# AUSTRALIAN COMBUSTION SYMPOSIUM

# 2015

# PROCEEDINGS

7 December - 9 December 2015

University of Melbourne, Parkville, Victoria


The Combustion Institute

Australian and New Zealand Section

*Editors: Yi Yang, Nigel Smith*

Each paper printed in this volume has been subject to a peer-review process which involved at least two independent expert reviewers. The reviewers provided written comments on the paper to the Technical Committee. The authors were then invited to revise their manuscript, considering the comments rendered by the peer-review process. The revised manuscript of each paper was then considered by the Technical Committee along with the review comments and authors response before acceptance for inclusion into the proceedings.



**The National Library of Australia**
Australian ISSN Agency print and online serial publications

**AUSTRALIAN COMBUSTION SYMPOSIUM**

**ISSN 1839-8170 (Print)**

and

**ISSN 1839-8162 (Online)**

The online version of the Proceedings of Australian Combustion Symposium can be found at
http://www.anz-combustioninstitute.org/ACS2015/ or http://www.anz-combustioninstitute.org/

# TABLE OF CONTENT



## Plenary Papers



## Session 1

## Session 2

# MESSAGE FROM THE CHAIRMAN

Combustion research in Australia continues to prosper and remains at the leading edge of this field. This is evident not only from the high number of top quality papers that will be presented at the 2015 Australian Combustion Symposium, but also from the diversity of topics spanning fundamental and applied areas. The conference program also brings together an outstanding team of invited speakers, three of whom are international.

The contribution of young scientists and research students is an essential part of these conferences. In this conference, it is refreshing to note that about two thirds of the registrants are students. To assist with their travel costs, twenty one grants were awarded by the Australia and New Zealand Section of the Combustion Institute.

A sad feature of this conference is the absence of Professor Bob Bilger who chaired the Australia and New Zealand Section of the Combustion Institute from 1980 to 1992 and was a regular supporter of its meetings. Bob passed away on October 2, 2015 at the age of eighty. His massive contributions to combustion research will continue to guide activities in this field for decades to come. Bob's kindness has touched the lives of many in our community and we'll always miss his wisdom and charming personality. The Australia and New Zealand Section of the Combustion Institute is eternally grateful for Bob's service who is commemorated through "The Bilger Lecture"; the opening lecture of our conference.

As Chairman of the ANZ-Section and on behalf of all our membership and delegates, I would like to thank **Professor Michael Brear** from Melbourne University and his outstanding team of organizers for their tireless work and dedication in making the 2015 Australian Combustion Symposium an outstanding success. Our thanks also go to:

Dr Robert Gordon, Conference Secretary, Melbourne University
Dr Peter Hield, Conference Treasurer, DST Group
Dr Yi Yang, Conference Technical Committee Co-chair, Melbourne University
Dr Nigel Smith, Conference Technical Committee Co-chair, DST Group
Dr Mohsen Talei, Conference Committee Member, Melbourne University

We hope you enjoy this conference and we look forward to seeing you at the upcoming 36$^{th}$ International Combustion Symposium in Seoul in 2106.

Assaad Masri

3 December 2015

# PREFACE

It is my pleasure to present these Proceedings of the Australian Combustion Symposium 2015 on behalf of the Symposium's Organising Committee.

The Australian and New Zealand Section of the Combustion Institute has held these biennial meetings for more than 30 years. They bring together combustion engineers and scientists from academia and industry, and provide a forum for papers in all aspects of fundamental and applied combustion research. Recent Symposia were held in Perth (2013), Newcastle (2011), Brisbane (2009), Sydney (2007) and Adelaide (2005).

These Proceedings contain five lectures given by invited speakers from Australia and overseas. We were very fortunate to have Doctor Thierry Poinsot (IMFT and CNRS, France) deliver the Bilger Lecture at the Symposium's opening. This was followed by fine Plenary Lectures given by Professor Andrea D'Anna (University of Naples Federico II, Italy), Professor Min Xu (Shanghai Jiao Tong University, China), Professor Evatt Hawkes (University of New South Wales) and Doctor Matthew Cleary (University of Sydney).

These Proceedings also contain another 88 papers that were selected from a total of 100 that were submitted for review. A total of 134 people attended the Symposium. The review process was coordinated by the Symposium's Technical Committee, and all papers received at least two reviews. These papers covered a broad range of topics across the following Sessions.

- Chemical Looping & VAM Combustion
- Combustion Kinetics
- Furnace Combustion
- IC Engine and Gas Turbine Combustion
- MILD Combustion
- Solids Combustion
- Soot
- Spray Combustion
- Turbulent & Laminar Flame Experiments
- Turbulent Combustion CFD

I also take this opportunity to honour the memory of Emeritus Professor Robert (Bob) W. Bilger BSc BE (N.Z.) D.Phil. (Oxford) FAA FTSE FIEAust, who recently left us. Prof. Bilger's substantial contributions to our field are very well known and do not need repeating. We also recall his leadership and mentoring of the broader combustion community. This extended far beyond his academic home at the University of Sydney, and he will be missed by many of us.

Finally, on behalf of the Organising Committee, I sincerely thank all who have contributed to this Symposium's success. We particularly thank the members of the Technical Committee and the Reviewers. We also sincerely thank our sponsors for enabling us to make this Symposium more affordable for all.

Professor Michael Brear
Organising Committee Chair
Melbourne
December, 2015

# ORGANIZING COMMITTEE

*Conference Chair*

Professor Michael Brear, University of Melbourne

*Secretary*

Dr Robert Gordon, University of Melbourne

*Treasurer*

Dr Peter Hield, Defence Science and Technology Group

*Committee Member*

Dr Mohsen Talei, University of Melbourne

*Technical Committee Co-Chairs*

Dr Yi Yang, University of Melbourne

Dr Nigel Smith, Defence Science and Technology Group

# LIST OF REVIEWERS

Professor Assaad Masri, University of Sydney (Chair, ANZ Section, The Combustion Institute)

A/Professor Evatt Hawkes, University of New South Wales
A/Professor Shawn Kook, University of New South Wales
Dr Qing Nian Shaun Chan, University of New South Wales
Dr Renlin Zhang, University of New South Wales
Dr Michele Bolla, University of New South Wales
Dr Haiou Wang, University of New South Wales

Professor Brian Haynes, University of Sydney
Dr Matthew Cleary, University of Sydney
Dr Matthew Dunn, University of Sydney
Dr Fatemeh Salehi, University of Sydney

Professor Guang Hong, University of Technology Sydney

Professor Eric Kennedy, University of Newcastle
Professor John Mackie, University of Newcastle
Dr Kalpit Shah, University of Newcastle
Dr Sazal Kundu, University of Newcastle

Professor Graham Nathan, University of Adelaide
Professor Bassam Dally, University of Adelaide
Professor John Abraham, University of Adelaide
Dr Paul Medwell, University of Adelaide
Dr Emmanuel Motheau, University of Adelaide
Dr Neil Smith, University of Adelaide

Professor Alex Klimenko, University of Queensland
Dr Bo Feng, University of Queensland
Dr Anand Veeraragavan, University of Queensland

A/Professor Richard Brown, Queensland University of Technology

Professor Michael Brear, University of Melbourne
Dr Yi Yang, University of Melbourne
Dr Robert Gordon, University of Melbourne
Dr Mohsen Talei, University of Melbourne
Dr Josh Lacey, University of Melbourne
Dr Nicolas Leplat, University of Melbourne
Farzad Poursadegh, University of Melbourne

Dr Nigel Smith, Defence Science & Technology Group
Dr Peter Hield, Defence Science & Technology Group

Professor Damon Honnery, Monash University
Dr Lian Zhang, Monash University

Professor Peter Nelson, Macquarie University
Professor Vladimir Strezov, Macquarie University

Dr Daniel Roberts, CSIRO Brisbane

Professor Hongwei Wu, Curtin University of Technology
A/ Professor Hari Vuthaluru, Curtin University of Technology

Dr Yasir Al-Abdeli, Edith Cowan University

Dr Xiangpeng Gao, Murdoch University

Professor Vasily Novozhilov, Victoria University

Professor Shusheng Pang, University of Canterbury

Dr Kai Morganti, Saudi Aramco Oil Company
Dr Tien Mun Foong, Australian Energy Market Operator
Dr Peter Dennis, Ford Australia
Dr Yuanjiang Pei, Argonne National Laboratory, USA

*The Organizing Committee would like to express their sincere gratitude to the reviewers for providing expert reviews and constructive feedback to the submitted papers, which helped in improving the quality and maintaining the standards of the Australian Combustion Symposium.*

***The Combustion Institute – Australian and New Zealand Section gratefully acknowledges the following organizations whose generous support contributed to the success of the 2015 Australian Combustion Symposium.***

## *Gold Sponsor*

AGL

Ford

Defence Science Institute

Melbourne Energy Institute

## *Silver Sponsor*

Coherent

MACS

NewSpec

Lastek

# AWARDS

## ***Best Student Paper Prizes***

**Brruntha Sundaram**, University of Queensland

*"Developments in Multiple Mapping Conditioning for turbulent premixed combustion"*

coauthored by A.Y. Klimenko, and M. J. Cleary

**Farzad Poursadegh**, University of Melbourne

*"A theoretical examination of spray supercriticality in compression ignition engines"*

coauthored by J. S. Lacey, M. J. Brear and R. L. Gordon

## ***The Terry Wall Best Student Paper Award*** *on Solid Fuel Combustion*

**Houzhi Wang**, University of Adelaide

*"Investigation of smouldering combustion of biomass fuel"*

coauthored by P. R. Medwell, C. H. Birzer, P. J. van Eyk, Z. F. Tian, and M. Possell

# TECHNICAL PROGRAM OVERVIEW

| | Woodward Conference Centre | Room GM16 | Room GM17 | Room 104 | Room 106 |
|---|---|---|---|---|---|
| **7 December** Morning | Opening Ceremony & Bilger Memorial | | | | |
| | Bilger Lecture (Poinsot) | | | | |
| | Plenary Lecture (D'Anna) | | | | |
| | IC Engine and Gas Turbine Combustion | MILD Combustion | Combustion Kinetics | Turbulent Combustion CFD | Spray Combustion |
| Afternoon | IC Engine and Gas Turbine Combustion | Solids Combustion | Combustion Kinetics | Turbulent Combustion CFD | Spray Combustion |
| **8 December** Morning | Plenary Lecture (Xu) | | | | |
| | Plenary Lecture (Hawkes) | | | | |
| | IC Engine and Gas Turbine Combustion | Solids Combustion | Combustion Kinetics | Turbulent Combustion CFD | Soot |
| Afternoon | IC Engine and Gas Turbine Combustion | Chemical Looping & VAM Combustion | Turbulent & Laminar Flame Experiments | Turbulent Combustion CFD | Soot |
| **9 December** Morning | Plenary Lecture (Cleary) | | | | |
| | Turbulent & Laminar Flame Experiments | Furnace Combustion | | | |
| Noon | Awards & Closing Ceremony | | | | |

| Monday 7 December | | | | | |
|---|---|---|---|---|---|
| 7:45 | **Opening Ceremony and Bilger Memorial**<br>Prof. Assaad Masri (Chair, Australian and New Zealand Section, the Combustion Institute)<br>Prof. Michael Brear (Chair, Conference Chair)<br>*Woodward Conference Centre* | | | | |
| 8:30 | Bilger Lecture (P1)<br>*Unsteady Combustion in Gas Turbines: Ignition, Instabilities and Control*<br>Dr. Thierry Poinsot, CERFACS, France<br>Chair: Prof. Assaad Masri, University of Sydney<br>*Woodward Conference Centre* | | | | |
| 9:30 | Plenary Lecture (P2)<br>*Combustion-Generated Fine and Ultrafine Particles*<br>Prof. Andrea D'Anna, University of Naples Federico II, Italy<br>Chair: Prof. Graham Nathan, University of Adelaide<br>*Woodward Conference Centre* | | | | |
| 10:30 | **Break** | | | | |
| | Woodward Conf. Centre | Room GM16 | Room GM17 | Room 104 | Room 106 |
| | **IC Engine and Gas Turbine Combustion**<br>Chair: Dr. J. Lacey | **MILD Combustion**<br>Chair: Dr. R. Gordon | **Combustion Kinetics**<br>Chair: Dr. Y. Yang | **Turbulent Combustion CFD**<br>Chair: Dr. M. Talei | **Spray Combustion**<br>Chair: Dr. S. Chan |
| 11:00 | 1A01: Impact of Triacetin as an oxygenated fuel additive to waste cooking biodiesel: transient engine performance and exhaust emissions<br>A. Zare, T. Bodisco, M.N. Nabi, H. M. Farhad, M.M. Rahman, D. Stuart, Z. Ristovski, R. J Brown<br>Queensland University of Technology | 1B01: Classification of Non-Premixed MILD and Autoignitive Flames<br>M. J. Evans, P. R. Medwell, H. Wu, A. Stagni, M. Ihme<br>University of Adelaide | 1C01: H2-Air Chemical Kinetic Evaluation for Pulse Detonation Engine Simulations<br>V.B.B. Rodrigues, E. C. Maciel, C. S. T. Marques<br>University of São Paulo, Brazil | 1D01: LES-MMC modeling of a partially-premixed turbulent dimethyl ether/air jet flame<br>G. Neuber, Y. Gao, A. Kronenburg, O.T. Stein , M. J. Cleary<br>University of Stuttgart, Germany | 1E01: Identification of Burning and Extinguishing Behaviour in Spray Flames with Spark Ignition<br>J. E. Baayens, Andrew P. Wandel<br>University of Southern Queensland |

| **MON** | Woodward Conf. Centre | Room GM16 | Room GM17 | Room 104 | Room 106 |
|---|---|---|---|---|---|
| 11:20 | 1A02: Modeling of the ion current developed in a direct injection diesel engine<br>R. Rao , D. Honnery<br>Monash University | 1B02: The impact of carrier gas on ethanol flame behaviour in a Jet in Hot Coflow (JHC) burner<br>J. Ye, P.R. Medwell, M.J. Evans, B.B. Dally<br>University of Adelaide | 1C02: Non-Oxidative Thermal Decomposition of Endosulfan<br>W.N.K. Dharmarathne, J.C. Mackie, E.M. Kennedy, M. Stockenhuber<br>University of Newcastle | 1D02: Acceleration of combustion simulations using GPUs<br>K.A. Damm, R.J. Gollan, A. Veeraragavan<br>University of Queensland | 1E02: A New Approach in Characterizing Secondary-Breakup Regimes for Newtonian Liquids<br>P.X. Pham, A. Kourmatzis, A. Masri<br>University of Sydney |
| 11:40 | 1A03: Experimental investigation of the effects of oxygenated fuels on exhaust emissions in a heavy duty diesel engine<br>F. M. Hossain, M.N. Nabi, M.M. Rahman, A. Zare, T.J. Rainey, D. Stuart,<br>Z. Ristovski, R. J. Brown<br>Queensland University of Technology | 1B03: The adequacy of laminar flame calculations for identifying MILD combustion<br>P.R. Medwell, M.J. Evans, Q.N. Chan, V.R. Katta<br>University of Adelaide | 1C03: Non-Oxidative Thermal Decomposition of Endosulfan II. Mechanism of Decomposition<br>J.C. Mackie, W.N.K. Dharmarathne, E.M. Kennedy, M. Stockenhuber<br>University of Newcastle | 1D03: Developments in Multiple Mapping Conditioning for turbulent premixed combustion<br>B. Sundaram, A.Y. Klimenko, M. J. Cleary<br>University of Queensland | 1E03: The effect of radiation heat transfer under ECN Spray A conditions<br>M. A. Chishty, M. Bolla, E. R. Hawkes, Y. Pei, and S. Kook<br>University of New South Wales |
| 12:00 | 1A04: Evaporation and mixing of ethanol-water mixture in a heavy duty common rail marine diesel engine intake air<br>E. Kim, V. Garaniya, R. Islam, R. Abbassi<br>University of Tasmania | 1B04: Effect of Turbulence on the MILD Combustion Characteristics of Victorian Brown Coal<br>M. Saha, B.B. Dally, P.R. Medwell, A. Chinnici<br>University of Adelaide | 1C04: Kinetics analysis and reaction characteristics of aluminium alloys in water vapor<br>T. Zhang, J. Liu, Z. Huang, W. Yang, J. Zhou<br>Zhejiang University, China | | 1E04: Effect of Impinging Angle on Non-Evaporative Diesel Wall-Jet<br>M.H. Jayed, J. Soria, D.R. Honnery<br>Monash University |
| 12:20 | **Lunch** (Woodward Conference Centre) | | | | |

| **MON** | Woodward Conf. Centre | Room GM16 | Room GM17 | Room 104 | Room 106 |
|---|---|---|---|---|---|
| | **IC Engine and Gas Turbine Combustion**<br>Chair: Dr. R. Zhang | **Solids Combustion**<br>Chair: Dr. Robert Gordon | **Combustion Kinetics**<br>Chair: Dr. M. Altarawneh | **Turbulent Combustion CFD**<br>Chair: Dr. M. Cleary | **Spray Combustion**<br>Chair: Prof. A. Masri |
| 13:10 | 1A05: Formulation of new oxygenated fuels and their influence on engine performance and exhaust emissions<br>M. N. Nabi, A. Zare, F.M. Hossain, M.M. Rahman, D. Stuart, Z. Ristovski, R. J Brown<br>Queensland University of Technology | 1B05: Effect of Boron Carbide on the Ignition and Combustion Characteristics of Amorphous Boron<br>D. Liang, L. Qiu, J. Liu, B. Chen, J. Zhou<br>Zhejiang University, China | 1C05: Magnitude of the deuterium kinetic isotope effect during the combustion of methane over a Pd/Al2O3 catalyst<br>B.A. Wright, E.M. Kennedy, and M. Stockenhuber<br>University of Newcastle | 1D05: The Flow Characteristics and Flame Statistics of an Experimental Turbulent CH4/air Premixed Flame using DNS<br>H. Wang, E.R. Hawkes, J.H. Chen<br>University of New South Wales | 1E05: A theoretical examination of spray supercriticality in compression ignition engines<br>F. Poursadegh, J.S. Lacey, M.J. Brear and R.L. Gordon<br>University of Melbourne |
| 13:30 | 1A06: Fuel Economy and CO2 Benefits of Dual-Fuel Combustion in Spark-Ignition Engines using Less Processed Petroleum-Derived Fuels<br>K. Morganti, M. Al-Abdullah and A. Zubail<br>Saudi Aramco Oil Company | 1B06: Investigation of smouldering combustion of biomass fuel<br>H. Wang, P. R. Medwell, C. H. Birzer, P. J. van Eyk, Z. F. Tian, M. Possell<br>University of Adelaide | 1C06: The role of HNO and NOH in NO formation during ammonia oxidation on Pt(111)<br>J.D. González, B.S Haynes and A. Montoya<br>University of Sydney | 1D06: Equivalence Ratio Effects on Turbulent Premixed Flames in Lean Methane/Air Mixtures<br>Z. Wang, E. Motheau, J. Abraham<br>Purdue University, USA | 1E06: Macroscopic Spray Characteristics of an Evaporating Diesel Spray<br>I.M. Rizwanul Fattah, W. Ren, C. Woo, Q.N. Chan, S. Kook, E.R. Hawkes<br>University of New South Wales |
| 13:50 | 1A07: The Effect of Nitric Oxide on Autoignition Onset of Toluene Reference Fuels (TRFs) in a CFR Engine<br>Z. Chen, H. Yuan, Y. Yang, M.J. Brear<br>University of Melbourne | 1B07: Degradation and Combustion Behaviours of Some Thermoplastics with Potential Use as Hybrid Rocket Fuels<br>P. Joseph, V. Novozhilov, R. Zhang<br>Victoria University | 1C07: Mechanism Development and Chemical Kinetics Analysis of HxNyOz Species in Gliding Arc Discharge<br>M. Zangouei, B. S. Haynes<br>University of Sydney | 1D07: Analysis of the flame brush of an acoustically perturbed swirling premixed flame<br>T.F. Guiberti, S. Bejaoui, D. Durox, T. Schuller<br>CNRS, France | 1E07: Flow Measurements of Compressed Natural Gas Jets Issued from Direct Injectors for Spark Ignition Engines<br>P. Lappas, T. J. Rogers, P. Petersen<br>RMIT University |

| **MON** | Woodward Conf. Centre | Room GM16 | Room GM17 | Room 104 | Room 106 |
|---|---|---|---|---|---|
| 14:10 | 1A08: Removal of secondary aerosols produced during plasma diesel particulate treatment<br>M. Babaie, P. Talebizadeh, K.H. Sia, A.J. Yi, Z. Ristovski, H. Rahimzadeh, R. Brown<br>Queensland University of Technology | 1B08: Use of Beneficiated Victorian Brown Coal for Blended Combustion in PCI Blast Furnaces<br>A. De Girolamo, A. Grufas, I. Lyamin, I. Nishio, Y. Ninomiya and L. Zhang<br>Monash University | 1C08: A Plug Flow Reactor for Investigating Autoignition Chemistry in Combustion Engines<br>N. Leplat, Z. Lu, Y. Yang, and M.J. Brear<br>University of Melbourne | 1D08: Local extinction and reignition in a turbulent lifted flame<br>S. Karami, M. Talei, E.R. Hawkes<br>University of New South Wales | 1E08: Common Rail Diesel Sprays from Twin-hole Nozzle<br>D. Nguyen, D. Duke, A. Kastengren, C. Powell, D. Honnery<br>Monash University |
| 14:30 | **Tour to Defence Science and Technology (DST) Group** (by advance registration only) | | | | |

## Tuesday 8 December

| | | | | | |
|---|---|---|---|---|---|
| 8:30 | Plenary Lecture (P3)<br>*Flash Boiling Spray Behavior and Combustion in a Direct Injection Gasoline Engine*<br>Prof. Min Xu, Shanghai Jiaotong University, China<br>Chair: Prof. Michael Brear, University of Melbourne<br>*Woodward Conference Centre* | | | | |
| 9:30 | Plenary Lecture (P4)<br>*Petascale Direct Numerical Simulations of Laboratory Flames*<br>Prof. Evatt Hawkes, University of New South Wales<br>Chair: Prof. Brian Haynes, University of Sydney<br>*Woodward Conference Centre* | | | | |
| 10:30 | **Break** | | | | |
| | Woodward Conf. Centre | Room GM16 | Room GM17 | Room 104 | Room 106 |
| | **IC Engine and Gas Turbine Combustion**<br>Chair: Prof. R. Brown | **Solids Combustion**<br>Chair: Prof. V. Novozhilov | **Combustion Kinetics**<br>Chair: Prof. E. Kennedy | **Turbulent Combustion CFD**<br>Chair: Dr. N. Smith | **Soot**<br>Chair: Prof. G. Nathan |
| 11:00 | 2A01: An Investigation of the Performance of a Gasoline Spark Ignition Engine Fuelled with Hot Ethanol Direct Injection<br>Y. Huang, G. Hong<br>University of Technology Sydney | 2B01: Pyrolysis Characteristics of Ionic Liquid and Solvent Treated Coals<br>J. Cummings, P. Tremain, D. Hamilton, S. Kundu, B. Moghtaderi, R. Atkin,and K. Shah<br>University of Newcastle | | 2D01: Lewis number effects on edge-flame propagation in lifted turbulent flames<br>S. Karami, M. Talei, E.R. Hawkes, H. Yu<br>University of New South Wales | 2E01: Soot measurements in a N2-diluted ethylene/air counterflow diffusion flame at elevated pressures<br>H.M.F. Amin and W.L. Roberts<br>King Abdullah University of Science and Technology, Saudi Arabia |

| **TUE** | Woodward Conf. Centre | Room GM16 | Room GM17 | Room 104 | Room 106 |
|---|---|---|---|---|---|
| 11:20 | 2A02: Emissions and Performance of a Gas Turbine Engine with Two and Three-Component Blends of Petroleum and Bio-fuels<br>F.L. Carter, R. N. Parthasarathy, and S. R. Gollahalli<br>University of Oklahoma, USA | 2B02: Numerical Modeling of Oxygen Enhanced Combustion and Transient Heating Characteristics in a Reheating Furnace<br>R. Prieler, P. Belohradsky, B. Mayr, M. Demuth, C. Hochenauer<br>Graz University of Technology, Austria | 2C02: Validation of oxidation mechanisms for pentane isomers<br>S. Cheng, H. Yuan, Y. Yang, M.J. Brear<br>University of Melbourne | 2D02: Large Eddy Simulation of Evaporating Acetone in a Turbulent Multiphase Flow<br>M. N. Khan and M. J. Cleary<br>University of Sydney | |
| 11:40 | 2A03: Ethanol-Fuelled Gasoline Compression Ignition (GCI) Combustion in a Common-Rail Diesel Engine<br>C. Woo, S. Kook, E.R. Hawkes<br>University of New South Wales | 2B03: A Bench-Scale TGA-FTIR Investigation of Tar Removal in a Modified Biochar Production Process<br>P. Tremain, F. Yin, F. Wilson, B. Moghtaderi, K. Shah<br>University of Newcastle | 2C03: Systematic study for H abstraction from alkanes by amine radical (NH2)<br>K. Siddique, M. Altarawneh, and B.Z. Dlugogorski<br>Murdoch University | 2D03: DNS of hydrogen auto-ignition under HCCI-like conditions with wall heat transfer; parametric study<br>J. Behzadi, M. Bolla, M. Talei, E.R. Hawkes, S. Kook<br>University of New South Wales | 2E03: High pressure considerations for Yield Sooting Index<br>S.A. Steinmetz, W.L. Roberts<br>King Abdullah University of Science and Technology, Saudi Arabia |
| 12:00 | | 2B04: XANES Iron K-Edge Speciation of Heat Transfer Tube Corrosion upon Victorian Brown Coal Oxy-Fuel Combustion.<br>I. Jabaz, J. Chen, K. Suzuki, Y. Ninomiya, L.Zhang<br>Monash University | 2C04: Reactions of SH radical with C1-C4 Hydrocarbons<br>Z. Zeng, M. Altarawneh, B.Z. Dlugogorski<br>Murdoch University | 2D04: Towards the LES-MMC Calculation of Turbulent Piloted Flames with Inhomogeneous Inlets<br>S. Galindo, M.J. Cleary and A.R. Masri<br>University of Sydney | 2E04: Variations of In-Flame Soot Particles in the Presence of a Neighbouring Flame in a Diesel Engine<br>R. Zhang, Y. Zhang and S. Kook<br>University of New South Wales |
| 12:20 | **Lunch** (Woodward Conference Centre) | | | | |

| **TUE** | Woodward Conf. Centre | Room GM16 | Room GM17 | Room 104 | Room 106 |
|---|---|---|---|---|---|
| | **IC Engine and Gas Turbine Combustion**<br>Chair: Prof. D. Honnery | **Chemical Looping and VAM Combustion**<br>Chair: Dr. A. Veeraragavan | **Turbulent and Laminar Flame Experiments**<br>Chair: Dr. P. Medwell | **Turbulent Combustion CFD**<br>Chair: Prof. A. Klimenko | **Soot**<br>Chair: Dr. Matt Dunn |
| 13:10 | 2A05: Effect of Injection Timing on Gasoline/Diesel and Gasoline/ Biodiesel Fuelled Dual-Fuel Engine: A Comparative Study<br>Y.H. Teoh, H.H. Masjuki, M.A. Kalam, H.G. How, S.M. Ashrafur Rahman, A.M. Ruhul<br>University of Malaya, Malaysia | 2B05: Chemical Looping Air Separation for Oxy-fuel Power Plants Using a Spray Dried CuO/MgAl2O4 Oxygen Carrier<br>H. Song, K. Shah, E. Doroodchi, A. Evans, B. Moghtaderi<br>University of Newcastle | 2C05: Suitability of micro-PIV for characterizing poly-disperse dilute sprays in combustion applications<br>A. Kourmatzis and A.R. Masri<br>Macquarie University | 2D05: Simulations of an n-dodecane flame with LES/sparse-Lagrangian MMC method<br>F. Salehi, M. J. Cleary, A.R. Masri<br>University of Sydney | 2E05: The influence of high flux broadband radiation on soot concentration and temperature in a sooty flame<br>X. Dong, Z. Sun, D. Gu, G.J. Nathan, P.J. Ashman, Z.T. Alwahabi, B.B. Dally<br>University of Adelaide |
| 13:30 | 2A06: Combustion and emission investigation of Calophyllum inophyllum biodiesel blends in an unmodified diesel engine<br>A. M. Ruhul, M. A. Kalam, H. H. Masjuki, S. Imtenan<br>University of Malaya, Malaysia | 2B06: Effect of Methane and coal dust Concentrations on Explosion Pressure Rise<br>M.J. Ajrash, J. Zanganeh, D. Eschebach and B. Moghtaderi<br>University of Newcastle | 2C06: Effect of multi-lateral fuel jet injection on the flow field of Methane-Air turbulent flame<br>C.X. Thong, B.B. Dally, P.A.M. Kalt, C.H. Birzer<br>University of Adelaide | 2D06: The effect of equivalence ratio on sound generation by turbulent premixed flames<br>A. Haghiri, M. Talei, M. J. Brear, E. R. Hawkes<br>University of Melbourne | 2E06: A technique for the measurement and classification of soot precursors and soot particles in turbulent flames<br>D. Bartos, M. Dunn, M. Sirignano, A. D'Anna, A.R. Masri<br>University of Sydney |
| 13:50 | 2A07: Effects of EDI on Combustion and Emissions of Small Spark Ignition Engine at Lean Mixture Conditions<br>N.F.O. Al-Muhsen, G. Hong<br>University of Technology Sydney | 2B07: Carbonation Reaction Kinetics at Low Partial Pressures of CO2 for a Novel Greenhouse Calcium Looping Combustion Process<br>M. Ramezani, K. Shah, E. Doroodchi, P. Tremain and B. Moghtaderi<br>University of Newcastle | 2C07: Scalar Dissipation Rates in Turbulent Flames of Methane with Inhomogeneous Inlets<br>H. Cutcherb, R.S. Barlowa, G. Magnottia , A.R. Masri<br>University of Sydney | 2D07: Flame interaction identification in turbulent premixed flames<br>D. Brouzet, A. Haghiri, T. Kulkarni, M. Talei, M. J. Brear, E.R. Hawkes<br>University of Melbourne | 2E07: The effect of Exit Strain Rate on Soot Volume Fraction in Turbulent Non-Premixed Jet Flames<br>S. M. Mahmoud, Z. W. Sun, B. B. Dally, Z. T. Alwahabi, P. R. Medwell and G. J. Nathan<br>University of Adelaide |

| **TUE** | Woodward Conf. Centre | Room GM16 | Room GM17 | Room 104 | Room 106 |
|---|---|---|---|---|---|
| 14:10 | 2A08: Comparative study on Gasoline-Ethanol Dual Fuel Injection Strategies in a Small Spark Ignition Engine<br>N.F.O. Al-Muhsen, G. Hong<br>University of Technology Sydney | 2B08: Derivation of Kinetic Parameters for the Stone Dust Looping Combustion Process for Ventilation Air Methane Abatement<br>S.Patel, O.Kubiak, P.Tremain, B. Moghtaderi, J. Sandford, K. Shah<br>University of Newcastle | 2C08: Performing High Spatial and Temporal Resolution Measurements on Forced Premixed Laminar Flames<br>S.M. Wiseman, M.J. Brear, R.L. Gordon, I. Marusic<br>University of Melbourne | 2D08: A study of pressure enhancement influence on the radiative reabsorption in CO2-diluted methane laminar premixed flames<br>S. Karimkashi, M. Bolla, H. Wang, E.R. Hawkes, H.G. Im, P.G. Arias<br>University of New South Wales | 2E08: Development of an in-flame thermophoretic soot sampling device<br>C. Wang, Q.N. Chan*, S. Kook, E.R. Hawkes, P.R. Medwell, J. Lee<br>University of New South Wales |
| 14:30 | | 2B09: VAM oxidation over palladium loaded on high silica BEA and MFI zeolites<br>H. HosseiniAmoli, L. Harvey, E.M. Kennedy, M. Stockenhuber<br>University of Newcastle | 2C09: An Experimental and Numerical Study into Laminar Flame Speeds of H2/CO/Air Mixtures with CO2 and N2 Dilution<br>R. Shang, Y. Zhang, M. Zhu, Z. Zhang, D. Zhang<br>University of Western Australia | 2D09: Preliminary Experimental and Computational Study of Time varying Laminar Non-Premixed Ethylene/Nitrogen Flames<br>K.K. Foo, A. Jocher, C.X. Thong, B.B. Dally, G.J. Nathan, P.R. Medwell, Z.T. Alwahabi, H. Pitsch<br>University of Adelaide | 2E09: External Irradiation Effect on the Evolution of In-flame Soot Species<br>C. Wang, Q.N. Chan, S. Kook, E.R. Hawkes, P.R. Medwell, J.Lee<br>University of New South Wales |
| 15:00 | **Tour to University of Melbourne Thermodynamics Laboratory** (register at reception desk on the 10th floor) | | | | |

| Wednesday 9 December | | |
|---|---|---|
| 9:00 | Plenary Lecture (P5)<br>*Conserved Scalar and Conditional Moment Models for Multiphase, Multicomponent and Multiscale Combustion*<br>Dr. Matthew Cleary, University of Sydney<br>Chair: Prof. Alex Klimenko, University of Queensland<br>*Woodward Conference Centre* | |
| 10:00 | **Break** | |
| | Woodward Conference Centre | Room GM16 |
| | **Turbulent and Laminar Flame Experiments**<br>Chair: Prof. B.B. Dally | **Furnace Combustion**<br>Chair: Dr. Peter Hield |
| 10:30 | 3A01: On the Structure of Turbulent Flames of DME/N2 with Inhomogeneous inlets<br>T.F. Guiberti, M. Juddoo, M. Dunn, W.L. Roberts, A.R. Masri<br>University of Sydney | 3B01: Assessment of natural draft combustion properties of a top-lit up-draft research furnace<br>T. Kirch, P.R. Medwell, C.H. Birzer<br>University of Adelaide |
| 10:50 | 3A02: Stabilization of Turbulent Auto-Igniting DME Jets Issuing in Hot Vitiated Coflows<br>A.R.W. Macfarlane, M. Dunn, M. Juddoo, A.R. Masri<br>University of Sydney | 3B02: Numerical simulation of premixed methane/air flame dynamics in narrow channels<br>X. Kang, R. J. Gollan, P. A. Jacobs and A. Veeraragavan<br>University of Queensland |
| 11:10 | 3A03: An Experimental Study of the Effect of Soap on Ignition and Combustion Characteristics of Single Droplets of Glycerol<br>H.Y. Setyawan, M. Zhu, Z. Zhang and D. Zhang<br>University of Western Australia | 3B03: Surface Temperature Distribution along the Brick-Clay or Porcelain Tube Due to the Flame Spreading<br>C Luo, J. Zanganeh, E. Doroodchi and B. Moghtaderi<br>University of Newcastle |
| 11:30 | 3A04: Soot Reduction in Cookstoves due to Turbulent Mixing<br>K.M. Lask, P.R. Medwell, C.H. Birzer, A.J. Gadgil<br>University of California Berkeley, USA | 3B04: Turbojet Exhaust Plume Heat Transfer<br>Y.D. Kuo, N.S.A. Smith, D.R. Honnery<br>Monash University |
| 12:00 | **Awards & Closing Ceremony – The Terry Wall Best Student Paper Award; Best Student Paper Prizes**<br>**Lunch** (Woodward Conference Centre) | |

**Proceedings of the Australian Combustion Symposium**
**December 7-9, 2015, The University of Melbourne**

# Unsteady combustion in gas turbines: ignition, instabilities and control

T.J. Poinsot *
[1]Institut de Mécanique des Fluides de Toulouse, CNRS
31400 TOULOUSE, FRANCE

**Abstract**

This paper presents recent progress in the field of unsteady combustion for two applications: ignition and combustion instabilities. Recent experimental obtained at CORIA and EM2C Paris are described and compared to LES results for flame ignition and propagation in gas turbines. For explosions in buildings, the comparison of LES with experimental results obtained on the venting chamber of Sydney and on scaled-up versions of this setup in Europe allows to describe the physics of these very fast flames but also to show the limits of present turbulent combustion models. For combustion instabilities, LES of full annular chambers are used together with recent theory and new experiments developed at Cambridge and EM2C Paris to analyse the structure of unstable azimuthal modes appearing in gas turbines and propose methods to mitigate these modes.

*Keywords: instabilities, ignition, propagation, gas turbines, safety*

## 1. Introduction

Unsteady combustion is a key question in multiple fields linked to combustion. Many combustion chambers used in gas turbine engines for example produce excellent steady operation characteristics but these performances are often impaired by poor unsteady behaviors: difficult ignition, unstable operating points, undesired quenching. In the field of safety and explosions in buildings, the whole process is always unsteady, beginning by the accidental ignition of a flammable mixture leading to unsteady flame propagation and overpressure generation.

Studying unsteady combustion is more difficult than it is for steady operation. The whole ignition process in an engine takes less than 100 milliseconds. Diagnostics have to be time-resolved. Repetitivity becomes an issue in turbulent flows. For simulations, by definition, unsteady phenomena are out of reach of RANS techniques which predict time or cycle-averages. To illustrate some typical unsteady combustion mechanisms, this paper describes studies in two fields:

- Ignition: two aspects of ignition will be discussed: (1) cases where ignition is desired and must occur, for example in gas turbines where ignition sequences must be both reliable and fast and (2) cases where ignition should not occur or if it occurs, should not lead to fast flames and to detonation (which may damage the structure), for example in buildings where a gas leak has taken place and where a flame propagates in a chamber filled with obstacles.

- Combustion instabilities: most combustion systems are designed to operate in stable regimes but all experimentalists working on steady combustion chambers (furnaces, gas turbines, power plants) know that 'sometimes', a chamber starts exhibiting unexpected oscillations. These oscillations (often called "thermoacoustic") lead to additional noise and vibration which can be ignored or tolerated if the level of oscillations remains small (a few Pa). In other cases, however, more serious consequences are observed: when the pressure RMS values go up to values of the order of a large fraction of the mean pressure, the chamber can quench, the flame can flashback and burn part of the injection system or the pressure oscillations can become so large that the structure cannot resist and either implodes (when pressure becomes too low) or explodes (when the pressure excursion is too high).

In this paper, the configuration corresponding to engines will correspond to annular chambers found in gas turbines where a single annular chamber is fed with multiple burners (from 10 to 25) fed by individual injectors. These configurations have significant specificities both for ignition and thermoacoustic phenomena. The annular shape of the chamber implies that flames have to jump from burner to burner to produce a complete light-around of the engine (usually only or two ignitors are used so that most sectors do not have their own ignitor). In terms of thermoacoustics, the annular shape generates a class of modes which are observed only in these engines: azimuthal unstable modes where acoustic modes propagate along the azimuthal direction and couple with unsteady combustion in all burners.

For both fields (ignition and thermoacoustics in large scale combustion chambers), the recent trend is to combine experimental and LES data in order to make faster progress. Section 2 focuses on ignition in gas turbines (Section 2.1) and in buildings (Section 2.2) while Section 3 will discuss thermoacoustics. The numerical LES tool used for all simulations is AVBP, the LES code of CERFACS. It will not be described here: the presentation will focus on the physics of the phenomena and not on the numerical aspects of LES

* Corresponding author:
Email: poinsot@imft.fr

which have already been discussed extensively in many other publications. Results presented here have been obtained in the PhDs of P. Quillatre, L. Esclapez, P. Wolf and M. Bauerheim at CERFACS, supervised by Dr B. Cuenot and Dr L. Gicquel.

## 2. Ignition

### 2.1 Ignition of swirled flames in gas turbines

Ignition of a gas turbine is a process going through three phases [1, 2, 3]: (1) a spark or a torch is used to ignite the first flame in one burner of the chamber, (2) this flame grows and ignites the whole sector, (3) the flame then propagates from the initial burner to its neighbours until a full light-round takes place. If any of these phases fails, the ignition process stops. When the altitude increases, ensuring that all these phases are successful and take place in a sufficiently small time becomes increasingly difficult. The first phase where the spark creates an initial flame kernel is quite difficult to study because it involves the formation of a shock wave, temperatures in excess of 10000 K and a plasma. It is not discussed here because in most cases, a very powerful spark is used to ensure that this step is indeed successful. This is obtained by using a spark energy much larger than the minimum ignition energy.

Even when the first flame kernel is ignited, phase 2 (the flame stabilization in the first sector) may not be certain: this kernel may be convected out of the chamber or be quenched near walls or by excessive strain. To ensure ignition, the kernel must travel back to the recirculation zone and find a stable position there to ignite the first burner. Finally, even if one burner in one sector is ignited, the propagation of the flame to the neighbouring sectors is also uncertain especially if the distance between injectors becomes too large. This question is critical to design chambers when the number of injectors (and therefore the distance between them) has to be determined. Minimizing the number of injectors is often desirable for cost reasons but this should not endanger the light-around mechanism necessary for ignition.

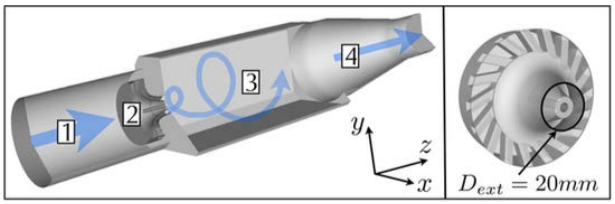

Fig. 1: swirled burner installed at CORIA [1,3].

These phenomena have been studied recently using LES and experiments. As an example, Fig. 2 first displays an LES of ignition in a single-injector swirled burner (Fig. 1) installed at CORIA, France [1,3]. The operating point is exactly the same but ignition is produced at two different instants, one of them leading to ignition and not the other one. This simple example shows another specific character of ignition: it is a random process where ignition does not take place at every sparking event but has to be quantified through its ignition probability. Certain locations will always provide ignition and they have to be identified: this is in general difficult to do in a real engine.

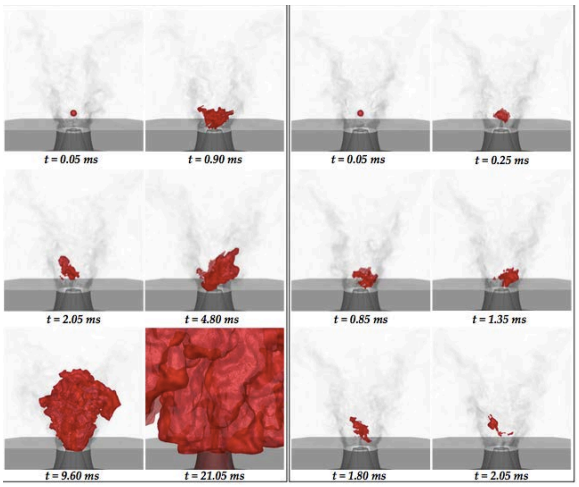

Fig. 2: successful (left) and failed (right) ignition sequences in the swirled burner of CORIA [1,3].

The same ignition studies were then performed in an engine with two to five similar injectors to investigate the effects of burner separation on flame propagation. LES and experiments agree and show that two modes of propagation can be found. For the first one, called radial, the flame jumps from burner to burner near the injection plane and this process is fast (Fig. 3). For the second mode (called axial), the flame has to fill the whole chamber before coming back eventually to the neighbouring burner (Fig. 4). Radial propagation is observed for small distances between burners while axial propagation is found for larger distances.

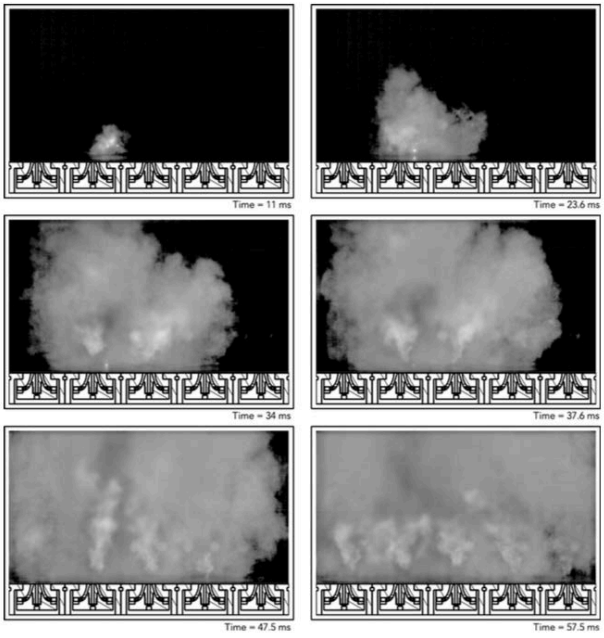

Fig. 3: radial propagation with five burners [1,3].

Radial propagation is obviously the one which is expected by engineers in real engines. It allows fast and reliable flame propagation. Hoping that axial propagation will ensure light-around is not acceptable: therefore this type of studies shows how far burners can be separated before ignition difficulties appear.

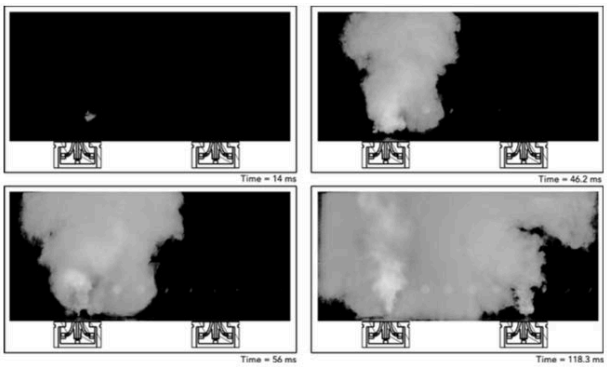


Fig. 4: axial propagation with two burners [1,3].

## 2.2 Explosions in venting chambers

Accidents due to gas explosion in industrial buildings are a major safety issue [4-7]. Although the primary objective is to prevent them, being able to understand mechanisms controlling explosions in buildings, typically in offshore oil and gas producing platforms or oil storage facilities, is a societal, economical and physical challenge of prime importance.

Typical explosion scenarios begin with an ignition of a quiescent flammable mixture inside a confined or semi-confined area. Then the flame propagates past the repeated obstacles, generating a strong overpressure. This overpressure is the parameter of critical interest for safety studies since it can induce the destruction of the facilities involved. In order to understand explosions in confined areas, small to medium scale configurations of vented chambers are usually considered. Experimental and numerical studies of explosion have extensively been performed in order to point out the mechanisms involved in flame acceleration and pressure increase genera- tion. Effects of geometric features or fuel type on this overpressure have also been studied.

As an example, a classic configuration is the setup of University of Sydney which consists in a square cross section premixed combustion chamber (25cm x 5cm x 5cm) with solid obstacles. The obstacles are three removable turbulence generating grids and one fixed central obstacle, as shown in Fig. 5 (left).

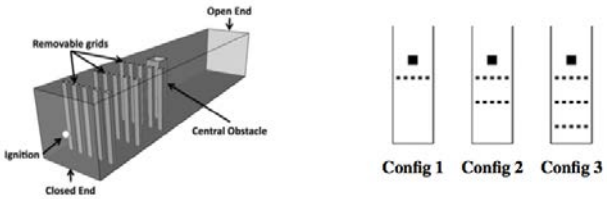


Fig. 5: the Sydney setup for explosions [10].

Fig. 6 displays a comparison of LES and experimental results during flame propagation. Such exercices have proved the quality of LES to capture the flame position as well as the overpressure generated by the explosion.

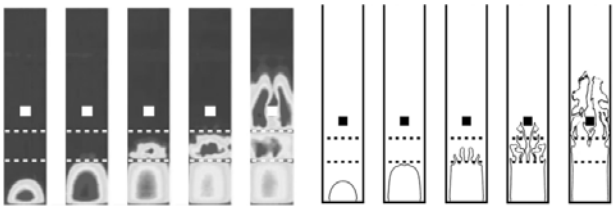

Fig. 6: Experimental (left) and LES (right) flame positions for the Sydney setup [8,9].

Note however that the PhD of P. Quillatre [8] also showed that when the experiment of Sydney was scaled up by a factor of 6 and then by 24 by GEXCON and experiments were repeated, predicting the overpressure accurately became much more difficult with LES even on very large grids (1 billion cells, Fig. 7). This demonstrated that present models for flame / turbulence interaction were working properly at the scale of the initial Masri chamber (where combustion develops in a volume of a few liters) but that when these models were applied to much larger configurations at Gexcon in which the total volume where the flame develops is 10000 times larger, they did not provide proper upscaling laws. Interestingly, this had not been observed before because very few systems allow such a large change in size and Reynolds numbers. Here the need to study real systems leads research back to a fundamental issue: the modeling of the interaction between flame and turbulent motions.

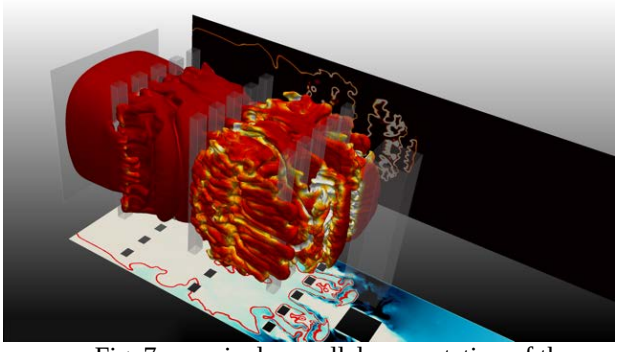

Fig. 7: massively parallel computation of the Sydney setup (1 billion cells) [8].

## 3. Combustion instabilities

Combustion instabilities (CIs), also called flame dynamics, can appear in almost any combustion system [11,18] but industry is not especially keen on studying them or in recognizing that they can be a problem in

their company's engines. The main reason for this is that CIs can be the cause of major problems which are difficult to master because they occur during the last stages of development and are still very difficult to predict today: having an unstable engine is still similar to catching some kind of disease for companies. Since the adventure of the F1 engine during the Apollo program in the 60s, which cost billions of dollars before a solution was found to mitigate CIs, all companies know that CIs can represent a major industrial danger for which communication may not be the best solution. CIs have been the hidden and feared problem of many combustion programs, starting with solid and liquid fuel rocket engines in the 50s and more recently gas turbines, industrial furnaces or even domestic heaters. Laboratories, on the other hand, have naturally no difficulty studying instabilities in canonical cases such as laminar premixed flames and the literature contains a very large amount of research work dedicated to CIs in simple laminar flames [13,14,16,18]. When it comes to real engines, the situation is different: here CI mechanisms involve not only those found in academic experiments but also introduce new physics which is often not studied in laboratories. Real flames are turbulent and many of them are swirled and confined in complex shape chambers. CIs in turbulent swirled flames are now commonly studied in laboratories but usually in simplified chambers which do not contain the complexities found in real engines.

- The range of pressures and volumetric powers reached in real engines drives unstable modes which cannot be reproduced in laboratories easily. The best example is transverse modes in rocket engines [19] which appear very easily on real systems but are difficult to trigger in laboratories because the power and the size of the experiments are not sufficient [20].

- Another example is liquid fuel injection: most laboratories study instabilities in gaseous flames. Even if research on CIs actually started in the 50s for liquid-fueled systems, studying instabilities in liquid fueled combustors remains much more complicated [19,21].

- The geometry of the chamber is a first-order parameter for CIs: in gas turbines, combustion chambers have annular shapes where azimuthal instability can develop, something which had never been studied in laboratories until very recent times [22,23,24] for obvious cost reasons. Therefore the physics of azimuthal modes was known mainly on the basis of limited experimental observations performed on real full turbines.

- Most instability modes studied in laboratories involve longitudinal acoustic modes which propagate along the flow direction. In real engines, modes can also be transverse, radial or azimuthal and more importantly, modes can be much more numerous than in a laboratory experiment simply because real configurations are geometrically complex. An industrial gas turbine can exhibit 30 acoustic eigenmodes between 0 and 250 Hz, many of them having the capacity to become self-excited [25]. This never happens in a laboratory system: simply being able to recognize which type of mode is appearing in such a system becomes much more complicated than in a laboratory scale experiment where only 2 to 5 modes can be found.

- Power density is known to be an important parameter for instabilities: when combustion chambers become smaller or when their power increases, CIs are more prone to appear and to lead to damages. This usually occurs for high-pressure systems which are also more difficult to study in laboratories.

- Finally, inlet and outlet conditions are usually well defined in laboratories where choked nozzles or imposed pressure sections can be imposed to control acoustic boundary conditions which are critical for CIs. In real engines, for example in gas turbines, the chamber is fed by a compressor and blows into a turbine (Fig. 8). Determining the impedances of these elements is a daunting task in itself.

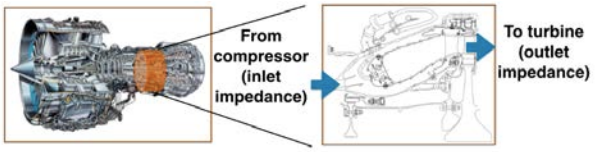


Fig. 8: the importance of inlet and outlet impedances to study combustion instabilities in the chamber.

An example of recent results on combustion instabilities in a full annular gas turbine is given in a recent series of papers using LES and theory [26,27] as well as new experimental systems based on annular chambers [23,24]. An example of LES results in an helicopter chamber is given in Fig. 9.

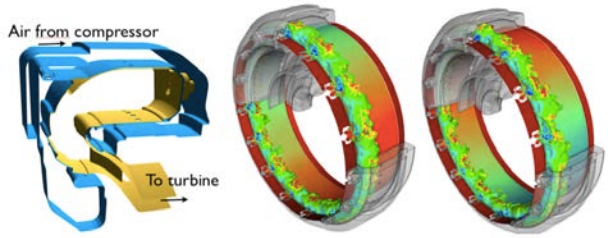


Fig. 9: LES of combustion instabilities in an annular helicopter chamber [28].

The pressure field produced by LES reveals that an azimuthal unstable mode is turning in the combustion chamber at a frequency of the order of 700 Hz with amplitudes or the order of kPa, as measured in the real engine.
In parallel with these LES, the setups installed at Cambridge (Fig. 10) and EM2C Paris (Fig. 11) have confirmed what LES suggested and added new insights. For example, both LES and experiments confirm that

azimuthal modes develop in annular chambers, that they are strong, dangerous and intermittent: their structure can change from standing to rotating modes (Fig. 10) without external cause, probably because this structure is excited by random turbulent forcing.
Experiments have also revealed new modes, unseen in LES like the slanted mode [23] observed at EM2C (Fig. 11) where two modes at the same frequency seem to combine to produce a very peculiar unsteady flame structure.

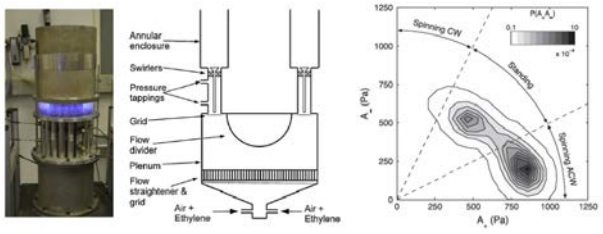

Fig. 10: the Cambridge setup for azimuthal modes in annular chambers [24]

An interesting development linked to the study of azimuthal modes in annular chambers is the renewal of purely theoretical methods [27,29,30], required to understand and guide the experimental and the simulation work in this field. Complete theories based on a network description of acoustic waves in the combustor and in the burners can be written analytically for azimuthal modes: despite the necessary simplifications required to build fully analytical solutions, these approaches reveal which parameters control azimuthal modes and can be used to mitigate them by using for example symmetry breaking where different burners are installed in the same chamber to limit possible resonances [27].

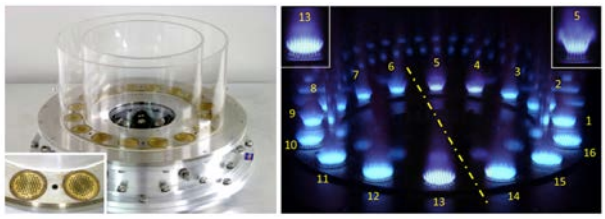
Fig. 11: the EM2C setup for azimuthal modes in annular chambers [23]

## 4. Conclusions

Unsteady combustion controls important phenomena such as ignition, quenching or instabilities which are crucial phases in all combustion systems. This field is the new frontier for research especially for real engines. The prediction of ignition and of optimal ignitor design is one first application where combined LES and experiments will allow significant progress. In the domain of thermoacoustics, full simulation methods able to predict instabilities before building engines remain out of reach for the moment, in laboratories as well as in industry but this will be the future target.

## 5. Acknowledgments

The support of the European Community ERC program INTECOCIS, of SAFRAN and of CTR (Stanford) is gratefully acknowledged. Many experimental results have been obtained through collaborations with University of Sydney, CORIA Rouen, EM2C Paris and Cambridge University and their help is gratefully acknowledged.

## 6. References

[1] Esclapez, L. (2015) Numerical study of ignition and inter-sector flame propagation in gas turbine. PhD Thesis. Université de Toulouse.

[2] Philip, M., Boileau, M., Vicquelin, R., Riber, E., Schmitt, T., Cuenot, B. and Candel, S. (2015). *Proc. Combust. Inst* 35(3), 3159-3166.

[3] Esclapez, L., Riber, E., & Cuenot, B. (2015). *Proc. Combust. Inst*, 35(3), 3133-3141.

[4] Dorofeev, S. *Proc. Combust. Inst.* 2011, *33*, 2161–2175 .

[5] Bradley, D.; Mitcheson, A. *Combust. Flame* 1978, *32*, 221–236.

[6] R. J. Martin, A. Reza, and L. W. Anderson. *Journal of Loss Prevention in the Process Industries*, 13(6):491–497, 2000.

[7] T. Abbasi, H. J. Pasman, and S. A. Abbasi. *J. Hazardous Materials*, 174(1-3):270–280, 2010

[8] Quillatre, P. (2014) Simulation aux grandes ´echelles d[´] explosions en domaine semi-confine. PhD Thesis, Université de Toulouse.

[9] Quillatre, P., Vermorel, O., Poinsot, T. & Ricoux, P. (2013) *Industrial & Engineering Chemistry Research*, 52.114

[10] A. R. Masri, A. Al-Harbi, S. Meares, and S. S. Ibrahim. *Industrial & Engineering Chemistry Research*, 2012, 14-11423.

[11] J. C. Oefelin, V. Yang, J. Prop. Power 9 (5), 1993, pp. 657–677.

[12] Hakim, L., Ruiz, A., Schmitt, T., Boileau, M., Staffelbach, G., Ducruix, S. and Candel, S. (2015). Proceedings of the Combustion Institute, 35(2), 1461-1468.

[13] S. Ducruix, T. Schuller, D. Durox, S. Candel, J. Prop. Power 19 (5), 2003, pp. 722–734.

[14] S. Ducruix, T. Schuller, D. Durox, S. Candel, Prog. Energy Comb. Sci. 210, 2005, p. 179.

[15] T. Lieuwen, J. Fluid Mech. 435, 2001, pp. 289–303.

[16] F. Boudy, D. Durox, T. Schuller, S. Candel, Proc. Combust. Inst. 33, 2011, pp. 1121–1128.

[17] C. O. Paschereit, W. Polifke, B. Schuermans, O. Mattson, J. Eng. Gas Turb. and Power 124, 2002, pp. 239–247.

[18] V. Kornilov, R. Rook, J. ten Thije Boonkkamp, L. de Goey, Combust. Flame 2009, pp. 1957–1970.

[19] F. E. C. Culick, P. Kuentzmann, Unsteady Motions in Combustion Chambers for Propulsion Systems, NATO Research and Technology Organization, 2006.

[20] Y. Méry, L. Hakim, P. Scouflaire, L. Vingert, S. Ducruix, S. Candel, *Comptes Rendus Mécanique* 341 (1), 2013, pp. 100–109.

[21] S. Hochgreb, D. J. C. Dennis, I. Ayranci, W. Bainbridge and S. Cant. Proceedings of ASME Turbo Expo 2013 - GT2013- 9531, 2013.

[22] J. Kopitz, A. Huber, T. Sattelmayer, W. Polifke, in: Int'l Gas Turbine and Aeroengine Congress & Exposition, ASME GT2005-68797 , Reno, NV, U.S.A., 2005.

[23] J. F. Bourgouin, D. Durox, J. P. Moeck, T. Schuller, S. Candel, *Proc. Combust. Inst.* 35 (3), 2015, pp. 3237–3244.

[24] N. Worth, J. Dawson, *Proc. Combust. Inst*. 34, 2012, pp. 1–8.

[25] W. Krebs, P. Flohr, B. Prade, S. Hoffmann, Combust. Sci. Tech. 174, 2002, pp. 99–128.

[26] Bauerheim, M., Parmentier, J. -F., Salas, P., Nicoud, F. and Poinsot, T. (2014) *Comb. Flame*, 161.1374-1389.

[27] Bauerheim, M., Salas, P., Nicoud, F. & Poinsot, T. (2014) *J. Fluid Mech.*, 760.431-465.

[28] Wolf, P., Balakrishnan, R., Staffelbach, G., Gicquel, L. Y. M. & Poinsot, T. (2012) *Flow, turbulence and combustion*, 88.191-206.

[29] Parmentier, J. -F., Salas, P., Wolf, P., Staffelbach, G., Nicoud, F. & Poinsot, T. (2012) *Comb. Flame*, 159.2374-2387.

[30] N. Noiray, M. Bothien, B. Schuermans, *Combust. Theory and Modelling* 2011, pp. 585–606.

# Combustion - Generated Fine and Ultrafine Particles

A. D'Anna[1,*]
[1]Dipartimento di Ingegneria Chimica, dei Materiali e della Produzione Industriale
Università degli Studi di Napoli Federico II Italy

**Abstract**

The processes by which carbonaceous nanoparticles are produced from combustion of liquid and gaseous fuels are reviewed in this talk. The focus is on the formation and properties of nanoparticles in laboratory flames - premixed and diffusion- and on the most advanced methods of sampling and detection. Measurements characterizing nanoparticles at the exhausts of engines and commercial burners are also analysed. A modelling analysis based on detailed chemical kinetic calculations and on a molecular dynamics approach is used to show how the chemical nature and the morphology of the emitted particles depend on combustion environments.

*Keywords: particulate matter, soot, diagnostics, chemical kinetics, engine emission.*

## 1. Introduction

Despite increasing emphasis on alternative energy sources, most of the energy consumed in the world is produced through fossil fuel combustion processes. Today, combustion of fossil fuels accounts for more than two-thirds of the world's primary energy utilization and this percentage will remain practically unchanged for the next decades [1].

Practical combustion devices produce and eventually emit particulate matter when incomplete combustion, i.e., locally fuel-rich conditions, results in a portion of the fuel carbon to be converted into high-molecular mass aromatic compounds. While many emission-free alternatives to fossil fuels are currently used or are being discussed for power generation (e.g., hydroelectricity, solar, wind, geothermal, tidal or wave energy), transportation systems requires high-density energy sources, primarily delivered as liquid fuels, and the only medium-term alternative to petroleum derived fuels is represented by biofuels of different origin, e.g., agricultural residue, food waste, woody plant parts, or algae biomass. Biofuels burn similar to fossil fuels and produce the same pollutants or even specific classes of pollutants which are of concern for human health.

Consequently, our life is exposed to combustion-generated particles and it will be exposed to these pollutants for a long time.

Engine industries and combustion technologists developed a combination of advanced engine technologies, exhaust control systems, and reformulated fuels to reduce particulate matter emission. Despite the newest combustion technologies which caused a strong reduction of the mass of emitted particulate in the atmosphere, our populated cities are still subject to traffic regulation in order to meet environmental standards. Moreover, there is still a great concern in the population about the health and environmental effects associated to particulate although recent studies have shown that "new-technology diesel exhaust" did not induce tumors or pre-cancerous changes in the lung and did not increase tumors in any other tissue [2].

The main concern is on the nanometer-sized and ultrafine fractions of the size distribution of the particulate matter. These particles have insignificant mass, but they dominate in terms of number concentration and have a larger surface area/mass ratio compared to larger particles. They can deposit far inside the airways, potentially reaching target organs. Due to elevated numerical concentration and large surface area, their health effect can go beyond what expected from such a low mass concentration [3]. Moreover, they can escape filters and are not easily measured at the engine exhausts and in the atmosphere so that are often overlooked.

Automotive sources are considered the major responsible for nanometer-sized and ultrafine particulate pollution but other combustion sources such as domestic heating and cooking as well as stationary power generation have to be considered too.

The processes by which carbonaceous nanoparticles are produced in combustion is reviewed in this paper. Starting from the formation mechanisms and the properties of nanoparticles in laboratory flames - premixed and diffusion- as detected by the most advanced methods of sampling and measurements, recent results obtained at the exhausts of engines and commercial burners are presented. A modeling analysis based on detailed chemical kinetic calculations and on a molecular dynamics approach is used to show how the chemical nature and their morphology depend on combustion environments.

## 2 Diagnostics for particles

Our understanding of particle formation in combustion has evolved in the last twenty years from a phenomenological description to almost quantitative understanding due to the progress of diagnostic tools, which today allow analysis on an almost atomic level of

* Corresponding author:
Email: andrea.danna@unina.it

the particles, either off-line and in-situ. Their use has improved our knowledge about the physical and chemical properties of soot and about the kinetics of particle formation in combustion. A complete overview of the current state-of-the-art of in-situ laser-based optical diagnostics for particle characterization is reported in refs. [4-6].

Combustion-formed particles range in size from near molecular dimensions up to some hundreds of nanometers and require an array of techniques for detailed chemical and physical characterization. The smallest particles, behaving like molecules, show spectroscopic properties such as absorption and fluorescence, which allow either identification of their chemical functionalities and/or their quantification both in-situ and in the sampled material [6-10]. The very low molecular mass associated with these particles makes the size measurements quite difficult. Interaction of light with particles results in static or dynamic light scattering. Static scattering from very small particles is of the same order of magnitude as scattering from the gas-phase products in which the particles are suspended making this technique unsuitable [11]. Diagnostics based on the detection of dynamic emissions, both scattering and fluorescence, improves the size measurement capability in the nanometer-sized range [12,13]. Larger particles are more suitable for laser induced incandescence and laser light scattering measurements. These two measurements together allow the direct evaluation of particle concentration and mean particle sizes in combustion systems [14-20].

Although in-situ measurements of nanoparticles are important for the determination of particle formation kinetics, additional structural and morphologic information is also of great interest to characterize particles and assess their role on the environment and on human health. This information is better retrieved from particle samples collected in the combustion systems and analyzed by off-line techniques. However, careful sampling is required to avoid artifacts formed from chemical and physical interactions during the collection and handling procedure [10].

Differential Mobility Particle Sizers (DMPS) are becoming a widely accepted tool for the determination of the size distribution of the particles extracted from the flame without any manipulation of the sample [21,22]. DMPS measurements require a high dilution sampling system to reduce the sample temperature and concentration and to avoid further reactions and particle coagulation in the sampling line. Particles are charged and separated in an electrostatic classifier based on their electrical mobility. A mobility, or size distribution is determined by counting the charged particles which exit the classifier, varying the applied voltage. When state of the art instrumentation is used, a size distribution from 1 to 100 nm can be measured [22]. The accuracy of the measurement relies on the correct evaluation of the dilution ratio required to suppress particle coagulation in the sampling line, charging efficiency and particle losses through the sampling lines/instrument. This is particularly problematic for particles down to 10 nm. Diffusion losses and the interpretation of particle mobility in terms of size are critical points [23]. Also DMPS is not able to qualify the result as a function of particle chemical nature.

Information on the molecular mass and structure of the particles can be retrieved by chemical and physical characterization by off-line measurements. Sampling procedure is the crucial point: the procedure should not falsify or change the particle properties in order that the sampled material be representative of the particles in the combustion environment. Although many precautions are adopted, the collection procedure inevitably modifies the samples and information obtained from off-line characterization of the sampled material has to account for possible sample modifications.

A way to withdrawn particles from combustion environments is by using suction probes. Combustion products are isokinetically sampled by means of water-cooled probes; total particle collected on the probe wall, on filters and in ice-cooled traps placed in the sampling line is extracted by solvents in order to separate the soluble species from soot. Soot samples are dried, weighed and suspended by ultrasonic agitation in suitable solvents for further analysis [24]. The soluble species are usually analyzed by high pressure liquid chromatography and mass spectrometry for the quantification of gas-phase Polycyclic Aromatic Hydrocarbons -PAH [24,25]. UV-visible absorption and fluorescence measurements are then used for the chemical characterization of the other absorbing and fluorescing species [26]. Size Exclusion Chromatography (SEC) analysis is used for the evaluation of molecular mass distribution of the sampled material [25]. SEC is performed by using a high pressure liquid chromatograph equipped with a diode array detector for absorbance measurements. Fourier-Transformed Infrared (FTIR) analysis, Raman spectroscopy and Surface-Enhanced Raman Scattering (SERS) have been employed to characterize nanoparticles produced in combustion by batch or in-situ [26,27]. The measured spectral features supply insight on the chemical properties of the combustion products through the identification of CC, CH and CO bonding. Coupled elemental analysis also gives information on the amount of C and H atoms in the samples [28].

Another common way of collecting particles is thermophoretic sampling. A cold surface placed in line with flow streamlines produces a strong temperature gradient making particles move towards the surface by thermophoretic forces [29]. We have recently shown that the transient response of the thermocouple, i.e., the temporal evolution of the detected temperature, contains information not only related to the particle volume fraction but also on the emissivity, i.e. optical properties, of the carbonaceous materials deposited on the thermocouple bead [30].

Size distribution functions of the particles deposited on substrates can be obtained by Atomic Force Microscopy (AFM) and High-Resolution Transmission Electron Microscopy (HR-TEM) [31-34]. AFM furnishes a 3D topological map of particles deposited on

atomically flat substrates, with angstrom resolution in height and nanometer resolution in the plane parallel to the surface [31]. This is a great advance relative to other microscopy techniques such as TEM, which only gives a 2D characterization of the particles. AFM operating in tapping mode collects a three dimensional map of the sample by precisely monitoring the position of a cantilever beam with a laser as it vibrates along the surface of the sample without having to further coat the sample. The vibrating tip of the cantilever beam is ideally ending in one atom. Determination of the interactions between the cantilever and the samples can also reveal information about the viscoelastic properties of the collected material [34]. In addition to AFM, HR-TEM observations can furnish information on the internal structure of the particles, although on a 2D image [33].

## 3 Experimental Evidences for Particle Formation

The first evidence of particle and in general of high-molecular-mass species in flame environments is the detection of a reasonable scattering signal in excess to gas phase compounds. Elastic light scattering of particles with sizes below the wavelength of the incident light is proportional to the sixth moment of the size distribution function in number concentration of the particles, so that this measurement is sensitive to smaller particles only if the larger ones are absent [11]. Absorption measurements help in discriminating the different characteristics of the formed particles [12]. Usually, the broadband UV-Visible absorption spectra measured in flames show a strong UV signal that decays at increasing wavelength in the visible range. The UV absorption in the range 200-250 nm is attributed to $CO_2$ molecules that have been found to exhibit strong absorption at high temperature [35]. The contribution of gaseous products does not account for the total UV signal measured in combustion nor soot particles can be responsible for such absorption because they mainly absorb visible light, so that other species UV-absorbing should be responsible for it. When the extra absorption in the UV is also associated with a scattering signal it is a clear indication of the presence of high-molecular-weight molecules/particles in the combustion environment. These compounds are transparent to the visible light. If also absorption in the visible range is detected, soot particles are present [6].

Taking advantage from the clearly distinct spectral behavior between soot and visible-transparent species, it is possible to follow their evolution in flame environments. Close to the main reaction zone of the flame, the volume fraction of visible-transparent species sharply increases and a large number concentration of particles of the order of $10^{13}$ $cm^{-3}$ can be measured. Particle size does not exceed 3 nm, as demonstrated by the low scattering measured in excess to gaseous compounds and the spectral behavior is limited to UV wavelengths. Beyond the maximum value, the volume fraction of visible transparent species decreases in correspondence with the formation of visible-absorbing, soot particles. These latter have a much lower number concentration of the order of $10^{11}$ $cm^{-3}$ but larger sizes ranging from 10 to 50 nm. Optical measurements do not allow determination of size and number concentration of the two classes of particles simultaneously because scattering is biased to the larger particles and the contribution to the scattering of the smaller particles become negligible. The number concentration and mean size can be calculated in the transparent region of the flames where larger particles are absent. The size of the visible transparent particles measured in-situ by scattering/extinction measurements in different flame conditions seems to remain quite unchanged and at about 2-4nm.

Laser induced fluorescence (LIF) in the UV helps qualify the chemical nature of the formed particles. The LIF spectra measured in the flame regions characterized by the prevalence of UV absorption show a broad signal in the region between 290 and 400 nm with a maximum at about 320. The spectra measured when also visible absorption is present show fluorescence signals which extend down to 500 nm and a continuum with a maximum above the 600 nm. The spectral behavior between 290 and 600 nm can be de-convoluted into two broad fluorescence bands: the first has a shape similar to that measured when only UV absorption is present whereas the second is broadband with a maximum at 420 nm. Both bands are typical of fluorescence from aromatic compounds whereas the continuum background which extends into the visible can be attributable to incandescence of soot particles. Time-resolved laser induced emission measurements have shown that LIF in the UV range centered at 320 nm can be attributed to high-molecular-mass aromatic compounds with sizes of the order of 2–3 nm constituted by 2-, 3-fused-rings species connected by aliphatic bonds whereas nanoparticles constituted by oligomers of larger PAHs or by clusters of PAHs are associated to visible fluorescence at 420 nm [36].

In-situ optical data unambiguously show the presence of two classes of particles: precursor nanoparticles with mean sizes between 2 and 4 nm, transparent to the visible radiation and fluorescing in the UV and visible, and visible absorbing particles, referred to as soot, with mean sizes between 10 and 50 nm.

Off-line measurements support the presence of different particles in combustion. Some peaks are observed in the molecular weight distribution obtained by SEC of the condensed species collected from flames by a suction probe [37]. A first peak is in the range of molecular mass between 500 and 2000 u close to the peaks of PAHs, a second one is in the molecular mass region of $10^4$-$10^5$u. Considering a density of 1.2 $g/cm^3$ typical of PAHs, the two broad peaks correspond to particles with an equivalent spherical diameter of 1–2 and 3–7 nm, respectively. Moving towards larger molecular weights, other two peaks become prevalent particularly in flame conditions where strong visible

absorption is measured in-situ. One peaks between $10^6$ and $10^7$u and the other at $10^8$–$10^{10}$u equivalent to spherical particles having sizes of 10-20 nm and 50-200 nm, respectively, if a density of 1.8 g/cm$^3$, typical of soot, is used for these particles.

Particle size distributions measured by DMPS confirm the optical and off-line measurements showing a bimodal shape of the particle size distributions with a first mode well below 10 nm and a second mode when soot particles were formed. Figure 1 reports the experimentally determined volume fraction of total particulates at 10 mm height in several premixed flames of ethylene/air with equivalence ratios ranging from 1.5 to 2.5. Total particulate concentrations were determined by absorption measurements in the UV using a volume attenuation coefficient of $3.5 \times 10^4$ cm$^{-1}$ for UV-absorbing particles and $8.8 \times 10^4$ cm$^{-1}$ visible absorbing particles [12]. The particulates comprise all of the carbonaceous species that have an appreciable absorption in the ultraviolet region. Experimental volume fractions of particles with sizes larger than 10 nm are also shown. These latter were detected by visible absorption [38]. In the same figure, the size distribution functions of the particles measured by DMPS at different equivalence ratios are also reported together with images of the flames. A rather mono-disperse peak with a modal mobility diameter of about 2.5 nm is detected at an equivalence ratio of 1.5, i.e., in a slightly rich bluish flame, whereas a second mode with diameters of the order of 7-8 nm appears when the flame becomes slightly yellow, i.e., at the equivalence ratio of 1.8. A third mode larger than 10 nm is observed in the richest analyzed flame, i.e., equivalence ratio of 2.5.

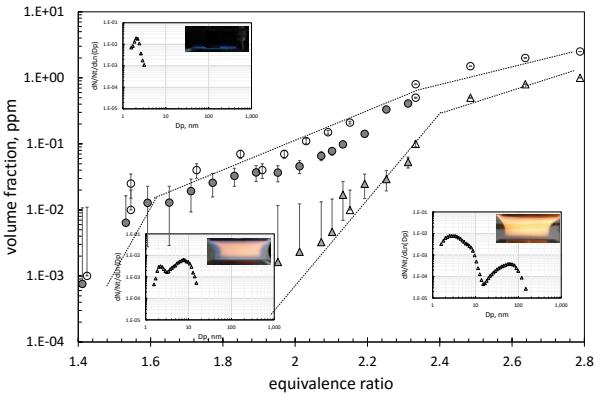


Figure 1: Soot volume fraction vs equivalence ratio at 10 mm along the flame axes of atmospheric pressure ethylene/air flames with a fresh gas flow velocity of 10 cm/s. Full and empty circles refer to total particulate matter retrieved from in-situ absorption measurement in the UV. Full and empty triangles represent the fraction of particles absorbing in the visible (Empty circles and triangles from [38,39]; full circles and triangles from [6]). Inserts are flame images and particle size distributions measured at the equivalence ratios of 1.5, 1.8 and 2.5 (Experimental data from [40]).

The smallest mode is measured in conditions where the extinction and fluorescence spectra are limited to the far UV with very low values of the scattering in excess to gaseous compounds. When a significant extinction in the visible wavelength range is detected and the scattering increases by orders of magnitude, the size distribution function includes the third mode with mobility diameters larger than 10 nm, in addition to the smaller peaks associated with nanoparticles. It is worth noting that when soot particles are detected, the first mode of the particle size distribution also includes nanoparticles with sizes around 5-8 nm indicating a continuous coagulation of nanoparticle in the process of soot formation.

A wide range of particles have been detected also in non-premixed flame conditions. These nanoparticles have some characteristics already found in premixed flames but also have some peculiarities. Indeed the presence of low-temperature regions with high concentrations of fuel and pyrolysis products such as PAHs can favor the nucleation of nanoparticles through physical coagulation mechanisms more than through chemical routes.

Small nanoparticles are also emitted from practical combustion devices but they are often considered not to be directly connected with combustion, but rather thought to nucleate during dilution and cooling of the exhausts. However, many of the features of the combustion-formed nanoparticles in laboratory studies may have pertinence to the emission from practical systems.

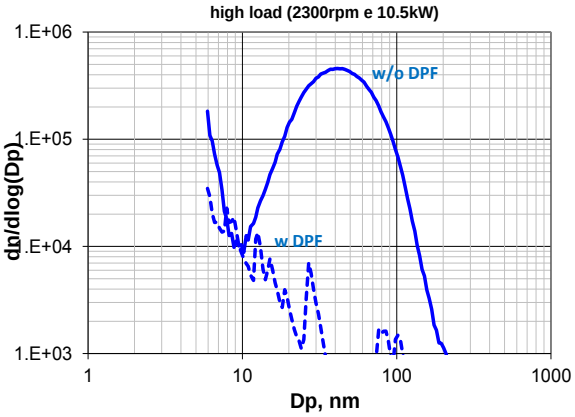


Figure 2: Particle size distribution measured at the exhaust of a diesel engine at a fixed rpm (2300) and engine load (10.5kW) with and without a DPF.

Figure 2 shows the particle size distribution functions by number measured with DMPS at the exhausts of diesel engine ran with and without a Diesel Particulate Filter (DPF). The particle size distribution emitted by the diesel engine shows two particle modes similar to those observed in premixed flames: nano-sized and soot particles. Measurements have been performed by maintaining the sampling line at a temperature of 450°C and diluting the sampled gases until a critical dilution is reached, i.e., the particle size distribution remains unchanged in its shape by increasing the dilution ratio. This sampling modality does not allow volatile compounds condensation on existing particles. The similarity in the size distribution function with those measured in flames suggests that nanoparticles measured in vehicle exhaust are generated in the combustion chamber and both nanoparticles and soot modes survive the exhaust system without significant growth. It is worth to note that the DPF efficiently filters particles

larger than 10nm but fails to collect all the sub-10nm particles.

The concentrations of high-molecular-mass tar-like species and soot during the combustion cycle in a single-cylinder direct injection diesel engine were measured in a pioneering work by Ciajolo and co-workers [41]. Samples were withdrawn with a fast in-cylinder gas sampling device during the combustion cycles and were analysed. They found that the formation of high-molecular-mass tar-like species occurs just after fuel ignition and precedes soot formation. The chemical characterization of the sampled species showed the presence of PAHs and aromatic compounds of high molecular mass exhibiting absorption and fluorescence in the UV similar to those found in laboratory flames. Extinction and scattering measurements performed in the combustion chamber of a ‘‘transparent” diesel engine have further confirmed the in-cylinder formation of nanoparticles during diesel combustion [42]. Recently, Kubo [43] measured the in-cylinder size distribution of the particles formed during the diesel cycle with a DMPS and found a unimodal particle size distribution with a peak at about 3 nm in the earlier stage of combustion, which moved from around 3-7 nm during combustion. As combustion proceeded, a second mode became clearly distinct at about 20 nm. Experimental data strongly support the hypothesis that the combustion process contributes to the emission of particles from engines although the Sulphur compounds and volatile organic compounds contribute to particle nucleation during dilution and cooling of the exhausts.

Measurements of particle size distributions were made also at the exhausts of a burner for home appliances and a cook-top stove, both fueled with methane. Figure 3 reports the size distribution functions determined by DMPS at the exhaust of a home-burner for different loads [44].

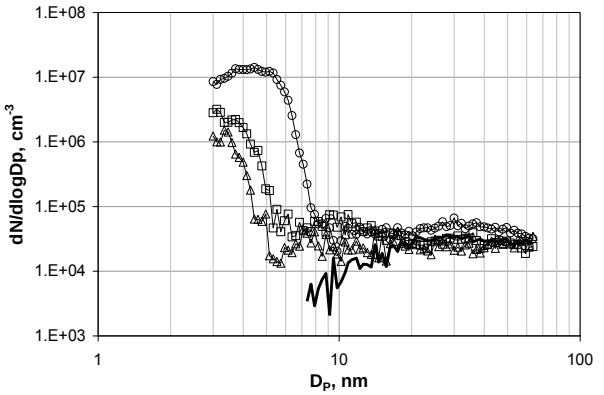


Figure 3: Particle size distribution measured at the exhaust of burner for home appliances [44].

Measurements have shown that particulate matter with size in the 1 nm-10 nm size range is formed in all the examined conditions. The emitted mass concentration of these compounds is very low, of the order 0.1 ppm. Primary soot particles in the 10 nm-50 nm range are not formed in all the conditions examined. In this size range, the number concentration of the particle measured at the exhaust of the combustion system is of the same order of magnitude of the number concentration of the particles present in the ambient air. The complete absence of particles larger than 10 nm is confirmed by the optical measurements, which show the complete absence of incandescence signals due to soot particles.

The cook-top stove also emits sub-10nm particles of organic carbon nature and nitrates and sulphates deriving from NOx and Sulphur contained in the fuel.

Trace amounts of metal nanoparticles are also measured at the exhausts of practical combustion devices.

## 4 Modelling approach

Significant progresses have been made towards quantitative prediction of soot mass, aggregate formation, detailed particle size distribution, and the evolution of the C/H ratio in soot. It is perceivable that in the next future the kinetic models of soot formation and oxidation will be able to provide predictions also for surface area, chemical composition, C/H and C/O ratios, and active surface sites. Ultimately, these models will evolve into tools that can predict toxicity, optical properties, and environmental impacts of soot directly.

A reliable and predictive kinetic model for soot prediction requires a detailed and correct description of the gas-phase chemistry that includes the kinetic behavior of all gas-phase aromatic molecules, including PAH in the stabilomer grid [45], and all the other aromatic networks present in combustion, and an appropriate coupling between gas-phase chemistry with aerosol dynamics and the chemistry governing particle formation and growth, including nucleation, hydrocarbon and PAH addition on particle surface, particle coalescence, aggregation, oxidation and oxidation-induced fragmentation.

We have recently developed a multisectional approach in which the molecular mass distribution is defined by a range of sections (lumped species) each containing a nominal C and H number. The level of agglomeration of the compounds is further defined by three entities: molecules, clusters of molecules and agglomerates of clusters [46-48]. The use of lumped species treats, numerically, all the compounds as gas phase species. This means that it is possible to evaluate a collision frequency and to assign an activation energy for each process in which gaseous compounds and particles are involved. The kinetic expression can be written in principle for each lumped species. Particles react in similar way, depending on some parameters, such as size, chemical composition and morphology. Kinetic expressions will be tailored on particle features, assuming specific dependence on these parameters. If these dependences are chosen on the base of physical meanings their validity can be wider. This approach tries to get more general expressions for particle reaction avoiding the tuning of kinetic rates for matching

experimental data. The model is fully coupled with the main pyrolysis and oxidation reactions of the fuel. The coupling between gas- and particle-phase is very important because of the role of abundant gaseous species such as $C_2H_2$, aromatic compounds and small radicals such as H and OH in the nucleation, growth and oxidation processes. The advanced multi-sectional method was broadly validated in rich premixed and non-premixed ethylene flames [46-48].

Particle nucleation remains one of the most intriguing and obscure steps in the process of particulate matter formation in flames. Although PAHs stacking/clustering has been individuated as a key step in the nucleation process, uncertainties remain on the size of the PAHs undergoing clustering, on the organization of the PAHs in the forming clusters and on the factors affecting the amount of order present in this texture organization. To systematically study the influence of the molecular structural and molecular weight of PAHs on the nucleation and coagulation processes and on the morphology of the formed clusters, a Molecular Dynamics approach has been used [49]. Two different types of macromolecules have been used in the simulations: PeriCondensed Aromatic Hydrocarbons (PCAH) and Aromatic Aliphatic Linked Hydrocarbons (AALH), known to be present in flame environment depending on flame temperature, equivalence ratio and fuel chemical structure. Calculations show that the presence of covalent bonds in the molecules such as in AALH improves the inception and growth mechanisms of the clusters and enhance the disorder of the clusters with an increased number of molecules not arranged in parallel planes. These results are in good agreement with experimental results on particle structure and morphology obtained by HR-TEM.

## 5 Final Remarks

Combustion of fossil fuels produces carbonaceous nanoparticles both in premixed and nonpremixed flame conditions. Two classes of carbonaceous material are mainly formed in combustion: nanoparticles with sizes in the range 1–5 nm, and soot particles, with sizes from 10 to 100 nm. Chemical and spectroscopic analysis give an indication of the chemical nature of the particles and show that the smaller particles can be thought as staked PAH structures or polymer-like structures containing sub-units with aliphatic and aromatic bonds.

Nanoparticles are also found in the exhaust of practical combustion systems. This has been mainly attributed to condensation of low volatility hydrocarbons during dilution and cooling of the exhausts. However, the similarity of the chemical properties and the size distribution functions of the emitted particles with those found in laboratory flames suggests that combustion-formed nanoparticles can escape the combustion process and be emitted into the atmosphere.

Thus combustion, as well as the fuel, may have a dominant role in determining the type and amount of particles emitted.

Nanoparticles are present in low mass concentration, but surprisingly high number concentrations due to their very low sizes. The emission of these particles into the atmosphere constitutes a serious concern for health and for their contribution to photochemical smog. The smallest particles play a particularly important role in health since they are able to penetrate deeper than larger particles into the respiratory system. They may also affect the radiation balance of the atmosphere by serving as condensation nuclei for cloud formation and for contrails in the upper atmosphere.

## 6 References


[1] Annual Energy Outlook 2015 with projections to 2040, DOE/EIA-0383(2015) U.S. Energy Information Administration

[2] Health Effects Institute, Advanced Collaborative Emissions Study -ACES-: Lifetime Cancer and Non-Cancer Assessment in Rats Exposed to New-Technology Diesel Exhaust, no.184, January 2015

[3] P. Pedata, T. Stoeger, R. Zimmermann, A. Peters, G. Oberdörster, A. D'Anna, Part Fibre Toxicol (2015) 12-34.

[4] A. Leipertz, F. Ossler, M. Aldén, in: K. Kohse-Höinghaus, J.B. Jeffries (Eds.), Applied Diagnostics, Taylor and Francis, New York-London, 2002, p. 359.

[5] P. Roth, Proc Combust Inst 31(2) (2007) 1773-1788.

[6] A. D'Anna, Proc Combust Inst 32 (2009) 593-613.

[7] A. D'Alessio, A. D'Anna, P. Minutolo, G. Gambi, Ber Bunseng Phys Chem 97 (1993) 1574-1582.

[8] A. D'Anna, A. D'Alessio, P. Minutolo, in: Bockhorn (Ed.), Soot formation in combustion: mechanisms and models, Springer-Verlag, Berlin 1994, p.83.

[9] P. Desgroux, X. Mercier, K.A. Thomson, Proc Combust Inst 34 (2013) 1713-1738.

[10] A. Ciajolo, in: Bockhorn, D'Anna, Sarofim, Wang (Eds.), Combustion Generated Fine Carbonaceous Particles, Karlsruhe University Press, Karlsruhe, 2009, p.333.

[11] A. D'Alessio, in: D.C. Siegla, G.W. Smith (Eds.), Particulate Carbon Formation During Combustion, Plenum Press, New York, 1981, p. 207.

[12] A. D'Alessio, A. D'Anna, A. D'Orsi, P. Minutolo, R. Barbella, A. Ciajolo, Proc Combust Inst 24 (1992) 973-980

[13] A. D'Alessio, A. D'Anna, G. Gambi, P. Minutolo, J Aerosol Sci 29 (1998) 397-409.

[14] C.J. Dash, Proc Combust Inst 20 (1984) 1231-1237.

[15] L.A. Melton, Appl Optics 23 (1984) 2201-2208.

[16] S. Will, S. Schraml, A. Leipertz, Optics Lett 20 (1995) 2342-2344.

[17] P. Roth, A.V. Filippov, J Aerosol Sci 27 (1996) 95-104.

[18] A.V. Filippov, M.W. Markus, P. Roth, J Aerosol Sci 30 (1999) 71-87.

[19] R.J. Santoro, C.R. Shaddix, in: K. Kohse-Höinghaus, J.B. Jeffries (Eds.), Applied Diagnostics, Taylor and Francis, New York-London, 2002, p.252.

[20] T. Lehre, B. Jungfleisch, R. Suntz, H. Bockhorn, Appl Optics 42 (12) (2003) 2021.

[21] B. Zhao, Z. Yang, J. Wang, M.V. Johnston, H. Wang, Aerosol Sci Technol 37 (8) (2003) 611-620.

[22] L.A. Sgro, A. Borghese, L. Speranza, A.C. Barone, P. Minutolo, A. Bruno, A. D'Anna, A. D'Alessio, Environ Sci Technol 42 (3) (2008) 859-863.

[23] P. Minutolo, A. D'Anna, A. D'Alessio, Combust Flame, 152 (2008) 287-292.

[24] R. Barbella, A. Ciajolo, A. D'Anna, Fuel 68(6) (1989) 690-695.

[25] B. Apicella, A. Ciajolo, A. Tregrossi, Anal Chem 76(7) (2004) 2138-2143.

[26] C. Russo, F. Stanzione, A. Tregrossi, A. Ciajolo, Carbon 74 (2014) 127-138.

[27] P. Minutolo, G. Rusciano, L.A. Sgro, G. Pesce, A. Sasso, A. D'Anna, Proc Combust Inst. 33 (2011) 649-657.

[28] C. Russo, A. Ciajolo, Combust Flame 162 (2015) 2431-2441.

[29] C.S. McEnally, U.O. Koylu, L.D. Pfefferle, D.E. Rosner, Combust Flame 109 (4) (1997) 701–720.

[30] G. De Falco, G. Trunfio, M. Commodo, P. Minutolo, A. D'Anna, in: D'Anna, Ciajolo, Commodo, De Giorgi, Gülder, Tregrossi (Eds.) Proc. XXXVIII Meeting of the Italian Section of the Combustion Institute, Lecce, 20-24 September 2015, p.IX4

[31] A.C. Barone, A. D'Alessio, A. D'Anna, Combust Flame 132(1/2) (2003) 181-187.

[32] A.B. Palotás, L.C. Rainey, C.J. Feldermann, A.F. Sarofim, J.B. Vander Sande, Microsc Res Tech 33 (3) (1996) 266-278.

[33] M. Alfè, B. Apicella, R. Barbella, J.-N. Rouzaud, A. Tregrossi, A. Ciajolo, Proc Combust Inst 32 (2009) 697-704.

[34] G. De Falco, M. Commodo, P. Minutolo, A. D'Anna, Aerosol Sci Technol 49 (5) (2015) 281-289.

[35] T. Joutsenoja, A. D'Anna, A. D'Alessio, M.I. Nazzaro, Appl Spectrosc. 55 (2) (2001) 130-135.

[36] M. Sirignano, A. Collina, M. Commodo, P. Minutolo, A. D'Anna, Combust Flame, 159 (4) (2012) 1663-1669.

[37] M. Sirignano, M. Alfè, A. Tregrossi, A. Ciajolo, A. D'Anna, Proc Combust Inst (2011), 633-640.

[38] A. De Filippo, L.A. Sgro, G. Lanzuolo, A. D'Alessio, Combust. Flame 156 (9) (2009) 1744-1750.

[39] A. D'Alessio, A. D'Anna, P. Minutolo, L.A. Sgro, A. Violi, Proc Combust Inst 28 (2) (2000) 2547-2554.

[40] M. Commodo, L.A. Sgro, P. Minutolo, A. D'Anna, J Phys Chem A 117 (2013) 3980-3989.

[41] R. Barbella, C. Bertoli, A. Ciajolo, A. D'Anna, Proc Combust Inst. 23 (1990) 1079-1085.

[42] B.M. Vaglieco, S.S. Merola, A. D'Anna, A., D'Alessio, J. Quant. Spectr Rad Transfer 73 (2–5) (2002) 443-450.

[43] S. Kubo, in: Bockhorn, D'Anna, Sarofim, Wang (Eds.), Combustion Generated Fine Carbonaceous Particles, Karlsruhe University Press, Karlsruhe, 2009, p.651.

[44] P. Minutolo, A. D'Anna, M. Commodo, R. Pagliara, G. Toniato, C. Accordino, Environ Eng Sci, 25(10) (2008) 1357-1363.

[45] A. Fahr, S.E. Stein, Proc Combust Inst 22 (1988) 1023-1029

[46] M. Sirignano, J. Kent, A. D'Anna, Combust Flame 157 (2010) 1211-1219.

[47] A. D'Anna, M. Sirignano, J. Kent, Combust Flame 157 (2010) 2106–2115.

[48] M. Sirignano, J. Kent, A. D'Anna, Energy Fuels 27 (2013) 2303-2315.

[49] S. Iavarone, M. Sirignano, A. De Candia, A. Fierro, L. De Arcangelis, A. D'Anna, Proceeding of the Ninth Mediterranean Combustion Symposium, Rhodes, Greece, June 7-11, 2015

# Flash-boiling spray Behavior and Combustion in a Direct Injection Gasoline Engine

Min Xu[1*], David L.S Hung[2], Jie Yang[1], Shengqi Wu[1]
[1] School of Mechanical Engineering, Shanghai Jiao Tong University, National Engineering Laboratory for Automotive Electronic Control Technology, Shanghai, China
[2]University of Michigan-Shanghai Jiao Tong University Joint Institute, Shanghai Jiao Tong University, Shanghai, China

## Abstract

Flash boiling occurs when heated fuel is injected into an ambient environment below its saturation pressure. Comparing with non-flash-boiling spray, namely the liquid spray, flash-boiling spray features a two-phase flow that vapour bubbles are generated constantly inside the liquid spray. In a constant volume chamber, the characteristics of flash boiling spray, including structure, flow field, droplet size and vapour concentration, have been extensively studied by means of various laser diagnostic techniques. Flash boiling spray, compared with typical high pressure liquid spray, has much shorter penetration, wider spray angle, smaller drop size, faster evaporation, and more uniform mass distribution, etc., which are ideal for direct-injection (DI) gasoline engine combustion. This could reduce the requirements of increasingly high injection pressure, thereby providing new opportunity for DI gasoline combustion system design. In this study, the flash-boiling spray is investigated in a single cylinder optical engine by heating the injected fuel at typical part load engine operating condition. The high-speed combustion flame images and cylinder pressure are recorded simultaneously with engine test data and exhaust emissions. Experimental results reveal that flash-boiling spray provides shorter spray penetration that delays and reduces impingement onto the piston comparing with liquid spray. In addition, flash-boiling spray leads to stronger flow-spray interaction and larger kinetic energy of the fuel-air mixing, which enhance the subsequent combustion characteristics. The flash-boiling spray also results in earlier flame kernel formation, faster flame propagation and more stable combustion, as well as reduced unburned hydrocarbon (UHC) and soot emissions.

*Key words: direct injection gasoline engine, flash boiling spray, spray characterization, engine combustion and emissions, optical engine, and laser diagnostics.*

## 1. Introduction

In recent years, high-pressure injection system has been utilized widely in spark ignition direct injection (SIDI) gasoline engines for atomizing the liquid fuel into small droplets. The smaller drop size and a wide spray distribution could enhance the interaction between liquid fuel and ambient air throughout intake and compression strokes so that the vaporization and mixing quality could be greatly improved. The benefits of high-pressure direct injection system include precise fuel metering, fast engine response, improved thermal efficiency and reasonable level of emissions [1, 2].

However, in the current generation of production SIDI engines, several issues such as wall wetting, soot formation, output cycle-to-cycle variation and knocking, remain as challenges. First of all, when the fuel injection pressure is high, due to high momentum, fuel spray usually over-penetrates in the cylinder, resulting in impingement onto the cylinder wall and/or piston surface. The evaporation for the adhered fuel is insufficient and liquid fuel remaining on the combustion chamber surface will lead to pool fire in combustion phase. Pool fire is a source for high level of unburned hydrocarbon (UHC) and soot emission [3, 4, 5]. Also the liquid fuel on the combustion chamber wall could easily leak into crankcase to dilute the lubricant oil, and then result in inefficient lubrication and excessive oil consumption. Secondly, cycle-to-cycle variation of combustion process prohibits the SIDI engine from reaching its full potential efficiency. Variation of intake airflow, fuel spray and mixture distribution before combustion all contribute to the combustion variation. Measures that stabilize such processes could suppress the engine output variation. The improved stability of a high-pressure injection system by flash boiling was reported [6]. Thirdly, engine knocking is believed to be associated with end gasoline auto ignition [7]. The current solution for knocking suppression is to implement close-loop ignition timing control based on cylinder block high frequency amplitude sensing [8]. This method could keep the engine from knocking but the engine efficiency would be degraded at the same time due to delayed combustion phasing. Improving the uniformity of the air-fuel mixture could potentially provide opportunity to suppress knocking probability while maintaining the engine running at MBT, due to fast flame propagation and less heterogeneity of the end gas. Moreover, as the emission legislation becomes increasingly stringent, better atomization of fuel in SIDI engines is required to achieve further improved combustion efficiency and reduced emissions.

Further increasing the injection pressure has been constantly proposed as a viable solution. However, the effect of high injection pressure on reducing fuel drop size diminishes since the injection pressure is already very high. Further increasing the injection pressure will not be cost effective. Changing the fuel temperature to improve the atomization quality, as an alternative control factor, has received more attention recently. When the

* Corresponding author: Min Xu
Phone: (+86) 13611728548
Email: mxu@sjtu.edu.cn

fuel is heated to a level that its saturated vapor pressure exceeds the ambient pressure, the spray injected is experiencing flash boiling. Studies of fuel temperature effects on fuel spray started since 1980s, and extensive research of superheated spray has been conducted in the past decades thanks to the fast development of the advanced laser diagnostic techniques [9,10,11]. In our previous works [12,13,14], a systematical study to fully characterize the flash boiling spray, in terms of macroscopic spray structure, drop size distribution, and spray particle flow field and liquid/vapor distribution, etc., was conducted in a constant volume chamber environment using various laser diagnostic instruments. The results have revealed the insight of the flash-boiling spray formation mechanism. Flash-boiling spray has many preferable characteristics, such as shorter penetration, faster evaporation, smaller drop size, and enhanced mixing, etc., which are ideal for SIDI engines as mentioned previously. In this study, the flash-boiling spray was investigated in a single cylinder optical engine using a heated water bath to control the superheated degree (SD) of fuel. High-speed Mie-scattering spray images were recorded to confirm the occurrence of flash-boiling and to study the impingement of spray under various SD conditions. Engine firing tests were conducted with simultaneously recording of flame propagation image, cylinder pressure and exhaust pipe emissions to evaluate the impact of flash-boiling spray on engine combustion and emissions.

## 2. Experimental setup and methodology

### 2.1 Constant volume chamber test setup

A systematic and parametric study has been conducted in a constant volume chamber to characterize the flash-boiling spray by various advanced laser diagnostics under a wide range of engine like conditions. Spray geometry, atomization and evaporation processes of an 8-hole DI injector have been investigated. Fig. 1 shows the schematic of experimental setup. It consists of a constant volume chamber, fuel supply system, fuel temperature control system, pressure control system, and imaging system. The constant volume chamber can achieve absolute ambient pressure between 10kPa and 2MPa. Various optical measurements could be applied via multi-direction optical access of this chamber, including backlit imaging, laser induced fluorescence, high-speed particle velocimetry, drop size measurement and etc. A piston accumulator pressurized by high-pressure nitrogen gas was used to generate various fuel pressures. A special water jacket was used to thermally regulate the fuel injector in order to achieve high fuel temperature. The whole system was synchronized via a multi-channel pulse generator.

Table 1 shows the test conditions. N-hexane was used as the test fuel. Injection pressure ranged from 3.0 MPa to 15 MPa, and injection duration was set as 1.0ms. Ambient pressure varied from 20kPa to 100 kPa at room temperature. Fuel temperature could be adjusted from room temperature to 90 ˚C.

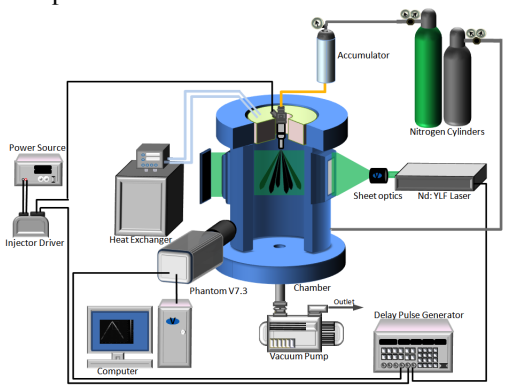


Figure 1. Schematic of experimental setup

Table 1. Test conditions

| Item | Specification |
|---|---|
| Test fuel | n-hexane |
| Test injector | 8-hole DI injector |
| Injection pressure (MPa) | 3.0 - 15.0 |
| Ambient temperature (˚C) | 25±1 |
| Fuel temperature (˚C) | 25, 40, 60,70, 80, 90 |
| Ambient pressure (kPa) | 20, 40, 60, 80, 100 |
| Injection pulse width (μs) | 1000 |

### 2.2 Single cylinder engine with optical access

A four-stroke single cylinder spark ignition direct injection engine (SIDI) running early injection homogeneous combustion was used for further investigation. Optical access includes two pent-roof windows on the cylinder head, a quartz liner and a quartz window on top of the piston with a 45° reflection mirror underneath the piston (Fig 2). The spark plug and the 8-hole SIDI fuel injector located at the central part of the cylinder head and the injector were arranged on the intake side while the spark plug was positioned on exhaust side. Fuel temperature was conditioned by a water bath in upstream close to the injector. The engine operated with a quartz liner for Mie-scattering imaging and with a geometrically–identical metal liner for combustion and emission tests. The engine was equipped with swirl control valve in one of the intake runner to provide different intake charge swirl level. When the SCV was completely closed, high swirl was introduced into the cylinder (swirl ratio of 5.68). When the SCV valve was at fully open position, swirl motion was much reduced (swirl ratio of 0.55). The swirl was measured in a steady flow rig [15]. A pressure transducer (Kistler 6125A) was installed on cylinder head to measure the cylinder pressure with 0.1° crank-angle (CA) resolution. The apparent heat release rate (AHRR) as well as net

indicated mean effective pressure ($IMEP_n$) were computed from cylinder pressure. Exhaust gaseous emission measurements were measured using a Horiba MEXA 7100EGR, in which HC was analyzed with a flame ionization detector (FID), whereas carbon monoxide (CO) and carbon dioxide (CO2) were examined with a non-dispersive infrared (NDIR) analyzer. The MEXA 1000 SPCS from Horiba was used to measure the exhaust particulate number (PN) [11]. The schematic and testing apparatus is shown in Fig.3.

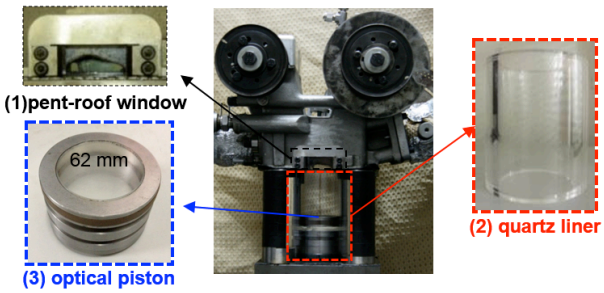


Figure 2 Single-cylinder engine with optical access through: (1) pent-roof window, (2) quartz liner, and (3) optical piston.

The specific engine parameters and experimental conditions are summarized in Table 2. The engine was running at typical dynamometer-based simulated cold start condition [16] at 1200 rpm and 40kPa MAP when the fuel experienced poor evaporation. As a result, large quantity of hydrocarbon and soot were generated and exhausted. The fuel temperature was regulated to 30ºC, 60ºC and 90ºC. With the ambient pressure of 40kPa at injection timing, the superheated degree of the injected fuel correspond to -10ºC, 20ºC, and 50ºC respectively, hence the fuel spray structure would be in non-flash-boiling spray, transitional flash-boiling spray, and flare flash-boiling spray accordingly [17]. The Mie-scattering imaging, and combustion test were conducted under the same condition separately to investigate the characteristics of these three forms of spray in real engine. The swirl control valve was adjusted to fully open or completely closed to investigate the effects of in-cylinder flow on these sprays.

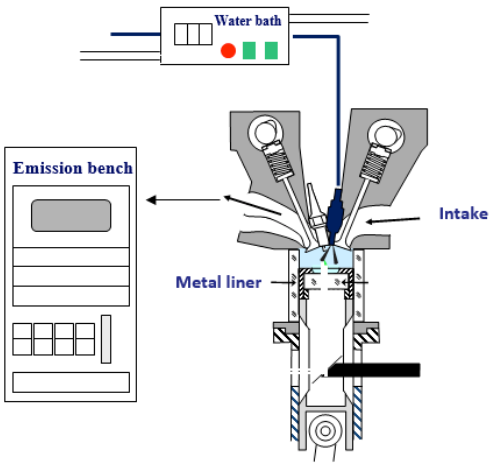


Figure 3 Schematic of engine and testing apparatus.

## 2.2 Optical diagnostics

In this study, a 14-bit monochrome CMOS high-speed camera (Vision Research phantom V7.3) was used in both experiments. For Mie-scattering spray imaging, a Nd:YLF laser (527nm wavelength, 24mJ/pulse @ 1000 Hz, 100ns pulse width) was used to illuminate the entire combustion chamber using a light diffuser to provide uniformly distributed laser beam through the top piston quartz insert from 45° mirror (Fig 4). High-speed camera captured the tumble plane spray images through pent-roof window and quartz liner with recording rate of 1 frame per crank angle degree from start of injection at 300 to 240 CA bTDC firing until the Mie-scattering signal of spray disappeared. The spray images were acquired for 50 consecutive cycles.

Table 2 Engine specifications and operating conditions

| Parameter | value |
|---|---|
| Bore | 86mm |
| Stroke | 94.6mm |
| Clearance Volume | 54.95cm$^3$ |
| Compression Ratio | 11.0:1 |
| Engine Speed | 1200rpm |
| Fuel injection pressure | 10MPa |
| Fuel mass/cycle | 17.6mg |
| Manifold Absolute Pressure (MAP) | 40kPa |
| Engine coolant and oil temperature | 30°C |
| Air/Fuel ratio | 14.7:1 |
| Start of injection | 300° BTDC |
| Spark timing | 15° BTDC |
| Swirl ratio level | 0.55,5.68 |
| Fuel temperature | 30, 60, 90ºC |
| Representative Superheated Degree (by n-hexane) | -10, 20,50ºC |

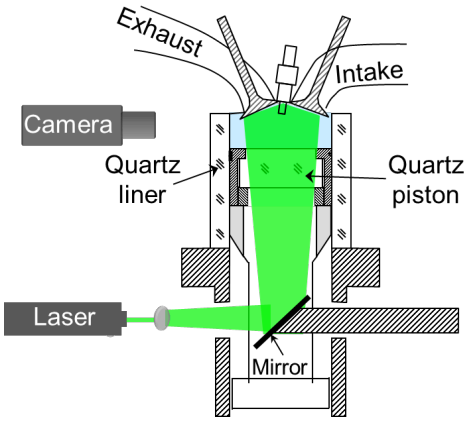


Figure 4 Experimental setup (laser beam was diffused to illuminate the combustion chamber).

In engine firing test with the metal liner, the flame natural illumination was acquired through the piston quartz insert via the 45° mirror using the high-speed camera. The piston insert provided a 62 mm (the bore was 86 mm) diameter view field which could capture the main process of the combustion flame propagation. The

flame detection camera was focused on the swirl plane across the ground electrode of the spark plug for better detection of early flame. The combustion flame image was recorded simultaneously with the cylinder pressure triggered by injection event for 200 continuous cycles.

Post processing of the acquired spray and combustion flame images was developed using Matlab. The detailed processing procedure was explained in [19].

## 3. Results and discussion

### 3.1 Characteristics of flash boiling spray

Figure 5 shows the complete spray characteristics, in terms of spray structure, spray pattern, near field spray at the beginning and the end of injection, nozzle internal flow, sauter mean diameter (SMD) of the spray, vapor concentration and spray/air velocity distribution, under non-flash-boiling condition, transitional flash-boiling condition and flare flash-boiling condition, defined by different Pa/Ps (ratio of ambient pressure to fuel saturation pressure) values into three zones: more than 1, between 0.3 and 1, and less than 0.3, respectively.

Spray structure changes dramatically according to different levels of the superheated degree. For the non-flash-boiling spray, individual fuel plumes clearly separate from each other. Narrow fuel plume penetrates fast along the nozzle direction with relatively poor atomization, which has resulted in long spray penetration. Once the fuel is superheated, fuel plumes expand significantly and start to move towards the central line of the injector, which is shown with shorter spray penetration and wider plume expansion angle under the transitional flash-boiling condition. Further superheating the fuel to the flare flash-boiling condition, has resulted in spray plumes collapsing into a larger single fuel plume. Spray penetration increases again as a single plume spray comparing to the transitional flash-boiling condition, but it is still shorter than that of liquid spray in the non-flash-boiling condition. These unique characteristics of shorter penetration, wider angle and more uniform fuel distribution caused by flash boiling can lead to less fuel impingement and more homogenous mixture formation. From the spray pattern images, which was recorded at 30 mm downstream the injector tip, it is evident that each fuel plume expands as the fuel is superheated, and eventually merges to the center under flare flash-boiling conditions.

Spray atomizes promptly once the fuel is injected out of the nozzle under transitional and flare flash-boiling conditions, which are shown as the near nozzle spray images soon after injection started. No liquid core or ligaments but only fuel mist can be seen under transitional and flare flash-boiling conditions. Near the end of injection, large ligaments were identified under non-flash-boiling condition, which will be the source of high level of HC and soot emissions. However, sprays with extremely tiny fuel droplets are observed under flash boiling conditions, which should be effective to mitigate issues of existence of large fuel drops generated at the end of injection caused by needle bounce. From the nozzle internal flow images, it shows that fuel evaporates at the nozzle exit before it is injected out of the nozzle. Internal vapor bubble size and volume fraction increase when the fuel becomes more superheated. These bubbles rupture instantaneously as soon as being discharged into the ambient, which has led to significant fuel atomization and evaporation.

According to the SMD results, the SMD difference between the injection pressure of 10 MPa and 3 MPa is obvious. Larger injection pressure results in much smaller fuel drop size. However, the difference becomes inconspicuous when the fuel is superheated, which implies that flash-boiling spray is much less dependent on the injection pressure to produce spray with fine droplets. The SMD distribution across the spray region of flash-boiling spray is more uniform than that of non-flash-boiling spray. Due to the significantly reduced SMD, the evaporation of the liquid droplets will be improved dramatically when the fuel is superheated. According to the vapor phase images obtained via laser induced exciplex fluorescence method, only slight amount of fuel vapor was detected under non-flash-boiling condition, but it increased substantially under transitional and flare flash-boiling conditions. The combined effects of direct vaporization due to flash boiling and the rapid evaporation of small liquid droplets due to improved atomization contribute to faster mixing and more homogeneous mixture formation. For the flow field, the LIF-PIV method was used to measure both the fuel spray velocity and ambient air velocity distribution simultaneously. It shows that the interaction between ambient air and fuel spray is enhanced when the fuel becomes superheated. More ambient air is entrained into the main fuel spray plume when further superheating the fuel. Flash-boiling spray promotes mass and momentum transfer between ambient air and fuel spray, which facilitates better mixture formation process.

Figure 6 shows the flash-boiling spray characteristics as a function of Pa/Ps value and the non-flash-boiling spray normalized characteristics as a function of Reynolds number. Under the non-flash-boiling condition (Pa/Ps>1), spray plume width, penetration, plume distance, SMD, and vapor quantity are almost independent of Pa/Ps (Fig. 6(a)). Weber number, Reynolds number, and air-to-liquid density ratio are normally used to characterize the spray characteristics of non-flash-boiling spray (Fig.6(b)).


| Item | Non-flash boiling condition (Pa/Ps≥1) | Transitional flash boiling condition (0.3≤Pa/Ps<1) | Flare flash boiling condition (Pa/Ps<0.3) | Flash boiling spray benefits |
|---|---|---|---|---|
| Spray structure | | | | • *Avoid wall impingement*<br>• *More uniform fuel distribution* |
| Spray pattern (30mm below the tip) | | | | • *Wider cone angle*<br>• *More uniform fuel distribution* |
| Near nozzle spray (Initial injection) | | | | • *Prompt atomization and boiling vaperization* |
| Near nozzle spray (end of injection) | | | | • *Improved atomization at the end*<br>• *Solve emission issues* |
| Nozzle internal flow | | | | • *Reduce liquid core*<br>• *Generate bubbles for flashing atomization* |
| SMD | 40 um 0 um | 40 um 0 um | 40 um 0 um | • *Smaller and uniformly distributed fuel drop size*<br>• *Less dependent of injection pressure* |
| Evaporation (vapor phase) | | | | • *Enhanced fuel vaporization* |
| Velocity distribution | | | | • *Faster mixture formation* |



Figure 5 Spray characteristics of non-flash-boiling and flash-boiling conditions.

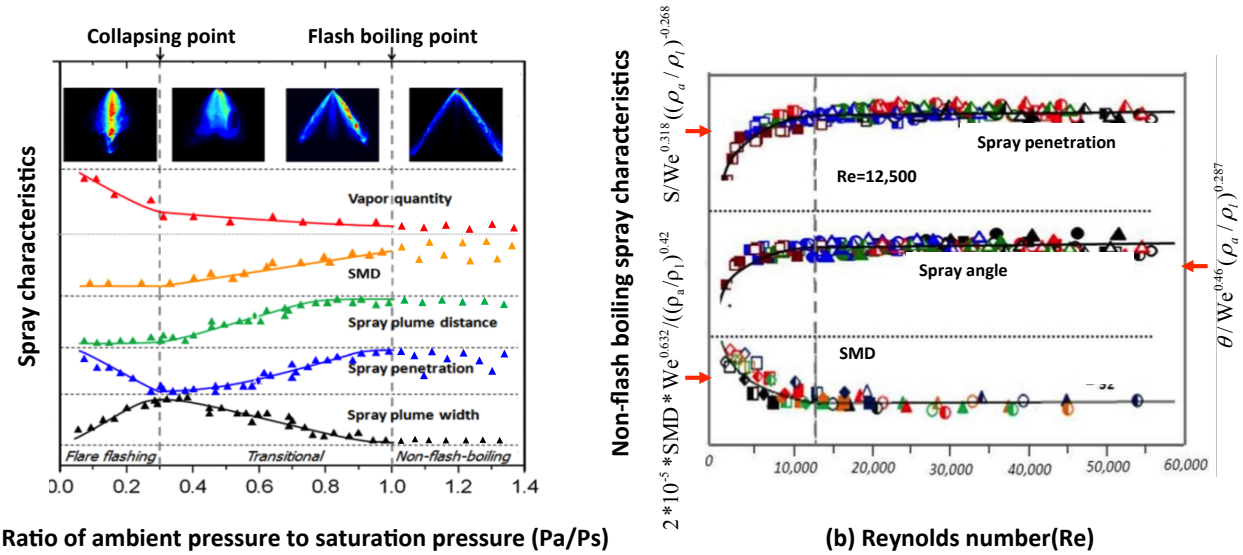


(a) Ratio of ambient pressure to saturation pressure (Pa/Ps) (b) Reynolds number(Re)

Figure 6 Spray characteristics versus Pa/Ps value and Reynolds number.

Figure 6 (b) shows the normalized characteristics of non-flash-boiling sprays versus Reynolds number. The spray breakup depends on the competition between the inertia force, surface tension force, viscous force and aerodynamic drag force acting on the liquid-jet surface. When Pa/Ps is smaller than 1.0, liquid spray undergoes flash boiling, and Pa/Ps value governs the spray characteristics. Fuel bubbles generated inside the nozzle hole and subsequent flash boiling effect trigger the prompt atomization and vaporization of spray, which leads to smaller SMD and stronger vapor concentration. When Pa/Ps is between 0.3 and 1.0, it leads to shorter spray penetration, wider spray plume width, smaller plume distance, smaller drop size, and increased vapor quantity with decreasing Pa/Ps value, as shown in Fig 6 (a). However, further decreasing Pa/Ps value (smaller than 0.3) leads to smaller plume width, longer spray penetration, much faster evaporation.

In summary, spray plume collapsing plays a vital role in these unique spray characteristics. Flash-boiling spray is shorter and wider spray with significantly enhanced atomization and evaporation characteristics even under very low injection pressure. It has great potential to solve some critical issues caused by the high-pressure liquid spray characteristics in today's SIDI engines. These claims need to be verified and assessed carefully in the real engine, and evaluated in terms of combustion and emissions, which are the main objectives presented in the next sections.

## 3.2 Spray in the optical engine and impingement study

Spray Mie-scattering images taken at 1.1ms ASOI (after start of injection) are shown in Figure 7, to demonstrate the effect of superheated degree on fuel spray structural transformation in an optical engine. It is clear that with the increase of fuel temperature, the spray shape changes significantly. At 30ºC fuel temperature, the spray in 7 (b) shows typical liquid spray structure that 8 plums can still be clearly identified while the spray angle is similar to those when the engine is not running (a). However, different from the quiescent conditions in the constant volume chamber, the spray structure is still affected by the in-cylinder airflow. With the increase of fuel temperature to 60ºC shown in Figure 7(c), the spray penetration decreases and it becomes wider. The plume-to-plume interaction demonstrates a vague boundary between different plumes. A vortex is found at the tip of the spray. It resembles a typical transitional flash-boiling spray. When further increasing the fuel temperature to 90ºC, the multiple spray plumes collapse into a single mass and a clear vortex can be observed at the tip of the spray. The spray structure change with temperature clearly agrees with prior knowledge of flash-boiling spray obtained in the constant volume chamber.

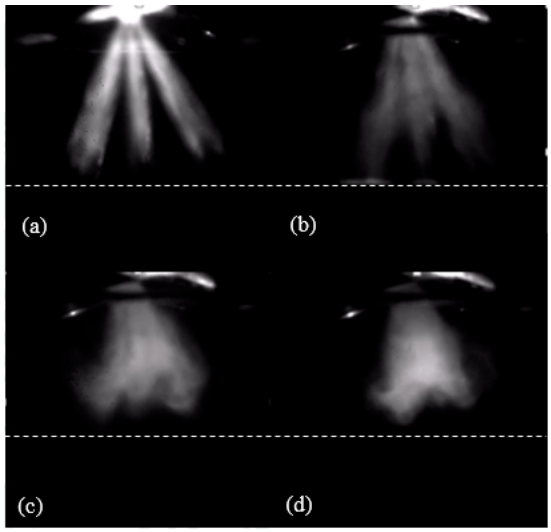


Figure 7 Spray images in engine recorded at 1.1ms ASOI (a) Engine not running; (b) 30ºC fuel temperature, 1200 rpm engine speed, low swirl ratio and -300 aTDC SOI; (c) and (d) are same condition as (b) but fuel temperature set to 60 and 90ºC respectively.

The dash lines in Fig.7 represent piston top surface at this crank angle. Liquid spray impinging on the piston surface is undesirable for combustion and emissions. To quantitatively evaluate the improvement of flash boiling on reducing impingement, the ensemble averaged impingement index among all 50 cycles for each crank-angle within the cycle was computed [20]. The results for liquid, transitional and flare flash-boiling sprays are depicted in Figure 8. Flash boiling delays the start of impingement by 2 CAD on average and 15% of impingement reduction at peak locations are found. Moreover, based on the constant chamber study, the collapsed flash-boiling spray contains large quantity of vapor. This could reduce the impinging liquid quantity even more.

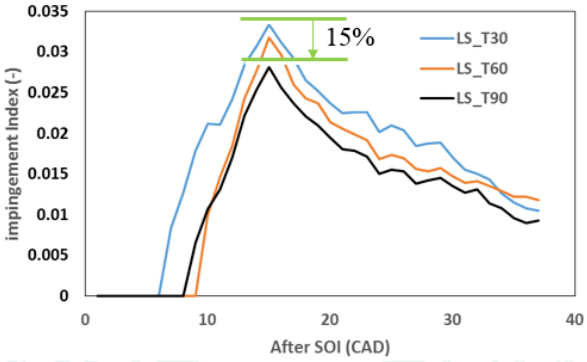


Figure 8 Averaged impingement index as a function of crank angle, for three fuel temperatures of 30, 60 and 90 ºC at low swirl ratio.

## 3.3 Engine combustion and emissions

Metal liner tests were carried out at 1200 rpm, at fixing the spark and injection timings of 15 and 300 CAD bTDC respectively. The results shown in Fig. 9 indicate the baseline condition when the engine coolant and oil as well as the fuel temperature were maintained at 30 ºC. The engine experiences severe cycle-to-cycle variation that the COV of IMEP is more than 6% while the IMEP output is low. The degraded engine performance is mainly attributed to the cold engine condition, which is unfavorable for fuel evaporation. With the increase of fuel temperature, the IMEP increases notably while the engine variation COV of IMEP falls below 3%, which is of significant importance to improve engine operation at cold start condition.

The combustion duration derived from cylinder pressure is shown in Fig. 10. The shorter combustion duration with increased fuel temperature indicates that both the increased combustion burn rate and decreased combustion duration should be the reasons for higher IMEP and reduced combustion variation. The poor fuel-air mixture formation at 30ºC fuel temperature should be the main reason for long combustion duration, while improved atomization and evaporation of flash-boiling spray enables better mixture preparation and results in better combustion performance.

Swirl ratio also exhibits additional positive effects on combustion. With the increased swirl ratio, the fuel temperature effect trends remain the same, but the magnitude increases. A higher swirl ratio leads to a larger IMEP, a smaller COV of IMEP, and narrower combustion duration.

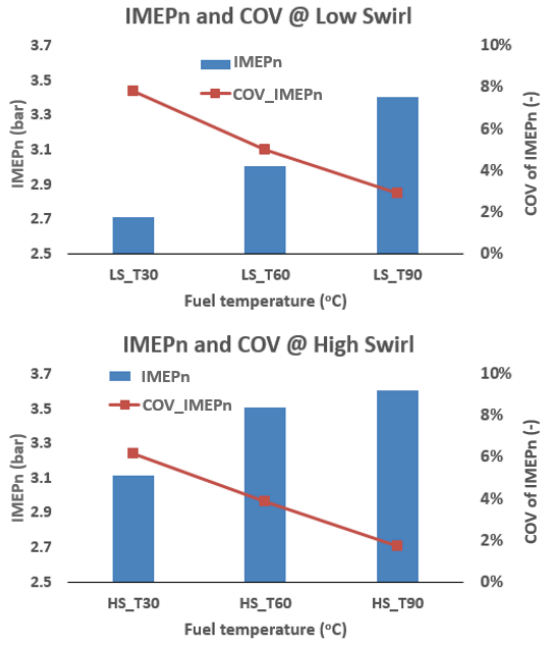


Figure 9 Combustion $IMEP_n$ and standard deviation of $IMEP_n$ under different fuel temperatures and swirl ratios.

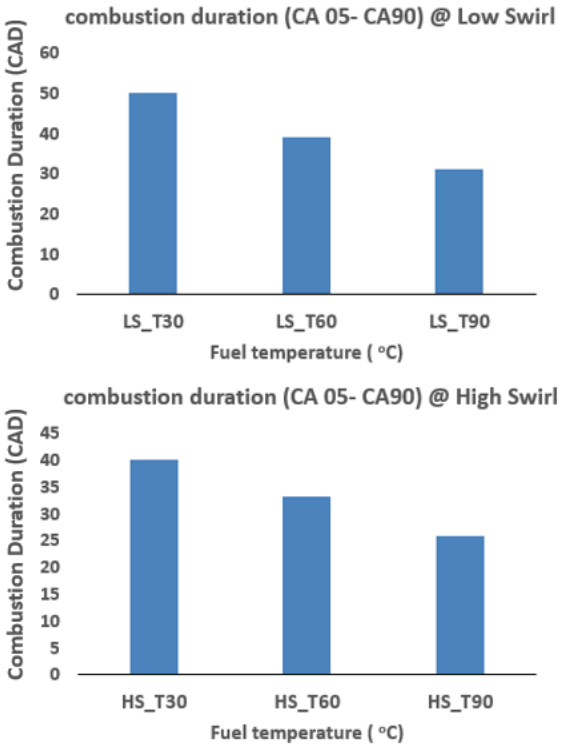


Figure 10 Combustion duration under different fuel temperatures and swirl ratios.

The regular engine-out emissions as well as particulate number measured in exhaust pipe are shown in Fig.11. The unburned hydrocarbons, CO and particulate mass are generated mainly by incomplete

combustion resulting from inefficient mixing. With the use of flash boiling spray, the mixing quality is improved while the impingement is reduced. Increasing the fuel temperature from 30ºC to 90ºC reduces THC, CO and PN by 9%, 30%, and 60%, respectively. The reduction of THC and PN is evident for better mixing while less CO also indicates the improvement of combustion efficiency. The rise of $NO_x$ reflects that the combustion temperature increases which also indicate that the combustion efficiency is improved. Since under engine cold start condition, increasing exhaust temperature to minimize catalyst light-off time and PN reduction is more important, and the influence of increasing $NO_x$ is less problematic.

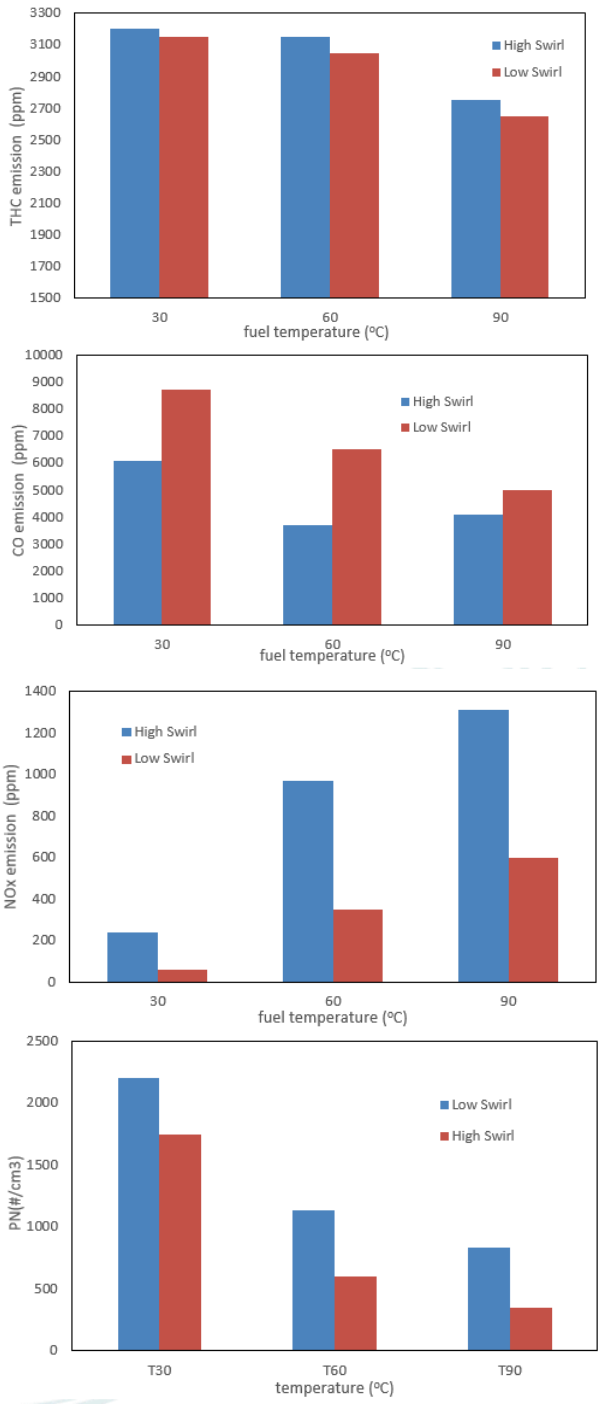


Figure 11 Exhaust emissions of THC, CO, NOx and PN in combustion test under various fuel temperatures.

Under high swirl condition, the effect of fuel temperature on emission shows the same trend. But with improved combustion efficiency the emission of CO and soot are even more reduced while more $NO_x$ is generated. The effect of different swirl ratio on THC is not so pronounced.

## 3.4 Combustion flame analysis

The flame area development trace is shown in Fig. 12 to provide more insight of the characteristics of flash-boiling spray combustion. The plateau of the flame area curve (3019mm$^2$) is the limitation of the piston view and close to the total piston area. For cold spray conditions (30ºC), the flame develops slowly and does not reach the full view area of the quartz piston, indicating incomplete combustion. When flash-boiling spray is introduced, the flame covers the entire piston view area. For 60ºC fuel temperature, the flame reaches the boundary before 25 aTDC. At 90ºC fuel temperature, the flame reaches the boundary around 10 aTDC. Steeper slope of flame area growth guarantees the combustion event to be completed immediately after passing the top dead center, which is important for improving engine efficiency and reducing engine out emissions. Swirl also increases flame speed and helps the flame reach the boundary sooner.

It can be also observed that after the early kernel development period when the flame area reaches a certain value, (for example dashed line in Fig 12), the flame area growth rate becomes stable. The flame area is estimated to be 300mm$^2$ in this study and further analysis will be conducted later.

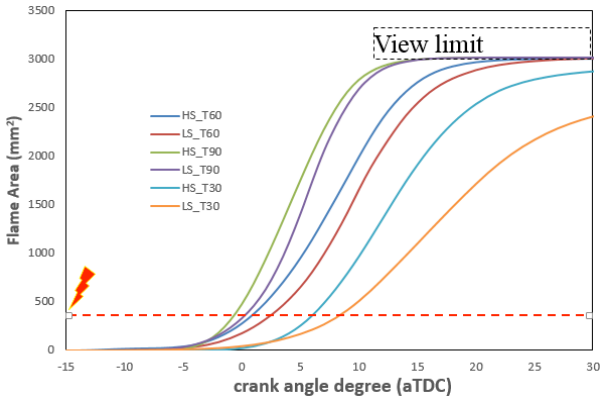


Figure 12 Flame propagating area under various fuel temperatures and swirl ratios, averaged 200 cycles for each condition

Figure 13 shows the flame-probability maps at different conditions to compare the combustion stability of non-flash-boiling and flash-boiling sprays at the crank angles of 3 CAD bTDC. The area whose probability is higher than 30% is provided in the top-right of each map to estimate the flame development of each condition and the stability of the combustion. Note that for few cycles of LS_T30 (note: LS_T30 corresponds to low swirl with fuel temperature of 30ºC) condition, the flame kernel is

not fully developed that the spark plug blocks part of the flame image, but this does not affect the conclusions of this study. For 30ºC fuel temperature tests, the flame develops slowly and the probability area higher than 30% is very small, indicating that the repeatability of the combustion is poor. As the fuel temperature increases, the flame area also develops faster and reaches larger area at the studied crank angle, which results in the area of probability higher than 30% increases dramatically compared with typical cold start condition. Area of probability larger than 90% is identified left to the spark plug for fuel temperature of 90ºC. However, it is not found for lower fuel temperatures. Faster and more repeatable flame development contributes to the improved combustion efficiency and reduced emissions.

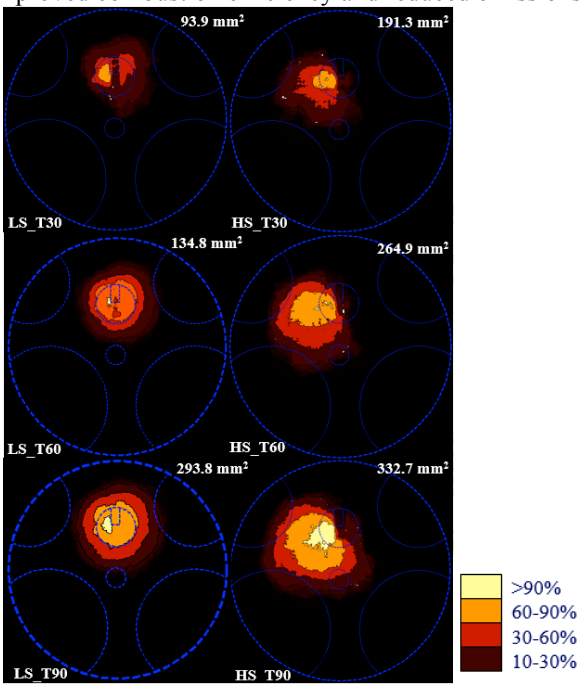


Figure 13 probability maps for flame development: bottom-left of each image shows the conditions; Top-right shows the area higher than 30% (200cycles average at 3 CAD before TDC).

In Fig.14, the distributions of number of flame cycles reaching 300 mm$^2$, which are considered to be stable initial flame size, are plotted. It can be observed that for fuel temperature of 30 ºC, the flame grows to a stable size very late after TDC, and the distribution of the crank angles reaching 300mm$^2$ is much wider. These indicate higher variability of combustion process. With the fuel temperature increase to 90ºC, the crank angle of peak count advances by 5-6 CAD while the distribution is more concentrated to illustrate more repeatable flame development. Therefore, faster and more repeatable flame can be achieved when flash-boiling spray is used.

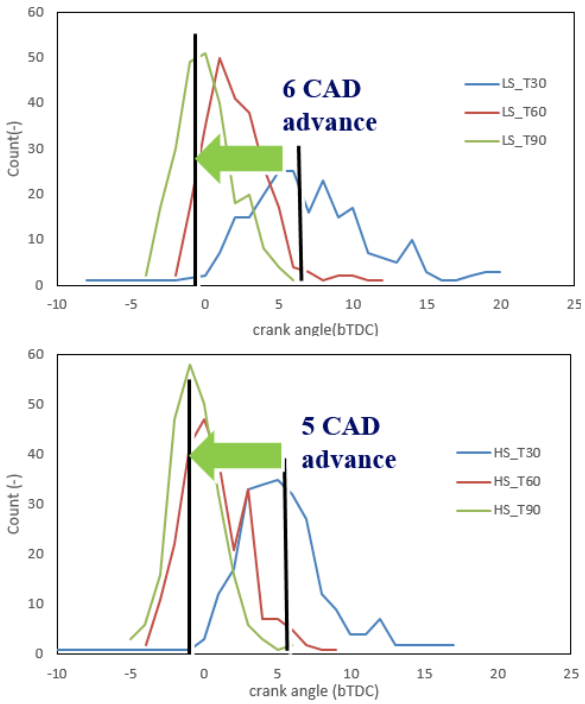


Figure 14 Distribution of the number of flame cycles reaching 300mm$^2$ under different conditions.

## 4. Conclusions

In this study, the flash-boiling spray was realized by controlling the fuel temperature in a single cylinder optical engine. Three temperatures of the liquid fuel provided distinct conditions of liquid spray, transitional flash-boiling spray, and flare flash-boiling spray to investigate the characterization of spray and combustion under simulated cold start condition in real engine. Following conclusions can be drawn:

(1) Mie-scattering imaging confirms the occurrence of flash-boiling spray during injection by controlling the fuel temperature. Analysis reveals that the delayed and reduced wall impingement is realized by flash boiling sprays.

(2) Combustion test shows that the higher engine performance, the lower engine cycle-to-cycle variation and lower emissions of THC, CO and PN can be achieved by increasing the fuel temperature.

(3) Flame image analysis reveals that at low fuel temperature, the flame develops slowly due to the poor spray atomization and mixture preparation. Flash-boiling spray elevates the flame development rate while the flame repeatability is also increased.

The flash-boiling spray could be a viable solution for more stringent legislation on emissions and lessens the requirement of increasingly high fuel injection pressure. It provides new opportunity for advanced SIDI combustion system design and development. The mechanism of combustion improvement by flash-boiling spray is still not sufficiently clear and will be further studied in future works.

## 5. Acknowledgments

This research is sponsored by National Natural Science Foundation of China (NSFC) under grants No. 51376119/E060502 and 51176115/E060404, and carried out at the National Engineering Laboratory for Automotive Electronic Control Technology of Shanghai Jiao Tong University.

## 6. References

[1] F. Zhao, M.-C Lai, and D.L. Harrington, Prog. Energy Combust. Sci. **25** (5) (1999), pp. 437-562.
[2] M.C. Drake, T.D. Fansler and A.M. Lippert, Proc. Combust. Inst. **30** (2) (2005), pp. 2683-2691.
[3] J.Serras-Pereira, P. G. Aleiferis, and D. Richardson, Fuel. **91** (1) (2012), pp.264-297.
[4] S.T. Chin and C.F. Lee, Proc. Combust. Inst. **29** (1) (2002), pp.767-773.
[5] T. Sagawa, H. Fujimoto and K. Nakamura, SAE Technical Paper No.2002-01-1647, 2002.
[6] H. Chen, Ph.D thesis, Shanghai Jiao Tong University, pp. 113-114, 2013.
[7] J.B. Heywood. Internal combustion engines fundamentals. McGraw-Hill Inc. 1988.
[8] M. Nakano, S. Nakahara and K. Akihama, SAE Technical Paper No.952408, 1995.
[9] R.D. Oza and J.F. Sinnamon, SAE Technical Paper No. 830590, 1983.
[10] M.M. Vieira and J. Simoes-Moreira, J. Fluid Mech. **572** (2007), pp. 121–144.
[11] E. Sher, T. Bar-Kohany and A. Rashkovan, Prog. Energy Combust. Sci. **34** (4) (2008), pp. 417–439.
[12] W. Zeng, M. Xu, G. Zhang, Y. Zhang and D.J. Cleary, Fuel, **95** (0) (2012), pp. 287-297.
[13] W. Zeng, M. Xu, M. Zhang, Y. Zhang and D.J. Cleary, Experimental Thermal and Fluid Science, **40** (0) (2012), pp. 81-92.
[14] M. Xu, Y. Zhang, W. Zeng, G. Zhang, M. Zhang, and D.J. Cleary, SAE Int. J. Fuels Lubr, **6** (1) (2013), pp.137-148.
[15] I.E. Karaiskos, PhD Thesis, University of London, 2005.
[16] D.J. Cleary and R.O. Grover, Jr., Proceedings of the ASME ICEF2013, Volume 1.
[17] J Su, M Xu, Y. Zhang, D.L.S Hung and T. Li, Proceeding of COMODIA **8**, Fukuoka, Japan (2012), pp. 98–103.
[18] H. Chen, D.L.S. Hung, M. Xu, H. Zhuang and J. Yang, Experiments in Fluids, **55** (4) (2014), pp.1-12.
[19] D.L.S. Hung, H. Chen, M. Xu, J. Yang and H. Zhuang, ASME J. Eng. Gas Turbines Power, **136** (10) (2014), pp. 101503.
[20] H. Chen, M. Xu, D.L.S. Hung, J. Yang and H. Zhuang, Proceedings of 16th Annual Conference on Liquid Atomization and Spray Systems - Asia, Nagasaki, Japan, (2013), p. 136-142.

**Proceedings of the Australian Combustion Symposium**
**December 7-9, 2015, The University of Melbourne**

# Petascale direct numerical simulations of laboratory flames

Evatt R. Hawkes[1,2*]
[1]School of Mechanical and Manufacturing Engineering,
[2]School of Photovoltaic and Renewable Energy Engineering,
The University of New South Wales,
Sydney, NSW 2052, Australia

**Abstract**
Achieving significant improvements of fuel efficiency and reductions of emissions (including $CO_2$) requires better understanding of the multi-physics turbulent flows that govern the performance of combustors. Direct numerical simulations (DNSs) have long been used to obtain this understanding, but until recently they were limited to very idealised scenarios. Advances in supercomputing have enabled rapid progress, such that DNSs of laboratory-scale experiments are now possible. In this article I will discuss recent examples of DNS performed in my group at the University of New South Wales, focussing on the stabilisation of lifted flames and on flame structure in high Karlovitz number lean premixed flames.

*Keywords: Direct numerical simulation; lifted flames; high Karlovitz number premixed flames*

## 1. Introduction

This century, the global energy sector will grow significantly, and it is imperative that it does so while making deep cuts in $CO_2$ emissions, dramatically improving urban air quality, adapting to new fuels, and integrating significant renewable generation. Cost-effectiveness is essential, especially considering that a massive 93% of the projected growth will be in non-OECD nations including China and India [1]. Cost-effectiveness is fundamentally what has driven the global dominance of combustion-based energy to date. It fundamentally derives from the exceptionally high stored energy density of fuels and their despatchability on-demand. Renewables such as photovoltaics and wind are progressing extremely rapidly and will gain significant market share – mostly by displacing coal-fired electricity – as they need to if we are to respond effectively to the challenge of climate change. However, it is important to recognise that their penetration will be insufficient to exclusively meet the diverse needs of the global energy sector in a cost-effective manner, especially in much of transportation (heavy duty, shipping, and aviation) and in the provision of high temperature industrial process heat. Even for electricity applications, highly despatchable combustion energy can significantly lower the overall cost of large-scale renewables. The IEA predicts that by 2035, 60% - 80% of energy needs will still be met from combustion [1], which implies that combustion research will be needed for decades at least.

It is important to understand that while existing combustion technologies have been developed incrementally over many decades, the drivers for these developments have radically changed in recent times, with development efforts now strongly focussed on lowering particulate, $NO_x$, and $CO_2$ emissions. However, current development cycles are too slow and costly, which is fundamentally driven by the complexity of the processes governing performance and emissions. They involve turbulent, multi-scale flows, which are highly complex, non-linear and which have interdependent physics. Existing understanding of these processes is insufficient and surprisingly lacking given the prevalence of combustion-based energy systems.

To gain this understanding, combustion science employs axes of experimentation and computation, which are both underpinned by combustion theory [2]. Experimental investigations of turbulent combustion have made great strides, e.g. [3-8], but even the most advanced experiments typically measure a only few relevant variables, such as a few species concentrations, temperature, or velocities, typically in two or fewer spatial dimensions.

Computational studies are increasingly recognised as a viable alternative to provide the required lacking information. These studies are categorised based on the level of resolution of turbulence they provide [9]. For practical combustion systems, it is rarely affordable to completely resolve all length- and time-scales of the problem, due to the large range of scales involved. Therefore, practically useful models such as Reynolds-averaged Navier-Stokes models and large-eddy simulations do not attempt to resolve small scales, which then requires approximations for the effects of unresolved phenomena. As a result, these approaches have only a limited utility in providing fundamental understanding of turbulent combustion. In contrast, direct numerical simulation (DNS) is an approach to modelling turbulent flows that completely resolves the smallest scales of turbulence and scalar fields. With the full three-dimensional, time-varying fields of all

* Corresponding author:
Phone: (+61) 2 9385 4602
Email: Evatt hawkes@unsw edu au

simulated variables available, it is an extremely useful tool for computational investigations of turbulent combustion phenomena.

To maximise its realism, it is usually desirable for DNS to represent a large dynamic range of scales, which has resulted in DNS being a computationally demanding exercise. Because of this inherent computational intensity, the development of the DNS technique has closely followed the development of supercomputing resources. DNS of non-reacting turbulent flows became feasible in the early 1970's with early work focussing on isotropic turbulence [10, 12]. Interest in DNS of combustion started to grow in the mid 1980's [13-15], with many significant studies being reported by the mid 1990's [16-20]. Obviously, these early studies required significant simplifications such as the use of small domains, highly idealised configurations, and considerable simplifications of chemistry models (such as infinitely fast or one-step chemistry assumptions).

Since 1993, the development of supercomputing power has been systematically monitored by the top500 project [21]. Figure 1 shows the computational power, measured in floating point operations per second as measured by the LINPACK benchmark, of the cumulative performance of the top 500 most powerful supercomputers in the world [21]. The trajectory has been very impressive, with the cumulative performance approximately doubling every 6.5 months, beating Moore's law considerably. Complementing these hardware developments has been the development of DNS codes that are able to make use of massively parallel supercomputing resources e.g. [4, 18, 22, 23]. As a result, significant progress has been made with the DNS approach such that DNS of some (but not all) laboratory-scale experiments has recently become possible. Notable examples of early work in this direction include DNS of lifted flames [24], premixed v-flames [25] and Bunsen-type flames [26].

In the above context, the objective of this article is to demonstrate what is now possible with the DNS approach using leadership-class supercomputing resources, which are capable of $10^{15}$ floating point operations per second (i.e. petascale computers). In this article I review advances in two areas. First, I review progress, originally reported in Refs. [27, 28], in performing the first DNS of laboratory-scale lifted hydrocarbon flame in a non-autoignitive environment, with the objective of understanding the stabilisation mechanism of this flame. Second, I review progress, reported in Refs. [29, 30], in performing the first DNS of a laboratory-scale premixed jet-type flame, using an accurate, multi-step chemical kinetic model for methane combustion, including $NO_x$ formation. The considered case represents a very high turbulence level, as measured by the Karlovitz number, and I report a direct comparison with experiment and an analysis of the internal structure of the flame.

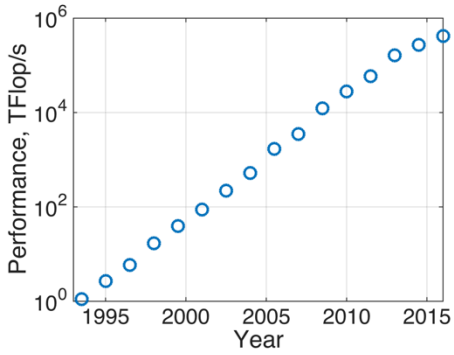


**Figure 1:** Summed performance of the top 500 most powerful supercomputers on the LINPACK benchmark, according to the top500 project [21].

## 2. DNS code

Both runs used versions of S3D [31]. Originally developed at Sandia National Laboratories, S3D is now in use by a number of groups worldwide. It solves the compressible governing equations of mass continuity, momenta, energy, and the mass fractions of chemical species including chemical reactions using finite difference methods. The equation sets are solved in a fully coupled way including the two-way interaction of heat release and flow.

The approach to solve the resulting set of coupled and non-linear partial differential equations is designed to exploit highly concurrent leadership computing architectures. The governing equations are solved on a conventional three-dimensional structured Cartesian mesh. Spatial differentiation is achieved through eighth-order finite differences. The differentiation and filtering require nine- and eleven-point centred stencils, respectively. Time advancement is achieved through a six-stage, fourth-order explicit Runge-Kutta (R-K) method, avoiding the expensive all-to-all communication required in implicit methods.

Figure 2 demonstrates the excellent strong scaling performance on a Cray XC-30 for a typical problem. (In a strong scaling test, the problem size remains fixed while the number of processing units is varied.) The reasons for this performance are explained as follows. In the S3D code, each rank is responsible for a piece of the three-dimensional domain; all message-passing interface (MPI) ranks have the same number of grid points and the same computational load under a Cartesian decomposition. Inter-rank communication is only between six nearest neighbours to exchange ghost-zones for derivative evaluation. The amount of data exchanged between neighbours is determined by the size of the finite difference stencil and is <15% of the data held by each process. Global communications are not a bottleneck and are mainly required for monitoring and synchronisation ahead of input/output. To minimise slow data transfers, care is taken with MPI rank placement to locate neighbours systematically first by cores on a socket then by sockets on a node. A

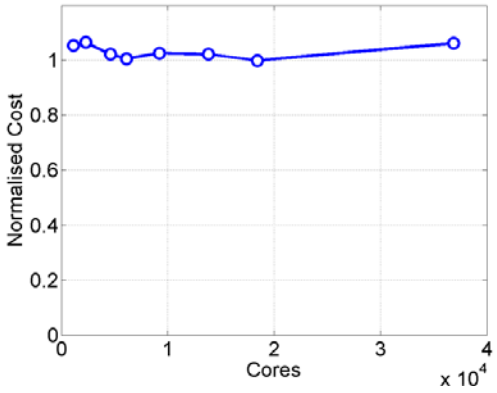


**Figure 2:** Strong scaling on a Cray XC-30; near-perfect scaling (near independence of total cost as core number is varied) is observed.

communication queue system ensures that MPI receives for non-blocking sends are pre-posted to enable use of remote direct memory access writes from the network interfaces. As a result of these features, S3D scales up to at least 200,000 processor cores, making it capable of conducting very large scale DNS as reported herein.

## 3. Lifted flame case

### 3.1 Objectives – lifted flame case

Lifted flames occur in many combustion applications including in certain types of gas turbines and in many industrial furnaces. The stabilisation of the flame is very important since it affects the overall combustion stability and pollutant emissions, as well the overall geometry and thus size of the combustor. Lifted flame stabilisation is therefore a topic that has been hotly debated in the combustion community for decades in hundreds of articles – see the reviews in Refs. [32, 33] – with no definitive conclusion having yet been arrived at.

The main theories for lifted flame stabilisation (in non-autoignitive environments) are now briefly reviewed. For flames having a large lifted height (over 20D), one theory posits that the region upstream of the flame is relatively well mixed and the flame is stabilised by a turbulent, premixed flame propagating into this flammable mixture [34, 35]. For lower lifted heights (less than 20D), the theory that has the most support is the edge-flame theory, where a partially premixed edge-flame, which may or may not have a tribrachial structure, propagates along the unburned stoichiometric iso-surface, with its propagation speed balancing oncoming flow. Another theory proposed for low lifted heights [36] is that stabilisation occurs due to a critical mixing rate being exceeded at locations further upstream, thus preventing more upstream stabilisation [36]. Several theories have also proposed a role played by large eddies, variously involving the turbulent transport of hot products, intermittency of turbulent and mixed regions, and modulation of lifted heights due to edge-flames propagating over large coherent jet structures [22, 37, 38].

In evaluating these theories, one of the key missing pieces of information is that the flame propagation velocity has never been instantaneously measured. Flow velocities have been measured and are generally shown to be the same order of magnitude as the laminar burning velocity, e.g. [38-40]. However, measurement of the flame propagation velocity relative to flow has not been possible because the flame locations were determined from two-dimensional measurements, e.g. by planar laser-induced fluorescence (PLIF) of radicals [32]. A consequence of the two-dimensionality is that out-of-plane flame motion could cause apparent in-plane motion if flame surfaces are not aligned perpendicular to the measurement plane. Due to the observed appearance of upstream flame islands in many measurements [23, 41] it is certainly known that out-of-plane motion exists.

Prior to this work, only a few DNS of lifted flames had been reported. An early study reported a simulation of hydrogen lifted flames [24, 42]. Although by today's standards, this simulation was not resolved well enough to be termed "DNS", it nonetheless provided some very important overall information with a vigorous inner premixed flame being identified and detached islands of diffusion flame being reported. The stabilisation mechanism was not analysed in detail, however. More recently, much larger DNS were reported modelling lifted hydrogen [43] and ethylene [44] flames; however these DNS were focussed on conditions of very hot co-flows, where autoignition was clearly the main mechanism of stabilisation.

In this context, the objectives of this part of the article are to report the first DNS of a hydrocarbon-relevant lifted flame in a non-autoignitive environment, and to study this flame to learn about the flame stabilisation mechanism.

### 3.2 Methods – lifted flame case

The DNS were completely described in Karami et al. [27, 28], so only a brief description of key details is reported here for orientation.

For these DNS, we considered it important to select parameters that were relevant to a typical laboratory-scale lifted methane flame. A considerable effort was spent on determining whether this could be done with a multi-step chemistry model. Methane lifted flames will not stabilise on small burners, so a reasonably large burner size of ~ 4 mm was selected. With a burner size this large, detailed chemistry was precluded due to the need to resolve a radical layer, which would have implied a computational cost that considerably exceeded what was available, not just in

Australia but overseas as well. Therefore, it was decided to employ a one-step chemistry model, which requires about a factor of 8 fewer grid points. The single-step chemistry model was, however, modified according to the approach suggested in Ref. [45] in order to correctly reproduce the dependence of the laminar flame speed on equivalence-ratio that is typical of hydrocarbon fuels.

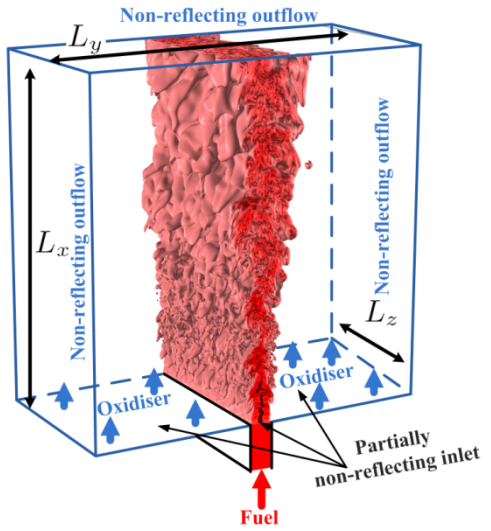


**Figure 3**: Schematic of the domain and the configuration of this study.

**Table 1**: Numerical and physical parameters of the simulation.

| Description | Value |
|---|---|
| Domain size ($L_x \times L_y \times L_z$) | 16H×24H×6H |
| Number of grid points ($N_x \times N_y \times N_z$ ) | 800×800×300 |
| Mean inlet jet Mach number ($U_j/a_{ref}$) | 0.48 |
| Laminar co-flow Mach number ($U_{co}/a_{ref}$) | 0.001 |
| Jet non-dimensional temperature ($T_{jet}$) | 2.5 |
| Co-flow non-dimensional temperature ($T_{co\text{-}flow}$) | 2.5 |
| Jet Reynolds number (Re) | 5280 |
| Inlet velocity fluctuation intensity | 5% |
| Fuel mass fraction in the fuel stream ($Y_{F,o}$) | 1.0 |
| Oxidiser mass fraction in the oxidiser stream ($Y_{O,o}$) | 0.233 |
| Stoichiometric oxidiser to fuel mass ratio (r) | 4.0 |
| Heat-release parameter (α) | 0.86 |
| Zel'dovich number (β) | 5.0 |
| Non-dimensionalisation Damköhler number (Da) | 800 |
| Lewis number (Le) | 1.0 |
| Prandtl number (Pr) | 0.7 |

It was decided to run a slot-jet case rather than a round jet case, as the latter are considerably more expensive due to the need to accommodate jet spreading in two directions and due to the longer run time required to converge statistics, particularly near the centreline. Figure Figure 3**: Schematic of the domain and the configuration of this study.**shows a schematic of the computational domain and the boundary conditions used. The mean inlet axial velocity and fuel mass fraction were specified using a tanh-based profile. The velocity fluctuations at the inlet were imposed using an auxiliary homogeneous isotropic turbulence field, produced based on a prescribed turbulent energy spectrum with a turbulence intensity of 5%. A non-reflecting boundary condition was imposed at the outflow while a partially non-reflecting boundary condition was imposed at the inflow. A periodic boundary condition was used in the spanwise direction.

Table 1 lists the physical and numerical parameters employed. To determine appropriate simulation parameters, the bulk parameters were approximately matched with an experimental jet flame reported in [46]. Therein, $S_L/U_j$=0.013, $\delta_L/H$=0.13, and Re=5,280 while in our simulation we have $S_L/U_j$=0.016, $\delta_L/H$=0.16, Re=5,280. The total grid number was 256 million. The resolution was selected both to provide a minimum Kolmogorov scale of more than 0.5 times the grid spacing and to resolve typical flame profiles with at least 10 grid points. The simulation was run for 18.0 jet flow through times, $t_j = L_x/U_j$ (where the $L_x$ is the length of the computational domain in the streamwise direction), to obtain a statistically stationary, solution and the data from the last $12.0t_j$ were used for the analysis. The simulation was performed on computational resources available at the Australian National Computational Infrastructure Facility (a Fujitsu Primergy) and required 400,000 CPU-hours on 8,000 Intel Xeon Sandy Bridge processors running for about 2.5 days. Further details of numerical methods are presented in Karami et al. [27, 28].

### 3.3 Results – lifted flame case

General flame structure

The volume rendering of logarithm of the scalar dissipation rate (blue/white) and reaction rate (red/orange) is presented in Figure 3. It may be observed that the flame has a complex structure. Overall there is a highly wrinkled leading partially premixed edge-flame followed by a trailing diffusion flame. Further aspects of the structure are described below.

Unlike the hydrogen DNS of Mizobuchi et al. [24, 42], a vigorous rich premixed flame core is not observed. This is attributed to the fact that hydrogen burns much more vigorously than hydrocarbons in rich mixtures. Islands of diffusion flame on the lean side that were noted by Mizobuchi et al. [24, 42] are also not observed. Rather, the trailing flame is a mostly connected diffusion flame with some flame holes. Diffusion flame islands also might have been a hydrogen-specific feature.

There is a proliferation of flame holes, not observed in earlier DNS studies of lifted flames [24, 42-44]. Although the analysis of the holes is not the focus of this paper, it is noted here that the holes originate by two different mechanisms. Some of the holes are generated by flame propagation at the leading edge to surround an unburned region with burning regions while others are caused by local flame

extinction. Both kinds of holes can either grow or shrink and disappear as they go downstream. They can also merge with other holes and split into multiple holes. The existence of extinction holes suggests that in this flame, the critical scalar dissipation rate can be locally exceeded, which suggests that extinction can locally moderate the stabilisation process [47].

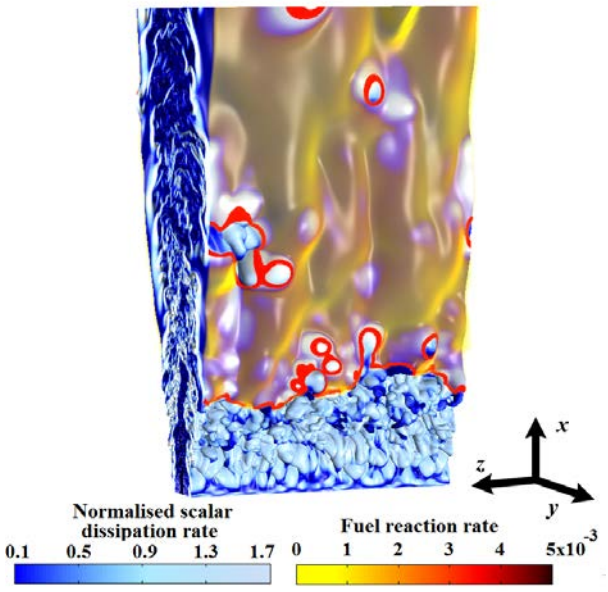


**Figure 3:** Three-dimensional volume rendering of the logarithm of the scalar dissipation rate (blue/white) and reaction rate (red/orange). (Only the region x < 14 is shown.)

Unconnected regions of high reaction rate ahead of the leading edge are not observed. Even though in a two-dimensional (2D) streamwise-transverse plane unconnected flame elements may be observed, all flame regions are actually connected if the three-dimensional topology is considered. Also not observed is any transport of hot products or even large scale folding of the flame into upstream unburned regions. The lack of any unconnected regions or large scale folding of the flame to upstream regions therefore rules out, for the present flame, the original large-eddy theory of flame stabilisation, wherein it was proposed by Broadwell et al. [37] that turbulent transport of pockets of hot products caused the flame to stabilise.

Consistent with many experimental observations of lifted flames [8, 47-49], the leading edges do not show a tribrachial structure. This lack of three distinct branches has been previously explained to result from mixture-fraction gradients ahead of the flame being too large to support distinct lean and rich branches [50]. The reaction rate is locally higher at the flame edges than further downstream, which is consistent with the existence of a premixed leading edge flame. It is also noted that in the present case, the premixed flame edges are quite narrow and of the order of the laminar flame thickness, which implies that the premixed edge flames are quite unlike a flat turbulent premixed flame.

The large degree of convolution of the flame edge implies it can consume stoichiometric reactants at a much greater rate than in a laminar flame (which would present a single straight line here), similar to how increased surface area causes the turbulent burning velocity to be larger than the laminar one in premixed flames.

Analysis of edge flame velocities

As mentioned in the previous section, the weight of experimental evidence supports a role of edge-flame propagation in lifted flame stabilisation at lower lifted heights. However, even the most advanced experimental measurements of lifted flames have not been able to measure the relative propagation velocity of local flames. As a result, prior to this work, it has not been demonstrated definitely that there is a balance between flame propagation and flow speeds.

To this end, the edge-flame velocities have been extracted. Following previous work by the author on extinction and reignition [51], the flame edge is defined as the intersection of a mixture-fraction iso-surface with a product mass-fraction iso-surface. The chosen mixture-fraction iso-value was 0.07, which corresponds to the mixture-fraction having the highest laminar flame speed in a one-dimensional flat premixed laminar flame, while the product iso-value was selected as the value corresponding to the maximum reaction rate in this same flame. By analysing a large number of flame images, it was found that this always corresponded very well with the upstream leading edge of the flame as judged from the reaction rate, as well as with the edge flames around flame holes. With this definition, it is possible to analytically define the edge velocity. The net edge-flame velocity is given by:

$$U = \mathbf{U} + \mathbf{V}_e. \qquad (1)$$

In the above, $U$ is the net velocity in the laboratory frame, $\mathbf{U}$ is the flow velocity, and $\mathbf{V}_e$ is the displacement velocity of the flame relative to the flow.

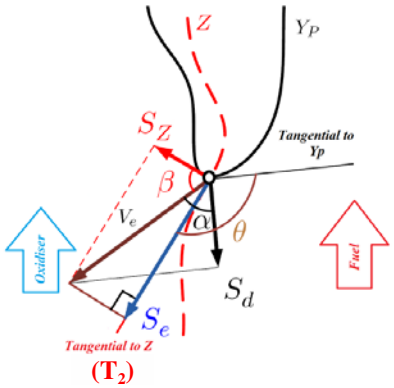


**Figure 5:** Coordinate system used to determine edge-flame velocities. The iso-surface of product mass-fraction is shown as the solid black line, the iso-surface of mixture fraction is shown as the dashed red line. $V_e$ is broken down into components that are normal and tangential to mixture-fraction iso-surfaces.

Previous work [52] demonstrated that $\mathbf{V}_e$ is given by:

$$\mathbf{V}_e = S_e\mathbf{T}_2 + S_Z\mathbf{N}_Z. \qquad (2)$$

This equation is best understood by consulting the diagram in Fig. 5. The quantity $S_e$ is the edge-flame displacement speed in the plane of the mixture-fraction

iso-surface in the direction $\mathbf{T}_2$, which is the tangent vector to the mixture-fraction iso-surface that is normal to the intersection line that defines the edge, pointing towards the unburned reactants. Here, $S_e$ is given in terms of the product mass-fraction self-displacement speed $S_d$, the mixture-fraction self-displacement speed $S_Z$, and the inner product of the normal vectors to product and mixture-fraction iso-surfaces k as:

$$S_e = \frac{S_d - kS_Z}{\sqrt{1-k^2}}, \quad (3)$$

The iso-surface self-displacement speeds are given by [53]:

$$\rho_u S_d^* = \rho S_d = \frac{\rho DY_P/Dt}{|\nabla Y_P|} \text{ and} \quad (4)$$

$$\rho_u S_Z^* = \rho S_Z = \frac{\rho DZ/Dt}{|\nabla Z|}.$$

It is then apparent that $S_z\mathbf{N_z}$ is the flame displacement in the mixture-fraction normal $\mathbf{N_z}$ direction.

Results are now presented for relevant speeds. First, Fig. 6a shows the probability density function (PDF) and mean streamwise velocity $U_x$, conditioned on the streamwise location. The key points to note are that the mean velocity is positive and the order of a few $S_L$, and fluctuations of velocity are significant relative to the mean. Next, Fig. 6b shows the PDF and mean streamwise net velocity $U_x + V_{e,x}$ conditioned on streamwise direction. The fact that the conditional mean of this quantity is nearly zero shows that the flow in net balances the flame propagation, thus demonstrating that flame propagation is the mechanism that controls the flame stabilisation.

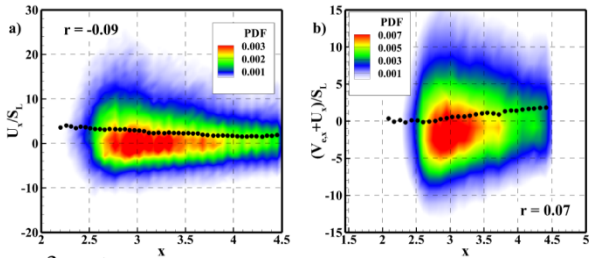


**Figure 6:** The joint PDF contours of a) streamwise flow velocity b) streamwise net velocity.

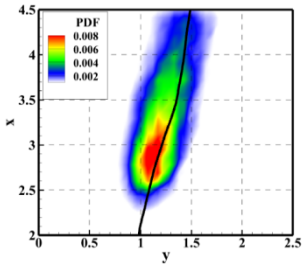


**Figure 7:** The PDF of the flame location points in a streamwise-transverse plane.

However, even after adding in the relative flame displacement speed, fluctuations are still significant. The sources of the fluctuations are therefore now examined in more detail. Figure shows the PDF of the flame location points in a streamwise-transverse plane, and the stoichiometric mean mixture fraction contour. It shows that the flame is stabilised around x=3.2H and y=1.2H, near the mean stoichiometric location, and experiences fluctuations that are larger in the direction aligned tangential to the mean stoichiometric contour than the direction normal to it.

To explain these fluctuations of the lifted height location, Fig. 8a shows the net streamwise edge-flame velocity conditioned on the flame location while Fig. 8b shows the transverse component. These figures clearly show that the flame tends to move on average in an elliptical pattern around the mean stabilisation location. On the on-average lean side, the streamwise velocity component is negative, moving the flame downstream. Once it reaches the downstream location, it then moves inwards, where it encounters a region of high positive streamwise velocity, which pushes it downstream again. Finally, it encounters a positive transverse velocity, moving it outwards to the on-average lean side again. (It is important to understand that the phrase on-average lean side is used rather than simply lean side, because instantaneously the flame is always found on the stoichiometric surface.)

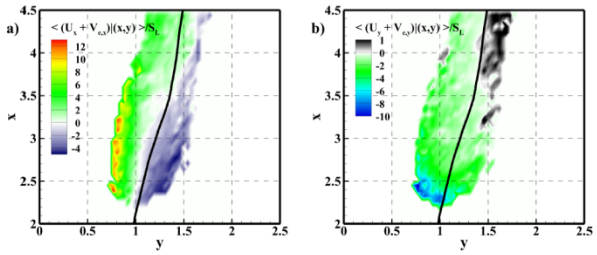


**Figure 8:** a) the net streamwise edge-flame velocity conditioned on the flame location and b) the net transverse edge-flame velocity conditioned on the flame location.

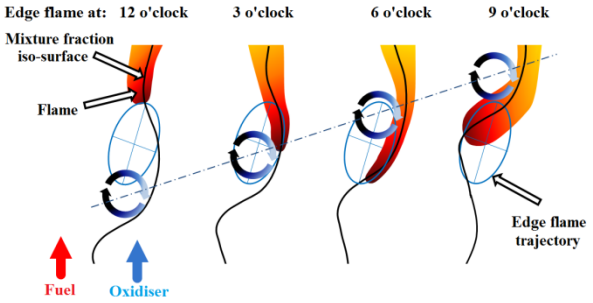


**Figure 9:** A schematic to explain the edge-flame response to the passage of a large eddy. The black line represents the mixture-fraction iso-surface. The red-orange contour represents the flame. The indicative clock-face is shown as the cross-hatched ellipse 12 o'clock, 3 o'clock, 6 o'clock and 9 o'clock marked. An indicative large eddy is shown as the blue, rotating arrow.

It is proposed that this pattern is connected with the passage of large eddies, as illustrated in Fig. 9. Starting at the 3'o-clock location on the lean side, the flame is proposed to exist on the outer side of a clockwise-rotating large eddy. The large eddy plus the flame propagation move the flame downstream while the centre of the eddy which is some distance away towards the centre of the jet is moving downstream. As

the large eddy passes the flame, the trailing edge of the eddy rapidly entrains the flame into the centre of the jet through 6 o'clock where it encounters a region of high streamwise velocity that pushes the flame downstream again at 9 o'clock. Eventually the flame encounters another large eddy, which moves it outwards again through 12 o'clock and downwards through 3 o'clock again. Overall, this picture is very consistent with several other proposals in the literature, notably those of Miake-Lye et al. [54] and Su et al. [38]. The role of large eddies is also consistent with observations of lifted flames in autoignitive conditions, where they moderate the autoignition stabilisation mechanism [43, 44].

## 4. Premixed flame case

### 4.1 Objectives – premixed flame case

The combined cycle gas turbine is well placed to contribute to the future energy mix, as it is the most efficient and lowest $CO_2$ emitting combustion-based power generation system currently available. Importantly, in contrast to coal-based energy, it is a technology that can enable high penetration renewable energy because of its fast starting capability.

Despite these benefits, gas-turbine technology needs to further reduce $CO_2$ emissions while also limiting other harmful emissions such as oxides of nitrogen, $NO_x$. To achieve this, new combustion modes are of great interest to gas-turbine manufacturers. The thrust of these new combustion modes is to achieve highly diluted, lower temperature combustion in intense mixing conditions, which improves combustion efficiency and radically reduces $NO_x$ [55]. Combustors must also be adapted to new low carbon fuels (e.g. hydrogen-rich fuels); or new oxidisers that replace nitrogen with recirculated products, which enables efficient capture of carbon dioxide for carbon storage.

Achieving these new combustion modes and fuels presents major challenges to the gas turbine industry. These combustion modes are susceptible to operability issues including combustion instability, blowout and flashback [55]. One fundamental feature that underpins all these problems is the interaction of intense turbulence with flames that are relatively weak, due to high dilution with air or recirculated products.

In turbulent premixed combustion, a non-dimensional parameter, the Karlovitz number (Ka), has been introduced to classify various scenarios of turbulence/flame interactions in the framework of the premixed combustion regime diagrams [56, 57]. Ka is defined as the ratio of the flame time scale $\tau_L$ to the Kolmogorov time scale $\tau_\eta$: $Ka = \tau_L/\tau_\eta$. In lean/diluted combustors, turbulent premixed flames are expected to be located in the high Ka thin/broken reaction zones regime, where turbulence can significantly penetrate and disrupt the inner structure of the flame [56].

Because of its technical importance, there has been significant interest from experimentalists in achieving high Ka conditions in the laboratory, which have reported features such as distributed preheat and/or reaction zones, and local extinctions [58-63]. The experiments reported by [58, 61] are not yet within range for DNS due to the high Reynolds numbers and large burner diameters. However, a series of coflowing turbulent premixed jet flame experiments at high Ka conditions in the thin and broken reaction zones regimes were performed recently at Lund University [64], and some of three cases are approachable with DNS. In the experiments, the fuel/air jet diameter was 1.5 mm, the jet Reynolds number (Re) ranged from 6,000 to 40,000 and Ka varied from 25 to 1470. A large coflow flame was used to prevent the entrainment of ambient cold air into the jet flame. Simultaneous planar laser-induced fluorescence (PLIF) measurements of OH and $CH_2O$ and Rayleigh scattering measurements of temperature were carried out. Among the experimental conditions, of particular interest and feasibility for performing DNS is a methane-air premixed flame at high Ka and moderate Re and at an equivalence ratio of 0.7. This flame is selected as the target flame for the present study using DNS. The lean conditions and high Ka result in spatial resolution requirements in the DNS constrained by resolving the turbulence scales.

In this context the objectives of this part of the article are to report the first DNS of a laboratory-scale, premixed jet-type flame, to demonstrate good agreement between the DNS and experiment, and to investigate the internal flame structure using the DNS.

### 4.2 Methods – premixed flame case

The experimental configuration is a round, piloted turbulent premixed methane-air burner described in Ref. [64]. The jet operates at atmospheric pressure and an ambient temperature, $T_j = 300$ K. A laminar $CH_4$/air coflowing pilot flame having a velocity $U_c$ of 1.8 m/s, a temperature $T_c$ of 1800K, and an equivalence ratio $\varphi$ = of 0.9 was used to stabilise the flame. The jet bulk velocity is $U_b = 110$ m/s and the equivalence ratio is $\varphi = 0.7$. At this condition, the laminar flame velocity $S_L$ is 0.193 m/s, the flame thermal thickness $\delta_L$ is 0.663 mm, and the flame time scale $\tau_L = \delta_L/S_L$ is 3.44 ms. A photograph of the flame from the experiment is shown in Fig. 9a. Fig. 9b illustrates the schematic of the configuration for the DNS, where the instantaneous flame front is delineated in red. The jet diameter D is 1.5 mm and the jet Re based on $U_b$ and D is 10,510. The small jet diameter and moderate jet Re render the DNS investigation computationally feasible, while retaining interesting features of high Ka flames.

(a)

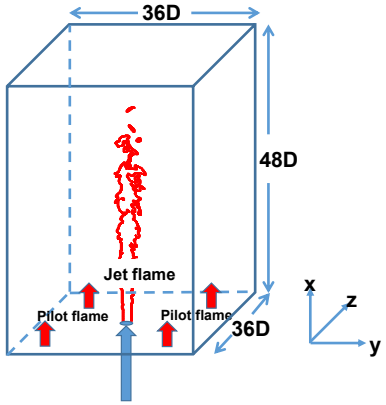


(b)

**Figure 10**. (a) Photograph of the turbulent flame from the experiment. (b) Schematic of the computational domain for DNS.

The mean jet axial velocity profile at the inlet is specified to match that of the experiment using a power law velocity profile for an axisymmetric fully developed turbulent flow [65]. Superimposed on this mean profile is a turbulence field with a fluctuation velocity of 4% of the bulk velocity. Ka is evaluated at the inlet to be 253. The Damköhler number (Da) defined as the ratio of the integral time scale $\tau_f$ to the flame time scale $\tau_L$ is 0.0545. For the large Ka and small Da in the present study, all turbulence time scales are smaller than the flame time scale, and the flame is in the broken reaction zones regime [56].

In the experiment the flame is attached to the rim of the burner, and the temperature and species profiles within the flame are somewhat ambiguous near the burner. We simply specify the following profile for a scalar $\psi$:

$$\psi = \psi_c + \frac{\psi_j - \psi_c}{2}\left(1 + \frac{\tanh\left(D/2 - r\right)}{\delta}\right), \quad (5)$$

where $\psi_j$ and $\psi_c$ denote the values of $\psi$ in the jet and coflow, respectively. r is the radial distance and $\delta$ is the thickness of the shear layer. $\psi_c$ is determined from an equilibrium calculation of a $CH_4$/air mixture with $\varphi$ = 0.9 at a defined temperature of 1800 K. $\psi_j$ is computed based on a $CH_4$/air mixture with $\varphi$ = 0.7 at 300 K.

The physical domain for the simulation is very large owing to the long flame length: $L_x \times L_y \times L_z$ = 48D × 36D × 36D in the streamwise x and lateral directions y and z, respectively, as illustrated in Fig. 9b. The resolution of the DNS is chosen to adequately resolve both of the flame and turbulence structures. A uniform grid spacing of $\Delta x$ = 30 μm is used in the streamwise direction x, while algebraic stretching is used in the lateral directions y and z outside of the shear zone. The grid in the y (z) direction is uniform with $\Delta y$ ($\Delta z$) = 30 μm in the region between y/D (z/D) = -5 and 5, and gradually stretched outside of this region with a maximum relative stretching rate of 1.9%. Approximately 22 grid points across $\delta_L$ are obtained with this spatial resolution. In the present high Ka case, the resolution of turbulence is more demanding. The Kolmogorov scale, defined as $\eta = (\nu^3/\varepsilon)^{1/4}$, has a minimum of 10 μm in a very narrow region near the potential core, where the flame does not overlap. The criteria, $\eta/\Delta x > 0.5$ [9], is satisfied elsewhere. Thus, the smallest scales of the turbulent flow are reasonably resolved in the flame region. The resultant number of grids is $N_x \times N_y \times N_z$ = 2400 × 900 × 900. To wash out artefacts from initialisation, the simulation was first advanced for $10\tau_j$ on a half-resolved grid, where $\tau_j$ is the flow through time defined as $\tau_j = L_x/U_b$. The results were then mapped to the fine grid. The solution was advanced for another $10\tau_j$ to provide stationary statistics. It was found that statistical results of the half-resolution run and the production run are very similar, confirming the resolution is adequate.

A reduced chemical mechanism for premixed $CH_4$/air flames with $NO_x$ was derived based on GRI-Mech3.0. The final skeletal mechanism contains 268 elementary reactions and 44 species, of which 16 species are identified as quasi steady state species due to their high reactivity and short lifetime. The remaining 28 species are transported on the DNS grid. The resultant mechanism has been validated against the detailed mechanism comprehensively [66].

The simulation was performed on Magnus, a Cray XC-40 located at the Pawsey Supercomputing Centre in Australia and required 10 million CPU-hours on 19,200 Intel Xeon Haswell processors for approximately 22 days.

### 4.3 Results – premixed flame case

Figure 10 presents a comparison of the radial variations of mean temperature at three axial stations between the DNS and experiments, where the experimental temperatures were determined from Rayleigh scattering. It may be noted that the agreement is generally quite good. There is a slight over-prediction of temperature towards the product side at

x/D=10; this is probably caused by heat loss to the burner not being properly accounted for in the DNS.

Figure 11 presents comparisons of planar-laser induced fluorescence of HCO, $CH_2O$ and OH with the DNS molar concentrations of the corresponding species. Qualitatively, the agreement is very good. Both the DNS and experiments show some regions of lower OH and HCO in the upstream region, suggesting local extinctions, while the $CH_2O$ and OH images show some evidence of distributed, non-flamelet combustion in the downstream region. The main difference between the DNS and the experiments is that the flame width in the DNS is slightly larger, though this does not seem to be borne out by the temperature profiles. Assuming both the experimental temperature profiles and PLIF measurements are correct, the most likely explanation seems to be that the DNS predicts the peak reaction rate to occur at a somewhat higher temperature than observed in the experiments. This could be attributed to a number of things, such as the chemistry model and the assumed boundary conditions in products and reactants. For example, the temperature of reactants might be slightly higher than reported due to heating from the burner, or the composition of the products could be different from equilibrium.

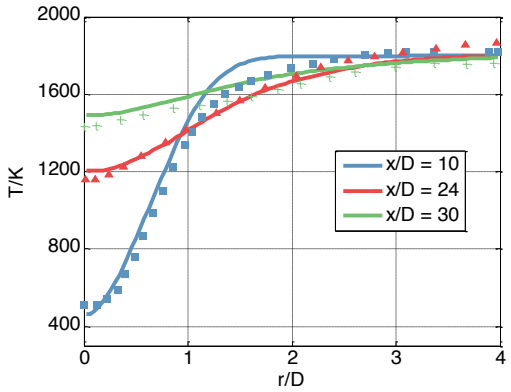


**Figure 11**. Comparison of radial variation of DNS and experimental mean temperatures at three axial stations.

Finally, the DNS are used to investigate the internal structure of the flame. In particular, the question of whether broadening of the preheat and reaction zones as a result of small-scale turbulence is addressed. This may be investigated by considering the magnitude of the progress variable gradient, which represents a reciprocal thickness. To this end, the probably density function and mean of the magnitude of the gradient of progress variable, conditional on progress variable, are plotted in Fig. 12 at x/D=8 and x/D=24. Also plotted is the profile of a laminar flame. Progress variable was defined based on the oxygen mass fraction. It is first noted that the gradient has large fluctuations, which is the expected behaviour at high Reynolds number for a passive scalar. Second, it is noted that at x/D=8, significant flame thinning (higher gradients) is observed for low values of progress variable. Further analysis, not presented here, shows this thinning results from the mean shear, which is significant at this axial location. In contrast at x/D=24 very substantial flame thickening has been observed, with gradients on average less than a half those observed in the laminar flame. Importantly, this thickening is also observed in the heat-releasing region, spanning roughly c = 0.5 to 0.9.

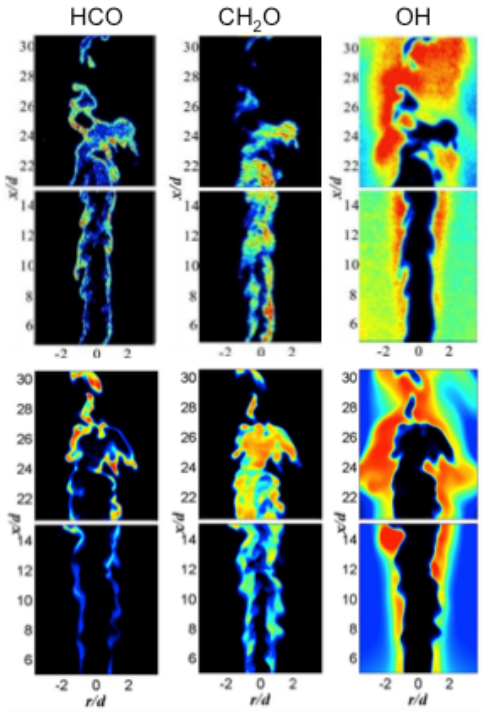


**Figure 12.** Comparisons of a typical snapshot of (top) the HCO, $CH_2O$, and OH PLIF images of experiment and (bottom) the HCO, $CH_2O$, and OH concentrations of DNS.

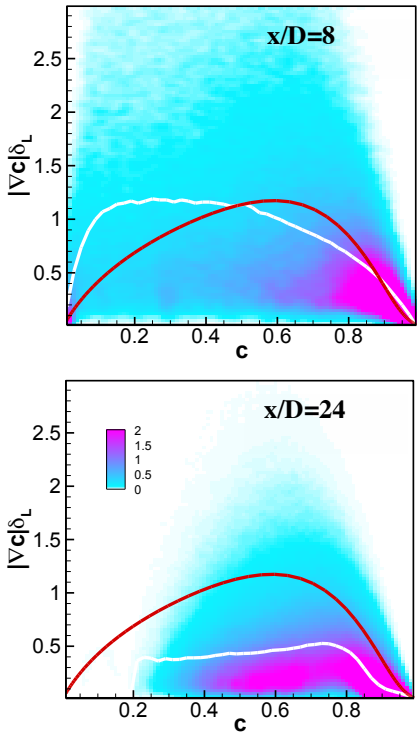


**Figure 13**. Joint PDFs of the progress variable gradient magnitude and the progress variable at various axial locations. White line: conditional mean. Red line: unstrained laminar flame results.

## 5. Conclusions

Direct numerical simulations have come a long way since their first application in combustion in the mid 1980s. In the petascale era of supercomputing, some laboratory-scale flames are now accessible. Two examples were discussed.

In the first example, a lifted jet flame was simulated using a one-step chemistry model, but with a relatively large (by DNS standards) 4 mm burner. The calculations were used to demonstrate several interesting features of the flame structure. It was shown for the first time that the edge-flame relative propagation velocity on averages matches the oncoming flow velocity, thus demonstrating the flame is stabilised by edge-flame propagation. Fluctuations of the edge-flame locations were however quite significant. The local velocities of edge flames were analysed and the results revealed an elliptical on-average motion of edge flames, which was proposed to be connected with the passage of large eddies. Large eddies first arrive at the flame location, pushing it first outwards towards the oxidiser, then downwards in the upstream direction, before passing the flame at which point the eddy entrains the flame into the jet core, where it finds a high velocity region and moves downstream again awaiting the passage of the next large eddy.

In the second example, an experimental lean premixed jet-flame at high Karlovitz number was simulated. In this case a small burner diameter (and a larger computational time allocation) enabled a detailed chemistry DNS. Results for mean temperature were compared quantitatively with experiment with good agreement. Qualitative comparisons were for key species including HCO, $CH_2O$ and OH were also very good with key features such as locally reduced concentrations corresponding to extinction and substantial thickening being reproduced in the DNS. The internal structure of the flame was examined and flame thinning was observed in the upstream, shear-dominated region while substantial flame thickening was observed downstream.

In perspective, I note that significant advances in computational power are expected over the next decades. The rate of progress will probably slow, due to power becoming the main cost driver for supercomputing as opposed to hardware. (This can already be detected in Figure 1). However, even a halved rate of progress, i.e. approximately a doubling of computational power each year, would imply that Reynolds numbers can increase by a factor of two every three years. Given we are already at around 10,000 jet Reynolds number, this means we could do Sadian Flame D [67-69] in less than 4 years and Flame F within 8 years.

These runs are very expensive, however. It is therefore worth thinking about what exactly we should do with DNS so that we can maximise the benefit to the wider combustion community, and indeed to society at large. I therefore conclude this article with some questions, and look forward to discussion after my talk. Should we be mainly targeting real laboratory flames, or are we better off sticking to simpler configurations and accessing more aggressive or wider parameter spaces? How can we coordinate and collaborate with experimentalists? Can/should we use DNS like the TNF workshop flames have been used, as benchmarks for development of practical models [70]? Can we go further, and provide insight to develop new models? How should we do this, given even analysing these data requires a supercomputer?

## 7. Acknowledgments

I would first like to acknowledge the main people that did the work. Dr. Shahram Karami (UNSW) carried out the lifted flame work, and Dr. Haiou Wang (UNSW) carried out the premixed flame work. We were supported by Dr. Mohsen Talei (University of Melbourne) who co-advised Shahram's Ph.D., and by my long-time collaborator Jacqueline H. Chen, who got me started on this combustion DNS journey and collaborated on both the lifted and premixed studies. Dr. Hongfeng Yu (University of Nebraska Lincoln) provided the fantastic animations of the DNS.

This work was supported by the Australian Research Council (ARC). The lifted-flame research was supported by access to computational resources on the Australian NCI National Facility through the National Computational Merit Allocation Scheme and Intersect Australia partner share. The premixed flame runs were carried out under the Petascale Pioneers Program and National Computational Merit Allocation Scheme at the Pawsey Supercomputing Centre with funding from the Australian Government and the Government of Western Australia.

## 5. References


[1] World energy outlook, International Energy Agency, (2012).

[2] R. Bilger, S. Pope, K. Bray, J. Driscoll, Proc. Combust. Inst. **30**(1) (2005), pp. 21-42.

[3] K. Kohse-Höinghaus, R. S. Barlow, M. Aldén, J. Wolfrum, Proc. Combust. Inst. **30** (1) (2005), pp. 89-123.

[4] M. Aldén, H. Edner, P. Grafström, S. Svanberg, Optics Communications **42** (4) (1982), pp. 244-246.

[5] A. R. Masri, Proc. Combust. Inst. **35** (2) (2015), pp. 1115-1136.

[6] M. Juddoo, A. R. Masri, Combust. Flame **158** (5) (2011), pp. 902-914.

[7] R. L. Gordon, A. R. Masri, E. Mastorakos, Combust. Flame **155**(1-2) (2008), pp. 181-195.

[8] I. Boxx, C. Heeger, R. Gordon, B. Böhm, M. Aigner, A. Dreizler, W. Meier, Proc. Combust. Inst. **32** (1) (2009), pp. 905-912.

[9] S. B. Pope,Turbulent flows, Cambridge University Press, (2000).

[10] S. A. Orszag, G. Patterson Jr, Phys. Rev. Lett. **28** (2) (1972), pp. 76.

[11] S. A. Orszag, G. Patterson Jr, Statistical Models and Turbulence (1972), pp. 127-147.

[12] R. S. Rogallo, Numerical experiments in homogeneous turbulence, NASA technical report, (1981).

[13] W. T. Ashurst, N. Peters, M. D. Smooke, Combust. Sci. Technol. **53** (4-6) (1987), pp. 339-375.

[14] J. J. Riley, R. W. Metcalfe, S. A. Orszag, Phys. Fluids **29** (2) (1986), pp. 406.

[15] P. A. Mcmurtry, W.-H. Jou, J. Riley, R. Metcalfe, AIAA J. **24**(6) (1986), pp. 962-970.

[16] T. Poinsot, S. Candel, A. Trouvé, Prog. Energy Combust. Sci. **21** (6) (1995), pp. 531-576.

[17] T. Poinsot, Proc. Combust. Inst. **26** (1) (1996), pp. 219-232.

[18] L. Vervisch, T. Poinsot, Ann. Rev. Fluid Mech. **30** (1) (1998), pp. 655-691.

[19] I. Shepherd, W. T. Ashurst, Symp. (Int.) Combust. **24** (1) (1992), pp. 485-491.

[20] T. Echekki, J. H. Chen, Combust. Flame **106** (1–2) (1996), pp.184-202.

[21] E. Strohmaier, J. Dongarra, H. Simon, M. Meuer, Top500 project, http://www.top500.org/

[22] C. P. Burgess, C. J. Lawn, Combust. Flame **119** (1-2) (1999), pp. 95-108.

[23] K. M. Lyons, K. A. Watson, C. D. Carter, J. M. Donbar, Combust. Sci. Technol. **179** (5) (2007), pp. 1029-1037.

[24] Y. Mizobuchi, S. Tachibana, J. Shinio, S. Ogawa, T. Takeno, Proc. Combust. Inst. **29** (2) (2002), pp. 2009-2015.

[25] J. B. Bell, M. S. Day, J. F. Grcar, M. J. Lijewski, M. R. Johnson, R. K. Cheng, I. G. Shepherd, Proc. Nat. Acad. Sci. **102** (29) (2003), pp. 10006-10011.

[26] J. B. Bell, M. S. Day, J. F. Grcar, M. J. Lijewski, J. F. Driscoll, S. A. Filatyev, Proc. Combust. Inst. **31** (1) (2007), pp. 1299-1307.

[27] S. Karami, E. R. Hawkes, M. Talei, J. Chen, Combust. Flame (Under review) (2014).

[28] S. Karami, E. R. Hawkes, M. Talei, J. H. Chen, J. Fluid Mech. **777** (2015), pp. 633-689.

[29] H. Wang, E. R. Hawkes, J. Chen, Science (in preparation) (2016).

[30] H. Wang, E. R. Hawkes, B. Zhou, J. Chen, M. Aldén, Proc. Combust. Inst. **36** (in preparation) (2016).

[31] J. H. Chen, A. Choudhary, B. De Supinski, M. Devries, E. R. Hawkes, S. Klasky, W. K. Liao, K. L. Ma, J. Mellor-Crummey, N. Podhorszki, R. Sankaran, S. Shende, C. S. Yoo, Comput. Sci. Disc. **2** (1) (2009), 015001.

[32] K. M. Lyons, Prog. Energy Combust. Sci. **33** (2) (2007), pp.211-231.

[33] C. J. Lawn, Prog. Energy Combust. Sci. **35** (1) (2009), pp. 1-30.

[34] L. Vanquickenborne, A. Van Tiggelen, Combust. Flame **10** (1) (1966), pp. 59-69.

[35] G. T. Kalghatgi, Combust. Sci. Technol. **41** (1) (1984), pp. 17-29.

[36] N. Peters, F. A. Williams, AIAA J. **21** (1983), pp. 423–429.

[37] J. E. Broadwell, W. J. A. Dahm, M. G. Mungal, Symp. (Int.) Combust. **20** (1) (1985), pp. 303-310.

[38] L. K. Su, O. S. Sun, M. G. Mungal, Combust. Flame **144** (3) (2006), pp. 494-512.

[39] E. F. Hasselbrink Jr, M. G. Mungal, Symp. (Int.) Combust. **27**(1) (1998), pp. 867-873.

[40] A. Upatnieks, J. F. Driscoll, C. C. Rasmussen, S. L. Ceccio, Combust. Flame **138** (3) (2004), pp. 259-272.

[41] R. Gordon, I. Boxx, C. Carter, A. Dreizler, W. Meier, Flow Turbul. Combust. **88** (4) (2012), pp. 503-527.

[42] Y. Mizobuchi, J. Shinjo, S. Ogawa, T. Takeno, Proc. Combust. Inst. **30** (1) (2005), pp. 611-619.

[43] C. S. Yoo, R. Sankaran, J. H. Chen, J. Fluid Mech. **640** (2009), pp. 453-481.

[44] C. S. Yoo, E. S. Richardson, R. Sankaran, J. H. Chen, Proc. Combust. Inst. **33** (1) (2011), pp. 1619-1627.

[45] D. Garrido-López, S. Sarkar, Proc. Combust. Inst. **30** (1) (2005), pp. 621-628.

[46] A. Cessou, C. Maurey, D. Stepowski, Combust. Flame **137** (4) (2004), pp. 458-477.

[47] K. A. Watson, K. M. Lyons, J. M. Donbar, C. D. Carter, Combust. Sci. Technol. **175** (4) (2003), pp. 649-664.

[48] A. Joedicke, N. Peters, M. Mansour, Proc. Combust. Inst. **30** (1) (2005), pp. 901-909.

[49] C. D. Brown, K. A. Watson, K. M. Lyons, Flow Turbul. Combust. **62** (3) (1999), pp. 249-273.

[50] S. H. Stårner, R. W. Bilger, J. H. Frank, D. F. Marran, M. B. Long, Combust. Flame **107** (3) (1996), pp. 307-313.

[51] E. R. Hawkes, R. Sankaran, J. H. Chen, Proc. Australian Combust. Symp. (2007), pp. 46-49.

[52] E. R. Hawkes, R. Sankaran, J. H. Chen, Proc. Combust. Inst. **33**(1) (2011), pp. 1447-1454.

[53] S. B. Pope, Int. J. Eng. Sci. **26** (5) (1988), pp. 445-469.

[54] R. C. Miake-Lye, J. A. Hammer, Symp. (Int.) Combust. **22** (1) (1989), pp. 817-824.

[55] T. Lieuwen, V. Mcdonell, E. Petersen, D. Santavicca, J. Eng. Gas Turbines Power **130** (1) (2008), pp. 011506.

[56] N. Peters,Turbulent combustion, Cambridge University Press, (2000).

[57] R. Borghi, Recent advances in the aerospace sciences, Springer, (1985).

[58] M. J. Dunn, A. R. Masri, R. W. Bilger, Combust. Flame **151** (1) (2007), pp. 46-60.

[59] M. Dunn, A. Masri, R. Bilger, R. Barlow, G.-H. Wang, Proc. Combust. Inst. **32** (2) (2009), pp. 1779-1786.

[60] M. S. Mansour, N. Peters, Y.-C. Chen, Proc. Combust. Inst. **27**(1) (1998), pp. 767-773.

[61] A. W. Skiba, T. Wabel, J. Temme, J. F. Driscoll, 51st AIAA/SAE/ASEE Joint Propulsion Conference (2015), pp. 4089.

[62] Z. Li, B. Li, Z. Sun, X.-S. Bai, M. Aldén, Combust. Flame **157**(6) (2010), pp. 1087-1096.

[63] C. Duwig, B. Li, Z. Li, M. Aldén, Combust.

Flame **159** (1) (2012), pp. 306-316.

[64] B. Zhou, C. Brackmann, Q. Li, Z. Wang, P. Petersson, Z. Li, M. Aldén, X.-S. Bai, Combust. Flame (2015), pp. 2937–2953.

[65] H. Yamaguchi, Engineering fluid mechanic, Springer, (2008).

[66] T. Lu, C. K. Law, Combust. Flame **154** (4) (2008), pp. 761-774.

[67] R. Barlow, J. Frank, Proc. Combust. Inst. **27** (1) (1998), pp.1087-1095.

[68] R. Barlow, J. Frank, A. Karpetis, J. Chen, Combust. Flame **143**(4) (2005), pp. 433-449.

[69] C. Schneider, A. Dreizler, J. Janicka, E. Hassel, Combust. Flame **135** (1) (2003), pp. 185-190.

[70] R. S. Barlow, Proc. Combust. Inst. **31** (1) (2007), pp. 49-75.

**Proceedings of the Australian Combustion Symposium**
**December 7-9, 2015, The University of Melbourne**

# Conserved Scalar and Conditional Moment Models for Multiphase, Multicomponent and Multiscale Combustion

M.J. Cleary
School of Aerospace, Mechanical and Mechatronic Engineering
The University of Sydney, NSW 2006 Australia

**Abstract**
Conserved scalar and conditional moment turbulent combustion models are well established, particularly for non-premixed combustion of gaseous fuels. As research increasingly focusses on solid and liquid fuel combustion, the utility, elegance and affordability of conserved scalar models is once again being demonstrated. The turbulent combustion of liquid and solid fuels is characterised by multiscale interactions of turbulence, chemistry, and interphase heat and mass transfer. This is further complicated when real fuels with multiple reactive and unreactive components are burned. Additionally, we may need to consider the multiscale interactions between gaseous and solid phases within the porous structure of solid fuels and pollutant adsorbents. This paper reviews recent advances in conserved scalar approaches to these issues. Some results are presented from a new conserved scalar model for combined evaporation, pyrolysis and char conversion of solid fuels in air and oxyfuel conditions. Comments are also made about future conserved scalar applications such as predictions of toxic NOx, SOx and trace metals.

*Keywords: conserved scalars, mixture fraction, conditional averages, multiphase, porous media*

## 1. Introduction

This paper is concerned with the modelling of the transport of scalar quantities in reacting flows. The conventional transport equation for a scalar, φ, is

$$\rho \frac{\partial \varphi}{\partial t} + \rho \boldsymbol{V} \cdot \nabla \varphi - \nabla \cdot (\rho \mathcal{D} \nabla \varphi) = W_\varphi \qquad (1)$$

where $\rho$ is the density, $\boldsymbol{V}$ is the velocity vector, $\mathcal{D}$ is the diffusivity and $W_\varphi$ is a source term. If the scalar in question is the mass fraction of a chemical species (i.e. $\varphi = Y$) then $W_Y$ is the rate of consumption or production of that species due to chemical reactions. The LHS of (1) is linear with respect to φ and does not pose any serious methodological problems for modellers. In contrast, the RHS consisting of the source term is generally non-linear (highly so in the case of reacting scalars) and this can pose a greater challenge. Burke and Schumann [1] first considered the case of a diffusion flame with infinitely fast chemistry resulting in an infinitely thin reactive surface, or flamesheet, coinciding with the stoichiometric mixture. From a mathematical perspective the troublesome non-linearity is confined to the flamesheet and it becomes possible to solve separate linear diffusion equations inside and outside of it, with the flamesheet acting as a boundary condition. Despite being conceptually simple the problem is ill-posed as the location of the flamesheet is unknown *a priori*. Burke and Schumann resolved this by linearly combining the fuel and oxygen mass fractions into a new, so called, conserved scalar, $\beta = Y_F - \frac{1}{s} Y_O$ (where s is the stoichiometric oxygen to fuel ratio), for which $W_\beta = 0$ everywhere in the flow. Hence, in the pre-computer era the diffusion flame problem was greatly simplified and consisted of solving (1) for the conserved scalar $\beta$ and subsequently obtaining fuel, oxygen and product mass fractions as piecewise linear functions of it.

With modern computing and advanced non-linear computational methods we might expect the Burke and Schumann approach to be obsolete but that is not the case. Of course, it still retains its pedagogical elegance [2]. But more than that, the flamesheet and models descendant from it find wide use in research and practice. In particular, this is common for modelling of turbulent and multiphase combustion, where affordable numerical grid resolution is insufficient to capture the multiscale nature of those flows [3]. The flamelet models [4, 5] are conceptually closely related to the flamesheet, whereby a thin turbulent flame brush is replaced by an ensemble of laminar flamelets. While the Burke and Schumann flamesheet was originally derived for infinitely fast chemistry, flamelet models incorporate more realistic chemistry with the models satisfying a balance between finite rate reactions and diffusion normal to the contours of a conserved scalar such as the mixture fraction. Other conserved scalar models have since been developed which, despite having alternative theoretical origins based on conditional averaging and probability density function (PDF) analysis, have practical implementations that are similar to flamesheets. These models include conditional moment closure (CMC) [6, 7], conditional source term estimation (CSE) [8, 9] and multiple mapping conditioning (MMC) [10-12]. The central premise and some examples of these are briefly reviewed now with a focus on gaseous flame cases. Following that, the extension of conserved scalars to multiphase, multicomponent and other multiscale flows is discussed at length.

* Corresponding author:
Phone: (+61) 2 9351 2346
Email: m.cleary@sydney.edu.au

## 2. Review of conditional moment models for turbulent combustion

While scalar transport in both laminar and turbulent flows is governed by (1), in turbulent flows unless all motions down to the Kolmogorov scale are resolved directly (this is impossible in simulations of practical engineering systems) then averaged or filtered versions of that equation are required. The mass-weighted (Favre) average rate of reaction of a species *i* with a species *j* in a turbulent flow is

$$\bar{W}_{Y_i} = \bar{\rho} k(\tilde{T}) \tilde{Y}_i \frac{\tilde{Y}_j}{M_j} \left(1 + \frac{\widetilde{Y_i'' Y_j''}}{\tilde{Y}_i \tilde{Y}_j} + \frac{E_a}{R_u \tilde{T}} \left( \frac{\widetilde{Y_i'' T''}}{\tilde{Y}_i \tilde{T}} + \frac{\widetilde{Y_j'' T''}}{\tilde{Y}_j \tilde{T}} + \left( \frac{E_a}{2 R_u \tilde{T}} - 1 \right) \frac{\widetilde{T''^2}}{\tilde{T}^2} \right) + \cdots \right) \quad (2)$$

where overbars and primes denote Favre averages and turbulent fluctuations, respectively, $k$ is the rate coefficient usually taking an Arrhenius form, $E_a$ is the activation energy, $R_u$ is the gas constant and $T$ is the temperature. Each turbulent correlation in (2) can be expressed exactly in terms of higher order correlations. This introduces two problems: (i) additional equations for those higher order terms need to be derived and solved and they in turn contain even higher order correlations; and (ii) the higher order correlations can be as large in magnitude as terms involving only mean quantities [6] so that truncation may produce significant modelling error.

Klimenko [13] and Bilger [14] independently demonstrated that this closure problem can be solved through taking conditional moments of (1) resulting in a replacement of the mean chemical source term with a conditional mean source term, $\overline{W_Y|\eta}$, having the same form as (2) but with mean temperature, mass fractions and correlations replaced by their conditionally averaged counterparts:

$$\overline{W_{Y_i}|\eta} = \overline{\rho|\eta} k(\overline{T|\eta}) \overline{Y_i|\eta} \frac{\overline{Y_j|\eta}}{M_j} \left(1 + \frac{\overline{Y_i'' Y_j''|\eta}}{\overline{Y_i|\eta}\,\overline{Y_j|\eta}} + \frac{E_a}{R_u \overline{T|\eta}} \left( \frac{\overline{Y_i'' T''|\eta}}{\overline{Y_i|\eta}\,\overline{T|\eta}} + \frac{\overline{Y_j'' T''|\eta}}{\overline{Y_j|\eta}\,\overline{T|\eta}} + \left( \frac{E_a}{2 R_u \overline{T|\eta}} - 1 \right) \frac{\overline{T''^2|\eta}}{\overline{T|\eta}^2} \right) + \cdots \right) \quad (3)$$

where $\overline{\quad|\eta} = \overline{\quad|\eta = \xi}$ and $\eta$ is the sample space for the conditioning variable, in this case the mixture fraction $\xi$. The rationale is that turbulent fluctuations relative to the conditional means are small and (3) can be accurately truncated at the lower order terms. The choice of conditioning variable(s) is regime dependent. In turbulent non-premixed flames the mixture fraction, a normalised conserved scalar having a value of unity in the fuel stream and zero in the oxidiser stream, is often a suitable conditioning variable. Figure 1 shows scatter plots of experimental instantaneous carbon dioxide mass fraction versus instantaneous mixture fraction for two non-premixed flames: Sandia flame D with Re=22,400; and Sandia flame F with Re=44,800 [15]. The conditional mean $CO_2$ mass fraction, $\overline{Y_{CO2}|\eta}$, and flamesheet $CO_2$ mass fraction are overlaid. The flamesheet is obtained from the instantaneous, one-step reaction of fuel and air. The difference between it and the conditional means represents the effects of the interactions between turbulent mixing and finite rate reactions. In both cases shown in Figure 1 the correlation between experimentally observed $CO_2$ and mixture fraction is evident. In the lower Reynolds number case there are only a few fluctuations relative to $\overline{Y_{CO2}|\eta}$ and the same trend also exists in plots of other chemical species and temperature (not shown). CMC modelling of flame D and similar flames with $\overline{W_Y|\eta}$ truncated at the leading order terms (so called 1st order closure) has proven to be very accurate [16-18]. In the higher Reynolds number flame F intense turbulent mixing leads to breakages in the thin flame near stoichiometric mixture fraction, effectively entraining fresh air into the fuel jet and introducing a level of premixing. Consequently the fluctuations relative to the conditional means are considerably larger. Autoignition, lifted flames and other cases with a Damköhler number of order unity or less reveal similar structures. The CMC hypothesis is not falsified but it does require more elaborate treatment of the conditional reaction rate. Modelling by Kim and Huh [19] with truncation at 2nd order terms in (3) (so called 2nd order closure) led to greatly improved predictions relative to 1st order closure for Sandia flame E which is intermediate between the D and F flames. Due to the complexity of 2nd order closure the assumption was applied only to a small number of species involved in rate limiting elementary reactions, and only marginal improvements were observed when performing 2nd order closure for flame F. De Paola et al. [20] had greater success using 2nd order closure in an n-heptane autoignition case without restriction on the species to which the advanced closure was applied.

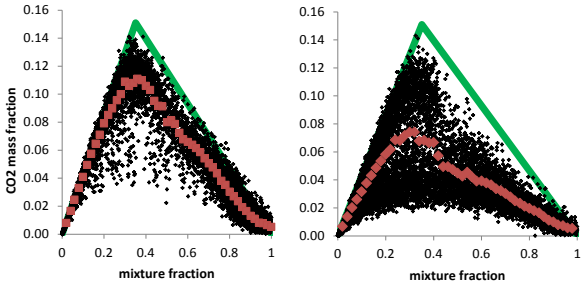


Figure 1: Instantaneous measurements of $CO_2$ mass fraction versus mixture fraction (black), measured conditional $CO_2$ mass fraction (red) and one-step flamesheet $CO_2$ mass fraction (green) in Sandia flames D and F at an axial station of 15 jet diameters. Experimental data is from [15].

The structure of turbulent premixed flames is very different to that of turbulent non-premixed flames. Since mixing of fuel and air is not the rate limiting process in premixed flames, mixture fraction is of little value as a conditioning variable. Experimental data indicates that a measure of reaction progress, such as sensible enthalpy or product mass fractions, is a better alternative from the point of view that fluctuations relative to mean values conditioned on it are small (see Fig.2 and 3 in [21]). Martin et al. [22] had success with conditioning on a

progress variable under lean premixed burning over a backward facing step. While reaction progress is a good conditioning variable, it is not a conserved scalar and the source term closure problem in (2) resurfaces. Furthermore the modelling of the turbulent distribution (i.e. the PDF) of a progress variable may be problematic. Recently Salehi et al. [23] developed a CMC model with standardised enthalpy as the conditioning variable for combustion under thermally stratified, but compositionally homogeneous HCCI engine conditions. Spontaneous ignition was well predicted using 1st order closure, while deflagrations were shown to require higher order methods. In the absence of radiation heat transfer the standardised enthalpy is a conserved scalar. Although it is a promising conditioning variable for some engine simulations, it does not appear to be applicable to cases without thermal variations in the premixture.

A closely related variation of CMC, known as conditional source-term estimation (CSE), was developed by Bushe and Steiner [24]. Rather than solving the conditionally averaged equation as is the case for CMC, CSE solves (1) in its original (unconditional) form. The CMC hypothesis is applied to the source term, $\overline{W}_Y$, which is estimated by inversion of an integral relationships between conditional and unconditional means via the PDF of the conditioning variable (see equation (4) below). CSE was subsequently validated in a number of studies including simulations of the non-premixed Sandia flame D [25], a premixed DNS flame [26] and an experimental premixed bluff-body flame [27]. In the latter two, mean values were conditioned on a reaction progress variable, which as previously mentioned is not a conserved scalar.

In non-premixed and premixed turbulent flames with sufficiently high Damköhler numbers, 1st order CMC closure is an accurate and computationally affordable approach. Modelling of mixed combustion modes, resulting from partial premixing of the fuel stream or flame breakages due to intense turbulent mixing or quenching, may be improved by 2nd order CMC closure. However, this substantially increases model complexity. An alternative is to use two conditioning variables while retaining the 1st order closure assumption. So called doubly-conditioned CMC was pioneered by Kronenburg [28] and Kronenburg and Kostka [29] who used mixture fraction and sensible enthalpy (the latter being a non-conserved scalar) for a DNS case and the Sandia D, E and F flames. Considerable improvements were observed with the addition of the second conditioning variable. Doubly conditioned CSE using two mixture fractions for three stream mixing in MILD combustion was recently developed by Labahn et al. [30]. The model has the advantage that both conditioning variables are conserved scalars and independent of each other. The same authors also applied CSE with double conditioning on the mixture fraction and a progress variable to a lifted flame in a cold coflow [9].

Flamelet, CMC and CSE models are sophisticated extensions (at least in concept) of the flamesheet model. Turbulent fluctuations are restricted to a manifold comprised of one or two conditioning variables. Preferably the conditioning variables are conserved scalars so that their turbulent distributions are independent and easily modelled. Mean quantities are then obtained by convolution of the conditional means and the PDF of the conditioning variable

$$\bar{\varphi} = \int_{\eta_0}^{\eta_1} \overline{\varphi|\eta} P(\eta)\, d\eta \qquad (4)$$

For mixture fraction the PDF may be accurately modelled as a Gaussian or $\beta$-function. Note that 2nd order CMC allows for conditional fluctuations relative to the manifold. Klimenko and Pope [10], through a generalisation of mapping closure called multiple mapping conditioning (MMC), extended this concept to manifolds of any size. For computational reasons it is desirable to limit the manifold to one or, at most, a few variables. Reference variables are used to assist the emulation of scalar turbulence and, in this original form of MMC, the reference variables act as conditioning variables. As MMC is in fact a full PDF model, there is no need to provide an external model for $P(\eta)$. To date MMC models with between one and four reference / conditioning variables have been used for non-premixed combustion[12, 31-33]. Sundaram et al. [34] developed an MMC model using a conserved distance-like reference / conditioning variable for premixed flames, obtaining good predictions of NOx from a lean premixed, high pressure combustor. A novel MMC model with side-stepping and a conserved reference variable for mixture fraction has also been developed for differential diffusion [35]. Generalised versions of MMC, whereby reference variables may not necessarily be conditioning variables, have also been developed [11, 36, 37] and are particularly attractive in the context of LES due to their ability to be combined with a sparse, and therefore computationally cheap, distribution of particles in the Monte Carlo scheme.

## 3. Conserved scalar models in multiphase combustion

The majority of combustors found in practical applications burn liquid or solid fuels such as diesel, kerosene, coal and biomass. Following the extensive development, testing and refinement of conserved scalar models for gaseous fuel combustion (see Section 2), the focus of modellers in recent years has turned to multiphase combustion [38-40]. The burning of liquid and solid fuels is a classical non-premixed combustion problem. Combustible vapours emanating from a phase change within or at the surface of a fuel particle, mix diffusively with the surrounding oxidiser and, if conditions permit, form a thin flame in the region of the stoichiometric mixture. That stoichiometric mixture and associated flame may form locally around isolated particles, around clusters of particles, or in the adjacent mixing superlayer separating the droplet or particle dispersion from the surrounding atmosphere. In intense

turbulence the combustion zone may thicken and premixing may also occur in parts.

Conserved scalars such as the mixture fraction are useful for modelling two aspects of multiphase combustion; namely interphase heat and mass transfer and turbulent reaction rate closure. Although different in nature, the need for special treatment arises for the common reason that practical modelling cannot adequately resolve the particle and Kolmogorov scales, respectively, at which these phenomena occur. Averaging or filtering is required and the aforementioned closure problem arises.

This section starts by deriving the multiphase scalar transport equation with focus on the mixture fraction transport. Then modelling of reactive scalars by CMC and flamelets is discussed, concentrating on the effects of interphase mass transfer on the flame structure. Finally conserved scalar models for the diffusive boundary layer around fuel particles are presented along with new model results from a unified conserved scalar model for multicomponent mass transfer due to evaporation, pyrolysis and char conversion of liquid and solid fuel particles.

### 3.1 Scalar transport in multiphase combustion

Within the interior of a single phase of a multiphase reacting flow scalar transport is governed by

$$\rho_k \frac{\partial \varphi_k}{\partial t} + \rho_k \boldsymbol{V}_k \cdot \nabla \varphi_k - \nabla \cdot (\rho_k \mathcal{D}_k \nabla \varphi_k) = W_{\varphi,k} \quad (5)$$

where the subscript $k \in [1,2,\dots n]$ is the phase index and $n$ is the number of phases present in the flow (typically $n = 2$). Equation (5) is valid right up to but not including the phase interface where mass transfer due to evaporation, pyrolysis and/or char conversion may occur. Following Kataoka [41], adoption of the separated flow model extends the equation so that it is valid for all phases and the phase interface. This perspective was considered by Mortensen and Bilger to formulate the spray CMC model [40] and similar notation is used below. For simplicity only two phases are considered, a dispersed phase, $k = 1$ (i.e. liquid or solid fuel particles) and the carrier or gas phase, $k = 2$.

A field variable variable $\gamma(x,t)$ is defined so that $\gamma = \gamma^I$ at the phase interface, the dispersed phase corresponding to $k = 1$ is found where $\gamma < \gamma^I$ and the gas corresponding to $k = 2$ is found where $\gamma > \gamma^I$. The interface may be tracked through the level set function

$$\frac{\partial \gamma}{\partial t} + \boldsymbol{V}^I \cdot \boldsymbol{\nabla} \gamma = 0 \quad (6)$$

where $\boldsymbol{V}^I$ is the interface velocity. Equation (6) can be expressed in terms of the phase velocity by adding and subtracting $\boldsymbol{V}_k \cdot \boldsymbol{\nabla}\gamma$ to give

$$\frac{\partial \gamma}{\partial t} + \boldsymbol{V}_k \cdot \boldsymbol{\nabla} \gamma = S_k \quad (7)$$

where

$$S_k = (\boldsymbol{V}^I - \boldsymbol{V}_k) \cdot \boldsymbol{n}_1 |\boldsymbol{\nabla}\gamma| \quad (8)$$

and $\boldsymbol{n}_1$ is the unit normal vector pointing from phase 1 into phase 2. Equation (7) can be used to track an interface and to determine which phase is present at location $x$ and time $t$. However, instead of tracking the interface directly, manipulations of (5) via the level set function produce a scalar transport equation which holds in both phases and at the interface. This is done through weighting the terms in (5) by a phase indicator function, $\theta_k$, which has a value of unity in phase 1 and zero in phase 2. In terms of $\gamma$

$$\theta_k = 0^{k-1} + (-1)^k H(\gamma - \gamma^I) \quad (9)$$

where $H$ is the Heaviside function. The transport equation of the indicator function then becomes [41]

$$\frac{\partial \theta_k}{\partial t} + \boldsymbol{V}_k \cdot \boldsymbol{\nabla} \theta_k = \Pi_k \quad (10)$$

where

$$\Pi_k = (-1)^k S_k \delta(\gamma - \gamma^I) \quad (11)$$

and $\delta$ is the Dirac delta function. Locally at a phase interface $\Pi_k$ is the volumetric rate of mass transfer per unit volume, i.e. $\Pi_k = \dot{m}_k / \rho V$.

Multiplying (5) by $\theta_k$, incorporating (10) and manipulating the result with the chain rule gives the phase weighted scalar transport equation

$$\begin{aligned} \rho_k \theta_k \frac{\partial \varphi_k}{\partial t} + \rho_k \theta_k \boldsymbol{V}_k \cdot \nabla \varphi_k - \nabla \cdot (\rho_k \theta_k \mathcal{D}_k \nabla \varphi_k) \\ = \theta_k W_{\varphi,k} + \rho_k \mathcal{D}_k \nabla \varphi_k \cdot \nabla \theta_k + \rho_k \varphi_k \Pi_k \end{aligned} \quad (12)$$

which is valid in both phases and at the phase interface. Modelling is required for the term involving the gradient of $\theta_k$. Since the interface is without mass, new species mass cannot be generated there, giving rise to the jump condition [41]

$$\textstyle\sum_{k=1}^{2} (\rho_k \mathcal{D}_k \nabla \varphi_k \cdot \nabla \theta_k + \rho_k \varphi_k \Pi_k) = 0 \,. \quad (13)$$

Since we are primarily interested in the transfer of mass from the dispersed phase to the gas phase and by neglecting compositional gradients within the fuel particles, from (13) we get

$$\rho_1 \mathcal{D}_1 \nabla \varphi_1 \cdot \nabla \theta_1 = 0 \quad (14)$$

$$\rho_2 \mathcal{D}_2 \nabla \varphi_2 \cdot \nabla \theta_2 = \rho_2 \Pi_2 (\varphi_1 - \varphi_2) \quad (15)$$

where it has been recognised that $\rho_2 \Pi_2 - \rho_1 \Pi_1$ . Incorporating (15) and dropping the phase index for clarity, the gas phase scalar transport equation finally becomes

$$\rho\theta \frac{\partial \varphi}{\partial t} + \rho\theta \boldsymbol{V} \cdot \nabla \varphi - \nabla \cdot (\rho\theta \mathcal{D} \nabla \varphi) = \theta W_\varphi + \rho \Pi \varphi_D \quad (16)$$

where $\varphi_D$ is the scalar value within the fuel particle.

For turbulent multiphase flows an averaged (or filtered) form of the scalar transport equation is needed. The LHS of (12) is conventional and taking an average poses no methodological obstacles, save the need for a suitable model for the turbulent flux (e.g. eddy diffusivity model). For dilute dispersions the volume fraction of the gas phase approaches unity such that $\bar{\theta} \approx 1$. The RHS of (12) contains the chemical rate and interphase mass transfer terms. In general, both are non-linear and averaging of them requires care.

The mixture fraction version (16), obtained by setting $\varphi = \xi$ and $W_\xi = 0$, remains a conserved scalar equation in the interior of a single phase as Π is zero everywhere except for at the interface between the phases. That interface is not resolved in any practical model and averaging is performed, viz.

$$\bar{\rho}\frac{\partial \tilde{\xi}}{\partial t} + \bar{\rho}\bar{\boldsymbol{V}} \cdot \nabla \tilde{\xi} - \nabla \cdot \left(\bar{\rho}(\mathcal{D} + \mathcal{D}_t)\nabla \tilde{\xi}\right) = \bar{\rho}\overline{\Pi}. \quad (17)$$

Note that a turbulent diffusivity closure has been shown for the turbulent scalar flux, although alternatives are possible. The average interphase transport, $\overline{\Pi}$, is in general non-zero in the gas phase. Particle source-in-cell models are commonly used for it:

$$\overline{\Pi} = \frac{1}{V}\sum_{n=1}^{N} \dot{m}_n'' A_n \quad (18)$$

Here, $N$ is the number of fuel particles in a computational cell, $\dot{m}_n''$ is the mass flux of vapour from an individual particle and $A_n$ is its surface area. The latter may be obtained from the Spalding transfer model [42] and this is discussed below. Although the mean mixture fraction equation in multiphase flows contains this source term due to interphase transport, fortunately it retains its conserved nature through the reaction zone and continues to be a useful quantity for turbulent multiphase combustion modelling, provided appropriate closures can be found for the conditional moments of Π. This is the subject of the next subsection. The modelling of the mixture fraction variance provides further challenges for modellers as interphase transport can have a large impact. The variance equation may be derived via the two-fluid approach either directly or by taking moments of the multiphase PDF transport equation [40]. It is convenient to determine the variance as the difference between the mean square and the square of the mean; $\overline{\xi''^2} = \overline{\xi^2} - \left(\tilde{\xi}\right)^2$. The model transport equations for the mean square of the gas phase mixture fraction is

$$\bar{\rho}\frac{\partial \overline{\xi^2}}{\partial t} + \bar{\rho}\bar{\boldsymbol{V}} \cdot \nabla \overline{\xi^2} - \nabla \cdot \left(\bar{\rho}(\mathcal{D} + \mathcal{D}_t)\nabla \overline{\xi^2}\right) = -2\bar{\rho}\mathcal{D}\overline{\nabla\xi \cdot \nabla\xi} + \bar{\rho}\overline{\xi\Pi} - \bar{\rho}\overline{\xi^2}\overline{\Pi}\,. \quad (19)$$

The last two terms on RHS are the transfer terms. Particle source-in-cell models similar to (18) are suggested by Borghesi et al. [43] and Srna et al. [44] in the RANS context for lifted, spray flames. Both papers show that the transfer terms dominate the variance equation, increasing the local value of the variance by up to 200%. In the former paper the stabilised flame base is well downstream of the liquid penetration length and it is shown that there is only a small effect on the ignition delay time by ignoring the interphase transport terms. In the latter paper the flame stabilised close to the region where liquid remains unevaporated and the interphase terms have a a profound effect on predicted ignition delay and lift-off length.

Various other models for the interphase transfer terms in the variance equation may be found in the literature [45, 46]. Kronenburg [47] has shown, via LES modelling, that predictions of local variance are extremely sensitive with order of magnitude differences between the models.

The scalar dissipation, $\bar{N} = \mathcal{D}\overline{\nabla\xi \cdot \nabla\xi}$, on the RHS of (19) also poses challenges to modellers. The steepening of mixture fraction gradients adjacent to fuel particles issuing new combustible vapour into the gas phase needs to be addressed. In the context of LES, Pera et al. [45] assume that equilibrium exists between dissipation and production of scalar variance at the subgrid scale, viz.

$$\bar{N} = \mathcal{D}_T\left|\nabla\tilde{\xi}\right|^2 + 2\left(\overline{\xi\Pi} - \tilde{\xi}\,\overline{\Pi}\right). \quad (20)$$

where $\mathcal{D}_T$ is the subgrid turbulent diffusivity. This model is subject to the same modelling uncertainties discussed above for the interphase transfer correlations, and a dynamic model may be required [45]. A model that adds the resolved and subgrid components is used in the LES of Ukai et al. [48] and De and Kim [49]

$$\bar{N} = (\mathcal{D} + C_N\mathcal{D}_T)\left|\nabla\tilde{\xi}\right|^2 \quad (21)$$

where $C_N$ is a tunable constant. Although practical, (21) is *ad hoc* and lacks a compelling physical basis.

Clearly, much new work is needed in order to convincingly model conserved scalar variance in multiphase flows. The challenge of model development is compounded by the dearth of data due to the difficulty faced by experimentalists in measuring the mixture fraction in multiphase flows. Ongoing efforts by Lowe and Masri to measure the mixture fraction in sprays using acetone LIF at the University of Sydney is hoped to make a significant contribution in this regard.

### 3.2 Turbulent multiphase combustion models

Turbulent multiphase combustion modelling includes all the difficulties of turbulent gaseous combustion modelling, and a host of additional difficulties. A growing number of recent papers have investigated the application of conserved scalar models such as CMC and flamelets to turbulent combusting sprays. Mortensen and Bilger formally derived the spray CMC equations [40], showing that upon taking conditional means of (16) a new conditional source term associated with interphase transport appears, namely $\overline{\Pi|\eta}/\bar{\theta}$. Note that in equation (52) in [40] $\overline{\Pi|\eta}/\bar{\theta}$ is multiplied by an already closed quantity involving the mass fraction of the evaporating species in the droplet

and the diffusion of that species in the droplet boundary layer. There is also another conditional source term involving the turbulent correlation of species and the volumetric evaporation rate, which are conventionally ignored under the assumption of 1st order CMC. With that assumption and further assuming that $\bar{\theta}$ is unity in dilute dispersions, the CMC spray equations of Mortensen and Bilger closely resemble the CMC equations for dilute biomass combustion derived earlier by Rogerson et al. [50].

The modelling of $\overline{\Pi|\eta}$ is an active area of research. Sreedhara and Huh [51] suggested a simple linear model

$$\overline{\Pi|\eta} = \begin{cases} \frac{\bar{\Pi}}{\int_{\bar{\xi}}^{\xi_S}(\eta-\bar{\xi})P(\eta)d\eta}\left(\eta-\bar{\xi}\right) & \text{for } \eta \geq \bar{\xi} \\ 0 & \text{for } \eta < \bar{\xi} \end{cases} \quad (22)$$

which performs well against DNS data in homogeneous, isotropic, decaying turbulence. More recently Seo and Huh [52] examined this model in the context of 3D DNS of a spray, observing that the model is reasonable for the mixture fraction range of meaningful probability but considerably underpredicts the conditional transfer rate for low probability fuel rich regions of the flow. Schroll et al. [53] suggested a model in the form of

$$\overline{\Pi|\eta} = \frac{\bar{\Pi}\delta(\eta-\bar{\xi}^*)}{P(\eta)} \quad (23)$$

whereby the mass transfer occurs as an impulse at the mixture fraction corresponding to some mean value, $\bar{\xi}^*$. Borghesi et al. [43] take the mean fuel particle surface mixture fraction within a computational cell, which is physically plausible as the mass transfer is confined to the surfaces. The model is applied to a lifted, autoigniting n-heptane spray, although as evaporation occurs upstream of the flame stabilization point the sensitivity of the results to the exact form of $\overline{\Pi|\eta}$ can be expected to be small. A refinement suggested by Ukai et al. [48, 54], and validated against the dilute combusting acetone spray data of Masri and Gounder [55], instead uses a mean value that is part way between the surface mixture fraction and the mean value of the gaseous mixture in the computational cell. That model accounts for the diffusion of mass between the droplet locations and the gas phase location at which the conditional moments are evaluated. For the that particular flame in which droplet evaporation, turbulence and finite rate chemistry have close interaction, it is shown that the refined model assigning the evaporative transfer to an intermediate mean value of the mixture fraction has a strong affect on the flame structure, while using the mean surface value of mixture fraction as suggested by Borghesi et al. [43] does not influence the flame structure at all.

Multiphase flamelet models are also under development. Olguin and Gutheil [56] derived the spray flamelet equations, which much like CMC, contain an interphase mass transfer term as a function of mixture fraction, $S_v(\xi)$. Closure models similar to those for $\overline{\Pi|\eta}$ are possible. Traditionally, the flamelet models have had a numerical advantage over CMC due to the ability to pre-tabulate reactive scalar source terms. Tabulation methods for multiphase flamelet models which include local interphase transfer terms, $S_v(\xi)$, are yet to be developed.

The CMC and flamelet models discussed above explicitly account for the effects of interphase transfer on flame structure through the conditional source term $\overline{\Pi|\eta}$ or $S_v(\xi)$. These models are in the early stages of development. However, a larger number of studies have more simply used the single phase CMC and flamelet models. Interphase mass transfer appears only through the modelling of the conserved scalar equations (17) and (19), and not through any special terms in the combustion model itself. While not general, such approaches are justified when there is a spatial separation between the dispersed phase and the reaction zone. Ignition of a lifted flame in a modern, compression ignition engine is a case in point [57]. A series of papers by Wright, Bolla and coworkers have considered CMC without conditional mass transfer due to evaporation in the modelling of large bore marine diesel engines [44, 58]. D'Errico et al. [59] and Knudsen et al. [60] have applied flamelet models to spray flames whereby flamelet structure is determined only by the local balance between finite rate chemistry and diffusion. D'Errico et al. [59] adapted the multiple representative interactive flamelet (mRIF) model, first suggested for two stage fuel injection by Barths et al. [61], to account for fuel spray evaporation in the far field. Knudsen et al. [60] used a flamelet model parameterised by both mixture fraction and a progress variable for partial premixing in a multiphase flow.

### 3.3 Conserved scalar models in the diffusive layer around fuel particles

A major part of the previous subsection is devoted to the modelling of the conditional volumetric transfer term $\overline{\Pi|\eta}$ in the CMC equation, for which there is a similar term in the multiphase flamelet equation, $S_v(\xi)$. The two models found in equations (22) and (23) distribute the interphase transport in mixture fraction space, consistent with the requirement that

$$\bar{\Pi} = \int_0^1 \overline{\Pi|\eta} P(\eta)\, d\eta \,. \quad (24)$$

First the mean rate, $\bar{\Pi}$, is calculated according to (18) and then the conditional means are given a certain distribution (i.e. linear in the case of (22) and a delta function in the case of (23)). A shortcoming of this approach is that it assumes that $\bar{\Pi}$ can be accurately modelled, but as the transfer occurs at the unresolved scales in a turbulent flow such accuracy is not assured. This interphase transfer rate closure problem is akin to that for the chemical reaction rate, $\bar{W}_Y$, albeit perhaps not as acute since (as will be shown below) the modelling of $\dot{m}_n''$ in (18) involves the logarithm of a turbulent quantity, whereas the chemical reaction rate involves an exponential.

Figure 2 shows a fuel particle (either liquid or a solid) surrounded by a diffusive gas layer. Since the fuel particle constitutes part of the dispersed phase, the subscript D is used to denote properties within it. The S and G states denote, respectively, the gas-side of the interface between the phases and the gaseous state at the outer edge of the diffusion layer. That layer has a characteristic thickness of $\delta$. In practical RANS or LES modelling the diffusive layer is not resolved by the grid. On the two sets of axes below the fuel particle, variations of scalar quantities through the diffusive layer are shown. The top one shows reactive species and mixture fraction. If there is no envelope flame around the fuel particle (e.g. in fuel-vapour rich regions of the flow near the inlet nozzle) then the fuel vapour mass fraction, *Y*, decays monotonically between its surface value and the value at the G state as shown by the solid line. Note that the G state fluctuates turbulently. If there is an envelope flame in the diffusive layer then the fuel vapour and oxidiser are consumed at a location corresponding to the stoichiometric mixture as shown by the dashed line. Being a conserved scalar, the mixture fraction decays monotonically according to the solid line curve through the diffusive layer for both the reactive and unreactive cases (although its exact distribution will vary due differences in fluid properties such as density). The lower axes show temperature which is strongly affected in the case where there is an envelope flame (dashed line) but varies monotonically (solid line) otherwise. The standardised enthalpy, which is the sum of the enthalpy of formation and sensible enthalpy, is however conserved and it varies monotonically regardless of the presence of a flame.

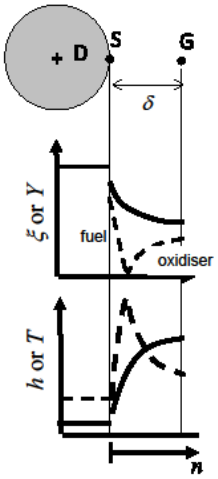


Figure 2: Schematic diagram of a fuel particle exchanging heat and mass with across a diffusive layer in the surrounding gas phase.

Spalding [42] derived an expression for the mass flux emanating from an evaporating droplet in both non-reacting and reacting conditions. Using contemporary notation it is

$$\dot{m}'' = Sh\frac{\rho\mathcal{D}}{L}ln(1+B) \qquad (25)$$

where *Sh* is the Sherwood number, *L* is the characteristic length of the fuel particle and

$$B = \frac{a_G - a_S}{a_S - a_D} \qquad (26)$$

is the Spalding transfer number, where $a$ is a conserved scalar. Models for turbulent spray evaporation commonly set $a = \bar{Y}_F$. For non-reacting sprays the fuel mass fraction is a conserved scalar, however $Y_F$ is a turbulent quantity thus introducing an error by taking only its average. In reacting flows $Y_F$ is not conserved. The most common and simple approach used in [43, 44, 48, 54, 58] and also found in Turns [2] is derived from the Burke and Schumann flamesheet model, effectively amounting to $a = \bar{h}$ (i.e the mean standardised enthalpy). Assuming that the envelope flame is infinitely thin and fast and that the gas specific heat, $C_p$, is constant this leads to

$$B = \frac{C_p(\bar{T}_G - T_S) + \Delta h_c/s}{h_{fg}} \ . \qquad (27)$$

where $\Delta h_c$ and $h_{fg}$ are the heat of combustion and enthalpy of vaporisation, repectively.

In an effort to eliminate the error associated with averaging the G state values in a turbulent flow, De et al. [62] used

$$B = \frac{\xi_G - \xi_S}{\xi_S - 1} \ . \qquad (28)$$

where the instantaneous mixture fraction at the G state is sampled from a β PDF and updated commensurate with the eddy turnover time. The S state values in the above equations can be obtained from knowledge of the surface, with phase equilibrium arguments commonly invoked.

The discussion above relates primarily to liquid droplets undergoing evaporation in a turbulent flame. Similar concepts apply to the turbulent combustion of dispersions of solid fuels such as coal and biomass. Stöllinger et al. [63, 64] developed a PDF model for coal volatile and char combustion. The gas composition seen by the multicomponent particles along their trajectory is determined by two mixture fractions; one for volatile species and one for char. Both mean and fluctuating mixture fraction models were used, and given the observed sensitivity further study is warranted.

In this light, a recent and ongoing collaboration between the University of Sydney and Universität Stuttgart [65] has unified the modelling of heat and mass transfer across the diffusive layer for liquid and solid fuels undergoing combinations of evaporation, pyrolysis and char conversion. Carbonaceous solid fuels are multicomponent, having free moisture, volatiles and char. The Spalding B numbers are defined for both the mixture fraction (one for each component) and standardised enthalpy, yielding closed form solutions for the mass flux, particle heating rate and composition in the diffusive layer. As is conventional, a quasi-steady assumption applies to the gas in the diffusive layer and,

at this stage, only species with small kinetic timescales can be predicted with accuracy. Here, both infinite rate flamesheet and flamelet generated composition fields are possible. Since the transfer physics across the diffusive layer are the same for evaporation, pyrolysis and char conversion a single set of analytical expressions exists for all three processes, with the different physics of the phase changes confined to the surface boundary conditions. A summary of the model follows.

From mass and heat transfer perspectives two different expressions are obtained for the mass flux across the diffusive layer surrounding an isolated fuel particle

$$\dot{m}'' = Sh\frac{\rho\mathcal{D}}{L}\ln(1+B_M) \tag{29}$$

$$\dot{m}'' = Nu\frac{\rho\alpha}{L}\ln(1+B_H)\,. \tag{30}$$

$Nu$ is the Nusselt number, $\alpha$ is the thermal diffusivity and $B_M$ and $B_H$ are the Spalding mass and heat transfer numbers defined in terms of the conserved scalars as

$$B_M = \frac{\xi_G-\xi_S}{\xi_S-1} \tag{31}$$

$$B_H = \frac{h_G-h_S}{h_S-h_D+q_D-q_R} \tag{32}$$

where $q_D$ and $q_R$ are the internal heating and radiation transfer rates per unit mass of the transferred species. The former is discussed below, while the latter would normally be obtained from an external model. Equations (29) and (30) are valid for conditions where there is an envelope flame and where there is not an envelope flame. Furthermore, there is no distinction between mass transfer due to evaporation, pyrolysis or char conversion.

There are two independent unknown quantities: $q_D$, and $\xi_S$. Closure for $q_D$ is found by equating Eq.(29) and (30):

$$q_D = \frac{h_G-h_S}{(1+B_M)^Z-1} - (h_S-h_D) + q_R \tag{33}$$

where $Z = Le^{-1}\,Sh/Nu$ and $Le = \alpha/\mathcal{D}$ is the Lewis number. Models for the second and third unknowns are found by consideration of the surface physics. Closure for $\xi_S$ is obtained from the kinetic rates of mass release due to either evaporation, pyrolysis or char reactions. For evaporation, phase equilibrium models such as the Clausius-Clapeyron relation are commonly. Pyrolysis is driven by temperature and rate of temperature rise at the surface and within the structure of the fuel particle. The simplest models use a two-parameter Arrhenius-type expression

$$\dot{m}_p'' = \Gamma\exp\left(-\frac{E_a}{R_uT_S}\right)\frac{m_v}{A} \tag{34}$$

where $\Gamma$ is a pre-exponential factor, $E_a$ an activation energy and $m_v$ is the volatile mass remaining in the fuel particle. Related but more sophisticated treatments of pyrolysis, such as CPD, FG-DVC, FLASHKIN and FLASHCHAIN are also available in the literature [66]. Simplicity is also desirable for the heterogeneous char reactions, e.g. the classical two-step oxidation-gasification kinetics scheme

$$C + \tfrac{1}{2}O_2 \overset{k_2}{\rightarrow} CO \tag{R2}$$

$$C + CO_2 \overset{k_3}{\rightarrow} 2CO \tag{R3}$$

where

$$\dot{m}_c'' = \mathcal{K}_2Y_{O_2,S} + 2\mathcal{K}_3Y_{CO_2,S} \tag{35}$$

and $\mathcal{K}_2$ and $\mathcal{K}_3$ are rate parameters. Equating (34) and (35) with (29) while substituting the definition of $B_M$ in (31) leads to expressions for the surface mixture fraction

$$\xi_S = 1 + \frac{\xi_G-1}{e^{\zeta}} \tag{36}$$

where

$$\text{for pyrolysis:}\quad \zeta = \frac{L\Gamma}{Sh\rho\mathcal{D}}\exp\left(-\frac{E_a}{R_uT_D}\right)\frac{m_v}{A} \tag{37}$$

$$\text{for char:}\quad \zeta = \frac{L}{Sh\rho\mathcal{D}}\left(\mathcal{K}_2Y_{O_2,S} + 2\mathcal{K}_3Y_{CO_2,S}\right). \tag{38}$$

The unified two-phase combustion model given by (29) to (38) has been verified against experimental data for evaporation of burning and non-burning ethanol and n-heptane droplets and sequential coal pyrolysis and char conversion in air and oxyfuel environments [65]. Each case is for a single fuel particle in a laminar flow and the modelling considers a static flame structure in the diffusive layer determined by a lightly strained laminar flamelet calculation. For brevity only the coal results are shown here. Figure 3 shows experimental and predicted particle temperatures versus time for six different cases with variable oxygen volume fractions (increasing from top to bottom in the figure) and with both $N_2$ and $CO_2$ as the major diluent gases (left and right). The former is related to air combustion, while the latter is associated with oxyfuel combustion with exhaust gas recirculation. Three stages of mass transfer are clearly evident in all six cases and are specifically indicated by Roman numerals in the top left figure. The first stage is pyrolysis without an envelope flame, the second stage is pyrolysis with an envelope flame (i.e. post particle ignition) and the third stage is char burnout. The model results given by the solid line clearly captures the transition between the stages and, importantly, the trends with varying levels of oxygen and when exchanging nitrogen for carbon dioxide as the diluent gas. This model appears to be both simple and accurate. Work to include it in a turbulent combustion code is ongoing.

## 4. Conserved scalar models for porous media

Conditional moment models (CMC and CSE) are well validated for turbulent combustion of gaseous fuels and they are now being intensively developed for multiphase combustion. Their benefits are derived from

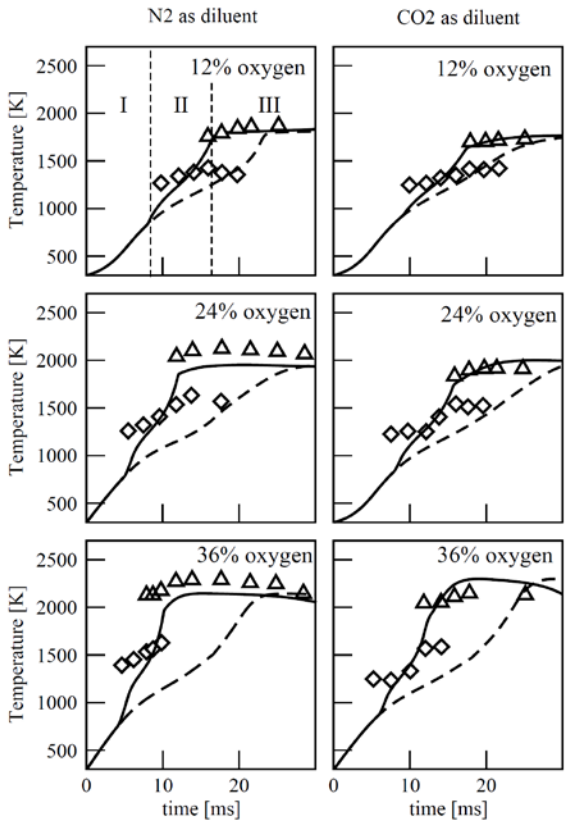


Figure 3: Particle temperature versus time for coal pyrolysis and char conversion with varying $O_2$ volume fractions. Cases have $N_2$ (left) and $CO_2$ (right) as the major diluent. Experimental data [67] - symbols, model results - lines. Figure is from [65].

a low order treatment of the mean of non-linear chemical reaction rates and increasingly for the simple treatment of the non-linear interphase transport terms. It is ideal if the conditioning variables are conserved scalars such as the mixture fraction, standardised enthalpy or a distance-like variable. There are models for other (possibly non-turbulent) reactive flow regimes which, in an attempt to avoid excessively large numerical resolution, also require the taking of averages of non-linear terms. In recent years conserved scalar models for reactive flows in porous media have emerged [68].

A porous medium has two phases: the fluid β-phase and the solid σ-phase. Heterogeneous reactions in the form of

$$A_{(g)} + B_{(s)} \rightleftharpoons C_{(g)}$$

occur at $\beta/\sigma$ -interface. The regime of this reaction depends on the Damköhler number, $Da = \tau_d/\tau_c$, which is the ratio of the timescale for diffusion of the gaseous reactant $A_{(g)}$ to the $\beta/\sigma$ - interface to the reaction timescale. The former is a function of the permeability of the gas. Since porous media consists of a very large number of interconnected pores with a wide range of sizes, practical models for reactive flow in porous media are required to solve for quantities that are spatially averaged on a grid that is numerically affordable. Conventional porous media models [69] solve for the $\beta$-phase-weighted spatial average (called the intrinsic average), which is the mean in the gas phase. Such modelling does not capture the potentially strong gradients in species concentrations in the direction normal to the reactive surface. This can be addressed by taking conditional moments on a conserved tracer species as explained below.

Three different regimes are shown in Fig.4 [70]. The solid lines show the variation in the concentration of species A with distance from the reactive surface. In the case of small Damköhler numbers ( $Da \ll 1$ ), the gaseous reactant is transported to the reactive surface much faster than it is consumed on the β/σ-interface. Changes in its concentration caused by the reaction will be compensated by the diffusive transport almost instantaneously. The regime is thus kinetically controlled. The concentration $C_A(x)$ varies insignificantly around $\langle C_A \rangle_\beta$ (the dashed line) which is the intrinsic average. Conventional porous media models which directly solve an equation for $\langle C_A \rangle_\beta$ perform well under the kinetics controlled regime [69]. When the reaction timescale is relatively small compared to the diffusion timescale ( $Da \gg 1$ ), gaseous reactant that arrives at the surface reacts immediately and the regime is said to be diffusion controlled. In the vicinity of the surface, the reactant concentration approaches zero (see Fig. 4(c)), while the intrinsic average remains large. Conventional porous media models do not account for this variation with distance from the surface. Klimenko and Abdel-Jawad [68] specifically investigated the intermediate regime for reactive flow in a static porous carbon structure, showing that the conventional approach based on instrinsic averages also gives poor predictions for $Da \sim 1$. As depicted in Fig. 4(b), the concentration of the gaseous reactant varies significantly and the intrinsic average can only be considered as a rough approximation for the actual concentration in this case.

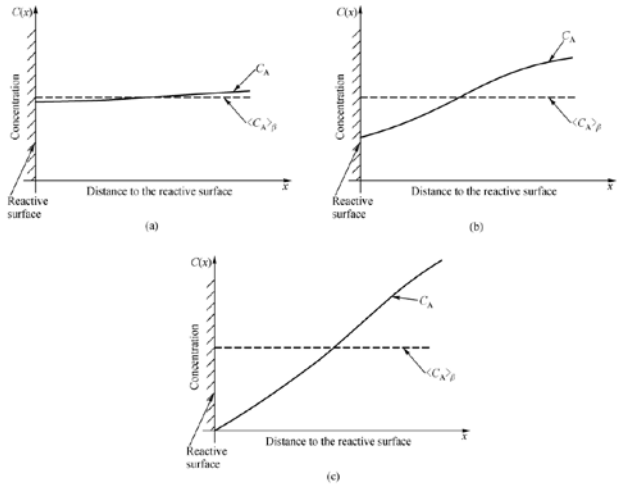


Figure 4: Schematic of the variation in the concentration of a gaseous reactant for three porous media reaction regimes: (a) kinetics controlled regime (Da≪1); (b) intermediate regime (Da~1); (c) diffusion controlled regime (Da≫1). Solid lines show concentrations varying

with distance from the reactive surface. Dashed lines show the intrinsic average, which does not vary with distance from the surface. Figure is from [70].

To address the shortcomings of intrinsic averaging in the intermediate ($Da \sim 1$) and diffusion controlled ($Da \ll 1$) regimes, Klimenko and Abdel-Jawad developed the porous conditional moment closure (PCMC) model [68]. A tracer variable, $Z$, which emulates diffusion to the reactive surface in a porous structure is introduced and the reactive scalar transport equations are conditionally averaged on it. The tracer is a conserved scalar in the $\beta$ - phase right up to the $\beta/\sigma$-interface where it is instantaneously consumed so at $Z = 0$ at that location. Thus the value of $Z$ which is non-zero away from the reactive surfaces, is related to the distance from the reactive surface. In that way the conditionally averaged mass fractions (typically both density and phase weighted)

$$\overline{Y|\eta} = \overline{Y|\eta = Z} = \frac{\overline{Y\rho\beta|\eta}}{\overline{\rho\beta|\eta}} \tag{39}$$

yields a distance dependent mass fraction that is needed for the intermediate and diffusion controlled regimes. A full derivation is found in [68].

Extensions and conceptual variations of PCMC have ensued. Saulov et al. [70] coupled the PCMC to a random pore model thus incorporating variations in the porous structure as it is consumed (e.g. char combustion) or grows (e.g. build-up of product layer). This was subsequently applied [71] to $CO_2$ capture in a gasifier whereby $CO_2$ which diffuses through a porous material reacts heterogeneously and exothermically with a solid calcium oxide doped surface to produce a product layer of calcium carbonate. Although not yet attempted, the calcination reaction whereby $CO_2$ is recycled upon endothermic reaction with oxygen would be very interesting. Klimenko and coworkers [72, 73] have also developed a related model, PDCMC, whereby the tracer is replaced by a more realistic distance variable and linked it to fractal properties of porous structures. Such models have application to a range of reactive flows in porous media. In addition to the carbon oxidation and $CO_2$ adsorption test cases mentioned above, PCMC and PDCMC have potential for modelling of underground coal fires and underground coal gasification and, depending on the Damköhler number, flow through reactive mineral networks e.g. those associated with $CO_2$ sequestration.

## 5. Pollutant formation

Conserved scalar models have been used for decades to predict pollutant formation in gaseous flames [74, 75]. The most difficult are pollutant species for which the Damköhler number is of order unity or less. For example, NOx and soot typically have chemical timescales that are much longer than the major species and often longer than the timescale of turbulent mixing. Conserved scalar models remain useful, provided they account for more than just the spatially local balance between reaction and diffusion which occurs within the thin stoichiometric zone. Conditional moment closure is suitable, while stationary laminar flamelet models are not [75]. Unsteady flamelets and representative interactive flamelets may circumvent the problems associated with their stationary counterparts.

A very challenging situation arises with the formation of pollutants in multiphase combustion, especially those pollutants derived from the fuel e.g. NOx, SOx and metal oxide emissions derived from fuel bound nitrogen, sulfur and trace heavy metal such as lead and mercury. The time and length scale ranges in multiphase flows are large, and the interactions between turbulence, homogeneous and heterogeneous chemistry, heat and mass transfer, radiation and intra-particle diffusion occur at scales not affordably resolved. Therefore subgrid or microscale models needs to account for these complex interactions taking account of the various timescales.

Power station NOx emissions are used as an example. About 70-80% of pulverised coal furnace NOx emissions are derived from the fuel bound nitrogen (fuel-N) [76]. Typical coals have fuel-N fractions of between 0.5 and 2.5% [77]. Biomass fuels sourced from agricultural residues exhibit a similar range. That fuel-N is partitioned between the fuel's volatile and char components. In high temperature combustion of pulverised coal, about 75 – 80% of the fuel-NOx comes from the volatiles with the remainder from the char. Pyrolysis of volatiles has a much shorter timescale than does char conversion. Figure 3, which was discussed above, shows experimental and model data for sequential pyrolysis and char conversion of coals at high temperature in various atmospheres [65, 67]. Defining the interphase mass transfer timescale as the ratio of the particle diameter to the Stefan flow velocity at the surface, $d/V_S$, the pyrolysis time scale is of order $10^{-5}\ s$ while the char conversion time scale is an order of magnitude larger at about $10^{-4}\ s$. Particle ignition delay and particle life times are of course much longer in the order of $10^{-3}\ s$ and $1 \times 10^{-1}\ s$, respectively. These need to be considered in the context of time scales for turbulent mixing and chemical reactions. A typical turbulent dispersion of coal would have a turbulent mixing time scale in the range of $10^{-4}$ to $10^{-3}\ s$. The chemical timescale for NOx production could be from $10^{-2}$ to $10^{-1}\ s$ whereas the timescale associated with the main oxidation reactions and heat release is usually an order of magnitude or so shorter than the turbulence time scale making it of the same order as the pyrolysis time scale. The three to four order of magnitude difference between the time scale associated with NOx production and that of the time scales associated with pyrolysis of volatiles (where much of NOx originates) and the main heat release reactions provides a challenge to modellers. While the flamesheet approximation [2, 43, 44, 48, 54, 58] or flamelet approximation [65] for the flame structure in the vicinity of a fuel particle are reasonable for predicting heating rates and major species production, NOx prediction is different as it is kinetically limited. More advanced treatments of the

diffusive layer are needed. As yet such models do not exist, spare fully resolved simulations of single fuel particles in fundamental studies.

Existing models for multiphase dispersions that are discussed in the previous sections assume that mass transfer occurs across a single interface between the gas and an impervious fuel particle. In reality coal particles are highly porous. Release of fuel bound pollutant species is thus further complicated by the need to consider that diffusion and reactions within that structure. The PCMC models may offer some new insights, while interaction of the PCMC with modelling of the diffusive layer and wider turbulent flow will pose a challenge to numericists.

## 6. Conclusion

Combustion models based on conserved scalars and conditional moments are presented as exemplars for accurate and affordable modelling. While well established for the modelling of gaseous fuel combustion, their application to multiphase regimes is still in the early stages. The recent examples are showing much potential with good predictions of the major quantities such as velocity and temperature in turbulent spray flames. The ability to predict pollutant species such as fuel derived NOx remains untested at this point. There are a number of continuing challenges associated with modelling the transfer of mass and heat between the liquid or solid fuel phase and the gas phase where turbulent reactions occur. Although the mixture fraction retains its conserved nature though the reaction zone, the appearance of vapour production terms due to evaporation, pyrolysis or char conversion add a source term whose closure remains uncertain. In particular the modelling of the mixture fraction variance may vary by orders of magnitude depending on which of the available closure models is chosen. The conditional interphase transport term in CMC (which has a counterpart in the multiphase flamelet equations) has also posed a challenge to modellers. To date two simple models have been suggested and tested with some ongoing refinement to improve their physical interpretation. The recent development and validation of a unified conserved scalar model for heat and mass transfer for combined evaporation, pyrolysis and char conversion also shows much potential although is yet to be tested in a turbulent flow.

The conditional moment closure hypothesis has a number of alternative or related implementations. Conditional source term estimation and multiple mapping conditioning are now well established for gaseous combustion although they have not yet been applied to multiphase cases. Porous CMC modelling is another novel development with a wide range of potential applications including combustion of porous materials such as char and sorption of pollutant species.

## 7. Acknowledgements

I devote this paper to the memory of Professor Robert W. Bilger who sadly died in October this year. Bob had a long and distinguished career developing and championing combustion research in general and conserved scalar models in particular. I am proud to acknowledge the large extent to which Bob as my supervisor, mentor and coauthor has influenced my career and research directions.

This work draws on research conducted over the past five years and funded by the Australian Research Council under grant numbers DP120102294 and DP130100763 and the Department of Resources, Energy and Tourism under the Australia-China Joint Coordination Group on Clean Coal Technology under funding agreement 001086. I would also like to acknowledge that my understanding of the topics addressed in the paper have been influenced over many long and enjoyable discussions with Andreas Kronenburg and Oliver Stein at Universität Stuttgart and Alex Klimenko at the University of Queensland.

## 8. References

1. S.P. Burke, T.E.W. Schumann, Ind. Engng Chem., 20 (1928) 998 - 1004.
2. S.R. Turns, in, McGraw-Hill, Singapore, 2012.
3. R.W. Bilger, S.B. Pope, K.N.C. Bray, J.F. Driscoll, Proc. Combust. Inst., 30 (2005) 21 - 42.
4. N. Peters, Prog. Energ. Combust. Sci., 10 (1984) 319 - 339.
5. A. Saghafian, V.E. Terrapon, H. Pitsch, Combust. Flame, 162 (2015) 652 - 667.
6. A.Y. Klimenko, R.W. Bilger, Prog. Energy Combust. Sci., 25 (1999) 595 - 687.
7. A. Kronenburg, E. Mastorakos, The conditional moment closure method, in: T.E.a.E. Mastorakos (Ed.) Turbulent Combustion Modeling - Advances, New Trends and Perspectives, Springer, 2011.
8. H. Steiner, W.K. Bushe, Phys. Fluids, 13 (2001) 754 - 769.
9. D. Dovizio, J.W. Labahn, C.B. Devaud, Combust. Flame, 162 (2015) 1976 - 1986.
10. A.Y. Klimenko, S.B. Pope, Phys. Fluids, 15 (2003) 1907 - 1925.
11. A.P. Wandel, R.P. Lindstedt, Phys. Fluids`, 21 (2009) 015103.
12. K. Vogiatzaki, M.J. Cleary, A. Kronenburg, J.H. Kent, Phys. Fluids, 21 (2009) 025105.
13. A.Y. Klimenko, Fluid Dynamics, 25 (1990) 327 - 334.
14. R.W. Bilger, Phys. Fluids A, 5 (1993) 436.
15. R.S. Barlow, J.H. Frank, Proc. Combust. Inst., 27 (1998) 1087 - 1095.
16. S.H. Kim, K.Y. Huh, L. Tao, Combust. Flame, 120 (2000) 75 - 90.
17. S. Navarro-Martinez, A. Kronenburg, F.D. Mare, Flow, Turbul. Combust., 75 (2005) 245 - 274.
18. G. Kim, S. Kang, Y. Kim, R.W. Bilger, M.J. Cleary, Combust. Theor. Model., 11 (2007) 527 - 552.
19. S.H. Kim, K.Y. Huh, Combust. Flame, 138 (2004) 336 - 352.
20. G.D. Paola, I.S. Kim, E. Mastorakos, Flow, Turbul. Combust., 82 (2009) 455 - 475.

21. M.J. Dunn, A.R. Masri, R.W. Bilger, R.S. Barlow, G.-H. Wang, Proc. Combust. Inst., 32 (2009) 1779 - 1786.
22. S.M. Martin, J.C. Kramlich, G. Kosaly, J.J. Riley, J. Eng. Gas Turb. Power, 125 (2003) 895 - 900.
23. F. Salehi, M. Talei, E.R. Hawkes, C.S. Yoo, T. Lucchini, G. D'Errico, S. Kook, Proc. Combust. Inst., 35 (2015) 3087 - 3095.
24. W.K. Bushe, H. Steiner, Phys. Fluids, 11 (1999) 1896.
25. H. Steiner, W.K. Bushe, Phys. Fluids, 13 (2001) 754.
26. B. Jin, R. Grout, W.K. Bushe, Flow, Turbul. Combust., 81 (2008) 563 - 582.
27. D. Dovizio, M.M. Salehi, C.B. Devaud, Combust. Theor. Model., 17 (2013) 935 - 959.
28. A. Kronenburg, Phys. Fluids, 16 (2004) 2640 - 2648.
29. A. Kronenburg, M. Kostka, Combust. Flame, 143 (2005) 342 - 356.
30. J.W. Labahn, D. Dovizio, C.B. Devaud, Proc. Combust. Inst., 135 (2015) 3547 - 3555.
31. M.J. Cleary, A. Kronenburg, Proc. Combust. Inst., 31 (2007) 1497 - 1505.
32. A.P. Wandel, A.Y. Klimenko, Phys. Fluids, 17 (2005) 128105.
33. K. Vogiatzaki, S. Navarro-Martinez, S. De, A. Kronenburg, Flow, Turbul. Combust., 95 (2015) 501 - 517.
34. B. Sundaram, A.Y. Klimenko, M.J. Cleary, U. Maas, Proc. Combust. Inst., 35 (2015) 1517 - 1525.
35. L. Dialameh, M.J. Cleary, A.Y. Klimenko, Phys. Fluids, 26 (2014) 025107.
36. M.J. Cleary, A.Y. Klimenko, Phys. Fluids, 23 (2011) 115102.
37. A.Y. Klimenko, Combust. Flame, 143 (2005) 369 - 385.
38. R.W. Bilger, Combust. Flame, 158 (2009) 191 - 202.
39. Y. Baba, R. Kurose, J. Fluid Mech., 612 (2008) 45 - 79.
40. M. Mortensen, R.W. Bilger, Combust. Flame, 156 (2009) 62 - 72.
41. I. Kataoka, Int. J. Multiphase Flow, 12 (1986) 745 - 758.
42. D.B. Spalding, Some fundamentals of combustion, Academic Press Inc., New York, 1955.
43. G. Borghesi, E. Mastorakos, C.B. Devaud, R.W. Bilger, Combust. Theor. Model., 15 (2011) 725 - 752.
44. A. Srna, M. Bolla, K. Boulouchos, Y. Wright, SAE Technical Paper, 2014-01-2738 (2014).
45. C. Pera, J. Reveillion, L. Vervisch, P. Domingo, Combust. Flame, 146 (2006) 635 - 648.
46. J. Reveillion, L. Vervische, Combust. Flame, 121 (2000) 75 - 90.
47. A. Kronenburg, in: 7th International Workshop on Conditional Moment Closure and Multiple Mapping Conditionoing, San Francisco, 2014.
48. S. Ukai, A. Kronenburg, O.T. Stein, Proc. Combust. Inst., 34 (2013) 1643 - 1650.
49. S. De, S.H. Kim, Combust. Flame, 160 (2013) 2048 - 2066.
50. J. Rogerson, R.W. Bilger, J.H. Kent, Proc. Combust. Inst., 31 (2007) 2805 - 2811.
51. S. Sreedhara, K.Y. Huh, Proc. Combust. Inst., 31 (2007) 2335 - 2342.
52. J. Seo, K.Y. Huh, Proc. Combust. Inst., 34 (2013) 1687 - 1695.
53. P. Schroll, E. Mastorako, R.W. Bilger, AIAA paper, (2010) 2010-2614.
54. S. Ukai, A. Kronenburg, O.T. Stein, Proc. Combust. Inst., 35 (2015) 1667 - 1674.
55. A.R. Masri, J.D. Gounder, Combust. Sci. Technol., 182 (2010) 702 - 715.
56. H. Olguin, E. Gutheil, Combust. Flame, 161 (2014) 987 - 996.
57. F. Salehi, M.J. Cleary, A.R. Masri, in: Australian Combustion Symposium, Melbourne, 2015.
58. M. Bolla, A. Srna, Y.M. Wright, B.V. Rotz, K. Herrmann, K. Boulouchos, SAE Technical Paper, 2014-01-1419 (2014).
59. G. D'Errico, T. Lucchini, F. Contino, M. Jangi, X.-S. Bai, Combust. Theor. Model., 18 (2014) 65 - 88.
60. E. Knudsen, Shashank, H. Pitsch, Combust. Flame, 162 (2015) 159 - 180.
61. H. Barths, C. Hasse, N. Peters, Int. J. Engine Research, 1 (2000) 249 - 267.
62. S. De, K.N. Lakshmisha, R.W. Bilger, Combust. Flame, 158 (2011) 1992 - 2008.
63. M. Stöllinger, B. Naud, D. Roekaerts, N. Beishuizen, S. Heinz, Combust. Flame, 160 (2013) 396 - 410.
64. M. Stöllinger, B. Naud, D. Roekaerts, N. Beishuizen, S. Heinz, Combust. Flame, 160 (2013) 384 - 395.
65. M.J. Cleary, O.T. Stein, A. Kronenburg, R.W. Bilger, Combust. Flame, submitted (2015).
66. P.R. Solomon, T.H. Fletcher, R.J. Pugmire, Fuel, 72 (1993) 587 - 597.
67. C.R. Shaddix, A. Molina, Proc. Combust. Inst., 32 (2009) 2091 - 2098.
68. A.Y. Klimenko, M.M. Abdel-Jawad, Proc. Combust. Inst., 31 (2007) 2107 - 2115.
69. M. Quintard, S. Whitaker, Tranport in Porous Media, 14 (1994) 163 - 177.
70. D.N. Saulov, C.R. Chodanka, M.J. Cleary, A.Y. Klimenko, Front. Chem. Sci. Eng., 6 (2012) 84 - 93.
71. D.N. Saulov, S. Watanabe, J. Yin, D.A. Klimenko, K. Hooman, B. Feng, M.J. Cleary, A.Y. Klimenko, Energies, 7 (2014) 1899 - 1916.
72. I.G. Vladimirov, A.Y. Klimenko, Multiscale Model. Simul., 8 (2010) 1178 - 1211.
73. A.Y. Klimenko, D.N. Saulov, P. Massarotto, V. Rudolph, Transp. Porous Media, 92 (2012) 745 - 765.
74. J.H. Kent, R.W. Bilger, Proc. Combust. Inst., 16 (1976) 1643 - 1656.
75. M.J. Cleary, J.H. Kent, Combust. Flame, 143 (2005) 357 - 368.
76. A. Williams, J.M. Jones, L. Ma, M. Pourkashanian, Prog. Energy Combust. Sci., 38 (2012) 113-137.
77. P. Glarborg, A.D. Jensen, J.E. Johnsson, Prog. Energy Combust. Sci., 29 (2003) 89-113.

# Impact of Triacetin as an oxygenated fuel additive to waste cooking biodiesel: transient engine performance and exhaust emissions

A. Zare[1,*], T. Bodisco[1], M.N. Nabi[1, 2], H.M. Farhad[1], M.M. Rahman[1, 2], D. Stuart[3], Z. Ristovski[1, 2], R.J Brown[1]

[1]Biofuel Engine Research Facility, Queensland University of Technology (QUT), QLD, 4000 Australia
[2]ILAQH, Queensland University of Technology (QUT), QLD, 4000 Australia
[3]Eco Tech Biodiesel Pty Ltd, QLD, 4504 Australia

## Abstract

The present work investigates the effect of oxygenated fuels on exhaust emission and engine performance under transient operation on a fully instrumented 6-cylinder turbocharged diesel engine with a common rail injection system. A range of oxygenated fuels based on waste cooking biodiesel with triacetin as an oxygenated additive were tested under transient operation. This investigation has shown that increasing the oxygen content of the fuel causes a decrease in exhaust particulate matter and particulate number. Increased oxygen in the fuel decreases the indicated power and the indicated mean effective pressure, while the brake specific fuel consumption increases. Different physical and chemical properties of the fuels are used to interpret the behaviour of the engine under transient operation. Owing to the use of oxygenated fuels, the oxygen ratio was used instead of the air to fuel ratio to better explain the phenomena during combustion.

*Keywords: Oxygenated fuel, Transient operation, Oxygen ratio, Engine performance, Exhaust emission,*

## 1. Introduction

To date, most studies of internal combustion engines have focused on steady-state operation [1]. However, in vehicles, engines are seldom used in steady state. Therefore, studies investigating transient operation are more likely to provide results reflective of reality than those investigating steady-state operation only. Here transient operation is defined as any operation in which the fuel injection or engine speed are changing frequently [1].

In general, combustion products under transient operation are more readily produced compared to steady-state operation. For example, 50% of NOx emissions during the European Driving Cycle stem from periods of acceleration. Similarly, PM (particulate matter) emissions during load increase have been measured to be higher than their respective quasi-steady-state values [1-4].

The complexity of transient operation experiments, and the availability of high-tech fast response measuring instruments and automatically controlled test-beds, have limited the research work done to date on transient engine operation. In addition, most of the current work investigating transient operation focused on driving cycles showing the mean values of the emission and engine performance parameters. Investigation into the effects of discrete modes of transient operation, such as load acceptance and free acceleration, to date, have been limited [1, 5].

High fuel price, global warming, environmental degradation and adverse health effects of fossil fuels have motivated a significant amount of recent engine research [1]. Fuel specific solutions investigated range from finding new sources of fuel or by adding additives to conventional fuels. The European Union issued a directive to offset fossil fuel usage with renewable biofuels by 10% by 2020 (EU Directive 2009/28/EC).

The current literature shows some advantages and disadvantages for the use of waste cooking biodiesel [6]. Previous studies, which were mostly under steady-state conditions, blended this fuel with diesel. A study reported that using waste olive oil decreased CO up to 58.9%, $CO_2$ up to 8.6%, however $NO_2$ and BSFC (brake specific fuel consumption) increased [7]. Another study reported lower PM, better engine performance and higher NOx on a commercial diesel engine [6].

Whilst biofuels have some advantages such as reducing PM, CO and HC, there are some disadvantages such as higher NOx. Hence, fuel additives could play an import role in improving the negative points of the blend. In addition to improving emission, fuel additives can improve the quality of combustion and ignition, and protect the engine from some issues such as wax deposition and abrasion [8].

As an additive to biofuel triacetin [$C_9H_{14}O_6$], which is the triester of glycerol acetic acid, could be introduced [9]. Glycerol is a byproduct of the production of biodiesel. A recent study of the effect of triacetin showed that adding triacetin to biofuels increases the density and viscosity of the blend. However, cetane number, heating value and flash point of the blend reduced [9].

This paper intends to study engine performance and exhaust emission under transient operation using a range of oxygenated fuels based on waste cooking biodiesel as the primary fuel and triacetin as an additive.

* Corresponding author: Ali Zare
Phone: (+61) 449857803
Email: ali.zare@qut.edu.au

## 2. Material and methods

### *Experimental facilities*

The engine used in this study was a 6-cylinder turbocharged diesel engine with a common rail injection system coupled to an electronically controlled water brake dynamometer. This engine research facility has the ability to program different test cycles that can be run automatically at 1 Hz resolution. For more specific information about the engine and experimental facilities readers can refer to Ref. [10].

### *Measuring instrumentation*

- DMS500 MkII Fast Particle Analyzer
- DUSTTRAK II AEROSOL MONITOR 8530
- California Analytical Instruments Models CAI-600 CLD NO/NOx digital analyzer and CAI-603 NDIR Gas Analyzer
- SABLE CA-10 Carbon Dioxide Analyzer

### *Fuel selection*

Table 1 shows the set of fuels used in this study. Except neat diesel, the blends were based on the waste cooking biodiesel as the primary fuel and triacetin as an additive. In this study, the oxygenated fuels are named according to their oxygen content.

### *Transient test*

In this experiment, a modal custom transient test was designed to evaluate the engine performance and exhaust emission during load acceptance. As it is shown in Fig. 1, this custom test has 2 main parts where each part is related to one speed, 1864 or 2257 RPM. In each part there are 3 loads, 25, 50 and 75%. Engine speed and torque were selected by mapping the engine according to the European Stationary Cycle (ESC) driving cycle pattern [11].

Table 1 Fuel properties.

| Properties | D100 | D60B35T5 | B100 | T4B96 | T8B92 | T10B90 |
|---|---|---|---|---|---|---|
| **O (wt%)** | **0** | **6.02** | **10.93** | **12.25** | **13.57** | **14.23** |
| C (wt%) | 85.1 | 80.46 | 76.93 | 75.81 | 74.73 | 74.19 |
| H (wt%) | 14.8 | 13.47 | 12.21 | 11.97 | 11.74 | 11.63 |
| Density @15°C (g/cc) | 0.84 | 0.866 | 0.87 | 0.882 | 0.893 | 0.898 |
| LHV (MJ/kg) | 41.77 | 38.92 | 37.2 | 36.38 | 35.57 | 35.16 |
| KV@40°C ($mm^2/s$) | 2.64 | 3.66 | 4.82 | 4.94 | 5.06 | 5.12 |
| Cetane number | 53.3 | 53.24 | 58.6 | 56.86 | 55.11 | 54.24 |

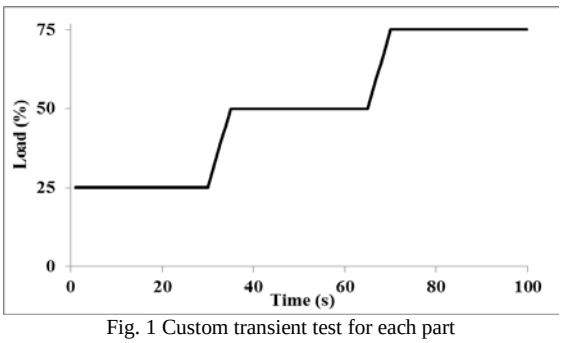

Fig. 1 Custom transient test for each part

## 3. Result and discussion

### *OR and OFR*

The proximity of the air and fuel mixture during combustion to its stoichiometric condition affects the exhaust emission and engine performance characteristics [12]. The equivalence ratio is a widely used parameter to quantify the mixture by using the actual and stoichiometric AFR (air to fuel ratio). AFR which is a commonly used parameter only shows the ratio of the intake air and fuel, and it cannot show the real amount of oxygen when the fuel is oxygenated. Since the presence of oxygen molecules during combustion can be a significant factor in the analysis of emission and engine performance, a different parameter should be used to show information about the real amount of oxygen molecules present during combustion.

In this regard, OR (oxygen ratio) and OFR (oxygen fuel ratio) can be used. These parameters have been proposed in the literature to show the oxygen presence of oxygenated fuels during combustion [12].

OFR is the ratio of the total oxygen atoms of the fuel to the total required oxygen atoms for the stoichiometric combustion [13]. OFR for diesel, which has no oxygen content, is zero. In this study, by increasing the oxygen content of the fuel, OFR increases linearly with $R^2$=0.985 up to 4.87 for the fuel with 14.23% oxygen content.

OR is defined in the below formula where "$Oxygen_{fuel}$" and "$Oxygen_{air}$" are the masses of oxygen within the fuel and the intake air, respectively. The "Stoichiometric oxygen requirement" is the theoretical amount of oxygen required for stoichiometric combustion.

$$OR = \frac{Oxygen_{fuel} + Oxygen_{air}}{\text{Stoichiometric oxygen requirement}} \quad (1)$$

Figure 2 shows the AFR and OR for the tested fuels at all the modes of the custom transient test. Also, it can be seen that by increasing the oxygen content of the fuel, the AFR decreases and the OR increases. Diesel has the highest AFR at all the modes. It shows that the OR provides different information about the presence of oxygen atoms during combustion that can be used to explain the other parameters in this study.

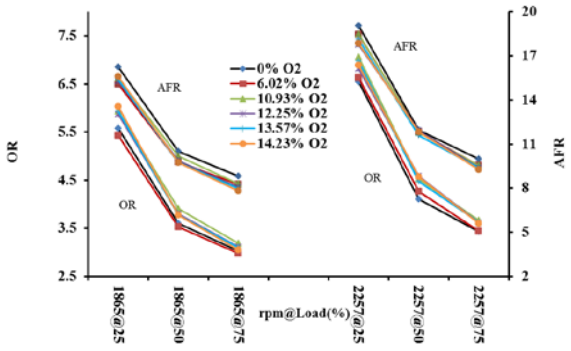

Fig. 2 Effect of 6 fuel oxygen content under the custom test on Oxygen ratio and Air fuel ratio

## Exhaust Emission

### *Nitrogen oxides*

As shown in Fig. 4(a), increasing the oxygen content of the fuel increases the NOx. Diesel with 0% oxygen content has the lowest NOx emission at 50% and 75% load for both speeds. The effective parameters of NOx formation can be the in-cylinder temperature, oxygen presence, ignition delay and fuel chemical properties [1].

Owing to the higher bulk modulus of the biofuel, as compared to neat diesel, the pressure rise in the injector will occur earlier. Consequently the advanced injection timing will lead to an extended premixed phase and total residence time; thereby the in-cylinder temperature will be increased leading to increased NOx formation. Additionally, the higher density of oxygenated fuels has been shown to cause a higher injected mass of fuel in some volumetric based injectors [1, 14] as it is shown by the BSFC in Fig. 3(b).

During turbolag, when the AFR is low, combustion is closer to stoichiometric, leading to higher in-cylinder temperature and consequently increased NOx formation. Moreover, in engines using mechanical fuel pumps, due to higher viscosity fuel leakage losses will be lower with biodiesel compared to diesel. Consequently the injection pressure will be higher leading to an increase in injected fuel quantity and lower AFR (Fig. 2 and Fig. 3(b)) thereby increasing NOx [1, 14]. NOx formation is highly correlated to the engine load which leads to higher temperature and lower AFR, as it can be seen in Fig. 2. Hence by increasing the load, NOx increases for each fuel separately, shown in Fig. 4(a).

Flame temperature is another parameter that can affect NOx formation. It has been reported that because of the double bonds in the molecules of biofuels the adiabatic flame temperature of biofuels is higher than diesel [15]. Another report stated that the adiabatic flame temperature is affected by in-cylinder radiative heat transfer from soot particle formation. It has been frequently reported that oxygenated fuels have a lower amount of soot compared to diesel, a conclusion mirrored in this study. Oxygenated fuels, therefore, have lower radiative heat transfer which leads to higher flame temperature and therefore increased NOx formation [1].

### *Particulate matter*

Generally, particulate matter is a liquid and solid mixture suspended in a gas. In compression ignition engines, injected fuel will be mixed with an oxidant in the combustion chamber; consequently, a great degree of heterogeneity characterises the combustion process. This process is defined as diffusion flame combustion, which is the main cause of PM emission. PM is a complicated pollutant that is not a chemically well-defined substance in terms of formation or composition. PM composition depends on various factors such as fuel type, lubricant type, engine load, engine speed, after-treatment devices, dilution level after being emitted and engine maintenance.

Figure 4(b) shows the diluted PM emission for the tested fuels under the custom transient test. Diesel, with 0% oxygen content, emits the highest amount of PM in all of the modes. It can clearly be seen that the PM reduces by increasing the oxygen content in the fuel. It should be mentioned that the normalised PM showed the same trend. PM formation is highly correlated to the engine load which leads to higher temperature and lower AFR, shown in Fig. 2.

Generally, PM formation takes place in the fuel-rich zone under high temperature decomposition during combustion. It mainly happens in the sprayed fuel core region. Apart from the type of fuel, the presence of oxygen helps the soot oxidation process. In addition to the intake air, in oxygenated fuels, the local fuel-rich zone within the core region of the sprayed fuel is reduced, preventing higher PM formation. Hence, the greater the oxygen content of the fuel, the less soot formation.

Owing to the higher bulk modulus of the biofuels the pressure rise in the injector will occur earlier; consequently, advancing the injection timing, leading to an extended premixed phase and total residence time, increasing the in-cylinder temperature. This process is beneficial since oxygenated fuel combustion has a higher duration after diffusion combustion, leading to lower PM [1].

### *Particle number*

Although the effect of increasing oxygen in fuel has been consistently reported in the literature to result in a decrease of PM, the corresponding effect on PN has not been consistent [1]. Some found an increase in PN such as reported during the NEDC (new European drive cycle) [16, 17]. On the other hand, a decrease in PN during the NEDC and Artemis transient driving cycle has also been reported [18].

Figure 4(c) shows the diluted PN emission for the tested fuels under the custom transient test. As can be seen by increasing the oxygen content of fuel, PN decreases. Diesel, with 0% oxygen content, has the highest value and the 14.23% oxygenated blend of waste cooking biodiesel and triacetin has the lowest emitted PN in all the modes. It should be mentioned that the normalised PN emission showed the same trend.

## Engine Performance

According to the Fig. 3(a) Diesel has the highest IMEP compared to the other oxygenated fuels. These parameters reduce by increasing the oxygen content of the fuel. This is due to the heating value of the fuels. As shown in Table 1, the lower heating value decreases by increasing the oxygen content of fuel.

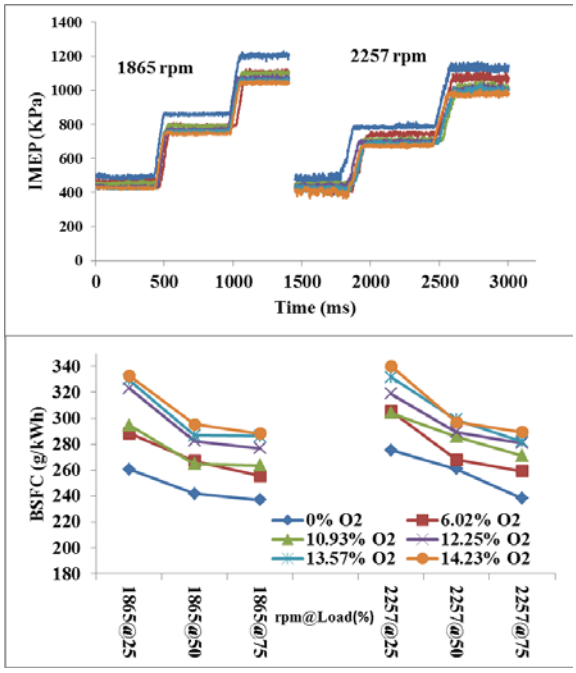


Fig. 3. Effect of 6 fuel oxygen content under the custom test (a) Brake specific fuel consumption (BSFC) and (b) Indicated mean effective pressure (IMEP)

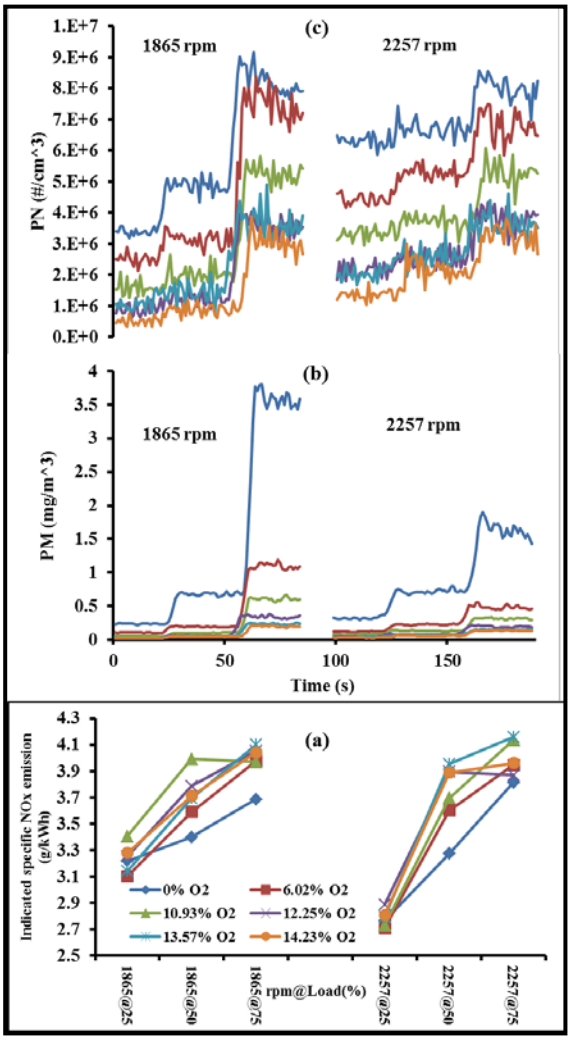


Fig. 4 Effect of 6 fuel oxygen content under the custom test on: (a) Normalised NOx emission; (b) diluted PM emission, (c) diluted PN emission

## 4. Conclusion

This work investigated the engine performance and exhaust emission under transient operation using a set of blended oxygenated fuels. The blends were based on waste cooking biodiesel as a primary fuel and triacetin as an additive. Results showed that increasing the oxygen content of the fuel leads to a reduction in IMEP, PM and PN, with the caveat that BSFC and NOx were increased. These results have been primarily attributed to the oxygen presence, heating value and density of the oxygenated fuels.

## 5. Acknowledgments

This research supported under Australian Research Council's Linkage Projects funding scheme (project number LP110200158). The author also would like to acknowledge the laboratory assistance from Mr. Noel Hartnett, DynoLog software development by Mr Andrew Elder from DynoLog Dynamometer Pty Ltd, Peak3 Pty Ltd for helping with measuring instruments, and Eco Tech Biodiesel for the supply of waste cooking biodiesel.

## 6. References

[1] E. G. Giakoumis; C. D. Rakopoulos; A. M. Dimaratos; D. C. Rakopoulos, Progress in Energy and Combustion Science **38** (5) (2012) , pp. 691-715 http://dx.doi.org/10.1016/j.pecs.2012.05.002.

[2] C. D. Rakopoulos; E. G. Giakoumis, Diesel engine transient operation, Springer, 2009

[3] B. K. Gullett; A. Touati; L. Oudejans; S. P. Ryan, Atmospheric Environment **40** (22) (2006) , pp. 4037-4047

[4] J. R. Hagena; Z. S. Filipi; D. N. Assanis, in: SAE Technical Paper No. 2006-01-1151 (2006)

[5] D. C. Rakopoulos; C. D. Rakopoulos; E. G. Giakoumis, Fuel **156** (2015) , pp. 1-19

[6] M. G. Kulkarni; A. K. Dalai, Industrial & engineering chemistry research **45** (9) (2006), pp. 2901-2913

[7] M. Dorado; E. Ballesteros; J. Arnal; J. Gomez; F. Lopez, Fuel **82** (11) (2003) , pp. 1311-1315

[8] P. V. Rao; B. A. Rao, Journal homepage: www. IJEE. IEEFoundation. org **3** (4) (2012) , pp. 629-638

[9] A. Casas; J. R. Ruiz; M. a. J. s. Ramos; A. Pérez, Energy & Fuels **24** (8) (2010) , pp. 4481-4489

[10] T. Bodisco; P. Tröndle; R. J. Brown, Energy **84** (2015) , pp. 186-195

[11] European Parliament and of the Council, in: *Directive 1999/96/EC*, Official Journal of European Union, L 044: 13 December 1999.

[12] C. J. Mueller; M. Musculus; L. Pickett; W. Pitz; C. Westbrook in: *The oxygen ratio: a fuel independent measure of mixture stoichiometry*, 30th International symposium on combustion, 2005

[13] P. X. Pham; T. A. Bodisco; Z. D. Ristovski; R. J. Brown; A. R. Masri, Fuel **116** (2014) , pp. 140-150

[14] J. Sun; J. A. Caton; T. J. Jacobs, Progress in Energy and Combustion Science **36** (6) (2010) , pp. 677-695

[15] R. L. McCormick; M. S. Graboski; T. L. Alleman; A. M. Herring; K. S. Tyson, Environmental science & technology **35** (9) (2001) , pp. 1742-1747

[16] G. Fontaras; G. Karavalakis; M. Kousoulidou; T. Tzamkiozis; L. Ntziachristos; E. Bakeas; S. Stournas; Z. Samaras, Fuel **88** (9) (2009) , pp. 1608-1617

[17] S.M. Chien; Y.J. Huang; S.C. Chuang; H.H. Yang, Aerosol and Air Quality Research **9** (1) (2009) , pp. 18-31

[18] A. Macor; F. Avella; D. Faedo, Applied Energy **88** (12) (2011), pp. 4989-5001

# Modeling of the ion current developed in a direct-injection diesel engine

Rahul Rao [1, *], Damon Honnery[1]
[1]Laboratory for Turbulence Research in Aerospace & Combustion
Monash University VIC 3800 Australia

**Abstract**

This paper presents a modelling study of the ion current produced in a direct-injection diesel engine. A phenomenological diesel engine model is developed that uses established spray, entrainment and heat transfer submodels and an ionic mechanism for n-heptane to solve for heat release, species concentrations and the ion current in the combustion chamber at different engine load settings. These predictions are compared to experimental results. Good agreement is found for the in-cylinder pressure and apparent heat release rate, with average absolute errors of 2.98% and 9.36% respectively. The ion current peaks are predicted fairly well with an average absolute error of 12.56%. The widths of the ion current peaks are significantly under-predicted and their positive offset due to soot is not modelled.

*Keywords: phenomenological engine model, ion current, diesel engine*

## Nomenclature

| | |
|---|---|
| $m_f$ | Mass of fuel in each packet |
| S | Spray penetration |
| $d_n$ | Diameter of nozzle hole |
| $t_b$ | Spray breakup time |
| $F_e$ | Entrainment factor |
| $u_i$ | Initial spray velocity |
| h | Convective heat transfer coefficient |
| B | Cylinder bore |
| P,T | Cylinder pressure & temperature |
| $\upsilon$ | Mean cylinder gas velocity |
| $m_e$ ,$\mu_e$, e | Electron mass, electron mobility & elementary charge |
| $v_{eH}$ | Collision frequency between electrons and heavy species |
| $F_G$ | Ion sensor geometric factor |
| $V_s$ | Voltage across ion sensor electrodes |
| $N_e$ | Number of electrons |

## 1. Introduction

Ion currents have been used in spark-ignition internal combustion engines for the prediction of several in-cylinder variables such as air-fuel ratio [1–3], in-cylinder pressure and peak pressure position [4, 5], as well as input for closed-loop control of spark-advance timing [6], knock and misfire [7]. Their use in compression-ignition engines includes the estimation of start of combustion [8], engine-out torque [9], combustion resonance [10] and soot emissions [11], and the closed-loop control of injection timing [12]. Additionally, given their low cost, it is clear that the ion current has many possible uses in internal combustion engine analysis and prediction of performance.

Chemical reaction mechanisms that are suitable for modelling the ion current are rare and are generally highly specialised for certain applications. Most detailed mechanisms [13–15] for hydrocarbon fuels, while comprising several hundred to a few thousand reactions, contain only neutral species. Some ionic mechanisms for methane [16] and propane [17] combustion exist and have been used successfully for single-dimensional modeling of the ion current in laminar flames, HCCI engines and constant-volume chambers. Rao & Honnery [18] developed a highly reduced ionic mechanism for methane combustion that was successfully used to reproduce experimental measurements of species concentrations in a laminar flame and pressure and ion current history during a constant-volume combustion event.

Phenomenological models for internal combustion engines are relatively computationally inexpensive compared to CFD models and, with good calibration techniques, can provide useful information on engine performance and emissions [19, 20]. Reaction mechanisms for surrogate fuels can be used in phenomenological models to simulate detailed chemistry. n-heptane is a commonly used surrogate fuel for diesel [14, 21]. An n-heptane mechanism was used in conjunction with 56 ion reactions in a 3-D CFD engine model to predict the ion current [22]. While accurate results were able to be achieved, complexity makes such a model computationally expensive. A smaller kinetic mechanism in a phenomenological engine model greatly reduces computational time. The aim of this work is to use a reduced chemical kinetic reaction mechanism in a phenomenological diesel engine model to predict experimentally observed in-cylinder pressure, heat release rate and ion current.

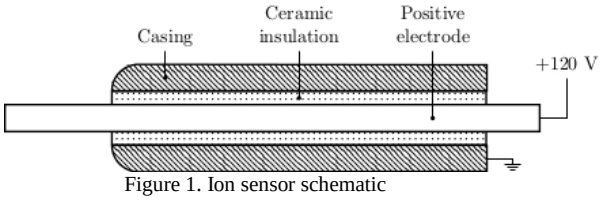

Figure 1. Ion sensor schematic

* Corresponding author:
Phone: (+61) 3 9905 1008
Email: Rahul.Rao@monash.edu

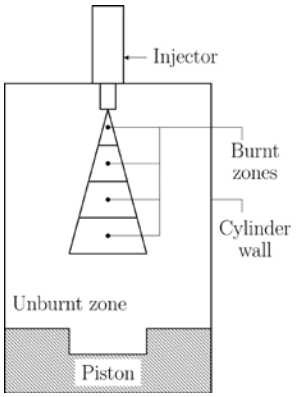

Figure 2. Division of the spray

## 2. Experiment

This study is based on experimental results obtained using a 4 L, 4 cylinder Hino W04D direct injection diesel engine coupled to a Heenan-Froude eddy current dynamometer and Froude-Hofmann V4 dynamometer controller. The combustion chamber is a bowl-in-piston design. Details on the engine can be found in Rao & Honnery [19]. In-cylinder pressure was logged every 0.2 crank angle degrees with an AVL piezoelectric high-pressure GU12P transducer. An AVL needle lift indicator was installed in cylinder 1 injector, with an SL31D2000 transducer measuring the pressure in the fuel line to this injector. This data was recorded as the average of 80 consecutive engine cycles using AVL Indicom software. Crank angle is measured using an AVL 346 angle encoder. The volumetric flow rate of intake air was measured using a turbine flowmeter and the flow rate of fuel measured using a strain gauge. These two measurements, therefore, represent averages over all four cylinders. Further details on the experimental setup for measurement of these parameters can be found in Rao & Honnery [19, 20].

The ion sensor used in these experiments is the same as that used by Rao & Honnery [9]. A schematic of the sensor is shown in Figure 1. The ion current is logged every 0.2 crank angle degrees to match the sampling rate of cylinder pressure. To match the AVL data, the experimental ion current is presented here as the average of 80 consecutive engine cycles. Further details on the design of the ion sensor and the experimental procedure can be found in Rao & Honnery [9].

## 3. Model

This section describes the various submodels used.

**Spray**

The spray is divided into axial zones (see Figure 2), with each zone corresponding to a single timestep during the injection period and containing a certain mass of fuel ('packet'). The spray tip correlations are the same as those used by Jung & Assanis [24, 25]. The nozzle discharge coefficient assumed was 0.7, the same as in previous modelling studies on the same engine [19, 20]. The spray evaporation model assumes a linear relationship between the droplet surface area and the evaporation time [26]. Jung & Assanis [25] found no difference in results when the evaporation sub-model was removed from their model and argue that the fuel can be assumed to be injected as a vapour. In this study, the results were found to be insensitive to the droplet evaporation rate.

**Air entrainment**

Air entrainment is modelled by assuming the conservation of momentum as the spray velocity decreases [24]. These equations have sometimes been found inadequate for a complete explanation of the entrainment of air, so empirical entrainment factors are sometimes added to the relation [19, 20], leading to Equation 1.

$$\dot{m}_a = -F_e \frac{m_f u_i}{(dS/dt)^2} \frac{d^2S}{dt^2} \quad (1)$$

The geometry of the piston crown in the experiment (see Figure 1) results in an early impingement of the spray on the piston. Bruneaux suggested that impinging jets may entrain less air at injection pressures below 150 MPa than free jets. The typical injection pressure seen during experiments is 10-17 MPa. Furthermore, the short distance travelled before impingement and the confined region within which all five sprays circulate increases the likelihood of spray-spray interaction, leading to a lower entrainment rate than before impingement. Therefore two different entrainment factors were used - a higher one before impingement and a lower one after.

**Combustion**

The mechanism used for this study is the reduced n-heptane mechanism developed by Patel et al. [27], modified to include four charged species (electrons, $HCO^+$, $H_3O^+$ and $O_2^-$) and their reactions. These additions were found to have a negligible effect on the performance of the parent mechanism. The ion reactions were obtained from Rao & Honnery [18]. The final mechanism consisted of 34 species and 56 reactions. Combustion is modelled using the Senkin routine of Chemkin.

**Heat transfer**

The Woschni model [28] is used for heat transfer to the cylinder walls (Equation 2).

$$h = 3.26B^{-0.2} P^{0.8} T^{-0.55} \upsilon^{0.8} \quad (2)$$

Optimisation of the pre-multiplication constant against the experimental pressure signal resulted in a change from 3.26 to 6.0.

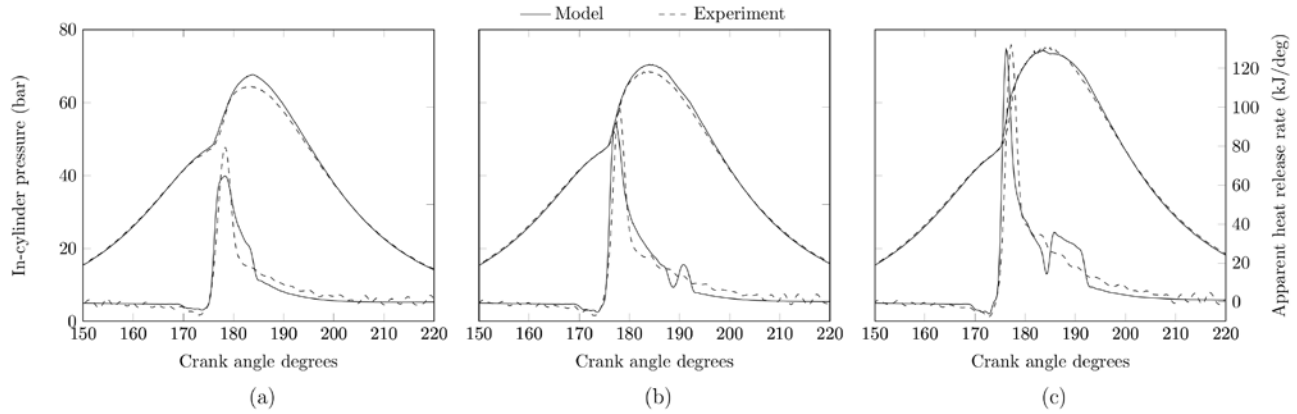


Figure 3. In-cylinder pressure and apparent heat release rate at 1600 RPM 80 Nm (a), 1600 RPM 120 Nm (b) and 1600 RPM 180 Nm (c)

**Ion current**

The ion current is calculated in the same way as in Rao & Honnery [18] (Equation 3). In the experiment, only the fuel packets in the vicinity of the ion sensor contribute to the ion current. With the use of a phenomenological model, several assumptions need to be made to obtain the spatial coordinates of any given fuel packet; these assumptions add extra complexity and empirical relations to the model and are highly specific to a particular spray pattern and combustion chamber geometry. It was therefore assumed that all electrons in the combustion chamber contribute to the ion current.

$$I(t) = F_G \, V_s \, e \, N_e \, \mu_e \qquad (3)$$

The geometric factor for the sensor used is difficult to estimate, considering the complex geometry of the sensor-cylinder head interface. When a radial current path between the sensor centre electrode and the cylinder head is assumed, the geometric factor is $12.6 \times 10^{-3}$ . Assuming a conical current path of radius equal to the sensor, an estimate of $3.7 \times 10^{-3}$ is obtained. When optimised for prediction of the ion current peak, a geometric factor of $2.5 \times 10^{-3}$ gives the lowest average absolute error in prediction. Given the assumption that all electrons contribute to the ion current, it is expected that the theoretical geometric factor will be significantly greater than that obtained from comparison to the experiment.

The time-step used for this model is 0.2 CAD. A time-step sensitivity analysis showed that the cylinder pressure and heat release rate showed no difference for time-steps of 0.4 CAD and lower, while the ion current showed no difference for time-steps of 0.2 CAD and lower.

## 4. Results

Comparisons of experimental and modelled data are presented in this section. Figure 2 shows the in-cylinder pressure and apparent heat release rates at engine-out torque settings of 80 Nm, 120 Nm and 180 Nm, all at 1600 RPM. The run times for these simulations were between 30 and 60 minutes each. It can be seen that the predictions of the in-cylinder pressure are fairly accurate in all three cases. The average error in peak pressure is 2.98% and the average absolute error in prediction of the peak pressure location is 0.4 CAD. At low torque settings, the in-cylinder pressure is over-predicted. This is largely corrected as the torque is increased. Predictions of the peak heat release rate are more inaccurate; the average percentage error in peak heat release rate prediction is 9.36%. The location of the peak heat release rate is predicted to an average absolute error of 0.6 CAD. Of particular interest is the more pronounced delineation between the premixed and mixing-controlled phases at higher torque settings - this is not seen in the experiment. This difference between experiment and model has been noticed in previous studies on the same engine [19, 20].

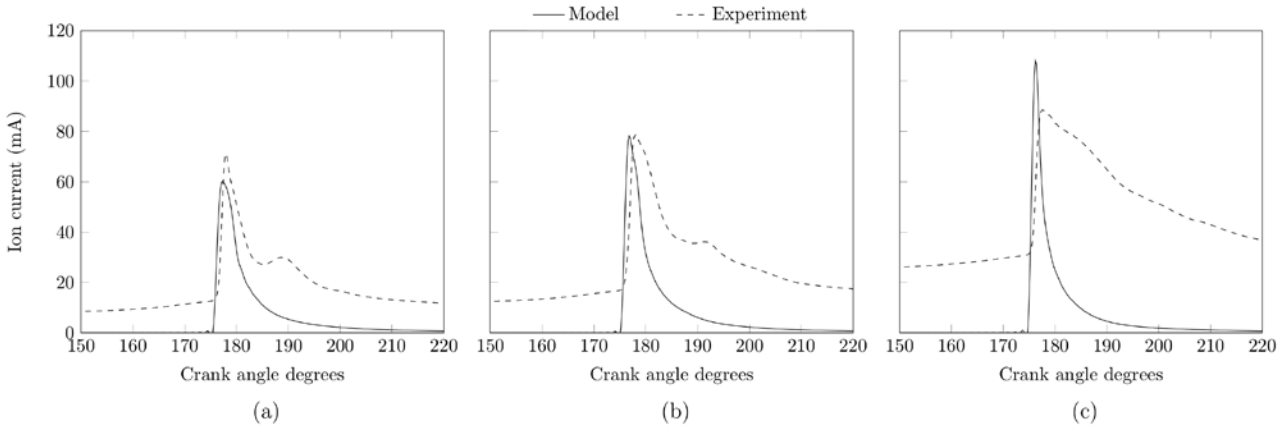


Figure 4. Ion current at 1600 RPM 80 Nm (a), 1600 RPM 120 Nm (b) and 1600 RPM 180 Nm (c)

The experimental and predicted ion current are shown in Figure 3 for the same three cases described above. Prediction of the trends in the ion current signal is accurate - increasing torque leads to increasing ion current. The ion current peaks are predicted to an average absolute error of 12.56% with the maximum error being at a torque setting of 180 Nm. The prediction of peak ion current location has an average absolute error of 1.1 CAD. There is also a positive offset in the ion current that has been suggested to be caused by soot formation on the ion sensor [9]. This offset is not seen in the model predictions, as would be expected since soot is not considered. The widths of the ion current peaks are significantly under-predicted. This is more apparent at higher values of torque, suggesting that soot formation may play a role in the elevated ion current seen in the experiment even after combustion has ceased. Furthermore, a study of sensitivity to number of radial zones shows that increasing the number of radial packets increases the width of the ion current peak; when more than one radial packet is used, central packets entrain air and burn slower than do packets on the spray periphery, resulting in a wider ion current peak. This is currently being investigated.

## 5. Conclusion

This paper presents a computationally efficient model for prediction of the ion current in a direct-injection diesel engine. The phenomenological model developed uses established sub-models for the fuel spray, air entrainment and heat transfer. A highly reduced n-heptane mechanism is used to model combustion. The predicted in-cylinder pressure, apparent heat release rate and ion current are compared to experimentally obtained results at different values of engine-out torque. Excellent agreement is found for the in-cylinder pressure, with an average absolute error of 2.98% in peak pressure prediction and average absolute error of 0.4 CAD in peak pressure location prediction. Peak heat release rate and location are predicted to an average absolute error of 9.36% and 0.6 CAD respectively. The ion current peaks and their location are predicted to an average absolute error of 12.56% and 1.1 CAD respectively. This model forms a good basis for further studies into the ion current in diesel engines via the inclusion of radial packets in the spray and a more detailed mechanism and also the testing of a wider range of engine operating conditions.

## Acknowledgments

The first author acknowledges the support of the Australian Government through its APA scholarship.

## References

[1] R. Reinmann, A. Saitzkoff, and F. Mauss. SAE 970856, 1997.

[2] E.N. Balles, E.A. VanDyne, A.M. Wahl, K. Ratton, and M. Lai. SAE 980166, 1998.

[3] Henrik Klövmark, Patrik Rask, and Urban Forssell. SAE 2000-01-1245, 2000.

[4] Nicholas Wickstrom, Mikael Taveniku, Arne Linde, Magnus Larsson, and Bertil Svensson. Intelligent Transportation System, 1997. ITSC'97., IEEE Conference, pages 972–977. IEEE, 1997.

[5] Andreas Gazis, Dimitris Panousakis, Rui Chen, and Wen-Hua Chen. Int J Engine Res, 7(3):271–282, 2006.

[6] M. Hellring, T. Munther, T. Rognvaldsson, N. Wickstrom, C. Carlsson, M. Larsson, and J. Nytomt. SAE 1999-01-1162, 1999.

[7] John Auzins, Hasse Johansson, and Jan Nytomt. Ion-gap sense in misfire detection, knock and engine control. SAE 950004, 1995.

[8] M. Glavmo, P. Spadafora, and R. Bosch. SAE 1999-01-0549, 1999.

[9] Rahul Rao and Damon Honnery. Int J Engine Res, 15 (3) (2014), pp. 370-380.

[10] Tamer Badawy, Amit Shrestha, and Naeim Henein. J Eng Gas Turb Power, 134(5):052802, 2012.

[11] Tamer Badawy, Fadi Estefanous, and Naeim Henein. SAE 2013-01-0555, 2013.

[12] Tamer Badawy, Naeim Henein, and Walter Bryzik. SAE 2011-01-2433, 2012.

[13] C.T. Bowman, R.K. Hanson, D.F. Davidson, Jr. W.C. Gardiner, V. Lissianski, G.P. Smith, D.M. Golden, M. Frenklach, and M. Goldenberg. GRI-Mech 3.0, 1995.

[14] HJ Curran, P Gaffuri, William J Pitz, and Charles K Westbrook. Combust Flame, 114(1):149–177, 1998.

[15] KJ Hughes, T Turanyi, AR Clague, and MJ Pilling. Int J Chem Kinet, 33(9):513–538, 2001.

[16] SM Aithal. Combust Sci Technol, 185(8):1184–1201, 2013.

[17] J.M. Rodrigues, A. Agneray, X. Jaffrezic, M. Bellenoue, S. Labuda, C. Leys, A.P. Chernukho, A.N. Migoun, A. Cenian, A.M. Savel'ev, N.S. Titova, and A.M. Starik.. Plasma Sources Sci T, 16(1):161–172, 2007.

[18] Rahul Rao and Damon Honnery. Combust Flame 162 (7), pp 2928-2936, 2015.

[19] V. Rao and D. Honnery. Fuel 107 pp 662-670, 2013.

[20] Varun Rao and Damon Honnery. Fuel, 135 pp 269–278, 2014.

[21] JT Farrell, NP Cernansky, FL Dryer, CK Law, DG Friend, CA Hergart, RM McDavid, AK Patel, Charles J Mueller, and H Pitsch. SAE 2007-01-0201, 2007.

[22] Fadi Estefanous. ASME 2013 Internal Combustion Engine Division Fall Technical Conference, pages V002T06A010–V002T06A010. American Society of Mechanical Engineers, 2013.

[23] John B Heywood. Internal combustion engine fundamentals. McGraw-Hill New York, 1988.

[24] Dohoy Jung and Dennis N Assanis. SAE 2001-01-1246, 2001.

[25] Dohoy Jung and Dennis N Assanis. KSME international journal, 18(5) pp 865–876, 2004.

[26] Nguyen, D., Honnery, D., & Soria, J. *Exp. Fluids*, *50*(4), 949-959, 2011

[27] Amar Patel, Song-Charng Kong, and Rolf D Reitz. SAE 2004-01-0558, 2004.

[28] Gerhard Woschni. SAE 670931, 1967.

**Proceedings of the Australian Combustion Symposium**
**December 7-9, 2015, The University of Melbourne**

# Experimental investigation of the effects of oxygenated fuels on exhaust emissions in a heavy duty diesel engine

F. M. Hossain[1*], M.N. Nabi[1, 2], M.M. Rahman[1, 2], A. Zare[1], T.J. Rainey[1, 2], D. Stuart[3], Z. Ristovski[1, 2], R. J. Brown[1, 2]

[1]Biofuel Engine Research Facility, Queensland University of Technology (QUT), QLD, 4000 Australia
[2]ILAQH, Queensland University of Technology (QUT), QLD, 4000 Australia
[3]Eco Tech Biodiesel Pty Ltd, QLD, 4504 Australia

**Abstract**

Physical and chemical properties of biofuels vary among various feedstocks and their subsequent conversions to fuels. The biofuels contain various amounts of oxygen, and this has a significant influence on exhaust emission. This oxygen content has been considered in order to investigate its effect on diesel engine exhaust emissions. The experiments have been conducted with a heavy duty diesel engine and various oxygenated fuels. It is found that the amount of oxygen in the fuel has a high level of influence on its exhaust emissions, and this provides agreement with diesel emissions results such as PN reduction. By increasing the amount of oxygen in the blend (by adding more biofuel), the particulate number (PN) is reduced and NOx increases gradually. However, the variation of PN and NOx are not similar for waste cooking biodiesel (WCBD) and butanol blend, even though their oxygen content are the same in the blends. This is due to the source of the biofuel and their internal chemistry.

*Keywords: Oxygenated fuel, Exhaust emissions, Particulate Number.*

## 1. Introduction

The reduction of environmental pollutants from direct injection heavy-duty diesel engines is mandated by the Australian New South Wales (NSW) federal government and international organization regulations. The increases in prices of diesel fuel coupled with stringent emission regulations provide a mandate, prompting the researcher to investigate alternatives to conventional fuel [1, 2]. A key feature of biodiesel fuels, which makes them different from conventional fossil fuels, is the oxygen bound in the fuel. While there are always two oxygen atoms in one fatty acid methyl ester (FAME), the oxygen content in the biofuels depends on the fatty acid ester profile, specifically carbon chain length and unsaturation level [3]. Rahman et al.(2014) found that saturated short chain length FAMEs reduce NOx and PN concentration, but higher levels of fuel consumption and unsaturated FAMEs can lower PN, and produce higher NOx [4]. High-quality biodiesel should have low- temperature performance and oxidative stability. Therefore, it is found that oxygen in the fuel can enhance the combustion process as well as provide increased combustion efficiency and lower soot levels [1, 5]. Biodiesel contains a higher concentration of reactive oxidative species that may enhance combustion efficiency and reduce exhaust emissions [4].

Internal combustion engines, such as diesel engines, are used to convert chemical energy (contained in the fuel) into mechanical energy. In the conversion process, emissions are produced. Diesel engine emissions contain pollutants that have adverse health and environmental effects [6]. This mechanical energy and the exhaust emissions depend on fuel properties such as chemical composition, higher heating value (HHV), density, viscosity, and cetane number [7]. These physical properties depend on chemical composition and molecular structure of the biofuels. [8]. Nabi et al. [9] theoretically investigate the engine performance and exhaust emissions for different oxygenated fuels. Based on this literature, the authors have been motivated to investigate the effect of oxygen content on exhaust emissions, especially PN and NOx.

There are many oxygenated fuels has been used including WCBD and butanol to reduce diesel engine emissions can be found [1, 5, 10]. Recently, butanol has received importance as oxygenated fuels due to their advantage compare to methanol and ethanol. It has a higher cetane number, lower volatility and a higher flashpoint [10, 11]. For this reason, the current study has been conducted experimentally using WCBD/diesel and butanol/diesel blends to investigate exhaust emissions. It is found that PN and NOx change for both blends when compared with diesel fuel. The results show inconsistent emissions for various oxygenated blends.

## 2. Engine and fuel specification

The experiments were conducted at QUT in the Biofuel Engine Research Facilities (BERF) lab with a heavy duty common-rail four stoke six-cylinder turbocharged diesel engine. The engine has a capacity of 5.9 L and maximum torque of 820 Nm at 1500 rpm. Figure 1 shows the schematic of the experimental engine setup. Further detail of the engine configuration and emission

* Corresponding author: Md Farhad Hossain
Phone: (+61) 424619932
Email: farhad.hossain@qut.edu.au

measuring instruments can be found in Bodisco et al. [6]. The Engine was operated at consistent speed of 1500 rpm (maximum torque speed), and at two different loads - including 50% and 100%. Maximum load at any particular engine speed depends upon the type of fuel used, therefore for each fuel at the first maximum load was determined when the engine was at full throttle for a particular speed. The measured load is then considered as 100% load for that speed and fuel, and then other load conditions were determined, based upon measured 100% load.

Table 1: Fuel properties

| Blends | O (wt%) | K.V@40°C (mm2/s) | Density(g/cc at 15° C) | HHV (MJ/kg) |
|---|---|---|---|---|
| Diesel [1] | 0 | 2.81 | 0.8411 | 44 |
| WCBD[5] | 10.89 | 4.82 | 0.87 | 39.9 |
| Bu [12] | 21.6 | 1.13 | 0.9074 | 36.02 |
| Bu_2 | 2 | 2.65 | 0.8381 | 43.26 |
| Bu_4 | 4 | 2.49 | 0.8351 | 42.52 |
| Bu_6 | 6 | 2.34 | 0.8321 | 41.78 |
| WCBD_2 | 2 | 3.18 | 0.8464 | 43.24 |
| WCBD_4 | 4 | 3.54 | 0.8517 | 42.49 |
| WCBD_6 | 6 | 3.92 | 0.857 | 41.74 |

Before conducting the experimental studies, a careful fuel analysis needed to be carried out. It is broadly accepted that the fuel properties influence the fuel spray characteristics, fuel evaporation, the formation of fuel droplet size, distribution of fuel atoms, and, therefore the exhaust emissions. Petroleum diesel and two biofuels (WCBD and butanol) were used to prepare different blends. Three different blends were prepared for each biofuel maintaining the total oxygen content in the blends of 2%, 4% and 6% respectively. The important physicochemical properties of pure fuels were experimentally measured. Then, the used blends' properties were calculated based on pure fuel properties that is shown in the Table 1 [5, 8].

## 3. Emission measurements and data collection

Figure 1 shows a schematic of the engine exhaust emission measurements. Various instruments were used for exhaust emission measurements, such as DMS500, DustTrack (Model 8530), SABLE (CA-10) and CAI 600. The Combustion DMS500 is uniquely suited for a variety of diesel particulate filter applications. CAI 600 series analysers were used to measure raw exhaust gases such as CO, $CO_2$, NOx, and HC, and Sable and DustTrack used to measure diluted $CO_2$ gas and particulate mass respectively. Further detail of the engine exhaust emission measurements can be found in Rahman et al. [8].

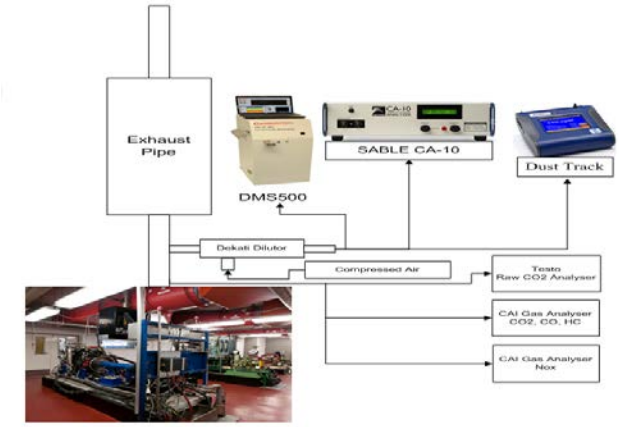

Figure 1: Experimental setup

## 4. Result and Discussion

The experiments were conducted with two different oxygenated biofuels - waste cooking biodiesel (WCBD) and butanol. The blends were prepared by adding a different amount of oxygenated fuel to the diesel. The blended fuel contained fixed amounts of oxygen, being 2%, 4% and 6% for each of the fuels.

### 4.1 Particulate number size distribution

The particulate number is the most complex emission parameter, and is receiving increased attention due to the associated possible adverse health effects [13]. Figures 2 and 3 present the PN size distribution at 50% and 100% load respectively. However, it was found from Figure 2 that the PN size distribution curve for WCBD blends was always under the diesel fuels curve. The pick point of the PN size distribution curve decreases with an increase in the oxygen amount - but not linearly. An exception was found for the 4% blend for both loads, that is, the range of particulate diameter was bigger when compared with other blends, and this can be found in Figures 2 and 3. The particulate diameter and number both reduced for 6% blends, compared with other fuels as shown in Figures 2 and 3.

Figures 4 and 5 present the PN distribution for butanol blends for 50% and 100% load respectively. The size distribution curve for butanol blends followed the same trend as for the WCBD blends. However, the particulate number was higher for butanol blends, when compared with WCBD blends for both loads. So, it could be said that PN size distribution not only depends on oxygen amounts, but it also depends on physiochemical properties of the fuel.

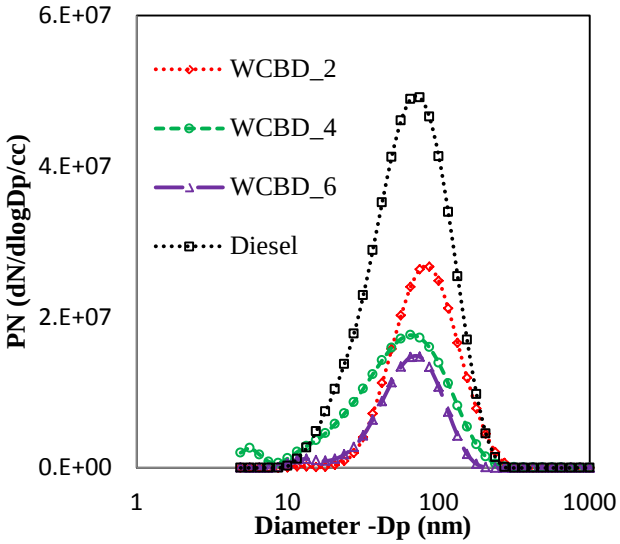


Figure 2: Variation of PN size distribution for oxygenated blends (WCBD) blends at 50% load.

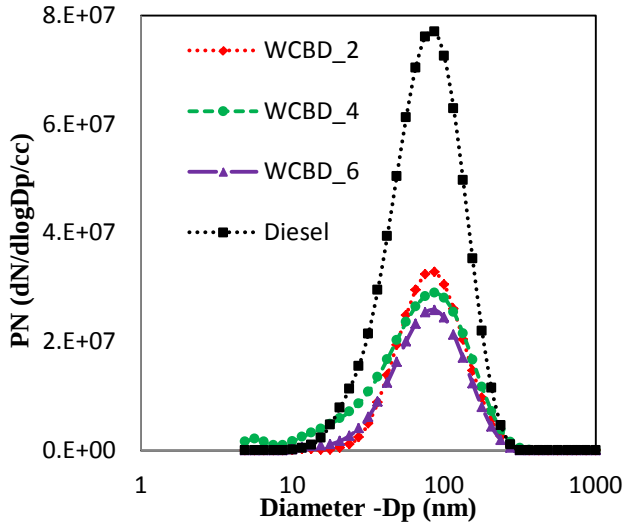


Figure 3: Variation of PN size distribution for oxygenated blends (WCBD) blends at 100% load.

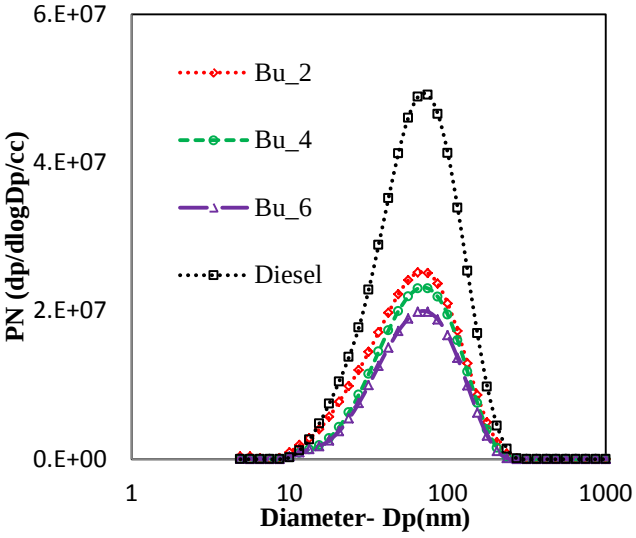


Figure 4: Variation of PN size distribution for oxygenated blends (butanol) blends at 50% load.

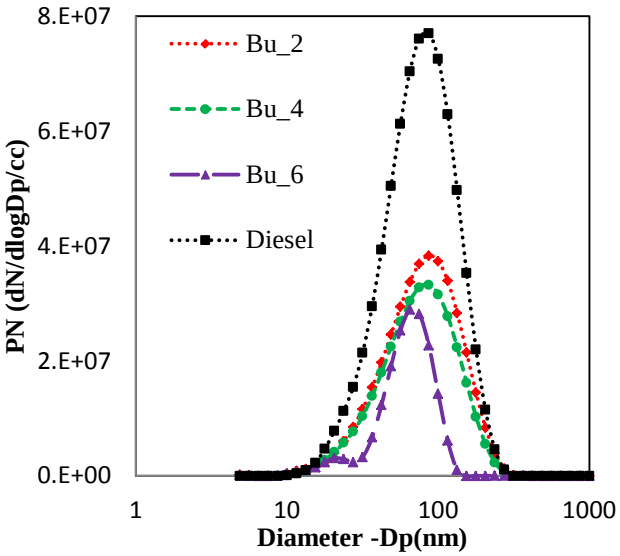


Figure 5: Variation of PN size distribution for oxygenated blends (butanol) blends at 100% load.

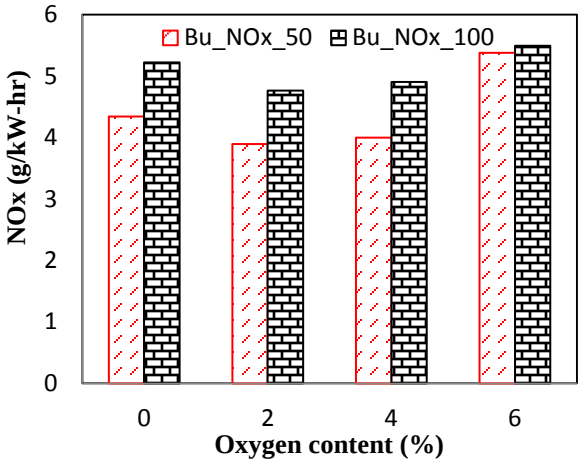


Figure 6: Variation of brake specific NOx emission for oxygenated blends (butanol) at two different loads including 50% and 100%.

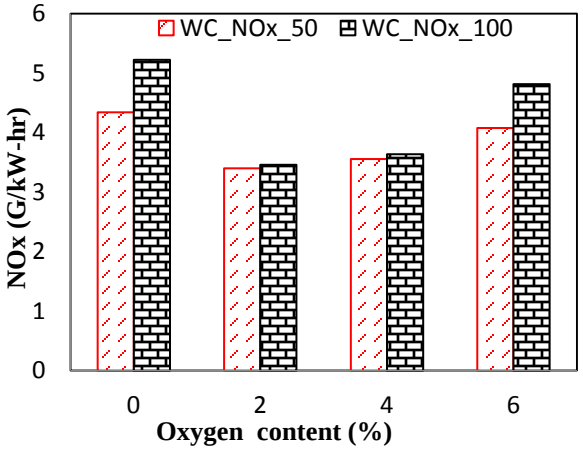


Figure 7: Variation of brake specific NOx emission for oxygenated blends (WCBD) at two different loads including 50% and 100%.

The specific NOx emissions were calculated against three different blends for both fuels and can be found in Figure 6 and 7. Noticeable variations in NOx emissions were observed among the three types of blends for two different types of oxygenated fuels. It was found that the specific NOx for all blends increased with increasing oxygen amounts except 0% oxygenated blends, as shown in Figure 6 and 7. The experiments were conduct at maximum torque conditions that could be reasons for the high specific NOx emissions for 0% oxygenated fuels. In additions, the further investigation could be helped to explain why specific NOx emission is the high for 0% blends. However, the rest of the results were similar to other publications, and can be found in Nabi et al. (2015) and Rahman et al. (2014) [1, 8]. It is also found that the rate of increase of NOx from 2% to 4% was low compared to the 4% to 6% blends for both fuels. The maximum increase in NOx was observed for 6% oxygenated blends, an observation common in the literature [14-16]. However, the oxygenated fuel came from a different feedstock. Therefore, the chemical and physical properties were different that influence combustion as well as combustion efficiency and exhaust emissions.

## 5. Conclusion

Experimental investigations on heavy duty engine exhaust emissions using three different oxygenated blends were prepared. The blends were prepared using diesel as a primary fuel, and WCBD and butanol were used as oxygenated fuels. It was found that the brake specific PN decreases with oxygen content in the blend, except for 4% oxygen blends for both types of oxygenated fuels. Conversely, the similar but opposite change was observed for variations of brake specific NOx emission. These results have primarily concluded that the increases of oxygen in the blend changes the chemical and physical properties that was influenced to change exhaust emissions.

## 6. Acknowledgments

This contribution is the result of the research supported by Australian Research Council's Linkage Projects funding scheme (project number LP110200158). The author would also like to acknowledge the laboratory assistance from Mr. Noel Hartnett, Dynolog software development by Mr Andrew Elder from DynoLog Dynamometer Pty Ltd, Peak3 Pty Ltd for assisstance with measuring instruments, and Eco Tech Biodiesel for the supply of waste cooking biodiesel.

## 7. References

1. M. N. Nabi; M. M. Rahman; M. A. Islam; F. M. Hossain; P. Brooks; W. N. Rowlands; J. Tulloch; Z. D. Ristovski; R. J. Brown, Energy Conversion and Management 96 (0) (2015) 588-598 .
2. NSWEPA, www.epa.nsw.gov.au (2014)
3. P. X. Pham; T. A. Bodisco; Z. D. Ristovski; R. J. Brown; A. R. Masri, Fuel 116 (0) (2014) 140-150 .
4. P. X. Pham; T. A. Bodisco; S. Stevanovic; M. D. Rahman; H. Wang; Z. D. Ristovski; R. J. Brown; A. R. Masri, SAE International Journal of Fuels and Lubricants 6 (1) (2013) 188-198
5. M. A. Islam; M. M. Rahman; K. Heimann; M. N. Nabi; Z. D. Ristovski; A. Dowell; G. Thomas; B. Feng; N. von Alvensleben; R. J. Brown, Fuel 143 (0) (2015) 351-360 .
6. T. Bodisco; R. J. Brown, Energy 52 (2013) 55-65 .
7. M. A. Islam; R. J. Brown; P. R. Brooks; M. I. Jahirul; H. Bockhorn; K. Heimann, Energy Conversion and Management 98 (2015) 340-347 .
8. M. M. Rahman; A. M. Pourkhesalian; M. I. Jahirul; S. Stevanovic; P. X. Pham; H. Wang; A. R. Masri; R. J. Brown; Z. D. Ristovski, Fuel 134 (2014) 201-208 .
9. M. N. Nabi, Applied Thermal Engineering 30 (8–9) (2010) 839-844 .
10. Z. Şahin; O. Durgun; O. N. Aksu, Energy Conversion and Management 103 (2015) 778-789 .
11. D. C. Rakopoulos; C. D. Rakopoulos; E. G. Giakoumis; R. G. Papagiannakis; D. C. Kyritsis, Energy 73 (2014) 354-366.
12. O. Armas; R. García-Contreras; Á. Ramos, Fuel Processing Technology 100 (2012) 63-72 .
13. DieselNet, https://www.dieselnet.com/(21/05/2015) (2015)
14. M. Lapuerta; O. Armas; J. Rodríguez-Fernández, Progress in Energy and Combustion Science 34 (2) (2008) 198-223
15. N. C. Surawski; B. Miljevic; G. A. Ayoko; S. Elbagir; S. Stevanovic; K. E. Fairfull-Smith; S. E. Bottle; Z. D. Ristovski, Environmental Science & Technology 45 (24) (2011) 10337-43 .
16. J. Xue; T. E. Grift; A. C. Hansen, Renewable and Sustainable Energy Reviews 15 (2) (2011) 1098-1116

# Evaporation and mixing of ethanol-water mixture in a heavy duty common rail diesel engine intake air

E. Kim *, V. Garaniya, R. Islam, R. Abbassi
Australian Maritime College
University of Tasmania TAS 7250 Australia

## Abstract

Limited crude oil resources and growing environmental awareness have provided enormous motivation to seek new techniques utilising alternative fuels for diesel engines. In this study, testing on a heavy duty common rail diesel engine was carried out to examine the evaporation and mixing of aqueous ethanol in the inlet air. The engine was maintained at 1800 RPM and 926 Nm torque. Aqueous ethanol was added at different energy substitution rates (5%, 15% and 20%). Two different types of jet configurations (3-jets and 5-jets) were used to inject an ethanol/water mixture into the air stream. Exhaust emissions of oxides of nitrogen (NOx), carbon monoxide (CO), hydrocarbons (HC), oxygen and carbon dioxide ($CO_2$) were measured. In general, the injection of ethanol resulted in reduction in the NOx whereas CO emission increased with increase in the rate of ethanol injection. To verify whether the aqueous ethanol was mixed and evaporated thoroughly, the temperatures across the pipe cross section were measured using a rotational two temperature probe device. For 5% energy substitution rate, the temperature distributions for both 3 and 5 jets were found to be uniform and ethanol was well mixed with air. However as the injection increased to 15%, the mixing of aqueous ethanol and compressed air did not occur homogenously across the pipe. Further for 20% substitution rate, the temperature across the pipe dropped sharply suggesting that 20% of ethanol/water mixture is above the maximum evaporation limit. To estimate the theoretical maximum amount of ethanol, the equilibrium temperature of the mixture was calculated. The results showed that a 5-jet configuration provided a better mixing compared to a 3-jet configuration.

*Keywords: Ethanol-water mixture, Evaporation and mixing, Aqueous ethanol fumigation, Heavy duty diesel engine, Apparent heat release rate*

## 1. Introduction

Recently diesel engines have increased in popularity partly due to their high efficiency and fuel economy. However, in spite of thermodynamic advantages, diesel engines still tend to produce much higher levels of oxides of nitrogen (NOx). Due to increasing emission standards, diesel engine industries are being forced to devise new techniques, but the emissions target levels are often difficult to achieve solely through engine design. The required level of PM and NOx emissions can be achieved by mixing alternative fuels with conventional fuels. When it comes to exhaust emissions from diesel engines, the utilization of cleaner-burning fuels,- such as ethanol, can be used [1].

Ethanol has been considered a vital alternative fuel for diesel engines since it can provide a solutions to the problems of greenhouse gases and particulates emissions [2]. In order to take advantage of ethanol in existing engines with relatively little modification, the fumigation technique in which ethanol is injected into the intake air stream is employed. Any modification of diesel engine injection system can be avoided while the volume of diesel required is reduced. [3].

The aim of the work is to investigate the evaporation and mixing behavior of aqueous ethanol injected into the air stream. The task was carried out using two different jet configurations and measuring thermodynamic properties.

## 2. Methodology

A Cummins QSG5.9-305MCD engine setup, similar to Goldsworthy[4] is used in the study. However the injection system was modified to improve ethanol mixing and vaporization.

As shown in Fig 1, a new injection system with 3-jet and 5-jet configuration was designed and developed. This system can be operated with either 3-jets or 5-jets open at one time by controlling the manual valve.

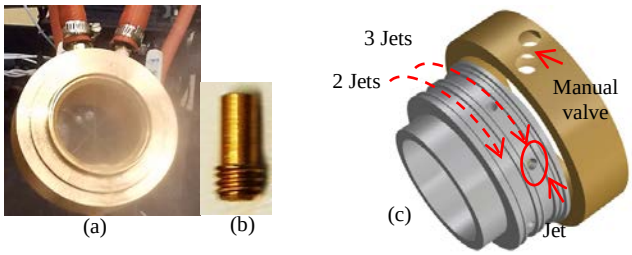


**Fig 1 (a) Cross view of ring nozzle, (b) a jet and (c) 3D drawing of jets installed in the ring nozzle**

As shown in Fig 2, the injection system was installed directly behind the turbocharger compressor, which allowed an approximate 60cm long duct for ethanol/water mixture to evaporate. If noticeable condensation occurred within the aftercooler, liquid would be apparent at the bleed point located on the aftercooler underside. If a small amount of condensate of ethanol/water appears at this bleed point, it shows that the amount of the ethanol injected is beyond the maximum evaporation limit.

* Corresponding author:
Phone: (+61)456010638
Email: eonjook@utas.edu.au

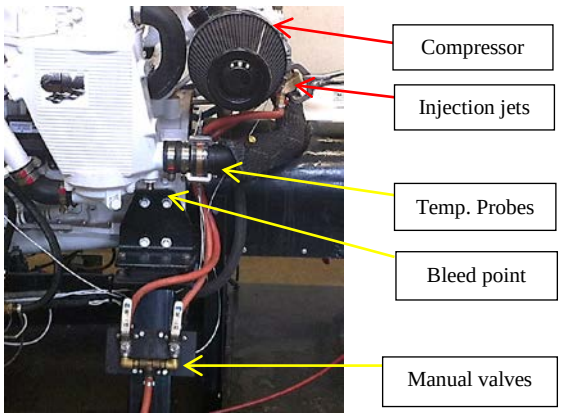


**Fig 2 Installation of ethanol/water injection system, temperature probes and manual valves**

A separate rotational temperature probe device Fig 3, was designed to measure the temperature inside the pipe at various locations. This device was installed just in front of the aftercooler. The probes configuration was able to measure the temperature profile across the airstream along the three orientations. The temperature was measured for six orientations (2~12) and three points along each orientation (A~C). In other words, temperatures at 18 points were recorded using two probes.

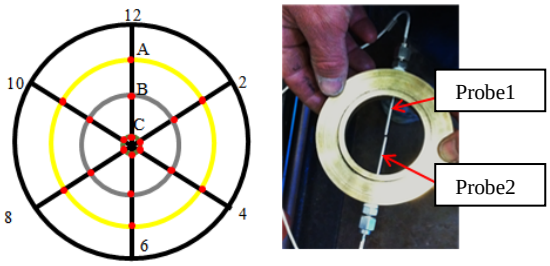


**Fig 3 Temperature probe configuration**

An aqueous ethanol (95%) was tested at 5%, 15% and 20% fuel energy substitution rate. Aqueous ethanol mixture substitution rate was defined as the percentage of the fuel energy from aqueous ethanol [5]. In order to inject aqueous ethanol into the air stream, a pressure vessel of nitrogen was used. Nitrogen was introduced at 10 bar into a vessel containing aqueous ethanol. The flowrate of aqueous ethanol was measured in liters per hour by a rotameter. The rotameter was calibrated using 3-jet or 5-jet configuration to find the relation between rotameter and ethanol flowrate.

Torque and speed were maintained as 1800 RPM and 926 Nm while the ethanol was injected. The engine governor was automatically controlled to normal fuel flow rate in order to compensate for the injected ethanol. [4]

## 3. Results and discussion

In order to verify whether the ethanol/water mixture is well mixed and evaporated, it is necessary to check whether the temperature across the pipe is constant. Figs 4(a) and (c) represent the temperature contours across 18 points inside the pipe. Figs 4(b) and (d) simply show the region of pipe where temperature was above the saturation temperature of ethanol. An interpolation was used to plot this scatter profile since there were only 18 points for each condition.

For 5% substitution rate, the temperature distribution for each radius layer is uniform, indicating that the mixing of ethanol/water and air occurred all around the pipe section. Also it is noticeable that the temperature at the centre of the pipe is higher than the temperature over the rim because most of the ethanol flowed close to the pipe surface and vaporized ethanol and air flowed in the centre of the pipe.

The observation shows that for 15% substitution rate, the mixing and evaporation was limited. In the upper section of the pipe temperatures were above the saturation temperature, but in the lower section these temperatures indicate ethanol in liquid form. This was also confirmed from the temperature plot in Fig 5.

For 20% substitution rate, the temperature inside the pipe was lower than the previous two cases. During testing at this point it was also observed that a small amount of ethanol was dripping at the bleed point, which confirmed the presence of liquid ethanol.

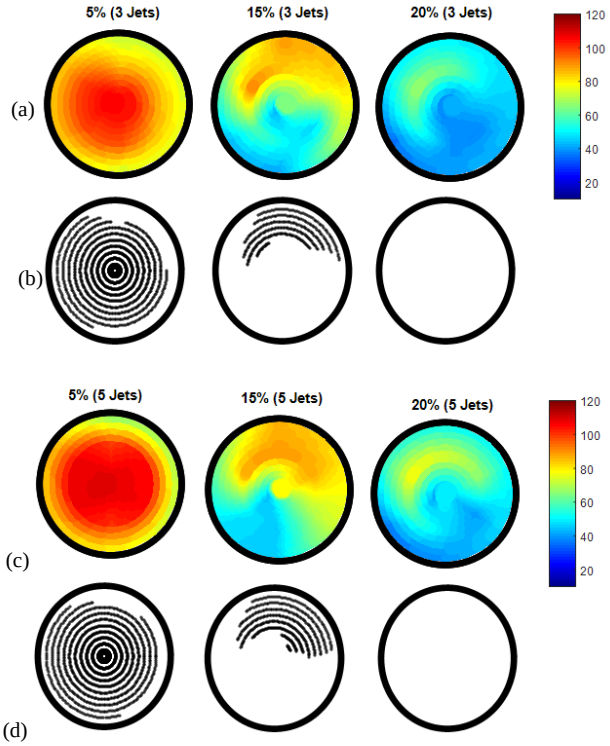


**Fig 4 Temperature contour across the pipe (a and c) and points where the temperature of ethanol/water and air mixture is higher than saturation temperature of ethanol (b and d) for 3 and 5 jets**

The limit of the amount of ethanol/water injection could be determined by estimating the theoretical temperature of ethanol/water and air mixture after the complete mixing process. In other words, if the calculated temperature of ethanol/water and air mixture is higher than saturation temperature of ethanol, it would have evaporated completely. The heat required

to vaporize ethanol/water mixture is calculated by taking three types of heat into account, being:

1. Heat taken from the air to bring ethanol to boiling point [6] :

$$Q_{Boiling} = \dot{m}_{eth} \times C_{Liquid} (T_2 - T_1) = 0.41 \text{ kW} \quad \text{(A)}$$

2. Heat required in vaporizing the ethanol mixture [6]:

$$Q_{Evap} = \dot{m}_{eth} \times L = 2.382 \text{ kW} \quad \text{(B)}$$

3. Heat taken to raise the ethanol mixture to equilibrium temperature[6]:

$$Q_{equilibrium} = \dot{m}_{eth} \times C_{gas} \times (T_3 - T_2) = 0.072 \text{ kW} \quad \text{(C)}$$

Where,

$\dot{m}_{eth}$ is ethanol/water mixture mass flowrate, 0.002513kg/s;

$T_1$ is aqueous ethanol injected temperature, 10°C;

$T_2$ is saturation temperature of ethanol, 78°C;

$T_3$ is the equilibrium temperature, °C;

$T_{air}$ is the temperature of airstream, 102.8°C;

$C_p$ is specific heat of dry air, 1.1 kJ/kg.K;

$C_{liquid}$ is specific heat of ethanol (liquid), 2.4 kJ/kg.K;

$C_{gas}$ is specific heat of ethanol (gas), 2.898 kJ/kg.K;

$L$ is latent heat of ethanol/water mixture, 948.1 kJ/kg

The total heat required to vaporize the ethanol/water mixture is the sum of three heats :

$$Q_{total} = Q_{boiling} + Q_{evap} + Q_{equilibrium} = 2.888 \text{ kW} \quad \text{(D)}$$

Using this total heat required, the outlet temperature of ethanol/water and air mixture at the end of the pipe is obtained as [6] :

$$T_3 = -\frac{Q_{total}}{\dot{m}_{air} \times C_P} + T_{air} = 87.9°C \quad \text{(E)}$$

The calculated outlet temperature of ethanol/water and air mixture is 87.9 $^0$C for 15% substitution rate for 3-jet. The calculated outlet temperatures are tabulated and plotted in Table 1 and Fig 5 respectively. During the experiments, attempts were made to maintain the same flow rates for both jet configurations, however there were slight variations in the flow rates, which resulted in minor variations in the calculated temperatures for 3-jet and 5-jet.

**Table 1 Estimated outlet temperature compared with the measured temperature for different substitution rate**

| Contents | Units | 3 Jets | | | |
|---|---|---|---|---|---|
| Substitution | [%] | 0% | 5% | 15% | 20% |
| Calculated Temp | [°C] | 110.1 | 105.6 | 87.9 | 82.9 |
| Measured Temp (Max.) | [°C] | 110.1 | 105.0 | 88.2 | 66.0 |
| Contents | Units | 5 Jets | | | |
| Substitution | [%] | 0% | 5% | 15% | 20% |
| Calculated Temp | [°C] | 110.1 | 101.0 | 89.2 | 83.4 |
| Measured Temp (Max.) | [°C] | 110.1 | 108.6 | 89.4 | 76.1 |

As shown in Fig 5, for 5% substitution rate, most temperatures were higher than 78°C saturation temperature so it could be considered that the ethanol/water and air mixed and evaporated completely. The estimated mixture temperature was exactly that of the maximum measured temperature.

For 15% substitution rate, average measured temperature was 65°C, which is lower than the saturation temperature of ethanol. This resulted in partial ethanol/water evaporation in the top part of the pipe as shown in Fig 4. It was noticed that evaporation of ethanol/water was better for 5 jets since it helped the ethanol/water mix through the pipe homogeneously. The calculated temperature was close to the highest measured temperature for both 3 and 5 jets.

At 20% substitution rate, measured temperatures dropped dramatically and all temperatures were lower than the saturation temperature as shown in Fig 5. It could be concluded that excessive ethanol/water was injected and it was not able to evaporate in the given amount of airstream even though estimated temperature is higher than boiling point.

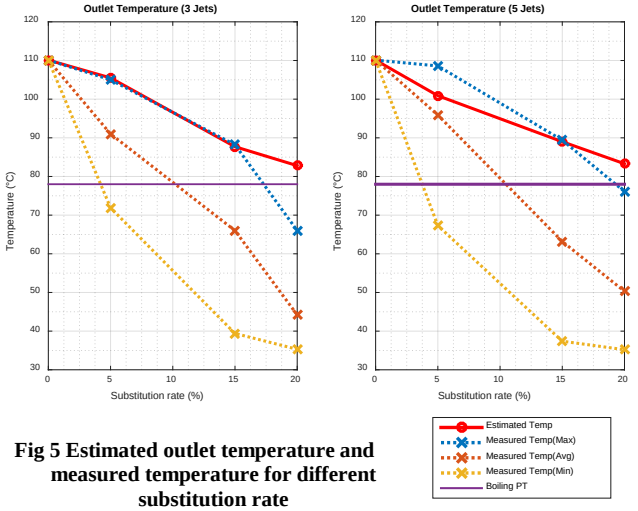


**Fig 5 Estimated outlet temperature and measured temperature for different substitution rate**

Thermal efficiency, exhaust temperature, NOx and CO under the above mentioned test condition were also measured. Fig 6 shows these results for different substitution rates of ethanol.

Thermal efficiency improves with the addition of ethanol injection, with the greatest improvement apparent for 5jets. This result is similar to the study by Shropshire, et al.[7] of single- and multiple- nozzle arrangements for ethanol fumigation. As expected, the multiple-nozzle configuration gave better ethanol distribution than single-nozzle arrangement. This was confirmed by both thermal efficiency and exhaust temperature.

Exhaust temperature drops dramatically with increased ethanol substitution rate. The evaporation of aqueous ethanol mixtures with air cause the inlet air temperature drop. The presence of water vapor in the combustion chamber lowers the combustion temperature due to the high specific heat capacity of water [8] .

NOx emissions fall steeply with increased energy substitution rates. As water vapor lowers the combustion temperature, it would be the main effect on reducing NOx emission.

CO emissions slightly increase with rising substitution rates and similar results are reported by

Karim[9] and Rakopoulos,et al.[10]. CO is intermediate in the combustion process and unoxidised CO will appear unless the combustion process is completed.

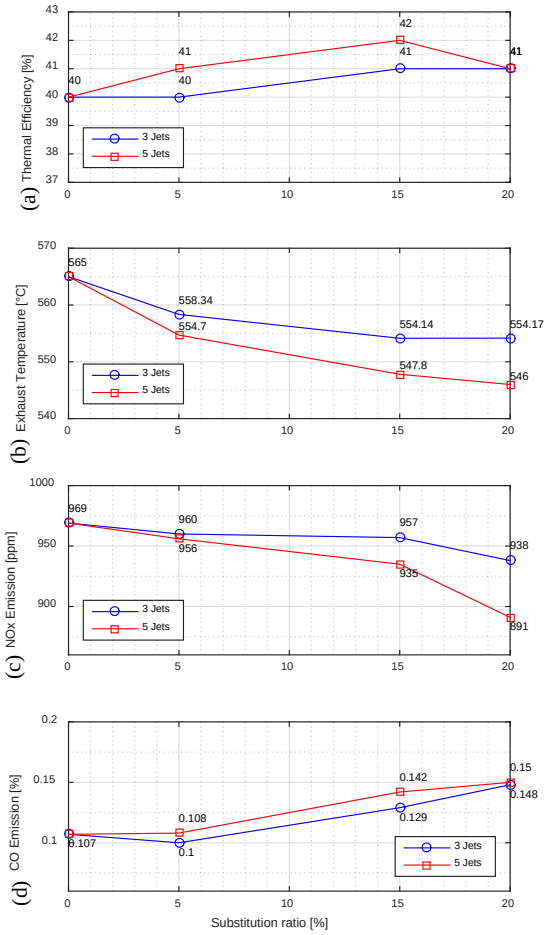


**Fig 6 (a) Thermal efficiencies, (b) Exhaust temperatures, (c) NOx emissions and (d) CO emissions**

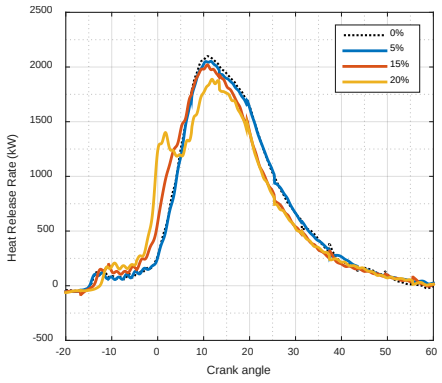


**Fig 7 Heat release rate for different energy substitution rates**

Fig 7 represents the heat release rate against crank angle for different substitution rates. At increased ethanol substitution rate, there is a clear shift of timing where the heat release rises above zero before Top Dead Centre. As further ethanol is added, the maximum heat release rate is reduced in intensity, but the early heat release rate is still greater than at lower ethanol addition rate. Heat release rate has two peaks for 20% ethanol substitution rate.

## 3. Conclusion

In this study, an experiment was designed to investigate the evaporation and mixing of the ethanol/water mixture. Ethanol/water mixture was injected by atomising jets into the turbocharger inlet air upstream. For 5% energy substitution rate, the temperature distributions for both 3 and 5 jets were found to be uniform and ethanol was well mixed with air. However the mixing of aqueous ethanol and compressed air did not occur homogenously as the injection increased to 15%. Further for 20% substitution rate, the temperature across the pipe dropped sharply suggesting that 20% ethanol/water mixture is above the maximum evaporation limit.

Thermal efficiency was slightly improved since injection of ethanol-air premixtures into the combustion chamber increased early combustion rate. The present study illustrated that maximum improvement of thermal efficiency was around 5.6% at 15% substitution rate. However CO emissions rose with increased ethanol substitution rate while NOx emissions dropped significantly when ethanol/water mixtures were added.

It is suggested that the ethanol partly evaporated and mixed across the pipe at 15% substitution rate and the maximum measured temperature was close to the estimated temperature.

Further work could include researching alternative ways to improve the mixing process of ethanol/water mixture with in the airstream. The combustion process would be further investigated using chemical kinetic modelling of combustion mechanism.

## 4. Acknowledgments

The authors are grateful for NCMEH's technical staff for their assistance in designing the experiment.

## 5. References

[1] M. Abu-Qudais,Haddad, O.,Qudaisat, M., Energy Conversion and Management **41** (4)(2000**)** 389-399.
[2] D. Nguyen,Honnery, D., Fuel **87** (2)(2008**)** 232-243.
[3] L. Lešnik,Vajda, B.,Žunič, Z.,Škerget, L.,Kegl, B., Applied Energy **111** (2013**)** 558-570.
[4] L. Goldsworthy, Experimental Thermal and Fluid Science **47** (2013**)** 48-59.
[5] L. Goldsworthy, Experimental Thermal and Fluid Science **42** (2012**)** 93-106.
[6] Y.A. Çengel,Boles, M.A., *Thermodynamics : an engineering approach*. New York : McGraw-Hill, c2011.
7th ed.: 2011.
[7] G.J. Shropshire,Bashford, L.L., Agricultural engineering **65** (5)(1984**)** 17-23.
[8] G.L. Borman,Ragland, K.W., (McGraw-Hill)(1998**)**.
[9] G.A. Karim, *Combustion in Gas-fueled Compression Ignition Engines of the Dual Fuel Type*. Wiley-VCH Verlag GmbH & Co. KGaA: 2010.
[10] D.C. Rakopoulos,Rakopoulos, C.D.,Papagiannakis, R.G.,Kyritsis, D.C., Fuel **90** (5)(2011**)** 1855-1867.

# Formulation of new oxygenated fuels and their influence on engine performance and exhaust emissions

M. N. Nabi[1,2,*], A. Zare[1,*], F.M. Hossain[1], M.M. Rahman[1, 2], D. Stuart[3], Z. Ristovski[1, 2], R. J Brown[1]
[1]Biofuel Engine Research Facility, Queensland University of Technology (QUT), QLD, 4000 Australia
[2]ILAQH, Queensland University of Technology (QUT), QLD, 4000 Australia
[3]Eco Tech Biodiesel Pty Ltd, QLD, 4504 Australia

## Abstract

The current study explores a series of oxygenated blends and their influence on engine performance and exhaust emissions on a 6-cylinder turbocharged common rail diesel engine. The fuel blends were prepared with waste cooking biodiesel as a base oxygenate, while triacetin, a derivative of biodiesel as an oxygenated additive. Triacetin was chosen for its high oxygen content and solubility with biodiesel and the experiments were conducted according to 13-mode European Stationary Cycle (ESC). Compared to baseline diesel fuel, all oxygenated blends led to an overall decrease in particle number (PN) over the entire particle size range, with significant reductions for the higher oxygen content fuel blends. NOx emissions however, were higher for the oxygenated blends which agreed with previously published literature. The results revealed that the fuel oxygen is a contributing factor for the reduction of PN and increase of the NOx emissions.

*Keywords: Oxygenate, Engine performance, DPM, PN and NOx emissions.*

## 1. Introduction

In order to meet the EU target of biofuel consumption for the year 2020, biodiesel production needs to be increased [1]. Glycerol is a by-product of the transesterification process, and with the increased volume of biodiesel, the use of glycerol/glycerol analogues as a fuel for internal combustion engine (ICE) would be a cost-effective option for this environmentally friendly fuel. However, due to some detrimental physical and chemical properties, glycerol cannot be directly used as a fuel [1]. Thus, it is necessary to upgrade glycerol and the conversion of glycerol into alternative oxygenated compounds could be an answer for the expanding glycerol stocks [2]. Crude glycerol can be used as a raw material for producing high value chemicals like monoacetin, diacetin and triacetin [3]. Triacetin is miscible with biodiesel and can be used as an additive to suppress smoke emissions in a direct injection diesel engine [4]. Previous studies revealed that fuels having oxygen in their molecular structure reduced carbon related emissions, particularly diesel particular matter (PM) emissions [5-11]. NOx emissions were generally reported higher for oxygenated fuels, but lower NOx emissions were also reported with the oxygenated fuels [12-15]. In this study, different oxygenated blends were formulated keeping the fuel oxygen in the range of 0-14.23%. The engine performance and exhaust emissions were investigated with the blends.

## 2. Material and methods

### 2.1. Tested Engine and fuels

All experimental measurements were conducted with a fully instrumented 6-cylinder turbocharged common rail diesel engine. The specifications of the tested engine are given in Table 1. A partial flow dilution tunnel was used for diluting the raw exhaust. The diluted exhaust was sent to DMS500 (Cambustion ltd), a SABLE CA-10 $CO_2$ analyser, and a DustTrak (TSI 8530). The raw exhaust was sent to a CAI 600 series CLD NOx analyser and a CAI 600 series $CO_2$ analyser. For engine particulars and gas sampling, details can be found in Rahman et al. [16]. The dilution ratio was calculated with the raw and diluted $CO_2$ data. For 13 different modes, the dilution ratios were in the range of 2-25. As per ESC 13-mode protocol, the engine was run for 13 different modes with a specific time for individual mode (Refer to Table 3) [17]. Oxygenated blends were designed in such a way so that the oxygen in the blends was in the range of 0-14.23%. Due to the solubility issue of triacetin to waste cooking biodiesel, a maximum of 10% triacetin was added to the waste cooking biodiesel. No phase separation was noticed in any of the blends for 96 hours at room temperature. Some important properties of the tested fuels are given in Table 2. In Table 2, the notation D100 indicates 100% diesel fuel (neat diesel); D60B35T5 denotes diesel 60%, biodiesel (waste cooking) 35% and triacetin 5%; B100 stands for biodiesel 100% (neat biodiesel), T4B96 represents triacetin 4% and diesel 96%; T8B92 designates triacetin 8% and biodiesel 92% and T10B90 symbolises triacetin 10% and biodiesel 90%.

Table 1. Engine specifications

| | |
|---|---|
| Engine model/type | Cummins ISBe220 31 |
| Number of cylinders | 06 |
| Injection type | High press common rail |
| Number of valves | 4 in each cylinder |
| Bore x stroke (mm) | 102 x 120 |
| Displacement volume (litre) | 5.9 |

* Corresponding author: Md Nurun Nabi
Phone: (+61) 0421110363
Email: nurun.nabi@qut.edu.au

| | |
|---|---|
| Maximum power @2500 rpm (kW) | 162 |
| Maximum torque @1500 rpm (Nm) | 820 |
| Compression ratio | 17.3:1 |
| Dynamometer type | Hydraulic |
| Emission standard | Euro III |

Table 2. Fuel properties

| Properties | D100 | D60B35T5 | B100 | T4B96 | T8B92 | T10B90 |
|---|---|---|---|---|---|---|
| O (wt%) | 0 | 6.02 | 10.93 | 12.25 | 13.57 | 14.23 |
| C (wt%) | 85.1 | 80.46 | 76.93 | 75.81 | 74.73 | 74.19 |
| H (wt%) | 14.8 | 13.47 | 12.21 | 11.97 | 11.74 | 11.63 |
| Density @15°C (g/cc) | 0.84 | 0.866 | 0.87 | 0.882 | 0.893 | 0.898 |
| LHV (MJ/kg) | 41.77 | 38.92 | 37.2 | 36.38 | 35.57 | 35.16 |
| KV@40°C ($mm^2/s$) | 2.64 | 3.66 | 4.82 | 4.94 | 5.06 | 5.12 |
| Cetane number | 53.3 | 53.24 | 58.6 | 56.86 | 55.11 | 54.24 |

Figure 1: Tested engine

Table 3. European Stationary Cycle (ESC) test mode [17].

| Mode | RPM | Load [%] | Weight [%] | Duration [min] |
|---|---|---|---|---|
| 1 | Low idle | 0 | 15 | 4 |
| 2 | A | 100 | 8 | 2 |
| 3 | B | 50 | 10 | 2 |
| 4 | B | 75 | 10 | 2 |
| 5 | A | 50 | 5 | 2 |
| 6 | A | 75 | 5 | 2 |
| 7 | A | 25 | 5 | 2 |
| 8 | B | 100 | 9 | 2 |
| 9 | B | 25 | 10 | 2 |
| 10 | C | 100 | 8 | 2 |
| 11 | C | 25 | 5 | 2 |
| 12 | C | 75 | 5 | 2 |
| 13 | C | 50 | 5 | 2 |

As per ESC 13-mode protocol, A, B C speeds for the BERF tested engine were determined by the following formula [17] and found to be 1472, 1865 and 2257 rpm respectively.

$A = n_{lo} + 0.25(n_{hi} - n_{lo})$
$B = n_{lo} + 0.50(n_{hi} - n_{lo})$
$C = n_{lo} + 0.75(n_{hi} - n_{lo})$

$n_{hi}$ was obtained by computing 70% of the declared maximum net power and that for $n_{lo}$ was 50% of the declared maximum net power.

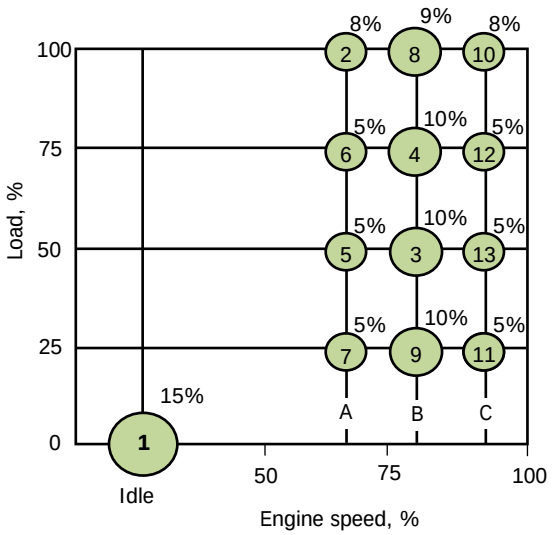


Figure 2: European Stationary Cycle (ESC) [17].

## 3. Results and discussion

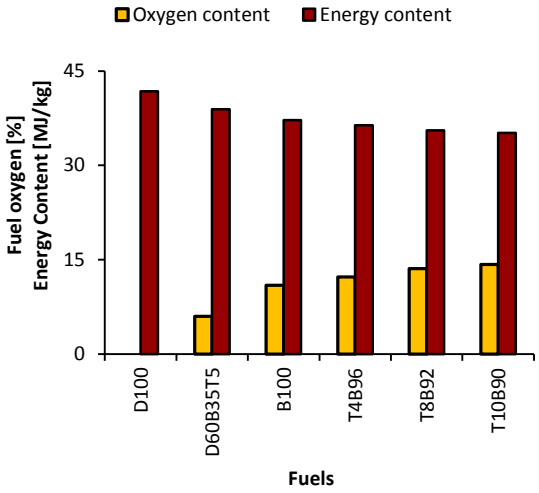


Figure 3: Oxygen and energy content of fuels

Figure 3 demonstrates fuel oxygen content and energy content of the blends. One can see from the Figure that the fuel oxygen varies from 0 to 14.23% corresponding to the energy content ranges from 41.77 to 35.16 MJ/kg. As can be seen from Figure 3 that the reference diesel fuel (D100) has 0% oxygen having the maximum energy level of 41.77 MJ/kg, while T10B90 has the highest oxygen content of 14.23% having the minimum energy content of 35.16 MJ/kg.

Figure 4 shows the power output (brake power) for D100 and a wide range of oxygenated blends. The brake power for D100 is higher than that of the oxygenated blends for all 13-mode. It is evident that the higher the oxygen content of the blends, the lower the brake power was observed. This was associated with the lower energy content of the blended fuels.

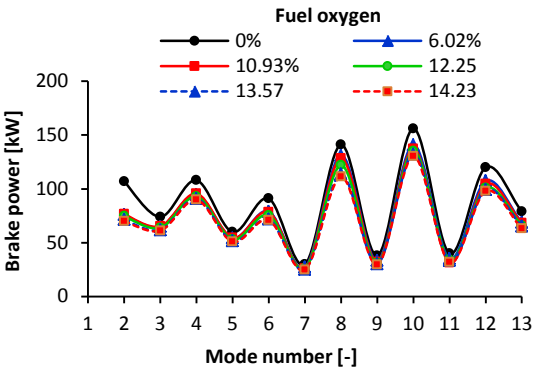


Figure 4: Brake power with D100 and oxygenated blends

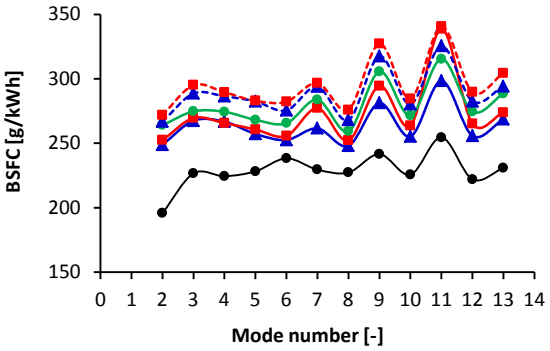


Figure 5: Brake specific fuel consumption (BSFC) with D100 and oxygenated blends. Figure legend as for Figure 4.

Figure 5 represents the brake specific fuel consumption (BSFC) of D100 and the different oxygenated blends. Compared to the D100, the blends show higher BSFC for every mode. As stated before that the oxygenated blends have lower energy content that results in a more fuel consumption for the same power output.

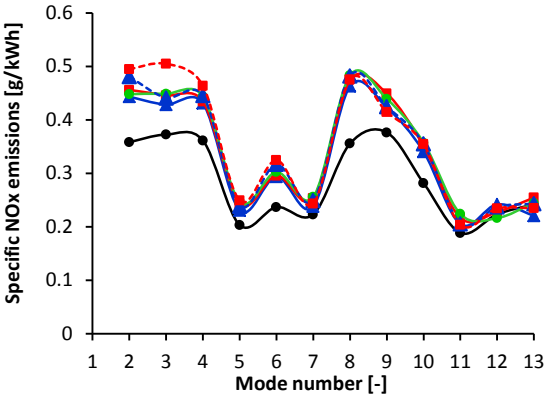


Figure 6: Weighted specific NOx emissions for D100 and oxygenated blends. Figure legend as for Figure 4.

Figure 6 depicts the weighted specific NOx emissions for D100 and the different oxygenated blends. As anticipated, NOx emissions for the oxygenated blends are higher for all 13-mode ranges compared to those of reference diesel fuel (D100). Fuels having higher density, viscosity, cetane number may also be the reasons for higher NOx emissions. Nabi et al. [18] did an experiment with 30% Licella biofuel (derived from *pinus radiata* wood flour) blended with neat diesel fuel (D100) that leads to an oxygen content of 2.88% in the blend. It was fuel oxygen that resulted in a higher NO emissions with 30% Licella biofuel compared to those of neat diesel fuel, authors reported. Several other studies [19-21] with oxygenated fuels reported higher NOx emissions. Concerning NOx emissions, the current study agrees with the studies of [18-21].

Figures 7-9 show the particle number (PN) size distributions for D100 and five oxygeanted blends. The three figures demonstrate the PN size distributions for a 50% load with three different engine speeds of 1472, 1865 and 2257 rpm (ESC mode-3, mode-5 and mode-13). The results (not shown) for other ESC modes exhibit the same trends. It can be seen from Figures 7-9 that the peaks of the PN size distributions for D100 can be found in the range of 56-75 nm, while for oxygenated blends the peaks can be found in the range of 36-64 nm. It is interesting to note that all oxygenated blends produce much lower PN over the entire size ranges compared to those of baseline D100 fuel. It is also noted that the reductions of PN is significant for the blends having higher oxygen content. The fuel oxygen promotes combustion in the fuel-rich region and/or oxidises soot that already formed in the combustion chamber results in a lower PN production. Tan et al. [22] reported lower accumulation mode PN for different biodiesel blends. Authors mentioned that fuel oxygen and absence of aromatics in the biodeisel were the reasons for reduction of PN with biodiesel blends. Pham et al. [23] also reported lower PN emissions with biodiesels compared to those of diesel fuel. The current investigation agrees with those of Tan et al. and Pham et al. [22, 23].

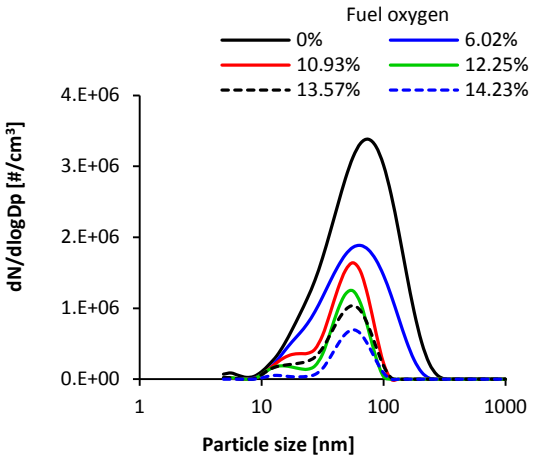


Figure 7: PN size distributions for D100 and oxygenated blends [load=50%, engine speed=1472 rpm]

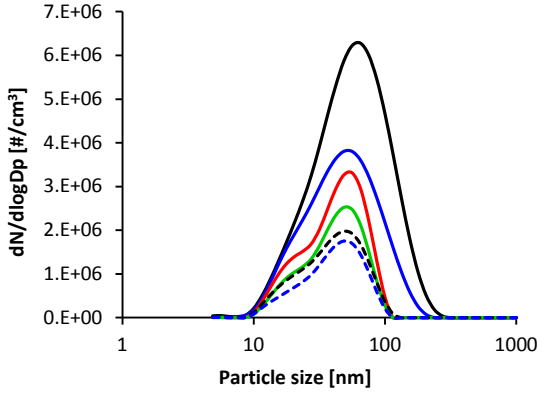


Figure 8: PN size distribution for oxygenated blends [load=50%, engine speed=1865 rpm]. Figure legend as for Figure 7.

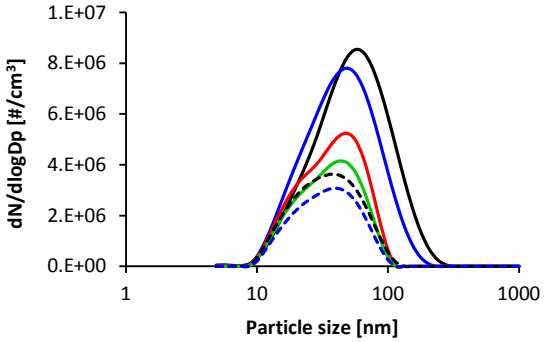


Figure 9: PN size distribution for oxygenated blends [load=50%, engine speed=2,257 rpm]. Figure legend as for Figure 7.

## 4. Conclusion

The current study investigated the engine performance and exhaust emission with a wide range of oxygenated blends using waste cooking biodiesel and triacetin under the 13-mode European Stationary Cycle. The experimental results revealed that the engine brake power reduced with the increase in oxygen content in the fuel blends. The reduction in power was due to the reduced energy content of the blends. The diesel particle numbers were much lower compared to those of commercial diesel fuel for the blends having higher oxygen content. Contrary to the particle numbers, NOx emissions were higher for all oxygenated blends.

## 5. Acknowledgments

The current investigation supported under Australian Research Council's Linkage Projects funding scheme (project number LP110200158). The author also would like to thank Mr. Noel Hartnett, Dynolog software development by Mr Andrew Elder form DynoLog Dynamometer Pty Ltd, Peak3 Pty Ltd for helping with measuring instruments, and Eco Tech Biodiesel for the supply of waste cooking biodiesel.

## 6. References

1. C. Beatrice; G. Di Blasio; M. Lazzaro; C. Cannilla; G. Bonura; F. Frusteri; F. Asdrubali; G. Baldinelli; A. Presciutti; F. Fantozzi; G. Bidini; P. Bartocci, Applied Energy 102 (2013) 63-71 10. 1016/j.apenergy.2012.08.006.
2. J. A. Melero; G. Vicente; G. Morales; M. Paniagua; J. Bustamante, Fuel 89 (8) (2010) 2011-2018 10.1016/j.fuel.2010.03.042.
3. Z. Mufrodi; R. Rochmadi; S. Sutijan; A. Budiman, Modern Applied Science 7 (10) (2013) 1 0.5539/mas.v7n10p70.
4. P. V. Rao; B. V. A. Rao, International Journal of Energy and Environment 3 (4) (2012) 629-638
5. D. Hernández; J. J. Fernández; F. Mondragón; D. López, Fuel 92 (1) (2012) 130-136 10.1016/j.fuel.2011.06.073.
6. A. K. Agarwal; T. Gupta; A. Kothari, Renewable and Sustainable Energy Reviews 15 (6) (2011) 3278-3300 10.1016/j.rser.2011.04.002.
7. H. Chen; J. Wang; S. Shuai; W. Chen, Fuel 87 (15-16) (2008) 3462-3468 10.1016/j.fuel.2008.04.034.
8. B. Kegl, Enery & Fuels 21 (2007) 3310–3316
9. M. N. Nabi; J. E. Hustad, Fuel 93 (2012) 181-188 10. 1016/j.fuel.2011.11.019.
10. R. Zhu; C. S. Cheung; Z. Huang; X. Wang, Journal of Aerosol Science 42 (4) (2011) 264-276 10.1016/j.jaerosci.2011.01.004.
11. Y. Di; C. S. Cheung; Z. Huang, Journal of Aerosol Science 40 (2) (2009) 101-112 10.1016/j.jaerosci.2008.09.004.
12. S. S. Gill, Tsolakis, A., Herreros, J.M., York, A.P.E., Fuel 95 (2012) 578–586
13. N. Miyamoto, Ogawa, H., Nabi, M.N., Obata, K., Arima, T., SAE Technical Paper Series 980506 (1998)
14. D. Agarwal; S. Sinha; A. K. Agarwal, Renewable Energy 31 (14) (2006) 2356-2369 10.1016/j.renene.2005.12.003.
15. J. P. Szybist; A. L. Boehman; J. D. Taylor; R. L. McCormick, Fuel Processing Technology 86 (10) (2005) 1109-1126 10.1016/j.fuproc.2004.11.006.
16. M. M. Rahman; A. M. Pourkhesalian; M. I. Jahirul; S. Stevanovic; P. X. Pham; H. Wang; A. R. Masri; R. J. Brown; Z. D. Ristovski, Fuel 134 (2014) 201-208 10.1016/j.fuel.2014.05.053.
17. DieselNet. European Stationary Cycle (ESC), (Accessed on 10 September 2015)
18. M. N. Nabi; M. M. Rahman; M. A. Islam; F. M. Hossain; P. Brooks; W. N. Rowlands; J. Tulloch; Z. D. Ristovski; R. J. Brown, Energy Conversion and Management 96 (2015) 588-598 10.1016/j.enconman.2015.02.085.
19. H. Kim; B. Choi, Renewable Energy 35 (1) (2010) 157-163 10.1016/j.renene.2009.04.008.
20. B. Tesfa; F. Gu; R. Mishra; A. Ball, Energies 7 (1) (2014) 334-350 10.3390/en7010334.
21. Z. Xusheng; G. Guanghai; L. Liguang; W. Zhijun; H. Zongjie; D. Jun, SAE Technical Paper Series 2008-01-1832)
22. P.-q. Tan; S.-s. Ruan; Z.-y. Hu; D.-m. Lou; H. Li, Applied Energy 113 (2014) 22-31 10.1016/j.apenergy.2013.07.009.
23. P. X. Pham; T. A. Bodisco; Z. D. Ristovski; R. J. Brown; A. R. Masri, Fuel 116 (0) (2014) 140-150 http://dx.doi.org/10.1016/j.fuel.2013.07.100.

**Proceedings of the Australian Combustion Symposium**
**December 7-9, 2015, The University of Melbourne**

# Fuel Economy and $CO_2$ Emissions Benefits of Octane-on-Demand Combustion in Spark-Ignition Engines

Kai Morganti*, Marwan Al-Abdullah and Abdullah Zubail

Fuel Technology R&D Division,
Saudi Aramco Research & Development Center, Dhahran, Kingdom of Saudi Arabia 31311

**Abstract**

This paper explores the use of Octane-on-Demand as a means of improving the efficiency and environmental impact of conventional light-duty vehicles. Engine fuel consumption maps are first presented for a standard market gasoline (RON 95), along with two dual-fuel combinations that utilize lower octane petroleum-derived fuels (RON 61 and 75) in combination with methanol (RON 109). The benefits of Octane-on-Demand in an otherwise conventional light-duty vehicle are then quantified using drive cycle simulations. The preliminary results indicate that Octane-on-Demand can be utilized to avoid unnecessary octane 'give away' during most urban driving, while still allowing downsized engines to operate at high specific outputs by eliminating the traditional constraints on high load operation. This approach is shown to provide small fuel economy benefits relative to an equivalent vehicle operated on gasoline, along with more substantial $CO_2$ emissions benefits of up to 27%. Overall, this suggests that Octane-on-Demand offers the potential to reduce the direct environmental impact of conventional light-duty vehicles, while also realizing the indirect benefits of petroleum-derived fuels that require less processing than those offered in the market today. 

*Keywords: Engine Downsizing, Octane-on-Demand, Octane Number, Knock, Methanol.*

## 1. Introduction

Reciprocating engines will remain the dominant energy conversion device utilized in the transport sector for the foreseeable future. This proven technology platform continues to offer cost advantages over competing technologies, while also benefiting from a comprehensive global fuel distribution network. In recent years, conventional powertrains have also benefited from varying degrees of hybridization, along with the inclusion of other low cost technologies that can further reduce fuel consumption. Engine downsizing has also proven to be an effective strategy for reducing fuel consumption, but is ultimately limited by the increased susceptibility to knock.

To address the need for fuels with higher anti-knock quality, many refiners 'splash-blend' high octane components into their gasoline blendstocks. Methanol and ethanol (RON ~109) have emerged as the most widely utilized components, but their concentrations are typically limited to around 15% (v/v) to maintain compatibility with existing vehicle systems. This produces a finished fuel with marginally higher anti-knock quality, but often with a much lower energy density than non-oxygenated gasolines. For these reasons, such fuels provide few benefits in non-optimized engine applications [1,2]. In particular, fuels with modest oxygenate levels often lead to a volumetric fuel consumption penalty at part-load conditions. And yet, such fuels do not appear to offer sufficiently high levels of anti-knock quality to offset these losses by enabling more extreme engine downsizing.

An alternative approach is to operate an otherwise conventional spark-ignition engine on two fuels that exhibit different levels of anti-knock quality. The lower octane fuel should provide both a high energy density and moderate levels of anti-knock quality for urban driving, while the high octane fuel should only be utilized to extend the engine performance envelope under more extreme driving conditions. This is likely to avoid excessive fuel consumption and octane 'give away' during most urban driving, but still allow downsized/boosted engines to operate at high specific outputs without encountering knock. Lower octane fuels can also be advantageous from an environmental perspective, since fewer $CO_2$ emissions are typically produced during the refining process.

Although a promising concept, there is still uncertainty surrounding the actual benefits that Octane-on-Demand can provide, and particularly whether these benefits justify the added complexities. This paper is therefore intended to be a contribution to this broader task. Engine fuel consumption maps are first presented for a standard market gasoline, along with two dual-fuel combinations that utilize lower octane petroleum-derived fuels in combination with methanol. Vehicle drive cycle simulations are then used to quantify the fuel consumption and $CO_2$ emissions for a light-duty vehicle equipped with a naturally aspirated engine and a downsized/turbocharged engine. The results indicate that Octane-on-Demand offers both fuel economy and $CO_2$ emissions benefits relative to an equivalent light-duty vehicle operated on gasoline.

## 2. Experimental and Numerical Methods

The vehicle drive cycle simulations were performed using the *ADVISOR* software [3]. The standard libraries were updated to simulate a modern vehicle with a curb mass of 1600 kg. This vehicle was equipped with both a baseline 2.5L inline four cylinder engine, and an equivalent engine that had been downsized to a displacement of 1.6L. Both engines produced a peak torque of 265 Nm, albeit at different speeds. The vehicle

* Corresponding author:
Phone: (+966) 13 876 7201
Email: kai.morganti@aramco.com

configurations were compared using the WLTP drive cycle, along with the more aggressive US06 drive cycle.

## 2.1 Fuel Properties

Two alternative naphthas were examined as candidates for the lower octane base fuel, while methanol was utilized as the high octane fuel (Table 1). A market gasoline (RON 95) served as the baseline case.

Table 1: Measured fuel properties.

| Property | Market Gasoline | Naphtha A | Naphtha B | Methanol |
|---|---|---|---|---|
| RON | 95.0 | 61.1 | 75.3 | 108.8 |
| MON | 86.3 | 59.0 | 73.0 | 88.7 |
| Net Heating Value (MJ/kg) | 42.1 | 44.6 | 45.4 | 20.1 |
| Hydrogen-to-Carbon Ratio | 1.82 | 2.18 | 2.24 | 4.00 |
| Density at 15°C (kg/m$^3$) | 752 | 710 | 680 | 796 |

## 2.2 Specific Fuel Consumption Maps

The instantaneous fuel consumption is computed using experimental brake specific fuel consumption (BSFC) maps derived with a single cylinder engine. The calibration procedure involved determining the minimum amount of methanol that must be added to obtain the baseline gasoline maximum brake torque (Figure 1). Examples of the resulting BSFC maps are presented in Figure 2. The tank-to-wheel $CO_2$ emissions were then computed using an elemental mass balance.

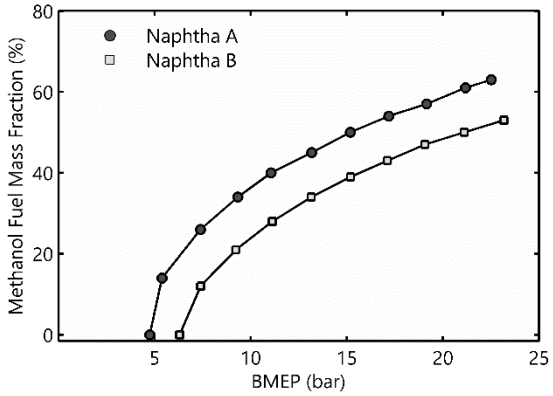


Figure 1: Minimum methanol requirement to maintain the baseline maximum brake torque (MBT) at 1500 rpm.

## 2.3 Numerical Engine Load Scaling

The effect of engine displacement on the engine load was accounted for using load scaling. This involved computed the equivalent brake mean effective pressure (BMEP) that would be required to maintain a given engine torque based on the revised engine displacement:

$$BMEP = \frac{Torque\ \ n_c\ \ 2\pi}{V_d} \qquad (1)$$

where $V_d$ is the engine displacement and $n_c$ is two for a four-stroke engine.

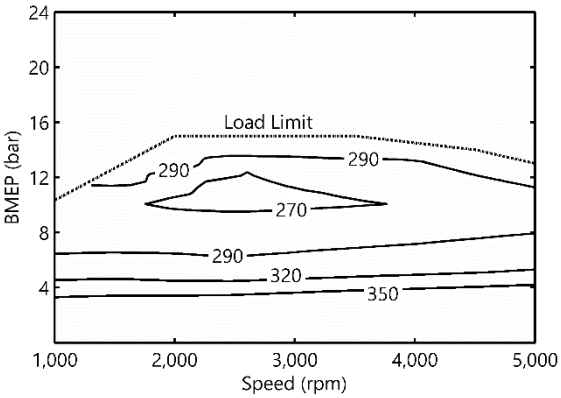


(a) Single Fuel: Market Gasoline (g/kWh).

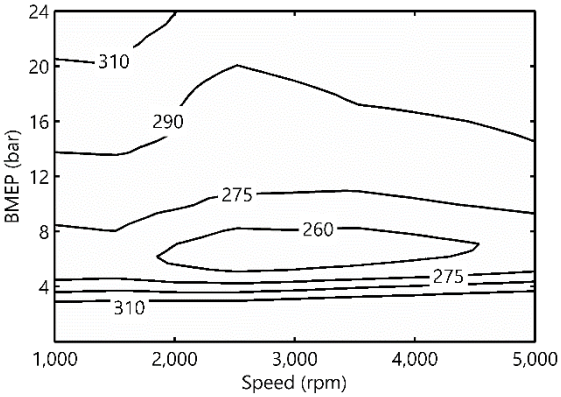


(b) Dual-Fuel: Naphtha B/Methanol (g/kWh).

Figure 2: Brake specific fuel consumption (BSFC) maps.

# 3. Results and Discussion

## 3.1 Baseline Engine Fuel Consumption

The simulated fuel consumption for the vehicle equipped with the baseline 2.5L engine is presented in Figure 3. Due to the lower energy density of both methanol and the naphtha fuels, the benefits of dual-fuel combustion in volumetric terms are particularly sensitive to the degree of methanol utilization. For example, in the WLTP drive cycle, the low rates of methanol utilization enable the Naphtha A/Methanol combination to provide a 5% fuel economy benefit relative to the market gasoline. This benefit is reduced to less than 1% in the more aggressive US06 drive cycle.

Nonetheless, each dual-fuel combination provides some degree of benefit in fuel economy terms relative to the market gasoline regardless of the methanol utilization. This can be attributed to the higher mass-based lower heating values (LHVs) for each of the naphtha fuels and differences in the stoichiometric air-fuel ratios (Table 1). In the case of the latter, a larger air requirement for a given fuel mass leads to reduced pumping losses, particularly at low engine loads.

## 3.2 Effect of Engine Downsizing

Dual-fuel combustion is evidently an enabling technology for engine downsizing, since the traditional

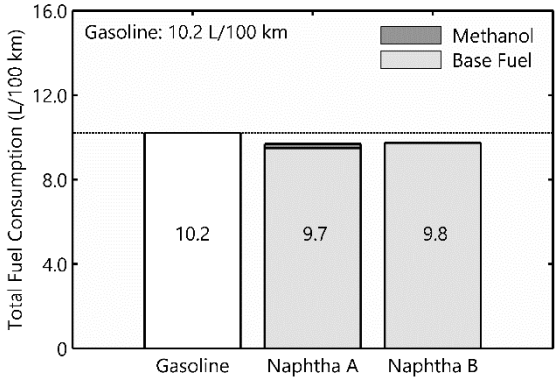


(a) WLTP drive cycle.

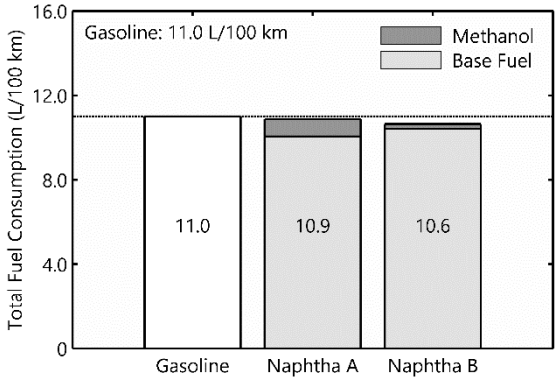


(b) US06 drive cycle.

Figure 3: Simulated fuel consumption for the vehicle equipped with the baseline 2.5L engine.

constraints on high load operation can be eliminated, i.e. spark retard and fuel enrichment. The effect of downsizing on the engine operating envelope during the US06 drive cycle is presented in Figure 4. Engine downsizing is shown to increase the maximum engine load from approximately 10 to 15 bar BMEP, while also shifting the intermediate load points to a lower engine speed (so-called 'down speeding'). This enables the engine to operate more frequently within the most efficient region of the operating envelope. Nonetheless, for the market gasoline, this presents somewhat of a trade-off, since a large proportion of the operating points have also been shifted into the less efficient high load regions where spark retard and fuel enrichment are required. This increases the vehicle fuel consumption.

## 3.3 Engine Octane Requirement

The effect of downsizing on the engine octane requirement during the US06 drive cycle is presented in Figure 5. The RON distribution correlates strongly with the degree of engine downsizing. In particular, the distribution is skewed towards the lower octane range for the baseline 2.5L engine, while the distribution is skewed towards the upper octane range for the downsized 1.6L engine. As a result, the vehicle equipped with the 2.5L engine could complete approximately 80% of the drive cycle on a fuel with a RON of 80. This includes the regular intervals where the octane demand of the engine is low,

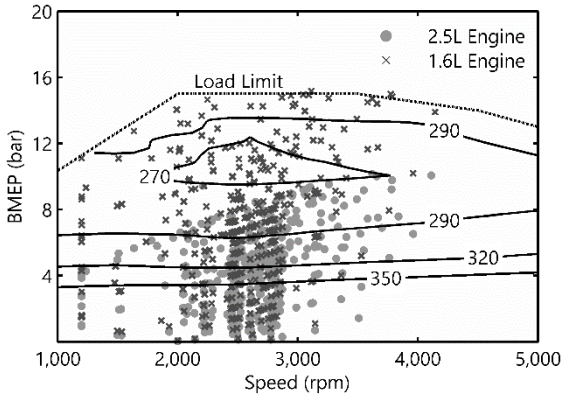


Figure 4: Operating envelopes for the 2.5L and 1.6L engines during the US06 drive cycle.

such as during idle and vehicle deceleration. However, the same fuel would only enable the vehicle equipped with the 1.6L downsized engine to complete less than half of the drive cycle. Nonetheless, the average octane requirement for the downsized 1.6L engine (RON 71) is still considerably lower than the minimum value typically specified for commercial gasolines. This highlights one of the key advantages of Octane-on-Demand, particularly when utilized in conjunction with lower octane fuels.

## 3.4 Downsized Engine Fuel Consumption

The simulated fuel consumption for the vehicle equipped with the downsized 1.6L engine is compared with the baseline 2.5L engine in Figure 6. In all cases, the benefits of Octane-on-Demand relative to the equivalent gasoline engine are reduced relative to those previously observed for the 2.5L engine (Figure 3). This is due to the lower volumetric energy density of both methanol and the naphtha fuels, along with the higher rates of methanol utilization for the downsized engine. This causes the total volumetric fuel consumption for the Naphtha A/Methanol combination in the US06 drive cycle to increase above the equivalent engine operated on gasoline, albeit by only 1%. This suggests that the anti-knock quality of Naphtha A (RON 61) may be too low to be used in conjunction with methanol in an engine with this degree of performance/downsizing.

## 3.5 Tank-to-Wheel $CO_2$ Emissions

The calculated tank-to-wheel $CO_2$ emissions for the vehicle equipped with the baseline 2.5L engine and the downsized 1.6L engine are presented in Figure 7. In all cases, the dual-fuel combinations provide lower tank-to-wheel $CO_2$ emissions than even the most efficient engine operated on the market gasoline (i.e. the 1.6L downsized engine). For example, the 2.5L engine operated on the Naphtha A/Methanol dual-fuel combination produces $CO_2$ emissions that are 3.5% lower than the 1.6L downsized engine operated on gasoline. For an equivalent degree of engine downsizing, the Naphtha B/Methanol dual-fuel combination produces $CO_2$ emissions that are 18% lower than the market gasoline. If the 2.5L engine is used as a baseline, then Octane-on-Demand can reduce the tank-to-wheel $CO_2$ emissions by up to 27%. These benefits can be attributed to a combination of the higher average

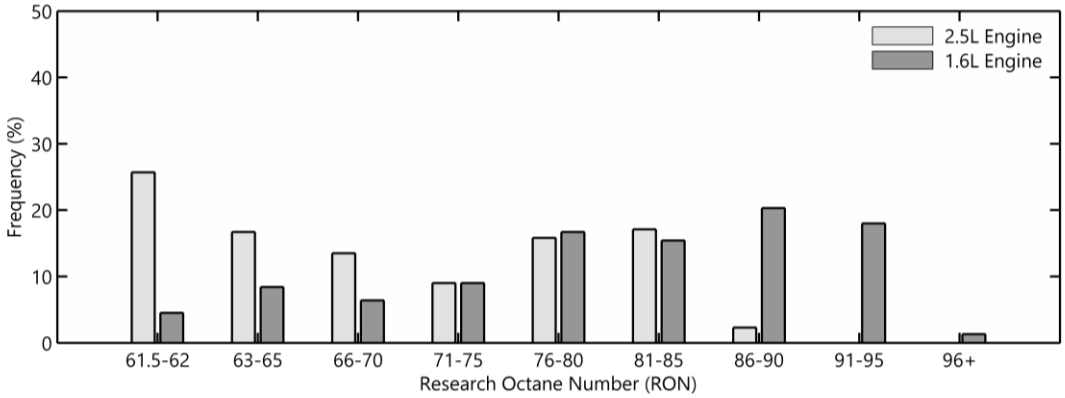


Figure 5: Engine RON requirement distribution for the Naphtha A/Methanol dual-fuel combination during the US06 drive cycle. The distribution was computed using an in-house octane model.

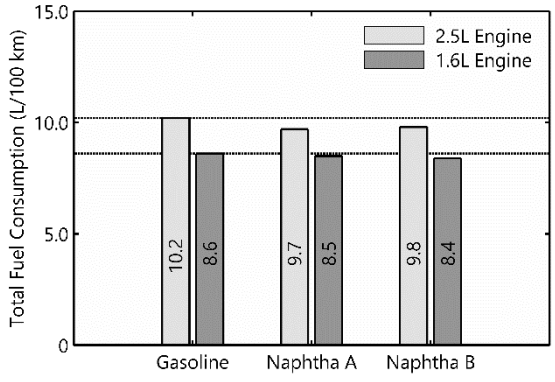


(a) WLTP drive cycle.

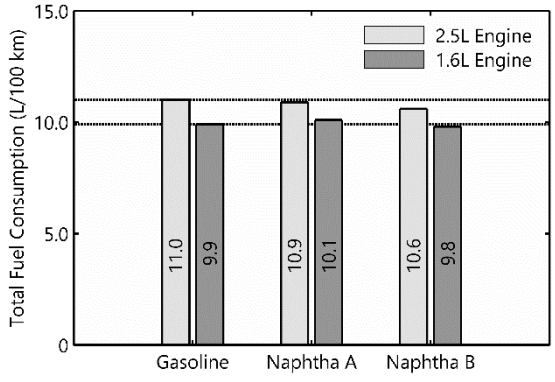


(b) US06 drive cycle.

Figure 6: Simulated fuel consumption for the vehicle equipped with the downsized 1.6L engine.

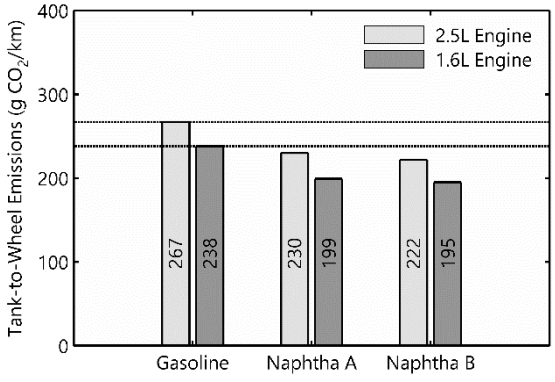


Figure 7: Simulated vehicle tank-to-wheel $CO_2$ emissions during the US06 drive cycle.

hydrogen-to-carbon ratios of the dual-fuel combinations, along with the more efficient operation of the engine in the downsized configuration.

## 4. Conclusions

This paper explored the use of dual-fuel combustion as a means of improving the efficiency and environmental impact of conventional light-duty vehicles. Engine fuel consumption maps were first presented for a market gasoline, along with two dual-fuel combinations that utilized lower octane petroleum-derived fuels in combination with methanol. Vehicle drive cycle simulations were then used to quantify the fuel consumption and $CO_2$ emissions for a light-duty vehicle equipped with a naturally aspirated engine and a downsized/turbocharged engine.

The simulation results indicated that Octane-on-Demand generally offers both fuel economy and $CO_2$ emissions benefits relative to an equivalent vehicle operated on gasoline. The fuel economy benefits were more pronounced for the vehicle equipped with the 2.5L engine, due to lower rates of methanol utilization. Nonetheless, small fuel economy benefits of up to 3% were also generally realized for the downsized 1.6L engine. This was not the case for the Naphtha A/Methanol dual-fuel combination in the US06 drive cycle, which suggested Naphtha A (RON 61) may not be suitable for an engine with this degree of performance/downsizing.

In all cases, Octane-on-Demand provided lower tank-to-wheel $CO_2$ emissions than even the most efficient gasoline engine. These benefits ranged from 3.5% up to 27%, depending on whether the 2.5L or 1.6L gasoline engine was used as the baseline. Overall, this study indicated that Octane-on-Demand offers the potential to reduce both vehicle fuel consumption and $CO_2$ emissions, while also realizing the environmental benefits of lower octane petroleum-derived fuels.

## 5. References

[1] R. Stein, D. Polovina, K. Roth, M. Foster et al., SAE Int. J. Fuels Lubr. **5** (2) (2012), pp. 823-843.

[2] M. Koç, Y. Sekmen, T. Topgül and H. Serdar Yücesu, Renew. Energ **34** (10) (2009), pp. 2101-2106.

[3] T. Markel, A. Brooker, T. Hendricks, V. Johnson et al., J. Power Sources 110(2)(2002), pp.255–266.

# The Effect of Nitric Oxide on Autoignition Onset of Toluene Reference Fuels (TRFs) in a CFR Engine

Zhongyuan Chen, Hao Yuan, Yi Yang*, Michael Brear
Department of Mechanical Engineering
University of Melbourne VIC 3010 Australia

## Abstract

This paper investigates the impact of nitric oxide (NO) on the timing of autoignition onset in a CFR octane rating engine fuelled with Toluene Reference Fuels (TRFs, i.e. mixtures of toluene, n-heptane and iso-octane). Four TRFs with the same research octane number (RON) of 91 and a varying toluene content (0-45 vol. %) are tested. NO is introduced at the engine intake where $O_2$ is maintained at 21 vol. %. A fuel rich operating condition ($\lambda = 0.7$) is used for all experiments in order to reduce the impact of the residual NO on autoignition [1]. The engine inlet temperature for the fuel and air mixture is set at 32$^{o}$C for all tests. Results show that the impact of NO on the timing of autoignition onset varies with both the NO concentration and the toluene fraction in the fuel. Chemical kinetic modelling is then undertaken and used to suggest the chemistry causing these variations.

*Keywords: Nitric Oxide, Autoignition, Toluene, Spark Ignition Engine.*

## Nomenclature

**CFR:** Cooperative Fuel Research
**IAP:** Intake Air Pressure
**IAT:** Intake Air Temperature, upstream of carburetor
**IMT** Inlet Mixture Temperature, downstream of carburetor
**EGR:** Exhaust Gas Recirculation
**CAD:** Crank Angle Degree
**TDC:** Top Dead Center
**CR:** Compression Ratio
**λ:** Air Excess Ratio

## 1. Introduction

Spark ignition (SI) engines have made remarkable advances in improving the efficiency and reducing pollutant emissions. However, today they are still considerably less efficient than diesel engines and one of the major reasons for this is that engine knock limits their compression ratio. Knock is a consequence of autoignition, which is due to compression of the unburned fuel/air mixture by the piston and flame. This process is controlled by the chemical kinetics, and can thus be affected by trace species in the reacting gas.

Nitric oxide (NO) is one such trace species, which exists inside the cylinder typically at 10-100 ppm levels in the residual gas. Residual NO is known to have a significant impact on autoignition in SI engines [2-4] and HCCI engines [5-7]. Fundamental kinetic experiments have also been conducted to understand the the impact of NO on fuel autoignition in jet-stirred reactors [8-10] and flow reactors [11, 12]. These studies reported that NO can enhance autoignition, particularly at low concentrations and high temperatures, and can also inhibit autoignition under other conditions. The promoting effect is mainly via

$$NO + HO_2 = NO_2 + OH \quad \text{R.1}$$
$$NO + ROO = NO_2 + RO \quad \text{R.2}$$

which convert $HO_2$ and ROO to more reactive OH and RO radicals. The inhibiting effect is via

$$NO + OH + M = HONO + M \quad \text{R.3}$$
$$HONO + OH = NO_2 + H_2O \quad \text{R.4}$$

which both remove reactive OH radicals from the chain reaction sequence.

Despite the significant impact of NO on SI engine knock, investigating this phenomenon in a firing SI engine is difficult. This is because the residual NO can be significant so its impact on engine knock can conceal the impact from externally added NO. Several approaches have been taken to address this issue, such as using skip firing techniques [2] or replacing atmospheric N2 with Ar [4]. Another difficulty of studying engine knock is that typical production SI engines cannot operate under continuous knocking conditions. In this study, a Cooperative Fuel Research (CFR) engine is used, which is a standard SI engine for octane number measurement. Its sturdy design has allowed wide use of this type of engines for engine knock studies. The engine experiments employ a fuel rich condition which produces low residual NO. This fuel-rich approach preserves the continuous firing nature of engine combustion and realistic temperatures, which is critical to autoignition.

Using this method, CFR engine experiments are performed to study the impact of NO on the timing of autoignition of toluene reference fuels (TRFs). Four fuels (PRF91, TRF91-15, TRF91-30, TRF91-45) with toluene content of 0, 15, 30 and 45 vol% and a research octane number (RON) of 91 were tested. The observed impact of NO on autoignition onset is discussed using known NO-hydrocarbon interaction chemistry.

* Corresponding author:
Phone: (+61) 3 83448104
Email: yi.yang@unimelb.edu.au

## 2. Experimental Methods

The CFR engine setup is shown in Fig. 1. Nitric oxide (10 mol% in $N_2$) is injected into the intake air upstream of the surge tank together with $O_2$ (99.999%). The addition of $O_2$ is to maintain the intake $O_2$% as in the air (20.95%), which otherwise could be reduced by the NO addition. The conversion of NO to $NO_2$ is negligible for the short residence time through the intake system and the low intake temperatures. An electric heater is used to control the intake mixture temperature (32±0.1°C) upstream of the fuel carburetor.

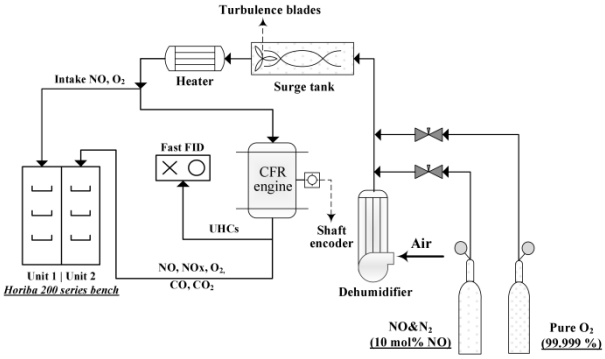


**Fig. 1. Schematics of the CFR engine setup**

The fuel is supplied via a standard carburetor of a CFR engine where the height of fuel reservoir was adjusted for varying flow rates. The air/fuel ratio (λ) was measured using a Bosch exhaust oxygen sensor. The combustion analysis was conducted via cylinder pressure measurement at 0.1 CAD resolution, which used a Kistler (6125C) pressure transducer mounted in the same port as the detonation pickup in the cylinder head. The engine operating conditions and cylinder pressures were collected using an in-house data acquisition system and LabView software. Exhaust gases (CO, CO2, $O_2$, NO, NOx) were measured using a Horiba emission bench, and unburned hydrocarbons (UHCs) were measured by a separate flame ionization detector (FID) beside the engine.

The experimental conditions for the four test fuels are shown in Table 1.

Table 1: Experimental conditions

| Fuel | PRF91 | TRF91-15 | TRF91-30 | TRF91-45 |
|---|---|---|---|---|
| RON | 91 | 91 | 91 | 91 |
| Toluene (v/v%) | 0 | 15 | 30 | 45 |
| Isooctane (v/v%) | 91 | 72.6 | 53 | 34.7 |
| n-Heptane (v/v%) | 9 | 12.4 | 17 | 20.3 |
| IAT (°C) | 55 | 60 | 67 | 74 |
| IMT (°C) | 32 | 32 | 32 | 32 |
| λ | 0.7 | 0.7 | 0.7 | 0.7 |
| CR | 7.4 | 7.4 | 7.4 | 7.4 |
| IAP | atmospheric | | | |
| Speed | 600±6 rpm | | | |
| Spark timing | 13 CAD before TDC | | | |
| NO addition | 0~300 ppm | | | |

Since λ = 0.7 is used for all experiments, exhaust NO levels are very low, i.e. 40~60 ppm, corresponding to only ~ 4 ppm residual NO. This allows investigation of the impact of externally added NO. Leaner cases were reported in a previous study on iso-octane [1], where considerably more residual NO was produced and effectively concealed the effect of external added NO on autoignition onset. The intake mixture temperatures of fuel/air/NO/$N_2$/$O_2$ were set at 32°C for all tests. Other parameters (i.e. IAP, Engine speed, Spark timing) were in compliance with the standard knocking test [13].

## 3. Results and Discussion

### 3.1 Experimental results

Figure 2 shows the measured in-cylinder pressure traces for PRF91 at NO addition from 0 to 310 ppm. The trace with median IMEP out of 600 sampled cycles is shown. Autoignition onset timing is determined as the crank angle at which a distinctive change in the pressure rise rate is observed.

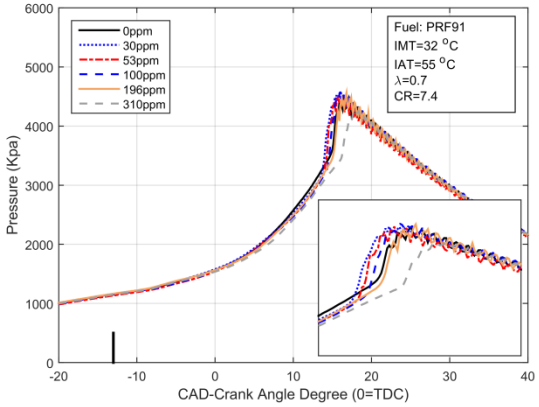


**Fig. 2. Measured pressure traces for PRF91**

These timings from Fig. 2 are then plotted against the level of NO addition in Fig. 3, together with the results for the other TRF91s. Results indicate that the effects of NO vary not only with the added NO concentration, but also with the fuel composition. For PRF91, a non-monotonic impact of NO is observed, where lower NO levels advance autoignition, relative to the zero NO case, but higher levels retard it. Similar non-monotonic trends were observed for the different TRFs.

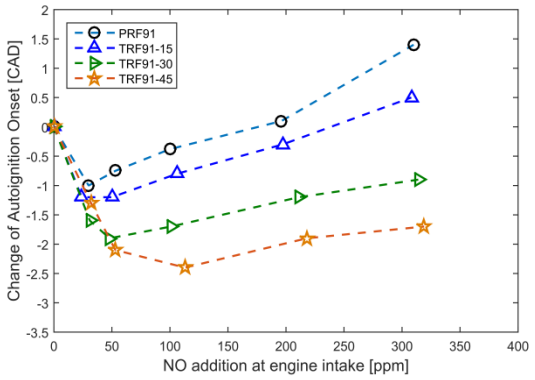


**Fig. 3. Measured impact of NO on autoignition timing for different TRFs, negative values denote more advanced autoignition timing.**

Figure 4 plots the same data as in Fig. 3 in a different way, i.e. change of autoignition onset vs. toluene content at different levels of NO addition. Overall, these results suggest that the autoignition behavior of commercial gasolines can have different sensitivity to NO inside the cylinder. Specifically, a stronger promoting effect of NO may be expected for gasoline containing more aromatics.

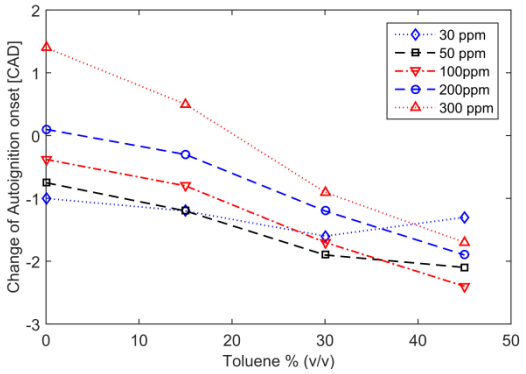


**Fig. 4. Measured change of autoignition onset by NO addition, negative values denote more advanced autoignition timing.**

### 3.2 Simulation results

In order to understand the impact of NO on the autoignition of fuels with different toluene content, kinetic modelling is now conducted using Chemkin [14] with a homogeneous constant-volume adiabatic reactor. Note that the objective here is not to model the CFR engine, but to verify if the trends seen in the experiments can be reproduced by the model, and thus gain some understanding on the impact of NO on autoignition of TRFs. The mechanism containing TRF and NO [15] was used. The starting temperature and pressure was set to 800K and 40bar, which is representative of the conditions at autoignition onset in the engine. The equivalence ratio was 1.43, which corresponds to a lambda of 0.7. The ignition delay was determined where the gas temperature rise exceeded 400 K.

Figure 5 and Fig. 6 show the effects of NO on ignition delay for different fuels. The overall trends of this modelling studied are similar to those observed in experiments. The promoting effect of NO is enhanced as the toluene content increases. All fuels again have a

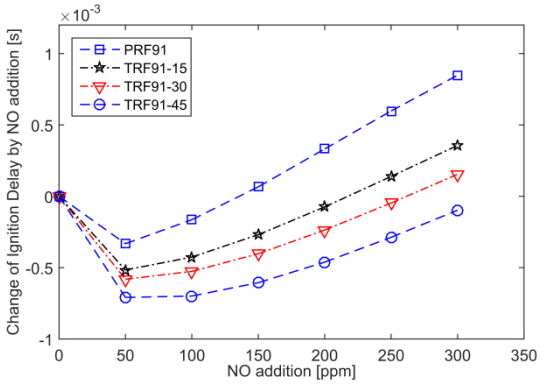


**Fig. 5. Simulated impact of NO on ignition delay for different TRFs, negative values denote more advanced ignition timing.**

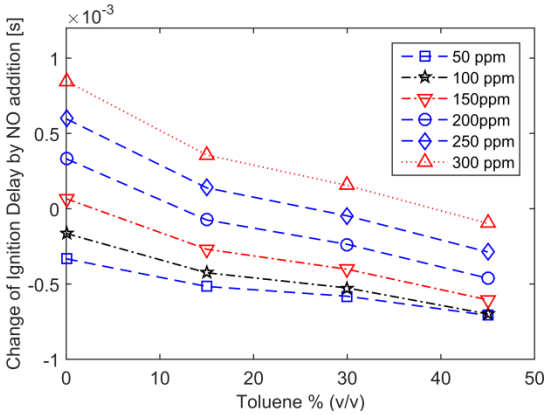


**Fig. 6. Simulated change of ignition delay by NO addition, negative values denote more advanced ignition timing.**

peak advance beyond which further NO retards autoignition.

The chemistry causing these interactions is generally via NO reactions that produce or scavenge reactive radicals [9, 11, 16, 17], among which the reactions R.1 and R.3 are particularly important:

$$NO + HO_2 = NO_2 + OH \qquad R.1$$
$$NO + OH + M = HONO + M \qquad R.3$$

Reaction R.1 is the key reaction leading to the promoting effect of NO on hydrocarbon oxidation, which can convert an unreactive $HO_2$ to a reactive OH. Reaction R.3 is responsible for the inhibiting effect of NO, by transforming a reactive OH into a relatively stable intermediate HONO. Low levels of NO addition can enhance the oxidation process through R.1, while excess NO addition may induce inhibition by scavenging OH in the radical pool through R.3.

In addition, NO can affect oxidation through other channels (i.e. R.5 and R.6) with toluene as the fuel [15].

$$C_6H_5\text{-}CH_2 + NO_2 = C_6H_5CH_2O + NO \qquad R.5$$
$$C_6H_5\text{-}CH_2 + NO_2 = C_6H_5CH_2NO_2 \qquad R.6$$

Toluene is unreactive and its consumption mainly forms resonance-stabilized benzyl radicals ($C_6H_5$-$CH_2$). In the presence of $NO_2$, benzyl radicals can react with $NO_2$ to generate alkoxybenzyl radicals ($C_6H_5$-$CH_2O$) and NO through reaction R.5, which has an important promoting effect for two reasons. First, it directly accelerates the production of alkoxybenzyl, which is a key step in toluene oxidation. Second, it converts $NO_2$ sourced from R.1 back into NO, thus regenerating NO to reinitiate the reaction sequence of R.1 to R.5 in a catalytic manner. This is consistent with both previous work [16] and the CFR engine results in this study that more toluene in the fuel enhanced the promoting effect of NO. However, benzyl radicals can also combine with $NO_2$ to form a $C_6H_5CH_2NO_2$ through R.6, which competes with reaction R.5 and has an inhibiting effect [15]. Thus, NO can influence toluene autoignition in a promoting or inhibiting way, but the overall promoting effect appears dominant for the fuels studied here.

## 4. Conclusions

CFR engine experiments were conducted to study the impact of NO on the timing of autoignition onset. Four fuels with toluene contents ranging from 0 to 45 vol.% and a RON of 91 were tested. Results showed that NO had a non-monotonic impact on the autoignition onset of these fuels, where it first advanced autoignition onset at low levels, but retarded it at high levels. Moreover, the promoting effect of NO became more important as the toluene fraction increased in the fuel.

Chemical kinetic modelling was then conducted to help understand the principles of the impact of NO on different fuels. Simulation results agreed qualitatively with experimental results and also showed that higher toluene content enhanced the promotion effect of NO on autoignition. Future kinetic modelling incorporating sensitivity analysis and reaction flux analysis is planned.

## 4. Acknowledgments

This research was supported by the Advanced Centre for Automotive Research and Testing (ACART, www.acart.com.au), and the Australian Research Council.

## 5. References

[1] Z. Chen; T. M. Foong; H. Yuan; Y. Yang; M. Brear, *19th Australasian Fluid Mechanics Conference*, Australasian Fluids Mechanics Society, Melbourne, Australia, 2014.
[2] P. J. Roberts; C. G. W. Sheppard, *SAE Int J Engines* 6 (2013) 2028-2043.
[3] O. Stenlaas; P. Einewall; R. Egnell; B. Johansson, *SAE transactions* 112 (2003) 906-913.
[4] Y. Kawabata; T. Sakonji; T. Amano, SAE International, 1999.
[5] J.-B. Masurier; F. Foucher; G. Dayma; P. Dagaut, *Proceedings of the Combustion Institute* 35 (3) (2015) 3125-3132.
[6] F. Contino; F. Foucher; P. Dagaut; T. Lucchini; G. D'Errico; C. Mounaïm-Rousselle, *Combustion and Flame* 160 (2013) 1476-1483.
[7] A. Dubreuil; F. Foucher; C. Mounaı¨m-Rousselle; G. Dayma; P. Dagaut, *Proceedings of the Combustion Institute* 31 (2) (2007) 2879-2886.
[8] G. Moréac; P. Dagaut; J. F. Roesler; M. Cathonnet, *Combustion and Flame* 145 (3) (2006) 512-520.
[9] P. Dagaut; G. Dayma, *The Journal of Physical Chemistry A* 110 (2006) 6608-6616.
[10] P. Dagaut; F. Lecomte, *Fuel* 82 (2003) 1033-1040.
[11] P. Glarborg; M. U. Alzueta; K. Dam-Johansen; J. A. Miller, *Combustion and Flame* 115 (1998) 1-27.
[12] J. H. Bromly; F. J. Barnes; S. Muris; X. You; B. S. Haynes, *Combustion Science and Technology* 115 (4-6) (1996) 259-296.
[13] ASTM D2699-13b,Standard Test Method for Research Octane Number of Spark-Ignition Engine Fuel,, A. International, West Conshohocken, PA, 2013,
[14] *Reaction Design CHEMKIN-RPO release 15112 (30-Jan-2012)* )
[15] J. M. Anderlohr; R. Bounaceur; A. Pires Da Cruz; F. Battin-Leclerc, *Combustion and Flame* 156 (2009) 505-521.
[16] G. Moréac; P. Dagaut; J. F. Roesler; M. Cathonnet, *Combustion and Flame* 145 (2006) 512-520.
[17] A. Dubreuil; F. Foucher; C. Mounaı¨m-Rousselle; G. Dayma; P. Dagaut, *Proceedings of the Combustion Institute* 31 (2007) 2879-2886.

# Removal of secondary aerosols produced during plasma diesel particulate treatment

Meisam Babaie[1, 2], Pouyan Talebizadeh[2, 3], Kok How Sia[2], Ang jia yi[2], Zoran Ristovski[2], Hassan Rahimzadeh[3], Richard Brown[2, *]

[1] Petroleum and Gas Engineering Division, School of Computing, Science and Engineering (CSE), University of Salford, Manchester, United Kingdom

[2] Biofuel Engine Research Facility, Queensland University of Technology, Queensland, Australia

[3] Department of Mechanical Engineering, Amirkabir University of Technology, Tehran, Iran

## Abstract

Non-thermal plasma (NTP) technologies have been examined to treat emissions and reduce $NO_x$ and particulate matter (PM) in recent years. In this study, diesel exhaust is exposed to NTP in a Dielectric Barrier Discharge (DBD) reactor, with a range of voltage amplitudes and frequencies to reduce PM mass and number. In some range of voltages and frequencies, numerous nano-particles in nucleation mode (diameter less than 40 nm) might be formed. The aim of this paper is to remove the generated nano-particles and to investigate the optimum voltage to employ the plasma. For this purpose, a Thermodenuder is used at the reactor outlet to remove the produced volatile particles from the exhaust gas. The results show a size reduction efficiency of 99 % and a mass reduction efficiency of 84 % at a frequency of 10 kHz and a voltage of 21 kV, with Thermodenuder is placed at the reactor outlet. The results of this paper show that this adaptation to the use of plasma for emission reduction is effective for future studies and experiments at very high voltages.

*Keywords: Non-thermal plasma, Diesel engines, Dielectric barrier discharge, Particle reduction, Thermodenuder*

## 1. Introduction

Diesel emissions reduction and control have been given increased attention due to increasingly stringent emissions standards and the associated adverse health effects. The emission produced by diesel engines is a complex mixture of gases, vapours and particles. However, diesel particulate matter (DPM) and nitrogen oxides (NOx) are acknowledged as some of the major harmful pollutants contributed by diesel engines. Many toxicological and epidemiological studies established the adverse health effects of diesel emissions [1-3].

DPM is recognised as the elemental carbon (EC) and heavy hydrocarbons derived from fuel and lubrication oil, and hydrated sulphuric acid derived from sulphur. DPM can vary with fuel composition, the type of diesel engine, environmental and operating conditions, as well as after-treatment devices (e.g. filters and catalysts) [4]. Up to date, various technologies have been used to eliminate DPM from exhaust gas, such as diesel oxidation catalysts (DOC) [5] and diesel particulate filters (DPF) [6, 7].

Non-thermal plasma technology has been introduced as a promising method for NOx reduction from diesel engine exhaust gas [2]; however, the effect of NTP on PM removal has not been well established until now. Plasma is known as the fourth state of matter where electrons, ions and molecules coexist together. Non-thermal plasma can be generated if the molecules are exposed to a strong electrical field where the temperature of its electron is higher than the background gases [2]. Non- thermal plasma (NTP) can be used to control diesel emissions [8]. Having a high energy content, it can be used in many applications including, but not limited to, producing ionised gas through electric current, and supplying sufficient energy to free electrons, allowing ions and electrons to coexist. The effective reduction of PM emissions using NTP technology has been discussed in literature [8-11].

The aim of this paper is to remove the nuclei mode particles formed by plasma at very high voltages by heating up the exhaust gas by a Thermodenuder after the plasma treatment. NTP treatment is used to reduce PM mass and number concentration in diesel engine exhaust gas. The purpose of the Thermodenuder use is to remove the generated nano-particles produced by NTP at high voltages. The addition of a Thermodenuder to the experiments is an innovative attempt aiming to provide results that may be used in future studies.

## 2. Composition of DPM

DPM are likely to be formed during the agglomeration process, where carbon particles react with other organic or inorganic (or both) components of diesel exhaust. Therefore, the composition of DPM can be divided into three basic components [12].

### *2.1. Dry carbon particles (soot)*

It is dispersed finely as a sooty substance which is the cause of black smoke from the exhaust. Soot formation occurs in the high temperature, fuel-rich reaction zone around individual fuel droplets, where hydrocarbons are oxidised under sub-stoichiometric oxygen conditions. Formation of soot takes place in a number of elemental steps: pyrolysis, nucleation, surface growth and coagulation, aggregation and oxidation.

* Corresponding author:
Phone: (+61) 7 3138 5157
Email: Richard.brown@qut.edu.au

*2.2. Soluble organic fractions (SOF)*

Most of the SOF compounds exist as vapours because the exhaust temperature is high. The proportion of SOF present in PM can be categorised into 'dry' and 'wet' particulates. In 'dry' particulates, the SOF content is low (less than 10%), whereas 'wet' particulates have high SOF contents. In wet particulates, the organic fraction may constitute over 50% of the total PM, with a multi-layer hydrocarbon adsorption on the surface of the particles [12].

*2.3. Sulphate particulates ($SO_4$)*

$SO_4$ are formed in the process of heteromolecular nucleation when sulphuric acid chemically reacts with water. Particles can be produced from small molecules and formed into stable nuclei particles. It is believed that sulphate particulates are separate from carbon particles and are present in the exhaust gas as nuclei mode particles [12].

The size distribution of diesel exhaust particulates can be typically presented using either particle mass or particle number distributions. Fig. 1 illustrates particle size and mass distribution represented in logarithmic scale.

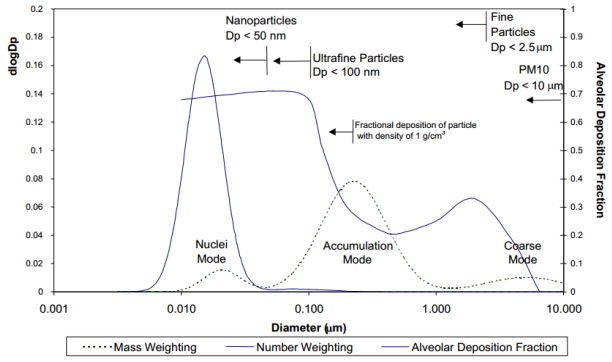


Fig.1. Typical engine exhaust size distribution [13]

From the Fig, it is observed that most of the particle mass distribution is in the accumulation mode where particle diameters are mostly in the fine particle range (>100nm). On the other hand, smaller particles are mostly in nuclei mode, where DPM comprises many nano-particles with less mass [13]. Similar size distribution findings have been published by other researchers and therefore this graph can be used as a reference to represent size distribution in general [12].

Small particles in the nucleation mode are usually numerous. As the accumulation of particles occurs, particles will have larger diameters and masses, but will be fewer in number and are hence in the accumulation mode of the size distribution. Nuclei mode particles are nano-particles (approximately 7 and 40nm) that are primarily volatile and unstable, possibly with a small amount of solid materials [2]. Agglomeration of these particles and other solid (carbon, metallic ash, etc.) materials, form the accumulation mode shown in Fig. 1 and in this mode, particles have larger diameters of up to 1 µm. These agglomerated particles compose most of the PM mass emission. [25]. The accumulation mode of particles is formed by the agglomeration of primary carbon particles and other solid materials. In the process of adsorption of gases and condensation of vapours, the primary carbon mix with its large number of hydrocarbons (other than sulphur compounds and metallic ash and wear metals) may be included in the process. PM mass distribution with small amounts of particle numbers determines the composition in the agglomeration process of particles [12].

## 3. Experimental setup

The experiments were conducted using a modern turbo-charged cylinder Cummins diesel engine with a maximum power of 162 kW at 2500 RPM at the Queensland University of Technology (QUT). An ultra-low sulfur diesel was used to run the engine, supplied by Intertek. The fuel specification is provided in Table 1.

Table 1 Fuel specification

| | Method | Results |
|---|---|---|
| Density @ 15°C (g/cm$^3$) | ASTM D 4052 | 0.8369 |
| Flash point °C | ASTM D 93 | 64 |
| Conductivity (pS/m) | ASTM D 2624 @ 25 °C | 548 |

A conventional DBD reactor consisting of two concentric quartz tubes was designed in the experiments. Fig. 2 shows the DBD reactor which connected to a pulsed power supply using the internal and external electrodes. As shown in Fig. 2, it consists of two concentric quartz tubes. Both tubes are 400 mm long and have a wall thickness of 1.5 mm [14]. The outside diameters of the inner and outer quartz tubes are 20 and 25 mm, respectively. Exhaust gas passes through the gap between these two quartz tubes. The internal electrode is a copper cylinder and the external electrode is made of copper mesh that wraps the exterior part of the DBD. The electrodes are placed in the middle of the DBD load with a length of 100 mm. Both tubes are fixed by two Teflon caps at each end. Exhaust enters the reactor at an angle of 45°, flows throughout the gap, and leaves the reactor with the same angle. The pulse power supply is based on the push–pull inverter topology which is described in [10].

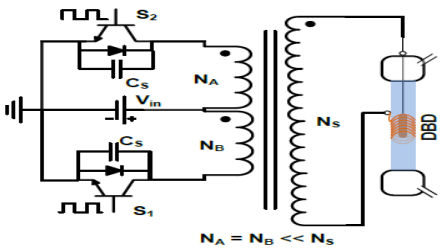


Fig. 2. Dielectric Barrier Discharge Reactor [8]

A Dust Trak II device was used in the experiment to measure the mass of the particles. A low flow Thermodenuder was also used to increase the

temperature of the exhaust gas at the reactor outlet. In all the experiments, exhaust gases obtained from the exhaust pipe were passed through the dilution tunnel before flowing through the DBD reactor. The purpose of the dilution tunnel was to lower the concentration of exhaust gas before flowing into the reactor. By applying high voltages using an AC power supply, plasma was generated in the reactor. The plasma then reduced the mass concentration of PM in the exhaust gas. During the combustion process, some particles were electrostatically charged, which may affect the accuracy of the measurements. A neutraliser was used to neutralise the charges and to increase the efficiency of the system. Fig. 3 shows a schematic of the experimental set-up A) without a Thermodenuder (TD) and B) with Thermodenuder (TD) at the outlet of the DBD reactor.

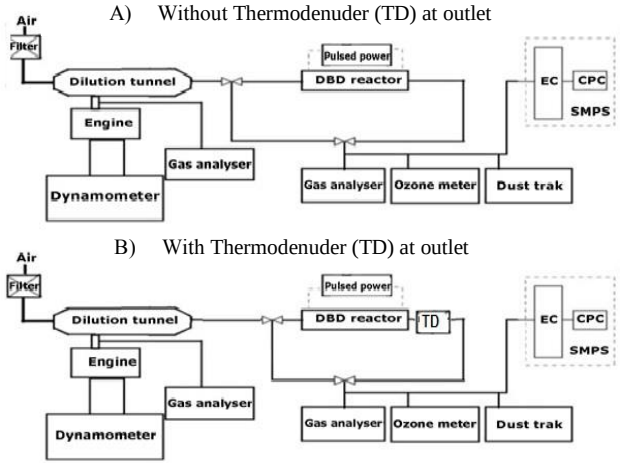


Fig. 3. Schematic diagram of plasma experiment withand Thermodenuder at outlet

Note that all the experiments were conducted at the voltage of 19 and 21 $kV_{pp}$ and the frequency of 10 kHz.

## 4. Results and Discussions

As shown in the previous paper by the authors, when using plasma at high power operating conditions, nano-particles which are mostly SOF and unstable solid materials are formed [10]. To provide a better understanding of this phenomenon, Fig. 4 displays the distribution of diesel particles at the reactor outlet for different applied voltages at the frequency of 10 kHz.

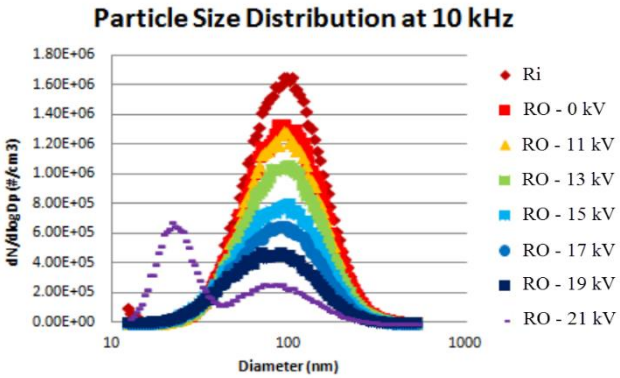


Fig. 4. Particle size distribution at the reactor outlet at various applied voltages as well as reactor inlet and outlet

As shown, at the applied voltage of 21 $kV_{pp}$, particles in nuclei mode are generated by the plasma. However, in the accumulation mode (which contains most of the particle mass), this voltage has a better performance than all other studied voltages. This paper concerns about the elimination of secondary nano-particles in nucleation mode. Note that in Fig. 4, Ri means the reactor inlet and RO means the reactor outlet.

In the following, the applied voltages of 19 and 21 kV are considered, which have particles at the accumulation and nuclei mode in the particle size distribution diagrams, respectively. The total concentration of particles before and after the reactor for 19 and 21 $kV_{pp}$ are listed in Table 2. As shown, the total PM concentration is higher at the applied voltage of 21 $kV_{pp}$ than 19 $kV_{pp}$ due to the formation of particles in the nuclei mode.

Table 2 Total PM number concentration (particle/$cm^3$) ($x10^6$)

| | Before the reactor | After the reactor | |
|---|---|---|---|
| | | 19 $kV_{pp}$ | 21 $kV_{pp}$ |
| PM concentration | 0.881 | 0.28 | 0.32 |

Fig. 5 displays the removal efficiency of the total PM concentration with and without using the Thermodenuder at the reactor outlet after treating the exhaust gas by NTP reactor.

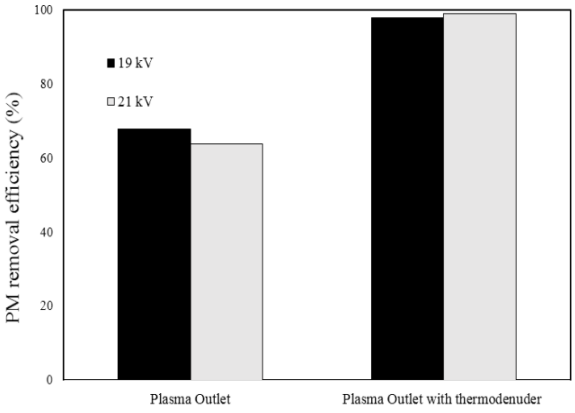


Fig. 5. PM concentration removal efficiency with and without using the Thermodenuder for the applied voltages of 19 and 21 $kV_{pp}$

As displayed in the Fig 5, by using the Thermodenuder for heating the exhaust gas after the plasma treatment, a higher number of particles are removed. This fact is due to the vaporization of nano-particles in the nuclei mode. As shown, PM concentration removal efficiency is equal for both 19 and 21 kVPP when using the Thermodenuder at the reactor outlet. However, it is higher for 19 kVPP without using the Thermodenuder. This indicates that the extra generated particles at the applied voltage of 21 kVPP are removed from the exhaust gas by using the Thermodenuder.

In Table 3, PM mass concentration at the inlet and outlet of the plasma reactor with and without using the Thermodenuder are schematised. Similar to the particle number, by using the Thermodenuder, more particles are removed from the exhaust gas. It should be noted that, unlike the plasma reactor, the Thermodenuder does not convert the particles to $CO_2$ and $H_2O$; rather it vaporizes the formed nucleation particles. However, the vaporised material is unlikely to renucleate in a practical diesel treatment system due to the rapid dilution that occurs to diesel emissions once they exit the tailpipe [15].

Table 3 The concentration of PM at different conditions

| Voltage $kV_{PP}$ | Initial PM concentration ($mg/m^3$) | PM mass removal efficiency after the plasma treatment ($mg/m^3$) | |
|---|---|---|---|
| | | Without Thermodenuder | With Thermodenuder |
| 19 | 0.5 | 72.8% | 83.9% |
| 21 | 0.5 | 59.8% | 84.0% |

Another important issue is that at 19 kV applied voltage, the particles are not going to the nuclei mode and therefore, higher PM mass removal can be achieved. However, at 21 kV applied voltage, since nano-particles are produced in the particle nuclei mode, lower removal efficiency by the plasma treatment is achieved. When using the Thermodenuder, by heating the plasma exhaust gas, the produced nano-particles are eliminated from the exhaust gas and then almost the same level of removal can be achieved.

## 5. Conclusion

The aim of this paper is to examine the effect of NTP on nuclei mode particles. This was done by applying a high voltage to the DBD reactor in a series of experiments. From the experiments, it was found that as the applied voltages increased from 19 $kV_{PP}$ to 21 $kV_{PP}$, there was an increase in the number of particles in the nuclei mode which are mostly SOF and other unstable materials. This is believed to be due to gas to particle change theory, leading to the formation of volatile particles in the nuclei mode. In order to eliminate the produced nano-particles from the exhaust gas, diesel particulates from the plasma reactor passed through the Thermodenuder aiming for heating. The results showed that the Thermodenuder had removed most of the volatile particles produced by the plasma. Furthermore, the results showed PM mass and concentration reduction at 21 $kV_{PP}$ and 10 kHz were equal to 84% and 99%, respectively by using the Thermodenuder at the reactor outlet. With the results obtained from this paper, it is concluded that with the aid of a Thermodenuder at the reactor outlet to remove volatile particles, PM reduction using an NTP reactor can be greatly improved.

## References


[1] J.L. Mauderly, E. Garshick, Diesel Exhaust, Environmental Toxicants, John Wiley & Sons, Inc.2008, pp. 551-631.

[2] P. Talebizadeh, M. Babaie, R. Brown, H. Rahimzadeh, Z. Ristovski, M. Arai, The role of Non-Thermal Plasma Technique in NOx treatment: A Review, Renewable and Sustainable Energy Reviews, 40 (2014) 886-901.

[3] S. Javadi Anaghizi, P. Talebizadeh, H. Rahimzadeh, H. Ghomi, The Configuration Effects of Electrode on the Performance of Dielectric Barrier Discharge Reactor for $NO_x$ Removal, Plasma Science, IEEE Transactions on, 43 (2015) 1944 - 1953.

[4] J.J. Schauer, Evaluation of elemental carbon as a marker for diesel particulate matter. Environmental Chemistry and Technology Program, Journal of Exposure Analysis and Environmental Epidemiology, 13 (2003) 443-453.

[5] B.J. Cooper, S.A. Roth, Flow-Through Catalysts for Diesel Engine Emissions Platinum Metals 35 (1991) 178-187.

[6] T. Kuki, Y. Miyairi, Y. Kasai, M. Miyazaki, S. Miwa, Study on Reliability of Wall-Flow-Type Diesel Particulate Filter, SAE2004-01-0959, (2004).

[7] K. Ohno, N. Taoka, T. Furuta, A. Kudo, T. Komori, Characterization of High Porosity SiC-DPF, SAE, 2002-01-0325., (2002 ).

[8] M. Babaie, P. Davari, P. Talebizadeh, Z. Ristovski, H. Rahimzadeh, R. Brown, Study of particulate matter removal mechanism by using non-thermal plasma technology, ICESP XIIIBangalore, India, 2013.

[9] K. Nakatani, S. Hirota, S. Takeshima, K. Itoh, T. Tanaka, K. Dohmae, SImultaneous PM and NOx Reduction System for Diesel Engines, SAE Technical Paper Series, (2002).

[10] M. Babaie, P. Davari, F. Zare, M.M. Rahman, H. Rahimzadeh, Z. Ristovski, R. Brown, Effect of pulsed power on particle matter in diesel engine exhaust using a DBD plasma reactor, Plasma Science, IEEE Transactions on, 41 (2013) 2349-2358.

[11] M. Babaie, P. Davari, P. Talebizadeh, F. Zare, H. Rahimzadeh, Z. Ristovski, R. Brown, Performance evaluation of non-thermal plasma on particulate matter, ozone and CO2 correlation for diesel exhaust emission reduction, Chemical Engineering Journal, 276 (2015) 240-248.

[12] W.A. Majewski, Diesel Particulate Matter, www.dieselnet.com/tech/dpm.php (2002).

[13] T. Kuroki, M. Ishidate, M. Okubo, T. Yamamoto, Charge-to-mass ratio and dendrite structure of diesel particulate matter charged by corona discharge, Carbon, 48 (2010) 184-190.

[14] T. Bodisco, R.J. Brown, Inter-cycle variability of in-cylinder pressure parameters in an ethanol fumigated common rail diesel engine, Energy, 52 (2013) 55-65.

[15] H. Bernemyr, Volatility and number measurement of diesel engine exhaust particles, 2007, Doctoral Thesis, KTH, School of Industrial Engineering and Management.

# Classification of Non-Premixed MILD and Autoignitive Flames

M. J. Evans[1, 2 *], P. R. Medwell[1], H. Wu[2], A. Stagni[2,3], M. Ihme[2]

[1]School of Mechanical Engineering, The University of Adelaide SA 5005, Australia

[2]Department of Mechanical Engineering, Stanford University CA 94305, USA

[3]Dipartimento di Chimica, Materiali ed Ingegneria Chimica "G. Natta", Politecnico di Milano 20133 Milan, Italy

## Abstract

Moderate or intense low oxygen dilution (MILD) combustion has been the subject of numerous studies in recent years. The boundaries of the MILD regime have, however, only been defined with respect to premixed configurations. These previous definitions have been based on the initial and final states of a perfectly-stirred reactor relative to the fuel self-ignition temperature or by defining a premixed MILD flamelet as a combustion without any distinct extinction or ignition events. This flamelet definition is applied to a non-premixed configuration to better understand the MILD combustion regime and classify previous experimental investigations. Through a simplified analysis, a simple quadratic inequality for the definition of MILD combustion is derived as a function of initial and final temperatures, and a one-step activation energy facilitating simple classification of non-premixed flames. This definition of MILD combustion qualitatively agrees with the premixed flamelet definition and provides insight into previous attempts to reconcile premixed and non-premixed classifications of MILD combustion. Subsequent comparison with experimental cases verifies the predictive capability to describe the ignition behaviour of jet flames in hot coflows in the MILD and autoignitive regimes.

*Keywords: MILD Combustion, Non-Premixed, Auto-Ignition, Flamelets*

## 1. Introduction

Moderate or intense low oxygen dilution (MILD) combustion is a regime with reduced pollutant emissions and efficiency improvements over conventional combustion [1]. Operation in the MILD, or flameless, regime is achieved by burning fuel in hot, low oxygen environments. This reduces chemical reaction rates, resulting in distributed reaction zones as opposed to the high temperature peaks in conventional flames [1]. As a result, jet flames in the MILD regime feature global Damköhler numbers (*Da*) near unity, such that finite-rate chemistry must be accounted for [2]. Despite numerous investigations into the unique characteristics of MILD combustion, the boundaries of the MILD regime have not been conclusively defined.

Ignition and combustion stability of the MILD combustion regime has been investigated experimentally [3] and numerically [3-5] in premixed reactors, resulting in premixed regime diagrams [1]. The regime diagrams produced through these analyses have been based on the initial temperature ($T_{in}$) and final temperature increase of the reacting mixture ($\Delta T$), demarcated by a self-ignition temperature ($T_{si}$) evaluated in a perfectly-stirred reactor (PSR) [1]. This $T_{si}$, defined as the autoignition temperature of the characteristic S-shaped curve at a constant level of reactant dilution, is set as 1000K for a mixture of $CH_4$ and $O_2$ diluted in $N_2$, and is mapped in Fig. 1 [1]. This figure has formed the basis of subsequent premixed [3-5] and non-premixed [6-7] analyses of MILD combustion, resulting in further reclassification in the case of ignition below the pre-defined $T_{si}$ [5-7]. This pre-defined $T_{si}$ description assumes that a definite ignition point exists for the mixture at each dilution point or that the autoignition temperature is constant for any dilution, which may not necessarily hold.

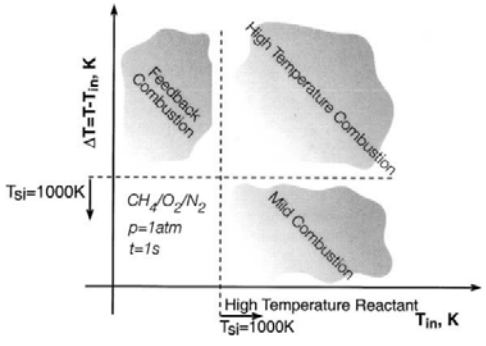


**Figure 1: Previously defined premixed MILD regime map [1].**

A description of the MILD combustion regime in a premixed reactor has been defined independently to the $T_{si}$ [1]. This definition arises from the absence of ignition or extinction points in MILD combustion [4], which is qualitatively consistent with the distributed nature of MILD combustion [1]. In this condition, the S-shaped curve, which describes the temperature as a function of residence time, is monotonic [4]. This definition provides explanation that the burning flame cannot be extinguished due to small fluctuations in scalar dissipation rate. This definition leads to a criterion for premixed MILD combustion, which, assuming constant specific heat at constant pressure, $c_p$, may be approximated as [1]:

$$\frac{E_{eff}/R}{T_{in}} \leq 4\left(1+\frac{T_{in}}{\Delta T}\right), \qquad (1)$$

where $R$ is the universal mass constant and $E_{eff}$ is the activation energy of an equivalent one-step reaction. This definition separates conventional autoignitive flames, which feature local ignition location points, from gradually igniting MILD flames. This definition of MILD combustion removes the explicit dependency on a pre-calculated $T_{si}$, with the regime boundary a

* Corresponding author:
Phone: (+61) 8 8313 3177
Email: m.evans@adelaide.edu.au

function of only $T_{in}$, $\Delta T$ and $E_{eff}$. The two alternate, premixed classifications of MILD combustion both propose distinct definitions of the MILD regime, based on a critical temperature, $T_{si}$, [1] or the global ignition process, $E_{eff}$, [4] respectively.

Studies of non-premixed MILD combustion have been limited to experimental observations [8,9], and numerical analyses [6,7] based on the PSR classification of Cavaliere and de Joannon [1]. Experimental observations of ethylene ($C_2H_4$) flames indicate a gradual ignition regime in hot, low oxygen coflows, corresponding to MILD combustion [8,9]. Increases in oxygen concentration leads to a transition to a conventional autoignitive flame structure [8,9]. This is consistent with the flame structure definition of Oberlack *et al.* [4], however the small temperature rises in these flames would lead to each of these being classified as MILD according to Cavaliere and de Joannon [1], despite their significantly different ignition characteristics [8,9].

Numerical investigations of the MILD regime in non-premixed combustion have included both laminar opposed-flow [6] and turbulent co-flow [7] fuel and oxidant configurations. The study of turbulent, non-premixed flames in hot and diluted coflows separates combustion $\Delta T < T_{si}$ into MILD, "Quasi-MILD" and "MILD-like" regimes [7]. The MILD definition is used in the same sense as [1] with an oxidant dependent, rather than fixed, value of $T_{si}$ [7]. The second regime, "Quasi-MILD", is classified as requiring forced ignition, through a simulated spark, with $\Delta T < T_{si}$ [7]. In this definition, $T_{si}$ takes the temperature of the oxidant at which a Reynolds-averaged Navier-Stokes (RANS) combustion model ignites and the limit of forced ignition is similarly defined through RANS simulation [7]. This definition of $T_{si}$ is dependent on the velocity field of the RANS simulation through strong coupling to turbulence and sensitivity to the Damköhler number, a subsequent chemical kinetics analysis by the same research group conversely describes "Quasi-MILD" in a PSR as being initiated by slow, exothermic reactions without autoignition [7]. The term "MILD-like" is used to describe the same condition as MILD at oxygen concentrations above the limit of forced ignition based on the "low oxygen" phrase in name of MILD combustion [7]. Neither [7] nor the following chemical kinetics analysis [5], however, offer any further, fundamental distinctions between the two suggested regimes.

The definitions of MILD combustion based on temperatures relative to some $T_{si}$ are not consistent between premixed and non-premixed configurations. The definition of MILD combustion provided by Oberlack *et al.* [4] may, however, be applied to non-premixed configurations through analysis of an idealised, one-dimensional flamelet analysis, similar to that by Pitsch and Fedotov [10]. This analysis facilitates the coupling of the reaction and the scalar dissipation rates ($\chi$) during combustion. Unlike the premixed analysis, however, the non-premixed approach separates the chemical and fluid terms in the expression for the reaction rate ($\omega$) at any given time (t) and mixture fraction ($Z$). This definition of non-premixed MILD combustion is qualitatively consistent with experimental observations of gradual ignition, rather than conventional autoignition, under MILD conditions. This definition is quantified through a non-premixed flamelet analysis, to produce a numerical criterion for non-premixed MILD combustion, which is compared to previous premixed regime classifications. This definition is then subsequently used to classify and explain previous experimental cases and observations.

## 2. Numerical Analysis

### *2.1 Non-Premixed Flamelet Analysis*

The one-dimensional, opposed-flow flamelet equations for a system consisting of a single fuel (F), oxidizer (O) and reaction product (P) with an irreversible, one-step reaction have previously been analysed by Pitsch and Fedotov [10]. Analysis of a stoichiometric (st) flamelet was shown to yield the equation for an S-shaped curve of $\theta_{st}$ versus $x$ as [10]:

$$\frac{d\theta_{st}}{d\tau} + x(\tau)\cdot\theta_{st} - \omega(\theta_{st}) = 0 \tag{2}$$

where:

$$x = \chi(\chi_{st,0})^{-1} \tag{3}$$

$$\theta = (T - T_{st,u})/\Delta T_{st} \tag{4}$$

$$\omega = Da\frac{(\nu+1)^2}{\nu}\frac{(1-\alpha)\exp(\beta_0-\beta)}{1-\alpha(1-\theta_{st})}\times (1-\theta_{st})^2\exp\left(-\alpha\beta\frac{1-\theta_{st}}{1-\alpha(1-\theta_{st})}\right) \tag{5}$$

$$\nu = (Z_{st})^{-1} - 1 \tag{6}$$

$$\alpha = \Delta T_{st}/T_{st,b} \tag{7}$$

$$\beta = E_{eff}/(RT_{st,b}) \tag{8}$$

and $Z_{st}$ is the stoichiometric mixture fraction, $\tau$ is a non-dimensional time and the subscript 0 denotes a chosen reference value, u denotes unburnt (fresh) mixture, and b denotes fully burnt mixture. Finally, in (5), $Da$ is a constant for any given fuel and oxidant combination with a one-step chemical reaction.

At steady-state, the derivative of non-dimensionalised strain-rate in (2) with respect to temperature can be shown to be:

$$\frac{\partial x}{\partial\theta_{st}} = -Da\frac{(\nu+1)^2}{\nu}\frac{(1-\alpha)\exp(\beta_0-\beta)}{\theta_{st}^2(1-\alpha(1-\theta_{st}))^3}\times (1-\theta_{st})\exp\left(-\alpha\beta\frac{1-\theta_{st}}{1-\alpha(1-\theta_{st})}\right)\times \left[\left(\alpha^2+(1+\beta)\alpha\right)(1-\theta_{st})^2 - \left(1+(3+\beta)\alpha\right)(1-\theta_{st})+2\right]. \tag{9}$$

From inspection of (9), only the final term can be zero in the interval $0 < \theta_{st} < 1$. Hence the condition for real solutions to the derivative of the S-shaped curve:

$$(\beta^2 + 6\beta + 1)\alpha^2 - (6\beta - 2)\alpha + 1 \geq 0. \quad (10)$$

This condition implies that (9) has local maxima and minima, which correspond to ignition (ign) and extinction (ex) given by:

$$\theta_{st} = 1 - \frac{(1+(3+\beta)\alpha) \pm \sqrt{\Delta}}{2\left(\alpha^2 + (1+\beta)\alpha\right)}, \quad \theta_{st,ex} \geq \theta_{st,ign} \quad (11)$$

where $\Delta$ is the left-hand side of (10). If $\theta_{st,ign}$ and $\theta_{st,ex}$ are real numbers, then the S-shaped curve has distinct autoignition and extinction points. If $\theta_{st,ign}$ and $\theta_{st,ex}$ are complex, that is $\Delta < 0$, then $x$ versus $\theta_{st}$ is monotonic indicating MILD combustion [4]. Finally, negative values of (11) indicate no physical solution.

### *2.2 S-Shaped Curve Generation*

The qualitative classifications of inequality (10) can be compared to a numerically solved S-shaped curve. S-shaped curves of $T_{st}$ versus $\chi$ were solved in FlameMaster 3.1 with the GRI-Mech 3.0 detailed chemical kinetics scheme [11], for $CH_4/H_2$ with three different oxidants [12].

## 3. Results and Discussion

The definitions of MILD combustion each map a quantitative region in the $T_{in}$ domain for different values of $\Delta T$. These regions are shown overlaid in Fig. 2. The blue region indicates the PSR definition of Cavaliere and de Joannon [1], bounded by $\Delta T < T_{si}$; the S-shaped curve definition of Oberlack *et al.* [4], where (1) holds, is indicated in green; and the current non-premixed study, where (10) is not met, is shown in red. The values of $T_{si}$ = 1000K and $E_{eff}$ = 40 kcal/mol are chosen for reference [1]. The three regime maps show the qualitative difference between the temperature-based, PSR definition and the S-shaped curve-based definitions. As a result of the different underlying approaches, the PSR definition contains both regions of gradual ignition and conventional autoignition. This is consistent with previous experimental investigations in which gradual ignition is observed for oxidants with 3% $O_2$, whilst autoignition is seen with 9% $O_2$ oxidants and higher $\Delta T$ [8], despite both conditions meeting the PSR definition of MILD combustion [1]. Whilst the PSR definition simply limits maximum the flame temperature to $T_{in}+T_{si}$, the premixed and non-premixed S-shaped curves indicate the shift from gradual ignition to autoignition. The maximum flame temperature of the S-shaped curve-based MILD regimes, however, increase with increasing $T_{in}$, indicating no correlation between $\Delta T \leq T_{si}$ and the flame ignition characteristics. Combustion is apparent below the pre-defined $T_{in}$ = 1000K PSR threshold [1] shown in Fig. 2. This region below 1000K exhibits what Wang *et al.* [5,7] would term "Quasi-MILD" combustion. Similarly, the regions of gradual ignition (red and green) with $\Delta T$ > 1000K meet the criteria of "MILD-like" proposed by the same group [5,7]. This demonstrates the link between the flame structure and the analyses of Wang *et al.* [5,7] in the classification of different flame regimes. Of the structural definitions of MILD combustion, the non-premixed MILD regime allows for greater $\Delta T$ compared to the premixed case for most $T_{in}$. At higher $T_{in}$, the non-premixed limit begins to approach a limiting value whilst the maximum $\Delta T/T_{in}$ for the premixed MILD regime continues to increase. Additionally, the non-premixed analysis features a region of low $\Delta T/T_{in}$ where a non-premixed solution does not exist. These effects demonstrate the differences between strain-induced mixing compared to analyses based on premixed residence times which exhibit significant differences, despite qualitatively similar trends. These different trends demonstrate that for a given fuel of some $E_{eff}$, there is a limiting value of $\Delta T/T_{in}$ for non-premixed MILD flames which does not exist in premixed configurations.

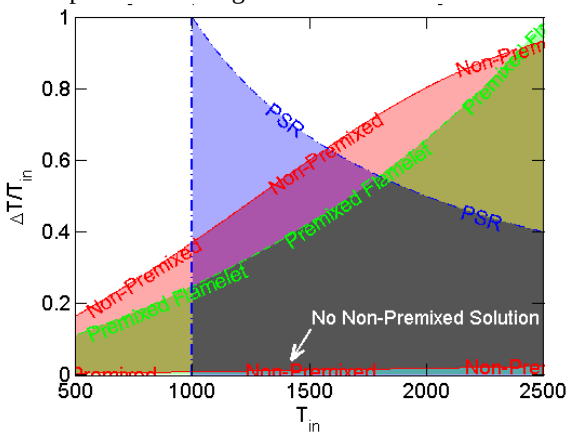


**Figure 2: Combined regime map for MILD combustion according to three different definitions: perfectly-stirred reactor (PSR) [1] (blue), premixed flamelet [4] (green), and non-premixed flamelet (red). With $\Delta T$ = 1000K, $E_{eff}$ = 40 kcal/mol [1] and $T_{in} = T_{st,u}$.**

Experimental studies of non-premixed combustion can be analysed as one-dimensional flamelets. Three fuel and oxidant combinations [12] are used to demonstrate the transition to the MILD regime. In each case, the fuel is 300K, 1:1 molar $CH_4/H_2$ and the oxidant is at 1300K with different levels of $O_2$ mass fraction ranging from 3-9% [12]. The stoichiometric temperature of the reacting mixtures are shown as a function of strain rate in Fig. 3. At 9% $O_2$ the autoignition and extinction points are identifiable as the locations where the S-shaped curve "folds" and physically represent conditions where a numerical solution jumps between the upper and lower branches of the curve. These points correspond to ignition and extinction conditions in a jet flame. At 3% $O_2$, the S-shaped curve is stretched such that there are no points of extinction or ignition and the flame is hence classified as MILD. The autoignitive flame at 6% $O_2$ borders the transition between the two regimes, however features autoignition and extinction points. These features are in accordance with the increasingly

defined ignition regions observed experimentally with increasing oxygen concentrations [12].

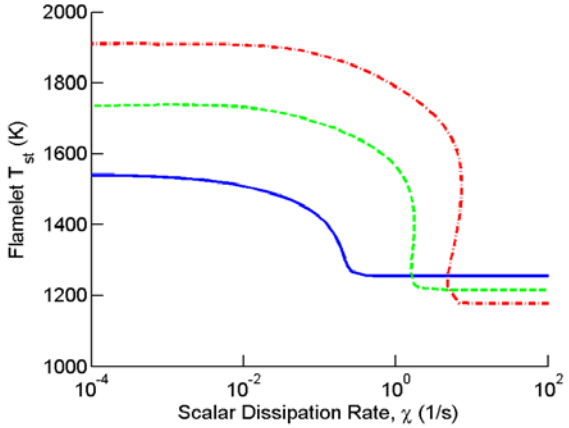


**Figure 3: S-shaped curves of $T_{st}$ vs $\chi$ for $CH_4/H_2$ flames in 1300K coflows at — 3, – – 6 and - · - 9% $O_2$ (by mass), designated HM1-3 [12].**

The MILD regime diagram in Fig. 2 may be expanded to an arbitrary fuel and oxidant combination by mapping to the $\alpha$ and $\beta$ axes, as defined by (7) and (8). The regime diagram in Fig. 4 shows contours of $\theta_{st,ign}$ in the three distinct regions defined by (11). This regime diagram is general for all fuels, for which a specific $E_{eff}$ may be estimated.

A selection of experimental cases are included in Fig. 4 to classify flames as either MILD or autoignitive flames. The HM1-3 and DJHC experimental cases use a $CH_4$-$H_2$ blend [12] and Dutch natural gas [13] respectively rather than pure $CH_4$ fuels, with $E_{eff}$, taken to be 47 kcal/mol [14]. Of the three data sets shown in Fig. 4, one case from each of [8] and [12] are well within the MILD regime, whilst another flame from each of these two experimental sets are in the autoignitive regime. The two MILD cases represent the two oxidants with $O_2$ ~ 3% and the three autoignitive flames correspond to oxidants $O_2$ ~ 9-10%. The remaining cases appear on the boundary of the MILD and autoignitive regimes. These are results consistent with the analysis of S-shaped curves of the HM1-3 flames from Fig. 3, and experimental observations of the ignition behaviour and structure of ethylene flames in hot coflows [8]. The classification of flames as MILD, autoignitive or bordering transition between the two regimes is, however, reasonably insensitive to variations in $E_{eff}$ in these cases due to the steep slope of the MILD-autoignitive boundary.

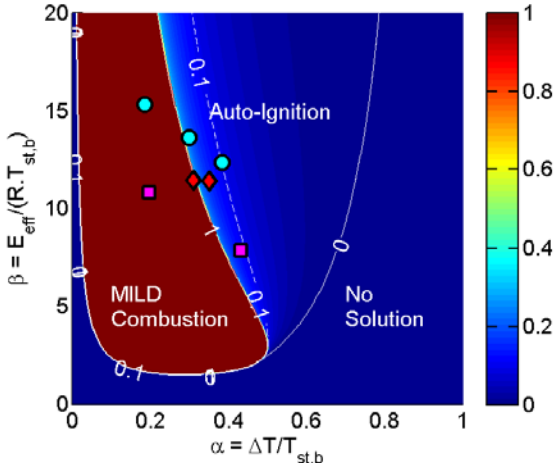


**Figure 4: Normalised autoignition temperature, $\theta_{st,ai}$, for a range of $\alpha$ and $\beta$. Experiments indicated: ● HM1-3 [12], ■ 3% and 9% $C_2H_4$ [8] and ♦ DJHC-I [13]. Lower O2 concentrations in each investigation give lower $\alpha$. $E_{eff|CH4}$ = 47 kcal/mol, $E_{eff|C2H4}$ = 29 kcal/mol [14].**

## 4. Conclusions

A non-premixed definition for MILD combustion has been determined and compared to previously defined criteria for premixed MILD combustion. This definition is consistent with the premixed definition of Oberlack *et al.* [4], however highlights differences at very high temperatures. Additional comparison with the definition of Cavaliere and de Joannon [1] indicates significant discrepancies in their boundaries of the MILD regime, defined for a PSR. Finally, the non-premixed definition of MILD combustion presented here is consistent with qualitative analyses of $CH_4/H_2$ flames and experimental observations of $C_2H_4$ flames in hot coflows.

## 5. Acknowledgements

The authors wish to acknowledge the support of The University of Adelaide, Stanford University and the Politecnico di Milano. The authors acknowledge funding support from the Australian Research Council (ARC) through the Discovery (DP and DECRA) grant scheme, the United States Asian Office for Aerospace Research and Development (AOARD) and the Australian Government funded Endeavour Scholarships and Fellowship grant programme.

## 6. References

[1] A. Cavaliere and M. de Joannon, Prog. Energ. Combust. 30 (4) (2004) 329-366.
[2] F. C. Christo and B. B. Dally, Combust. Flame 142 (2005) 117-129.
[3] P. Sabia, M. de Joannon, A. Picarelli, R. Ragucci, Combust. Flame 160 (2013) 47-55.
[4] M. Oberlack, R. Arlitt and N. Peters, Combust. Theor. Model. 4 (2000) 495-509.
[5] F. Wang, P. Li, Z. Mei, J. Zhang and J. Mi, Energy 72 (2014) 242-253.
[6] M. de Joannon, G. Sorrentino and A. Cavaliere, Combust. Flame 159 (2012) 1832-1839.
[7] F. Wang, J. Mi and P. Li, Energy Fuels 27 (2013) 3488-3498
[8] P. R. Medwell, P. A. Kalt and B. B. Dally, Combust. Flame 152 (2008) 100-113.
[9] B. C. Choi and S. H. Chung, Combust. Flame 157 (2010) 2348-2356.
[10] H. Pitsch and S. Fedotov, Combust. Theor. Model. 5 (2001) 41-57.
[11] G. P. Smith, D. M. Golden, M. Frenklach, N. W. Moriarty, B. Eiteneer, M. Goldenberg, C. T. Bowman, R. K. Hanson, S. Song, W. C. Gardiner, Jr., V. V. Lissianski, and Z. Qin http://www.me.berkeley.edu/gri_mech/
[12] B. B. Dally, A. N. Karpetis and R. S. Barlow, Proc. Combust. Inst. 29 (2002) 1147-1154.
[13] E. Oldenhof, M. J. Tummers, E. H. van Veen, D. J. E. M. Roekaerts, Combust. Flame 157 (2010) 1167-1178.
[14] J. Göttgens, F. Mauss and N. Peters, Proc. Combust. Inst. 24 (1992) 129-135.

# The impact of carrier gas on ethanol flame behaviour in a Jet in Hot Coflow (JHC) burner

J. Ye*, P.R. Medwell, M.J. Evans, B.B. Dally
School of Mechanical Engineering
The University of Adelaide, South Australia 5005, Australia

## Abstract

This paper presents the impact of carrier gas on the flame behaviour in a Jet in Hot Coflow (JHC) burner operated with prevaporised ethanol, emulating MILD combustion conditions. The appearance of flames carried by different carrier gases is similar, though the flame is more luminous when air is used. However, OH chemiluminescence ($OH^*$) imaging indicates that the type of carrier gas has a significant impact on the flame structure. The use of nitrogen as a carrier gas is found to produce similar effects to diluting the coflow. In particular, the $OH^*$ intensity in the axial direction peaks at the flame base when it is carried by air, indicating an existence of a high temperature zone with rapid reactions. However, no peak $OH^*$ intensity in the axial direction is observed in the flame carried by nitrogen, which suggests a more uniform temperature distribution.

*Keywords: MILD combustion, Prevaporised liquid fuels, Carrier gas, Hydroxyl radical chemiluminescence, JHC burner*

## 1. Introduction

Moderate or intense low-oxygen dilution (MILD) combustion is a very promising technology for low emissions and high thermal efficiency. MILD combustion occurs in an environment with low local oxygen concentration and high reactant temperature, which is often achieved through an enhanced mixing of hot exhaust gases with reactants. This environment suppresses the temperature increase across the reaction zone, which significantly reduces the emissions of $NO_x$ and soot [1-3]. These characteristics of MILD combustion are favoured in many industrial applications. For instance, the volumetric reaction resulting from the hot and diluted mixture leads to a larger radiating volume and a higher net radiation flux, which is highly desired in furnaces and boilers [4]. In a gas turbine application, due to a uniform temperature distribution with a lower peak temperature, a higher efficiency is achieved by raising the mean temperature of exhaust gases, while maintaining low $NO_x$ formation and the durability of gas-turbine components, even though a high radiant flux is not favourable. Due to the advantages of MILD combustion and the wide use of liquid fuels, it is of great value to extend this technology to liquid fuels.

Liquid fuel is prevalently fed into a combustion chamber in a form of spray, which is formed by an atomisation process. During atomisation, the liquid fuel is broken into droplets with diameter smaller than the orifice diameter, which accelerates the evaporation of liquid fuels. To improve the atomisation of liquid fuels, high-speed gas is often applied to exert additional shear force on liquid fuels. Atomisation is followed by spray penetration, mixing, evaporation and burning processes, which strongly couple with each other. To separate the impact of chemistry from the spray characteristics, liquid fuels are prevaporised in this study.

In the case of prevaporisation, heated gas is required as a carrier to help deliver prevaporised liquid fuels and stop them from condensing. A previous experimental study on MILD combustion of prevaporised liquid fuels showed that $NO_x$ emissions were increased when air was used as a carrier instead of $N_2$ in a reversed-flow combustor [5]. It is speculated that the premixing of fuel and carrier air led to the formation of higher temperature flame pockets with higher local oxygen concentration, leading to higher $NO_x$ emissions.

The type of carrier gas was reported by Stårner et al. [6], to impact the structure of an open flame in a piloted spray burner [6]. It was found that the behaviour of an acetone flame carried by air was more like a premixed flame, in which combustion took place at the jet centerline [6]. In contrast, the flame carried by $N_2$ behaved closer to a non-premixed flame [6]. This phenomenon was also observed in a diluted methanol spray flame issuing into 12% $O_2$ coflow in a vitiated coflow burner [7]. This vitiated coflow burner is similar to the Jet in Hot Coflow (JHC) burner [1, 3]. The JHC burner provides optical access for fundamental research on MILD combustion, and is suitable for a range of operating conditions. Medwell et al. [3] observed a pool of precursors upstream of an apparent lift-off height in a hot diluted coflow, which is referred to as "transitional" behaviour. This build-up of flame intermediates, followed by the initiation of combustion and the formation of a steady flame, helps stabilise "lifted" jet flames in vitiated coflows [8]. The formation rate of one of the key intermediates, $CH_2O$, was found to be greatly enhanced by the diffusion of $O_2$ to the fuel-rich side in a JHC burner [9]. Hence, it is speculated that using air as a carrier promotes the formation of $CH_2O$, thereby stabilising the flame.

* Corresponding author:
Phone: (+61) 8 8313 5460
Email: jingjing.ye01@adelaide.edu.au

In summary, the type of carrier gas has been reported to affect the mixing and flame structure [6-7] in spray burners, and affect the $NO_x$ formation in a MILD combustor [5]. Although using $N_2$ for atomisation may not be directly applicable to industrial applications, part of the hot exhaust gases are expected to be mixed with liquid fuels for heating and dilution when MILD combustion of liquid fuels is commercialised. The exhaust gas is composed of oxidiser and inert, which can be represented by air and $N_2$. It is important to understand the impact of those species in the exhaust gas. By changing the type of carrier gas in a JHC burner, this issue can be explored in a controlled and simplified environment. Therefore, this paper intends to further investigate the impact of carrier gas under MILD combustion conditions with the aid of OH chemiluminescence imaging in a JHC burner. The fuel used here is prevaporised ethanol, which is carried by either air or nitrogen.

## 2. Experiment Details

Figure 1 shows the experimental setup in the present study. The basic configuration and operation of this JHC burner are the same as a previous study [3]. The JHC burner consists of a central fuel jet (ID=4.6 mm) in a coflow of hot exhaust products from a secondary porous bed burner located upstream of the exit plane (ID=82 mm). The hot coflow is produced from the combustion of a lean mixture of natural gas, air, $H_2$ and $N_2$. The mole fractions of natural gas, air, $H_2$ and $N_2$ are manipulated to generate 3%, 6% and 9% excess oxygen by volume in the hot coflow, while the total volumetric flow rates and the temperature of the hot coflow are kept constant. The adiabatic flame temperature for the various coflow conditions is close to 1400 K.

As shown in Fig. 1, ethanol is heated and mixed with carrier gas in a Controlled Evaporator and Mixer (CEM). The temperature of the heater inside the CEM is set by the control unit, which also controls the mass flow rates of ethanol and carrier gas. The preheat temperature is set to 413 K, which is higher than the boiling point of ethanol to prevent condensation. The pipeline from the CEM to the burner is thermally insulated, and no condensation of the fuel is observed. The mass flow rates of ethanol and carrier gas are 0.38 g/s and 0.49 g/s, respectively, resulting in an equivalence ratio of 6.9 in the jet. Note that when switching between air and $N_2$ as carrier gas, the flow rates of ethanol and carrier gas are kept constant. At the same flow rates, the jet Reynolds number and the bulk jet velocity are kept around 10,000 and 50 m/s, respectively. Due to the lower viscosity and density of $N_2$, the jet Reynolds number of ethanol carried by $N_2$ is 1% higher than that of ethanol carried by air, while the bulk jet velocity is 2% higher. After prevaporisation, the mixture of ethanol and carrier gas is fed into the JHC burner via the central fuel jet.

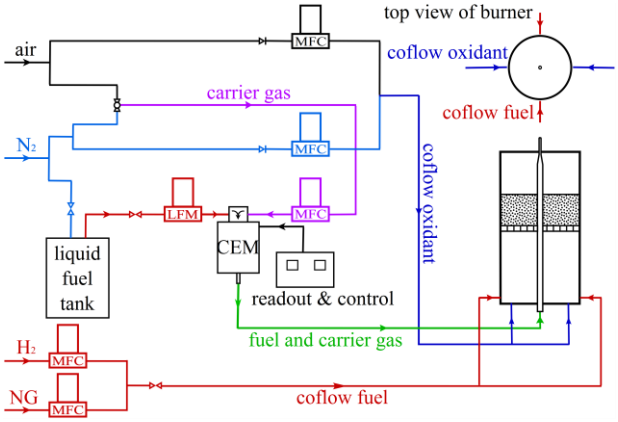


Fig. 1: Experimental Setup: CEM is the Controlled Evaporator and Mixer, MFC is the mass flow controller for gases, and LFM is the liquid flow meter.

Imaging of the flames is achieved both through conventional photography and OH chemiluminescence ($OH^*$), which is detected with an electronically gated pco.pixelfly camera equipped with a Lambert Instruments intensifier. The camera system is equippedwith a 50 mm f/3.5 UV transmissive lens and a 310 nm bandpass optical filter with a bandwidth of 10 nm. The photographs of the flames are taken with a Canon EOS 60D SLR camera with a standard 50 mm f/1.8 lens.

## 3. Results and Discussions

### 3.1 Flame Appearance

Figure 2 shows photographs of the ethanol flames carried by air or nitrogen under the three coflow conditions considered in this paper (3, 6 and 9% $O_2$ by volume). All the photographs are taken with an ISO sensitivity of 1600, exposure time of 4 seconds and an f-number of 16. The bottom edge of the photograph coincides with the jet exit plane. From the photographs, all the ethanol flames are clean of soot and visually appear lifted. The apparent lift-off height seems independent of the excess oxygen level in the coflow, which has not been reported in previous studies on this type of burner burning with methane- or ethylene- based fuels [10-11]. The lift-off heights of the flame in a given coflow are also similar when different carriers are used. Considering that the jet velocity is almost identical for the different carrier gases, this seems to suggest that the type of carrier gas does not affect the ignition delay. This observation is confirmed by ignition delay calculations performed in the Closed Homogeneous Batch Reactor model in the CHEMKIN software, which shows the type of carrier gas has little impact on the ignition delay. The flames become more luminous when carried by air instead of $N_2$. This observation is more pronounced in a coflow with a lower oxygen level. It is suspected that the stronger luminosity of flames carried by air results from a stronger reaction intensity and higher temperature, which will be examined from the $OH^*$ imaging in the proceeding section.

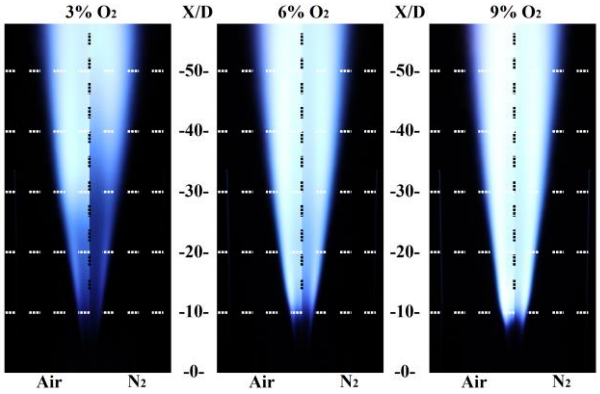


Fig. 2: Photographs of the ethanol flames carried by air or $N_2$ issuing into a coflow with 3%, 6% and 9% excess $O_2$. X is the axial distance above the jet exit plane; D is the jet diameter.

### 3.2 OH* chemiluminescence

The chemiluminescence of $OH^*$ is a natural emission of light within the flame when chemically excited OH relaxes from an upper electronic state to a lower electronic state. To better understand the use of $OH^*$, laminar flame calculations are performed for ethanol flames carried by air with the OPPDIF code of CHEMKIN. The strain rate is defined as $a = (U_O+U_F)/H$, where $U_O$, $U_F$ is the velocity of oxidiser and fuel at the nozzle exit planes, and $H$ is the separation distance between the two nozzles [12]. The strain rate used here is 125 $s^{-1}$. The chemical kinetic mechanism used includes the ethanol chemical kinetic mechanism by Marinov [13] and $OH^*$ kinetics provided in [12] and [14]. Figure 3 compares the formation of $OH^*$ with the temperature distribution in mixture fraction space for ethanol flames carried by air in the 9% $O_2$ coflow. The stoichiometric mixture fraction in this case is 0.12, as indicated by the vertical dashed line. The peak flame temperature occurs on the rich-side of the stoichiometric mixture fraction, which is attributed to lower mass weighted heat capacity of the richer mixture. It can be seen that $OH^*$ is formed within the high temperature region, and the mole fraction of $OH^*$ peaks at the maximum flame temperature. Hence, $OH^*$ can be used to indicate high flame temperature.

Figure 4a displays examples of instantaneous $OH^*$ images corrected for background and vignetting from ethanol flames carried by air or $N_2$ in the 9% $O_2$ coflow.

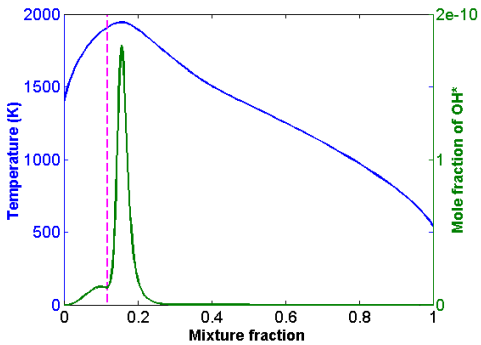


Fig. 3: Flame temperature and $OH^*$ mole fraction as a function of mixture fraction for ethanol flames carried by air in the 9% $O_2$ coflow. The vertical dashed line indicates the stoichiometric mixture fraction.

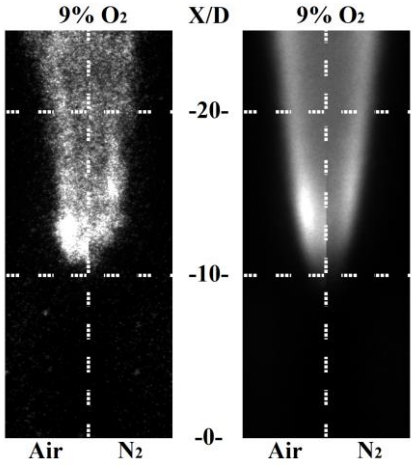


a. Instantaneous images b. Averaged images

Fig. 4: Instantaneous and averaged $OH^*$ images from ethanol flames carried by air or $N_2$ in the coflow with 9% excess $O_2$. X is the axial distance above the jet exit plane; D is the jet diameter

These images are taken with a gate time of 1 ms. The bottom edges of these images coincide with the jet exit plane, which suggests that the flames are lifted. For both flames, a peak $OH^*$ intensity exists at the flame base, especially for the carrier air case, which indicates the occurrence of high flame temperature. This indicates that the fuel jet is partially mixed with the hot coflow upstream of the lift-off height, which is consistent with previous measurements in this burner [3]. For the rest of the flame length, a conventional non-premixed flame structure is observed for both cases; such that the signal at the edges of the flames is stronger than that in the centre of the flames. The flame carried by air shows a higher $OH^*$ intensity than that carried by $N_2$, which is in agreement with the higher flame luminosity observed in the flame photographs.

Figure 4b shows the corresponding corrected and averaged $OH^*$ images, which are averaged from 146 instantaneous images. In the averaged image, the location of the high temperature zone in the flame carried by air changes slightly, and its size is reduced relative to the instantaneous image. As for the flame carried by $N_2$, there is no peak $OH^*$ along the axial direction in the averaged image. The comparison of instantaneous and averaged images suggests that both the location of the peak $OH^*$ and the $OH^*$ intensity vary shot-by-shot, which are attributed to the fluctuations in the turbulent flames. For example, the flame base fluctuates up and down shot-by-shot, which makes the lift-off height and its appearance in the averaged image differ from those in an instantaneous image. Hence, interpretation of the results requires an analysis of both the instantaneous and averaged images.

Figure 5 plots the corrected normalised total $OH^*$ signal in the averaged images against the axial distance above the jet exit plane normalized by the jet diameter (X/D) for various coflow conditions. The surrounding air entrainment has an affect on the flame above 100 mm downstream the jet exit plane (X/D=22) [3]. The impact of cold air entrainment on the reaction zone has been

discussed in a previous study [3], and is not the focus of the current paper. Total $OH^*$ signal here refers to radially integrated $OH^*$ across the whole width of the flame. Given the same coflow condition, the $OH^*$ intensity is higher when the flame is carried by air. In addition, the spatial gradient of $OH^*$ in the axial direction is greater when carrier air is used instead of $N_2$. Given the same carrier, the $OH^*$ intensity in the flame increases significantly with the excess oxygen level in the coflow. This observation is different from a previous study on MILD combustion in jets in cross-flow [15], which reported that the oxygen level had little impact on the $OH^*$ intensity. This is likely because the adiabatic flame temperature of the coflow was increased instead of being kept constant at a lower oxygen level in the previous study.

The build-up of total $OH^*$ changes significantly with the excess oxygen level in the coflow. For flames carried by air in the 6% and 9% $O_2$ coflow, three distinguishable regions are formed: in the first region no chemiluminescence is produced; in the second region a rapid production of $OH^*$ occurs, where the $OH^*$ intensity peaks; in the third region a decline in the $OH^*$ intensity is apparent. However, in a 3% $O_2$ coflow, there is neither a rapid build-up of $OH^*$ nor a decrease in the $OH^*$ intensity regardless of the carrier gas. Instead, the intensity of $OH^*$ increases gradually with the axial distance in the 3% $O_2$ coflow. This suggests that the flame temperature becomes more spatially distributed in a more diluted coflow. The peak in the $OH^*$ intensity disappears when $N_2$ is used as a carrier instead of air in the 6% $O_2$ coflow. Despite the higher (6%) excess oxygen level, flames carried by $N_2$ behaves closer to flames issuing into a 3% $O_2$ coflow. Hence, the use of $N_2$ as carrier gas produces a similar impact to diluting the coflow, which also leads to a more uniform temperature distribution. When the ethanol flames are carried by $N_2$ in a 6% $O_2$ coflow, the local oxygen concentration in the stoichiometric mixture is calculated to be 5.7%, while it is 6.6% in the flames carried by air. It is suspected that the more uniform temperature distribution is not only caused by the fuel dilution, but also caused by the actual changes in the flame structure, which will be examined with planar laser diagnostics in the future. It is worth noting that the instantaneous $OH^*$ images display the same trends mentioned above, despite the turbulent fluctuations in the flames.

## 3. Conclusions

To understand the impact of carrier gas on the flame behaviour under MILD combustion conditions, this paper presented OH chemiluminescence ($OH^*$) imaging of prevaporised ethanol flames in a Jet in Hot Coflow (JHC) burner. The appearance of flames carried by different carrier gases is similar, though the flame is more luminous when air is used. However, $OH^*$ imaging indicates that the type of carrier gas has a significant impact on the flame structure. The use of nitrogen as a carrier is found to produce similar effects to diluting the coflow. In particular, $OH^*$ intensity in the axial direction peaks at the flame base when it is carried by air, indicating an existence of a high temperature zone with rapid reactions. However, no peak $OH^*$ intensity in the axial direction is observed in the flame carried by nitrogen, which suggests a more uniform temperature distribution.

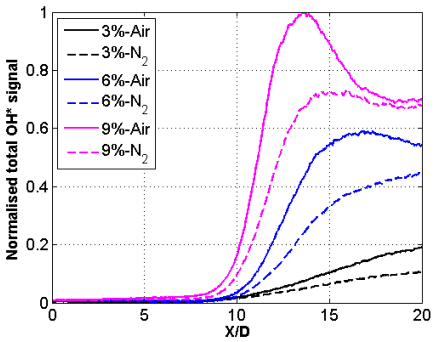


Fig. 5: Normalised radially integrated total $OH^*$ signal as a function of axial distance above the jet (X) normalized by jet diameter (D) in the coflow with 3%, 6% and 9% excess $O_2$

## 4. Acknowledgments

This research is funded by the China Scholarship Council and The University of Adelaide. Funding from the Australian Research Council (ARC) and the United States Air Force Asian Office of Aerospace Research and Development (AOARD) is gratefully acknowledged. The authors thank Kathleen Lask and Chia Thong for their assistance during the experiments.

## 5. References

[1] B.B. Dally, A.N. Karpetis and R.S. Barlow, Proc. Combust. Inst. 29 (2002), pp. 1147-1154.
[2] M. Derudi and R. Rota, Proc. Combust. Inst. 33 (2011), pp. 3325-3332.
[3] P.R. Medwell, P.A.M. Kalt and B.B. Dally, Combust. Flame 148 (2007), pp. 48-61.
[4] R. Weber, S. Orsino, N. Lallemant and A. Verlaan, Proc. Combust. Inst. 28 (2000), pp. 1315-1321.
[5] J. Ye, P.R. Medwell, E. Varea, S. Kruse, B.B. Dally and H.G. Pitsch, Appl. Energy 151 (2015), pp. 93-101.
[6] S.H. Stårner, J. Gounder and A.R. Masri, Combust. Flame 143 (2005), pp. 420-432.
[7] W. O'Loughlin and A.R. Masri, Flow Turbul. Combust. 89 (2012), pp. 13-35.
[8] R.L. Gordon, A.R. Masri and E. Mastorakos, Combust. Flame 155 (2008), pp. 181-195.
[9] P.R. Medwell, P.A.M. Kalt and B.B Dally, Combust. Sci. Technol. 181 (2009), pp. 937-953
[10] E. Oldenhof, M.J. Tummers, E.H. van Veen, D.J.E.M. Roekaerts, Combust. Flame 157 (2010), pp.1167-1178
[11] P.R. Medwell and B.B. Dally, Energy Fuels, 26 (2012), pp. 5519-5527
[12] C. S. Panoutsos, Y. Hardalupas, and A.M.K.P. Taylor. Combust. Flame 156.2 (2009), pp. 273-291.
[13] Marinov NM, Int. J. Chem. Kinet. 31(1999), pp.183–220
[14] J. M. Hall and E. L. Petersen, Int. J. Chem. Kinet. 38 (2006), pp. 714-724
[15] J. Sidey and E. Mastorakos, Proc. Combust. Inst. 35 (2015), pp. 3537-3545

# The adequacy of laminar flame calculations for identifying MILD combustion

P.R. Medwell[1*], M.J. Evans[1], Q.N. Chan[2], V.R. Katta[3]

[1]School of Mechanical Engineering, The University of Adelaide, SA, Australia

[2]School of Mechanical and Manufacturing Engineering, University of New South Wales, NSW, Australia

[3]Innovative Scientific Solutions Inc., Dayton, Ohio, USA

## Abstract

Moderate or Intense Low oxygen Dilution (MILD) combustion is well established to provide low $NO_x$ emissions and high thermal efficiency. The required conditions to achieve MILD combustion are commonly reported based on well-stirred reactor calculations. The validity of this approach for classifying nonpremixed jet flames is unclear. Flames that meet a common definition of MILD combustion have been observed to behave very differently to other flames that display more classic MILD combustion characteristics. This paper considers two jet flame conditions; one classified as being in the MILD domain, and another representative of more conventional combustion. A series of experimental results, well-stirred reactor calculations and jet flame modelling results are presented. The validity of laminar flame calculations at predicting the basic trends of flame behaviour in the transition to MILD combustion is demonstrated to require great care in interpretation, but the calculations can replicate the experimental observations.

*MILD combustion; Lifted flames; Hot coflow; Jet in hot coflow burner*

## 1. Introduction

The Moderate or Intense Low oxygen Dilution (MILD) combustion regime is characterised by high thermal efficiency and low $NO_x$ emissions. MILD combustion is achieved under hot and depleted oxygen conditions, leading to a distributed reaction zone. Although this approach is well established [1] there remains uncertainty in the conditions required to achieve this regime in a general sense.

To develop understanding of the MILD combustion regime, a series of experimental and computational studies have been performed in a jet in hot coflow (JHC) burner configuration [2, 3]. The JHC burner is similar to other vitiated coflow burners [4] that have been used for the study of autoignitive lifted flames [5]. Both burners consist of a central fuel jet that issues into a coflow of products from a premixed burner mounted upstream of the jet exit plane. A variety of flames that meet the definition of MILD combustion can be established in these burners, however very different behaviour has been reported [6]. It is worth noting that both the MILD combustion and lifted flames are autoignitive, but the conditions that lead to the different regimes are not yet explained.

The various JHC-style burner studies have each focussed on a narrow range of operating conditions. This has prevented a comprehensive study to develop a unified approach for classifying flame behaviour. Moreover, existing definitions of MILD combustion stem from simplified zero- and one-dimensional calculations. Whilst these analyses provide a good framework for developing regime diagrams spanning conventional to MILD combustion, the criteria used to distinguish flame behaviour in a generalised sense has not been established. In particular, the link between jet flames and regime maps generated from well-stirred reactor calculations is not known. Thus, this paper aims to set in place a framework to classify flames under hot and vitiated oxidant conditions, with a particular emphasis on identifying MILD combustion conditions.

## 2. Methodology

### 2.1 Flames of interest

For this paper only two flames are chosen, although this number will be extended in later studies. The two flames are ethylene fuel jets (at 300 K) which issue into a coflow at 1100 K and with either 3% or 9% $O_2$ (by volume). The coflow stream consists of the products of a natural gas / hydrogen / air / nitrogen premixed secondary flame upstream of the jet exit plane. These flame conditions have been presented previously [7].

### 2.2 Chemkin laminar flame calculations

For a detailed assessment of the chemical kinetics of interest to this study, the well-stirred reactor (WSR) model of the AURORA routine in the Chemkin software suite (version 4.1) is used. For all fuels, the University of California at San Diego (UCSD) kinetic mechanism scheme is used (version CK_2014-07-31).

Well-stirred reactor (WSR) models are widely used as a tool to investigate “most reactive mixtures” in lifted flames [8]. Although the experimental flames considered in this paper are predominately nonpremixed, previous attempts at replicating experimental trends using opposed-flow calculations have not performed well [9].

* Corresponding author:
Phone: +61 (0)8 831 35460
Email: paul.medwell@adelaide.edu.au

One of the key objectives of the paper is to identify whether the WSR approach predicts the flame behaviour in the transition to MILD combustion without resorting to detailed two-dimensional time-dependent simulations; however such detailed simulations are also performed for comparative purposes in this paper.

A series of runs for a stoichiometric well-stirred mixture of $C_2H_4/O_2/N_2$ are performed. The reactant temperature and $O_2$ concentration are independently varied, with $N_2$ adjusted to balance the composition.

### 2.3 UNICORN calculations

One-dimensional opposed-flow laminar flame calculations of the flames considered in this study have been reported previously [9]. Such calculations have inherent weaknesses when studying lifted flames. Firstly, the mixing that occurs in lifted flames creates premixed flame pockets, which are believed to be one of the primary stabilisation mechanisms for these types of autoignitive flames [8]. Secondly, the time-dependent nature of the ignition processes is difficult to capture accurately in most opposed-flow simulations. To circumvent these issues, the use of the UNICORN (UNsteady Ignition and COmbustion using ReactioNs) solver is used to perform axisymmetric two-dimensional time-dependent laminar flame calculations. Further details of the UNICORN code have been presented previously [10, 11]. In brief, it is a time-dependent mathematical model for the simulation of unsteady reacting flows. For the current study, only steady laminar flows are considered. Under these conditions UNICORN performs direct numerical simulations (DNS). For consistency with the Chemkin calculations, the University of California at San Diego (UCSD) kinetic mechanism is used. The composition of the mixtures mimics those of the Chemkin runs and the experiments.

## 3. Results

### 3.1 Experimental observations

Figure 1 presents experimental observations for ethylene flames which appear attached in a 3% $O_2$ coflow or "transitional" (lifted) in a 9% $O_2$ coflow [7]. The experimental photograph (Figure 1a) of the flame in a 3% $O_2$ coflow has very low luminosity, consistent with the "flameless" nature of MILD combustion. The low level of luminosity gives a false impression of a lifted flame, but in reality it is possible to distinguish a faint reaction zone to the jet exit plane. This is supported by laser diagnostic images (Figure 1b) of the OH radical, formaldehyde and temperature centred at 35mm downstream of the jet exit plane. An OH layer is clearly present between the jet centreline and the coflow oxidant stream, indicative of a reaction zone in the 3% $O_2$ flame, despite its low luminosity at this height. Further evidence of a reaction in this region is the strong formaldehyde ($H_2CO$) signal measured. Subsequent computational modelling of this flame also predicts an attached jet flame [3].

The experimental measurements of the 3% $O_2$ flames suggest that they are attached jet flames. When the coflow $O_2$ concentration is increased to 9% the flames visually appear lifted. At around the 35mm location, the OH images in the 9% $O_2$ flame base frequently show a strong reaction zone at the top of the image. Upstream of the strong OH signal it is possible to identify a weak OH tail that seems to extend to the jet exit plane. The presence of OH upstream of the apparent lift-off height, coupled with high levels of formaldehyde in the lifted region of these flames tends to indicate that they are not lifted according to the typical definition. It is therefore inappropriate to classify them with other (lifted) flames in other combustion regimes that do not display this type of behaviour. Due to the appearance of the features, they have instead been referred to as "transitional" flames [7]. Highly resolved DNS studies support the assertion that the intense build-up of precursors in the lifted region of these types of flames is different to conventional lifted flames [12, 13].

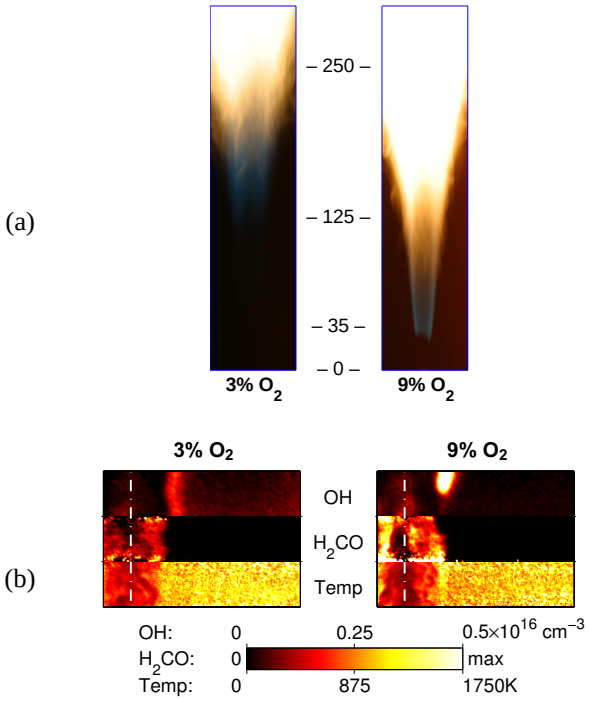


**Figure 1:** Experimental measurements of $C_2H_4$ flames in a 3% and 9% $O_2$ coflow ($T_{coflow}$=1100K). $Re_{jet}$=10,000. [7]. (a) Experimental photographs, with locations shown in millimetres. (b) Laser diagnostic images at a measurement height of 35mm above jet exit plane, with jet centreline marked by white dashed vertical line.

### 3.2 Ignition delay calculations

Figure 2 presents the calculated ignition delay times for $C_2H_4$ flames across a range of $O_2$ levels and temperatures. A reduction in the $O_2$ concentration is seen to increase the ignition delay across the entire range of conditions. Whilst expected, this observation contradicts the trends noted in the experimental flames where the 3% $O_2$ flame appears attached while the 9% $O_2$ flame appears lifted. The ignition delay is 6.2ms and 5.0ms, for the 3% and 9% $O_2$ cases, respectively.

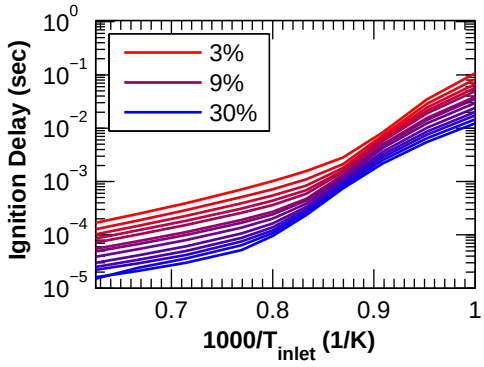


**Figure 2:** Calculated ignition delays for a $C_2H_4/O_2/N_2$ mixture ($\Phi$=1) across a range of $O_2$ levels.

## 3.3 Combustion regime diagram

Figure 3 demonstrates the MILD combustion operating regime in the domain of oxygen ($O_2$) concentration and reactant temperature. For each combination of reactant temperature and $O_2$ concentration the equilibrium temperature and auto-ignition temperature are determined. Four combustion domains are defined in Table 1, based on definitions previously suggested by Cavaliere and de Joannon [1].

The regime diagram presented in Figure 3 is a simplified map to give an indication of the combustion domains. The reactants do not include other major and/or minor species that would be encountered in a practical system. It also assumes stoichiometric conditions ($\Phi$=1) and not the most reactive mixture [8]. Furthermore this diagram does not reveal the unsteady/lifted flame region that occurs between the "hot" flames and the MILD combustion domains [6]. Detailed analyses of the transient solutions that occurs in this transitional region have been presented elsewhere [14, 15]. Despite the limitations, this type of regime map has been reported previously to indicate the conditions required to achieve MILD combustion. Figure 3 indicates that both of the flames considered in this study are classified as MILD combustion, despite having clearly different features (Figure 1).

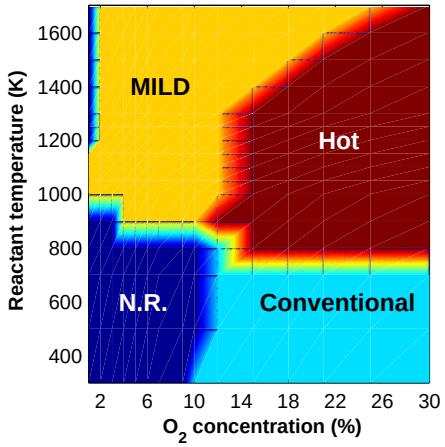


**Figure 3:** Regime diagram for a $C_2H_4/N_2/O_2$ mixture ($\Phi$=1) showing four combustion domains. 'N.R.' = no reaction; 'Conventional' = conventional combustion; 'Hot' = hot flames; 'MILD' = MILD combustion.

| $\Delta T=T_{equil}-T_{inlet}$ | $T_{inlet} < T_{a.i.}$ | $T_{inlet} > T_{a.i.}$ |
|---|---|---|
| $\Delta T < T_{a.i.}$ | No reaction | MILD combustion |
| $\Delta T > T_{a.i.}$ | Conventional | Hot flame |

**Table 1**: Definition of combustion domains based on reactant temperature ($T_{inlet}$), equilibrium temperature ($T_{equil}$) and auto-ignition temperature ($T_{a.i.}$) from well-stirred reactor calculations [1].

## 3.4 Temporal evolution

Figure 4 presents the time evolution of the OH radical in the $C_2H_4$ flames in 3% and 9% $O_2$ coflow cases from WSR calculations. The ignition delay for the 3% $O_2$ flame appears to be significantly longer, despite the experimental observation of this flame appearing attached. Comparison of the temporal profiles of OH demonstrates that the ignition process is very different between the 3% and 9% $O_2$ cases. At 9% $O_2$ the OH profile is seen to undergo a continuous increase in OH concentration until ignition, whereas at 3% $O_2$ after an initial increase the OH concentration remains relatively constant for a prolonged period ahead of the rise to the peak OH concentration. The long ignition process of the 3% $O_2$ flame supports the common description of MILD combustion being a "distributed" reaction – distributed both in time and space.

The temporal profile of the 3% and 9% $O_2$ flames are different, yet both occur within the MILD combustion regime in the definition from Table 1. This is consistent with different behaviour noted experimentally (Figure 1). Although these two flames may be broadly grouped together it is clear that they have different flame stabilisation mechanisms. A fundamental difference between natural gas jet flames in a 3% and 9% $O_2$ environment has been discussed previously [16] but not taken into consideration temporal differences. It is therefore apparent that within the MILD combustion regime there exists multiple flame stabilisation mechanisms and flame behaviour. Whilst this has been reported previously [6] there has been no attempt to relate these differences to the definition and classification of MILD combustion in the JHC burner to the WSR configuration.

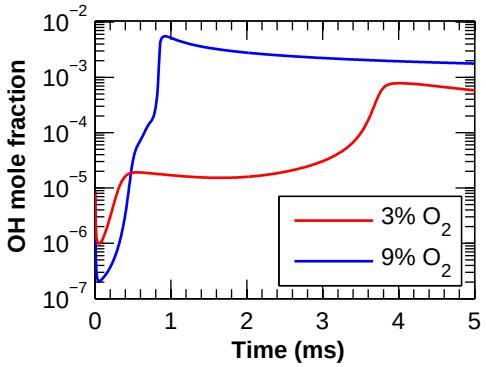


**Figure 4:** Temporal profile of OH mole fraction for a $C_2H_4/O_2/N_2$ mixture ($\Phi$=1) at two $O_2$ levels.

### 3.5 Two dimensional structure

The WSR calculations presented provide some insight into mapping turbulent nonpremixed jet flames in a vitiated coflow to the combustion operating regime diagram. However, the WSR ignores the nonpremixed nature of the experimental flames. To provide more detailed analysis, while avoiding the complexity of turbulent flows, a two-dimensional laminar axisymmetric streaming flow CFD model has been generated using the UNICORN code. A simplified case of a fuel jet in a depleted oxygen hot coflow is considered, where the velocity of both streams is 1.0 m/s. This configuration enables an investigation without shear or turbulent transport. Figure 5 presents the temperature and OH mass fraction for a $C_2H_4$ fuel stream in a 3% and 9% $O_2$ coflow, with compositions consistent with the flames presented in Figure 1.

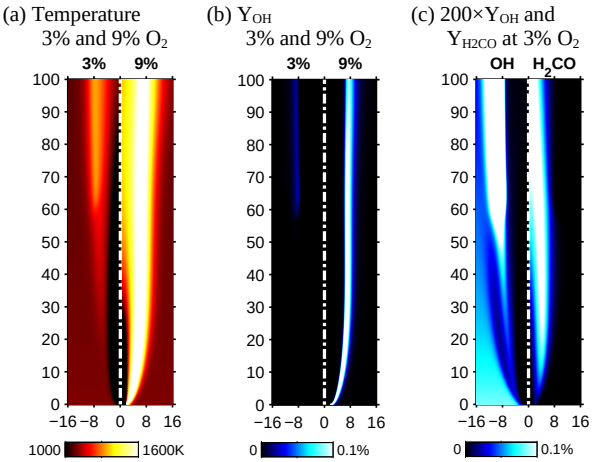


**Figure 5:** Calculated temperature, OH mass fraction and $H_2CO$ mass fraction for $C_2H_4$ flame in a 3% and 9% $O_2$ coflow. $T_{jet}$=300K, $T_{coflow}$=1100K. $U_{jet}$ = $U_{coflow}$ = 1.0 m/s. Note that (c) is only for 3% $O_2$ coflow and OH mass fraction is multiplied by 200. All dimensions in millimetres.

It is essential to emphasise that the flow conditions between the calculations and the experiments are very different – the experiments have both shear and turbulence, neither of which is included in the calculations presented in Figure 5. Nevertheless, the OH profiles in Figure 6 tend to follow a similar trend to the measurements in Figure 1.

Experimentally, the 3% $O_2$ coflow flame appeared lifted, but on closer inspection it is indeed attached. The temperature profile in Figure 5(a) and OH profile in Figure 5(b) both tend to indicate a lifted flame. However, if the colour-scaling is increased 200 times (to highlight lower concentrations) a clear reaction zone is revealed in Figure 5(c), which also shows significant $H_2CO$ presence.

The 9% $O_2$ coflow flame experimentally appeared lifted, with a weak OH tail extending to the jet exit plane. In contrast, the calculations presented in Figure 5 indicate a completely attached flame. This is consistent with a conventional flame attaching at low velocities and becoming lifted at higher velocities.

## 4. Conclusions

Jet in Hot Coflow (JHC) burners have previously been used to study both MILD combustion and autoignitive lifted flames. Many of the lifted flames fall under the classification of MILD combustion, yet their lifted behaviour is inconsistent with the expected behaviour of flames in the MILD combustion regime. This paper has compared two flames; one unquestionably in the MILD regime and another in the transition from conventional to MILD combustion. On first inspection the trends reported in experimental flames are not reproduced by only comparing simple ignition-delay-based metrics. It appears that the widely established definition of MILD combustion based entirely on initial, final and autoignition temperatures of a well-stirred reactor may not be a good identification tool for nonpremixed flames. However, the trends in the flame behaviour observed experimentally can be inferred from thorough inspection of the calculations. Future work is required for a more generalised classification of these flames.

## 5. Acknowledgments

The authors gratefully acknowledge support by The University of Adelaide, the Australian Research Council (ARC), the United States Asian Office of Aerospace Research and Development (AOARD) and the United States Air Force Office of Scientific Research (AFOSR).

## 6. References

[1] A. Cavaliere, M. de Joannon, *Prog. Energy Combust. Sci.* **30** (2004), pp. 329-366.
[2] B.B. Dally, A.N. Karpetis, R.S. Barlow, *Proc. Combust. Inst.* **29** (2002), pp. 1147-1154.
[3] S.R. Shabanian, P.R. Medwell, M. Rahimi, A. Frassoldati, A. Cuoci, *Appl. Therm. Eng.* **52** (2013), pp. 538-554.
[4] R. Cabra, T. Myhrvold, J.Y. Chen, R.W. Dibble, A.N. Karpetis, R.S. Barlow, *Proc. Combust. Inst.* **29** (2002), pp. 1881-1888.
[5] R.L. Gordon, A.R. Masri, E. Mastorakos, *Combust. Flame* **155** (2008), pp. 181-195.
[6] P.R. Medwell, B.B. Dally, *Energ. Fuel* **26** (2012), pp. 5519-5527.
[7] P.R. Medwell, P.A.M. Kalt, B.B. Dally, *Combust. Flame* **152** (2008), pp. 100-113.
[8] E. Mastorakos, *Prog. Energy Combust. Sci.* **35** (2009), pp. 57-97.
[9] P.R. Medwell, D.L. Blunck, B.B. Dally, *Combust. Flame* **161** (2014), pp. 465-474.
[10] V.R. Katta, L.P. Goss, W.M. Roquemore, *AIAA J.* **32** (1994), pp. 84-94.
[11] V.R. Katta, W.M. Roquemore, *AIAA J.* **46** (2008), pp. 1640-1650.
[12] C.S. Yoo, E.S. Richardson, R. Sankaran, J.H. Chen, *Proc. Combust. Inst.* **33** (2011), pp. 1619-1627.
[13] Z. Luo, C.S. Yoo, E.S. Richardson, J.H. Chen, C.K. Law, T. Lu, *Combust. Flame* **159** (2012) pp. 265–274.
[14] M. de Joannon, P. Sabia, A. Tregossi, A. Cavaliere, *Combust. Sci. Tech.* **176** (2004), pp. 769-783.
[15] P. Sabia, G. Sorrentino, A. Chinnici, A. Cavaliere, R. Ragucci, *Energ. Fuel* **29** (2015), pp. 1978-1986.
[16] P.R. Medwell, P.A.M. Kalt, B.B. Dally, *Combust. Sci. Tech.* **181** (2009), pp. 937-953.

**Proceedings of the Australian Combustion Symposium**
**December 7-9, 2015, The University of Melbourne**

# Effect of Turbulence on the MILD Combustion Characteristics of Victorian Brown Coal

Manabendra Saha*, Bassam B. Dally, Paul R. Medwell and Alfonso Chinnici
Centre for Energy Technology, School of Mechanical Engineering
The University of Adelaide, SA 5005, Australia

## Abstract

In this experimental work, a vertical furnace of 1200 mm long with a cross section of 260 x 260 $mm^2$ is used to investigate the MILD (Moderate or Intense Low oxygen Dilution) combustion characteristics of pulverised Victorian brown coal. The furnace consists of a central fuel jet, from which coal particles are fed with a carrier gas into a hot and vitiated co-flow from a secondary swirling burner. The furnace walls as well as co-flow temperature and local oxygen concentrations are controlled by the secondary swirling burner using non-premixed natural gas combustion. The aim of this paper is to investigate the interaction of volatiles released from the coal particles with a vitiated co-flow and its impact on the formation and emission of $NO_x$ and other pollutants under MILD combustion conditions. The Loy-Yang brown coal from the Latrobe valley, Victoria, with particle sizes in the range of 53-125 µm, is injected into the furnace using $CO_2$ as a carrier gas through the insulated water cooled central jet. The co-flow in the furnace was operated under lean fuel conditions with an excess $O_2$ concentration of 5.9% (by volume). The turbulent fuel jet Reynolds number was varied from $Re_{jet}$ = 5,527 to $Re_{jet}$ = 20,000 to investigate the impact of turbulence on volatiles' release and reactions under MILD combustion conditions. Detailed measurements of in-furnace temperatures and in-furnace CO and $NO_x$ concentrations are presented and discussed, together with visual observations at the bottom, middle and top region of the furnace.

*Keywords: MILD combustion, pulverised Victorian brown coal, turbulent fuel jet, temperature, CO, NO.*

## 1. Introduction

The Loy-Yang brown coal in Victoria, Australia, is a low rank and Tertiary aged coal which is named as lignite [1]. The Victorian brown coal is one of the lowest cost energy sources in the world. Furthermore, the Victorian brown coal has a high volatile and oxygen content, as well as low in ash, sulphur and heavy metals, which makes Victorian brown coal unique when compared with other solid fuels such as biomass, peat, bituminous coal and anthracite [1]. However, the Victorian brown coal has an high moisture content (about 60 – 70 wt%) [2] that reduces its effective energy content. Furthermore, typical Victorian brown coal-fired system plants are characterised by an high emission intensity (≈ 1.22 ton-$CO_2$/MWh) and $NO_x$ emissions [3, 4] that restrict the use of this coal drastically. Thus the efficient and environment friendly usage of Victorian brown coal is a major challenge.

Moderate or Intense Low oxygen Dilution (MILD) combustion is an innovative technique that offers ultra-low pollutant emissions, improved thermal efficiency, enhanced combustion stability, thermal field uniformity, and broad fuel flexibility. MILD combustion differs from conventional combustion because of the absence of any visible or audible flame at optimized conditions. As a result, MILD combustion is often called 'flameless combustion' or 'flameless oxidation' (FLOX®) [5].

There is a progressive base of knowledge of the MILD combustion regime in-particular for gaseous and liquid fuels. Moreover, MILD combustion technology has been successfully implemented in various industrial sectors for gaseous fuels. Nevertheless, MILD combustion of solid fuels, in particular low-rank pulverised fuels such as brown coal has received much less attention than that of gaseous fuels.

The first significant attempt to apply MILD combustion technology to pulverised coal was conducted by Kiga et al. [6] by burning a high volatile pulverised coal with high-temperature preheated air in a drop tube furnace. An experimental study on the MILD combustion behaviour of high volatile bituminous coal was conducted in a 0.58MW furnace by Weber et al. [7] at the International Flame Research Foundation (IFRF). The measured $NO_x$ emissions at the furnace exit were in the range of 160-175 ppm (at 3% $O_2$ concentrations) showing high $NO_x$ reduction potential of the technology. However, the basic mechanism of $NO_x$ formation is not clearly understood from the experiments. Previously, the current authors published a comprehensive set of experimental and numerical results [8] from pulverised brown and black coal in a recuperative furnace to better understand the formation and destruction of pollutants, like $NO_x$ under MILD combustion conditions.

The main focus of the current work is to investigate the burning characteristics of pulverised Victorian brown coal under MILD combustion conditions. In particular, the present experimental study investigates the influence of jet inlet velocities of $CO_2$ carried Loy-Yang brown coal stream (at room temperature) on the flame stability and pollutants formation and destruction. The turbulent fuel jet Reynolds number was varied from $Re_{jet}$ = 5,527 to $Re_{jet}$ = 20,000 to investigate the impact of turbulence on the devolatilisation as well as volatiles' release and reaction under MILD combustion conditions. It is well established that the devolatilization mode of coal

* Corresponding author:
Phone: +61 (0)8 8313 5460
Email: manabendra.saha@adelaide.edu.au

combustion, and especially the release position and rate of volatiles, are the main controlling parameters, which regulate the flame shape and length [9]. Detailed measurements of in-furnace gas concentration of CO, and $NO_x$ and in-furnace temperatures along with exhaust emissions are analysed and discussed. To the best of our knowledge, the burning characteristics of Victorian brown coal have not been previously reported for MILD combustion conditions, either in an enclosed (furnace) or in open flame system.

## 2. Experimental Setup

### 2.1 Experimental details

A schematic diagram of the MILD combustion furnace used in this project is shown in Figure 1. The furnace has an inner cross-section of 260 × 260 $mm^2$ and a height of 1200 mm. The furnace wall is well insulated, with 100-mm-thick high-temperature ceramic fibre-board refractory. A secondary swirling burner operating on the non-premixed combustion mode supplies hot combustion products under different stoichiometry. A duct configuration is built to transport the hot combustion products from swirling burner to the furnace at a uniform flow speed. Two porous beds filled with ceramic beads materials (~mean diameter of 4 mm of each ceramic bead) of 20 mm layers are used to help create a uniform co-flow.

The water cooled and well insulated central jet with an internal diameter ($D_j$) of 19 mm is used to inject coal into the furnace. A summary of the operating conditions and measured gas concentrations in the co-flow is shown in Table 1. The internal temperatures of the furnace were measured on the centreline (X = 0 mm) along the height (Y-axis) of the furnace for all experiments. Furnace temperatures were measured using 6-mm-diameter sheathed Pt/Pt 13%Rh (R-Type) thermocouples at heights of 70, 170, 270, 370, 470, 570, 670, 770, and 870 mm from the fuel jet exit. All temperature measurements are logged using a PC and USB-TC data logger. A water cooled sampling probe was introduced through the thermocouple ports to measure in-furnace $O_2$, CO, $CO_2$ and $NO_x$ mole fraction using a TESTO Model 350XL portable gas analyser. The absolute errors of these measurements, according to the manufacturer's specifications, are ±0.8% (by volume) for O2, ±10 ppmv for CO, and ±5 ppmv for NO of measured value. The sampling probe was traversed in the horizontal directions (Z-axis) at three positions (Z = 0, Z = 50, and Z = 100 mm) across different planes at eight holes of various vertical locations (Y-axis) of the furnace to provide a total of 24 points of measurement.

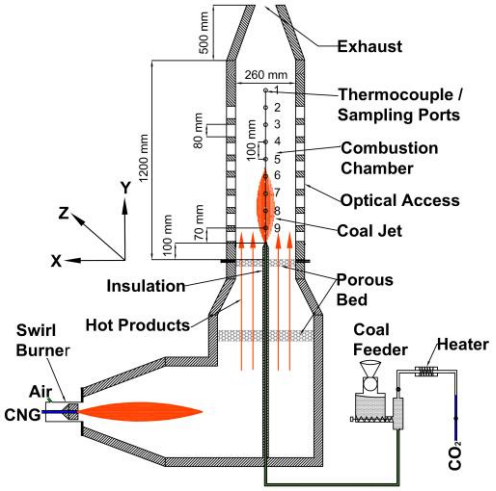


Fig. 1 Schematic diagram of the MILD combustion furnace and supply system

### 2.2 Characteristics of Coal

A Victorian brown coal, Loy-Yang, was milled and sieved into the 53 μm <d ≤125 μm size range. The coal was dried in an oven at 105 ºC for 4 hours to remove all moisture and then stored in a sealed container under ambient condition. Proximate and ultimate analyses of the coals are presented in Table 2. The gross dry calorific value of Loy-Yang brown coal is measured to be 24.5 MJ/kg.

Three different experiments were conducted using Loy-Yang brown coal with $CO_2$ as a carrier gas. A twin-screw volumetric coal feeder was specially built for this project to decouple the carrier gas flow rate from the solid particle supply rate. The coal feeder is operated using an AC motor controlled the amount of coal fed into the furnace. The coal feeding rate was constant and set to 1.47 kg/ hr for 10 kW heat input by the pulverised coal.

## 3. Results and Discussion

Figure 2 shows the photographs of Loy-Yang brown coal combustion under MILD conditions, taken from a side window close to the bottom (y = 80 mm), middle (y = 500 mm), and top (y = 995 mm) of the furnace for the three jet Reynolds number cases. The photographs imply that for all cases (i) no flame is visible at the jet exit where the volatiles are released by the coal particles and rapidly mixed with the surrounding co-flow; (ii) for the $Re_{jet}$ = 5527 case

Table 1 Operating parameters of secondary burner and measured gas concentrations of co-flow

| Fuel | Co-flow Velocity (m/ s) | Co-flow Temp. (K) | Wall Temp. (K) | $O_2$ (%db) | CO (ppmv dry) | $CO_2$ (%db) | $NO_x$ (ppmv dry) |
|---|---|---|---|---|---|---|---|
| Natural gas | 1.56 | 1284 | 1112 - 1236 | 5.9 | 19 | 8.9 | 98 |

Table 2 Coal analyses

| Fuel | Proximate analysis (wt % db) | | | Ultimate analysis (wt % daf) | | | | |
|---|---|---|---|---|---|---|---|---|
| | Fixed carbon | Volatile | Ash | C | H | N | S | O (by difference) |
| Loy-Yang brown coal | 47.3 | 51.3 | 1.4 | 66.8 | 4.8 | 0.4 | - | 28.0 |

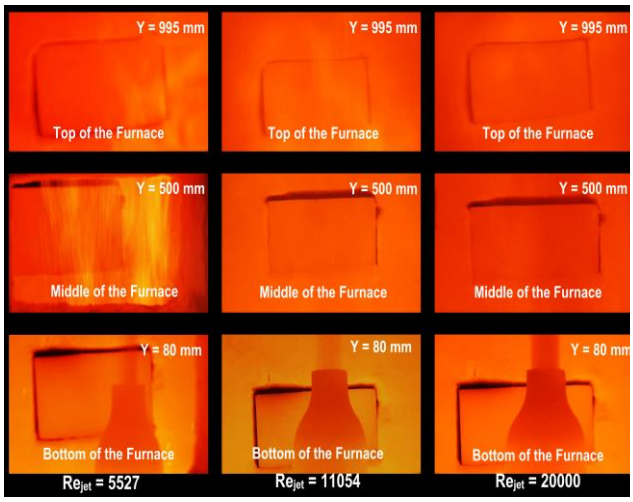

Fig. 2 Photographs of the furnace when operating under MILD combustion conditions

multiple intermittent soot sheets exist in the middle and top of the furnace, and (iii) for the case of $Re_{jet}$ = 11054 and $Re_{jet}$ = 20000 no visible flame at the middle and top of the furnace.

The in-furnace gas composition and temperatures were measured along various vertical positions (along the y–axis) of the furnace centreline ($x$ = 0 mm) for all cases. The comparisons between measured mean temperatures for the jet Reynolds number of $Re_{jet}$ = 5,527, $Re_{jet}$ = 11,054, and $Re_{jet}$ = 20,000 are shown in Fig. 3. Temperature difference at various locations of the furnace is less than 100 K which implies that a homogeneous temperature distribution is achieved in brown coal MILD combustion. However a clear distinction exists between those measured temperatures for different jet Reynolds numbers along the furnace centreline (x = 0, z = 0). The furnace temperature for $Re_{jet}$ = 20,000 case is lower than $Re_{jet}$ = 5,527 case, because heating of carrier gas takes more energy for higher Reynolds number case.

Figure 4 represents a comparison of in-furnace CO mole fraction between three different jet velocities. The measured in-furnace CO levels for the $Re_{jet}$ = 20,000 case were generally higher in these experiments than the cases of lower jet Reynolds numbers. This is because, with higher Reynolds number there is a better mixing and hence better reaction of the volatiles produces more CO. At the top part of the furnace, CO levels are found at their lowest concentration, suggesting that gaseous volatiles are completely burned by then. It is remarkable that the CO peak level has been elongated with increased Reynolds number that speculates the flame length increased by increasing jet Reynolds number.

No major differences between three cases for the measured NO mole fraction can be observed from Fig. 5, although for $Re_{jet}$ = 5,527 case, the NO mole fraction in the middle part of the furnace is measured to be higher than other two cases. This can be explained by the higher residence time of coal particles for the lowest jet Reynolds number. The long residence time allows to producing more fuel-NO by the oxidation reaction of the incorporated nitrogen (N) in the coal particles. It is presumed that the nitrogen (N) in the coal particle is entirely released during the devolatilization process. In comparing the cases between $Re_{jet}$ = 20,000 and $Re_{jet}$ = 5,527, it is clear that the particles' residence time is four times higher for the $Re_{jet}$ = 5,527 case and thus it is speculated that for this case (i) a share of nitrogen incorporated in the coal is converted into fuel-NO, by the devolatilization process; and (ii) a share of the remaining nitrogen in the char is converted into fuel-NO, by the reaction with oxygen. Furthermore, higher in-furnace temperature for the case of $Re_{jet}$ = 5,527 contributes to generate relatively higher NO, by

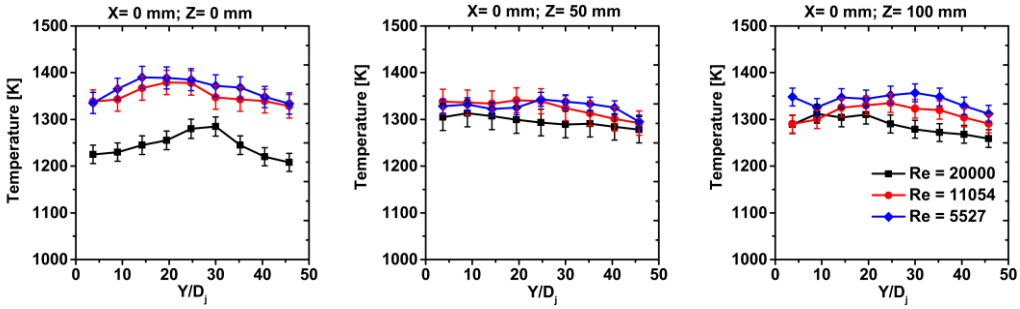

Fig. 3 Measured temperature profiles at the centreline (X = 0) along the vertical locations (the Y-axis) at different horizontal distances (the Z-axis) from the centre of the furnace

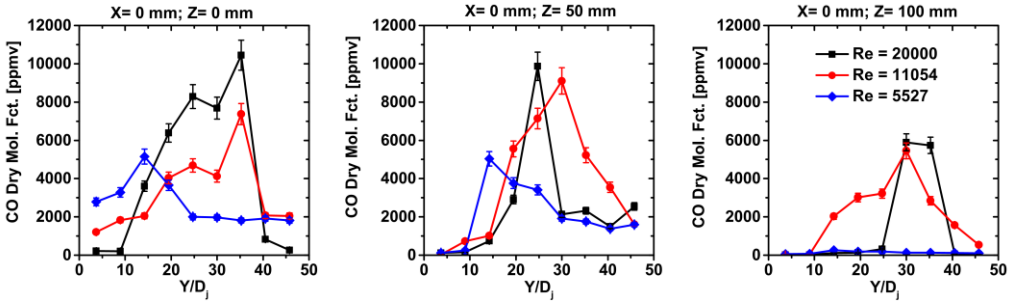

Fig. 4 Measured in-furnace CO dry molar fractions at the centreline (X = 0) along the vertical locations (the Y-axis) at different horizontal distances (the Z-axis) from the centre of the furnace

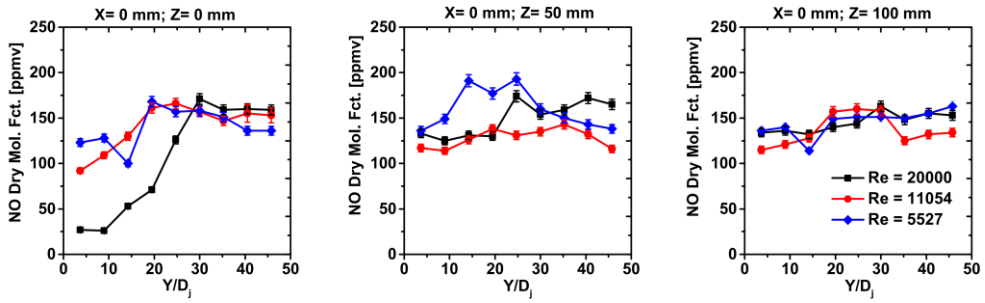


Fig. 5 Measured in-furnace NO dry molar fractions at the centreline (X = 0) along the vertical locations (the Y-axis) at different horizontal distances (the Z-axis) from the centre of the furnace

following the thermal-NO route.

The comparison of the measured exhausts gas concentrations (NO, $O_2$, CO, and $CO_2$) between the three different jet Reynolds number cases investigated in this study, are illustrated in Fig. 6. The largest NO emissions was measured for the $Re_{jet}$ = 5,527 case which is ≤ 147 ppm, whilst for the case of $Re_{jet}$ = 11,054 the value is ≤ 118 ppm and for the highest Reynolds number ($Re_{jet}$ = 20,000) case the value is ≤ 106 ppm. The overall NO formation is impacted by the dilution of the flows with additional $CO_2$ volume flow rate into the mixture for the higher jet Reynolds number. It is measured that the additional $CO_2$ volume flow rate of the mixture increases about 72% for the $Re_{jet}$ = 20,000 case when compared with $Re_{jet}$ = 5,527 case. It is interesting to note that for all the cases the value of exhaust NO is reduced from the in-furnace NO concentration, which can be explained by the NO-reburning mechanism. This depends primarily on the NO recombination with hydrocarbons according to reaction ( $C_xH_y + NO \rightarrow HCN + product$ ) and consequently reduces the overall- NO emission. At higher jet Reynolds number case, the NO-reburning reaction is favoured due to the higher jet turbulence and better mixing. The exhaust CO level was measured to be 2410~2500 ppmv for the lowest Reynolds number ($Re_{jet}$ = 5527) case while for the highest Reynolds number ($Re_{jet}$ = 20000) case the CO level was 1650~1780 ppmv. The higher CO emissions for $Re_{jet}$ = 5527 case is related to the more eminent char burnout by the heterogeneous reactions between char ($C_{(s)}$) and gaseous products ($C_{(s)} + 1/2O_2 \rightarrow CO$, $C_{(s)} + CO_2 \rightarrow 2CO$, $C_{(s)} + H_2O \rightarrow CO + H_2$) of the combustion reaction. It is believed that, coal particles have a sufficient time to burn char for the $Re_{jet}$ = 5527 case due to the higher residence time. On the other hand, similar values of oxygen concentration at the furnace outlet were measured for all cases and thus the overall equivalence ratio was almost same for each case.

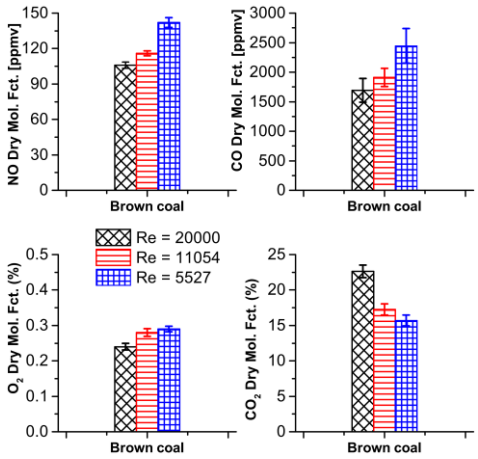


Fig. 6 Measured values of exhaust gas concentrations

## 4. Conclusions

This paper reports on the successful burning of Victorian brown coal carried by $CO_2$ in a furnace under MILD combustion conditions. Results point to a minor difference associated with the carrier gas velocities regarding furnace temperatures and in-furnace $NO_x$ concentration, whilst a major difference is found regarding in-furnace CO concentrations. The temperature distribution inside the furnace became quite uniform for both cases. Generally, higher $NO_x$ is measured in the middle part of the furnace. This is attributed to the flame sheets observed in this part of the furnace, which are a sign of conventional combustion and the associated higher thermal $NO_x$ formation. For all of the investigated cases, very low $NO_x$ emissions were found, providing strong evidence of the potential benefits of MILD Combustion application to Victorian brown coal. Future work is planned to better understand the devolatilisation region under MILD condition using advanced non-intrusive laser based techniques.

## 5. Acknowledgment

M. Saha acknowledges the financial support received from The University of Adelaide and Brown Coal Innovation Australia (BCIA).

## 6. References

[1] C.-Z. Li, Fuel **86** (12) (2007) 1664-1683.

[2] E. Binner; L. Zhang; C.-Z. Li; S. Bhattacharya, Proc. Combust. Inst. **33** (2) (2011) 1739-1746.

[3] A. H. Al-Abbas; J. Naser; D. Dodds, Fuel **102** (2012) 646-665.

[4] Z. F. Tian; P. J. Witt; M. P. Schwarz; W. Yang, Energy Fuels **24** (9) (2010) 4971-4979.

[5] J. Wünning; J. Wünning, Prog. Energy Combust. Sci. **23** (1) (1997), pp. 81-94.

[6] T. Kiga; K. Yoshikawa; M. Sakai; S. Mochida, J. of Propul. Power **16** (4) (2000), pp. 601-605.

[7] R. Weber; J. P. Smart, Proc. Combust. Inst. **30** (2) (2005), pp. 2623-2629.

[8] M. Saha; B. B. Dally; P. R. Medwell; E. M. Cleary, Energy Fuels 28 (9) (2014) 6046-6057.

[9] A. Williams; M. Pourkashanian; J. Jones, Prog. Energy Combust. Sci. **27** (6) (2001) 587-610.

# Effect of Boron Carbide on the Ignition and Combustion Characteristics of Amorphous Boron

D. Liang[1], L. Qiu[2], J. Liu[1,*], B. Chen[1], J. Zhou[1]
[1]State Key Laboratory of Clean Energy Utilization, Zhejiang University, Hangzhou 310027, China
[2]Zhejiang Energy Group R&D, Zhejiang Provincial Energy Group Company LTD., Hangzhou 310027, China

## Abstract

Boron carbide ($B_4C$) is one of the main components of boron (B)-based propellant primary combustion products. It has important influence to the secondary combustion. A laser ignition experimental system was designed to study the ignition and combustion characteristics of B/$B_4C$ mixtures in different mass ratios. A scanning electron microscope (SEM) was used for the micro-morphology analysis of the mixtures before and after combustion. The mass contents of $B_4C$ in the mixed samples were set to be 0 %, 20 %, 40 %, 60 %, 80 %, and 100 %. As the content of $B_4C$ increases, the maximum combustion intensity and average combustion temperature both decrease. However, the average combustion intensity during the combustion initially increases and then decreases. When the content of $B_4C$ is 40 %, the average combustion intensity reaches the maximum value. The ignition delay time also changes with the content of $B_4C$, and reaches a minimum value (111 ms) when the content of $B_4C$ is 40 %. After combustion, an oxide layer generated and covered on the surface of the samples. The porosity decreased significantly.

*Keywords: boron carbide, amorphous boron, ignition and combustion, spectra, temperature*

## 1. Introduction

Amorphous boron (B) has high gravimetric calorific value (58.28 MJ/kg) [1], and is considered to be an ideal fuel for solid-ducted rocket propellants. In practical applications, limiting factors of the performance of B-based propellants mainly include: the high melting and boiling points, ignition temperature, and oxygen demand of B [2-4]. Therefore, study on the formulation and incomplete combustion products of B-based propellants are helpful to improve the combustion efficiency of B, and the ignition and combustion characteristics of B-based propellants [5-8].

The main source of boron carbide ($B_4C$) in the B-based propellant is the combination reaction between carbon (from the adhesive) and boron during the combustion. According to the working principle of solid-ducted rockets [9], the combustion and decomposition of the adhesive usually takes place during the primary combustion (combustion in the gas generator). Earlier study results [10] show that $B_4C$ is one of the main components of B-based propellant primary combustion products. In addition, the numerical calculation results of Liu et al. [11] shows that $B_4C$ occurs in the primary combustion products of B-based propellant when the mass content of B in the propellant is larger than 32 %. Since the gravimetric calorific value of $B_4C$ is also high (52 MJ/kg) [12], it has important influence to the secondary combustion (combustion in the afterburning chamber). Besides, since $B_4C$ has better ignition characteristics than B, sometimes it is added in the B-based propellant, artificially, as a kind of additive or coating material [13]. Therefore, studying the effect of $B_4C$ on the ignition and combustion characteristics of B can provide reference for the performance improvement of B-based propellants.

In the present study, the ignition and combustion characteristics of B/$B_4C$ mixtures with different mass ratios were analyzed using a laser ignition experimental system. The ignition delay time, combustion intensity and temperature of these samples were compared. The comprehensive change rules of the ignition and combustion characteristics of the mixed samples were obtained.

## 2. Experimental section

### 2.1 Materials

The B sample used in this study was purchased from Baoding Zhongpuruituo Technology Co., Ltd., China. It has a nominal purity of 99 %, and an average particle size of 1 μm. The sample is brown at room temperature.

The $B_4C$ sample was purchased from Aladdin Industrial Co., China. It is analytically pure, and the average particle size is 1-5μm. This sample is dark grey at room temperature.

A planetary mixer was used for mechanical mixing of the samples. Six mixed samples with different mass content of $B_4C$ were prepared (Tab. 1).

### 2.2 Devices and Methods

The structure of the laser ignition experimental system designed for the experiments was showed in Fig. 1.

Tab. 1 Formulation of the samples (by mass)

| No. | Content of $B_4C$ (%) |
|---|---|
| 1 | 0 |
| 2 | 20 |
| 3 | 40 |
| 4 | 60 |
| 5 | 80 |
| 6 | 100 |

* Corresponding author: J. Liu, Dr. /Prof.
Phone: (+86) 057187952884
Email: jzliu@zju.edu.cn

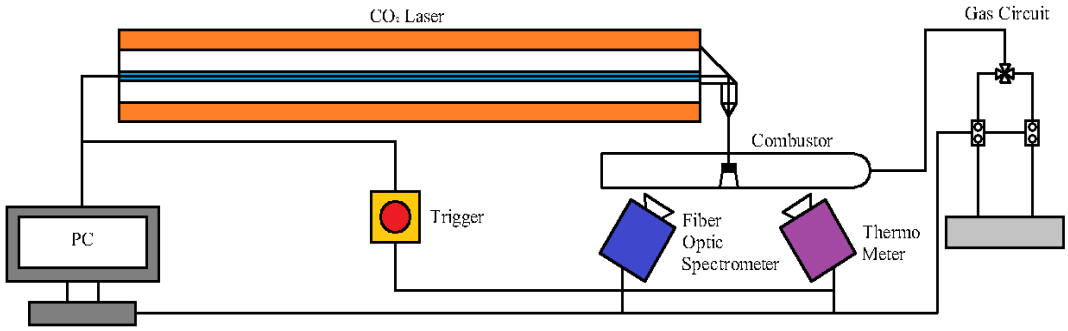


Fig. 1 Schematic of the laser ignition experimental system

The system contains four parts: the ignition module, the gas regulation module, the combustion diagnostics module, and the data acquisition module. In the system, an AvaSpec-3648 fiber optic spectrometer and a KLEIBER Infrared GmbH thermodetector were used for the real-time measurement of the ignition combustion process of the samples. The carbon dioxide ($CO_2$) laser, the fiber optic spectrometer and the thermodetector were connected by a synchronous trigger. In the experiments, the laser power was set to 150 W, and the heating time was set to 2 s. The reaction gas was air, with a constant gas flow of 1L/min. The sampling interval of the fiber optic spectrometer was set to 3 ms, and the sampling period was set to 3 s. The sampling period of the thermodetector was also set to 3 s, and the sampling frequency was set to 100 Hz. The samples were packed using a quartz crucible, approximately 50 mg for each time. At least three repeated tests were conducted for each sample.

A Hitachi S-3700N scanning electron microscope (SEM) was used for the micro-morphology analysis of the sample with 40 % $B_4C$, before and after combustion. The sample was treated by spray-gold before the analysis.

## 3. Results and Discussion

### 3.1 Combustion Intensity Analysis

The characteristic spectrum during the combustion process is recorded by the fiber optic spectrometer. It reflects the combustion intensity of the samples. The maximum spectral intensity curves of the samples are picked out, and presented in Fig. 2.

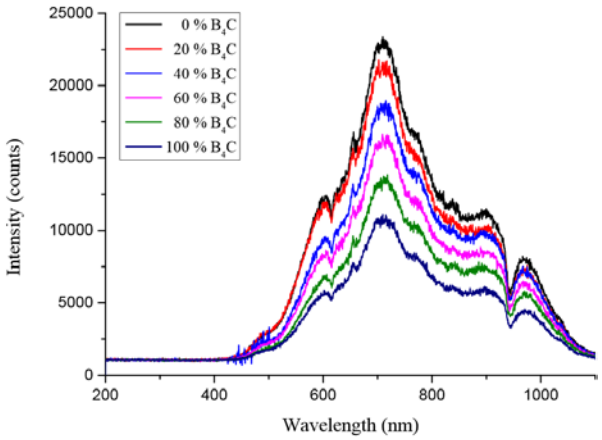


Fig. 2 Maximum spectral intensity curves at full wave of the samples

As the content of $B_4C$ increases, the maximum combustion intensity decreases. This is because the gravimetric calorific value of $B_4C$ is lower than that of B. All the curves have similar peak pattern, and reach the maximum value at 710 nm. To analyze the combustion intensity during the whole combustion process, the full-time spectral intensity at 710 nm are presented in Fig. 3.

The combustion intensity gradually rises after the laser is turned on. However, once the laser is turned off, the combustion intensity decreases sharply. At the beginning of the combustion, the sample with 40 % $B_4C$ shows the largest combustion intensity. Later, the combustion intensity of the sample with 20 % $B_4C$ turns larger than that of any other samples. At last, the combustion intensity of the B sample rises up rapidly and becomes the largest. As a result, $B_4C$ can promote the rise of the combustion intensity when its mass content is no more than 40 %. This can be attributed to the ignition point of $B_4C$ is lower than that of B. However, samples with larger $B_4C$ content ($\geq$ 60 %) show lower combustion intensity than the B sample all the time, under the effect of gravimetric calorific value.

To further compare the combustion intensity, the spectral intensity area was obtained by integrating the spectral intensity curves in Fig. 2 and Fig. 3. The results are showed in Fig. 4.

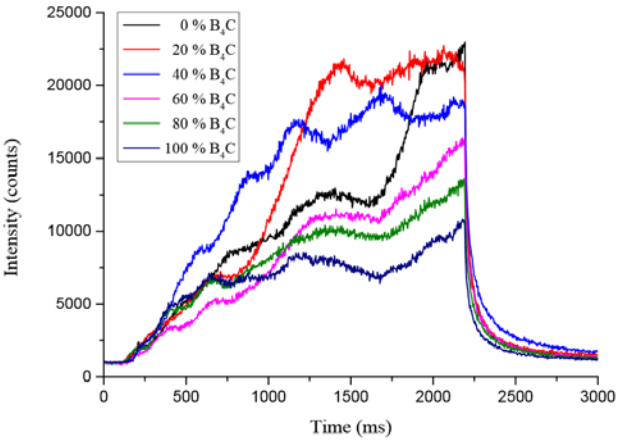


Fig. 3 Full-time spectral intensity curves of the samples at a wavelength of 710 nm

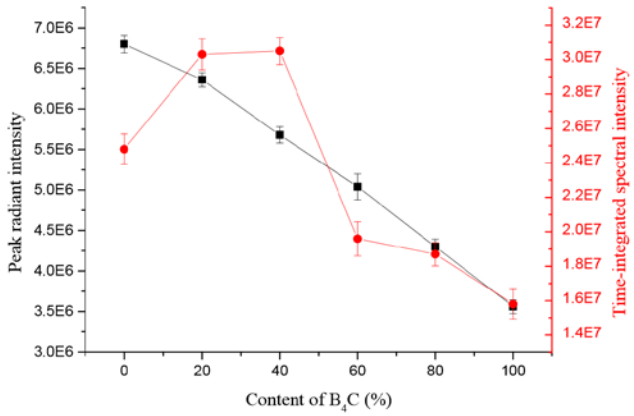


Fig. 4 Spectral intensity area of the samples

As the content of $B_4C$ increases, the peak radiant intensity decreases. The time-integrated spectral intensity also changes with the content of $B_4C$, and reaches the maximum value (3.05E7) when the content of $B_4C$ is 40 %. Therefore, when the mass content of $B_4C$ is 40 %, the average combustion intensity of the sample is the largest. This is attributed to the $CO_2$ gas generated during the combustion of $B_4C$ can help to break the liquid $B_2O_3$ oxidation film [14-15]. Thus, it can promote the contact between B and environmental oxygen (O).

## 3.2 Ignition Delay Time Analysis

Since the laser and the fiber optic spectrometer were connected by a synchronous trigger, the ignition delay time can be calculated by counting the appearance frame of the characteristic spectrum [16] (Fig. 5).

The ignition delay time initially decreases and then increases. It reaches the minimum value (111 ms) when the mass content of $B_4C$ is 40 %. This is because the heating rate of the laser is very fast [14], and the ignition delay time is influenced by both the ignition point and the temperature rise rate of the samples. On the one hand, the ignition point of $B_4C$ is lower than that of B, which is beneficial to the ignition. On the other hand, the $CO_2$ gas generated by $B_4C$ carries away a large amount of heat [17] and will slow the temperature rise rate.

## 3.3 Combustion Temperature Analysis

The average combustion temperature is defined as the average temperature in 2 s after the laser is turned on [18]. The change rules of the average combustion temperature are showed in Fig. 6.

As the content of $B_4C$ increases, the average combustion temperature decreases monotonically. This result indicates that although the addition of $B_4C$ is helpful to the increase the average combustion intensity, the effect of the heat loss caused by $CO_2$ is more important. It is noteworthy that the heat loss is a specimen surface heat loss. In the practical application of propellants, the heat taken away by $CO_2$ may also contribution to the engine working [19].

## 3.4 Micro-morphology analysis

Fig. 7 shows the micro-morphology of the sample with 40 % $B_4C$ before (a) and after (b) combustion.

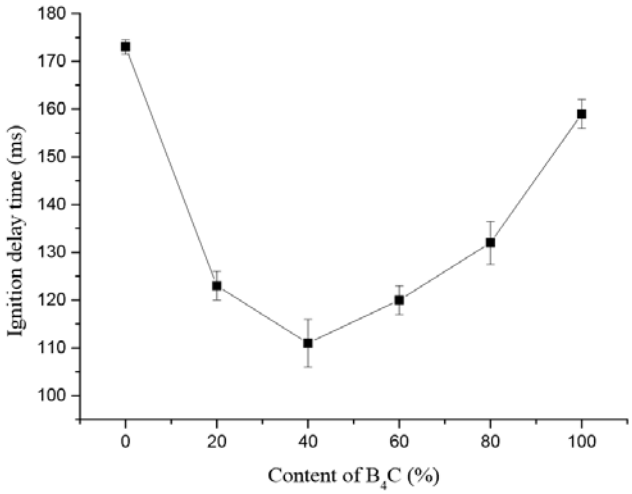


Fig. 5 Ignition delay time of the samples

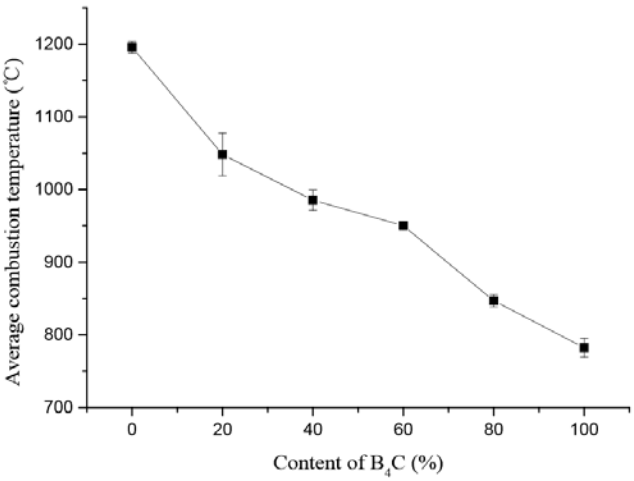


Fig. 6 Average combustion temperature of the samples

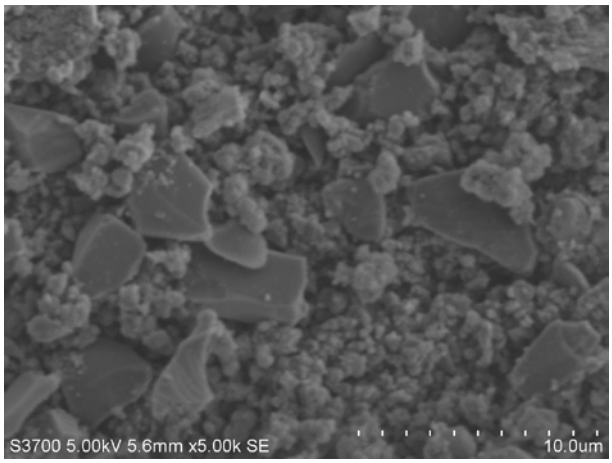

(a) Before combustion

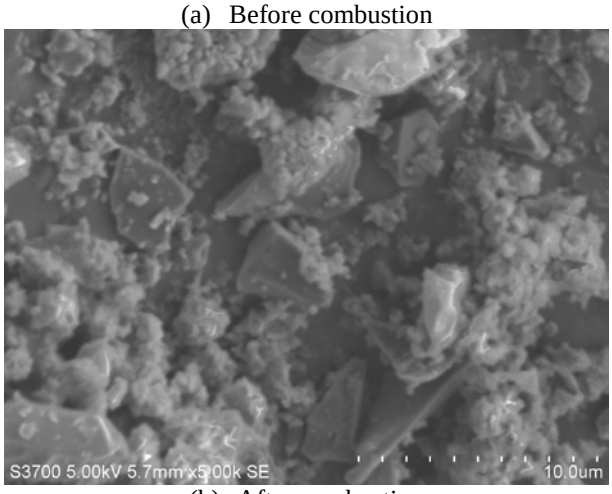

(b) After combustion

Fig. 7 SEM images of the sample with 40 % $B_4C$

Before combustion, large particles and small particles are independent and decentralized in the sample. According to the particle size information of the original materials, the large particles are mainly $B_4C$, and the small particles are mainly B. After combustion, the large particles are still recognizable. However, the small particles have agglomerated. During the combustion, an oxide layer generated and covered on the surface of the sample. The porosity of the sample decreased significantly.

## 4. Conclusion

The content of $B_4C$ has a significant effect on the ignition and combustion characteristics of $B/B_4C$ mixtures. As the content of $B_4C$ increases, the average combustion intensity increases at first, and decreases then. Inversely, the ignition delay time first decreases and then increases. When the mass content of $B_4C$ is 40 %, the average combustion intensity reaches the maximum value, and the ignition delay time reaches the minimum value (111 ms). The maximum combustion intensity and the average combustion temperature of the mixed samples decrease with the increase of $B_4C$ content. The micro-morphology of the sample with 40 % $B_4C$ changed a lot during the combustion. An oxide layer generated and covered on the surface of the sample. The porosity of the sample decreased significantly. Generally speaking, the addition of appropriate amount of $B_4C$ can improve the ignition characteristics of B, and is also beneficial to increase the average combustion intensity of B.

## 5. Acknowledgments

This work was funded by the National Natural Science Foundation of China (Grant No. 51106135).

## 6. References

[1] C. Mao, B. Li, S. Hu, Y. Wang. J. Propul. Technol. 22 (1) (2001) 6-9.
[2] A. Gany, Y.M. Timnat. Acta Astronaut. 29 (3) (1993) 181-187.
[3] L. Zang. J. Propul. Technol. 4 (1990) 56-62.
[4] M. A. Trunov, V. K. Hoffmann, M. Schoenitz, E. L. Dreizin. J. Propul. Power 24 (2) (2008) 184-191.
[5] J. Xi, J. Liu, Y. Wang, D. Liang, H. Li, J Zhou. Propell. Explos. Pyrot. 39 (6) (2014) 844-851.
[6] L. Liu, G. He, Y. Wang. J. Therm. Anal. Calorim. 114 (2013) 1057-1068.
[7] A.M. Mellor. AIAA J. 9 (1971) 1944-1947.
[8] C.L. Yeh, W.H. Hsieh, W. Felder. Int. J. Energ. Mat. Chem. Propul. 3 (1994) 1-6.
[9] K. Obuchi, M. Tanabe, T. Kuwahara. AIAA Paper. 46 (2008) 1-8.
[10] D. Liang, J. Liu, J. Xiao, J. Xi, Y. Wang, Y. Zhang, J. Zhou. Acta Astronaut. 112 (2015) 182-191.
[11] L. Liu, G. He, Y. Wang. Chin. J. Explo. Propel. 36 (2013) 46-51.
[12] W. Zhang, H. Zhu, D. Fang. Chin. J. Explo. Propel. 52 (1) (2002) 25-28.
[13] C. Li. Proc. Int. Pyroteeh. Semin. 20 (1994) 653-661.
[14] W. Ao, Y. Wang, H. Li, J. Xi, J. Liu, J. Zhou. Propell. Explos. Pyrot. 39 (2) (2014) 185-191.
[15] M.K. King. J. Spacecraft and Rockets 19 (4) (1982) 294-306.
[16] H.J. Fan, N.F. Wang, X. Z. Fan, D. L. Guan. J. Propul. Technol. 29 (1) (2008) 102.
[17] D. Liang, Z. Wang, J. Liu, Y. Zhang, W. Ao, J. Xi, J. Zhou. Chin. J. Energ. Mater. Chem. Propuls. 22 (2014) 386-91.
[18] D. Liang, J. Liu, J. Xiao, J. Xi, Y. Wang, J. Zhou. J. Therm. Anal. Calorim. (2015) DOI 10.1007/s10973-015-4750-6.
[19] A. M. Mellor. AIAA J. 9 (1971) 1944-1947.

**Proceedings of the Australian Combustion Symposium**
**December 7-9, 2015, The University of Melbourne**

# Investigation of smouldering combustion of biomass fuel

H. Wang[1,4,*], P. R. Medwell[1], C. H. Birzer[1], P. J. van Eyk[2], Z. F. Tian[1], M. Possell[3,4]

[1]School of Mechanical Engineering, The University of Adelaide, SA 5005 Australia

[2]School of Chemical Engineering, The University of Adelaide, SA 5005 Australia

[3]Faculty of Agriculture and Environment, The University of Sydney, NSW 2006 Australia

[4]Bushfire and Natural Hazards CRC, Melbourne, VIC 3002 Australia

## Abstract

Smouldering combustion can be a serious hazard because of its low ignition temperature, high toxic emissions and particulate matter emissions. Smouldering combustion plays an important role in bushfires, as most forest biomass fuels such as grass, leaves, bark and coarse woody debris are prone to smoulder. The majority of studies on smouldering combustion have been carried out on polyurethane foam, due to its importance in residential fires. However, there have been comparatively few studies on smouldering combustion with an emphasis on the initiation and spread of bushfires. In this paper, a smouldering combustion reactor is introduced which is used to initiate smouldering combustion by radiant heat flux and measure the product gas content and temperature inside the reactor. The aims of this preliminary study are to: identify the initiation of smouldering combustion in forest biomass fuel using the experimental apparatus; develop a method to determine the smouldering ignition of forest biomass fuel and; investigate the effects of radiant heat flux and air flowrate on the initiation of smouldering combustion. The results indicate that under the conditions presented in this paper solid biomass fuel directly transitions from pre-ignition to flaming combustion in a short period of time. However, it is found that radiant heat flux and air flow rate have a significant influence on the transition time. Hence, these parameters will be the focus of future work on the initiation of self-sustaining smouldering combustion.

*Keywords: Smouldering, Radiant ignition, Biomass combustion, Transition to flaming.*

## 1. Introduction

Smouldering combustion is a slow and low temperature form of combustion, which shows no flame. Smouldering combustion is sustained by the heat evolved when oxygen directly reacts at the surface of a condensed-phase fuel [1]. Biomass solid fuel subjected to external heating typically leads to three regimes: preheating, smouldering and flaming. This makes smouldering important to bushfires, especially in fire front propagation, because it provides a critical pathway from virgin biomass solid fuel to flaming combustion. As solid biomass fuel is heated, it first undergoes a preheating stage. Water evaporation and devolatilisation occur in this stage. After the preheating stage, the combustion of biomass solid fuel will occur in one of three ways, namely, smouldering combustion, smouldering to flaming combustion or direct flaming combustion. The conditions that lead to the three different regimes are complex and not well understood.

Smouldering combustion burns large amounts of biomass, because a fire-front typically only burns the superficial parts of biomass solid fuel, while self-sustained smouldering combustion can consume the biomass solid fuel almost completely [2]. Smouldering combustion causes significant damage to the forest ecosystem and prolongs its restoration time after a bushfire. Smouldering also causes significant damage to the soil ecosystem and contributes to atmospheric pollutant and greenhouse gas emissions [3]. Smouldering combustion is a serious fire hazard. From the point of ignitibility, smouldering can be initiated by weak heat sources (~6 kW/m$^2$), while flaming ignition typically requires fluxes of about 20 kW/m$^2$ or higher [4]. Once ignited, smouldering can last for a long period of time (typically days or weeks) and is difficult to extinguish [5]. Smouldering typically produces more toxic gases, such as carbon monoxide, than flaming combustion [1]. Although smouldering combustion has been widely investigated, fundamental understanding of smouldering, in particular the transition from ignition to self-sustained smouldering, still remains unknown. The conditions that lead to different combustion regimes are not well understood. The combustion characteristics, such as temperature, spread (propagation) rate, gas emissions and particulate matter are varied in the different combustion regimes. Hence, it is crucial to develop a comprehensive understanding of the effects of different conditions on smouldering ignition and identify which conditions leads to the various combustion regimes in solid biomass fuel.

Conduction, convection and radiation are the three major heat transfer mechanisms in a fire [6]. Previous research on smouldering combustion has largely focused on fires started by conduction or convection heat transfer mechanisms, because the majority of the work is for residential fires, where radiation may be less important than the other heating mechanisms. Radiation has effects on bushfire initiation and spread because it is one of the major heat transfer mechanisms. Despite a lack of experimental studies, there has been some previous modelling work done on smouldering combustion started

* Corresponding author:
Email: houzhi.wang@adelaide.edu.au

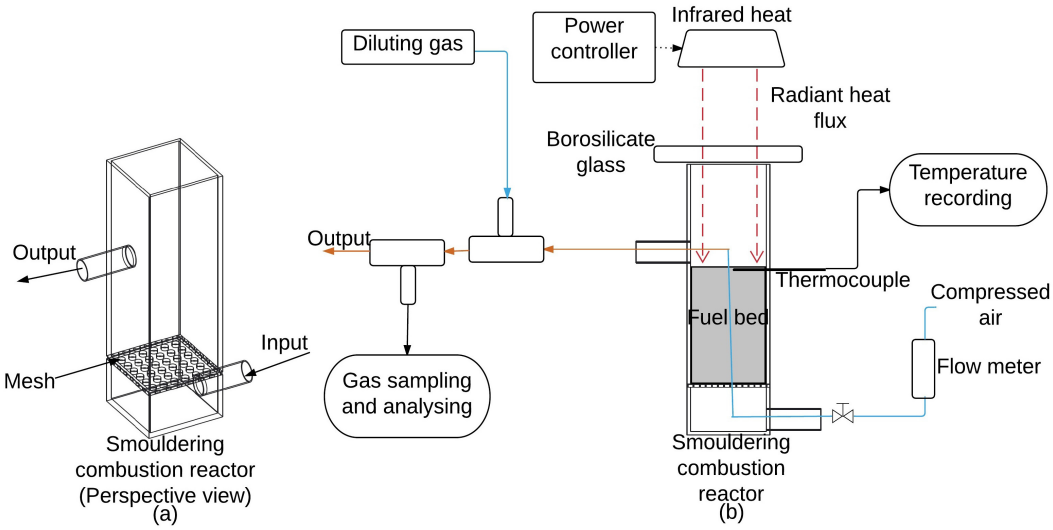


**Figure 1.** Experimental setup (a): Perspective view of smouldering combustion reactor, b): schematic diagram of the experimental setup)

by external radiant heating [7,8,9]. Therefore, the current study will concentrate on experimentally initiating smouldering combustion by radiant heating flux.

There are various approaches to characterise smouldering ignition. Temporal and spatial temperature profiles and mass-loss rates have been demonstrated to characterise two types of smouldering ignition: assisted ignition and true ignition (the initiation of self-sustained smouldering) [10,11]. During assisted smouldering combustion, the reactions are dominated by the external heating flux. The heat from the exothermic reactions cannot overcome the heat losses; therefore, the ignition will cease if the external heating input is eliminated. For self-sustained smouldering, the exothermic reactions provide sufficient heat to overcome the heat losses and drive the reactions. In this case, smouldering combustion is controlled by the heat generated by the exothermic reactions, but not external heating flux. Therefore, self-sustained smouldering combustion can continue without any external heating. However, to-date, there is no effective method to identify the initiation of the various type of smouldering combustion.

Smouldering combustion is a common type of combustion that occurs in fires; and it is difficult to detect the initiation of smouldering combustion. Common methods, such as temperature profile of fuel and visual observation cannot effectively identify the initiation of smouldering combustion [10,13]. This is mainly because smouldering combustion is a low-temperature and slow type of combustion. The potential of smouldering combustion to be a serious hazard requires investigations into other factors that could be used as indicators of the initiation of smouldering combustion and the transition from smouldering to flaming combustion. The focus of this research is on the fundamental study of smouldering combustion. The aims of this research are to understand the initiation of smouldering combustion and its transition to flaming combustion by radiant heat, indicate the initiation of smouldering combustion and flaming combustion using product gas content and temperature profile, and investigate the effects of radiant heat flux on the initiation of smouldering combustion.

## 2. Experimental Setup

The smouldering combustion reactor used for the experiments is shown in Figure 1(a). It has an air input near the bottom of the reactor, an output for sampling product gas, and a stainless steel mesh inside the reactor to distribute the air flow and support the biomass fuel sample. The reactor has a square cross-section of 35 mm × 35 mm and a height of 115 mm. Figure 1(b) shows a schematic diagram of the experimental apparatus. An infrared heat lamp (Research Inc. Model 5306B; United States) is placed above the reactor to heat the testing sample. The electrical power input into the heat lamp is a controlled variable during the experiments, spanning the range from 555W to 790W, which gives a range of radiant heat flux of 11.2 $kW/m^2$ to 15.9 $kW/m^2$ (measured with Medtherm Corp. 64 series heat flux sensor; United States) A gas analyser (Testo Ltd. Testo 350; Germany) is directly connected to the output of the reactor, which measures the CO, $CO_2$ and $O_2$ contents (dry basis) in the product gas. Based on the specifications of the gas analyser (Testo 350), the response times for the CO sensor (40 seconds) and $CO_2$ sensor (10 seconds) were taken into account when analysing the data. During the experiments, the flowrate of the gas analyser pump is 0.98 L/min, and the tube used to connect the gas analyser and reactor has an inner diameter of 8 mm and length of 1.5 m. Therefore, the flow time delay is calculated to be 4.6 seconds, based on the average pump flowrate, inner diameter and length of the silicone tube.

A type-K thermocouple (TC-Direct; Australia) is buried in the fuel bed, 2 – 3 mm beneath the fuel surface (below one pine chip particle). According to the specifications of the thermocouple, the response rate is $210ºC \cdot s^{-1}$. The air supply is set to 7 grams/min. This flowrate avoids the entrainment of ambient air into the top of the reactor. Pulverized and dried pine chips are

used as fuel in the study. The pine chips were milled and sieved (2 mm < d < 3 mm size) and then were dried in an oven at 100ºC for 12 hours. This was done to maintain a consistent particle size in the experiments and eliminate a potential source of uncertainty. During the experiment, the testing sample is heated for 25 minutes or until flaming combustion occurs. The gas analyser and temperature recording are started when the heat lamp is turned on. The infrared heat lamp was switched off after flaming ignition occurred and the air input was temporarily closed to extinguish the flaming combustion. After the flaming combustion was extinguished, the air flow rate was turned back on to the previous value (7.0 grams/min).

## 3. Results and Discussion

In Figure 2, it was found that char combustion occurs after flaming combustion is extinguished. As the measurements of CO and $CO_2$ concentration indicate that ongoing combustion occurred. Therefore, it is evident that the continued smouldering combustion after the flaming ignition is self-sustained in this case, as the external heat source is eliminated. Figure 2 indicates that under these smouldering combustion conditions the $CO_2$ emissions are approximately twice as much as the CO (~20,000 ppm and ~10,0000 ppm, respectively). Compared to the flaming ignition, the average gas concentration of CO and $CO_2$ during the sustained smouldering combustion are much less than during the transition from no ignition to flaming ignition, although the emissions during steady-state flaming combustion are expected to yield a higher CO to $CO_2$ conversion.

The temporal gas contents and temperature profiles under radiant heat flux 11.2 kW/m$^2$ are shown in Figure 3. The results in Figure 3 shows a transition from no ignition to flaming combustion, as both CO and $CO_2$ gas contents are in the flaming combustion range (according to Figure 2). The transition takes place in a short period of time (35 seconds). The sensors of the gas analyser have a longer response time than the time of the transition; therefore, it is difficult to accurately interpret the transition based on the emission curves of carbon monoxide and carbon dioxide. Flaming combustion was visually observed at the end of the curve (1242 seconds) in Figure 3, which can be indicated by the rapid temperature rise in the temperature profile. However, the heat lamp was still on during the transition, hence, it is difficult to determine whether the transition from smouldering to flaming combustion is initiated by the radiant heat flux. It may be the case that the transition from smouldering to flaming combustion is dominated and initiated by the heat generated by the smouldering combustion. Future research will concentrate on understanding the transition from smouldering to flaming combustion; and the conditions that lead to the transition.

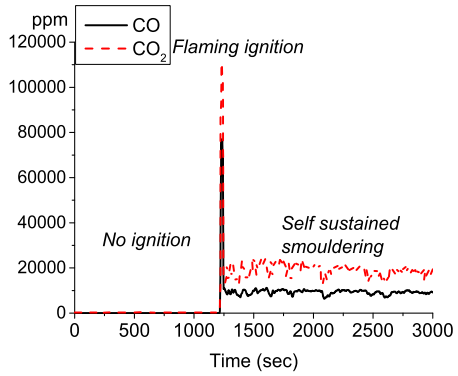


**Figure 2.** Temporal CO and $CO_2$ profile during three phases: no ignition, flaming ignition and self-sustained smouldering (output power: 555W (11.2 kW/m$^2$) and the external heating was removed after the flaming ignition, air flow rate: 7.0 grams/min, dry basis)

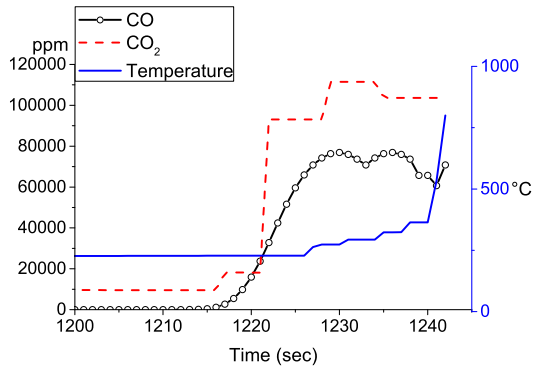


**Figure 3.** Temporal CO, $CO_2$ and temperature profile during the transition from no ignition to flaming combustion (output power: 555W (11.2 kW/m$^2$), air flow rate: 7.0 grams/min, dry basis)

The temporal gas content profiles for CO, $CO_2$ and $O_2$ in the product gas under different radiant heat flux are shown in Figure 4. The curves stop at the '×', as flaming combustion occurs. Flaming combustion (rapid increasein both CO and $CO_2$) occurs in less than 960 seconds when the radiant heat flux is equal or greater than 11.2 kW/m$^2$. In the cases of 11.2 kW/m$^2$, 13.5 kW/m$^2$ and 15.9 kW/m$^2$, the transition from no ignition to flaming combustion occurs. The results in Figure 4 indicate that the transition from no ignition to flaming combustion occurs when the radiant heat flux is equal or greater than 11.2 kW/m$^2$ for 1240 seconds. Gratkowski *et al.* [13] suggest the minimum radiant heat flux required for the smouldering ignition of wood is 12.5 kW/m$^2$ for 1800 seconds. The minimum required radiant heat flux for the studies are of a similar order of magnitude, but the ignition time in the Gratkowski *et al.* study is 560 seconds longer than the current study. This difference indicates that fuel type, air flow and particle size could have influences on the minimum required radiant heat flux for smouldering ignition. These results suggest that under the current experimental setup and settings, smouldering combustion will be initiated and followed by a transition to flaming combustion. There are several possible reasons for the direct transition to flaming combustion. For example, the high air flowrate in the current experiment could provide high oxygen availability, which facilitates oxidation reactions, and cause the transition to flaming combustion. This may explain why the minimum radiant heat flux for flaming

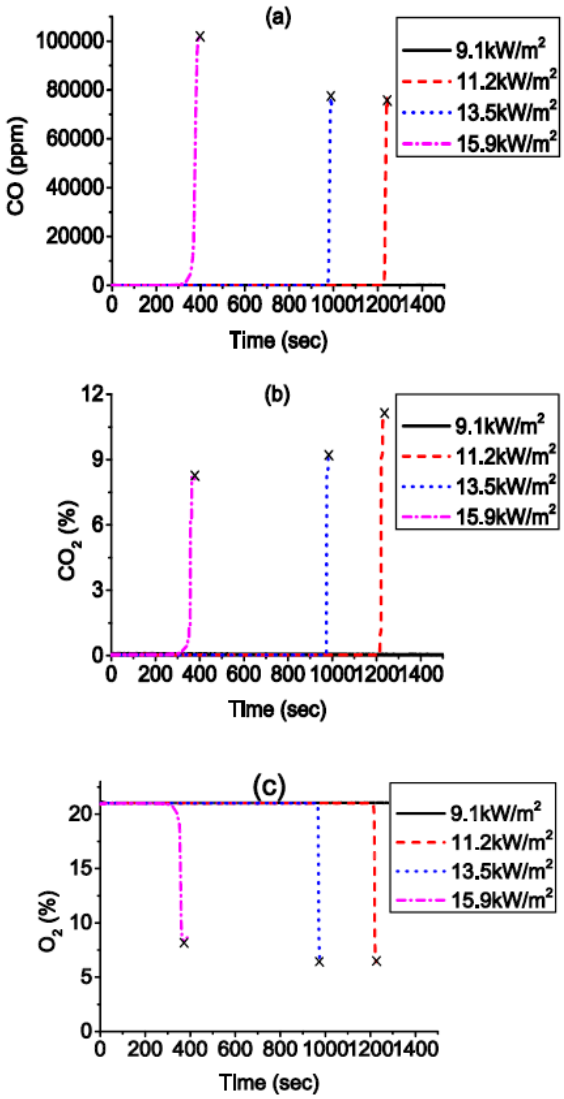


**Figure 4.** Effects of radiant heat flux on the time required to initiate flaming ignition and gas emissions of pulverised pine chips at air flow rate of 7 grams/min (a) CO, (b) $CO_2$, (c) $O_2$.

ignition of wood, as reported by various studies, are much higher than the minimum radiant heat flux found in this study; as most of the previous studies were conducted in quiescent air [12,13,14]. It is also possible to hypothesise that small particle size may increase the oxygen access, which makes it easier to initiate flaming combustion. Therefore, further research is required to examine these hypotheses.

## 4. Conclusion

Smouldering combustion is common in bushfires and other fire events. It is usually easier to initiate smouldering combustion than flaming combustion, as the initiation of smouldering combustion normally requires less heat than flaming combustion. Moreover, it is difficult to extinguish or detect smouldering combustion, as smouldering combustion does not have obvious indications, such as high temperature or visible flame. In the context of bushfires, smouldering combustion can be initiated by the radiation emitted from the fire front. Once ignited, smouldering combustion can last for a long period of time, and can transition to flaming combustion under certain conditions. This study investigated the initiation of smouldering combustion in biomass fuel by radiant heating. Pulverised pine chips with a particle size between 2 mm and 3 mm were heated by an infrared heat lamp. The effects of radiant heat flux on the initiation of smouldering combustion and the characteristics of smouldering ignition were measured using temperature and gas concentration profiles. The results demonstrate that the radiant heat flux and air flow rate have influences on the CO and $CO_2$ emissions during the transition. It was found that the minimum radiant heat flux required to initiate the transition from no ignition to flaming combustion is around 11.2 kW/m$^2$, which is less than the values reported previously. However, only the transition from pre-ignition to flaming combustion was achieved. Based on the parameters used in this study, the transition from smouldering to flaming combustion occurred over a short time. The results have indicated that radiant heat flux and air flow rate has a great effect on the time to the transition and should be the focus of future experiments.

## 5. Acknowledgments

The support of the University of Adelaide and the Bushfire and Natural Hazards CRC are gratefully acknowledged. The authors would like to thank Mr Marc Simpson for his assistance throughout the experimental campaign.

## 6. References

[1] Ohlemiller, T. SFPE Handbook of Fire Protection Engineering, Massachusetts, U.S., 2002, pp. 2-200.
[2] Hyde, J., Smith, A., Ottmar, R., Alvarado, E. and Morgan, P. Int J Wildland Fire **20** (2) (2011), pg. 163.
[3] Rein, G. Int Rev Chem Eng **1** (2009), pp. 3-18.
[4] McAllister, S. Fire Safety J **61** (2013), pp. 200-206.
[5] Svensen, H., Dysthe, D., Bandlien, E., Sacko, S., Coulibaly, H. and Planke, S. Geology **31** (2003), pg. 581.
[6] Drysdale, D. Fire Safety J **9** (1985), pg. 301.
[7] Sullivan, A., Ellis, P. and Knight, I. Int J Wildland Fire **12** (2003), pg. 101.
[8] Weber, R. Combust Flame **78** (1989), pp. 398-408.
[9] Morandini, F., Perez-Ramirez, Y., Tohay, V., Santoni, P. and Barboni, T. Int J Therm Sci **70** (2013), pp. 83-91.
[10] Anderson, M., Sleight, R. and Torero, J. Fire Safety J **35** (2000), pp. 131-147.
[11] Hadden, R., Alkatib, A., Rein, G. and Torero, J. Fire Technol **50** (2012), pp. 673-691.
[12] Bilbao, R., Mastral, J., Aldea, M., Ceamanos, J., Betrán, M. and Lana, J. Combust Flame **126** (2001), pp. 1363-1372.
[13] Lawson, D. I., and D. L. Simms. BR J Appl Phys **3** (1952), pg. 288.
[14] Gratkowski, M., Dembsey, N. and Beyler, C. Fire Safety J **41** (2006), pp. 427-443.

# Degradation and Combustion Behaviours of Some Thermoplastics with Potential Use as Hybrid Rocket Fuels

P. Joseph[1, *], V. Novozhilov[1], R. Zhang[2]
[1]Centre for Environmental Safety and Risk Engineering, Victoria University, PO Box 14428, Melbourne 8001, Victoria, Australia
[2]School of Mechanical and Aerospace Engineering, Queen's University Belfast, BT9 AH, Northern Ireland, UK

## Abstract

In our quest for the identification of safer fuels for hybrid rocket propulsion, we have evaluated the degradation behaviours and combustion attributes of some common commodity plastics in small scale laboratory scale experiments. These mainly included: thermo-gravimetry (TGA), oxygen bomb calorimetry, and optionally, pyrolysis combustion flow calorimetry (PCFC). During the course of our investigations, we have also tried to seek correlations between the kinetic parameters, obtained through the TGA analyses, and other related intrinsic properties of some of the materials, to the fuel regression rates in the context of hybrid rocket propulsion. It was also observed that the heat release capacity values from the PCFC measurements, for materials that underwent single step degradation leaving little, or no char residues, correlated well with the data obtained from oxygen bomb calorimetry. It was inferred that the heat release capacity, an intrinsic and intensive property of material, could be considered as a reliable indicator of the flammability, and hence directly related to the heat release rates and the maximum enthalpy of combustion of the materials in question. Therefore, the heat release capacity can be taken as a suitable indicator of the heat release rate per unit surface area of a material, and hence reflects its suitability as a safer alternative fuel for hybrid rocket propulsion.

*Keywords: Chain-growth polymers; Thermal degradation; Heats of combustion; Regression rate; Heat release capacity*

## Nomenclature

| | |
|---|---|
| $E_a$ | activation energy (kJ/mol) |
| $A$ | Arrhenius parameter (1/s) |
| $\beta$ | heating rate (K/s) |
| $\eta_c$ | heat release capacity (J/g K) |
| $k$ | reaction rate constant (1/s) |
| $h_c$ | specific heat of combustion (J/g) |
| $\dot{Q}''$ | heat release rate per unit area |
| $\partial$ | degradation zone thickness |

| | |
|---|---|
| HRR | heat release rate |
| pHRR | peak heat release rate |
| PCFC | pyrolysis combustion flow calorimetry |
| TGA | thermo-gravimetric analysis |
| THR | total heat released |

| | |
|---|---|
| EVA | polyethylene-co-vinyl acetate |
| E/P | ethylene/propylene copolymer |
| HDPE | high density polyethylene |
| HTPBD | hydroxy-terminated polybutadiene |
| LDPE | low density polyethylene |
| PE | polyethylene |
| PiB | polyisobutylene |
| PMMA | polymethyl methacrylate |
| PP | polypropylene |
| R/C | natural rubber containing Carbon black |
| VA | polyvinyl alcohol |

| | |
|---|---|
| B | Boron |
| Si | Silicon |

## 1. Introduction

Hybrid propulsion has been developed as an attractive alternative to conventional liquid and solid rocket motors with the view of achieving safer and more flexible space vehicle launching and manoeuvring [1]. It is well known that traditional liquid and solid rocket motors suffer from certain drawbacks. For example, liquid systems require quite complex and costly plumbing. Solid systems, on the other hand, are inherently unsafe due to uniform mixing of fuel and oxidizer.

Hybrid systems provide an alternative to both conventional technologies by executing combustion in diffusion mode, i.e. with initial separation of fuel and oxidizer. Most often, solid fuel (non-energetic polymer) and liquid oxidizer are used. Such arrangement provides operationally flexible, safe and reasonably priced technology.

A major disadvantage of hybrid systems is low thrust. This is a major obstacle for a wider use of Hybrid Rocket Engines [2]. Essentially, the non-energetic nature of fuels gives rise to requirement of very high regression rates, in order to achieve the required thrust. In practice this leads to necessity to use multiple ports, and other modifications that complicate the design.

Encouraged by the results from our previous work, we report here on our continuing efforts to identify safer fuel systems, among ordinary thermoplastic materials, as

* Corresponding author:
Phone: (+61) 3 99198134
Email: paul.joseph@vu.edu.au

potential and safer candidates for hybrid rocket propulsion [3].

## 2. Materials and Methods

In the present work, with a view to screening a wider range of common chain-growth polymers, we have selected the following materials: LDPE, HDPE, PP, E/P, PiB, R/C, EVA and EVOH. The polymeric materials were sourced locally, except PiB and EVOH (from Aldrich chemical company), and all of them were used without further purification. R/C (with about 5 wt.% loading of carbon powder) was chosen to see if the filler has any effect on the general degradation profile of the base elastomer [1]. EVA and EVOH, owing to their oxygenated nature, are assumed to possess lower calorific values; however they are related to each other and EVA to the polyethylene-analogues that were selected for the study (i.e. LDPE and HDPE). In addition, we envisaged a two-stage decomposition for EVA, and smaller but noticeable char residues for EVOH, as compared to the corresponding polyolefin-based fuels (i.e. LDPE, HDPE, PP, E/P and R/C).

The TGA runs were carried out, either in nitrogen or in oxygen and at different heating rates (5, 10, 15, 20 and 25$^{o}$C/min), on sample masses in the range of *ca.* 10-20 mg, from 30 to 700$^{o}$C in a Mettler Toledo TGA/SDTA851e instrument. Specific heats of combustion, $h_c$, were measured using an oxygen bomb calorimeter using IKA C200 instrument (Table 1). PCFC measurements were carried out using a Fire Testing Technology Ltd (FTT) Micro Calorimeter, which basically works on the principle of oxygen consumption calorimetry [4]. The instrument generates plots of the heat release rates (HRR) against time, and gives values for the maximum amount of heat released per unit mass per degree of temperature (i.e. heat release capacity measured in J/g K), the latter being a reliable indicator regarding flammability of a material. Furthermore this quantity, $\eta_c$, is proven to be an intensive and intrinsic property of the material under consideration [5].

## 3. Results and Discussion

Table 1. Values of the specific heats of combustion (from bomb calorimeter experiments)

| Sl. No. | Sample | Specific heats of combustion (J/kg) |
|---|---|---|
| 1 | LDPE | 46.4 |
| 2 | HDPE | 46.5 |
| 3 | PP | 46.4 |
| 4 | E/P | 46.5 |
| 5 | PiB | 46.4 |
| 6 | R/C | 43.3 |
| 7 | EVA | 40.7 |
| 8 | EVOH | 29.4 |

As can be seen from the table, the specific heat of combustion values for the polyolefins are remarkably constant (around 46.5 J/g). Here, as the combustion was performed in an excess amount of oxygen, we could also assume that runs resulted in complete combustion of the materials. Therefore, the values obtained should be their gross calorific values, and thus reflect the total heat energy obtainable under very rapid combustion conditions similar to those prevailing in a typical hybrid rocket engine. In principle, these values could be computable from the individual bond dissociation energies, under standard conditions, and assuming that the materials are pure (i.e. from their standard heats of formation).

The specific heat of combustion of a material is an intrinsic and intensive quantity, and should be able to be correlated with fundamental quantities of similar nature, for instance the heat release capacity (as measured in PCFC). In addition, as in common with any other additive property of a polymeric material, both $h_c$ and heat release capacity values ($\eta_c$) are computable from considering the corresponding molar group contributions [5].

It can be also noticed from the table that for the elastomeric material (R/C), the $h_c$ value is comparatively lower (43.3 MJ/kg), and this could be attributed to the presence of internal double bonds, and hence higher C/H ratio as compared to the saturated counterparts (i.e. LDPE, HDPE, PP and PiB), and to the presence of the carbon filler (*ca.* 5 wt.%). However, owing to radiative heat transfer mode associated with carbon black, under the operating conditions and the time scales prevailing in a real life hybrid motor, the presence of carbon particles could be of an added value [1].

As is expected with oxygenated substrates, like EVA and EVOH, the $h_c$ values were lower, with further and marked decrease with lowering of the C/O ratio (EVOH). Considering the above factors, we chose PP, E/P and PiB, as representative and promising materials for further kinetic evaluations, and with a view to identifying any possible correlations between the measured parameters.

The thermograms obtained for PP, E/P and PiB, in oxygen atmosphere and at different heating rates were analyzed using the method of Flynn and Wall to obtain the Arrhenius parameters. Here the relation assumes the following form [6]:

$$\log \beta = -2.315 + \log\left(\frac{AE_a}{R}\right) - \log g(\alpha) - 0.4567\left(\frac{E_a}{RT_\alpha}\right) \quad (1)$$

where $\beta$ is the heating rate and $\alpha$ is the fraction of the material degraded. Therefore, plots of *log$\beta$ vs 1/T* were constructed for each value of $\alpha$, and then the $E_a$ values were calculated from the slopes of the linear dependence (see, for example, Fig. 1 and Fig. 2 for PP). From the plots, the values of $E_a$ and $A$ were calculated for each value of $\alpha$ (Table 2). Even though the three chosen substrates (PP, E/P and PiB) underwent degradation through a steep one-step process, the values of $E_a$ and particularly $A$ were found to vary, and that the degrees of variations were also different for the three materials. The

major pathways of degradation of the materials could be considered to be of random chain scissions followed by various amounts of chain stripping. Closer examinations of the thermograms of the materials, obtained under nitrogen and oxygen, do bring out noticeable changes in their overall profiles.

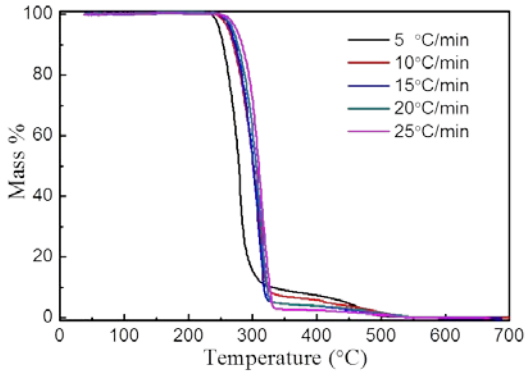

Fig. 1 Thermograms of PP in oxygen at different heating rates

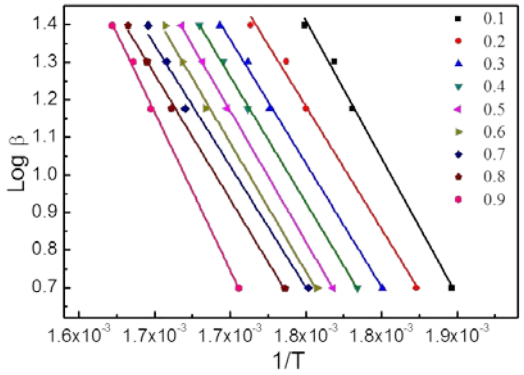

Fig. 2 Log β vs 1/T plots for PiB at different values of α

However, such differences can be assumed to be absent in bomb calorimetric runs, as a near complete and rapid combustion is effected by using a large excess of oxygen under a very high pressure. Here, given that all three substrate are saturated alkanes in chemical composition, and that the effects of any additives present are negligible, then their gross calorific values should be quite similar, and indeed this was found to be true (see Table 1).

In TGA analyses, since the sample is subjected to a pre-determined heating ramp, the thermal, or thermo-oxidative, degradations and the absence of any flaming mode of combustion make the situation substantially different to what the sample will be made to undergo in a bomb calorimeter, or in a test rocket motor. Therefore, the correlations, if found, between the Arrhenius parameters obtained from TGA thermograms with those of the empirical quantities, such as the regression rate obtained from a test rocket motor, should be treated with caution.

Table 2. Arrhenius parameters for PP, E/P and PiB obtained from TGA runs in oxygen (quoted at α = 0.5)

| Sl. No. | Sample | $E_a$ (kJ/mol) | A (1/s) |
|---|---|---|---|
| 1 | PiB | 80 | $10^9$ |
| 2 | PP | 127 | $10^{13}$ |
| 3 | E/P | 166 | $10^{17}$ |

The heat release capacity, $\eta_c$, which can be determined using PCFC, could be taken as a more reliable indicator of the performance of the fuel materials in the context of hybrid rocket propulsion. It was shown to be an intrinsic and intensive property for pure materials, and owing to the additive nature of the particular contributions from the molar constituents of a material, $\eta_c$, can be calculated from the relevant data [5]. In addition, as forced combustion in the presence of an excess amount of oxygen is also ensured during the final stage of a PCFC run, the value of $\eta_c$ so obtained should be a true reflection of the gross calorific value of a fuel- see for example the data, for some common fuel types used in hybrid rocket engines, obtained in our laboratories (Table 3).

Table 3. Specific heats of combustion and heat release capacity values for typical hybrid rocket fuels (from PCFC runs)

| Sl. No. | Sample | $h_c$ (J/g) | $\eta_c$ (J/K g) |
|---|---|---|---|
| 1 | PMMA | 25.51 | 397.00 |
| 2 | HTPBD | 40.83 | 560.06 |
| 3 | Wax | 44.56 | 575.64 |
| 4 | PP | 50.59 | 1282.62 |

It is evident from the table that as the gross calorific values of the fuels increase, their heat release capacity values also increases. Therefore, assuming near complete combustion in hybrid rocket engines, where liquid oxygen is commonly used as the oxidant, the heat release capacity could be taken to be directly related to the fuel regression rate. The validity of such an assumption precludes the dependence of the regression rates on the size morphology, configuration and the operating constraints of the rocket motor [7].

From a practical point of view, the Arrhenius parameters are deduced from dynamic TGA runs at comparatively low heating rates (*ca.* 5 to 25°C/min) where competing reactions are practically more resolved and the consecutive reaction can be assumed to occur sequentially. Under these conditions, the calculated activation energies could be of value, however, the *A* values do not necessarily reflect the underpinning physio-chemical processes occurring when a solid polymer undergoes degradation. In addition, the situation can be further complicated owing to the presence of multi-components and/or phases [8].

The heat release capacity, $\eta_c$, values can be obtained considering an appropriate analytical relation, of the following form [5]:

$$\eta_c = \frac{h_c^0(1-\mu)E_a}{eRT_p^2} \qquad (2)$$

Where $h^o{}_c$ (J/g) is the heat of complete combustion of the pyrolysis gases, $\mu$ (g/g) is the the weight fraction of the solid residue after pyrolysis or burning, $E$ (kJ/mol) is the global activation energy for the single-step mass-loss process or pyrolysis, $T_p$ (K) is the temperature at peak mass loss rate, and $e$ is the natural logarithm base and $R$ is the Universal gas constant. Extensive PCFC data has been collated for a wide variety of common polymers,

and these include: the heat release capacity (J/g K), total heat release (kJ/g) and the char yields (g/g)- here the former quantities denote the calorific value of a material, whilst the latter reflects the degree of completion of the combustion process itself [5].

Generally, there are two main problems that must be distinguished when addressing the issue of insufficient thrust in hybrid rocket motors. If a particular solid fuel is chosen then the problem translates into the necessity to increase fuel regression rate (this is the problem statement most often found in the literature devoted to hybrid engines). Another problem, however, appears when one has a choice of fuels, or proposing new fuel formulation. In comparing different fuels the relevant parameter is a heat release rate per unit surface area of the solid fuel, $\dot{Q}"$, and not just its regression rate.

It is this latter problem that is being considered in the present paper. Prediction of exact values of fuel regression and heat release rates in hybrid engines is a difficult task. It has to be achieved by either very demanding CFD modeling, or at least by experimentally verified phenomenological correlations. The latter are also fairly complicated [7]. We argue however that the problem of *solid fuel ranking* in terms of their quality for application in hybrid engines is simpler. We propose to use for this purpose a Heat Release Capacity as introduced by Walters and Lyon [5]. Heat Release Capacity is a parameter that can be measured using the standardized procedure.

Furthermore, in their investigation [see for example, in 9] Walters and Lyon directly and experimentally demonstrated that average flaming Heat Release Rate of the material (under external flux, which in case of a hybrid engine will be heat feedback from flame sheet to the material surface) linearly increases with the material's Heat Release Capacity. Most importantly, Heat Release Capacity can be theoretically calculated from additive molar group contributions. This makes this parameter extremely useful in testing new potential hybrid fuel formulations.

In the context of hybrid rocket propulsion, ideally a promising fuel should have relatively higher values for the HRR, THR and the Heat Release Capacity, while the amount residue after combustion should be the minimum. Given that the chemical constituent structures of the three potential fuels under consideration are known, we could also calculate the heat release capacity by treating the molar group contributions as additive in nature [5]. The data thus obtainable for hydrocarbon based polymeric substrates could be then utilized to gauge their efficacies as hybrid rocket fuels.

In any case, it would be highly desirable to correlate simple and empirical intrinsic properties such as gross calorific values, heat release capacity, etc., with the actual fuel heat release rate per unit area, $\dot{Q}"$. In terms of the degradation rate, $\dot{Q}"$ , can be related taking also into account of the relationship given by Lengelle et al. [10]:

$$\dot{Q}" = \rho \dot{r} h_c \approx \rho h_c k(T_s) \partial = \rho h_c A exp(-\frac{E_a}{RT}) \partial \qquad (3)$$

where $k$ is the degradation rate, $T_s$ is the temperature of the surface of the fuel, $\partial$ is the degradation zone thickness of the fuel. According to Lengelle et al. the typical temperature of the fuel surface of polyethylene (PE) in a hybrid rocket engine is about 950 K, which will also ensure the complete degradation of the three substrates under consideration, as inferred from their thermograms. The results obtained through our previous work, on chemically modified PP and PMMA systems with Si-containing groups, we were able to successfully correlate $k(T_s)$, i.e., the degradation rate constant of the modified and virgin PP and PMMA, to their possible regression rates, $\dot{r}$ [3].

## 3. Main conclusions

By carrying out PCFC measurements, we have now identified that the heat release capacity factor, $\eta_c$, can truly reflect the efficacy of a material and its possible performance in a test rocket motor, and thus can be correlated to regression rates, $\dot{r}$ . Given that this parameter are computable for most of the common polymers, such correlations opens up enormous opportunity to screen a wide variety of polymeric substrates in the context of finding safer fuel systems for hybrid rocket propulsion. As the next step, we intend to carry out simple chemical modifications of the promising substrates, with either Si-, or B-, containing groups, and then compare their efficacies, relative to the un-modified counterparts.


### 4. Acknowledgements

One of us, RZ, is grateful to the Zhejiang University, China, for the provision of post-doctoral fellowship. The authors also wish to thank the Engineering and Physical Sciences Research Council (EPSRC), UK, for the financial support (grant number: EP/F068867/1).


## 5. References


[1] V. Novozhilov, P. Joseph, K. Ishiko, T. Shimada, H. Wang and J. Liu. Energies. **4** (2011), pp. 1779-1839

[2] M.J. Chiaverini, N. Serin, D.K. Johnson, Yeu-Cherng Lu, K.K. Kuo, and G. A. Risha. Journal of Propulsion and Power. **16** (1) (2000), pp. 125-132

[3] K. Kitagawa, P. Joseph, V. Novozhilov and T. Shimada. Int. J. Energ. Mater. Chem. Propul. **11** (6) (2012), pp. 549-566

[4] S. Tretsiakova-McNally and P. Joseph. Polymers.**7**(3), (2015), pp. 453-467

[5] R.N. Walters and R.E. Lyon. J. Appl. Polym. Sci. **87**, (2003), pp. 548-563

[6] J.H. Flynn and L.A. Wall. Polym. Lett. 4, (1966), pp. 323-328

[7] G. Zilliac, M.A. Karabeyoglu, Hybrid Rocket Fuel Regression Rate Data and Modeling, 42nd AIAA/ASME/SAE/ASEE Joint Propulsion Conference and Exhibition, California, 2006, p.1

[8] P. Budrugeac. Polym. Deg. Stab. **71**, (2001), pp. 185-187

[9] R.E. Lyon. Fire Mater. **24**, (2000), pp. 179-186

[10] G. Lengelle, B. Fourest, J. Godon and C Guin, Condensed-phase Behavior and Ablation Rate of Fuels for Hybrid Propulsion, 29th AIAA/ASME/SAE/ASEE Joint Propulsion Conference and Exhibition, California, 1993, p.1

**Proceedings of the Australian Combustion Symposium**
**December 7-9, 2015, The University of Melbourne**

# Use of Beneficiated Victorian Brown Coal for Blended Combustion in PCI Blast Furnaces

Anthony De Girolamo[1], Alex Grufas[1], Ilia Lyamin[1], Iori Nishio[2], Yoshihiko Ninomiya[2] and Lian Zhang[1, *]
[1]Department of Chemical Engineering, Monash University VIC 3800, Australia
[2]Department of Applied Chemistry, Chubu University, Aichi 387-8501, Japan

## Abstract

The prospect of blending PCI coal with a lower cost char, derived from Yallourn brown coal, is evaluated in this study by means of thermogravimetric analysis (TGA), flat flame burner reactor and drop tube furnace experiments at four different blending ratios as well as CFD modelling. Yallourn char has desirable properties compared to the PCI coal including a lower ash content and higher heating value, although the reactivity is lower and ignition temperature is higher. The combustion behaviour of a blend is not always easily predicable based on the performance of the individual fuels. The drop tube furnace used in this study has a unique system for preheating secondary gas to achieve similar conditions to that in a blast furnace. The blends were tested at three temperatures (800, 900, 1000°C) and four $O_2$/C ratios (range 0.7-1.3). The results indicate that the behaviour of blends is synergistic, i.e. better burnout performance from blending can be obtained compared to predictions based on weighted-averages of pure components. The increase in ignition temperature and time delay with blending ratio was less than expected from a linear weighted-average prediction model. At a blend ratio of 40-60%, the burnout was maximised in the drop tube furnace with higher $O_2$/C ratios, although the ignition of blends is delayed compared to the pure PCI.

*Keywords: Pulverised coal injection, blending, lignite, brown coal, Victorian brown coal*

## 1. Introduction

One of the promising applications for Victorian brown coal (VBC) is as a substitute for bituminous coals used in pulverised coal injection (PCI) in a blast furnace. This may be achieved as a blend or as a complete replacement. VBC contains a relatively high amount of moisture and has a low ash yield. It is predominantly used for electricity generation at local power plants where it is inefficient and very carbon intensive [1].

A previous study has confirmed the viability of a complete replacement of commercial PCI coal with two chars derived from Yallourn brown coal [2]. The brown coal char replacement shows both beneficial and detrimental effects on the performance. Yallourn char has a lower cost compared to PCI coal and contains a higher calorific value, meaning it can replace a greater portion of coke. It also has lower ash and moisture contents. On the other hand, the previous study showed that Yallourn char has a higher ignition temperature due to the its lower volatile content, which in turn would cause a delay before combustion can begin as well as having lower char reactivity. Char can be blended with the normal PCI coal to balance these characteristics, however it is not easily foreseeable how the created blend will behave due to possible synergistic interactions between different coals or chars [3]. This means that measured performance indicators such as ignition and burnout may differ from a linear prediction based on the individual fuel. In addition, since blending is always the first strategy to be used for a new fuel, this work is expected to shed light on the use of Yallourn char as a blend fuel for the combustion in an industrial boiler/furnace.

This study aims to clarify the ignition and burnout of Yallourn semi-coke blended with a commercial PCI coal in a lab-scale DTF, which is able to pre-heat the gas temperature up to 1000°C to mimic the raceway region where hot blast temperature is 1000 to 1200° [4]. Understanding the behaviour of a solid fuel in the raceway of a blast furnace is pivotal, which will help minimise the amount of unburnt particles to be entrained into and block the gas passage in the blast furnace. It is of interest to maximise the replacement of PCI coal and thus have a greater content of Yallourn char in the blend in order to reduce fuel costs and ash burden. Additionally, if a Yallourn char blend is chosen with a higher calorific value than PCI coal, a higher coke replacement ratio would be achieved and thus additional cost savings in coke requirement would ensue. The obtained results can provide an insight into the previously unexplored application of brown coal to blast furnaces via the PCI method. Such a prospect would reduce the reliance on more expensive PCI coal as well as coking coals, diversify the use of Victorian brown coal by creation of a product that can be exported to the international market.

## 2. Method

Yallourn char for this study is obtained by pyrolysis of raw wet Yallourn brown coal in a pilot scale shaft furnace. As in the previous study [2], two types of Yallourn char were produced under different conditions. These will be referred to as Yallourn char 1 (YC-1) and Yallourn char 2 (YC-2). The most common size fraction was taken from each of these (1-4 mm), ground to a size of <106 microns and mixed with a commercial PCI coal at four different blending ratios from 20% (mass fraction) to 80% char with the remaining PCI coal. The

* Corresponding author:
Phone: (+61) 3 9905 2592
Email: lian.zhang@monash.edu

proximate and ultimate analysis of both fuels is shown in Table 1.

Table 1: Proximate and ultimate analysis of fuels

| | YC-1 | YC-2 | PCI coal |
|---|---|---|---|
| Proximate analysis | | | |
| Moisture % *ar* | 10.2 | 1.2 | 1.9 |
| Ash % *db* | 6.7 | 5.2 | 8.7 |
| Volatile matter % *db* | 5.8 | 4.5 | 20.7 |
| Fixed carbon % *db* | 77.3 | 90.3 | 70.6 |
| Ultimate analysis % *db* | | | |
| Carbon | 87.1 | 93.22 | 80.84 |
| Hydrogen | 1.2 | 0.49 | 3.90 |
| Oxygen | 3.310 | 0.00 | 4.894 |
| Nitrogen | 0.66 | 0.76 | 1.20 |
| Sulfur | 0.33 | 0.38 | 0.47 |
| Lower heating value (MJ/kg) | 27.2 | 32.3 | 30.5 |

## 2.1 Thermogravimetric analysis (TGA)

TGA (Shimadzu DTG – 60H) was used to determine the ignition temperature of the coal-char blends, the intrinsic reactivity kinetic parameters for pure fuels (both activation energy and pre-exponential factors) and the ash% of the unburned residues collected after the drop tube furnace experiments.

A Kissinger plot was used to determine the intrinsic reactivity including activation energy and pre-exponential factor for the two Yallourn char samples and PCI coal [5]. Although the intrinsic reactivity wil become less important at higher temperatures in a commercial blast furnace, it is still expected that that intrinsic char reactivity is a significant factor in burnout due to the highly turbulent regions in the flame and small particle sizes used in PCI combustion [6]. Ignition temperature is defined as the temperature at which the combustion rate, for a certain heating rate, rises to 1 *wt%/min* of the current mass [7].

## 2.2 Flat flame burner experiments

Ignition tests were also carried out in a flat flame burner reactor (FFBR). The FFBR was operated at atmospheric pressure with a measured flame temperature of approximately 1062°C before the feeding of coal/char. Oxygen fraction was fixed at 0.21 and the $O_2$/C molar ratio was fixed at 2.5. At least 100 images were analysed for each blend to measure the ignition point of each sample as a distance from the burner base. A high speed camera was used to measure particle velocity and thus calculate the ignition time. Further information about the FFBR can be found in a previous study [8].

## 2.3 Drop tube furnace experiments

A 2 m high drop tube furnace (DTF) was used to combust the coal and char sample and a gas analyzer recorded the combustion gases exiting the furnace. The sample enters the drop tube furnace with a low volume primary gas, while a secondary gas is preheated to the furnace temperature and mixes with the coal or char at the injection point. Such a unique pre-heating system for the gas can resemble the blast furnace condition where coal is injected into a hot air stream. Further details including a schematic are available in a previous study [9].

The coal/char feeding rate was approximately 0.7 g/min. Primary and secondary gas flow rates were set to 1 L/min and 9 L/min respectively. Oxygen was added to the secondary gas to achieve the desired $O_2$/C ratio. The following parameters were varied in this study: Blending ratio (with respect to Yallourn char content): 0%, 20%, 40%, 60% 80% and 100%; Furnace temperature: 800°C, 900°C and 1000°C; and $O_2$/C ratio: 0.7, 0.85, 1.0 and 1.3.

## 2.4 Computational fluid dynamics modelling

A three-dimensional CFD model of the DTF was used to gain a better understanding of the interactions of different blends. The mesh for this was taken from a previous study [9]. Blends were added to the model as two coal injections added at the same inlet surface. This method may be used to study the interactions caused by differences in volatile content and reactivity. This mesh was validated in a grid independence test as well as with measurements of particle temperature. The models used in the simulation are summarized as follows: Turbulence – Realizable k-ε model; Radiation – Discrete ordinates (DO) model; Radiation absorption: weighted-sum-of-gray-gases model (WSGGM); Particle reactions – Multiple surface reaction model; and Gas reactions – Westbrook & Dryer mechanism [10].

# 3. Results and Discussion

## 3.1 Thermogravimetric analysis (TGA)

The kinetic parameter analysis (Table 2) showed a large variation in activation energy between YC-1 and YC-2 char, (103.0 and 151.6 kJ/mol respectively), although these two chars possess the similar properties in terms of the content of remaining volatiles and ash content. Likely the pyrolysis condition is critical in affecting the char structure and its reactivity.

Figure 1 shows the TGA measured ignition temperature as a function of the Yallourn char blending ratio. It generally increases with increasing Yallourn char content. This is due to the lower VM %. However, the ignition temperature of blends increases non-linearly with reduced volatile matter content in the coals. Thus, the ignition temperature of the blends is lower than the weighted average of each respective coal and is not additive, indicating the strong synergistic behavior between Yallourn char and the PCI coal. Moreover, the increase extent for the blending of YC-1 with PCI coal is much lower than that of YC-2, although they bear the same volatile content as evident in Table 1. This further indicates a distinctive char structure for YC-1, which is

clearly more reactive and prone to ignite heterogeneously.

Table 2 Kinetic parameters: Yallourn char and PCI coal

| | Pre-exponential constant ($s^{-1}$) | Activation energy (kJ/mol) | Reaction rate at 1000°C ($s^{-1}$) |
|---|---|---|---|
| YC-1 | 5.33E+04 | 103.0 | 3.16 |
| YC-2 | 3.90E+06 | 151.6 | 2.35 |
| PCI coal | 8.20E+05 | 129.0 | 4.19 |

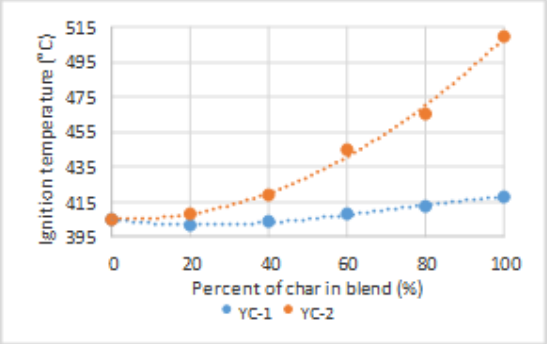


Figure 1: Ignition temperature of blends by TGA

## 3.2 Flat flame burner experiments

The direct observation of coal/char ignition in FFBR in Figure 3 show an agreement with the ignition prediction by TGA. That is, the ignition for char-coal blends was unaffected by blending at low ratios. As expected, YC-2 blends shows a larger ignition delay than for YC-1 blends. In addition, the flame for the blend using YC-2 char is more non-continuous, indicative of the difficulty for the ignition. For YC-1, blends 60% and below showed similar flame length and ignition points to that of PCI coal. In contrast, increasing the amount of YC-2 will drastically increase the ignition distance after 40% and increase flame length due to the higher energy value.

Figure 2 further quantifies the ignition time as a function of Yallourn char blending ratio. Clearly, the ignition delay for blending YC-1 with PCI coal is less obvious. The use of up to 60% YC-1 char resulted in the same ignition time with the pure PCI coal. On the other hand, the use of maximum 40 *wt%* is only allowed for the YC-2 char, otherwise the ignition would be delayed considerably. Such a finding is consistent with the TGA results in Figure 2.

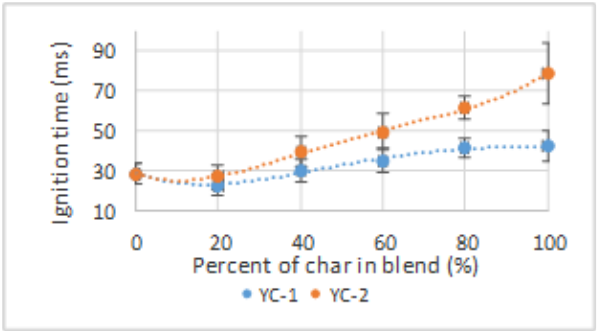


Figure 2 Ignition time for char blends as measured in the flat flame burner.

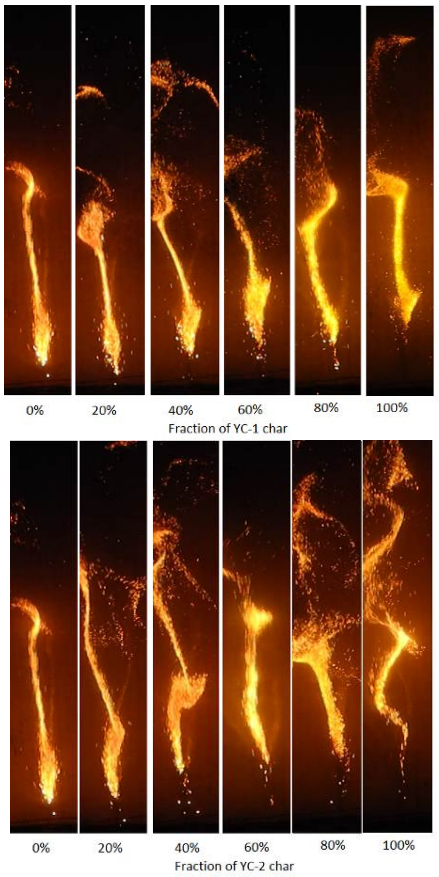


Figure 3 Effect of blend ratio on flame structure for YC-1 (top) and YC-2 (bottom).

## 3.3 Drop tube furnace (DTF) experiments

Figure 4 shows that at 1000°C in the DTF, PCI shows higher burnout and faster burnout rate at lower O/C ratios (below 1.0) for YC-2, however is closely followed by 40-60% blends (with burnout amounts seen above 85% and 90% at these ratios). As the $O_2$/C ratio increases above 1.0, 40-60% YC-2 blends show best burnout performance (faster rate and higher values). At higher $O_2$/C ratios (above 1.2), the burnout of all blends shows similar or better burnout performance than PCI.

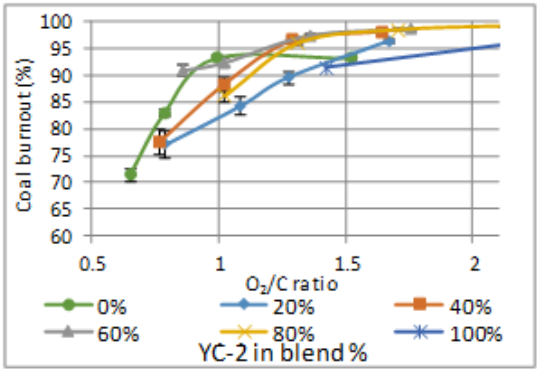


Figure 4 Burnout in the drop tube furnace for different blends of YC-2

### 3.4 Computational fluid dynamics modelling

Since the experimental conditions in the DTF are difficult to control, and hence, the influence of individual parameters are difficult to be assessed. In this sense, CFD modelling has been conducted to manipulate the conditions so as to assess the influence on individual variables such as burnout and temperature. By comparing the burnout under a constant $O_2$/C ratio of 1.0 at wall temperature 1000℃ in Figure 5, it can be seen that burnout decreases as Yallourn char fraction is increased. YC-1 shows more comparable burnout to PCI coal at all blend ratios with burnout decreasing less than 1.5% compared to pure PCI coal, while the burnout for YC-2 char drops as far as 2.5%.

Figure 6 shows the temperature profile along the reactor for YC-2 char under the same condition. As can be seen, adding 20 *wt%* YC-2 into PCI led to a marginal temperature drop at the distance of 0.1 m. Increasing the blending ratio to 40 *wt%* and beyond clearly reduces the peak temperature by minimum 50°C. Such a temperature gap is clearly influential in delaying the burnout rate.

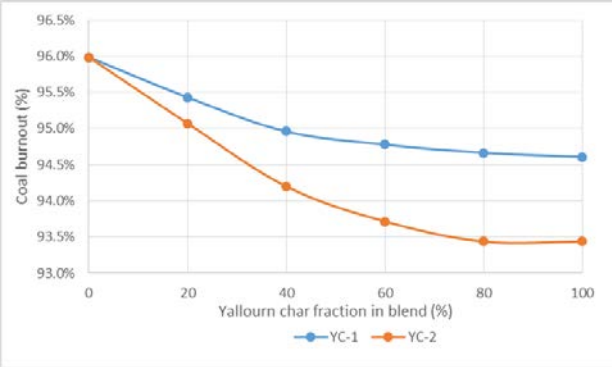


Figure 5 Effect of Yallourn char % in blend on coal burnout for at 1000°C and $O_2$/C=1.0

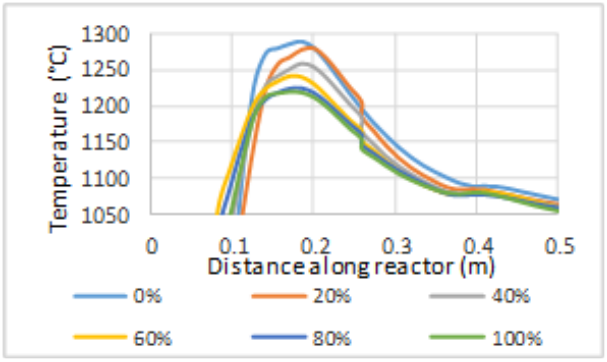


Figure 6 Effect of blend ratio on gas temperature profile for YC-2 char at 1000°C

## 5. Conclusions

There is strong synergetic behavior for the coal-char blend combustion. The ignition temperature increased non-linearly and was lower than the expected weighted averages. Burnout for the blends in the drop tube was maximized for a low blend ratio at low $O_2$/C ratios but for blends of similar Yallourn char and PCI coal contents at higher $O_2$/C ratios. While YC-1 and YC-2 were created from the same parent coal, differences in ignition and burnout indicate that char preparation condition is critical in affecting the maximum blending ratio of the char.

## 6. Acknowledgments

This work is supported by Coal Energy Australia (CEA), Brown Coal Innovation Australia (BCIA) and the Joint Partnership program between Australian Academy of Technological Science and Engineering, and Japan Society for the Promotion of Science (JSPS).

## 6. References

[1] Y. Traa, Is a renaissance of coal imminent?—challenges for catalysis, Chemical Communications, 46 (2010) 2175-2187.
[2] A. De Girolamo, N.K. Lameu, L. Zhang, Y. Ninomiya, Ignitibility and Combustibility of Lignite Pyrolysis Char under Simulated Blast Furnace Conditions, Submitted to Fuel, (2015).
[3] Y. Shen, B. Guo, A. Yu, P. Zulli, A three-dimensional numerical study of the combustion of coal blends in blast furnace, Fuel, 88 (2009) 255-263.
[4] A.M. Carpenter, Use of PCI in blast furnaces, IEA Clean Coal Centre, 2006.
[5] H.E. Kissinger, Reaction Kinetics in Differential Thermal Analysis, Analytical Chemistry, 29 (1957) 1702-1706.
[6] L. Lu, V. Sahajwalla, C. Kong, A. Mclean, Chemical structure of chars prepared under conditions prevailing in the blast furnace PCI operation, ISIJ international, 42 (2002) 816-825.
[7] C.a. Wang, Y. Liu, X. Zhang, D. Che, A study on coal properties and combustion characteristics of blended coals in Northwestern China, Energy & Fuels, 25 (2011) 3634-3645.
[8] W. Prationo, J. Zhang, H.A.A. Abbas, X. Wu, X. Chen, L. Zhang, Influence of External Clay and Inherent Minerals on Lignite Optical Ignition and Volatile Flame Propagation in Air-Firing and Oxy-Firing, Industrial & Engineering Chemistry Research, 53 (2014) 2594-2604.
[9] J. Zhang, W. Prationo, L. Zhang, Z. Zhang, Computational Fluid Dynamics Modeling on the Air-Firing and Oxy-fuel Combustion of Dried Victorian Brown Coal, Energy & Fuels, 27 (2013) 4258-4269.
[10] C.K. Westbrook, F.L. Dryer, Simplified Reaction Mechanisms for the Oxidation of Hydrocarbon Fuels in Flames, Combustion Science and Technology, 27 (1981) 31-43.

# $H_2$-Air Chemical Kinetic Evaluation for Pulse Detonation Engine Simulations

V.B.B. Rodrigues[1,3], E. C. Maciel[2,3*], C. S. T. Marques[2,3*]
[1]Engineering School of Lorena
University of São Paulo SP 12602-810 Brazil
[2]Spatial Sciences and Technologies
Technological Institute of Aeronautics SP 12228-900 Brazil
[3]Aerothermodynamics and Hypersonics
Institute for Advanced Studies SP 1228-001 Brazil

## Abstract

In this work, previous evaluation of the $H_2$-air chemical reaction mechanisms for multidimensional CFD simulation of pulse detonation engines was carried out using a one-dimensional ZND model. OH* chemical subsets were added to improve the accuracy of simulations for optical diagnostics development in the future. ZND time scales, OH and OH* mole fraction profiles were applied for comparison among the small kinetic models to those detailed reaction sets from the Explosion Dynamics Laboratory at Caltech. The recent reduced reaction mechanism with any of the two different OH* chemical kinetics considered are more appropriate reaction chemical sets for 2-D/3-D pulse detonation engine simulations, albeit with higher computational time.

*Keywords: $H_2$-air, chemical kinetics, ZND, pulse detonation engines.*

## 1. Introduction

Pulse detonation engines (PDEs) have extraordinary potential to replace current propulsion systems due to high efficiency, simplicity, low cost, scalability and wide flight range [1]. The interest in PDEs has been mainly focused on high-speed flight and for access to space [2]. However, the requests for faster, more efficient and low pollutant emission systems have also motivated jet engines for commercial aviation that include detonation devices, as PDEs [3].

In these engines, the combustible mixture is instantaneously compressed by a shock wave and burned at high pressure and constant volume with successive ignitions to generate controlled periodic detonation waves that propagate intermittently to produce thrust [4].

Detonation cycle engines have thermodynamic advantages over those based on deflagration, which lead to higher performance and fuel economy. Furthermore, hydrogen as a fuel is important to pollutant reduction and it is supposed to be applied for PDEs, in spite of the peculiarities of hydrogen combustion kinetics, the reason that the wide use of hydrogen engines has been avoided [5].

The main characteristic of hydrogen chemical kinetics is the inverse dependence of the reaction rates on pressure [5], making it a very difficult task to develop a small reaction set for a wide range of combustion conditions.

Computational fluid dynamics (CFD) has been widely employed for PDE simulations to optimize and determine operation parameters, and to validate reaction mechanisms and optical diagnostics [5-8].

In this work, $H_2$-air reaction mechanisms were evaluated through a one-dimensional (1-D) Zel'dovich-von Neumann-Döring (ZND) model to select suitable small reaction set for two-dimensional (2-D) PDE simulations with reduced computational time.

## 2. Kinetic Models

Nine different $H_2$-air kinetic models for PDE simulation were evaluated by comparing with those detailed by Shepherd [9]. Six of them, which are next to those detailed, are presented here.

Table 1 presents these six reaction mechanisms (1-6) and their main characteristics.

The skeletal reaction set from Jachimowski [10], widely applied for supersonic combustion, was updated with Arrhenius parameters from Konnov [11] and Westbrook [12]. The recent skeletal mechanism from Liberman was discarded [13]. Three reduced mechanisms [5,14,15] for deflagration, deflagration-to-

Table 1. Kinetic models for $H_2$-air detonation

| | Kinetic model | Species | Reactions | Ref |
|---|---|---|---|---|
| 1 | Skeletal from Jachimowski | 7 | 7 | [10] |
| 2 | Reduced without nitrogen chemistry | 9 | 19 | [5] |
| 3 | Skeletal from Jachimowski with OH* kinetics from Schulz | 8 | 15 | [10] [17] |
| 4 | Reduced with OH* kinetics from Schulz | 10 | 27 | [5] [17] |
| 5 | Skeletal from Jachimowski with OH* kinetics from Mével | 8 | 15 | [10] [18] |
| 6 | Reduced with OH* kinetics Mével | 10 | 27 | [5] [18] |
| 7 | Detailed from the Shepherd's group without OH* kinetics | 12 | 24 | [9] |

* Corresponding author:
Phone: (+55) 12 39475445
Email: emilio.c.maciel@gmail.com, carlatm@ieav.cta.br

detonation transition and detonation were tested. They include $HO_2$ kinetics, which are very important for detonation propagation through ground-state OH radicals [16], and chain termination reactions for $H_2O_2$; but they do not include nitrogen chemistry. Only the reaction set from Smirnov [5] is comparable to those detailed set[9].

Both skeletal [10] and reduced [5] kinetic models, previously selected were also tested with recent OH* excited radical kinetics [17-19] for comparison. In both subsets, only the reaction O + H + M = OH* + M was taken into account for the excited radical formation with different Arrhenius parameters and there is a single different reaction step between these two subsets. Moreover, they are applied to different pressure ranges.

The OH* radical is a spatial and temporal reaction zone marker and its kinetics gives more accurate simulations for optical diagnostics. Thus, in spite of two slightly different reaction sets for the OH* radical, it is important to verify their accordance due to the high sensitivity of the $H_2$-air mechanisms to pressure, mainly for the skeletal set, which can properly simulate only some combustion parameters.

## 3. Calculation of ZND Scales

$H_2$-air kinetic models were evaluated through time scales from the ZND model [20], which is a steady 1-D theory and the simplest model for detonation. It considers a planar shock wave followed by a finite reaction zone. Equations of shock wave theory are applied to establish the flow conditions behind a normal shock and the Euler equations set is employed for the reaction zone to solve the 1-D steady flow. The Chapman-Jouguet (CJ) condition is determined at the end of the reaction zone [8].

From detonable mixture composition ($P_1$, $X_{H2}$, $X_{ar}$, $\Phi$) and CJ detonation velocities, previously calculated [21], the detonation structure through 1-D ZND simulation was determined for different $H_2$-air reaction mechanisms (Table 1). ZND time scales and mole fraction profiles were obtained for comparison.

Induction times ($\tau_i$) and the times ($\tau_{eq}$) to reach the CJ thermodynamic state (sonic flow at equilibrium) were determined for stoichiometric $H_2$-air detonable mixtures at 0.5, 1.0 and 1.5 atm and for mixtures with equivalence ratios ($\Phi$) from 0.6 to 1.4 at 1 atm. Mole fraction profiles were established for stoichiometric $H_2$-air detonable mixtures at 0.5, 1.0 and 1.5 atm and for those with $\Phi = 0.8$ and $\Phi = 1.4$ at 1 atm.

## 4. Results and Discussion

Figures 1 and 2 show the induction times ($\tau_i$) and times ($\tau_{eq}$) to reach the CJ condition for stoichiometric $H_2$-air detonable mixtures at 0.5 1.0 and 1.5 atm and for mixtures with $0.6 \leq \Phi \leq 1.4$ at 1 atm calculated from the ZND model for different reaction sets.

Independent of the OH* reaction subset applied, the OH* kinetics added to both skeletal and reduced kinetic

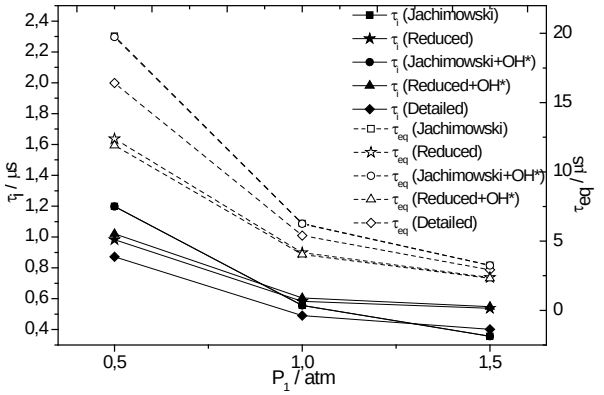


**Figure 1.** Induction times ($\tau_I$, solid symbols) and times ($\tau_{eq}$, open symbols) to reach CJ condition from different kinetic models for stoichiometric $H_2$-air detonable mixtures at different initial pressures.

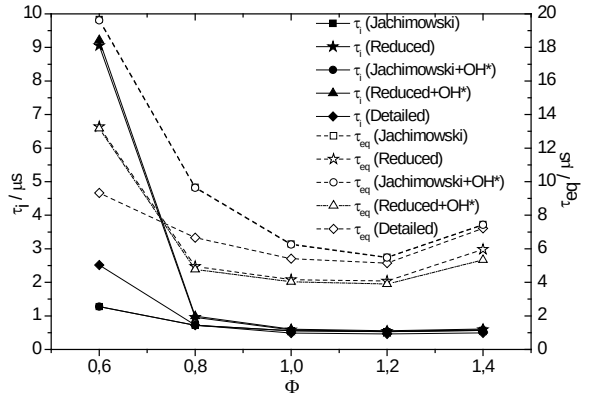


**Figure 2.** Induction times ($\tau_I$, solid symbols) and times ($\tau_{eq}$, open symbols) to reach CJ condition from different kinetic models for $H_2$-air detonable mixtures at 1atm and different equivalent ratios ($\Phi$).

models slightly change the calculated ZND time scales. Furthermore, almost the same results were obtained from both reaction subsets (deviations lower than 0.3%). For this reason, only those for the OH* model from Mével [18,19] are presented (Fig. 1 and 2).

The induction times from all kinetic models applied were similar to the values obtained through a detailed model for stoichiometric ($\Phi = 1.0$) $H_2$-air detonations and for fuel-riches ($\Phi = 1.2$ and $\Phi = 1.4$) at 1 atm, with deviations of around 15%. The same deviations were verified for induction times at 0.5 atm obtained from the reduced mechanism and at 1.5 atm obtained from skeletal kinetics. At $\Phi = 0.8$, the skeletal kinetics were able to reproduce the same value as those from the detailed reaction set. Discrepancies among induction times were observed for detonation at $\Phi = 0.6$, the highest for the reduced model.

For all reaction mechanisms tested, the times to reach the CJ condition were similar to those from the detailed model with increasing fuel (equivalence ratio) and pressure. For reduced kinetics, the deviations were found to be 18-25%, except at $\Phi = 0.6$ (30%). The skeletal kinetics resulted in higher deviations for fuel-lean ($\Phi = 0.6$ and $\Phi = 0.8$) detonations. However, the deviations are lower for stoichiometric conditions (10-17%) and for fuel-rich detonations (3-7%).

Figures 3 and 4 present OH and OH* mole fraction profiles for stoichiometric $H_2$-air detonable mixtures at 0.5, 1.0 and 1.5 atm.

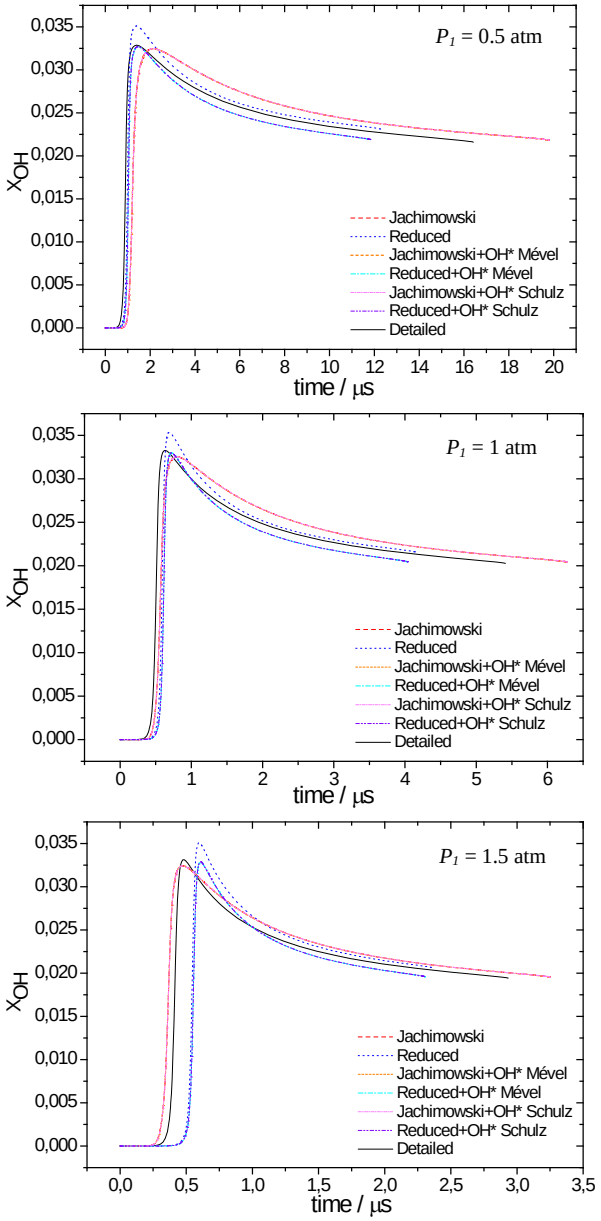


**Figure 3.** OH mole fraction profiles for stoichiometric $H_2$-air detonable mixtures at different initial pressures.

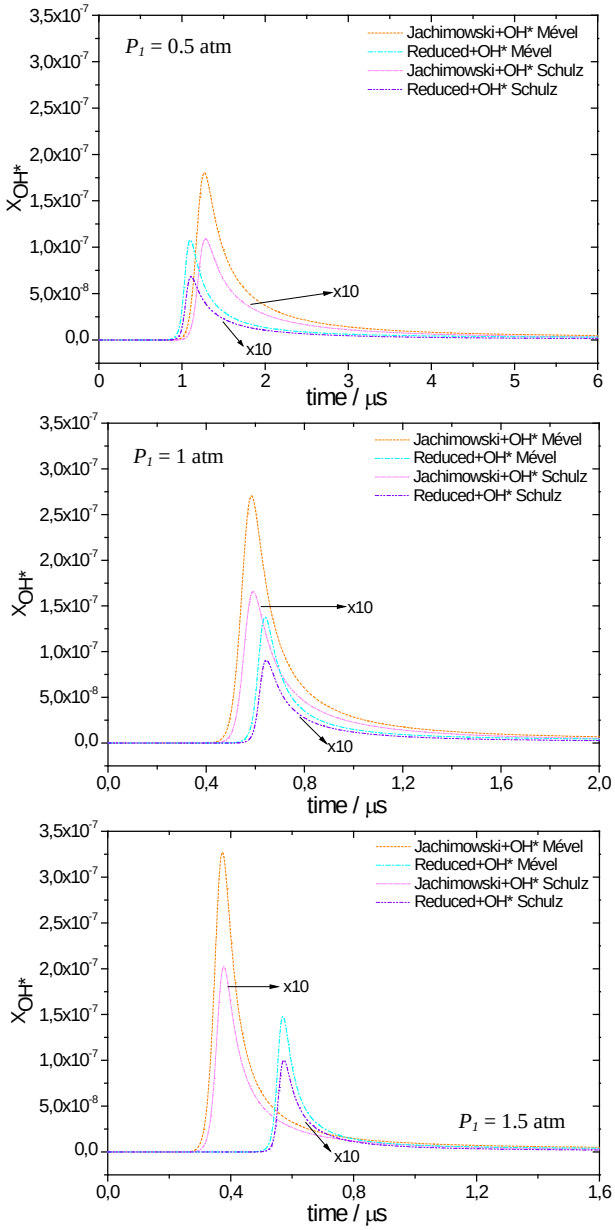


**Figure 4.** OH* mole fraction profiles for stoichiometric $H_2$-air detonable mixtures at different initial pressures.

The OH mole fraction profiles were better simulated by the reduced reaction model with OH* kinetics subsets for stoichiometric $H_2$-air detonation at 0.5 and 1.0 atm. At an initial pressure of 1.5 atm, the skeletal reaction mechanism with or without the OH* chemical kinetics produced better profiles than the reduced models. Although, the OH profile shape simulated from the reduced reaction mechanisms were more similar to those produced by the detailed set, but the fraction mole peaks are shifted.

Both OH* chemical subsets added to the reduced kinetics improved equally the OH mole fraction profiles. However, they had no effect on the skeletal set.

The same behaviour was verified for $H_2O$ mole fraction profiles, which are not presented here.

Figure 5 shows OH mole fraction profiles for a fuel-lean ($\Phi$ = 0.8) and a fuel-rich ($\Phi$ = 1.4) detonation.

CJ pressures are higher as pressure increases and for fuel-rich detonation conditions [21]. In inverse mode those for initial pressure change (Fig. 3), the reduced chemical kinetics with OH* subsets were better simulated for a fuel-rich ($\Phi$ = 1.4) detonation condition, in which the CJ pressure is higher and the skeletal reaction model leads to better results for the fuel-lean ($\Phi$ = 0.8) detonation condition, where CJ pressure is lower.

Again, both OH* reaction subsets improved the reduced kinetics, fitting the OH fraction mole peak to those obtained from the detailed reaction mechanism, while they had no effect on results from skeletal set.

OH mole fractions are unchanged as pressure increases and are slightly decreased with detonable mixture enrichment. In addition, the profiles are narrowed for higher pressure and fuel-richer detonations.

In contrast, OH* mole fractions (Fig. 4) are substantially increased as pressure increases, mainly from the skeletal model, for which they increased of around 80% for both subset applied (orange and magenta lines). There are no experimental data to support that the

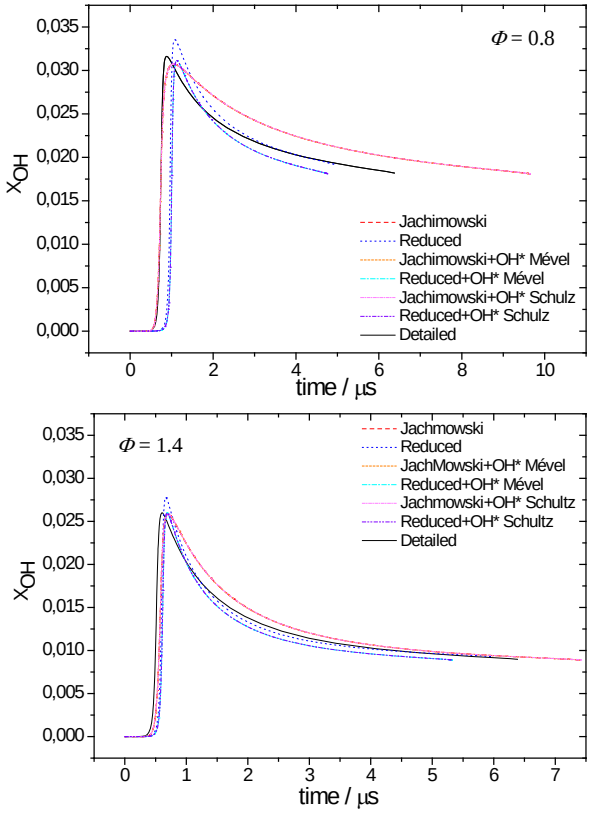


**Figure 5.** OH mole fraction profiles for $H_2$-air detonable mixtures at 1 atm with Φ=0.8 and Φ=1.4.

increase of the OH* mole fraction predicted is excessive, but the results revealed more sensitivity of this skeletal chemical set to pressure changes.

Furthermore, the OH* reaction subset from Mével [18,19] simulated mole fractions one order higher than those from Shulz [17].

OH* radicals are predominantly thermal in detonation conditions and their mole fractions are expected to be higher as pressure and temperature increases. Both reaction subsets were able to provide higher mole fractions as pressure increased. However, the subset from Mével [18,19] corresponds to reactions with higher temperatures and global reaction rates than those from Shulz [17]. In any case, it is necessary to validate against experimental data for fine adjustment.

The intrinsic unstable nature of detonations is well captured through multidimensional simulation and the OH and OH* radical profiles are essential to achieve accuracy. OH radicals are responsible for detonation propagation and, consequently, for velocity field and OH* radicals could supply a better description of the temperature and pressure fields. Therefore, the reduced reaction set with OH* chemical kinetics is more suitable for 2-D/3-D PDE simulations, despite higher computational time. Moreover, the addition of OH* kinetics can enable and improve optical diagnostics.

## 5. Conclusion and Outlook

Kinetic models for $H_2$-air deflagration/detonation were evaluated by applying the 1-D ZND model. Further, two OH* chemical kinetics subsets were added for comparison.

In general, all reaction mechanisms were well fitted to the detailed reaction model for ZND time scales, with higher deviations for the times to reach CJ condition. Discrepancies were verified for the most fuel-lean detonation condition. OH mole fraction profiles were better simulated from reduced reaction kinetics with OH* reaction subsets, except for detonation at 1.5 atm and they are considered more suitable for multidimensional PDE simulations.

Thereafter, KIVA will be applied to 2-D PDE simulations to generate pressure profiles and images for comparisons with experimental data.

## 6. Acknowledgments

The authors thank IEAv for fellowships and CNPq (Proc. 471052/2012-4) for financial support.

## 7. References

[1] K. Kailasanath, AIAA Journal.41 (2003) 145–159

[2] F.K. Lu, D.R. Wilson, Proc. Int. Symp. on Shock Waves 24, 2004, p. 75.

[3] F. Giuliani, A. Lang, M. Irannezhad, A. Lundbladh, Proc Int.Cong. Aeronaut. Sci. 27, 2010, 10p.

[4] D. Allgood, E. Gutmark, J. Hoke, R. Bradley, F. Shauer, J. Prop. Power 22 (2006) 70-77.

[5] N.N. Smirnov, V.F. Nikitin, Int. J. Hydrogen Energy 39 (2014) 1122-1136.

[6] H.B. Ebrahimi, C.L. Merke, J. Prop.Power, 18 (2002) 1042-1048.

[7] R. Mével, D. Davidenko, J.M. Austin, F. Pintgen, J.E. Shepherd, Int J Hydrogen Energy 39 (2014) 6044-6060.

[8] G. Bechon, R. Mével, D. Davidenko, J.E. Shepherd, Combust Flame 162 (2015) 2191-2199.

[9] S. Browne, Z. Liang, J.E. Shepherd, Fall 2005 Western States Section Combust. Inst. (2005) 274-291.

[10] D.R. Eklund, S.D. Stouffer, Proc. AIAA/ASME/SAE/ASEE Joint Prop. Conf. 30, 1994, 20p.

[11] A.A. Konnov, Combust Flame, .152 (2008) 507-528.

[12] M. O'Conaire, H.J. Curran, J.M. Simmie, W.J. Pitz, C.K. Westbrook, Int. J. Chem Kin. 36 (2004) 603-622.

[13] M.F. Ivanov, A.D. Kiverin, M.A. Liberman, Int. J. Hydrogen Energy 36 (2011) 7714-7727.

[14] V. Zhukov, ISRN Mech. Eng. 2012 (2012) Article ID 475607, 11p.

[15] E.L.Petersen, R.K. Hanson, J. Prop Power 15 (1999) 591-600.

[16] Z. Liang, S. Browne, R. Deiterding, J.E. Shepherd, Proc. Combust. Inst. 31 (2007) 2445-2453.

[17] T. Kathrotia, M. Fikri, M. Bozkurt, M. Hartmann, U. Riedel, C. Schulz, Combust. Flame 157 (2010) 1261-1273.

[18] R. Mével, S. Javoy, F. Lafosse, N. Chaumeix, G. Dupré, C.E. Paillard, Proc. Combust. Inst. 32 (2009) 359-366

[19] R. Mével, Étude de mécanismes cinétiques et des propriétés. explosives des systèmes hydrogène-protoxyde d'azote et silane-protoxyde d'azote. Application à la securité industrielle, PhD Thesis, Université d'Orléans, 2009.

[20] S. Kao, J.E. Shepherd, Numerical Solution Methods for Control Volume Explosions and ZND Detonation Structure, Report Nº FM2006.007, GALCIT, 2008.

[21] C.S.T. Marques, A.C de Oliveira, F.B. Dovichi Filho, W.C. Ferraz, J.B. Chanes Jr., Proc. Braz. Cong. Thermal Sci.Eng., 13, 2010, 10p.

**Proceedings of the Australian Combustion Symposium**
**December 7-9, 2015, The University of Melbourne**

# Non-Oxidative Thermal Decomposition of Endosulfan

W.N.K. Dharmarathne, J.C. Mackie, E.M. Kennedy*, M. Stockenhuber
Priority Research Centre for Energy, Faculty of Engineering & Built Environment
The University of Newcastle, Callaghan NSW 2308
Australia

## Abstract

Endosulfan is a member of the cyclodiene pesticide group of compounds, commonly used on the major crops of tobacco, cotton and fruits. This article presents the results of an experimental study on the non-oxidative thermal decomposition of endosulfan. The objective of the study was to identify its decomposition pathways and to gain an understanding into the formation of toxic species which may be introduced in the environment during its thermal decomposition. The experiments were conducted using a tubular reactor placed in a three zone heating furnace and operated with a dilute heated stream of endosulfan vapour in 99.999% helium. Gaseous species such as HCl, CO, $C_2H_2$ and $SO_2$ were detected and quantified by online Fourier Transform Infra-red spectroscopic analysis. The pyrolysis of endosulfan started at 300°C and the formation of HCl and CO commenced at 375°C. The initiation of the decomposition of endosulfan involves retro Diels-Alder elimination to hexachlorocyclopentadiene (HCCP) and the seven-membered ring compound, 4,7-dihydro-1,3,2-dioxathiepine-2-oxide (cyclic S=O). $SO_2$ was quantitatively eliminated from this cyclic S=O compound at increased temperatures, forming 2,5-dihydrofuran. As the temperature increased, we observed a rise in tertiary products including pentachlorocyclopentadiene (PCCP), tetrachlorostyrene (TCS) and different isomers of chlorinated styrene products. At 550°C, chlorinated benzene products were identified comprising pentachlorobenzene and tetrachlorobenzenes.

*Keywords: Endosulfan, Pyrolysis, Hexachlorocyclopentadiene.*

## 1. Introduction

Endosulfan is a chlorinated cyclodiene insecticide. It was introduced commercially as a broad spectrum insecticide in 1954 by Farbwerke Hoechst, Germany [1]. Technical grade endosulfan is a mixture of two stereoisomers, α and β endosulfan, in a ratio of 7:3. It has been in use for ~5 decades and is effective against a broad number of insect pests and mites [2, 3]. It destroys a wide variety of insect and mite species and hence it is also used as a wood preservative. It has been used extensively on fruit, cereal and vegetable crops such as green peppers, rice, corn, cotton, sorghum, etc [4, 5]. Endosulfan and its degradation products, which have been detected in different environmental samples, many of which are persistent in the environment and have estimated half-lifes of 3–6 months or longer [6].

Toxic products released in pesticide fires or in the burning of pesticide-treated biomass can result in adverse effects on the surrounding environment and people's health. In 1978 Chopra et al made a systematic study on the pyrolysis of α endosulfan at 900 °C in a nitrogen atmosphere, as a method for predicting the fate of pesticides in tobacco and cigarette smoke. Chlorobenzene was one of the major products during the pyrolysis of α endosulfan [7]. Chlorinated benzenes are considered to be a probable threat to health due to their notoriety as acting as precursors for the formation of dangerous pollutants, such as dioxins, under some thermal conditions.

Although the use of endosulfan is prohibited in many countries, its residues can be detected in soils and biomass from previous use. The current understanding of the products of combustion of endosulfan is quite limited. Significant quantities of endosulfan are handled and stockpiled at manufacturing sites and storage facilities. Consequently, an evaluation of the risks associated with accidental fires should be included in or to assess the possible environmental impact of endosulfan that may generate toxic products upon their combustion. Non-oxidative thermal analysis is a useful tool in establishing suitable conditions for the degradation of these compounds and endosulfan-contaminated biomasses. In this study, we concentrate on the thermal decomposition of technical endosulfan in a non-oxidative atmosphere to determine the formation of Volatile Organic Carbon (VOC) products and gases.

## 2. Experimental Setup

### 2.1 Experimental Apparatus

The apparatus consists of two major components, a three zone quartz flow reactor/furnace, and a collection system for different types of products. Figure 1 illustrates a schematic of the experimental setup. Under pyrolysis experiments, ultra-high purity He (99.999 % purity) was employed as a bath gas to maintain non-oxidative conditions.

Reactor system

The reactor used in this study is a 10mm inner diameter quartz tube (purity 99.5%) reactor.

* Corresponding author: E. Kennedy
Phone: (+61) 2 49854422
Email: eric.kennedy@newcastle.edu.au

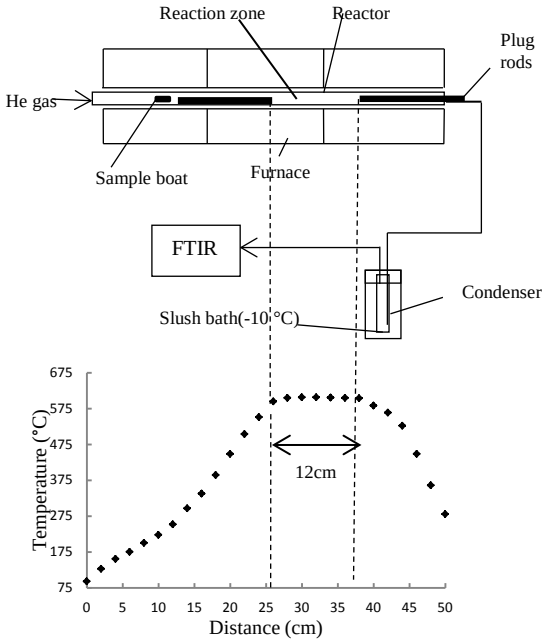


Fig. 1, A sketch of experimental setup with the axial temperature profile at 600 °C

The reactions take place in the central zone of the quartz tube, denoted in Figure 1 as the reaction zone. The volume of the reactor was adjusted by inserting two quartz rods, 9.5mm in outside diameter (o.d) to ensure that the vapour reaches the reaction zone rapidly, minimising decomposition in the lower temperature regions.

Technical grade endosulfan (> 96% purity) was purchased from Sigmachem, China. The sample was placed in a small quartz boat (30mm in length and 8mm width) and positioned in the entry zone of a three-zone furnace, each zone controlled independently (Eurotherm, Marrickville, Australia). The entry zone of the furnace was maintained at 180 °C to permit slow but controlled rate of evaporation of the endosulfan, with the other zones of the furnace heated to 300, 350, 375, 390, 400, 425, 450 °C in separate experiments. The evaporation rate of endosulfan was approximately 1.2 mg/min. The experiment lasted 1 hour with 5s residence time.

Product collection system

Product gases were trapped in a chilled condenser, submerged in a slush bath (ice and acetone) maintained at -10 °C. The PTFE connection tube was heated to 130 °C to ensure the complete trapping of all VOC reaction products. After each experiment, condenser, reactor, PTFE tube and quartz rods were rinsed with DCM (dichloromethane) and the dissolved contents analysed. We cleaned the tube further with DCM and then baked it at 105°C to remove trace contaminants that could have affected the results of subsequent experiments.

### 2.2 Analysis

Gaseous product analysis

The gaseous products were analysed on a Fourier transform infrared (FTIR) spectrometer (Perkin Elmer Spectrum 100) equipped with a 0.19m path length PTFE cell. 16 scans were recorded per analyses, in the range of 4000-500 $cm^{-1}$ with a resolution of $1cm^{-1}$. For the identification of gaseous products, we used the reference spectra of QASoft software package. The software also provided a region integration and subtraction routine for quantitative analysis. In addition to FTIR analysis, GC–MS (Shimadzu QP 5000) was utilized for detecting other gases products present in the gas stream.

GCMS analysis of VOC liquid products

Analysis of VOCs was performed on an Agilent 7200 quadruple time-of-flight GC/MS. One µL of the solution was injected into the GC/MS, equipped with a DB-5MS column (30 m length, 0.25 mm i.d., 0.25 µm film thickness). The oven temperature program was held at 30 °C for 4 min, then a rise to 290°C at 10 °C/min and held 4 min at 290 °C. Helium was used as the carrier gas at a constant flow rate of 1.2 mL/min. MS ionisation electron impact voltage was 70 eV.

## 3. Results and Discussion

### 3.1 Gaseous products analysis

A typical FTIR spectrum is shown in Figure 2. The three major identified species are HCl, $SO_2$ and CO. CO and HCl produce distinct absorption bands at around 2060-2220 $cm^{-1}$ and 2680-3045 $cm^{-1}$ respectively. The asymmetric stretching vibration of $SO_2$ generates absorption bands in the range of 1300-1400$cm^{-1}$.

HCl and CO form at a temperatures higher than 375°C. The yields of each compound was quantified as a mole fraction of initial endosulfan input feed concentration, with the yield-temperature profiles of gases displayed in Figure 3. The yields of all gaseous species exhibit a slow increase in the temperature range of 300 - 375 °C and a rapid ascent in the region of 390 - 450 °C . The yields of CO and $SO_2$ followed a similar trend while large increases in HCl yield were observed at 450°C. An additional gas phase product, 2,5-dihydrofuran, was observed in GC-MS analysis of gases produced from experiments performed at 400- 450°C.

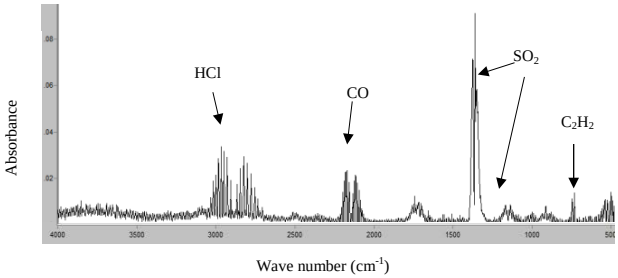


Fig. 2, FTIR spectrum of experiment at 425 °C

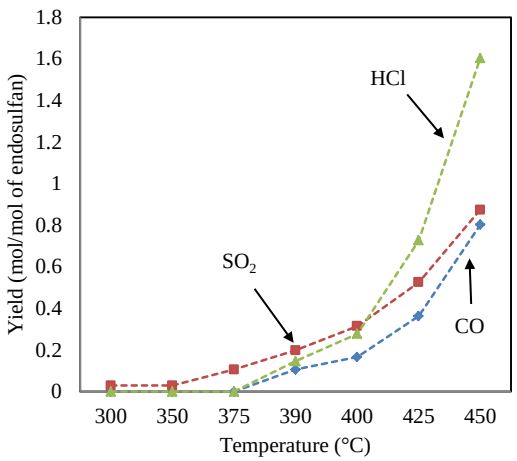


Fig. 3, The yield temperature profile of gaseous products

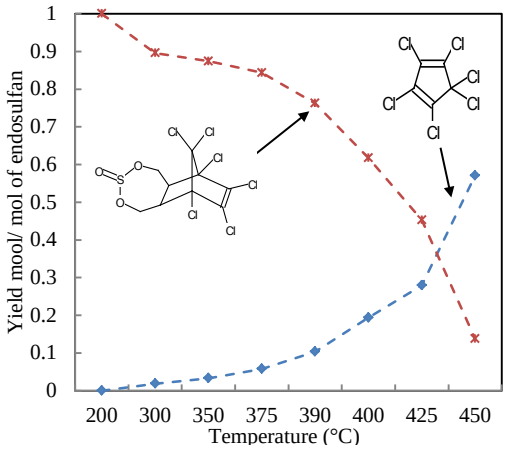


Fig. 4, Yield temperature profile of undecomposed endosulfan and HCCP

## 3.2 VOC analysis

Figure 6 presents a chromatogram for the pyrolysis of endosulfan at 450 °C. Identification of HCCP, endosulfan-ether and endosulfan were confirmed by the injection of authentic standards and other products were identified using NIST library only.

At 450 °C, the chromatograph of species indicated four major products comprising undecomposed endosulfan, HCCP, PCCP and TCS. In Figure 4, we report the yield-temperature profiles for HCCP and endosulfan as the mole fraction of the initial moles of endosulfan loading. The amount of undecomposed endosulfan initially follows a slow decrease and then, above 375 °C, a steep conversion increasing to 90% at 450 °C. Although present initially as a trace impurity, HCCP constitutes the dominant product at 450 °C with a yield of more than 60%. PCCP and TCS started to form at temperature > 375°C (Fig. 5). The unavailability of authentic standards for these components prevented us from performing quantitative analysis of PCCP and chlorinated styrene products. A higher yield of PCCP was noticed at a temperature 450°C due to Cl atom fission from HCCP and production of HCl by H atom abstraction by Cl atoms from endosulfan. We conducted experiments where the reaction temperature was the 180 °C as the vaporizer temperature, and no any decomposition occurred. Decomposition of endosulfan commenced at 300 °C and resulting about 10% of degradation at 300°C.

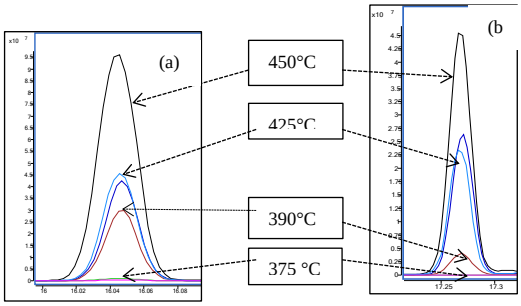


Fig. 5, Counts vs retention time chromatograph of PCCP (a) and TCS (b)

The mass spectrum of PCCP was not found in the NIST library, PCCP was identified comparing m/z data and peak intensity with literature values [8].

Table 1, Comparison of m/z data of PCCP

| m/z | 203 | 201 | 205 | 238 | 240 | 131 | 242 |
|---|---|---|---|---|---|---|---|
| Literature (%) | 100 | 72.5 | 46.1 | 22.4 | 16.9 | 8.9 | 5.2 |
| Our (%) | 100 | 73 | 48 | 21.8 | 17 | 8 | 6 |

Table 2 lists the minor VOC products with their corresponding Retention Times (RTs) and compound ID in figure 6. We detected endosulfan ether (EE), an impurity remaining in endosulfan after its synthesis. EE evaporates from endosulfan and passes undecomposed through the reactor, owing to its relatively low boiling temperature. Another two isomers of PCCP were detected with identical mass spectra. The same three isomers have been detected in previous studies with one of the products being in excess [8].

## 3.3 Mass balance

An overall 96% mass balance obtained in the experiments conducted at a temperature 300-390°C. An 88% of mass balance estimated for experiments at 390-450°C may be due to the unavailability of authentic standards for all the compounds which appear as products at reaction temperatures higher than 390°C. Calculated elemental sulfur mass balance in all experiments exceeds 94%.

Table 2 Identified minor VOC products at 450°C

| ID | Compound | RT |
|---|---|---|
| a,b | Isomers of PCCP | 14.6,14.7 |
| c | Pentachlorocyclohexene | 15.87 |
| d | Benzene,1,4-dichloro-2-(2-chloroethenyl)- | 16.41 |
| e | 1,2,4,5 tetrachlorobenzene | 16.9 |
| f | Isomer of 1,4-Dichloro-2-chloromethyl-5-dichloromethylbenzene | 17.91 |
| g | Pentachlorobenzene | 18.75 |
| h | Unknown (m/z 216, 278, 170) | 19.6 |
| i | Pentachlorostyrene isomer | 21.1 |
| j | p-(Trichlorovinyl)benzoylchloride | 22.44 |

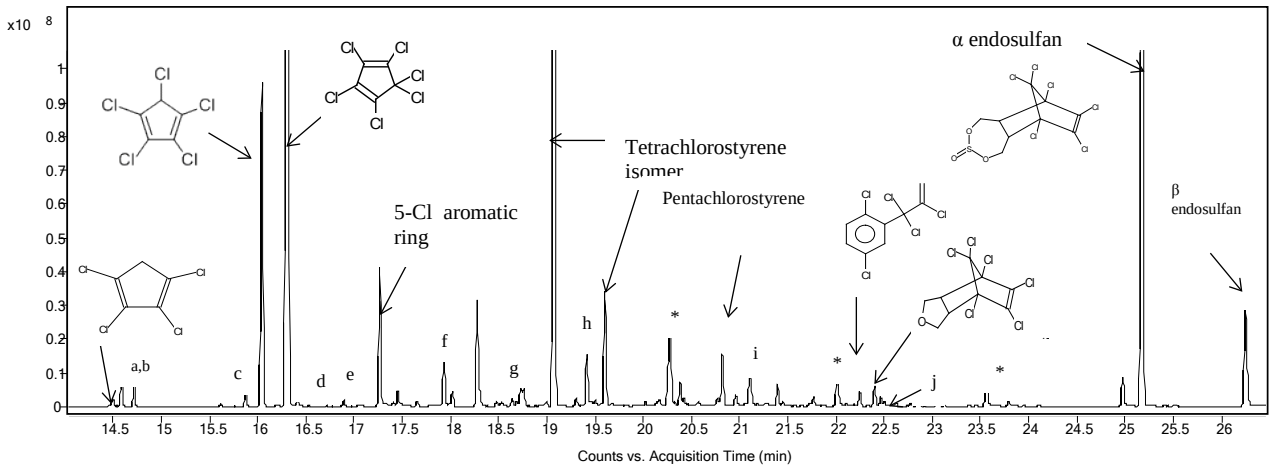


Fig. 6, Assignment of peaks in the zoomed chromatogram from the analysis of pyrolysis products of endosulfan at a residence time of a 5s *impurity

### 3.4 Decomposition of endosulfan - mechanistic considerations

The mechanism of thermal decomposition of endosulfan has been investigated by quantum chemical techniques. This theoretical study is the basis of a subsequent submission to this meeting. A brief summary of the quantum chemical analysis follows.

At the lowest temperatures at which decomposition can be detected, the reaction is initiated by a retro-Diels-Alder dissociation into HCCP and 4,7-dihydro-1,3,2-dioxathiepine-2-oxide. The latter product can undergo a two-channel decomposition in which both channels eliminate $SO_2$ and produce either 2,5-dihydrofuran (an observed product) or 3-butenal. CO is eliminated from 3-butenal via a hydrogen transfer from the carbonyl carbon to produce propene.

HCCP has two weakly bound Cl atoms, one of which can fission off with increase in temperature, producing the resonance stabilized pentachlorocyclopentadienyl radical. This radical can abstract a hydrogen atom from endosulfan to produce PCCP. Cl atoms can also abstract H from endosulfan leading to the observed HCl.

Abstraction of a hydrogen atom from endosulfan engenders a rapid and progressive rupture of the double ring structure, eliminating $SO_2$ in the process and leading to the formation of an open-chain structure which eventually recyclises to six-membered aromatic rings, forming chlorobenzenes and chlorinated styrenes. The products observed in our study are consistent with those observed by Chopra et al who investigated the pyrolysis of endosulfan at 900°C [7]. At 550°C, chlorinated benzene products were identified comprising pentachlorobenzene, different isomers of tetrachlorobenzenes and other chlorinated aromatic compounds. These are recognized precursors for PCDD/F formation.

## 4. Conclusion

In this paper, we describe a laboratory scale apparatus to study the pyrolysis of endosulfan. We have assmbled FTIR, GC-QTOF MS, GC-MS, µGC to detect and identify a wide range of pyrolysis products. Decomposition of endosulfan commenced at about 300 °C. In our experiments, HCCP was a major product detected in the pyrolysis products of endosulfan over the temperature range of 300 - 450°C. $SO_2$ is quantitatively eliminated at temperatures around 450°C with no other sulphur products detected. Quantitative results obtained from this study may contribute to an improved understanding of thermal decomposition of endosulfan. The oxidative mechanism for decomposition is being further investigated.

## 5. Acknowledgments

The authors would like to thank the Australian Research Council for financial support of this project and the University of Newcastle, Australia for a postgraduate research scholarship.

## 6. References

[1] H. Maier-Bode, Rev. Envi. Conta. Toxi 22 (1968) 1-44.
[2] R. J. Douthwaite, Appl Ecol 19 (1982) 133-141.
[3] D. M. Roberts, A. Karunarathna, N. A. Buckley, G. Manuweera, M. H. R. Sheriff, M. Eddleston, Bulletin of the WHO 81 (11) (2003) 789-798.
[4] T. Siddique, C. B. Okeke, M. Arshad, W. T. Frankenberger, Agric. Food Chem 51 ( 2003) 8015–8019.
[5] W. F. Schmidt, C. J. Hapeman, C. P. Rice, S. Bilboulian, J. Fettinger, Agr. Food Chem 45 (1997) 1023-1026.
[6] N. Awasthi, R. Ahuja, A. Kumar, Soil Biology and Biochemistry 32 (11) (2000) 1697–1705.
[7] N. M. Chopra, B. S. Campbell, J. C. Hurley, Agric. Food Chem 26 (1) (1978) 255-258.
[8] G. H. Irzl, C. T. Vijayakumar, J. K. Fink, K. Lederer, Polymer Degradation and Stability 16 (1986) 53-71.
[9] M. A. Bell, R. A. Ewing, G. A. Lutz, Reviews of the environmental effects of pollutants: XII. Hexachlorocyclopentadiene, Report No. EPA-600/1-78-047, U.S. Environmental Protection Agency, 1979.

**Proceedings of the Australian Combustion Symposium**
**December 7-9, 2015, The University of Melbourne**

# Non-Oxidative Thermal Decomposition of Endosulfan

# II. Mechanism of Decomposition

J.C. Mackie*, W.N.K. Dharmarathne, E.M. Kennedy, M. Stockenhuber
Priority Research Centre for Energy, Faculty of Engineering & Built Environment
The University of Newcastle, Callaghan NSW 2308
Australia

**Abstract**

The mechanism of thermal decomposition of endosulfan has been investigated by quantum chemical calculation. Under pyrolysis conditions, endosulfan initially decomposes via a retro-Diels-Alder decomposition into hexachlorocyclopentadiene (HCCP) and 4,7-dihydro-1,3,2-dioxathiepine-2-oxide (a seven-membered ring compound). The latter undergoes decomposition via two competing channels – one eliminates $SO_2$ and 2,5-dihydrofuran, the second also eliminates $SO_2$, forming additionally 3-butenal which further eliminates CO and propene. At higher temperatures, HCCP undergoes fission of a Cl atom, which promotes further decomposition of endosulfan via abstraction of a hydrogen atom to form HCl. The resulting endosulfan radical undergoes a sequence of low barrier steps leading to ring opening and finally to ring closure to a series of chlorinated styrenes and chlorobenzenes – known precursors of dioxins under oxidative conditions.

*Endosulfan, pyrolysis, quantum chemistry, reaction mechanisms.*

## 1. Introduction

Our experimental flow reactor study [1] of the pyrolysis of endosulfan vapour between 300 and 550°C at 5 s residence time revealed the extensive formation of toxic volatile compounds including many chlorinated styrenes and benzenes. These are known precursors of the polychlorinated dioxins and dibenzofurans (PCDD/F). Although endosulfan usage has been banned in many countries and its usage is to be phased out in others, there are still large stockpiles in existence and there are considerable risks associated with accidental fires. Endosulfan is an important member of the chlorinated cyclodiene group of pesticides which also include aldrin and dieldrin and an understanding of the mechanism of formation of the PCDD/F precursors is important in avoiding dioxins' formation in strategies for destruction of this class of pesticides.

To develop an understanding of the mechanism of pyrolysis and the formation of products, we employ quantum chemical computational techniques to identify minimum energy reaction pathways and transition states linking reactants and products. Our experimental study revealed that decomposition commenced at approximately 300°C where the initial detected product was hexachlorocyclopentadiene (HCCP). $SO_2$ was also an important product at low temperatures. Above 375°C, HCl and CO are detected, with rapid rises in these products and in endosulfan decomposition taking place at around 400°C. Chlorinated aromatics including chlorinated styrenes and benzenes are observed above about 500°C. We present a quantum chemical analysis to explain these observations and predict major observed products. Ultimately we aim to develop a chemical kinetic mechanism of formation of dioxin precursors to be used in modelling studies of PCDD/F formation under oxidative conditions.

## 2. Computational Methodology

Quantum chemical calculations were carried out using the Gaussian 09 suite of programs [2]. Molecular geometry optimizations were mainly carried out using density functional theory at the M062X/6-31+G(d,p) level of theory and improved energy calculations were made using the extensive G3Large basis set. Because of the very many heavy atoms in endosulfan and similar sized products the highly accurate G4MP2 methodology could only be carried out on molecules such as HCCP with about 11 heavy atoms. Transition states (TSs) were located and barrier energies computed. Where necessary, intrinsic reaction coordinate (IRC) analyses were carried out to establish links between reactants and products.

## 3. Results and Discussion

### 3.1 Initial Decomposition

* Corresponding author:
Phone: (+61) 2 49854439
Email: john.mackie@newcastle.edu.au

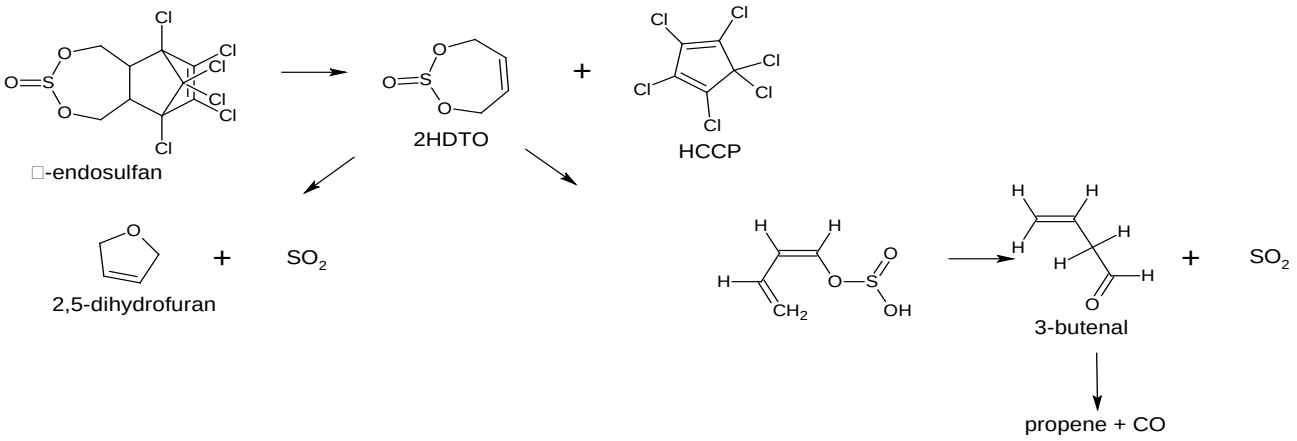


Fig. 1: Initial decomposition reactions of endosulfan

The lowest energy decomposition of endosulfan was found to be the retro-Diels-Alder decomposition into HCCP + 4,7-dihydro-1,3,2-dioxathiepine-2-oxide (2HDTO). (See Fig. 1.) This reaction passes through a TS whose barrier is 204 kJ/mol (at 0 K) and is 130 kJ/mol endothermic. 2HDTO undergoes decomposition via two competing reaction channels. The first, which is endothermic by 15.5 kJ/mol with a barrier of 205 kJ/mol produces $SO_2$ + 2,5-dihydrofuran – a product identified in our experimental study [1]. The second channel, endothermic by 25.5 kJ/mol, involves a H transfer to the S=O group with a comparable barrier of 207 kJ/mol. A second step, exothermic by 18.8 kJ/mol produces $SO_2$ + 3-butenal with a modest barrier of 76 kJ/mol. 3-Butenal is the source of the CO observed above 375°C. Elimination of CO results from a 1,4-H transfer to produce propene. We compute a barrier of 179 kJ/mol and an exothermicity of 13.4 kJ/mol for this reaction. Our barrier energy is in excellent agreement with a previous experimental determination [3] of 177.8±0.8 kJ/mol.

## 3.2 Decomposition of HCCP

Above about 375°C, HCCP begins to decompose, experimentally observable from the presence in the products of pentachlorocyclopentadiene (PCCP) together with the observation of significant yield of HCl. These are associated with fission of a weakly bound Cl atom from the C1 position in HCCP. As indicated by a potential energy scan, fission of a Cl atom from HCCP has no discrete TS, hence the barrier (at 0 K) for the reaction HCCP $\rightarrow$ Cl + pentachlorocyclopentadienyl radical will equal the energy change (0 K), $\Delta_r E_0$ = 231 kJ/mol as calculated at the M062X/G3Large level of theory.

Pentachlorocyclopentadienyl radical is resonance stabilized and therefore relatively long-lived. It can abstract a H atom from endosulfan to form PCCP. Also, Cl transfer around the five-membered ring is facile and will lead to observed [1] isomers of PCCP.

## 3.3 Free Radical Initiated Decomposition of Endosulfan

At 400°C and above, yields of HCl increase dramatically with a similar extent of decomposition of endosulfan. At these temperatures, fission of Cl from HCCP is very rapid and HCl arises from abstraction of H from endosulfan by Cl atoms. Abstraction of one of the H atoms from a methylene carbon in the seven-membered ring is the most probable leading to the radical structure (I) shown in Fig. 2.

Radical I readily undergoes β-bond scission at one of the O-S bonds. The barrier for this is only 18 kJ/mol and the reaction energy is -85 kJ/mol (to radical II). Loss of $SO_2$ from radical II is endothermic by 105 kJ/mol via a barrier of 126 kJ/mol. Radical III thus formed also undergoes facile β-scission with a low 56 kJ/mol barrier to form radical IV. This radical has a 3-butenal moiety and eliminates CO as described in Section 3.1 Owing to the hydrogen atom transfer taking place in IV $\rightarrow$ V, radical V now possesses a terminal methyl group.

The residual five-membered ring structure in radical V is destroyed by a further β-scission and the radical VI thus formed now has an open-chain structure. This now allows for the transfer of a methyl hydrogen on C1 to C4, which also bears a chlorine atom. The barrier for this transfer is 162 kJ/mol. The C-Cl bond on C4 now becomes very weak, as signified by its bondlength increasing to 1.819 Å. Fission of this Cl atom is quite facile, requiring only 107 kJ/mol. According to a relaxed potential energy scan, this fission does not have a discrete barrier.

After an energetically, near-trivial and essentially free rotation of the $H_2C$=CH=CH=CH- moiety about the –CCl=CCl-CC=$CCl_2$ moiety in radical VIII, the structure can readily undergo ring closure to a cyclohexadienyl compound IX. This process has a barrier of 135 kJ/mol. Finally, elimination of HCl via a four-centre TS of barrier 135 kJ/mol leads to the product 2,3,4,5-tetrachlorostyrene. It is to be noted that in our experimental work [1], a tetrachlorostyrene was identified as a major product above about 400°C.

Figure 2 shows the complete reaction scheme described in Section 3.3 and gives barriers and reaction energies at 0 K for each step in the reaction mechanism.

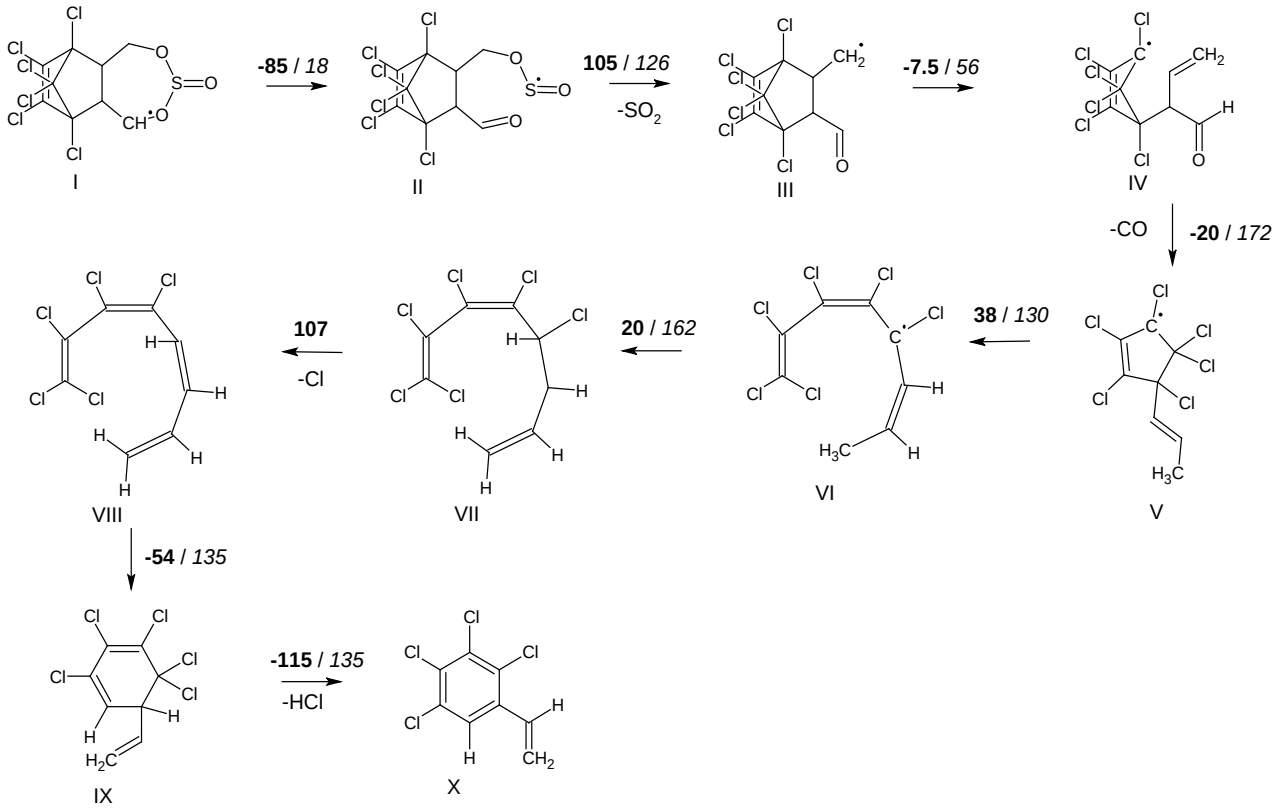


Fig. 2: Decomposition mechanism of an endosulfan radical. Numbers in bold are reaction energies at 0 K. Numbers in italics are barrier heights at 0 K. Units are kJ/mol.

## 3.4 Minor Product Formation

In the only previous study of pyrolysis of endosulfan by Chopra et al [4] carried out between 880-900°C, a large number of chlorinated benzenes was observed, together with some unidentified chloro-aromatics. Also observed were chlorohydrocarbons containing one or two carbon atoms, but no higher.

Our experimental observations are in accord with the results of Chopra et al [4]. However, these workers attributed the formation of the chlorobenzenes to loss of the bridging $CCl_2$ group by cycloelimination [5]. We calculate the barrier to cycloelimination of $CCl_2$ to be 310 kJ/mol at the M062X/G3Large level of theory. While this large barrier is probably surmountable at 900°C, cycloelimination is unlikely to contribute significantly to the chlorobenzenes formation in our experiments around 500°C. A further problem with attributing $CCl_2$ cycloelimination as the mechanism for chlorobenzene formation is that because of the low (204 kJ/mol) barrier for HCCP elimination from endosulfan, the bridging $CCl_2$ structure will no longer exist at temperatures sufficiently elevated for the large cycloelimination barrier to be overcome.

Instead, we believe that the tetrachlorostyrene (X) as shown in Fig. 2 is the most probable precursor of the chlorobenzenes. Cl atoms have a propensity to undergo ipso addition to an aromatic ring and to displace the substituent atom or group [6]. Hence Cl addition at the carbon atom bearing the vinyl group can facilitate its displacement. Pentachlorobenzene thus formed has been observed in significant yield [1]. Acetylene (also observed) would be expected to arise from H loss from vinyl.

Vinyl radical is probably the source of the chloroethanes and chloroethenes reported by Chopra et al [4]. Recombination between Cl and vinyl will produce chloroethene, and addition reactions of Cl would lead to the polychlorinated ethanes and ethenes observed.

As can be seen in the reaction scheme of Fig. 2, there are two intermediates which possess a terminal methyl group, viz., V and VI. Whilst hydrogen transfer from the methyl group as in VI $\rightarrow$ VII has a lower barrier, scission of the $CH_3$ group is possible leading to the formation of $CH_3Cl$ and other chlorinated methanes.

The large range of observed chlorobenzene isomers arises not only from facile ring Cl migration but also from H ipso addition and Cl displacement reactions which take place with only small barriers.

## 3.5 Dioxins' Formation from Endosulfan

Although most members of the cyclodienes including aldrin, dieldrin and endosulfan are now banned in most developed countries, large quantities of stockpiles, especially of endosulfan remain. The

cyclodienes are produced by Diels-Alder addition reactions of hexachlorocyclopentadiene. As our experimental and computational results indicate, liberation of the powerful chlorinating agent, hexachlorocyclopentadiene, is facile. In a recent report, Wang et al [7] found elevated levels of endosulfan and chlorinated benzenes in the Australian environment as a consequence of bushfire activity. Thus we would expect that the large quantities of chlorinated aromatics which we find in pyrolysis would be readily converted under oxidative conditions into chlorinated phenoxy intermediates – the direct precursors of PCDD/Fs [8].

If large concentrations of endosulfan are combusted such as might occur in an accidental stockpile burning, dioxin precursors will not only be formed as we have described above, but in addition, very large concentrations formed of HCCP and the pentachlorocyclopentadienyl radical will lead to precursors by a different route. This route which has been extensively studied in non-chlorinated cyclopentadiene itself by Kislov and Mebel [9] involves addition of pentachlorocyclopentadienyl radical to HCCP. We have investigated this route by quantum chemistry and find that, analogous with that followed by cyclopentadiene itself, after several low barrier steps, fully chlorinated styrene and chlorinated naphthalenes are produced. Thus, we expect that under fuel-rich and high endosulfan fuel combustion, very high levels of polychlorinated dioxins and dibenzofurans will result.

## 4. Conclusion

From the results of a quantum chemical study, initiation of inert gas pyrolysis of endosulfan takes place via a retro-Diels-Alder decomposition into hexachlorocyclopentadiene (HCCP) and 4,7-dihydro-1,3,2-dioxathiepine-2-oxide (2HDTO). Decomposition commences at about 300°C in a flow reactor at a residence time of 5 s. At comparable temperatures, the seven-membered ring of 2HDTO further decomposes via two competing reaction channels, both eliminating $SO_2$ – one also forming 2,5-dihydrofuran, the other, in a two-step process, forms the intermediate, 3-butenal, which then undergoes fission into CO and propene.

At higher temperatures, HCCP undergoes Cl scission and the Cl radicals thus released, lead to acceleration in the rate of decomposition of endosulfan promoted by abstraction of a methylene hydrogen from the seven-membered ring. The endosulfan radical thereby formed undergoes several low barrier decompositions, liberating, in turn, $SO_2$, CO, Cl and finally, HCl, in forming 2,3,4.5-tetrachlorostyrene. The last-named product is the precursor of the many chlorobenzene isomers observed experimentally. These are likely to be formed by ipso Cl atom addition and displacement of a vinyl radical.

Vinyl radicals and methyl radicals arising from scission of a terminal $CH_3$ group from intermediates in the decomposition of endosulfan radicals are the probable precursors of chlorohydrocarbons possessing one or two carbon atoms.

## 5. Acknowledgments

This research was undertaken with the assistance of resources from the National Computational Infrastructure (NCI), which is supported by the Australian Government. W.N.K.D. acknowledges the award of a postgraduate studentship by the University of Newcastle. JCM thanks Dr George Bacskay for bringing to his attention the environmental effects in residual endosulfan in soils.

## 6. References

[1] W.N.K. Dharmarathne, J.C. Mackie, E.M. Kennedy, M. Stockenhuber, Proc. Aust. Combust. Symp. University of Melbourne, Melbourne, 2015.

[2] M.J. Frisch, G.W. Trucks, H.B. Schlegel et al, Gaussian 09, Revision D.01, Gaussian, Inc., Wallingford CT, 2013.

[3] R.J. Crawford, S. Lutener, H. Tokunaga, Canad, J. Chem. **55** (1977), pp.3951-3954.

[4] N.M. Chopra, B.S. Campbelland J.C. Hurley, J. Agric. Food Chem. **26** (1) (1978), pp. 255-258.

[5] R.W. Hoffmann, Angew. Chem. Int. Ed. **10** (8) (1971), pp. 520-590.

[6] J.P Cui, Y.Z. He, W. Tsang, J. Phys.Chem. **93** (1989), pp. 724-727.

[7] X. Wang, K. Kennedy, J. Powell et al, Environ. Sci – Processes & Impacts, **17** (3), (2015), pp. 525-532.

[8] M. Altarawneh, B.Z. Dlugogorski, E.M. Kennedy and J.C. Mackie, Prog. Energy Combust. Sci **35** (2009), pp. 245-274.

[9] V.V. Kislov and A.M. Mebel, J. Phys. Chem. A **111** (2007), pp. 9532-9543.

# Kinetics analysis and reaction characteristics of aluminum alloys in water vapor

Tianyou Zhang, Jianzhong Liu, Zhenyu Huang, Zhijun Zhou, Weijuan Yang*, Junhu Zhou
State Key Laboratory of Clean Energy Utilization, Zhejiang University, Hangzhou 310027, China

**Abstract**

Aluminum has a high energy density. In order to investigate the activation mechanism of aluminum powder reaction in water vapor, experiments were carried out on the thermo-balance to study the reaction characteristics of aluminum samples with different low-melting metals in water vapour. The results showed that the weight gain of binary or ternary alloy outweighed pure aluminum. Single curve integral method was adopted to calculate kinetic parameter of the reaction of aluminum and aluminum alloys (Al-Li, Al-Mg and Al-Mg-Li) with $H_2O$. The apparent activation energy (E) and pre-exponential factor (A) were calculated. Al-Mg-Li had the activation energy of 65.52kJ/mol which was the smallest one among the four samples. Lower E presented easier condition of reaction startup. The activation mechanism of binary or ternary alloy was studied. The reaction product of aluminum alloy with $H_2O$ was measured by XRD and SEM. $LiAlO_2$ was observed in the product of Al-Li, and new crystalline hexagonal grain changed the morphology in the surface of sample. Al-Li or Al-Mg-Li alloy could be used as hydrogen carrier in underwater propulsion.

*Keywords: Aluminum alloy, water vapor, kinetic analysis.*

## Nomenclature

WG = the ratio of the final weight gain to the theoretical weight gain
WGR = weight gain rate

## 1. Introduction

Aluminum, the most abundant metallic element on the earth, is a promising energy storage and energy conversion material and has attracted much attention [1-3]. Since the middle of last century, metallic fuels have begun to be used as solid propellant[4]. Researchers had added aluminum into solid propellant to produce a new type of propellant with high energy density. Aluminum contributed greatly to improve the specific impulse and increased the energy density [1, 2, 5].

In neutral conditions, the release of hydrogen was observed through cutting, drilling, or grinding of freshly exposed Al surfaces in water[6, 7]. However, this reaction stopped soon because of the rapid passivation of the Al surface. The main problem is that the $Al_2O_3$ produced could form a solid film and hindered the continuous reaction of Al with water. Hydroxide ions (OH-1) in alkaline solutions can destroy the protective oxide layer on the Al surface [8-10]. The most commonly used hydroxide is sodium hydroxide (NaOH). Milling Al with different oxide modifiers, such as $Bi_2O_3$, $Cr_2O_3$, $TiO_2$, and ZnO, was proved to be an effective method to improve reaction efficiency [11, 12]. The adding of low-melting metals was also common used in improving the reactivity of Al. Mg, Li, In, Ga, Hg, Zn were effective in improving the hydrogen production rate and yield[13-17]. Li could be a good activator in promoting Al-$H_2O$ reaction in aqueous solution.

This study focused on the reaction of molten Al with $H_2O$ vapor at an elevated temperature. To facilitate the wide use of aluminum in propellant and hydrogen production material, different alloy elements were selected as activators in the reaction of pure aluminum with $H_2O$. Li and Mg were chosen in our study because of their reactivity and nontoxicity. By thermogravimetry and kinetic analysis, the reactivity of different samples was obtained. X-ray diffraction (XRD) and scanning electron microscopy (SEM) were used to analyze the products and to explore the activation mechanism.

## 2. Experimental section

### 2.1 Reagents

There were three kinds of powders. One is aluminum powder obtained by commercial way and it has an average size of 10 μm with a purity of 99.9%. The Li content of aluminum-lithium alloy is 20% with a mean particle size of 45 μm and a purity of 99.99%. Magnesium has the same particle size and purity with Al-Li alloy. The sample of Al-Mg-Li was obtained by hand-mixing using these three reagents. Al-Li and Al-Mg are binary alloy with 80% Al content. Al-Mg-Li is composed of 80%Al, 10%Mg and 10%Li. It was made through grinding in a crucible.

### 2.2 Measurements and methods

Experiments were conducted with a high-temperature thermogravimetric analyzer (CAHN THERMAX500, Thermo Electron Corporation, USA) to investigate the reactivity of different Al-based samples at a heating rate of 25 K/min up to 1000 ℃. The samples (10 mg) were placed in a crucible, which was in the argon atmosphere. The flux of argon and $H_2O$ vapor were 500 and 100 ml/min respectively. TG (thermo-gravimetric) and DTG (differential thermo-

* Corresponding author: W. Yang, Dr. /A.P.
Phone: (+86) 13906528790
Email: yangwj@zju.edu.cn

gravimetric) curves can be obtained to analyze the reaction kinetics.

The products were collected after the test ended and then measured using XRD (X'Pert PRO, Netherlands) and SEM (SU-70, Japan).

## 3. Results and discussion

### 3.1 Kinetic analysis

The TG and DTG results of Al, Al-Li, Al-Mg and AL-Mg-Li were depicted in Fig.1. The sample with 20% of Li (Al-Li) presented a better reactivity, and it had a greater final WG and a higher peak of DTG. The pure aluminum had the least WG, and it had no obvious WG before 800 ℃ .Except for Al, their DTG curves all had significant peak in relatively low temperature.

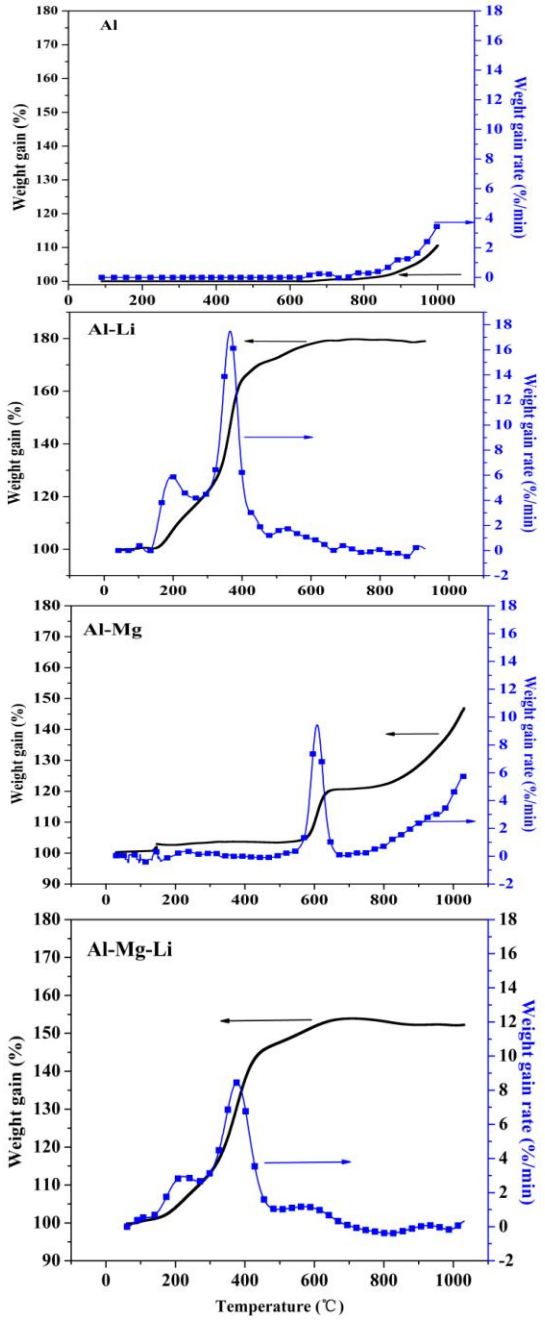


Fig.1 TG and DTG curves of samples: Al, Al-Li, Al-Mg, Al- Mg- Li

Thermal reaction parameters were summarized in Tab.1. Al-Li and Al-Mg-Li achieved the maximum WGR at a temperature lower than 400℃ , 354 and 376.9, respectively. As for the WG, Al-Mg-Li had lower WG than that of Al-Li, but both of them far outweighed Al. This meant that Li could promote the reaction of Al with water vapor. And, the percentage of aluminum reacted increased with the increase of Li content. Al-Mg and Al-Li with the same content aluminum (80%) presented a great difference, both in WG and WGR. With a higher activity, Li showed advantage over Mg in promoting the Al-$H_2O$ reaction.

Tab.1 Thermal reaction parameters

| Samples | WG (%) | Maximum WGR (%/min) | Temperature at The maximum WGR (℃) |
|---|---|---|---|
| Al | 111.2 | 3.57 | 1000 |
| Al-Li | 179.8 | 17.68 | 354 |
| Al-Mg | 148.5 | 9.75 | 608.3 |
| Al-Mg-Li | 153.6 | 8.63 | 377 |

Doyle single curve integral method was used to calculate the kinetic parameters based on the thermo-gravimetric results[18, 19]. The expression for this method is as follows:

$$F(\alpha) = \frac{AE}{\beta R} e^{-5.33-1.0515E/RT}$$

Where F(α) is reaction mechanism function; α is conversion rate; A is frequency factor, $s^{-1}$ ; E is reaction apparent activation energy, J/mol; β is the rate of temperature rise, K/s; R is gas constant, R=8.314K/(mol·K). Choosing the proper mechanism function, the apparent activation energy and frequency factor can be calculated.

As shown in Tab.2, the apparent activation energy (E) and pre-exponential factor (A) were listed, as well as their temperature range. In the atmosphere of water vapor, the activation energy of pure Al was 399.05kJ/mol, but E of Al-Mg-Li was only 65.52kJ/mol which was the smallest one among the four samples. Lower E presented easier condition of reaction startup. The reaction of Al-$H_2O$ started up over 700 ℃ while Al-Mg-Li and Al-Li with water below 200℃. The ternary and binary alloys were easier to be reacted with water vapor than pure aluminum. In comparison with the WG results above, the reaction of ternary alloy with water vapor was easy to start, but not achieved the greatest final WG.

Tab.2 Reaction kinetic parameters of Al, Al-Li, Al-Mg, and Al- Mg- Li under the atmosphere of water vapor

| Samples | E (kJ/mol) | A($s^{-1}$) | Temperature range (℃) |
|---|---|---|---|
| Al | 399.05 | $1.68\times10^{11}$ | 880-1000 |
| Al-Li | 77.17 | $5.54\times10^{4}$ | 200-440 |
| Al-Mg | 221.76 | $1.24\times10^{14}$ | 320-600 |
| Al-Mg-Li | 65.52 | $3.8\times10^{4}$ | 200-450 |

### 3.2 Activation mechanism of binary or ternary alloy

Based on previous studies [1, 20, 21], it was easy to form oxide film on the Al surface when exposed to air or other oxidants. In view of the fact that the addition of Li or Mg promoted the Al-$H_2O$ reaction,

they might have some influence in preventing the formation of oxide film. The reaction products after thermogravimetric experiments were measured using XRD for the crystalline species.

Fig. 2 presented XRD patterns for the reaction products collected after the experiments. Significant differences occurred in the XRD patterns after Li or Mg was added into Al. Peaks of Al, $Al_2O_3$, and $Al_{2.667}O_4$ were present in the products of pure Al with $H_2O$ reaction. For the Al-Li sample, XRD peaks included Al, $Al_2O_3$, and $LiAlO_2$. Similarly, Al, $Al_2O_3$, and $MgAl_2O_4$ peaks were detected in Al-Mg. Al-Mg-Li had both $MgAl_2O_4$ and $LiAlO_2$ peaks. The XRD results showed that the $Al_2O_3$ and the oxide of Li or Mg reacted and generated new products.

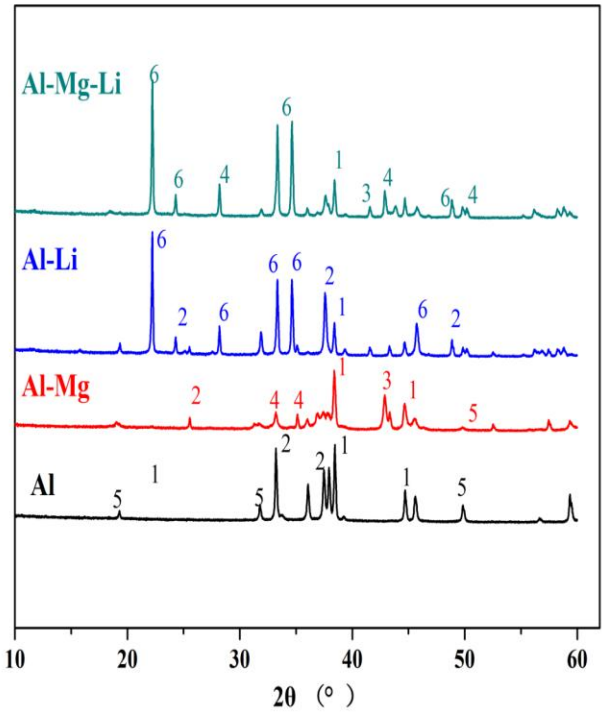


Fig.2 XRD patterns of products: Al, Al-Li, Al-Mg, Al-Mg-Li (1-Al, 2-$Al_2O_3$, 3-MgO, 4-$MgAl_2O_4$, 5-$Al_{2.667}O_4$, 6-$LiAlO_2$)

As depicted in Fig.3, the particles were generally spherical with few pitting for the products of Al. This result verified the fact that the main residuum of the Al-$H_2O$ reaction was unreacted Al. From the SEM images of the product for Al-Li, the surface appearance was markedly different from that of pure Al, and solid oxide film was not formed. Hexagonal crystals were clearly observed and flakes could be seen as well. In contrast to the corresponding XRD pattern, the crystalline hexagonal grain was $LiAlO_2$. For the sample of Al-Mg, fine oxide grains covered the surface, and fluidized products were also can be seen. Some needles were coated by fluidized products. These needles were predicted to be $MgAl_2O_4$ based on the corresponding XRD pattern. It could be predicted that adding Mg to Al promoted the crack of Al oxide film, thus facilitating the Al-$H_2O$ reaction. As for the Al-Mg-Li, Hexagonal crystals, flakes and needles were all observed. After the addition of Li or Mg, the crystals were not compact, and interspaces between crystals were visible. The appearance of $LiAlO_2$ and $MgAl_2O_4$ were different from $Al_2O_3$ in structure, which contributes to the promotion of Al-$H_2O$ reactivity. In conclusion, adding low-melting metal is an effective activator that drives the Al-$H_2O$ reaction.

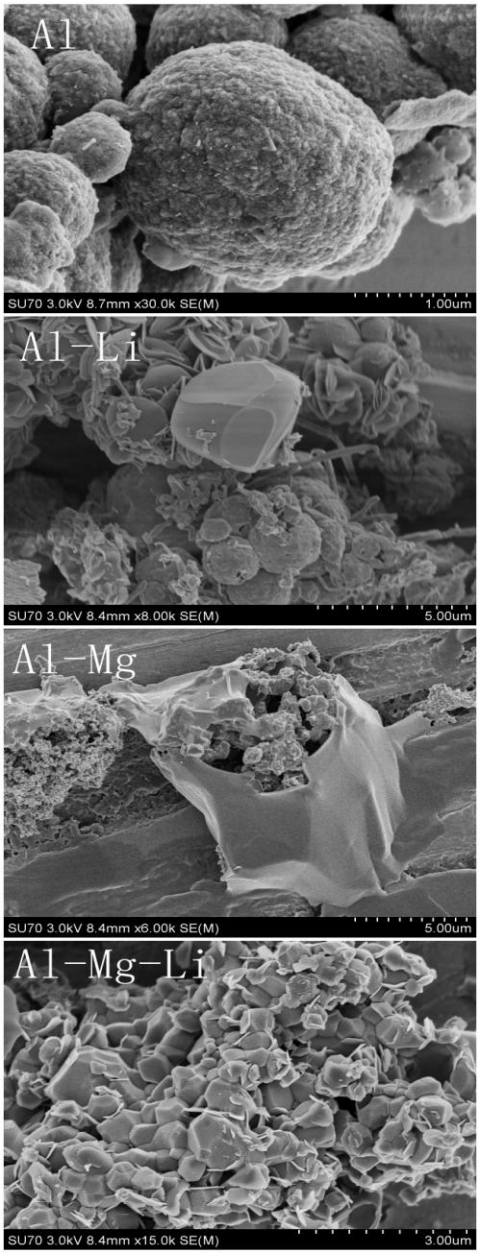


Fig.3 SEM micrographs of products: Al, Al-Li, Al-Mg, Al-Mg-Li

## 4. Conclusion

Li and Mg were added into Al as additives to investigate the effect on Al-$H_2O$ reactivity by thermogravimetric analyzer. The sample Al-Li presented a better reactivity and it had a greater final WG and a higher peak of DTG. Al-Li and Al-Mg-Li achieved the maximum WGR at a temperature lower

than 400℃. After the addition of Li, the reaction started in advance. The activation energy of Al-Mg-Li was the smallest among these four samples. The ternary and binary alloys were easier to be reacted with water vapor than pure aluminum.

The XRD results showed that $LiAlO_2$ or $MgAl_2O_4$ was generated after adding the Li or Mg. Based on the SEM images, it was found that new crystals change the surface morphology and increased voids between crystals. This explained the promoting mechanism of Li or Mg in Al-$H_2O$ reaction. More in-depth research still needs to be done in the future.

## 5. Acknowledgments

This work was financially supported by the National Natural Science Foundation of China (51376160) and the Fundamental Research Funds for the Central Universities (2015FZA4010).

## 6. References

[1].A. Ingenito; C. Bruno, J Propul Power 20 (6) (2004) 1056-1063 Doi 10.2514/1.5132.
[2].J. P. Foote; J. T. Lineberry; B. R. Thompson; B. C. Winkelman, AIAA paper 3086 (1996) 1996
[3].H. Wang; D. Leung; M. Leung; M. Ni, Renewable and sustainable energy reviews 13 (4) (2009) 845-853
[4].A. Davis, Combust Flame 7 (1963) 359-367
[5].T. F. Miller; J. L. Walter; D. H. Kiely, Proceedings of the 2002 Workshop on Autonomous Underwater Vehicles (2002) 111-119 Doi 10.1109/Auv.2002.1177213.
[6].P. Fleming; T. Bloodworth; G. Cook; A. Strauss; D. Wilkes; D. DeLapp; C. Cox, Science and Technology of Welding and Joining. Submitted January 13 (2009)
[7].K. Uehara; H. Takeshita; H. Kotaka, J Mater Process Tech 127 (2) (2002) 174-177
[8].E. Czech; T. Troczynski, Int J Hydrogen Energ 35 (3) (2010) 1029-1037
[9].L. Soler; J. Macanás; M. Muñoz; J. Casado in: *Hydrogen generation from aluminum in a non-consumable potassium hydroxide solution*, Proceedings International Hydrogen Energy Congress and Exhibition IHEC, 2005; 2005; pp 13-15.
[10].D. Stockburger; J. Stannard; B. Rao; W. Kobasz; C. Tuck in: *On-line hydrogen generation from aluminum in an alkaline solution*, Proc Symp Hydrogen Storage Mater Batteries Electrochem, 1992; 1992; pp 431-44.
[11].P. Dupiano; D. Stamatis; E. L. Dreizin, Int J Hydrogen Energ 36 (8) (2011) 4781-4791 DOI 10.1016/j.ijhydene.2011.01.062.
[12].H.-W. Wang; H.-W. Chung in: *Hydrogen generation by the reaction of oxide-modified aluminum powders with tap water*, SPIE Solar Energy+ Technology, 2010; International Society for Optics and Photonics: 2010; pp 77701E-77701E-6.
[13].Z. W. Zhao; X. Y. Chen; M. M. Hao, Energy 36 (5) (2011) 2782-2787 10.1016/j.energy.2011.02.018.
[14].V. Rosenband; A. Gany, Int J Hydrogen Energ 35 (20) (2010) 10898-10904
[15].M. Q. Fan; L. X. Sun; F. Xu, Energy 35 (3) (2010) 1333-1337 DOI 10.1016/j.energy.2009.11.016.
[16].M. q. Fan; L. x. Sun; F. Xu, Energy 35 (7) (2010) 2922-2926
[17].M.-Q. Fan; F. Xu; L.-X. Sun; J.-N. Zhao; T. Jiang; W.-X. Li, J Alloy Compd 460 (1) (2008) 125-129
[18].Z. S. Petrović; Z. Z. Zavargo, J Appl Polym Sci 32 (4) (1986) 4353-4367
[19].J. H. Flynn; L. A. Wall, Journal of Polymer Science Part B: Polymer Letters 4 (5) (1966) 323-328
[20].S. Mohan; L. Furet; E. L. Dreizin, Combust Flame 157 (7) (2010) 1356-1363 DOI 10.1016/j.combustflame.2009.11.010.
[21].M. Schoenitz; C. M. Chen; E. L. Dreizin, J Phys Chem B 113 (15) (2009) 5136-5140 Doi 10.1021/Jp807801m.

# Magnitude of the deuterium kinetic isotope effect during the combustion of methane over a $Pd/Al_2O_3$ catalyst

B.A. Wright, E.M. Kennedy* and M. Stockenhuber
Chemical Engineering, Faculty of Engineering & Built Environment
The University of Newcastle, Callaghan NSW 2308, Australia

**Abstract**

The deuterium kinetic isotope effect during combustion of methane (7,000 ppm in air) over a $Pd/Al_2O_3$ catalyst at 270 °C has been determined. The overall rate ratio, $CH_4$ vs $CD_4$ is 3.1±0.2 which was consistent with the rate ratio predicted (2.9) if the rate determining step of the reaction is largely governed by the rate of bond breaking in methane. In additional experiments involving the oxidation of humid $CH_4$ or $CD_4$ feed gases, which have been saturated in $H_2O_{(v)}$ or $D_2O_{(v)}$ respectively, the rate of reaction decreases significantly in the presence of a high concentration of water vapour (ca 12,000 ppm) but the overall rate ratio, $CH_4$ / $H_2O_{(v)}$ vs $CD_4$ / $D_2O_{(v)}$ increases only slightly, to 3.2 ±0.6. This suggests that the effect of water vapour on the reaction rate is attributable to an equilibrium isotope effect (EIE) but under all reaction conditions studied at 270 °C, the rate limiting step involves methane activation.

*Keywords: Ventilation Air Methane, catalytic combustion, Kinetic isotope effect*

## 1. Introduction

Methane comprises 17% of the worlds anthropogenic greenhouse gas emissions with roughly 8% coming from coal mines of which 70% is in the form of ventilation air methane (VAM). Further details are given in [1]. VAM has a $CH_4$ concentration of 0.1-1 vol% but a flow rate in the range of 300 $m^3 \cdot s^{-1}$ making beneficial reuse difficult. Hence, much of the current research focuses on mitigation through combustion processes to produce $CO_2$.

One option is the use of low temperature, flameless, catalytic combustion. This is attractive due to the low temperature operation. This has the potential to reduce system energy use compared to standard autoignition systems, along with potential safety benefits.

The most active catalyst for methane oxidation is palladium [2], which was the focus of this study. Despite extensive study there is still no agreement on the methane oxidation reaction mechanism in fuel lean conditions when the catalyst is in the oxide phase which would be typical for a VAM system [2]. This study examined potential mechanisms for the catalytic combustion of methane over a commercial $Pd/Al_2O_3$ catalyst. The main focus was on isotopic jump experiments using both dry and humid feeds as the role of water in the mechanism was considered crucial.

## 2. Experimental Setup

### 2.1 Time on Stream Experiments

Apparatus

In order to obtain intrinsic rate data, a plug flow reactor, operating under differential reaction conditions was used. Gas chromatography (GC) (GC-2014 Shimadzu GC with thermal conductivity detector and Labanalysis software), and gas phase Fourier transform infra-red spectroscopy (FTIR) equipped with 10 metre multi-pass cell (IR Prestige 21 Shimadzu FTIR QP 5000) were used to quantify feed and reaction products.

Reactor System and Materials

The reactor used in this study was ¼" stainless steel with stainless steel piping, valves and fittings. The reactor was heated by a 3 zone XD-1200 NT furnace (Brother). Gas flow was controlled using either an Aalborg Command Module or a Model 5878 Brooks Command Module with mass flow controllers. The temperature of the $H_2O$ and $D_2O$ saturators was controlled using a Huber CC-K6 chiller system with Pilot One Command Module. A layout of the apparatus is presented in Fig. 1.

The gas flow consisted of compressed air and $CH_4$ (99.95%, Coregas) or $CD_4$ (99%, Aldrich). The methane concentration was maintained at 7000 ppm to simulate a typical VAM flue gas composition. While elevated $CO_2$ levels would be anticipated in a typical VAM system, it was only present as a background component in the air. The $CO_2$ peak in the GC was used to determine conversion (and thus rate). In order to humidify the feed with $H_2O$, a distilled water saturator was used, while the $D_2O$ used was 99.9% (NovaChem). The catalyst used was a commercial 1 wt% $Pd/Al_2O_3$ supplied by Sigma Aldrich. This was supplied in powder form, which was used to make pellets in the size fraction 250-425 μm.

The catalyst had a Pd dispersion of 14.2% with details of the preparation and properties given in [3]. To prevent catalyst bypassing but also maintain differential conditions γ-alumina (Sigma Aldrich) pellets of the same size fraction were blended with the catalyst in a ratio of 3 parts alumina to 1 part catalyst. Experiments showed the γ-alumina was inert. Before conducting experiments the catalyst was calcined at 500 °C using a heating rate of 10 °C·$min^{-1}$. The catalyst was cooled to the reaction temperature of 270 °C with a He flow. For each run fresh catalyst was used to avoid H and D cross contamination.

* Corresponding author: E. Kennedy
Phone: (+61) 2 49854422
Email: eric.kennedy@newcastle.edu.au

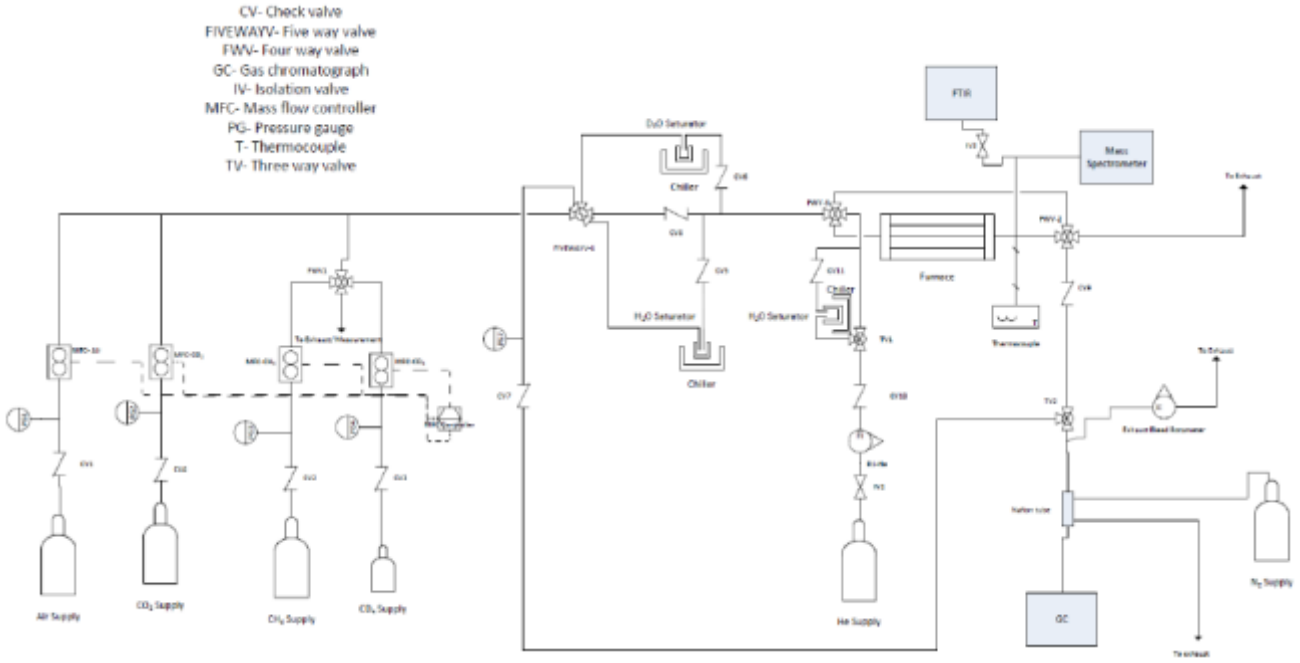


Fig. 1- Experimental layout

Experimental Runs

For all runs, the experiment was operated with a gas hourly space velocity (GHSV) of 100,000 $h^{-1}$. This excluded any $Al_2O_3$ diluent pellets in the calculation. Approximately 50 mg of $Pd/Al_2O_3$ was used. The reaction temperature was 270 °C to maintain differential conditions for both $CH_4$ and $CD_4$. For the runs, the dry feed was initially run for four hours, the humid feed for two hours and then the dry feed was run again for two hours. There were three different types of runs conducted:

- $CH_4$, $H_2O$ (2 runs)
- $CD_4$, $D_2O$ (2 runs)
- $CH_4$, $D_2O$ (1 run)

The dry feed involved running the air-methane mix without modification while the wet feed involved bubbling the mix through the appropriate $H_2O$/ $D_2O$ saturator. To maintain a constant water concentration the saturators were held at 10 °C using a chiller.

## 2.2 Analysis

The primary conversion analysis was performed using the GC which could detect for all major compounds in the system apart from water. The GC had a TCD detector and used a molecular sieve column and a Hayesep D column. The column temperature was set at 100 °C and a six minute analysis time was used. Labanalysis software was used to view the results. As the reactor was operated under conditions of low conversion ($X_{CH4}$ <15%), the rate of conversion was based on the measurements of $CO_2$ formation.

The conversion data was used to calculate reaction rates. In the range of 4-8 (generally 6-8) repeat reaction rates measurements were calculated in each period (dry, wet, dry), with an average taken. To estimate the error in the reaction rate, the standard deviation was used. The average reaction rates were used to calculate turnover frequencies (TOF) with standard uncertainty propagation calculations used to determine the final uncertainty.

Gas phase FTIR was used to determine if isotopomers of methane were produced, based on published characteristic wavelengths of these species [4]. The sample chamber was evacuated to 2.5 torr or lower before the reaction sample was introduced to the multi-pass cell, with 16 scans being accumulated for each spectra.

# 3. Results and Discussion

## 3.1 Time on Stream Experiments

An example of the conversion plots for the various $CH_4/H_2O$ and $CD_4/D_2O$ runs is given in Fig. 2. There are a number of features that give insight into the reaction mechanism. Firstly, the initial dry $CH_4$ conversion is around 8-10% compared to the $CD_4$ conversion being in the 2-4% region. This is strong evidence for a KIE for dry feeds, which agrees with [5]. The two most likely reasons are that methane activation was rate limiting or that an O-D moiety was more strongly bound to the surface, which increased the surface coverage. Of these options methane activation being rate limiting is considered most likely.

The significant deactivating effect of humid feeds on the catalyst is highlighted in Fig. 2. For both $H_2O$ and $D_2O$ exposure, the conversion dropped almost immediately. For $H_2O$ the conversion was approximately 0.5% while for $D_2O$ the conversion was between 0.3 and 0.4%.

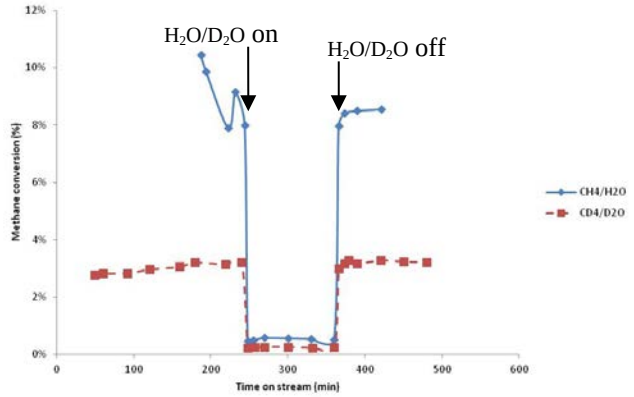


Fig. 2- Plot of change in conversion during isotope "jump"

From Fig. 2 it appears that the catalyst deactivation due to water vapour was reversible. The recovery in activity of the catalyst was rapid once the water was switched off. This highlights that the presence of water vapour has a significant impact on the reaction rate. There are three possible reasons for this, including a likely increase in surface water coverage of the catalyst, the increased partial pressure of water in the gas phase creates a thermodynamic barrier to desorption from the surface and the water reducing the oxygen mobility of the support, which could occur in a Mars and van Krevelen (MVK) mechanism. The rapid recovery in activity when water was removed indicates that the rate of desorption of surface hydroxyls is not slow in dry feeds. This indicates that the partial pressure of the water in the gas phase is playing a role and could indicate the thermodynamic barrier to desorption or a MVK mechanism.

## 3.2 Mixed isotope run

To assess the extent of isotope scrambling and the reversibility of methane adsorption, a reaction involving $CH_4/D_2O$ was undertaken. If methane was reversibly adsorbed to the surface during reaction, then mixed isotopic species such as $CH_3D$, would form once $D_2O$ was introduced into the system. Gas phase FTIR was used with the 2000-2500 $cm^{-1}$ wavenumber region was investigated and the results are shown in Fig. 3.

Figure 3 highlights that as the $D_2O$ exposure increased, a signal at the 2199 $cm^{-1}$ formed, which corresponds to $CH_3D$ [4]. After 30 min of $D_2O$ exposure the signal to noise ratio was 1.4 and after 90 min of $D_2O$ exposure it was 1.5. Further, 30 min after the $D_2O$ had been switched off the ratio had increased to three but 90 min after switching off the $D_2O$, there was no signal in this region. It is thought that the reason for the highest signal to noise ratio being obtained after the $D_2O$ was switched off was that significantly more methane was being activated as the conversion was higher and there was still some $D_2O$ left in the system.

While there was strong evidence for $CH_3D$ formation, there was no evidence for any of the other isotopomers of methane forming. This could either be because they were not present or they were not in sufficient concentration to be detected. The formation of $CH_3D$ is evidence that methane is reversibly adsorbed to

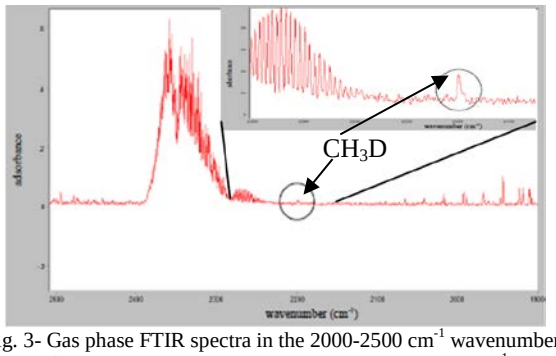


Fig. 3- Gas phase FTIR spectra in the 2000-2500 $cm^{-1}$ wavenumber region after 90 min exposure to $D_2O$ with zoom on 2199 $cm^{-1}$ signal

the surface. Given that no other isotopes are formed it suggests that breaking the first C-H bond is reversible but subsequent hydrogen abstraction is irreversible although the extent of reversibility was difficult to assess due to the low conversion of methane and weak signal rendering quantitative analysis difficult.

## 3.3 Turnover frequencies

A summary of the TOF data is presented in Table 1. The initial and final dry conversions were within experimental uncertainty of each other except for the second $CH_4$ /$H_2O$ run. For the dry $CH_4$ data, the TOF were within the range of 0.03 to 0.179 $s^{-1}$ as published by [6] for a $Pd/ZrO_2$ catalyst. There was no known published deuterated data for comparison.

Table 1 shows that the dry TOF is an order of magnitude larger than the humid rate which highlights the extent of water poisoning. However, in all cases the final dry conversion was at least within 10% of the initial dry conversion if not within experimental uncertainty. This highlights the water poisoning was reversible.

## 3.4 Kinetic isotope effect

Based on the data in Table 1, an estimation of the rate of $CH_4$ vs $CD_4$ was undertaken. Under conditions where the feed gas is free of water vapour (although some water vapour is generated during reaction).

Table 1- Turnover frequencies

| Run Type | Run Number | Condition | TOF ($s^{-1}$) |
|---|---|---|---|
| $CH_4$/ $H_2O$ | 1a | Dry | 0.088±0.011 |
| | 1b | Wet | 0.0051±0.0004 |
| | 1c | Dry | 0.081±0.003 |
| | 2a | Dry | 0.061±0.0006 |
| | 2b | Wet | 0.0063±0.0005 |
| | 2c | Dry | 0.076±0.002 |
| $CD_4$/ $D_2O$ | 3a | Dry | 0.029±0.002 |
| | 3b | Wet | 0.0023±0.0002 |
| | 3c | Dry | 0.031±0.001 |
| | 4a | Dry | 0.02±0.003 |
| | 4b | Wet | 0.0013±0.0002 |
| | 4c | Dry | 0.02±0.002 |

$$\frac{k_H}{k_D}(dry) = \frac{average\ TOF\ (run\ 1a, 1c, 2a, 2c)}{average\ TOF(run\ 3a, 3c, 4a, 4c)} = 3.1 \quad (1)$$

This estimate is based on the assumption that the number of active site on the catalyst remains constant. Comparing the value of 3.1±0.2 obtained experimentally with that predicted if the rate-limiting step involves dissociation of the C-H (or C-D) bond:

$$\frac{k_H}{k_D} = e^{\frac{\Delta G^{\ddagger}_D - \Delta G^{\ddagger}_H}{RT}} = e^{\frac{4.785}{RT}} = 2.9 \quad (2)$$

where $\Delta G^{\ddagger}_D - \Delta G^{\ddagger}_H$ is approximately equal to the difference in C-D and C-H bond dissociation energies (4,785 J $mol^{-1}$), $R$ is the ideal gas constant and $T$ is the reaction temperature (543K).

The similarity in the experimental and theoretical $\frac{k_H}{k_D}$ values suggests that C-H (C-D) bond cleavage in methane is rate limiting under these reaction conditions.

Under conditions where the feed methane/air stream was saturated in water vapour, the rate of reaction decreases significantly due to the high concentration of water vapour (ca 12,000 ppm). We again estimate of the rate of $CH_4$ / $H_2O_{(v)}$ vs $CD_4$ / $D_2O_{(v)}$.

$$\frac{k_H}{k_D}(wet) = \frac{average\ TOF\ (run\ 1b, 2b)}{average\ TOF(run\ 3b, 4b)} = 3.2 \quad (3)$$

Under these conditions, the overall rate ratio, $CH_4$ / $H_2O_{(v)}$ vs $CD_4$ / $D_2O_{(v)}$ increases only slightly, to 3.2±0.6. This suggests that the effect of water vapour on the reaction rate is attributable to an equilibrium isotope effect (EIE) but under all the reaction conditions studied at 270 °C, the rate limiting step remains methane activation.

## 3.5 Implications for mechanism

From this data some assertions about the reaction mechanism can be made. For dry feeds, it is apparent that there was a KIE, with the $CD_4$ conversion being significantly lower than the $CH_4$ conversion. This is strong evidence for methane activation being rate limiting for dry feeds at least initially. It is also clear that water has a significant deactivating effect.

In the literature several different mechanisms have been proposed by authors such as [6] and [7]. While no conclusive results were obtained with respect to the number of active sites from this work, the most likely mechanism is a single site mechanism like that proposed by [6] with some modifications. In [6], water adsorption from the gas phase was not considered which this work shows it is important for humid feeds. The FTIR also indicated that at least the cleavage of the first C-H bond is reversible rather than irreversible. A modified mechanism is given in (4), with changes the mechanism given by [6] bolded (steps (4c) and (4e)).

| | |
|---|---|
| $O_{2(g)} + S \overset{K_1}{\rightleftharpoons} O_2^*$ (a) | Oxygen adsorption from gas phase |
| $O_2^* + S \overset{k_2}{\rightarrow} 2O^*$ (b) | |
| $\boldsymbol{H_2O_{(g)} + S + O^* \overset{K_3}{\rightleftharpoons} 2OH^*}$**(c)** | Water adsorption from gas phase |
| $CH_{4(g)} + S \overset{K_4}{\rightleftharpoons} CH_4^*$ (d) | |
| $\boldsymbol{CH_4^* + O^* \overset{K_5}{\rightleftharpoons} CH_3^* + OH^*}$**(e)** | Adsorption and hydrogen abstraction from methane molecule |
| $CH_3^* + O^* \rightarrow CH_2^* + OH^*$(f) | |
| $CH_2^* + O^* \rightarrow CH^* + OH^*$(g) | |
| $CH^* + O^* \rightarrow CHO^* + S$ (h) | |
| $CHO^* + O^* \rightarrow CO^* + OH^*$(i) | Surface rearrangements |
| $CO^* + O^* \rightarrow CO_2^* + S$ (j) | |
| $CO_2^* + O^* \rightarrow CO_3^* + S$ (k) | |
| $2OH^* \overset{K_3}{\rightleftharpoons} H_2O_{(g)} + O^* + S$(l) | Product water desorption from surface |
| $CO_2^* \overset{K_6}{\rightleftharpoons} CO_{2(g)} + S$ (m) | Carbon dioxide desorption from surface |
| $CO_3^* \overset{K_7}{\rightleftharpoons} CO_{2(g)} + O^*$ (n) | |

(4)

## 4. Conclusion

In this paper we describe experiments to try to shed light on the reaction mechanism for the catalytic combustion of methane over $Pd/Al_2O_3$ in humid feeds at low temperatures. Deuterated isotopes of methane and water were used to gain insight into the reaction mechanism using GC and FTIR to determine conversion and different methane isotopes. Our mechanism was similar to other authors, although it is clear that water plays a significant deactivating role. It is also hypothesised that methane is only reversibly adsorbed to the surface initially and that at 270 °C, the rate limiting step in the reaction involves methane activation.

## 5. Acknowledgments

The authors would like to thank the Australian Coal Association Research Program (ACARP) for financial support of this project grant number G1200592.

## 6. References

1. Su, S. and J. Agnew, Fuel, 2006. **85**(9): p. 1201-1210.
2. Ciuparu and L. Pfefferle, Catalysis Today, 2002. **77**(3): p. 167-179.
3. Setiawan, A., et al., Catalysis Science & Technology, 2014. **4**(6): p. 1793-1802.
4. Wilmshurst, J.K. and H.J. Bernstein, Canadian Journal of Chemistry, 1957. **35**(3): p. 226-235.
5. Au-Yeung, J., et al., Journal of Catalysis, 1999. **188**(1): p. 132-139.
6. Fujimoto, K.-i., et al., Journal of Catalysis, 1998. **179**(2): p. 431-442.
7. Cortés, J., E. Valencia, and P. Araya, Journal of Physical Chemistry C, 2010. **114**(26): p. 11441-11447.

# The role of HNO and NOH in NO formation during ammonia oxidation on Pt(111)

Juan D. González, B.S Haynes and Alejandro Montoya*
School of Chemical and Biomolecular Engineering
The University of Sydney 2006 Australia

## Abstract

A new thermodynamically-consistent microkinetic model for $NH_3$ oxidation on Pt(111) is developed. Molecular modelling methods were employed to obtain the thermodynamic and kinetic parameters of 30 reversible elementary reactions including $NH_3$ dehydrogenation, oxidation, and products formation. Emphasis is placed on the role of HNO and NOH in the reaction network due to ambiguities in the open literature on the rates for NO formation. Several pathways including *i*) N*+O*↔NO*, *ii*) HNO*↔NO* +H* and *iii*) NOH*↔NO +H* were studied. Although vibrational surface properties of HNO* are consistent with experimental reported values, a kinetic analysis reveals that pathway *i)* is the most relevant in the NO formation. A method that links binding energies and vibrational properties of surface species with thermodynamic properties required in the surface module of Chemkin will be discussed.

*Keywords: Density Functional Theory, Ammonia oxidation, Mechanism, Microkinetics, Modelling.*

## 1. Introduction

The oxidation of ammonia to $HNO_3$ is one of the largest processes in the chemical manufacturing industry, with a worldwide production of about 70 million tonnes in 2010 [1]. The oxidation of $NH_3$ is typically carried out with air over a Pt/Rh alloy between 750 and 900 °C, and 1 to 15 bar. The oxidation conditions allow a variety of surface morphologies of the catalyst to be present during steady-state operations [2], affecting the rate of elementary reactions and, therefore, the rate-limiting step(s) of the reaction network.

Intermediates that might be present during the $NH_3$ oxidation have been identified using Ultra High Vacuum (HUV) techniques [3-8], and elementary reaction steps of $NH_3$ dehydrogenation leading to NO, $N_2$, and $N_2O$ have been studied with molecular modelling techniques[2, 9]. Most of these studies have focused on Pt(111) because this face is the most thermodynamically stable at high temperatures[10, 11] The $NH_3$ oxidation is assisted by adsorbed oxygen (O*) and hydroxyl (OH*) species ultimately leading to N* on the surface [9, 12]. This N* recombines to form $N_2$, NO and $N_2O$ as presented in reactions (3)-(5) [2]. In a recent study, Warner and Haynes[13] developed a model that combines a fundamental surface reaction mechanism with mass transfer effects for $NH_3$ combustion on Pt. The model indicates according to (1) that the activation energy ($E_a$) for reaction (2) minus twice $E_a$ of reaction (3) should be in the order of -87 kJ.mol$^{-1}$ to reproduce the experimental observations of $N_2$ production in a wide range of industrial conditions.

$$E_{app_{N_2}} = E_{aN_2} - 2E_{aNO} = -87\ kJ.mol^{-1} \quad (1)$$

The authors also found that the available values for $E_a$ from density functional theory (DFT) calculations for reactions (2) and (3) on different platinum surfaces are inconsistent with the relationship (1). We explored new reaction pathways leading to NO involving HNO* and NOH* intermediates, reactions (5)-(8) on Pt(111). Smirnov *et al.* [14] and Asscher and Somorjai [15] using HREELS and molecular beam techniques first have proposed that HNO* and NOH* are surface intermediates for NO formation during $NH_3$ oxidation on Pt(111). However, the kinetic relevance of (5)-(8) relative to (3) is not known.

| | |
|---|---|
| N*+N*↔$N_2$ | (2) |
| N*+O*↔NO* | (3) |
| N*+NO*↔$N_2$O* | (4) |
| HNO*↔NO* +H* | (5) |
| NOH*↔NO +H* | (6) |
| HNO*+O*↔NO*+OH* | (7) |
| NOH*+O*↔NO*+OH* | (8) |

Here, a detailed thermodynamically-consistent surface mechanism that includes the presence of HNO* and NOH* during $NH_3$ oxidation on Pt(111) is developed to understand the role of reactions (5)-(8) in NO formation.

## 2. Methodology

### 2.1 Molecular modelling simulations

A periodic slab of Pt(111)-p(2x2) with a spacing of 15 Å between slabs was used to obtain changes in enthalpy ($\Delta H$), entropy($\Delta S$), activation energies ($\Delta E$) and pre-exponential rate factors ($A$) of elementary reactions. Figure 1 shows a schematic representation of the periodic slab and the surface adsorption sites tested for site selectivity analysis. Electronic energies and equilibrium configurations were obtained with the

* Corresponding author:
Phone: +61 2 9351 2040
Email: alejandro.montoya@sydney.edu.au

VASP program [16-18] using the PBE functional, and the Methfessel-Paxton method with a smearing of 0.2 eV, a (5×5×1) k-point mesh and an energy cut-off of 400 eV.

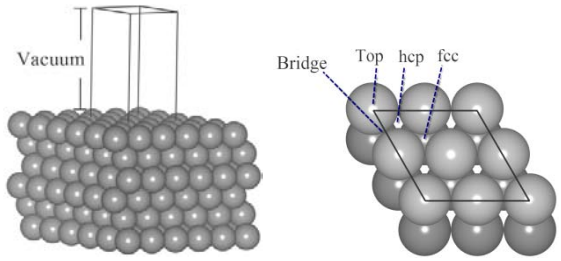


**Figure 1.** Side and top views of a supercell model of a Pt(111) surface. Symmetry sites are shown in the top side view for clarity.

The CI-NEB method [19, 20] with at least five images was used to obtain $E_a$ values. The convergence of the CI-NEB was achieved when the force of the band was lower than 0.05 eV/Å. The validity of the transition states was confirmed with a single imaginary frequency in the direction of the reaction coordinate. All the energies presented here are corrected by vibrational energy at zero kelvin.

## 2.2 Microkinetic simulations

Microkinetic simulations were carried out using the Chemkin-pro software package [21]. A shear flow reactor (SFR) with a diameter of 0.06 cm, 5 cm long and a site density of $2.3*10^{-9}$ mol.cm$^{-2}$ was used to simulate previous experimental studies carried out in a platinum tube between 100 and 900°C [22]. The reactions were simulated at 1 bar, with an inlet flow of 300 sccm and an inlet concentration of 1000 ppm of $NH_3$ and 2000 ppm of $O_2$ in argon.

Sensitivity coefficients for selected species $S_{ij}$ were obtained according to equation 2:

$$S_{ij} = \frac{\partial ln\alpha_i}{\partial ln\beta_j} \quad (8)$$

Where $\alpha_i$ represents the surface fraction of the species $i$, and $\beta_j$ represents rate constant of the reaction $j$. In particular, changes in the rate constant were obtained by varying pre-exponential factor. The rate constant in the forward direction for each elementary reaction was calculated following an Arrhenius expression:

$$k_f(T) = A_f exp(-\frac{E_{af}}{RT}) \quad (9)$$

Where $A_f$ is the pre-exponential factor, $E_{af}$ the forward activation energy and R is the gas constant. The rate constant for the reverse reaction was calculated using the equilibrium expression of the elementary reaction:

$$k_r(T) = A_f exp(-\frac{E_{af}}{RT})\ exp(-\frac{\Delta S}{R}) exp(\frac{\Delta H}{RT}) \quad (10)$$

This methodology results in a thermodynamically-consistent kinetic model, a constraint that is often neglected in heterogeneous kinetic models. The method of calculating $\Delta H$, $\Delta S$, and $A$ factors, and the evaluation of the relevant NASA polynomials coefficients will be presented in detail elsewhere [23, 24].

## 3. Results and Discussion

### 3.1 Species binding on Pt(111)

The binding energies (BE) and the preferred sites of adsorption of all the species involved in NO formation are shown in Fig. 2. Binding energies for species other than HNO and NOH have been extensively reviewed [9, 25] and the values showed in Fig. 2 are within 4 kJ mol$^{-1}$ of those reported in the literature. The BE of HNO* and NOH* are similar and relatively high, indicating that surface recombination and decomposition may be preferred than their desorption to the gas phase. The BE of HNO* and NOH* (387 and 397 kJ.mol$^{-1}$) are lower than the BE of N*, similar to NH* and O*, and higher than OH*, H* and NO*. The stability of HNO* and NOH* is in the range of the thermal stabilities of other species known to be involved in the NO desorption process.

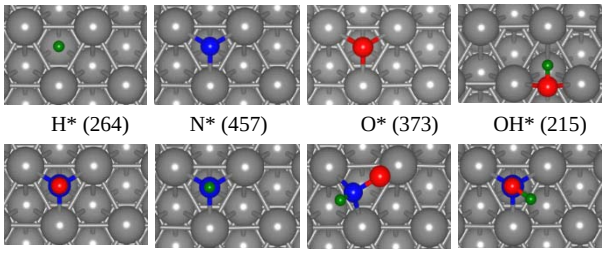


**Figure 2.** Top view of preferred sites for adsorption and BE for species involved in reactions (2) and (3) and (5)-(8). Blue: nitrogen atom, green: hydrogen atom, gray: platinum atom and red: oxygen atom.

The binding characteristics of HNO* and NOH* are somewhat different. While HNO* binds N-O down with N above a bridge site and O above atop site, the NOH binds N-down above an fcc site. The change in binding characteristics results in differences in the molecular frequencies of HNO* and NOH*. The calculated frequencies and modes for HNO* and NOH* are presented in Table 1. It is observed that the intramolecular stretching of NH at 3311 cm$^{-1}$ and the NO asymmetrical stretching at 1009 cm$^{-1}$ for HNO* are close to the bands at 3280 and 800 cm$^{-1}$ found by Smirnov et al.[14] in a HREELS study. These bands which are not found in any known adsorption states of nitrogen oxides or $NH_x$* (x=1-3), were assigned to the NH and NO stretchings, respectively, of an HNO* species bonded to the Pt(111) surface via both nitrogen and oxygen atoms. There is no experimental data available to compare with the computed frequencies for NOH*.

**Table 1**. Vibrational modes and frequencies ($cm^{-1}$) for HNO and NOH adsorbed on Pt(111).

| Modes | Adsorbate | |
|---|---|---|
| | HNO* | NOH* |
| Stretching | 3311 | 3556 |
| Scissoring | 1279 | 1302 |
| stretching | 1009 | 909 |
| Frustrated rotation | 766 | 544 |
| Frustrated rotation | 536 | 543 |
| Frustrated rotation | 415 | 345 |
| Frustrated translation | 373 | 181 |
| Frustrated translation | 254 | 161 |
| Frustrated translation | 216 | 129 |

## 3.2 Pathways analysis for NO formation on Pt(111).

A schematic representation of a selected set of elementary steps leading to NO* is shown in Figure 3, and the corresponding minimum energy pathways are presented in Figures 4 and 5.

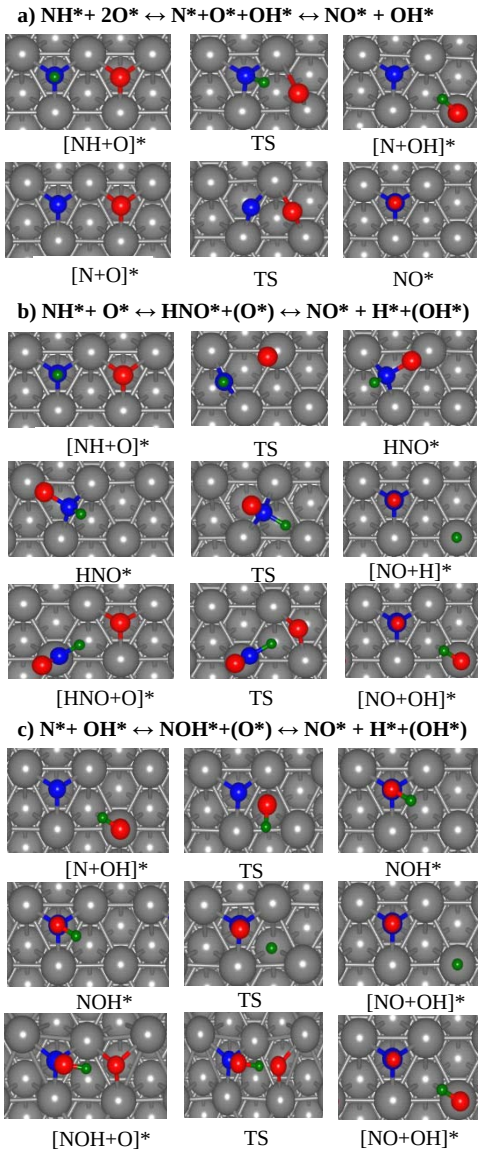


**Figure 3**. Pathways for NO formation on Pt(111) surface. TS: transition state. NH*+O* represents reactants adsorbed in a separate unit cell without lateral interaction. [NH+O]* represents co-adsorbed reactants in the same unit cell with lateral interaction.

The reaction of NH* with O* is presented in fig 3a, and its corresponding reaction profile is shown with blue lines in fig 4. The reaction of NH* with O* leading to HNO* and formation of NO* assisted by Pt and O* is presented in Fig 3b, with its corresponding energy profiles in fig 4. The reaction of N* with OH* leading to NOH* and formation of NO* assisted by Pt and O* is presented in fig 3c, with its corresponding energy profiles in Fig. 5.

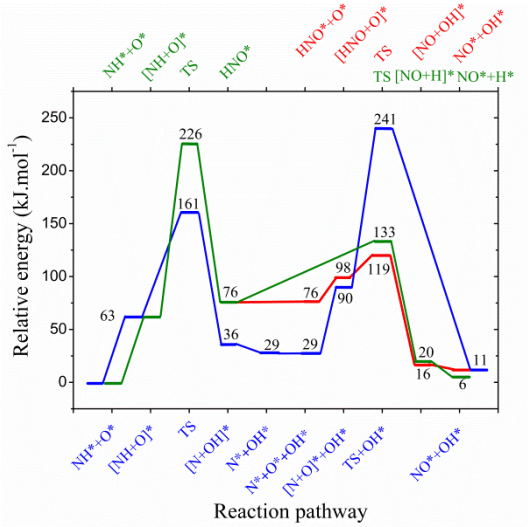


**Figure 4**. Reaction energy diagram for NO formation via HNO* and N*+O* recombination. All energies are referenced to NH*, 2O* and Pt(111).

For reaction N*+O*→NO* the first step has lower activation energy (161 vs. 226 $kJ.mol^{-1}$) compared with HNO* formation step. The second, corresponding to the NO* formation is highly activated with an energy barrier of 212 $kJ.mol^{-1}$. In contrast, NO formation via HNO* dissociation shows lower energy barriers (133 and 119 $kJ.mol^{-1}$ in the presence or absence of oxygen respectively). Since the overall energetic cost for NO* formation via N*+O*→NO* is 14 $kJ.mol^{-1}$ lower than any considered HNO* pathway, we expect pathway (3) be favoured against (5) and (7) pathways.

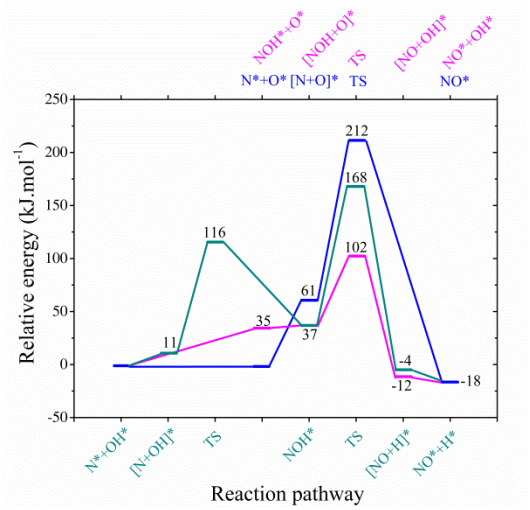


**Figure 5**. Reaction energy diagram for NO formation via NOH* and N*+O* recombination. All energies are referenced to NH*, 2O* and Pt(111) and are ZPE corrected.

NO* formation via NOH* along with N*+O*→NO* pathway is presented in Fig. 5. The NOH* formation has an energy barrier of 116 kJ.mol$^{-1}$. The subsequent NOH* dissociation in the presence or absence of oxygen are 168 and 102 kJ.mol$^{-1}$ activated, respectively. The NOH* pathway leading to NO* is less activated than the N* +O*→NO* recombination.

We have also examined the interconversion reaction of HNO*→NOH* by the intramolecular migration of H to O in the HNO molecule but this step is highly activated with an energy barrier of 253 kJ.mol$^{-1}$ and exothermic by -10 kJ.mol$^{-1}$. Although the activation energy for NO* formation via NOH* is lower than N*+O* recombiantion, the species surface concentration (i.e OH*) can modify the rate constant of the reactions and therefore a more strict analysis need to be carried out. The results are presented in the next section

### 3.3 Sensitivity Analysis

After computing the energetics and energy barriers of the elementary steps, a thermodynamically consistent model for $NH_3$ oxidation on Pt(111) was developed. DFT results and experimental sticking coefficients are used as input parameters. To identify the elementary steps contributing to NO formation, a local sensitivity analysis (8) was carried out. The results are shown in figure 6. The sensitivity analysis for NO formation reveals that the overall rate of NO production is affected mainly by the $N_2$ formation. There is also a minor effect coming from $O_2$ dissociation, $NH_3$ adsorption, $N_2O$ formation, OH formation, water dissociation by oxygen and NO formation itself. Additional analysis including rate of progress and contribution analysis allow us to conclude that HNO and NOH intermediates have a negligible weight in the overall NO formation rate.

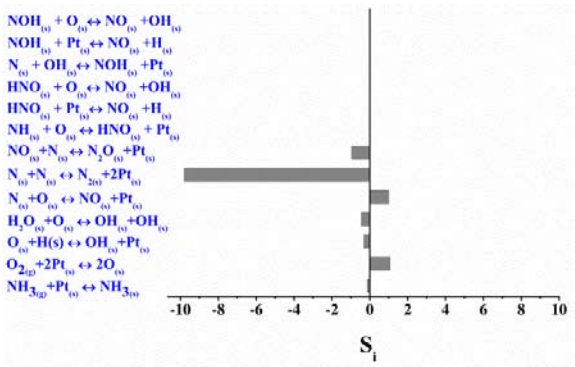


**Figure 6.** Local sensitivity for NO formation in a SFR with a diameter of 0.47 cm, a length of 5cm and a site density of 2.3*10$^{-9}$ mol.cm$^{-2.}$ Inlet conditions: 1000 ppm of $NH_3$ and 2000 ppm of $O_2$ in argon at 300 sccm.

## 4. Conclusions

The developed DFT-based microkinetic model and sensitivity analysis reveals that HNO and NOH intermediates have a negligible role in the overall rate of NO formation. The role of HNO and NOH on different platinum surfaces and the coverage effect on the activation energies for reactions (2)-(8) need further investigation. The inclusion of these effects in the calculated activation energies might result in a better agreement between DFT values and fundamental relationships like (1) derived from experimental studies.

## 5. Acknowledgments

This research was undertaken with the assistance of resources provided at the National Computational Infrastructure Facility (NCI) supported by the Australian Government. Juan D. Gonzalez would like to thanks to the Australia Awards Scholarship and Australian Leadership Awards programs.

## 6. References

[1] S. T. Hatscher; T. Fetzer; E. Wagner; H.-J. Kneuper, in: Handbook of Heterogeneous Catalysis, Wiley-VCH Verlag GmbH & Co. KGaA: 2008.
[2] M. Baerns; R. Imbihl; V. A. Kondratenko; R. Kraehnert; W. K. Offermans; R. A. van Santen; A. Scheibe, Journal of Catalysis 232 (1) (2005) 226-238.
[3] T. Pignet; L. D. Schmidt, Chemical Engineering Science 29 (5) (1974) 1123-1131.
[4] T. Pignet; L. D. Schmidt, Journal of Catalysis 40 (2) (1975) 212-225.
[5] M. Kim; S. J. Pratt; D. A. King, Journal of the American Chemical Society 122 (10) (2000) 2409-2410.
[6]A. Scheibe; M. Hinz; R. Imbihl, Surface Science 576 (1–3) (2005) 131-144.
[7]A. Scheibe; U. Lins; R. Imbihl, Surface Science 577 (1) (2005) 1-14.
[8]J. L. Gland; V. N. Korchak, Journal of Catalysis 55 (3) (1978) 324-336.
[9]W. K. Offermans; A. P. J. Jansen; R. A. van Santen, Surface Science 600 (9) (2006) 1714-1734.
[10]D. W. Blakely; G. A. Somorjai, Surface Science 65 (2) (1977) 419-442.
[11]G. A. Somorjai; J. Carrazza, Industrial & Engineering Chemistry Fundamentals 25 (1) (1986) 63-69.
[12]W. D. Mieher; W. Ho, Surface Science 322 (1–3) (1995) 151-167.
[13] M. Warner; B. S. Haynes, Proceedings of the Combustion Institute 35 (2) (2015) 2215-2222.
[14] M. Y. Smirnov; V. V. Gorodetskii; J. H. Block, Journal of Molecular Catalysis A: Chemical 107 (1–3) (1996) 359-366.
[15] M. Asscher; W. L. Guthrie; T. H. Lin; G. A. Somorjai, The Journal of Physical Chemistry 88 (15) (1984) 3233-3238.
[16]J. Hafner, Journal of Computational Chemistry 29 (13) (2008).
[17] G. Kresse; J. Furthmüller, Physical Review B 54 (16) (1996) 11169-11186
[18] G. Kresse; D. Joubert, Physical Review B 59 (3) (1999) 1758-1775
[19] G. Henkelman; H. Jónsson, The Journal of Chemical Physics 113 (22) (2000) 9978-9985.
[20] G. Henkelman; B. P. Uberuaga; H. Jónsson, The Journal of Chemical Physics 113 (22) (2000) 9901-9904.
[21] Chemkin-Pro 15112, Reaction Design: San Diego, 2013.
[22] X. Traversac. Experimental and microkinetic modelling study of ammonia oxidation over platinum, PhD Thesis, The University of Sydney, 2007.
[23] A. Andreasen; H. Lynggaard; C. Stegelmann; P. Stoltze, Surface Science 544 (1) (2003) 5-23.
[24] F. J. Zeleznik; S. Gordon, in: NASA-TN-D-767: 1961.
[25] D. C. Ford; Y. Xu; M. Mavrikakis, Surface Science 587 (3) (2005) 159-174.

# Mechanism Development and Chemical Kinetics Analysis of $H_xN_yO_z$ Species in Gliding Arc Discharge

M. Zangouei, B. S. Haynes*
School of Chemical and Biomolecular Engineering
The University of Sydney NSW 2006 Australia

## Abstract

A comprehensive mechanism for the chemical reactions of $H_xN_yO_z$ species in the gliding arc plasma discharge was developed and validated versus a wide range of experimental conditions. The rate constant of electron-species reactions were calculated using the electron energy distribution function (EEDF), and excitation and dissociation cross sections of species. In contrast to the traditional modelling technique in which the concentration of species is modelled in a microdischarge for a single pulse, and subsequently integrated over the multiple pulses, here, the whole discharge is considered as one macrodischarge, produced in one pulse with a wavelength equal to the residence of gas in the discharge. Some results such as effect of $N_2/O_2$ ratio on the concentration of formed NO and $NO_2$, and also the effect of humidity on the concentration of products are presented here. The calculated results are in a very good consistency with the experimental results. Using the normalised rate of reactions, the main pathways of formation of products were also extracted. The current model can be extended for the ignition and combustion of hydrocarbons.

*Keywords: Gliding Arc Discharge, Chemical Kinetics Study, Plasma Modelling.*

## 1. Introduction

While several types of plasma discharges are available, the "gliding arc discharge" has been of particular interest in fuel processing studies. It has been used in different processes such as biomass tar gasification into syngas [1], hydrogen production from hydrogen sulphide [2], liquid fuel reforming [3, 4], and natural gas oxidation to syngas [5, 6]. Such plasmas may also be useful in augmentation of ignition in practical combustors [7]

The modelling of plasma chemistry in most studies reported in the literature has been carried out in one pulse and subsequently, extended over the multiple pulses. The rate constant of electron-neutral collisions is calculated in a single microdischarge based on the applied reduced electric field. Each microdischarge has a high electric field region at its head, followed by the low electric field region in the streamer channel. The accuracy of this technique for the rate constant calculation relies on estimates of several parameters such as microdischarge dimension, density of microdischarges on the surface of electrodes, variation of electric field by time and rate of occurrence of streamer channels which are not entirely known. These uncertainties ultimately may not lead to an accurate evolution of real reactor data [8]. Here, in order to bypass these inaccuracies, we use a different technique to calculate the temporal evolution of species in a discharge based on the method introduced in [9]. In this technique, the applied power on the plasma discharge is immediately averaged over the entire discharge volume and the rate constant of electron-neutral reactions is calculated based on the power density (J/cm$^3$ s), electron energy distribution function (EEDF), excitation and dissociation cross sections of species as is explained in details in the next section. A comprehensive mechanism for the chemical reactions of $H_xN_yO_z$ in a gliding arc discharge was developed and validated versus a wide range of experimental conditions.

## 2. Methodology

### 2.1 Chemical Kinetics Gas-Phase Model

In order to develop the mechanism, two types of reactions were considered: neutral-neutral and electron-neutral reactions. The rate constants of neutral-neutral reactions are taken primarily from the evaluated chemical kinetics data published by JPL [10], Tsang and Herron [11], Tsang and Hampson [12], Baulch *et al.* [13], Atkinson *et al.* [14], and Herron [15]. The rate of neutral-neutral reactions were defined as following:

$$r_{neutral-neutral} = \sum k_{jl}N_jN_l + \sum k_{jlm}N_jN_lN_m + \sum -k_{ij}N_iN_j + \sum -k_{ijl}N_iN_jN_l \quad (1)$$

The rates of electron-neutral reactions were defined as following:

$$r_{ei} = \frac{W_d}{V_d} \times \frac{1}{\varepsilon_{ei}} \times \frac{W_{ei}}{\sum W_{ei} + \sum W_i} \quad (2)$$

In this equation, $W_d$ is the discharge power (eV/sec, 1eV=1.602×10$^{-19}$ J), and $V_d$ is the discharge volume (cm$^3$). It is assumed that the discharge power ($W_d$) and, consequently, electrons are uniformly distributed (i.e.

* Corresponding author:
Phone: (+61) 2 93513435
Email: brian.haynes@sydney.edu.au

0-D model) over the discharge volume ($V_d$). $\varepsilon_{ei}$ is the bond dissociation enthalpy of species $i$ (eV/molecule) through electron-species collision. $W_{ei}$ is the power density consumed for the bond dissociation or excitation of species $i$ with the threshold energy of $\mathcal{E}_{ei}$:

$$W_{ei} = \sqrt{\frac{2q}{m}} \cdot n_e \cdot N_i \cdot \varepsilon_{ei} \cdot \int_0^\infty \varepsilon \cdot Q_{ei}(\varepsilon) \cdot f(\varepsilon) \cdot d\varepsilon \quad (3)$$

where $q$ is $1.602\times10^{-12}$ erg eV$^{-1}$, $m$ is electron mass (g), $n_e$ is the electron concentration (cm$^{-3}$), $N_i$ is the number of species $i$ per unit of volume (molecule/cm$^3$), $Q_{ei}$ is the dissociation or excitation cross section of species (cm$^2$/molecule), and $f(\varepsilon)$ is the electron energy distribution function.

In Eq. 2, $W_i$ is the power density deposited into the elastic processes:

$$W_i = \frac{2m}{M_i} \sqrt{\frac{2q}{m}} \cdot n_e \cdot N_i \cdot \varepsilon_{ei} \cdot \int_0^\infty \varepsilon^2 \cdot Q_i(\varepsilon) \cdot f(\varepsilon) \cdot d\varepsilon \quad (4)$$

Where $Q_i$ is elastic momentum transfer cross section (cm$^2$/molecule) and $M_i$ is the molecular mass of species $i$ (g/molecule). The Bolsigplus software [16] was used to calculate the Electron Energy Distribution Function (EEDF, $f(\varepsilon)$). Note that the developed mechanism does not include any ionised species since the ionisation energy of species is much higher (>12 eV) than the average energy of electrons (up to 4 eV) in our experiments.

The governing kinetic of the model formed a system of non-linear ordinary differential equations (ODE), solved numerically by means of an in-house MATLAB code.

### 2.2 Gliding Arc Discharge Reactor (GADR)

The GADR (Figure. 1) was designed and built by Etudes Chimiques et Physiques Company, France, commissioned at The University of Sydney. The reactor comprises two zones: the discharge zone (V≅2 cm$^3$) and the post-discharge zone (V=1400 cm$^3$). The discharge zone includes two inlets, one before the discharge gap and one after. Both inlet flows enter tangentially to create a 3D discharge which promotes uniform gas treatment.

The high voltage (HV) electrode (cathode), made of stainless steel, was insulated by a high voltage ceramic insulation. The arc formed between cathode and anode (reactor body) was powered by a single-phase transformer (6 kV, 25 mA). The outer surface of the discharge zone was insulated by a multi-layer glass wool to minimise the heat loss through the wall.

The post-discharge zone was equipped with a capillary sampling tube (quartz material), located just after the discharge zone. The reactor is also equipped with a sampling tube at the end of post-discharge zone. The axial temperature was monitored using a K-type thermocouple placed in a hollow quartz tube with one sealed end.

Product concentrations (NO, $NO_2$, $N_2O$, $HNO_3$, $HNO_2$) were determined by FTIR (Varian 7000, 4000-400 cm$^{-1}$, resolution of 0.25 cm$^{-1}$). Measurements were taken relative to a transparent background, using 20 kHz speed and 64 scans to co-add at 0.25 cm$^{-1}$ resolution. In order to measure the quantity of each component in the sample flow, the spectrum of the sample flow was compared to the calibration spectrum, which was created for each component (NO, $NO_2$, $N_2O$) separately using a certified gas standard.

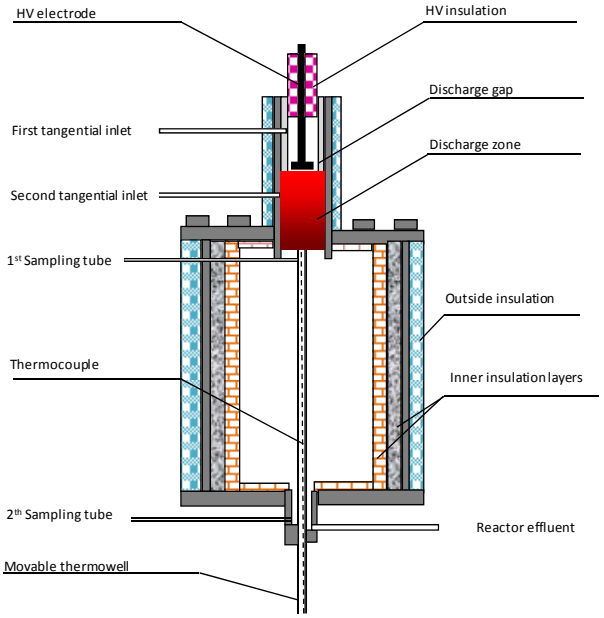


Fig. 1 Schematic diagram of the gliding arc reactor used for the experiments.

## 3. Results and Discussion

### 3.1 NOx formation in dry $N_2/O_2$ mixture

In order to validate the developed mechanism, a series of experiments were carried out using different $N_2/O_2$ ratios, namely 90/10, 79/21, 70/30, 60/40, and 50/50, feed flow rate of 20 slpm, atmospheric pressure, and energy density of 0.45 J/cm$^3$. The gas temperature in the discharge was assumed to be equal to the attainable adiabatic temperature corresponding to the applied energy density.

The results are presented in Figure 2. As can be seen from Figure 2a, the formation of NO is greatest (1065 ppm) for $N_2/O_2$ = 70/30, decreasing to ~700 ppm at either higher (90/10) or lower (50/50) values of the $N_2/O_2$ ratio. However, the formation of $NO_2$ rises steadily with increasing $O_2$ in the mixture (Fig. 2b). Overall, the formation of NOx ($NO+NO_2$) depends only weakly on the mixture composition. The trend for NOx (not presented) is similar to that NO, i.e formation of ~1400 ppm for $N_2/O_2$=70/30, decreasing to ~900 – 1000 ppm for either higher (90/10) or lower $N_2/O_2$ ratios (50/50).

The results of the model are also presented in Figure 2. There is good quantitative agreement between model and experiment in all cases. Over studied range of $N_2/O_2$, the average of $NO_{model}/NO_{exp}$ is 1.11 with a

standard deviation of 0.10, where that of $NO_{2,model}/NO_{2,exp}$ is 1.00 with a standard deviation of 0.13.

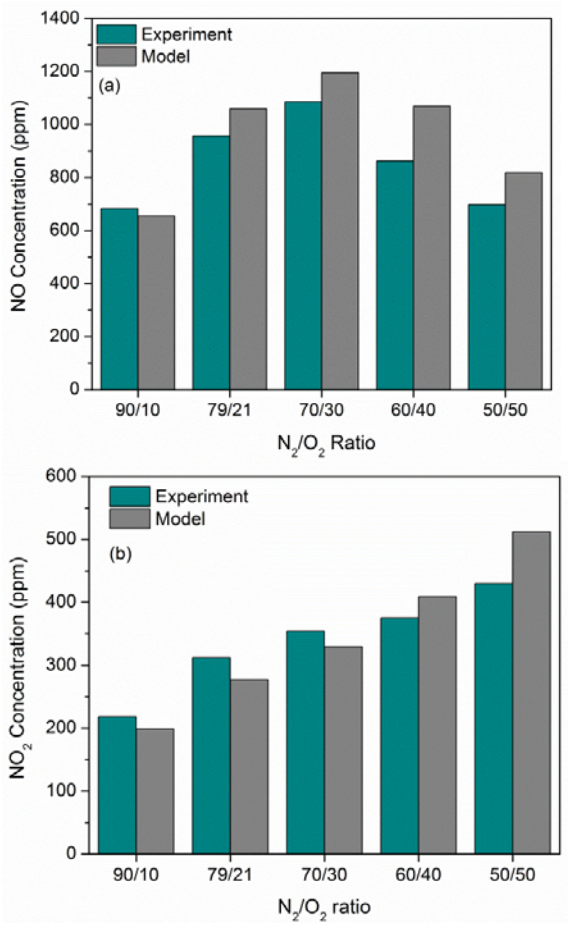


Fig. 2 Calculated and measured (a) NO and (b) $NO_2$ concentration for different $N_2/O_2$ ratios. Energy density of 0.45 J/cm$^3$ feed (dry). P=1 atm.

The temporal evolution of products predicted over both the discharge and post-discharge zones are presented in Figure 3. The reactive centres are produced initially by electron-$O_2$ and electron-$N_2$ collisions, forming O, O($^1$D), N, N($^2$D), and $N_2(A^3\sum_u^+)$. The O($^1$D) reaches its quasi-steady concentration in $\tau \leq 0.01$ μs, due to collision with the background gas and quenching to the ground state:

$O(^1D)+O_2 \rightarrow O+O_2$

$O(^1D)+N_2 \rightarrow O+N_2$

N($^2$D) and $N_2(A^3\sum_u^+)$also reach their quasi-steady concentration in $\tau \leq 0.1$ μs, due to collision with the background gas:

$N(^2D)+N_2 \rightarrow N+N_2$

$N(^2D)+O_2 \rightarrow NO+O$

$N_2(A^3\sum_u^+)+O_2 \rightarrow N_2O+O$

The most important pathways for the production and consumption of $NO_2$ are:

$NO+O+M \rightarrow NO_2+M$,

$NO_2+O \rightarrow NO+O_2$,

$NO+O_3 \rightarrow NO_2+O_2$,

Regardless of $N_2/O_2$ ratio, the same reactions are responsible for NOx formation:

$NO+N \rightarrow N_2+O$

$N+O_2 \rightarrow NO+O$

$N(^2D)+O_2 \rightarrow NO+O$

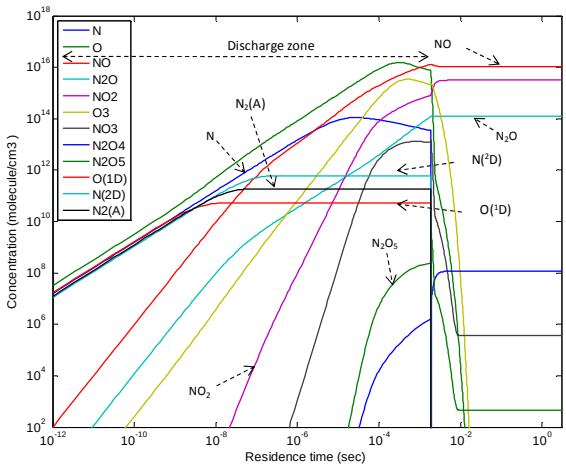


Fig. 3 Temporal evolution of products over the both discharge and post-discharge zones. Dry air ($79N_2/21O_2$) as feed at 298 K, discharge zone temperature 636 K (adiabatic temperature), pressure 1 atm, and energy density 0.45 J/cm$^3$.

In the post-discharge zone, the product distribution is governed only by the neutral-neutral reactions due to the absence of electron-neutral reactions. As can be seen in Figure 3, the concentrations of N($^2$D), N, $N_2$, $N_2(A^3\sum_u^+)$, O($^1$D), O and $O_3$ drop sharply to zero at the end of the discharge zone due to their rapid consumption in the absence of electron-neutral reactions.

### 3.2 NOx formation in humid-$N_2$

The experimental and modelled concentrations of products from a discharge in humid-$N_2$ (RH=90% at 21 °C and 1 atm) are presented in Figure 4. As is seen from Figure 4a, the measured concentration of NO (342 ppm) is in good agreement with the modelled concentration (326 ppm). There is very little $NO_2$ formed in this system which is also found in the modelling (Fig 4b), but the model now overpredicts this by a factor of 2 (4 ppm vs 2ppm) – given the difficulty of sampling and measuring small concentrations of $NO_2$ in much higher concentrations of NO, this is considered to be satisfactory agreement. Also shown in Fig 4.b in the fact that there is a small amount of $N_2O$ formed in this discharge and that this is accurately captured by the model.

Figure 5 depicts the temporal evolution of different components in the humid-$N_2$ discharge. In contrast to the case of dry air in which NO is mainly formed through the reactions of atomic nitrogen and $O_2$ ($N+O_2 \rightarrow NO+O$, $N(^2D)+O_2 \rightarrow NO+O$), here NO is produced predominantly by the following reactions:

$N+OH \rightarrow NO+H$

$NH+OH \rightarrow H_2+NO$

$NH+O \rightarrow H+NO$

$NO_2$ is mainly produced via $OH+HNO_2 \rightarrow H_2O+NO_2$ and $NO+O+M \rightarrow NO_2+M$. Around 76% of $N_2O$ is formed through $NH+NO_2 \rightarrow N_2O+OH$, while the rest (24%) is formed via reaction of excited molecular nitrogen and $O_2$: $N_2(A^3\sum_u^+)+O_2 \rightarrow N_2O+O$.

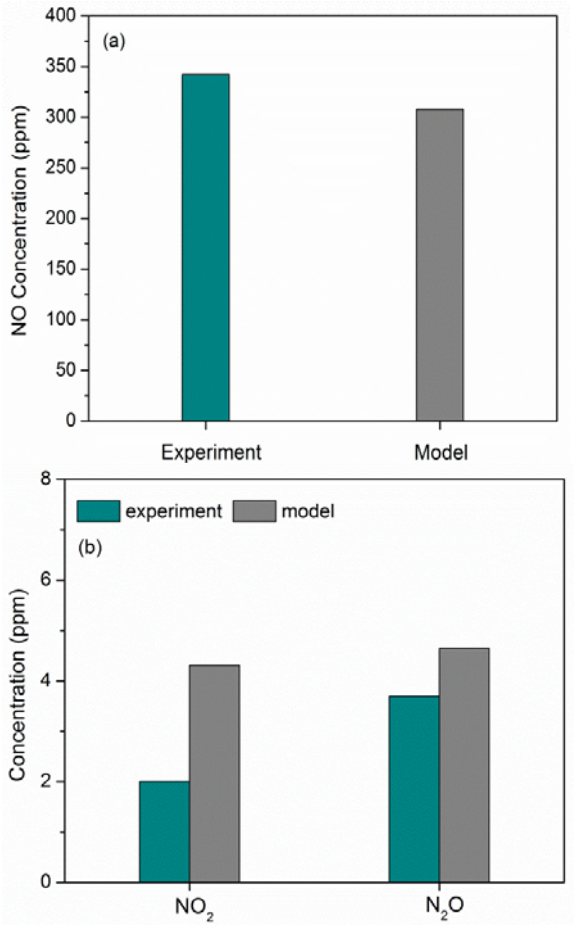


Fig. 4 The measured and calculated (a) NO concentration, (b) $NO_2$ and $N_2O$ concentration. Feed composition: humid-$N_2$ (RH=90% at 21 °C and 1 atm), P=1atm, $T_{modelling}$=936 K, energy density 0.9 J/cm$^3$.

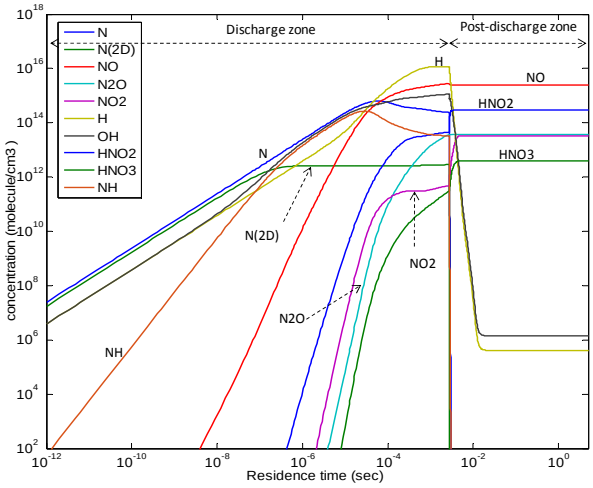


Fig. 5 Temporal evolutions of different species in humid-$N_2$ discharge (RH=90% at 21 °C and 1 atm). $T_{modell}$=936 K (adiabatic temperature), feed flow rate=10 slpm, P= 1 atm. Energy density of 0.9 J/cm$^3$.

## 4. Conclusion

We have developed a comprehensive mechanism for the chemical reactions of $H_xN_yO_z$ species in the gliding arc plasma discharge capable of replicating a wide range of experimental conditions. The capability of model for the prediction of the products distribution for $N_2/O_2$ and humid-$N_2$ feed was presented here. A very good consistency between the measured and modelled results was observed. The model can be extended for the ignition and combustion of hydrocarbon species.

### 5. References


[1] Y. N. Chun, S. C. Kim, K. Yoshikawa, Chemical Engineering and Processing: Process Intensification 57-58 (2012), pp. 65-74.

[2] T. Nunnally, K. Gutsol, A. Rabinovich, A. Fridman, A. Starikovsky, A. Gutsol, R. W. Potter, International Journal of Hydrogen Energy 34 (18) (2009), pp. 7618-7625.

[3] M. H. Rafiq, J. E. Hustad, International Journal of Hydrogen Energy 36 (14) (2011), pp. 8221-8233.

[4] G. P. J. Gonzalez-Aguilar, A. Lebouvier, J. D. Rollier, A. Darmon, L. Fulcheri, , Energy & Fuels 23 (10) (2009), pp. 4931-4936.

[5] A. Rabinovich, M. Gallagher, A. Fridman, A. Plevich, A. Gutsol. World Intellectual Property Organization, USA patent (2011).

[6] M. H. Rafiq; J. E. Hustad, Industrial & Engineering Chemistry Research 50 (9) (2011), pp. 5428-5439.

[7] S. M. Starikovskaia, Journal of Physics D: Applied Physics 39 (16) (2006), pp. R265-R299.

[8] G. Sathiamoorthy, S. Kalyana, W. C. Finney, R. J. Clark; B. R. Locke, Industrial & engineering chemistry research 38 (5) (1999), pp. 1844-1855

[9] D. Levko, A. Shchedrin, V. Chernyak, S. Olszewski, O. Nedybaliuk, Journal of Physics D: Applied Physics 44 (14) (2011), pp. 145206-145219.

[10] S. P. Sander, R. R. Friedl, D.M. Golden, M. J. Kurylo, P. H. Wine, A. R. Ravishankara, J. P. D. Abbatt, J. B. Burkholder, C. E. Kolb, G. K. Moortgat, R. E. Huie, V. L. Orkin, (2011)

[11] W. Tsang, J. T. Herron, Journal of Physical and Chemical Reference Data 20 (4) (1991), pp. 609-663.

[12] W. Tsang; R. F. Hampson, Journal of Physical and Chemical Reference Data 15 (3) (1986), pp. 1087-1279

[13] D. D. L. Baulch, C. C. J. Cobos, R. R. A. Cox, C. C. Esser, P. P. Frank, T. Just; J. A. Kerr, M. J. Pilling, J. Troe; R. W. Walker, Journal of Physical and Chemical Reference Data 21 (3) (1992), pp. 411-734.

[14] J. M. Heimerl, T. P. Coffee, Combustion and Flame 35 (1979), pp. 117-123.

[15] J. T. Herron, Journal of Physical and Chemical Reference Data 28 (5) (1999), pp. 1453-1483.

[16] http://www.bolsig.laplace.univ-tlse.fr/)

**Proceedings of the Australian Combustion Symposium**
**December 7-9, 2015, The University of Melbourne**

# A Plug Flow Reactor for Investigating Autoignition Chemistry in Combustion Engines

N. Leplat, Z. Lu, Y. Yang* and M.J. Brear
Department of Mechanical Engineering
The University of Melbourne, Parkville VIC 3010 Australia

**Abstract**

A Plug Flow Reactor (PFR) facility has been constructed at the University of Melbourne for investigating fuel oxidation at temperatures up to 1000 K and pressures up to 50 bar. These conditions correspond to the low-to-intermediate temperature regimes of hydrocarbon combustion and where the chemistry can lead to autoignition in engines. Turbulent flow is employed in a quartz tube reactor of 25 mm diameter and 1020 mm length. Chemical reaction inside the reactor is highly diluted by excess air, and this slows down the reaction rates and thus facilitates kinetic investigations. Fuel and air are preheated separately and mixed upon entering the reactor. A novel mixer is implemented in order to achieve fast mixing, thereby minimizing initialization issues. A sample probe travels along the flow direction, extracting reaction intermediates at different effective reaction times. The sampled gases can be analysed with a gas chromatograph to provide detailed species evolution as a function of reaction progress. The main features of this facility are reported, together with updates on the validation experiments. In particular, the turbulent plug-like flow field is verified inside the reactor, and the fast mixing of fuel and air flows is achieved.

*Keywords: Plug Flow Reactor, Fuel chemistry, Low temperature combustion.*

## 1. Introduction

With the advances in engine technology and the increasing use of alternative fuels, understanding combustion chemistry becomes increasingly important. Achieving this task requires the acquisition of accurate experimental data. A wide range of experimental facilities are used in this regard, including static reactors, flow and stirred reactors, shock tubes, rapid compression machines (RCM), and burner stabilized laminar flames. Fundamental kinetic data, such as ignition delays, laminar flame speeds, and species compositions have been obtained by using these techniques. Based on these data, detailed kinetic mechanisms have been assembled and validated, which, coupled with CFD models, can enable simulation of the combustion chemistry encountered during practical combustion processes.

Plug flow reactors (PFR) are a continuous flow device in which a mixture flows and reacts inside a tube [1]. Compared to compression-ignition experiments, e.g. shock tubes and RCMs, which are useful for obtaining ignition delay data, PFR experiments are more adapted for species concentration measurements in steady reacting flows.

The PFR at the University of Melbourne has recently been built for investigating fuel autoignition chemistry, which occurs at the low-to-intermediate temperature regime of hydrocarbon oxidation (600–1100 K for engine conditions). Under such conditions, temperatures are not high enough to decompose the fuel molecules into small species. Instead, the reaction kinetics is predominantly controlled by species of similar size to the fuel [2]. Autoignition finds common applications in combustion engines; it is the process initiating engine knock in spark-ignition engines and causing ignition delay post fuel injection in diesel engines. These processes are heavily affected by fuels used.

## 2. Design

The PFR at the University of Melbourne is designed for continuous operation at pressures up to 50 bar and temperatures up to 1000 K. This high pressure limit was a priority in designing this reactor, in response to the increasingly higher operating pressures in modern engines, and the fact that the kinetics of combustion reactions are pressure dependent. In contrast, most PFR results reported in the literature are at pressures of 10 bar and below.

The dilution gas, which is required to slow down the reaction rates so that the chemistry can be probed over a sufficiently long flow distance, is chosen to be air supplied by an oil free air compressor. Using other gases, e.g. nitrogen as in [1, 3], is not feasible due to the high-flow rates during continuous operation at high-pressure. For the same reason, bundled gas bottles are not suitable for extended period of testing. Under typical conditions, the air flow is kept in large excess relative to the fuel flow, which is well below the lower flammability limit of the investigated mixture. This provides very lean and non-flammable system in which the observed reactivity only arises from auto-ignition (low temperature oxidation) chemistry.

The reacting mixtures are prepared via a pre-heating system, where the fuel and air are heated separately and mixed upon entering the reactor. It is critical to achieve fast mixing in this setup because reactions could start during the mixing of the two hot gases, causing

* Corresponding author:
Phone: (+61) 03 8344 8104
Email: yi.yang@unimelb.edu.au

initialization issue for kinetic modeling. A mixer of novel design (as detailed below) is used for achieving this fast mixing. The pre-heating method is considered better than the alternative pre-mixing method (i.e. mixing first then heating), because heating gases is an inherently slow process.

## 3. Facility Setup

The setup of the PFR facility is shown in Fig. 1, which includes subsystems for air supply, fuel supply, reactor vessel (including sample probe), and exhaust line.

Air Supply - The air is supplied by an oil-free compressor. The flow rate is controlled by a needle valve and measured by a flowmeter. Flow rates up to ~10 g/sec and pressure up to 10 bar can be established at present, with an upgrade to a higher pressure compressor planned. Before entering the reactor, the air is heated to the required temperature for the experiments (up to 1000 K) by means of an inline heater (8 kW). Secondary air flow, called balance air, is supplied in the space between the quartz tube and the inner wall of the pressure vessel (where the reactor heaters are located) (see right part of Fig. 1). This secondary flow is used to maintain a similar pressure across the reactor wall, minimizing pressure differences that might damage the reactor.

Fuel Supply -Liquid fuels are supplied to the reactor after vaporization. The fuel is stored in two stainless steel cylinders: one is the working cylinder that delivers the fuel to the reactor, and the other is a transfer cylinder used to refill the first one. Nitrogen at up to 120 bar can be applied to the working cylinder to drive the fuel flow, which can be adjusted by a metering valve downstream. The fuel flow rate is measured from the temporal mass loss of the working cylinder using a load cell. Liquid fuels are preheated to below their boiling point and then injected into a stream of hot nitrogen where they are vaporized and mixed with the nitrogen prior to the reactor. The mixture temperature is set so that the fuel vapor does not condense or pyrolyze. Heating required in this part of the system is achieved by cable heaters (500W each).

Reactor - The reactor tube is made of quartz (fused silica) with ID = 25 mm, OD = 33 mm, and $L$ = 1020 mm (Fig. 1). It is enclosed in a stainless steel vessel rated for 50 atm at 1000 K. Quartz was used for its inertness at high temperatures, thereby minimizing surface reactions. The reactor is set up vertically in order to minimize gravity-induced inhomogeneity in the mixture which might be significant at high pressures. The reactor is surrounded by three tubular heaters (between the quartz tube and the vessel wall) to compensate for the heat loss from the reacting gases and to achieve close-to adiabatic conditions.

Reacting gases are extracted using a sample probe which travels along the centerline of the reactor (Fig. 1). The sampled gas is analyzed by a gas chromatograph (Shimadzu GC2010) equipped with a thermal conductivity detector (TCD) and a flame ionization detector (FID) for quantitative determination of gas compositions. The probe (OD = 12.7 mm, $L$ = 1020 mm) consists of a glass-lined stainless steel tube (OD = 1.6 mm, ID = 0.7 mm) for gas extraction, a thermocouple for measuring local gas temperature, and an aerodynamic tip with a 0.3 mm orifice. The gas extraction tube is cooled by hot water surrounding it to rapidly quench reactions in the sampled gas.

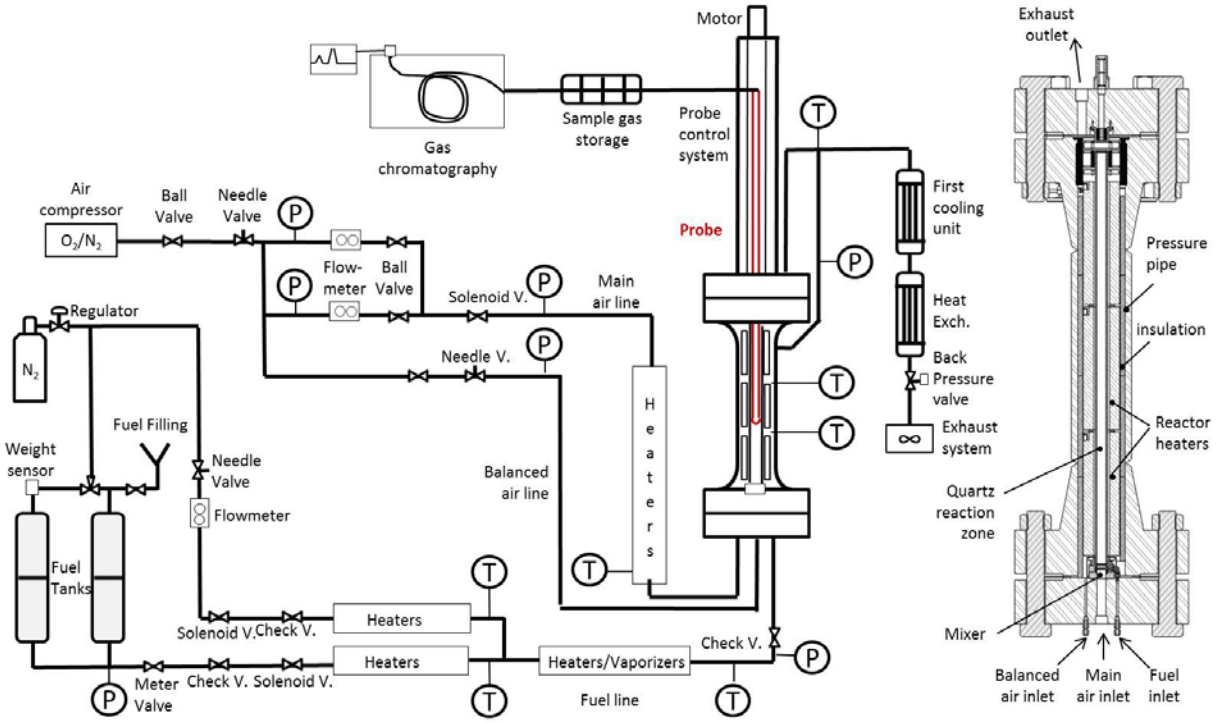


Figure 1. Schematic diagram of the plug flow reactor facility at the University of Melbourne with the detail of the reactor on the right side

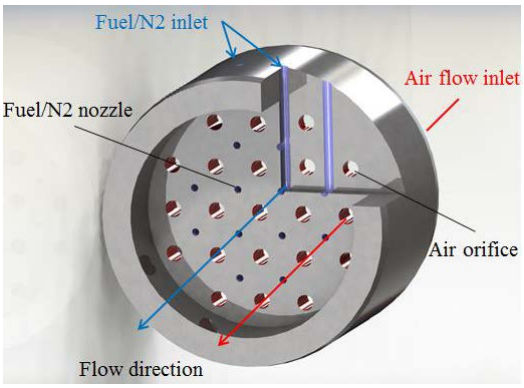


Figure 2. Scheme of the mixer configuration

A distinct feature of the reactor is the mixer (Fig. 2) with a unique design that contrasts with those used in similar facilities [3, 4]. A rapid mixing to minimize reactions during the preparation of a thermally and compositionally homogeneous mixture is important in such experiments [1]. The mixer is a circular plate (ID = 25 mm) with 21 separate 1.75 mm diameter holes for the air flow. The fuel (vapor in $N_2$) is injected through 12 much smaller nozzles that are at a regular pitch relative to the air flow holes. CFD calculations demonstrated that the overall mixing process can substantially be improved with this mixer in comparison with other common designs in the literature [5]. This improvement is considered resulting from the localized fuel /air mixing via the evenly distributed air holes and fuel nozzles on the mixer. This is in contrast to former designs where fuel was always injected into a single stream of air, either from the holes on the reactor wall (so called external injection [6]) or from holes on a cone located at the center of the reactor (internal injection [3, 4]). The new design substantially enhances local mixing and results in much fast mixing overall.

The reactor pressure is controlled by a backpressure valve located on the exhaust line (Fig. 1). A heat exchanger is used upstream of the valve to cool the gases to a temperature such that this valve may operate safely.

Validation tests have been conducted to verify some of the major assumptions for PFR experiments, including the approximation of isobaric and adiabatic conditions, steadiness, radial uniformity, and rapid mixing of the reactants. Some of these results are presented below.

## 3. Temperature Field Characterization

Given the major impact of temperature on chemical kinetics, achieving a homogeneous temperature field inside the reactor is important for PFR experiments. With reactions occurring in the flow, the temperature may increase or decrease along the reactor under adiabatic conditions, depending on the exothermic or endothermic nature of the reaction. Without reactions, adiabatic conditions simply correspond to isothermal conditions in the flow. As shown in Fig. 1 and 2 above, three tubular heaters are used, which surround the reactor tube and compensate

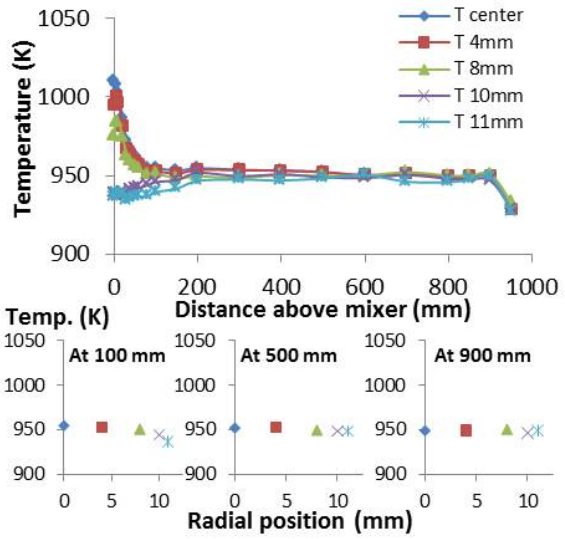


Figure 3. Axial and radial temperature profiles at 950K, 8bar and $F_{air}$=5.44g/s (1.83 l/s for the reactor temperature and pressure).

for heat loss at the wall. Tests have been conducted to characterize the temperature field inside the reactor. A specially designed probe containing five thermocouples is used for this purpose. The thermocouples are located at the same radial plane but at five different radial positions (the center and 4, 8, 10, 11 mm radii).

Figure 3 presents examples of such measurements in the absence of chemical reaction, for an air flow of 5.4 g/s and a reactor temperature of 950 K and pressure of 8 bar. To achieve this temperature inside the quartz tube, the inlet air heater has been set to 1125K. This temperature drop is due to the heat loss of the air flow at the unheated section from the exit of the air heater to the entrance of the reactor. Such heat loss also causes the temperatures of the five thermocouples to vary by roughly 75 K at the start of the reactor (right downstream of the mixer), as noted in Fig. 3. However, the large temperature gradient at the initial radial planes is rapidly diminished along the flow, as evident from the five thermocouples reporting nearly the same temperatures at ~100 mm downstream of the mixer. This indicates that the turbulence in the flow mixes the air streams issued from the 1.75 mm holes on the mixer effectively, and rapidly achieves homogeneous temperature distribution along the radial plane. Along the reactor, the temperature difference between the centerline and the temperature measured closest to the wall (11mm) is roughly 5 K, which is reasonably small. Moreover, along the flow, Fig. 3 shows that a nearly constant temperature can be maintained for approximately 800 mm. The reactor can thus provide a relatively long tube length for the study of low temperature combustion chemistry using the sample probe. The reactor temperature field has also been characterized for other air flow rates, temperatures and/or pressures, and similar results have been obtained. Major improvements have since been made to reduce the initial temperature gradient at the reactor entrance, including better insulation of the unheated section, and adding a band heater to the bottom flange of the pressure vessel.

## 4. Mixing Length Characterization

The temperature probe used in characterizing the temperature field can also be used to estimate the mixing length at which the air and the fuel/$N_2$ are homogeneously mixed. In this case, a non-reacting flow is used where $N_2$ without vaporized fuel is injected into the air (from the small holes on the mixer). Since the $N_2$ is unheated and the air is approximately 1000 K, the species mixing ($N_2$ and air) can be approximated by the mixing of the two temperatures. Further, out of the 5 radial positions of the thermocouples, some align with hot air streams and some align with cold $N_2$ streams. Figure 4 presents an example of such measurements, where the conditions are the same as those shown in Fig. 3, except that a cold nitrogen flow was applied in the fuel supply line.

It is recognized that the temperature variation inside the reactor is determined by both heat loss of the gas flow and mixing of the hot and cold streams. In order to isolate the latter for characterizing the mixing length, a normalized temperature ratio below is used.

$$\frac{\left(T_{4mm}/T_{center}\right)_{with\ N_2}}{\left(T_{4mm}/T_{center}\right)_{without\ N_2}}$$

Here the temperature measured at 4 mm radius ($T_{4mm}$) represents a cold $N_2$ stream, and the temperature at the centreline ($T_{center}$) represents a hot air stream, and the ratio of the two can be used to characterize the mixing process. This ratio is normalized by the same ratio for the case without $N_2$ (data shown in Fig. 3), to remove the impact of the heat loss on $T_{4mm}/T_{center}$ ratio. Such normalization assumes $N_2$ jets having a negligible impact on the flow heat loss, which is reasonable given the $N_2$ flow being much smaller than that of air.

It is apparent in Fig. 4 that the ($T_{4mm}/T_{center}$) ratio fluctuates near the mixer, due to the large temperature difference between the $N_2$ and air streams just issued from the mixer. However, the two gases mix quickly downstream, and the normalized ($T_{4mm}/T_{center}$) ratio approaches unity in ~ 60 mm if a value of 1±0.001 is defined as homogenous. This mixing length is considerably shorter than those of similar PFR experiments [3, 4], where a mixing length of 250 mm or longer is typically cited for reactors of similar length.

Tests were conducted to understand the impact of operation parameters, including $F_{air}$, $F_{N2}$, reactor temperature and pressure, on the mixing length. It appears that the mixing length is negligibly affected by temperature, the pressure and $F_{N2}$. However, experimental results have demonstrated that the mixing length decreases with an increase of the air flow as shown in Fig. 5.

## 5. Conclusions

A high-pressure plug flow reactor has been established for investigating fuel autoignition chemistry at conditions that are relevant to modern engines. Measurement of the temperature field confirmed that the plug flow regime was achieved inside the reactor. The novel mixer design therefore successfully achieved rapid mixing of fuel and air flows.

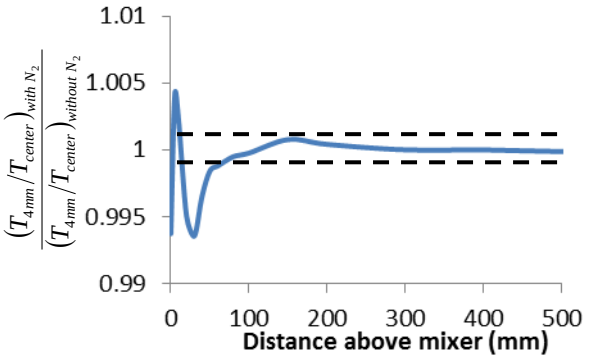


Figure 4. Estimation of the mixing length by comparing the ratio $T_{4mm}/T_{center}$ with or without flow of cold $N_2$ through the fuel supply line at 950K, 8bar, $F_{N2}$=0.241g/s and $F_{air}$=5.44g/s

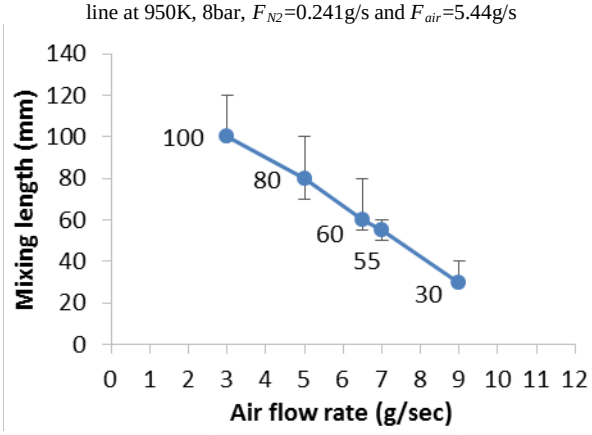


Figure 5. Dependence of the mixing length with the flow in air at $P$ = 5 bar and 800 K

## 6. Acknowledgments

This project is supported by the University of Melbourne, the Australian Research Council (DP140100846) and the Advanced Centre for Automotive Research and Testing (ACART, www.acart.com.au). The authors also thank Mr. Alistair Knox for his technical support in building the facility.

## 7. References

1. F.L. Dryer, F.M. Haas, J. Santner, T.I. Farouk, and M. Chaos, Prog. Energy Combust. Sci. **44** (2014), pp. 19–39.
2. H.J. Curran, P. Gaffuri, W.J. Pitz, C.K. Westbrook, Combust. Flame **114** (1998), pp. 149-117
3. D.N. Koert and N.P. Cernasky, Meas. Sci. Technol. **3** (1992), pp. 607-613.
4. Li, J. Ph.D Thesis, 2004, Princeton University, United States.
5. J. Cochet, Y. Yang, M.J. Brear, Proc. Austral. Combust. Symp. (2013).
6. M.K. Christensen, 2012, Ph.D Thesis, The Pennsylvania State University, United States.

**Proceedings of the Australian Combustion Symposium**
**December 7-9, 2015, The University of Melbourne**

# LES-MMC modeling of a partially-premixed turbulent dimethyl ether/air jet flame

G. Neuber[1] , Y. Gao[1], A. Kronenburg[2,*], O.T. Stein[1] , M. J. Cleary[2]
[1]Institut für Technische Verbrennung, University of Stuttgart, Herdweg 51, 70174 Stuttgart, Germany
[2]School of Aerospace, Mechanical and Mechatronic Engineering, The University of Sydney, New South Wales 2006, Australia

## Abstract

A turbulent, piloted dimethyl ether (DME)/air jet flame with a Reynolds number of 29,300 has been simulated using a sparse Lagrangian filtered density function (FDF) approach coupled to an LES flow field solver. Mixing between the Monte-Carlo (MC) particles is modelled by a generalized form of multiple mapping conditioning (MMC) that requires about 100 times fewer stochastic particles than standard FDF approaches. This can be achieved by pairwise mixing of particles that are selected dependent on their distance in both physical and reference space, the latter being the LES filtered solution of mixture fraction. We use three different kinetic reaction mechanisms to describe the finite-rate chemistry. LES-MMC method successfully predicts the flame structure and composition field of the DME flame. Conditional means and variances obtained from the different DME mechanisms are in very good agreement with experimental data and existing LES-CMC computations [4]. In comparison to conventional dense particle methods with 20-50 particles per LES cell, the savings in computational cost are substantial, while a high accuracy is maintained.

*Keywords: dimethyl ether, turbulent combustion modeling, multiple mapping conditioning*

## 1. Introduction

Dimethyl ether (DME) is a second generation biofuel and may be a potential "green" alternative to conventional diesel fuels. DME is an oxygenated fuel and the absence of a direct bond between two carbon atoms will lead to a notable reduction of CO and soot emissions during the DME fuel conversion process. Most flames of practical interest are turbulent and the use of DME in industrial applications requires a detailed understanding of the interactions between turbulence and chemical kinetics specific to DME. We therefore investigate a canonical setup of a turbulent reacting jet that provides well-defined boundary conditions for combustion model investigations.

Experiments were conducted using the geometry of the well known Sandia jet flames series (Sandia Flames A-F) [1]. The original flame series was based on a diluted methane jet into air with different Reynolds numbers. The same setup is now used for the present DME case. The change of fuel constitutes a noticeable increase in the complexity of the combustion chemistry and can help to enhance our understanding of the combustion of oxygenated fuels. The current setup is a piloted, partially-premixed DME/air jet flame (Sandia DME D) with a jet exit Reynolds number of 29,300. Raman measurements by Fuest et al. [2, 3] provide species data while Coriton et al. [4] measured formaldehyde, hydroxyl and velocities. Computational results were published by Coriton et al. [4] and by Popp et al. [5].

Both of these studies used Large Eddy Simulation (LES) for the modeling of the flow field. Here, small-scale processes such as turbulence and chemical reactions and their interactions are unresolved and require closure. Different models for the turbulence-chemistry interactions such as mixture fraction based methods [6, 7] or PDF methods [8] exist. This paper will couple a Lagrangian particle PDF method for modelling the interactions between combustion chemistry and turbulence with the LES solver.

All Lagrangian MC particle methods need a mixing model for closure. Standard mixing models are the interaction by exchange with the mean (IEM) [9], the Curl's model [10], modified Curl's model [11] and the Euclidean minimum spanning tree (EMST) model [12], the characteristics of which were recently reviewed in [13]. Especially in the context of an LES simulation the MC particle method can be computationally expensive. A sparse Lagrangian particle method together with an intelligent particle selection for the mixing particles allow for a massive reduction of the computational effort. Here, we use the Multiple Mapping Conditioning (MMC) model [14], which mixes pairs of particles dependent on their distance in both physical and reference space, the latter being the filtered mixture fraction obtained from LES. A generalized version of the MMC-LES model was presented by Cleary and Klimenko [15, 16], comprising constant and variable density reacting jet flows. The approach has been successfully validated by application to the Sandia flame series (D-F) [16,17].

## 2. Numerical methods

A hybrid Euler/Lagrange approach is used consisting of an Eulerian LES for the computation of the velocity, pressure and mixture fraction fields and a

* Corresponding author:
Permanent Affiliation: Institut für Technische Verbrennung, University of Stuttgart, Phone: (+49) 711 685 65635
Email: andreas.kronenburg@itv.uni-stuttgart.de

Lagrangian formulation of the FDF for the simulation of the transported (reactive) scalars.

The direct solution of the FDF transport equations for the species is computationally prohibitive due to the high dimensionality of the system. For any realistic treatment of the chemical kinetics, a high number of species in the reaction system is needed and the numerical effort scales exponentially with the number of dimensions. In [15] and [18] it is shown that the use of a Lagrangian particle scheme provides an equivalent solution, however, the computational cost scales only linearly with the number of dimensions. Therefore, two sets of stochastic differential equations have to be solved for a representative number of stochastic Monte Carlo particles, viz.

$$\mathrm{d}x_i^p = A_i^p \mathrm{d}t + b_{ij}^p \mathrm{d}\omega_j \,, \quad (1)$$

$$\mathrm{d}\phi_\alpha^p = \left(W_\alpha^p + S_\alpha^p\right)\mathrm{d}t \,. \quad (2)$$

The particle movement is given by Eq. (1) where $A_i^p$ is the drift and $b_{ij}^p$ is the diffusion coefficient [15]. The index i indicates the direction in physical space. Here $\mathrm{d}\omega_j$ is an independent Wiener process with zero mean and $\sqrt{\Delta t}$ variance, which models a random walk and represents the sub-grid fluctuations. Eq. (2) describes the temporal evolution of the transported scalars $\phi_\alpha^p$. $W_\alpha^p$ is the chemical reaction rate of scalar α and appears in closed form. $S_\alpha^p$ is the mixing operator representing the conditional sub-filter scalar dissipation and needs closure. In the context of a sparse particle method, the MMC mixing model uses a variant of Curl's mixing model where two particles, p and q, mix linearly at each time step according to

$$\phi_\alpha^p(t+\Delta t) = \phi_\alpha^p(t) + \gamma\left(\bar{\phi}_\alpha^{p,q}(t) - \phi_\alpha^p(t)\right) , \quad (3)$$

$$\phi_\alpha^q(t+\Delta t) = \phi_\alpha^q(t) + \gamma\left(\bar{\phi}_\alpha^{p,q}(t) - \phi_\alpha^q(t)\right) . \quad (4)$$

Here, $\bar{\phi}_\alpha^{p,q}$ is the weighted mean of two particles and $\gamma = 1 - e^{\Delta t/\tau}$ controls the extent of mixing and is dependent on a mixing timescale $\tau$, which is determined locally and instantaneously [15]. The particle pairs are selected by minimization of the effective square distance representing localness in both physical and mixture fraction space

$$d_{p,q}^2 = \sum_{i=1}^{3}\left(\frac{d_{x_i}^{p,q}}{r_i}\right)^2 + \left(\frac{d_{\tilde{f}}^{p,q}}{f_m}\right)^2 , \quad (5)$$

where $r_i$ and $f_m$ are weighting parameters, with $r_i = r_m/\sqrt{3}$. The reader is referred to reference [15] for a more detailed description of the mixing model.

A two-way coupling scheme connects the Eulerian LES scheme and the Lagrangian FDF scheme, whereby the LES provides velocity, turbulent diffusivity and mixture fraction to the Lagrangian fields. The FDF scheme provides a density feedback to the LES field. This density feedback is achieved by a conditional form of the equivalent enthalpy method that was first developed by Muradoglu et al. [19] and then extended by Raman et el. [20, 21] to intensive Lagrangian FDF simulations. Here, the coupling is realized by the solution of LES filtered equivalent species transport equations with source terms that ensure relaxation of the LES solutions towards the particle solutions.

## 3. Numerical setup

We investigate a piloted, partially-premixed turbulent DME/air jet flame with a jet diameter of D = 7.45 mm and a jet exit bulk velocity of $U_b$ = 45.9 m/s. The corresponding Reynolds number is $Re_D$ = 29,300. Our computational domain extends 60D in axial and 18.5D in radial direction. The pilot and co-flow inlet velocities are set to 5.8 m/s and 0.9 m/s, respectively. The jet diameter, the circumferential and the axial directions of the domain are resolved by 35, 60 and 480 cells, respectively, resulting in an overall cell number of about 1.5 Mio. A second much coarser mesh with 5760 cells covering the same spatial domain is used for the stochastic MC particle management. Separate simulations of pipe flow inside the fuel nozzle are carried out and used as the jet inlet boundary condition. A zero gradient boundary condition is set to the pressure inlet and the velocity outlet boundaries. A total pressure boundary condition is set for the pressure at the outlet boundary. To minimize numerical diffusion a central difference scheme is used for the filtered momentum conservation equations. All other transport equations are discretised by the total variation diminishing (TVD) scheme. Sub-grid stresses are modelled using a Smagorinsky LES-model with a constant of $C_s$ = 0.175. 150,000 particles are used for the whole flow domain, with only 50,000 being located in a reaction zone and being chemically active. The number of particles corresponds to 0.1 particles per LES cell, which is more than two orders of magnitude below common values for dense LES/PDF simulations. We set $f_m$ = 0.03 and $r_i$ = 0.0025. We use three different kinetic reaction mechanisms to describe the detailed chemistry, namely the mechanism by Kaiser et al. [22] consisting of 78 species and 351 reaction, by Zhao et al. [23] employing 55 species and 290 reactions and by Metcalfe et al. [24] consisting of 124 species and 766 reactions. The particle libraries in the OpenFOAM® 2.3.0 toolbox has been extended to account for the requirements of an LES-MMC simulation. To achieve statistical convergence the simulations have been run in MPI parallel mode on 24 Intel Xeon E5-2680 processors for approximately 2 weeks.

## 4. Results and discussion

In the present work we focus on the investigation of the capacity of the MMC-LES approach to simulate the DME combustion in a turbulent jet flame using detailed chemistry. Radial profiles of the mean axial velocity (see Fig. 1) show an over-prediction of the centerline velocity and a velocity deficiency at outer positions. Compared to the experimental data the peak of the standard deviation is shifted slightly towards the inside. Reasons are not

entirely clear and may be related to the boundary layer of the superimposed turbulent velocity at the jet inlet that is over-predicted. Overall agreement of CMC computations [4] using the mechanism by Zhao et al. [23] seems slightly better, but there a dynamic Smagorinsky model was used and current LES may be improved by the use of an equivalent closure of the sub-grid stresses.

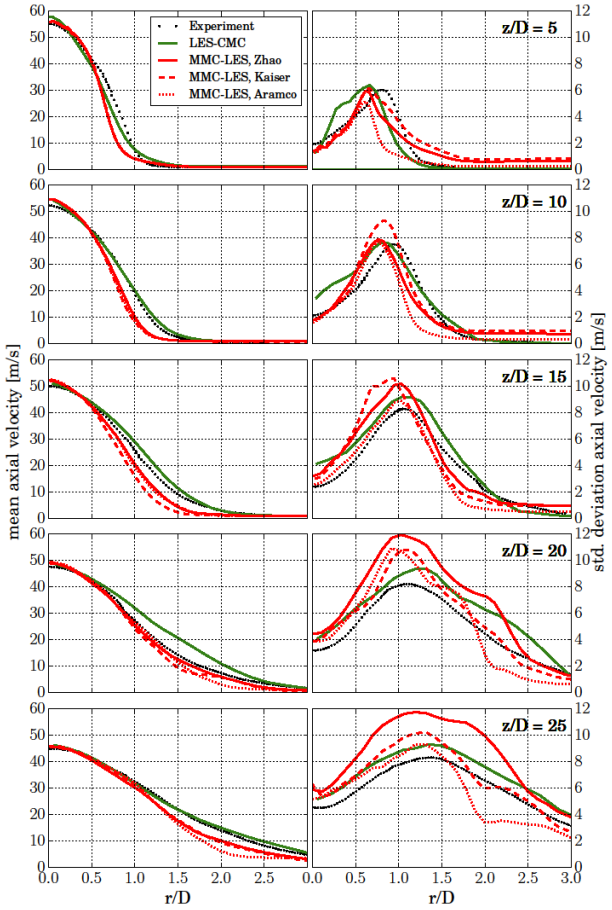


**Figure 1:** Spatial mean and std. deviation for axial velocity at axial locations of $z/D$ = 5, 10, 15, 20 and 25

Most important is, however, the correct transport and mixing of the stochastic MC particles. Fig. 2 shows the time averaged mean and standard deviation of the mixture fraction on the stochastic MC particles and compares them with experiments and CMC-LES results [4]. The results of the MMC-LES simulations are relatively independent of the chemical mechanism and comparable in quality to the CMC-LES results. The local maxima of variance are somewhat better captured by the current simulations.

The mixing distance in mixture fraction space, $f_m$, is a modeling parameter and input to the mixing model. Its correct choice is therefore important and has direct influence on the model behavior. The effect of $f_m$ and $r_m$, the latter resulting from $f_m$, are shown in Fig. 3 at three different positions. The mean $d_{\tilde{f}}$ represents the mean mixing distance in mixture fraction space and the mean $d_x$ indicates the mean distance in physical space. Correct modeling should drive these two values close to $f_m$ and $r_m$. The two peaks of $d_{\tilde{f}}$ and $d_x$ close to the jet

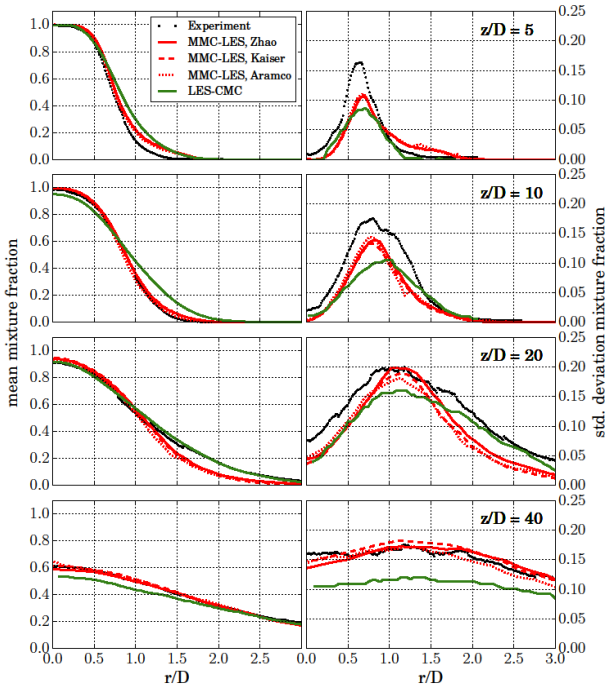


**Figure 2:** Time averaged mean and std. deviation of the mixture fraction at different downstream positions

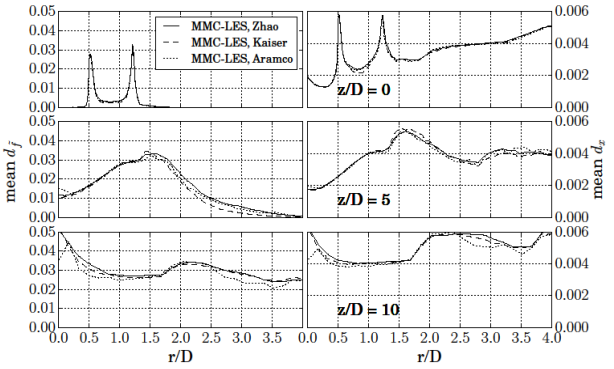


**Figure 3:** mean mixing distance in mixture fraction space (left) and physical space (right) for $f_m$ = 0.03 and $r_m$ = 0.0043m

exit can be associated with the shear layers between jet and pilot and pilot and co-flow. The $d_{\tilde{f}}$ and $d_x$ are meaningless in region of zero mixture fraction gradient. Overall, the achieved distances in mixture fraction and physical space agree well with the target value as imposed by the selection of $f_m$. Figure 4 present the spatial mean and std. deviation of temperature at different downstream positions. Despite the deviations from measurements very close to the nozzle, we get good agreement at z/D = 10 and z/D = 40. The reasons for the notable over-prediction at the outer edge of the shear layer can be associated with errors in the prediction of the velocity and mixture fraction fields (cf. Figs. 1 and 2). It is therefore standard practice for turbulent non-premixed combustion to validate reactive species predictions by comparisons of conditionally averaged quantities rather than unconditional averages. Fig. 5 depicts conditional mean profiles of the fuel species, $H_2O$, CO, $CO_2$ and $H_2$ and an overall very good agreement with experimental data can be seen. The clear deviations on the very rich side (at z/D = 40) can primarily be associated with uncertainties in the

measurements and potentially differential diffusion effects. Our results are consistent with computations by Popp et al. [5].

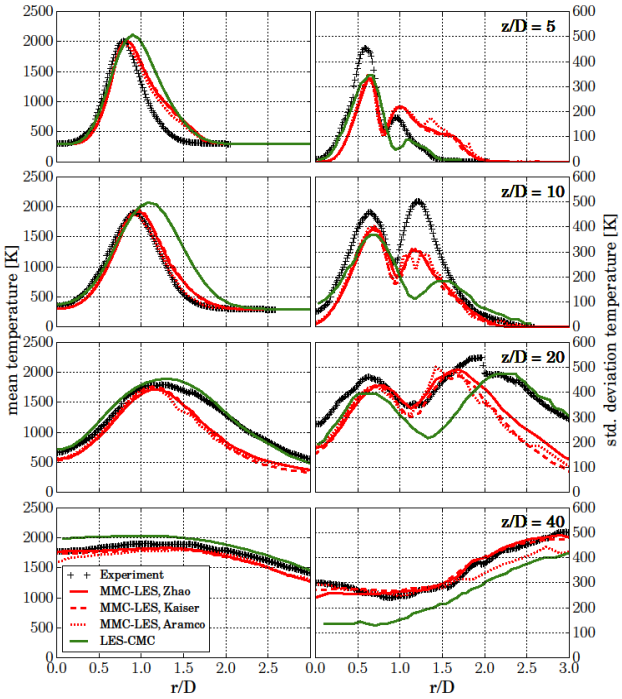


**Figure 4:** Spatial mean and std. deviation values of temperature at axial locations of $z/D$ = 5, 15, 20 and 25

## 5. Summary and conclusions

A numerical investigation of a piloted, partially-premixed turbulent dimethyl ether/air jet flame with a Reynolds number of $Re_D$ = 29,300 was performed. The computed results of velocity, mixture fraction, reacting species distributions and temperature compared favourably with measurements. The flame structure is well captured and the very moderate degree of extinction is correctly predicted.

## 6. Acknowledgements

Grants from DFG (AK – grant number KR3864/10-1) and ARC (MJC – grant number ARC PD130100763) are acknowledged with thanks.

## 7. References

[1] International Workshop on Measurement and Combustion of Turbulent Non-Premixed Flames (TNF), available at https://www.sandia.gov/TNF.

[2] F. Fuest, R.S. Barlow, J. Chen and A. Dreizler, Comb. Flame **159** (2012), pp. 2533–2562.

[3] F. Fuest, G. Magnotti, R.S. Barlow and J.A. Sutton, Proc. Combust. Inst. **35** (2015), pp. 1235–1242.

[4] B. Coriton, M. Zendehdel, S. Ukai, A. Kronenburg, O.T. Stein, S. Im, M. Gamba and J.H. Frank, Proc. Combust. Inst. **35** (2015), pp. 1251–1258.

[5] S. Popp, F. Hunger, S. Hartl, D. Messig, B. Coriton, J.H. Frank, F. Fuest and C. Hasse, Comb. Flame **162** (2015), pp. 3016–3029.

[6] N. Peters, Prog. Energy and Comb. Science **3** (1984), pp. 319–339.

[7] A.Y. Klimenko and R.W. Bilger, Prog. Energy and Comb. Science **25** (1999), pp. 595–687.

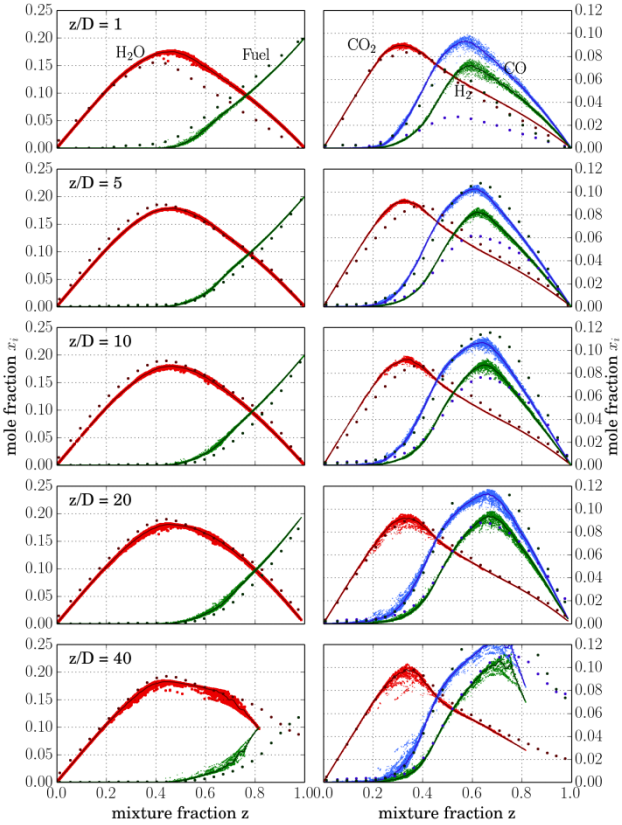


**Figure 5:** Comparison of experimental and numerical conditional mean profiles of Fuel (DME + $C_xH_y$), $H_2O$, $CO_2$ and $H_2$ at axial locations of $z/D$ = 1, 5, 10, 20 and 40 for the Zhao mechanism

[8] A.Y. Klimenko and S.B. Pope, Physics of Fluids **15** (7) (2003), pp. 1907–1925.

[9] J. Villermaux and J.C. Devillion, 2nd Int. Symp. Chem. Reac. Eng. (1972), pp. 1–13.

[10] R.L. Curl, AIChE J. **9** (2) (1963), pp. 175–181.

[11] J. Janicka, W. Kolbe and W. Kollmann, J. Non-Equilib. Thermodyn. **4** (47) (1979), pp. 47–66.

[12] S. Subramanian and S.B. Pope, Comb. Flame **115** (4) (1998), pp. 487–514.

[13] C. Celis and L.F. Figueira da Silva, Flow Turbulence Combust. **94** (2015), pp. 643–689.

[14] M.J. Cleary and A.Y. Klimenko, Flow Turbulence Combust. **82** (2009), pp. 477–491.

[15] M.J. Cleary and A.Y. Klimenko, Physics of Fluids **23** 115102 (2011), pp. 1–19.

[16] M.J. Cleary, A.Y. Klimenko, J. Janicka and M. Pfitzner, Proc. Combust. Inst. **32** (2009), pp. 1499–1507.

[17] Y. Ge, M.J. Cleary and A.Y. Klimenko, Proc. Combust. Inst. **34** (2013), pp. 1325–1332.

[18] C.W. Gardiner, Handbook of Stochastic Methods, Springer Verlag, 2010.

[19] M. Muradoglu, S.B. Pope and D.A. Caughey, J. Comput. Phys. **172**(2) (2001), pp. 841–878.

[20] V. Raman, H. Pitsch and R.O. Fox, Combust. Flame **143**(1-2) (2005), pp. 56–78.

[21] V. Raman and H. Pitsch, Proc. Combust. Inst. **31** (2) (2007), pp. 1711–1719.

[22] E.W. Kaiser, T.J. Wallington, M.D. Hurley, J. Platz, H.J. Curran, W.J. Pitz and C.K. Westbrook, J. Phys. Chem. **104**(35)(2000), pp. 8194–8206.

[23] Z. Zhao, M. Chaos, A. Kazakov and F.L. Dreyer, Int. J. Chem. Kinet. **40**(1) (2008), pp. 1–18.

[24] W.K. Metcalfe, S.M. Burke, S.S. Ahmed and H.J. Curran, Int. J. Chem. Kinet. **45**(10) (2013), pp. 638–675.

**Proceedings of the Australian Combustion Symposium**
**December 7-9, 2015, The University of Melbourne**

# Acceleration of combustion simulations using GPUs

K.A. Damm[1], R.J. Gollan[1], A. Veeraragavan*,[1]
[1]School of Mechanical & Mining Engineering
The University of Queensland, Queensland 4072, Australia

**Abstract**

The solution of the chemical kinetics problem in reacting flow simulations requires the integration of a large set of Ordinary Differential Equations. This paper explores the use of general purpose graphic processing unit (GPGPU) programming to accelerate this costly computation via the implementation of a chemical kinetics ODE solver on a GPU using OpenCL. The GPU solver is coupled into the University of Queenslands in-house Navier-Stokes code *Eilmer*. Three reaction mechanisms are simulated for two case studies: a well-stirred reactor and a shock-induced combustion flow. Results from the well-stirred reactor simulation show that the GPU implementation outperforms an identical CPU implementation for problem sizes exceeding 64 to 256 cells, depending on reaction mechanism complexity. The performance is shown to scale with both number of cells and reaction mechanism complexity. The results of simulating shock-induced combustion showed that branch divergence limited the performance of the GPU implementation.

*Keywords: Chemical Kinetics, reacting flow simulation, GPGPU*

## 1 Introduction

Modelling of chemical kinetics requires the solution of a possibly stiff system of Ordinary Differential Equations (ODE), given by Eq. 1 where $X_i$ is the concentration of the $i^{th}$ species.

$$\frac{d[X_i]}{dt} = f([X_0],[X_1].....[X_i]) \tag{1}$$

Since detailed reaction mechanisms can be made up of hundreds of reactions and tens of species, it is currently impractical to simulate complex reacting flows using detailed reaction mechanisms, especially if one wants to do simulations on an engineering workstation. To reduce the compute time of such simulations, it is proposed that the system of ODEs be solved in a massively parallel manner using general purpose graphics processing units (GPUs). When comparing CPUs and GPUs, Hwu et al [1] concluded that GPUs are the superior processor architecture for computational power. The authors compared the current GFLOPS (*GIGA* Floating Point Operations Per Second) achievable for both CPUs and GPUs and found that GPUs perform on the order of 1000s of GFLOPS compared to CPUs which perform less then 200 GFLOPS.

Recent papers by Niemeyer and Sung [2] and Shi et al [3] have reported promising results for the use of GPUs in reactive flow simulations. Niemeyer and Sung [2] cited accelerations of 126x, 59x and 4.5x faster than the single-core CPU implementation for several reaction mechanisms ranging from a non-stiff hydrogen-oxidation mechanism (9 species, 28 irreversible reactions), moderately stiff hydrogen/carbon-monoxide mechanism (13 species, 54 irreversible reactions) and a severely stiff ethylene oxidation mechanism (111 species, 1566 irreversible reactions). The implementation used a Runge-Kutta-Cash-Karp 5th order algorithm for the non-stiff systems, and a stabilized explicit Runge-Kutta Chebyshev algorithm for moderately stiff and severely stiff systems. Shi et al [3] implemented the CHEMEQ2 solver [4] on a GPU. The published results show that for the GPU solver using the CHEMEQ2 algorithm the GPU performed similar to that of 13 parallel 2.8 GHz CPU processors.

A broader literature review of the GPU vs CPU comparisons uncovers some inconsistency in reported accelerations. This inconsistency in published results sparked an investigation by Lee et al [5]. In their paper, the authors re-evaluated a number of published works in an effort to explain the spread of results. They found that in many cases comparisons between CPU and GPU code were not judicious. The paper's results showed that on average GPUs performed only 2.5x times faster than the CPU counterpart. We make this point about the spread of reported accelerations to give some context to our present work. We have made a dedicated attempt to keep algorithmic consistency in our present work comparing a CPU and GPU implementation and our results should be viewed in that light. The aim of this paper is to contribute to the growing body of work in accelerating combusting flow simulations by identifying suitable benchmarking cases. The University of Queensland's newly developed chemical kinetics GPU solver is presented and the results of a benchmarking study, where the new GPU solver is benchmarked against an identical CPU solver are reported.

## 2 Background

A standard GPU architecture consists of one or more compute units. Housed on each compute unit are a number of processing threads. These threads are the

*Corresponding author:
Phone: +61 7 336 54069
Email: anandv@uq.edu.au

elements on which floating point operations are executed [6]. GPUs are built on a Single Instruction Multiple Data (SIMD) architecture. This format allows the concurrent execution of a single operation on a set of multiple data.

The processing threads on a GPU are grouped into smaller subsets called warps. Warps vary in size for different vendors. In NVIDIA devices, for example, a warp consists of 32 processing elements [1]. Only one warp on a GPU will be executing at one point in time. Hence, the 32 processing elements will be truly executing concurrently. For peak runtime performance, all 32 processing threads in a warp execute the same instruction path. If any conditional statements (such as *if* or *else*) cause two threads in a warp to travel down different instructional paths then divergence will occur. This is a direct consequence of the SIMD structure. When divergence occurs in a warp, the thread which is taking a different instructional path must wait until the other 31 threads have finished executing before being executed. In the worst case, where the 32 threads are all on differing instructional paths, this leads to the code running in serial [1]. Divergence is a major concern since GPU threads are far less superior than CPU cores at performing tasks serially. We mention this issue of performance degradation due to divergence as it is an issue that requires some attention for solving complex ODEs in parallel on GPU architectures.

## 3 Implementation

In this work, the chemical kinetics solver for the GPU architecture is written using OpenCL [7]. Operator Splitting [2] is used to separate the update of the chemical kinetics terms from the other physical processes, such as convection and diffusion. This allows the species concentrations change due to chemical reactions to be updated independently on the GPU each time step and added to the other flow variable updates at the conclusion of each global time step. The GPU chemical kinetics solver is coupled to the University of Queenslands flow solver *Eilmer*[8]. The set of ODEs governing the species concentrations updates are solved on the GPU using the $\alpha - QSS$ method developed by Mott [4]. The GPU solver maps each of the cells in the fluid domain to a physical thread on the GPU. This facilitates the concurrent update of multiple cells' species concentrations. The cell data is stored in the GPU's low latency global memory. In this work, we compare this new hybrid CPU/GPU implementation for a complete timestep update to our original work which is implemented for the CPU only. The two variations of update algorithm are shown in Figure 1.

In order to get optimal performance from the GPU, some care must be taken with the code written for the GPU such that the nuances of the architecture are considered. For example, the GPU implementation uses memory coalescing as suggested by Stone et al [9]. Also, the GPU implementation is designed to overpresribe the workload on the GPU such that all the available resources are being utilized. This helps to lessen the effects of GPU overhead costs, where GPU overhead costs are defined as wall-clock time spent performing operations which are not required for an identical CPU implementation, such as data transfer to/from the GPU.

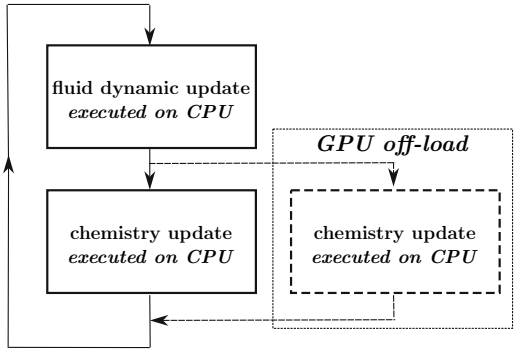


Figure 1: Flow diagram for update algorithm with both CPU-only and CPU/GPU updates shown.

## 4 Results and Discussion

Note that the flow code *Eilmer* had an existing chemistry module that executes on the CPU prior to this work on a GPU implementation. In what follows, we compare the performance of running the simulation code in pure CPU mode (pre-existing implementation) versus the CPU/GPU hybrid implementation (present work) wherein the chemistry module is executed on the GPU (see Figure 1). For simplicity, the CPU/GPU hybrid approach will be referred to as the GPU solver. All CPU based code was executed on a single core of an Intel(R) Xeon(R) CPU E5-2680 v2 @ 2.80GHz. The GPU code was executed on a NVIDIA Tesla K40m with all 2880 CUDA cores being utilised.

Two case studies are used to benchmark the GPU solver against the standard *Eilmer* CPU solver. Firstly a well-stirred reactor is simulated to provide the best case scenario for the GPU, since all the cells in the domain will have identical conditions, so no divergence will occur. To test the GPU solver in a typical reacting flow simulation, shock-induced combustion in supersonic flow due to a sphere fired into a premixed fuel/oxidiser mixture is simulated. In this latter case, divergence is anticipated to be a limiting factor.

Two reaction mechanisms are simulated for the well-stirred reactor: the Evans and Schexnayder reduced hydrogen-air mechanism (6 species, 8 reactions) [10] and the DRM19 methane combustion mechanism (19 species, 84 reactions) [11]. The initial conditions for the hydrogen-air reactor simulation were mole fraction ratios of 2:1 for $H_2 : O_2$, temperature of 1000 K and a pressure of one atmosphere. The initial conditions for the methane reactor simulation were mole fraction ratios of 1:2:7.52 for $CH_4 : O_2 : N_2$, temperature of 2000 K and a pressure of one atmosphere. The reactors were simulated through ignition to steady state.

The results for the well-stirred reactor simulations are presented in Figures 2 through 5. The average wall-clock time to execute a global step (which includes the time spent updating fluid dynamic properties serially on the CPU) and the average wall-clock time spent in the chemistry solver are plotted against number of ODEs (species x cells). Results are plotted comparing the time spent in the chemistry update for both the CPU and GPU implementations. A second set of results are plotted for the global time spent doing a complete timestep update, that is, both the fluid dynamic update and chemistry update combined. Three important features can be derived from these plots. First, it

is apparent that for coarser meshes the CPU implementation executes an integration step faster than the GPU implementation. In this case, the GPU is not being overprescribed with work and has idle compute resources. For finer meshes, the GPU implementation surpasses the CPU implementation for faster execution; the GPU now is over-prescribed with work and all compute resources are being utilised. For the Evans and Schexnayder scheme this performance cross-over occurs at 256 cells, and for the DRM19 scheme cross-over occurs at 64 cells. Second, soon after the cross-over region, where the GPU begins to outperform the CPU implementation, the acceleration factor asymptotes to its maximum value. The GPU can only process a finite number of cells at one point in time. If the GPU is tasked with more work than it can perform concurrently, it will queue cells until it has finished with the current batch. Once the GPU has reached its limit for processing cells in parallel, its performance gain over the CPU asymptotes. Third, it is noted that global time step acceleration is lower than the chemistry time step acceleration. This result is a direct consequence of the fraction of the algorithm time spent in the chemistry update compared to the fluid dynamic update. For smaller mechanisms such as the reduced hydrogen mechanism, only 40% of the flow solver update is spent updating the species concentrations. For larger mechanisms such as DRM19, the global reduction is closer to the chemistry reduction since the chemistry solver takes up a larger portion of the overall solver time.

For the well-stirred reactor, there is no divergence occurring since all threads are performing identical calculations on identical data. As such the average time it takes one thread on the GPU to integrate a single cell, and likewise, the average time it takes a single CPU core to integrate a singe cell may be estimated. Since the CPU is solving each cell sequentially the average time is a trivial calculation.

$$t_{cpu,avg} = \frac{dt_{global}}{N_{cells}} \tag{2}$$

For the GPU implementation, since the tests were performed on NVIDIA hardware it can be assumed that the warp size is 32, thus 32 cells are being executed concurrently.

$$t_{gpu,avg} = \frac{dt_{global}}{N_{cells}/32} \tag{3}$$

The average times to solve one cell on a single core/thread are presented in Figures 6 and 7. As expected the CPU is executing each cell faster, owing to its superiority in sequential code execution. For finer meshes, the GPU's compute resources become increasingly utilized until all threads are active. As such the CPU solves each cell 20x faster than a GPU thread compared to 30-40x faster for coarser meshes. This result confirms that GPUs become progressively more efficient for larger grid sizes via overprescription of GPU resources.

Three reaction mechanisms are simulated for the supersonic flow over a sphere: the Evans and Schexnayder reduced hydrogen-air mechanism (6 species, 8 reactions) [10], the Stanford Hydrogen-Air reaction mechanism (19 species, 38 reactions) [12], and the DRM19 methane combustion mechanism (19 species, 84 reactions) [11]. The inflow mole fraction ratios of 2:1 for $H_2 : O_2$, were used for the two hydrogen-air combustion mechanisms. The inflow mole fraction ratios of 1:2:7.52 for $CH_4 : O_2 : N_2$ were used for the methane combustion mechanism. These simulations were computed through to steady state.

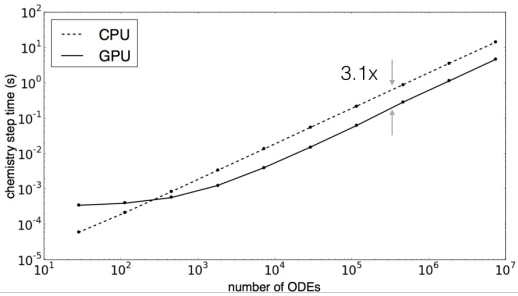


Figure 2: Evans and Schexnayder Chemistry Time

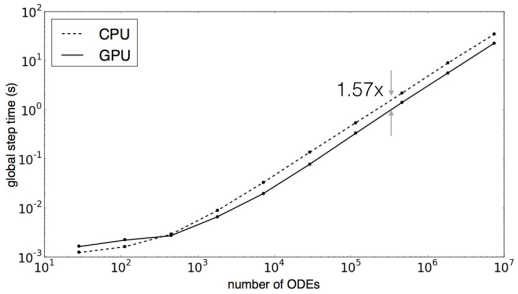


Figure 3: Evans and Schexnayder Global Time

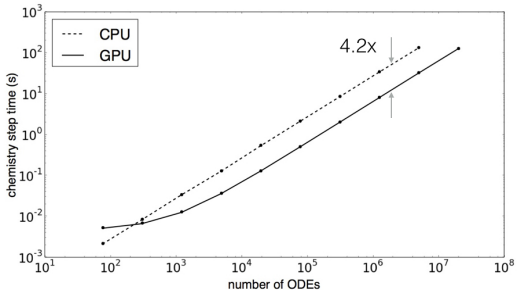


Figure 4: DRM19 Chemistry Time

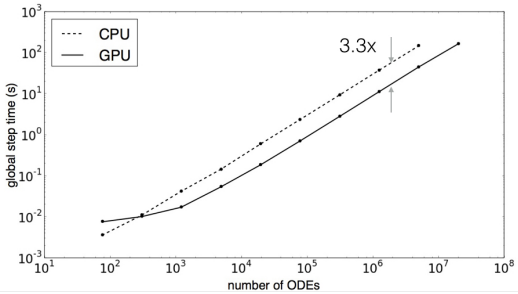


Figure 5: DRM19 Global Time

The results for the shock-induced combustion simulations are presented in Figures 8 and 9. The plots show the acceleration factor ($CPU_{time}/GPU_{time}$) for the sphere and reactor simulations for comparison. It is clear that these simulations have poorer performance compared to the reactor simulations. Two major reasons that this has occurred are as follows. First, divergence

has occurred and some warps are now executing sequentially rather than concurrently. This is a direct result of the differing chemical composition causing neighbouring cells to take different paths through the conditional statements in the $\alpha - QSS$ algorithm. Second, the chemistry time is only a small fraction of the overall flow time. This is largely because there is only a portion of the cells which are computationally demanding in terms of chemistry calculation compared to the reactor case where all cells went through ignition. Hence any acceleration in the chemistry will only have a small effect on the reduction of the total wall-clock time.

## 5 Conclusion

A GPU chemical kinetics solver was added to UQ's *Eilmer* Navier-Stokes solver. Two case studies were used to benchmark the GPU implementation against an identical CPU solver. A well-stirred reactor and shock-induced combustion test cases were simulated for a number of reaction mechanisms. The results for the well-stirred reactor showed that the GPU out performed the CPU on reducing the wall-clock time for all simulations with grid sizes greater than 64 to 256 cells depending on reaction mechanism complexity. The results for the shock-induced combustion simulations found that divergence severely limited the performance of the GPU. GPU and coupled message-passing interface (MPI) simulations will be examined in future work.

## 6 Acknowledgements

Computational resources were provided by the HPC and Research Support Group, Queensland University of Technology, Brisbane, Australia

## References

[1] W.-m. Hwu and D. Kirk, *Programming massively parallel processors*. Elsevier, 2009, vol. 92.

[2] K. E. Niemeyer and C.-J. Sung, "Accelerating moderately stiff chemical kinetics in reactive-flow simulations using GPUs," *Journal of Computational Physics*, vol. 256, no. 0, pp. 854 – 871, 2014.

[3] Y. Shi, W. H. Green, H.-W. Wong, and O. O. Oluwole, "Accelerating multi-dimensional combustion simulations using GPU and hybrid explicit/implicit ODE integration," *Combustion and Flame*, vol. 159, no. 7, pp. 2388 – 2397, 2012.

[4] D. R. Mott, E. S. Oran, and B. van Leer, "A quasi-steady-state solver for the stiff ordinary differential equations of reaction kinetics," *Journal of Computational Physics*, vol. 164, no. 2, pp. 407 – 428, 2000.

[5] V. W. Lee *et al.*, "Debunking the 100x GPU vs. CPU myth: an evaluation of throughput computing on CPU and GPU," in *ACM SIGARCH Computer Architecture News*, vol. 38, no. 3. ACM, 2010, pp. 451–460.

[6] B. Gaster, L. Howes, D. R. Kaeli, P. Mistry, and D. Schaa, *Heterogeneous Computing with OpenCL: Revised OpenCL 1*. Newnes, 2012.

[7] (2015). [Online]. Available: https://www.khronos.org/opencl/

[8] R. J. Gollan and P. A. Jacobs, "About the formulation, verification and validation of the hypersonic flow solver Eilmer," *International Journal for Numerical Methods in Fluids*, vol. 73, pp. 19–57, 2013.

[9] C. P. Stone and R. L. Davis, "Techniques for solving stiff chemical kinetics on graphical processing units," *Journal of Propulsion and Power*, vol. 29, no. 4, pp. 764–773, 2013.

[10] J. S. Evans and C. J. Schexnayder, "Influence of chemical kinetics and unmixedness on burning in supersonic hydrogen flames," *AIAA Journal*, vol. 18, no. 2, pp. 188–193, 1980.

[11] A. Kazakov and M. Frenklach, "Drm19 reaction mechanism," http://www.me.berkeley.edu/drm/.

[12] Z. Hong, D. F. Davidson, and R. K. Hanson, "An improved $H_2/O_2$ mechanism based on recent shock tube/laser absorption measurements," *Combustion and Flame*, vol. 158, no. 4, pp. 633–644, 2011.

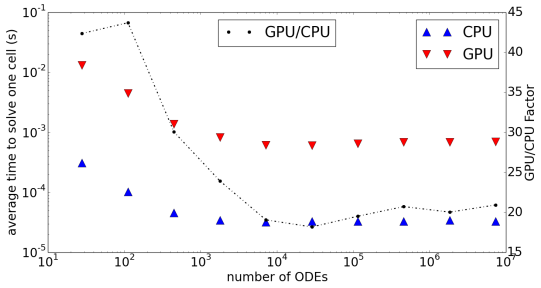


Figure 6: Evans and Schexnayder average time to solve one cell

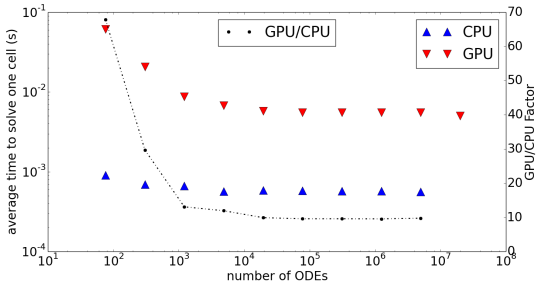


Figure 7: DRM19 average time to solve one cell

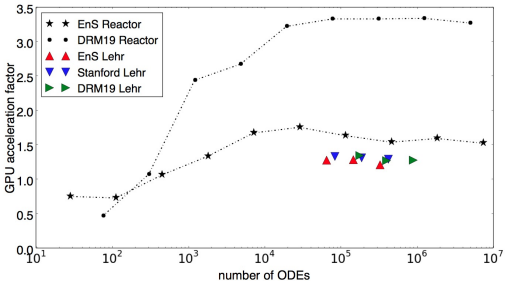


Figure 8: Acceleration factor (global time)

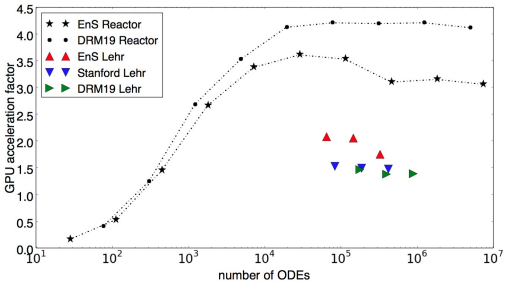


Figure 9: Acceleration factor (chemistry time)

# Developments in Multiple Mapping Conditioning for turbulent premixed combustion

B. Sundaram[1,*], A.Y. Klimenko[1], M. J. Cleary[2]
[1]School of Mechanical and Mining Engineering, University of Queensland QLD 4072 Australia
[2]School of Aerospace, Mechanical and Mechatronic Engineering, University of Sydney NSW 2006 Australia

## Abstract

The modelling of turbulent combustion is one of the key areas in combustion research. One recent trend in turbulent combustion modelling is the appearance of universal, flexible models that combine features of existing categories. One of these approaches involves Filtered Density Function (FDF) methods, generalised Multiple Mapping Conditioning (MMC) and sparse-Lagrangian modelling. Jointly, these approaches allow for flexibility and the combination of useful properties of the original categories, most importantly generality and low computational cost. We discuss the general principles of universal modelling using MMC conditioning and sparse-Lagrangian simulations and present some working examples. Attention is paid to the application of MMC to premixed combustion.

*Keywords: PDF methods, Multiple Mapping Conditioning, Premixed combustion*

## 1. Introduction

The complexities of modelling turbulent combustion, which involves non-linear, multi-scale interactions between turbulent fluctuations and chemistry have been discussed in many publications, and a number of approaches to the problem have been suggested. These approaches can be divided into two major categories: 1) those based on utilising the mixture fraction [1-3] in one way or the other; and 2) those involving modelling of joint Probability Density Functions (PDF) of reactive scalars [4, 5]. The first category (fast chemistry, flamelet, Conditional Moment Closure (CMC), etc.) is characterised by relatively low computational cost, while the second category involves more general, albeit more computationally expensive methods . These two groups can be used in context of both Reynolds Averaged Navier-Stokes (RANS) and Large Eddy Simulations (LES) [6, 7, 8]. There exists another option --- Direct Numerical Simulation (DNS) --- which while useful, can hardly be used in complex practical applications with realistic kinetics due to prohibitive computational costs. While most of these categories were conventionally seen as being distinct and incompatible, research in recent years is marked by an emergence of universal and flexible approaches that combine useful features of the different categories. This presentation discusses and illustrates these new approaches

The universality of probability density function (PDF) methods is based on the application of instantaneous non-linear chemical reaction rates, which thus appear in the model in closed form. However, the PDF equations contain unclosed conditional scalar dissipation terms, which necessitate the involvement of mixing models; Interaction by Exchange with the Mean (IEM [9, 10], Curl's [11], Modified Curl's (MC) [12, 13] and Euclidean Minimum Spanning Tree (EMST) [14] are noted to be the most popular choices of mixing models.

## 2. Conditioning of Mixing

Models that utilise mixture fraction are computationally efficient and involve accurate specification of mixing, but have limited applications and lack the generality required to handle cases involving complex combustion phenomena such as extinction and re-ignition. PDF methods are a more general, albeit more computationally expensive approach, which can accurately treat complex kinetics but have difficulties in precise modelling of mixing. In the past, the mixture fraction approach and PDF methods were viewed as distinct (and to some extent competing) approaches for modelling turbulent combustion. With the introduction of MMC, this is no longer the case [15]. MMC enforces conditional properties (such as conditional expectations modelled by CMC) on mixing while improving emulation of mixing and retaining the generality of the PDF methods.

In addition to the conventional dissipation time, MMC models possess an additional parameter, called *localness*. While the former parameter is selected to match large-scale properties of the simulated turbulent flow, the choice of the latter parameter reflects more refined properties of turbulent mixing determined by the scales of the inertial interval of turbulence. Hence, MMC is explicitly aimed not only at simulation of the macroscopic effects of mixing but also some of the microscopic effects of mixing. At this stage MMC is the only approach that is explicitly directed at modelling micromixing. Practically, the MMC localness parameter is selected to match the conditional variances, which are generated by small-scale fluctuations of the scalar dissipation.

* Corresponding author:
Email: brruntha.sundaram@uqconnect.edu.au

MMC has evolved from its original version to a more flexible and simple to use generalised from. Its main feature is conditioning of mixing on MMC reference variables. Different types of reference variables have been explored in MMC modelling, including mixture fraction, scalar dissipation and implied or shadow position [16, 17].

## 3. Resolution of large scales alongside modelling of small scales

LES is known to improve simulation of turbulent flows in comparison with RANS-based models. LES also avoids the computational expense associated with resolving the smallest of turbulent scales which is performed in DNS. The additional computational expense of LES, relative to RANS, is rewarded by well-simulated dynamic fields. Conversely, LES of reacting flows tends to fall below the expected quality. This happens due to the neglect of subgrid fluctuations of reactive species, which are quite substantial (as long as the LES is not over-refined to approach the full DNS regimes).

The shortcomings of LES for reacting flows can be remedied by combining the LES and PDF methods into approach called the Filtered Density Function (FDF) [3]. In this approach the large scales are resolved by LES while the subgrid distributions of species are not neglected but emulated. This can be done by Lagrangian particles or by multiple Eulerian fields (in the stochastic field method). It is possible for FDF approaches to produce very good result but their application is limited due to high computational cost incurred by the necessity of many particles per each cell or many stochastic fields.

The computational cost of FDF methods can be substantially reduced in sparse-Lagrangian simulations. These simulations aim not to reproduce a subgrid FDF of reactive scalars within each Eulerian cell, but instead, aim to have a representative stochastic value which is distributed with the modelled FDF. These values are evaluated at Lagrangian particles, which while having very few particles per cell or even having several cells per one particle, can be sufficient for good simulations. In simple terms, the reactive scalars are simulated on a Lagrangian grid, while dynamic characteristics of turbulence are evaluated on the Eulerian grid. The variations of Lagrangian representations of the scalars emulate subgrid fluctuations.

## 2. Non-premixed combustion

Practically, a substantial reduction in the number of particles is impossible to achieve without improving the control of mixing. Sparse-Lagrangian methods work in conjunction with MMC modelling of mixing with conditioning on the mixture fraction. Simulations of Sandia flame D [18] with as few as 10000 reactive particles [19] have been performed with a thousand-fold reduction of computational cost as compared to conventional FDF simulations (which might deploy 20-50 million particles for a similar case). Simulations of the whole series D-F [18] have also been performed by sparse-Lagrangian MMC-LES simulations with only ~30 thousand particles [20]. Flame F is very close to extinction and is very difficult to reproduce correctly. The whole series has been simulated with exactly the same set of the model parameters.

The Cabra lifted hydrogen flame [21] has been simulated with approximately one particle per 32 LES cells. Accurate modelling of mixture fraction, shown in Fig. 1, is necessary to reproduce other reactive scalars. Axial temperature is shown in Fig. 2. The OH radical is an indicator of liftoff height, and is determined to be 9.4 diameters from the inlet compared to the experimental value of 10. Unconditional axial and conditional means of OH are shown in Figs. 3 and 4 respectively.

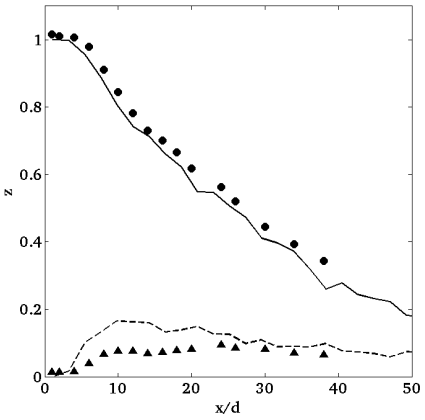


Fig. 1: Axial profile of mean and RMS particle mixture fraction. Circles - experimental mean, triangles - experimental RMS, solid line – simulated mean, dashed line - simulated RMS.

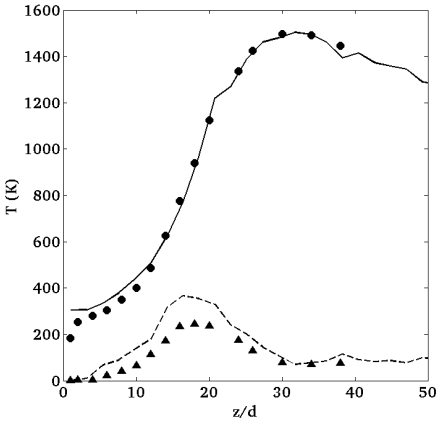


Fig. 2: Axial profile of mean and RMS temperature. Circles - experimental mean, triangles - experimental RMS, solid line – simulated mean, dashed line - simulated RMS.

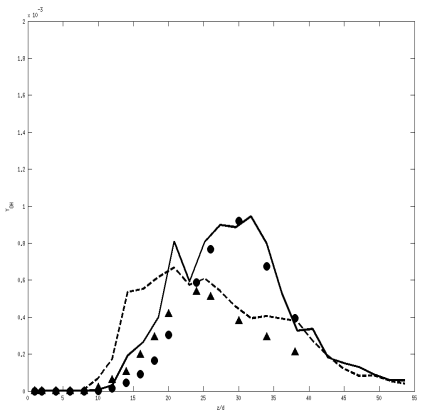

Fig. 3: Axial profile of mean and RMS OH fraction. Circles - experimental mean, triangles - experimental RMS, solid line – simulated mean, dashed line - simulated RMS.

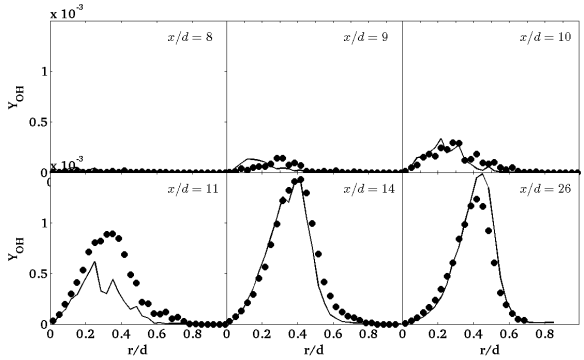


Fig. 4: Conditional means of OH mixture fraction. Circles - experimental mean, triangles - experimental RMS, solid line – simulated mean, dashed line - simulated RMS.

## 3. Premixed combustion

PDF methods are known to work well for distributed regimes but have difficulties in reproducing flamelet regimes of premixed flames. The main problem is non-localness of simulated mixing that allows a direct mixing of the fresh and burned mixture (which is unphysical). MMC can be used as a remedy, localising mixing within the flame structure. The desired properties of the turbulent flames can be enforced by conditioning of mixing, while the selection of different values for the MMC localness parameter allows for simulating distributed regimes, flamelet regimes or any regimes in between.

The selection of the MMC reference variable $\xi$ that controls localization of mixing is illustrated in Fig. 5. This variable can be qualitatively understood as the distance from the flame surface into the fresh mixture (this is conceptually similar to the level set approach). A constant density flow is assumed for simplicity. The area $A$ of the surfaces of $\xi = const$ increases as the flame is approached, while the flow of Lagrangian particles (each representing a certain mass) through these surfaces remains the same. Hence, the velocity of these particles in the reference space decreases from turbulent propagation speed $u_t$ at a large distance from the flame to the laminar propagation speed $u_0$ at the flame.

The details of the law associated with this decrease are very interesting, but it is still uncertain if this law is consistent with the relations of the inertial interval of turbulence. Fortunately, we do not need to emulate the whole distribution of the reference variables and are concerned only with the range near $\xi = \xi_f$ where the flame is located. Practically, the stochastic differential equation for simulation of the reference variables can be selected in different ways.

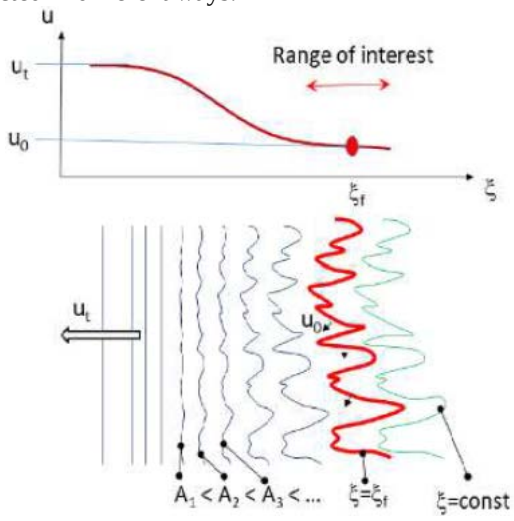


Fig. 5: Schematic of the choice of the MMC reference variable

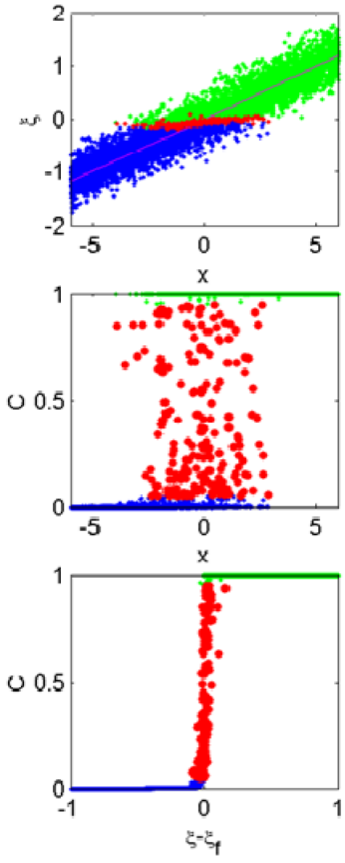


Fig. 6: Illustrative simulation of flame propagation in physical and reference spaces.

The flame is thin in the reference space $\xi$ and propagates in this space with velocity close to the laminar propagation speed. The same flame is much wider in the physical space $\xi$ and propagates in this space with the turbulent propagation speed. The structure of sample simulations with a simple one-step reaction mechanism is shown in Fig. 6. The case under consideration corresponds to $Re \approx 1000$, $Ka \approx 0.6$ and the flame speed amplification $u_t/u_0 \approx 5$. The red dots represent particles at the flame, the blue dots represent the fresh mixture and green dots represent the burned mixture. The flame is much thinner in the reference space than in the physical space. The top figure presents a snapshot of the $x$-$\xi$ plane, while the bottom figures show scatter plots of the reaction progress variable C versus $x$ and $\xi$ correspondingly. The bottom figure is very close to the laminar flamelet solution, although some fluctuations with respect to this solution are also apparent.

This model for premixed flames has been extended through the addition of a second reference variable to simulate two-dimensional rod-stabilised V-flames in the corrugated and thin wrinkled flamelet regimes. Simple, one-step irreversible chemistry is currently being applied alongside the model to predict the stabilisation angle of the flames under a range of localisations in the reference and physical spaces.

## 4. Conclusion and Submission Instructions

The development of MMC over the last decade has brought unification of previously unrelated approaches to modelling of turbulent combustion. The most notable steps are the incorporation of the PDF methods into an LES framework and the merging of the mixture-fraction based models with the PDF methods. These developments stimulate joint application of different turbulent models in a way that amplifies their strengths and negates their weaknesses.

## 4. Acknowledgments

This research is financially supported by the Australian Research Council.

## 5. References

[1] R. W. Bilger, Turbulent Reacting Flows, Ch. 3, Springer (1980).

[2] A. Y. Klimenko, R. W. Bilger, Prog. Energy Combust. Sci. **25** (1999), pp. 595-687.

[3] N. Peters, Turbulent Combustion, Cambridge University Press (2000).

[4] S. B. Pope, Prog. Energy Combust. Sci. **11** (1985), pp. 119-192.

[5] D. C. Haworth, Prog. Energy Combust. Sci. **36** (2009), pp. 168-259.

[6] P. J. Colucci, F. A. Jaberi, P. Givi, S. B. Pope, Phys. Fluids **10** (1998), 499-515.

[7] R. Fox, Computational Models for Turbulent Reacting Flows, Cambridge University Press (2003).

[8] V. Raman, H. Pitsch, Proc. Combust. Inst. **31** (2007), pp. 1711-1719.

[9] J. Villermaux, J. Devillon, Proc. 2nd Int. Symp. Chem. Reac. Eng. (1972), pp. 1-13.

[10] C. Dopazo, E. O'Brien, Acta Astronautica **1** (1974), pp. 1239-1266.

[11] R. Curl, AIChE Journal **9** (1963), pp. 175-181.

[12] J. Janicka, W. Kolbe, W. Kollmann, J. Non-Eq. Thermo. **4** (1977), pp. 47-66.

[13] R. Lindstedt, S. Louloudi, E. Vos, Proc. Combust. Inst. **28** (2000), pp. 149-156.

[14] S. Subramaniam, S. B. Pope, Combust. Flame **115** (1998), pp. 487-514.

[15] M.J. Cleary and A.Y. Klimenko in T. Echekki, E. Mastorakos (editors) Turbulent Combustion Modelling Advances, New Trends and Perspectives, New York, Springer, 2011.

[16] B. Sundaram, A. Y. Klimenko, M. J. Cleary, U. Maas, Proc. Combust. Inst. **35** (2015), pp. 1517-1525.

[17] S.B. Pope, Phys. Fluids **25** (2013), 110803.

[18] R. Barlow, J. Frank, Proc. Combust. Inst **27** (1998), pp. 1087-1095.

[19] M. J. Cleary, A. Y. Klimenko, Flow Turb. Combust. **82** (2009), pp. 477-491.

[20] Y. Ge, M.J. Cleary and A.Y. Klimenko, Proc. Combust. Inst. **34** (2013), pp. 1325-1332.

[21] R. Cabra, T. Myhrvold, J.Y. Chen, R.W. Dibble, A.N. Karpetis, R.S. Barlow, Proc. Combust. Inst. **29** (2002), pp. 1881-1888.

# The Flow Characteristics and Flame Statistics of an Experimental Turbulent $CH_4$/air Premixed Flame using DNS

Haiou Wang[1*], Evatt R. Hawkes[1, 2], Jacqueline H. Chen[3]
[1] School of Mechanical and Manufacturing Engineering
The University of New South Wales, NSW 2052 Australia
[2] School of Photovoltaic and Renewable Energy Engineering
The University of New South Wales, NSW 2052 Australia
[3] Sandia National Laboratories, Livermore, CA 94550, USA

## Abstract

Direct numerical simulation of an experimental turbulent $CH_4$/air lean premixed jet flame was performed. At the inlet, a $CH_4$/air mixture with an equivalence ratio of 0.7 was issued through a round nozzle surrounded by a laminar coflow with hot products at an equivalence ratio of 0.9. The flame features a moderate jet Reynolds number and high Karlovitz number requiring two billion grids to resolve the turbulence and flame structure. A reduced chemical mechanism for premixed $CH_4$/air flames with $NO_x$ based on GRI-Mech3.0 was used. The mechanism includes 268 elementary reactions, and 28 transported species. The DNS database is employed to study the characteristics of the flow. It is shown that compared with a non-reacting round turbulent jet, the reacting turbulent jet decays more slowly. The mean velocity approaches its self-similar state shortly after $x/D$ = 20, while the fluctuating axial velocity does not become self-similarity until $x/D$ = 30. The profiles of the three components of the fluctuating velocity are different, suggesting the existence of anisotropic turbulence. The flame structure is studied in terms of the flame area, stretch factor and turbulent flame velocity. The normalized wrinkled flame surface area increases linearly in the streamwise direction. The stretch factor is found to be below unity throughout the domain due to the intense strain rate, which influences the flame structure and leads to partial-extinction of the flame upstream.

*Keywords: Direct numerical simulation, turbulent flame, self-similarity, turbulent flame velocity, stretch factor*

## 1. Introduction

Turbulent lean premixed combustion is a promising approach for low $NO_x$ gas turbine combustors. However, it is susceptible to thermoacoustic instabilities and flashback [1]. A thorough understanding of the dynamics of turbulent lean premixed combustion is required to control these processes and develop appropriate predictive combustion models.

The flow field of turbulent round jets has been extensively studied to understand free shear flow and facilitate the development of turbulence models. The self-similar solution of the axisymmetric jet was established. In the self-similar region, cross-stream profiles of all statistics could be expressed in terms of a single similarity function, regardless of downstream distance. Similarity analysis of non-reacting turbulent jet flows was performed both experimentally [2] and numerically [3]. However, the self-similarity in reacting turbulent jet flames has been rarely reported [4].

Turbulent flame velocity $S_T$ is an important quantity both from a fundamental understanding and a modelling viewpoint. It is known that turbulent eddies wrinkle the flame and significantly increase its surface area, which increases the turbulent burning velocity. Another quantity that influences the turbulent flame velocity is the stretch factor, which measures the ratio of the burning rate of the turbulent flame per unit surface area with respect to a laminar flame. This factor can be different from unity, particularly in highly stretched flames.

In this paper, direct numerical simulation (DNS) is employed to provide insights of the detailed structures of the flow field and the statistics of the turbulent flame evolution.

## 2. DNS database description

### 2.1 Configuration

The DNS modelled an experimental high Karlovitz number round jet turbulent premixed burner [5]. While DNS of other laboratory flames such as V-flames [6] and swirl-stabilised flames [7] have been reported, it is believed that this is the first detailed chemistry DNS of an experimental round jet-type flame. Figure 1 illustrates the schematic of the configuration. The jet operates at atmospheric pressure and room temperature of $T_j$ = 300 K. The jet bulk velocity is $U_b$ =110 m/s and the equivalence ratio of the reactant is $\Phi_j$ =0.7. A laminar $CH_4$/air coflow flame ($U_c$ =1.8 m/s, $T_c$ = 1800K, $\Phi_c$ = 0.9) was established surrounding the jet to provide a hot environment and thus enable flame stabilisaztion. The coflow is large (40$D$) and shelters the flame from the surrounding air. The jet diameter is $D$ = 1.5 mm and the Reynolds number based on $U_b$ and $D$ is $Re_j$ =10510. The Karlovitz number of the flame Ka is 253.6 based on jet-exit conditions. Note that Ka is a local number and remains high (Ka > 100) as the flow develops. It is

* Corresponding author:
Phone: (+61) 0413 625 612
Email: haiou.wang@unsw.edu.au

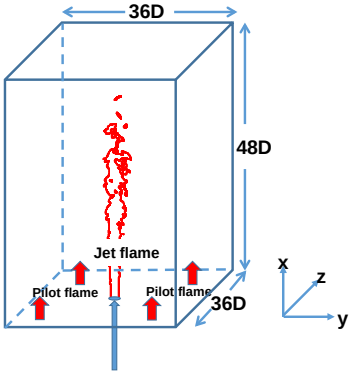


Figure 1. Schematic of the computational domain for DNS.

therefore a flame that is expected to lie in the distributed reaction or broken reaction zones regimes, which are of technical interest to gas turbine manufacturers.

The physical domain for the simulation is very large owing to the long flame length: $L_x \times L_y \times L_z$ = 48D × 36D × 36D in the streamwise $x$ and lateral directions $y$ and $z$, respectively, as illustrated in Fig. 1. The jet flow-through time based on $L_x$ and $U_b$ is $t_j$ = 0.645 ms. The resolution of the DNS is chosen to adequately resolve both of the flame and turbulence structures. A uniform grid spacing of $\Delta x$ = 30 μm is used in the streamwise direction $x$. The grid in the $y$ ($z$) direction is uniform with $\Delta y$ ($\Delta z$) = 30 μm in the region between $y/D$ ($z/D$) = -5 and 5, and gradually stretched outside of this region. The unstrained laminar flame thickness is 0.663 mm, which corresponds to 22 grid points with the DNS resolution. In the present case, the resolution of turbulence is more demanding. The Kolmogorov scale $\eta$ exhibits its minimum of 10 μm in a very narrow region near in the potential core, where the flame does not overlap. $\eta/\Delta x > 0.5$ is satisfied elsewhere. Thus, the smallest scales of the turbulent flow are reasonably resolved. The resultant number of grids is $N_x \times N_y \times N_z$ = 2400 × 900 × 900. The simulation was advanced for 9 flow-through times to provide stationary statistics.

## 2.2 Numerical Method

The DNS code 'S3D' was employed to solve the compressible equations for continuity, momentum, species mass fractions and total energy [8]. The code has been widely used in DNS studies of turbulent combustion. The equations were integrated in time in a fully coupled manner with a fourth order, six-stage, low-storage Runge–Kutta method [9]. An eighth order explicit finite difference scheme was used to obtain spatial derivatives, and a tenth order explicit low dissipation filter was applied every ten time steps to remove spurious fluctuations close to the grid size. The non-reflecting boundary condition [10] was applied in all the directions. CHEMKIN and TRANSPORT software libraries were linked with S3D to evaluate thermodynamic and transport properties.

A reduced chemical mechanism for premixed $CH_4$/air flames with $NO_x$ was derived based on GRI-Mech3.0 [10]. The final skeletal mechanism contains 268 elementary reactions and 44 species, of which 16 species are identified as quasi steady state species due to their high reactivity and short lifetime. The other 28 species are transported on the DNS grid.

Although it will be reported elsewhere, the DNS shows good quantitative agreement with the experimental mean temperatures and good qualitative agreement with experimental planar laser-induced fluorescence measurements of OH, $CH_2O$ and CH.

# 3. Results and Discussion

## 3.1 Characteristics of the flow

The development of the turbulent flow may be characterised by the axial evolution of $\Delta U_0$ and $\delta_{1/2}$, as illustrated in Fig. 2. $\Delta U_0$ is the mean axial velocity excess at the centerline defined as $\Delta U_0 = U_0 - U_c$. $\delta_{1/2}$ is the jet half-width defined as the radial distance at which the mean axial velocity excess reaches half of the corresponding mean axial velocity excess at the centerline, and it is employed as a measure of the growth of the jet. Fig. 2 shows that the mean axial velocity excess remains almost constant in the near-field for $x/D$ < 6, and decays in the far-field inversely with distance after $x/D$ =20. The analysis of round jets gives the following relationship between the mean axial velocity excess and the streamwise distance:

$$\frac{\Delta U_b}{\Delta U_0} = \frac{1}{C}\left(\frac{x}{D} - \frac{x_0}{D}\right) \qquad (6)$$

where $C$ is the decay constant and $x_0$ is the so-called virtual origin. The current DNS database predicts values for the coefficients of $C$ = 19.27 and $x_0$ = -4.76. These values are in contrast with $C$ = 5.9 and $x_0$ = 5 for a non-reacting round turbulent jet [2] indicating that due to heat release and hot coflow the jet decays more slowly, and the virtual origin moves from the positive side of $x$ to the negative side. Fig. 2 also shows that the jet half-width increases almost linearly in the far-field, so that the jet envelope adopts a nearly conical shape. The growth of the jet half-width starts earlier than the increase of the inverse of the mean axial velocity excess at the centerline.

Figure 3 shows the radial profiles of the mean and fluctuating axial velocities at various streamwise locations. The radial distance is normalised by the corresponding jet half-width $\delta_{1/2}$. It is shown that the mean velocity approaches its self-similarity quickly after $x/D$ = 20. The fluctuating axial velocity profiles are much more complex as revealed in Fig. 3b. The location of the highest fluctuation in the upstream coincides with the centre of the shear characterised by the jet half-width. However, it shifts towards the centerline at more downstream locations. At $x/D$ = 30 and 40, the highest fluctuation occurs at $r/\delta_{1/2}$ = 0.5. Upstream, the fluctuating axial velocity in the shear is much larger than that at the centre, while downstream the fluctuating

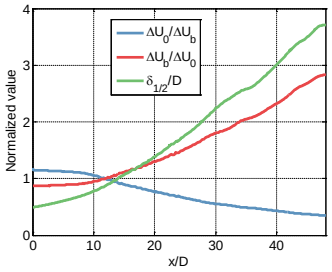


Figure 2. Axial evolution of the mean axial velocity excess, the inverse of the mean axial velocity excess, and the jet half-width along the streamwise direction.

axial velocity is more homogeneous in the radial direction. The fluctuating axial velocity does not demonstrate a self-similar profile until $x/D$ = 30, in contrast with the mean axial velocity.

Turbulent intensities are studied in terms of the axial, radial and azimuthal components of the fluctuating velocity ($u_x'$, $u_r'$, and $u_\theta'$). It has been experimentally observed that the three components have different profiles in the self-similar region in a round turbulent jet [2]. It should be noted that in free turbulent shear flows, energy is mainly transferred from the mean flow to $u_x'$, and the pressure interaction term exchanges energy between the three components, without changing the total amount energy, which is responsible for anisotropic turbulence. Fig. 4 shows radial profiles of the three components at various streamwise locations. It is clear that the magnitudes of $u_r'$ and $u_\theta'$ are smaller than the axial component $u_x'$. At $x/D$ = 5, the fluctuating velocities increase considerably near the rim of the burner and $u_x'$ is about twice of $u_r'$ and $u_\theta'$. $u_x'$ shows its maximum at $x/D$ = 10. By $x/D$ = 20, the three components of the fluctuating velocity are comparable, indicating the relaxation of the turbulence to isotropic conditions.

## 3.2 Turbulent flame statistics

Next, we focus on the turbulent flame statistics. The degree of flame wrinkling is quantified by the wrinkled flame area. The flame location is instantaneously identified from an iso-surface of progress variable, $c$, defined from the $O_2$ mass fraction, where the chosen iso-value $c$ = 0.8 corresponds the location of the maximum heat release rate in a laminar flame. The instantaneous turbulent flame surface area $\Delta A_T(x)$ within a slab of thickness $\Delta x$ at the streamwise location $x$ is calculated by triangulating the iso-surface, finding the area of each triangle at this location, and then summing all of the triangle areas. $\Delta A_L(x)$ is the unwrinkled flame surface area defined on the averaged progress variable $\overline{c}$ = 0.8. The evolution of the unwrinkled and wrinkled flame surface area is illustrated in Fig. 5a. It is seen that both $\Delta A_L$ and $\Delta A_T$ initially increase and then decrease with $x$ due to flame annihilation. $\Delta A_L$ peaks at $x/D$ = 21 while $\Delta A_T$ peaks at $x/D$ = 25.

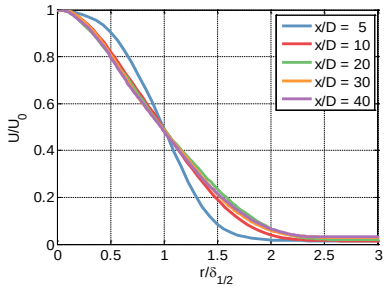


(a)

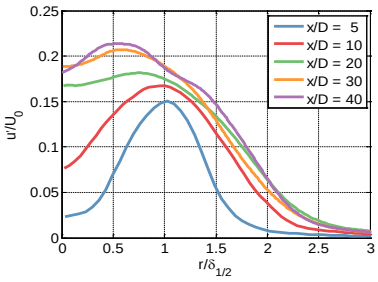


(b)

Figure 3. (a) Radial profiles of the mean axial velocity at various streamwise locations. (b) Radial profiles of the fluctuating axial velocity at various streamwise locations.

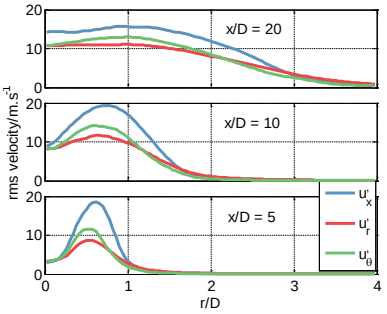


Figure 4. Radial profiles of the axial, radial and azimuthal fluctuating velocities at various locations along the streamwise direction.

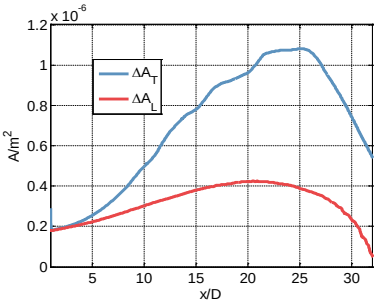


(a)

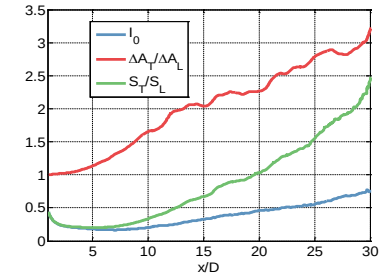


(b)

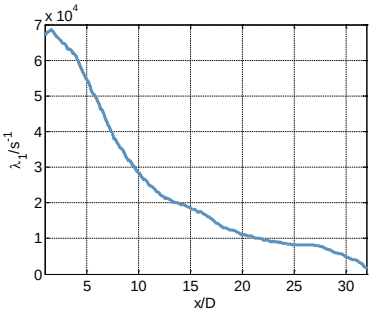


(c)

Figure 5. (a) $\Delta A_L$ conditioned on $\overline{c}$ = 0.8 and $\Delta A_T$ conditioned on c = 0.8. (b) The profiles of $I_0$, $\Delta A_T/\Delta A_L$ and $S_T/S_L$. (c) The profiles of the most extensive strain rate $\lambda_1$ of the mean flow conditioned on $\overline{c}$ = 0.8.

As the flame is spatially developing, we are interested in the local turbulent flame velocity $S_T$ at various downstream locations. By assuming a local balance between the consumption of reactants and turbulent flame propagation, the local stretch factor $I_0$ may be determined. Finally, the local turbulent flame velocity $S_T$ is calculated as [12]:

$$S_T(x) = S_L I_0(x) \Delta A_T(x) / \Delta A_L(x) \quad (7)$$

The computed results are shown in Fig. 5b. It is seen that the ratio of $\Delta A_T$ to $\Delta A_L$ increases by a factor of three from the inlet to the downstream location near the flame tip, and the increment is almost linear. In contrast, $S_T/S_L$ is found to decrease near the inlet, and exhibits its minimum at $x/D$ = 5. The magnitude of $S_T/S_L$ is always smaller than that of $\Delta A_T/\Delta A_L$, which indicates that the stretch factor $I_0$ is below unity throughout the domain. The profile of $I_0$ suggests that $I_0$ is significantly reduced upstream due to turbulent strain and gradually increases as the flame develops downstream. The fuel consumption rate is considerably weaker compared with the corresponding unstrained laminar flame near the inlet. This is due to the large flame strain rates encountered near the inlet. Fig. 5c shows the profile of the most extensive strain rate $\lambda_1$ of the mean flow conditioned on $\overline{c}$ = 0.8. Note that the mean flow is statistically two-dimensional in the *x*-*r* plane. The non-zero components of the strain rate tensor of the mean flow include $\partial Ux/\partial x$, $0.5(\partial Ux/\partial r + \partial Ur/\partial x)$, $0.5(\partial Ur/\partial x + \partial Ux/\partial r)$ and $\partial Ur/\partial r$. $\lambda_1$ is calculated as the largest eigenvalue of the mean strain rate tensor. It is clear that $\lambda_1$ is large near the inlet and decays downstream. Upstream, the strain rate is intense and pushes the flame towards the product side, leading to partial quenching of the oxidation layer due to radical depletion. Although not shown here, we do observe negative displacement velocity of the flame in the upstream region.

## 4. Conclusion

A DNS model of an experimental turbulent CH4/air lean premixed flame was employed to study the flow and flame characteristics. The potential core has a length of about 6 nozzle diameters. The mean axial velocity remains constant in this region and decays in the far-field inversely with distance after *x/D* = 20. The mean velocity approaches a self-similar state earlier than the fluctuating velocity. The ratio of the wrinkled flame surface area to the unwrinkled flame surface area increases by a factor of three from the inlet to the downstream location near the flame tip, and rate of increase with distance is nearly linear. The evolution of the stretch factor indicates that the flame is considerably weaker compared with the corresponding unstrained laminar flame, which is due to large stain rate on the flame front. This implies that turbulent combustion models will need to take into account stretch effects in order to capture even basic flame behaviour in these high Karlovitz number conditions.

## 5. Acknowledgments

This work was supported by the Australian Research Council. The work at Sandia National Laboratories was supported by the Division of Chemical Sciences, Geosciences and Biosciences, the Office of Basic Energy Sciences, the US Department of Energy (DOE). This research used resources provided by the Pawsey Supercomputing Centre with funding from the Australian Government and the Government of Western Australia. The research was also supported by computational resources at Pawsey awarded through the National Computational Merit Allocation Scheme.

## 6. References

[1] J. F. Driscoll. Prog. Energy Combust. Sci. 34 (2008), pp 91–134

[2] H. J. Hussein, S. P. Capps, W. K. George. J. Fluid Mech. 258 (1994), pp 31–75

[3] B. J. Boersma, G. Brethouwer, F. T. M. Nieuwstadt. Phys. Fluids 10 (1998), pp 899-909

[4] J. E. Rehm, N. T. Clemens. Combust. flame 116 (1999), pp 615–626

[5] B. Zhou, C. Brackmann, Q. Li, Z. Wang, P. Petersson, Z. Li, M. Aldén, and X. Bai. Combust. Flame 162 (2015), pp 2937–2953.

[6] J. B. Bell, M. S. Day, I. G. Shepherd, M. R. Johnson, R. K. Cheng, J. F. Grcar, V. E. Beckner, M. J. Lijewski. PNAS 102 (2005), pp 10006–10011

[7] J. B. Bell, M. S. Day, M. J. Lijewski. Proc. Combust. Inst. 34 (2013), pp 1173–1182

[8] J. H. Chen, A. Choudhary, B. de Supinski, M. DeVries, E. R. Hawkes, S. Klasky, W. K. Liao, K. L. Ma, J. Mellor-Crummey, N. Podhorszki, R. Sankaran, S. Shende, C. S. Yoo. Comput. Sci. Disc. 2 (2009), 015001

[9] C.A. Kennedy, M.H. Carpenter. Appl. Numer. Math. 14 (1994), pp 397–433.

[10] T.J. Poinsot, S.K. Lele. J. Comput. Phys. 101 (1992), pp 104–129

[11] Smith, Gregory P., David M. Golden, Michael Frenklach, Nigel W. Moriarty, Boris Eiteneer, Mikhail Goldenberg, C. Thomas Bowman et al. "GRI-Mech 3.0." (1999)

[12] R. Sankaran, E. R. Hawkes, C. S. Yoo, J. H. Chen. Combust. Flame 162 (2015), pp 3294-3306

# Equivalence Ratio Effects on Turbulent Premixed Flames in Lean Methane/Air Mixtures

Zhiyan Wang[1,*], Emmanuel Motheau[2], John Abraham[1,2,3]
[1]School of Mechanical Engineering, Purdue University, West Lafayette, IN 47907-2088, USA
[2]School of Mechanical Engineering, University of Adelaide, South Australia 5005, Australia
[3]Department of Mechanical Engineering, San Diego State University, San Diego, CA 92182-1323, USA

**Abstract**

Direct numerical simulations (DNS) of turbulent premixed methane/air flames are carried out to investigate the effects of equivalence ratio on the turbulent flame speed in lean mixtures. Turbulent flames are simulated as statistically stationary following a Lagrangian framework using an inflow-outflow configuration. The inflow velocity is dynamically adjusted at run-time to stabilize the flame brush location within the computational domain. Linear forcing is applied inside the unburned mixtures to maintain the turbulent intensities at desired levels. Velocity and length scales of the imposed turbulence are selected such that Karlovitz number and Damköhler numbers remain constant for flames of different equivalence ratios. Simulations are run for more than 80 eddy turnover times and the turbulent flame speed is derived by averaging the inflow velocity. The results show that equivalence ratio does not have an explicit effect on the turbulent flame speed above the lean limit. The flame surface normal is found to be preferentially parallel to the most compressive strain rate direction for all equivalence ratios.

*Keywords: DNS of turbulent premixed flames, premixed flame speed, lean burn natural gas combustion*

## 1. Introduction

In recent years, natural gas has received increased attention as an alternative fuel source for internal combustion engines employed in transportation and power generation applications. It is known that natural gas produces 25-30% less carbon emissions per unit energy than conventional fuels [1, 2]. Lean burn natural gas engines are particularly attractive because of their potential of lower $NO_x$ emissions and enhanced thermal efficiency compared to engines operating under stoichiometric conditions. However, lean burn also increases the likelihood of misfire due to combustion instabilities that results in increased exhaust emissions and reduced efficiency [3-5]. To address the challenges associated with lean burn combustion, various strategies have been proposed including using elevated inlet manifold temperatures, hot-gas jet ignition and introducing greater swirl and turbulence at the end of compression [6]. The effectiveness of these approaches is often accessed with the aid of high-fidelity numerical tools.

Flamelet-based models are one of the most widely used models in modeling premixed turbulent combustion. Williams (1985) and Abraham *et al.* (1985) have proposed the G-equation model based on the premise that the premixed turbulent flame could be represented by the isosurface of a scalar field $G$ [7, 8]. The instantaneous flame front, assumed to be infinitely thin, is represented by an isosurface of the scalar quantity $G$ at $G \equiv 0$. In the transport equation of $G$, turbulent flame speed $S_T$ is used to model the global effects of turbulence on enhancing chemical reaction rates through flame surface augmentation mechanism and enhanced transport. The use of a single variable $S_T$ greatly simplifies the modeling by eliminating the stiff chemistry source terms. Indeed, by assuming a priori closure for the turbulent premixed flame speed, multi-dimensional simulations have been carried out in rather complex geometries such as bombs [9, 10], SI engines [11, 12] and industrial burners [13, 14].

It is important to note that several definitions of turbulent flame speeds exist. To avoid ambiguity, in this paper we will define turbulent flame speed as the velocity at which the unburned mixture enters the flame zone in the direction normal to the mean flame front. Numerous correlations for $S_T$ has been proposed in the past and a majority of the existing correlations involves the ratio of velocity, i.e. $u_{rms}/S_L$, and that of the length scales, i.e. $L_o/\delta_L$ [13, 15-17]. Here, $S_L$ and $\delta_L$ denote the flame speed and flame thickness of an unstrained laminar flame, respectively, while $u_{rms}$ and $L_o$ represents the root-mean-square of turbulent velocity fluctuation and the integral length scale, respectively. Alternatively, correlations relating $S_T$ to velocity and length scale ratios can be recast into a unique form involving ratios of the timescales, using Karlovitz number (Ka) and Damköhler number (Da). The Karlovitz number represents the ratio of characteristic chemical timescale to the Kolmogorov timescale while Damköhler number represents the ratio of integral eddy turnover time to the chemical time scale. Their respective definitions used in this paper are given as,

$$\mathrm{Ka} = \frac{\tau_c}{\tau_\eta} \sim \left(\frac{\mathrm{u_{rms}}}{\mathrm{S_L}}\right)^{\frac{3}{2}} \left(\frac{\delta_\mathrm{L}}{\mathrm{L_o}}\right)^{\frac{1}{2}}, \quad (1)$$

$$\mathrm{Da} = \frac{\tau_t}{\tau_c} \sim \frac{\mathrm{S_L}}{\mathrm{u_{rms}}} \frac{\mathrm{L_o}}{\delta_\mathrm{L}}. \quad (2)$$

The effects of equivalence ratio (φ) on $S_T$ are still not well understood. Specifically, it is not known whether equivalence ratio has an explicit effect on $S_T$ or it only exerts its influences on $S_T$ through the laminar flame speed $S_L$. Limited work has been carried out to

* Corresponding author:
Phone: (+1)603 892-2815
Email: wang1695@purdue.edu

characterize the equivalence ratio effects. Bell *et al.* (2006) performed 2D simulation of premixed methane flames at equivalence ratios $\phi$ = 0.55 and 1.00 [18]. They have found a change in the Markstein number as $\phi$ is varied, hence modifying the turbulent flame speed. Fru *et al.* (2011) carried out direct numerical simulations (DNS) of premixed methane-air flame kernels subjected to various turbulence intensities at five equivalence ratios [19]. They have observed that for a fixed value of $u_{rms}/S_L$, $S_T/S_L$ varies with equivalence ratios. However, neither of the two works has taken into account the effects of length scales, i.e. $L_o/\delta_L$. In addition, the studied flames are subjected to decaying turbulence field which introduces ambiguity into the definition of $u_{rms}/S_L$.

In this work, we set out to investigate the influence of equivalence ratio on the turbulent flame speed using direct numerical simulations. By forcing the turbulence inside the fresh mixtures, we have ensured that the premixed flame is interacting with non-decaying turbulence such that velocity and length scale ratios between the flow field and flame (consequently Da and Ka) are clearly defined and held invariant. The rest of the paper is organized in the following manner. Section 2 will be dedicated to the discussion of numerical methods, chemistry mechanisms and the simulation setup. Section 3 presents the results of turbulent flame speed at various equivalence ratios. The effects of flow strain rates with respect to the flamelet are also discussed. The paper then closes with conclusions in Section 4.

## 2. Computational Setup

### 2.1 The Numerics

All of the results presented in this work are obtained using the in-house code HOLOMAC (High-Order LOw-MAch number Combustion). It solves the 3D conservation equations under the low-Mach-number assumption for multi-component mixtures with CHEMKIN interface for computing the chemical reactions and transport properties. Spatial discretization is performed using 6th-order implicit compact schemes. The time integration is based on an Strang operator-split strategy. Convection terms are advanced in time using a 2nd-order Adams-Bashforth (AB2) scheme while the diffusion terms are integrated using a stabilized explicit Runge-Kutta-Chebyshev (RKC) method. The momentum equation is solved using a projection-correction method. The divergence condition is enforced up to machine precision by solving a variable-coefficient Poisson equation using a spectral solver based on Fast Fourier Transform (FFT). Readers are advised to consult [20] for more details about the numerics of the code.

### 2.2 Reaction Mechanism

A global chemical mechanism has been developed, based on the 17-species, 73-step skeletal mechanism developed by Sankaran *et al.* (2007), as part of this work to describe methane oxidation [21]. The global mechanism takes the form:

$$\dot{\omega} = A\mathrm{T}^{b}[\mathrm{CH_4}]^{m}[\mathrm{O_2}]^{n}\exp(-\mathrm{T}/\mathrm{T_a}). \qquad (3)$$

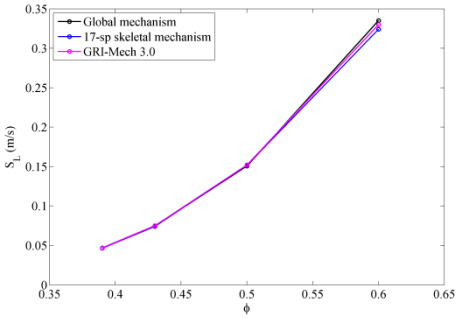


Fig. 1. Computed laminar flame speed as a function of $\phi$ for unburned temperature of 810K at pressure 20 bar.

The parameters are calibrated such that the heat release rate of the laminar flame in the temperature space matches that obtained using the 17-species reduced mechanism. Figure 1 shows the computed laminar flame speeds with the global chemistry, the reduced mechanism and the GRI-Mech 3.0. It is evident that the global mechanism shows agreement with the other two within 2% for the range of equivalence ratios considered in this work.

### 2.3 Computational Setup

In this work, the turbulent premixed flame is simulated as statistically stationary inside the computational domain by employing a Lagrangian framework, i.e. the frame of reference is placed on the mean flame front and the cold premixed flow is "seen" as propagating toward a locally-evolving but globally-stationary flame. This can be realized using an inflow-outflow configuration as shown in Fig. 2. Periodic boundary conditions are applied to the lateral boundaries parallel to the mean flow direction. Inflow of unburned methane-air mixture is specified at the left boundary while the burned charge passes through a sponge zone and exits from the right. To maintain the flame stationary, *a priori* knowledge of the flame speed is required to specify the inflow boundary condition. To account for this, a predictive control is employed on the flame position to correct the inflow velocity toward the "true" flame speed. For the current simulations, two forms of control loop have been implemented. A differential loop is used to adjust inflow velocity until the mean flame front is stationary within a characteristic time period $\tau_d$. In addition, an integral control is applied to return the mean flame front to its initialized position over some characteristic time $\tau_i$. To minimize interference between the two forms of feedback loop, the characteristic time scale of the integral control $\tau_i$ has been selected to be much longer than $\tau_d$.

The domain is initialized with a laminar flame front. To maintain the desired turbulence intensity inside the cold flow, turbulent fluctuations are imposed on the mean inflow velocity from the moving slice of a homogeneous isotropic turbulent field generated in an auxiliary simulation. In addition, the cold flow ahead of the flame is forced using the linear forcing scheme of Carroll and Blanquart (2003) [22]. In essence, a forcing term of the form

$$f_i = \mathrm{M(T)B}\left(\frac{k_o}{k}\right)\rho \mathrm{u_i}, \qquad (4)$$

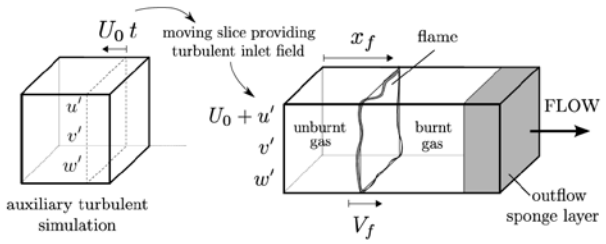


Fig. 2: Schematic for simulating a statistically stationary turbulent flame using an inflow-outflow configuration.

Table 1. Computational conditions and average turbulent flame speeds

| | Case 1 | Case 2 | Case 3 | Case 4 |
|---|---|---|---|---|
| **P (bar)** | 20 | 20 | 20 | 20 |
| **$T_u$ (K)** | 810 | 810 | 810 | 810 |
| **Φ** | 0.5 | 0.6 | 0.43 | 0.39 |
| **$S_L$ (m/s)** | 0.1506 | 0.3351 | 0.07445 | 0.04650 |
| **$\delta_L$ (μm)** | 100 | 50 | 200 | 300 |
| **$u_{rms}$ (m/s)** | 2.160 | 4.806 | 1.068 | 0.667 |
| **$L_o$ (mm)** | 0.640 | 0.320 | 1.280 | 1.920 |
| **$u_{rms}/S_L$** | 14.3 | 14.3 | 14.3 | 14.3 |
| **$L_o/\delta_L$** | 6.4 | 6.4 | 6.4 | 6.4 |
| **Ka** | 21.5 | 21.5 | 21.5 | 21.5 |
| **Da** | 0.45 | 0.45 | 0.45 | 0.45 |

is added to the momentum equation to represent the energy cascade from scales which are larger than the domain size. Here, $k$ is the instantaneous turbulent kinetic energy (TKE) and $k_o$ is the desired steady-state TKE; M(T) represents a temperature mask which ensures that turbulence is only forced inside the unburned flow; B is the forcing constant which is proportional to the inverse of the desired eddy turnover time. It has been reported that the integral length scale of the forced turbulence will always converge to approximately 20% of the domain size independent of the initial state or the choice of forcing constant B [23]. This means that $L_o$ can be controlled by simply adjusting the domain size and consequently a constant ratio of $L_o/\delta_L$ can be maintained throughout the simulation. Table 1 lists the physical conditions employed for the simulations. The pressure is set at 20 bar and unburned mixture temperature $T_u$ is at 810 K to mimic the conditions inside lean-burn natural gas engines. Turbulent velocity fluctuations are varied between 0.67 - 4.81 m/s such that $u_{rms}/S_L$ remains constant at 14.3. The computational domain size is selected at $80 \times 32 \times 32\delta_L$ such that $L_o$ is always 6.4 times the laminar flame thickness.

## 3. Results and Discussion

We will now present results from the parametric studies exploring the effects of equivalence ratio on turbulent flame speed under lean-burn conditions. Each simulation was performed over more than 80 eddy turnover times to obtain a large sample space for meaningful statistics to be collected. Figure 3a shows the time history of the dynamically adjusted mean velocity $U_0$ at the inflow boundary for all four cases. Evidently, there is a transient phase of approximately 20 eddy turnover times before $U_0$ becomes steady. This corresponds to the time over which the initialized laminar flame front is stirred by the approaching turbulent mixture and transitions into a fully-developed turbulent brush. The evolution of the mean flame brush

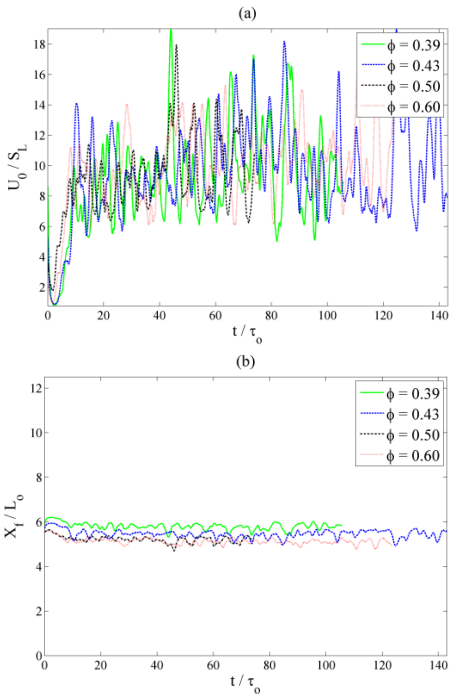


Fig. 3: (a) Time history of the mean inflow velocity normalized by the laminar flame speed (top); (b) evolution of the mean flame brush location (bottom) for $\phi$ = 0.39, 0.43, 0.5 and 0.6.

locations are shown in Fig. 3b. It is seen that the mean front position fluctuation is less than one integral length scale and this indicates the success of our feedback mechanism for simulating statistically stationary flame.

The turbulent flame speed $S_T$ can be obtained from the time average of the inflow velocity once the turbulent flame becomes fully-developed and stationary in the statistical sense. Figure 4 shows the values of $S_T$ obtained by averaging increasing number of time snapshots. For all four cases, self-convergence of $S_T$ is noted as the sample size increases. More interestingly, the normalized turbulent flame speed $S_T/S_L$ converges to a similar value around 10. This suggests that the most dominant effects of equivalence ratio on turbulent flame speed is through its influence on the laminar flame speed $S_L$ and flame thickness $\delta_L$. In other words, turbulent flame speed has a weak (if any) explicit dependence on φ. Instead, changes in φ only results in changes in the flame velocity and length scale ratios, i.e. $u_{rms}/S_L$ and $L_o/\delta_L$, should the flame be subjected to the same turbulent flow, which cause $S_T$ to vary. For the case of $\phi$ = 0.39 (indicated by green circles in Fig. 4), a reduction in $S_T/S_L$, albeit small (less than 5%), is evident. This suggests that extinction may be beginning to play a role. Statistics of the alignment of principal strain rate directions with the flamelet normal direction have been studied. This provides insights on whether passive scalar gradients are created or destroyed by turbulence [24]. The principal strain rates are computed from the strain rate tensor $S_{ij}$ at three different isotherm surface by solving the eigenvalues. The largest eigenvalue, denoted as $\lambda_1$ is called the most extensive strain rate and the eigenvalue $\lambda_3$ is called the most compressive strain rate. Figure 5 shows the pdf of the orientation (expressed as cosine of the angle) between the strain rate directions

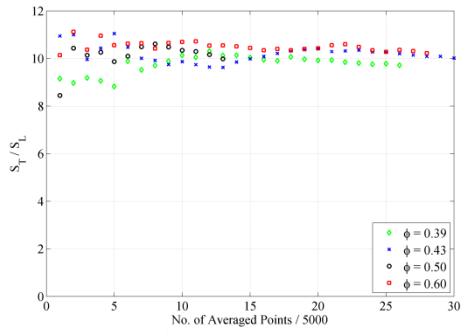


Fig. 4: Normalized turbulent flame speed $S_T$ obtained from averaging increasing sample size.

and the flame surface normal on the temperature isosurface at T = 1694, 1394 and 1094 K.Here, 1694 K corresponds to the temperature where heat release rate is maximum and 1094 K corresponds to the preheat zone of the flame at $\phi$ = 0.43. It is shown that the most compressive strain rate direction is preferentially aligned to the flame surface normal while the most extensive strain rate direction is preferentially parallel to it. This suggests that the flame is strained in such a way that the isosurface of temperature (and also species mass fractions) are packed closer together and thereby facilitating steeper scalar gradients. Furthermore, the alignments do not show noticeable difference at various points across the flame. Comparison of the alignment in the preheat zone of flames at different equivalence ratios are illustrated in Fig. 6. The isotherm contour where data is analyzed is at 30% of the maximum temperature rise. Similar trend is observed for all four cases. This suggests that $\phi$ has limited explicit influence on turbulence-flame alignment in lean premixed flames.

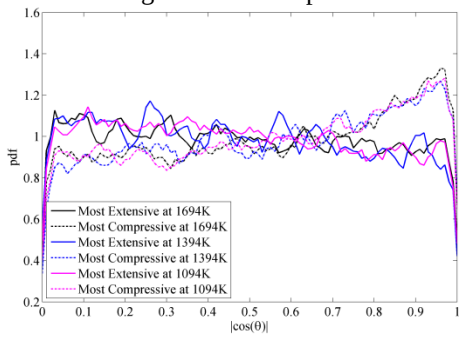


Fig. 5: Pdf of alignment between stain rate directions and flamelet normal on the isosurface of T = 1694K, 1394K and 1094K for φ = 0.43.

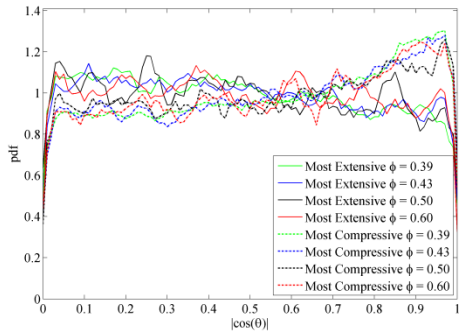


Fig. 6: Pdf of alignment between stain rate directions and flamelet normal in the flame preheat zone for φ = 0.39, 0.43, 0.5 and 0.6.

## 4. Conclusion

Direct numerical simulations of turbulent premixed methane flames are carried out under lean conditions using an inflow-outflow configuration. The flames are simulated as stationary by dynamically adjusting the mean inflow velocity. It is found that the normalized turbulent flame speed, i.e. $S_T/S_L$, does not change with equivalence ratio above the lean limit when Ka and Da are fixed. This implies that $\phi$ only influences $S_T$ implicitly by affecting ratios of length scales and velocities between turbulent flow and the flame.

## 5. Acknowledgments

The authors thank Caterpillar, Inc. for their financial support of this work. This work used the Extreme Science and Engineering Discovery Environment (XSEDE) which is supported by National Science Foundation grant number ACI-1053575, and computational resources provided by Information Technology at Purdue (ITaP).

## 6. References

[1] K. Kato, K. Saeki, H. Nishide, T. Yamada, JSAE Rev. 22 (2001), 365-368.
[2] R. Tilagone, G. Monnier, A. Chaouche, Y. Baguelin, S. De Chauveron, SAE Technical Paper 961080 (1996).
[3] A. Das, H.C. Watson, Proc. Inst. Mech. Eng. 211 (1997) 361-378.
[4] K.S. Varde, G.M.M. Asar, SAE Technical Paper 2001-28-0023.
[5] M.L. Franklin, D.B. Kittelson, R.H. Leuer, M.J. Pipho, SAE Technical Paper 940546 (1994).
[6] H.M. Cho, B.Q. He, Energy Convers. Mgmt. 48 (2007) 608-618.
[7] F.A. Williams, Combustion Theory, Westview Press, Boulder CO, 1985.
[8] J. Abraham, F.A. Williams, F.V. Bracco, SAE Technical Paper 850345 (1985).
[9] B. Lewis, G. von Elbe, Combustion, flames and explosions of gases, Academic Press, New York, 1961.
[10] T.W. Lee, G.L. North, D.A. Santavicca, Combust. Sci. Tech. 84 (1992) 121-132.
[11] Y. D'Angelo, G. Joulin, G. Boury, Combust. Theory Model 4 (2000) 317-338.
[12] R.N. Paul, K.N.C. Bray, Proc. Combust. Inst. 26 (1996) 259-266.
[13] V. Zimont, W. Polifke, M. Bettelini, W. Weisenstein, J. Eng. Gas Turbines Power 120 (3) (1998) 526-532.
[14] P. Flohr, H. Pitsch, Proc. CTR Summer Program (2000) 169-179.
[15] P. Clavin, F.A. Williams, J. Fluid Mech. 116 (1982) 251-282.
[16] A.R. Kerstein, Proc. Combust. Inst. 21 (1988) 1281-1289.
[17] S. Daniele, P. Jansohn, J. Mantzaras, K. Boulouchos, Proc. Combust. Inst. 33 (2011) 2937-2944.
[18] M.S. Day, J.B. Bell, J.F. Grcar, M.J. Lijewski, Proc. ECCOMAS-CFD (2006).
[19] G. Gru, D. Thevenin, G. Janiga, Energies 4 (2011) 878-893.
[20] E. Motheau, J. Abraham, J. Comp. Phys. under review.
[21] R. Sankaran, E.R. Hawkes, J.H. Chen, T.F. Lu, C.K. Law, Proc. Combust. Inst. 31 (2007) 1291-1298.
[22] P.L. Carroll, G. Blanquart, Phys. Fluid 25 105114 (2013).
[23] C. Rosales, C. Meneveau, Phys. Fluid 17 095106 (2005).
[24] N. Chakraborty, N. Swaminathan, Phys. Fluid 19 (2007).

# Analysis of the flame brush of an acoustically perturbed swirling premixed flame

T.F. Guiberti[1,2,3 *], S. Bejaoui[1], D. Durox[1], T. Schuller[1]
[1]Laboratoire EM2C, CNRS, CentraleSupelec, Grande Voie des Vignes, 92290 Châtenay-Malabry, France
[2]Clean Combustion Research Center, KAUST, Thuwal 23955, Saudi Arabia
[3]School of Aerospace, Mechanical and Mechatronic Engineering, The University of Sydney, NSW 2006, Australia

## Abstract

An analysis of the thickness of the flame brush of an acoustically perturbed premixed swirling flame is conducted by post-processing planar OH laser induced fluorescence measurements. Experiments are carried out at two distinct frequencies of the flame describing function (FDF) and two different forcing amplitudes. Modifications of the flame brush thickness reveal effects of swirl number fluctuations and flame-vortex roll-up, the two mechanisms that control the flame frequency response. It is found that the flapping motion induced by swirl number fluctuations takes place over all the flame brush length and drastically increases with the forcing amplitude. The second mechanism of flame-vortex interaction only takes place away from the anchoring point and remains weakly sensitive to the forcing level. These data help to shed light on mechanisms controlling the nonlinear dynamics of premixed swirling flames subjected to flow oscillations.

*Keywords: Flame dynamics, Flame brush, Swirl flame, OH-PLIF, Hydrogen enrichment.*

## 1. Introduction

The flame describing function (FDF) is widely used to analyze the dynamics of a combustor and examine its stability with respect to self-sustained thermo-acoustic oscillations. This weakly nonlinear representation of the flame frequency response is generally determined experimentally or more rarely represented by a low order model. To reduce the gap between FDF measurements and low order models, it is necessary to sort out the main mechanisms controlling the FDF and identify their respective contributions as a function of frequency and amplitude.

Palies et al. [1] proposed a linear low-order model combining effects of swirl number oscillations and flame-vortex interactions to represent the flame describing function of premixed swirling flames subjected to acoustic oscillations. It is now generally admitted that these two elementary mechanisms control the response of swirling flames to flow oscillations [2], but their respective contribution as a function of frequency and amplitude has not been investigated yet.

Experiments conducted in this study shed light on these contributions by comparing the thickness of the flame brush of a swirling flame submitted to acoustic modulations.

## 2. Experimental set-up

The experimental set-up presented in Fig. 1 is similar to that use in [3] for the investigation of the impact of heat loss and hydrogen enrichment on the shape of confined swirling flames. The burner includes a radial swirling vane located 35 mm upstream the exit plane of an annular injector featuring a central bluff body

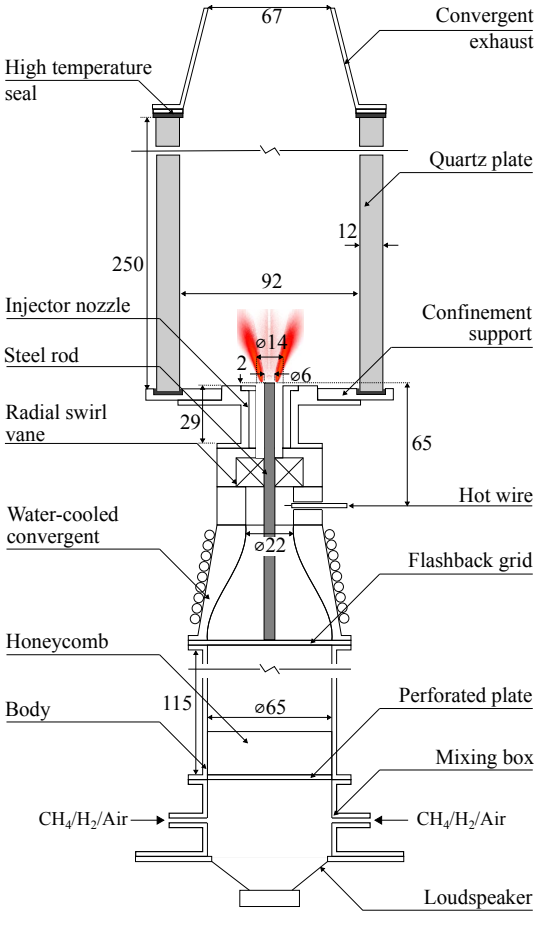


**Figure 1: Schematics of the test-rig with the main dimensions in mm. An image of the flame chemiluminescence gives an indication of the flame size.**

that helps stabilizing the flame. The swirl number at the injector outlet has been determined with particle imaging

* Corresponding author:
Phone: (+61) 4 06964242
Email: Thibault.guiberti@kaust.edu.sa

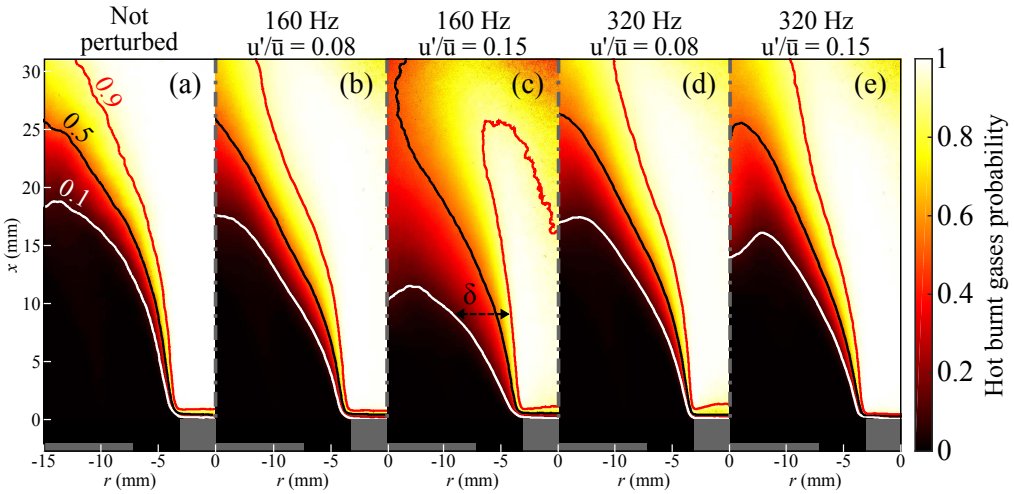


**Figure 2: Distribution of hot burnt gases probability for the unperturbed flame (a) and four acoustically perturbed flames (b-e). Only the left side of the flame is represented. Iso-contours of probability 0.1 (white), 0.5 (black), and 0.9 (red) are indicated. The gray zones show the central rod and the combustor dump plane.**

velocimetry (PIV) and is S = 0.4. The flame is stabilized in a combustion chamber with a square cross-section and four quartz windows. The flame is perturbed acoustically using a loud-speaker located at the base of the burner. A hot-wire, installed upstream the swirling vane, is used to control the velocity fluctuation produced by the loud-speaker in the injector.

The response of premixed $CH_4/H_2$/air flames at an equivalence ratio $\phi = 0.7$ and a thermal power $P = 4$ kW is investigated. The $H_2$ enrichment is expressed by the molar fraction of $H_2$ in the $CH_4/H_2$ mixture and is $X_{H2}^{fuel} = 0.60$. The bulk flow velocity is $u_b = 14$ m.s$^{-1}$ in the annular injection tube exhausting in the chamber. Two distinct harmonic modulation frequencies $f_1 = 160$ Hz and $f_2 = 320$ Hz are chosen to perturb the flame acoustically. These frequencies respectively correspond to the first minimum and the global maximum of the FDF gain [1,2]. At $f_1 = 160$ Hz, the flame motion is mostly associated to swirl number fluctuations. At $f_2 = 320$ Hz, large fluctuations of flame surface area and heat release rate result from a large flame-vortex roll-up taking place at the flame tip. The response at $f_1$ and $f_2$ is investigated at two forcing amplitudes $u'/\bar{u} = 0.08$ and $u'/\bar{u} = 0.15$ determined with the hot wire (Fig. 1), where $u'$ denotes the rms value of the velocity signal and $\bar{u}$ its mean value.

Laser induced fluorescence measurements of the OH radical (OH-PLIF) in the vertical symmetry plane of the burner are used to infer the probability of presence of hot burnt gases. The OH-PLIF system comprises a dye laser (Continuum, ND6000) with Rhodamine 590 dye, pumped by a Nd:YAG Laser (Continuum, Precision) operated at 10 Hz, and delivering 20 mJ/pulse. The laser is tuned to the $Q_1(6)$ transition at 282.927 nm and the fluorescence is collected with a UV lens (UV-NIKKOR 105 mm) equipped with a 10 nm bandpass filter centered at 310 nm (Asahi Spectra Co., ZBPA310) and imaged onto a 1024x1024 pixels ICCD camera (Princeton Instruments, PI-MAX 3). The laser sheet has a 50 mm width and a 0.5 mm thickness. No attempts to correct for flat field or beam energy variations were made.

Instantaneous OH-PLIF snapshots are first binarized using an arbitrary threshold to delineate the hot burnt gases, featuring a high signal intensity, from the cooler regions of the flow. The threshold value always corresponds to 20 % of the individual image maximum pixel intensity and therefore compensates for eventual laser pulse energy fluctuations. Taking the mean value of a set of 1000 binarized images yields an estimate of the probability of presence of OH radicals in the laser sheet. A pixel value of 1 corresponds to a region always filled with hot burnt gases. A value of 0 indicates a region filled with fresh reactants or cold burnt gases, featuring no OH-PLIF signal.

## 2. Results and discussions

Figure 2a shows the location of the hot burnt gases probability for the unperturbed flame, in the absence of external forcing. Only the left side of the flame is represented. The inner recirculation zone downstream the central rod tip yields a probability of 1 and is always filled with hot burnt gases. The annular jet at the injector outlet (-7 mm < $r$ < -3 mm) is filled with fresh reactants and yields a probability of 0. The burnt gases located in the outer recirculation zone ($r$ < -7 mm and $x$ < 10 mm) are cooled by the heat losses to the combustion chamber walls [3]. The probability of hot burnt gases in this region is then 0 or is very low.

The distance between the iso-contours of probability 0.1 and 0.9 in Fig. 2a gives an indication of the flame brush thickness $\delta$. This thickness $\delta$ changes when the distance $x$ to the rod tip increases. Figure 3 shows the evolution of the flame brush thickness $\delta$ as a function of the distance $x$ to the rod tip. The flame brush thickness of the unperturbed flame (solid black line) increases regularly and monotonously from $\delta = 0.7$ mm at 0.5 mm above the rod tip to $\delta = 4.1$ mm at $x = 15$ mm. The turbulent flame is anchored at the tip of the central rod in a region of low speed, with small fluctuations of its horizontal position for low values of $x$. When $x$ increases,

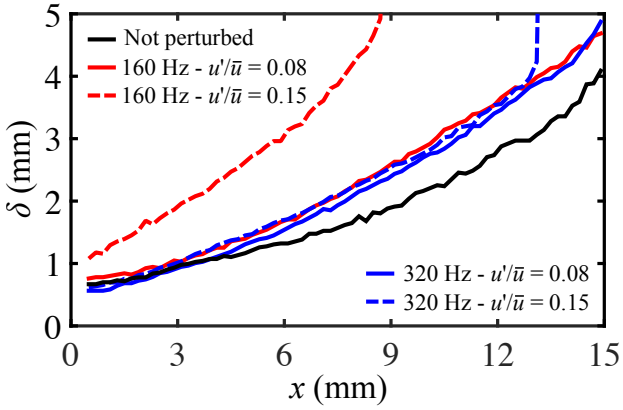


**Figure 3: Evolution of the flame brush thickness $\delta$ as a function of the distance $x$ to the rod tip. Results are presented for the unperturbed flame and four acoustically perturbed flames.**

turbulent fluctuations increase yielding a thicker flame brush.

Figures 2b and c show the mean distribution of the burnt gases probability when the flame is perturbed at $f_1 = 160$ Hz with an 8 % and a 15 % relative velocity forcing level, respectively. The distribution of the burnt gases probability differs from the unperturbed case shown in Fig. 2a. Perturbing the flame at $f_1 = 160$ Hz increases the thickness $\delta$ of the flame brush. At this frequency, increasing the forcing amplitude drastically increases $\delta$. Figures 2d and e show similar images for the forcing frequency $f_2 = 320$ Hz. Again, perturbing the flame acoustically yields a thicker flame brush than the unperturbed flame shown in Fig. 2a. However, thickening only takes place at larger $x$ distances and the forcing level only weakly alters the flame topology compared to experiments carried out at $f_1 = 160$ Hz.

Figure 3 shows the evolution of $\delta$ as a function of $x$ for the unperturbed flame and the four perturbed cases explored. In all cases, $\delta$ increases regularly and monotonously with $x$. Results for the unperturbed flame (black solid line) serve as a baseline to compare effects of the modulation frequency and modulation level.

At a low forcing level, results are very similar for the two forcing frequencies $f_1 = 160$ Hz and $f_2 = 320$ Hz. The flame brush thickness reaches $\delta \approx 3.2$ mm for $x = 12$ mm in comparison to $\delta \approx 2.6$ mm for the unperturbed flame at the same axial position. In the two cases, the acoustic modulation has only a weak influence on $\delta$ for $x < 4$ mm. The size of the flame brush near the flame base is however slightly thicker at $f = 160$ Hz than the unperturbed case, which is itself thicker than for a flame perturbed at $f = 320$ Hz, but these differences are hardly visible. Particle imaging velocimetry (PIV) experiments (not shown here) reveal that a relatively small vortex is shed at the injector lip during the modulation cycle, but this vortex does not directly interact with the flame brush near the flame base. Interaction between the flame and this vortex has only a visible effect at larger distances to the injector $x > 5$ mm, where the thickness of the flame brush increases with respect to the unperturbed flame.

It is now worth analyzing results for a higher forcing level of 15% to highlight differences in the flame behavior. Results are first analyzed for $f_1 = 160$ Hz. This case differs from the previous ones at small amplitudes. Figure 3 (red dashed lines) shows that the flame brush thickness increases rapidly with the distance $x$. It reaches $\delta \approx 5.0$ mm for $x = 9$ mm compared to $\delta \approx 1.9$ mm for the unperturbed flame at the same position. It is also remarkable that the flame brush is thicker $\delta \approx 1.1$ mm near the flame base $x = 0.5$ mm compared to $\delta \approx 0.7$ mm for the unperturbed flame. This is due to the particular motion of the flame at this forcing frequency and forcing amplitude, which is driven by large swirl number oscillations and flame vortex interactions [2]. Two components laser Doppler velocimetry (LDV) experiments, realized 1 mm above the rod tip under non reactive conditions (not shown here), indicate that the swirl number fluctuation rms amplitude reaches roughly 30 % for $f_1 = 160$ Hz and a forcing level of 15%.

When the swirl number varies during a modulation period, the flame opening angle changes as well. The flame front at the base of the flame follows an inverted pendulum motion and swings around the tip of the central rod. As a consequence, the flame brush thickness increases drastically for this forcing frequency and amplitude level. For $x < 6$ mm, $\delta$ increases roughly linearly with $x$ due to the flapping motion of the flame caused by the swirl number oscillation. For $x > 6$ mm, PIV experiments (not shown here) also reveal a fully developed vortex interacting with the flame brush. This additional mechanism increases the flame brush thickness more rapidly near the flame tip. For $f_1 = 160$ Hz, both swirl number fluctuations and flame-vortex roll-up contribute to the flame brush broadening.

Results are now examined for the same relative forcing level 15% at the frequency $f_2 = 320$ Hz. Longitudinal and azimuthal waves do not propagate at the same speed in the injection tube. Longitudinal acoustic waves propagate at a high speed equal to the sum of the speed of sound and the bulk flow velocity $u_b$. Azimuthal vortical waves are only transported by the flow with a velocity $u_b$. Therefore, the phase difference between longitudinal and azimuthal waves changes as the distance from the swirler increases. LDV measurements show that azimuthal vortical waves produced downstream the swirler and longitudinal acoustic waves are in phase at the outlet of the injector for $f_2 = 320$ Hz. This leads to weak fluctuations of the swirl number, with a measured rms amplitude lower than 8 %. As a consequence, the flapping motion of the flame is reduced and the flame brush thickness barely deviates from the unperturbed case shown in black line in Fig. 3 when $x < 4$ mm. Only the interaction of a vortex shed at the injector lip broadens the flame brush at larger distances $x > 4$ mm when it enrolls the flame. The flame brush thickness follows in this case the same evolution as for a lower modulation level $u'/\bar{u} = 0.08$. Differences only appear near the flame tip, where the flame brush suddenly broadens for $u'/\bar{u} = 0.15$ near $x \approx 13$ mm. This evolution is analyzed in more details in Fig. 4.

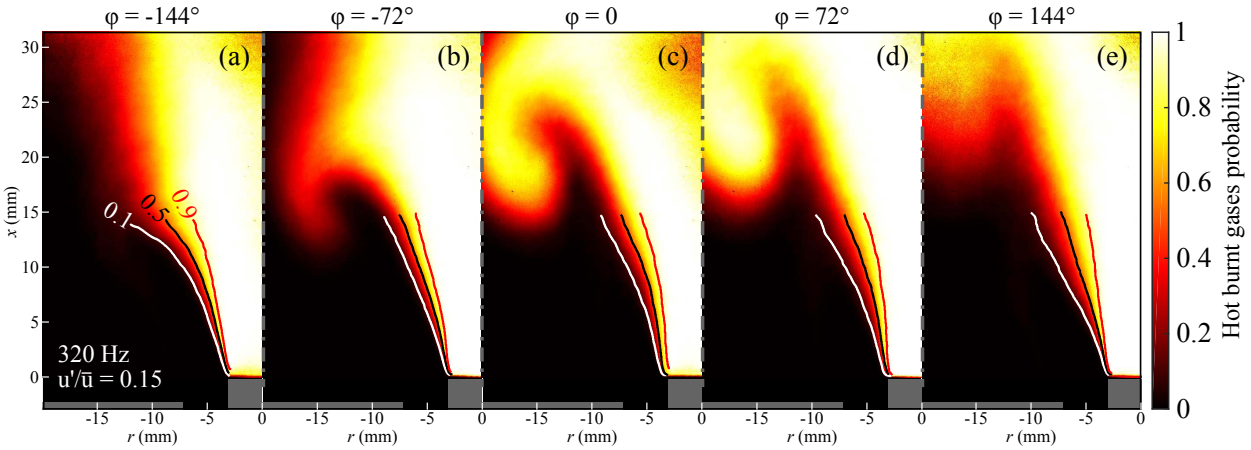


**Figure 4: Distribution of hot burnt gases probability for five phases regularly distributed in a modulation period at $f_2$ = 320 Hz and a modulation level of 15 %.**

Figure 4 shows the distribution of the hot burnt gases probability for five phases regularly distributed in a modulation period when the flame is perturbed at $f_2 = 320$ Hz and $u'/\bar{u} = 0.15$. We resorted to phase conditioned averages to obtain these images. At phase $\varphi = 0$, the bulk axial velocity is roughly equal to the mean bulk flow velocity $u_b = 14$ m.s$^{-1}$ and has a positive temporal derivative. We follow here the sequence of flame roll-up process. A vortex is shed from the burner lip at $\varphi \approx -144°$, it enrolls the flame tip between $-72° \leq \varphi \leq 72°$ and leads to a large extinction of the flame tip when $\varphi \approx 144°$. This cyclic motion generates toroidal pockets of hot burnt gases, which are convected upstream through the external recirculation zone. PIV experiments (not shown here) confirm the direct relation between the evolution of these pockets of hot burnt gases and the convection of a vortex.

The 0.1 and 0.9 iso-contours lines of probability of burnt gases being present shown in Fig. 4a-e also reveal that the flame brush thickness slightly changes during a modulation period for $x > 5$ mm. The flame brush thickness is minimum just before the generation of a vortex ring at $\varphi \approx -144°$ and reaches its largest width for $\varphi \approx 144°$ when a vortex ring is disrupting the flame tip. This flame wrinkling process near the flame base is attributed to the sudden and large flame motion taking place near the flame tip by the vortex roll-up and detachment.

## 4. Conclusions

The influence of acoustic perturbations on the thickness of the flame brush has been analyzed for a premixed $CH_4/H_2$/air swirling flame. It has been shown that perturbing the flame acoustically broadens the flame brush above a certain distance downstream the flame anchoring point.

When the flame motion is only driven by flame vortex roll-up, the flame brush thickness is altered away from the anchoring point where the vortex interacts directly with the flame front. In this situation, increasing the forcing amplitude does not have a significant influence on the flame brush thickness.

When the flame motion is controlled by swirl number fluctuations and flame vortex roll-up, the flame brush thickens immediately above the flame anchoring point. In addition, the forcing amplitude has in this case a large influence on the flame brush thickness, which increases rapidly with the distance to the flame anchoring point at the highest forcing amplitude investigated.

## 5. Acknowledgments

This work is supported by Agence Nationale de la Recherche, France, VALOGAZ project (ANR-10-EESI-0005). We wish to thank Y. Le Teno and S. Bouamama from EM2C for their assistance during the design and construction of the laboratory room and test-rig.

## 6. References

[1] P. Palies, T. Schuller, D. Durox, S. Candel (2011), Proc. Combust. Inst., **33** (2011) pp. 2967-2974.
[2] S. Candel, D. Durox, T. Schuller, J.F. Bourgouin, J.P. Moeck, Ann. Rev. Fluid Mech., **46** (2014), pp. 147-173.
[3] T.F. Guiberti, D. Durox, P. Scouflaire, T. Schuller, Proc. Combust. Inst. **35** (2) (2015), pp. 1385–1392.

**Proceedings of the Australian Combustion Symposium**
**December 7-9, 2015, The University of Melbourne**

# Local extinction and reignition in a turbulent lifted flame

Shahram Karami[1,*], Mohsen Talei[2], Evatt R. Hawkes[1,3]
[1] School of Photovoltaic and Renewable Energy
The University of New South Wales, NSW 2052, Australia
[2] Department of Mechanical Engineering
University of Melbourne, Melbourne, VIC 3010, Australia
[3] School of Mechanical Engineering
The University of New South Wales, NSW 2052, Australia

## Abstract

Direct numerical simulation (DNS) was used to analyse local extinction and reignition in a lifted turbulent flame. The edge flame propagation velocity appears to be dependent on the scalar dissipation rate consistent with previous experimental and numerical studies. This dependency is analysed with a model proposed for laminar triple flames, showing a good agreement for moderate scalar dissipation rates and an under- and over-predictions of the DNS results in very low and high scalar dissipation rates, respectively. These discrepancies are then explained based on the model's assumptions. The extinction and reignition are also analysed separately where the distinction is made based on the average hole diameter. It is revealed that during the extinction process, the edge flame is primarily a nonpremixed flame and propagation velocity reduces in a non-linear manner as scalar dissipation rate increases. In the reignition process, the flame experiences a wide range of premixed and non-premixed modes and the edge propagation velocity, conditionally averaged on the scalar dissipation rate decreases linearly when the scalar dissipation rate increases.

*Keywords: Local extinction, Reignition, Strain rate, Curvature.*

## 1. Introduction

The rate of mixing between fuel and air plays an important role in the flame stability and pollutant emissions for nonpremixed flames. A low mixing rate will affect the device efficiency and produce pollution, whereas the mixing rate higher than a specific value will result in local or even global extinction. As a result, local extinction and reignition have received a great attention in the literature.

Extinction and reignition have been a topic of a number of numerical studies. For instance, the extinction of a laminar triple flame with a pair of vortices was studied by Favier and Vervisch [1, 2] wherein it was shown that the scalar dissipation rate is the controlling parameter. However, it was observed that the scalar dissipation of growing holes is lower than that which has initiated the local extinction. In another study of a non-premixed flame in a counter-flow configuration under oscillating strain-rate conditions [3], it was observed that the flame was extinguished as the strain rates exceed the critical extinction strain rate of steady flames. In a DNS study of a piloted flame, Pantano [4] observed that extinction is controlled by the scalar dissipation rate. Furthermore, some of the extinction events were encountered in regions with a higher scalar dissipation rate than that for the extinction limit in a laminar flame. Sripakagorn et. al. [5] studied the effect of turbulence on extinction and reignition of flame holes in a isotropic three-dimensional decaying turbulence with a single-step chemistry model and an assumption of negligible density variations. They found that the edge-flame propagation and engulfment of neighbour hot products to the unburned portion of stoichiometric surface are the main mechanisms of reignition. In addition, independent flamelet scenario has a minor contribution in reignition. Pantano and Pullin [6] proposed a model for local extinction holes where the holes dynamics are assumed to be controlled by the edge-propagation velocity which is only a function of the scalar dissipation rate in their theory. A general transport equation for the joint probability density function of the hole area and scalar dissipation rate was proposed. A simplified form of this equation was solved for small holes. They assumed that the net rate of production–distribution of the holes area and the folding effects of mixture fraction iso-surfaces are negligible.

The physical mechanisms of extinction and reignition in turbulent lifted flames are not yet understood. Experimental studies reveal that large vortical structures and high strain rates on the stoichiometric surface can extinguish the flame [7, 8]. Some recent experimental studies with access to high-resolution measurements discuss the effects of the scalar dissipation rate; however, these studies are limited to two-dimensional measurements. One should note that interpreting the observations of two-dimensional measurements in turbulent lifted flames for which the third dimension is crucially important [9] can be misleading. The authors are not aware of any numerical studies of extinction and reignition in turbulent lifted flames. The available studies are limited to simpler configurations and hence their findings cannot be easily extended to turbulent lifted flames.

Therefore, the main focus of this paper is to analyse extinction and reignition in a lifted turbulent flame using direct numerical simulation (DNS). The analysis will reveal the mechanisms involved in

* Corresponding author:
Phone: (+61) 2 9385 4602
Email: s.karami@unsw.edu.au

extinction and reignition and the role of key parameters, namely the scalar dissipation rate and normalised flame index.

## 2. Description of the DNS database

### 2.1 Configuration

The DNS data used here was previously introduced in our previous study on the stabilisation mechanism of a turbulent lifted flame [10]. The details of the run are given in Ref. [10], so only a brief overview is given here. The configuration is a slot-jet flame where fuel is injected at the velocity, $U_j$, into a slower co-flow of oxidiser having the velocity $0.01U_j$. The mean inlet axial velocity, $U_{in}$, was specified to vary between the pure streams using a *tanh* profile with the momentum thickness of 0.05H, where H is the jet width. Turbulence in the fuel jet was specified with a frozen turbulent velocity field, based on a prescribed turbulent Passot-Pouquet energy spectrum, which is convected into the domain by applying Taylor's hypothesis. A uniform grid spacing of 0.02H was used in the streamwise and spanwise directions, which is approximately twice the Kolmogorov length scale, considered to be a good resolution in DNS [11]. An algebraically stretched mesh was used in the transverse direction which maintained uniform spacing of 0.02H in $|y| < 5H$, where y is the transverse coordinate, and less than 3 % stretching in the region of $|y| > 5H$. The simulation was performed for 18.0 jet flow through times, $t_j = L_x/U_j$, where $L_x$ is the streamwise domain length.

Table 1: Numerical and physical parameters of the simulation.

| Description | Value |
|---|---|
| Domain size ($L_x \times L_y \times L_z$) | 16H×24H×6H |
| Number of grid points ($N_x \times N_y \times N_z$ ) | 800×800×300 |
| Mean inlet jet Mach number ($U_j/a_{ref}$) | 0.48 |
| Laminar co-flow Mach number ($U_{co}/a_{ref}$) | 0.001 |
| Jet non-dimensional temperature ($T_{jet}$) | 2.5 |
| Co-flow non-dimensional temperature ($T_{co\text{-}flow}$) | 2.5 |
| Jet Reynolds number (Re) | 5280 |
| Inlet velocity fluctuation intensity | 5% |
| Fuel mass fraction in the fuel stream ($Y_{F,o}$) | 1.0 |
| Oxidiser mass fraction in the oxidiser stream ($Y_{O,o}$) | 0.233 |
| Stoichiometric oxidiser to fuel mass ratio (r) | 4.0 |
| Heat-release parameter (α) | 0.86 |
| Zel'dovich number (β) | 5.0 |
| Non-dimensionalisation Damköhler number (Da) | 800 |
| Lewis number (Le) | 1.0 |
| Prandtl number (Pr) | 0.7 |

### 2.2 Physical model and parameters

To limit the computational cost, a single-step irreversible reaction of F+rO→(1+r)P with an Arrhenius source term was used. A modified activation energy approach, initially developed by Garrido-López and Sarkar [12], was used to capture the realistic dependence of laminar burning velocity on equivalence ratio that is typical of the hydrocarbon fuels. A comprehensive justification of the choice of chemistry model is described in our previous article [10]. The reaction and thermochemical parameters are chosen to result in the $H/\delta_L$ and $U_j/S_L$ being comparable to experimentally measured methane flames[13], where $\delta_L$ is the laminar flame thickness and $S_L$ is the laminar burning velocity.

The parallel DNS code, S3D_SC was employed. S3D_SC is a one-step chemistry version of S3D, developed at Sandia National Laboratories [14]. The compressible Navier-Stokes, sensible energy, and species transport equations are solved on a structured 3D Cartesian mesh using high order methods [14]. Non-reflecting outflow boundary conditions are used in the streamwise and transverse directions, and periodic boundary conditions are applied in the spanwise direction [15-17]. Other simulation parameters are summarised in Table 1.

## 3. Mathematical background

In this study focussing on extinction and reignition, it is useful to define a concept of flame edges, which separate the burning and nonburning regions of a mixture-fraction isosurface. Following previous studies [4, 10, 18, 19] the flame edges are defined as the intersection points of a mixture-fraction iso-surface with a product mass-fraction iso-surface. The mixture-fraction iso-value is 0.07, which corresponds to the mixture-fraction having the highest flame speed in a one-dimensional flat premixed laminar flame, while the product iso-value was selected as the value corresponding to the maximum reaction rate in the same flame. A sensitivity analysis of the edge-flame statistics to these criteria is shown in Ref. [10].

The holes identified using this methodology were extensively visualised to understand the holes behaviour and their interaction with each other. The extinction holes might grow and shrink independently, split into multiple holes, and/or merge with neighbour holes, which is consistent with the observations in previous experimental studies [7, 20-22].

As an orientation, first we discuss the behaviour of all extinction holes away from the flame base. Then, we focus on extinction and reignition of individual holes. For this purpose, *thirty* individual holes with no splitting and merging and far from other neighbouring holes were selected to minimise the hole-hole interaction. These individual holes, however, do not have a simple structure and are commonly convoluted due to the effects of turbulence. This is in contrast to the assumption made by Pantano and Pullin [6] in their model for local extinction holes.

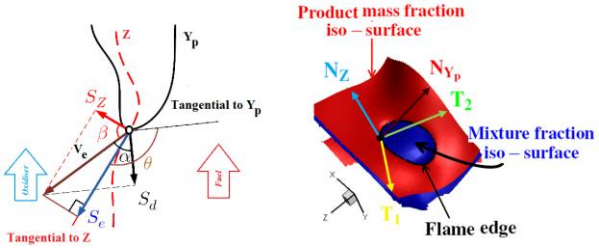


Figure 1. Schematic of the hole and edge propagation velocities.

The edge-flame displacement speed, $S_e$, is defined as the motion of the flame edge relative to the flow (defined positive if towards reactants), projected into the plane of the mixture-fraction iso-surface. The edge speed is given in terms of the product mass-fraction self-displacement speed $S_d$, the mixture-fraction self-displacement speed $S_z$, and the inner product of the normal vectors to product and mixture-fraction iso-surfaces k as [19]:

$$S_e^* = \frac{S_d^* - kS_Z^*}{\sqrt{1-k^2}}, \rho_u S_d^* = \frac{\rho DY_P/Dt}{|\nabla Y_P|} \text{ and } \rho_u S_Z^* = \frac{\rho DZ/Dt}{|\nabla Z|}. \quad (1)$$

The normalised flame index (NFI) [23] is also used here to distinguish between premixed and nonpremixed combustion modes and is defined as:

$$NFI = \frac{\mathbf{N}_Z.\mathbf{N}_{Yp}}{|\mathbf{N}_Z.\mathbf{N}_{Yp}|}. \quad (2)$$

## 4. Results and discussion

For orientation, the dependence of the edge-flame propagation velocity on scalar dissipation rate is compared with the proposed model by Pantano and Pullin [6]. In those studies the edge-flame propagation velocity was parameterised as a function of

$$\varepsilon = \frac{l_{LF}}{L/\beta}, \quad (3)$$

where $l_{LF}$ and L are respectively the laminar flame and mixing layer thicknesses and defined as,

$$l_{LF} = \frac{\lambda}{\rho C_P S_L} \text{ and } L/\beta = \sqrt{\frac{2\lambda}{\rho C_P \chi}}, \quad (4)$$

where β is the Zel'dovich number, ρ is the density, $C_P$ is the specific heat coefficient, λ is the thermal conductivity and χ is the scalar dissipation rate. Pantano and Pullin [6] assumed that for small holes, i.e. holes which can be characterised by their area, the edge-flame propagation velocity can be modelled as:

$$\frac{S_e^*}{S_L} = 1 - \frac{1+\frac{1}{\frac{\varepsilon}{\varepsilon_{ex}}-1}}{1+\frac{1}{\frac{\varepsilon_0}{\varepsilon_{ex}}-1}}, \quad (5)$$

where $\varepsilon_{ex}$ is the value of extinction limit beyond which no flame exists and $\varepsilon_0$ is the value of ε where $S_e^*$ is zero [6]. The joint PDF of the edge-flame propagation velocity and ε for all holes in the region of 5<x<12 is presented in Fig 2. The black circles are the conditional average of edge-flame propagation velocity on ε and the red circles are the model presented by equation 5. There is a reasonable agreement between the model and the DNS results in particular for moderate scalar dissipation rates. The departure of the conditional mean from the model for low ε values can be due to the interaction of holes boundaries in the healing process. When the extinction holes heal, edge flames seek to meet and close the holes completely. The visualisation of the healing process shows that when the holes reach to a diameter less than two times of the thermal flame thickness, the healing accelerates because of the edge-flames interactions. There is also a deviation from the model for high ε values and the model over-predicts the edge-flame propagation velocity. The main reason for this difference is that the model was developed for small and less disturbed holes; however, the holes in this study are highly contorted and are as big as three times of the jet width.

Now, the question arises, how the scalar dissipation rate contributes to the extinction and reignition processes and what mode of combustion, e.g. premixed or non-premixed is dominant? To answer these questions, extinction and reignition of thirty holes are analysed where the distinction of reignition from extinction was achieved using the rate of change in the average hole radius. The average radius of each hole at each instant was calculated by averaging the distance of the edge-flame locations from centroid of the hole.

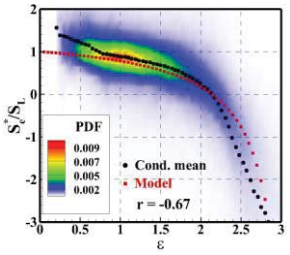


Figure 2. The joint PDF of edge-flame propagation velocity and ε (black circles are conditional means and the red squares are the model proposed by Pantano and Pullin [6]).

### 4.1 Extinction mechanism

The joint PDF of the edge propagation velocity and the scalar dissipation rate during extinction is shown in Fig. 3a. The edge propagation velocity is negatively correlated with the scalar dissipation rate. The joint PDF is narrow with low fluctuations over the conditional mean. The conditional mean shows a non-linear behaviour as expected for extinction events [24]. The joint PDF of the edge-propagation velocity and scalar dissipation rate also shows that even though a high scalar dissipation rate is required for formation of the holes, the hole can grow with lower values of scalar dissipation rate [2].

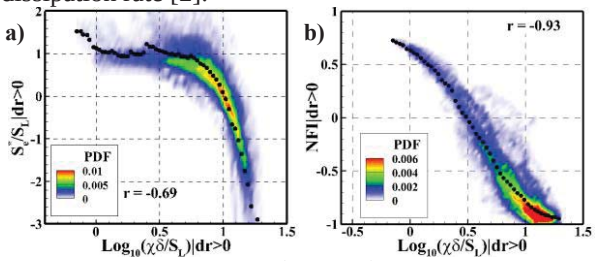


Figure 3. The joint PDF of a) edge-flame propagation velocity and b) NFI when the local extinction occurs with the normalised scalar dissipation rate (black circles are conditional means).

The normalised flame index (NFI) which is widely used to distinguish premixed from non-premixed flames is presented in Fig. 3b. The joint PDF of the NFI and scalar dissipation rate shows the dominant presence of non-premixed flames in the local extinction process. These observations suggest that local extinctions occur when a highly straining turbulent structure intrudes into the flame sheet, resulting in squeezing of the product mass fraction and mixture-fraction iso-surfaces such

that the flame could not be sustained due to the excessive dissipation of heat.

### 4.2 Reignition mechanism

In contrast to the extinction process, the conditional edge-flame propagation velocity on the scalar dissipation rate exhibits a mostly linear (but still decreasing) response to an increase in the scalar dissipation rate from low to moderate values as can be observed in Fig. 4a. The edge-propagation velocity at low values of scalar dissipation rate corresponding to the final stages of healing increases due to flame-flame interaction. Figure 4b shows a wide range of possibilities for premixed or nonpremixed edge flames in the reignition process. Extensive observation of the animations suggests that the combustion mode alters from nonpremixed at the beginning of the healing to premixed as the healing is advanced.

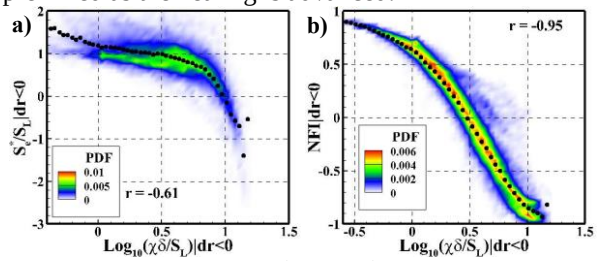


Figure 4. The joint PDF of a) edge-flame propagation velocity and b) NFI with the normalised scalar dissipation rate when holes are healing (black circles are conditional means).

## 5. Discussion

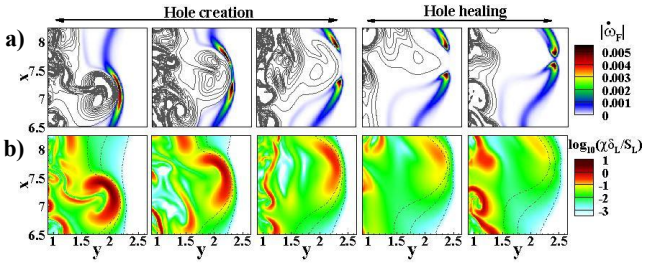


Figure 5. Instantaneous contour plots of a) reaction rate and b) scalar dissipation rates at local extinction and reignition (grey lines in a) are vorticity and dot-lines in b) are mixture fraction iso-contours).

To summarise the main findings, the instantaneous local extinction and reignition process for a given hole is presented in Fig. 5. As can be seen, the extinction occurs as a large structure hits the mixture-fraction iso-surface. After extinction, the scalar dissipation rate is high and the flame front has a comet shape similar to highly strained counter-flow flames [25]. The reignition process starts with propagation of the comet shape structures towards each other as the large structure moves away. It appears that the reignition starts with a nonpremixed structure, approaching a triple flame structure as the healing is progressed.

## 6. Conclusion

The local extinction and reignition in a turbulent lifted flame were studied using direct numerical simulation (DNS). The conditional mean of edge-flame propagation velocity on the scalar dissipation rate shows a good agreement with the predictions of the model proposed by Pantano and Pullin [6]. Separate analyses of extinction and reignition were performed. It was revealed that a high scalar dissipation rate is required for the extinction, whereas the generated hole can nonetheless grow with significantly lower values of scalar dissipation rate. The flame shows a nonpremixed nature during extinction while it can be either premixed or non-premixed during reignition.

## 7. Acknowledgments

This work was supported by the Australian Research Council (ARC). The research was also supported by access to computational resources on the Australian NCI National Facility through the National Computational Merit Allocation Scheme and Intersect Australia partner share.

## 8. References

[1] V. Favier, L. Vervisch, Combust. Flame **125** (1–2) (2001), pp. 788-803.
[2] V. Favier, L. Vervisch, Symp. (Int.) Combust. **27** (1) (1998), pp. 1239-1245.
[3] F. N. Egolfopoulos, Int. J. Energy Res. **24** (11) (2000), pp. 989-1010.
[4] C. Pantano, J. Fluid Mech. **514** (2004), pp. 231-270.
[5] P. Sripakagorn, S. Mitarai, G. Kosály, H. Pitsch, J. Fluid Mech. **518** (2004), pp. 231-259.
[6] C. Pantano, D. I. Pullin, J. Fluid Mech. **480** (2003), pp. 311-332.
[7] J. Hult, U. Meier, W. Meier, A. Harvey, C. F. Kaminski, Proc. Combust. Inst. **30** (1) (2005), pp. 701-709.
[8] K. M. Lyons, K. A. Watson, C. D. Carter, J. M. Donbar, Combust. Flame **142** (3) (2005), pp. 308-313.
[9] R. L. Gordon, A. R. Masri, E. Mastorakos, Combust. Flame **155** (1-2) (2008), pp. 181-195.
[10] S. Karami, E. R. Hawkes, M. Talei, J. H. Chen, J. Fluid Mech. **777** (2015), pp. 633-689.
[11] J. Göttgens, F. Mauss, N. Peters, Symp. (Int.) Combust. **24** (1) (1992), pp. 129-135.
[12] D. Garrido-López, S. Sarkar, Proc. Combust. Inst. **30** (1) (2005), pp. 621-628.
[13] A. Cessou, C. Maurey, D. Stepowski, Combust. Flame **137** (4) (2004), pp. 458-477.
[14] J. H. Chen, A. Choudhary, B. De Supinski, M. Devries, E. R. Hawkes, S. Klasky, W. K. Liao, K. L. Ma, J. Mellor-Crummey, N. Podhorszki, R. Sankaran, S. Shende, C. S. Yoo, Comput. Sci. Disc. **2** (1) (2009), pp.
[15] J. C. Sutherland, C. A. Kennedy, J. Comput. Phys. **191** (2) (2003), pp. 502-524.
[16] C. S. Yoo, Y. Wang, A. Trouvé, H. G. Im, Combust. Theor. Model. **9** (4) (2005), pp. 617 - 646.
[17] C. S. Yoo, H. G. Im, Combust. Theor. Model. **11** (2) (2007), pp. 259 - 286.
[18] E. R. Hawkes, R. Sankaran, J. H. Chen, Proc. Combust. Inst. **33** (1) (2011), pp. 1447-1454.
[19] E. Hawkes, R. Sankaran, J. Chen, 16th Australasian Fluid Mechanics Conference (AFMC) (2007), pp. 1271-1274.
[20] I. G. Boxx, C. D. Carter, W. Meier, AIAA SciTech, 13-17 January 2014, National Harbor, Maryland (52nd Aerospace Sciences Meeting) (2014), pp.
[21] R. Gordon, I. Boxx, C. Carter, A. Dreizler, W. Meier, Flow Turbul. Combust. **88** (4) (2012), pp. 503-527.
[22] S. Noda, H. Mori, Y. Hongo, M. Nishioka, JSME Int. J. B **48** (1) (2005), pp. 75-82.
[23] E. Knudsen, H. Pitsch, Combust. Flame **159** (1) (2012), pp. 242-264.
[24] N. Darabiha, Combust. Sci. Technol. **86** (1-6) (1992), pp. 163-181.
[25] G. Amantini, J. H. Frank, A. Gomez, Proc. Combust. Inst. **30** (1) (2005), pp. 313-321.

**Proceedings of the Australian Combustion Symposium**
**December 7-9, 2015, The University of Melbourne**

# Identification of Burning and Extinguishing Behaviour in Spray Flames with Spark Ignition

Jocelyn Baayens[1], Andrew P. Wandel[2,*]
[1]School of Mechanical and Electrical Engineering
University of Southern Queensland Qld 4350 Australia
[2]Computational Engineering and Science Research Centre, School of Mechanical and Electrical Engineering
University of Southern Queensland Qld 4350 Australia

## Abstract

The Gaussian Mixture Model (GMM) is used to analyse Direct Numerical Simulation results for sprays which are ignited using spark ignition. The variables considered in the GMM are the reaction progress variable and its dissipation. It is found that a case which sustained a self-propagating flame produces a burning branch, where a strong flame front is developed, and an extinguishing branch, which contains droplets which are offset from the main spark energy. These branches are distinctly observed through the various clusters that are formed by the GMM. In contrast, cases which ignite but subsequently undergo global extinction do not produce clusters that are distinctly from the burning branch or extinguishing branch near the flame kernel. However, the clustering does display a strong extinguishing branch near the leading edge of the flame front.

*Keywords: Direct Numerical Simulations, Spark Ignition, Spray Flames, Extinction, Gaussian Mixture Model*

## 1. Introduction

Spark ignition for spray combustion is common in gas turbine engines while the automotive industry is adopting it as DISI (Direct-Injection Spark-Ignition) engine technology: an active research area [1–5]. Classic experiments showed that spray flames need more spark energy than equivalent gaseous mixtures to overcome the latent heat of vaporisation, with turbulence impacting negatively on ignition success [6, 7]. The behaviour is sensitive to the droplet size, with fine droplets able to sustain lean flames (when the equivalent gaseous flame cannot) because the gaseous distribution of fuel is more variable, producing local stoichiometric conditions [6].

This paper is the continuation of a sequence of investigations into the cause of extinction in spray flames [8–10]. It draws heavily on the findings of the most recent paper, where a quantitative measure distinguishing between burning and extinguishing flames was established. This paper will explore a different means of analysing the cases to describe the distinct behaviour of these two types of cases.

### 1.1 Simulations

Direct Numerical Simulations (DNS) of sprays using spark ignition are investigated; the simulations have been comprehensively described previously [10]. In summary, droplets are initially randomly distributed in pure air that is preheated to 500°C; the droplets are located in the central slab of the domain, with no droplets near the non-reflecting boundary conditions that allow the flame to exit the domain. A spark is activated in the middle of the droplet field and this paper analyses the field when the spark is deactivated.

The cases studied in Ref. [10] are investigated here (Table 1). The base case is chosen as one which successfully burns throughout the simulation (the flame front reaches the boundaries), while the remaining droplet cases are chosen to show progressively-increasing global extinction. Case BE burns throughout the simulation (the flame front propagates throughout), but extinction was about to commence when the simulation was stopped. The I cases ignited, but global extinction commenced soon after the spark was deactivated. The F cases did not ignite at all. The parameters that were varied to achieve these cases were the equivalence ratio $\Phi$ (which is the value within the droplet field if all the fuel was vapour), the square of the ratio of initial droplet diameter to the same quantity for the base case, and ratio of the initial turbulent kinetic energy to the same value for the base case. Having fewer droplets (reduced $\Phi$) or larger droplets are well-known to reduce the flammability of the mixture. The increased turbulence in these simulations moves the flame kernel away from the spark, so the spark is less effective [10].

Table 1: DNS Cases investigated here. Columns are: equivalence ratio ($\Phi$), the square of the ratio of initial droplet diameter to base case, and ratio of turbulent kinetic energy to base case. Case BE is Burning, but about to Extinguish; "I" means "ignited"; "F" means "failed to ignite".

| Name | $\Phi$ | Rel. Diam. Sq. | $k/k_b$ |
|---|---|---|---|
| Base | 2.0 | 1 | 1 |
| BE | 1.7 | 1 | 1 |
| I1 | 1.6 | 1 | 1 |
| I2 | 2.0 | 1.5 | 1 |
| F1 | 1.0 | 1 | 1 |
| F2 | 1.0 | 1 | 8 |

* Corresponding author:
Phone: (+61) 7 4631 2230
Email: andrew.wandel@usq.edu.au

### 1.2 DNS data to be analysed

The reaction progress variable was calculated using

$$c = \frac{\left(1-Z\right)Y_{\mathrm{O},i} - Y_{\mathrm{O}}}{\left(1-Z\right)Y_{\mathrm{O},i} - \max\left(0, \frac{Z_{\mathrm{st}}-Z}{Z_{\mathrm{st}}}\right)Y_{\mathrm{O},i}} \qquad (1)$$

where $Z$ is the mixture fraction, $Z_{\mathrm{st}}$ the stoichiometric mixture fraction and $Y_{\mathrm{O},i}$ is the mass fraction of the oxidiser in the oxidiser stream. Also of interest is the dissipation of $c$:

$$N_{cc} = D\nabla c \cdot \nabla c \qquad (2)$$

with $D$ the diffusivity. It has previously been shown that the joint-probability density function (jpdf) of these two quantities provides an indication of whether extinction is imminent [10]. This paper investigates another description of the behaviour, which provides another perspective on why the extinction occurs. To achieve this description, data mining is used to distinguish between the burning behaviour of successfully-propagating flames and extinguishing behaviour of isolated droplets.

## 2. Data Mining Method

The Gaussian Mixture Model (GMM) is a density-based method used to find clusters of arbitrary shape [11]. A cluster is defined to be a collection of data points which are considered to have similar properties and are thereby classified to belong to a group (with a total of $M$ groups). Each group contains data points which are close together in space. The data points from a different group can be considered to have different properties.

The derivation follows Ref. [12]. A GMM is a weighted sum of component Gaussian densities given by the equation

$$P\left(\mathbf{x}\middle|\lambda\right) = \sum_{i=1}^{M} w_i g\left(\mathbf{x}\middle|\mu_i, \Sigma_i\right) \qquad (3)$$

where $\mathbf{x}$ is an $n$-dimensional continuous-valued data vector; $w_i$ are the mixture weights; $g(\mathbf{x}|\mu_i,\Sigma_i)$ are the component Gaussian densities (clusters), which are $n$-dimensional Gaussian functions; $M$ is the number of clusters; $\mu_i$ is the mean vector; and $\Sigma_i$ is the covariance matrix. This mixture distribution has the constraints

$$0 \le w_i \le 1 \quad \text{and} \quad \sum_{i=1}^{M} w_i = 1 \qquad (4)$$

The complete Gaussian Mixture Model is parameterised by the mean vectors, covariance matrices and mixture weights from all component densities:

$$\lambda = \left\{w_i, \mu_i, \Sigma_i\right\} \qquad (5)$$

A maximum-likelihood estimation is used to find λ.

## 3. Results and Discussion

The reaction progress variable and its dissipation are the quantities to be considered in the GMM, hence $n = 2$. For this paper, $M = 20$ was chosen. The nodes with $c < 0.02$ were excluded to reduce processing effort. These nodes account for the vast majority of data and the nodes of interest here have $c > 0.9$.

The cluster plots for the Base case and case BE are shown in Figs. 1 and 2 respectively. For $0 < c < 0.3$, the behaviour is similar, with multiple clusters in the leading edge of the flame front. The behaviour for $0.3 < c < 0.7$ is substantially different. For the Base case, there is a very large, dominant cluster for the highest values of $N_{cc}$, which is overwhelmed in case BE by the clusters which are on the shoulders and penetrate closer to $c = 0.5$ than in the Base case. This uppermost cluster was identified as belonging to a burning branch [10], which has a high probability in the Base case, i.e. a large region of space takes these values. The extinguishing branch for $0.3 < c < 0.7$ is also more segmented in case BE than the Base case. This large number of clusters in case BE is probably due to multiple flame fronts being created around individual droplets (see Fig. 23(b) [10]), while the Base case produced a large, strong flame kernel.

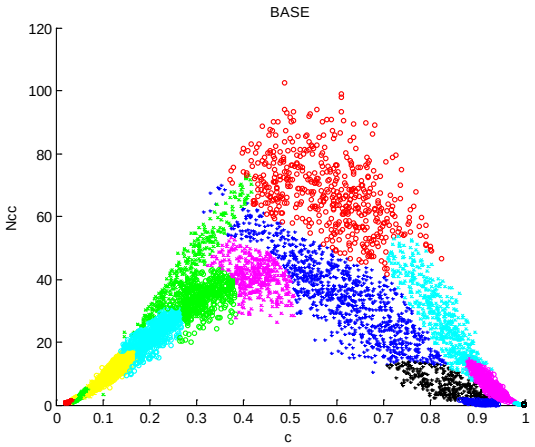


Figure 1: Cluster plot of $N_{cc}$ vs $c$ for Base case. The colours are randomly chosen to distinguish between clusters and cannot be matched to other cases.

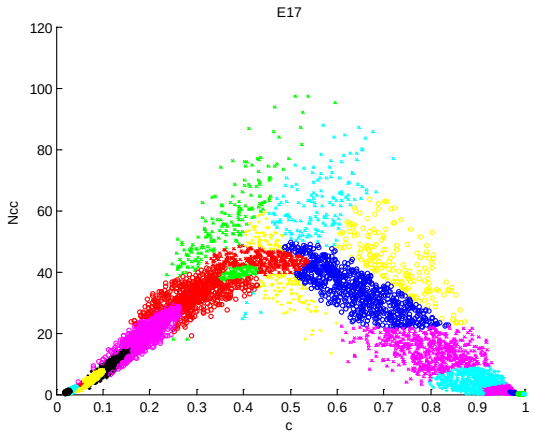


Figure 2: Cluster plot of $N_{cc}$ vs $c$ for case BE.

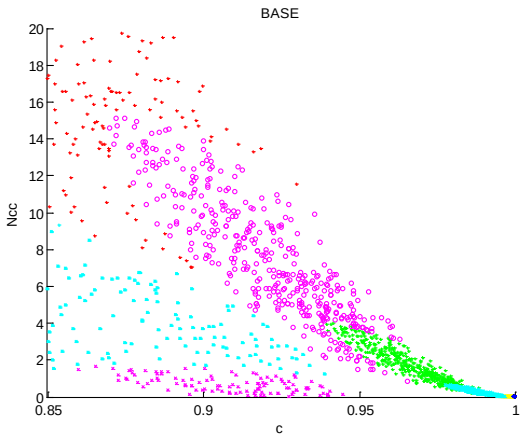


Figure 3: Zoomed-in image of Fig. 1.

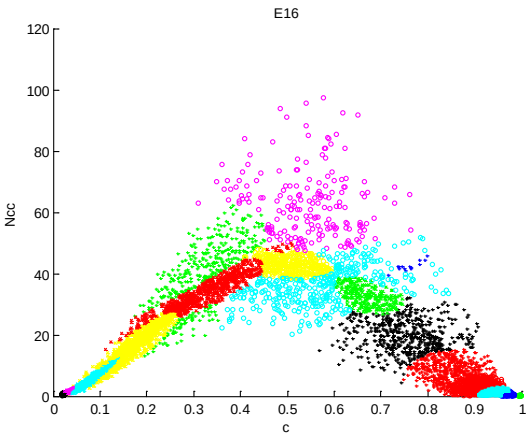


Figure 5: Cluster plot of $N_{cc}$ vs $c$ for case I1.

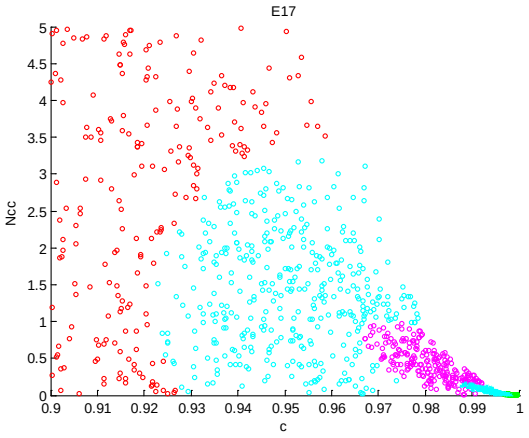


Figure 4: Zoomed-in image of Fig. 2.

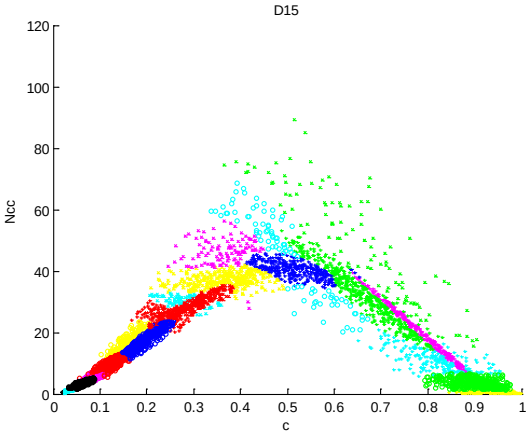


Figure 6: Cluster plot of $N_{cc}$ vs $c$ for case I2.

For the region closest to the flame kernel ($c > 0.7$), the clustering is completely different. In the Base case, the separation of clusters is parallel to the edges of the data, while in case BE, the separation is essentially for constant $N_{cc}$. In the successfully-burning Base case, this behaviour is caused by a large, stable flame kernel which supports the burning branch, while some droplets are separated from the flame kernel and produce the extinguishing branch. In case BE, the primary flame kernel is not sufficiently strong to support combustion, so there is no clear distinction between that region and the region around separated droplets.

To investigate this further, Figs. 3 and 4 zoom in on the highest values of $c$ in Figs. 1 and 2. The separation of the clustering in the Base case is fundamentally caused by the burning branch being fed by the strong flame kernel at $c = 1$, while the extinguishing branch is sourced by incomplete combustion from isolated droplets. This completely different behaviour produced the findings of Ref. [10]. It is interesting that the burning branch contains multiple clusters for $c > 0.98$. By contrast, the clustering for case BE is only separated radially from $c = 1$: the flame kernel is insufficiently strong to produce self-sustaining flame fronts which could be considered a burning branch.

The cluster plot for case I1 (Fig. 5) shows similar behaviour to case BE in the vicinity of $c = 1$ in that the clusters do not separate into burning and extinguishing branches. The more immediate extinction in case I1 can be heralded by the lack of any distinct burning branch cluster except for the few nodes with the highest values of $N_{cc}$. At lower values of $c$ in case I1, there is an intense series of narrow clusters that overlays broader clusters. This is caused by the predominance of droplets which have not sustained flames (the narrow clusters), with a small number of droplets which have produced reasonable flames that have insufficient energy to sustain the entire field.

Case I2 (Fig. 6) continues this trend, with a very strong extinguishing branch overlaying weakly-burning clusters at lower values of $c$ and no clear separation of burning and extinguishing branches at the highest values of $c$. A distinct feature of this case is the thin cluster present in $0.6 < c < 0.9$, which, when compared to Fig. 1, is in the middle of the extinguishing branch. This case has a very small flame kernel (Fig. 23(e) [10]), with a substantial, very lean secondary structure and a tiny tertiary flame kernel around a single droplet. It is likely that the thin cluster is caused by the substantial secondary structure which cannot sustain combustion due to insufficient fuel.

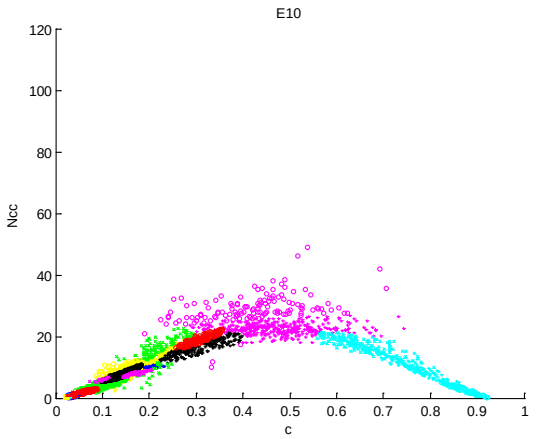


Figure 7: Cluster plot of $N_{cc}$ vs $c$ for case F1.

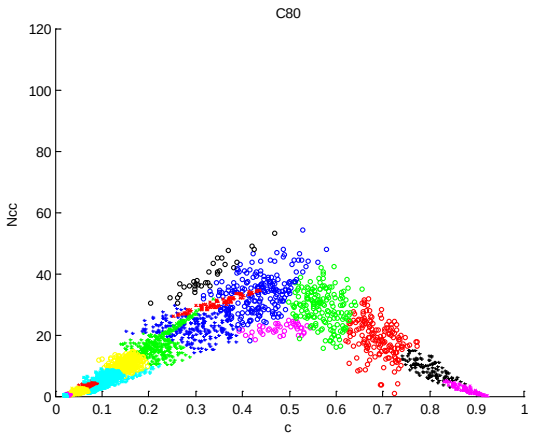


Figure 8: Cluster plot of $N_{cc}$ vs $c$ for case F2.

Case F1 (Fig. 7) does not show a burning branch because this case fails to ignite. There is weak scatter for $c \approx 0.5$ due to the discrete nature of the droplet field. This discrete nature also produces parallel clusters for lower values of $c$; the large number of such clusters is probably due to the high value of $M$ given that there are only two clusters for $c > 0.4$.

The higher turbulence in case F2 significantly distorts the field, thereby producing a few clusters for the highest values of $c$ as well as a number of very thin clusters for $0.3 < c < 0.5$ (Fig. 8). The primary mechanism by which the turbulence suppresses ignition is to push the heated region away from the centre of the spark, thereby preventing sufficient time for ignition to commence.

## 4. Conclusions

A data mining tool, the Gaussian Mixture Model, has been used to analyse Direct Numerical Simulation results for a spray which is ignited using a spark. It has been found that the case with a self-sustaining propagating flame produces clustering which distinctly shows a burning and extinguishing branch for values of the reaction progress variable above 0.4. In contrast, cases which extinguished did not produce similarly-distinct clusters.

The clustering method identified that for cases where extinction is imminent, a strong extinguishing branch is visible for values of reaction progress variable lower than 0.5. This distinction was not apparent when considering the joint-probability density functions [10].

Future work will consider the sensitivity of the method to the number of clusters $M$ and compare a wider range of simulation parameters to confirm that the identified trends are observed for the different types of behaviour.

## 5. Acknowledgments

Some of this work was performed at Cambridge University, where it was funded by Rolls–Royce plc. The authors are grateful to Prof. R. S. Cant for the use of the SENGA code to produce the DNS results.

## 6. References

[1] R. Anderson, A New Direct Injection Spark Ignition (DISI) Combustion System for Low Emissions, Technical Report P0201, FISITA, 1996.

[2] P. G. Aleiferis, J. Serras-Pereira, Z. van Romunde, J. Caine, M. Wirth, Combust. Flame 157 (2010) pp. 735–756.

[3] H. Kwon, H. Choi, J. Kim, K. Min, Combust. Theory Modelling 16 (2012) pp. 1089–1108.

[4] M. Sjöberg, D. L. Reuss, Proc. Combust. Inst. 34 (2013) pp. 2933–2940.

[5] D. Goryntsev, A. Sadiki, J. Janicka, Proc. Combust. Inst. 34 (2013) pp. 2969–2976.

[6] S. K. Aggarwal, Progr. Energy Combust. Sci. 24 (1998) pp. 565–600.

[7] A. H. Lefebvre, Gas Turbine Combustion, Taylor and Francis, 1999.

[8] A. P. Wandel, N. Chakraborty, E. Mastorakos, Proc. Combust. Inst. 32 (2009) pp. 2283–2290.

[9] A. P. Wandel, Proc. Combust. Inst. 34 (2013) pp. 1625–1632.

[10] A. P. Wandel, Combust. Flame 161 (2014) pp. 2579–2600.

[11] M. Kantardzic, Data Mining: Concepts, Models, Methods and Algorithms, 2nd Ed., IEEE Press, 2011.

[12] D. Reynolds, Encyclopedia of Biometrics, Springer, 2009, pp. 659–663.

**Proceedings of the Australian Combustion Symposium**
**December 7-9, 2015, The University of Melbourne**

# A New Approach in Characterizing Secondary-Breakup Regimes for Newtonian Liquids

Phuong X. Pham[1, *], Agisilaos Kourmatzis[2], Assaad Masri[1]
[1]Clean Combustion Research Group – School of Mechanical and Mechatronic Engineering
University of Sydney - NSW 2006 - Australia
[2] Department of Engineering, Macquarie University - NSW 2109 - Australia

## Abstract

An image processing technique developed earlier using backlit shadowgraph for primary and secondary atomization study has been extended in this work to investigate the breakup evolution of a broad range of biodiesels, ethanol and fossil diesel. The backlit system uses a high speed CMOS camera in conjunction with a long distance microscope objective lens with the aid of a diffused light beam generated from a diode stack high-speed Nd-YAG laser. In the current work, a new approach of using the spatial gradient of area of fragment shapes is developed to improve understanding of the droplet-to-fragment and fragment-to-fragment breakup processes. A definition of breakup length is given here as the length between the initial location of the parent droplet and the location where the spatial gradient of area of ligaments and unbroken objects becomes close to zero. The non-dimensional breakup-time characteristic is then estimated using the measured breakup length and an appropriate velocity scale. This quantitative approach is capable of comparing the breakup time amongst different fuels and could be used to improve current breakup-time models. The trend of breakup-time observed in this study matches quite well with that reported by Pilch and Erdman [1]. The time however, is one order of magnitude shorter than that noticed by Pilch and Erdman. This is attributed to the difference in the breakup time definitions and the experimental techniques used in Pilch and Erdman's work and those in this study, as has also been observed elsewhere [1].

*Keywords: Secondary atomization, Biodiesel, Breakup evolution, Breakup length, Breakup time*

## 1. Introduction

Secondary atomization, a phenomenon describing the process of parent droplets breaking up into fragments under interfacial aerodynamic forces, is relevant to many power generation systems such as IC engines and boilers. An extensive review on this topic can be found in [2]. Under aerodynamic forces, a parent droplet will break up into different fragments (droplet-to-fragment breakup) and then the fragments break up to form smaller liquid shapes downstream (fragment-to-fragment breakup). Size distributions of the fragments arising from secondary atomization are amongst the most important parameters but very difficult to measure accurately [2]. Kourmatzis et al. [3, 4] recently developed a backlit technique to classify and quantify different liquid shapes yielded from primary and/or secondary atomization. The liquid fragments arising from the atomization process have classified into three well-characterized shapes (small drops, ligaments, and unbroken objects) and their quantifying parameters (e.x. probability, SMD, and area) were averaged for each image [3]. The experiment uses a high speed CMOS camera in conjunction with a long distance microscope objective lens in order to visualize a small scale. However, averaging the whole image is inadequate when it comes to examining the evolution of droplet-to-fragment and fragment-to-fragment breakup. This paper extends the image processing technique to examine the breakup evolution by dividing each image into smaller equal horizontal bins to observe the gradient of quantifying parameters (e.x. size and area) through the bins.

Since the fragments arising from secondary breakup result from air-liquid interfacial aerodynamic forces, this process depends on the air stream conditions which lead to different breakup regimes. The common used breakup regime diagram is shown in [5] where the breakup modes are classified by the droplet Weber and Ohnesorge number and they include deformation, oscillation, bag, multi-mode, shear breakup regime. The classification is made using critical Weber numbers [2]. However, there exist difficulties in interpreting experimental observations which leads to inconsistencies in the available critical Weber number as well as breakup regimes. For example, Pilch and Erdman [1] found transition between multimode and sheet-thinning at We = 100 while Gelfand [7] reported We = 40. The vibrational breakup regime is not always observed [2] and the catastrophic breakup is not mentioned in the commonly used breakup regime diagram developed by Hsiang and Faeth [5].

Breakup time of the parent droplets is a critically important and commonly reported parameter in secondary atomization, however, the definitions of breakup time are numerous, generic and can be vague in the literature. This is due to difficulties in interpreting the experimental data [1]. Pilch and Erdman [1] defined the total breakup time as the time when all fragments have ceased. Patel and Theofanous [7], however, reported breakup as the time required to

* Corresponding author:
Phone: (+61) 2 93517144
Email: x.pham@sydney.edu.au

double the diameter of initial droplets. More details about other definitions can be found in [1]. The temporal evolution of bag breakup has been studied by Chou and Faeth [8]. A number of continuous processes have been pointed out in their work including droplet deformation, bag growing, bag and ring breakup. However, it is observed from our previous work [9] that the bag and ring breakup events are not the end of the secondary atomization process, the ligaments and unbroken blobs arising from the events still continue to generate small drops downstream.

As such, more quantitative work is needed to improve understanding of the breakup models for secondary atomization. This work will examine the breakup evolution of different liquid shapes generated from secondary atomization of different fluids including a range of biodiesels, ethanol and fossil diesel. A new approach will be developed to measure breakup-length and breakup-time for these liquids.

## 2. Experiment setup

An air-cross flow system, shown schematically in Figure 1 consists of compressed air supplied to a mini-tunnel which contains the final air discharge nozzle at its exit. Upstream of the nozzle, a number of laminarizing grids are inserted to eliminate flow instability at the exit plane. Mono-dispersed droplets were generated and delivered vertically to the cross flow using a syringe pump and a needle with an internal diameter ID = 210 um. The injection rate is kept constant at 150 ml/h. The mean diameter of the mono-dispersed droplets was measured using a long distance microscope lens providing an initial diameter equal to 400 um (±5%) independent of the tested liquids. The observation reveals that droplet generation process is driven by a Rayleigh dripping regime where the droplet diameter d = 1.89*ID. More details about this system and data processing can be found in [3, 9].

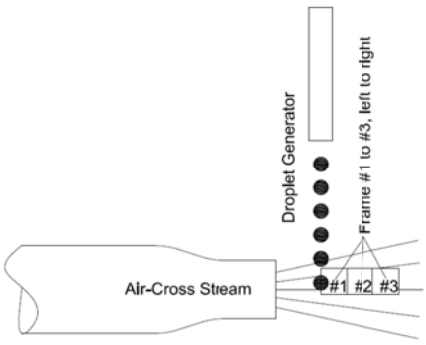


Figure 1. Schematic of the cross-flow experimental system (three 4x4mm frames, #1 to #3, corresponding to 3 different visualizing positions downstream)

Six fuels are selected here including ethanol (E), fossil diesel (D) and four different biodiesels (B1 to B4). Selected properties for these fuels are listed in Table 1 and more details of these fuels have already appeared elsewhere [9]. Dimensionless parameters (We, Re, and Oh) controlling the testing conditions are shown in Table 2. The reader is directed to [9] for computing the dimensionless parameters. A sequence of 1,000 consecutive 4x4mm images with 512x512 pixels is recorded for each atomization condition and three downstream locations corresponding with frame #1, #2 and #3 (see Figure 1) are investigated.

Table 1. Selected physical properties of the tested fuels

| Fuel | **B1** | **B2** | **B3** | **B4** | **E** | **D** |
|---|---|---|---|---|---|---|
| Density, [kg/m3] | 877 | 871 | 873 | 879 | 789 | 848 |
| Viscosity, [Pa.s]*$10^{-3}$ | 1.71 | 3.81 | 4.32 | 4.65 | 1.3 | 3.2 |
| Surface tension, [N/m] *$10^{-3}$ | 25 | 33 | 44 | 28 | 22 | 26 |

Table 2. Breakup regimes and conditions (Local We numbers are the same amongst the tested fuels; minimum Re and Oh numbers in each regime are for E, the lowest viscosity fuel, while maximum values are for B4, the highest viscosity fuel)

| Breakup Regime | Bag | Bag | Multi-mode | Sheet Stripping | Catastrophic |
|---|---|---|---|---|---|
| Local We | 20 | 45 | 95 | 245 | 400 |
| Local Re | 700-950 | 1,050-1,400 | 1,520-2,050 | 2,480-3,300 | 3,100-4,200 |
| Oh | 0.018-0.047 | 0.018-0.047 | 0.018-0.047 | 0.018-0.047 | 0.018-0.047 |

## 3. Results and discussion

### 3.1 Breakup evolution

In this study, the liquid shapes arising from secondary atomization are well classified into three groups: small drops, ligaments, and unbroken objects based in their major characteristic dimension ($d_{max}$) and their aspect ratio (AR), the ratio between their major and minor characteristic dimensions ($d_{max}/d_{min}$). The categories are described as below:

- Small drop: $d_{max} < d_o$ and AR < 3
- Ligament: AR > 3, and
- Unbroken objects: $d_{max} > d_o$ and AR < 3, where $d_0$ is the parent droplet diameter.

As observed in this work, the small drops will not breakup again downstream, which is attributable to their small local Weber number, owing to (i) their small size and (ii) small relative liquid-air velocity. Therefore, this work will focus on examining the spatial gradient of area of ligaments and unbroken objects in each image, which is horizontally divided into 9 equal bins. This is done by taking the area of all fragments that are binned in a particular shape class (e.x ligaments) and using their geometric centroids to define a spatial bin. Since the bins are quite narrow (approximately 300 um in this work), the centroid of each bin is simply assumed as the axial location of all liquid shapes having their centroids appearing in the bin.

An example of the approach is given in Figure 2a and 2b for fuel B1 and We = 245. The area of ligaments, unbroken objects and the sum of those two

are plotted versus axial location for frame #1 (Figure 2a) and #2 (Figure 2b). The area is normalized by the parent droplet diameter, $d_o$. Although the image was divided into 9 bins, only 8 axial centroids shown for each image, as can be seen in Figures 2a and b, corresponding to those of bin #2 to bin #9, respectively. The first bin was left out from the processing to avoid the issue of shapes' morphology unexpectedly cut off by the left edge when they enter the image from the edge.

It is evident from Figure 2a that the area of ligaments and unbroken objects dramatically decreases in the first-haft of the frame #1, up to axial location of 275 pixel (approx. 2.15mm) in that frame (the location of arrow shown in Figure 2a). Then, the area levels off (from the arrow's location shown in Figure 2a and in whole Figure 2b). The arrow's location shown in Figure 2a could be a useful indicator for total breakup length of the parent droplets. The feasibility of this technique for breakup evolution including breakup length and breakup time will be investigated in detail in the following sections.

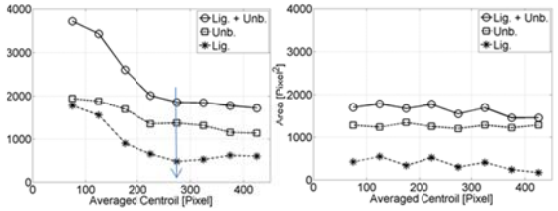


*a, Frame #1* *b, Frame #2*

*Fig 2. Area of unbroken objects and ligaments during catastrophic breakup (We = 400) of biodiesel B1 as a function of the liquid shapes' axial location*

## 3.2 Evolutions during bag breakup

The area of ligaments and unbroken objects is normalized by the area of parent droplet and plotted versus the bins' centroid in Figure 3a (for low viscosity fuels: D, B1 and E) and Figure 3b (for higher viscosity fuels: B2, B3 and B4). Both locations shown in these figures are at We = 20, which is a bag breakup mode.

Two steps, bag growing and fragment generation, in the breakup evolution are evident from these figures. These two steps are demonstrated by two arrows shown in each figure, the solid arrow represents the first step (bag growing) and the dotted one is following to show fragment-to-fragment generation when ligament and unbroken objects continue breaking up downstream to generate small drops. It is also evident from these figures that higher viscosity liquids (see Figure 3b) show their longer bag-growing durations than their counterparts (see figure 3a), however, at the end of the second step the area of these fragments are almost similar which may illustrate that the effect of fuel viscosity on atomization characteristics is minimal when breakup has ceased, even though some differences exist in the breakup evolution of liquids with different viscosity as discussed above.

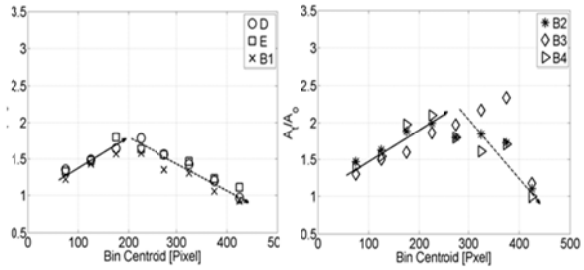


*a, Frame #1* *b, Frame #2*

*Fig 3. Normalized sum area of unbroken and ligament by initial droplet's area during bag breakup (We = 20) as a function of the*

## 3.3 Evolution of catastrophic breakup regime

Determination of catastrophic breakup evolution is quite difficult because the fragmentation processes happen rapidly and the mist formed by the wave crest stripping completely obscures the event [1]. The feasibility of the technique using the gradient of area used in previous section for bag breakup regime is tested here for catastrophic condition, We = 400.

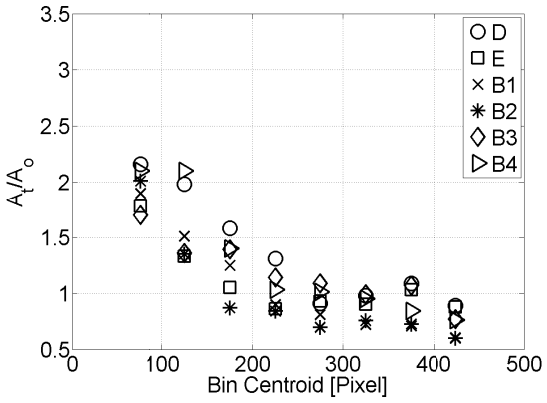


*Fig 4. Normalized sum area of unbroken and ligament by initial droplet's area during catastrophic breakup (We = 400) as a function of the liquid shapes' axial location (Frame #1)*

Similar to Figure 3, the normalized area of ligaments and unbroken objects is presented in Figure 4 but for We = 400. It is clear from Figure 4 that there is a small difference in the area of those fuels tested especially when the axial location exceeds 275 pixel in this image (corresponding to 2.15 mm). It is clear that only a decreasing area is observed in the trend prior to the axial location of 275 pixel where the area levels off, and this is unlike the case for bag break-up. In agreement with previous work [9], the small difference in the area amongst fuels tested demonstrates that the influence of liquid properties on atomization characteristics at high Weber number (such as We>200 in this study) is minimal.

### 3.4 Total breakup time

Along with dimensionless parameters including We and Oh, the non-dimensional time characteristic (T) of drop breakup by Rayleigh-Taylor and Kelvin-Helmholtz instabilities is commonly used for secondary atomization analysis and can be computed using the following equation:

$$T = t\frac{U_o}{d_o}.\frac{1}{\varepsilon^{0.5}} \quad (1)$$

where, t is the dimensional time, $U_o$ is the initial relative velocity of the drop and air, $d_o$ is the initial diameter of parent droplets, and ε is the density ratio of droplet and air.

In this current work, the dimensionless breakup time, $T_b$, will be estimated through the experimental breakup length, $L_b$, which is determined as in Figure 2, discussed in Sections 3.1 to 3.3. The relationship between $T_b$ and $L_b$ is given in Equation (2).

$$T_b = \frac{L_b}{d_o}.\frac{1}{\varepsilon^{0.5}} \quad (2)$$

Values of $T_b$ are plotted versus Weber number in Figure 5 for all of the liquids tested. It can be seen that the breakup times of D, E and B1 reach a peak at We = 45 before decreasing towards We=400. This agrees well with the report of Dai and Faeth [10], who noticed a local peak of breakup time near We=40. The local maximum of breakup time could be an important indicator for the transition of bag and sheet-thinning breakup regimes [2]. High viscosity fuels including B2, B3 and B4, however, show their slight decreases in their breakup time as We increases from 20 to 45 (see Figure 5). It is notable that the commonly used breakup time model by Pilch and Erdman [1] was qualitatively developed using very wide scattered data (see Figure 5 in their article [1]). The approach here may give a better quantitative capability of comparing the breakup time among different liquids.

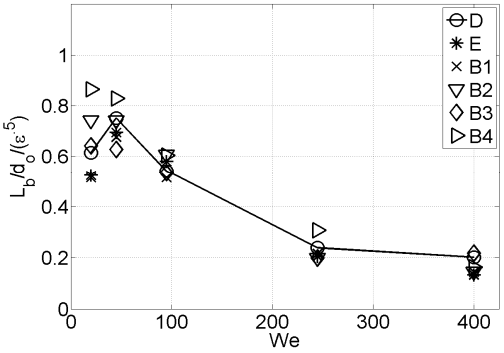


*Fig 5. Total dimensionless time as a function of Weber number*

The trend of breakup time shown in Fig. 5 matches well with that reported by Pilch and Erdman [1], albeit the values of breakup time are in one order of magnitude shorter than Pilch and Erdman's. The gap in the breakup time was also noted by other authors [1] and this could be due to the difference in definitions of the breakup length and/or in experimental methods used here and Pilch and Erdman's work. Pilch and Erdman [1] defined total breakup time as the time when the drop and all of its fragments no longer further breakup without further clarification. Our understanding of the total breakup time is similar to Pilch and Erdman's definition, however, the time is quantitatively measured using the spatial gradient of size or area of well-classified fragments (ligaments and unbroken objects) downstream. It was reported by Pilch and Erdman [1] that the difference in the data of breakup time available in literature is also in one order of magnitude. Regarding the experiment methods, difference in experimental systems leads to different types of aerodynamic forces acting the droplets which could also attribute to the difference in the breakup time measured amongst the different experiments. For example, shocktube (used by Pilch and Erdman) provides a nearly spatially uniform step change in relative velocity while an air-cross stream (used in this work) has a shearing effect. The parent droplets in the latter experimental method also experience turbulence in shear layer in the air-cross stream system, and this may result in a shorter breakup time. Therefore, this quantitative methodology may assist in isolating critical parameters which dictate the atomization process.

## 4. Conclusion

A new approach in characterizing secondary atomization characteristics for different fuels has been developed. The breakup length and breakup time of parent droplets are quantified using the spatial gradient of total area of ligaments and unbroken objects. The quantitative information may be useful for improving secondary breakup models.

## 5. Acknowledgement

This research is supported by the Australian Research Council.

## 6. References

[1] M. Pilch and C. A. Erdman, Int J Multiphase Flow 13(6) (1987), pp. 741–757

[2] D. R. Guildenbecher, C. Lo´pez-Rivera, and P. E. Sojka, Exp Fluids 46 (2009), pp. 371–402

[3] A. Kourmatzis, P. X. Pham, and A. R. Masri, Combustion and Flames 162(4) (2015), pp. 978-996.

[4] A. Kourmatzis, P. X. Pham, and A. R. Masri, Fuels, 108 (2013), pp. 758-777

[5] L. P. Hiang and G. M. Faeth, Int. J. Multiphase Flow 18(5) (1992), pp. 635-652

[6] B. E. Gelfand, Prog. Energy Combust. Sci. 22(1996), 201-265

[7] P. D. Patel and T. G. Theofannous, J. Fluid Mech. 103 (1980), pp. 207-223

[8] W. H. Chou and G. M. Faeth, Int. J. of Multiphase Flow 24 (1998), pp. 889-912

[9] P. X. Pham, PhD Thesis (2015), The Uni. Of Sydney

[10] Z. Dai and G. M. Faeth, Int. J. Multiphase Flow 27 (2001), pp. 217-236

# The effect of radiation heat transfer under ECN Spray A conditions

M. A. Chishty[1, *], M. Bolla[1], E. R. Hawkes[1, 3], Y. Pei[2], and S. Kook[1]
[1]School of Mechanical and Manufacturing Engineering
University of New South Wales NSW 2055 Australia
[2]Energy System Division, Argonne National Laboratory, IL, 60439, USA
[3]School of Photovoltaic and Renewable Energy Engineering
University of New South Wales NSW 2055 Australia

## Abstract

This article examines the effect of radiation in a model of a canonical diesel spray flame known as Spray A. In spray A, liquid *n*-dodecane spray was injected with 1500 bar fuel pressure into a constant volume chamber at temperature, oxygen mole fraction and density of 900K, 15% and 22.8 kg/m$^3$, respectively. The unsteady Reynolds-averaged Navier-Strokes (RANS) model equations coupled with a reduced 53 species *n*-dodecane chemical mechanism and a two-equation soot model are solved. The effect of radiation has been introduced using three different radiation models (spherical-harmonics and discrete ordinate method) along with the optically thin (i.e. emission only, no absorption) assumption and results are compared with the case without radiation. At Spray A conditions the contribution of gas phase radiation (mainly from $CO_2$ and $H_2O$) is more dominant than the soot radiation. Moreover, the effect of radiation absorption is found to be important and a moderate influence on the temperature distribution of the order of 10-20K at the most in the fuel lean region has been noticed. The radiative emission rate is similar for all three radiation models. However, the higher absorption rate has been noticed for the DOM model in comparison with the P1 model. The flame lift-off length is not affected by the radiation and differences in the soot formation are perceivable but only minor. The performance of the DOM and P1 models is comparable, whereas the optically thin assumption leads to a higher cooling effect.

*Keywords: Engine Combustion Network, Spray A, Radiation modelling, Spray combustion, Discrete Ordinate Method, Soot modelling.*

## Nomenclature

ECN= Engine Combustion Network
RTE = Radiative Transfer Equation
TRI = Turbulence Radiation Interaction
TCI = Turbulence Chemistry Interaction
$Y_s$ = Soot mass fraction
$N_s$ = Particle number density
ISAT = In-Situ Adaptive Tabulation
$S_{qrad}$= Radiation source term
$\alpha_{total}$ = Total absorption coefficient (m$^{-1}$)
G = Radiation Intensity (Wm$^{-2}$)
$\sigma$ = Stefan-Boltzmann const. $5.67\times10^{-8}$ W m$^{-2}$ K$^{-4}$
$fv_{soot}$ = Soot volume fraction (ppm)
$\alpha_{soot}$ = Soot absorption coefficient (m$^{-1}$)
$T_{rate}$ = Temperature rate of change (Ks$^{-1}$)
$T_{No\ Rad.}$ = Temperature without radiation (K)
$T_{Rad.}$. = Temperature with radiation (K)
$\Delta T = T_{Rad.} - T_{No\ Rad.}$ (K)

## 1. Introduction

Radiative heat transfer is an important phenomenon which plays a significant role in the overall heat transfer prediction in the majority of the combustion applications such as flames, gas combustors, industrial furnaces and fires [1]. Radiative heat transfer has been ignored in many applications which can result in severe over-predictions of the temperature and hence may affect the species distribution [2]. The combined effects of temperature fluctuations and absorption coefficient can increase the radiative fluxes up to 2-3 times based on the mean properties [3]. Radiation can account for 50% of the total heat loss in very large bore, heavy duty diesel engines [4]. In case of pollutant modelling, the soot radiation is non-linearly coupled to soot formation/oxidation processes and in a heavy-duty diesel engines this can affect the peak temperature of the flame by 20-25K as well as having an impact on the formation of nitric oxide ($NO_x$) and other pollutants by 12-25% [5]. Therefore, it is important at a minimum understand, and possibly to account for, radiation for the accurate calculation of temperature, heat transfer rates and pollutant emissions in turbulent flames [6].

Various challenges occur in the modelling of chemically reacting turbulent flows such as turbulence, chemistry and turbulence-chemistry interactions (TCI) and by considering radiation three new difficulties are introduced. First, the absorption coefficient has a strong dependence on the wavelength of participating gas-phase species (specifically $CO_2$, $H_2O$, CO and $CH_4$) and additional issues arise when soot is considered. Second, the structure of the radiative transfer equation (RTE) is a high order integro-differential equation and the direct solution using finite volumes or finite differences is not efficient and therefore special approaches are required, such as the Monte Carlo method [7, 8]. And third, unresolved turbulent fluctuations in temperature and composition lead to nonlinear interactions between turbulence and radiation, which can considerably

* Corresponding author:
Phone: (+61) 416470867
Email: m.chishty@unsw.edu.au

increase the radiative emissions [9, 10]. There are only few studies reported for radiation heat transfer modelling in diesel engines, e.g. [4, 11-16]. In this paper, an initial attempt to investigate the role of radiation under the ECN Spray A conditions is presented. This choice is made because this flame has been extensively measured and the conditions are very relevant to modern heavy-duty engines. The nominal Spray A condition is considered, namely the ambient temperature, density and oxygen volume fraction are 900K, 22.8 kg/m$^3$ and 15%, respectively. The objective of this paper is to analyse the relative contributions to the Planck mean absorption coefficient and to radiation heat transfer from major gas-phase species as well as from soot.

# 2. Numerical Methodology

## 2.1 Numerical setup

Numerical simulations have been conducted on ANSYS FLUENT 14.5 finite volume based CFD commercial code. The unsteady Reynolds Navier Strokes (RANS) equations have been solved and the realizable k-ε model has been used for the turbulence modelling. Liquid n-dodecane is injected at a pressure of 1500 bar and the spray is modelled using the Lagrangian discrete phase approach. A similar case setup has been employed to that which has been used in our previous case studies [17, 18].

A reduced 53 species *n*-dodecane chemical mechanism [19] with an improved ignition delay prediction compared with previous mechanisms has been employed in conjunction with the two-equation soot model by Leung et al. [20]. The transport equation of soot mass fraction ($Y_s$) and particle number density ($N_s$) are solved and acetylene is used as a soot precursor. This soot model has been successfully applied for Spray A by the same authors in Ref. [21] and more information can be found in Ref. [22]. The unresolved turbulent fluctuations of the thermochemical state have been neglected, assuming each cell in the CFD domain is approximated as "well-mixed". Generally, the well-mixed model is able to predict the qualitative trends of general combustion indicators like the ignition delay and flame lift-off length. This approach neglects TRI, which will be considered in future work.

## 2.2 Radiation modelling

Three different solvers for the RTE have been employed: the discrete ordinate method (DOM), the spherical-harmonics method (P1 method) and the optically thin assumption. The radiation source term, $S_{qrad}$, is computed as:

$$S_{qrad} = \alpha_{total}\,(4\sigma T^4 - G) \quad (3)$$

where the first and second terms on the right hand side are the radiation emission and absorption, respectively. Radiative properties are considered to be grey. The total Planck mean absorption coefficient ($\alpha_{total}$) includes the effect of soot particles as $\alpha_{soot} = 2370 \times f v_{soot} \times T$ [23] as well as major gas-phase species ($CO_2$, $H_2O$, $CH_4$ and CO) as function of temperature and their respective mass fractions following Ref. [24]. For the optically thin method, the radiation absorption is neglected and there is no need to solve the RTE. For the DOM [25] RTE is solved for a finite number of solid angles – the angular discretization used here is 4x4, resulting into 64 directions solved. Radiation scattering has been neglected. The P1 method [26] is based on the expansion of the radiation intensity into an orthogonal series of spherical harmonics, resulting in a transport equation for incident radiation, G. Further details can be found in the Fluent theory guide [27].

# 3. Results and Discussion

This section is divided into two parts: first, the flame structure is presented along with radiation-relevant quantities as the mean absorption coefficient. Second, simulation results for three different radiation models are compared in terms radiation source term and the corresponding impact on the temperature field.

The flame penetration length, ignition delay, lift-off length and soot peak location are validated in our previous study [21]. The flame lift-off length is not affected by the radiation and differences in the soot formation are perceivable but only minor.

Figure 1 shows the spatial distributions of the three most relevant species (soot, $CO_2$ and $H_2O$) contributing to radiation and their corresponding Planck mean absorption coefficients at 4 ms after start of injection – during the quasi-steady period of the lifted spray flame. The black line represents the stoichiometric mixture fraction.

The soot is confined in the fuel-rich region and is completely oxidised outside the stoichiometric line. The peak soot volume fraction is around 8 ppm and the maximal absorption coefficient is 35 m$^{-1}$. The spatial extent of soot radiation emission and absorption is limited within the fuel rich region.

A different picture is observed for $CO_2$ and $H_2O$. The maximal $CO_2$ mass fraction is found at around stoichiometric conditions. At fuel-rich conditions, high equilibrium values of CO rather than $CO_2$ are present. On the other hand, $H_2O$ shows a more homogeneous distribution of the high concentration within the entire fuel-rich cross-section. Soot absorption is more dominant inside the flame, while the gas phase radiation effects are more important in the fuel lean region because of the temperature dependence on absorption coefficient which is higher for colder region. The peak magnitude of $\alpha_{CO2}$ is 3.75 times higher, while $\alpha_{H2O}$ is 1.3 times lower in comparison with $\alpha_{soot}$. The radiation effects of gas-phase species are more important than the soot radiation at Spray A conditions. It is important to note that the high concentration of $CO_2$ and $H_2O$ in the ambient gas results from the premixed combustion to obtain the target pressure and temperature before the start of injection. This leads to an increase of the optical thickness and to a more prominent role of gas phase radiation.

As simulation results using the DOM and the P1 models are similar, Fig. 2 shows only the spatial distributions of the DOM model. From left to right, temperature and its difference with the case without radiation ($\Delta T = T_{Rad.} - T_{No\ Rad.}$), radiative emission and absorption rate, radiation source term (defined with sign positive for a heat loss) and the rate of temperature

change induced by radiation ($T_{rate}=S_{qrad}/(\rho c_p)$). The temperature contour shows the overall spread of the flame. The effect of radiation as an energy coupling can be noticed in the ΔT iso-contour.

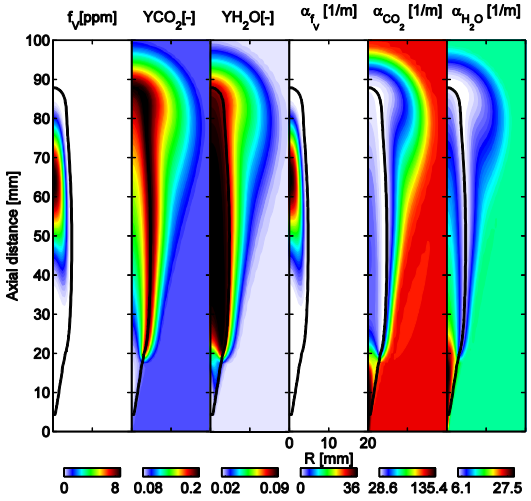


Figure 1: Spatial distribution of flame structure quantities at 4 ms. From left to right: $fv_{soot}$, mass fraction of $CO_2$, $H_2O$ and their respective mean absorption coefficients, respectively. Black iso-lines denote the stoichiometric mixture fraction.

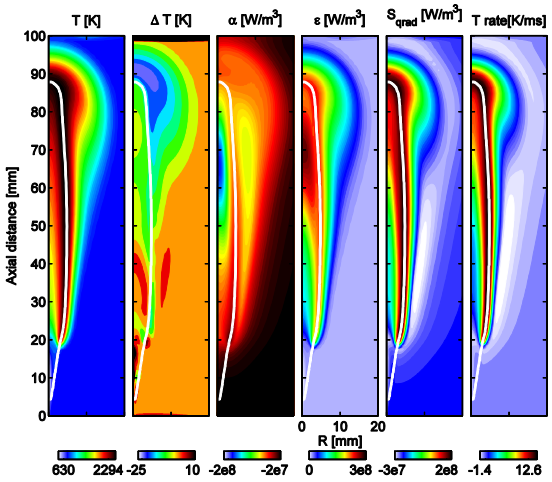


Figure 2: Spatial distribution of temperature, temperature difference, radiative absorption, emission, source term and temperature rate of change at 4 ms for DOM model. White iso-lines denote the stoichiometric mixture fraction.

The maximal difference in temperature is around 20K at the head of the jet on the fuel lean side. This difference in temperature can have a significant influence on the rate of $NO_x$ formation [6], which is formed in this region. On the fuel rich side the difference in temperature is smaller (around 5-10 K) and the difference in soot formation rate is minor. A very high absorption rate has been observed at the soot peak location, while the peak emission rate location is axially shifted 5 mm downstream. The peak value $S_{qrad}$ and $T_{rate}$ is along the stoichiometric line in concomitance with highest temperatures.

This study has neglected the influences of unresolved turbulent fluctuations in temperature and composition space, neglecting the interaction between turbulence and radiation, which can further enhance the radiative emission [10]. The temperature rate distribution shows the characteristic cooling rate in [K/ms] to provide a useful measure for the effect of radiation on the local temperature and thus assess whether turbulent fluctuations could be important. The temperature rate of change is the order of around 10 K/ms, consistent in order of magnitude with ~20K temperature change for this 4 ms injection duration. Considering turbulence timescales should be significantly shorter than the injection duration; this suggests the inclusion of fluctuations is probably not important. It is important to note however that the residence time plays a major role for radiation and for the case of Spray A (typical for automotive-size diesel engines) the characteristic time scale is of the order of a couple of milliseconds while it becomes considerably longer for larger heavy-duty and marine diesel engines. Therefore, the role of radiation and turbulence-radiation interactions is expected to become more prominent for larger engines.

Figure 3 shows the radial distribution of different radiation-relevant quantities at 60 mm axially from the injector at 4 ms for the three different radiation models. The first row from left to right represents the temperature difference with respect to the case without radiation, emission rate and absorption rate, respectively. While the second row shows the net radiation source term, ratio of absorption rate to emission rate and temperature rate of change, respectively.

The effect of radiation absorption is found to be important and a moderate influence on the temperature distribution of the order of 10K at the most in the fuel lean region has been noticed in the temperature difference plot. The performance of the DOM and P1 models is comparable, whereas the optically thin assumption leads to a higher cooling effect - as expected – because of the absence of radiation absorption. The emission rate is similar for all three radiation models, as the same radiative properties have been employed. However, the higher absorption rate is observed for the DOM model in comparison with the P1 model. The $T_{rate}$ gives the characteristic cooling rate and similar profiles are observed as that of the radiation source term. The main differences between P1 and DOM are in the first 5 mm radially and later both are cooled at the same rate.

## 4. Conclusion

The effect of radiative heat transfer under ECN Spray-A conditions has been studied numerically using three different radiation models: the discrete ordinate method (DOM), the spherical-harmonics method (P1 method) and the optically thin assumption. It has been noticed that at Spray-A conditions the contribution of gas phase radiation (mainly from $CO_2$ and $H_2O$) is more dominant than the soot radiation. This is partly the result of the pre-burn constant-volume chamber operation leading to elevated concentrations of $CO_2$ and $H_2O$ in the ambient gas composition. Moreover, the effect of radiation absorption is found to be important and a moderate influence on the temperature distribution of the order of

10-20K at the most in the fuel lean region has been found, having a potential influence on $NO_x$ formation. The results from the DOM and P1 models are comparable, whereas the optically thin assumption leads to a higher cooling effect. The emission rate is similar for all three radiation models. However, a somewhat higher absorption rate has been observed for the DOM model compared to the P1 model. The flame lift-off length is not affected by radiation and differences in the soot formation are perceivable but only minor. The effects of turbulence-chemistry interaction (TCI) as well as turbulence-radiation interaction (TRI) are in progress and will be included in future studies.

## 5. Acknowledgments

The research was supported by the Australian Research Council (ARC) and by the United States Navy. Muhammad Aqib Chishty acknowledges the support of University of New South Wales, Sydney, Australia via University International Postgraduate Award. The authors would also like to acknowledge the computational support of the Australian NCI National Facility, the partner share of the NCI facility provided by Intersect Australia Pty Ltd., the UNSW Faculty of Engineering and iVEC (Western Australia).

## References

[1] M. F. Modest, Radiative Heat Transfer, Academic Press, 2003, pp. 503.
[2] R. Yadav, A. Kushari, A. K. Verma and V. Eswaran, Numer. Heat Trasnfer, Part B, **64** (2) (2013), pp. 174-197.
[3] T. H. Song and R. Viskanta, J. Thermophys Heat Transfer, **1** (1) (1987), pp. 56-62.
[4] G. Borman and K. Nishiwaki, Prog. Energy Combust. Sci., **13** (1) (1987), pp. 1-46.
[5] M. Musculus, SAE Technical Paper No. 2005-01-0925, 2005.
[6] L. Wang, D. C. Haworth, S. R. Turns and M. F. Modest, Combust. Flame, **141** (1–2) (2005), pp. 170-179.
[7] R. S. Mehta, D. C. Haworth and M. F. Modest, Combust. Flame, **157** (5) (2010), pp. 982-994.
[8] A. Gupta, D. C. Haworth and M. F. Modest, Proc. Combust. Inst., **34** (1) (2013), pp. 1281-1288.
[9] D. C. Haworth, Prog. Energy Combust. Sci., **36** (2) (2010), pp. 168-259.
[10] P. J. Coelho, Prog. Energy Combust. Sci., **33** (4) (2007), pp. 311-383.
[11] T. Yoshikawa and R. D. Reitz, J. Therm. Sci. Technol., **4** (1) (2009), pp. 86-97.
[12] J. Wiedenhoefer and R. Reitz, SAE Technical Paper No. 2003-01- 0560, 2003.
[13] R. Houshiar and C. Najafi, SAE Technical Paper No. 2006-01-1386, 2006.
[14] S. Skeen, J. Manin, L. Pickett, K. Dalen and A. Ivarsson, SAE Technical Paper No. 2014-01-1252, 2014.
[15] D. C. Haworth, S. P. Roy, J. Cai, A. Sircar, A. Imren and M. F. Modest, International Multidimensional Engine Modeling User's Group Meeting at the SAE Congress, Detroit, MI, US, 2015.
[16] J. Abraham and V. Magi, Numerical Heat Transfer, Part A: Applications, **31** (6) (1997), pp. 597-610.
[17] Y. Pei, E. R. Hawkes, S. Kook, G. M. Goldin and T. Lu, Combust. Flame, **162** (5) (2015), pp. 2006-2019.
[18] M. A. Chishty, M. Bolla, Y. Pei, E. R. Hawkes and S. Kook, 10th Asia-Pacific Conference on Combustion, Paper No. 124, Beijing, China, 2015.
[19] T. Yao, Y. Pei, B.-J. Zhong, S. Som and T. Lu, 9th U.S. National Combustion Meeting, Paper No. 1C02, Cincinnati, Ohio, 2015.
[20] K. M. Leung, R. P. Lindstedt and W. P. Jones, Combust. Flame, **87** (3–4) (1991), pp. 289-305.
[21] M. A. Chishty, M. Bolla, Y. Pei, E. R. Hawkes, S. Kook and T. Lu, SAE Technical Paper No. 2015-01-1849, 2015.
[22] M. Bolla, Y. M. Wright, K. Boulouchos, G. Borghesi and E. Mastorakos, Combust. Sci. Technol., **185** (5) (2012), pp. 766-793.
[23] J. F. Widmann, Combust. Sci. Technol., **175** (12) (2003), pp. 2299-2308.
[24] R. S. Barlow, A. N. Karpetis, J. H. Frank and J. Y. Chen, Combust. Flame, **127** (3) (2001), pp. 2102-2118.
[25] E. H. Chui and G. D. Raithby, Numer. Heat Trasnfer, Part B, **23** (3) (1993), pp. 269-288.
[26] P. Cheng, AIAA Journal, **2** (9) (1964), pp. 1662-1664.
[27] ANSYS FLUENT 14.5 Theory Guide, ANSYS Inc., USA, 2012.

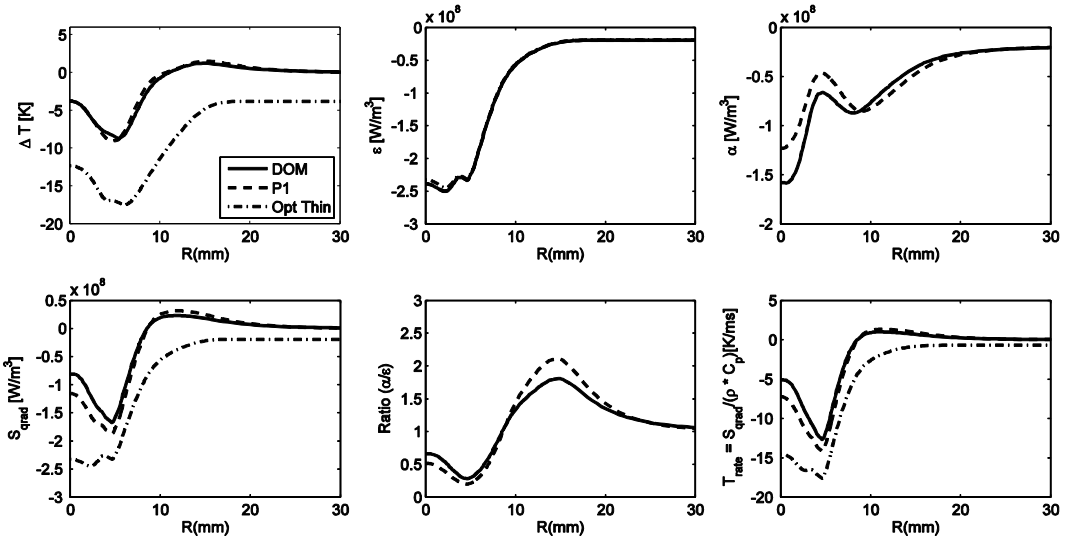


Figure 3: Radial distribution of different radiation relevant quantities at 60 mm axially from the injector at 4 ms for three different radiation models: DOM (solid lines), P1 (dashed lines) and optically thin assumption (dashed-dotted lines).

# Effect of Impinging Angle on Non-Evaporative Diesel Wall-Jet

M.H. Jayed[1, *], J. Soria D.R. Honnery,
[1]Laboratory for Turbulence Research in Aerospace and Combustion (LTRAC),
Department of Mechanical and Aerospace Engineering, Monash University,
Clayton, VIC 3800, Australia

## Abstract

This paper presents an experimental study on the wall-impinging diesel spray issued from a single-hole nozzle. To examine the effect of impingement angle on spray-wall interaction, repeated non-evaporative diesel spray is injected at 150 MPa pressure and impinged on a wet flat steel plate placed at a characteristic length where spray reaches peak velocity in the pressure chamber at 5 MPa in ambient temperature. The flow regimes resulting from the impact is closely observed by an ultra-high-speed camera. It is found that, spray-wall impact causes a huge loss of kinetic energy and reduces wall-jet penetration distance over the wall compared to free-jet. Wall-jet velocity slows down as a decaying turbulent jet as it travels further from the impinging point entraining more air and getting effected by growing aerodynamic drag. Compared to normally impinging sprays, wall-jet produced by higher impinging angle travels faster and breaks up its dense zones by diffusing easily into chamber. A new empirical formula is developed to express temporal evolution of radial wall-jets considering pressure gradient of issued spray, incident angle on solid wet plate and impingement distance.

*Keywords: impingement, wall-jet, impinging distance, injection pressure, impinging angle, diesel spray.*

## Nomenclature

$\delta P$ Pressure difference between injection pressure and chamber back pressure (Pa)
$\rho_a$ Air density at chamber pressure (kg/m$^3$)
$X_p$ impingement distance (mm)
$\theta$ impingement angle (degree)
$t_i$ Time after impingement (ms)
t Time after start of injection (SOI) (ms)

## 1. Introduction

In a small high speed direct injection diesel engine, the impingement of spray on to the piston cavity cannot be avoided because of the short distance between the nozzle tip and wall. So, predicting impingement spray behaviour is very important for understanding and simulating diesel combustion to develop cleaner fuel-economic diesel vehicles. Due to insufficient technological advancement in experimentation, initial attempts of diesel combustion descriptions were based on free turbulent jet relying on free jet theory. Donaldson and Snedeker [1] tested free air jet issuing from a converging nozzle on a flat circular plate. They described three different flow regimes on impinging jet: These free jet descriptions on different zones of spray combustion continued long after advanced measuring technique had been developed. Adding two more regimes Weclas and Cypris [2] described impinging diesel jet in five regions as shown in figure 1.

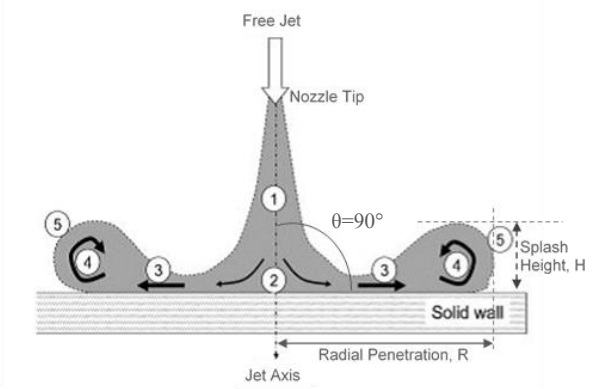


**Fig 1. Basic geometry of impinged spray on a solid wall: 1- free jet region; 2- impingement region; 3-main wall–jet region; 4- wall-jet vortex region; 5 – leading edge [2].**

Most impinging jet models [3-5] used experimental results of non-reacting jets, especially single drop models. Whereas, some studies [6-9] are reported on combusting or reacting droplets. Apart from great detail of work venturing into estimating spray impaction phenomena by splash pattern of single droplet and its atomization on wet and dry wall, there are heat transfer models of spray-wall based on droplet properties like velocity [10], volume flux [11] and mass flux [12]. But such models are not found consistent with experimental results of fuel spray impinging on solid surface as multiple drop interaction and dense spray cores effect on heat transfer are not considered in single drop analysis. So, better understanding of spray break-up and mixing is necessary for numerical modelling and complex engine design. Moreira et al. [13] critically reviewed this approach finding that it fails to accurately describe quantitatively many of the complex phenomena occurring in impinging dense spray. In order to gather adequate information on highly transient nature of the

* Corresponding author:
Phone: (+61) 426064080
Email: md.hussan@monash.edu

diesel spray impingement phenomena sufficient to enable models to be improved, and also improve our understanding of these complex flows, a wider range of experimental study is required in engine-like conditions.

There are many factors affecting spray impingement, these include, the type of nozzle used, chamber and injection pressure, impingement plate standoff distance and angle, and the plate wetting [14, 15]. Here, some of this parameters are neutralized in this study by using an injector with fixed nozzle geometry and impinging all sprays on same steel wall inside a chamber pressurized at 50bar. Impingement plate stand-off distance is fixed a single location corresponding to the point at which the impingement spray leading edge reaches its maximum velocity as this has been shown to be an important scaling parameter in free sprays. Impingement plate angle is varied, with three angles considered.

Measurements are limited to a number of important macroscopic properties of the spray, including leading edge penetration and velocity, and wall spray splash height. Penetration is compared to a number of the existing models, leading to the development of a new empirically based model.

## 2. Experimental Set-up

The experimental set up is discussed in detail in [16, 17]. A common rail injection system was used to inject a highly turbulent diesel spray at 150 MPa an air filled 5 MPa pressurized chamber. Spray images were captured by an ultra-high-speed digital camera (Shimadzu Hyper Vision, HPV-1) at 250 kfps and 125kfps in free-jet and impingement test respectively, at a fixed resolution of 312 pixels by 260 pixels. The CCD exposer duration was controlled by frame rate. The spray video is divided into 102 frames. The scaling factor of the image was 15pixel/mm. Image processing involves image noise reduction and analysis by the Canny algorithm to detect the spray edge. The spray edge is used to define the penetration of the spray in the axial direction before impingement (free spray), and in the radial direction after impingement (wall spray). The instant the free jet impacts the plate is used to set the wall jet time zero and wall jet (radial) penetration is measured from the point of impaction (centreline of the free jet, Fig. 1). A flat, round plate of 50 mm diameter is used for impingement. Since each experimental condition examined consist of many spray events, the data presented is for a wetted plate

### 2.1 Experimental conditions

Standard Australian automotive diesel fuel with density 830 kg/m$^3$ was injected into quiescent air at a temperature of approximately 20°C. A heat exchanger is used to maintain the pressurized fuel temperature below 30°C as it circulates in the closed loop high pressure system. Fuel injection duration is kept at 0.6 ms in all spray events. The common rail delivered fuel pressure fluctuates~ 0.5 MPa of the set value. A Bosch diesel injector was used operating with a nozzle with a single hole of 0.15mm in diameter. The opening pressure is 22 MPa. Three different impingement angles are created by tilting the flat plate 10° and 20° from normal impinging position as shown in fig. 1 and cases are presented in table 1.

## 3. Results and discussion

3.1 Determining impinging distance, $X_p$

Kostas et al. [15, 16] has shown that the penetration corresponding to the maximum leading edge is an important scaling parameter in free spray penetration. Near field penetration of the spray is dominated initially by the injector opening process (needle lift), which typically takes less than 50μs. During this process, and depending on the injection pressure, the starting vortex of the spray interacts with the high pressure chamber air to give rise to a maximum velocity of the leading edge of the spray, after which edge velocity decreases. Velocity is determined by differentiating the leading edge penetration. For 150 MPa injection pressure used here, the averaged spray tip reaches a peak velocity of 199.4 m/s after traveling 7.3 mm down from the nozzle tip ( fig. 2). The impingement plate is set to this distance for the impinged spray tests.

Also shown in Fig. 2 is the root mean square of the edge velocity relative to the mean penetration velocity. As the edge detection method used is pixel accurate, as the edge slows, frame to frame movement drops and chances of error in locating the edge increases. There is also greater shot to shot variation as the edge moves farther from the nozzle as large scale turbulent mixing starts to dominate the structure of the edge. To limit the resulting uncertainty, each condition consists of 200 individual injection events.

**Table 1. Experiment design**

| Case | Injection Pressure (MPa) | Impingement angle (degree) |
|---|---|---|
| Flat | 150 | 90 |
| 10 Plate | 150 | 100 |
| 20 Plate | 150 | 110 |

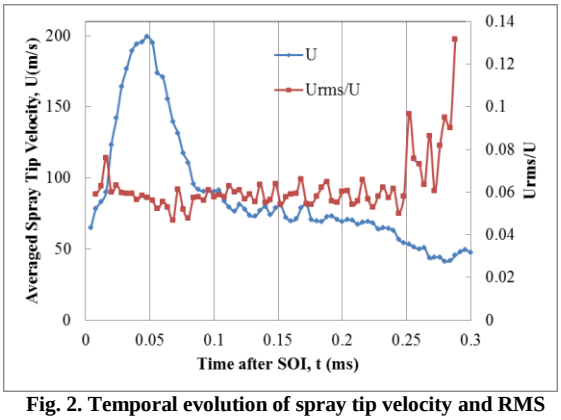


**Fig. 2. Temporal evolution of spray tip velocity and RMS velocity/velocity for 150 MPa injections. The times are relative to SOI (i. e. t = 0).**

3.2. Wall-spray penetration

Wall spray penetration over a wet flat plate changes at different impinging angle. As shown in fig. 3, the spray leading edge after 0.1ms of impingement has travelled further for higher impinging angle in 20° inclined plate than normally impinged one. The momentum of the

leading edge is much higher for 20° inclined plate than sprays impinged at lower angles.

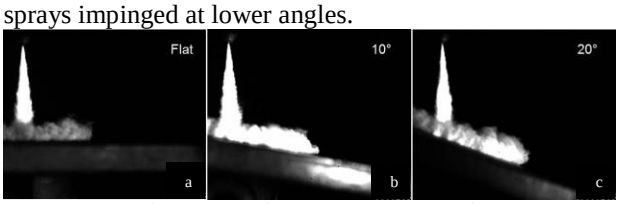


**Fig. 3. Spray after 0.1ms of impingement on a) flat (θ =90°), b) 10Plate (θ =100°) and c) 20Plate (θ =110°).**

Figure 4 shows the radial penetration (R) and splash height (H) of wall-sprays for three different plate inclination angles. Results show that the normally impinged spray has the highest splash height and lowest radial penetration. Splash height is lowest and radial penetration highest for the 20° inclined plate.

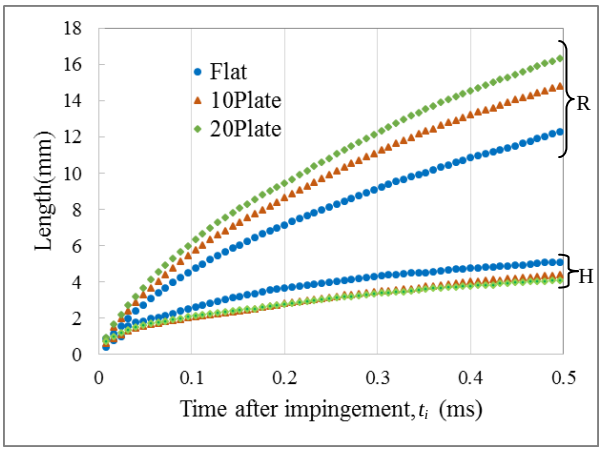


**Fig. 4. Wall-spray radial penetration (R) and splash height (H) on flat (θ =90°), 10Plate (θ =100°) and 20Plate (θ =110°).**

As many empirical models [18, 19] of wall impingement penetration are based on modification of free spray penetration, it is interesting to compare impinged spray with the free spray case in same condition as shown Fig. 5. For the free spray, penetration is axial penetration relative to the stand-off distance $X_p$. Several observations can be made from this figure. Wall sprays have lower penetration than the free spray case and they all appear to have a similar scaling with time from impact.

Kostas et al. [16] showed that penetration for the free spray consists of three separate phases, each of which has a separate scaling relationship. For the wall sprays here, two separate phases are present, a near impingement phase and are far impingement phase. Scaling with time in the near field is found to be propotional to $t^{0.65}$, while for the far field $t^{0.5}$. Ebara et al. [20] found diesel wall-spray penetration to grow linearly with time in the near field as shown below,

$R=A' t_i$ , for near nozzle field

$R= A' t_i^{0.5}$, for far field

$A'= F_1L_w +F_2 \theta +F_3L_w \theta +F_4$

Here, $F_1$, $F_2$, $F_3$, $F_4$ are co-efficient for test nozzle, $L_w$ is the impingement distance.

An attempt to fit the Ebara derived empirical model to the data here for the 90° impingement is shown in fig. 6. As to be expected given the differences in scaling, the model shows limited agreement to the measured data. Using the scaling found here, a new empirical model is introduced to express penetration R (mm) at different impingement angles variation and the effect of pressure difference between injection pressure and chamber back pressure, impinging angle and distance.

Wall-spray penetration is given by,

$R= A\, t_i^{0.65}$, for near nozzle field, $0<t_i<0.25$

$R=A\, t_i^{0.5}$, at far field, $t_i>0.25$

The scaling constant is given by

$A= k_1 (\delta P/\rho_a)^c d_o \theta$ (rad) + $k_2 \sin\theta + k_3 X_p$

Here, $\delta P$ is the pressure drop across the nozzle (Pa), $\rho_a$ the chamber density (kg/m$^3$), $d_o$ the nozzle diameter (m) and θ. c is the coefficient for near nozzle field (c=0.65) and far field (c=0.5). For the near field the values for $k_1$, $k_2$ and $k_3$ are 19.686, 135.123 and -24.604. Whereas, for far field, the values for $k_1$, $k_2$ and $k_3$ is 104.817, 43.553 and -8.887, respectively.

The fit to the experimental data is shown in Fig. 6. While highly empirical, this model demonstrates the complexity of the parameter space controlling the spray impingement process. However, this type of empirical models useful in thermodynamic engine models.

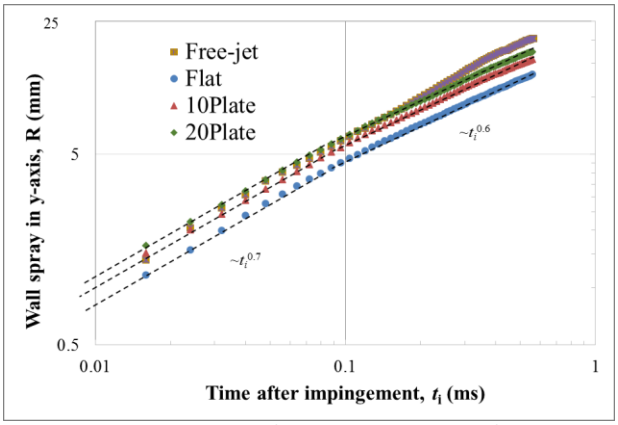


**Fig. 5. Temporal evolution of spray tip penetration of diesel wall-jet and free- jet from impingement.**

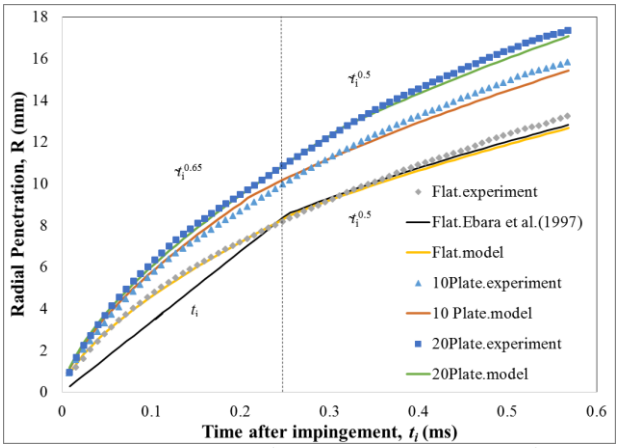


**Fig. 6. Comparison of wall-jet penetration curves for 150 MPa injection pressure between new empirical formula predictions with Ebara et al. [20] model and experimental measurements.**

## 4. Conclusions

A series of experiments has been undertaken to examine the complex interaction of a high pressure diesel spray with a flat wall set at different inclination angles. These new experimental data plays a vital role in development and improving models by providing insights of wall-jet macroscopic properties. Wall sprays are found to penetrate slower than an equivalent free spray. Scaling is shown to be similar in time for the leading edge penetration for the three wall spray cases examined, with two penetration phases found, which gives rise to a near are far field scaling. Based on this scaling, an empirical fit to the experimental data was developed to account for the controlling parameter space (injection pressure, chamber pressure, nozzle diameter and plate inclination angle). While highly empirical, this model demonstrates the complexity of the parameter space controlling the spray impingement process. Further experiments are planned to test and extend this to different chamber and injection pressures.

## 4. Acknowledgments

Authors would like to acknowledge the funding support from the Australian Research Council.

## 5. References

[1] Donaldson, C. D. & Snedeker, R. S. 1971. A study of free jet impingement. Part 1. Mean properties of free and impinging jets. *Journal of Fluid Mechanics,* 45**,** 281-319.

[2] Weclas, M. & Cypris, J. 2010. Role of jet core in splashing patterns of diesel jet impingement on a solid wall. *International Journal of Engine Research,* 11**,** 29-46.

[3] Bai, C. & Gosman, A. 1995. Development of Methodology for Spray Impingement Simulation. *International Congress & Exposition, Detroit, Paper no. 950283.* Michigan, United States: SAE.

[4] Cossali, G., Coghe, A. & Marengo, M. 1997. The impact of a single drop on a wetted solid surface. *Experiments in fluids,* 22**,** 463-472.

[5] Rioboo, R., Tropea, C. & Marengo, M. 2001. Outcomes from a drop impact on solid surfaces. *Atomization and Sprays,* 11.

[6] Burgoyne, J. & Cohen, L. 1954. The effect of drop size on flame propagation in liquid aerosols. *Proceedings of the Royal Society of London. Series A. Mathematical and Physical Sciences,* 225**,** 375-392.

[7] Chigier, N. & Mccreath, C. 1974. Combustion of droplets in sprays. *Acta Astronautica,* 1**,** 687-710.

[8] Godsave, G. Studies of the combustion of drops in a fuel spray—the burning of single drops of fuel. Symposium (International) on Combustion, 1953. Elsevier, 818-830.

[9] Sirignano, W. A. 1983. Fuel droplet vaporization and spray combustion theory. *Progress in Energy and Combustion Science,* 9**,** 291-322.

[10] Arcoumanis, C. & Chang, J.-C. 1993. Heat transfer between a heated plate and an impinging transient diesel spray. *Experiments in fluids,* 16**,** 105-119.

[11] Estes, K. A. & Mudawar, I. 1995. Correlation of Sauter mean diameter and critical heat flux for spray cooling of small surfaces. *International Journal of Heat and Mass Transfer,* 38**,** 2985-2996.

[12] Sawyer, M., Jeter, S. & Abdel-Khalik, S. 1997. A critical heat flux correlation for droplet impact cooling. *International Journal of Heat and Mass Transfer,* 40**,** 2123-2131.

[13] Moreira, A. L. N., Moita, A. S. & Panão, M. R. 2010. Advances and challenges in explaining fuel spray impingement: How much of single droplet impact research is useful? *Progress in Energy and Combustion Science,* 36**,** 554-580.

[14] Mohammadi, A., Kidoguchi, Y. & Miwa, K. 2002. Effect of Injection Parameters and Wall-Impingement on Atomization and Gas Entrainment Processes in Diesel Sprays. SAE International.

[15] Ko, K. & Arai, M. 2002. Diesel spray and adhering fuel on an impingement wall. *SAE paper no. 2002-01-1628*.

[16] Nguyen, D. and D. Honnery, Combustion of bio-oil ethanol blends at elevated pressure. Fuel, 2008. 87(2): p. 232-243.

[17] Kostas, J., Honnery, D. & Soria, J. 2011. A correlation image velocimetry-based study of high-pressure fuel spray tip evolution. Experiments in fluids, 1-12.

[18] Hiroyasu, H. and M. Arai, Structures of fuel sprays in diesel engines. 1990, SAE Technical Paper: 900475.

[19] Roisman, I. V., Araneo, L. & Tropea, C. 2007. Effect of ambient pressure on penetration of a diesel spray. International Journal of Multiphase Flow, 33, 904-920.

[20] Ebara, T., Amagai, K. & Arai, M. 1997. Movement and structure of diesel spray impinging on an inclined wall. SAE Technical Paper: 970046.

**Proceedings of the Australian Combustion Symposium**
**December 7-9, 2015, The University of Melbourne**

# A theoretical examination of spray supercriticality in compression ignition engines

Farzad Poursadegh*, Joshua S. Lacey, Michael J. Brear and Robert L. Gordon
Department of Mechanical Engineering
University of Melbourne VIC 3010 Australia

## Abstract

The potential supercriticality of fuel injection has received significant recent attention due to the high pressure and temperature conditions that occur in modern compression ignition (CI) engines. Several recent works have argued the case both for and against its likelihood. This paper revisits two particular aspects of the relevant theory. Using the microscopic length scales of a gas/liquid interface in a properly formulated mixture, we first find that a locally discontinuous phase boundary exists under all injection conditions relevant to diesel engines, and then infer that subcriticality should almost always occur in CI engines. Examining the thermodynamic properties of n-dodecane/nitrogen mixtures, it is then found that the dissimilarity of the hydrocarbon fuel and nitrogen molecules leads to critical pressures at intermediate fuel mass fractions that are much higher than those of either contributing components, and higher than engine pressures. Together, these two results suggest that supercriticality is unlikely in modern diesel engines.

*Keywords: Fuel supercriticality, Phase boundary, Thermodynamic Discontinuity, Compression ignition engine*

## 1. Introduction

Understanding the fundamental mechanisms involved in supercritical fuel injection is of significant current interest, due to the possibility of its occurrence in some modern internal combustion (IC) engines. In contrast to conventional sprays that are dominated by liquid breakup and evaporation processes, the reduced surface tension and heat of vaporization under certain high pressure and temperature conditions may suppress classical spray behavior and promote diffusional, gas-like dynamics [1-3]. While the underlying physics of conventional spray phenomena is relatively well-characterized, those of fuel sprays at elevated pressures and temperatures are not well-understood. This is primarily due to the complex thermodynamics and transport at these conditions. Gas phase solubility effects also add further complexity by introducing nonlinear effects on the critical properties of the mixtures, particularly for those with strongly dissimilar components, like nitrogen and hydrocarbons [4].

Dahms et al. [5,6] recently presented a detailed theoretical framework for examining the physics of liquid fuel spray formation under supercritical pressures. They proposed that beyond a certain ambient temperature and pressure, relevant to the context of modern diesel engines, the classical liquid injection process transitions to a continuous, diffusional mixing regime. That phenomenon was attributed to the transition of the phase boundary to a continuum regime with diminished interfacial tension force. Later experiments exploring these arguments [7,8] were however unable to be conclusive as to whether transitions between sub- and supercriticality were actually observed. The recent detailed thermodynamic analysis by Qiu and Reitz [9] suggested that local temperature reductions due to liquid evaporation in diesel engine-like environments leads to the presence of multiple stable liquid-containing phases. Earlier studies by Abraham et al. [10,11] also questioned the importance of fuel supercriticality in the absence of combustion in similar supercritical environments.

Considering these two different viewpoints, this paper reconsiders the physics of liquid hydrocarbon fuel sprays in diesel engines. The framework of Dahms et al. [6] is first revisited and employed to investigate the structure of multicomponent liquid/gas interfaces formed under given fuel injection conditions. The gradient theory of heterogeneous fluids [12] combined with vapor-liquid equilibrium (VLE) and an adiabatic mixing assumption is used to study the molecular structure of the phase boundaries at diesel engine-like environments. Then, the critical points of the mixture are calculated and employed to investigate the thermodynamic state of the simulated interface across the fuel mass fraction domain.

## 2. Theoretical Model

Gradient theory [12], which has been widely employed to describe the distribution of matter through phase interfaces, transforms the statistical mechanics of an inhomogeneous fluid into non-linear boundary value problems, the solutions of which provide information on the interface. According to this theory, in the absence of an external potential, the interfacial tension σ of a multicomponent planar vapor-liquid interface at phase equilibrium is

$$\sigma = \int_{\rho_{r,v}}^{\rho_{r,l}} \sqrt{2(\varphi - \bar{\varphi}_B) \sum_{i=1}^{N} \sum_{j=1}^{N} \kappa_{ij} \frac{\partial \rho_i}{\partial \rho_r} \frac{\partial \rho_j}{\partial \rho_r}} \, d\rho_r \qquad (1)$$

* Corresponding author:
Phone: (+61) 3 8344 8876
Email: farzadp@student.unimelb.edu.au

and the corresponding density profile $\rho(z)$ across the interface can be evaluated from the following formulation for distance along the interface, z

$$z(\rho_r) = z_0 + \int_{\rho_{r,v}}^{\rho_r} \sqrt{\frac{\sum_{i=1}^{N}\sum_{j=1}^{N}\kappa_{ij}\frac{\partial\rho_i}{\partial\rho_r}\frac{\partial\rho_j}{\partial\rho_r}}{2(\varphi-\bar{\varphi}_B)}}\, d\rho_r \qquad (2)$$

where $\varphi_B = -P_s$ is the equilibrium pressure, $\varphi$ is the mixture's grand thermodynamic potential energy density and $\kappa_{ij}$ is the cross influence parameter. The subscript *r* denotes the reference component which has the maximum density difference between coexisting phases, indicated by subscripts *v* for vapor and *l* for liquid phase. Readers are referred to [6] for further details.

In order to use gradient theory, the densities of homogeneous coexisting phases at equilibrium, the Helmholtz free-energy density and the chemical potentials must be determined. The volume corrected Peng-Robinson equation of state is employed in this study in conjunction with the van der Waals mixing model to account for mixture states over the range of pressures and temperatures of interest. With the density distribution of each individual component across the interface from the phase equilibrium calculations, (1) and (2) are then employed to compute interfacial properties. In this work, the interface's characteristic length-scale, $\delta$, is quantified following Lekner et al. [13]. To identify the simulated interface's regime from a macroscopic point of view, its characteristic length is compared to the local mixture's molecular mean-free-path (MFP) calculated following Bird [14]

$$\lambda = \sum_{i=1}^{N} 4x_i \left[\pi N_A \sum_{j=1}^{N} \rho_j \left(d_i + d_j\right)^2 \sqrt{1+\frac{m_i}{m_j}}\right]^{-1} \qquad (3)$$

where $N_A$ is the Avogadro constant, $\rho_j$ is the molar density of component *j* in the vapor phase, *d* and *m* are the effective molecular diameter and mass of contributing species, respectively. Consistent with the sphericity assumption applied in the derivation of (3), the effective molecular size of each component is calculated using the vapor-phase viscosity coefficient following Bird [14] and Hirschfelder et al. [15]

$$d_i = \left[\frac{5}{16\mu_i}\sqrt{\frac{m_i k_B T}{\pi}}\right]^{1/2} \qquad i = 1, \ldots, N \qquad (4)$$

where T and μ are the temperature and viscosity of pure species in a gas phase. Employing (4) results in the effective molecular sizes for nitrogen and n-dodecane of 3.64 and 9.1 [Å], respectively.

To investigate the thermodynamic state of the simulated interface and determine the fuel/gas mixing behavior in a macroscopic level, the critical properties of the mixtures must be calculated first. Similar to pure fluids, the intensive properties of coexisting phases at the critical point of a mixture are equal. This thermodynamic state is referred to the critical mixing point, above which vapor-liquid equilibrium cannot exist. In this paper, the phase stability criterion, given by Michelsen [16], is used to calculate the critical mixing points of a given binary system.

## 3. Results and Discussion

In this study, n-dodecane and nitrogen are considered as surrogates for diesel fuel and the ambient gas, respectively. Based on the VLE assumption, pressure and temperature remain constant across the phase interface as composition varies, such that the Helmholtz free energy density of the interface is minimized. Figure 1 depicts the impact of equilibrium temperature on the interface thickness and fuel's enthalpy of vaporization for a binary system of n-$C_{12}$/$N_2$ at a constant pressure. Here, the dimensionless interface thickness is defined as the ratio of the interface thickness to the molar average of the molecular diameters of the mixture components. It is noticed that the phase boundary thickens and the energy barrier for the phase transition process decreases with interface temperature. At the critical mixing point, the interface thickness approaches infinity and the latent heat of vaporization becomes null, as the coexisting phases become indistinguishable.

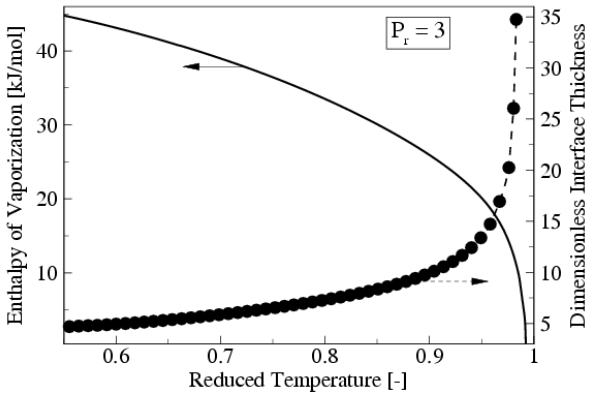


**Figure 1** Interface thickness and latent heat of vaporization of n-dodecane in a mixture with nitrogen at a reduced pressure of 3 as a function of equilibrium temperature.

To investigate the dominant mechanisms involved in the formation and mixing of liquid fuel sprays at selected injection conditions, the interface state first needs to be determined. This is achieved by obtaining the intercepts of the adiabatic mixing temperature loci with the corresponding VLE curves [6]. The procedure is illustrated in Fig. 2 with liquid n-dodecane at a fixed fuel temperature of 363 K injected into gaseous nitrogen at $T_A$ = 750 K and $P_A$ = 50 bar (approximating light-load late-injection scenario). Applying the adiabatic mixing assumption, a temperature distribution for all possible mixtures of fuel and ambient gas at each

injection condition is calculated. The intersection of this temperature profile with the corresponding VLE curves determines the equilibrium thermodynamic state and composition of the interface at the given injection condition. Incorporating the calculated interface state into (1)-(3), information regarding its detailed structure is extracted.

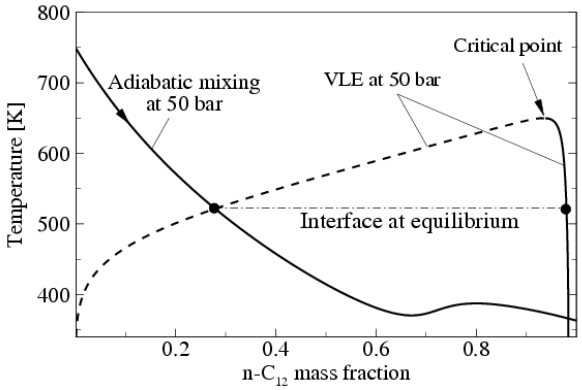


**Figure 2** Adiabatic mixing temperature distribution superimposed onto the VLE curves to calculate the corresponding interface state at $P_A$ = 50 bar.

Table 1 summarizes some of the key interface properties calculated under representative diesel engine-like conditions. As quantified in Tab. 1, the interfacial thickness increases and its molecular structure becomes weaker as the fuel is injected into hotter and higher pressure conditions. Through this process, there will eventually be an appreciable shift in the mechanisms that govern the interface. Following [6], a Knudsen-number criterion is employed to examine this potential shift in interface regime. According to [6], when $Kn = \delta/\lambda \leq 0.1$, the gradients of macroscopic variables across the interface become gradual enough that the continuum description is reasonable. This threshold is intended to identify diffusional gaseous jet-like behavior as opposed to the classical two-phase spray formation where the interface is governed by discontinuous thermodynamic jump conditions.

As summarized in Tab. 1, under the injection conditions considered in this study, the vapor composition at the VLE point along the adiabatic mixing trajectory is nitrogen dominated on a molar basis, e.g. over 90% $N_2$ under the most extreme injection scenario. This suggests that the error associated with modeling n-dodecane molecules as elastically colliding, hard spheres in (3) is small. A combination of increased number density and concentration of larger fuel molecules in the local mixture results in a shorter molecular pathway under higher pressure and temperature conditions. Using these calculated MFPs and interfacial thicknesses, the corresponding local Knudsen-numbers are calculated, which shows that $Kn > 0.1$ under all representative conditions. This suggests that an instantaneous spray transition to a purely diffusional jet is not relevant to the context of diesel engines.

**Table 1** Calculated details of gas/liquid interfaces formed under representative modern CI engine-like conditions

| | $T_A$ [K] | $P_A$ [bar] | $x_{F,v}$ | $\delta$ [Å] | $\sigma$ [$\frac{mN}{m}$] | $Kn_v$ |
|---|---|---|---|---|---|---|
| I | **450** | **30** | 0.009 | 11.5 | 12.8 | 2.8 |
| II | **600** | **40** | 0.034 | 14.5 | 8.70 | 1.72 |
| III | **900** | **60** | 0.084 | 20 | 4.94 | 0.86 |
| IV | **1000** | **80** | 0.097 | 24 | 3.20 | 0.57 |

To further analyze the phase transition behavior under representative CI engine conditions, the corresponding mixture states are compared against the true thermodynamic critical values. For this purpose, conditions (I) and (III) are considered to simulate cold engine early-injection and high-load scenarios, respectively. Figure 3 shows the mixture states of normal dodecane and nitrogen at these conditions superimposed onto the corresponding critical curves. According to Konynenburg and Scott [4], mixtures of nitrogen and a normal alkane exhibit "Type III" behavior consisting of two distinct critical curves. The first branch starts from the critical point of the pure n-alkane and rises steeply in pressure. The second branch, which occurs at temperatures far colder than those relevant to CI engines, starts from the critical point of nitrogen and meets at the end of the three-phase equilibrium line. Unlike pure fluids, the critical temperature of a mixture is not necessarily the highest temperature at which two phases coexist [15]. Thus, the cricondentherm, which is the maximum temperature at which condensation can occur, is used in this analysis to determine the region where the mixture enters into a single-phase regime regardless of its pressure. As demonstrated in Fig. 3, the difference between the loci of the mixtures' cricondentherm and critical points rapidly increases as the fuel mass fraction drops below a value of 0.7.

Under injection condition (I), the compressed liquid-core vaporizes and mixes with the background nitrogen by passing through the saturation zone. Eventually the mixture enters the superheat region, where the temperature is greater than that of the mixture's cricondentherm and critical temperature but remains subcritical with respect to pressure. The spray therefore would exhibit conventional atomization and vaporization behavior at this injection condition. Under the late-injection scenario, that is condition (III), compressed liquid fuel is injected into supercritical conditions for that of the pure fuel. The mixture then follows a similar mixing path as that of condition (I) and will eventually transition to a supercritical state once the mixture is almost pure nitrogen. This is consistent with the presence of a distinct molecular interface as predicted by the earlier microscopic simulations, and implies that a transition to a supercritical state does not occur without first passing through the saturation region.

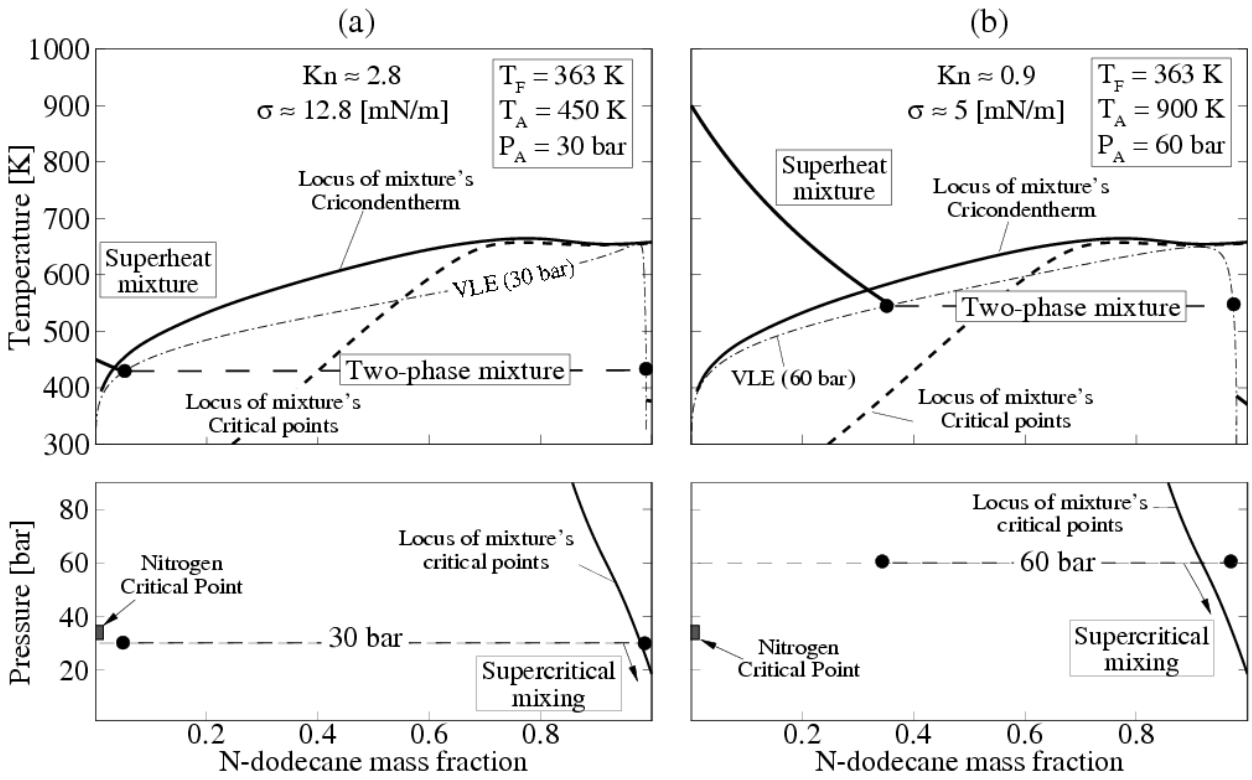


**Figure 3** Mixture state profiles superimposed on the corresponding VLE curves and the locus of mixture critical pressure for conditions (a) (I) and (b) (III).

## 4. Conclusions

Simulations using n-dodecane and nitrogen as surrogates for multicomponent diesel fuel and ambient gas suggest that a transition to a purely diffusional mixing regime does not appear relevant to CI engines. Unlike the transition of pure fluids subjected to conditions well above their critical point, mixtures of liquid alkanes and nitrogen must pass through a region where multiple liquid-containing phases coexist, such that there is no direct transition to the supercritical state. Critical temperature for hydrocarbons increases with chain length, hence the chamber conditions required for transition of mixtures with longer-chain hydrocarbons, which may be better surrogates for diesel fuels, should be even more extreme than those discussed in this paper.

## 5. Acknowledgment

This research was supported by the Advanced Centre for Automotive Research and Testing (ACART, www.acart.com.au) and the Australian Research Council.

## 6. References

[1] W.O.H. Mayer, A.H.A. Schik, B. Vielle, C. Chauveau, D.G. Talley, and R.D. Woodward, J. Propulsion Power **14** (5) (1998), pp. 835–842

[2] B. Chehroudi, D. Talley, and E. Coy, Phys. Fluids **14** (2) (2002), pp. 850–861

[3] C. Muthukumaran and A. Vaidyanathan, Phys. Fluids **27** (3) (2015)

[4] P. Van Konynenburg and R. Scott, Phil. Trans. R. Soc. A **298** (1442) (1980), pp. 495–540

[5] R. Dahms, J. Manin, L. Pickett, and J. Oefelein, Proc. Combust. Inst. **34** (1) (2012), pp. 1667–1675

[6] R. Dahms and J. Oefelein, Phys. Fluids **25** (2013), pp. 1–24

[7] Z. Falgout, M. Rahm, Z. Wang, and M. Linne, Proc. Combust. Inst. **35** (2) (2014), pp. 1579–1586

[8] J. Manin, M. Bardi, L. Pickett, R. Dahms, J. Oefelein, Fuel **134** (2014), pp. 531–543

[9] L. Qiu and R. D. Reitz, Int. J. Multiphase Flow **72** (2015), pp. 24–38

[10] S.D. Givler, J. Abraham, Prog. Energy Combust. Sci. **22** (1996), pp.1-28

[11] J. Abraham, S.D. Givler, SAE Technical Paper, No. 1999-01-0511 (1999)

[12] J.W. Cahn and J.E. Hilliard, J. Chem. Phys. **28** (2) (1958), pp. 258–267

[13] J. Lekner and J. Henderson, Phys. A: Statistical Mechanics and its Applications **94** (3) (1978), pp. 545–558

[14] G.A. Bird, Molecular gas dynamics and the direct simulation of gas flows, Clarendon, 1994

[15] J. Hirschfelder, C. Curtiss, and R. Bird, Molecular theory of gases and liquids, Wiley New York, 1954

[16] M. Michelsen, Fluid Phase Equilibria **16** (1) (1984), pp. 57–76

**Proceedings of the Australian Combustion Symposium**
**December 7-9, 2015, The University of Melbourne**

# Macroscopic Spray Characteristics of an Evaporating Diesel Spray

I.M. Rizwanul Fattah[1], W. Ren[1], C. Woo[1], Q.N. Chan[1, *], S. Kook[1], E.R. Hawkes[1, 2]
[1]School of Mechanical and Manufacturing Engineering
[2]School of Photovoltaic and Renewable Energy Engineering
UNSW Australia NSW 2052 Australia

## Abstract

The liquid spray cone angle and penetration behaviors of a modified single-hole injector, which is operated at an injection pressure of 100 MPa and injection duration of 1.95 ms (actual), are assessed in a well-controlled high-pressure (6 MPa), high-temperature (900 K), and non-reacting (0% vol. $O_2$) environment inside a constant-volume combustion chamber. The liquid spray cone angle is observed to be wide after the start of injection, dropping gradually to a quasi-steady minimum value of 12°, before increasing again when approaching the end of injection. The spray penetration, on the other hand, is observed to progress in an opposite manner to the spray cone angle, and is found to reach a maximum distance of ~16 mm, when the spray cone angle is at minimum. The transient macroscopic spray trends do not appear to be correlated to the mass flow rate profile.

*Keywords: Spray penetration, Spray cone angle, Constant-volume combustion chamber, Diesel injector.*

## 1. Introduction

The macroscopic liquid spray features of an injected fuel jet have a significant impact on the atomization, vaporization and fuel-air mixing processes, and hence, the ensuing combustion and emission formation in diesel engines [1]. Assessing the macroscopic spray characteristics, such as spray cone angle and penetration, and correlating them to the fuel injector nozzle design and operation mode are therefore an important aspect of diesel engine studies. The study of injection events in a highly-controlled, simplified environment, such as a constant-volume combustion chamber (CVCC), is important, as it permits the spray characteristics to be interrogated in pressure and temperature settings that are typically encountered in diesel engines, but without the complication of in-cylinder phenomena. The high-fidelity data acquired in the well-defined boundary conditions has the potential to improve the fundamental understanding of the spray events, and to enable the development of more accurate computational models, which can be used to improve engine design [2]. The importance and applicability of the approach are recognized internationally, as demonstrated through the research activities of Engine Combustion Network (ECN) [3].

The aim of the current work is therefore to assess the macroscopic liquid spray behavior of a modified single-hole injector, which was previously used in the authors' optical engine studies [*e.g.*, 4]. The common-rail solenoid injector is tested in an optically accessible constant-volume combustion chamber. The diesel fuel jet is injected into a charge gas, at an elevated temperature and pressure conditions of ~900 K and 6 MPa, with a 0% oxygen environment. The liquid spray cone angle and penetration of the jet, under the vaporizing, non-reacting condition, are subsequently derived from the processing of the high-speed Mie-scattered images, which are acquired from the chamber. The current work also assesses the temporal liquid spray cone angle and penetration characteristics in relation to the injection rate profile of the injector, acquired using a Bosch tube-type injection rate meter.

## 2. Experimental Details

The experiments were conducted in an optically-accessible, UNSW Australia constant-volume combustion vessel (CVCC). A schematic of the vessel is given in Fig. 1, along with the high-speed Mie-scattering setup described in Section 2.2. The vessel has a cubical combustion chamber (114 by 114 mm), with optical access (102 mm diameter) provided by side-port windows. A single-hole fuel injector was mounted at the center of a metal side-port of the CVCC. A 0% oxygen environment was used for the current study to provide the vaporizing condition in the absence of combustion. The test condition was simulated by metering acetylene, hydrogen, oxygen and nitrogen gases into the CVCC. The combustible gas mixture was subsequently spark-ignited to create a high-temperature, high-pressure environment in the vessel. Following the premixed combustion, the combustion products was then allowed to cool over a relatively long time (~8 s, see Fig. 2) through heat transfer to the cooler vessel walls (electrically heated to 403 K). The pressure (temperature) was monitored using an in-vessel pressure sensor (Kistler 6052C) during the cool-down period, and the injector was triggered for fuel injection when the targeted pressure (temperature) condition was reached. For the current study, an ambient condition with a gas pressure and temperature of 6 MPa and ~900 K, respectively, was targeted. The targeted condition

* Corresponding author:
Phone: (+61) 2 9385 4116
Email: qing.chan@unsw.edu.au

corresponds to a low-temperature combustion state in engines with moderate exhaust gas recirculation [2, 3]. The time-resolved in-vessel pressure for all the injection cycles (5 runs) were acquired and plotted as shown in Fig. 2. Shaded error bars (1 standard deviation) are used shown the statistical uncertainty associated with each data point. A mass averaged approximation of ambient gas temperature due to unavailability of fast response thermocouples translates into some uncertainties. An uncertainty of 10 K is usually expected to yield about 1 mm variation in liquid length [2]. From the figure, it can be seen that the run-to-run fluctuations in the measured pressures were not significant, therefore ensuring that the fuel injection events were compared at nominally identical conditions. Throughout the experiments, an agitator mounted at the top of the CVCC was activated to maintain a spatially uniform temperature environment in the vessel right up to the time of diesel fuel injection. It is noted that the gas velocities induced by the agitator were assessed to be small in comparison to that of the fuel jet [2], so the environment within the CVCC can be considered quiescent. The fuel injection system used for the experiments comprised of a Bosch common-rail (CP4) system and a single-hole solenoid injector (Bosch, P/N: 0445110258). The injection system was controlled using an injection driver (Zenobalti, ZB-5100) and was used to deliver conventional diesel fuel with a cetane number of 51. At a fixed rail pressure of 100 MPa, an injection duration of 1.95 ms (actual) was specified for the single-hole injector to give 10 mg of diesel fuel per injection. The injected fuel mass was measured using a Bosch-tube type injection rate meter [5]. It should be noted that the injector used originally had seven equally-spaced holes, each with 134 µm nozzle hole diameter and an included angle of 150° (See Table 1 for details). It is noted that the injection angle is accounted when computing the spray penetration plot. The injector, was modified for single-hole injection by laser welding the six other nozzle holes for the present study. The single-hole injector was used to avoid the complexity that can arise from jet-jet interaction.

High-speed Mie-scattering imaging was performed, using the setup shown schematically in Fig. 1, to visualize the liquid phase of the vaporizing spray. The spray was illuminated using high-speed LEDs (Central wavelength: 455 nm, FWHM: 18 nm, P/N: M455L3, Thorlabs), which were driven and controlled using a DC4104 LED driver (Thorlabs), through the side windows of the CVCC. The light from each LED was diffused through an engineered diffuser to achieve homogeneous illumination, and was collimated using a 60 mm FL convex lens to improve its directionality. The elastically-scattered light from the spray was captured with a high-speed camera (Photron SA-5) that was positioned in front of the chamber (directly facing the injector tip). The camera was equipped with $f_{\#}1.4$ lens (Nikkor) and was operated at a frame rate of 20k frames per second (fps). The pixel resolution of the image was about 195 µm per pixel. For the lens setup, an aperture opening of f/4 was selected to optimize image depth-of-field and sharpness. A camera exposure time of 50 µs was also specified to freeze the motion of the sprays.

The macroscopic dimensions of the liquid spray, *i.e.* spray cone angle and penetration, were derived from the

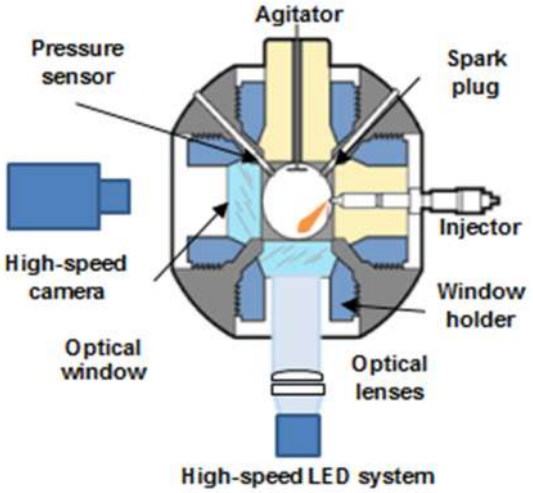


Figure 1: Cross-sectional schematic drawing of the constant-volume combustion chamber (CVCC) and Mie-scattering imaging setup.

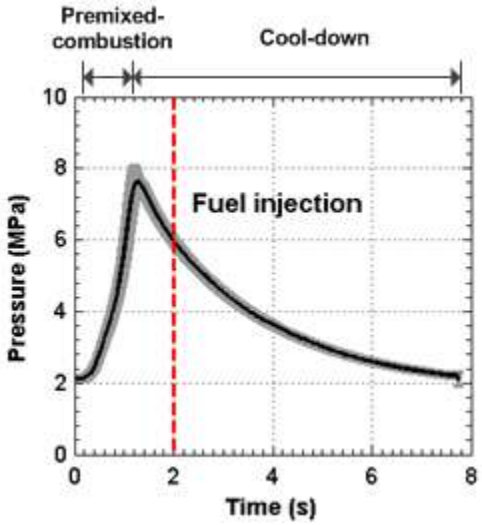


Figure 2: Pressure history of the CVCC when simulating the diesel engine condition. The red dashed line indicates the instance when the fuel was injected into the chamber. Error bars (1 standard deviation, in grey) are used to indicate show the run-to-run uncertainties.

Table 1: Experimental specifications and operating conditions.

| | |
|---|---|
| CVCC ambient condition at injection | |
| Temperature | ~900 K |
| Pressure | 6 MPa |
| Composition (product) | 0% vol. $O_2$ |
| | 6.52% vol. $CO_2$ |
| | 89.71% vol. $N_2$ |
| | 3.77% vol. $H_2O$ |
| Chamber wall temperature | 403 K |
| Injector conditions | |
| Fuel | Conventional diesel |
| Cetane number | 51 |
| Common rail | Third generation Bosch |
| Nozzle | Minisac, hydro-grounded |
| | K1.5/0.86 |
| Number of holes | 7 (original) |
| | 1 (modified) |
| Hole diameter | 134 µm |
| Included angle | 150° |
| Rail pressure | 100 MPa |
| Injection duration | 1.1 ms (electronic) |
| | 1.95 ms (actual) |
| Injected mass per injection | 10 mg |

Mie-scattered images that were captured sequentially

after the triggering of the injector. The images were pre-processed in several steps. The Mie-scattered images obtained were first median-filtered to reduce impulse noises in the image. The images were also corrected for background, dark charge and detector attenuation (flat-field correction) [6, 7]. Each image was subsequently binarized with a fixed intensity threshold at 10 % of the maximum image intensity. It is noted that the threshold value was selected based upon the result of a sensitivity analysis. The preparatory steps are illustrated in Fig. 3, with a typical Mie-scattering image captured at 0.25 ms after start of injection (aSOI). The SOI is defined as the instance when the spray is first detected by the camera. The binarized images generated were used to provide spray contour data, from which the spray cone angle and penetration information are derived. The determination of the spray penetration and cone angle requires an iterative process to evaluate, as the definition used for each depends on the other. The pixel on the spray boundary with the maximum distance ($S$) from the nozzle was first identified using an in-house MATLAB code [8]. The spray was then subdivided at the position of average distance ($S/2$), between the nozzle and the identified pixel, into two sub-regions. The near-nozzle sub-region was subsequently used to determine the spray cone angle ($\theta$), via:

$$\theta/2 = tan^{-1}(\frac{A_{S/2}}{(S/2)^2}), \qquad (1)$$

where $A_{S/2}$ is the projected spray area of the near-nozzle spray region. The subdivision process was necessary to exclude the unsteady spray head region, so that the derived value is representative of the outer boundary of the steady, near-nozzle portion of the spray [9]. The penetration is obtained by averaging the distances between the pixels, located in an arc of $\theta/2$ centered on the $S$-axis, to the nozzle. The averaging step was necessary to ensure that the values obtained are less sensitive to instantaneous spray fluctuations.

## 3. Results and Discussion

Prior to the CVCC experiments, the diesel fuel injection rate of the nozzle was measured using a Bosch-tube-type injection rate meter [5], at an injection pressure of 100 MPa and a back-pressure of 6 MPa, which corresponds to the targeted CVCC pressure condition. The injection event was repeated 20 times, and the averaged injection rate profile and the error bars (1 standard deviation) are presented in Fig. 4(a). The vertical red dashed-lines are used in the figure to indicate the four characteristic time intervals/stages that are typically observed in rate of injection measurements. In Fig. 4(a), it can be seen that there is a measurable delay of 0.35 ms between the start of the electronic command (SOE) and the start of injection (SOI) – the instance when the initial injection rate climb is detected. The delay, which is generally termed as hydraulic delay, is attributed to the time required to active the solenoid valve and the actual needle lift [5, 10]. The injection rate curve is also observed to exhibit transient behavior immediately after both SOI and end of injection (EOI) events, which corresponds to the periods when the mass flow rates are either ramping up or down. Between the two transient periods, the injection rate is observed to approach a quasi-steady average mass flow rate value of ~5 mg/ms, albeit with slight oscillation. The assessment of the origin of the oscillation is beyond the scope of the present study. It is noted, however, a recent study [10] has identified the displacement of the injector tip in the testing volume of the rate meter to be the cause of the oscillations observed in long-tube type mass flow rate measurements. In Fig. 4(a), it can be seen that there is a relatively long delay of ~1.2 ms between the end of electronic command (EOE), which would initiate the closing stage of the injector, and the actual EOI event. A slight leveling in the profile is also observed after the EOI, which is most likely due to needle bounce [11].

The spray cone angle, which can be used to indicate the degree of dispersion of the spray, influences plays a significant role in the vaporization and mixing [12]. The temporal evolution of the spray cone angle is therefore plotted in Fig. 4(b). It is noted that the injection event was repeated 5 times. The average spray cone angle profile and the error bars are presented in the figure. In Fig. 4(b), it can be seen that the spray cone angle is larger (~20°) at the beginning of the injection event (SOI). The spray cone angle, however, is found to transit to a narrower spray during the quasi-steady part of the injection process to reach a minimum value of ~12° at 1.4 ms after SOE, before increasing again when approaching EOI. It is noted the same experiment was repeated with different injection pressures, whereby the injection durations were varied to maintain the injected fuel mass and the spreading of the sprays were found to stabilize at ~12°. The small error bars associated with the plot indicate that the spray cone angle trend is repeatable between runs. The widely varying cone angle with time implies that for the selected injection pressure (100 MPa) and duration (1.95 ms, actual), the spray cone behavior is mainly transient, and only reaches a steady-state behavior between 1.1 and 1.6 ms after SOE.

In addition to the observations of the spray cone angle, the temporal spray penetration behavior is also

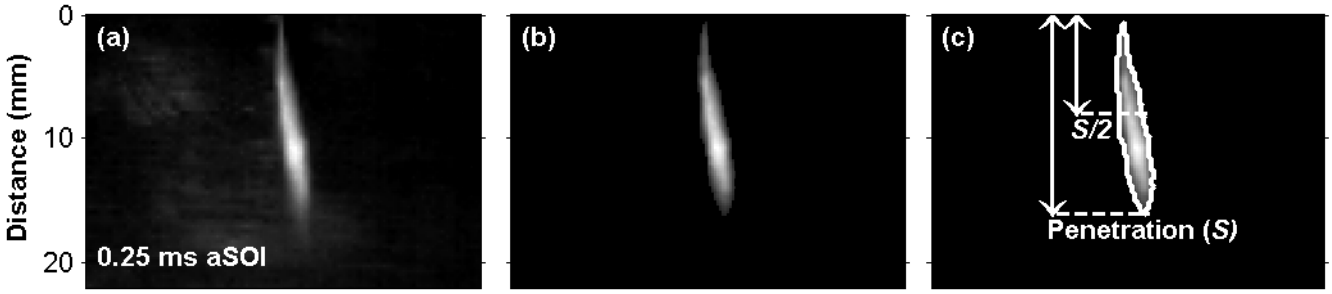


Figure 3: The Mie-scattering image pre-processing steps: (a) A typical Mie-scattering image acquired at 0.25 ms aSOI. (b) The same Mie-scattering image after median-filtering, background, dark charge and detector attenuation correction. (c) The parameters of interest of the spray were derived from the boundary of the resulting image. The definition of the maximum spray tip penetration ($S$) is shown.

plotted in Fig. 4(c). From the figure, the liquid spray penetration is observed to increase or decrease rapidly in the periods when the mass flow rate is ramping up or down in Fig. 4(a), which is to be expected. In the figure, the liquid spray penetration appears to reach a local maximum at 0.6 ms after SOE, before settling to a lower penetration value. The reason behind the overshoot is unclear, but may be attributed to the injector or injector driver configurations [2]. The rapid opening of the injector, when responding to the electronic command, can cause a slug of fuel to accelerate and therefore penetrate past the quasi-steady liquid length [2]. From the figure, the liquid penetration can be observed to increase progressively with time to reach a maximum distance of ~16 mm at 1.4 ms after SOE. Between 1.4 and 2.3 ms after SOE, however, the liquid length is observed to recess to distances closer to the nozzle, when approaching the EOI. The spray penetration is generally found to increase when the spray cone angle is decreasing, and vice versa. The finding is expected from a mixing standpoint, given that a higher spray cone can enhance the entrainment of hot air into the jet, thereby shortening the spray penetration [12]. It is noted that both liquid spray cone angle and penetration are observed to vary throughout the injection event, despite the near constant mass flow rate over the same time period. The observation implies that the changes in the macroscopic spray behaviors are not related to the needle motion within the injector, but may be due to complicated internal flow transients [12]. Some low frequency variations are observed in both the liquid spray angle and spray penetration plots. However, it is unclear at present if the observed variations are related to the oscillations in the mass flow rate profile.

## 4. Conclusions

The liquid spray cone angle and penetration behaviors of a modified single-hole injector, operated at an injection pressure and duration of 100 MPa and 1.95 ms (actual), respectively, were assessed in a well-controlled high-pressure (6 MPa), high-temperature (900 K) and non-reacting (0% vol. $O_2$) environment inside a constant-volume combustion chamber. The liquid spray cone angle was observed to be wide after the start of injection, dropping gradually to a quasi-steady minimum value of 12°, before increasing again when approaching the end of injection. The spray penetration, on the other hand, progressed in an opposite manner to the spray cone angle, and was found to reach a maximum distance of ~16 mm, when the spray cone angle was at minimum. The transient macroscopic spray trends do not appear to correlate to the mass flow rate profile.

## 5. Acknowledgments

The authors wish to acknowledge the financial support of Australia Research Council (ARC) and UNSW Australia.

## 6. References

1. J. Lee, N. Kim, H. Lee and K. Min, SAE Paper 2011-01-0684, 2011.

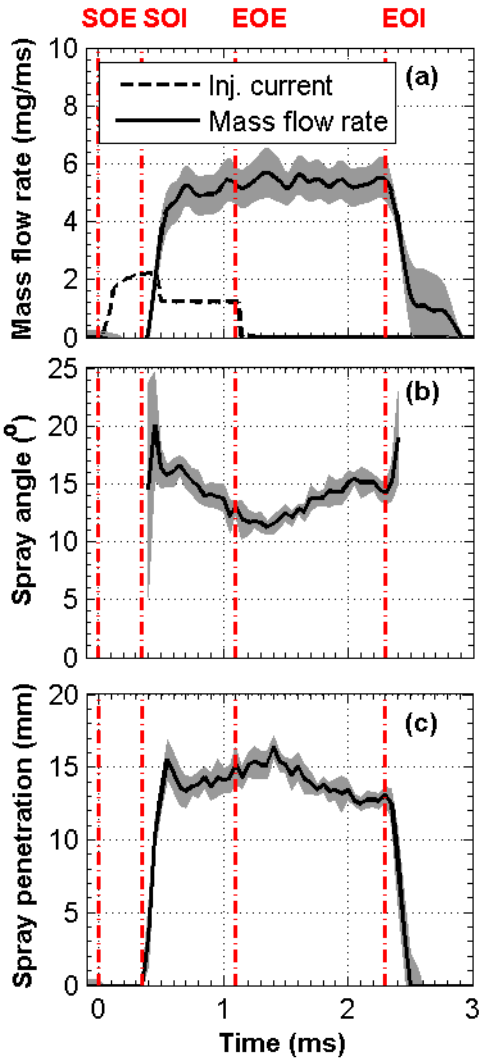


Figure 4: The (a) injection rate, (b) the liquid spray tip penetration and (c) the spray cone profile for the diesel liquid spray as a function of time. Red-dashed lines are used to indicate the four injection characteristic times: start of energizing (SOE), start of injection (SOI), end of energizing (EOE) and end of injection (EOI). Error bars (in grey) are used to indicate the run-to-run uncertainties.

2. L.M. Pickett, C.L. Genzale, G. Bruneaux, L.-M. Malbec, L. Hermant, C. Christiansen and J. Schramm, SAE Paper 2010-01-2106, 2010.
3. Engine Combustion Network (ECN), http://www.sandia.gov/ecn/dieselSprayCombustion.php
4. R. Zhang and S. Kook, Environ. Sci. Technol., **48** (2014), pp 8243–8250.
5. C. Woo, S. Kook, P. Rogers, C. Marquis, E.R. Hawkes and S. Tupufia, SAE Paper 2015-24-2489, 2015.
6. Y. Bao, Q.N. Chan, S. Kook and E.R. Hawkes, SAE International Journal of Fuels and Lubricants **7** (2014), pp. 1010-1026.
7. Q.N. Chan, Y. Bao and S. Kook, Fuel **130** (2014), pp. 228-240.
8. Q.N. Chan, G.J. Nathan and P.R. Medwell, Exp Fluids **55** (2014), pp. 1827-1838.
9. J.D. Naber and D. L. Siebers, SAE Paper 960034, 1996.
10. J. Manin; A. Kastengren and R. Payri, J Eng Gas Turb Power **134** (2012), pp. 122801-122801.
11. J.H. Lee, S. Cho, S.Y. Lee and C. Bae, Proceedings of the Institution of Mechanical Engineers, Part D: Journal of Automobile Engineering **216** (2002), pp. 691-700.
12. Y. Jung, J. Manin, S. Skeen and L.M. Pickett, SAE Paper 2015-01-0946, 2015.

# Flow Measurements of Compressed Natural Gas Jets Issued from Direct Injectors for Spark Ignition Engines

P. Lappas[1, *], T. J. Rogers[1], P. Petersen[2]
[1]School of Aerospace, Mechanical and Manufacturing Engineering, RMIT University, VIC 3083, Australia
[2]School of Media and Communication, RMIT University, VIC 3001, Australia

**Abstract**

Using high-speed high-fidelity schlieren photography and Particle Image Velocimetry (PIV), high pressure ratio (PR) compressed natural gas (CNG) jets are studied under realistic spark-ignited (SI) engine conditions, with the exception that the environment into which the jets flow is quiescent. The CNG jets were issued impulsively with a modified gasoline direct injector into an optically accessible constant volume chamber (CVC). The pressure ratio, defined by the supply pressure of the injector divided by the pressure inside the CVC, covered a broad range of values (8.3<PR<400). Non-dimensional scaling laws applied to the schlieren data show that the jet penetration rate, which is an important determinant of fuel targeting, can be represented by a single monotonic relationship. The jet's spread angle and the development of the barrel length, which is a key transient underexpanded jet feature are also reported. Particle image velocimetry (PIV) maps taken at multiple after start of injection (aSOI) instances detail the flow speeds within the jet core and the ambient regions. Using the jet core centreline velocity, the Mach disc location (barrel length) is measured to within 7% of schlieren measurements.

*Keywords: Natural gas, direct injection, PIV, schlieren, high-speed photography, transient jet.*

## 1. Introduction

The necessity to reduce specific fuel consumption and engine emissions has driven the development of direct-injection gaseous engines as both dual [1] and single fuel solutions [2]. In order to optimise the application of CNG to SI engines, the air-fuel mixture formation and its combustion characteristics need to be well known. The latter topic is well covered in the literature, however, the mixture formation and in-cylinder flow [3] resulting from gaseous injection into the cylinder requires further investigation, especially for the transient period soon after the SOI in SI engines.

The study of direct injection gaseous fuel delivery and mixture preparation is not new. Several studies have shown the freestream targeting behaviour of gas jets experimentally [4, 5] and numerically [6, 7]. Jets impinging on the piston and cylinder walls at engine-relevant conditions have also been investigated experimentally [8, 9, 10] and numerically [11, 12]. Within this existing literature, CNG jets issued at conditions relevant to SI engines are poorly covered. This is typically due to surrogates being used in lieu of CNG for: safety concerns (i.e. nitrogen), imaging quality enhancement (i.e. helium) or more fundamental studies (methane). Three main areas have been largely neglected for SI engines: the transient flow and mixing processes of fuel injection within the first few milliseconds of delivery, high pressure ratio (PR>40) compressed natural gas (CNG) delivery and the effect of late injection timing (close to Top Dead Centre—TDC) on the in-cylinder flow. These three areas are addressed in the present article using a quiescent environment with unobtrusive optical diagnostics as the measurement method.

The transient flow processes of gaseous fuel injection within the first few milliseconds of delivery is important because they can occupy much of the delivery period, especially for low engine loads. There is also strong incentive to investigate high pressure ratios, because of the trend toward substantial fuel delivery in short periods close to TDC. The effect of gaseous fuel injection on the in-cylinder flow is also an important topic because this flow strongly influences the ignition and combustion characteristics in the combustion chamber.

## 2. Experimental Methods

### 2.1 The Test Volume

The central component of the experimental system is the constant volume chamber (CVC). This 7 litre chamber has four orthogonally positioned fused-silica windows (Ø120 mm) that provide access for the optical diagnostic techniques used, namely, schlieren high-speed photography and planar PIV. The orthogonal configuration was used to avoid optical distortion. The fuel injector is mounted centrally at the top of the CVC in a vertical orientation. Before each test, the CVC is filled with high-purity nitrogen as the ambient medium at a given pressure and temperature.

A gasoline multi-hole fuel injector made by Bosch (part no. 0 261 500056) was modified to have a single 1.00 mm diameter orifice. The design is similar to that described in [5] except for a reduced bore length to provide a more realistic internal geometry.

The exact composition of the CNG used in this study is unknown. It is, however, representative of stock which fuels passenger and light-commercial vehicles

* Corresponding author:
Phone: (+61) 3 99258084
Email: petros.lappas@rmit.edu.au

locally. By volume, this representative stock contains 90% methane, 5% ethane, 3% carbon dioxide and traces of nitrogen propane and butane [13].

For the current study, both freestream and impinging jets were investigated. Freestream jets were allowed to develop to relative lengths of ~200x/d, where x denotes the penetration length of the jet and d represents the injector nozzle diameter. The impinging tests represent late SOI when the piston is relatively close to TDC. A flat square surface approximated the piston crown at 50° bTDC. To the best of the authors' knowledge, the current study is the first to experimentally investigate the temporospatial flow characteristics of CNG jets for late direct injection conditions. A large range of pressure ratios were examined, representing realistic SI engine conditions. The range of conditions tested is presented in Table 1. The amount of fuel injected was kept at 12 mg for all tests, corresponding to 600 Joules of heat release. This approximate heat release is expected per cylinder of a small 4 cylinder automotive engine running at cruise conditions where stratified operation is likely. To fix the mass of fuel injected, the opening duration of the injector was varied depending on the CNG supply pressure.

**Table 1. CNG jet delivery conditions**

| Upstream pressure | Down-stream pressure | Pressure ratio | Jet type | No. of tests |
|---|---|---|---|---|
| Po (bar) | Pa (bar) | Po/Pa | | N |
| 20—100 | 0.25—2.40 | 8.33-400 | Free | 14 |
| 20—100 | 0.25—2.45 | 4.56-219 | Impinging | 21 |

## 2.2 Schlieren high-speed imaging (S-HSV)

S-HSV is a line-of-sight unobtrusive method which provides time-resolved images, at the camera's frame rate, of the dynamic processes in jet formation. Subsequent planar PIV measurements complement S-HSV by providing instantaneous, high-fidelity images in which velocity fields are quantified. The S-HSV set-up used in this work is similar to that described by Rogers et al. [14], but is briefly outlined as follows.

Images were acquired using a folded Z-Type configuration in which a continuous Xenon lamp (300w Xenon lamp Olympus CLV U20) illuminated an imaging field up to 152 mm in diameter using parabolic mirrors of focal length 1524 mm. The camera used in this work was a Vision Research Phantom v1610 coupled to either a Sinar Sinaron S 300mm or a Rodenstock Apo-Ronar 800 mm lens for the freestream and nearfield tests, respectively. This combination resulted in a spatial resolution of 0.157 mm/pixel (frame size of 384px × 640px) at 46,000 fps (21.74 µs between frames) for the freestream conditions. For the impinging jet experiments, the spatial resolution was 0.087 mm/pixel (256px × 400px frame size) at 80,000 fps (12.50 µs between frames). The image and data processing for the S-HSV measurements is described by Rogers et al. [14].

## 2.3 Particle Image Velocimetry (PIV)

A photograph of the planar PIV set-up is shown in fig. 1. An Nd:YAG pulsed laser (QuantaRay PIV-400) was operated at a wavelength of 532 nm. For each measurement two light pulses, usually microseconds apart, were passed through commercial sheet forming optics to illuminate flow seeding particles in the test volume. The light sheet formed, was ~40 mm tall, ~0.5 mm thick with an energy level of 180 mJ/pulse. The light scattered from the particles was recorded on a CCD still camera (HiSense MKII 620) fitted with a 60 mm f2.8 lens (Nikkor). The particles were titanium dioxide (TiO2) and sized in accordance with typical considerations [15]. Consequently, the nominal diameter of the particles used to seed the jet gas and the ambient environment was 0.1 µm and 1 µm respectively. In order to differentiate between jet flow and flow originating from the ambient medium, only one gas was seeded for any one experiment.

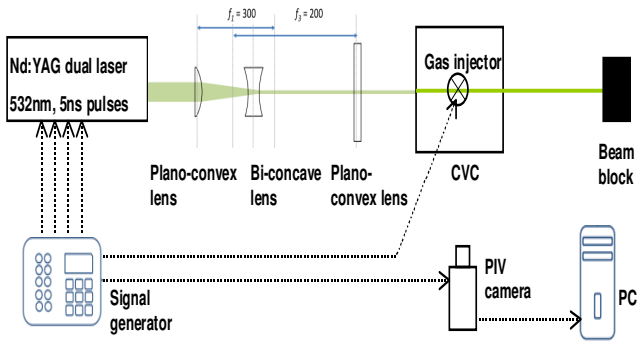


**Fig. 1. PIV experimental configuration.**

Delivery of the ambient tracer particles into the CVC was achieved through a novel seeding device which comprised three main parts: a fuel injector, a fluidised bed and a distribution nozzle. The fluidised bed contained a small volume of particles which were agitated into an aerosol through several high pressure (15 bar) nitrogen jets issued from the fuel injector. The aerosol was then distributed into the CVC through a nozzle (Bete PJ20), which has a single orifice (508 µm) opening. The distribution pattern of the aerosol was a ~90° hollow-cone. The particles once issued to the CVC required a stabilization period but once suspended, the distribution density was visibly homogeneous.

The in-jet seeding was achieved through the use of a modified filter body, loosely representative of a fluidized bed. The aerosol of CNG and 0.1 µm TiO2 was created in-line to the fuel supply. Distribution of the particles was largely dependent on the injection gas dynamics. This method yielded ample clarity on the in-jet features studied.

Laser pulse separation times were kept small enough to ensure that groups of particles in the PIV interrogation zones for the 1st image were distinguishable in the 2nd image. As a result, a separation time of ~0.25 µs was selected for the high-velocity in-jet flow, and values between 1 to 20 µs (depending on the delivery pressure

ratio and time aSOI) were used for the ambient flow experiments.

PIV velocity maps of the entire jet and surrounding in-cylinder region were taken for two instances after start of injection: 215 and 415 µs. They were also acquired when the fuel occupied 30% and 50% of the combustion chamber volume. The image and data processing for the PIV measurements is described by Rogers et al. [14].

## 3. Results and Discussion

Select frames from high speed schlieren videos of freestream and impinging jets are depicted in fig. 2. These images show the jet features discussed in this study, which are also defined in the schematic of fig. 3.

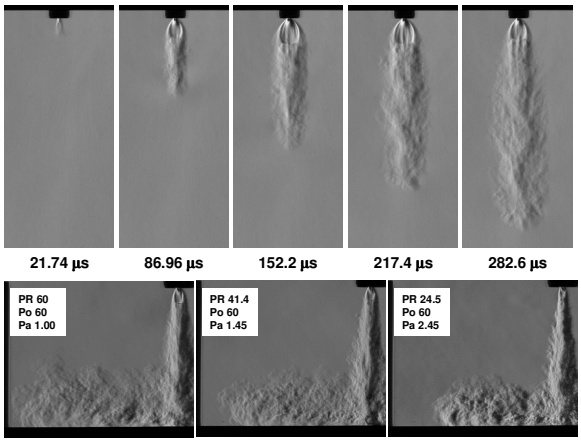


**Fig. 2. Upper row: Freestream PR400 CNG jet sequence. Every forth image presented. Lower row: High PR CNG jets impinging at 976 µs aSOI for an increasing ambient pressure.**

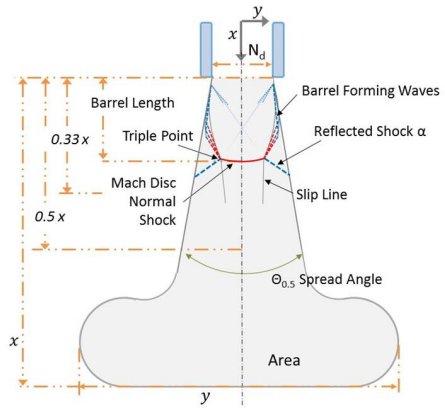


**Fig. 3. Simplified underexpanded impinging jet anatomy with typical measurement locations.**

### 3.1 Macro-Properties of Jets

The macro structure jet dimensions are generally external such as axial and radial penetration, spread angle and self-similarity.

The axial penetration of a jet is probably the most studied and most relevant parameter for engine related flows. Prior to surface contact, the jet inside the cylinder of an engine will typically behave as a free jet, even at late SOI conditions. The penetration rate of a free turbulent jet is influenced by the fuel momentum injection rate and ambient air entrainment. Equation 1 is a universal dimensionless relation that represents these influences for sonic nozzle exit flow [8].

$$\frac{x}{d_{eq}} = \Gamma\left(\frac{\pi}{4}\right)^{1/4}\left(\frac{t\,u_n}{d_{eq}}\right)^{1/2} \quad \textbf{Equation 1}$$

where, $d_{eq} = d_e\,(\rho_e/\rho_a)^{1/2}$, is the equivalent exit diameter. d and ρ denote diameter and density respectively. The subscripts e and a represent the nozzle exit and the ambient environment respectively. The proportionality constant, Γ, is known as the rate of penetration. A number of values have been reported for Γ, ranging from 2.14 to 3.00 [5].

Figure 4 shows that even for substantially high pressure ratios, where the compressible features are large, the CNG jets scale well to equation 1, with a slope (Γ) value of 3.19. This slope value is in direct agreement with the literature range reported and is closest in magnitude to that measured by Ouellette and Hill [7].

The spread angle was also measured by averaging the freestream jet angles to the 3 different penetrations of 33, 50 and 70%, as shown in fig. 3. The angles considered are for jets which have developed for x/d > 20. The mean spread angle for the freestream CNG jets is 23.33°; a value in close agreement to a commonly reported value of 24° for gaseous jets [16].

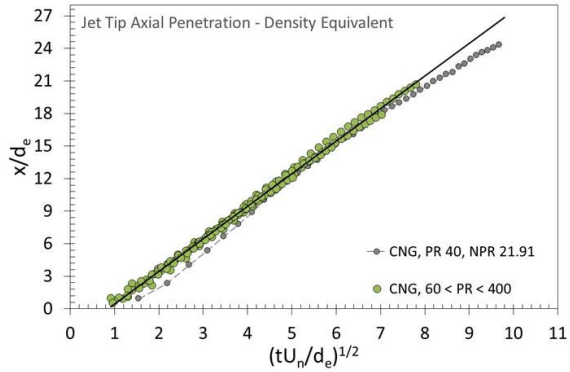


**Fig. 4. Normalised axial penetration rate for high pressure ratio jets.**

Using the projected jet and cylinder areas, the percentage of cylinder filling was also calculated for impinging jets. The filling percentage was recorded against PR and time aSOI, with all three variables plotted in fig. 5. A best fit empirical relation between the variables was determined and is shown in equation 2.

$$\sqrt{t_{\%\,filled}} = 167\,f^{11/15}\left(\frac{P_o}{P_a}\right)^{-0.234} \quad \textbf{Equation 2}$$

where, $t_{\%filled}$ is the time to reach a nominal fill level $f$ and $P_o/P_a$ is the pressure ratio.

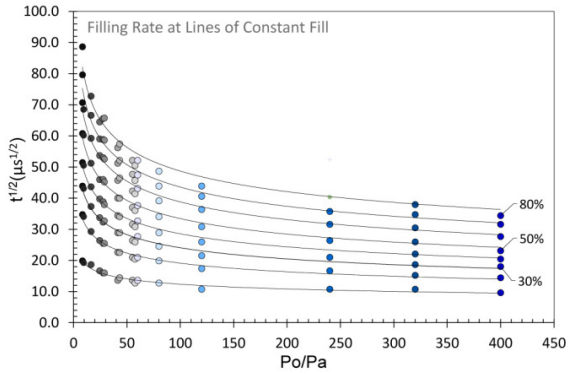


**Fig. 5. CVC fill times for various fill levels and PRs.**

## 3.1 Compressible Nearfield Features of Jets

As shown in fig. 3, the barrel length is the downstream distance between the orifice exit and Mach disc. Within the barrel region of the underexpanded jets, the flow is supersonic where negligible mixing occurs. Immediately downstream of this region, post Mach disc, ambient flow is able to penetrate into the jet core and hence mixing of fuel and air begins. Mixing downstream of this region is a result of the high turbulent shear at the jet-to-air boundary layer and entrainment of ambient air. The processes in this region are responsible for the mixing behaviour, which in turn affects engine operation. Therefore the location of the Mach disc is important to predict.

Using the jet core centreline velocity, the Mach disc location (barrel length) is measured to within 7% of schlieren measurements. The dimensionless Mach disc locations of the steady state CNG jets were found to depend on the pressure ratios tested in accordance with the best fit curve shown in equation 3.

$$\frac{x_{MD}}{d} = 0.363\sqrt{\frac{P_o}{P_a}} + 0.779 \qquad \textbf{Equation 3}$$

The gradient in equation 3 is about half of previously reported values [17], because the latter values were measured from jets issued from needle-less orifices. This was confirmed by conducting PIV tests on our CNG injector with its needle removed.

## 4. Conclusions

With schlieren imaging and PIV, transient CNG jets issued at an unprecedented range of PRs at freestream and impinging conditions have been characterised. The time for a CNG jet to disperse inside a particular cylinder volume was found to collapse to a single novel relationship between PR and fill time (Eqn. 2). Jet penetration rates were found to agree well with previous work. Barrel lengths were found to be up to 50% smaller than previously reported values, because of the influence of the needle on nozzle geometry.

## 5. References


1. McTaggart-Cowan, G., Jones, H., Rogak, S., Bushe, W. et al., "Direct-Injected Hydrogen-Methane Mixtures in a Heavy-Duty Compression Ignition Engine," SAE Technical Paper 2006-01-0653, 2006, doi:10.4271/2006-01-0653.

2. Caley, D. and Cathcart, G., "Development of a Natural Gas Spark Ignited Direct Injection Combustion System," Technical Paper, vol. Technical Paper, 2006.

3. Salazar, V. and Kaiser, S., "Interaction of Intake-Induced Flow and Injection Jet in a Direct-Injection Hydrogen-Fueled Engine Measured by PIV," SAE Technical Paper 2011-01-0673, 2011, doi:10.4271/2011-01-0673.

4. Baert, R., Klaassen, A., and Doosje, E., "Direct Injection of High Pressure Gas: Scaling Properties of Pulsed Turbulent Jets," SAE Int. J. Engines 3(2):383-395, 2010.

5. Johansen, L., de Benito Sienes, E., and Dahlander, P., "Analysis of Transient Compressible Gas Jets Using High Speed Schlieren Imaging," SAE Technical Paper 2013-01-0871, 2013, doi:10.4271/2013-01-0871.

6. Abraham, J., "Entrainment Characteristics of Transient Gas Jets," Numerical Heat Transfer, Part A: Applications: An International Journal of Computation and Methodology, vol. 30, pp. 347-364, 1996.

7. Ouellette, P. and Hill, P. G., "Turbulent Transient Gas Injections," Journal of Fluids Engineering, vol. 122, pp. 743-752, 2000.

8. Owston, R., Magi, V., and Abraham, J., "Fuel-Air Mixing Characteristics of DI Hydrogen Jets," SAE Int. J. Engines 1(1):693-712, 2009, doi:10.4271/2008-01-1041.

9. Salazar, V. and Kaiser, S., "An Optical Study of Mixture Preparation in a Hydrogen-fueled Engine with Direct Injection Using Different Nozzle Designs," SAE Int. J. Engines 2(2):119-131, 2010, doi:10.4271/2009-01-2682.

10. Bruneaux, G., Causse, M., and Omrane, A., "Air Entrainment in Diesel-Like Gas Jet by Simultaneous Flow Velocity and Fuel Concentration Measurements, Comparison of Free and Wall Impinging Jet Configurations," SAE Int. J. Engines 5(2):76-93, 2012, doi:10.4271/2011-01-1828.

11. Gerke, U., "Numerical Analysis of Mixture Formation and Combustion in a Hydrogen Direct-Injection Internal Combustion Engine," Doctor of Science, Swiss Federal Institute of Technology, 2007.

12. Baratta, M., Catania, A., Spessa, E., Herrmann, L. et al., "Multi-Dimensional Modeling of Direct Natural-Gas Injection and Mixture Formation in a Stratified-Charge SI Engine with Centrally Mounted Injector," SAE Int. J. Engines 1(1):607-626, 2009, doi:10.4271/2008-01-0975.

13. Rietzschel, J., Stadler, S. and Zhu, Y., "Fuel Composition Sensing of Compressed Natural Gas," Masters thesis, School of Aerospace, Mechanical and Manufacturing Engineering, RMIT University Melbourne, 2012.

14. Rogers, T., Petersen, P., Lappas, P., "Flow Characteristics of Compressed Natural Gas Delivery for Direct Injection Spark Ignition Engines" SAE paper 2015-01-0002

15. Melling, A., "Tracer particles and seeding for particle image velocimetry," Measurement Science and Technology, vol. 8, p. 1406, 1997.

16. Horn, G. and Thring, M. W., "Angle of Spread of Free Jets," Nature, vol. 178, pp. 205-206, 07/28/print 1956.

17. Ashkenas, H. and Sherman, F. S., "The Structure and Utilization of Supersonic Free Jets in Low Density Wind Tunnels," Rarefied Gas Dynamics, Proceedings of the 4th International Symposium held at the Institute for Aerospace Studies, vol. 2, 1966.

# Common Rail Diesel Sprays from Twin-hole Nozzle

D. Nguyen[1,*], D. Duke[2], A. Kastengren[3], C. Powell[2], D. Honnery[1]
[1]Laboratory for Turbulence Research in Aerospace and Combustion (LTRAC)
Department of Mechanical and Aerospace Engineering
Monash University VIC 3800 Australia
[2]EnergySystems Division, Argonne National Laboratory IL 60439 USA
[3]X-ray Science Division, Argonne National Laboratory IL 60439 USA

## Abstract

This paper presents two techniques used to study peripheral parameters of non-evaporating high pressure diesel sprays from common rail injectors equipped with a twin-hole nozzle during the initial, highly transient stages. To characterise the spray, high speed optical imaging and X-ray radiography were used. The former was performed at the LTRAC laboratory at Monash University, while the latter was performed at the Advanced Photon Source at Argonne National Laboratory. The optical imaging made use of high temporal/spatial resolution spray recordings on a digital camera while the X-ray radiography relied on a point wise basis at roughly similar sampling rate. Results have shown some differences in spray tip penetration and jet merging length between two measurement types. Tip velocities were found much different from those typical of single-hole nozzles.

*Keywords: Twin-hole nozzle, diesel, spray, penetration, X-ray radiography*

## 1. Introduction

To date, most of the studies on high pressure transient fuel sprays have made use of single-hole nozzles, purpose designed for laboratory experiments [1]-[5]. In engine fuel systems, the nozzles are typically multi-hole. Multi-hole nozzles provide greater fuel-air mixing for a fixed fuel mass flow over a single hole. Further to this, jet to jet interaction can be expected among the individual jets, and the fuel flow in the nozzle itself is more complex than would occur for a single-hole nozzle.

The optical study of multi-hole nozzles is more complex than for a single-hole nozzle [6]-[9]. The spatial extent of the measurement domain is larger, and the flow is generally no longer symmetric. To overcome the difficulties, we make use of a twin-hole nozzle in this study, with each hole directed at a fixed angle. This arrangement allows investigation of sprays which are more realistic of multi-hole nozzles while minimizing measurement difficulties.

A focus of interest in this study is the merging properties of the individual jets. In addition to this, we are interested in the axial penetration and leading edge velocity. We measure these macroscopic properties using two different techniques. The first uses high speed optical imaging of volume illuminated sprays, while the second makes use of X-ray radiography. Apart from obvious differences between these two techniques, both have very different signal sensitivities and spatial resolution, so an additional interest is how these two techniques compare. To enable precise calculations of spray penetration while maintaining simplicity, a new case-adaptive edge detection method is introduced.

* Corresponding author:
Phone: (+61) 3 99051300
Email: dungt.nguyen@monash.edu

## 2. Experimental Methodology

### *2.1 Experimental Facilities*

The high speed optical imaging experiments were undertaken in the Laboratory for Turbulence Research in Aerospace and Combustion (LTRAC). A Bosch common rail injector is located at the top of a fully instrumented constant volume vessel measuring 150mm in diameter and 132mm in height [1]. The injector is equipped with a twin-hole nozzle (each hole 212μm in diameter), which directs two jet sprays downwards. The holes are separated by 0.62mm and their axes set with a subtended angle θ of 5° directed outwards. High pressure diesel fuel is supplied to this injector through a common rail from a feedback controlled pump able to maintain the pressure to within ±5bar of the set value. Standard automotive diesel is circulated in the fuel system and its temperature is maintained between 30-32°C. The injection pressure used is 1000Bar, with the vessel pressurised to 20Bar using compressed air at 22°C.

A HPV1 Shimadzu digital camera operating at 500kfps is used to image the sprays. Integration time is 1/8 of the frame rate. The camera is able to record 100 images, giving a total of 200μsec recording time. CCD size is 312x260px$^2$ with image area 21x17.5 mm$^2$. Volume illumination of the sprays is done via two high power flash units. A 200mm focal length micro Nikon lens (f-stop set to 5.6) is used to capture the scattered light from the sprays

Optical techniques using visible light sources are limited in the near-field due to multiple scattering in the dense spray region close to the

nozzle tip. X-ray radiography is used to overcome this limitation [4]. X-rays are capable of penetrating dense flow fields with relatively little scattering. Using a high-flux monochromatic beam, radiography provides a local quantitative measurement of the fuel mass distribution by measuring line of sight transmission, which can be related to the sample projected density by the Lambert-Beer law;

$$\frac{I}{I_0} = e^{-\mu M} \quad (1)$$

where $I$ and $I_0$ are the transmitted and incident X-ray beam intensities, $\mu$ is the absorption coefficient (determined by calibration of the fuel) and $M$ is the projected density (units mass per area);

$$M = \int \rho dz \quad (2)$$

($\rho$ being density). Detail can be found in [5],[9],[10].

The X-ray radiography was performed at the 7-BM beamline of the Advanced Photon Source (APS) at Argonne National Laboratory [11]. In these experiments, a monochromatic X-ray beam of mean energy 8 keV at 1.4% full width at half maximum bandpass was used. The beam was focused to a spot approximately 5x6μm$^2$ in size using a pair of X-ray focusing mirrors. The beam focus is aligned with the spray, which was placed in a pressurized chamber (20bar $N_2$ at ambient temperature) fitted with X-ray transparent polyimide windows. Time-resolved point measurements are combined to a 2D representation of the projected density field by translating the spray across the fixed beam position. Measurements are made on an unstructured grid of several hundred points, with increasingly fine resolution near the nozzle tip. Figure 1 illustrates the actual orientation of the APS spray chamber set-up, with the injector mounted to the left spraying towards the right (angle θ also illustrated).

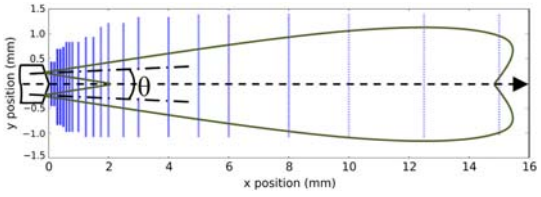


Figure 1: X-ray measurement points set up at Argonne Lab.

Each point measurement is captured with a temporal resolution of 3.68μs (the orbit period of the synchrotron storage ring). The reference intensity $I_0$ is determined by both the incoming beam intensity and the intensity of the transmitted beam for several hundred microseconds before the spray event, normalizing out the absorption due to the ambient gas and other components in the beam path. 32 measurements were recorded at each sampling position to compute an ensemble average. Figure 2a) shows a sequence of instantaneous images from a single spray event, while Fig. 2b) shows a sequence of ensemble-averaged contours of projected density from the X-ray measurements.

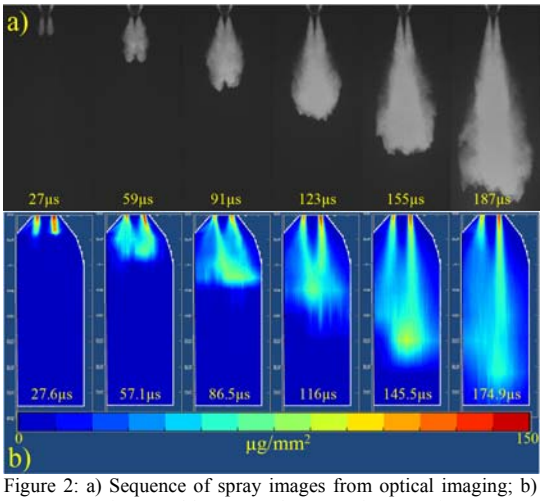


Figure 2: a) Sequence of spray images from optical imaging; b) Sequence of ensemble-averaged spray images from X-ray radiography. Time stamp in each image represents time after SOI.

### 2.2 Calculation Approaches

Characterization of the LTRAC spray data is done by dividing the image into the left and right hand sides from the centerline passing through the middle point between the two nozzle holes. These represent the two individual jets. The penetration of the leading edge is calculated for these sides as well as the penetration of the leading edge along the centerline of the spray. There are a number of options available for such calculations including binarisation [1], use of algorithms such as Canny [12], and strip-wise cross-correlation [3]. The first two methods are typically pixel accurate, the third, similar to PIV, is able to return subpixel accuracy for the edge location. Leading edge detection can provide the distribution of vertical velocities (radial velocity deemed negligible), a new approach is developed for this work based on direct quadratic function fit on the intensity profile along the one-pixel-wide strip of the region surrounding the spray leading edge. This operation, illustrated in Fig. 3, is very fast and sub-pixel accurate. Two thresholds are used, a lower "threshold 1" for skipping image noise and a higher "threshold 2" for determining the edge which is reckoned to be the intersection between the function and the line of "threshold 2". The black arrow points to the position defined as the edge if binarisation is used while the green arrow points to the so defined position using this method.

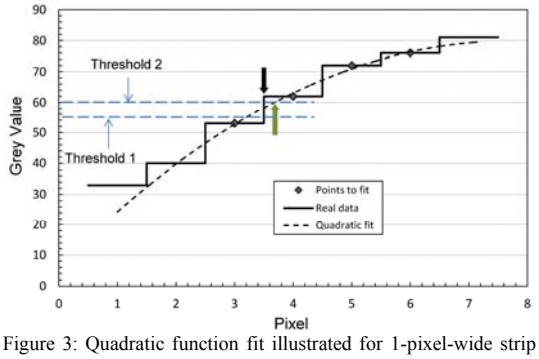


Figure 3: Quadratic function fit illustrated for 1-pixel-wide strip to find the spray leading edge.

Due to the sparse nature of the X-ray data, the spray penetration against time is found from a threshold applied to the leading edge of the time dependent integrated fuel mass profile for each axial measurement position, Fig. 1. A few examples of integrated mass profiles are shown in Fig. 4. To find the merging point of two individual jets, a threshold method is also used for both techniques with the point wise APS data being interpolated using a Delaunay Triangulation method onto a structured 2D array of data as in Fig. 2b).

## 3. Results

Figure 4 shows the variation of integrated mass with time at selected axial ($x$) positions from the X-ray data. The time is relative to when diesel first appears closest to the nozzle tip ($x$=0.1mm). All profiles have the same trend of an initial rapid rise from zero to a peak followed by a gradual decrease to a more steady flow condition. This peak represents the passing of the head of the spray seen in Fig. 2b). The head of the spray is a product of the formation of a leading edge vortex, created when the fuel first leaves the nozzle [1]. The head is defined by the region of high mass, with each jet clearly showing separate heads before the merge point. The presence of the spray head is not as evident in the volume illumination images shown in Fig. 2a). The ability of each of the two imaging techniques to detect the low density spray region surrounding the main part of the spray is also different. This region is clearly evident in the volume illumination images. A further difference between the images shown in Fig. 2 is that Fig. 2a) is a single injection event, while Fig. 2b) is created by averaging 32 separate injections. An additional point of interest is asymmetry in the spray mass distribution of the X-ray images. This property reveals itself in the difference between the leading edge penetrations of the two jets in the volume illumination images.

For the condition used, it takes the spray less than 200μs to reach the far end of the viewing window. From the data in Fig. 4, it is clear that it takes much longer (nearly 500μs) for the spray to reach steady state as characterised by the stable integrated mass period following the passing of the spray head transient.

Fig. 5 shows the maximum tip penetrations on both sides of the spray and centerline for the LTRAC data; and a single common penetration curve for the X-ray data. The optical imaging data are the average of ~200 spray events, with the APS data based on pointwise averaging of 32 spray events. Both measurement techniques yield roughly similar penetration, with the change in penetration gradient (leading edge velocity) at around 110μs evident. Penetration over this time is generally dominated by the injector opening dynamics [8],[9], so greatly depends on the nozzle geometry.

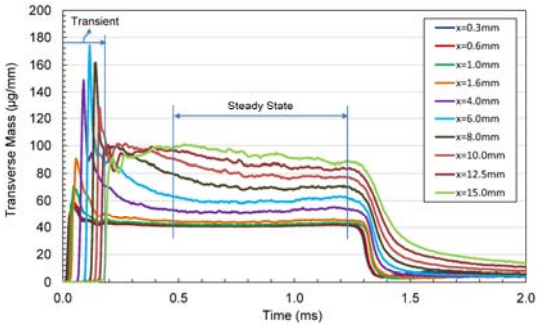

Figure 4: Variation of integrated mass with time at a few axial positions as examples.

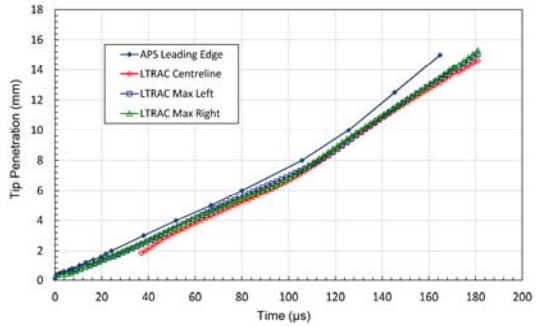

Figure 5: Spray tip penetrations calculated from LTRAC data compared with tip penetration calculated from APS data.

From the optical imaging data, it is seen that the left and right hand side averaged penetrations are very close to each other and ahead of the centerline penetration. The APS penetration data appear to be slightly ahead of the LTRAC data. The penetration data obtained in Fig. 5 have low uncertainty. For optical imaging, the error at 95% confidence level reaches its maximum absolute value of around ±0.07mm (±0.5% relative) near the end while the maximum relative error of ±3.2% occurs at 0.1mm from the nozzle tip (±0.06mm absolute). For X-ray radiography, the maximum error in timing is only about ±2.2μs, similar to the variability of the single jet in [13]. It is possible that the much lower sample number of the APS data is playing a role here, too.

An interesting observation for this nozzle is the shot-to-shot variability in which hole dominates. This can result from factors such as the nozzle geometry and inconsistent internal flow cavitation. While this is more apparent in the APS data (Fig. 2b), the greater sample numbers of the LTRAC data tend to average this effect out as is evident by the similarity of the left and right side penetration curves.

Jet interaction can be characterised partly by studying the merging length, the distance from the nozzle at which the jets first merge. Figure 6 shows this for both measurement types. Jet merging happens close to the nozzle (< 2mm), and varies as the spray transitions from the passing of the head transient to the steady flow condition. While their general trends are similar, there are differences between the two data sets. As observed in the

images shown in Fig. 2, detecting the merge point depends to a great extent on the ability to detect the low density region surrounding the core of the spray, the spatial resolution of the measurement, and the number of spray events sampled. Interestingly, the X-ray data shows the merge point to be closer to the nozzle exit during the initial opening period. If image sensitivity was not to play a role here, the result would more likely be the reverse.

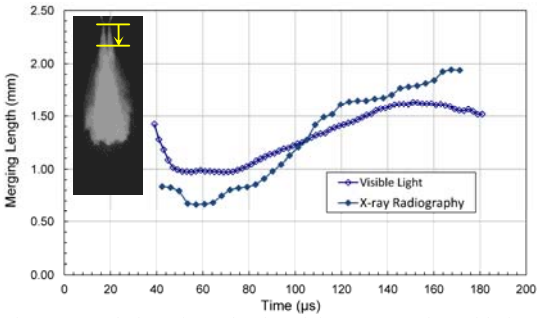


Figure 6: Evolution of merging length between two jets with time for both LTRAC and APS data.

LTRAC spray leading edge penetration speeds calculated based on averaged penetration data in Fig. 5 are shown in Fig. 7. The radiography data cannot provide an accurate penetration speed for this particular dataset due to the coarse sampling resolution. Leading edge velocities seen are much lower than single-hole data ([1]-[3]) operating at similar conditions. The slower penetration velocities seen here are in agreement with the findings in [7],[9] for the isolated jet of multi-hole nozzles. This is understood to be a consequence of increased flow though larger hole areas for the multi-hole nozzles leaving a lower pressure in the nozzle sac volume. Despite the slower speeds, the general trends seen are similar to those found for single-hole nozzles. An initial region of rapid acceleration, as the injector first opens, is followed by a region of relatively constant velocity, although this region is longer for this twin-hole nozzle than for the single-hole nozzle of [2],[3]. After this region, the leading edge undergoes a second period of acceleration. This second acceleration typically corresponds to the peak leading edge velocity of the penetration, after which the velocity decays [3]. Given the reduced coverage of the spray domain, it is not clear from this data if the tip has reached its peak velocity [1]. Increased optical noise from reflections is likely to be playing a role in the fluctuations near the end.

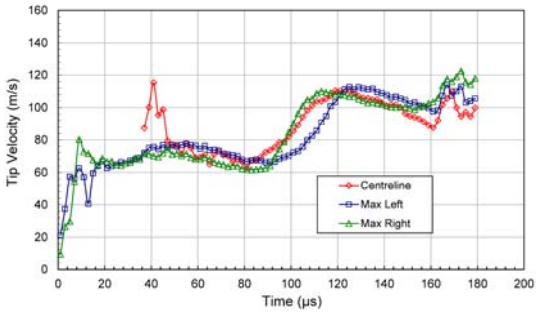


Figure 7: Leading edge velocities calculated from LTRAC data.

## 4. Conclusion

Two techniques have been applied to investigate the development of a diesel spray produced from a twin-hole nozzle. Preliminary results have been found to be very similar, although some differences are noted. The APS X-ray data was found to yield slightly faster penetration than for the volume illumination data. Spray merge length was found to be initially shorter for the X-ray data, although the general trends were very similar for both methods, with this length found to increase with time as the spray starting transient moved to the far field. An interesting finding is the twin-hole nozzle that showed lower leading edge velocity than for single-hole nozzles operating at similar conditions. Another interesting feature is the short to shot variability in hole dominance. Important differences between the two measurement techniques such as the quantity being measured, sensitivity and the sample number could be the source of the small differences noted.

## Acknowledgments

We acknowledge the Australian Research Council for funding the LTRAC component of this project. The X-ray component was performed at the 7-BM beam line of the APS at Argonne National Laboratory. Use of the APS is supported by the U.S. Department of Energy (DOE) under Contract No. DE-AC02-06CH11357. Mr. Matthew Wills is thanked for his help in processing the APS data.

## References

[1] J. Kostas, D. Honnery and J. Soria, Fuel 88 (2009), pp. 2225-2237.

[2] J. Kostas, D. Honnery, J. Soria, A. Kastengren, Z. Liu, C.F. Powell and J. Wang, Applied Physics Letters 95 (2009), DOI: 10.1063/1.3182821.

[3] J. Kostas, D. Honnery and J. Soria, Exp. Fluid 51 (2011), pp. 667-678.

[4] A. Kastengren and C.F. Powell, Exp. in Fluids 55 (3) (2014), DOI: 10.1007/s00348-014-1686-8.

[5] A. Kastengren, F. Tilocco, D. Duke, C. Powell, X. Zhang and S. Moon, Atomization and Sprays 24 (3) (2014), pp. 251–272.

[6] W. Zhong, Z. He, Q. Wang, Z. Shao and X. Tao, Heat and Mass Transfer 59 (2014), pp. 1–10.

[7] S. Moon, Y. Matsumoto, K. Nishida and J. Gao, Fuel 89 (2010), pp. 3287–3299.

[8] K. Nishida, J. Tian, Y. Sumoto, W. Long, K. Sato and M. Yamakawa, Fuel 88 (2009), pp. 1634–1642.

[9] A.I. Ramirez, S. Som, S.K. Aggarwal, A.L. Kastengren, E.M. El-Hannouny, D.E. Longman and C.F. Powell, Exp. Fluids 47 (2009), pp. 119–134.

[10] A.L. Kastengren, C.F. Powell, Z. Liu and J. Wang, SAE Technical Paper No. 2009-01-0840.

[11] A.L. Kastengren, C.F. Powell, D. Arms, E.M. Dufresne, H. Gibson and J. Wang, Journal of Synchrotron Rad. 19 (4) (2012), pp. 654–657.

[12] J. Canny, IEEE Trans. Pattern Anal. Mach. Intel. 8 (6) (1986), pp. 679–698.

[13] A.L. Kastengren, C.F. Powell, Y.J. Wang, J. Wang, Proceedings of the ASME Internal Combustion Engine Division 2007 Fall Technical Conference ICEF2007-1663, Charleston, South Carolina USA, October 2007.

# An Investigation of the Performance of a Gasoline Spark Ignition Engine Fuelled with Hot Ethanol Direct Injection

Yuhan Huang [1, 2 *], Guang Hong[1]
[1]School of Electrical, Mechanical and Mechatronic Systems
University of Technology Sydney NSW 2007 Australia
[2]School of Energy and Power Engineering
Huazhong University of Science and Technology Wuhan 430074 China

## Abstract

Ethanol direct injection (EDI) is a promising technology to address the issue of knock in downsized spark ignition (SI) engines due to the strong cooling effect of EDI and ethanol's large octane number. However, the evaporation rate of ethanol is lower than that of gasoline fuel because of its low volatility (saturation vapour pressure) in low temperature conditions and large enthalpy of vaporization. This might have caused the increased HC and CO emissions in an ethanol direct injection plus gasoline port injection (EDI+GPI) engine when EDI was applied. To address this issue, the combustion and emission performance of an EDI+GPI engine fuelled with hot ethanol fuel was experimentally investigated in the present study. The experiments were conducted on a 249 cc single cylinder SI engine at medium load (IMEP 6.0-6.3 bar) and stoichiometric fuel/air ratio condition. The injected ethanol fuel temperature ranged from 45 ℃ (no fuel heating) to 105 ℃ (flash-boiling spray) with an increment of 15 ℃. Experimental results showed that the IMEP decreased slightly with the increase of ethanol fuel temperature. However, the ISCO and ISHC emissions decreased significantly and ISNO increased moderately with the increase ethanol fuel temperature.

*Keywords: Ethanol direct injection, Fuel temperature, Flash-boiling, Spark ignition, Combustion performance.*

## 1. Introduction

Ethanol fuel is considered promising as an alternative transportation fuel because it can be produced from bio-mass via established and new processes [1]. Comparing with gasoline fuel, ethanol fuel has many advantages including greater enthalpy of vaporization, larger octane number, faster laminar flame speed and smaller air/fuel ratio. Recently, ethanol direct injection (EDI) has been developed as a new technology to address the issue of knock in downsized spark ignition (SI) engines due to the strong cooling effect of EDI and ethanol's large octane number.

However, as neat fuel, EDI may be not suitable to power SI engines in some conditions because of its low volatility, low heating value and high enthalpy of evaporation, especially under cold conditions [2, 3]. It was reported that gasoline-fuelled engine could be started at ambient temperature as low as -40 ℃, while ethanol fuelled engine could not be started at temperature lower than 13 ℃ without an auxiliary cold start system [2]. Therefore, ethanol direct injection plus gasoline port injection engine (EDI+GPI) needs to be investigated to address this issue. As reported, EDI+GPI utilizes ethanol fuel more efficiently and flexibly in SI engines than the E10 or E85 in the current market [4]. It integrates the advantages of both port injection and direct injection fuel systems. Dual-injection concept offers the flexibility to change the gasoline-ethanol blending ratios online in terms of engine loads. The GPI can be used to address the cold start issue of ethanol fuel. The EDI can be started once the engine is warmed up and the percentage of ethanol fuel can be increased when engine load is increased to suppress the knock propensity.

To exploit the potential of the dual-injection concept, a single cylinder SI engine equipped with EDI+GPI has been developed at the University of Technology Sydney. Experimental results showed that the engine thermal efficiency was increased and knock propensity was reduced when EDI was applied [4, 5]. On the other hand, the HC and CO emissions of the engine were increased with the increase of ethanol ratio [4, 5]. It was found from the numerical modelling of the EDI+GPI engine that the low evaporation rate of ethanol fuel might have resulted in the poor mixing and increased HC and CO emissions [6].

The mixing and evaporating processes of a spray can be affected by a number of factors. The fuel temperature is an important factor that determines the saturation vapor pressure and thus the evaporation rate of a liquid fuel. The effect of fuel temperature on the EDI spray characteristics was investigated experimentally in a constant volume chamber [7]. The results showed that the ethanol evaporation rate did not increase much and could be considered as non-evaporating spray when the fuel temperature was increased from 275 K to 325 K, but increased significantly with further increase of fuel temperature. The cold start and mixing can be big issues for engines fuelled with neat ethanol or high percentage of ethanol/gasoline blends. Increasing the fuel temperature is an effective way to reduce the viscosity and increase the vapor pressure of the fuel, and consequently increase the break-up and evaporation rates. Studies were conducted to investigate the cold start

* Corresponding author: Yuhan Huang
Phone: (+61) 415040942
Email: yuhan.huang@student.uts.edu.au

and emission characteristics of engines fuelled with heated ethanol fuel [2, 8-12]. Experimental results showed that the cold-start time was shortened and emissions were reduced with the heated ethanol fuel.

The aim of the present study is to investigate the potential of increasing ethanol fuel temperature on improving the emission performance of an EDI+GPI engine.

## 2. Experimental Setup

The experiments were conducted on a four-stroke single-cylinder SI engine equipped with an EDI+GPI dual-injection fuel system. Table 1 shows the specifications of the engine. The original engine was an SI engine with gasoline port injection. It was modified to EDI+GPI engine by adding an EDI fuel system. Both GPI and EDI injectors were controlled by an engine control unit (ECU). More details about the engine modification and test rig can be found in [4].

Table 1. Engine specifications.

| | |
|---|---|
| Engine type | Single cylinder, air cooled, four-stroke, Spark ignition |
| Displacement | 249.0 cc |
| Stroke × Bore | 58.0 mm × 74.0 mm |
| Connecting rod | 102.0 mm |
| Compression ratio | 9.8:1 |
| Valve timings | IVO: 22.20° BTDC; IVC: 53.80° ABDC<br>EVO: 54.60° BBDC; EVC: 19.30° ATDC |
| Ethanol delivery system | Direct injection |
| Gasoline delivery system | Port injection |

Figure 1 is the schematic of the fuel heating system. An electronic resistance heater made of Kanthal A1 heating resistance wire was used to heat the ethanol fuel in the high pressure rail. The heater was wrapped on the fuel rail upstream the injector. A T-type thermocouple was attached to the surface of the fuel rail at the entrance of the EDI injector. The temperature was fed to a 2132 Eurotherm PID temperature controller, which controlled the relay of the heating system, so that the heating process stopped when the fuel temperature reached the preset value. Therefore, the fuel rail temperature at the injector entrance was regarded as the fuel temperature in the present study. The accuracy of the temperature control was within ±3 ℃. The power required for EDI heating is dependent on the fuel flow rate and the heating temperature. The maximum heating power is 150W which is about 3% of the engine output power.

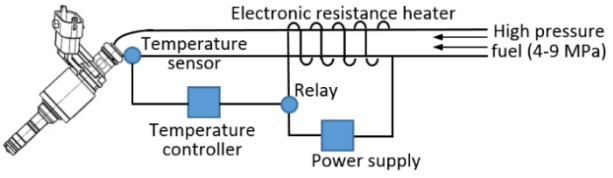


Fig. 1. Schematic of the EDI fuel heating system.

The ethanol fuel mixed with 0.1% gasoline fuel was provided by the Manildra Group. The gasoline fuel was the Unleaded Petrol from the Caltex Australia with an Octane number of 91. The experiments were conducted at medium load (6.0-6.3 bar IMEP) and engine speeds of 3500 rpm or 4000 rpm. The lambda was maintained around one during the experiments. A MEXA-584L gas analyzer was used to measure the lambda of EDI+GPI dual-fuelled conditions by setting the atomic ratios of hydrogen to carbon (H/C) and oxygen to carbon (O/C) in the blended fuel. The GPI pressure was 0.25 MPa and the EDI pressure was 4 MPa. The spark timing was 15 CAD BTDC. The GPI timing was 410 CAD BTDC and EDI timing was 300 CAD BTDC. The ethanol volume ratio was fixed at 50% (8.0 mg GPI plus 8.8 mg EDI). The investigated ethanol temperature varied from 45 ℃ (no fuel heating applied) to 105 ℃ (flash-boiling spray) with an internal of 15 ℃.

## 3. Results and Discussion

This section presents and discusses the experimental results in two sub-sections, the effect of ethanol fuel temperature on the engine combustion and emissions characteristics.

### 3.1 Combustion characteristics

To understand the effect of ethanol fuel temperature on the combustion characteristics of the EDI+GPI engine, the in-cylinder pressure, heat release rate (HRR), mass fraction burnt (MFB), indicated mean effective pressure (IMEP) and indicated thermal efficiency are discussed in this section.

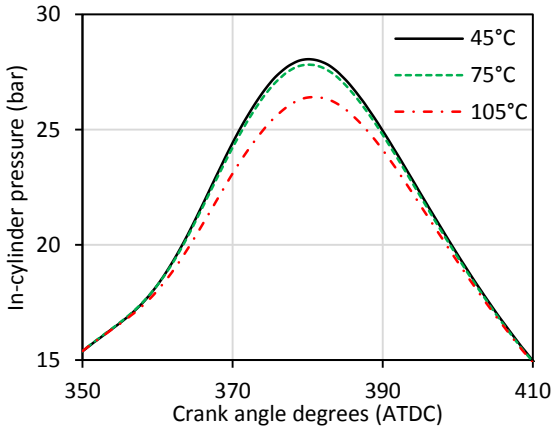


Fig. 2. In-cylinder pressure of different ethanol fuel temperatures at 3500 rpm.

Fig. 2 shows the in-cylinder pressure at the ethanol fuel temperatures of 45 ℃ (no fuel heating), 75 ℃ and 105 ℃ at the engine speed of 3500 rpm. As shown in Fig. 2, the peak in-cylinder pressure decreases slightly when the ethanol temperature is increased from 45 ℃ to 75 ℃, but decreases noticeably from 75 ℃ to 105 ℃. The corresponding HRR and MFB with different ethanol fuel temperatures at 3500 rpm are depicted in Figs. 3 and 4. Consistently, the HRR and MFB derived from the cylinder pressure shown in Fig. 2 demonstrate no noticeable difference when the fuel temperature is increased from 45 ℃ to 75 ℃. However when the fuel temperature is further increased to 105 ℃, the peak HRR value decreases and the slope of the MFB curve becomes smaller, indicating slower combustion speed.

The decrease of combustion speed with increased ethanol fuel temperature may be caused by the following two reasons. Firstly, the fuel density and viscosity

decrease when the fuel temperature is increased, which affect the injection process. Experiments and simulations on the injection process of a compression ignition engine found that the injection timing was retarded, the peak line pressure was decreased and the injection duration was prolonged when the fuel temperature was increased [13, 14]. The fuel mass flow rate also decreased when the fuel temperature was increased due to the decrease of fuel density [15]. These indicate that the mass of ethanol fuel injected into the combustion chamber is reduced with the increase of fuel temperature.

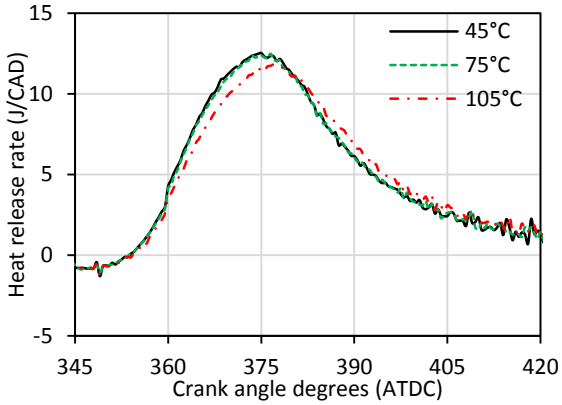


Fig. 3. Heat release rate of different ethanol fuel temperatures at 3500 rpm.

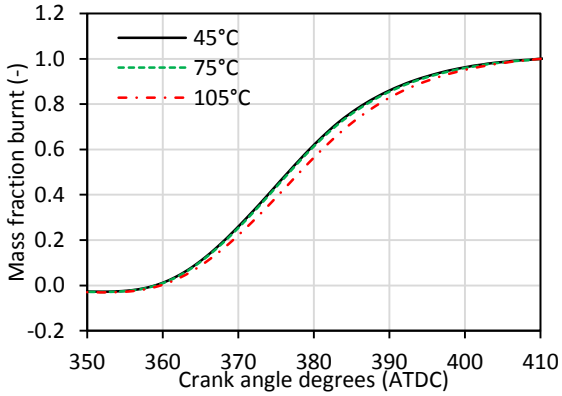


Fig. 4. Mass fraction burnt of different ethanol fuel temperatures at 3500 rpm.

The second reason is that the fuel spray process is affected significantly by the fuel temperature. The direct injection injector used in the engine tests was a six-hole nozzle. Fig. 5 shows the spray structures at 2.0 ms after the start of injection in a constant volume chamber with different fuel temperatures. The injection pressure was 6 MPa and the ambient pressure was 1 bar. More details about the spray experiments in the constant volume chamber can be found in reference [7]. Fig. 5 shows that the two side plumes of the ethanol spray converge towards the middle one when the fuel temperature is increased from 52 ℃ to 77 ℃, and collapse completely when the temperature reaches 102 ℃. In the EDI+GPI engine, the EDI injector was installed with the spray plumes bend towards the spark plug to create an ignitable mixture around the plug gap by the time of ignition. However, the results in Fig. 5 indicate that the spray was not collapsed at 45 ℃ and 75 ℃, but collapsed at 105 ℃. This may have destroyed the desired fuel distribution in the combustion chamber, and consequently deteriorated the ignition and combustion processes.

(a) 52 ℃ (b) 77 ℃ (c) 102 ℃

Fig. 5. Effect fuel temperature on the EDI spray structure.

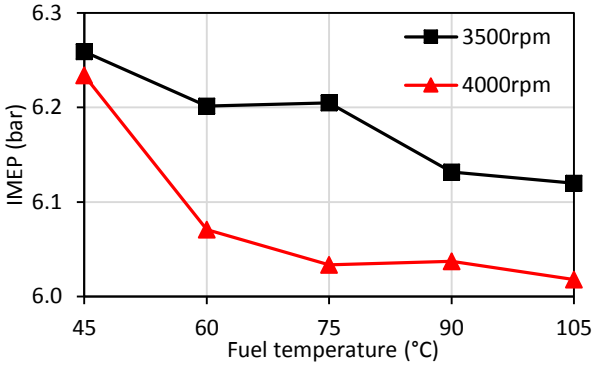


Fig. 6. Effect of ethanol fuel temperature on IMEP.

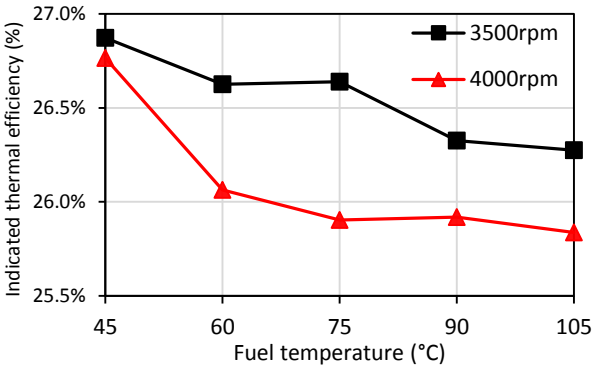


Fig. 7. Effect of ethanol fuel temperature on indicated thermal efficiency.

Fig. 6 shows the effect of ethanol fuel temperature on the IMEP at the engine speeds of 3500 rpm and 4000 rpm. As shown in Fig. 6, the IMEP decreases slightly from 6.26 bar to 6.12 bar at 3500 rpm and from 6.23 bar to 6.02 bar at 4000 rpm when the fuel temperature is increased from 45 ℃ to 105 ℃. The decrease of IMEP with increased fuel temperature is caused by the decreased combustion speed, as discussed in Figs. 3 and 4. Consistently, the indicated thermal efficiency decreases slightly from 26.9% in 45 ℃ to 26.3% in 105 ℃ at 3500 rpm, and from 26.8% in 45 ℃ to 25.8% in 105 ℃ at 4000 rpm, as shown in Fig. 7. The heating load is not included in the decrease of thermal efficiency.

## 3.2 Engine emissions

Although increasing ethanol fuel temperature decreases the thermal efficiency slightly, the emission performance of the EDI+GPI engine can be significantly improved with heated ethanol fuel. Figs. 8 and 9 show the effect of ethanol fuel temperature on the indicated specific carbon monoxide (ISCO) and hydrocarbon (ISHC) emissions. As shown in Fig. 8, the ISCO decreases from 24.27 to 15.81 g/kw-h at 3500 rpm and from 38.13 to 14.10 g/kw-h at 4000 rpm when ethanol temperature is increased from 45 ℃ to 105 ℃. The ISHC also decreases from 2.26 to 1.20 g/kw-h at 3500 rpm and from 2.47 to 0.77 g/kw-h at 4000 rpm, as shown in Fig 9. The decrease of ISCO and ISHC emissions are the results of improved evaporation and mixing processes

with heated ethanol fuel. Previous CFD simulation on the spray and combustion processes of the EDI+GPI engine showed that the low evaporation rate of ethanol fuel in low temperature environment before combustion led to a large number of liquid droplets not evaporated before the combustion took place, which consequently resulted in incomplete combustion and increased CO and HC emissions when EDI was applied [6]. In the present study, the ethanol fuel temperature is increased, which should increase the spray evaporation of ethanol fuel and thus improve the consequent combustion process and reduce the ISCO and ISHC emissions. Fig. 10 illustrates the effect of fuel temperature on the indicated specific nitric oxide (ISNO) emission. As shown in Fig. 10, the ISNO increases moderately from 13.38 or 10.73 g/kw-h at 45 ℃ to 14.32 or 12.30 g/kw-h at 105 ℃. The ISNO is increased due to the higher combustion temperature which might be resulted from the higher temperature of the ethanol fuel.

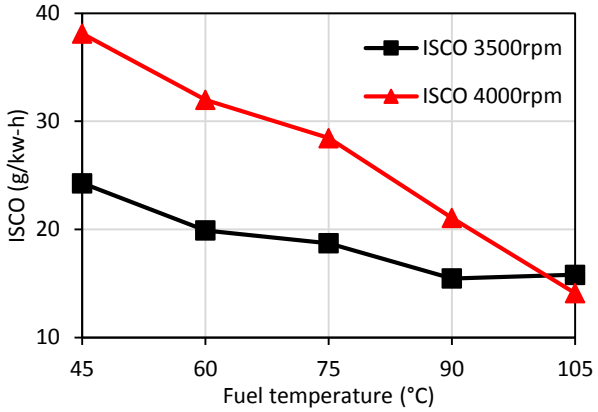


Fig. 8. Effect of ethanol fuel temperature on ISCO.

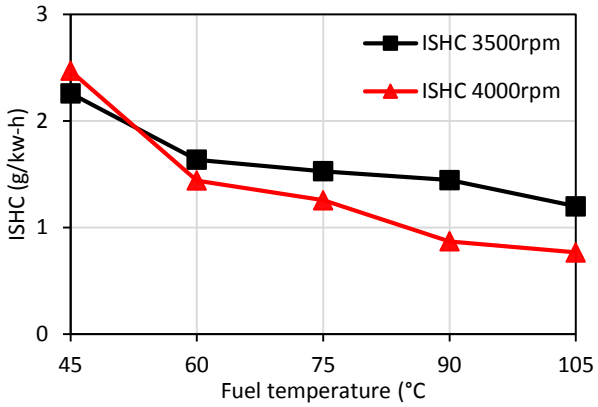


Fig. 9. Effect of ethanol fuel temperature on ISHC.

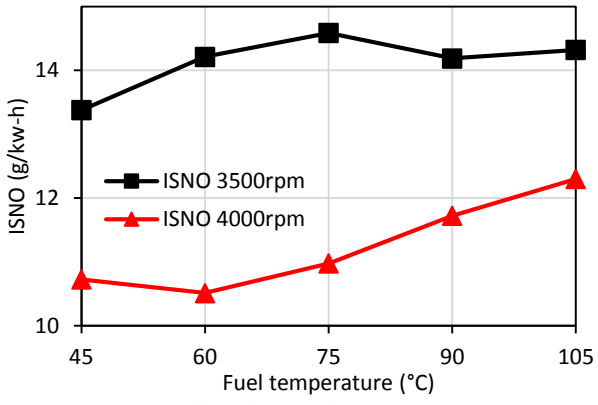


Fig. 10. Effect of ethanol fuel temperature on ISNO.

## 4. Conclusions

Experiments were conducted to investigate the effect of ethanol fuel temperature on the combustion and emission performance of a single-cylinder SI engine equipped with EDI+GPI dual-injection fuel system. The engine was operated at medium load (IMEP 6.0-6.3 bar) and stoichiometric air/fuel ratio at engine speeds of 3500 rpm or 4000 rpm. The ethanol fuel temperature was increased from 45 ℃ (no fuel heating) to 105 ℃ (flash-boiling spray).

The ISCO emission is decreased by 35% at 3500 rpm and 63% at 4000 rpm and the ISHC is decreased by 47% at 3500 rpm and 69% at 4000 rpm when ethanol temperature is increased from 45 ℃ to 105 ℃. On the other hand, the penalties of heating ethanol fuel are only 2% or 4% of decrease in thermal efficiency, and 7% or 15% of increase in ISNO emission. However even the increased ISNO emission is still smaller than that of GPI only condition due to the lower combustion temperature and stronger cooling effect of EDI. These indicate that increasing fuel temperature can be effective on reducing the CO and HC emissions while keeping the high thermal efficiency of the EDI+GPI engine.

## 5. Acknowledgments

The scholarship provided by the China Scholarship Council (CSC) is gratefully appreciated. The authors would like to express their great appreciation to Manildra Group for providing the ethanol fuel.

## 6. References

[1] S. M. Sarathy, P. Oßwald, N. Hansen, et al., Progress in Energy and Combustion Science, 44 (2014) 40-102.
[2] L. C. Monteiro Sales, J. R. Sodré, Applied Thermal Engineering, 40(0) (2012) 198-201.
[3] C. Liang, C. Ji, B. Gao, et al., Energy Conversion and Management, 58(0) (2012) 19-25.
[4] Y. Zhuang, G. Hong, Fuel, 105(0) (2013) 425-431.
[5] Y. Zhuang, G. Hong, Fuel, 135(0) (2014) 27-37.
[6] Y. Huang, G. Hong, R. Huang, Energy Conversion and Management, 92(0) (2015) 275-286.
[7] Y. Huang, S. Huang, P. Deng, et al., SAE Int. J. Fuels Lubr., 7(3) (2014) 792-802.
[8] L. Hildebrand, M. V. Feitosa, M. T. Ávila, et al., SAE paper 2000-01-3193, 2000.
[9] R. Krenus, M. R. V. Passos, T. Ortega, et al., SAE paper 2014-01-1369, 2014.
[10] L. C. M. Sales, J. R. Sodré, Fuel, 95(0) (2012) 122-125.
[11] D. F. Kabasin, Y. Joseph, W. Fedor, et al., SAE Int. J. Engines, 3(1) (2010) 982-995.
[12] D. Kabasin, K. Hoyer, J. Kazour, et al., SAE Int. J. Fuels Lubr., 2(1) (2009) 172-179.
[13] G. Guangxin, Y. Zhulin, Z. Apeng, et al., Journal of Energy Resources Technology, 135(4) (2013) 042202-042202.
[14] G. Chen, Journal of Engineering for Gas Turbines and Power, 131(2) (2008) 022802-022802.
[15] R. Mamat, N. R. Abdullah, H. Xu, et al., SAE International 2009-01-1896, 2009.

# Emissions and Performance of a Gas Turbine Engine with Two and Three-Component Blends of Petroleum and Bio-fuels

F.L. Carter[1], R. N. Parthasarathy[1], and S. R. Gollahalli[1,*]
[1]Combustion and Flame Dynamics Laboratory, University of Oklahoma, Norman, OK 73019, USA

## Abstract

Measurements of NO, CO, $CO_2$, and $O_2$ concentrations in the exhaust and performance characteristics (turbine inlet temperature, exhaust temperature, brake specific fuel consumption, overall equivalence ratio) of an auxiliary power unit gas turbine generator, fuelled with Jet A, a blend of Jet A and SME (soy methyl ester), and a blend of Jet A, SME and butanol are presented. The objective was to determine the effect of addition of alcohols on the emissions of petroleum-biofuel blends. Results indicate that the three component blend can mask the impact of the two component blend in terms of emissions at the rated full power.

*Keywords: Gas turbine, Emissions, Biofuels and Blends of Petroleum fuels and Biofuels*

## Nomenclature

| | |
|---|---|
| APU | Auxiliary power unit |
| BSFC | Brake specific fuel consumption |
| EIM | Mass-based emission index |
| EIE | Energy-based emission index |
| LHV | Lower heating value |
| MW | Molecular weight |
| SME | Soy methyl ester |

## 1. Introduction

Efforts to extend the availability of the crude oil reserves, such as conservation techniques, horizontal drilling and fracking to liberate otherwise nonviable deposits and the removal of oils locked within shales and sands, have become the focus of many technical advances. These efforts have more recently involved the use of fuels derived from biological sources. However, these biological replacements do not exist in large cost-effective quantities to warrant the wholesale conversion to their use; also, their inability to be used as direct replacements prohibits their use within the existing infrastructure. One solution to this either/or dilemma has been the blending of the fossil fuel with its biological counterpart in such a manner that the properties and consequences of the blend remain within the acceptable limits that have been established for the fossil fuel. It is generally known that the use of vegetal source-derived fatty methyl esters, such as soy methyl ester (SME) or their blends with petroleum fuels, results in a significant increase in NO emissions, but a decrease of the emission of soot and carbon monoxide [1-6]. Alcohols, however, have the potential to reduce NO emissions, particularly in lean-burning environments such as gas turbine engines. This motivated the logical step of combining the two biofuels with petroleum counterparts to tailor a composite blend which could be the optimal fuel from an environmental point of view. This paper presents the results of such an attempt.

### 1.1 Experimental Details

An auxiliary power unit (APU) gas turbine direct current generator used for ground starting of helicopters was the key component of this experimental setup. The electrical generator (28 V and 10 kW) was powered by a gas turbine engine with a single stage centrifugal compressor, an annular combustor and a one-stage axial turbine. The engine, originally meant for military outdoor applications, was adapted for laboratory application by installing thermocouples at salient locations, connecting to an alternate fuel supply system that enabled fuel flow rate measurement, construction of a low voltage, high amperage controllable load rack for output power measurement, and installation of a data-acquisition system. Also, the starting power source was modified for use with conventional automotive 12 V batteries. The engine exhaust system that served to discharge the combustion products outside the laboratory and reduce noise was fabricated in house.

The fuel supply rate to the engine was measured gravimetrically with a digital scale and a graduated cylinder. The engine loading was accomplished by constructing a load bank consisting of forty 250 W, 24 V, 500 hr lamps that were connected in parallel by 20 pairs of 15A circuit interrupters. This arrangement allowed output load dissipation at increments of 15 A (5% of full load). The heat generated by the lamps mounted in a duct was removed by the positive pressure airflow from a 110 V, 200 W centrifugal fan.

The data acquisition software "LabView" (National Instruments Inc. USA) was used for gathering temperature data from six thermocouples that were mounted at different locations in the engine. The data were acquired at a rate of 50 Hz and averaged over 10 seconds. Gas samples were withdrawn from the exhaust through tapered uncooled stainless steel probes (expanding from 1 mm diameter to 6 mm diameter over a length of 25 mm). Since the samples were taken from the exhaust, local reactions were expected to be minimal and frozen satisfactorily by this arrangement. The gases were passed through ice-cooled condensers to remove

* Corresponding author:
Phone: (+01) 405-325-1728
Email: gollahal@ou.edu

**Table 1: Properties of Fuel Components**

| | Jet A | SME | Butanol |
|---|---|---|---|
| LHV (J/kg) | $4.33x10^7$ | $3.7x10^7$ | $3.44\ x10^7$ |
| Density (kg/m3) | 810 | 879 | 810 |
| MW (kg/kmol) | 182 | 294 | 74 |
| C atoms/ kmol | 13 | 19 | 4 |
| H atoms/kmol | 26 | 34 | 10 |
| O atoms/kmol | 0 | 2 | 1 |

moisture and fiber wool (coarse) and balsa (fine) filters to trap particulate matter to protect the instruments. Thus, the concentrations of species were reported on a dry sample basis. The analytical instruments consisted of non-dispersive infrared detector of CO and $CO_2$ concentrations and chemical detectors for $O_2$ and NO concentration measurements. Several runs were repeated about 5 times and the uncertainties were estimated using Student's t–distribution at 95% confidence level. Typical uncertainty bars are shown in the figures of the measurements.

## 2. Results and Discussion

### 2.1 Brake Specific Fuel Consumption

Figure 1 shows the variation of brake specific fuel consumption (BSFC) with output power of the electrical generator. Since the electrical generator efficiency was not available, the engine output itself could not be determined. However, for the purpose of comparing the performance of the fuels, the measurements are plotted against the measured electrical power. As expected in typical gas turbine engines, BSFC decreases rapidly with the increase in output power and levels off at the rated full load. These measurements validated the modifications made in adapting the field engine to the

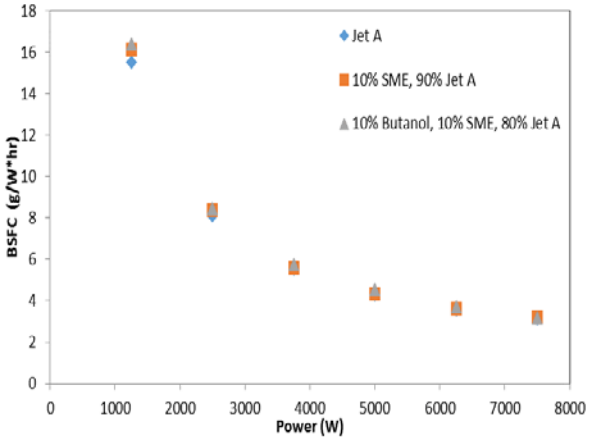


Fig. 1. Variation of BSFC with Output Power

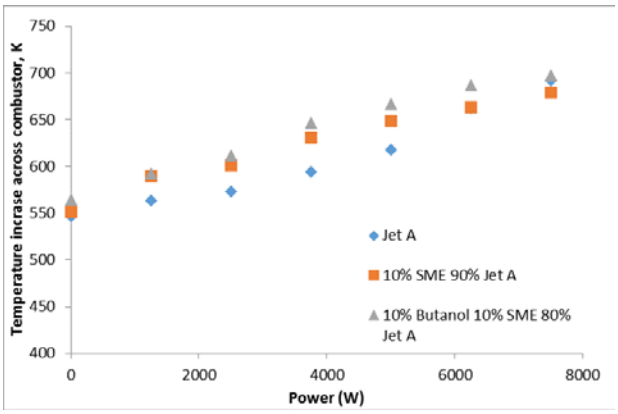


Fig. 2. Variation of the Temperature Increase Across Combustor with Output Power.

laboratory tests. It is interesting to note that the BSFC of the two-component and three-component blends was higher than that of Jet A fuel at the lowest load and the difference gradually vanished as the output power increased even though the LHV of biofuels is smaller, which suggests an improvement of combustion with biofuels. The thermal efficiency-output power curve is almost an inverse image of this curve [7], and hence is not shown here. The asymptotic full-load value of BSFC after accounting for the inertial and friction powers of the electrical generator and the large speed reduction gear unit is equivalent to a thermal efficiency of about 14.2%, 13.1% and 17.8% for Jet A, Jet A-SME, and Jet A-SME-Butanol blends. Although it appears smaller than the theoretical Brayton air-standard cycle efficiency of 35%, the measured efficiency is typical of APU gas turbines.

### 2.2 Temperature Increase in Combustor

Figure 2 shows the variation of the temperature increase in combustor with output power for different fuels. It is clear that the temperature differentials across the combustor are larger for the Jet A-SME blend and is even higher for the Jet A-SME-butanol blend in the mid-operating power range of the generator, although they

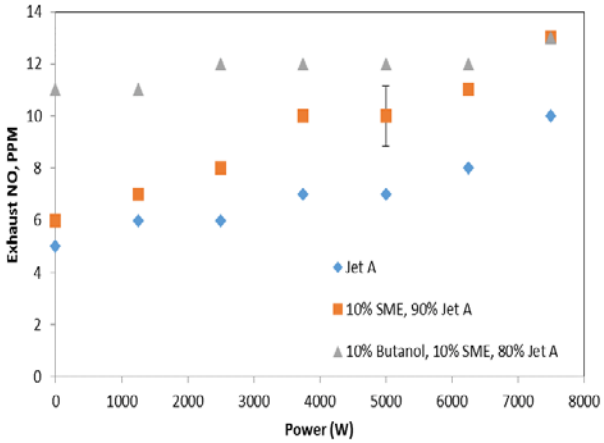

Fig. 3. Measured NO Volumetric Concentration in the Exhaust over the Output Power Range.

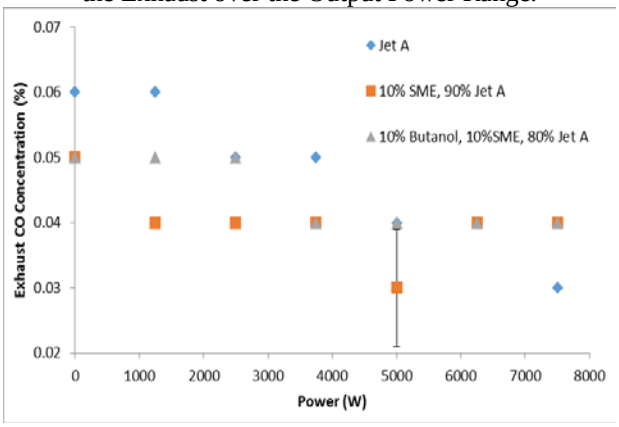


Fig. 4. Measured CO Volumetric Concentration in the Exhaust over the Output Power Range.

become closer at low and higher loads. This is an evidence of lower radiant heat loss from the biofuel flame than that from Jet A flame [6]. Also, the temperature differential across the combustor increases more rapidly for the two-component blend than that for Jet A and becomes almost the same as that of the three-component blend at the full load.

## 2.3 Measured NO and CO concentrations

Figure 3 shows the variation of the measured volumetric concentration of NO with output power. It seems that the oxygen content of SME and butanol are more effective at low loads in enhancing NO production, particularly that of butanol. This trend does not conform to the temperature variation, suggesting that deviation from the thermal mechanism occurs at low loads. At high loads, with more fuel present in the combustor and higher temperatures, the differences become smaller. The exponential effect of temperature dominates the NO production over the concentration of oxygen in the Zeldovich mechanism of NO production. Measured CO concentration values of CO are shown in Fig. 4. At low loads, the CO concentration is higher due to low combustion temperatures and decreases with power as the heat tease rates and flame temperatures increase with an increase in

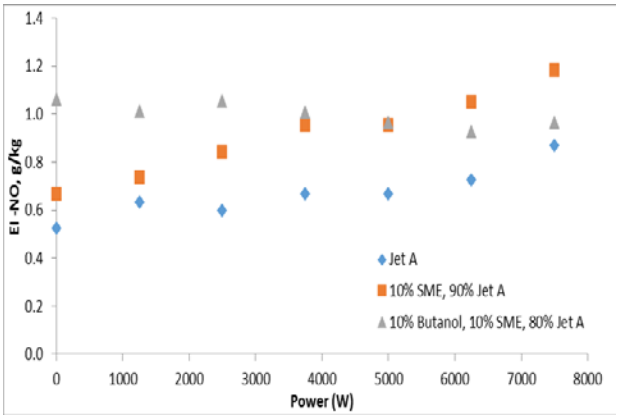


Fig. 5: Mass-based NO Emission Index over the Output Power Range.

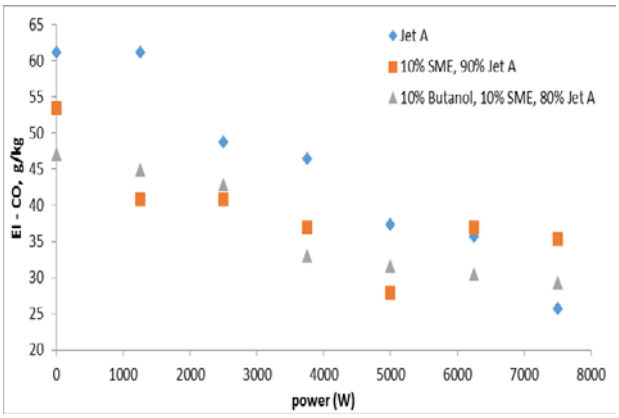


Fig. 6: Mass-based CO Emission Index over the Output Power Range.

power. It should be noted that the uncertainty in CO measurements was the highest of all the variables measured in this study and thus the scatter in the data is also high. Nevertheless, the trends are clear. Jet A produces the highest CO at low load and the two component (JetA-SME) blend results in the lowest CO emission. Alcohols, due to high latent heat and consequent quenching on the combustor, contribute to higher CO than the two-component blend.

## 2.4 Emission Indices of NO and CO

Figures 5 and 6 are plots of mass-based emission index (mass of pollutant emitted per unit mass of fuel consumed-EIM) of NO and CO with output power for the three fuels tested. Although this emission index is often used in combustion literature, when the heating value of fuels is different, energy-content based emission index (mass of pollutant emitted per unit energy output-EIE) is a better and more relevant comparison of fuel potential of environmental damage in engines. This emission index also accounts for the combustion efficiency of fuels. Figures 7 and 8 show the corresponding data on energy-based emission indices of

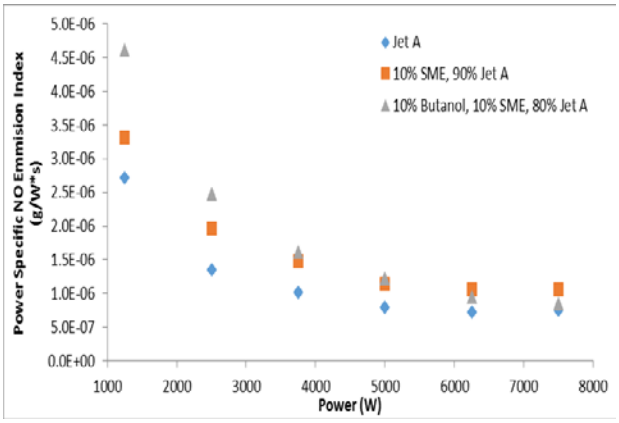

Fig. 7: Energy-based NO Emission Index over the Output Power Range.

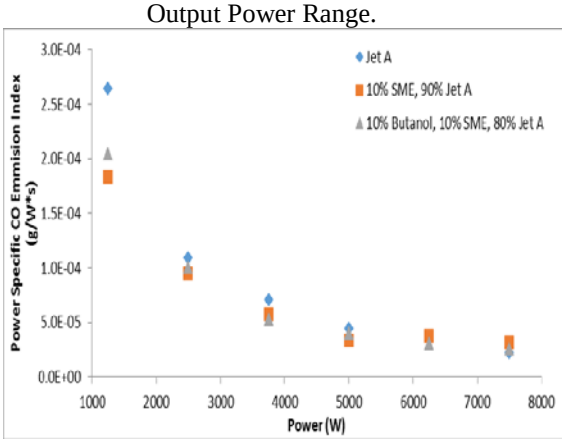


Fig. 8. Energy-based CO Emission Index over the Output Power Range.

NO and CO over the output power range. The no-load data has been omitted in these figures for obvious reasons of this emission index being infinite at zero output.

The mass-based emission index of NO (EIENO) increases with output power for all fuels, indicating that more NO is produced per unit mass of fuel at high power. This result is in conformity with the variation of mass-based emission index with equivalence ratio in a small-scale gas turbine engine for jet engine applications [8, 9]. As the output power and equivalence ratio are directly correlated in gas turbine engines, this comparison is valid. This behavior is attributed to the increasing combustion temperature with the output load. As the mixtures are overall lean in gas turbines, the thermal mechanism is dominant.

Habib et al. [8] noticed that the (EIENO) leveled off and even decreased with an increase in equivalence ratio for Jet A-SME blends. Mendez et al. [9] noted that the EIENO increased more slowly with output power for JetA-butanol blends. The present observations agree well with those from previous studies. The additional oxygen in the blends that could push the reactants towards leaner conditions is a source of the changing behavior of blends.

The mass-based CO emission index (EIMCO), on the other hand, decreases monotonically with the increase in output power for all fuels (Fig. 6), and is in full conformity with the results reported in [8, 9]. As the load and equivalence ratio increase, combustion temperature increases and CO oxidation rates are enhanced resulting in the observed variation.

The energy-based emission indices of NO and CO (EIENO, EIECO) show trends similar to those of the mass-based emission indices, but exhibit smoother variation with output power than the former. As mentioned earlier, these emission indices account for the variation in heating values and combustion efficiency and hence are superior indicators for the comparison of fuels. It is clear that energy-based emission indices decrease with output power. The thrust-based emission index showed non-monotonic variations with equivalence ratio [7, 8] presumably because the overall equivalence ratio is not a good representation of the flame tube equivalence ratio in a gas turbine engine. At low loads, the EIENO is lowest for Jet A and EIECO is lowest for the blends, and the differences diminish significantly at high loads.

## 3. Conclusions

This study on the effects of blending biofuels with Jet A in a small gas turbine shaft power engine driving an electrical generator has shown these results: (a) the BSFC is higher for blends in the low and mid-load ranges and the difference decreases at the high loads; (b) the temperature increase in combustor was the highest for the three-component blend; (c) at low loads NO emission index is higher, and CO emission index is lower for bio-fuel-Jet A blends with the differences decreasing significantly at high loads, and (d) at high loads, the emissions indices of three component blends with butanol are closer to those of Jet A than those with the two-component blend (SME-JetA).

## 4. Acknowledgments

The financial support of the US Department of Energy is gratefully acknowledged.

## 5. References

[1] M. Canakci and J. van Gerpen, Transactions. American Agriculture and Bioengineering, **46** (2003), pp. 937-944.

[2] S. Fernando, C. Hall and S. Energy and Fuels, **20** (2006), pp. 376-382.

[3] G. Labeckas and S. Slavinskas, Energy Conversion Management, **47** (2006), pp. 1954–1967.

[4] J. Tsai, S. Chen, K. Huang, Y. Lin, W. Lee, C. Lin and W. Lin, Journal of Hazardous Materials, **179** (2010), pp. 237-243.

[5] S.K. Hoekman and C. Robbins, Fuel Processing Technologies, **96** (2010), pp. 237-249.

[6] N.D. Love, R.N. Parthasarathy and S.R Gollahalli, International Journal of Green Energy **6** (2009), pp. 323–332.

[7] F.L. Carter, M.S. Thesis, Aerospace and Mechanical Engineering, University of Oklahoma, Norman, Oklahoma, USA (2015).

[8] Z. Habib, R. N. Parthasarathy and S. R. Gollahalli, Applied Energy, **87** (2010), pp. 1701–1709.

[9] C. Mendez, R.N. Parthasarathy and S.R. Gollahalli, Applied Energy, **118** (2014), pp. 135–140.

**Proceedings of the Australian Combustion Symposium**
**December 7-9, 2015, The University of Melbourne**

# Ethanol-Fuelled Gasoline Compression Ignition (GCI) Combustion in a Common-Rail Diesel Engine

C. Woo[1], S. Kook[1, *], E.R. Hawkes[1]

[1]School of Mechanical and Manufacturing Engineering
The University of New South Wales NSW 2052 Australia

## Abstract

Gasoline compression ignition (GCI) engines achieve high brake efficiency and simultaneous reduction of smoke and nitrogen oxides ($NO_x$) emissions via partially premixed charge (PPC) combustion owing to the extended ignition delay associated with the use of low cetane number fuel. Compared to kinetics-controlled homogenous charge compression ignition (HCCI) and its variants, GCI engines are more practical because the combustion phasing is closely coupled with the fuel injection timing. In this study, ethanol produced from biomass has been selected as a GCI fuel, considering its higher octane number (i.e. lower cetane number), evaporative cooling and oxygen contents than gasoline, all of which could further improve the GCI combustion. The ethanol-fuelled GCI was investigated in a single-cylinder automotive-size diesel engine connected to an Eddy Current (EC) dynamometer, with a particular emphasis on the effect of common-rail pressure on GCI combustion. The results show that the friction loss plays a significant role in GCI combustion such that the increased friction loss with increasing common-rail pressure leads to the increased brake specific fuel consumption (BSFC) and decreased fuel conversion efficiency. The engine-out emissions also show an increasing trend with increasing common-rail pressure due to the over-penetration of fuel sprays and wall wetting, which suggests that the common-rail pressure for GCI applications should remain low for both the efficiency and emissions. Compared to the diesel reference case, the ethanol-fuelled GCI combustion at low 50-MPa common-rail pressure achieves 50% higher fuel conversion efficiency, 5% lower BSFC and 27% lower $NO_x$ emissions while smoke emissions are kept at a negligible level.

*Keywords: Ethanol-fuelled gasoline compression ignition (GCI), Partially premixed charge (PPC), Common-rail pressure.*

## 1. Introduction

The simultaneous reduction of smoke and nitrogen oxides ($NO_x$) emissions while maintaining high efficiency of diesel engines has long been and will be of high interests to engine developers. Many have investigated new combustion regimes achieving this goal. The low-temperature combustion (LTC) diesel [1] uses a high rate of exhaust gas recirculation (EGR) for long ignition delay to increase the premixed charge while keeping the flame temperature below the soot and NO formation limit and due to the late injection timing, the combustion phasing is closely coupled with the fuel injection event. The homogeneous charge compression ignition (HCCI) [2] uses port or direct injection of fuel at the intake stroke or early at the compression stroke for long ignition delay to achieve soot- and $NO_x$-free combustion via lean homogenous mixtures but the combustion phasing is decoupled from injection timing and dominated by the kinetics of chemical reactions [3, 4]. However, these regimes cannot operate at high loads since LTC requires high EGR and thus the high load operation is not feasible [5, 6] and HCCI causes excessive pressure rise rates leading to pressure ringing and audible noise [3, 4].

One idea to overcome these hurdles is gasoline compression ignition (GCI) [7, 8] via direct injection of low cetane number fuel (e.g. gasoline) for realising the extended high-load limit with the help of fuel characteristics. While the direct injection of gasoline is similar with HCCI engines, the GCI does not modify engines for a low compression ratio and low-pressure injection system but shares exactly the same hardware of common-rail diesel engines with a high compression ratio of up to 18 [9, 10] and thus the GCI achieves very high efficiency due to a high compression ratio [10, 11]. As the injection timing of GCI is close to top dead centre (TDC), the extended ignition delay is controlled predominantly by low auto-ignition characteristics of gasoline [11]. The relatively shorter premixing time than HCCI means that the mixture is neither homogenous nor fully premixed but partially premixed [12] and thus the combustion phasing is closely coupled with the fuel injection event [12-14], offering a practical advantage over HCCI. Furthermore, the partially premixed charge (PPC) combustion helps achieve successful engine operation at high load and high speed conditions [13, 14] with the lower smoke and $NO_x$ emissions than those of conventional diesel combustion [7, 8].

This paper explores an alternative strategy: ethanol-fuelled GCI. The low auto-ignition quality of ethanol together with its high evaporative cooling can achieve even longer ignition delay than that of gasoline. Moreover, the oxygenated ethanol is well known to produce negligible amounts of soot [15], which in turn allows for a better $NO_x$ control [16]. The focus of the present study is the effect of common-rail pressure on GCI combustion considering that highly evaporative fuel and extended ignition delay time would not require high injection momentum needed for a conventional diesel fuel, which can potentially reduce friction loss and thereby increasing the brake efficiency.

* Corresponding author:
Phone: (+61) 2 93854091
Email: s.kook@unsw.edu.au

## 2. Experiments

The physical properties of ethanol and petroleum diesel fuel are summarised in Table 1. It is shown that ethanol has 43% lower kinematic viscosity and 35% lower calorific value than those of petroleum diesel. The ethanol has high research octane number (RON) of 108.6 and very low cetane number of 5~15, which is directly opposite to the low RON of 15~25 and high cetane number of 51 found in petroleum diesel. It is notable that ethanol contains 34.8% oxygen in fuel, which would reduce soot formation and enhance oxidation [17].

Figure 1 shows a single-cylinder diesel engine and measurement tools used in the present study. The single-cylinder diesel engine shares the production engine head and common-rail fuel injection system of a four-cylinder small-bore engine, and connected to an eddy current (EC) dynamometer (Froude Hoffmann, AG-30HS). The engine specifications are summarised in Table 2. The displacement volume of engine is 497.8 $cm^3$ with a compression ratio of 17.7. The swirl ratio of the engine head was 1.4. Two 60-litre surge tanks were used to minimise pressure fluctuations associated with the single-cylinder engine operation both upstream of the intake ports and downstream of the exhaust ports. The intake surge tank includes 4.5-kW electric heaters for the air temperature control. A common-rail fuel injection system (Bosch CP3) and a solenoid-type injector were used for direct injection of both ethanol and petroleum diesel. The common-rail pressure, injection duration and timing were controlled independently using a universal control unit (Zenobalti ZB-9013P).

The coolant temperature and intake air temperature were held constant at 90°C and 80°C, respectively. The engine speed was fixed at 2000 rpm where the maximum torque is measured from the corresponding production engine. The common-rail pressure was varied between 50 and 100 MPa. The double injection strategy with half of the fuel being injected at 170°CA bTDC and the other half being injected at 3°CA bTDC was implemented in the present study. The injection duration was adjusted for the fixed brake mean effective pressure (BMEP) of 426 kPa. It was noted that higher common-rail pressure conditions required the increased fuel mass to match the BMEP (this will be discussed in the following section). The injected fuel mass was measured using a Bosch-tube-type injection rate meter [18, 19]. A piezo-electric pressure transducer (Kistler 6056A) was used to record crank-angle-resolved in-cylinder pressure. Simultaneously, the exhaust emissions of smoke (Horiba Opacimeter MEXA-600S) and $NO_x$ (Ecotech 9841 AS) were measured. The unburnt hydrocarbon (HC) and carbon monoxide emissions were also recorded using a HC/CO analyser (Horiba MEXA-584L).

## 3. Results and Discussion

The results are shown in Fig. 2 for the in-cylinder pressure and aHRR traces of GCI combustion together with those of the diesel reference case. The increased common-rail pressure appears to impact both the magnitude and phasing of GCI combustion significantly. For example, the peak in-cylinder pressure and aHRR become higher with increasing common-rail pressure. For the 100-MPa case, the peak in-cylinder pressure is very high exceeding the diesel reference case. The start of combustion of the 100-MPa

Table 1. Fuel properties

| Property / Fuel | | Ethanol | Diesel |
|---|---|---|---|
| Density (@ 15℃), kg/$m^3$ | | 789 | 848 |
| Viscosity (@40 ℃), $mm^2/s$ | | 1.08 | 1.9 |
| Research octane number (RON) | | 108.6 | 15-25 |
| Cetane number | | 5-8 | 51 |
| Lower heating value, MJ/kg | | 26.80 | 41.66 |
| CHO wt.% | C | 52.17 | 86.2 |
| | H | 13.02 | 13.8 |
| | O | 34.78 | 0 |

Table 2. Engine specifications and operating conditions

| **Engine Specifications** | | | | |
|---|---|---|---|---|
| Displacement | 497.8 $cm^3$ | | | |
| Bore | 83 mm | | | |
| Stroke | 92 mm | | | |
| Compression ratio | 17.7 | | | |
| Swirl ratio | 1.4 | | | |
| Injector | 7-hole Bosch common-rail<br>Nominal hole diameter: 134 µm<br>K-factor: 1.5<br>Discharge coefficient: 0.86<br>HFR: 400 $cm^3$ for 30s<br>Included angle: 150° | | | |
| **Operating Conditions** | **Ethanol-fuelled GCI** | | | **Diesel** |
| Coolant temperature [°C] | 90 | | | |
| Intake air temperature [°C] | 80 | | | 27 |
| Engine speed [ rpm] | 2000 | | | |
| Injection timing [°CA bTDC] | 170, 3 | | | 13 |
| Injection Pressure [MPa] | 50 | 70 | 100 | 130 |
| Total injection mass [mg] | 24.8 | 28.2 | 33.0 | 26.0 |

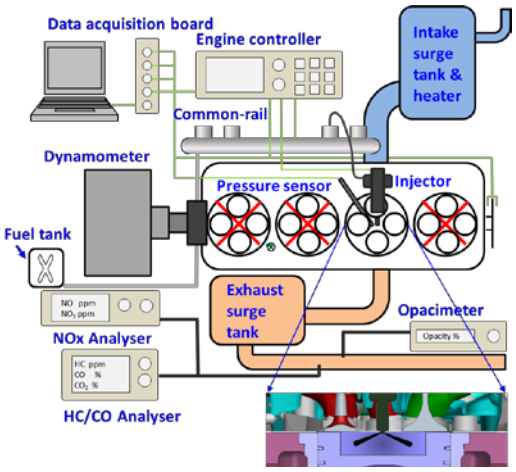


Fig.1. Schematic diagram of engine and diagnostic tools

case is also earlier than the diesel reference case, placing the peak in-cylinder pressure right at TDC. The observed trends could be explained with the improved air entrainment and mixing due to the increased injection momentum [9]. Previously, however, Table 2 showed higher injected mass of ethanol with increasing common-rail pressure, which was required to achieve the target BMEP of 426 kPa. It was implied that the wall wetting played a significant role on GCI combustion employing early fuel injection such that the issue would become worse at higher injection-momentum conditions and thus needed over-fuelling. This suggests that the increased in-cylinder pressure shown in Fig. 2 was a result of the second injection executed at 3°CA bTDC. That is, the near-TDC second injection at higher common-rail pressure could lead to improved ethanol combustion despite the worse wall wetting occurred in the early first injection. Fig. 2 also shows an interesting trend in aHRR traces. The GCI combustion shows a higher proportion of the mixing-controlled burn phase than that of the diesel reference case, which was simply due to the split injection of ethanol compared to the single injection of diesel. This secondary peak aHRR shows an increasing trend with decreasing common-rail pressure as annotated by the dashed-line arrow. This was because the air entrainment and mixing of the second injection occurred at a slower rate, leading to the combustion mode dominated by the mixing-controlled burn phase. The observed trends confirm that the GCI combustion employing a double-injection strategy is predominantly controlled by the second injection executed near TDC, which offers a practical advantage in controlling the combustion phasing.

The higher peak in-cylinder pressure and aHRR at higher common-rail pressure conditions led to the increased IMEP as shown in Fig. 3 (top-left). The coefficient of variation of IMEP (CoV of IMEP) shown in Fig. 3 indicates a slight increase in the cyclic fluctuation at higher common-rail pressure, which however is all within 4% meaning the stable engine operation. The combustion phasing is represented via the crank angle degree of 50% heat release (CA50). The CA50 decreases with increasing common-rail pressure as the proportion of premixed burn increases. However, the increased IMEP does not simply result in the increased BMEP. As mentioned previously, the BMEP was fixed at 426 kPa when the common-rail pressure was varied. This means the increased IMEP was used to compensate the increased friction loss. Fig. 3 (top-right) shows the increasing FMEP with increasing common-rail pressure due to the higher requirement for the fuel pumping power. The single-cylinder engine used in the present has a common-rail pump connected to the cam shaft which is driven by the crank shaft via a belt connection. The higher common-rail pressure therefore means the increased pumping loss. For the fixed BMEP, the increased fuel mass at higher common-rail pressure conditions (see Table 2) leads to the decreased fuel conversion efficiency and increased BSFC as shown in Fig. 3. The partially premixed, high-efficiency GCI combustion results in higher fuel conversion efficiency than the diesel reference case regardless of the common-rail pressure; however, only the 50-MPa condition shows a fuel economy benefit over the diesel reference case.

Figure 4 shows the measured emissions for various common-rail pressures. The increased uHC emissions due to the wall wetting from the early first injection

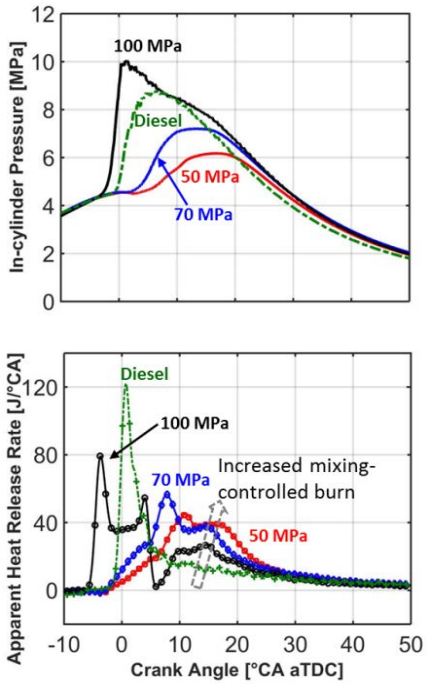


Fig. 2 Effect of common-rail pressure on the in-cylinder pressure and aHRR traces

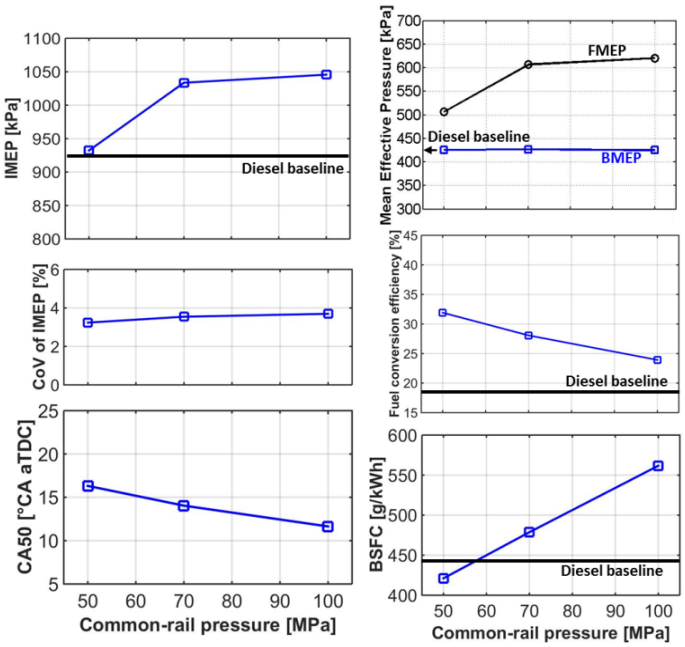


Fig. 3 Effect of common-rail pressure on mean effective pressure (MEPs), combustion phasing (CA50), fuel conversion efficiency, and BSFC

become worse at higher common-rail pressure conditions. The CO emissions shown below also increase leading to the significantly lower combustion efficiency. For example, the estimated combustion efficiency at common-rail pressure of 100 MPa is 90%, which is 8% lower than the diesel reference case. However, both smoke and $NO_x$ emissions are much lower than the diesel reference case at all common-rail pressures tested in the present study. Trend-wise, the smoke and $NO_x$ emissions increase with increasing common-rail pressure. It was noted that the high opacity level included white smoke from unburnt ethanol, which once again demonstrates the significance of wall wetting. The increased $NO_x$ emissions at higher common-rail pressures are consistent with the higher peak aHRR shown in Fig. 2 suggesting higher bulk-gas temperature and thus increased thermal NO formation. All of the measured engine-out emissions as well as fuel conversion efficiency and BSFC therefore suggest that low common-rail pressure is preferred for ethanol-fuelled GCI combustion.

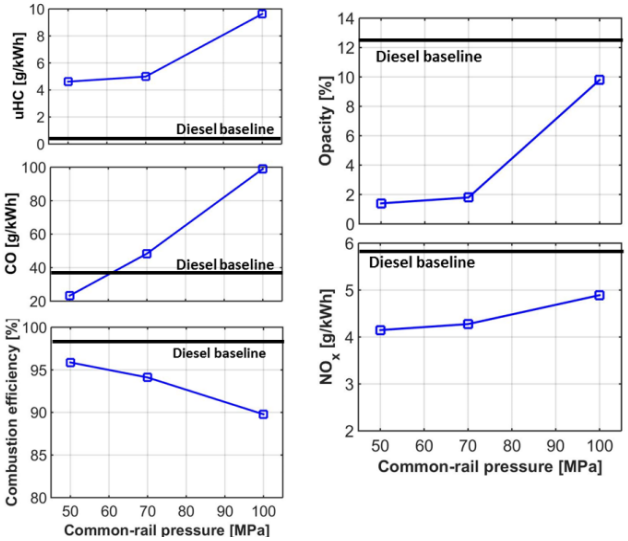


Fig. 4 Effect of common-rail pressure on engine-out emissions of uHC, CO, smoke (opacity) and $NO_x$

## 4. Conclusions

The performance and emissions of ethanol-fuelled gasoline compression ignition (GCI) engine has been investigated in a single-cylinder light-duty diesel engine equipped with a conventional common-rail fuel injection system. The major findings of the present study are summarised as follows:

- The common-rail pressure variations at fixed brake power conditions show that the peak in-cylinder pressure and heat release rate increase with increasing common-rail pressure due to the improved mixing, which results in increased indicated power.
- However, the friction loss increases with increasing common-rail pressure, which outperforms the increased indicated power. At fixed brake power conditions, this means increased BSFC suggesting that the common-rail pressure for GCI applications should remain low for the efficiency gain.
- The engine-out emissions of uHC, CO, and white smoke show an increasing trend with increasing common-rail pressure due likely to the increased wall wetting. The increased peak aHRR also cause the increased $NO_x$ emissions, all of which support the advantages of low common-rail pressure for GCI applications.
- Compared to the diesel reference case of the present study, the optimised ethanol-fuelled GCI combustion at low common-rail pressure of 50 MPa achieves 50% higher fuel conversion efficiency and 5% lower BSFC despite 36% lower calorific value of ethanol. The $NO_x$ emissions are decreased by 27% while smoke emissions are kept at a negligible level.

## 5. Acknowledgments

Experiments were performed at the UNSW Engine Research Laboratory, Sydney, Australia. Support for this research was provided by the Australian Research Council.

## 6. References

[1] S. Kook, C. Bae, P.C. Miles, D. Choi and L.M. Pickett, SAE Technical Paper No. 2005-01-3837; 2005.

[2] J.E. Dec, Proc Combust Inst 32 (2) (2009), pp. 2727-2742.

[3] R.K. Maurya and A.K. Agarwal, SAE Technical Paper No. 2008-28-0064; 2008.

[4] Y. Zhang, B.Q. He, H. Xie and H. Zhao, SAE Technical Paper No. 2006-01-0631; 2006.

[5] S. Kimura, O. Aoki, Y. Kitahara and E. Aiyoshizawa, SAE Technical Paper No. 2001-01-0200; 2001.

[6] A. Wimmer, H. Eichlseder, M. Klell and G. Figer, Int. J. Veh. Des. 41 (1-4) (2006), pp. 32-48.

[7] G.T. Kalghatgi, P. Risberg and H.E. Ångström, SAE Technical Paper No. 2006-01-3385; 2006.

[8] G.T. Kalghatgi, P. Risberg and H.E. Ångström, SAE Technical Paper No. 2007-01-0006; 2007.

[9] L. Hildingsson, G. Kalghatgi, N. Tait, B. Johansson and A. Harrison, SAE Technical Paper No. 2009-01-2648; 2009.

[10] V. Manente, B. Johansson, P. Tunestal and W. Cannella, SAE Int. J. Engines 2 (2) (2009), pp. 71-88.

[11] V. Manente, C.G. Zander, B. Johansson, P. Tunestal and W. Cannella, SAE Technical Paper No. 2010-01-2198; 2010.

[12] L. Hildingsson, B. Johansson, G.T. Kalghatgi and A.J. Harrison, SAE Int. J. Engines 3 (1) (2010), pp. 440-460.

[13] M. Sellnau, M. Foster, K. Hoyer, W. Moore, J. Sinnamon and H. Husted, SAE Int. J. Engines 7 (2) (2014), pp. 835-851.

[14] M.C. Sellnau, J. Sinnamon, K. Hoyer, J. Kim, M. Cavotta and H. Husted, SAE Technical Paper No. 2013-01-0272; 2013.

[15] S. Padala, C. Woo, S. Kook and E.R. Hawkes, Fuel 109 (0) (2013), pp. 597-607.

[16] A. Mohammadi, S.-S. Kee, T. Ishiyama, T. Kakuta and T. Matsumoto, SAE Technical Paper No. 2005-01-3712; 2005.

[17] V. Manente, B. Johansson and P. Tunestal, J. Eng. Gas Turbines Power 132 (8) (2010), pp. 082802.

[18] S. Padala, S. Kook and E.R. Hawkes, Energy Fuels 28 (1) (2014), pp. 340-348.

[19] C. Woo, S. Kook, P.L. Rogers, C. Marquis, E. Hawkes and S.C. Tupufia, SAE Technical Paper No. 2015-24-2489; 2015.

# Effect of Injection Timing on Gasoline/Diesel and Gasoline/ Biodiesel Fuelled Dual-Fuel Engine: A Comparative Study

Y. H. Teoh [1, 2, *], H. H. Masjuki [1, *], M. A. Kalam [1], H. G. How [1], S. M. Ashrafur Rahman [3], A. M. Ruhul [1]
[1] Centre for Energy Sciences, Faculty of Engineering, University of Malaya, 50603 Kuala Lumpur, Malaysia
[2] School of Mechanical Engineering, Universiti Sains Malaysia, Engineering Campus, 14300 Nibong Tebal, Penang, Malaysia
[3] Queensland University of Technology (QUT), Australia

## Abstract

Biodiesel can be considered as an alternative substitute to fossil diesel fuels used in the transport sector. However, the drawbacks such as higher specific fuel consumption and lower thermal efficiency were usually arises with the use of biodiesel in conventional diesel combustion engines. Using alternative fuels and switching to promising combustion technologies such as low temperature combustion (LTC) are reliable approaches to solve this issue. This research aims to apply biodiesel as an alternative fuel source for engines operating in dual-fuel combustion mode. The effects of direct fuel injection timing on engine out-responses were studied under constant EGR of 35%. This dual-fuel combustion mode employed gasoline as port injection fuel and diesel/ biodiesel as direct injection fuel with rapid in-cylinder fuel blending. The results of engine performance, emissions, and cylinder pressure were recorded and analyzed. The results showed that engines operating under biodiesel-gasoline dual-fuel combustion mode could achieve high efficiency at SOI timing of -13°ATDC. With this strategy, near zero nitrogen oxide ($NO_x$) emission can be achieved under early or late SOI timing. Biodiesel-gasoline dual-fuel combustion mode showed lower hydrocarbon (HC) and carbon monoxide (CO) emissions than diesel-gasoline dual-fuel combustion mode. The oxygen content in biodiesel is especially useful in limiting locally fuel rich regions, resulting in improved combustion and thereby reducing HC and CO emissions simultaneously.

*Keywords: low temperature combustion, combustion, gasoline, diesel, biodiesel.*

## 1. Introduction

In the present scenario of a worldwide energy crisis coupled with its detrimental impact on environment, the world is compelled to focus on developing clean alternative fuel that is economically competitive, technically feasible, easily available, and environmentally acceptable [1-3]. Biofuels from bio-based products are an alternative to fossil fuels used in transport sector. Biodiesel in its neat or blended form can be used in diesel engines without modification of the engine or fueling process, thus greatly simplifying the system's integration and adoption.

Recently, another type of promising combustion strategies have evolved that are called low temperature combustion (LTC) in addition to spark ignition (SI) and compression ignition (CI). LTC is an in-cylinder approach of advanced combustion strategies for the simultaneous reduction of particulate matter (PM) and nitrogen oxides ($NO_x$) emissions [4, 5]. LTC can be achieved with a new emerging dual-fuel engine combustion strategy, called reactivity controlled compression ignition (RCCI) by Kokjohn et al. [6]. RCCI is a dual-fuel engine combustion technology and offers better control of combustion and resolve the load range limitation issue of homogeneous charge compression ignition (HCCI) and premixed charge compression ignition (PCCI) strategies [7]. Usually, RCCI uses port injection of relatively low reactive fuel (i.e., gasoline) along with direct injection of higher reactive fuel (i.e., diesel) to control in-cylinder charge conditions. Mixing fuels of varied reactivity in the cylinder offers another powerful dimension of combustion control parameters.

The application of biodiesel in conventional diesel combustion engines has usually caused higher $NO_x$ and specific fuel consumption [8-10]. Using alternative fuels and switching to promising combustion technologies such as LTC can be reliable approaches to addressing this issue [11]. In fact, LTC is a promising concept for $NO_x$ emission reduction not only for petroleum diesel, but also for biodiesels [12]. However, the main challenge for most LTC strategies is the higher hydrocarbon (HC) and carbon monoxide (CO) emissions that result from low combustion temperature and higher exhaust gas recirculation (EGR) rate. Using oxygenated fuel of biodiesel can be a good alternative to this problem, and yet these fuels are derived from renewable sources. However, very few studies have investigating engines operating on biodiesel in RCCI combustion mode. In a RCCI dual-fuel combustion engine system, biodiesel fuel has a higher cetane number and higher oxygen content and can be used as the ignition source. Apparently, combining the two, LTC and biodiesel, could potentially address both the emissions and efficiency challenges observed with petroleum-diesel based LTC [13]. Therefore, this research study focuses on the utilisation of biodiesel as an alternative fuel source for engines operating in RCCI dual-fuel combustion mode.

* Corresponding author: Y.H. Teoh & H.H. Masjuki
Phone: (+60) 3 79674448
Email: yewhengteoh@gmail.com, masjuki@um.edu.my

## 2. Experimental Apparatus

In this study, fossil diesel fuel and palm oil were obtained in commercial form. Table 1 describes the key physicochemical of the converted neat palm methyl ester (PME) compared with American Society for Testing and Materials (ASTM) and European Standards (EN). The important properties of petroleum diesel and gasoline are also listed in this table.

Table 1: The fuel properties of petroleum diesel, PME biodiesel and gasoline

| Properties | Diesel | Biodiesel Limit (ASTM D6751) | Test method | PME | Gasoline |
|---|---|---|---|---|---|
| Kinematic viscosity @ 40°C ($mm^2/s$) | 3.34 | 1.9-6.0 | D445 | 4.4 | 0.567 |
| Density @ 15°C ($kg/m^3$) | 851.9 | 880 | D127 | 882.5 | 0.745 |
| Acid number (mg KOH/g) | 0.12 | 0.5 max | D664 | 0.2 | - |
| Calorific value (MJ/kg) | 45.31 | - | D240 | 39.98 | 43.5 |
| Flash point (°C) | 71.5 | 130 min | D93 | 155.5 | -36 |
| Pour point (°C) | 1 | Not specified | D2500 | 4 | - |
| Cloud point (°C) | 8 | Not specified | D2500 | 5 | - |
| Oxidation stability @ 100°C (hours) | >40 | 3 min | EN14112 | 15 | - |
| Cetane number | 52 | 47 min. | D6890 | 75 | - |

In this study, all experiments were conducted under a constant speed of 1500 rpm and direct injection fuel pressure of 600 bar. Two kinds of dual-fuel experiments, i.e. the direct injection (DI) diesel coupled with port fuel injection (PFI) gasoline and the DI PME fuel coupled with PFI gasoline, are compared in terms of performance, emissions, and combustion characteristics. Gasoline was port fuel injected onto the opened intake valve at −360° ATDC. Experiments were performed at 35% EGR and the start of injection (SOI) timing was varied from -5° ATDC and advanced up to the point at which potential unstable combustion starts to occur. For each type of DI fuel, the injection quantity was set to 6.5 mg/stroke for baseline diesel fuel and 7.6 mg/stroke for PME fuel, respectively. Considering the lower calorific value of PME fuel compared to baseline diesel, higher injection quantity is necessary to ensure equivalent fuel energy is injected for every cycle. The ratio of energy of the premixed gasoline fuel to the total energy was maintained at 0.6 for both direct injected diesel and PME dual-fuel combustion. In addition, the total supplied fuel energy is approximately 760 J/cycle. The test engine used in this study is based on a modified single-cylinder compression ignition diesel engine. The related engine modifications of the fuel delivery system of this engine and instrumentations have been discussed in the author's previous work [14].

## 3. Results and Discussions

The indicated specific fuel consumption (ISFC) as a function of SOI timing for baseline diesel/gasoline and PME/gasoline dual-fuel experiments is shown in Fig. 1. In general, the results indicated that as the SOI timing is advanced, the ISFC increases to a point then decreases. Furthermore, the ISFC for PME/gasoline operation is constantly greater than that of baseline diesel/gasoline across all SOI timings. The higher ISFC of PME/gasoline corresponds to less efficient operation, thus requiring a greater amount of DI fuel to accomplish the same amount of indicated power. This is due to the low calorific value of PME compared with diesel, which was about 12% lower than that of baseline diesel fuel. Subsequently, the results also indicate that the ISFC tends to be highly sensitive to variation in SOI timing. For both the dual-fuel operations, advancing the SOI timing resulted in an increase in ISFC initially that reached the highest value at SOI timing of -45°ATDC and then was reduced. The lowest achievable ISFCs for diesel/gasoline and PME/gasoline operation are found to be 190.0 and 213.9 g/kWhr, respectively, at an optimum SOI timing of −7 °ATDC.

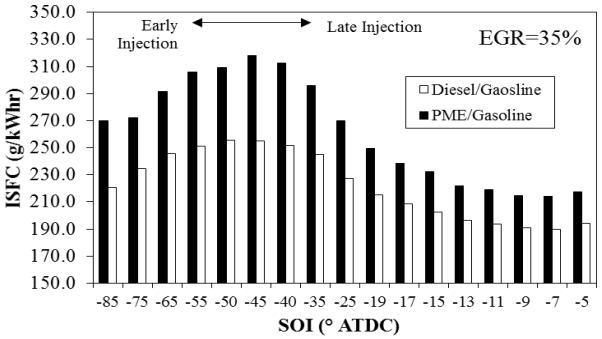


Fig. 1: ISFC at various SOI timings.

Fig. 2 illustrates the variations in brake thermal efficiency (BTE) with different SOI timings for engines fuelled with diesel/gasoline and PME/gasoline dual-fuel combustion at 35% EGR. The PME/gasoline operation shows slightly higher BTE than diesel/gasoline with SOI of -5 and -7°ATDC, and somewhat lower with further SOI advancement. The highest reported BTE for diesel/gasoline and PME/gasoline are found to be 34.8% and 34.7%, respectively, at SOI timing of -13°ATDC. In both the dual-fuel operations, advancing the SOI timing resulted in an increase in BTE initially, reached the peak value at SOI timing of -13°ATDC, and then was reduced. Some improvement in BTE was gained with SOI beyond -50°ATDC.

The variation of $NO_x$ under various SOI timings is illustrated in Fig. 3. Generally, the PME/gasoline operation shows slightly lower $NO_x$ emissions than diesel/gasoline across all SOI timings. With advancing SOI, $NO_x$ is initially increased and reaches the maximum value of 6.7 and 6.4 for diesel/gasoline and PME/gasoline, respectively, at SOI -35°ATDC, and then is reduced. A substantially lower level of $NO_x$ below EURO VI emission standards can be achieved by early or late SOI timing for both fuel operations. With

advanced SOI cases, the early injection tend to lean out the local equivalence ratio resulting from extended mixing time and retards the combustion phasing, resulting in lower peak flame temperatures and therefore lower $NO_x$ emissions. In contrast, with late injection cases, the combustion phasing is progressively retarded and shifted away from top dead center (TDC) in expansion stroke. This effect leads to reduced combustion temperature and lower $NO_x$ formation via thermal or Zeldovich mechanism. Besides, the effect of SOI timing on combustion phasing can be realised from the crank angle of mass fraction burned of 50% (CA50) plot as shown in Fig. 4. As can be seen, later or earlier SOI timing will all shift the CA50 away from TDC in the expansion stroke, which explains the decreased $NO_x$ emissions. A minimum point of CA50 versus SOI timing presents for both cases. With advanced SOI timing, the leaner local equivalence ratios prolonged the ignition delay and thus caused ignition to occur late. However, when SOI was retarded, ignition delay became shorter due to the considerably higher cylinder pressure and temperature at that moment, which led to immediate combustion after DI fuel was injected.

Fig. 5 shows the variations in HC emissions with different SOI timings for engine fuelled with diesel/gasoline and PME/gasoline dual-fuel combustion at 35% EGR. The PME/gasoline operation reveals lower HC than diesel/gasoline across all SOI timings. The oxygen content in PME fuel is especially useful in limiting locally fuel rich regions, resulting in improved combustion and thereby reducing HC emissions. Furthermore, it can be seen that the highest HC emissions resulting from diesel/gasoline and PME/gasoline operation are 1.7 and 1.6 g/kWhr, respectively, with earliest SOI timing of -85°ATDC. As previously discussed, the earliest SOI timing tends to lean out the local equivalence ratio and caused the engine to begin running rough with intermittent misfiring, thereby resulting in higher HC emissions. Subsequently, the effect of SOI timing on CO emissions for engines fuelled with diesel/gasoline and PME/gasoline dual-fuel combustion as shown in Fig. 6. Similarly to the HC variation trend, it can be seen that CO emissions first decrease with advancing SOI timing, reaching a minimum at an SOI of -13°ATDC, and then showing a gradual increase. Besides, it can be seen that CO emissions were lower for PME/gasoline than diesel/gasoline across all SOI timings. The use of oxygenated fuel of PME biodiesel would be expected to enhance combustion efficiency, thereby reducing CO emissions.

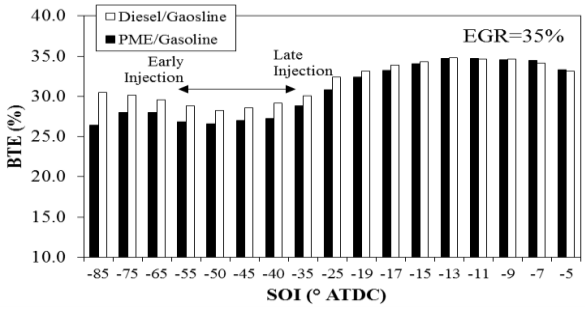


Fig. 2: BTE at various SOI timings.

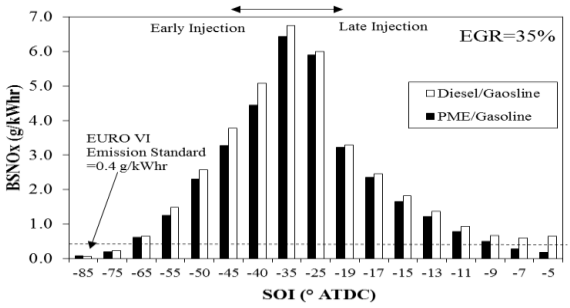


Fig. 3: Brake specific NOx ($BSNO_x$) emissions at various SOI timings.

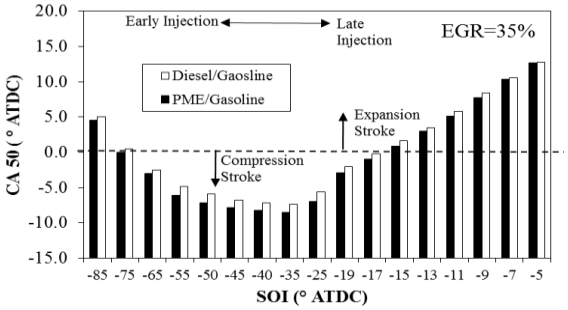


Fig. 4: CA50 at various SOI timings.

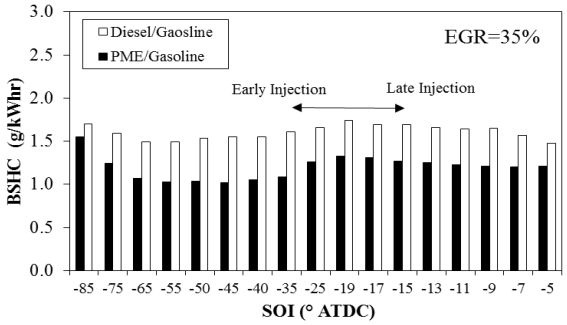


Fig. 5: Brake specific HC (BSHC) emissions versus SOI timing sweeps.

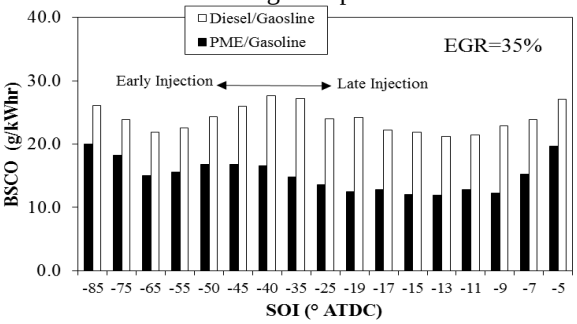


Fig. 6: Brake specific CO (BSCO) emissions versus SOI timing sweeps.

Combustion characteristics resulting from SOI timing variation for both the dual-fuel operation is shown in Fig. 7. At advanced SOI timing, peak cylinder pressure is initially increased and reaches the maximum at SOI timing of -45°ATDC, and then is reduced. Besides, it can be seen that at different SOI timings, the peak heat release rate (HRR) of the PME/gasoline is marginally higher than those of diesel/gasoline cases except for the considerably advanced SOI timing past -25°ATDC. Compared to the case of SOI of -45°ATDC, both late and early SOI timings will reduce the peak cylinder pressure and retard the corresponding crank angle toward the expansion stroke. This interesting effect can be

explained because as the SOI advanced, the in-cylinder mixture became more homogenous, and the low equivalence ratio extended the ignition delay of DI fuel, thereby delaying the combustion phasing. For retarded SOI cases, on the other hand, the combustion process becomes more coupled with the variation in SOI timing. From the HRR profile, it can be observed clearly that a remarkable two-stage high temperature heat release (HTHR) occurred for late SOI timing of -5° to -25°ATDC. In contrast, for advanced SOI timing cases, the combustion process is characterised by single-stage low temperature heat release (LTHR) and followed by single-stage HTHR. The changes of HRR profile from two-stage HTHR for late SOI case to single-stage HTHR for early SOI case indicates that the typology of combustion shifts from partially diffusion controlled to almost totally kinetically controlled. Clearly the variation of SOI timing have significant effect on combustion characteristics for the engine operating in dual-fuel combustion mode. As the SOI is advanced from -45 to -65°ATDC, the peak of second stage HTHR increases and becomes narrower. However, further advancing the SOI past -65°ATDC caused a reduction in this peak, resulting in lower locally combustion temperature, thereby caused reduction in $NO_x$ emissions. In addition, in general, under most of the SOI timing conditions except for the earliest and latest SOI, all PME/gasoline operations exhibited advanced SOC timing than the diesel/gasoline operations owing to their relatively higher cetane number.

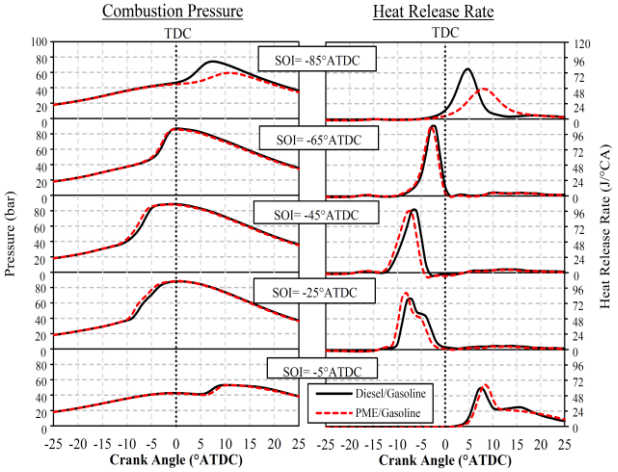


Fig. 7: Effect of SOI timing on combustion pressure and heat release rate.

## 4. Conclusions

The following main conclusions can be drawn from this investigation.

1. The lowest achievable ISFCs for diesel/gasoline and PME/gasoline operation are found to be 190.0 and 213.9 g/kWhr, respectively, at an optimum SOI timing of −7 °ATDC.

2. The PME/gasoline operation shows slightly higher BTE than diesel/gasoline with SOI of -5 and -7°ATDC. The highest reported BTE for diesel/gasoline and PME/gasoline are found to be 34.8% and 34.7%, respectively, at SOI timing of -13°ATDC.

3. A substantially lower level of $NO_x$ below EURO VI emission standards can be achieved by early or late SOI timing for both fuel operations. Besides, the same CA50 is possibly obtained by early or late SOI timing.

4. The PME/gasoline operation reveals lower HC and CO than diesel/gasoline across all SOI timings. The oxygen content in PME fuel is especially useful in limiting locally fuel rich regions.

In conclusion, the results from this study suggest that alternative fuels from bio resources have high potential as substitutes for petroleum-based fuels for engines operating with low temperature combustion strategies. Meanwhile, the engine operating in RCCI dual-fuel combustion mode is capable of achieving high efficiency with near zero $NO_x$ emissions.

## 5. Acknowledgments

The authors would like to acknowledge the Ministry of Higher Education (MOHE) of Malaysia and University of Malaya for financial support through HIR grant (UM.C/HIR/MOHE/ENG/07) and Postgraduate Research Grant (PPP) (grant number PG035-2012B).

## 6. References

1. M. Mofijur; H. H. Masjuki; M. A. Kalam; A. E. Atabani; M. Shahabuddin; S. M. Palash; M. A. Hazrat, Renewable and Sustainable Energy Reviews 28 (0) (2013) 441-455 http://dx.doi.org/10.1016/j.rser.2013.07.051.

2. A. M. Liaquat; M. A. Kalam; H. H. Masjuki; M. H. Jayed, Atmospheric Environment 44 (32) (2010) 3869-3877 http://dx.doi.org/10.1016/j.atmosenv.2010.07.003.

3. B. Tesfa; R. Mishra; F. Gu; A. D. Ball, Renewable Energy 37 (1) (2012) 333-344 http://dx.doi.org/10.1016/j.renene.2011.06.035.

4. J. E. Dec, Proceedings of the Combustion Institute 32 (2) (2009) 2727-2742 http://dx.doi.org/10.1016/j.proci.2008.08.008.

5. W. F. Northrop; D. N. Assanis; S. Bohac, SAE Int. J. Engines 4 (1) (2011) 1431-1444 10.4271/2011-01-1186.

6. S. L. Kokjohn; R. M. Hanson; D. A. Splitter; R. D. Reitz, SAE Int. J. Engines 2 (2) (2009) 24-39 10.4271/2009-01-2647.

7. R. D. Reitz; G. Duraisamy, Progress in Energy and Combustion Science 46 (0) (2015) 12-71 http://dx.doi.org/10.1016/j.pecs.2014.05.003.

8. M. F. Al-Dawody; S. K. Bhatti, Energy Conversion and Management 68 (0) (2013) 96-104 http://dx.doi.org/10.1016/j.enconman.2012.12.025.

9. S. M. Palash; H. H. Masjuki; M. A. Kalam; B. M. Masum; A. Sanjid; M. J. Abedin, Energy Conversion and Management 76 (0) (2013) 400-420 http://dx.doi.org/10.1016/j.enconman.2013.07.059.

10. S. M. A. Rahman; H. H. Masjuki; M. A. Kalam; M. J. Abedin; A. Sanjid; H. Sajjad, Energy Conversion and Management 76 (0) (2013) 362-367 http://dx.doi.org/10.1016/j.enconman.2013.07.061.

11. A.-H. Kakaee; P. Rahnama; A. Paykani, Journal of Natural Gas Science and Engineering 25 (0) (2015) 58-65 http://dx.doi.org/10.1016/j.jngse.2015.04.020.

12. M. K. Veltman; P. K. Karra; S.-C. Kong, SAE International (2009) 10.4271/2009-01-0485.

13. B. Tompkins; T. Jacobs, Spring technical meeting of the central states section of the combustion institute 2 (2012)

14. Y. H. Teoh; H. H. Masjuki; M. A. Kalam; M. A. Amalina; H. G. How, RSC Advances 4 (92) (2014) 50739-50751 10.1039/C4RA08464K.

**Proceedings of the Australian Combustion Symposium**
**December 7-9, 2015, The University of Melbourne**

# Combustion and emission investigation of *Calophyllum inophyllum* biodiesel blends in an unmodified diesel engine

A. M. Ruhul[1,*], M. A. Kalam[1], H. H. Masjuki[1,*], S. Imtenan[1], A. Sanjid[1], Y. H. Teoh[1, 2], H. G. How[1]
[1]Centre for Energy Sciences, Department of Mechanical Engineering
University of Malaya, 50603 KL Malaysia.
[2]School of Mechanical Engineering, Universiti Sains Malaysia, Engineering Campus,
14300 Nibong Tebal, Penang, Malaysia.

**Abstract**

Recently, *Calophyllum inophyllum* oil is considered as one of the most promising biodiesel sources among all non-edible sources. In this study, combustion and emission characteristics of 20% (v/v) *Calophyllum inophyllum* biodiesel (CB20) with 80% (v/v) ordinary diesel (OD) were investigated in a 4-cylinder, turbocharged and unmodified diesel engine. Constant torque of 80 Nm at variable engine speed ranging from 1000 to 3000 rpm with 1000rpm interval was considered as the operating condition. Combustion parameters such as in-cylinder pressure, heat release rate (HRR), start of combustion (SOC) and emission parameters like nitric oxide (NO), carbon mono-oxide (CO), unburned hydrocarbon (HC) and smoke opacity were considered in this investigation. CB20 increased NO by 15.71% and reduced CO, HC and smoke opacity by 21.89%, 25.36%, and 7.33%, respectively compared to OD.

*Keywords: Combustion, Emission, Calophyllum inophyllum, diesel engine.*

## 1. Introduction

Biodiesel is thought to be the most realistic alternative of petrodiesel due to their availability, non-toxic, biodegradable and eco-friendly nature. Biodiesel, an esterified item effortlessly got from vegetable oil or animal fats of which vegetable oils are observed to be promising feedstock [1]. Biodiesel is the most convenient alternative source that could play a very important role to meet the energy demand, especially in automobile and power generation sector. Generally it is synthesized from edible oils due to abundance and low free fatty acid content. Consideration is essentially engaged towards biodiesel from non-edible feedstocks as depending on edible source poses a threat to food supply. In addition, production of biodiesel from non-edible feedstocks decreases the expense of biodiesel as these are fundamentally less expensive [2].

*Calophyllum inophyllum* is a member of Clusiaceae or Guttiferae (mangosteen) family which is commonly known as Penaga Laut in Malaysia [3]. Nowadays this non-edible sources which have recently drawn the attention of the researchers [4, 5]. However, a new target has been set for the European members by the European Renewable Energy Directive (RED) that, at least 10% biofuel have to be used on all forms of transport by 2020 [6]. Higher density and viscosity, poor atomization and evaporation quality, advanced combustion and higher $NO_X$ emissions and poor cold flow properties, etc. are the main problems regarding the use of biodiesel in diesel engines. Eradicating such problems to make biodiesel more viable for the diesel engines is the key to modern biodiesel research works. Rahman et al. [7] studied performance and emission at high idling conditions. Venkanna and Reddy [8] and Rizwanul et al. [9] were tested the variable percentage of CB blended with OD. In a different study, some authors[10] studied the effect of injector opening pressure on engine performance running with CB biodiesel blends. It is very rare to investigate the combustion in the variable speed of CB blended with OD. In this study, 20% *Calophyllum inophyllum* biodiesel blended with diesel (80Nm constant torque with variable engine speed), has been used for investigation of replacement of diesel in terms of combustion and emission to the environment.

## 2. Materials and methodology

### 2.1 Biodiesel production

The feedstock of *Calophyllum inophyllum* and all relevant chemicals associated with biodiesel production such as $H_2SO_4$, $CH_3OH$, KOH, and $Na_2SO_4$ were purchased from the local market of Malaysia. *Calophyllum inophyllum* biodiesel was produced in a fixed batch glass reactor in laboratory scale through esterification and then transesterification process as it possessed higher acid value (greater than 4 mgKOH/g) [9]. Esterification was carried out for 3h with 18:1 methanol to oil molar ratio, 1% (v/v) $H_2SO_4$ catalyst loading, 60°C reaction temperature and 800rpm stirring speed. After separation of excess methanol and other impurities, esterified products were prepared for transesterification process. In transesterification process 6:1 methanol to oil molar ratio, 1% (w/w) KOH catalyst loading, 60°C reaction temperature and 800rpm stirring speed were maintained for 2h. After completing the transesterification process, separation, purification, mechanical drying, chemical drying and filtration were performed and finally obtained pure *Calophyllum inophyllum* biodiesel. Produced biodiesel and diesel were poured into a vessel

* Corresponding author: A. M. Ruhul & H. H. Masjuki
Tel.: +603 79674448; Fax: +603 79675317
Email: ruhulamin07ruet@gmail.com, masjuki@um.edu.my

with a certain amount (v/v) and blended at 4000 rpm with the help of a blending machine for 15–20 minutes. Some major physicochemical properties of produced biodiesel and diesel-biodiesel blends were reported in Table 1.

**Table 1: Major physicochemical property of the *C. inophyllum* and ordinary diesel**

| Property | CB100 | CM20 | OD |
|---|---|---|---|
| Viscosity @40°C ($mm^2/s$) | 4.71 | 3.60 | 3.46 |
| Density @40°C ($kg/m^3$) | 868.6 | 837.0 | 829.6 |
| Calorific value (MJ/kg) | 39.38 | 43.69 | 44.66 |
| Acid value (mgKOH/g) | 0.33 | 0.27 | 0.24 |
| Oxygen stability (h) | 3.29 | 15.6 | 21.25 |
| Flash point (°C) | 141.5 | 77.5 | 69.35 |
| Cetane number | 56.3[a] | n. s. | 48[b] |

n.s.=not specified, [a]Calculated, [b]Provided by the supplier

## 2.2 Experimental setup and engine testing condition

In this study an unmodified, inline 4-cylinder, turbocharged, water-cooled high-speed diesel engine was used for investigation the combustion and emission parameter. Engine test bed setup layout was represented in Fig. 1. An eddy current dynamometer was coupled to the engine to provide load. BOSCH BEA-350 exhaust gas analyzer was connected in the exhaust system of the engine to measure the NO, HC and CO. AVL DiCom 4000 was used to measure smoke opacity. The measuring methods for HC and CO emissions were non-dispersive infrared, NO was electrochemical, and smoke opacity was photodiode receiver method. For data acquisition, REO-DEC data control system was used, which was interfaced with a computer with the help of REO-DCA software. Both engine combustion and emission investigation were carried out varying the engine speed ranging from 1000 to 3000 rpm with 1000 rpm interval at constant 80 Nm torque.

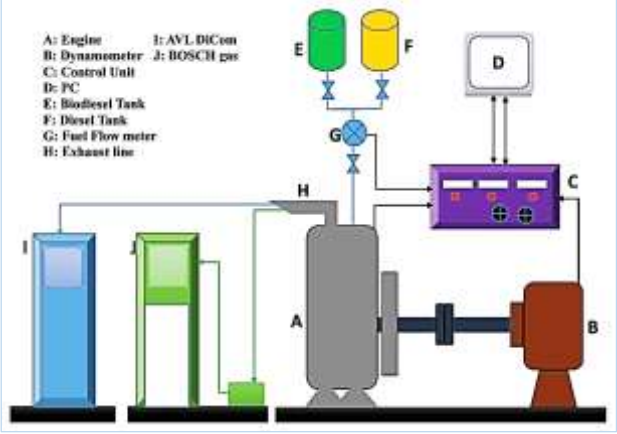


Fig.1. Engine Test Bed Setup

## 3. Result and Discussion

For combustion character analysis, a Kistler 6058A pressure sensor was installed through the glow plug port for measuring the in-cylinder pressure. Kistler 2614B4 type charger amplifier was used to amplify the charge signal output from the pressure sensor. 2614A type high precision incremental encoder was used to acquire the top dead centre (TDC) position and crank angle signal for each engine rotation. The test bed (integrated with all the sensor and other system) connected with a computer interface and data was obtained from the Dewe-30-8-CA data acquisition card. Combustion parameter like heat release rate (HRR) and start of combustion (SOC) were obtained by using Matlab® R2009a software. In this study, in-cylinder pressure, heat release rate (HRR) and start of combustion (SOC) parameter was briefly discussed for combustion parameter analysis.

Theoretically, the identification of the start of combustion (SOC) timing and differences in combustion rates obtained from the HRR versus crank angle diagram [11]. Hence, HRR analysis is a significant parameter in understanding the combustion mechanism. Average in-cylinder pressure data of 100 consecutive cycles with a 0.1°crank angle (°CA) resolution was used to calculate HRR. The analysis was derived from the first law of thermodynamics, as shown in (1) without taking heat loss into account through cylinder walls.

$$\frac{dQ}{d\theta} = \frac{V\frac{dP}{d\theta} + \gamma P\frac{dV}{d\theta}}{\gamma - 1} \quad (1)$$

Where $\frac{dQ}{d\theta}$ = rate of heat release (J/°CA), V=instantaneous cylinder volume ($m^3$), θ = crank angle (°CA), P = instantaneous cylinder pressure (Pa), γ = specific heat ratio which is considered constant at 1.35 [12].

In cylinder Pressure and cylinder volume with respect to crank angle considered as the input value. The volume (V) and the volume changes ($dV/d\theta$) with respect to every crank angle are represented by (2) and (3), respectively.

$$V = V_c + Ar\left[1 - cos\left(\frac{\pi\theta}{180}\right)\right] + \frac{1}{\lambda}\left\{1 - \sqrt{1 - \lambda^2 Sin^2\left(\frac{\pi\theta}{180}\right)}\right\} \quad (2)$$

$$\frac{dV}{d\theta} = \left(\frac{\pi\theta}{180}\right) \times r \left[Sin\left(\frac{\pi\theta}{180}\right) + \frac{\lambda^2 Sin^2\left(\frac{\pi\theta}{180}\right)}{2 \times \sqrt{1 - \lambda^2 Sin^2\left(\frac{\pi\theta}{180}\right)}}\right] \quad (3)$$

### 3.1 In-cylinder pressure

Considering 'hot' part around top dead Centre (TDC), at constant 80Nm torque, cylinder pressure with respect to crank angle diagram for OD and CB20 represented in Fig. 2(a), 2(b) and 2(c) at 1000, 2000 and 3000 rpm, respectively. It was illustrated that maximum cylinder pressure arises for OD and CB20 fuels varies within 8-10°CA after TDC among all the variable speed. From the figures it was clear that there is no significant difference on the maximum in-cylinder pressure for OD and CB20 for a certain engine speed. Which reflects conversion of fuel energy into mechanical energy was almost same for OD and CB20 [13]. It also illustrated in-cylinder pressure increases with increasing engine speed and OD shows slightly higher maximum pressure compared with CB20 for all speeds. High viscosity (high density), low volatility (high flash point), poor atomization and air-fuel mixing due to higher speed resulted reduced the premixed charge, consequently reduced premixed charge [14]. The maximum in-cylinder pressure was obtained at 3000rpm. From Fig.2 (c) 88.81 bar for OD and 86.20 bar for CB20, at 9° and 10° after TDC, respectively. Peak in-cylinder

pressure at 1000rpm Fig.2 (a) for OD and CB20 was 64.54 bar and 62.48 bar, at 8° and 9°, respectively, after TDC which was the maximum for the given operating condition. Peak in-cylinder pressure at 2000rpm Fig.2 (b) for OD and CB20 was 72.38 bar and 70.23 bar, respectively at 9°after TDC, respectively which was maximum for the given operating condition. Combustion phenomenon makes clear combining in-cylinder pressure to heat release rate (HRR)

## 3.2 Heat release rate (HRR)

The heat release rate (HRR) analysis is the most effective way to gather information for the in-depth understanding of combustion mechanisms in diesel engines. Combined with HHR analysis, in-cylinder pressure characteristic of the tested fuel can be explained properly. A distributed type pump-line-nozzle fuel injection system (157 bar injection pressure) was integrated with the experimented engine, which can affect the start of injection (SOI) due to higher denser fuel and higher bulk modulus of compressibility [15]. Thus, SOC was given preference instead of measuring the ignition delay (ID) in this present study. SOCs were obtained from the HRR against the crank angle diagram. Theoretically, as the piston is near the TDC, fuel vaporization causes a negative heat release and with the start of combustion, heat release momentarily becomes positive at a point. This point is called SOC.

HHR of OD and CB20 at 1000, 2000 and 300rpm were represented by Fig. 2(a), Fig. 2(b) and Fig. 2(c), respectively. It is clear that the area under the first sharp peak in the HRR diagram which is premixed combustion is higher for OD compare to CB20, except at lower speed 1000rpm. This is due to little higher maximum pressure developed in the cylinder during combustion [14]. At 1000 rpm, SOC of the OD was -3.5° ATDC and CB20 were observed at -2.7°ATDC while at 2000 and 3000 rpm SOCs were almost same as -1.5°ATDC. It is essentially a reflection of hampers of proper atomization of CB20 and subsequently at higher speed, higher crank angle revolution was needed to make the charge combustible.

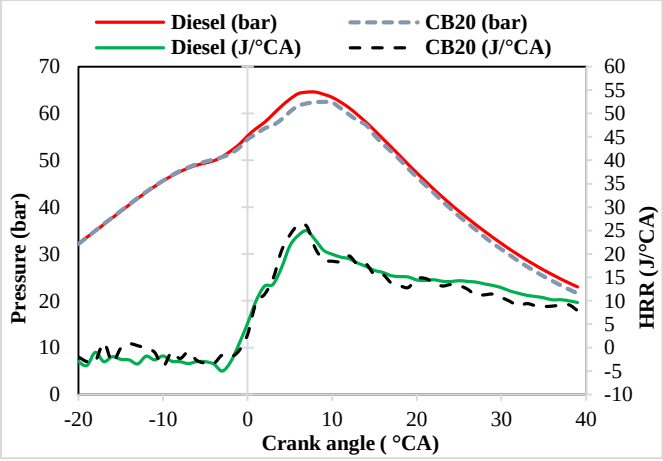


(a) 1000rpm

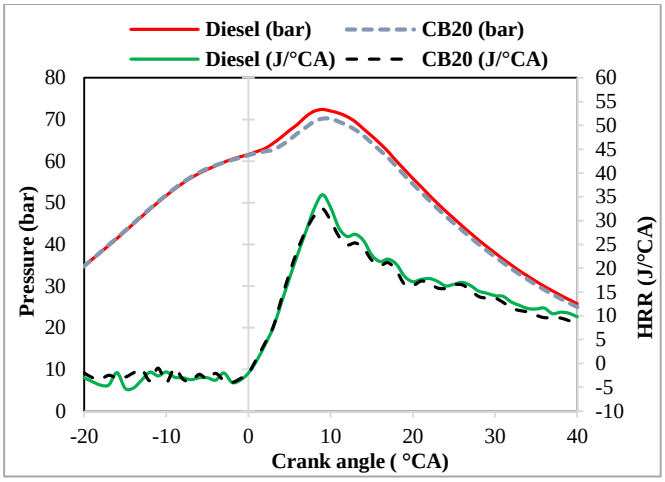


(b) 2000rpm

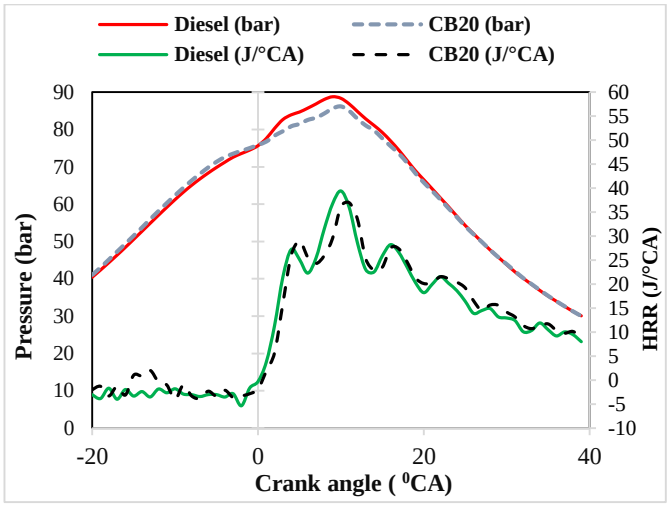


(c) 3000rpm

Fig.2. Pressure and HRR with VS. crank angle diagram for OD and CB20 at (a) 1000rpm (b) 2000rpm and (c) 3000rpm

## 3.3 Emissions

Emission parameter such as NO, CO, HC and smoke opacity were studied throughout the experiments. Fig. 5 represents the NO emission and CO emission of both diesel and CB20 with incremental engine speed ranging from 1000rpm to 3000rpm. Atmospheric nitrogen, which comes with intake air is the main sources for NO emission during combustion. Tripled bonded, inert in nature, gasses splits up in high combustion temperature and undergoes with some series of reaction with oxygen. This NO formation mechanism is well known as Zeldovich mechanism [16]. The amount of NO formation mainly depends on oxygen concentration, air surplus coefficient, in-cylinder temperature and residence time [17]. It was illustrated that NO emission is increased with increasing engine speed and higher that of OD in every condition. This can be ascribed as the higher combustion temperature which provides the in-cylinder pressure high in-cylinder temperature for both premixed and diffusion combustion condition rather than diesel [18]. Compared with OD, CB20 increases NO emission by 15.71%.

The main reason of CO formation is an overly lean mixture or overly rich mixture which provides poor oxidation of the fuel. The flame cannot propagate through the mixture in overly lean mixtures, consequently, fuel pyrolysis with partial oxidation causes CO. Fig. 3 shows that CO emission decreases with increasing the engine speed and CB20 reduces CO emission on an average 21.98% compared with OD. This can be attributed to time available for oxidation mechanism [17] in higher engine speed.

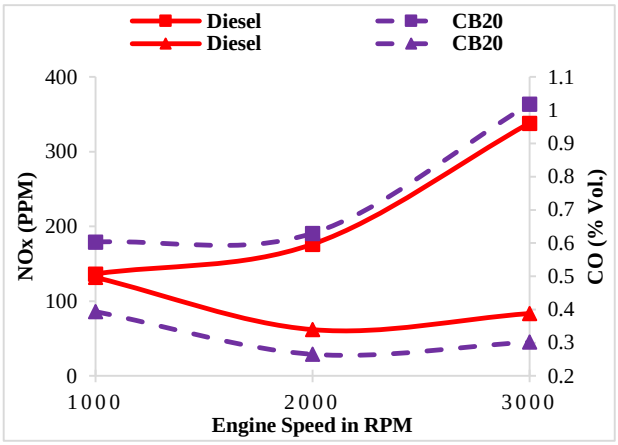


Fig. 3. $NO_X$ and CO emission with different engine speed

Fig. 4 represented the HC emission and smoke opacity with incremental engine speed. Compared with OD, CB20 reduces HC and smoke emission by 25.36% and 7.33%, respectively. HC emission significantly decreases with the incremental engine speed. This can be attributed to high in-cylinder temperature due to the high in-cylinder pressure during combustion [19].

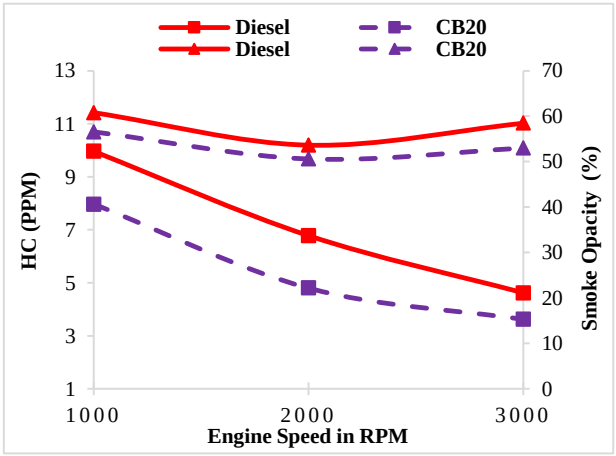


Fig. 4. HC and Smoke emission with different engine speed

## 4. Conclusions

*Calophyllum inophyllum* is a potential non-edible source of biodiesel and a substitutable fuel of diesel. During this investigation, comparative improvement of combustion and exhaust emission characteristics of the CB blend (CB20) was studied with high-speed, water-cooled turbocharged diesel engine. Based on the experimental investigation, the following conclusions can be drawn.

- CB20 produced about 15.71% higher NO than diesel.
- CB20 showed about 21.98% decrement of CO emission than diesel.
- CB20 showed 25.36% decrement of HC emission than diesel,
- Smoke opacity was also reduced for CB20 about 7.33% than diesel.
- The higher engine speed provides better combustion behaviour of CB20 compared to diesel.

Therefore, regarding combustion and emission characteristics, 20% *Calophyllum inophyllum* biodiesel (CB20) at the aforementioned operating condition of an unmodified diesel engine at higher engine speed.

## 5. Acknowledgments

The authors would like to thank the University of Malaya for financial support through High Impact Research grant titled: “Clean Diesel Technology for Military and Civilian Transport Vehicles” having grant no. UM.C/HIR/MOHE/ENG/07 and “Fundamental Research Grant Scheme (FRGS)” having grant no. FP051-2014B.

## 6. References

[1] G. Kafuku; M. Mbarawa, Applied Energy 87 (8) (2010) 2561-2565.
[2] M. Tabatabaei; K. Karimi; I. S. Horváth; K. Rajeev, Biofuel Research Journal 2 (2015) 258-67.
[3] H. Ong; T. Mahlia; H. Masjuki; R. Norhasyima, Renewable and Sustainable Energy Reviews 15 (8) (2011) 3501-3515.
[4] V. SathyaSelvabala; D. K. Selvaraj; J. Kalimuthu; P. M. Periyaraman; S. Subramanian, Bioresource technology 102 (2) (2011) 1066-1072.
[5] S. Imtenan; H. Masjuki; M. Varman; I. R. Fattah, RSC Advances 5 (22) (2015) 17160-17170.
[6] P. UNION, (2009).
[7] S. A. Rahman; H. Masjuki; M. Kalam; M. Abedin; A. Sanjid; H. Sajjad, Energy Conversion and Management 76 (2013) 362-367.
[8] B. Venkanna; C. V. Reddy, International Journal of Agricultural and Biological Engineering 4 (3) (2011) 48-57.
[9] I. R. Fattah; M. Kalam; H. Masjuki; M. Wakil, Rsc Advances 4 (34) (2014) 17787-17796.
[10] V. K. Belagur; V. R. Chitimini, International Journal of Ambient Energy 33 (2) (2012) 65-74.
[11] M. Canakci; A. N. Ozsezen; A. Turkcan, Biomass and Bioenergy 33 (5) (2009) 760-767.
[12] J. B. Heywood, Internal combustion engine fundamentals, Mcgraw-hill New York, 1988.
[13] A. N. Ozsezen; M. Canakci; C. Sayin, Energy & Fuels 22 (2) (2008) 1297-1305.
[14] S. Sivalakshmi; T. Balusamy, Fuel 106 (2013) 106-110.
[15] S. Imtenan; H. Masjuki; M. Varman; I. R. Fattah; H. Sajjad; M. Arbab, Energy Conversion and Management 94 (2015) 84-94.
[16] P. Benjumea; J. R. Agudelo; A. F. Agudelo, Energy & Fuels 25 (1) (2010) 77-85.
[17] S. Imtenan; M. Varman; H. H. Masjuki; M. A. Kalam; H. Sajjad; M. I. Arbab; I. M. Rizwanul Fattah, Energy Conversion and Management 80 (2014) 329-356.
[18] D. Kannan; S. Pachamuthu; M. N. Nabi; J. E. Hustad; T. Løvås, Energy Conversion and Management 53 (1) (2012) 322-331.
[19] M. Mofijur; H. Masjuki; M. Kalam; A. Atabani; I. R. Fattah; H. Mobarak, Industrial Crops and Products 53 (2014) 78-84.

# Effects of EDI on Combustion and Emissions of Small Spark Ignition Engine at Lean Mixture Conditions

Nizar F.O. Al-Muhsen*, Guang Hong
School of Electrical, Mechanical and Mechatronic Systems
University of Technology Sydney (UTS), NSW, 2007, Australia

## Abstract

Running the spark ignition engine under lean mixture operating conditions can improve the engine efficiency and reduce the fuel consumption and emissions. However, the cycle-to-cycle variation can limit the lean burn spark ignition engine improvement. This experimental work investigates the effect of the ethanol direct injection strategy on the engine combustion and emissions in lean mixture conditions. Three equivalent air/fuel ratios (λ=1.0, 1.1 and 1.2) and five ethanol direct injection (EDI) percentages, 0%, 25%, 50%, 75% and 100% were adopted. The experiments were carried out on a small spark ignition engine equipped with a dual fuel injection system. The experimental results show that to the limit of lean mixture condition (λ=1.1) the ethanol direct injection improved the combustion performance and thus engine thermal efficiency (2.6%) by taking the advantages of ethanol fuel properties such as high laminar burning velocity and great latent heat. The engine volumetric efficiency was significantly improved with the increase of air/fuel ratio. The EDI demonstrates a superior potential in engine emission reduction in the lean mixture conditions than that in stoichiometric conditions. The coefficient of variation of the indicated mean effective pressure at λ=1.2 was also reduced considerably when ethanol starts to be injected into combustion chamber.

*Keywords: Lean Burn, Ethanol Direct Injection Engine, Combustion.*

## 1. Introduction

Recently, engine performance improvement and emissions reduction have become a main concern among the researchers and the automotive companies worldwide. Reducing the pumping and heat losses can be an interested outcomes as a consequence of lean mixture operating conditions [1, 2]. Diluting the stoichiometric air/fuel ratio with extra amount of air (lean mixture) can significantly improve the combustion quality and then reduce the emissions [1, 3]. Consequently, the engine thermal efficiency and volumetric efficiency can be significantly improved. However, when the conventional naturally aspirated gasoline engines are adopted, the highly diluted mixture will lower the laminar burning velocity and mixture homogeneity increasing the difficulties to start the combustion and enlarging the magnitude of cycle-to-cycle variations [4, 5]. This undesirable combustion behaviour will obviously limit the engine performance development. Lately, ethyl alcohol (Ethanol fuel) as a green environmentally friendly biofuel has been targeted as an alternative fuel that can enhance the gasoline fuel performance [3, 6-8]. Adopting an ethanol fuel to the spark ignition engines may promote more complete and stable combustion that may result in better engine thermal efficiency, engine volumetric efficiency and thus less emissions production [6, 9-11]. This can be mainly attributed to the ethanol fuel properties such as laminar burning velocity, the latent heat of vaporization and octane number when it is compared with gasoline fuel as shown in table1. A partial-burn and misfire occurring possibility can be increased due to the deceleration of flame propagation with lean burn engines [12]. The greater ethanol flame speed (~39cm/sec) compared with gasoline one (~33cm/sec) can substitute the reduction in the air/gasoline mixture combustion velocity due to adopting lean combustion mode. Employing ethanol direct injection (EDI) strategy to the lean burn engine can enhance the combustion stability and thus engine performance by taking better of the advantages of ethanol properties. Therefore, this paper aims to investigate the leveraging effect of the EDI combined with the lean burn on a small spark ignition engine (SSIE) performance. Three engine parameters that were examined which are the combustion and emissions performance in addition to coefficient of variation of the indicated mean effective pressure ($COV_{IMEP}$).

| Properties | Units | Gasoline | Ethanol |
|---|---|---|---|
| Chemical formula | ---- | $C_2$-$C_{12}$ | $C_2H_5OH$ |
| Molecular weight | kg/kmol | 114.15 | 45.07 |
| H/C | Atom ratio | 1.795 | 3 |
| O/C | Atom ratio | 0.7-0.78 | 0.794 |
| Density (at 288.15K) | $kg/m^3$ | 750-765 | 785-809.9 |
| Stoichiometric air-fuel ratio | w/w | 14.2:1-15.1:1 | 8.97:1 |
| Octane number | ---- | 91 | 108.61 |
| Higher heating value (HHV) | MJ/kg | 44.0 | 26.9 |
| Laminar flame speed at 100kPa, 325K | cm/s | ~33 | ~39 |
| Latent heat of vaporization | kJ/kg | 298 | 948 |
| Saturation vapour pressure | kPa | 28.828 | 8.773 |

Table1. Gasoline and Ethanol Properties [3, 7, 13-15]

* Corresponding author: Nizar F.O. Al-Muhsen
Phone: (+61) 423095545
Email: Nizar.Al-Muhsen@student.uts.edu.au

## 2. Engine and Experimental Procedure

### 2.1 Research Engine

The experiments were conducted on a small naturally aspirated spark ignition engine. This single-cylinder four-stroke engine was originally designed with a port fuel injection only before it was modified to be equipped with an EDI system. An electronic control unit (ECU) developed by Hents Technology was used to adjust and control the engine operating parameters such as throttle position and the mass of fuels in gasoline port injection (GPI) and ethanol direct injection (EDI). In order to set the required engine speed and measure the engine torque, an eddy current dynamometer with control system was coupled to the engine. A Kistler 6115B spark plug cylinder pressure transducer was used to monitor and record the in-cylinder pressure. More details about the research engine can be found in [8].

### 2.2 Experimental Procedure

Five volume-based ethanol direct injection percentage (EDIP) were set to be started from 0.0% (GPI only), 25%, 50%, 75% and EDIP100% (ethanol only). In order to achieve lean mixture operating conditions at each EDIP, the throttle opening percentage (throttle position) was set to be changed from 32% at λ=1.0 to 43% at λ=1.2 as shown in table 2. During the test, the engine was set to a medium load, a constant engine speed of 3500 RPM, EDI timing of 300 crank angle degree before top dead centre (CAD BTDC) and fixed spark timing of 15CAD BTDC. In different EDI percentages and lean burn conditions, the total amount of fuel heating energy (~580J) per cycle was kept the same. The indicated mean effective pressure (IMEP) and $COV_{IMEP}$ were calculated based on the mean value of 100 consecutive engine cycles of the recorded in-cylinder pressure data at a sample rate of 1/0.5CAD. Each cylinder pressure recording was repeated three times and the average of the IMEP and $COV_{IMEP}$ was used into the result analysis. With regard to other output data such as engine torque and emissions, five samples were taken and the theoretical calculations were based on the sample mean value.

| | |
|---|---|
| Engine speed | 3500 RPM |
| EDI percentage (v/v) | 0%, 25%, 50%, 75%, 100% |
| Percentage of GPI (v/v) | 100%, 75%, 50%, 25%, 0% |
| Equivalence Air/Fuel ratio (λ) | 1.0, 1.1, 1.2 |
| Throttle position | 32%, 37%, 43% |
| EDI pressure | 40 bar |
| GPI pressure | 2.5 bar |

Table2. Engine operating conditions.

## 3. Results and Discussion

Experimental results will be presented and discussed in this section to understand the effect of EDI on the engine performance, combustion and emissions in lean mixture conditions.

### 3.1 Engine Performance

Figure 1 shows the variation of the IMEP with EDI percentages (EDIP) at three different air/fuel ratios. As shown in Fig. 1 the IMEP is increased with the increase of EDIP at all air/fuel ratios. This is possibly attributed to the advantages of direct fuel injection and the greater laminar burning velocity of ethanol fuel than gasoline. At λ=1.1 the IMEP slightly greater than that in stoichiometric conditions at all EDIP. However, at λ=1.2 the IMEP is slightly lower than that in stoichiometric conditions. Firstly, at λ=1.1, the IMEP improvement could be attributed to the combined effect of ethanol fuel laminar burning speed, oxygen content and the charge cooling effect with pumping loss reduction and excess amount of air that provide more oxygen promoting more completed combustion process [3, 6]. These factors could improve the value of the IMEP considerably [16]. Secondly, at λ=1.2, even though the extra amount of air could enhance the chemical reaction of fuel leading to better fuel oxidation that will be noticed in the emissions performance section, the mixture might be too lean to keep the mixture quality and the flame speed [1, 2, 4].

Figure 2 shows the variation of the $COV_{IMEP}$ with EDIP at different values of λ. Cycle-to-cycle variation represents the main challenging to the lean burn engine improvement. It is assumed that the highly diluted mixture could lead to a slow burning rate, so that the combustion process could not completed [4]. As shown in Figure 2, the $COV_{IMEP}$ is dramatically increased with the increase of λ, especially when the λ is increased from 1.1 to 1.2. This result is consistent with that in previous research, mainly due to the mixture's low quality and non-uniform distribution. Figure 2, however, also shows that the $COV_{IMEP}$ reduces with the EDIP until the EDIP is greater than 80%. The reduced $COV_{IMEP}$ with the EDI might be attributed to the improved mixture distribution with direct fuel injection, ethanol's greater laminar burning velocity and better low temperature combustion stability than gasoline's [3].

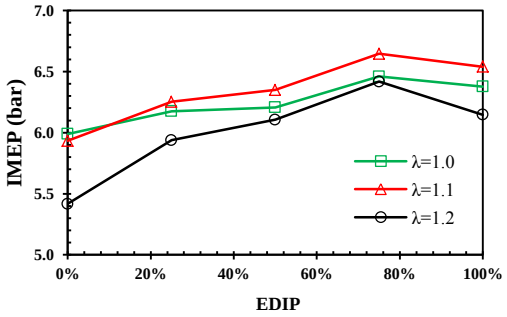


Figure 1. Variation of IMEP with EDIP and λ

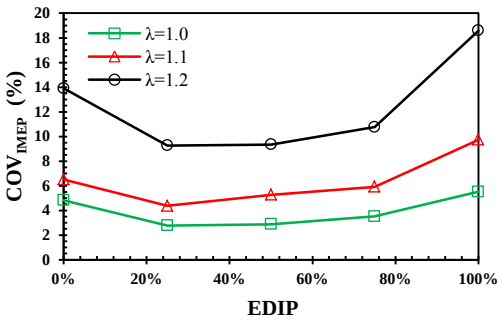

Figure 2. Variation of $COV_{IMEP}$ with EDIP and λ

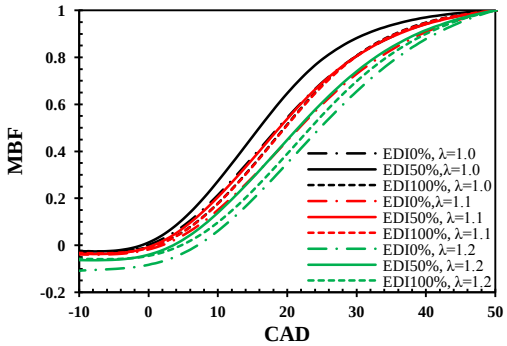

Figure 3. Variation of MBF with CAD

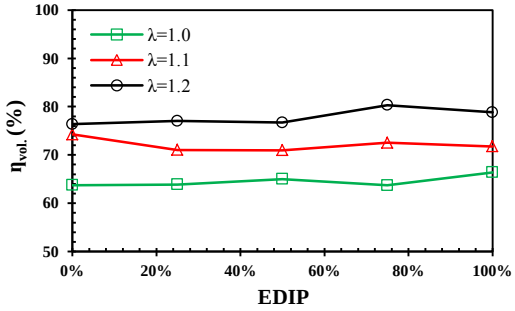

Figure 4. Variation of $\eta_{vol.}$ with EDIP and λ

The effects of the combination of EDIP and lean mixture on the combustion performance are illustrated by the mass burnt fraction (MBF) in Fig. 3. As shown in Figure, the combustion duration is shortened and thus more quantity of fuel is consumed with the increase of EDIP up to 80%. Consequently, more heat is released from the burnt fuel, resulting in reduction of HC and CO emissions which will be discussed in the next section. This result might be attributed to the ethanol greater flame speed combined with the oxygen contents. However, MBF in 100% EDIP condition shows a slower combustion than that with EDIP of 50%. This could be attributed into two main reasons. Firstly, injecting the entire amount of ethanol fuel that has around three times greater latent heat of vaporization than that of gasoline directly into the combustion chamber will significantly decrease the chemical reaction temperature. Consequently, the burning rate will be relatively decelerated and thus less stable combustion. Secondly, the combination of the ethanol lower volatility compared to that of gasoline with the high fuel impingement into the combustion chamber surfaces possibly deteriorate the air/fuel mixture quality and thus lower combustion performance compared to that of EDIP 50%. EDI 25% and 75% were omitted in order to demonstrate the effect of the EDI at different lean burn cases clearly.

Figure 4 shows the cylinder pressure from 40 CAD BTDC to 80 CAD ATDC. The solid lines with different colors in Fig. 4 illustrate the combustion pressure of EDIP of 50%. It can be clearly observed that the results for EDIP of 50% demonstrate maximum in-cylinder pressure at different air/fuel ratios. This tendency might be attributed to the relatively greater laminar burning velocity of ethanol combined with the ethanol charge cooling effect.

Figure 4 shows the variation of the engine volumetric efficiency with the EDIP and different value of λ. As it can be observed in Fig. 3, the leveraging effects of the EDI combined with lean burn mixture on the engine volumetric efficiency result in an important improvement. This could be attributed to two main reasons. Firstly, regarding ethanol effect, the charge cooling effect due to the higher latent heat of vaporization compared with gasoline might play an important job to increase the fresh charge density and then improve the engine capacity. Moreover, the ethanol oxygen content is also assumed to play a significant role in the volumetric efficiency increment. Secondly, concerning lambda effect, run the engine with excess air could promote more complete and stable combustion which are also possibly effect positively on the engine capacity performance.

## 3.2 Emission performance

Operating the engine with lean mixture conditions can dramatically reduce the indicated specific carbon monoxide (ISCO) emissions. The more oxygen proportion in the mixture the more oxidation can be promoted. As a result of this, the amount of ISCO emissions are reduced dramatically with the lean combustion compared to the stoichiometric one [4, 16]. However, Fig. 5 does not show any ISCO reduced by lean mixture when λ is increased from 1.0 to 1.1, ISCO is significantly increased. In general, the ISCO increases with the increase of the EDIP.[11, 16].

Figure 6 shows the variation of the indicated specific hydrocarbon (ISHC) emissions with EDIP and λ. For EDI percentages between 0% and 50%, the ISHC emissions are decreased probably due to excess amount of air for both lean burn conditions which result in better combustion process. However, when the EDIP is greater than 75%, the ISHC emission starts to increase and then becomes to be greater than that at stoichiometric conditions. This result could be attributed to the increase of the amount of the directly injected ethanol fuel that impinged into the combustion chamber walls or not evaporated, resulting in a poor mixture and combustion quality [8, 13].

Figure 7 demonstrates the effect of the EDI and lean mixture on the indicated specific oxides of nitrogen ($NO_x$) emissions. Because the $ISNO_x$

emissions are highly related to the combustion temperature, the $ISNO_x$ emissions are substantially reduced with the increase of EDIP due to the ethanol fuel's greater latent heat than gasoline's [7]. However, $ISNO_x$ slightly increased when EDIP increases from 0% to 25% and from 80% to 100% at λ=1.1. This might be due to the combustion was advanced, and hence the in-cylinder temperature and pressure were increased leading to slightly increase in the $NO_X$ emission [11].

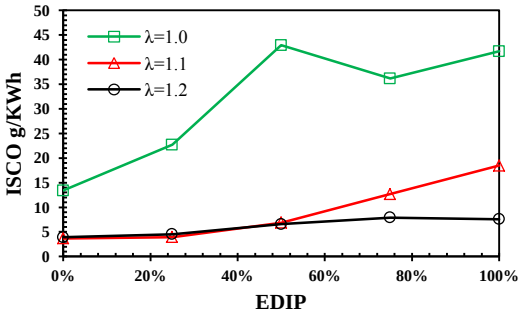

Figure 5. Varation of ISCO wtih EDIP and λ

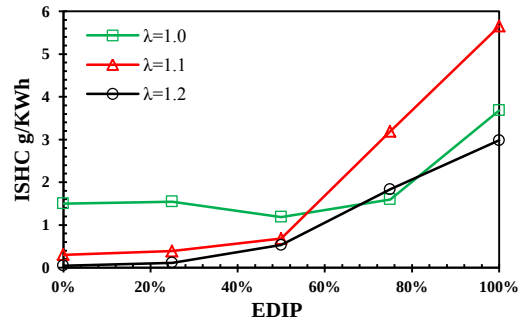

Figure 6. Variation of ISHC with EDIP and λ

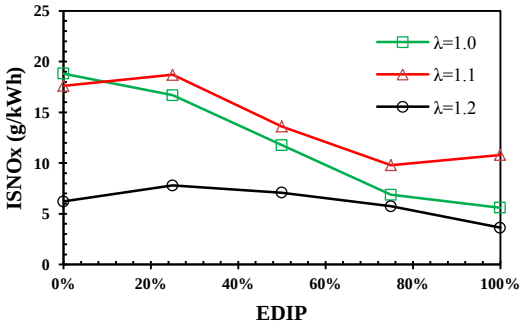

Figure 7. Variation of ISNOx with EDIP and λ

## 4. Conclusion

The effect of the EDI on the engine performance and emissions at lean burn conditions was examined. Experiments were conducted on a spark ignition engine equipped with dual fuel injection system (EDI+GPI). Five volumetric percentages of ethanol fuel were chosen as shown in table 2. Three lambda values of 1.0, 1.1 and 1.2 and fixed engine speed (3500RPM) were chosen at medium engine load.

The engine performance (IMEP) could be improved by adopting EDI strategy in to the gasoline port injection engine at all air/fuel ratios. EDI could substitute the flame speed reduction in the lean mixture conditions due to ethanol's greater burning velocity compared to gasoline. However, the IMEP is slightly decreased at EDI 100% compared to EDI 75% at the tree values of λ (1.0, 1.1 and 1.2) probably due the overcharge cooling effects combined with a relatively poor mixture quality.

Once the EDI start working at 25%, the $COV_{IMEP}$ was dramatically decreased at all air/fuel ratios especially at highly lean mixture conditions (λ=1.2). This positive behaviour could be attributed to the greater laminar flame speed and better low temperature combustion stability of ethanol compared to that of gasoline [3]. However, at all air/ fuel ratios and at EDI 100% operating conditions, the $COV_{IMEP}$ back to increase. This might be attributed to the deterioration of the mixture quality as a result of highly percentage of ethanol direct injection.

ISCO and ISHC emissions were reduced at leaner combustion when the value of lambda (1.1 and 1.2) at most of the EDIP possibly due to the excess amount of air that might improve the fuel oxidation. However, ISHC emission was increased with EDIP over 50% probably due to the poor mixture quality and the oil film formation. In contrast, ISNOx emission was decreased with EDI percentage at values of λ 1.0 and 1.2 possibly due to the charge cooling effects. However, $ISNO_X$ at the point of EDI 25% and EDI 100% at λ=1.1 was slightly increased which might be due to the combustion advancing resulting in higher in-cylinder pressure and temperature [11].

## 5. References


[1] A. DeFilippo; S. Saxena; V. Rapp; R. Dibble; J.-Y. Chen; A. Nishiyama; Y. Ikeda, in: SAE International: 2011.

[2] M. Sjöberg; W. Zeng; D. Singleton; J. M. Sanders; M. A. Gundersen, SAE Int. J. Engines 7 (4) (2014) 1781-1801.

[3] Y. Zhuang; G. Hong, Fuel 135 (0) (2014) 27-37.

[4] J. B. Heywood, Internal Combustion Engine Fundemantales McGraw-Hill, Inc., 1988, p.^pp.

[5] M. Pan; G. Shu; H. Wei; T. Zhu; Y. Liang; C. Liu, Applied Thermal Engineering 64 (1–2) (2014) 491-498.

[6] P. Bajpai, Advances in Bioethanol, Springer New Delhi Heidelberg New York Dordrecht London, India, 2013, p.^pp. 100.

[7] B. M. Masum; H. H. Masjuki; M. A. Kalam; I. M. Rizwanul Fattah; S. M. Palash; M. J. Abedin, Renewable and Sustainable Energy Reviews 24 (2013) 209-222.

[8] Y. Zhuang; G. Hong, Fuel 105 (2013) 425-431.

[9] F. Catapano; S. Di Iorio; P. Sementa; B. M. Vaglieco, in: SAE International: 2014.

[10] E. Kasseris; J. B. Heywood, SAE Int. J. Engines (2012).

[11] D. Turner; H. Xu; R. F. Cracknell; V. Natarajan; X. Chen, Fuel 90 (5) (2011) 1999-2006.

[12] A. A. Quader, in: SAE International: 1976.

[13] L. Chen; R. Stone; D. Richardson, Fuel 96 (0) (2012) 120-130.

[14] K. Kar; T. Last; C. Haywood; R. Raine, SAE Int. J. Fuels Lubr. 1 (1) (2008) 132-144.

[15] Y. Huang; G. Hong; X. Cheng; R. Huang, SAE Int. J. Engines (2013).

[16] W. W. Pulkrabek, Engineering Fundamenatals of the Internal Combustion Engines, Prentice-Hall, Inc., United State of America, 1997, p.^pp.

# Comparative study on Gasoline-Ethanol Dual Fuel Injection Strategies in a Small Spark Ignition Engine

Nizar F.O. Al-Muhsen*, Guang Hong
School of Electrical, Mechanical and Mechatronic Systems
University of Technology Sydney (UTS), NSW, 2007, Australia

## Abstract

Combined ethanol as oxygenated fuel with gasoline fuel can have significant synergies with a small spark ignition engines (SSIE) due to the higher ethanol's latent heat of vaporization, laminar flame speed and research octane number than that of gasoline. This paper reports an experimental investigation to the effect of three dual injection strategies, gasoline port injection (GPI) plus ethanol direct injection (EDI), GPI plus gasoline direct injection (GDI) and GPI only, on the engine performance and the emissions. Experiments were conducted on a modified 249cm3 single cylinder spark ignition engine at a stoichiometric air-fuel ratio ($\lambda$=1), constant engine speed and medium engine load. Five injection volumetric percentages were chosen; 0, 25, 50, 75 and 100%. Among the three injection strategies EDI+GPI demonstrated the best engine performance in terms of the increase of IMEP and nitric oxide emission reduction and GPI the second. However, when the percentage of the fuel directly injected increased to 44% for ethanol and 76% to gasoline, the combustion becomes more unstable and more CO and HC emitted than that in GPI only.

*Keyword: Dual injection, Ethanol direct injection, Gasoline direct injection, Port injection.*

## 1. Introduction

Developing a recent fossil fuel or adopting an alternative environmentally friendly one is a common topic among the worldwide researchers in the last few years. Recently, ethyl alcohol (Ethanol) as an oxygenated biofuel has been seen as an attractive fuel that can improve the gasoline performance or even replace it [1-4]. Practically, ethanol fuel can help to improve the combustion quality and its efficiency that will lead to enhance the engine thermal efficiency, engine capacity and emissions [5-7]. This can be mainly attributed to the ethanol's excellent properties such as the latent heat of vaporization, octane number and laminar burning velocity if it is compared with gasoline fuel as shown in table1.

The dual injection strategy is a new technology that utilized to optimize the spark ignition engine performance providing more flexibility to the direct fuel injection to port fuel injection ratio that can be immediately changed according to the needed operating conditions. Gasoline direct injection engines has been commercially produced due to its high performance comparing with the conventional port fuel injection engines. However, these engines produce a larger amount of emissions (particular matter) because the mixture before combustion might be non-homogeneous [8, 9]. In contrast, the directly injected ethanol can relatively enrich more completed and less emission combustion due to its remarkable properties [5, 7]. The high research octane number of ethanol fuel could contribute significantly to the engine anti-knock ability [4, 10]. The charge cooling effects due the great latent heat of vaporization of ethanol could significantly promote higher compression ratio, improve the volumetric efficiency and reduce the NOx emissions significantly [3, 6, 11]. Moreover, the high laminar burning velocity of ethanol could significantly improve the combustion characteristics, and hence the engine performance [11, 12].

The presented work aims to investigate fuel injection strategies in combination of multiple fuels used to optimize the engine performance, maximize the thermal efficiency and minimize the emissions at a medium engine load of a small SI engine. In order to do that, two injection strategies were investigated and compared with the conventional port fuel injection strategy as a baseline. Moreover, combustion and emissions taking into account as a main two parameters that can indicate to engine performance.

| **Property** | **Unit** | **Gasoline** | **Ethanol** |
|---|---|---|---|
| Chemical formula | - | $C_2$-$C_{12}$ | $C_2H_5OH$ |
| Molecular weight | kg/kmol | 114.15 | 45.07 |
| H/C | Atom ratio | 1.795 | 3 |
| O/C | Atom ratio | 0.7-0.78 | 0.794 |
| Density (at 288.15K) | $kg/m^3$ | 750-765 | 785-809.9 |
| Stoichiometric air-fuel ratio | w/w | 14.2:1-15.1:1 | 8.97:1 |
| Kinematic viscosity | $mm^2/s$ | 0.5-0.6 | 1.2-1.5 |
| Octane number | - | 91 | 108.61 |
| Higher heating value (HHV) | MJ/kg | 44.0 | 26.9 |
| Laminar flame speed at 100kPa, 325K | cm/s | ~33 | ~39 |
| Latent heat of vaporization | kJ/kg | 298 | 948 |
| Saturation vapour pressure | kPa | 28.828 | 8.773 |

Table1. Ethanol and Gasoline Fuel Properties [2, 4, 13-15]

## 2. Experimental Setup and Methodology

* Corresponding author: Nizar F.O. Al-Muhsen
Phone: (+61) 423095545
Email: Nizar.Al-Muhsen@student.uts.edu.au

## 2.1 Test Rig Engine

A 4-stroke single cylinder has been adopted to conduct this experimental work. This spark ignition engine was modified from conventional port fuel injection engine to be equipped with flexible dual fuel injection system that can be controlled by a computer. An engine control system was developed by Hents Technology to adjust and monitor the spark timing, the mass of fuel injected, fuel injection timing and pressure, throttle position and engine speed (RPM). An eddy current dynamometer with control system was coupled to the engine to uphold the engine speed and measure the engine torque. The in-cylinder pressure was recorded using a Kistler 6115B measuring spark plug pressure transducer. More details about the engine test rig can be found in [3].

## 2.2 Experimental Methodology

Three fuel injection strategies: Gasoline port injection only (GPI) which was set as a baseline, EDI+GPI and GDI+GPI were set at about stoichiometric air/fuel ratio (λ=1), a fixed engine speed of 4000 RPM, spark timing of 15 crank angle degree before top dead center (CAD BTDC) and the direct injection timing of 300CAD BTDC for both GDI and EDI. In different injection strategies and direct injection volumetric percentages (DIVP), the total fuel heating energy (~580J) is kept the same. During the engine tests, methodical comparisons were implemented to the three combustion modes as shown in the matrix test (Table 2) with a focus on the effect of the injection strategy on the engine performance and emissions. The DIVP of fuel was changed from 0% as GPI only, which represented as a baseline for the experimental tests, to 100% as DFI only. This includes ethanol direct injection (EDI) and gasoline direct injection (GDI). The engine was started and warmed up to 200 $^{o}$C, as the designated engine operating temperature, with GPI only, and then DIVP gradually increased from 0% to 100%. Five samples were taken for each data and then the average was used in calculations and analyses. The in-cylinder pressure was recorded three times for each 100 consecutive cycles at a rate of 0.5 crank angle degree (CAD) intervals and then averaged to be counted into the theoretical calculations.

| Test | Symbol | Port injection | Direct injection | DIVP% |
|---|---|---|---|---|
| Baseline | GPI only | Gasoline | - | 0 |
| Strategy1 | GPI+EDI | Gasoline | Ethanol | 0-100 |
| Strategy2 | GPI+GDI | Gasoline | Gasoline | 0-100 |

Table2. Test matrix

# 3. Results and Discussion

Results of engine performance and emissions are represented and discussed to show the effect of different fuel injection strategies.

## 3.1 Engine Performance

Figure 1 shows the variation of IMEP with DIVP at 4000 RPM. It compares the three injection strategies GPI only, EDI+GPI and GDI+GPI. As shown in Figure 1, the IMEP increases significantly once the EDI starts at DIVP of 25% ethanol fuel and reaches the maximum IMEP at DIVP of 75% ethanol fuel. This result could be attributed to two main reasons. Firstly, the Oxygen content of ethanol fuel might improve the combustion phasing resulting in higher IMEP comparing with the other two injection strategies. Secondly, the higher ethanol laminar burning velocity than that of gasoline fuel might play a significant role in improving the combustion quality resulting in IMEP enhancement [3, 16, 17]. In contrast, at DIVP of 100% ethanol fuel, the IMEP is reduced. This could be attributed to lower heating value of ethanol coupled with overcharge cooling effect and lower saturation vapor pressure resulting in reducing the heat released and poor mixture quality around the vicinity of the spark plug at the moment of the spark discharge [7].

Concerning GDI, the reduction in IMEP can be attributed to the high-pressure injector's position might suit EDI but not GDI. Direct injection of gasoline fuel in this engine might cause a higher fuel impingement into the combustion chamber surfaces resulting in higher oil film formation and thus low mixture quality which might cause the IMEP reduction.

Figure 2 shows the variation of DIVP with the coefficient of variation of IMEP ($COV_{IMEP}$) which denotes to the cyclic variability of the engine that must not exceed 10% [18]. As shown in Figure 2, the $COV_{IMEP}$ in the dual fuel injection strategies is smaller than that of GPI only until the DIVP reaches 76% in GPI+EDI and 44% in GPI+GDI.

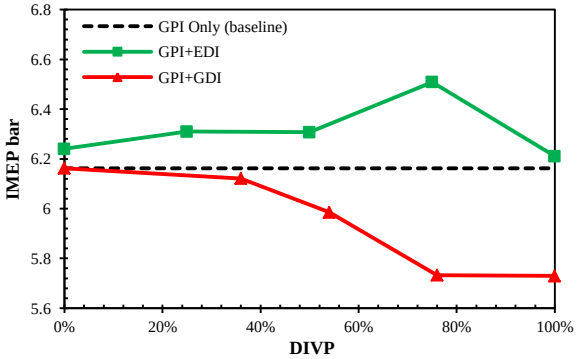


Fig. 1 Variation of IMEP with DIVP

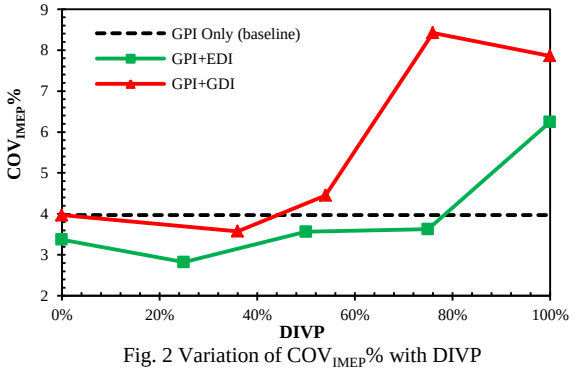


Fig. 2 Variation of $COV_{IMEP}$% with DIVP

This can be attributed to the greater ethanol latent heat of vaporization and burning velocity that may reduce the combustion temperature and shorten the combustion duration respectively. However, for GDI injection, the $COV_{IMEP}$ increased dramatically when the amount of DIVP moved from 54% to 100%. It is assumed that, the high amount of the impinged fuel might cause a more oil film formation on the walls of the combustion chamber resulting in less homogenous and leaner mixture which it is also believed that it might increase the engine cycle-to-cycle variations [18]. Furthermore, $COV_{IMEP}$ increased when EDI move from 75% to 100%. This mainly because the 100% EDI could cause an overcharge cooling effect and thus further increasing of combustion duration resulting in more unstable combustion [19].

Figure 3 shows that the engine volumetric efficiency is slightly improved with the increase of the EDI percentage gradually. It is assumed that inject ethanol directly into the combustion chamber may reduce the mixture temperature and increase its density [3, 17]. However, turning up into 100% EDI can adversely affect the engine volumetric efficiency compared with 75% EDI, possibly due to the combustion deterioration that may happen as a results of the over cooling effect. In contrast, the volumetric efficiency in GDI+GPI is slightly lower than that in GPI only. This may be due to the inferior mixture quality compared with the baseline injection strategy (GPI only).

Figure 4 shows the cylinder pressure in four conditions: GPI only, EDI only, GDI only and 50%EDI+50%GPI. As shown in Fig. 4, the charge cooling effect and laminar flame speed of ethanol combined with oxygen content may speed up the combustion process and then increase the cylinder pressure [16, 17]. This is consistent with the IMEP results shown in Fig. 1. However, the overcharge cooling effect may negatively affect these processes. This can be observed previously in Fig. 1 when the IMEP increased with specified amount of ethanol directly injected (25%≤ EDI ≤75%) and then starts to be decreased when the overcharge cooling happened at 100% EDI.

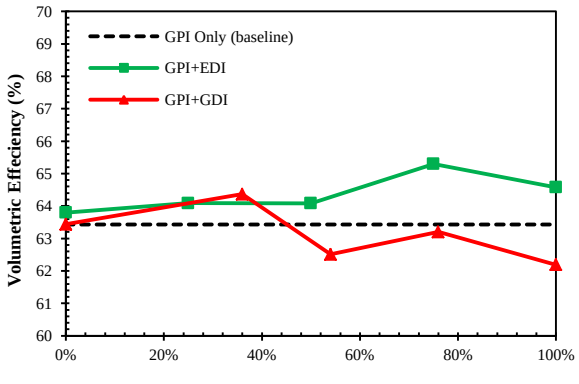

Fig. 3 Variation of the Engine Volumetric Efficiency with DIVP

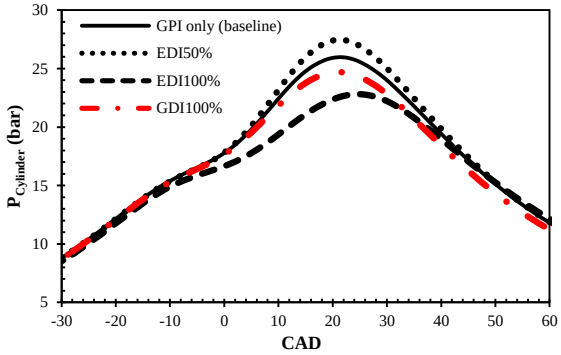

Fig. 4 Variation of Cylinder Pressure with CAD

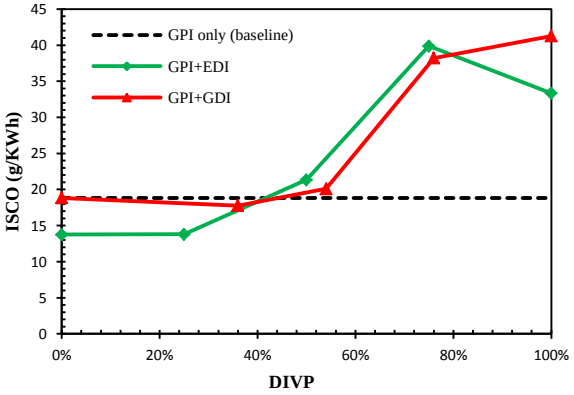

Fig.5 Variation of ISCO with DIVP

## 3.2 Emissions

As shown in Fig. 5 the indicated specific carbon monoxide (ISCO) emissions are slightly reduced with the increase of DIVP. However, once the DIVP is greater than 42%, the ISCO then increases quickly with the increase of DIVP. This result could be attributed to three reasons. Firstly, focusing on ISCO reduction period, ethanol fuel is an oxygenated fuel providing combined with fast laminar flame speed effect could improve the combustion quality resulting in ISCO reduction [7]. Secondly, for both direct injection strategies, when DIVP moves from 42% to 100%, the overcharge cooling effect may reduce the combustion temperature resulting in less ISCO oxidation and thus higher amount of carbon monoxide emissions [18]. Finally, the poor mixture quality after 42% DIVP for both direct injection strategies may adversely affect the combustion quality enlarging the ISCO emissions compared with GPI only.

Figure 6 shows the variation of indicated specific hydrocarbon (ISHC) emissions with DIVP. The ISHC values decrease with increase DIVP reaching a minimum value at 50% in GPI+EDI and at 56% in GPI+GDI and then the ISHC increase reaching the maximum at 100% DIVP. The difference between two strategies is possibly because of the fuel properties. The greater laminar flame speed and the oxygen content of ethanol might contribute to reduce ISHC until 50% of EDI whereas the overcharge cooling effect and lower ethanol volatility may result in lower mixture quality leading to more oil

film formation and thus higher amount of ISHC emissions [18]. These can be the main reasons that might contribute increasing ISHC dramatically between 50-100% EDI. In contrast, for GPI plus GDI strategy, the higher gasoline volatility compared with ethanol may play a significant role in the ISHC reduction.

The indicated specific nitric oxide (ISNOx) emissions varied with DIPV are represented in Fig. 7. In fact, the combustion temperature influences directly the NOx formation inside the combustion chamber [20]. It can be clearly seen that the charge cooling effect of both injection strategies in the ISNOx reduction. Actually, ethanol fuel is more efficient in the ISNOx reduction than gasoline. This can be attributed mainly to the higher latent heat of vaporization which might play an essential job in the combustion temperature decreasing resulting in the ISNOx emissions reduction [2].

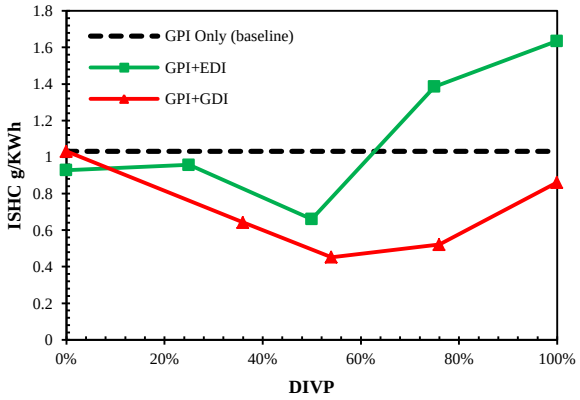


Fig. 6 Variation of ISHC with DIVP

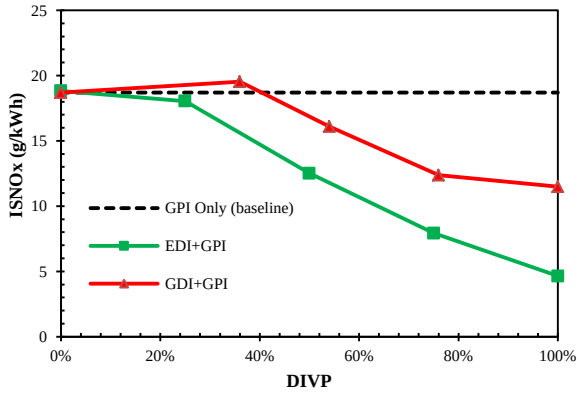


Fig. 7 Variation of ISNOx with DIVP

## 4. Conclusion

An experimental investigation was conducted to investigate dual injection strategies. Experiments were carried out on a small SI engine at GPI only, EDI+GPI and GDI+GPI at medium load and 4000RPM engine speed. The Results of engine performance and emission varied with the percentage of fuel directly injection are presented and discussed. Conclusions can be drawn as follows.

1. Adopting EDI plus GPI strategy improved the combustion quality and thus enlarged IMEP comparing with the other two injection strategies, possibly because of the oxygen contain of ethanol combined with the greater laminar burning velocity compared to that of gasoline.

2. Using GPI plus EDI strategy enhanced the combustion stability by reducing the cycle-to-cycle variation comparing with the other two injection strategies, possibly due to ethanol greater laminar flame speed coupled with the oxygen content.

3. Engine volumetric efficiency slightly improved using GPI plus EDI strategy compared with the other two injection strategies, perhaps due to the high utilizing of ethanol latent heat of vaporization.

4. GPI plus GDI strategy performed better in HC emissions reduction compared with GPI plus EDI strategy, perhaps due to the greater gasoline volatility compared with ethanol fuel.

5. GPI plus EDI strategy behaved better in NOx emissions reduction compared with the other two injection strategies, probably due to the ethanol greater latent heat of vaporization compared with gasoline.

## 5. References


[1] P. Bajpai, Advances in Bioethanol, Springer New Delhi Heidelberg New York Dordrecht London, India, 2013, p.^pp. 100.

[2] B. M. Masum; H. H. Masjuki; M. A. Kalam; I. M. Rizwanul Fattah; S. M. Palash; M. J. Abedin, Renewable and Sustainable Energy Reviews 24 (2013) 209-222.

[3] Y. Zhuang; G. Hong, Fuel 105 (2013) 425-431.

[4] Y. Zhuang; G. Hong, Fuel 135 (0) (2014) 27-37.

[5] F. Catapano; S. Di Iorio; P. Sementa; B. M. Vaglieco, in: SAE International: 2014.

[6] E. Kasseris; J. B. Heywood, SAE Int. J. Engines (2012).

[7] D. Turner; H. Xu; R. F. Cracknell; V. Natarajan; X. Chen, Fuel 90 (5) (2011) 1999-2006.

[8] F. Bonatesta; E. Chiappetta; A. La Rocca, Applied Energy 124 (2014) 366-376.

[9] C. Wang; H. Xu; J. M. Herreros; J. Wang; R. Cracknell, Applied Energy 132 (0) (2014) 178-191.

[10] E. Kasseris; J. B. Heywood, SAE Int. J. Engines (2012).

[11] Y. Huang; G. Hong; R. Huang, Energy Conversion and Management 92 (0) (2015) 275-286.

[12] C. Jiang; X. Ma; H. Xu; S. Richardson, in: SAE International: 2012.

[13] L. Chen; R. Stone; D. Richardson, Fuel 96 (0) (2012) 120-130.

[14] K. Kar; T. Last; C. Haywood; R. Raine, SAE Int. J. Fuels Lubr. 1 (1) (2008) 132-144.

[15] Y. Huang; G. Hong; X. Cheng; R. Huang, SAE Int. J. Engines (2013).

[16] H. Bayraktar, Renewable Energy 30 (11) (2005) 1733-1747.

[17] Z. Wang; H. Liu; Y. Long; J. Wang; X. He, Energy 82 (2015) 395-405.

[18] J. B. Heywood, Internal Combustion Engine Fundemantales McGraw-Hill, Inc., 1988, p.^pp.

[19] G. Zhu; D. Hung; H. Schock, Proceedings of the Institution of Mechanical Engineers, Part D: Journal of Automobile Engineering 224 (3) (2010) 387-403.

[20] H. Wei; T. Zhu; G. Shu; L. Tan; Y. Wang, Applied Energy 99 (2012) 534-544.

**Proceedings of the Australian Combustion Symposium**
**December 7-9, 2015, The University of Melbourne**

# Pyrolysis Characteristics of Ionic Liquid and Solvent Treated Coals

J. Cummings [1], P. Tremain [2], D. Hamilton [2], S. Kundu [2], B. Moghtaderi [2], R. Atkin [1] and K. Shah [2*]

[1] Discipline of Chemistry, The University of Newcastle, Callaghan, NSW 2308, Australia

[2] Discipline of Chemical Engineering, Faculty of Engineering and Built Environment, The University of Newcastle, Callaghan, NSW 2308, Australia.

## Abstract

Two coals, one lignite and one sub-bituminous, were treated at low temperatures with four different ionic liquids (ILs), 1-butylpyridinium chloride [Bpyd][Cl], 1-ethyl-3-methylimidazolium dicyanamide [Emim][DCA], 1-butyl-3-methylimidazolium chloride [Bmim][Cl] and 1-butyl-3-methylimidazolium tricyanomethanide [Bmim][TCM]. These IL treated coals were then washed with n-methyl-2-pyrrolidone (NMP). The pyrolysis characteristics of the treated coals were probed via thermogravimetric analysis (TGA) with the aim of investigating the differences among the raw coal, the IL treated coal and the IL & NMP treated coals. After low temperature IL treatment, all coal samples lost more mass during pyrolysis in comparison to the raw coal. This indicated that IL treatment had broken the macrostructure of the coal apart; resulting in an increase in the volatilization of lower molecular weight species during pyrolysis. The pyrolysis characteristics of the IL & NMP treated coals, saw some samples, specifically those treated by [Bpyd][Cl] lose less mass after NMP treatment, indicating that the lower molecular weight species may have been extracted by the NMP treatment. Other samples showed little to no difference after NMP treatment, and in the case of coal P treated [Emim][DCM], an increase in mass loss was observed after NMP treatment. The observed differences in pyrolysis characteristics appeared to be coal and IL specific, with [Bpyd][Cl] appearing to be the most effective in liberating lower molevular weight species to be extracted by NMP. These results are promising for utilising lower grade coals as feedstocks for valuable chemicals and tars, and producing coals with less volatile matter and a higher carbon content.

*Keywords: Coal treatment, Coal extraction, Ionic Liquids, Pyrolysis, Thermal extraction.*

## 1. Introduction

Coal is an important fuel source that is used in a variety of conversion and utilization processes such as gasification, liquefaction and combustion in power plants. Coal is also used as an organic feedstock to generate valuable aromatic and phenolic based chemicals, along with tars and gases from gasification. Solvent treatment of coal is carried out in order to extract certain components, alter its structure, swell and fragment it and gain a greater understanding of the chemistry of coal [1]. This is essential to allow for more efficient utilisation and conversion of coal in industrial processes [2].

A large range of organic solvents have been shown to be able to solublise, swell and fragment coals, which is advantageous for a variety of industrial applications such as liquefaction and combustion [3-5]. Typical organic solvents utilised include, pyridine, n-,ethyl-2-pyrrolidone (NMP), and carbon disulfide ($CS_2$). These solvents have been shown to solubilize a variety of lower grade coals, resulting in swelling and fragmentation [6]. It has been suggested that this is due to the ability of these solvents to disrupt certain types of secondary interactions, such as hydrogen bonds and ionic interactions, which are known to occur more significantly in lower grade coals such as lignite and sub-bituminous coal [7-9].

Ionic liquids (ILs) are molten salts which have a melting point below 100 °C [10]. ILs as solvents possess a range of unique properties such as a high thermal stability, a low vapour pressure and the ability to tune properties by altering the combinations of cation/anions that make up their composition [11].

ILs have been investigated previously as solvents for cellulose, lignin, and lignocellulose [12-15]. These studies found that certain ILs were able to deconstruct the structure of cellulose and lignin, by disrupting the hydrogen bonding that occurs between biomass units, allowing the biomass to be solubilized. A small number of studies have been carried out investigating the ability of ILs to solubilize coal [16-18]. Painter et al. [16] initially showed that 1-butyl-3-methylimidazolium chloride ([Bmim][Cl]) was able to solubilize the Illinois No. 6 coal. Lei et al. [19] investigated the effect of

* Corresponding author:
Phone: (02) 4033 9332
Email: kalpit.shah@newcastle.edu.au

temperature and the ratio of IL to coal on the efficiency of lignite extraction by [Bmim][Cl]. They found that an increase in temperature and IL/coal ratio resulted in an increase in extraction yield. The effect of coal maceral content on IL extraction was investigated by Shah et al. [17]. It was shown that coal/IL interactions appear to be maceral specific, with the vitrinite rich coal being swollen by IL treatment and the inertinite rich coal appearing fragmented. The extraction of the vitrinite rich coal was also found to be 30% greater than that of the inertinite rich coal.

In a previous investigation, it was shown that specific ILs were able to alter the morphological and thermal properties of sub-bituminous coals favourably for conversion processes [20]. Extensive fragmentation was observed along with an increase in mass loss during pyrolysis. In an additional study, compositional changes and thermal changes to coals after IL treatment were probed via Fourier Transform Infrared spectroscopy (FTIR), and thermogravimetric analysis (TGA). It was found that the IL treated coals appeared to lose larger amounts of mass at lower temperatures, indicating an increase in lower molecular weight species after treatment [21, 22]. This was corroborated with the FTIR data, which showed that there was an increase in aliphatic hydrocarbons after IL treatment. The aim of the present study is to determine whether these lower molecular weight species can be extracted after IL treatment by investigating the pyrolysis characteristics of raw coal, IL treated coal and IL & NMP treated coal.

## 2. Experimental

One lignite and one sub-bituminous coal, Coal P and R respectively, with a particle size range of 150 – 212 μm, were used in this investigation. The ultimate analyses of these coals are presented in Table 1.

**Table 1.** Ultimate analyses of the coals P and R.

| Coal | Ultimate analysis | | | | |
|---|---|---|---|---|---|
| | C (%) | H (%) | N (%) | S (%) | O (%) |
| P | 65.1 | 5.3 | 1.2 | 0.7 | 27.9 |
| R | 77.2 | 5.2 | 2.0 | 0.7 | 15.0 |

*O calculated by difference

Four IL's were employed in this study: 1-butylpyridinium chloride [Bpyd][Cl], 1-ethyl-3-methylimidazolium dicyanamide [Emim][DCA], 1-butyl-3-methylimidazolium chloride [Bmim][Cl] and 1-butyl-3-methylimidazolium tricyanomethanide [Bmim][TCM]. All ILs were purchased from io-li-tec at 99% purity and were selected based upon previous work carried out on coal and biomass/IL pretreatments [13, 15, 23, 24]

Samples were prepared in a 1:5 mass ratio of coal to IL, respectively. The IL and coal mixtures were magnetically stirred in sealed jars that were placed in an oil bath at 100 °C for 3 hours. After 3 hours, samples were removed from the oil bath, and the coal-IL mixture placed in a centrifuge tube in order to separate and recover each phase. The supernatant was then carefully removed from the centrifuge tube with a pipette.

The IL was then placed in an oven at low temperatures (60 – 80 °C) to evaporate water and recover the IL. The coal was then washed multiple times with distilled water in order to ensure negligible amounts of IL remained on the surface. The electrical conductivity of this water was then measured; the washing process was repeated until the recovered water had a similar conductivity to that of distilled water. These samples were then placed in the oven to dry at 100 °C.

The dry IL treated coal samples were then treated with NMP for 3 hours at 100 °C. The NMP/coal mixture was separated via filtration and each component was recovered, the coal was then placed in the oven to dry.

The pyrolysis characteristics of the coal samples were then analysed using a thermogravimetric analyser (Model Q50 V20.10 Build 36, TA Instruments, U.K.). Each raw, IL treated and IL & NMP treated coal sample (10 – 20 mg) was placed in a platinum crucible and a nitrogen flow rate of 60 mL/min. Pyrolysis of each sample was then carried out from 0 - 1100 °C with a temperature ramp rate of 30 °C/min.

## 3. Results and Discussion

The thermal pyrolysis profile of the raw, IL treated and IL & NMP treated coal samples were carried out via TGA. Figure 1 shows the TG profiles, from 100 - 1100 °C, for each of the different treatments of the coal P and coal R samples. The trends observed between the raw, IL treated and IL & NMP treated coal samples appeared to vary with the coal and IL used.

During pyrolysis, raw coal P lost roughly 55 % of its mass over the 100 - 1100 °C. When coal P was treated with each of the ILs, changes in pyrolysis characteristic were observed. The [Bpyd][Cl] treated coal P sample (Fig. 1a) was observed to lose roughly 65 % of its mass during pyrolysis over the 100 - 1100 °C range. This increase in mass loss compared to raw coal P occurred after 400 °C, the point at which the macrostructure begins to decompose, indicating an increase in lower molecular weight species after treatment. When NMP was used to further treat this sample, the thermal properties were observed to change again. The NMP treated [Bpyd][Cl] coal P sample (Fig. 1a) was observed to lose roughly the same amount of mass as the raw sample (roughly 55 %), indicating that the lower molecular weight species liberated from the IL treatment were extracted by the NMP treatment.

The [Bpyd][Cl] treated coal R samples exhibited a similar trend to the coal P samples. The raw coal R sample lost close to 35 % of its mass, whereas the IL treated sample lost 50 % of its mass over the same temperature range. Furthermore after NMP treatment, it was observed to lose roughly 42 % of its mass.

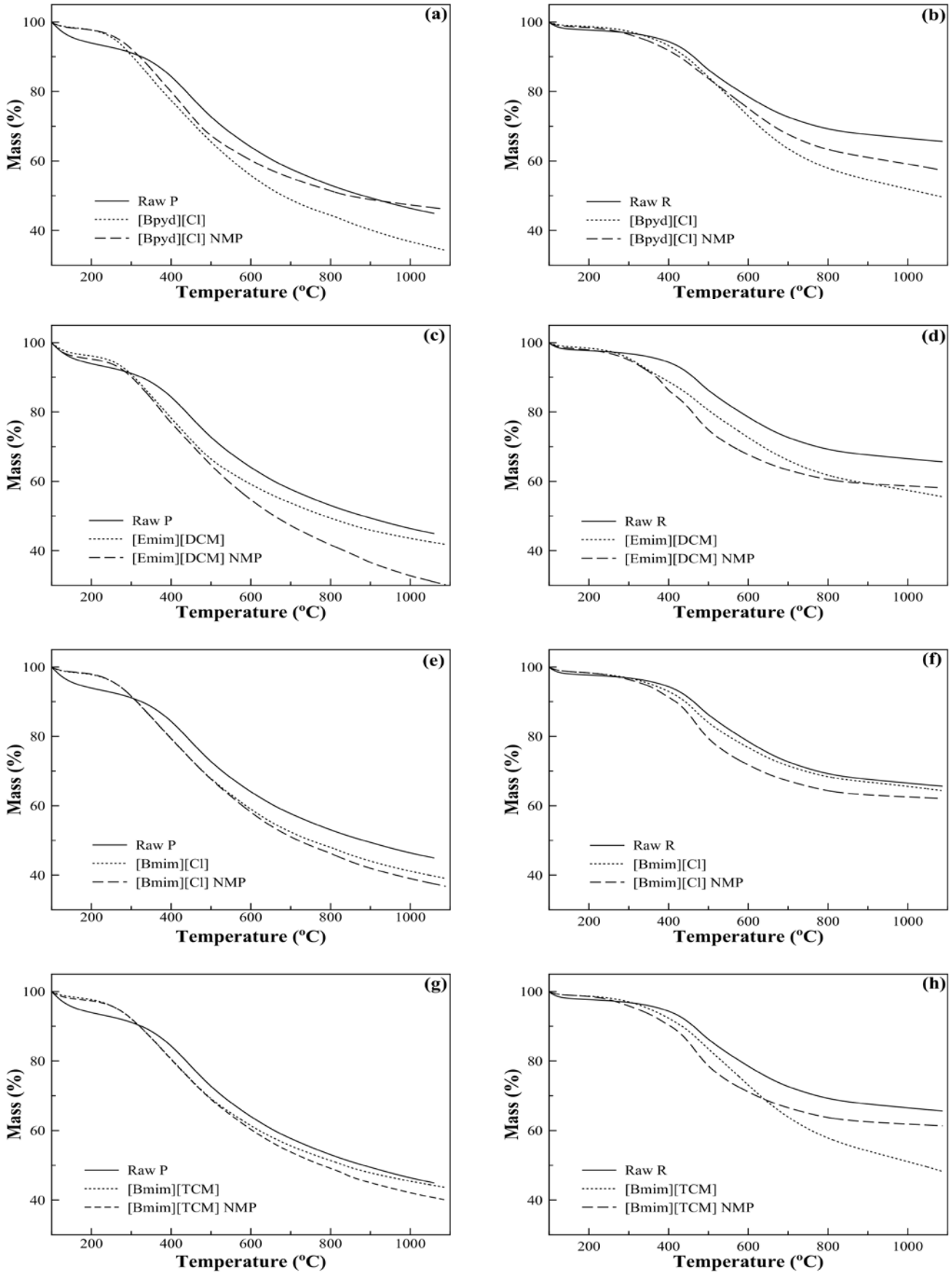


**Figure 1.** Thermal profiles of coals P and R treated by [Bpyd][Cl] and NMP (a and b), [Emim][DCM] and NMP (c and d), [Bmim][Cl] and NMP (e and f), and [Bmim][TCM] and NMP (g and h)

indicating that the lower molecular species were extracted.

The [Emim][DCM] treated coals (Fig. 1c & d) exhibited a different trend. For coal P, the IL treated sample lost roughly the same mass as the raw coal (42 %), whereas after NMP treatment it lost close to 70 % of its mass over the same temperature range. For coal R, the IL and NMP treated samples appeared to lose roughly the same amount of mass over the 100 - 1100 °C temperature range.

The [Bmim][Cl] treated coals (Fig. 1e & f) also displayed differing trends, for both coals P and R, there were minimal differences observed in the thermal properties between the IL treated samples and the NMP treated samples, this seems to illustrate that the effectiveness of the treatment process is IL dependent.

The ability of [Bmim][TCM] to alter the thermal properties of the coals appeared to be coal dependent (Fig. 1g & h). The IL treated sample lost 52 % of its mass; close to 20 % more than the raw coal over the same temperature range. After being treated with NMP, this sample lost 38 % of its mass.

It appears that overall, the effectiveness of the treatment is dependent on both the IL and grade of coal being used, with the lignite coal P being most effectively extracted by [Bpyd][Cl], and the sub-bituminous coal being most effectively extracted by [Bpyd][Cl] and [Bmim][TCM]. This difference may be due to the difference in oxygen contents between each coal.

These results indicate that low temperature IL treatment resulted in the degradation of the macrostructure of each coal used, to differing degrees, liberating lower molecular weight species, resulting in higher mass losses during pyrolysis. This has been observed in previous investigations [20-22]. After solvent extraction of these samples with NMP, multiple samples appeared to have lost these lower molecular weight species, although this was dependent on the coal and IL used, with [Bpyd][Cl] appearing to be the most effective.

Ultimately this means that it may be possible to extract valuable fine chemicals and tars from these IL treated coals with solvents such as NMP, leaving the coal with less volatile matter and a higher carbon content.

## 4. Conclusion

Two coals, one lignite and one sub-bituminous were treated with four different ILs at 100 °C, these coals were then treated with NMP. The thermal properties of these coals were analysed and compared via TGA. It was found that low temperature IL treatment resulted in an increase in mass loss during pyrolysis to differing degrees. This indicated that the ILs had broken the macrostructure of the coal apart during the treatment process; resulting in an increase in the liberation of lower molecular weight species in the treated samples. When the IL treated samples were treated with NMP, another change in thermal properties was observed. These changes appeared to be coal and IL specific, with the [Bpyd][Cl] treated samples appearing to lose the most volatile matter after IL treatment, with a significant decrease in mass loss observed after NMP treatment. The [Bmim][Cl] treated samples on the other hand appeared to show little to no differences in both coals.

These results are promising for utilising lower grade coals as feedstocks to produce valuable chemicals and tars, as well as producing coals with less volatile matter with a higher carbon content.

## 5. Acknowledgments

The authors wish to acknowledge the financial support provided by the University of Newcastle Australia for the work presented in this paper.

## 6. References

[1] H. H. Schobert; C. Song, Fuel **81** (1) (2002) pp. 15-32.

[2] J. Hayashi; C.-Z. Li, in: Advances in the Science of Victorian Brown Coal, C.-Z. Li, (Ed.) Elsevier Science: Amsterdam, 2004; pp. 11-84.

[3] N. Wijaya; L. Zhang, Energy & Fuels **25** (1) (2011) pp. 1-16.

[4] F. Pinto; I. Gulyurtlu; L. S. Lobo; I. Cabrita, Fuel **78** (6) (1999) pp. 629-634.

[5] S. Vasireddy; B. Morreale; A. Cugini; C. Song; J. J. Spivey, Energy & Environmental Science **4** (2) (2011) pp. 311 - 345.

[6] J. P. Mathews; C. Burgess-Clifford; P. Painter, Energy & Fuels **29** (3) (2015) pp. 1279-1294.

[7] M. Iino, Fuel Processing Technology **62** (2–3) (2000) pp. 89-101.

[8] J. W. Larsen; M. Mohammadi, Energy & Fuels **4** (1) (1990) pp. 107-110.

[9] M. Nishioka; J. W. Larsen, Energy & Fuels **4** (1) (1990) pp. 100-106.

[10] Y. I. Rika Hagiwara, Journal of Fluorine Chemistry 105 (2000) pp. 221-227.

[11] R. Hayes; G. G. Warr; R. Atkin, Chemical Reviews (2015) pp. 6357–6426.

[12] J. B. Binder; M. J. Gray; J. F. White; Z. C. Zhang; J. E. Holladay, Biomass and Bioenergy **33** (9) (2009) pp. 1122-1130.

[13] W. Li; N. Sun; B. Stoner; X. Jiang; X. Lu; R. D. Rogers, Green Chemistry **13** (8) (2011) pp. 2038-2047.

[14] A. Brandt; J. Grasvik; J. P. Hallett; T. Welton, Green Chemistry **15** (3) (2013) pp. 550-583.

[15] K. C. Badgujar; B. M. Bhanage, Bioresource Technology **178** (2015) pp. 2-18.

[16] P. Painter; N. Pulati; R. Cetiner; M. Sobkowiak; G. Mitchell; J. Mathews, Energy & Fuels **24** (3) (2010) pp. 1848-1853.

[17] K. Shah; R. Atkin; R. Stanger; T. Wall; B. Moghtaderi, Fuel **119** (2014) pp. 214-218.

[18] N. Pulati; M. Sobkowiak; J. P. Mathews; P. Painter, Energy & Fuels **26** (6) (2012) pp. 3548-3552.

[19] Z. Lei; L. Wu; Y. Zhang; H. Shui; Z. Wang; C. Pan; H. Li; S. Ren; S. Kang, Fuel **95** (0) (2012) pp. 630-633.

[20] J. Cummings; K. Shah; R. Atkin; B. Moghtaderi, Fuel **143** (2015) pp. 244-252.

[21] J. Cummings; K. Shah; E. Heldt; B. Moghtaderi; R. Atkin; S. Kundu; H. Vuthaluru, in: *International Conference on Coal Science and Technology*, Fuel Processing Technology Melbourne, 2015.

[22] J. Cummings; S. Kundu; P. Tremain; B. Moghtaderi; R. Atkin; K. Shah, Energy & Fuels **(Accepted)** (2015).

[23] M. Francisco; A. van den Bruinhorst; M. C. Kroon, Green Chemistry **14** (8) (2012) pp. 2153-2157.

[24] S. Xia; G. A. Baker; H. Li; S. Ravula; H. Zhao, RSC advances **4** (21) (2014) pp. 10586-10596.

# Numerical Modeling of Oxygen Enhanced Combustion and Transient Heating Characteristics in a Reheating Furnace

R. Prieler[1, *], P. Belohradsky[2], B. Mayr[1], M. Demuth[3], C. Hochenauer[1]
[1]Institute of Thermal Engineering
Graz University of Technology, Inffeldgasse 25/B, A-8010 Graz, Austria
[2]Institute of Process and Environmental Engineering
Brno University of Technology, Technicka 2, 61669 Brno, Czech Republic
[3]Messer Austria GmbH – Kompetenzzentrum Metallurgie, Industriestraße 5, A-2352 Gumpoldskirchen, Austria

## Abstract

In this work an experimental and numerical investigation of oxygen enhanced combustion (OEC) was done for different oxygen concentrations on a 750 kW lab-scale furnace. Temperatures in the furnace and heat fluxes to the walls were measured and used to validate the CFD model especially the chemical reaction mechanism for applicability in OEC. Flame temperature and shape were in good agreement as well as the heat fluxes to the walls for all combustion cases. An increase of the furnace efficiency was determined from 61% for combustion with air and 73.4% for OEC with an $O_2$ concentration of 30.8vol% in the oxidizer. The same trend was predicted by the numerical simulations. Additionally an industrial walking hearth furnace to reheat steel billets was simulated by the CFD model for air-fuel and OEC with an enrichment level of 25vol% $O_2$. Furnace operation revealed a fuel saving of 8% compared to the air case. The transient simulation of the billets showed that the similar billet surface temperature was achieved with OEC.

*Keywords: Oxygen-enhanced combustion, Computational fluid dynamics, Reheating furnace, Furnace efficiency*

## 1. Introduction

The combustion of hydrocarbon fuels like natural gas is used in many industrial processes producing the anthropogenic greenhouse gas $CO_2$. A tremendous amount of fossil fuels are fired in high temperature processes like melting, annealing, reheating etc. High efforts were made on recuperation systems, wall refractory and process control to improve such processes driven by environmental and economic issues. Most combustion processes use air with a typical composition of 21vol% $O_2$ and 79vol% $N_2$. In addition the nitrogen has to be heated up by the heat released from the combustion. Hence, the nitrogen prevents higher flame temperatures and has no contribution to the radiative heat transfer in the furnace. Therefore the efficiency in combustion processes can be increased by the reduction or complete removal of the nitrogen which are called oxygen enhanced combustion (OEC) [1]. Retrofit of existing combustion systems can be an opportunity to improve the energy efficiency for example in cement, glass or steel industry.

Numerical modeling of OEC processes is significantly different from conventional air-fired combustion. Higher flame temperature due to the lack of nitrogen and increased radiative heat transfer in OEC are the main challenges for accurate CFD simulations. For common air-fuel combustion global reaction mechanisms might be applicable considering just a few reactions. Hence, higher flame temperature occur in OEC intermediate species like radicals and CO have to be taken into account with more detailed reaction mechanisms. Investigations on the impact of different reaction mechanisms and radiation models in OEC were carried out by several authors for gas fired furnaces, e.g., Yin et al. [2,3], Galletti et al. [4] and Al-Abbas and Naser [5].

This study mainly focuses on the reheating process in the steel industry which, in combination with the rolling mill, is the second largest energy consumer in steel manufacturing [6,7]. Oliveira et al. [8] already determined the potential of oxy-fuel combustion in reheating processes to increase the efficiency. An experimental and numerical investigation on the furnace efficiency depending on the oxygen enrichment was published in [9]. In this work test runs were carried out on a 750 kW furnace with OEC for 21, 25.4 and 30.8vol% $O_2$ in the oxidizer. Experimental results were used to validate a numerical model using the steady flamelet approach for prediction of the gas phase combustion in OEC and air-fired conditions. The steady flamelet model offers a time saving method in combustion modeling compared to conventional used eddy dissipation model and eddy dissipation concept. As a consequence large scale furnaces can be analyzed without expensive test runs. Furthermore, a walking hearth furnace for reheating steel billets was simulated with the CFD model for air-fuel and OEC (25vol% $O_2$). Predicted heat fluxes to the steel billets were used to predict the temperature distribution in the billets for both operating conditions by coupling gas phase combustion and transient heating.

## 2. Experimental setup

### 2.1 Lab-scale furnace

In Fig. 1 a 3D model of the experimental furnace can be seen. The furnace consists of a horizontal combustion chamber with a length of 4 m and inner

* Corresponding author:
Phone: (+43) 316 873 7810
Email: rene.prieler@tugraz.at

diameter of 1 m. The burner is located at the front of the chamber. The walls of the combustion chamber are water cooled and are divided into seven cooling zones. Six sections have the length of 0.5 m; the seventh section has the length of 1 m. For each zone the absorbed heat flux can be determined through measuring the water mass flux and the in- and outlet temperatures. Additionally the temperature was measured at a distance of 0.75, 1.25, 1.75, 2.25, 2.75, 3.25, and 3.75 m from the front wall of the furnace and different radial positions. The flue gas temperature was measured using thermocouples of type R. The correction of the measured temperature due to radiation from the thermocouples to the cold walls was neglected because only a small part of the thermocouple surface was exposed to radiation. The lab-scale furnace was considered to be in a steady-state when the maximum change of the flue gas temperature over 30 minutes was below 10 K and the local wall heat fluxes did not change over 10 minutes [10]. The numerical grid for the simulation was made of 1.6 million cells. The furnace was investigated under oxygen concentration of 21, 25.4 and 30.8vol% $O_2$. Premixing of air and pure oxygen was carried out before entering the burner to achieve the desired OEC level. More detailed information can be found in [10,11].

### 2.2 Industrial walking hearth furnace

In Fig. 2 a 3D model of the walking hearth type furnace is shown. The furnace is fired by 48 swirl burners with natural gas which is located at the roof of the furnace. This furnace operates under air-fuel and an oxygen enrichment of 25vol% $O_2$ with an equivalence ratio of 0.97. The oxidizer was pre-heated up to 310 °C. According to the operating conditions of the furnace the fuel input was 18.2 MW (air-fuel) and 16.74 MW (25vol% $O_2$) which is a fuel saving of 8%. The billets enter the furnace from the left and leave the furnace at the right. Three different zones can be identified in the furnace namely the pre-heating, heating and soaking zone. In this furnace billets were heated up from ambient temperature to about 1200 °C with a residence time of 6400 seconds. The billets have a dimension of 0.12 x 0.12 m and are 12 meters long. For the numerical simulations the furnace was modeled with a grid of approximately 5.7 million cells including the furnace walls.

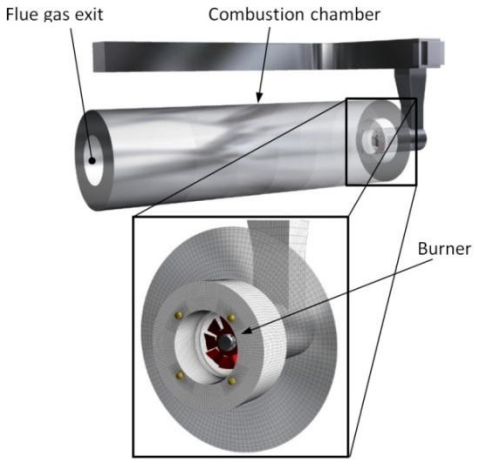


Fig. 1. 3D model of the 750 kW test furnace.

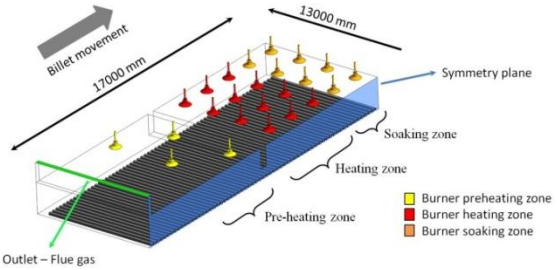


Fig. 2. CFD model of the industrial walking hearth furnace for reheating steel billets.

## 3. Numerical method

### 3.1 Modeling of the reactive flow

The turbulent flow was modeled by solving the Reynolds-averaged Navier-Stokes (RANS) equations with a steady-state pressure-based solver. For the Reynolds stresses the realizable k-epsilon model was used.

In this work the SFM model was used to investigate the OEC combustion. The turbulent flame is represented by an ensemble of small one dimensional laminar diffusion flames. For these laminar flames the thermochemical state (temperature, species concentrations and density) is related to a single parameter called mixture fraction. The mixture fraction is defined as the mass fraction of all fuel (C, H, etc.) and oxidizer (O, etc.) elements in all species (CO2, H2O, CO, etc.). It is defined in (1), where $Z_i$, $Z_{i,ox}$ and $Z$ are the elemental mass fractions of element $i$ in oxidizer and fuel.

(1)

The big advantage of this approach is that the one dimensional laminar diffusion flames can be calculated with a detailed mechanism before the actual CFD calculation. Solving the transport equations in CFD is related to the Favre-averaged values of the scalars like temperature, species concentrations, etc. Therefore a presumed $\beta$-probability density function (PDF) was appropriate for the turbulence-chemistry interaction which describes the relationship of the instantaneous and averaged values. Also to integrate the PDF the mixture fraction variance has to be introduced. The solution of this calculation is stored in look up tables depending only on three variables for which transport equations have to be solved during the CFD simulation. These are the mixture fraction, the mixture fraction variance and in non-adiabatic condition the enthalpy. In the CFD calculation only two additional equations for the mixture fraction and the mixture fraction variance must be solved to describe the chemical reaction which leads to vast calculation time reduction. Therefore this approach with the detailed reaction mechanisms with 17 species and 25 reversible reactions [12] was used in this study to describe the combustion process.

Due to the fact that more than 90% of the heat flux in reheating furnaces is transported by radiation, the modeling of the radiative heat transfer is crucial for the accuracy of the simulation. It was found that the impact of OEC on the radiative heat flux is more sensitive for

large beam length. Hence the investigated furnaces have moderate beam lengths the weighted-sum of grey gases model (WSGGM) [13] with coefficients from Smith et al. [14] was applied to determine the radiative properties of the flue gas. The radiative transport equations were solved by the discrete ordinates model (DOM) [15, 16].

### 3.2 Iterative solution procedure for the transient heating of steel billets

In the walking hearth type furnace the transient effects of the reheating of the billets were considered by an iterative procedure of the steady-state furnace simulation and the transient simulation of the billet. In the furnace simulation a temperature boundary condition of the billet surface was defined. The heat fluxes, which were determined in the steady-state furnace simulations, were the boundary conditions for the following transient simulation of the billets. The calculated surface temperatures of the billet in the transient simulation are the new temperature distribution of each billet in the next steady-state furnace simulation. This procedure is done until the change of temperature of the billet is below 1% which can be seen as sufficient convergence criteria.

## 4. Results

### 4.1 Lab-scale furnace

Based on the measured temperatures in the furnace contour plots were created of the temperature distribution. This contour plots were compared to the simulation results for all three combustion cases in Fig. 3. In this figure only one half of the furnace was displayed because the thermocouples were inserted into the furnace from one side and temperatures were measured from the wall to the axis of the combustion chamber.

For the air-fired case similar flame temperatures right after the burner were detected for experiments and CFD. Also a slight deflection of the flame to the left was found due to the inhomogeneous inflow to the burner. This is caused by the air supply duct (see Fig. 1). With OEC the flame temperature increases which can be seen for 25.4vol% and 30.8vol%. Nevertheless the deflection of the flame to the left wall decreases because of the lower volume-flow rate of oxidizer which reduces the momentum induced by the swirl burner. In all cases the predicted flame is longer and hotter than in the measurement. This can be explained by the additional heat losses of the inspection windows and the rear and front walls of the furnace which were not considered in the CFD model. Furthermore the air leakage occurs during the experiments and additionally decreases the temperature especially in OEC.

In Fig. 4 the calculated and measured heat fluxes to the furnace walls (sections) are displayed. The sections 1 to 3 showed an increase of the heat flux for both measurement and simulation. It was also examined that the heat flux in this sections increases with the OEC level. From section 3 to section 4 the heat flux for 30.8vol% $O_2$ enrichment decreases because of the shorter flame. For 21 and 25.4vol% $O_2$ the heat flux starts to decrease between section 4 and 5. In section 7 all cases showed higher heat fluxes compared to section 6. This is because the last section was 1 m compared to 0.5 of the other sections which results in an increase of the heat exchange area with the factor 2. The comparison of the CFD results with the measured temperatures and heat fluxes revealed a good agreement and the applicability for OEC and air-fuel combustion.

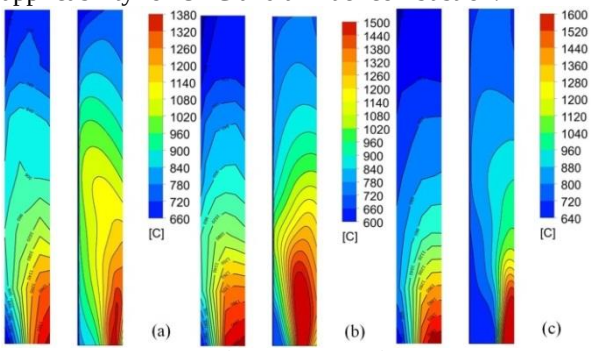


Fig. 3. Contour plots of the measured (left) and calculated (right) temperatures: (a) 21vol%, (b) 25.4vol%, (c) 30.8vol% $O_2$.

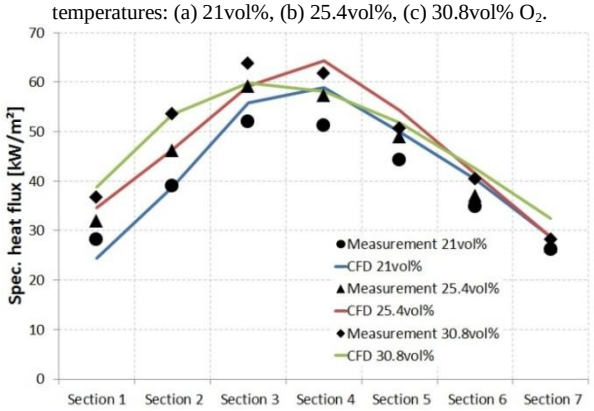


Fig. 4. Heat fluxes to the furnace wall.

As already mentioned in section 1 higher efficiencies of combustion processes can be achieved by OEC. The furnace efficiency is defined in (3), where $\dot{Q}$ is the heat flux to the wall (or billets in section 4.2) and $\dot{Q}_{fuel}$ is the fuel input.

$$\frac{\dot{Q}}{\dot{Q}} \qquad (3)$$

In Fig. 5 the efficiency displayed for measurement and CFD. An increase of the efficiency can be clearly identified for predicted and measured values. The measurement showed an increase from 61% (air-fuel) to 73.4% for 30.8vol% $O_2$ which is a difference of 12.4%. Approximately the same trend was observed in the simulation with values of 66% (air-fuel) and 74.4% (OEC for 30.8vol%)

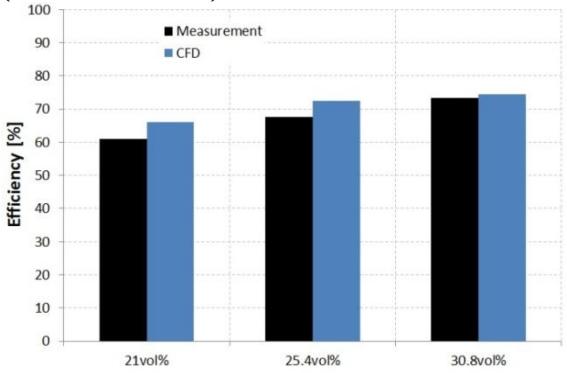


Fig. 5. Predicted and measured furnace efficiency for the three combustion cases.

### 4.2 Walking hearth furnace

CFD simulation of the walking hearth furnace was carried out with the same numerical model as for the lab-scale furnace. In Fig. 6 the simulated heat fluxes for both cases are displayed. The simulation predicted similar heat fluxes (deviation of 0.2 MW) to the billets although the fuel input was reduced with a value of 8%. The heat losses through the flue gas can be reduced in OEC from 5.38 MW to 3.95 MW. This leads to a higher efficiency of the reheating process of 61.4% compared to air-firing with 57.6%.

Results of the transient simulation of the billets are presented in Fig. 7. This figure shows the billet temperatures at different positions in the furnace and examined although the fuel input was decreased the target temperature of the billets was reached in both cases. Not only the target temperature was achieved also the temperature uniformity of the discharged billet is similar for both conditions which is important for the following deformation process on the rolling mill.

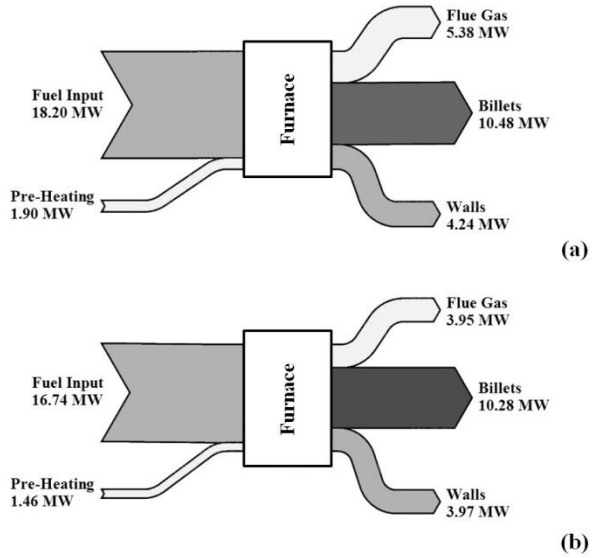


Fig. 6. Calculated heat fluxes in the walking hearth furnace: (a) air-fired, (b) 25vol% $O_2$.

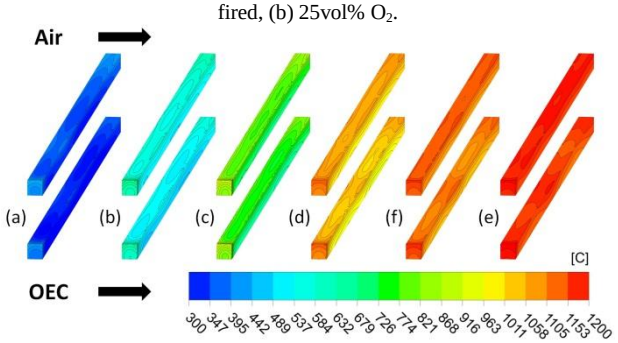


Fig. 7. Billet surface temperatures for air-fuel (top) and OEC (bottom): (a) 4.9 m, (b) 7.6 m, (c) 10.3 m, (d) 13.8 m, (e) 15.1 m and (f) 17 m.

## 5. Conclusion

A lab-scale furnace was experimentally investigated by measurement of the temperatures in the furnace and the heat flux to the chamber walls. Air-fuel and 2 OEC (25.4vol% $O_2$ and 30.4vol% $O_2$) cases were tested to determine the impact of OEC on the efficiency in the combustion process. The measurements were compared to a CFD model which uses the SFM to predict the gas phase combustion. A reaction mechanism of 17 species and 25 reversible reactions was applied. A comparison with measurement showed that the simulation was able to predict the flame temperatures as well as the heat fluxes to the walls under OEC and air-fuel conditions. An increase of the efficiency was detected for OEC compared to air-fuel combustion with the measured data and CFD simulations. Furthermore a walking hearth furnace was simulated for air combustion and 25vol% $O_2$. A fuel saving of 8% compared to air-fuel was determined with the same heat flux to the billets. Therefore the furnace efficiency was increased up to 61.4%.

## 6. Acknowledgments

This work was supported by the Austrian Research Promotion Agency (FFG), "Competence-Headquarter: Ökologische und ökonomische Optimierung von industriellen Hochtemperaturprozessen durch Sauerstoffeinsatz" (project 848281, eCall 4944044).

## 7. References

[1] C. Baukal, Oxygen-Enhanced Combustion, CRC Press, Boca Raton, FL, US, 2013, p. 792.

[2] C. Yin, L.A. Rosendahl, A.K. Kaer, Fuel. **90** (7) (2011), pp. 2519–2529.

[3] C. Yin, L.C.R. Johansen, L.A. Rosendahl, A.K. Kaer, Energy Fuels. **24** (12) (2010), pp. 6275–6282.

[4] C. Galletti, G. Coraggio, L. Tognotti, Fuel. **109** (2013), pp. 445–460.

[5] A.H. Al-Abbas, J. Naser, Energy Fuels. **26** (2) (2012), pp. 952–967.

[6] Y. Sakamoto, Y. Tonooka, Y. Yanagisawa, Energy Conv. Management. **40** (11) (1999), pp. 1129–1140.

[7] S.H. Han, D. Chang, Heat Mass Transf. **55** (2012), pp. 4079–4087.

[8] F.A.D. Oliveira, J.A. Carvalho, P.M. Sobrinho, A. de Castro, Energy. **78** (2014), pp. 290–297.

[9] R. Prieler, M. Demuth, C. Hochenauer, In: 15th Int. Conference on Numerical Combustion. Avignon, France, April 2015.

[10] P. Belohradský, P. Skryja, I. Hudak, Energy. **75** (2014), pp. 116–126.

[11] P. Belohradský, P. Skryja, I. Hudak, In: 10th European on Industrial Furnaces and Boilers. Gaia (Porto), Portugal, April 2015.

[12] T.W.J. Peeters, PhD thesis. Delft Technical University, Delft, The Netherlands, 1995.

[13] H.C.Hottel, A.F. Sarofim, Radiative transfer, McGraw-Hill Book Company, New York, US, 1967, p. 52.

[14] T.F. Smith, Z.F. Shen, J.N. Friedman, J Heat Transf. **104** (1982), pp. 602–608.

[15] E.H. Chui, G.D. Raithby, Num Heat Transf, Part B. **23** (1993), pp. 269–288.

[16] E.H. Chui, G.D. Raithby, J Heat Transf. **112** (1990), pp. 415–423.

# A Bench-Scale TGA-FTIR Investigation of Tar Removal in a Modified Biochar Production Process

P. Tremain, F. Yin, F. Wilson, B. Moghtaderi, K. Shah*
Priority Research Centre for Frontier Energy Technologies and Utilisation School of the Engineering
The University of Newcastle NSW 2308 Australia

## Abstract

Biochar is an emerging soil amendment and carbon sequestration candidate. The current study proposes to enhance biochar production by reducing tar production in the pyrolysis process while concomitantly improving biochar nutrient properties by introducing lime (CaO) to the pyrolysis process. Preliminary thermogravimetric analysis coupled with Fourier transform infrared spectroscopy (TGA-FTIR) experiments with sugarcane bagasse have shown the addition of CaO, in the form of limestone dust, to the pyrolysis process can significantly decrease volatile tar production when mixed at ratios of 0.5 and 1 CaO to biomass. Scanning electron microscopy of the biochar produced revealed no structural changes to biochar with the addition of CaO. Future studies will investigate a wider range of biomass sources and investigate its potential as a soil amendment.

*Keywords: biochar, tar, pyrolysis, stone dust, calcium oxide, TGA-FTIR.*

## 1. Introduction

Biochar is char created from a biomass feedstock via a pyrolysis process, for specific use as a soil amendment [1]. Biochar has garnered significant attention in the scientific community over the past decade due to its soil amelioration properties and carbon sequestration potential [2, 3]. Biochar application to soil has been conducted by numerous groups with a general consensus that the application of biochar to soils can be beneficial in terms of increasing crop yield [4-9], improving WHC [10-12] and altering the pH of soils [13, 14].

The production of biochar is typically conducted via a slow pyrolysis process, i.e. ramp rate 3-10°C/min, to ensure char yields are maximized. However, one commonly encountered issue with biochar production is the evolution of tars during the pyrolysis process. Tars are inherently toxic and pose significant handling and cleanup issues. Hence cracking and removal of tars during the pyrolysis process is of significant benefit to biochar producers.

The use of lime (CaO) to catalytically pyrolyse and gasify biomass to reduce tar production has been presented by a number of studies. Investigations performed by Wang et al. [15] and Han et al. [16] both reported a significant reduction in volatile tar related compounds, such as carbonyl and phenolic groups, when biomass pyrolysis or gasification was performed in the presence of CaO.

Furthermore, CaO is commonly used in agriculture to control soil pH imbalances and serve as a source of calcium for plants, with the addition of biochar to soil often completed in conjunction with liming practices. Hence this study proposes a novel modification to the biochar production process by introducing CaO, in the form of limestone dust, to the pyrolysis process in order to promote cracking of tars in situ and ultimately enhance the liming properties of biochar produced.

**Table 1.** Proximate analysis of sugarcane bagasse on a dry basis (d.b.).

| Biomass | M (%) | V (% d.b.) | FC (% d.b.) | Ash (% d.b.) |
|---|---|---|---|---|
| Bagasse | 8.5 | 86.6 | 6.6 | 6.9 |

M: Moisture content;V: Volatile Matter; FC: Fixed Carbon

In this study a preliminary TGA-FTIR investigation is presented for the pyrolysis of one type of biomass with different amounts of CaO to gauge its effect on tar formation and the structural morphology of biochar produced. The experimental methods are detailed in the following section.

## 2. Experimental Methods

A series of preliminary experiments were conducted using a Q50 thermo-gravimetric analyser (TGA) coupled with a Varian IR-660 Fourier transform infrared (FTIR) spectrometer for online gas analysis. Biomass samples were pyrolysed with and without limestone dust (i.e. CaO) in situ. Sugarcane bagasse, with a particle size of 75-150 µm, was the biomass sample utilized, with its proximate analysis presented in Table 1. XRF analysis of the limestone dust (particle size 75-150 µm) utilized in this study is presented in Table 2.

The pyrolysis experiments were carried out in the TGA under a nitrogen atmosphere (100 mL/min) and 5°C/min heating rate up to a maximum temperature of 600°C. During the experiments, gases exiting the TGA were transferred to the FTIR spectrometer via a heated transfer line set at 240°C. FTIR spectra were taken at 10°C increments with 24 scans per spectra over a scan range of 500 – 4000 $cm^{-1}$ and resolution of 2 $cm^{-1}$. FTIR operating conditions consisted of a gas cell length of 10 cm and gas cell temperature of 240°C. The experimental apparatus is pictured in Figure 1.

**Table 2.** XRF elemental analysis of stone dust.

| Element | Ca | Fe | Mg | Al | Si | Mn | K |
|---|---|---|---|---|---|---|---|
| Abundance (%) | 97.56 | 0.23 | 0.38 | 0.15 | 1.21 | 0.43 | 0.04 |

* Corresponding author:
Phone: (+61) 2 40339332
Email: kalpit.shah@newcastle.edu.au

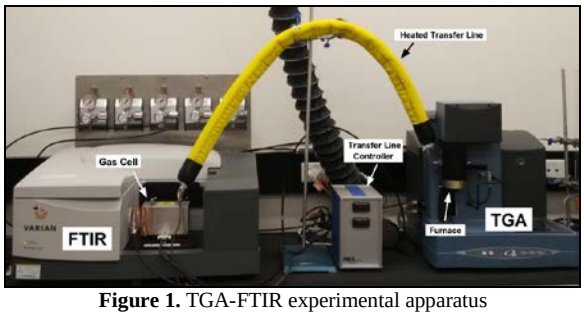


**Figure 1.** TGA-FTIR experimental apparatus

The biochar samples produced were subsequently examined via scanning electron microscopy (SEM). Sample preparation for SEM involved gold coating samples before examination on a Philips XL30 SEM located at the EMXRAY unit at the University of Newcastle.

## 3. Results and Discussion

### 3.1 Thermal analysis

The derivative mass loss (DTG) as a function of temperature for three different CaO to biomass (CaO:B) ratios is presented in Figure 2. It can be seen that each curve followed relatively the same trend, with peak devolatilisation achieved at approximately 350°C for all treatments. A slight decrease in the magnitude of the DTG curve was observed for increasing CaO content attributed the capture of a portion of the $CO_2$ produced during biomass devolatilisation and the cracking of tars.

### 3.2 Gas analysis

Online FTIR measurements allowed for the characterization of volatile components during the pyrolysis of bagasse with and without CaO. An example FTIR spectra obtained for pyrolysis of CaO and bagasse and in a 0.5:1 ratio at 350°C is presented in Figure 3. For all treatments, the primary volatile constituents observed were $CO_2$ (~2400 $cm^{-1}$), as well as tar functional group constituents; carbonyl C=O (~1600 $cm^{-1}$), phenol C-O (~1100 $cm^{-1}$) and aromatic =C-H (~800 $cm^{-1}$). Other volatiles observed included CO (~2100 $cm^{-1}$), $CH_4$ (~2900 $cm^{-1}$) and $H_2O$ (~3700 $cm^{-1}$). To gain a qualitative understanding of the in situ tar cracking ability of CaO, the area under the curve of the carbonyl, phenol and aromatic peaks were taken for each of the

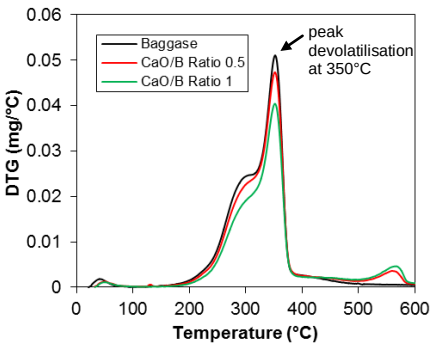


**Figure 2.** Derivative mass loss as a function of temperature for three different CaO to Biomass ratios

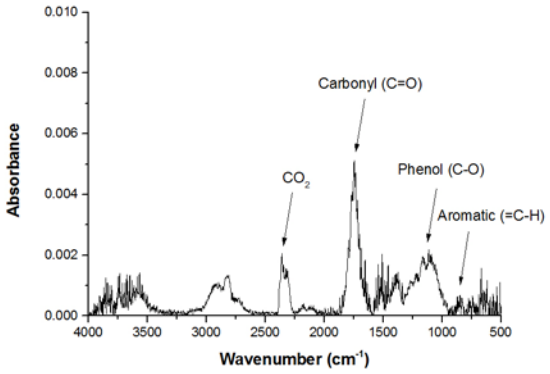


**Figure 3.** FTIR spectra for CaO to Biomass ratio of 0.5 and temperature of 350°C

different treatments, i.e. CaO:B ratios of 0, 0.5 and 1, at a temperature of 350°C. The temperature of 350°C was chosen as this was the point of peak devolatilisation as illustrated in Figure 2 as well as the point where each of the tar related peaks reached a maximum.

The area under the curve for the carbonyl, phenol and aromatic peaks for each of the different CaO to biomass ratios is presented in Figure 4. It can be seen in Figure 4 that the area under the curve for each of the three functional groups decreased with the addition of CaO to the pyrolysis process. Carbonyl group evolution reduced by 53% and 55% for CaO:B of 0.5 and 1 respectively, phenol group evolution reduced by 37% and 38% for CaO:B of 0.5 and 1 respectively and the aromatic peak area reduced by 46% and 49% for CaO:B of 0.5 and 1 respectively. The observed decreases were directly attributed to the tar cracking abilities of CaO in situ. It was also observed that peak intensity increased for lower molecular weight species such as $CO_2$, CO and $CH_4$ for the 0.5 and 1 CaO:B ratio treatments, which was again attributed to the cracking of light hydrocarbons.

It was interesting to note for the peak areas presented in Figure 4, that there was not as significant a reduction in peak area when the CaO:B ratio was increased from 0.5 to 1 in comparison to when the CaO:B ratio was increased from 0 to 0.5. At this stage it is unknown whether this was biomass specific or CaO specific. Future experiments will investigate this trend.

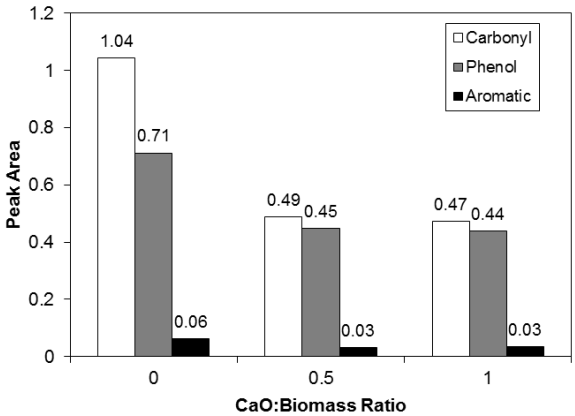


**Figure 4.** Integrated area under the curve for carbonyl, phenol and aromatic groups for different CaO:Biomass ratios

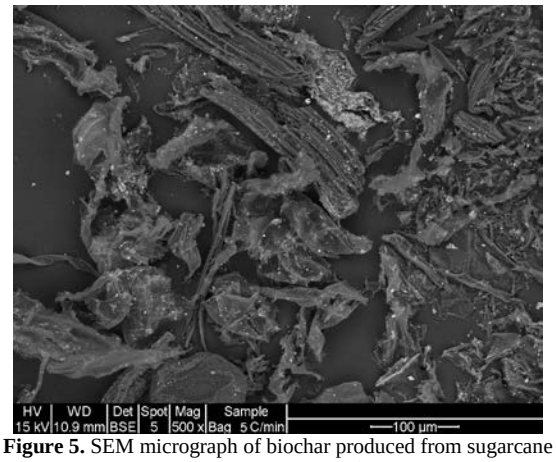


**Figure 5.** SEM micrograph of biochar produced from sugarcane bagasse in the absence of CaO.

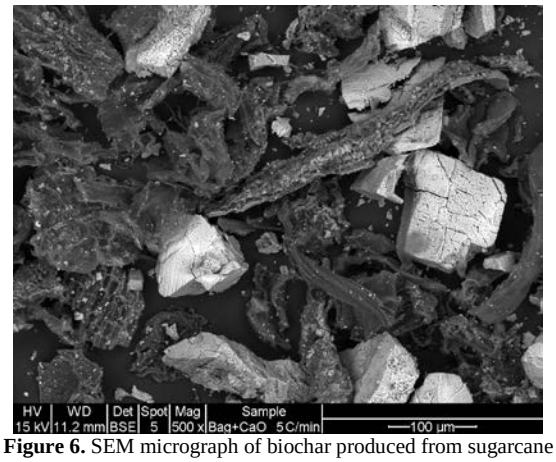


**Figure 6.** SEM micrograph of biochar produced from sugarcane bagasse and CaO in a 1 to 1 ratio.

### 3.3 Biochar morphology

At the conclusion of the pyrolysis experiment, the biochar samples produced were retained and subjected to SEM. Figure 5 and Figure 6 present SEM micrographs of the biochar produced for CaO:B ratios of 0 and 1 respectively. The back scattered electron (BSE) detector was used when performing SEM allowing for the differentiation of elements based on colour. In Figure 6, the CaO particles can be clearly seen as the white cubic particles, while in both Figure 5 and 6 the carbon rich biochar particles are seen as dark grey. Examination of the char particles in Figure 5 and 6 revealed no significant differences in particle morphology between the two treatments apart from the presence of some small CaO particles on the surface of the chars in Figure 6.

### 3.4 Implications for future biochar production

Currently, there has not been widespread adoption of biochar application at large scale farming operations, primarily due to the associated cost and scale of spreading required to gain benefits, i.e. application of 20-100 t/ha. From this preliminary study it was observed that addition of CaO to the pyrolysis of sugarcane bagasse resulted in a reduction in volatile tar components. This is significant for future biochar production as the reducing tars, reduces the hazards associated with biochar production and waste disposal. Furthermore, CaO is an important part of agricultural practices globally. CaO is commonly applied to farming soils to improve soil pH and improve crop productivity, with the incorporation of CaO into farming soil typically occurring once every 1-5 years in some case. Hence the application of a biochar rich in CaO as may be significantly more attractive to farm operators as liming requirements as well as the benefits of biochar can be achieved by the incorporation of the CaO rich biochar reducing the economic outlay and spreading time.

## 4. Conclusions

From the bench scale TGA-FTIR investigation conducted, it was concluded that addition of CaO to a biochar production process can significantly reduce the tar formation, with a CaO to biomass ratio of 0.5 resulting in 53, 37 and 46 % reduction in carbonyl, phenol and aromatic group peak areas respectively in comparison to only bagasse pyrolysis. No significant changes in biochar morphology were observed with and without CaO. Ultimately addition of CaO to the biochar production process may help reduce tar production eliminating toxic hazards as well as producing a biochar product of higher quality and use than typical biochars. Future work will expand the current investigation to include a greater variety of biomass feedstock as well as pyrolysis operating conditions, in addition the analysing the further physical and chemical properties of the biochars produced.

## 5. Acknowledgments

The authors wish to acknowledge the financial support provided by the University of Newcastle, Australia for the work presented in this paper.

## 6. References

[1] J. Lehmann; S. Joseph, in: Biochar for environmental management: science and technology, J. Lehmann; S. Joseph, (Eds.) Earthscan: Sterling, VA, 2009; pp 1-9.

[2] J. Lehmann; J. Gaunt; M. Rondon, Mitigation and Adaptation Strategies for Global Change **11** (2) (2006) pp. 395-419.

[3] M. P. McHenry, Agriculture, Ecosystems & Environment **129** (1-3) (2009) pp. 1-7.

[4] J. Major; M. Rondon; D. Molina; S. Riha; J. Lehmann, Plant Soil **333** (1-2) (2010) pp. 117-128.

[5] P. Blackwell; E. Krull; G. Butler; A. Herbert; Z. Solaiman, Soil Res. (Collingwood, Aust.) **48** (7) (2010) pp. 531-545.

[6] S. Kishimoto; G. Sugiura in: *Charcoal as a soil conditioner*, Symposium on Forest Products Research International Achievements and the Future, Pretoria, 22-26 April, 1985; CSIR Conference Centre: Pretoria, 1985; pp 12-23.

[7] K. Y. Chan; L. Van Zwieten; I. Meszaros; A. Downie; S. Joseph, Aust. J. Soil Res. **46** (5) (2008) pp. 437-444.

[8] K. Y. Chan; L. Van Zwieten; I. Meszaros; A. Downie; S. Joseph, Aust. J. Soil Res. **45** (8) (2007) pp. 629-634.

[9] Y. Chen; Y. Shinogi; M. Taira, Soil Res. (Collingwood, Aust.) **48** (7) (2010) pp. 526-530.

[10] R. T. Barnes; M. E. Gallagher; C. A. Masiello; Z. Liu; B. Dugan, PLoS One **9** (9) (2014) pp.

[11] J. M. Novak; I. Lima; B. Xing; J. W. Gaskin; C. Steiner; K. C. Das; M. Ahmedna; D. Rehrah; D. W. Watts; W. J. Busscher; H. Schomberg, Annals of Environmental Science (2009) pp. 195-206.

[12] K. Uzoma; M. Inoue; H. Andry; A. Zahoor; E. Nishihara, Journal of Food, Agriculture & Environment **9** (3&4) (2011) pp. 1137-1143.

[13] B. Smider; B. Singh, Agriculture, Ecosystems & Environment **191** (2014) pp. 99-107.

[14] R. Xu; A. Zhao; J. Yuan; J. Jiang, J. Soils Sediments **12** (4) (2012) pp. 494-502.

[15] D. Wang; R. Xiao; H. Zhang; G. He, J. Anal. Appl. Pyrolysis **89** (2) (2010) pp. 171-177.

[16] L. Han; Q. Wang; Q. Ma; C. Yu; Z. Luo; K. Cen, J. Anal. Appl. Pyrolysis **88** (2) (2010) pp. 199-206.

**Proceedings of the Australian Combustion Symposium**
**December 7-9, 2015, The University of Melbourne**

# XANES Iron K-Edge Speciation of Heat Transfer Tube Corrosion upon Victorian Brown Coal Oxy-Fuel Combustion

Iman Jabaz[1], Barbara Etschmann[2], Juan Chen[3], Koichi Suzuki[3], Yoshihiko Ninomiya[3], Lian Zhang[1,*]

[1]Department of Chemical Engineering, Monash University, Clayton, Victoria 3800, Australia
[2]School of Geosciences, Monash University, Clayton, Victoria 3800, Australia
[3]Department of Applied Chemistry, Chubu University, 1200 Matsumoto-Cho, Kasugai, Aichi, Japan

## Abstract

Oxy-fuel combustion is one of the most promising technologies for $CO_2$-capture in the energy industry. It is based on burning fossil fuels in a mixture of recirculated flue gas and high-purity oxygen, rather than in air. Ash deposits and corrosion on heat transfer tube surfaces play a critical role on coal fired boiler performance. Understanding tube corrosion mechanisms allows the deployment or retrofit of advanced tube materials for a long lifetime in an oxy-firing boiler. In this study, a variety of laboratory tests have been conducted to compare the corrosion of various tubes upon the exposure to Victorian brown coal fly ashes in both air-firing and oxy-firing conditions, at a furnace temperature of 650°C for the duration of 50 hr. The tube materials studied include carbon steel, austenitic stainless steels and commercial ferrite steels. The cross-section of the tube after exposure tests were examined using optical microscopy (OM), scanning electron microscopy (SEM) equipped with an energy dispersive x-ray (EDX) detector, and synchrotron X-ray absorption near edge spectroscopy (XANES). The observed corrosion behavior shows accelerated corrosion substantially under the oxy-fuel combustion mode, as compared to air-firing mode. The analyses confirmed the severe corrosion for SUS347and T23 under the oxy-fuel mode compared to the air-firing mode, whereas SS400 was affected slightly by flue gas composition. EXANES analysis indicates that, hematite ($Fe_2O_3$), siderite ($FeCO_3$) and augite are the major Fe-bearing species on the corroded tube surfaces. The iron speciation was also found varying greatly with the tube material. For Hazelwood fly ash tested under the oxy-fuel mode, it was confirmed that, siderite is the major Fe-bearing form on the low-Cr tube surface; magnetite ($Fe_3O_4$), hematite and augite ($(Ca,Na)(Mg,Fe,Al,Ti)(Si,Al)_2O_6$) are prevalent in middle-Cr tubes; and augite and maghemite ($Fe_2O_3$) are abundant on the high-Cr tube surface.

*Keywords: Oxy-fuel combustion, Victorian brown coal, Tube corrosion, XANES Fe K-Edge.*

## 1. Introduction

All over the world, coal is the most abundant fossil fuel [1].Based on the Key World Energy Statistics 2006 the recoverable reserves of coal are estimated approximately 120 billion tons [2]. Energy demand in the worldwide is forecast to increase about 40% by 2030. However, the electricity generated by coal is predicated to decline by 2040 [3]. The amount of coal consumed through the combustion process in power plants resulting in $CO_2$ emissions which contributes to global warming [4]. In order to reduce the $CO_2$ produced from coal-fired power plants, A variety of technologies for carbon capture and storage (CCS) have being developed in the world [5].Oxy-fuel combustion is an attractive technology for curtailing greenhouse gas emissions from coal combustion [6]. In comparison to air-firing mode, oxy-fuel mode is able to deliver a flue gas mainly consisting of $CO_2$ and $H_2O$ [7]. However, the impure components such as $SO_2/SO_3$ and HCl in the oxy-fuel flue gas are increased due to the flue gas recirculation, therefore, the tube corrosion in the heat-exchanger zone is supposedly altered [8, 9].

In this work, we presented the results for the influences of oxy-fuel combustion on the tube corrosion during Victorian brown coal combustion. Apart from two Victorian brown coal fly ashes (i.e. Hazelwood and Yallourn fly ash), three extra lignite fly ash samples were tested. A total of six different tube materials were tested as well. For each test, a tube was mounted in a fly ash sample, which was subsequently immersed in a typical oxy-firing flue gas environment for 50 hours. The temperature was maintained at 650°C throughout the test, as this temperature has been found being the worst temperature for tube corrosion in the super-heater zone in a boiler [10]. With regard to the tubes after test, each tube was quickly mounted and solidified into epoxy resin to avoid the surface oxidation in the ambient air. The cross-section was further polished and subjected to a variety of characterisation, optical microscopy (OM) to quantify the corrosion depth, scanning electron microscopy (SEM) equipped with energy dispersive x-ray (EDX) detector to reveal the microstructure of corroded layer and the concentration profile of a variety of elements of interest, and synchrotron X-ray absorption near edge spectroscopy (XANES) to quantify the speciation of iron (Fe) along the tube cross-section.

* Corresponding author:
Phone: (+61)-3- 9905-2592
Email: lian.zhang@monash .edu

### 2.1 Tube corrosion test set – up and conditions

A horizontal test furnace was used for tube corrosion test, the schematic diagram of which is shown in Figure 1. The temperature was fixed at 650°C to mimic post-combustion flue gas temperature with a range of 500-800°C, which is similar with the conditions near super-heater and re-heater in an industrial furnace. For each run, the ash sample of ~ 100 *mg* were placed on the square specimen (tube plate). The fly ash powder was spread uniformly over the plate surface using a paint brush to mimic the ash deposition on a real steam tube surface. The tube specimen was then loaded on a quartz-made sample holder and pushed to the middle zone in the furnace, as shown in panel (a). The flue gas Compositions used are shown in Table 1 to mimic the typical air-firing and oxy-firing conditions. The gas flow rate is 300 mL/min. Six tube materials were tested, including SS400, SUS304, SUS347, T23, T91, 12Cr1MoV whose properties are shown in Table 2. Furthermore, the elemental compositions of five fly ash samples used are shown in Table 3, including two Xinjiang ash (sub-bituminous coal, XJ and XJ_C), Hazelwood fly ash (HW), modified Hazelwood ash (HW_NaK) for the raw Hazelwood fly ash mixed with $Na_2SO_4$ (10 *wt%*) and $K_2SO_4$ (10 *wt%*), and Yallourn fly ash (YL). The concentration of $Na_2SO_4$ decreases in a sequence of HW < XJC < YL < XJ < HW_NaK.

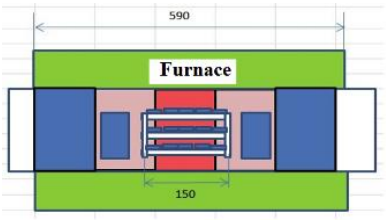

Fig. 1 Schematic diagrams of the hot corrosion furnace

Table 1 Flue gas compositions used

| Gas composition | | Air-firing | Oxy-firing |
|---|---|---|---|
| $O_2$ | [vol%] | 4.0 | 4.0 |
| $CO_2$ | [vol%] | 15.0 | Bal. |
| $SO_2$ | [ppm] | 300 | 3000 |
| HCl | [ppm] | 260 | 1000 |
| $H_2O$ | [vol%] | 8.0 | 30 |
| $N_2$ | [vol%] | Bal. | 10 |

### 2.2 Metallographic studies

The macro-structures for the cross-sections of corroded tubes were carried out on a computerized photometallurgical microscope (Olympus) to establish the thickness of scale and depth of intergranular penetration, if any in the alloys. Prior to the analysis, the corroded tube was mounted in epoxy resin, which was then cut by wire meshing to achieve its cross-section. The resulting cross-section was further polished by the use of silicon carbide paper.

Table 2 Tube materials tested in this study

| **Specimen** | **Steel grade** | **Composition** | **Cr Content, *wt%*** |
|---|---|---|---|
| SS400 | Carbon steel (JIS SS400-ASTM A283) | | |
| SUS304 | Austenite stainless steel (JIS SUS304-ASTMS30400) | 18Cr-8Ni | 18-20 |
| SUS347 | Austenite stainless steel | 18Cr-8Ni-Nb | 17-19 |
| T91 | High alloy steel | 9Cr-1Mo-V-Nb | 9 |
| T23 | Low alloy steel | 2.25Cr-1.6W-V-Nb | 2.25 |
| 12Cr1MoVG | Low alloy steel | 12Cr-1Mo-V | 0.9-1.2 |

### 2.3 Scanning electron microscopic (SEM) studies

Microstructure studies were performed using (JEOL 7001F) to identify the morphological features of corrosion product phases in the scale layers. The SEM was coupled with EDS that allows for both spot and line analysis to establish the concentration profiles of the elements of interest.

### 2.4 Synchrotron X-ray absorption spectroscopy (XAS) studies

The K-edge XANES spectra of Fe on the cross-section of tube surface were obtained from beamline BL16A1 at the National Synchrotron Radiation Research Centre (NSRRC). All spectra were normalised using ATHENA and the linear combination fitting (LCF) feature was used on the normalized sample spectra for the quantification of iron speciation.

Table 3 Elemental compositions of five fly ash samples tested in this study, *wt%*

| Ash samples | $Na_2O$ | MgO | $Al_2O_3$ | $SiO_2$ | $P_2O_5$ | $SO_3$ | $K_2O$ | CaO | $Fe_2O_3$ |
|---|---|---|---|---|---|---|---|---|---|
| XJ (Ash 1) | 10.4 | 12.46 | 8.27 | 16.24 | 0.45 | 10.58 | 0.45 | 38.82 | 0.38 |
| XJ_C (Ash 2) | 6.62 | 9.1 | 12.11 | 34.83 | 0.27 | 6.49 | 0.87 | 24.55 | 3.75 |
| HW (Ash 3) | 0.2 | 29.3 | 3.01 | 5.82 | 0.0 | 12.8 | 0.17 | 32.4 | 14.0 |
| HW_NaK (Ash 4) | 4.53 | 23.4 | 2.4 | 4.6 | 0.0 | 12.8 | 5.6 | 25.9 | 11.2 |
| YL (Ash 5) | 3.12 | 23.95 | 3.03 | 2.91 | 0.0 | 6.25 | 0.15 | 9.67 | 49.0 |

## 3. Results and Discussion

### 3.1 Structures and Microstructures for Corroded Tubes Caused by the Interaction with Hazelwood and Yallourn Fly ash

The structures for the corroded tubes upon the interaction with Hazelwood fly ash in oxy-firing mode are illustrated in Figure 2. Taking the SS400 tube as an example, it is obvious that an interface in dark brownish colour was formed, which refers to the corrosion caused for this tube material. With regard to the other tubes including 12CrMoVG, T23 and SUS347, a peeled-off layer was even observed, which sticks to the ash layer and shows in dark greyish colour. Clearly, all the tubes have been corroded significantly under the oxy-fuel case. However, the interface is unclear and even invisible for the same tubes exposed to Hazelwood fly ash in air-firing mode, as shown in Figure 3. The discrepancy between these two figures is a strong indication of the severe corrosion under the oxy-firing mode.

Statistical analysis was conducted to quantify the thickness of the corrosion interface for each tube under the oxy-fuel mode. Based on the interface depth, the corrosion rate or interface growth rate was further calculated by dividing by the exposure time, 50 hr employed in this study. The results are depicted in Figure 4. Irrespective of fly ash type, the Cr content in tube material is generally in reverse proportion to the growth rate. That is, the SUS347 tube having the highest Cr content showed the least corrosion rate which is consistent to the literature finding [8]. For the tube T23 alloyed steel with the lowest Cr content, it was found to have the highest oxide thickness that is consistent with the literature too [7]. The effect of fly ash type is marginal, given the fact that the experimental error is relatively large. The growth rate 0.2-1.2 $\mu m/h$ found here is also broadly consistent with the literature report on the tested alloy tubes with the similar Cr contents [11].

Figure.5 further illustrates the microstructure of the corroded SUS347 tube exposed to Hazelwood fly ash in the oxy-fuel mode, and its line analysis results for the distribution of the elements of interest along the cross-section of the corroded tube. Same as that has been observed by the optical microscopy, a peeled-off layer/scale was confirmed here. The line analysis demonstrates the penetration of oxygen in both the interface and peeled-off layer. Moreover, the abundance of sulphur was confirmed for these two layers too. Apparently, apart from oxygen, sulphur also played a key role under the oxy-firing mode. This is different from the air-firing mode where the penetration of oxygen into tube was only observed (data not shown).The abundance of chromium in the peeled-off scale is also interesting. Its abundance is even comparable to that of iron in this layer. The oxidation of chromium is apparently more intense than iron, which caused the peeling-off of the tube surface accordingly. Figure 6 for the elemental mapping of the corroded SUS347 further proved this hypothesis. The penetration of both oxygen and sulphur occurred on the interface. Compared to iron, chromium preferentially stayed on the top layer of the interface, indicative of its protection effect towards iron.

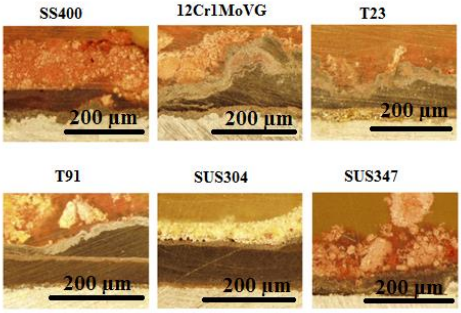


Fig.2 Structures for the cross-section of corroded tubes upon the adhesion of Hazelwood fly ash under the oxy-firing mode

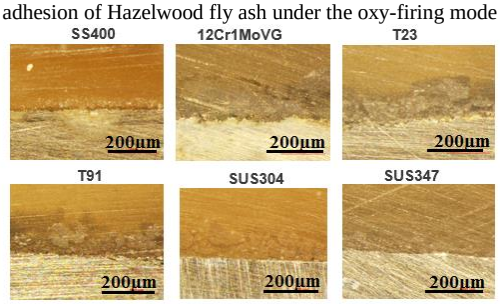


Fig.3 Structures for the cross-section of corroded tubes upon the adhesion of Hazelwood fly ash under the oxy-firing mode

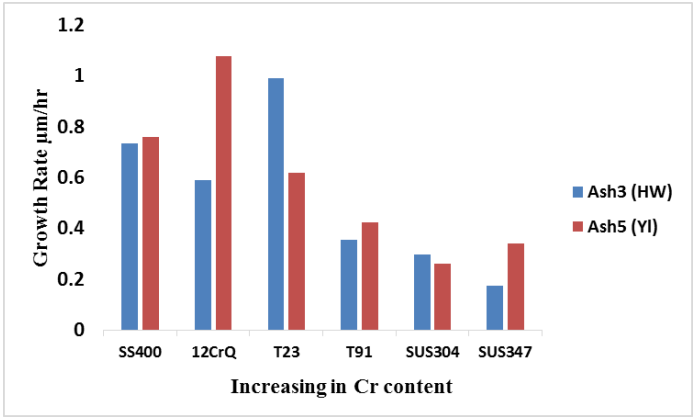


Fig.4 Growth rate of the tube specimens on exposure to Hazelwood and Yallourn ash in oxyfuel mode.

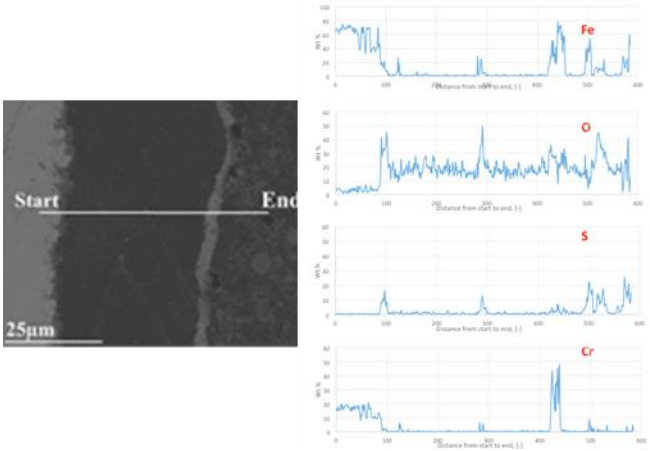

Fig.5 Line analysis of the corroded SUS347 upon the exposure to Hazelwood fly ash in oxy-firing mode

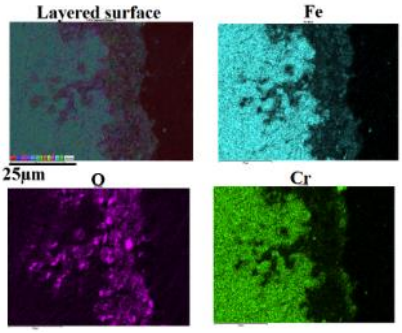


Fig.6 Elemental mapping of the corroded SUS347 upon the exposure to Hazelwood fly ash in oxy-fuel mode

### 3.2 Effect of tube material on the corrosion by Hazelwood fly ash under oxy-fuel combustion.

Figure.7 depicts the XANES spectra and fitting results for the interface zones of the six tubes exposed to Hazelwood fly ash in the oxy-firing mode. The Fe-bearing compounds on the interfacial layers of these tubes are broad. In general, the fraction of augite $(Ca,Na)(Mg,Fe,Al,Ti)(Si,Al)_2O_6$ was increased upon increasing the content of Cr in the tubes, whereas the amount of siderite ($FeCO_3$) was decreased on the tubes with elevated Cr content.

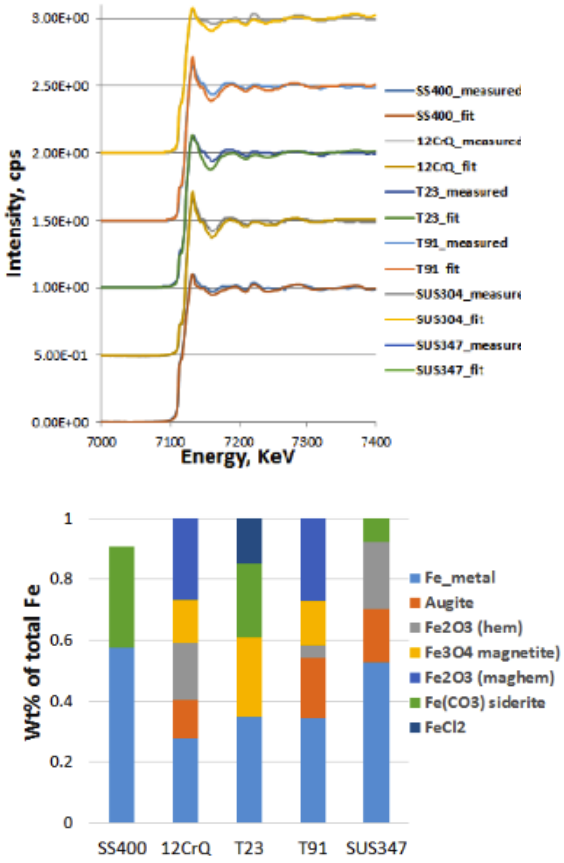


Fig.7 EXANS spectra and fitting results for the interfacial layer of tubes exposed to Hazelwo1od ash in oxy-firing mode

## 4. Conclusion

The following conclusions can be drawn from this work. Corrosion rate is around 0.2-1.0 μm/hr under oxy-fuel mode of 50 hours, decreasing with the increase on the content of Cr in tube, except T23. Penetration of oxygen is the main cause for tube corrosion in air-firing mode; whereas the penetration of both sulphur and oxygen corroded tube in the oxy-firing mode. EXANES analysis indicates that, hematite ($Fe_2O_3$) siderite ($FeCO_3$) and augite ($NaFeO_2$) are the major Fe-bearing species on the corroded tube surface.

## 5. Acknowledgments

The authors are grateful to BCIA and ANLEC who have supported this work. Appreciation is also extended to beamline scientists, in NSRRC of Taiwan for the XANES operation support.

## 6. References

[1] British Petroleum, BP statistical review of world energy, BP, London 1-49, 2011.
[2] Z. Li, X. Zhang, Y. Sugai, J. Wang, K. Sasaki, Properties and developments of combustion and gasification of coal and char in a CO 2-rich and recycled flue gases atmosphere by rapid heating, Journal of Combustion, 2012 (2012) 1-11.
[3] International Energy Agency, Key world energy statistics, OECD/IEA, Paris, France, 2007.
[4] A. Hjörnhede, M. Montgomery, M. Bjurman, P. Henderson, A. Gerhardt, J. Lecomte-Beckers, Preliminary Experiences with Materials Testing at the Oxyfuel Pilot Plant at Schwarzepumpe, Materials for Advanced Power Engineering 2010, (2010) 1220-1235.
[5] G. Stein-Brzozowska, J. Maier, G. Scheffknecht, Impact of the oxy-fuel combustion on the corrosion behavior of advanced austenitic superheater materials, Energy procedia, 4 (2011) 2035-2042.
[6] Y. Tan, E. Croiset, M.A. Douglas, K.V. Thambimuthu, Combustion characteristics of coal in a mixture of oxygen and recycled flue gas, Fuel, 85 (2006) 507-512.
[7] M. Montgomery, M. Bjurman, A. Hjørnhede, H. Rombrecht, A. Lisk, H. Krautz, High temperature corrosion investigation in an oxyfuel combustion test rig, Materials and Corrosion, 66 (2015) 257-269.
[8] R. Abang, A. Lisk, H.J. Krautz, Fireside corrosion of superheater materials under oxy-coal firing conditions, Energy Procedia, 40 (2013) 304-311.
[9] J. Maier, B. Dhungel, P. Mönckert, R. Kull, G. Scheffknecht, in: Proceedings of the 33rd international technical conference on coal utilization and fuel systems. Clearwater, Florida, 2008.
[10] K. Natesan, J. Park, Fireside and steamside corrosion of alloys for USC plants, International Journal of Hydrogen Energy, 32 (2007) 3689-3697.
[11] S. Tuurna, P. Pohjanne, P. Auerkari, Performance of superheater materials in simulated oxyfuel combustion, Research Report VTT-R-02456-11, 37(1-20), 2011.

# Chemical Looping Air Separation for Oxy-fuel Power Plants Using a Spray Dried $CuO/MgAl_2O_4$ Oxygen Carrier

H. Song, K. Shah, E. Doroodchi, A. Evans, P. Tremain, B. Moghtaderi *
Priority Research Centre for Frontier Energy Technologies & Utilisation, The Newcastle Institute for Energy and Resources
The University of Newcastle NSW 2308 Australia

## Abstract

Chemical looping air separation (CLAS) is a novel technique for acquiring high purity oxygen from ambient air, providing an efficient alternative to the commercial cryogenic distillation. As for the successful application of CLAS process, the oxygen transport media, i.e. oxygen carrier, plays a crucial role. Such a carrier may continuously fetch oxygen from air via oxidation and subsequently release it by reduction in the present of an inert environment, e.g. $CO_2$, $H_2O$ and combination of each. This study presents the redox characteristics obtained via a thermogravimetric analysis for a spray dried $CuO/MgAl_2O_4$ oxygen carrier. Various reaction mechanisms have been used herein to determine the underling behaviour of both oxidation and reduction reactions of $CuO/MgAl_2O_4$ at temperatures between 800 and 975°C. Results have shown that the oxygen release reactivity for $CuO/MgAl_2O_4$ increases as the temperature rises. Oxidation reactivity also perform a similar trend at temperatures lower than 900°C. However, at temperatures higher than 900°C, the oxidation reactivity tends to decrease with an increase in temperature. The Avrami-Erofe'ev random nucleation and subsequence growth model (*A2*) and phase boundary reaction model (*R2*) were found to achieve the best fitting for oxygen release and oxidation respectively among all investigated mechanisms. Based on the two mechanisms, the kinetic parameters were calculated as $E$ = 259 kJ/mol and $A$ = 2.79E+11 $min^{-1}$ for oxygen release, and $E$ = 59 kJ/mol, $A$ = 835 $m^{3/2}mol^{-1/2}min^{-1}$ and $E$ = -21 kJ/mol, $A$ = 0.21 $m^{3/2}mol^{-1/2}min^{-1}$ corresponding to the temperature range of 800-900°C and 925-975°C. In addition, the oxygen release level for $CuO/MgAl_2O_4$ was also investigated in a quartz packed bed reactor. The oxygen content in the outlet stream was able to attain a value very close to the equilibrium concentration.

*Keywords: Chemical looping air separation, oxygen carrier, redox characteristics.*

## 1. Introduction

With the increase of global demand for solid fossil energy, the release of polluted gases, in particular $CO_2$, has also markedly increased from 280ppm to the current level of about 400 ppm over past decades. As one of the major contributors to global warming, it has forced mankind to adopt more efficient and clean technologies for the use of solid fuels. One of the emerging technologies, i.e. oxy-fuel combustion, shows great potential for the sequestration of $CO_2$, and therefore enables the storage of $CO_2$ in the consequent steps. However, it somehow suffers from certain difficulties towards commercialization. The cost in associated with high purity oxygen is probably one of the key issues need to be solved before commercialization. Conventionally, the gaseous oxygen is generated by cryogenic air separation technique, which is believed to be a highly energy concentrated process. A more recent development named as chemical looping air separation by Moghtaderi offers a comparatively low energy consumption, i.e. 0.08 kW per standard cubic meter of oxygen product, which is only about 30% of the specific power of an advanced cryogenic air separation.[1] Such a low energy penalty for oxygen production make this technique a very attractive option for oxy-fuel power plants.

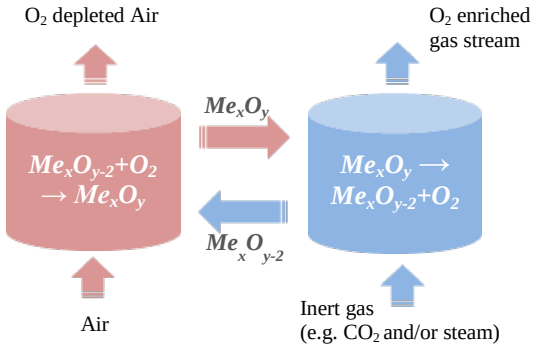


**Fig. 1.** Principle of chemical looping air separation

The CLAS process relies on the oxygen transport capability of metal oxide which need to have reasonable thermodynamic properties. Namely, it can release oxygen and subsequently be oxidized by air at relatively low temperatures. To ensure a constant oxygen stream, the oxidation and reduction processes can be carried out in two parallel reactors, i.e. oxidation reactor and reduction reactor. Meanwhile, the oxygen carrier particles are exchanged between the two reactors for continuously transporting oxygen. Figure 1 has illustrated the whole CLAS process. By using $CO_2$ and/or steam to purge reduction reactor, the metal oxide can keep releasing oxygen to build equilibrium concentration of oxygen. Higher concentration of oxygen than equilibrium level can be produced via the condensation of steam at the outlet of reduction reactor if the steam is used as purging gas. The reduced particles

* Corresponding author:
Phone: (+61) 2 40339062
Email: Behdad.Moghtaderi@newcastle.edu.au

are then transported to oxidation reactor. After regeneration, the oxidized particles will return to the reduction reactor for participating the next redox cycle.

Thus far, Cu-, Mn-, and Co-based oxides have been found to be the most viable oxygen carrier candidates for CLAS from thermodynamic point of view.[1, 2] Various oxygen carriers, such as $CuO/SiO_2$, Mn-Fe and $Co_3O_4/CoAl_2O_4$, were developed and extensively studied. [2-9] In this study, a spray dried $CuO/MgAl_2O_4$ oxygen carrier was evaluated for the use in CLAS. The spray dried technique offers uniform spherical particles, which are preferred for fluidized bed CLAS systems. The reactivity and kinetic parameters for $CuO/MgAl_2O_4$ carrier were determined by thermogravimetric analysis under conditions pertinent to CLAS. Its oxygen release property was additionally investigated in a quartz packed-bed reactor.

## 2. Experimental

### 2.1 Oxygen carrier preparation

The $CuO/MgAl_2O_4$ oxygen carrier particles were prepared via a spray dried method. The commercial CuO and $MgAl_2O_4$ powders in a weight ratio of 3:2 were mixed and milled with deionized water containing polyvinyl alcohol as organic binders and Darvan C as dispersant. The resulted suspension was continuously stirred with a propeller blade mixer, and at the same time pumped to a spray drier to form spherical particles. The raw oxygen carrier particles were then sintered at 1100°C for 24 hours. Finally, the particles in range of 106-212 um were sieved out for further investigations.

### 2.2 Apparatus

A TA-Q50 thermogravimetric analyzer was employed for investigating the redox reactivity for $CuO/MgAl_2O_4$. During test, the oxygen carrier particles about 10 mg were loaded in a platinum pan (10 mm in diameter and 2 mm in height) and heated in the furnace of TGA to temperatures in the range of 800-975$^oC$. The weight profile was monitored continuously for oxygen carrier at isothermal conditions.

A quartz packed bed reactor with 10 mm OD and 8 mm ID was used to determine the oxygen release property for $CuO/MgAl_2O_4$. About 6 g of particles were used during test. The oxygen concentration was analysed at the outlet of reactor for the isothermal tests at 800, 850, 900 and 950$^oC$ via a Varian CP-4900 Micro GC equipped with a 5A molecule sieve column.

For both TGA and packed bed experiments, air was used for oxidation and $N_2$ was used as purging gas for oxygen release. Flow rate was set at 200 ml/min for both air and $N_2$ in TGA studies. This high flow rate was chosen to minimize the diffusion effect of reaction gas on reaction rate.[8] Whereas in packed bed studies, low flow rate at 40 ml/min was selected.

In general, five cycles of redox reaction were performed for each experiment in TGA. Only the experimental data at the fifth cycle was used for analysis. The conversion of oxygen carrier for oxygen release and oxidation is calculated based on

$$\alpha_{red}=(m_{ox}-m)/(m_{ox}-m_{red}) \quad \text{for oxygen release} \quad (1)$$

$$\alpha_{ox}=(m-m_{red})/(m_{ox}-m_{red}) \quad \text{for oxidation} \quad (2)$$

here, $\alpha_{red}$ and $\alpha_{ox}$ are solid conversion for oxygen release and oxidation respectively. m, $m_{ox}$ and $m_{red}$ correspond to the instantaneous weight, fully oxidation weight and reduction weight, respectively.

## 3. Results and discussion

Fig. 2 shows the weight factions for the five redox cycles test at 850 $^oC$ for $CuO/MgAl_2O_4$. During the feed of $N_2$ purging gas, the weight fraction was continuously reduced to about 94% by releasing oxygen, which is equal to the theoretical weight loss of CuO containing in $CuO/MgAl_2O_4$. This implies that nearly all CuO were completely decomposed. With switching $N_2$ to air, the weight fraction was found to increase due to the oxidation reaction of $Cu_2O$, and attain 100% conversion at the end of each oxidation. No decline of oxygen transport capacity was noticed within 5 redux cycles.

The surface morphology for fresh and reacted particles was analyzed by a scanning electron microscopy (SEM) and has been shown in Fig. 3. As can be found in Fig. 3a, the $CuO/MgAl_2O_4$ particles exhibit a regular spherical shape. The majority of the particles were found to have a hole in the middle, which may be expected to form during the fast decomposition of organic binders and dispersant, as well as the rapid evaporation moisture during sintering process. The surface of reacted particles have not shown any obvious changes compared to that of fresh sample except for the cracks formed as shown in Fig. 3b.

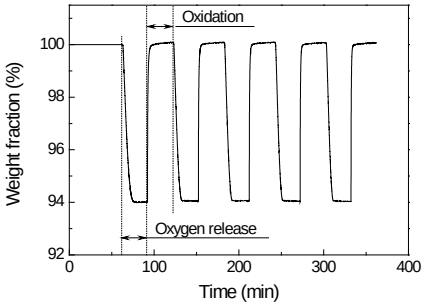


**Fig. 2.** Weight fraction of five oxygen release and oxidation cycles test for $CuO/MgAl_2O_4$ at 850$^oC$

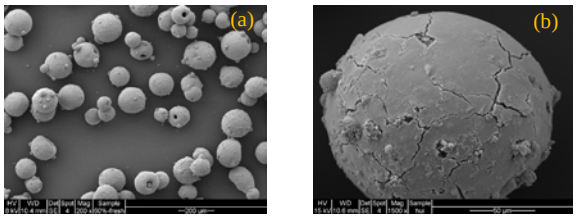


**Fig. 3.** SEM images for (a) fresh and (b) 900$^oC$ reacted $CuO/MgAl_2O_4$ particles

To derive kinetic parameters for $CuO/MgAl_2O_4$, further experiments in TGA at 800, 825, 875, 900, 950 and 975°C have been conducted. Various reaction models, e.g. diffusion mechanism, chemical reaction model, Avrami-Erofe'ev random nucleation and subsequence growth model, phase boundary reaction model and Mampel power law were applied to simulate the experimental results. The reaction model can be express as a universal equation according to

$$G(\alpha) = k\cdot(C - C_{eq})^n\cdot t \quad (3)$$

here, $G(\alpha)$ is determined by reaction mechanism and can be seen in Table 1. The Exponent $n$ is the reaction order.The value of $n$ is zero for oxygen release and 1/2 for oxidation. $t$ stands for time, $C$ and $C_{eq}$ will stand for the oxygen concentration used for oxidation and the equilibrium oxygen concentration used for cupric oxide decomposition at tested temperatures, respectively. $k$ is the reaction constant following the Arrhenius equation of

$$k = A\cdot exp\ (-E/RT) \quad (4)$$

here, A, E, R, and T are the pre-exponential factor, activation energy, gas constant and reaction temperature, respectively.

The equilibrium oxygen concentration $C_{eq}$ can be calculated based on equations (5) and (6). [5]

$$P_{O2,\,e} = exp(-\Delta G/RT) \quad (5)$$

$$\Delta G = 292+0.051\cdot T\cdot logT-0.37T\ (298K < T < 1323K) \quad (6)$$

here, $P_{O2,\,e}$ is oxygen equilibrium partial pressure, $\Delta G$ is Gibbs free energy.

It was found that Avrami-Erofe'ev random nucleation and subsequence growth model (A2) and phase boundary reaction model (R2) achieve the best fitting results among all the mechanisms for oxygen release and oxidation reactions, respectively.

Figures 4a and 4b show the Arrhenius plots determined by A2 and R2 models for oxygen release and oxidation, respectively. As informed in Fig. 4a, a very good linear fitting between oxygen release results and A2 model was obtained, attaining a $R^2$ value of 0.9965.

**Table 6.1.** Summarisation of $G(\alpha)$ equations for different reaction mechanisms

| Reaction mechanism | $G(\alpha)$ | Reaction mechanism | $G(\alpha)$ |
|---|---|---|---|
| D1 | $\alpha^2$ | A3 | $[-ln(1-\alpha)]^{1/3}$ |
| D2 | $(1-\alpha)ln((1-\alpha)+\alpha$ | R2 | $1-(1-\alpha)^{1/2}$ |
| D3 | $[1-(1-\alpha)^{1/3}]^2$ | R3 | $1-(1-\alpha)^{1/3}$ |
| D4 | $1-2\alpha/3-(1-\alpha)^{2/3}$ | P1 | $\alpha$ |
| C1 | $-ln(1-\alpha)$ | P2 | $\alpha^{1/2}$ |
| C2 | $(1-\alpha)^{-1}-1$ | P3 | $\alpha^{1/3}$ |
| A2 | $[-ln(1-\alpha)]^{1/2}$ | P4 | $\alpha^{1/4}$ |

Note: D1, one dimensional diffusion; D2, two dimensional diffusion; D3, three dimensional diffusion (Jandar function); D4, three dimensional diffusion (G-B function); C1, first order chemical reaction; C2, second order chemical reaction; An, Avrami-Erofe'ev random nucleation and subsequence growth, where n = 2 or 3; Rn, phase boundary reaction, where n = 2 or 3; Pn, Mampel power law, where n = 1, 2, 3 or 4.

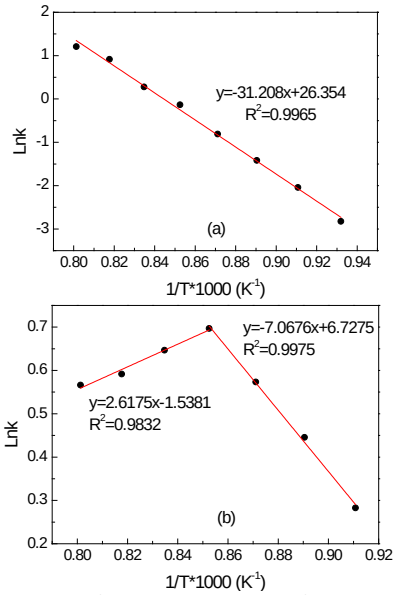


**Fig. 4.** Arrhenius plots for (a) oxygen release from Avrami-Erofe'ev random nucleation and subsequence growth model (A2) and (b) oxidation from phase boundary reaction model (R2)

The pre-exponential factor and activation energy were calculated from the slope and intercept to be 259 kJ/mol and $2.79\times10^{11}$ $min^{-1}$, respectively. Although two distinct zones, i.e. 825-900 and 925-975°C, were observed for oxidation reaction, the fitting results also indicate good fittings between oxidation and R2 in both zones. Corresponding to the slopes and intercepts for the two temperature zones in Fig. 4b, the oxidation activation energy E and pre-exponential factor A were determined as 59 kJ/mol and 835 $m^{3/2}mol^{-1/2}min^{-1}$ for the temperature range of 825-900°C and -21 kJ/mol and 0.21 $m^{3/2}mol^{-1/2}min^{-1}$ for the temperature range of 925-975°C, respectively.

The observed two temperature zones can be explained to the fact that the diffusional effect caused by the thermodynamic properties of CuO may be more intense at lower temperatures compared to the higher temperatures. According to the calculations from equations (5) and (6), the equilibrium oxygen partial pressure will increase from a very low value of 0.11 to 7.19% (i.e., ~65 times higher) as the temperature increases from 800 to 975°C. For reduction, the equilibrium oxygen pressure can be more readily reached at low temperatures compared to that under high temperatures. Although the gas flow rate is selected as high as possible for the experiments to reduce the diffusion effect, the equilibrium pressure can still be attained at the boundaries surrounding the unreacted grains inside the $CuO/MgAl_2O_4$ particles. Once the equilibrium is reached, the reduction rate will be significantly reduced because of the transportation difficulties for the produced oxygen, viz., diffusion effect. However, such a diffusion effect can be expected to decrease with an increasing temperature because of the increase in the equilibrium oxygen partial pressure. Therefore, the decrease in activation energy (i.e., 176 kJ/mol) at temperatures higher than 900°C should be the result of combined effects of diffusion/equilibrium oxygen partial pressure and structural transformations.

Figures 5 and 6 illustrate the fitting results for oxygen release and oxidation reactions using A2 and R2 models, respectively, based on above determined kinetic parameters. The simulations as performed for oxygen release at the temperature range of 825-975°C fit the oxygen release experimental data nearly in a full conversion range, i.e. 0-1 (See Fig. 5). As for oxidation, only the conversion range of 0-0.8 was well fitted for experimental data at the high temperature range, viz. 900-975°C (See Fig. 6b), while a narrower conversion range was fitted for those data obtained at low temperatures in the range of 825-900°C. However, in a realistic reactor, full conversion for solids generally cannot attained. [9] Such fitting results will be qualified for predicting the reaction in a real reactor system.

Apart from above kinetic analysis, the oxygen release property was also analyzed by employing a packed-bed reactor. Fig.7 has listed the oxygen profile as measured at the outlet of packed-bed reactor. The oxygen concentration in the product stream was found to be 0.25, 0.60, 1.67, and 4.81% corresponding to the temperatures of 800, 850, 900 and 950°C, which are in good agreement with the equilibrium concentrations of 0.12, 0.46, 1.5 and 4.53%, respectively, for the pure $CuO/Cu_2O$ system.

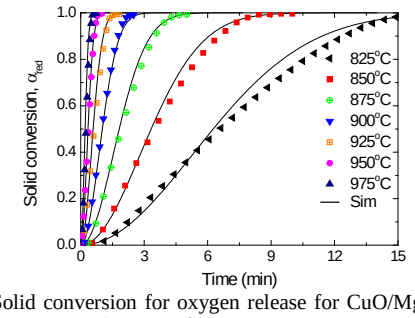


**Fig. 5.** Solid conversion for oxygen release for $CuO/MgAl_2O_4$ at the temperature range of 825-975°C. Symbols represent the experimental results and the solid lines denote the simulation of A2 model.

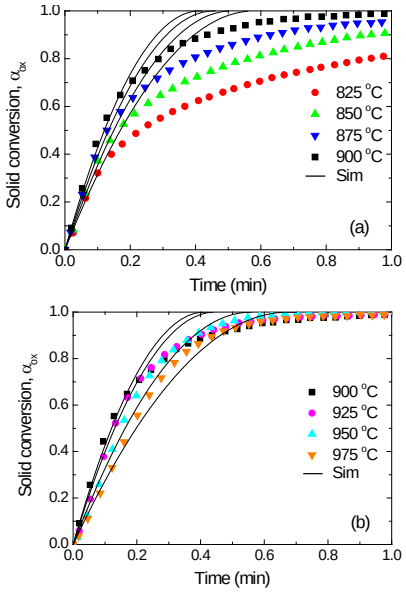


**Fig. 6.** Solid conversion for oxidation obtained for $CuO/MgAl_2O_4$ at the temperature range of (a) 825-900°C and (b) 900-975°C. Symbols represent the experimental results and the solid lines denote the simulation of R2.

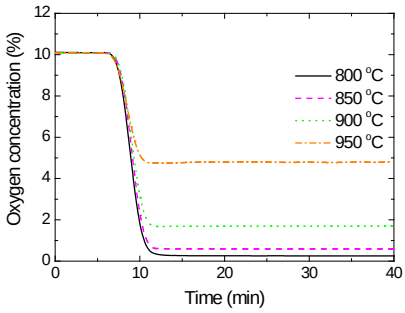


**Fig. 7.** Oxygen release profile for $CuO/MgAl_2O_4$ at temperatures of 800, 850, 900 and 950°C in packed-bed reactor

## 3. Conclusion

The use of spray dried $CuO/MgAl_2O_4$ oxygen carrier was evaluated under conditions pertinent to chemical looping air separation. Both kinetic parameters and oxygen release property were analyzed by using thermogravimetric analysis and packed bed reactor. Results show that Avrami-Erofe'ev random nucleation and subsequence growth model (A2) and phase boundary reaction model (R2) are the best mechanisms among all employed models for predicting the oxygen release and oxidation for $CuO/MgAl_2O_4$, respectively. In addition, the oxygen concentration during oxygen release process for $CuO/MgAl_2O_4$ can attain the level close to equilibrium value for all investigated temperatures.

## 4. Acknowledgments

Authors gratefully acknowledge the financial support provided by Australian National Low Emissions Coal Research & Development.

## 5. References

[1] B. Moghtaderi, Energy & Fuels. **24** (2010), pp. 190-198.

[2] H. Song, K. Shah, D. Elham, T, Wall and B. Moghtaderi, Energy & Fuels. **28** (2014), pp. 1284-1294.

[3] G. Azimi, H. Leion, T. Mattisson and A. Lyngfelt, Energy Procedia. **4** (2011), pp 370-377.

[4] Z.S. Li, T. Zhang, and N.S. Cai, Ind & Eng Chem Res. **47** (2008), pp. 7147-7153.

[5] H. Song, PhD. Thesis (2015), the University of Newcastle, Australia, pp. 1-275.

[6] H. Song, K. Shah, D. Elham and B. Moghtaderi, Energy & Fuels. **28** (2013), pp. 163-172.

[7] H. Song, K. Shah, D. Elham, T, Wall and B. Moghtaderi, 2nd International Conference on Chemical Looping (2012), 26-28, Sep. Darmstadt, German, pp. 1-9.

[8] H. Song, K. Shah, D. Elham, T, Wall and B. Moghtaderi, Energy & Fuels. **28** (2013), pp. 173-182.

[9] B. Moghtaderi and H. Song, Energy & Fuels. **24** (2010), pp 5359-5368

**Proceedings of the Australian Combustion Symposium**
**December 7-9, 2015, The University of Melbourne**

# Effect of Methane and coal dust Concentrations on Explosion Pressure Rise

Mohammed Jabbar Ajrash, Jafar Zanganeh , Daniel Eschebach, Sazal Kundu and Behdad Moghtaderi*

The Frontier Energy Technologies Centre, Chemical Engineering,
School of Engineering, Faculty of Engineering & Built Environment,
The University of Newcastle, Callaghan, NSW 2308, Australia

## Abstract

Explosion pressure rate rise (dp/dt) experiments for coal dust and methane-coal dust-air hybrid mixtures in a modified 20 L explosion apparatus were conducted to provide data on explosion characteristics in Ventilation Air Methane (VAM) systems. Coal dust concentrations of 10, 25, 50 and 100 $g.m^{-3}$; methane concentrations of 0.75, 1.25, 2.5 and 5%; and initial ignitor energies of 1, 5 and 10 kJ were investigated. The dp/dt of dilute coal dust-methane-air hybrid mixtures were strongly affected by the ignitor energy. The potential of higher energy boosting the fuel combustion from the flammable to the explosion phase was demonstrated. There was no observed influence on dp/dt at 10 $g.m^{-3}$ coal dust concentration. In contrast, 25 $g.m^{-3}$ of coal dust concertation had significant influence on the dp/dt for methane-coal dust-air hybrid mixtures

***Keywords***: *Explosion pressure rate, Hybrid mixture, Initial ignition energy, VAM safety, ASTM E2021.*

## 1. Introduction

Hybrid mixture is all important for safety in the mining industry. The characteristics of coal dust explosions have been studied since the 1930s in the US Bureau Institute of Mines by developing the Hartman apparatus (ASTM E2019, 1.2 Liter, electrical ignition source). Coward noticed that flammable clouds enhanced the explosion characteristics of combustible dust cloud particles [1].

By using the Hartman apparatus, many researchers have investigated the explosions characteristics of hybrid mixtures. A number of limitations were identified with the use of the Hartman apparatus. For instance, dust dispersion inside the vessel was not uniform [2], and there was a significant difference in the pressure measurement Cashdollar (1985) compared the 20 L and 1 $m^3$ apparatus results, finding good agreement between pressure rate (dp/dt), Minimum Explosion Concentration (MEC) and deflagration index ($K_{st}$). Moreover, higher energy did boost the fuel combustion from flammability to explosion phase. a Consequently, the 20 L apparatus is currently the accepted standard for primary testing before large scale tests [3]. Hertzberg 1988 , Cashdollar 2012 and Niansheng 2013 included in their studies the effects of ignitor energy on the characteristics of coal dust using a 20 L apparatus; Specifically, $P_{max}$ (maximum pressure rise) and $K_{st}$ (deflagration index). They concluded there is an influence of the ignitor's energy on the $P_{max}$, $K_{st}$ and MEC [4,5]. In ventilation air-methane systems, the coal dust cloud is not the only hazardous material. The other concern is the presence of methane gas with coal dust, with may produce a more explosive mixture. Torrent 1989, investigated the effects of methane on coal dust cloud hybrid mixtures. They proved that presence of methane increase the risk of coal dust cloud explosions [6]. Despite the many studies in the field of coal dust cloud explosions, there is little information available regarding the effects of dilute methane, typically found in ventilation air methane, on coal dust cloud explosions. This study was therefore aimed at investigating the effects of dilute methane concentrations that may be present in VAM capture ducts on the characteristics of coal dust cloud explosions. To achieve these goals, a comprehensive set of experiments were conducted. The pressure rise rate (dp/dt) for a wide range of ignitor energies were determined for coal dust and methane/coal dust/air hybrid mixtures.

## 2. Methodology and definitions

A modified 20 L dust explosion apparatus located at the University Of Newcastle, Australia; was employed to investigate the explosion characteristics of hybrid mixtures as shown in Figure 1. The methane line connected to the 20 L apparatus was modified to allow methane addition, to mitigate the effects of an explosion of methane mixed with coal dust. The mitigation system consists of a methane bottle, stainless steel pipe, plug valve, needle valve, flash-back arrestor and check valve.

* Corresponding author:
Phone: (+61) 2 4033 9335
Email: behdad.moghtaderi@newcastle.edu.au

**Figure 1: 20 L dust explosion apparatus**

The coal dust used was obtained from a coal mine located in NSW, Australia. The sample was transported to the laboratory in an air-sealed package and stored in cool conditions to reduce any further oxidation. Representative sub-samples were dispatched to third party laboratories for proximate analyses. The results are shown in Table 1.

**Table 1: Proximate analysis**

| Carbon % | Moisture% | Ash% | Volatile Matter% |
|---|---|---|---|
| 56 | 1.1 | 10.3 | 31.7 |

All experiments were carried out to the ASTM E1226[7] standard. Three different energy chemical ignitors were used (1, 5 and 10 kJ), and instrument air was used to prevent addition of impurities and moisture found in plant air. The coal dust is dispersed in the vessel by triggering a remote control unit. The ignitors are energized 88 ms after the dispersion process (as shown in Fig.3). The parameters were measured and calculated according to the ASTM 1226[8] standard. Each test was repeated three times to ensure reproducibility of the tests. The standard deviation of the pressure transducer measurement was less than 5%.

## 3. Results and Discussion

### 3.1 Coal dust over pressure explosions

As mentioned previously, the concentration of coal dust in the VAM capture duct is low. Thus dilute concentrations of coal dust cloud (Mine B sample) were used for this study (10, 25, 50 and 100 g.m$^3$). A plot of pressure rise rate (dp/dt) vs coal dust concentrations for the three ignition energies (1, 5 and 10 kJ) are shown in Fig. 2.

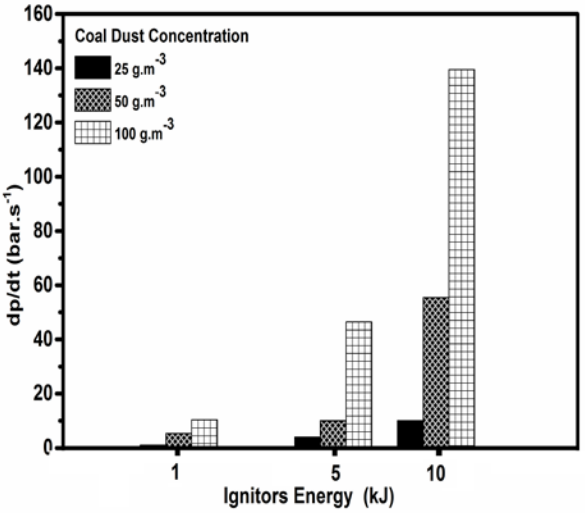


**Figure 2 Pressure rise rate (dp/dt) for 25, 50 and 100 g.m$^{-3}$ coal dust concentrations with 1, 5 and 10 kJ chemical ignitor energies**

For 10 g.m$^{-3}$, dp/dt values recorded were equal to the initial chemical ignitor dp/dt. It has been noted that the initial ignition energy has an effect on dp/dt (see Figure 2). For a coal dust concentration of 25 g.m$^{-3}$ and 50 g.m$^{-3}$, the dp/dt increased ten-fold as the initial ignition source was increased from 1 to 10 kJ. For a 100 g.m$^{-3}$ coal dust concentration, the dp/dt increased by fifteen-fold as the initial ignition source was increased from 1 to 10 kJ. To sum up, at low coal dust concentration, the initial ignition energy is an important factor.

### 3.2 Methane influence

In VAM capture ducts, methane gas presents an additional hazard to the coal dust cloud. In this work, the influence of methane on dp/dt of methane coal dust is investigated. The influence of methane concentration on the dp/dt for 10 g.m$^{-3}$ coal dust concentration is shown in Fig. 3.

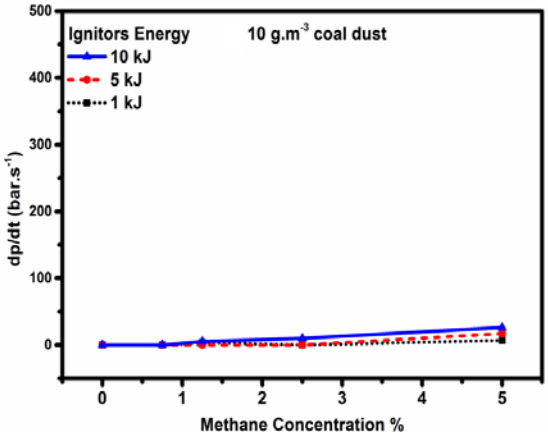


**Figure 3: Pressure rate rise (dp/dt) of 10 g.m$^{-3}$ coal dust mixed with methane with 1,5 and 10 kJ intial ignition energy ignitors**

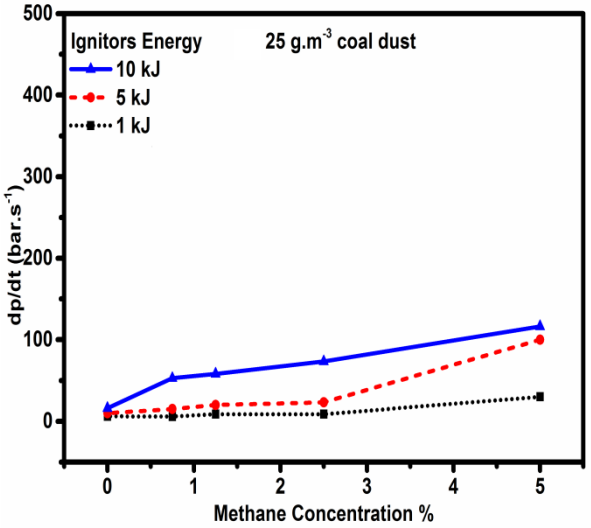


**Figure 4: Pressure rate rise (dp/dt) of 25 g.m-3 coal dust mixed with methane with 1,5 and 10 kJ intial ignition energy ignitors**

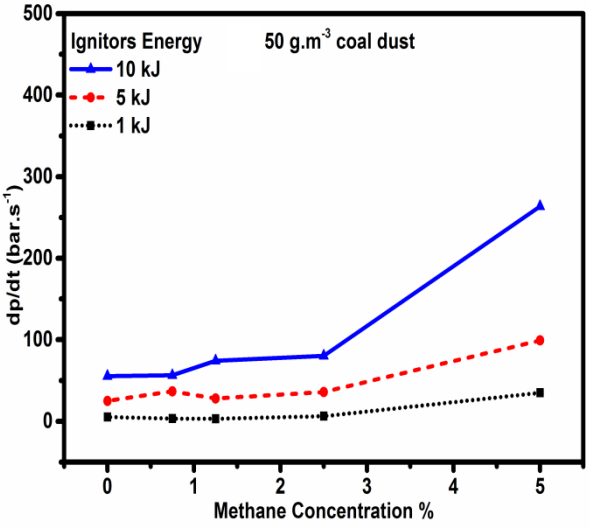


**Figure 5:Pressure rate rise (dp/dt) of 50 g.m$^{-3}$ coal dust mixed with methane for 1,5 and 10 kJ intial ignition energy ignitors**

The results show no significant change in dp/dt at 10 g.m$^{-3}$ concentration of coal dust. A slight rise at 5% methane is due to the methane concertation being in the flammable rage. These indicate that there is no explosion in coal dust methane mixture had taken place at previous fuel composition.

The influence of methane on dp/dt values at 25 g.m$^{-3}$ coal dust concentrations is shown in Figure 4

At 25 g.m$^{-3}$ coal dust concentration, the enhanced influence of methane gas on dp/dt is obvious compared to results at 10 g.m$^{-3}$ coal dust concentrations. This is due to the fact the Minimum Auto Ignition Concentration (MAIC) of a coal dust clouds is 15 g.m$^{-3}$, as reported in a study using similar coal dust samples. By using 10 kJ initial ignition source, only 0.75% of methane caused the dp/dt to rise from about 5 bar.s$^{-1}$ to 60 bar.s$^{-1}$. The dp/dt increased gradually until reaching 110 bar.s$^{-1}$. At 5 kJ initial ignition energy, an increasing dp/dt rate is observed for 5% methane concentration.

The dp/dt rose from 15 bar.s$^{-1}$ to 100 bar.s$^{-1}$ and could be related to a change in fuel combustion from the flammable to explosion phase. The effect of the lowest methane concentration (0.75%) on dp/dt values is clearly observed at 10 kJ ignitor energy but not for 1 and 5 kJ. The 1 kJ initial ignition lines, Fig 3 and Figure 4, the influence of methane on dp/dt is not obvious, even when a 5% of methane concentration is added to the mixture. By using 5 kJ ignition source, 5% concentration of methane tripled the value of dp/dt from 30 bar.s$^{-1}$ to 95 bar.s$^{-1}$. By using 1 kJ initial ignition energy, no significant increase in dp/dt was recorded, and the values were quite similar to the behavior observed in Fig. 3.

The influence of methane on the dp/dt values of 50 g.m$^{-3}$ coal dust concentrations is shown in Fig. 5.

At 50 g.m$^{-3}$ coal dust concentration and 10 kJ initial ignition source, the dp/dt shows significant rise in all methane concentrations. The dp/dt increased about three-fold when 5% concentration of methane was added as compared to 2.5% concentration of methane. At an initial ignition energy source of 5 kJ, A similarly large increase in dp/dt was observed at 5% methane concentration for 25 g.m$^{-3}$ coal dust concentrations, Figure 4, as compared to 50 g.m$^{-3}$, Fig 5. For 1 kJ initial ignition energy source, the dp/dt did not increase above the initial ignitor energy below 5% methane concentration. At 5% methane concentration and 50 g.m$^{-3}$ coal dust concentration, the dp/dt reached 30 bar.s$^{-1}$. When the coal dust concentration was decreased to 25g.m$^{-3}$, the dp/dt decreased to 20 bar.s$^{-1}$. Finally, the span between dp/dt values for 5 kJ and 10 kJ energy ignitors significantly increased when 5% concentration of methane was added with the coal dust. The influence of methane on the dp/dt values of 100 g.m$^{-3}$ coal dust concentrations is shown in Fig. 6.

For 100 g.m$^{-3}$ coal dust concentration, the results show the span between dp/dt values for 10 kJ and 5kJ initial ignition energy increased for all methane concentrations, including 0%. This is due to the fact that explosion severities are much higher for coal dust concentrations of 100 g.m$^{-3}$ than for 50 g.m$^{-3}$, in agreement with Cashdollar et al.

By using 1 kJ initial ignition source, the dp/dt is more sensitive for methane when only 1.25% of methane concentration added. This point indicates the phase of combustion change from flammable to explosion

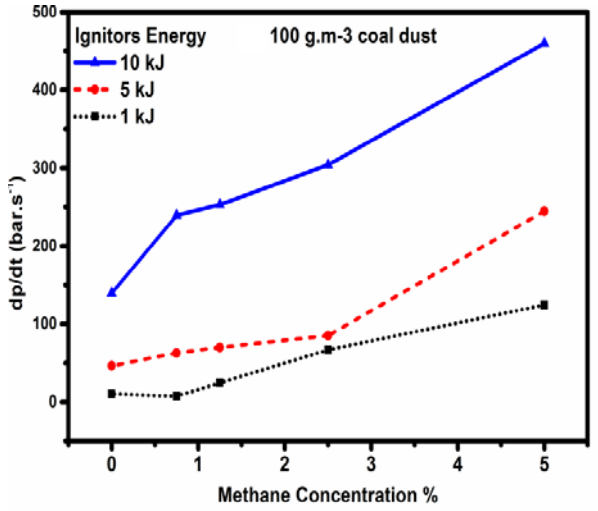


**Figure 6: Pressure rise rate (dp/dt) of 100 g.m$^{-3}$ coal dust mixed with methane for 1, 5 and 10 kJ intial ignition energy ignitors**

From all the above, dp/dt rise was observed according to four combustion phases: (i) the ignitors' energy explosion; (ii) fuel combustion during the flame ignitors' explosion traveling in the vessel; (iii) flammable mixture; and (iv) the explosion. For 10 g.m$^{-3}$ coal dust concentrations, the dp/dt recorded was due to the ignitors' explosion and fuel combustion during the flame traveling from ignitors (phase one and two). For 25 g.m$^{-3}$ coal dust concentrations, in addition to phase 1 and 2, phase 3 was also observed. For 50 and 100 g.m$^{-3}$ coal dust concentrations, all phases had been observed due to sufficient fuel, initial ignition energy and oxygen.

## 4. Conclusion

It has been found that a dilute percentage of methane influenced the dp/dt of dilute coal dust concentrations, for instance 0.75% methane concentration doubled the dp/dt of a 100 g.m$^{-3}$ coal dust-air mixture for a 10 kJ initial ignition source. The Initial ignition energy plays an important role of determining the dp/dt, especially for dilute methane-coal dust-air hybrid mixture explosions. The influence of 0.75% methane concentration was more obvious at higher concentrations of coal dust and /or when there was a high ignition source. There was no influence of 10 g.m$^{-3}$ of coal dust concentrations on the dp/dt. In contrast, a concentration of 25 g.m$^{-3}$ coal dust had significant influence of the dp/dt of methane-coal dust-air mixtures.

5. Acknowledgement

The authors wish to acknowledge the financial support provided to them by Australian Coal Association and Low Emission Technology (ACALET), Australian Department of Industry and the University of Newcastle (Australia). In addition, special gratitude is given to the Higher Committee for Education Development (HCED) and Midland Refineries Company (MRC) from the Iraqi government for sponsoring a postgraduate candidate working in this project.

## 6. References

[1] H.F. Coward, G.. Jones, Limits of Flammability of Gases and Vapors, . U.S. Bur. Mines, , US Gov. Print. Off. (1952).

[2] L.A. Eggleston, A.J. Pryor, The limits of dust explosibility, Fire Technol. 3 (1967) 77–89.

[3] K.L. Cashdollar, M. Hertzberg, 20-L Explosibility Test Chamber for Dusts and Gases, Rev. Sci. Instrum. 56 (1985) 596. doi:10.1063/1.1138295.

[4] M. Hertzberg, K.L. Cashdollar, I. a. Zlochower, Flammability limit measurements for dusts and gases: Ignition energy requirements and pressure dependences, Symp. Combust. 21 (1988) 303–313. doi:10.1016/S0082-0784(88)80258-3.

[5] N. Kuai, W. Huang, B. Du, J. Yuan, Z. Li, Y. Gan, et al., Journal of Loss Prevention in the Process Industries Experiment-based investigations on the effect of ignition energy on dust explosion behaviors, J. Loss Prev. Process Ind. 26 (2013) 869–877. doi:10.1016/j.jlp.2013.03.005.

[6] J.G. Torrent, J.C. Fuchs, Flammability and explosion propagation of methane/coal dust hybrid mixtures, in: 23 Int. Conf. SMRI, 1989.

[7] W. Conshohocken, Standard Test Method for Minimum Explosible Concentration of Combustible Dusts, Am. Soc. Test. Mater. (2014) 1–9.

[8] ASTM Standard, Test Method for Explosibility of Dust Clouds 1, (2014). doi:10.1520/E1226-12A.

# Carbonation Reaction Kinetics at Low Partial Pressures of $CO_2$ for a Novel Greenhouse Calcium Looping Combustion Process

M. Ramezani[1], K. Shah[1], E. Doroodchi[1], P. Tremain[1] and B. Moghtaderi[1*]

[1] The Priority Research Centre for Frontier Energy Technologies & Utilisation, Chemical Engineering, School of Engineering, Faculty of Engineering and Built Environment, The University of Newcastle, Callaghan, New South Wales 2308, Australia

## Abstract

The kinetic parameters for the carbonation reaction of a limestone sorbent were determined under the unique conditions of a greenhouse calcium looping (GCL) process. Considering a wide range of reaction mechanisms and Arrhenius plots, the carbonation reaction kinetics were determined over low $CO_2$ partial pressure ranges from 500 to 1000 ppm (0.05-0.1%) and a temperature range of 400 to 500 $^oC$. The reaction order was found to be close to first order and increased with increasing temperature, while the activation energy was 19.47 kJ $mol^{-1}$.

*Keywords: Carbonation reaction, kinetic parameters, Calcium Looping Processes, Reaction mechanism, Arrhenius Plot.*

## 1. Introduction

Food production in greenhouses has become an important source of sustainable food supplies for millions of people worldwide [1]. In Australia, the greenhouse horticulture industry produces about 20% of the value of total vegetable and cut flower production [1]. Similar to other countries, Australian greenhouse growers face challenges such as high energy use, fertiliser requirements, $CO_2$ emissions/management and labour costs all of which have a significant impact on their industry's growth. Vegetable greenhouses need heat, light and carbon dioxide ($CO_2$) to provide an appropriate environment to enhance crop productivity [2]. The current study proposes a novel Greenhouse Calcium Looping (GCL) process to provide heat and carbon dioxide ($CO_2$) enrichment in greenhouses currently being developed at the University of Newcastle in conjunction with a suite of other chemical/calcium looping processes [3, 4].

The GCL process is based on the carbonation/calcination cycle of limestone ($CaCO_3$), providing heat and $CO_2$ enrichment through two steps ($\Delta H_{r,\,298k}$ values were determined using HSC Chemistry 6 software):

1. The carbonation reaction takes place during the night (night half-cycle) where calcium oxide (CaO) undergoes an exothermic carbonation reaction (1) as a result of contact with $CO_2$ emitted from growing plants.

Carbonation (Exothermic)

$$CaO + CO_2 \rightarrow CaCO_3 \qquad \Delta H_{r,298K} = -178.175\, {kJ}/{mol} \qquad (1)$$

2. The calcination reaction takes place during the day (day half-cycle) where the calcium carbonate ($CaCO_3$), formed in the night half-cycle, is calcined (2) by combusting small quantities of a hydrocarbon fuel.

Calcination (Endothermic)

$$CaCO_3 \rightarrow CaO + CO_2 \qquad \Delta H_{r,298K} = 178.175\, {kJ}/{mol} \qquad (2)$$

The main product from the carbonation reaction (1) is heat which can be used locally to provide the appropriate temperature in greenhouses during night especially in cold or mild climate zones. The produced heat can also be transferred to a waste heat recovery unit for power generation (e.g. an organic Rankine cycle unit). In comparison, through the calcination reaction (2), $CO_2$ is produced during day which may be used to aid photosynthetic processes as $CO_2$ enrichment in the range of 800-1800 ppm can boost plant growth by up to 40% [5].

In our previous work [4], the thermodynamic feasibility of the GCL process was investigated considering an RGibbs unit operation in ASPEN Plus. The RGibbs block simulates the reaction based on the minimization of Gibbs free energy and predicts the thermodynamic equilibrium of reactants and products at given process conditions, without needing the reactions' stoichiometry kinetics. However, to predict the required reactor size using the RPlug unit operation in ASPEN Plus, the stoichiometry and kinetic parameters of the reaction are paramount. In our previous publication [4] it was reported that the energy required for the GCL process can be supplied by natural gas, biomass or solar energy. It is also possible to use coal to provide the required energy for the calcination reaction.

Sun et al. [6] determined the intrinsic kinetic parameters of the carbonation reaction in a range of $CO_2$ partial pressures from 6 % to 100%. A grain size model was used to determine the carbonation rate constants of two sorbents namely Strassburg limestone and Arctic dolomite. Their activation energy were reported to be near each other valued at 29±4 kJ $mol^{-1}$ and 24±6 kJ $mol^{-1}$, respectively. The reaction rate was concluded to change from first order to zero order when the $CO_2$ partial pressure increased above 10%.

Most of the literature has focused on determining the carbonation/calcination reaction rate at higher $CO_2$ partial pressures [7, 8]. However, in the GCL process, calcium looping is performed under lower $CO_2$ levels

* Corresponding author:
Phone: (+61) 2 40339062
Email: Behdad.Moghtaderi@newcastle.edu.au

(less than 0.2%) for which the kinetics of carbonation/calcination reactions may be different in comparison to those of higher $CO_2$ concentrations. Thus, establishing the kinetic parameters of the carbonation/calcination reactions for low $CO_2$ partial pressures is required. The aim of this research was to determine the kinetic parameters of the carbonation reaction at $CO_2$ partial pressures of less than 0.1% (1000 ppm).

## 2. Experimental

All experiments were carried out in a Q50 thermo-gravimetric analyser (TGA) where 2 mg of limestone sorbent, provided by a local supplier, were inserted into a platinum crucible. The limestone particle size was 75 to 150 µm. To remove impurities, the sample was initially heated to 700 $^oC$ at a 20 $^oC$ $min^{-1}$ ramp rate and held isothermally for 10 minutes. Industrial grade $CO_2$ diluted in air at a concentration of 2000 ppm, supplied by Coregas Co., was then introduced to the TGA by a mass flow controller (MFC). The carbonation reaction experiments were performed in a temperature range of 400 to 500 $^oC$ and $CO_2$ partial pressures of 0.05 to 0.1% (500 to 2000 ppm). The total flow rate of gases was set at 100 ml $min^{-1}$ at atmospheric pressure inside the TGA. All experiments were repeated 3 times to obtain reliable data.

Table 1 details the entire TGA experimental method. After calcination at 700 $^oC$ in 100 ml $min^{-1}$ of air, the gas was switched to 50 ml $min^{-1}$ $CO_2$ at 2000ppm concentration and 50 ml $min^{-1}$ air while the temperature was reduced to 450 $^oC$, at 20 $^oC$ $min^{-1}$, at which the carbonation reaction occurred. The air flow rate was selected based on diluting 2000ppm $CO_2$ to the required $CO_2$ level in the TGA, which in this case was 1000 ppm. The system was held isothermally for 120 minutes in which data was recorded every millisecond. External mass transfer resistance due to the formation of gas films around the particles was minimised by conducting the experiments at a high flow rate of 100 ml $min^{-1}$.

## 3. Reaction Mechanism Description

The conversion of CaO particles via the carbonation reaction was calculated on a molar basis through following equation:

$$x = \frac{\frac{m_{CaO}(t) - m_{CaO}(0)}{44}}{\frac{m_{CaO}(0)}{56}} \tag{3}$$

Table 1. Details of carbonation reaction study in TGA at 450 $^oC$, $CO_2$ partial pressure of 0.1% (1000 ppm) and total flow rate of 100 ml $min^{-1}$.

| Step | Method |
|---|---|
| 1 | Air at flowrate of 100 ml $min^{-1}$ |
| 2 | Ramp temperature at 20 $^oC$ $min^{-1}$ to 700 $^oC$ |
| 3 | Isothermal for 10 mins |
| 4 | Jump to 450 $^oC$ |
| 5 | Air at flowrate of 50 ml $min^{-1}$ |
| 6 | 2000 ppm $CO_2$ at flowrate of 50 ml $min^{-1}$ |
| 7 | Isothermal for 120 mins |
| 8 | Equilibrate at 40 $^oC$ |
| 9 | Mark end of cycle |

Table 2. *G(x)* functions for different reaction mechanisms.

| Reaction mechanism | $G(x)$ |
|---|---|
| D1 | $x^2$ |
| D2 | $(1-x)\ln(1-x)+x$ |
| D3 | $\left[1-(1-x)^{\frac{1}{3}}\right]^2$ |
| D4 | $\left[1-(1-x)^{\frac{1}{3}}\right]^2$ |
| C1 | $-\ln(1-x)$ |
| C2 | $(1-x)^{-1}-1$ |
| A2 | $[-\ln(1-x)]^{\frac{1}{2}}$ |
| A3 | $[-\ln(1-x)]^{\frac{1}{3}}$ |
| R2 | $1-(1-x)^{\frac{1}{2}}$ |
| R3 | $1-(1-x)^{\frac{1}{3}}$ |
| P1 | $x$ |
| P2 | $x^{\frac{1}{2}}$ |
| P3 | $x^{\frac{1}{3}}$ |

Where $x$ is CaO conversion, $m_{CaO}$ $(t)$ is the weight of sample at time $t$ and $m_{CaO}$ (0) is initial sample weight. 44 and 56 are the molecular weights of $CO_2$ and CaO, respectively.

The general equation for a gas-solid reaction is a function of equilibrium gas pressure ($P_{CO_2,eq}$), temperature and reaction mechanism as follows [9]:

$$\frac{dx}{dt} = kf(x)\left(P_{CO_2} - P_{CO_2,eq}\right)^n \tag{4}$$

Where $t$ is time, $n$ is the reaction order, $f(x)$ represents a function for the reaction mechanism and $k$ is the reaction rate constant following the Arrhenius-type equation:

$$k = k_0 \exp\left(\frac{-E}{RT}\right) \tag{5}$$

Where $k_0$ is the pre-exponential factor, $E$ is the activation energy, $R$ is the gas constant and $T$ is the temperature.

The $CO_2$ equilibrium partial pressure depends on the carbonation/calcination reaction temperature according to the correlation suggested by Baker [10]:

$$\log P_{CO_2,eq}[kPa] = 9.079 - \frac{8307.83}{T[k]} \tag{6}$$

Integrating (4) gives $G(x)$ of which various forms were postulated to show different reaction mechanisms:

$$G(x) = \int_0^x \frac{1}{f(x)}dx = \int_0^t k\left(P_{CO_2} - P_{CO_2,eq}\right)^n dt = k\left(P_{CO_2} - P_{CO_2,eq}\right)^n t \tag{7}$$

Table 2 summarises $G(x)$ functions for various reaction mechanisms which were used to determine the carbonation reaction mechanism in this study.

## 4. Results and Discussion

The CaO conversion versus time, calculated by (3), over a temperature range of 400-500 $^{o}$C and for a $CO_2$ partial pressure of 1000 ppm (0.1%) is shown in Fig. 1. At 500 $^{o}$C, nucleation growth occurred for approximately 10 minutes causing a sigmoidal shape for carbonation reaction rate. The nucleation and nuclei growth occurs for particular gas-solid reactions at specific temperatures and gas phase compositions [11]. Nucleation is a dynamic process which initiates the carbonation reaction and the progress of this reaction depends on the rate of nuclei growth. Following this step, the chemical reaction plays a key role in making a linear slope which was considered the intrinsic reaction rate in this study. Subsequently, the reaction rate was reduced as a result of the formation of a carbonation layer on the surface of the CaO particles, hence hindering the access of $CO_2$ to the surface of the particles. The reaction progress became almost zero at around 50, 43 and 35% CaO conversion at 500, 450 and 400 $^{o}$C, respectively. It can be noticed that the reaction rate was almost the same for 430 and 450 $^{o}$C while at 500 $^{o}$C it decreased as this temperature is close to the equilibrium temperature at which the carbonation/calcination reactions occur for $CO_2$ partial pressures less than 1000 ppm.

The right hand term in (7) is temperature dependent and the most appropriate reaction mechanism can be determined by plotting $G(x)$ functions, tabulated in Table 2, versus time. For the range of 100-1000 ppm $CO_2$ partial pressures and over the temperature range of 400-500 $^{o}$C, $G(x)$ functions were plotted and the highest $R^2$ value of the least-square linear fits was considered to be the most appropriate reaction mechanism for the carbonation reaction.

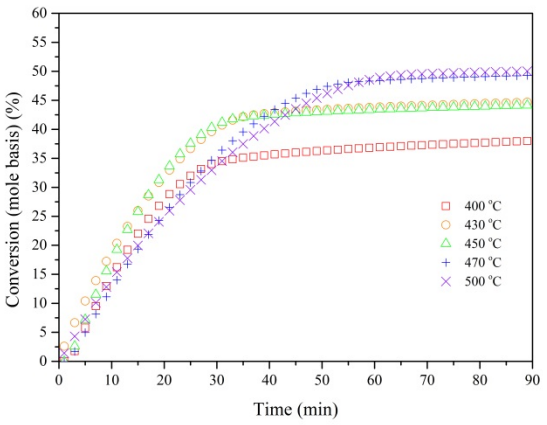


Figure 1. Calcium oxide (CaO) conversion, on a molar basis, versus time for different carbonation temperatures and the following conditions: $CO_2$ partial pressure: 1000 ppm (0.1 %), total pressure: 1 atm, total flow rate: 100 ml min$^{-1}$, sample size: 2 mg, particle size: 75-150 μm.

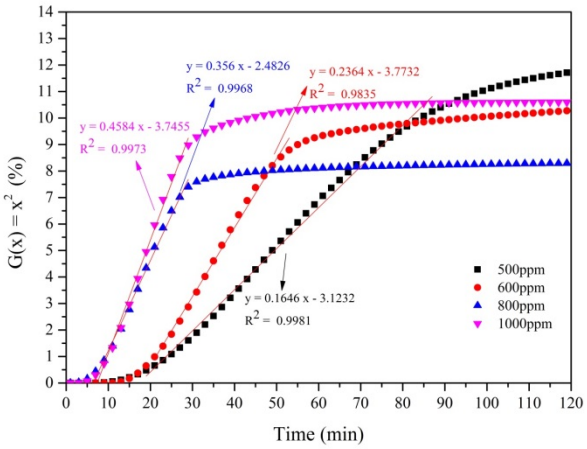


Figure 2. $G(x) = x^2$ reaction mechanism versus time for determination of $k(C - C_{eq})^n$ of the carbonation reaction at 450 $^{o}$C and $CO_2$ partial pressures of 500-1000 ppm. Symbols represent experimental data calculated by the D1 model and the continuous lines are the linear fits of the data which are time based on the linear least-square regression method.

The averaged $R^2$ values for all of the reaction mechanisms can be seen in Table 3, highlighting that the most appropriate reaction mechanism was D1 or $G(x)=x^2$. The effect of $CO_2$ partial pressure on conversion, existed in the $G(x)$ function, at a temperature of 450 $^{o}$C is demonstrated at Fig. 2. As can be clearly seen, the carbonation reaction increases as the $CO_2$ partial pressure increases from 500 to 1000 ppm, due to Le Châtelier's principle in which increasing the $CO_2$ partial pressure shifts the equilibrium and promotes the carbonation reaction forward.

The slope of the least-square linear regression presented in Fig. 2 determines the value of $k(C - C_{eq})^n$ at 450 $^{o}$C. These values were also determined, with the same trend, for 400 and 500 $^{o}$C, as presented in Fig. 3 in the format of $\ln\left[k(P - P_{eq})^n\right]$ versus $\ln(P - P_{eq})$ to establish the order of reaction ($n$) and the reaction constant ($k$).

Table 3. Average $R^2$ values for linear fitting of reaction mechanisms

| Reaction mechanism | Average $R^2$ of linear fitting |
|---|---|
| D1 | 0.977 |
| D4 | 0.976 |
| D3 | 0.975 |
| D2 | 0.970 |
| C2 | 0.951 |
| C1 | 0.940 |
| R3 | 0.936 |
| R2 | 0.934 |
| P1 | 0.927 |
| A2 | 0.857 |
| P2 | 0.837 |
| A3 | 0.800 |

| | |
|---|---|
| P3 | 0.779 |
| P4 | 0.745 |

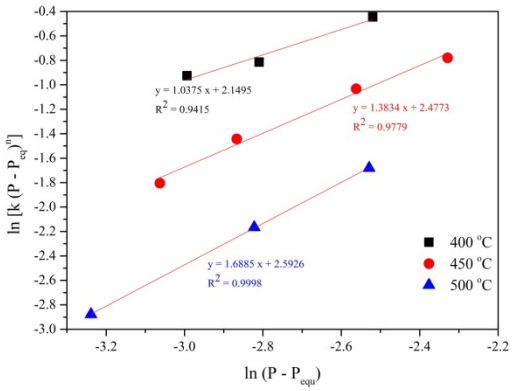


Figure 3. $\ln\left[k\left(P-P_{eq}\right)^{n}\right]$ versus $\ln\left(P-P_{eq}\right)$ in the range of 500-1000 ppm $CO_2$ partial pressure and 400, 450 and 500 $^{o}$C.

Through least-square linear fitting of plots in Fig. 3 the values of ln *k* and *n* are the intercept and slope of the linear fits, respectively.

The activation energy and pre-exponential factor were determined via Arrhenius plots as depicted in Fig. 4, which shows ln (*k*) versus 1/T for the temperature range of 400 to 500 $^{o}$C and $CO_2$ partial pressures of 500 to 1000 ppm. The activation energy was determined by least-square linear fitting of the slope, while the pre-exponential factor was determined by linear fitting of the intercept. The activation energy, order of reaction and pre-exponential factors determined are summarised in Table 4. The activation energy was less than that of Sun et al. [6] who reported a value around 30 kJ mol$^{-1}$ , but it was higher than zero which was reported by Bhatia and Perlmutter [12].

The discrepancy between our results and previous studies likely related to the differences in the samples structure and impurities. During nucleation and solid product formation, a sorbents structure changes and the extent of changes may differ from one sorbent to another.

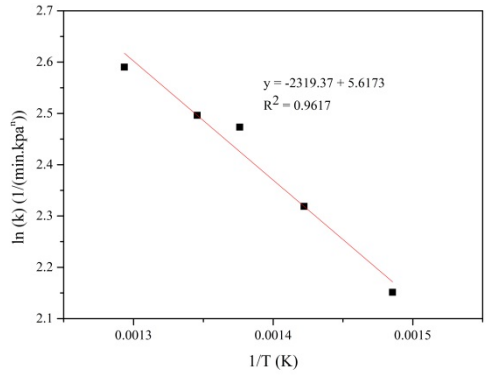


Figure 4. Arrhenius plot for the carbonation reaction at 400 to 500 $^{o}$C and $CO_2$ partial pressures of 500-1000 ppm.

Table 4. Carbonation kinetic parameters for $CO_2$ partial pressures of 500-1000 ppm and the temperatures of 400-500 $^{o}$C.

| Temperature ($^{o}$C) | Order of reaction (n) | Activation energy (E) (kJ mol$^{-1}$) | Pre-exponential factor ($k_0$) (min$^{-1}$ kpa$^{-n}$) |
|---|---|---|---|
| 400 | 1.04 | 19.28 | 275.13 |
| 450 | 1.38 | 19.28 | 275.13 |
| 500 | 1.69 | 19.28 | 275.13 |

Moreover, the activation energy for the gas-solid reaction is not only dependent on the chemical energy but also on the mechanical energy. This implies that greater impurities in the sorbent result in a lower mechanical energy between grains, leading to a lower activation energy.

## 5. Conclusion

The kinetic parameters of the carbonation reaction for a limestone sorbent were determined considering a wide range of reaction mechanisms. Through conducting least-square linear fitting, the reaction mechanism with the function $G(x) = x^2$ predicted the conversion of carbonation reaction better than others. The order of reaction, activation energy and pre-exponential factor were calculated considering an Arrhenius plot in which the activation energy was 19.47 kJ mol$^{-1}$ while the order of reaction was approximately first order at 400 $^{o}$C and increased with increasing temperature. The kinetic parameters determined in this study were in a good agreement with previous literature.

## 6. References


1. RIRDC Rural Industries Research and Development Corporation Report HSA-9.
2. P. V. Nelson, Greenhouse operation and management, Prentice Hall, 1991, p. 1-612.
3. K. Shah; C. Zhou; H. Song; E. Doroodchi; B. Moghtaderi, Energy Fuels 29 (2) (2015) 602-617 10.1021/ef502389t.
4. M. Ramezani; K. Shah; E. Doroodchi; B. Moghtaderi, Energy Convers. Manage. 103 (0) (2015) 129-138 http://dx.doi.org/10.1016/j.enconman.2015.06.044.
5. ASABE Heating, Ventilating and Cooling Greenhouses. ASABE EP406.4 https://elibrary.asabe.org/abstract.asp?aid=45682&t=3&dabs=Y&redir=&redirType=
6. P. Sun; J. R. Grace; C. J. Lim; E. J. Anthony, Chem. Eng. Sci. 63 (1) (2008) 47-56
7. F. Garcıa-Labiano; A. Abad; L. De Diego; P. Gayan; J. Adanez, Chem. Eng. Sci. 57 (13) (2002) 2381-2393
8. D. P. Hanak; E. J. Anthony; V. Manovic, Energy & Environmental Science (2015) 10.1039/C5EE01228G.
9. J. Szekely; J. W. Evans, Gas-solid reactions, Academic Press, UK, 1976, p. 1-400.
10. E. Baker, J. Chem. Soc. (Resumed) (1962) 464-470
11. M. M. Hossain; H. I. de Lasa, Chem. Eng. Sci. 63 (18) (2008) 4433-4451 http://dx.doi.org/10.1016/j.ces.2008.05.028.
12. S. Bhatia; D. Perlmutter, AIChE J. 29 (1) (1983) 79-86

# Derivation of Kinetic Parameters for the Stone Dust Looping Combustion Process for Ventilation Air Methane Abatement

S.Patel[1], O.Kubiak[1], P.Tremain[1], B. Moghtaderi[1], J. Sandford[2], K. Shah[1] *
[1]Priority Centre for Frontier Energy Technologies and Utilisation, Discipline of Chemical Engineering,
School of Engineering, Faculty of Engineering and Built Environment,
The University of Newcastle, Callaghan, NSW 2308, Australia
[2]Glencore Coal Assets, Bulga Complex, Singleton, Australia

**Abstract**
Intrinsic kinetics of the carbonation reaction in a carbonator were studied for a novel stone dust looping (SDL) process and a dilute $CO_2$ calcium looping (CL) process. The random pore model (RPM) was applied to estimate the kinetic parameters. A series of experiments were performed in a single lab scale fluidised bed reactor to evaluate the kinetic parameters for an SDL process with catalytic oxidation (1 vol. % $CH_4$ in air) and a CL process (1 vol. % $CO_2$ in air). The calcination process was carried out for particles size (150-212 μm), calcination temperatures (850 $^0$C) and three inventory sizes (8, 12 and 16 g). In addition, the effect of temperature (500-600 $^0$C) on carbonation reaction was also studied. The activation energy and pre-exponential factor determined for the carbonation reaction in the SDL and CL process were close agreement. Hence with sufficient temperature and/or CaO inventory for catalytic oxidation of methane, similar $CO_2$ capture can be achieved in the SDL and CL processes.

*Keywords: Stone dust, combustion, methane oxidation, Ventilation air methane, Kinetics etc.*

## 1. Introduction

Methane is the second most abundant greenhouse gas emitted by anthropogenic activities after carbon dioxide ($CO_2$) and has a global warming potential 25 times higher than that of $CO_2$ [1]. This suggests that growing methane emissions may have an influence on rising temperatures, while decreasing methane emissions may have short-term benefits in reducing the rate of climate change. Coal mining operations are a large source of fugitive methane emissions. Of the total fugitive methane emissions from coal mines, approximately 64% are a result of the Ventilation Air Methane (VAM) stream [2].

In the current marketplace there is an increasing need to abate VAM and thus lower the greenhouse footprint of mining activities. Hence, efforts have been made in recent times to design systems that can either destruct VAM through thermal oxidation process or make use of it for heat or power generation. In this regard, the research team at the University of Newcastle has come up with a novel VAM abatement process called "Stone Dust Looping (SDL)". Unlike the conventional calcium looping (CCL) process where lime (CaO) is introduced directly to the flue gas from a thermal power plant with $CO_2$ at concentrations as high as 12-15%, the SDL process uses VAM with concentrations of $CH_4$ up to 0.1 to 1 vol. % and inert $CO_2$ up to 0.3 to 2 vol. %. and can be configured into $CO_2$ capture/no $CO_2$ capture mode [3].

The CCL process uses calcium-based sorbents in a heterogeneous non-catalytic gas-solid reaction for the capture of carbon dioxide ($CO_2$). This has been extensively presented for different applications, such as fluidized bed combustors with in situ $CO_2$ capture [4, 5], and steam reformers [6-8]. In comparison the SDL process uses a calcium-based sorbent for a heterogeneous catalytic gas-solid reaction in which methane is catalytically oxidized by the calcium based sorbent to produce $CO_2$ which can then be captured [3]. In catalytic gas-solid reactions, there are several reaction steps that take place, i.e. the external and internal mass transfer of the gaseous reactants and the reaction which takes place at the reaction surface. There are many parameters that affect non-catalytic and catalytic gas-solid reactions, such as temperature, solid particle physical structure, and particle size. Therefore, the use of an appropriate mathematical model is essential to show the performance of the complex interactions between gaseous and solid reactants without any mathematical complexities.

The un-reacted shrinking core model and the grain model are frequently used for gas-solid reactions of non-porous and porous solid reactants, respectively. However, a pore model describes the carbonation reaction with higher precision as they account for the evolution of pore size distribution during cycling [9].

Modification of a pore model to a grain model, with an appropriate modification to structural parameters, was established by Bhatia and Perlmutter [10] with good agreement between a grain model and their random pore model (RPM)[10, 11] The RPM model deliberates the pore structure as a network of randomly interconnected

* Corresponding author:
Phone: (+61) 240339332
Email: kalpit.shah@newcastle.edu.au

pores, expresses the particle structural parameters based on this geometry and to end with, when it is applied to the carbonation reaction, delivers kinetic parameters by fitting the experimental reaction rate data obtained from 'fresh lime'[12]. In this study we aimed to determine the carbonation reaction kinetics of the $CO_2$ capture process for Omya limestone via a series of SDL and dilute $CO_2$ calcium looping (CL) fluidized bed experiments and implementing the RPM model.

## 2. Experimental

### 2.1. Material and Methods

Experiments were performed in a laboratory scale fluidized bed reactor as shown in Fig. 1. The setup was comprised of a fluidized bed reactor, furnace, condenser, gas control unit and gas analyser. The reactor was a cylindrical fused-quartz tube (Monash Scientific Ltd.) with a height of 700 mm and diameter of 25 mm. A frit (distributor plate) of porosity 3 (16-40 µm) was placed 280 mm from the bottom of the reactor to ensure that the feed gas was pre-heated before entering the fluidized bed. The reactor temperature was maintained during the experiment by the furnace controller and measured using a Pt/Rh thermocouple. Stone dust ($CaCO_3$) material (Omya limestone) was sieved to the preferred particle size of 150-212 µm and kept in an oven at $100^0$C prior to experimentation. XRF analysis of the fresh Omya limestone is provided in Table 1.Stone dust material was calcined at 850 $^0$C for 3 hours to produce fresh calcined lime (CaO) for use in experiments. Each experiment was performed three times to ensure repeatability of results.

### 2.2. SDL process

To simulate the SDL process, stone dust particles of the desired particle size were fed into the top of the reactor and were fluidized in either air or a high-purity VAM environment (i.e. a mixture of 1 vol. % $CH_4$ in air) through the gas control unit.

**Table 1:** XRF Analysis of Stone dust

| Ca | Fe | Mg | Al | Si | Mn | K |
|---|---|---|---|---|---|---|
| 97.56 | 0.23 | 0.38 | 0.15 | 1.21 | 0.43 | 0.04 |

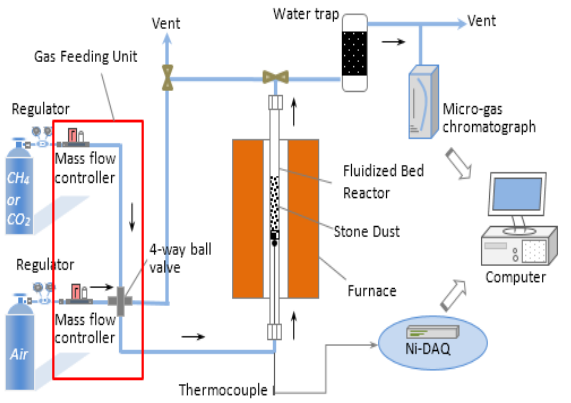


**Figure 1:** Schematic View of Laboratory Scale Fluidized Bed Reactor [3]

The gas control unit consisted of mass flow controllers to initially allow for calcination of stone dust in air at $850^0$C and then catalytic oxidation of VAM via fresh calcined lime (CaO) followed by carbonation at temperatures of 500-$600^0$C. The product gas stream was led to a gas analyzer (Agilent Micro-GC 4900) after the condenser (water trap) where the concentrations of $CH_4$, $CO_2$, CO, $H_2$, and $O_2$ were measured in real time. The exhaust was then vented to the atmosphere. The overall reaction occurring in the SDL carbonator is follows:

$$CaO + CH_4 + 2O_2 \rightarrow CaCO_3 + 2H_2O \qquad (1)$$

The $CO_2$ capture in the SDL carbonator is defined in Equation (2), which can be expressed as the ratio of $CO_2$ reacting with CaO in the bed after catalytic oxidation of methane to the amount of $CH_4$ entering the reactor, which can be written as:

$$\text{SDL } CO_2\text{Capture} = \frac{F_{CH4}X_{CH4} - F_{CO2,out}}{F_{CH4}} \qquad (2)$$

where $F_{CO_{2,out}}$ is the molar flowrate of $CO_2$ exiting the carbonator, $F_{CH_4}$is the molar flowrate of $CH_4$ entering the carbonator and $X_{CH_4}$ is the conversion of methane to $CO_2$.

### 2.3. Dilute $CO_2$ CL process

In this study the dilute $CO_2$ CL process was defined as 1 vol.% $CO_2$ in air and represents the hypothetical case of the SDL Process where 100% $CH_4$ conversion to $CO_2$ is obtained. The CL process experiments were performed under the same conditions as discussed above for the SDL process, however in the CL process 1 vol.% $CO_2$ in air was fed into the reactor during carbonation instead of 1 vol.% $CH_4$ in air. The product gas stream concentrations of $CO_2$, CO, $H_2$, and $O_2$ were also measured by gas analyzer in real time. The reaction occurring in the carbonator during the CL process is as follows:

$$CaO + CO_2 \rightarrow CaCO_3 \qquad (3)$$

The $CO_2$ capture in the CL carbonator was defined as the ratio of $CO_2$ reacting with CaO in the bed to the amount of $CO_2$ entering the reactor, which can be written as:

$$\text{CL } CO_2\text{Capture} = 1 - \frac{F_{CO_{2,out}}}{F_{CO_{2,in}}} \qquad (4)$$

where $F_{CO_{2,out}}$ is the molar flowrate of $CO_2$ exiting the carbonator, $F_{CO2,in}$is the molar flowrate of $CO_2$ entering the carbonator.

Experiments were conducted to investigate the effect of inventory size and carbonation temperature on the performance of both the SDL and CL processes as well as reaction kinetics. An experimental matrix is presented in Table 2 for all fluidized bed experiments performed in this study.

**Table 2.** Experimental matrix of fluidised bed experiments

| Case | T (°C) | $CH_4$ flowrate (mL/min) | $CO_2$ flowrate (mL/min) | Inventory (gm) |
|---|---|---|---|---|
| A | 500 | 500 | 500 | 8 |
| | 550 | | | |
| | 600 | | | |
| B | 500 | 500 | 500 | 12 |
| | 550 | | | |
| | 600 | | | |
| C | 500 | 500 | 500 | 16 |
| | 550 | | | |
| | 600 | | | |

The RPM was used to estimate the kinetic parameters and this model was previously established and applied for other gas-solid reactions [10-14]. According to this model, the reaction rate of a gas-solid reaction in the presence of a product layer diffusion resistance is expressed by Equation (5)[12].

$$\frac{dX}{dt}_{reactor} = \frac{k_s S_0 (C_{CO_2} - C_{e,CO_2})(1-X)\sqrt{1-\psi \ln(1-X)}}{(1-\varepsilon_0)\left[1+\frac{\beta Z}{\psi}(\sqrt{1-\psi \ln(1-X)}-1)\right]} \quad (5)$$

where $k_s$is the rate constant for the surface reaction, $S_0$ is the reaction surface area per unit of volume, $\varepsilon_0$ is the porosity of the particle, $C_{CO_2}$ is the concentration of $CO_2$ in the gas bulk, $C_{e,CO_2}$is the equilibrium concentration of $CO_2$ at reaction conditions[15], $X$ is solids conversion at the exit of the carbonator, $\psi$ relates the internal pore structure of the particle as defined in Equation (6), $\beta$ is defined in Equation (7) and $Z$ is defined in Equation (8):

$$\psi = \frac{4\pi L_0 (1-\varepsilon_0)}{{S_0}^2} \quad (6)$$

where $L_0$ represents the initial pore length per unit of volume and $S_0$, $L_0$ and $\varepsilon_0$ can be directly calculated from mercury porosimetry data[12] applied to fresh calcines.

$$\beta = \frac{2 k_s \rho_{CaO} (1-\varepsilon_0)}{PM_{CaO} D_p S_{ave}} \quad (7)$$

where $\rho_{CaO}$ is the density of CaO, $PM_{CaO}$ is the molecular weight of CaO, $D_p$ is the apparent product layer diffusion and $S_{ave}$ is maximum average reaction surface.

$$Z = 1 + \frac{\rho_{CaO}(v_{CaCO_3} - v_{CaO})}{PM_{CaO}} \quad (8)$$

where $v_{CaCO3}$ is the molar volume of $CaCO_3$ and $v_{CaO}$ is the molar volume of CaO.

In Equations (6–8), a number of structural parameters for the limestone used were required. Table 3 presents the structural parameters for Katowice limestone as obtained from Grasa et al.[9] which bears significant similarities to Omya limestone used in our experimental study both structurally and compositionally. For this reason, as well as the fact that the parameters were obtained from experiments performed under similar reaction conditions, the parameters presented in Table 3 were applied in our model.

**Table 3.** Structural parameters of calcined fresh Katowice limestone input to carbonator model from obtained from literature data[9].

| Parameter | Value |
|---|---|
| $S_0$ ($m^2/m^3$) | $35 \times 10^3$ |
| $L_0$ ($m/m^3$) | $2.63 \times 10^{14}$ |
| $\varepsilon_0$ (-) | 0.46 |
| $\psi$ (-) | 1.41 |

The reaction rate constant ($k_s$) was derived by simplifying and integrating the terms in Equation (5) assuming a first order reversible reaction to give:

$$f(\psi) = \frac{1}{\psi}\left[\sqrt{1-\psi \ln(1-X)} - 1\right] = \frac{k_s S_0 (C_{CO_2} - C_{e,CO_2}) t}{2(1-\varepsilon_0)} \quad (9)$$

In the fast reaction regime, a plot of the reaction rate constant,$k_s$, can be represented by the Arrhenius equation:

$$k_s = k_{s0} \exp(-E_{aK}/RT) \quad (10)$$

Arrhenius plots of ln$k_s$ versus 1/T, where $k_s$ was determined from Equation (9), were then used to determine the activation energy, $E_{aK}$, and pre-exponential factor, $k_{s0}$, for each of the experimental conditions detailed in Table 2.

## 3. Results and discussion

### 3.1. Overall $CO_2$ capture

The overall efficiency of the SDL and CL processes were determined based on the amount of $CO_2$ captured by the CaO bed in the carbonator. For the SDL process, the amount $CO_2$ captured is dependent on the conversion of $CH_4$ to $CO_2$ via catalytic oxidation. Fig. 2 provides the amount of $CO_2$ captured in the CaO bed for the SDL carbonator reactor at three different temperatures (500, 550 and 600 °C) and a flow rate of 500 mL/min of 1 vol. % of methane in air. In Fig. 2 it can be seen that as the temperature increases, so too does $CH_4$ conversion, i.e. more $CO_2$ is produced, and hence the amount of $CO_2$ captured ultimately increases.

Fig. 3 presents a comparison of the total amount of $CO_2$ captured in the CaO bed for both the SDL and CL processes for the three inventory sizes, three temperatures and a flow rate of 500 mL/min of the respective gas.

At lower temperatures it can be seen that the CL process has superior $CO_2$ capture, while the SDL process is limited due to insufficient conversion of methane. For the SDL process an increase in inventory directly relates to an increase in $CO_2$ capture due to an increase in the amount of active sites for $CH_4$ oxidation. As the temperature the CL process capture decreases as the carbonation/calcination temperature is approached, however for the SDL process methane conversion increases to near 100% and $CO_2$ captured in CaO is higher in comparison to the CL process for the same inventory size.

### 3.2. Carbonation reaction kinetics

An example of the Arrhenius plots obtained for the SDL and CL experiments are presented in Fig. 4 for Case A (Table 2).Table 4 presents a comparison of the experimentally determined SDL and CL kinetic parameters. It can be seen that the average

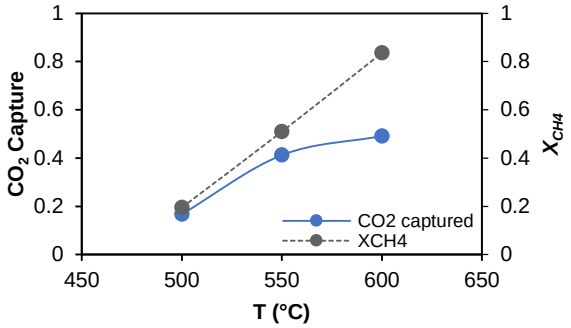


**Figure 2:** $CO_2$ Captured in CaO bed vs. temperature and methane conversion ($X_{CH4}$) as a function of temperature at a 500 ml gas flow rate for Case C.

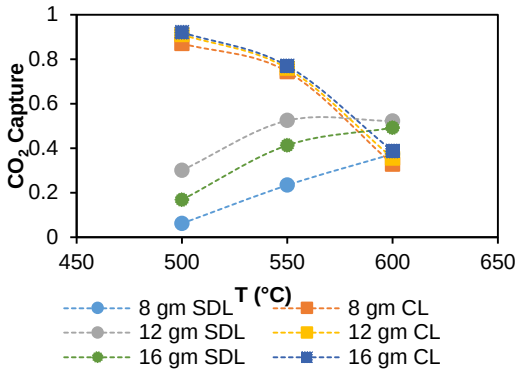


**Figure 3:** Amount of $CO_2$ captured in CaO vs. temperature at 500 ml flow rate with different inventory size.

carbonation kinetic parameters for the SDL and CL process were similar with a $k_{s0}$ of 8.05 × $10^{-6}$ $m^4$/kmol.s and 9.62 × $10^{-6}$ $m^4$/kmol.s respectively and activation energy of 20.87 × $10^3$ kJ/kmol and 25.22 × $10^3$ kJ/kmol, respectively. These are in close agreement with the values reported by Grasa et al.[9]: $E_{aK}$ of 19.2 × $10^3$ kJ/kmol) and $k_{s0}$ of 5.29×$10^{-6}$ $m^4$/kmol.s for Katowice limestone.

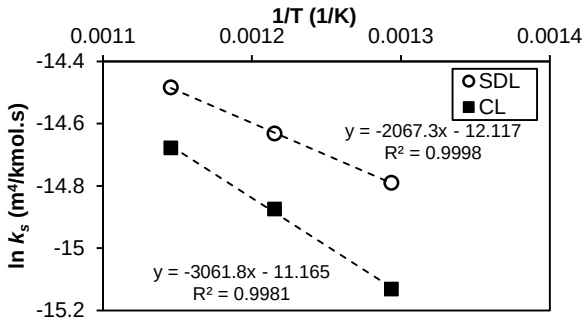


**Figure 4.**Carbonation reaction kinetics Arrhenius plot for Case A.

## 4. Conclusion

The RPM model was used to describe the intrinsic rate of carbonation reaction kinetics with Omya limestone for an SDL and dilute $CO_2$ CL process. The effect of temperature and inventory size on the carbonation reaction were also investigated.

**Table 4.** Comparison of SDL and CL carbonation kinetic parameters

| Case | SDL | | CL | |
|---|---|---|---|---|
| | $E_{aK}$ (kJ/kmol) | $k_{s0}$ ($m^4$/kmol.s) | $E_{aK}$ (kJ/kmol) | $k_{s0}$ ($m^4$/kmol.s) |
| A | 17.24 ×$10^3$ | 5.46 ×$10^{-6}$ | 25.53 ×$10^3$ | 1.41 ×$10^{-5}$ |
| B | 24.08 ×$10^3$ | 9.64 ×$10^{-6}$ | 16.92 ×$10^3$ | 3.80 ×$10^{-6}$ |
| C | 21.30 ×$10^3$ | 9.05 ×$10^{-6}$ | 33.21 ×$10^3$ | 1.09 ×$10^{-5}$ |
| Avg. data | 20.87 ×$10^3$ | 8.05 ×$10^{-6}$ | 25.22 ×$10^3$ | 9.62 ×$10^{-6}$ |

Activation energies for the carbonation reaction of SDL and CL processes were found to be 20.87 × $10^3$ kJ/kmol and 25.22 × $10^3$ kJ/kmol, respectively which were in close agreement with literature values. As the carbonation reaction kinetics were similar, it was concluded that if sufficient inventory and or temperature is provided to facilitate catalytic oxidation of methane, similar $CO_2$ capture to the CL process can be achieved by the SDL process.

## 5. Acknowledgement

The authors wish to acknowledge the financial support received from University of Newcastle (Australia) and Australian Coal Association Research Program (Project ID: C23052) for the work presented in this paper.

## 6. References

[1]D. Reay; P. Smith; A. Van Amstel, Methane and climate change, Earthscan, 2010.
[2] Y. Zhongqing; Z. Li; T. Qiang, Natural Gas Industry **2** (2010) 033
[3] K. Shah; B. Moghtaderi; E. Doroodchi; J. Sandford, Fuel Processing Technology **140** (2015) 285-296
[4] J. C. Abanades; E. J. Anthony; D. Y. Lu; C. Salvador; D. Alvarez, AIChE Journal **50** (7) (2004) 1614-1622
[5] H. An; T. Song; L. Shen; C. Qin; J. Yin; B. Feng, International Journal of Hydrogen Energy **37** (19) (2012) 14195-14204
[6] B. Balasubramanian; A. L. Ortiz; S. Kaytakoglu; D. Harrison, Chemical Engineering Science **54** (15) (1999) 3543-3552
[7] A. Lopez Ortiz; D. P. Harrison, Industrial & Engineering Chemistry Research **40** (23) (2001) 5102-5109
[8] K. Johnsen; H. Ryu; J. Grace; C. Lim, Chemical Engineering Science **61** (4) (2006) 1195-1202
[9] G. Grasa; R. Murillo; M. Alonso; J. C. Abanades, AIChE journal **55** (5) (2009) 1246-1255
[10] S. K. Bhatia; D. D. Perlmutter, AIChE Journal **26** (3) (1980) 379-386 10.1002/aic.690260308.
[11] S. K. Bhatia; D. D. Perlmutter, AIChE Journal **27** (2) (1981) 247-254 10.1002/aic.690270211.
[12] S. Bhatia; D. Perlmutter, AIChE Journal **29** (1) (1983) 79-86
[13] G. R. Gavals, AIChE Journal **26** (4) (1980) 577-585 10.1002/aic.690260408.
[14] R. Barker, Journal of applied Chemistry and biotechnology **23** (10) (1973) 733-742
[15] E. Baker, Journal of the Chemical Society (Resumed) (1962) 464-470

# VAM oxidation over palladium loaded on high silica BEA and MFI zeolites

H. HosseiniAmoli, L. Harvey, E.M. Kennedy, and M. Stockenhuber*
Priority Research Centre for Energy, Faculty of Engineering & Built Environment
The University of Newcastle, Callaghan NSW 2308
Australia

## Abstract

The catalytic combustion of lean air methane in the presence of water vapour is investigated. High silica zeolites with MFI and BEA topology are used as support for the Pd-based catalyst. The thermal stability of 1% Pd/H-BEA (Si/Al=175), 1% Pd/H-ZSM-5 (Si/Al=140) and 1%Pd/Silicalite (Si/Al=1100) during methane conversion as a function of time on stream is examined. The results display slight reduction in activity for H-BEA, moderate deactivation for MFI silicalite and rapid deactivation for HZSM-5 catalyst over 40 hours' time on stream. The deactivation indicates the presence of water vapour in the feed could be the primary factor of catalyst deactivation. BEA zeolite was shown to be more stable compared to the MFI structure catalyst over 40 h of time on stream. It is suggested that that the nature of BEA support facilitates a higher level of palladium particle distribution in compare to MFI. Also, the silicalite-supported catalyst demonstrated superior activity and stability to the HZSM-5, suggesting that increasing the ratio of Si/Al leads to a reduction in aluminium concentration and a more neutral framework which results in higher hydrophobicity and thermal stability. In order to have better understanding of catalyst performance, the stability results were supported by catalyst characterization such as $N_2$-adsorption and desorption, ICP, XRD and TEM analyses.

*Keywords: BEA, MFI, Hydrophobicity, Stability, Methane Conversion.*

## 1. Introduction

During underground mining of coal, high volumes of methane, which is diluted in air to a concentration of less than 1%, can be emitted. In addition to methane, water vapour is also typically present, further hindering combustion. This ventilation air methane (VAM) is below the lower flammability limit of methane (5 % in air). Catalytic combustion is a potential solution, particularly for lean methane mixtures, whereby methane is converted to carbon dioxide over Pd-based catalyst such as $Pd/Al_2O_3$, $Pd/SiO_2$, $Pd/ZrO_2$ and Pd/Zeolite [1-7].

Catalyst deactivation is a major challenge associated with catalytic processes. There are several reasons for the deactivation of Pd-based catalysts. The inhibition of Pd-based catalysts by water for methane oxidation has been reported in previous investigations [1, 8-11]. Water, generated during reaction, notably decreases the activity of the catalyst at lower temperatures due to competition with methane for active sites. This deactivation is suggested to be due to transformation of the active site (PdO) into a less active site ($Pd(OH)_2$)[1, 7, 12, 13].

In heterogeneous catalytic processes, the reaction occurs on the surface of the solid catalyst. Therefore, surface properties are very important for catalyst performance [14]. The presence of strong polar groups such as hydroxyl groups or metal–oxygen bonds on the surface and inside the catalyst pore structure are the main source of hydrophilicity of the conventional heterogeneous materials such as zeolites [14-16]. Zeolites are well-known to have strong affinity for water adsorption even at low water vapour pressures. The hydrophobicity of zeolites largely depends on the population of the Al atoms in the framework. [17-19]. Aluminium in a zeolite structure causes a charge imbalance. Increasing the ratio of Si/Al leads to a reduction in aluminium concentration and a more neutral framework which results in higher hydrophobicity and thermal stability [16, 20].

Zeolite structures such as MFI and BEA with high silica content show high affinity to the organic phase (hydrophobicity) during coadsorption of water and volatile organic compounds (VOCs) [21-23]. For example, silicalite-1 with MFI ratio of Si/Al > 1000 is largely applied for removal of water contaminated with organic impurities[24]. MFI and BEA are micro-porous zeolites with a three dimensional channel systems built from T12 units with 10-rings channel and T16 units with 12-ring channels, respectively. Moreover, BEA framework provides approximately 20.5 % accessible volume which is almost double amount of accessible volume for MFI framework [25]. Also, according to Andreia and Walter's investigation on the physicochemical properties of HBEA and HZSM-5 (MFI structure), the surface area, average pore diameter and total pore volume of HBEA pores revealed the largest value in comparison to HZSM-5. A similar consideration shows the largest value of micro-pore volume and micro-pore area for ZSM-5. They used $N_2$ adsorption/desorption isotherms at 77 K [26].

In this research, the catalyst activity and stability as a function of Si/Al ratio and zeolite framework in VAM oxidation is investigated. Thus, we investigate the effect of using MFI and BEA as supports for the catalytic combustion of methane under humid feed condition.

* Corresponding author:
Phone: (+61) 2 4985 4433
Email: Michael.stockenhuber@newcastle.edu.au

## 2. Experimental

### 2.1 Catalyst Preparation

HZSM-5 and HBEA were purchased from Zeolyst International, Kansas, USA. Tetrapropylammonium bromide ((TPA)Br, Fluka 98%), ammonium fluoride ($NH_4F$, ≥99.99% trace metals basis) and palladium (II) nitrate were purchased from Sigma-Aldrich. Fumed silica (Aerosil 210, 99%) was obtained from Degussa. Silicalite-1 of the MFI structure type was synthesized with the methods reported by Guth and Kessler[25]. First, a solution of 72 g distilled water, 4.26 g (TPA)Br and 0.3 g $NH_4F$ were prepared and stirred until dissolved. 12 g of fumed silica were then added gradually to the solution and stirred until homogenized and reached a pH of 6. The gel was then added to a PTFE-lined autoclave and crystallized at 200°C for 16 days. Finally, the products were filtered, washed with distilled water and dried at 80°C overnight. All samples were calcined at 550°C for 3 h under air flow. Finally 1.2 wt% palladium was loaded on calcined samples through incipient wetness method with Pd(II) nitrate solution (10 wt% in 10 wt% nitric acid) and dried at 110°C overnight and calcined at 500°C for 2 h under air flow.

### 2.2 Characterization

For measuring the surface area of the catalyst, Micromeritics Tristar surface area analyser by nitrogen adsorption and desorption at 77 K and Micromeritics Vacprep 061 for sample degassing was used. The X-Ray diffraction patterns (XRD) of the catalysts were measured with Cu Kα incident radiation (λ= 1.5406A)° were obtained using a Philips X'Pert diffractometer. A JEOL 2100 Transmission Electron Microscope (TEM) was used for TEM images. The quantity of palladium loaded on catalysts was measured by a Varian 715-ES inductively coupled plasma optical emission spectrometer (ICP-OES).

### 2.3 Catalytic activity measurements

Catalytic combustion of lean methane was performed in a tubular stainless steel fixed bed micro reactor. While for a VAM combustion system the most appropriate reactor type is expected to be a monolithic reactor, fixed bed reactors can be used for evaluation of the catalyst performance [1, 3, 27]. Prior to the test the catalyst was calcined at 500°C for 2 h under 100 mL/min air flow. The inlet methane concentration was set at 0.7% in air with a high gas hourly space velocity (GHSV) of 50 000 $h^{-1}$. The total flow rate of VAM emission in a typical coalmining shaft is approximately 150–300 $m^3/s$. At a space velocity of 50,000 $h^{-1}$ it is estimated a 10 $m^3$ - 20 $m^3$ size reactor is needed for the combustion reaction. Methane conversion was monitored using a gas chromatograph (Shimadzu GC-2014) with packed Hysep and Molecular Sieve dual column and a thermal conductivity detector (TCD). The temperature of bed was measured by a thermocouple placed into the catalyst bed. An average carbon balance of 96% was obtained for all experiments. The average water vapour concentration was determined by a humidity probe and determined to be constant, with approximately 85% relative humidity (RH), corresponding to approximately 30 000 ppm of $H_2O$ vapour pressure, falling within the humidity range of 70-100% RH typically reported for VAM [1, 29].

## 3. Result and discussion

### 3.1 Structural properties of catalysts

Surface area and pore volume analyses were performed by $N_2$ adsorption and desorption. Table 1 shows the surface area, pore volume and pore diameter of HBEA, ZSM-5 and silicalite as determined by nitrogen adsorption experiments. As expected the surface area, pore volume and diameter of BEA is greater than in the MFI structure of silicalite and HZSM-5. The results show the langmuir surface area of 811 $m^2g^{-1}$, 473 $m^2g^{-1}$ and 487 $m^2g^{-1}$ for Pd/HBEA, Pd/HZSM-5 and Pd/Silicalite, respectively. The ICP results of Si/Al ratio for all supports summarized in table 1. Also ICP confirmed the range of 1% to 1.12% palladium loading on all zeolite supports.

The XRD pattern of synthesised silicalite with Si/Al ratio 1100 is shown in Fig. 1. The diffraction pattern shows high crystallinity in which high peaks were found in the 2θ range of 5-10° and 22-26°, compatible with literatures about the MFI structure[25, 30, 31].

Fig. 2, Fig. 3, and Fig. 4, provide palladium particle size and distribution of fresh catalysts under transmission electron microscope (TEM). According to the statistical analysis by digital micrograph software, the average palladium particle size on Pd/HBEA nm and Pd/Silicalite-1(MFI) is 4.4 nm and 6.3 nm, respectively.

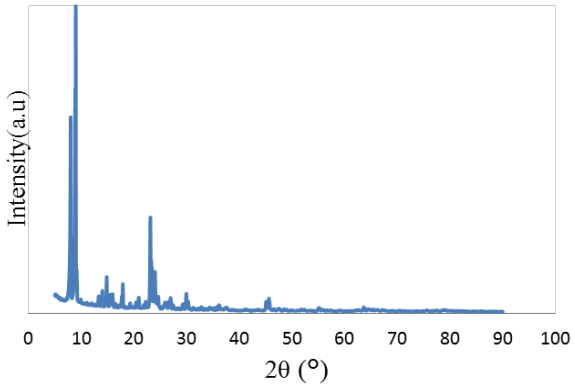


Fig. 1, XRD pattersn of silicalite synthesised

Table 1, Surface Area and Pore volume

| Sample | Surface Area($m^2/g$) | Pore volume ($cm^3/g$) | Average Pore diameter(nm) |
|---|---|---|---|
| Pd/HBEA, Si/Al=175 | 811 | 0.34 | 2.56 |
| Pd/HZSM-5, Si/Al=140 | 473 | 0.19 | 2.1 |
| Pd/Silicalite, Si/Al=1100 | 487 | 0.17 | 2.04 |

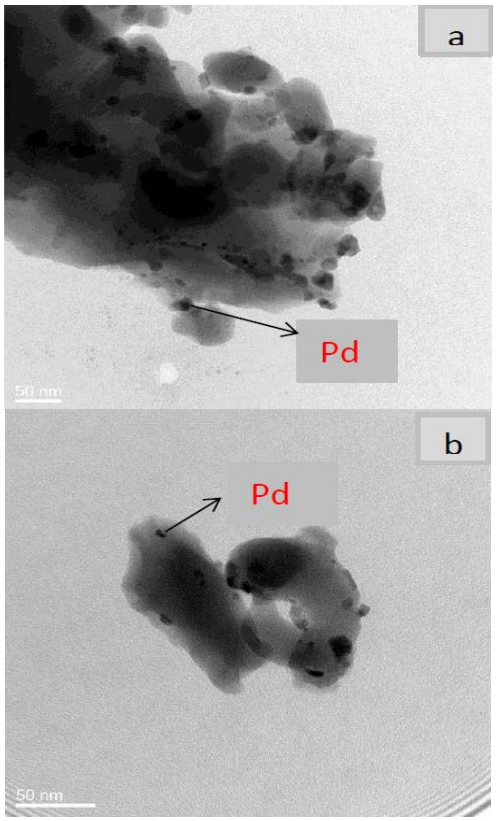

Fig. 2, TEM images (a) fresh Pd/HBEA; (b) fresh Pd/Silicalite-1(MFI)

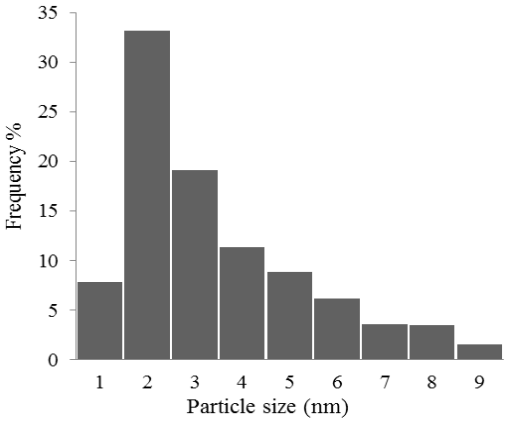

Fig.3, Palladium particle size distribution of fresh catalysts Pd/HBEA

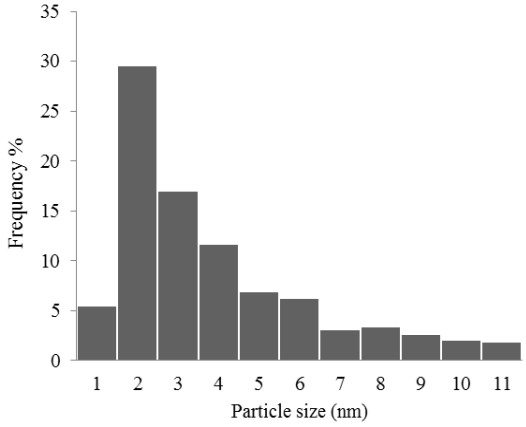

Fig.4, Palladium particle size distribution of fresh catalysts Pd/Silicalite-1(MFI)

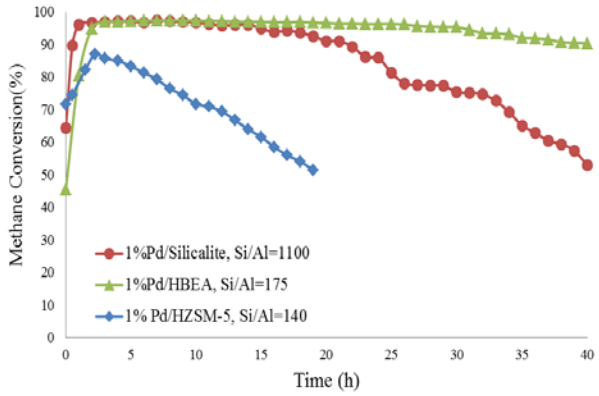

Fig. 5, Methane conversion as function of time on stream, humid feed at a constant bed temperature 400°C, GHSV 50 000 $h^{-1}$.

## 3.2 Catalyst activity and stability

Methane conversion as a function of time on stream is plotted in Fig. 5, Evaluation of catalyst stability was performed under humid feed at constant temperature and 400°C. Deactivation can be observed for all samples, though at different rates. As it has been mentioned previously, the presence of water vapour in the feed is a significant factor contributing to catalyst deactivation in addition to water vapour generated by the reaction[1].

Comparing MFI structures with different Si/Al ratio shows a significant difference in stability between silicalite with Si/Al=1100 and HZSM-5 with Si/Al=140. This difference is likely to be due to the negative framework charge caused by presence of aluminium in the zeolite structure [16, 20]. Further, BEA (Si/Al=175) exhibits much higher stability, i.e., conversion over 40 h time on stream in comparison to MFI (Si/Al=140). This difference can be attributed to the larger pore volume, pore diameter and approximately double the accessible volume of BEA structure [25, 26] which provide more volume for palladium particles to disperse. It is suggested that that the nature of BEA support helps in providing a better palladium particle distribution in comparison to the MFI support which is confirmed by TEM images in Fig. 2. Furthermore, the average Pd particle size of Pd supported on BEA is significantly smaller (4.4 nm) than Pd supported on MFI (6.3 nm). This suggests significant differences in the Pd dispersion dependent on the support which is confirmed by calculation dispersion value. Using dispersion equation based on particle size, shows 25.4 % Pd dispersion on BEA support in comparison to 17.7% Pd dispersion on MFI support[32]. This attribution has been reported in previous literature that the nature of support influences the distribution and morphology of palladium nanoparticles [13, 33, 34].

## 4. Conclusion

We have investigated methane conversion over palladium loading on BEA and MFI zeolites. Methane conversion, as a function of time on stream under humid

conditions results in enhanced stability of BEA compared to MFI. This may be a result of the larger dimensional framework of BEA than MFI which provides a greater accessible volume for palladium to disperse. TEM images as shown in Fig. 2, disclose the presence of= nano-size palladium particles distributed on the MFI and BEA frameworks. The average palladium particle size for fresh Pd/HBEA catalyst and Pd/Silicalite-1(MFI) is 4.4 nm and 6.3 nm, respectively, suggesting higher palladium dispersion on BEA framework. Also, a catalyst with the same MFI structure and less aluminium content showed much better thermal stability. Since, high Si/Al ratio leads to reduction in aluminium concentration and a more neutral framework which results in higher hydrophobicity and thermal stability.

## 5. Acknowledgment

We would like to acknowledge ACARP for their generous financial support of the project. We thank Hongwei Liu for assistance with TEM analysis. We are grateful to acknowledge financial support provided by University of Newcastle.

## 6. Reference

[1] A. Setiawan; J. Friggieri; E. M. Kennedy; B. Z. Dlugogorski; M. Stockenhuber, Catalysis Science & Technology 4 (6) (2014) 1793-1802.
[2] S. Su; A. Beath; H. Guo; C. Mallett, Prog. Energy Combust. Sci. 31 (2) (2005) 123-170.
[3] S. Su; J. Agnew, Fuel 85 (9) (2006) 1201-1210.
[4] B. Kucharczyk, Polish Journal of Chemical Technology 13 (4) (2011) 57-62.
[5] P. Araya; S. Guerrero; J. Robertson; F. Gracia, Applied Catalysis A: General 283 (1) (2005) 225-233.
[6] K. Baris, Energy for Sustainable Development 17 (1) (2013) 13-23.
[7] P. Gélin; M. Primet, Applied Catalysis B: Environmental 39 (1) (2002) 1-37.
[8] K. Yasuda; T. Masui; T. Miyamoto; N. Imanaka, Journal of materials science 46 (11) (2011) 4046-4052.
[9] D. Ciuparu; E. Perkins; L. Pfefferle, Applied Catalysis A: General 263 (2) (2004) 145-153.
[10] D. L. Mowery; R. L. McCormick, Applied Catalysis B: Environmental 34 (4) (2001) 287-297.
[11] C. H. Bartholomew, Applied Catalysis A: General 212 (1–2) (2001) 17-60.
[12] D. Ciuparu; N. Katsikis; L. Pfefferle, Applied Catalysis A: General 216 (1) (2001) 209-215.
[13] L. Wenge; G. Deyong; X. Xin, China Petroleum Processing & Petrochemical Technology 14 (3) (2012) 1-9.
[14] C. Chen; S. Shi; M. Wang; H. Ma; L. Zhou; J. Xu, Journal of Materials Chemistry A 2 (21) (2014) 8126-8134.
[15] A. Sah; H. Castricum; A. Bliek; D. Blank; J. Ten Elshof, Journal of membrane science 243 (1) (2004) 125-132.
[16] N. Chen, The Journal of Physical Chemistry 80 (1) (1976) 60-64.
[17] T. Kawai; K. Tsutsumi, Colloid Polym Sci 270 (7) (1992) 711-715.
[18] K. Tsutsumi; K. Mizoe, Colloids and Surfaces 37 (1989) 29-38.
[19] N. Y. Chen, The Journal of Physical Chemistry 80 (1) (1976) 60-64.
[20] A. V. Goretsky; L. W. Beck; S. I. Zones; M. E. Davis, Microporous and Mesoporous Materials 28 (3) (1999) 387-393.
[21] Q. Hu; J. Li; S. Qiao; Z. Hao; H. Tian; C. Ma; C. He, Journal of hazardous materials 164 (2) (2009) 1205-1212.
[22] N. Navascués; C. Téllez; J. Coronas, Microporous and Mesoporous Materials 112 (1) (2008) 561-572.
[23] Q. Hu; B. J. Dou; H. Tian; J. J. Li; P. Li; Z. P. Hao, Microporous and Mesoporous Materials 129 (1–2) (2010) 30-36.
[24] J. M. Thomas; J. Klinowski; M. W. Anderson, Chemistry Letters (10) (1983) 1555-1556.
[25] http://www.iza-online.org/
[26] A. A. Costa; W. B. Wilson; H. Wang; A. D. Campiglia; J. A. Dias; S. C. L. Dias, Microporous and Mesoporous Materials 149 (1) (2012) 186-192.
[27] A. Setiawan; E. M. Kennedy; B. Z. Dlugogorski; A. A. Adesina; O. Tkachenko; M. Stockenhuber, Energy Technology 2 (2014).
[28] H. Schultz; P. Carothers; R. Watts; R. McGuckin, United States Environmental Protection Agency, Air and Radiation (US-EPA) (2003).
[29] S. Su; H. Chen; P. Teakle; S. Xue, Journal of environmental management 86 (1) (2008) 44-62.
[30] H. Zhou; Y. Su; X. Chen; S. Yi; Y. Wan, Separation and Purification Technology 75 (3) (2010) 286-294.
[31] O. Larlus; V. Valtchev; J. Patarin; A. C. Faust; B. Maquin, Microporous and Mesoporous Materials 56 (2) (2002) 175-184.
[32] T. Paryjczak; J. A. Szymura, Zeitschrift für anorganische und allgemeine Chemie 449 (1) (1979) 105-114.
[33] Y. Liu; S. Wang; T. Sun; D. Gao; C. Zhang; S. Wang, Applied Catalysis B: Environmental 119 (2012) 321-328.
[34] L.-f. Yang; C.-k. Shi; X.-e. He; J.-x. Cai, Applied Catalysis B: Environmental 38 (2) (2002) 117-125.

**Proceedings of the Australian Combustion Symposium**
**December 7-9, 2015, The University of Melbourne**

# Validation of oxidation mechanisms for pentane isomers

Song Cheng, Hao Yuan, Yi Yang*, Michael, J. Brear
Department of Mechanical Engineering
The University of Melbourne, VIC 3010, Australia

## Abstract

Alkanes are a major constituent of gasoline fuels. Their combustion chemistries, however, have attracted relatively less attention compared to their shorter and longer chain counterparts. As a part of an international collaboration on studying C5 combustion chemistry, this paper reports kinetic modeling of the oxidation of *normal*-, *iso*-, and *neo*-pentane using existing mechanisms and compares these to experimental results in the literature. The objective is to identify a suitable mechanism for a study of engine knock currently being undertaken in authors' group. Four detailed combustion mechanisms, each containing sub-mechanisms for the three C5 isomers, are used to simulate a wide range of experimental data in the literature. The experimental data include ignition delays from rapid compression machines and shock tubes, as well as species profiles from jet stirred reactors, which cover reaction temperatures from 600 to 1400 K, pressures from 1 to 520 atm, equivalence ratios from 0.2 to 2, residence times from 0.05 to 0.25 s, and a dilution level from 70% to 90%. Results indicate that the mechanism from Bugler et al. [1] performs best for the three isomers overall. Further opportunity to improve mechanisms is then identified for *n*-pentane at low-to-intermediate temperatures and for very lean and very rich conditions.

*Keywords: chemical kinetic mechanisms, modelling, pentane.*

## 1. Introduction

Alkanes containing five carbon atoms have three isomers: *normal*-, *iso*-, and *neo*-pentane (Figure 1).

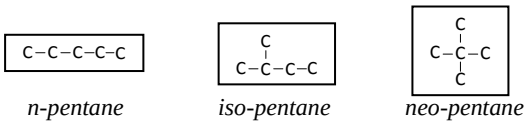


Figure 1. The isomers of pentane.

Pentanes are major constituents of gasoline and contribute significantly to the required vapor pressure. Their content in gasoline worldwide varies from 10 to 40% by volume [2, 3]. Despite this, the combustion chemistry of pentanes has not been studied as much as C1-C4 alkanes or C7 and C8 primary reference fuels. To address this issue, further study of C5 combustion chemistry was nominated as a topic for collaborative research in the International Workshop on Flame Chemistry at the 2014 International Symposium on Combustion.

As part of this effort, this work examines existing combustion mechanisms of pentane isomers which are often enclosed in part or entirely in the mechanisms of longer chain alkanes. However, these C5 sub-mechanisms have often been overlooked during the validation of these larger compounds, even though experimental data for C5 oxidation are available from a number of studies (as reviewed below). This work will therefore identify the best C5 mechanism as a first step to modeling C5 autoignition during engine knock in spark-ignition engines. The engine experiment is currently being undertaken in the authors' group since the knock propensity of pentane isomers is not well understood and only their octane numbers are reported in the literature.

Four published mechanisms, named M1 to M4, are examined. Each of these covers the detailed combustion chemistry of the three pentane isomers. Individual mechanisms for single isomers are also available in the literature, but these were not considered so as to avoid inconsistency with thermal and kinetic data across mechanisms.

Mechanisms M1-4 are defined as follows. M1 is a mechanism developed specifically for the three pentane isomers at the National University of Ireland, Galway (NUI-G) [1]. M2 is a gasoline surrogate mechanism developed by Andrae [4]. M3 is an *iso*-octane mechanism developed by Contino et al [5]. M4 is a gasoline surrogate mechanism from Lawrence Livermore National Laboratory (LLNL) [6].

The selected mechanisms are validated against a wide range of experimental data previously reported in the literature. These include ignition delay times (IDTs) from shock tubes [7-9] and rapid compression machines (RCMs) [10-13], as well as species profiles from jet stirred reactors (JSRs) [14, 15].

## 2. Modelling Methods

Ignition delay times in RCMs and shock tubes were modelled using CHEMKIN-PRO [16] Closed Homogeneous Reactor. The reaction is considered as an adiabatic, constant-volume process. Heat loss during RCM experiments was not considered as the data was unavailable. The ignition was defined as the timing to reach a temperature rise of 400 K unless otherwise noted. Species profiles from JSRs were modelled using a Perfectly Stirred Reactor.

## 3. Results and Discussion

### 3.1 *neo*-pentane

* Corresponding author: Yi Yang
Phone: (+61) 3 8344 8104
Email: yi.yang@unimelb.edu.au

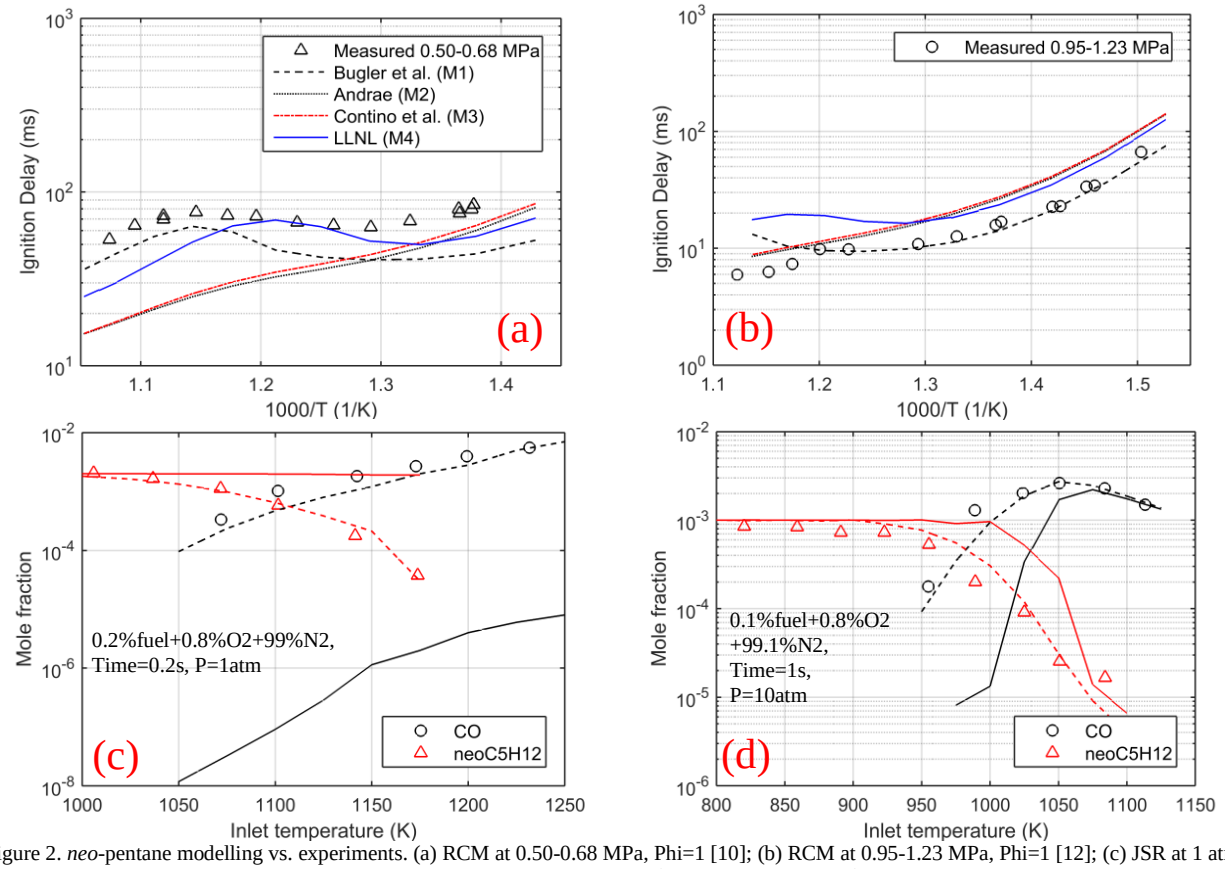


Figure 2. *neo*-pentane modelling vs. experiments. (a) RCM at 0.50-0.68 MPa, Phi=1 [10]; (b) RCM at 0.95-1.23 MPa, Phi=1 [12]; (c) JSR at 1 atm, Phi = 2; (d) JSR at 10 atm, Phi = 1 [15], dashed lines for M1 and solid lines for M4 in (c) and (d).

The four mechanisms were first compared against *neo*-pentane ignition delay times in RCMs, as shown in Fig. 2 (a) and (b). The NUI-G and LLNL mechanisms, M1 and M4 respectively, reproduced the overall negative temperature coefficient (NTC) behaviours in these RCMs. For M1, the discrepancy between the model and experiment in Fig. 2a is likely in part due to heat losses which were not considered in our modeling. As the pressure doubles from Fig. 2 (a) to 2 (b), the ignition delay becomes much shorter and the impact of heat losses should also become considerably smaller. This is consistent with the significant improvement between the model and experiment. On the other hand, mechanisms M2 and M3 fail to reproduce the NTC behaviours observed experimentally, and the similarity between these two mechanisms suggests that their C5 sub-mechanisms have the same origin.

The species profiles from the JSR are reproduced for M1 and M4 in Fig. 2 (c) and (d). M2 and M3 were not attempted due to their poor performances in the earlier RCM results. The mole fractions of the fuel and CO are shown as the major species in the reacting mixture. Excellent agreement is observed between M1 and the experimental results for the two species, at both 1 and 10 atm. However, M4 substantially under-predicts the reactivity of *neo*-pentane, showing the fuel consumption and CO formation two orders of magnitude lower than the experimental results.

It is evident from these results that M1 produced the best agreement with experiment among the four mechanisms compared.

## 3.2 *iso*-pentane

A comparison between the 4 mechanisms for *iso*-pentane is shown in Fig. 3. At these low temperatures (< 900 K) and elevated pressures (7-12 atm), M1 matched the experiments quite well and outperformed the other three mechanisms. The fact that M1 consistently under-predicts the experiment may again be due to our model not considering the heat losses. The LLNL mechanism M4 is the second best, whereas M2 and M3 were the poorest and again reproduced nearly identical results.

M1 and M4 were further compared for IDTs in shock tubes in Figs. 3 (c) and (d). The simulated IDTs here were defined using the criterion of maximum OH production rates, instead of a 400 K temperature rise, due to the highly diluted mixtures used. At high temperatures (> 1200 K) and low pressures (< 5 atm), M1 performs better than M4 in most cases, and the agreement between both mechanisms, in particular M1, is overall excellent. Note that IDTs in shock tubes are orders of magnitude shorter than those in RCMs; therefore heat loss should have a small impact on IDTs [17].

From comparing the IDT data, M1 is clearly the best among the four mechanisms for modeling *iso*-pentane oxidation. No species profile data have been found in the literature for *iso*-pentane.

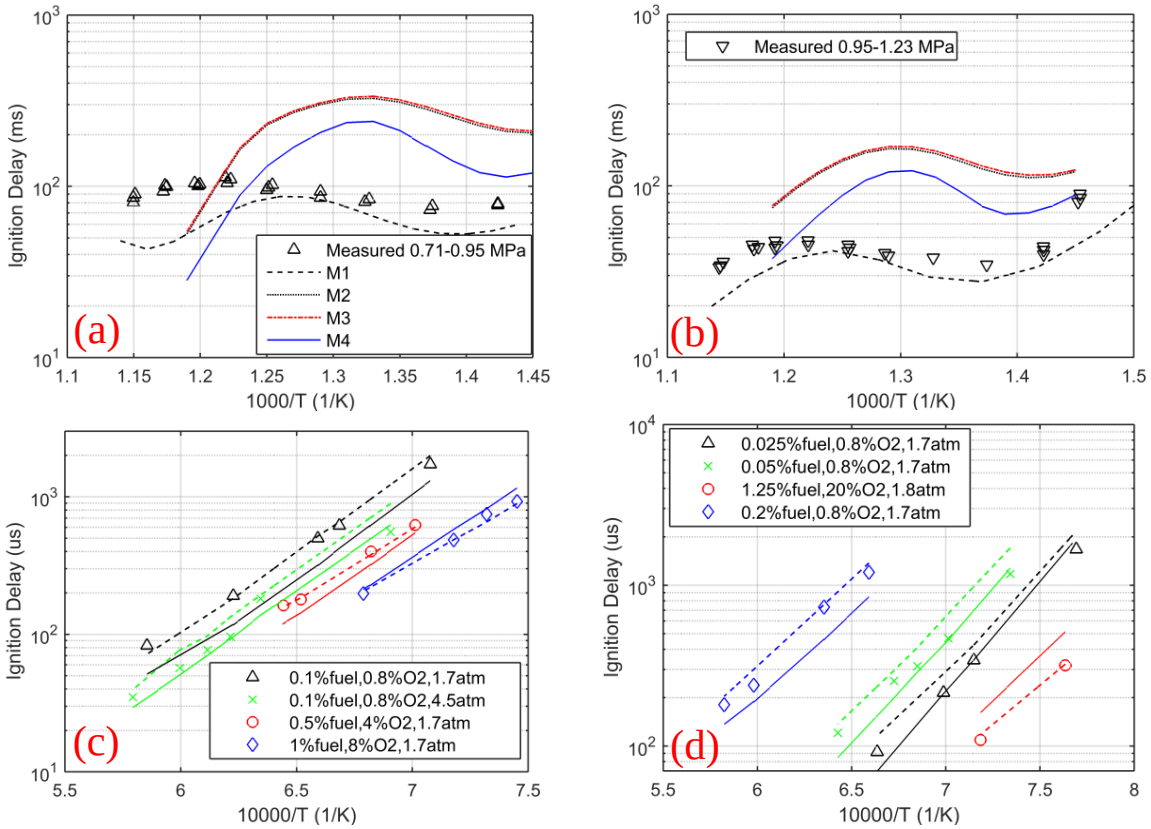


Figure 3. *iso*-pentane modelling vs. experiments. (a) RCM at 0.71-0.95 MPa, Phi=1, (b) RCM at 0.95-1.23 MPa, Phi=1 [12], (c) Shock tube at ~2 atm, Ar as diluent, (d) Shock tube at Phi=1, Ar as diluent [8], dashed lines for M1 and solid lines for M4 in (c) and (d).

### 3.3 *n*-pentane

*n*-Pentane is the most studied isomer of C5 alkanes. Figure 4 compares the four mechanisms against RCM (a, b), shock tube (c, d) and JSR results (e, f). Low pressure RCM results (Fig. 4a) show that the NTC behaviour of differing strengths are observed in all four mechanisms, and all are stronger than that observed experimentally. At 15-21 bar (Fig. 4b), all mechanisms over-predicted the IDTs in a RCM. Note that the modelled IDTs being longer than the measured (as observed in Fig. 4b) cannot be explained by the impact of heat loss, indicating that all *n*-pentane mechanisms needs further validation at these conditions.

Comparison against IDTs in shock tubes is further conducted for M1 and M4. Figures 4 (c) and (d) show a close match between the experiment and the M1 simulations, except for the ultra-high pressure cases (250 and 530 atm) which are not applicable to engine combustion. M1 also performs overall better than M4 under these high temperature conditions.

JSR species profiles modelled by M1 and M4 are compared in Fig. 4 (e) and (f). For a fuel rich case, both models under-predict the fuel reactivity, as evidenced by both having lower fuel consumption and CO formation than the experiment. In contrast, for a fuel lean case, both models substantially over-predict the fuel reactivity. This is demonstrated by a sudden drop in the fuel fractions and a sharp rise of $CO_2$ fraction at ~ 0.1 s residence time, indicating that the fuel oxidation was nearly completed by that moment. These simulated results are significantly different to that observed experimentally and are unlikely to be correct, since CO to CO2 reaction generally requires ~1500 K and the temperature of the JSR experiment was only 1000 K.

The above results indicate that the *n*-pentane mechanism in M1 overall works the best among the four mechanisms considered at high pressures and high temperatures. However, it still needs improvement at low temperatures (< 1000 K) and at substantially lean and rich equivalence ratios. Further study on identifying the chemistry responsible for these inconsistencies is currently being conducted.

## 5. Conclusion

Kinetic modelling of the oxidation of pentane isomers were conducted using four existing mechanisms and published experimental data from RCMs, shock tubes, and JSRs. Simulation results demonstrated that the NUI-Galway mechanism [1] overall produced the best results when compared to three other mechanisms. Agreement was particularly good for *neo*-pentane and *iso*-pentane. Significant differences with experiment were nonetheless observed for the ignition delay time for *n*-pentane at temperatures less than 1000 K and for JSR experiments at equivalence ratios of 0.2 and 2.

## 6. Acknowledgements

This research was supported by the Advanced Centre for Automotive Research and Testing (ACART, www.acart.com.au) and the Australian Research Council.

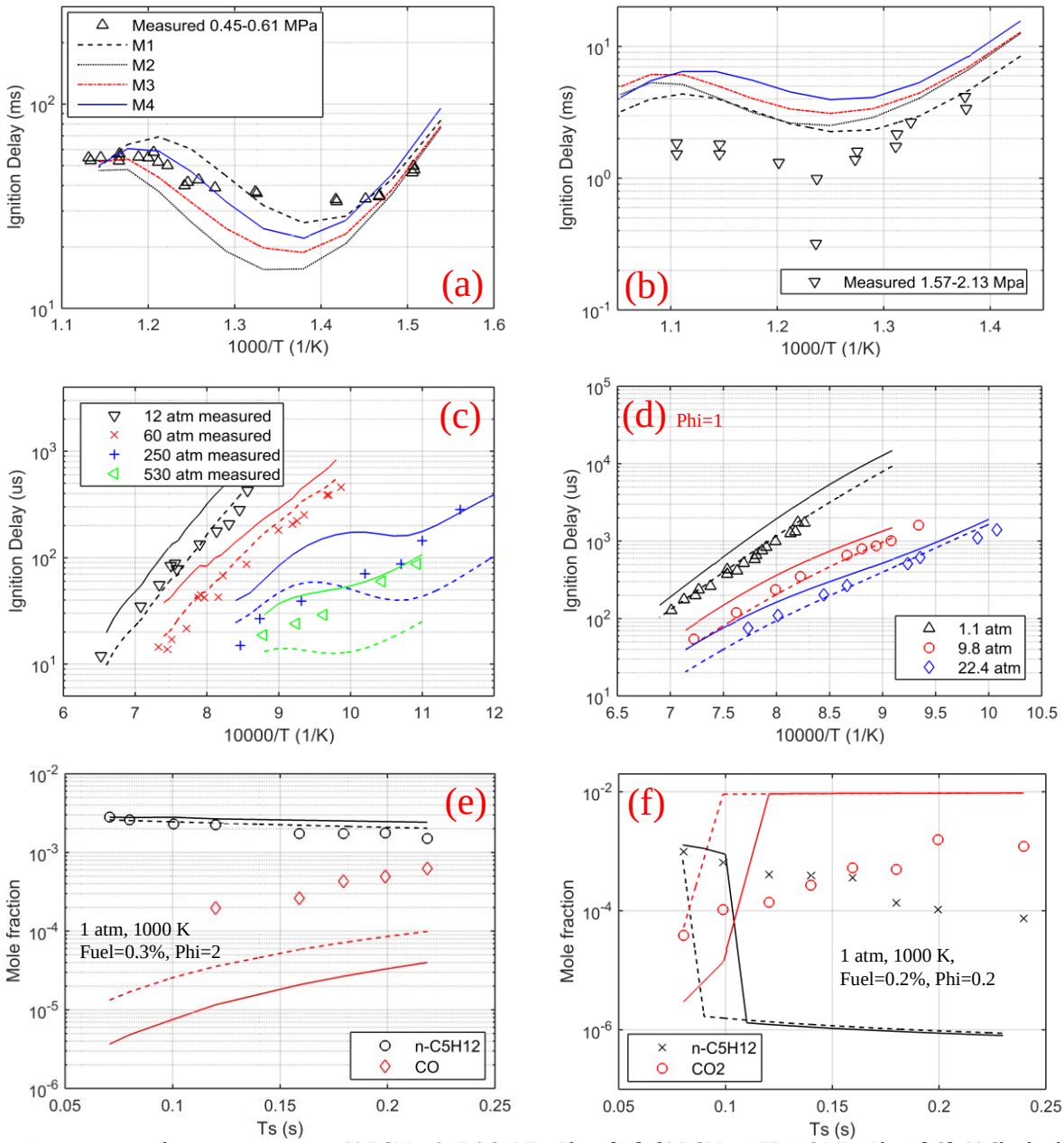


Figure 4. *n*-pentane simulation vs. experiments. (a) RCM at 0.45-0.61 MPa, Phi=1 [11], (b) RCM at 1.57-2.13 MPa, Phi=1 [13], (c) Shock tube at *n*-pentane:O2:N2:Ar=13:207:771:9 [18], (d) Shock tube at Phi=1 [7], (e) JSR at 1 atm, Phi=2, (f) JSR at 1 atm, Phi=0.2 [14], dashed lines for M1 and solid lines for M4 in (c)-(f).

## 7. Reference


[1] J. Bugler, K. P. Somers, E. J. Silke, H. J. Curran, The Journal of Physical Chemistry A 119 (28) (2015), pp. 7510-7527.

[2] P. Aleiferis, Z. Van Romunde, Fuel 105 (2013), pp. 143-168.

[3] A. A. May, N. T. Nguyen, A. A. Presto, T. D. Gordon, E. M. Lipsky, M. Karve, A. Gutierrez, W. H. Robertson, M. Zhang, C. Brandow, Atmospheric Environment 88 (2014), pp. 247-260.

[4] J. C. Andrae, Fuel 87 (10) (2008), pp. 2013-2022.

[5] F. Contino, F. Foucher, P. Dagaut, T. Lucchini, G. D'Errico, C. Mounaïm-Rousselle, Combustion and Flame 160 (8) (2013), pp. 1476-1483.

[6] M. Mehl, W. J. Pitz, C. K. Westbrook, H. J. Curran, Proceedings of the Combustion Institute 33 (1) (2011), pp. 193-200.

[7] B. Marks, O. Mathieu, R. Archuleta, E. Petersen, G. Bourque, in: 2012.

[8] M. Oehlschlaeger, D. Davidson, J. Herbon, R. Hanson, International journal of chemical kinetics 36 (2) (2004), pp. 67-78.

[9] C. K. Westbrook, W. J. Pitz, M. M. Thornton, P. C. Malte, Combustion and flame 72 (1) (1988), pp. 45-62.

[10] R. Minetti, M. Ribaucour, M. Carlier, L. R. Sochet, Combustion science and technology 113 (1) (1996), pp. 179-192.

[11] M. Ribaucour, R. Minetti, E. Sazhina, S. Sazhin, (2007).

[12] M. Ribaucour, R. Minetti, L. Sochet, H. Curran, W. Pitz, C. Westbrook, Proceedings of the Combustion Institute 28 (2) (2000), pp. 1671-1678.

[13] C. Westbrook, H. Curran, W. Pitz, J. Griffiths, C. Mohamed, S. Wo, Symposium (International) on Combustion, 27 (1) (1998), pp. 371-378.

[14] A. Chakir, M. Belumam, J. Boettner, M. Cathonnet, Combustion science and technology 77 (4-6) (1991), pp. 239-260.

[15] P. Dagaut, M. Cathonnet, Combustion and flame 118 (1) (1999), pp. 191-203.

[16] CHEMKIN-PRO 15131, Reaction Design: San Diego, 2013.

[17] H.-P. S. Shen, J. Vanderover, M. A. Oehlschlaeger, Combustion and Flame 155 (4) (2008), pp. 739-755.

[18] V. Zhukov, V. Sechenov, A. Y. Starikovskii, Combustion and flame 140 (3) (2005), pp. 196-203.

# Systematic Study for H Abstraction from Alkanes by Amine Radical ($NH_2$)

Kamal Siddique, [1] Mohammednoor Altarawneh*,[1] Jeff Gore[2] and Bogdan Z. Dlugogorski[1]
[1]School of Engineering and Information Technology, Murdoch University
90 South Street, Murdoch, WA 6150, Australia
[2]Dyno Nobel Asia Pacific Pty Ltd, Mt Thorley, NSW 2330, Australia

**Abstract**
This contribution studies the thermokinetic parameters pertinent to bimolecular gas phase reaction of alkanes with the amine ($NH_2$) radical at the CBS-QB3 level of theory. The $NH_2$ radical originates from the oxidation of ammonia and hydrogen cyanide in systems involving conversion of nitrogenous fuels, with important implications to atmospheric and combustion systems. The underlying reactions comprise abstraction of hydrogen atoms from methane, ethane, propane, *n*-butane, *i*-butane and 2-methylbutane by the $NH_2$ radical. The computed mechanistic and kinetic parameters (fitted in temperature range of 300- 2000 K) entail high level of accuracy and concur with the available experimental measurements. The calculated activation enthalpy or enthalpy barrier ($\Delta H^{\#}$) for the $CH_4 + NH_2$ reaction amounts to 50.1 kJ/mol, exceeding the enthalpy barriers for the abstraction of hydrogen attached to primary carbons in $C_2H_6$, $C_3H_8$, *n*-$C_4H_{10}$ and *i*-$C_4H_{10}$ that fall between 34 and 37 kJ/mol. The enthalpy barrier decreases to 25.1 kJ/mol and 24.9 kJ/mol for abstraction of hydrogen atoms from secondary carbons in *n*-$C_4H_{10}$ and $C_3H_8$, respectively. For hydrogen atoms attached to tertiary carbons in 2-methylbutane and *i*-butane, the activation enthalpies correspond to 18.2 kJ/mol and 18.8 kJ/mol, respectively, in line with weakening strength of the C-H bonds, compared with secondary C-H bonds in linear alkanes. The dissociation enthalpies of the weakest C-H bonds in alkanes trace a linear relationship with the activation enthalpy on the Evans-Polanyi plot, in the temperature range of 300 – 2000 K.

*Keywords: Enthalpy barrier, Transition state structure, Hydrocarbon, CBS-QB3, ChemRate*

## 1. Introduction

Reactions of $NH_2$ play a significant role in various combustion systems such as pyrolysis and oxidation of ammonia[1-2], oxy-steam combustion technology[3], coal nitrogen gasification[4] and oxidation of volatile nitrogen-bearing compounds in biomass.[5] $NH_2$-derived reactions assume central importance in $NO_x$ abatement technologies such as in the thermal DeNOx and NOxOUT processes.[6] In the aforementioned systems, $NH_2$ originates mainly from two pathways, oxidation of $NH_3$ and decomposition of HCN. Hydrogen cyanide (HCN) appears as a product when nitrogen atom forms part of an aromatic ring. Ammonia evolves when the nitrogen content exists in an amine form. Furthermore, the pyrolysis of fuel nitrogen gives off ammonia and cyanuric acid (HNCO).[7] Formation of $NH_2$ from oxidative decomposition of HCN proceeds via a complex reaction mechanism, summarised by the following reactions:

$$HCN + NCO \rightleftharpoons CN + HNCO$$
$$HNCO + H \rightleftharpoons NH_2 + CO$$

The direct abstraction of hydrogen atoms from alkanes by $NH_2$ produces ammonia and alkyl radicals. Literature reports numerous experimental measurements of the kinetic parameters, over a wide range of operational *T-P* conditions (300-3000 K, 0.4-93 kPa). For example, Hack et al.[8-9] operated an isothermal flow reactor equipped with a laser-induced fluorescence to measure histories of $NH_2$ consumption in a temperature range of 400 to 1080 K, for reactions of $NH_2$ with $CH_4$, $C_2H_6$, $C_3H_8$, *i*-$C_4H_{10}$, and cyclohexane. In another study, Hennig and Wagner[10] deployed the shock tube method to measure the reaction rate constant of $NH_2$ with methane, ethane, and propane at temperatures between 1500 and 2100 K. Demissy and Lesclaux[11] implemented flash photolysis employing laser-resonance absorption for detection of $NH_2$ that reacted with a series of alkanes at temperatures between 300 and 520 K.

In contrast to experimental work, the available theoretical analyses are scarce and limited to the reactions of $NH_2$ with few saturated hydrocarbons. Leory et al.[12] investigated the reaction of methane with $NH_2$ at the CL//UHF/6-31G level of theory. Another computational study employed UMP2, CCSD(T)//UMP2 and B3LYP approaches with 6-311++G(2d,p) basis set to examine the reaction of methane with $NH_2$.[13] Mebel and Lin[14] performed G2M computation of potential energy surfaces for alkanes ($CH_4$, $C_2H_6$, $C_3H_8$, and *i*-$C_4H_{10}$) reacting with $NH_2$. Their calculations comprised the H abstraction from secondary and primary sites to obtain rate constants in temperature range of 300-3000 K.

The current contribution reports accurate CBS-QB3 calculations of relative enthalpy for the

* Corresponding author: Mohammednoor Altarawneh
Phone: +61 8 9360 7507
Email: M.Altarawneh@Murdoch.edu.au

reactions of $NH_2$ with the complete series of $C_1$-$C_4$ alkanes and 2-methylbutane. In addition to the reactions considered by Mebel and Lin[14], we also explore the reaction of $NH_2$ with *n*-butane. As will be evident later, *n*-butane and *i*-butane exhibit different enthalpy barriers ($\Delta H^{\#}$).

$$CH_4 + NH_2 \rightarrow NH_3 + CH_3 \quad (R1)$$
$$C_2H_6 + NH_2 \rightarrow NH_3 + C_2H_5 \quad (R2)$$
$$C_3H_8 + NH_2 \rightarrow NH_3 + n\text{-}C_3H_7 \quad (R3a)$$
$$C_3H_8 + NH_2 \rightarrow NH_3 + i\text{-}C_3H_7 \quad (R3b)$$
$$n\text{-}C_4H_{10} + NH_2 \rightarrow n\text{-}C_4H_9 + NH_3 \quad (R4a)$$
$$n\text{-}C_4H_{10} + NH_2 \rightarrow i\text{-}C_4H_9 + NH_3 \quad (R4b)$$
$$i\text{-}C_4H_{10} + NH_2 \rightarrow i\text{-}C_4H_9 + NH_3 \quad (R5a)$$
$$i\text{-}C_4H_{10} + NH_2 \rightarrow t\text{-}C_4H_9 + NH_3 \quad (R5b)$$
$$C_5H_{12} + NH_2 \rightarrow C_5H_{11} + NH_3 \quad (R6)$$

The study has two aims: (i) to compute the reaction rate constants in terms of the Arrhenius parameters fitted over a temperature range of 300 - 2000 K, and (ii) to develop a relationship between the activation enthalpy and the bond dissociation enthalpy (BDH) for the title reactions at more accurate level of theory (CBS-QB3). The current analysis provides closer agreement with experimental values reported in literature, as compared to the previous systematic studies.

## 2. Calculation methods

We perform geometry optimisations, vibrational frequency calculations and total energy computations at the CBS-QB3 level of theory, as implemented in the Gaussian 09[15] suite of programs. The absence of imaginary frequencies verifies the true minima of reactants and products while a transition structure retains one, and only one, imaginary frequency along the specified reaction coordinate. The CBS method encompasses low-level, SCF and ZPE computations on large basis sets, mid-sized sets for second-order corrections, and small sets for high-level corrections. CBS employs the Møller–Plesset second-order energies, empirical and spin-orbit interaction corrections to extrapolate the results to the infinite basis set.[16] The ChemRate code facilitates calculations of reaction rate constants at the high-pressure limit according to the conventional transitional state theory. We quote all calculated activation and reaction enthalpies at 298.15 K. For $C_1$-$C_4$ alkanes, we have obtained bond dissociation enthalpies (BDHs) for hydrogen attached to primary, secondary, and tertiary carbons; the latter two, as allowed by the structure of alkane species. For 2-methylbutane, we have calculated H abstraction only from the tertiary carbon. The computed BDHs concur with the corresponding experimental values[17] to within 5.0 kJ/mol.

## 3. Results and discussion

### 3.1 Reaction dynamics

Figure 1 portrays the optimised transition structures of adducts of the selected alkanes with $NH_2$. Labels of the transition structures reflect the reactions enunciated in the introduction. Figure 2 depicts the schematic diagram of the potential energy profiles of the entire system. For methane (R1), the enthalpy barrier rises to 50.1 kJ/mol. Reaction R2 has an enthalpy barrier of 37.3 kJ/mol at 298.15 K. The BDH of the primary H-atom in ethane of 410.6 kJ/mol is weaker than that of methane of 429.9 kJ/mol. Our calculated activation enthalpy for the hydrogen abstraction in R2 decreases by 12.8 kJ/mol compared with the corresponding value for R1. This trend concurs with a higher exothermicity of R2 with respect to R1. The activation energies for R1 and R2 calculated at the G2MP2 method amount to 62.3 kJ/mol and 51.1 kJ/mol,[14] respectively. Clearly, our calculated CBS-QB3 values underestimate previous G2M-based theoretical values.

H abstraction from propane by $NH_2$ may involve primary and secondary C-H sites. Breaking of the C-H bond (for H attached to the secondary carbon) incurs lower BDH of 399.0 kJ/mol contrasted with the primary H-atom (413.2 kJ/mol). Reaction R3b that produces *i*-$C_3H_7$ displays elevated exothermicity in comparison to R3a that generates *n*-$C_3H_7$, justifying their corresponding enthalpy barriers. The enthalpy barrier of Reaction R3b attains a value of 24.9 kJ/mol, i.e., lower by 10 kJ/mol than that of Reaction R3a. Mebel and Lin[14] reported activation enthalpies for reactions R3a and R3b of 29.0 kJ/mol and 25.9 kJ/mol. These values somewhat underestimate the analogous values computed herein of 34.9 kJ/mol and 24.9 kJ/mol, correspondingly.

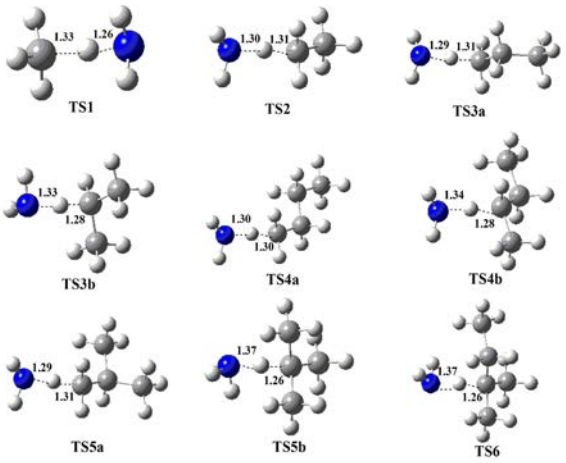


Figure 1. Optimised (CBS-QB3) geometries of the transition states for the reactions of the $NH_2$ radical with alkanes. Distances are in Å.

Similarly to propane, reactions of *n*-$C_4H_{10}$ with $NH_2$ proceed via H abstraction from primary and secondary carbon atoms. The BDH value of primary C-H bond in *n*-$C_4H_{10}$ overshoots that of a secondary C-H bond by 15.6 kJ/mol, resulting in elevated exothermicity of Reaction R4b in comparison to R4a. The strengths of C-H bonds for secondary and primary carbons agree with the literature values. The activation enthalpy associated with Reaction R4a surpasses that for R4b by 9.4 kJ/mol.

Furthermore, the reactions of $NH_2$ with *i*-$C_4H_{10}$ ensue by two exit channels: (i) the H abstraction from a primary and (ii) tertiary C−H bonds. The BDH of the tertiary H-atom in *i*-$C_4H_{10}$ is weaker than that of the primary atom, resulting in the higher exothermicity of the R5b channel as compared to the R5a corridor. Our BDH for tertiary C−H bond in *i*-$C_4H_{10}$ (386.9 kJ/mol) compares well with the analogous theoretical and experimental values of 397.5 kJ/mol reported in the literature.[17] The enthalpy barriers attain 35.1 kJ/mol and 18.8 kJ/mol at 298.15 K for Reactions R5a and R5b, respectively. For comparison, Demissy and Lesclaux reported equivalent experimental values at room temperature as 25.5 kJ/mol and 20.5 kJ/mol.[11] The G2M (rcc, MP2) activation barriers amount to 51.8 kJ/mol and 34.7 kJ/mol, correspondingly, for the same reactions.[14]

H abstraction from the tertiary carbon in 2-methylbutane requires an activation enthalpy similar to that of R5b. Reaction R5b is associated with the more reactant-like transition state among all located transitions states. This transition state exhibits the shortest length of the breaking C−H bond (1.26 Å) and the longest length of the forming N−H bond (1.37 Å). Overall, geometries of transition structures remain insensitive to the size of the carbon chain in alkanes.

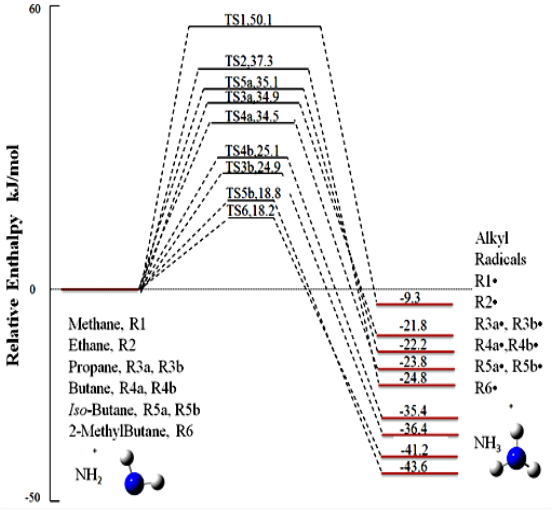


Figure 2. Schematic diagram of the relative enthalpies for the systems of $NH_2$ + alkanes. Enthalpies are obtained from the CBS-QB3 calculations.

## 3.2. Reaction kinetics

ChemRate software served to predict the rate constants for the abstraction of hydrogen by $NH_2$, over a temperature range from 300 K to 2000 K at the high-pressure limit. Overall, our estimated reactions rate constants remain in good agreement with the analogous values in literature. Table 1 assembles the Arrhenius parameters for the title reactions. Our calculated rate constants match reasonably well the relevant values reported in literature. For instance, for Reaction R1, our rate expression appears as $k = 1.21\times10^{-11}$ exp(-64900/(*RT*)) cm$^3$ s$^{-1}$ molecule$^{-1}$, i.e., in close agreement with the theoretically fitted rate constant of Mebel and Lin[14] at $k = 2.77\times10^{-11}$ exp(-55700/(*RT*)) cm$^3$ s$^{-1}$ molecule$^{-1}$. Hennig and Wagner[10] obtained $k = 1.99\times10^{-11}$ exp(-63400/(*RT*)) cm$^3$ s$^{-1}$ molecule$^{-1}$ from the shock tube experiments for Reaction R1, for temperatures between 1500 and 2100 K. Demissy and Lesclaux[11] estimated a rate constant of $k = 8.30\times10^{-13}$ exp(-43900/(*RT*)) cm$^3$ s$^{-1}$ molecule$^{-1}$ for the low temperature range of 300 to 520 K.

For Reaction R2, the theoretically estimated[14] rate constant $k = 1.54\times10^{-11}$ exp(-40700/(*RT*)) cm$^3$ s$^{-1}$ molecule$^{-1}$ concurs well with our expression of $k = 3.39\times10^{-11}$ exp(-52400/(*RT*)) cm$^3$ s$^{-1}$ molecule$^{-1}$. Hennig and Wagner,[10] using the same experimental setup for Reaction R2 as for Reaction R1, for temperatures between 1500 and 2100 K, reported $k = 1.61\times10^{-11}$ exp(-47900/(*RT*)) cm$^3$ s$^{-1}$ molecule$^{-1}$. Finally, Demissy and Lesclaux[11] estimated a rate constant of $k = 6.14\times10^{-13}$ exp(-29900/(*RT*)) cm$^3$ s$^{-1}$ molecule$^{-1}$ for the low temperature range of 300 to 520 K. Overall, The estimated activation energies from experiments [8,9,10,11] fitted in the range 600–2000 K display a good agreement with values calculated herein, if compared with analogous theoretical values reported in previous investigations.

Table 1. Rate parameters for the abstraction reactions, between 300 and 2000 K. Values of the Arrhenius parameters (*A* and $E_a$) are in units of cm$^3$ s$^{-1}$ molecule$^{-1}$ and J mole$^{-1}$; $k = A$ exp(-$E_a$/(*RT*)).

| Reaction | Transition state | *A* | $E_a$ |
|---|---|---|---|
| R1 | TS1 | $1.21\times10^{-11}$ | 64900 |
| R2 | TS2 | $3.39\times10^{-11}$ | 52400 |
| R3a | TS3a | $5.96\times10^{-12}$ | 49800 |
| R3b | TS3b | $4.46\times10^{-12}$ | 39900 |
| R4a | TS4a | $2.24\times10^{-12}$ | 49800 |
| R4b | TS4b | $2.50\times10^{-12}$ | 40700 |
| R5a | TS5a | $1.96\times10^{-12}$ | 49800 |
| R5b | TS5b | $3.56\times10^{-12}$ | 34900 |
| R6 | TS6 | $7.34\times10^{-13}$ | 34000 |

### 3.3. Evans-Polanyi Correlation

Figure 3 elucidates a correlation between BDHs and activation enthalpy ($\Delta H^{\#}$). The rate of H abstraction generally depends on bond strengths (as expressed by BDH) undergoing the fission process. We found a linear correlation between $\Delta H^{\#}$ and BDHs for a series of analogous reactions. For a certain attacking radical X, the same X-H bond forms in all reactions. Therefore, the Evans-Polanyi assumes a linear relationship in the form of

$$\Delta H^{\#} = \alpha\,[\mathrm{BDH}_{298\mathrm{K}}\,(\mathrm{C\text{-}H}) + C]$$

where $\alpha$ and $C$ denote constants.[11]

The activation enthalpies of H abstractions from alkanes by $NH_2$ correlate with the relevant BDHs. The least square slope coefficient lies within the expected range for the Evans-Polanyi plots (0.0-1.0). The present Evans-Polanyi plot affords estimation of the activation enthalpy for the reaction of $NH_2$ with other hydrocarbons not reported herein.

## Conclusion

The calculated enthalpy barrier ($\Delta H^{\#}$) for $CH_4$ + $NH_2$ rises to 50.1 kJ/mol, exceeding the barriers for the removal of primary H atoms from other alkanes, such as $C_2H_6$, $C_3H_8$, *n*-$C_4H_{10}$ and *i*-$C_4H_{10}$. The enthalpy barrier reduces to 25.1 kJ/mol and 24.9 kJ/mol for H abstraction from secondary C-H bond in *n*-$C_4H_{10}$ and $C_3H_8$, respectively. For the hydrogen placed on the tertiary carbon in $C_5H_{12}$ and *i*-$C_4H_{10}$ molecules, the enthalpy activation barrier declines to 18.2 kJ/mol and 18.8 kJ/mol, correspondingly, in line with the decreasing strength of the relevant C-H bonds. The trends in the computed kinetic parameters reflect those of the bond dissociation enthalpies (BDHs), following the decreasing order of tertiary > secondary > primary. The rate of the abstraction of hydrogen increases from primary carbon to the tertiary carbon of the C1-C4 alkane chain. The current study well compares the thermokinetic parameters with the experimentally reported values in the literature.

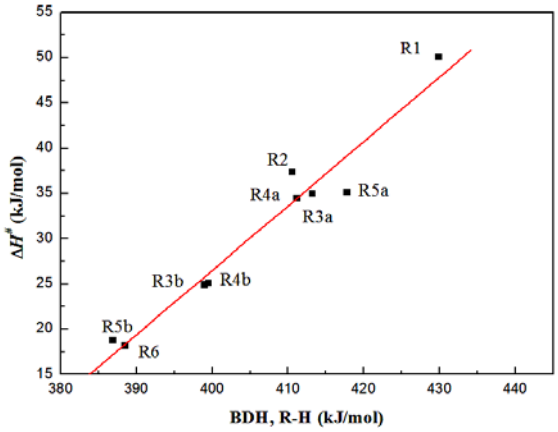


Figure 3. Evan-Polanyi plot for the H abstraction reaction $NH_2$ + R-H → $NH_3$ + $R^{*}$.


## Acknowledgements

This study was funded by the Australian Research Council and supported by grants of computing time from the National Computational Infrastructure (NCI), Canberra, Australia and the Pawsey Supercomputing Centre, Perth, Australia. K.S. thanks Anam Saeed for helpful comments.


## References


[1] I. Rahinov, N. Ditzian, A. Goldman and S. Cheskis, Appl. Phys. B. **77** (5) (2003), pp. 541-546.

[2] J.A. Miller, M.D. Smooke, R.M. Green and R.J. Kee, Combust. Sci. Technol. **34** (1-6) (1983), pp. 149-176.

[3] C. Zou, Y. He, Y. Song, Q. Han, Y. Liu, F. Guo, C. Zheng, Fuel **158** (2015), pp. 874-883.

[4] L.J. Mckenzie, F.J. Tian, C.Z. Li, Environ Sci Technol. **41** (2007), pp. 5505–5509.

[5] T. Mendiara and P. Glarborg, Combust. Flame **156** (10) (2009), pp. 1937-1949.

[6] M.T. Javed, N. Irfan and B.M. Gibbs, J. Environ. Manage. **83** (3) (2007), pp. 251-289.

[7] P. Glarborg, A.D. Jensen and J.E. Johnsson, J. Environ. Manage. **83** (3) (2003), pp. 251-289.

[8] J. Ehbrecht, W. Hack, P. Rouveirolles and H.G. Wagner, Ber. Bunsenges. Phys. Chem. **91** (7) (1987), pp. 700-708.

[9] W. Hack, H. Kurzke, P. Rouveirolles and H.G. Wagner, Ber. Bunsenges. Phys. Chem. **90** (12) (1986), pp. 1210-1219.

[10] G. Hennig and H.G. Wagner, Ber. Bunsenges. Phys. Chem. **99** (6) (1995), pp. 863-869.

[11] M. Demissy and R. Lesclaux, J. Am. Chem. Soc. **102** (9) (1980), pp. 2897-2902.

[12] G. Leroy, M. Sana, A. Tinant, Can. J. Chem. **63** (7) (1985), pp. 1447-1456.

[13] H. Basch and S. Hoz, J. Phys. Chem. A. **101** (24) (1997), pp. 4416-4431.

[14] A.M. Mebel and M.C. Lin, J. Phys. Chem. A. **103** (13) (1999), pp. 2088-2096.

[15] M.J. Frisch, G.W. Trucks, H.B. Schlegel, G.E. Scuseria, M.A. Robb, J.R. Cheeseman, G. Scalmani, V. Barone, B. Mennucci, G.A. Petersson,; et al. Gaussian 09, revision A.1., Gaussian, Inc., Wallingford, CT, 2009.

[16] R. Casasnovas, J. Frau, J.O. Castro, A. Salva, J. Donoso and F. Munoz, Int. J. Quant. Chem.**110** (2) (2010) , pp. 323-330.

[17] Y.R. Lou, Handbook of Bond Dissociation Energies in Organic Compounds, Taylor & Francis, 2002, pp. 20-22.

[18] W. Hack, H. Kurzke, P. Rouveirolles, H. G. Wagner, Proc. Combust. Inst. **21** (1) (1998), pp 905-911.

[19] Y.X Yu, S.M. Li, Z.F. Xu, Z.S. Li, C.C. Sun, Chem. Phys. Lett. **302** (3–4) (1999), pp. 281-287.

**Proceedings of the Australian Combustion Symposium**
**December 7-9, 2015, The University of Melbourne**

# Reactions of SH radical with $C_1$-$C_4$ Hydrocarbons

Zhe Zeng,[1] Mohammednoor Altarawneh[*,1] Bogdan Z. Dlugogorski[1]
[1] School of Engineering and Information Technology
Murdoch University, WA 6150 Australia

**Abstract**

This study investigates H abstraction reactions from $C_1$-$C_4$ hydrocarbons by SH radicals. H abstraction from the weakest C-H site in alkenes and alkynes are noticeably exothermic and irreversible, whereas H abstractions from primary and secondary sites in alkanes are endothermic with shallow reverse barriers. This finding prompts two remarks: (i) the well-documented inhibition effect of $H_2S$, on oxidation of alkanes, does not apply to alkenes and alkynes; and, (ii) the activity of $H_2S$ and its SH radical (inhibition versus promotion) during combustion of hydrocarbons depends on the reversibility of the H abstraction process. An alkyl radical readily abstracts an H atom from $H_2S$, whereas the analogous process for alkenes and alkynes proceeds in the reverse direction; i.e., SH abstracts an H atom from an alkene or alkyne, generating alkenyl or alkynyl radical. The Evans-Polanyi plots display linear correlations between the bond dissociation enthalpies of the abstracted hydrogens and the relevant activation energies, for the three groups of hydrocarbons. In the case of methane, we have demonstrated that, the reactivity of SH radicals towards abstracting H atoms exceeds that of $HO_2$ but falls below those of OH and $NH_2$ radicals.

*Keywords: H abstraction, HS· radical, reaction activity, Evans-Polanyi relationship*

## 1. Introduction

Hydrogen sulfide ($H_2S$) exists as a major impurity in natural gas and crude oil. Pipeline-quality natural gas typically contains 2000 ppm of sulfur species, in which the $H_2S$ constitutes the predominant sulfur carrier [1]. At higher temperature (above 603 K), $H_2S$ inhibits the oxidation of hydrocarbons, as reported by Nguyen et al. [2, 3] who studied the thermal pyrolysis of *n*-octane and $H_2S$ mixtures at 70 MPa, and by Selim et al. who reported the effect of $H_2S$ additive to $H_2$/air and $CH_4$/air flames [4, 5]. However, the literature presents no details of the interaction between $H_2S$ and hydrocarbons, and the $H_2S$ inhibition mechanism remains open to speculations. Along the same line of enquiry, sulfur oxides ($SO_x$) represent potent inhibitors for gas-phase reactions. These species act as scavengers for O/H radical, and subsequently slow down the active reaction sequence [6, 7].

A pioneering study of Gray et al. [8] employed photolysis of azomethane to produce methyl radicals to react with $H_2S$. A methyl radical readily abstracts an H atom from $H_2S$ in Reaction R1 at a rate constant of $k(T) = 8.32 \times 10^{-14} \cdot \exp(-14\,600/T)$ $cm^3 \cdot molecule^{-1} \cdot s^{-1}$. While another experimental work by Perrin D. et al. found that a HS radical can extract one H from 2-(Z)-$C_5H_{10}$ to form $H_2S$ at a rate constant of $k(T) = 7.77 \times 10^{-14} \cdot \exp(-101/T)$ $cm^3 \cdot molecule^{-1} \cdot s^{-1}$.[9]

$$CH_3 + H_2S \rightarrow CH_4 + SH \qquad (R1)$$

To the best of our knowledge, literature provides no experimental or theoretical measurements for reactions of $H_2S$ or its SH radical with other alkanes, alkenes or alkynes.

While oxidation of hydrocarbons commences with abstraction of H atoms by the O/H radical pool, the presence of appreciable concentrations of SH (e.g., in natural gas processed at elevated temperatures) could contribute to the overall oxidation mechanism of the relevant hydrocarbons. For this reason, we investigate the reactivity of SH radicals with all $C_1$-$C_4$ hydrocarbons, with only typical results described in this contribution. We limit our analysis to the initial H abstraction step from hydrocarbons, i.e., by investigating the backward pathway in Reaction R1. From a kinetic perspective, we report rate constants for the generic reaction ($RH + SH \rightarrow R + H_2S$) and plot Evans-Polanyi curves to relate the dependence of the estimated activation energies on the dissociation enthalpies of the relevant C-H bonds. Finally, we comment on the relatively slow rates of H abstractions by SH radicals, by examining the corresponding bimolecular reactions of other radicals, namely OH, $HO_2$ and $NH_2$.

## 2. Calculation Methods

All structure optimisations and enthalpy calculations were conducted with the Gaussian 09 suite of programs [10], at the composite CBS-QB3 level of theory [11]. The CBS-QB3 based calculations produce reliable results for H-abstraction reactions in gas phase. For instance, a concise study of Pokon et al. compared reactions and activation enthalpies predicted by the CBS-QB3 methodology with those obtained experimentally or theoretically (but at other levels of theory), to demonstrate an accuracy of 8.4 kJ/mol [12]. We further confirm the identity of each transition structure by performing intrinsic reaction coordinates

*Phone: (+61) 8 9360-7507
E-mail: *M.Altarawneh@Murdoch.edu.au

(IRC) calculations to link each transition state with its corresponding reactants and products.

The ChemRate program deployed the classical transition state theory (TST) [13] to obtain the reaction rate constants. We then fitted, in the least-square sense, the Arrhenius rate parameters $E_a$, $A$, and $n$ in the form of:

$$k=A\cdot T^{n}\cdot\exp(-E_a/RT)$$

in the temperature range from 300 to 2000 K, to the calculated reaction rate constants.

## 3. Results and Discussion

### 3.1 H abstraction from alkanes

Before presenting the results for the title reactions, we first inspect the transition structure and the activation barrier for abstraction of an H atom from methane:

$$CH_4 + SH \rightarrow CH_3 + H_2S \qquad (R2)$$

Figure 1 illustrates the geometry of the transition state for Reaction R2. In this structure, the distance between the C atom and the dissociated H atom increases to 1.64 Å, while the distance between the H and S atom achieves 1.44 Å. As indicated in Fig. 2, the activation enthalpy of Reaction R2 attains a value of 65.9 kJ/mol at 298.15 K, whereas the enthalpy of the reaction products ($CH_3$ + $H_2S$) exceeds that of the reactants ($CH_4$ + SH) by 56.1 kJ/mol. This means that, the reverse reaction (R1) prevails over the forward reaction (R2), concurring with the experimental results of Gray et al. [8]. Table 1 compares the calculated kinetic parameters of Reaction R1 with the experimental measurements. The reaction rate corresponds to $5.12 \times 10^{-14}$ cm$^3$·molecule$^{-1}$·s$^{-1}$ at 423 K, in a relatively good agreement with the equivalent experimental value of $2.63 \times 10^{-15}$ cm$^3$·molecule$^{-1}$·s$^{-1}$.

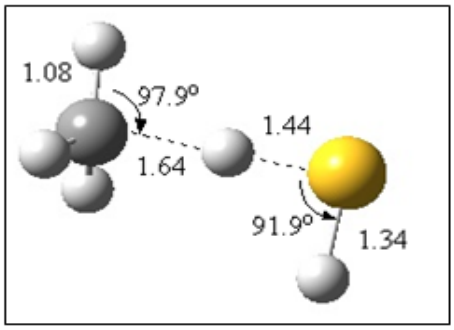


Fig.1 Geometry of the TS of $CH_4$ + SH reaction. Distances are in Å and angles in degrees.

Table 1. Arrhenius parameters fitted between 372 and 444 K for Reaction R1, $k=A\cdot\exp(-E_a/RT)$ for experimental measurements and theoretical calculations.

| Reaction | $A$ (cm$^3$·molecule$^{-1}$·s$^{-1}$) | $E_a$ (kJ/mol) | Ref. |
|---|---|---|---|
| **R1** | $8.32 \times 10^{-14}$ | 12.1 | [8] |
| **R1** | $6.31 \times 10^{-12}$ | 17.0 | This work |

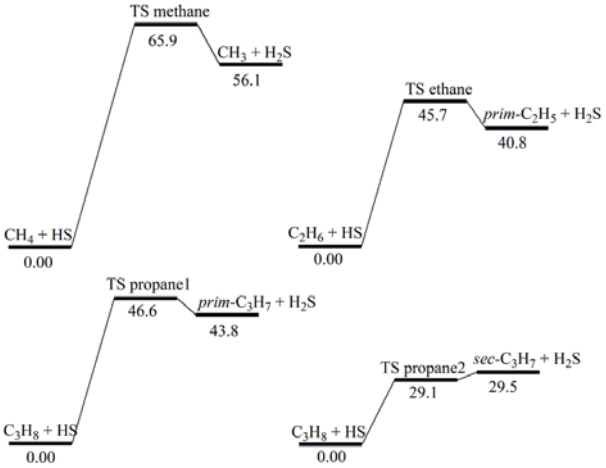


Fig. 2 Potential energy surface of $C_1$-$C_3$ alkanes + SH radical, computed at CBS-QB3 level of theory. Enthalpies are in kJ/mol at 298.15 K.

H abstractions from primary sites in ethane, and propane display similar reaction and activation enthalpies. As these reactions are considerably endothermic with a shallow reverse barrier, the backward reaction dominates over the forward channel, with insignificant formation of $H_2S$ and $CH_3$ (e.g., less than 1 % conversion at temperatures below 700 K). Rather, alkyl radicals ($CH_3$, $C_2H_5$, $C_3H_7$ and $C_4H_9$) readily abstract H atoms from $H_2S$ to produce alkane molecules and SH radicals. For $C_2H_5$ and *prim*-$C_3H_7$, trivial activation barriers amount to 4.90 kJ/mol and 2.87 kJ/mol at 298.15 K. For the remaining alkyl radicals, the reaction proceeds via a negligible-barrier or even barrierless process (e.g. *sec*-$C_3H_7$). Table 2 lists the Arrhenius parameters for the forward and reverse reactions for H abstractions from the primary sites in the three $C_1$- $C_3$ alkanes.

### 3.2 H abstraction from alkene and alkyne

Prior to analysing reactions between SH radical and unsaturated hydrocarbons (alkenes, alkynes), we conduct calculations of bond dissociation enthalpies (BDH) to locate the weakest C-H bonds in these species. This approach is reasonable, as SH radical attacks first the weakest C-H bonds in alkenes and alkynes. In Fig. 3, we present the calculated PES for propene, 1-butene, *iso*-butene, allene, propyne and 1-butyne. All illustrated reactions comprise the abstraction of H atoms from the weakest C-H bond in each molecule. As opposed to alkanes, these reactions proceed with plausible activation barriers, resulting in the enthalpy of separated products lying significantly below that of the reactants. For 1-butene, the reaction incurs a trivial activation enthalpy of 1.80 kJ/mol and -39.4 kJ/mol for enthalpy change. The activation barriers rise to 16.7 kJ/mol and 13.0 kJ/mol, for propene and 1-butyne, respectively. But for *iso*-butene, allene and propyne, the reactions are slower with higher activation enthalpies of 39.8 kJ/mol, 35.5 kJ/mol and 34.7 kJ/mol, correspondingly. Table 3 assembles the fitted Arrhenius parameters, *Ea*, *A*, and *n*.

Table 2. Arrhenius parameters fitted between 300 and 2000 K (100 K interval) for alkane + SH radical, $k=A\cdot T^{n}\cdot\exp(-E_a/RT)$. Both forward and backward reactions are included.

| Reaction | $\log_{10}A$ ($cm^3\cdot molecule^{-1}\cdot s^{-1}$) | $n$ | $E_a$ (kJ/mol) |
|---|---|---|---|
| $CH_4$ +HS → $CH_3$ + $H_2S$ | $6.92\times10^{-22}$ | 3.91 | 61.2 |
| $CH_3$ + $H_2S$ → $CH_4$ + HS | $4.57\times10^{-22}$ | 3.52 | 4.9 |
| $C_2H_6$ + HS → $C_2H_5$ +$H_2S$ | $4.37\times10^{-22}$ | 3.41 | 42.2 |
| $C_2H_5$ + $H_2S$→ $C_2H_5$ + $H_2S$ | $5.89\times10^{-23}$ | 3.06 | 1.09 |
| $C_3H_8$ + HS → *prim*-$C_3H_7$ + $H_2S$ | $8.51\times10^{-22}$ | 3.39 | 43.2 |
| *prim*-$C_3H_7$ + $H_2S$ → $C_3H_8$ + HS | $5.25\times10^{-22}$ | 2.74 | 0.41 |

## 3.3 Relationship between BDH and activation energy of reactions of SH + hydrocarbon

To explain the difference in H abstraction from alkane and alkene/alkyne with an SH radical, we introduce the Evans-Polanyi plots, as illustrated in Fig. 4. The activation energies for the reaction between hydrocarbons and SH form a linear relationships with the BDH of the weakest C-H bond. In the three cases, a linear relationship prevails between the BDH and the activation energy, with separate lines for alkanes, alkenes and alkynes. In the next sections, we highlight some insights prompted by the analysis of the Evans-Polanyi plots, by answering why we have different linear fits for alkane, alkene and alkyne, separately.

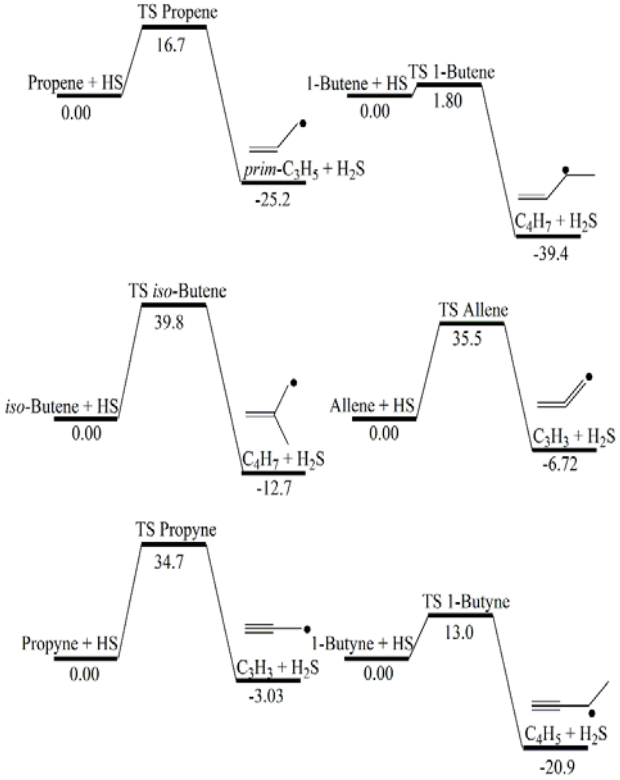


Fig. 3 Potential energy surface for alkene/alkyne (propene, 1-butene, *iso*-butene, allene, propyne, 1-butyne) + SH reaction, computed at CBS-QB3 level of theory. H atom is abstracted from weakest C-H, as illustrated by the product radicals. Values of relative enthalpy at 273.15 K, are in kJ/mol.

Table 3. Fitted Arrhenius parameters between 300 and 2000 K for alkene/alkyne + SH radical, $k=A\cdot T^{n}\cdot\exp(-E_a/RT)$.

| Reaction | $A$ ($cm3\cdot molecule^{-1}\cdot s^{-1}$) | $n$ | $E_a$ (kJ/mol) |
|---|---|---|---|
| Propene + HS → $C_3H_3$ + $H_2S$ | $2.00\times10^{-24}$ | 3.79 | 9.91 |
| 1-Butene + $H_2S$ → $C_4H_7$ +HS | $2.19\times10^{-23}$ | 3.40 | 0.43 |
| *iso*-Butene + HS → $C_4H_7$ +HS | $2.69\times10^{-22}$ | 3.32 | 36.5 |
| Allene + $H_2S$ → $C_3H_3$ + $H_2S$ | $2.51\times10^{-22}$ | 3.37 | 30.2 |
| Propyne + HS → $C_3H_3$ + $H_2S$ | $2.24\times10^{-21}$ | 3.36 | 29.1 |
| 1-butyne + $H_2S$ → $C_4H_5$ + HS | $1.10\times10^{-22}$ | 3.32 | 8.01 |

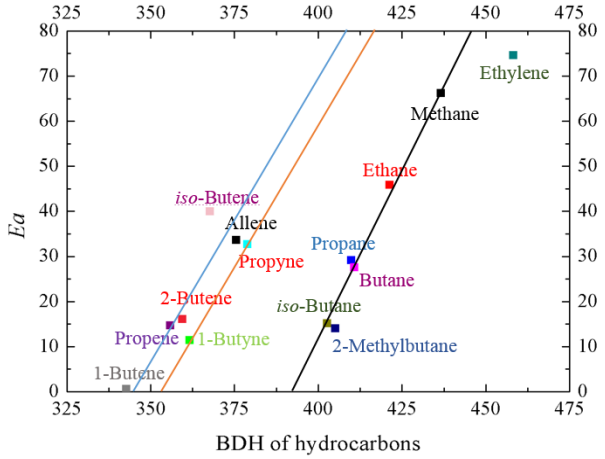


Fig. 4 Evans-Polanyi plots (activation energy of SH + hydrocarbons versus BDHs of the weakest C-H bonds in hydrocarbon molecules). All numbers are in kJ/mol at 298.15 K.

The orbital hybridisation in double and triple bonded carbon leads to strong C-H bonds on the unsaturated C atoms. For example, all H atoms of ethylene rest on unsaturated carbon atoms. This results in higher BDH if compared with other unsaturated hydrocarbons that comprise saturated carbon atoms in their structure. A hydrogen atom attached to such a carbon displays much weaker BDH. More orbital overlap for unsaturated C clearly weakens the C-H bond on the saturated C, resulting in lower BDH for the remaining alkenes and alkynes compared to alkanes. This explains why the weakest C-H bond for alkenes and alkynes occur on the saturated carbon vicinal to an unsaturated carbon. Ethylene has no saturated carbon, which renders it an exception in the Evan-Polanyi plots.

Due to weaker primary/secondary C-H bonds in alkenes and alkynes, such as that in 1-butene, the SH radical abstracts an H from these locations in unsaturated hydrocarbons more readily than from the two corresponding hydrogen sites in alkanes. Based on our kinetic analysis, we report that, the forward reaction predominates for alkenes and alkynes whereas the backward process governs the reactions involving alkanes.

The following linear relationships arise separately for alkanes, alkenes and alkynes. The three lines look

parallel to each other. It might be due to they share SH to dissociate the corresponding C-H bond. Small errors in $E_a$ explain slight differences in the slopes.

$E_a$ (alkane) = -614.69 + 1.56 × BDH
$E_a$ (alkene) = -511.36 + 1.49 × BDH
$E_a$ (alkyne) = -525.15+ 1.47 × BDH

### 3.4 Activity of SH compared with those of OH, $NH_2$ and $HO_2$

In this section, we compare the reactivity of SH radical toward H abstraction, as calculated in the present study, with that of $NH_2$, OH and $HO_2$ from literature. Figure 5 contrasts the rate constants for H abstraction from methane by all four radicals. Interestingly, H abstraction from methane by SH and $NH_2$ radicals display overlapping rate constants. Theoretical calculations by Mebel and Lin yielded 60.2 kJ/mol as the activation energy for the reaction $CH_4 + NH_2 \rightarrow CH_3 + NH_3$ [14]; i.e., very close to the value of 61.2 kJ/mol calculated herein for the reaction involving SH rather than $NH_2$. Abstraction by OH and $HO_2$ radicals incurs the fastest and the slowest reaction rates, respectively [15, 16]. The reaction of $NH_2 + CH_4 \rightarrow NH_3 + CH_3$ proceeds predominantly in the forward direction, in contrast to the analogous reaction involving SH. The $HO_2$ radical seems inactive with a reported activation barrier of 87.9 kJ/mol. Thus, we conclude that, the radical activity follows the order of: OH > $NH_2$ > HS > $HO_2$.

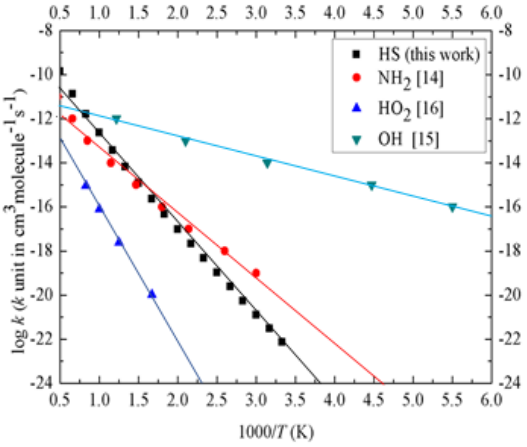


Fig. 5 Rate constants for H abstraction from $CH_4$ by SH, $NH_2$, $HO_2$ and OH radicals, units of $k$ are in $cm^3 \cdot molecule^{-1} \cdot s^{-1}$. Results are taken from this work (SH + $CH_4$) and literatures ($NH_2$/$HO_2$/OH + $CH_4$).

While elucidating explanations for the observed reactivity sequence seems to be out of scope of the current work, it is stimulating to note that, this ordering follows the bond strengths of the freshly formed O-H, N-H and S-H bonds. For example, the S-H bond is weaker than O-H and N-H bonds and hence OH and $NH_2$ are more effective in abstracting H atom from the hydrocarbon chain. Along the same line of enquiry, the O-H bond in $H_2O_2$ constitutes the weaker bond justifying its low reaction activity.

## 4. Conclusions

This contribution reported thermokinetic parameters for reactions of SH radicals with $C_1$-$C_4$ hydrocarbons. The inhibition effect of $H_2S$ on oxidation of alkanes stems from the facile abstraction of an atom from $H_2S$ by alkyl radicals. The presence of weaker C-H bonds in alkenes and alkynes forces the overall reaction to proceed in the forward direction; i.e. formation of $H_2S$ and an alkenyl or alkynyl radical. We discovered a linear relationship between activation energies and bond dissociation enthalpies of the attacked C-H sites. By studying the H abstraction from methane, we compared the reactivity of the HS radical with that of OH, $HO_2$ and $NH_2$ radicals to obtain the following reactivity sequence: OH > $NH_2$ > HS > $HO_2$.

## 5. Acknowledgments

This study has been supported by grants of computing time from the National Computational Infrastructure (NCI) Australia and the Pawsey Computing Centre in Perth as well as funds from the Australian Research Council (ARC). Z. Z. thanks Murdoch University for a postgraduate scholarship.

## References

[1]. P. Jaramillo, W. M. Griffin, and H. S. Matthews, Environ. Sci. Tech., 2007. 41(17): p. 6290-6296.
[2]. V. P. Nguyen, V. Burklé-Vitzthum, P. M. Marquaire, R. Michels, J. Anal. Appl. Pyroly., 2013. 103(0): p. 307-319.
[3]. V. P. Nguyen, V. Burklé-Vitzthum, P. M. Marquaire, R. Michels, J., J. Anal. Appl. Pyroly., 2015. 113(0): p. 46-56.
[4]. H. Selim, A. Al Shoaibi, and A. K. Gupta, Appl. Energy, 2011. 88(8): p. 2593-2600.
[5]. H. Selim, A. Al Shoaibi, and A. K. Gupta, Appl. Energy, 2012. 92(0): p. 57-64.
[6]. M. U. Alzueta, R. Bilbao, and P. Glarborg, Combust. Flame, 2001. 127(4): p. 2234-2251.
[7]. C. L. Rasmussen, P. Glarborg, and P. Marshall, Proc. Combust. Inst., 2007. 31(1): p. 339-347.
[8]. Gray, P., A. A. Herod, and L. J. Leyshon, Can. J. Chem., 1969. 47(4): p. 689-690.
[9]. Perrin, D., C. Richard, and R. Martin, Int. J. Chem. Kinetic., 1988. 20(8): p. 621-632.
[10]. M. J. Frisch et al., Gaussian 09, Revision B.01. 2009: Wallingford CT.
[11]. M. J. Frisch, G. W. Trucks, H. B. Schlegel, et al., Gaussian 98, Revision A.11. 1998, Gaussian Inc.
[12]. Emma K. Pokon, Mathew D. Liptak., Steven Feldgus, George C. Shields, J. Phys. Chem. A, 2001. 105: p. 10483-10487.
[13]. V. Mokrushin, V. Bedanov, W. Tsang, M. Zachariah, V. Knyazev, ChemRate. 2002, NIST: Gaithersburg, MD.
[14]. Mebel, A.M. and M.C. Lin, J. Phys. Chem. A, 1999. 103(13): p. 2088-2096.
[15]. Atkinson, R., Atmos. Chem. Phys., 2003. 3(6): p. 2233-2307.
[16]. Jorge Aguilera-Iparraguirre, Henry J. Curran, Wim Klopper, John M. Simmie, J. Phys. Chem. A, 2008. 112(30): p. 7047-7054.

**Proceedings of the Australian Combustion Symposium**
**December 7-9, 2015, The University of Melbourne**

# Suitability of micro-PIV for characterizing poly-disperse dilute sprays in combustion applications

A. Kourmatzis[1] * and A.R. Masri[2]
[1]Department of Engineering
Macquarie University NSW 2109 Australia

[2]Aerospace, Mechanical and Mechatronic Engineering
The University of Sydney NSW 2006 Australia

## Abstract

Micro-PIV (μPIV) has the potential to be applied to combusting turbulent poly-disperse sprays, and can be considered as an extension to a standard shadow sizing technique. Commercial software which allows for the determination of both the size and velocity of the observed fragments is readily available. However, a key limitation of these shadow based techniques is the dependence on the measurement depth of the lens due to the absence of a planar light sheet. Whilst this presents a limitation, it is also the key advantage of μPIV, given the removal of droplet scattering and the ability to instantaneously visualize both the size and velocity of arbitrarily shaped fragments. In this contribution, by studying sprays dominated by spherical objects and comparing with LDA/PDA, we examine the limitations of applying μPIV towards the characterization of velocities in dilute poly-disperse turbulent flows with different initial velocity profiles. The results indicate that the μPIV technique can be biased towards larger droplet sizes, providing an effective 'size sub-ranged' velocity profile which is linked to the limited spatial resolution of the lens. By binarizing the images with a threshold closer to the background, the bias is reduced in the centreline, but leads to a reduction of the out-of-plane resolution due to an increase in the measurement depth. These results suggest the need for a balanced normalized background threshold for accurate resolution of planar velocities. Velocity profile shapes can be accurately recovered, and, with an accurate threshold choice, the magnitudes of the turbulence intensity and centerline mean velocities are in excellent agreement with PDA results. The measurements provide insights into the limitations of using μPIV in poly-disperse turbulent sprays and guide future development in this area.

*Keywords: Sprays, Micro-PIV, Image Processing*

## 1. Introduction

In the context of spray combustion and atomization, the use of a `shadowgraph' type layout to determine droplet or fragment sizes has been employed by multiple groups [2], who have also assessed sprays using non-spherical metrics [3]. This has been possible by utilizing long working distance microscope lenses in combination with sufficiently powerful light sources, coupled to high speed cameras. With the addition of a double pulsed light source this shadowgraph layout can be easily converted to a micro-PIV (μPIV) system. However, the accuracy of such a measurement technique towards the determination of gradients in the velocity profile in practical poly-disperse sprays remains open to speculation. Determination of velocities in polydisperse sprays, which can be sub-ranged on droplet size, is of paramount importance in combustion where quantities such as strain rate, slip velocity, and Stokes numbers are required [4].

Micro-PIV (μPIV) has been widely used to measure velocities in gaseous flows at very high spatial resolution [5]. Generally this is applied in situations where a laser sheet as in conventional PIV is not desired due to scattering effects, such as for Poiseuille flows in small channels where the measurement volume is surrounded by walls [5]. Additionally, μPIV is an attractive option given that conventional PIV used in sprays cannot provide particle sizes, unless used in conjunction with LIF/Mie scattering. Both LIF/Mie, LDA/PDA and diffraction sizing have the additional in-built assumption that all fragments are spherical. Therefore, μPIV can be particularly useful in situations where non-spherical objects are present and/or instantaneous size and shape conditioned or "sub-ranged" velocities would be needed.

Micro-PIV uses a double pulsed diffused light source and hence has the further distinct advantage of simple alignment given that no beam overlap is required. There have been a number of publications over the last decade or so [5-6] which have examined the advantages and limitations of μPIV. A common problem with μPIV is that, due to the lack of a planar laser sheet, it becomes a line-integrated method and therefore for certain flows with steep velocity gradients, the out-of-plane resolution is not sufficient. Substantial work has analyzed the effect of the lens depth of field and PIV settings on the measurement accuracy of the system [6-7]. The choice of interrogation window size is particularly important, due to the practical difficulty in achieving a high seed particle number for a small field of view.

In this contribution, we use a well-defined dilute spray geometry to assess the suitability of a shadow based μPIV system in determining planar velocity and turbulence profiles sub-ranged on droplet size, by

* Corresponding author:
Phone: +61 2 9850 9071
Email: agi.kourmatzis@mq.edu.au

comparing to a commercial LDA/PDA system. Combination of this technique with other work currently underway in quasi-3D imaging of non-spherical fragments [8] has the potential of yielding both size and shape conditioned volume flux in moderately dense spray flows.

Firstly, the experimental set-up is described, including the test conditions, methodology employed, and PIV post-processing settings. Results will concentrate on demonstrating the influence of background threshold choice on the shape and absolute magnitudes of the velocity and turbulence profiles. These velocity profiles will be plotted alongside the analogous measurements from an LDA/PDA system. Results will be shown for a particular mean velocity condition for two flows that contain a different initial velocity profile, one having the characteristics of a fully developed pipe flow as presented elsewhere [9].

## 2. Experimental Methodology

The geometry used for spray delivery included an ultrasonic nebulizer located upstream of the exit plane of a tube of length 196mm and diameter 4.6mm. The nebulizer delivers an acetone spray carried by air as fully described elsewhere [9]. The long tube results in a fully developed profile. A shorter tube, of length 22mm is also employed here in order to produce a different velocity profile at the exit plane. This allowed for an independent investigation of the influence of velocity gradients on the accuracy of µPIV. The bulk mean velocity of the air flow examined here is 80m/s. A comprehensive set of LDA/PDA data describing these geometries is available elsewhere [10] and this includes full details on the LDA/PDA system and associated uncertainties.

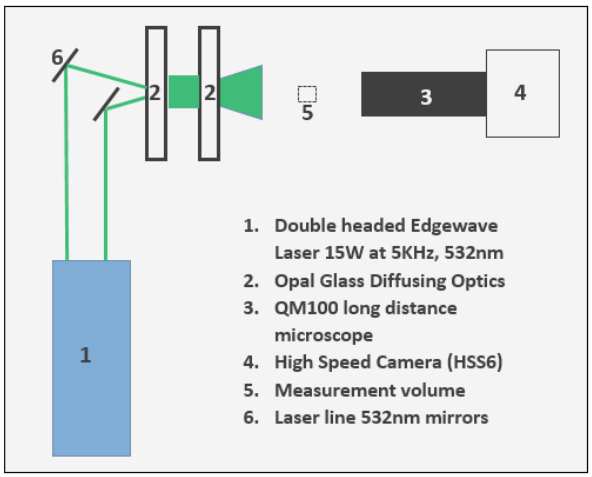

Figure 1: Schematic of Shadow based µPIV system

The µPIV system consists of a double headed Edgewave high speed pulsed diode laser delivering two 532nm beams at a repetition rate of 5kHz each. The time separation between each beam is 1.6µs and the high speed camera, connected to a QM100 long distance microscope lens, is run in PIV mode synchronized to the lasers using a LaVISION high speed controller.

Multiple iterations were done in order to optimize the PIV interrogation settings, which depended strongly on the number of particles per image. An interrogation window smaller than 64x64 pixels was not possible, providing a spatial resolution for the velocity of the order of 200µm on a total field of view of 2.4mm, which is sufficient to resolve integral scale fluctuations. This, however, is substantially larger than the pixel resolution which is approximately 3.1µm. Multiple passes of decreasing size from 128x128 were applied to the post processing routine with 50% overlap and a constant window shift. Spurious vectors were removed and a median filter was utilized. Due to the sparse droplet number density, there was no condition set on a minimum number of vectors per interrogation window. Throughout the contribution, where binary thresholds are referred too, the quantities are calculated as (intensity for binarization/background intensity). The binary threshold used is applied globally throughout the image however full details of the routine are presented elsewhere [1].

## 3. Results

### 3.1 Fully developed profiles

Figure 2a shows the mean axial velocity normalized by the centerline value plotted vs radial location for the long tube (196mm), for different binarization thresholds from µPIV. Also plotted alongside are the LDA results at the exit plane. Importantly, for this fully developed flow, the shape of the velocity profile is largely unaffected by the choice of binarization threshold and this is true even in the shear layer where a steep velocity gradient is observed. Processing the µPIV image pairs with no applied background threshold (‘nothresh’) also results in a recovery of the profile measured by the LDA instrument to within 5% close to the centreline. However, amongst all thresholds chosen for binarization of the PIV image pairs, the velocity profiles from the µPIV measurements are consistently of a lower magnitude compared to the LDA results past r=1mm. The reason for this can be described through observation of Fig. 2b.

Figure 2b shows that the LDA profile closest to the µPIV results is that which has been subranged on droplet sizes larger than 30 micrometers, indicating a bias towards larger sizes. This shall be explored further upon discussion of Fig. 3. The reason for this bias is predominately due to the limited spatial resolution of the lens camera pair, which while 3µm, after binarizing and filtering for noise removal, results in a minimum size of approximately 20µm as described elsewhere [1]. This indicates a limitation of the µPIV setup. However, compared to conventional light scattering based PIV where no droplet size can be inferred, this is a substantial improvement.

These results indicate that application of shadow based sizing techniques to velocity estimation of droplets or other fragments must be done with the knowledge of this bias. The bias can be minimized by increasing the background threshold chosen for

binarization. However that will result in a larger measurement depth, which will result in a poor recovery of gradients as will be described further upon presentation of Figure 3.

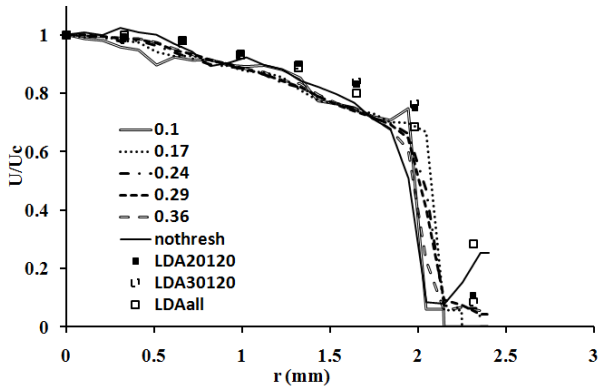


(a) Mean axial velocity (U) normalized by centerline mean velocity ($U_c$) vs. r

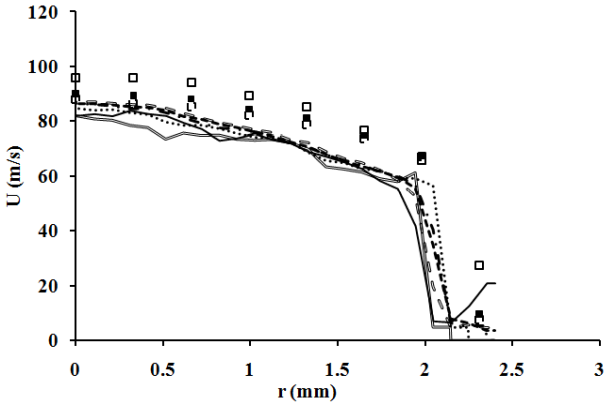


(b) Mean axial velocity (U) vs. r

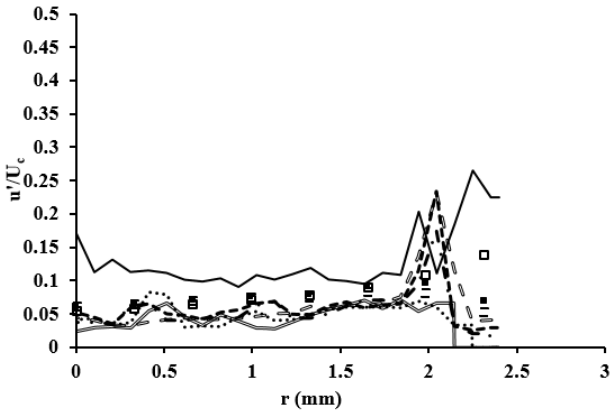


(c) Turbulence Intensity (centerline normalized) vs. r

Figure 2: Measured quantities of mean axial U and rms of fluctuations plotted vs radial position as a function of the threshold chosen for binarization (lines). Results are shown alongside LDA measurements subranged on sizes from 20<d<120, 30<d<120, and no subrange, for the long tube at the exit plane.

Figure 2c shows the turbulence intensity for the same cases plotted vs radial position. The case of no threshold ('nothresh') now shows a distinct deviation from all other processed measurements providing an artificially high turbulence intensity across the full radial profile of the spray. This is largely attributed to uneven background illumination and the presence of noise from the raw images. All other binary cases show an excellent recovery of the turbulence intensity profile, both with the correct magnitudes being recovered as well as an accurate recovery of the profile up until r=2mm. Due to the lack of statistics past that point, results tend to exhibit a lower signal-noise ratio.

## 3.2 Effect of velocity profile

With a short tube (22mm), the initial velocity profile will not be close to parabolic, which means use of the shadow based µPIV will not be as straightforward for a number of reasons. First of all, with the short tube there will be a much larger slip velocity between different size classes [10] and secondly there is a velocity gradient that occurs both in the centerline of the flow and in the shear layer [10]. In the context of a poly-disperse spray as is present here, these gradients are largely attributed to dispersion of the droplet stream resulting in a slow moving droplet dominated core surrounded by a faster moving air stream. These types of flows are the norm in spray combustion and therefore we examine here the ability of the µPIV system to capture subranged velocity profiles.

Figure 3 shows the mean velocity plotted vs radial location for the short tube. The substantial slip velocity present amongst cases from the LDA measurements is very apparent when comparing Fig. 3 to Fig. 2b. While changing the threshold chosen for binarization still has a minor effect on the magnitude of the µPIV measurements, the results of Fig. 3 indicate that an increase in background threshold reduces the bias towards larger droplet sizes. For instance a threshold of 0.375 now over-predicts the centerline velocity magnitude of the d>30 droplets.

However, observing the region from r=1.5-2.5mm shows the precise opposite. An increase in the background threshold (the most extreme case being no threshold) will result in a severe under prediction of the velocity magnitude in the shear layer. Whilst the increase in threshold allows for smaller droplets to be detected, the effective measurement depth also increases [1] and this results in an inability to correctly recover gradients. An increase in the lens magnification should improve this, and "SFOV .17" in Fig. 3 indicates a µPIV result from a magnification of 2x compared to the other results. No improvement is observed here, and is due to an inadequately diffused light source for such a small field of view (of approximately 1.2mm) resulting in pixelated images. For higher magnification to be advantageous, it is likely that at least three diffusing optics must be used, which also require more light intensity. This additional diffusion would allow for higher background thresholds to be employed with a lens that has a smaller measurement depth, hence improving the out of plane spatial resolution. This is subject to future work.

Figure 4 shows the influence of the background threshold chosen for binarization on the normalized

velocity profile for the case of the short tube flow. Whilst Fig. 3 did show that an increase in threshold resulted in a reduction in bias of the velocity magnitude with size in the spray centerline, Fig. 4 very clearly shows the negative influence that such an increase in threshold has on the velocity profile. The shape of the profile, as opposed to the absolute magnitude, is more recoverable with a decrease in the background threshold whilst in the fully developed case of Fig. 2a, this sensitivity was not apparent. In this instance, a very low threshold of 0.05 shown in Fig. 4 resulted in no data past r=0.5mm.

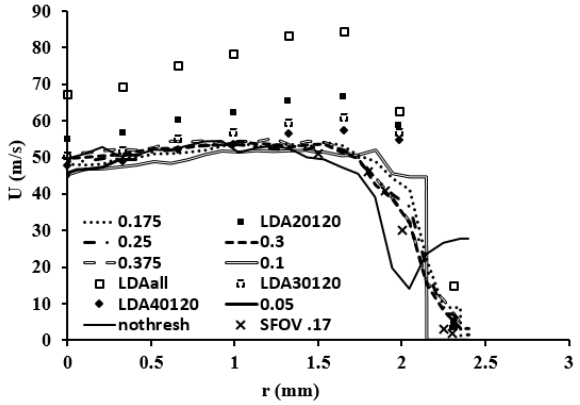


Figure 3: Mean velocity vs radial position as a function of the threshold chosen for binarization (lines) and shown alongside LDA measurements subranged on sizes from 20<d<120, 30<d<120, 40<d<120, and no subrange for short tube at the exit plane. Also shown is a μPIV case from a higher magnification (SFOV) at a threshold of 0.17.

However, extrapolating from the trend going from no threshold ('nothresh') to 0.375, 0.3, 0.25, 0.175 and finally 0.1 shows a very clear improvement in the profile measurement with a decrease in threshold. Similar results were also obtained with the higher magnification lens. Additionally, a feature of these normalized velocity measurements is that the slip between the lowest threshold (0.1) and highest threshold cases (0.375) increases with radial position. This is physically consistent with the subranged LDA results, suggesting that the choice of threshold will dictate which droplet sizes the μPIV result will be most representative of. With further development, the μPIV technique will therefore be able to accurately provide subranged velocity profiles.

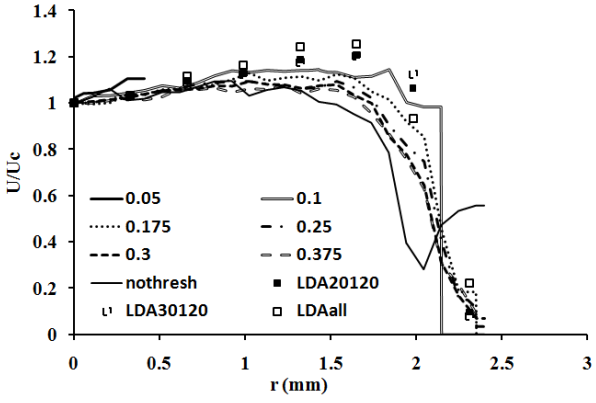


Figure 4: Mean velocity (U) normalized by centerline mean velocity ($U_c$) vs radial location as a function of the threshold chosen for binarization (lines) and shown alongside LDA measurements subranged on sizes 20<d<120, 30<d<120, 40<d<120, and no subrange for short tube at the exit plane.

These results indicate that in situations where a qualitative understanding of the velocity profile is desired, a minimum background threshold should be used to replicate a planar measurement. However, in flows where gradients are not as severe, a maximized threshold may be preferable.

## 3. Conclusion

Micro-PIV, a diagnostic technique commonly used in small-scale laminar flows, has been applied to a poly-disperse turbulent spray in a shadow-type arrangement. The limitation of μPIV in terms of accurately determining planar velocity magnitudes and turbulence levels as a function of the droplet size had not been adequately examined in the literature. It is found that the background threshold chosen for binarization is critical in determining both the degree of bias of the velocity profiles towards larger sizes and the measurement depth (out of plane resolution) which affects estimation of velocity gradients. The results here have outlined key parameters which dictate the suitability of μPIV in poly-disperse sprays and this will guide future measurements in this area. A higher magnification lens with a highly diffused light source would improve the out of plane spatial resolution of the system. In instances where only larger droplet sizes are present, and a high spatial resolution is not necessary (such as in atomizing sprays) this technique can be extremely powerful in determining simultaneous velocities and sizes of arbitrarily shaped fragments whilst also size sub-ranged velocity profiles.

## 4. Acknowledgments

The work was funded by the Australian Research Council. The assistance of Dr. Mrinal Juddoo with the experiments is highly appreciated.

## 5. References

[1] A. Kourmatzis, P.X. Pham and A.R. Masri, Comb. Flame. **162** (4) (2015), pp. 978-996

[2] C. Dumouchel, Expts. Fluids. **45** (2008), pp. 371–422.

[3] S. Ghaemi, P. Rahimi and D.S. Nobes Atom. Sprays. **19** (9) (2009), pp. 809-831.

[4] Y-C. Chen, S.H. Starner and A.R. Masri, Int. J. Mult. Flow. **32** (4) (2006), pp.389-412.

[5] C.D. Meinhart, S.T. Wereley and J.G. Santiago, Expts. Fluids. **27** (1999), pp.414-419.

[6] A. Kloosterman, C. Poelma and J. Westerweel, Expts. Fluids. **50** (2011), pp. 1587-1599.

[7] C.J. Bourdon, M.G. Olsen and A.D. Gorby, Meas. Sci. Tech. **15** (2004), pp. 318-327.

[8] A. Kourmatzis and A.R. Masri, 13th FLUCOME, Doha, Qatar, Nov. 2015

[9] W. O'Loughlin and A.R. Masri, Comb. Flame. **158** (8) (2011), pp. 1577-1590.

[10] A. Kourmatzis and A.R. Masri, 12th ICLASS, Heidelberg, Germany, Sep. 2012

# Effect of multi-lateral fuel jet injection on the flow field of Methane-Air turbulent flame

C.X. Thong[1, *], B.B. Dally[1], C.H. Birzer[1], P.A.M. Kalt[1]
[1]Centre for Energy Technology
School of Mechanical Engineering
The University of Adelaide SA 5005 Australia

## Abstract

Multi-lateral jet injection concepts have a long history in industry and for various purposes, be it for hot combustion product quenching or for general mixing applications. The current study involves injecting fuel (CNG) through lateral side jets, a short distance upstream of a round jet air nozzle exit, with a flame stabilizing at the jet exit. Flame photography and Particle Imaging Velocimetry measurements were conducted as part of a preliminary study to investigate the effect of lateral injection on flame flow field, stability and appearance. For this study, the bulk flow velocity is kept constant whilst mass-flows of air and fuel are varied, which effectively changes the jet-to-cross-flow momentum ratio and equivalence ratio, $\phi$. The resulting velocity maps are processed to acquire the flow field and the resulting turbulence intensity. It is found that the change in flow conditions upstream in the nozzle affects the nearfield in both the lifted and attached flames up to two diameters downstream. The correlation between the sidejet-to-primary-flow momentum ratio, flow turbulence intensity, and their corresponding flames are presented and discussed.

*Keywords: Partially Premixed Flame, Particle Imaging Velocimetry, Jet in Cross Flow, PIV.*

## Nomenclature

| | |
|---|---|
| $V_b$ | Bulk velocity (m/s) |
| JICF | Jet in Cross Flow |
| $G_{inj}/G_P$ | Fuel to cross-flow momentum ratio |
| $G_{inj}$ | Fuel injection momentum(kg.ms$^{-2}$) |
| $G_P$ | Primary flow momentum ratio |
| U | Mean velocity (ms$^{-1}$) |
| $u'$ | Velocity root mean square (ms$^{-1}$) |
| $u'/U$ | Turbulence intensity |
| $\phi$ | Equivalence ratio |
| NOx | Nitrous oxide |
| CNG | Compressed Natural Gas |
| $Re_{Db}$ | Bulk flow Reynolds Number based on primary jet diameter |

## 1. Introduction

Jet in cross-flow (JICF) is a classical fluid mechanics case that has been studied extensively over the decades. Although the most common cases involve flow out of chimneys that results in counter rotating vortices, JICF arrangements can be found mostly in chemical mixing, fuel and combustion quenching, and for fume dispersion. In most JICF applications in the industry, the main flow is often confined with multiple lateral jets involved [1,3]. Confinements can significantly influence the JICF behavior, in particularly the jet spread, jet trajectory and etc, but little studies on the effect of confinement on jets interaction can be found.

Studies have been conducted to investigate the effectiveness of multiple JICF to quench hot combustion products [1,7]. These studies have contributed much to the foundation of the Rich Burn Quick Quench Lean Burn (RQL) combustors, which have been proven to reduce NOx in combustion. The quick quenching and mixing effect of JICF is attributed to its complex induced structures and vortices such as counter rotating vortex pairs (CVP) and horse-shoe vortices. However, the effects of the JICF induced fuel-air mixing have not been investigated for turbulent jet flames.

Previous work by the authors [2] has classified the resulting flow of JICF in terms of momentum ratio of the side-jet to the primary flow:

$$\frac{G_{inj}}{G_P} = \frac{(\rho V^2 A)_{inj}}{(\rho V^2 A)_P} \quad (1)$$

where $\rho$ is fluid density [kg/m$^3$], $V$ is the velocity [m/s], and $A$ is the hydraulic area for both the jet ($inj$) and primary confinement ($P$) [m$^2$]. Equation (1) will be used throughout this study to classify the various flows and mixing regimes by varying the $G_{inj}/G_P$ of the flow. This ratio has consequences on the flow downstream, in particularly towards the potential core of the jet outflow [2,3].

The potential of JICF in partial premixing fuel and air for combustion is untapped. Partial premixing of the fuel and air offers advantages in terms of pollutants control and flame stability. Other example of premixing method includes recessing a fuel tube

* Corresponding author:
Phone: (+61) 8 8313 1120
Email: chia.thong@adelaide.edu.au

concentric to a central jet of air (effectively an air co-flow) [4]. Partial premixing of fuel with air prior to combustion helps to increase flame stability and delay flame lift-off.

In this paper, the flow field of a multilateral jet burner is investigated by varying both fuel (sidejet) and air (central flow) velocities whilst keeping the bulk flow a constant. This effectively varies the $G_{inj}/G_P$ and equivalence ratio ($\phi$) of the fuel mixture. Particle Imaging Velocimetry is conducted to study the planar flow field along the centerline of the flow within the flame. Flame photography is used to compare different flames in relations to the varying fuel momentum ratio and $\phi$.

## 2. Experimental set up

### 2.1 Multi-lateral jet burner

Figure 1 shows the experimental set up, the top view and the cross section of the symmetrical 4-jets configuration burner used in the experiments. The primary diameter ($D_P$) measures 25.4mm whilst the side jets are each 3mm in bore diameter ($D_{inj}$) and are attached laterally to the primary pipe nozzle and placed 90 degrees relative to the adjacent jets. The jets are located at approximately 1 $D_P$ upstream of the nozzle exit.

The flames investigated here comprise of compressed natural gas (CNG) – jets issuing into a primary cross-flow of air. The cases tested have conserved bulk velocity ($V_b$) of approximately ~3.1 m/s which translates to $Re_{Db}$ ≈5000. The air and fuel mass flow rate are varied, which effectively manipulates the jet injection to cross-flow momentum ratio ($G_{inj}/G_P$), and the fuel-air equivalence ratio ($\phi$). The experimental parameters are presented in Table 1. Both air and fuel flow rates are controlled using ABB rotameters with pressure regulators.

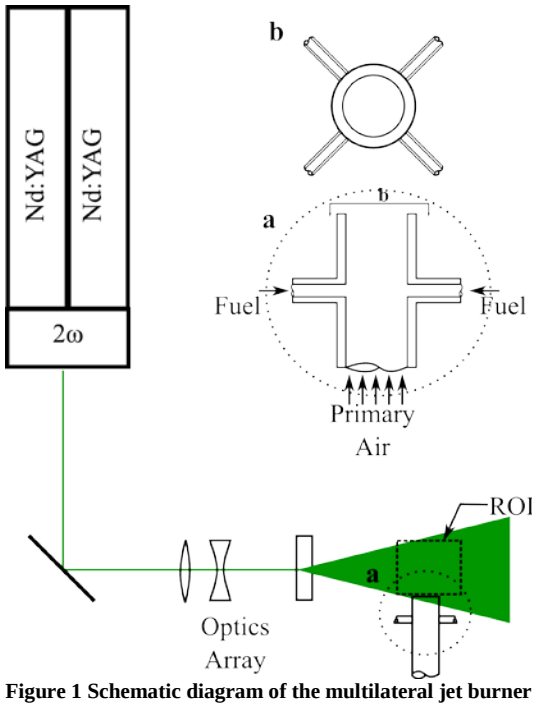


**Figure 1 Schematic diagram of the multilateral jet burner experimental set up.**

### 2.2 Optical set up

Velocity field was measured using cross correlation Particle Imaging Velocimetry technique, conducted in the TEC Laboratory at the University of Adelaide. The region of interest (ROI) is illuminated by a Quantel Brilliant B, double-pulsed Nd:YAG laser using the second harmonics at 532nm. Laser power was set to approximately 800mW. The time delay between successive laser pulses was 70$\mu$s. Both fuel and air flow streams are seeded with Sigma-Aldrich Titanium(IV) dioxide, rutile powder (<5μm) via external cyclone seeders.

The imaging system comprised of a Princeton Instruments Megaplus II ES4020 camera running in triggered double exposure mode at a 2.5Hz duty cycle. Collection optics were a Tamron 90-200 compound lens fitted with a 532nm band-pass interference filter imaging a region of approximately 86mm by 86mm onto a CCD detector of 2048 pixels by 2048 pixels. The spatial resolution is therefore ~24px/mm. The imaging was repeated for both the $45^o$ and $90^o$ plane (angle of imaging plane relative to the adjacent jets). The resulting Mie-scattering of titanium dioxide particles (<5$\mu$m) introduced into the flow were processed using PIVView software [5]. Cross-correlation was performed on an interrogation window of 32 pixels by 32 pixels with 50% overlap. Gaussian peak fitting was selected to avoid peak locking effect and give sub-pixel on the displacements. The PIV ensemble consisted of 500 image pairs. The PIVView output data are imported into freeware OMA-X[6] for compiling and further processing.

The flame photographs are taken with a standard NIKON Digital Single Lens Reflex (DSLR) camera. Different exposure time, ISO, and aperture were tested, and a suitable setting is used for all the presented photographs. The photographs are taken at constant height throughout the flame sets.

## 3. Results and Discussion

The flame photographs in Fig. 2 are arranged in decreasing order of jet-to-cross-flow momentum ratio with Fig. 2(a) corresponding to the $G_{inj}/G_P$=0.8 case and Fig. 2(e) corresponding to the $G_{inj}/G_P$=0.2

**Table 1 Experimental parameters for the tested flame conditions**

| Cases | Jet to cross flow momentum ratio, $G_{inj}/G_P$ | Fuel to air equivalence ratio, $\phi$ |
|---|---|---|
| i63p40 | 0.8 | 5.3 |
| i57p42 | 0.6 | 4.6 |
| i50p44 | 0.4 | 3.8 |
| i44p46 | 0.3 | 3.2 |
| i37p48 | 0.2 | 2.6 |

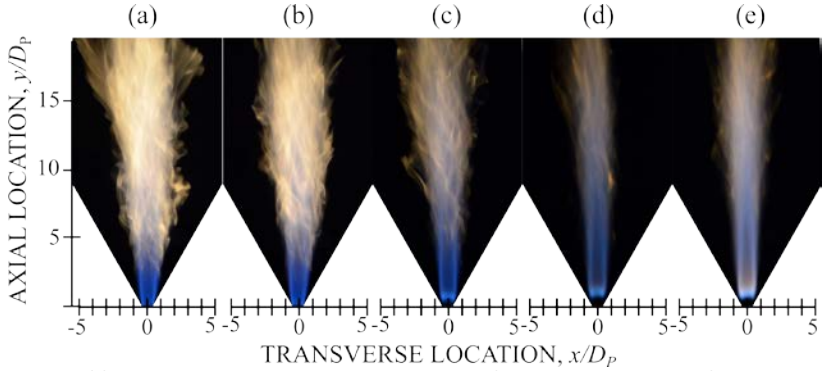


**Figure 2 Photographs of flames taken by a standard DSLR exposed for 1.0s at ISO 400 and f#32 under different mixing conditions: a)$G_{inj}/G_P$=0.8; b)$G_{inj}/G_P$=0.6; c)$G_{inj}/G_P$=0.4; d)$G_{inj}/G_P$=0.3; and e)$G_{inj}/G_P$=0.2.**

case. Decreasing the $G_{inj}/G_P$ also decreases equivalence ratio, $\phi$ of the mixture. The $\phi$ value is reduced from 5.3 for the case in Fig. 2(a) to 2.6 in Fig. 2(e), transiting from richer to leaner flame. The decreasing $\phi$ in the tested cases are reflected by the flames' luminosity in Fig. 2. The flame in Fig. 2(a) shows a brighter and sootier flame as compared with the leaner flames seen in Fig. 2(e). The photographs in Fig. 2 were taken at 1.0s exposure time, at ISO 400 and apperture (f#) 32.

From Fig. 2, it is clear that the different momentum ratios impact on the flames' appearances. The flame for both $G_{inj}/G_P$=0.8 and 0.6 are observed to be attached to the nozzle exit, and at $G_{inj}/G_P$=0.4, the flame transitions intermittently from attached to lifted; hence it is termed the "transitional flame". Flame lift-off can be seen more prominently for cases $G_{inj}/G_P$=0.3 and $G_{inj}/G_P$=0.2. From these figures, the lift-off height is estimated to be approximately $1D_P$ above the nozzle exit.

The $G_{inj}/G_P$ values that denote the tested cases also reflect the different mixing regimes within the primary jet that are achieved before being expelled out to be burnt, which include [2]:

a) Backflow mode
b) Impinging mode
c) Streaming mode

Cases $G_{inj}/G_P$=0.8 and $G_{inj}/G_P$=0.6 corresponds to the backflow mode, as shown in the isothermal studies, whilst $G_{inj}/G_P$=0.4 to $G_{inj}/G_P$=0.2 correspond to that of an impinging flow mode.

For backflow mode, the fuel injected into the air cross-flow propagates upstream into the nozzle before being expelled. This partial premixing does not lead to flame propagation into the burner due to the flow conditions and rich mixtures.

Figure 3 shows the mean velocity field images with no smoothing and filter applied, for the different flames. Figure 3(a) to 3(e) show the axial velocity magnitude for the cases $G_{inj}/G_P$=0.8 to $G_{inj}/G_P$=0.2. The images to the left of each plot show the velocity field captured at the 45° plane (relative to the adjacent jets as indicated by the accompanying schematic drawings) whilst the right side of the plots show the velocity field captured at the 90° plane. The measurements cover the flow from centerline to $1D_P$ in the transverse location, and from the nozzle exit to approximately $2.5D_P$ downstream.

Figure 3(a) and 3(b) shows a flow-field that is similar to a round jet flow exit. Comparing the 45° plane to the 90° plane shows that both planes are symmetrical despite the location of the jets. Figure 3(c), 3(d) and (e) shows a "necking" in the flow field. The necking of the flow happens further downstream with reducing $G_{inj}/G_P$. This necking also coincides with the lift-off distance of the respective cases, which is observed to increase with reducing $G_{inj}/G_P$.

Figure 4 shows the centreline velocity decay plots for all tested cases. The outflow centerline velocity, $U_C$ for each of the cases are normalized to their

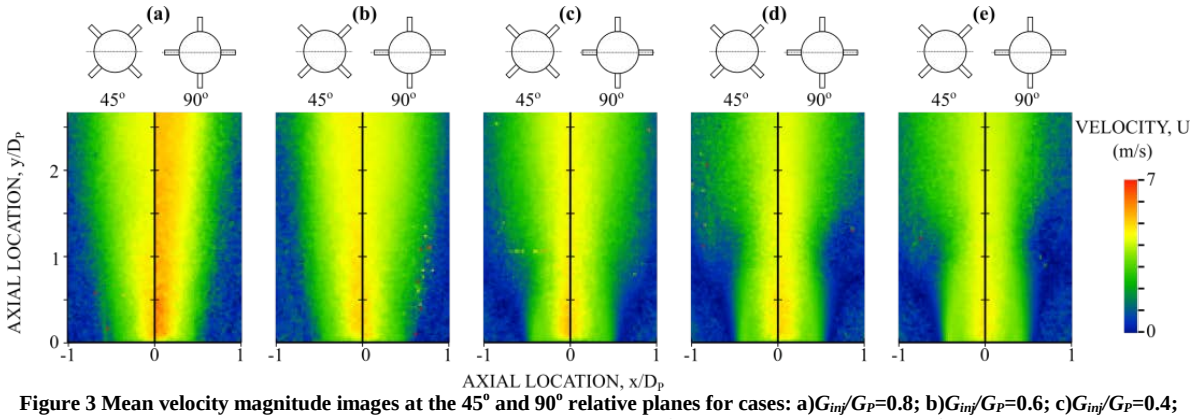


**Figure 3 Mean velocity magnitude images at the 45° and 90° relative planes for cases: a)$G_{inj}/G_P$=0.8; b)$G_{inj}/G_P$=0.6; c)$G_{inj}/G_P$=0.4; d)$G_{inj}/G_P$=0.3; and e)$G_{inj}/G_P$=0.2. The schematic diagram above each sub-figure shows the orientation of the side jet nozzles relative to the laser plane (dashed line).**

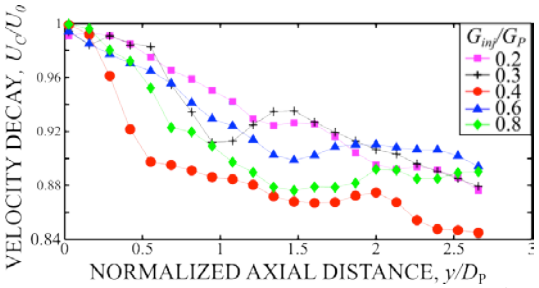


**Figure 4 Normalized centreline velocity decay, *Uc/Uo* for the studied cases, measured at the centreline from the burner nozzle exit to approximately 2.5$D_P$ downstream.**

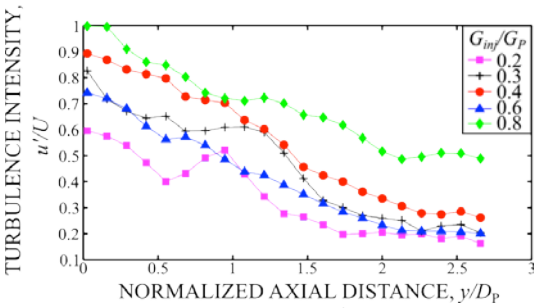


**Figure 5 Turbulence intensity, *u'/U* for the studied cases, measured at the flow centreline from the nozzle exit to approximately 2.5$D_P$ downstream.**

respective centerline nozzle exit velocity, $U_0$ and is measured to approximately 2.5$D_P$ downstream.

It is clear from Fig. 4 that the centerline velocity decay for these flames is different from a standard decay of a simple jet. The virtual origin seems to have shifted and the velocity decay is accelerated close to the jet exit, recovers slightly at $y/D_P$=1.5~2.0, before decaying again. The increase in decay rate close to the exit increases with the momentum ratio. Also noticeable is that the axial location of the velocity recovery for the $G_{inj}/G_P$=0.2 and 0.3 cases coincident with the lift-off height of these flames. The transitional case ($G_{inj}/G_P$=0.4) exhibits the largest drop in mean centerline velocity, i.e. 12% from the exit to around 0.5$D_P$ before it plateaus and decays further past 2$D_P$. Modelling of similar cases in isothermal condition using commercially available Computational Fluid Dynamics package, ANSYS CFX reveals similar trend where the decay pattern further downstream (>2.5$D_P$) is similar to round jets with no side injection. This observation corroborates the fact that the side jets effect is limited to the flow in the near field region.

Figure 5 shows the turbulence intensity, $u'/U$ at the flow centerline plotted from the nozzle exit to approximately 2.5$D_P$ downstream. The turbulence intensity is obtained by normalizing fluctuating component of ($u'$) to their respective local mean velocity ($U$). Similar to the trends observed in Fig. 4, the turbulence intensity is affected up to the measured axial location in this study and becomes quite similar further downstream. While there is a clear trend of an increase in turbulence intensity at the jet exit corresponding to the increase in the momentum ratio, the case $G_{inj}/G_P$=0.6 does not follow this trend. The increase in turbulence intensity around $y/D_P$=1 seems to be associated with flame ignition and coincides with lift-off height location. Most of the tested cases reduces to a consistent $u'/U$ = 0.2~0.3 except for $G_{inj}/G_P$=0.8 case which remains much higher at around $u'/U$≈0.6.

Generally, despite the increase in $\phi$, the lift off distance is decreased. This particular trait of this fuel-air mixing method shows the increasing flame stability with increasing $G_{inj}/G_P$. By increasing the momentum ratio, the side jets interact with the adjacent jets, which promotes more mixing and hence producing a delayed flame lift off.

## 4. Conclusion

The flow field and stability of a multi-lateral jet burner of methane-air mixture are presented in this paper. It is found that changes in the jet to cross-flow momentum ratio has significant effect on the resulting flows up to 2 primary diameter downstream, and this is reflected in both the velocity decay plot and the turbulence intensity. However, the short downstream distance that is affected by the change in jet to primary flow momentum-ratio is sufficient to affect the flame stability drastically. Further work is underway to investigate the flame structures generated by the multilateral jet mixing technique and correlated to the velocity field, and flame stability.

## 4. Acknowledgments

This work was made possible using the equipment at the Centre for Energy Technology at the University of Adelaide and the financial support of ARC Discovery.

## 5. References

[1] J.D. Holdeman, D.S. Liscinsky, V.L. Oechsle, G.S. Samuelsen and C.E. Smith, Journal of Engineering for Gas Turbines and Power. **119** (1997), pp. 852–862

[2] C.X. Thong, P.A.M. Kalt, B.B. Dally and C.H. Birzer, Exp Fluids. **56** (15) (2015), pp. 1–16

[3] T. New and W. Tay, Journal of Turbulence **7** (57) (2006), pp. 1–20

[4] S. Meares and A.R. Masri, Combustion and Flame **161** (2014), pp. 484–495

[5] PIVTEV GmbH [www.pivtec.com]

[6] P.A.M. Kalt and M.B. Long, [www.oma-x.org]

[7] M.Y Leong and G.S. Samuelsen, Journal of Propulsion and Power, **16** (5)(2000), pp. 729-735.

**Proceedings of the Australian Combustion Symposium**
**December 7-9, 2015, The University of Melbourne**

# Scalar Dissipation Rates in Turbulent Flames of Methane with Inhomogeneous Inlets

H. Cutcher[b], R.S. Barlow[a], G. Magnotti[a] , A.R. Masri[b*]
[a]School of Mechanical and Mechatronic Engineering, The University of Sydney, NSW 2006 Australia
[b]Combustion Research Facility, Sandia National Laboratories, Livermore CA 94550, USA

## Abstract

This paper presents highly resolved measurements of scalar dissipation rates in turbulent piloted flames of methane with compositionally inhomogeneous inlets. Earlier measurements in such flames have shown that the first few diameters downstream of the jet exit plane are critical in determining stability limits. In such region, and when the inlets are inhomogeneous, multi-modes of combustion may occur with premixed-stratified flames closer to the jet exit transitioning to non-premixed further downstream. The role of scalar dissipation in such transition remains unclear and the new measurements have sufficient resolution to shed light on these issues. It is found that in the inhomogeneous case, the scalar dissipation rate remains low for flammable mixtures throughout the early flame stabilization region (x/D<5). The evolution of local maxima in the conditional mean scalar dissipation rate may be a potential indicator for the transition from premixed to non-premixed mode of combustion.

*Keywords: Turbulent flames, scalar dissipation rates, inhomogeneous composition, stratified flames*

## 1. Introduction

Compositional inhomogeneity in turbulent combustion systems is quite common due to the inherent difficulty associated with achieving uniform mixing in small spaces. This is compounded with the possible formation of acoustic instabilities and flow pulsations which tend to induce such concentration gradients [1,2]. Early laboratory studies of such flows include various designs of stratified burners which essentially involve two adjacent streams with different compositions both being within the flammability limits [3–6]. The turbulent piloted burner with inhomogeneous inlets, which is the subject of this paper, broadens the scope of these investigations to include compositional gradients that could span the entire mixture fraction range from zero to one. This is achieved by introducing two concentric pipes within the pilot stream where the inner pipe which carries fuel, can be recessed within the outer pipe which carries air, hence introducing compositional inhomogeneity at the jet exit plane.

In earlier papers [7–9] it has been found that with methane as fuel, the flame stability may be significantly improved at intermediate recess distance of the fuel pipe, and hence at some optimal level of compositional inhomogeneity in the inlet profile. At such conditions, detailed measurements of species concentration and temperature have revealed that fluid mixtures in the region adjacent to the hot pilot stream are generally premixed and/or stratified hence enabling higher rates of heat release which in turn lead to enhanced flame stability. This is in contrast to the standard case when the mixture at the jet exit plane is homogeneous so that diffusion and mixing are required before combustion can take place. It is also found that this mode of premixed-stratified combustion gradually transitions to non-premixed within the first five to ten diameters of the jet exit plane.

The measurements reported earlier while detailed and informative, are of limited spatial resolution so that the resulting scalar dissipation rates have modest signal to noise ratios. In addition, insufficient scans were collected close to the pilot which is a region of interest. Recently, these measurements were repeated at Sandia's Combustion Research Facility using an improved set-up where the spatial resolution of the system is enhanced and where more refined measurements were obtained near the pilot in flames of both homogeneous as well as inhomogeneous inlet. While the remainder of the data is still being processed, this paper reports initial results not only to confirm earlier findings but also to report some novel trends in the scalar dissipation rates as measured in the early regions of the these flames.

## 2. Experiment setup

Figure 1 shows a schematic of the burner with two tubes surrounded by an 18mm diameter pilot. The inner tube (4mm inner diameter and 0.25 mm wall thickness) can be recessed at a distance, *Lr*, within the outer tube (7.5mm inner diameter and 0.25 wall thickness). One of the tubes issues fuel and the other air so the degree of mixing can be controlled at the exit plane by varying the recession distance. At sufficiently large recess distances (Lr > 300mm) the issuing mixture is close to homogeneous and at Lr=0 it is purely non-premixed. At intermediate distances, the mixture is non-uniform with varying degrees of inhomogeneity. The burner was located in a

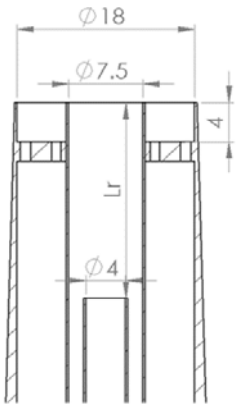

Fig. 1: Schematic of burner.

* Corresponding author:
Phone: (+61) 2 93512288
Email: assaad.masri@sydney.edu.au

300 mm x 300 mm wind tunnel giving a 15 m/s uniform air co-flow.

For the flames discussed in this paper the overall volumetric air/fuel ratio is $V_A/V_F$= 2.0 with the inner tube issuing methane and the outer tube (annulus) flowing air. The pilot is a mixture of acetylene, hydrogen, air, nitrogen and carbon dioxide designed to have the same C/H ratio and adiabatic equilibrium temperature as a stoichiometric methane/air mixture. To provide a pilot heat release rate of $H_r$ = 2.22 kW as used previously [7–9] the unburnt bulk pilot velocity was $U_p$ = 3.72 m/s.

Multi-scalar measurements were taken using combined line imaging of Raman and Rayleigh scattering, and laser induced fluorescence of CO at the Turbulent Combustion Laboratory (Sandia National Laboratories) [10,11]. This provides single shot profiles of temperature and major species ($O_2$, $N_2$, $CH_4$, $H_2O$, $H_2$, $CO_2$ and CO) across 6 mm segments in the flow. The distinguishing feature of this campaign over previous work on the same flames [7,9] is a much improved spatial resolution where radial axis binning was reduced from 100µm to 20µm. In addition the shot density was increased at regions of interest.

Four frequency doubled Nd:YAG lasers were combined to achieve ~1.8J/pulse for use for Raman and Rayleigh line imaging. A 230.1 nm UV laser beam aligned along the same axis as the Nd:YAG laser beams was used to excite CO. Three CCD cameras were used to collect the line imaged Raman/Rayleigh/CO-LIF signals after passing through a pair of 150 mm achromats with an optical resolution of 60µm. The oversampling rate is chosen to maximise signal to noise ratio and take full advantage of the optical resolution [6].

A wavelet denoising algorithm was applied to the Raman-Rayleigh-LIF measurements to enable the finer spatial resolution. The wavelet adaptive thresholding and reconstruction method has been shown to give superior performance to other algorithms [6]. This allows the resolution of accurate measurements despite the inherently low Raman signal levels.

Two cases, listed in Table 1, were selected for comparison with previous work [7–9] and the initial analysis presented in this paper. The bulk jet velocity $U_j$ is calculated from the total volumetric flow rate at the exit plane. The bulk jet velocity at blow off $U_{bo}$ is similar for the earlier as well as the current measurements and these may be found in [7]. These cases were chosen to distinguish between near-homogeneous and highly inhomogeneous conditions at the exit plane and these will be referred to as FJ-300-59 and FJ-75-80, respectively. Equal departure from blow off (Uj/Ubo =0.7) improves the comparability of the two flames.

Table 1: Table of selected cases

| Case | Lr (mm) | $U_j$ (m/s) | $U_{bo}$ (m/s) | $U_j/U_{bo}$ (%) | $Re_j$ |
|---|---|---|---|---|---|
| FJ-59mps-Lr300 | 300 | 59 | 84.3 | 70 | 27600 |
| FJ-80mps-Lr75 | 75 | 80 | 114.3 | 70 | 37500 |

## 3. Results and discussion

### 3.1 High resolution comparison

Instantaneous scatter data of temperature and mass fraction of CO and $H_2$ versus mixture fraction is shown in Fig. 2. Contrasting the two left columns with the two right shows the difference between homogeneous (FJ-300-59) and inhomogeneous flames (FJ-75-80) respectively at two axial locations, x/D=1 (top three rows) and x/D=5 (bottom three rows).

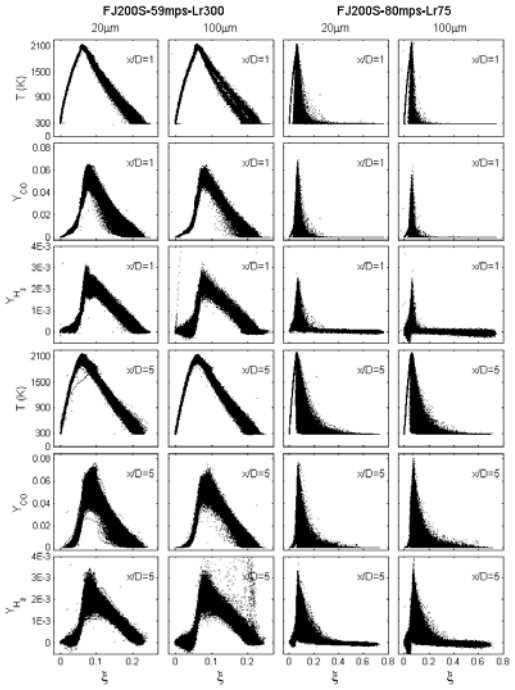


Fig. 2: Instantaneous scatter data for temperature, carbon monoxide and hydrogen mass fractions versus mixture fraction. This figure shows the similarity of the data presented previously by Meares et al. (2014) [7] and higher resolution data presented here at two axial locations, x/D=1 and x/D=5.

The three scalars in Fig. 2 provide the opportunity to compare the two data sets collected in 2013 and 2105. The agreement of Rayleigh, LIF and Raman based diagnostics can be seen in temperature, CO mass fraction and $H_2$ mass fraction respectively. The two data sets which have different spatial resolution demonstrate sufficiently similar characteristics and confirm accurate repetition of the past work in this high resolution campaign.

Some asymmetry can be seen in the lower resolution data as demonstrated by separation of the temperature data points on the rich side of the flame. This has been improved in the current, higher resolution data with no visible sign in the scatter plots. The current data set shows a reduction in the number of stray scatter points and reduced over-correction of Raman signals.

The agreement in the data of the two campaigns validates the use of the higher resolution data for an improved study of the phenomena demonstrated in previous work.

Histograms of mixture fraction gradient across a 1000K increment (700-1700K) are shown in Fig. 3 for

the two selected flames for the both high and low resolution data sets. The gradient $\Delta\xi/\Delta T$ has been shown previously to be an adequate indicator of the combustion mode [7] such that values of $\Delta\xi/\Delta T \sim 0K^{-1}$ are indicative of premixed flames while values around $-10^{-4}K^{-1}$ refer to non-premixed combustion. The results remain consistent between the high and low resolution data sets which feature similar trends. The impact of the increased resolution is minimised across a large temperature range improving its use an indicator of the mode of combustion that dominates each of these flames.

For the homogeneous mixture at x/D=1 (FJ-59mps-Lr300) the distribution of $\Delta\xi/\Delta T$ in Fig. 3 is narrowly centred on approximately $-9x10^{-5}$ $K^{-1}$. The narrow range reflects the uniformity of the mixture at the exit plane. In contrast the partial premixed case (FJ-80mps-Lr75) is centred at near zero at x/D=1 and is much broader than its near-homogeneous counterpart. At five diameters downstream there is little change in the homogeneous case as the air and fuel are already well mixed but the inhomogeneous case shows a broadened distribution with the centre moving closer to that seen for FJ-59mps-Lr300.

Moving downstream, the increasing number of negative values is indicative of the increasing prevalence of fuel-rich reactants mixing with pilot. Upstream in the inhomogeneous flame, the primary mode of combustion is premixed/stratified and subsequently sees only small changes in mixture fraction over the burning region. As the mixture approaches homogeneity and the flame becomes diffusion-dominated, the mixture fraction gradient increases and $\Delta\xi/\Delta T$ moves further from zero. These trends are similarly observed in both the 2013 and 2015 data sets.

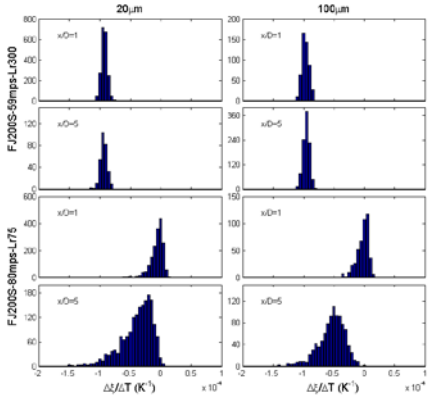


Fig. 3: Histograms of $\Delta\xi/\Delta T$ across the span 700K < T <1700K for two configurations.

## 3.2 Scalar dissipation development

The effect of increased spatial resolution can be seen in the development of the radial component of scalar dissipation. Results from the high resolution data set demonstrate greater values for $\chi_r$ than for the coarser data. This is potentially due to the resolution of smaller scale mixture fraction gradients that couldn't be observed with the previous measurements. The qualitative features of both data sets with respect to $\chi_r$ are similar, and this section takes advantage of the increase in resolution and shot density to explore the evolution of dissipation measurements at additional axial locations. An increased number of axial locations in the near field allow further examination of the evolution of the flames than has been previously possible.

Fig. 4 shows the conditional mean profiles of $\chi_r$ for x/D = 0.5, 1, 2, 3, 5, 7 and 10. The right hand column has been filtered spatially to include data close to the reactive edge of the jet but exclude pilot flows. This leads to some truncated profiles on the conditional plots due to the absence of these leaner mixtures from the spatial range considered here (see plots on the right hand side of Fig. 4). Note, as well, the differences in the y axis scale between the plots.

For the inhomogeneous case (FJ-80mps-Lr75), and as the axial distance increases, the trend is for the overall magnitude of scalar dissipation rate to decrease and this is expected since due to the shallower concentration gradients that form further downstream. At x/D=10, we can see the beginning of the localised peak just rich of stoichiometric analogous to that clearly seen in the near homogeneous case. This supports the previously reported statement [7,9] that most of the mixing has occurred by x/D = 5-10 and the characteristics of both flames converge.

In the case of the FJ-59mps-Lr300 flame the noticeable trend moving downstream is the increasing distinction of the local maximum near $\xi$ = 0.08. With the exception of at x/D = 3, the magnitude of these peaks relative to the rest of the mixture continues to increase. In a similar manner to the inhomogeneous case, the mean value across the profile continually decreases as the distance from the exit plane increases however at an initially increased rate.

For the near homogeneous flame, diffusion is the dominant mode of combustion. Similarly, for downstream locations in the inhomogeneous case FJ-80mps-Lr75, transition to non-premixed combustion modes occurs at x/D $\approx$ 7. The localised peak in density weighted scalar dissipation occurs near $\xi$ = 0.08 over the same range where diffusion is dominant. That it exists over the entire axial range for the near homogeneous flame but only appears downstream in the partially premixed case suggests that it may be useful as an indicator of a non-premixed combustion mode.

Fig. 5 shows the evolution of scalar dissipation along the first couple of diameters. These are conditional on specific mixture fraction ranges as indicated on each plot. Note also that the same logarithmic scale is used throughout on the horizontal axis to facilitate comparison between the homogeneous (left) and inhomogeneous cases (right). For the stoichiometric rage ($0.05<\xi<0.06$), both cases are similar except for a slightly broader distribution for FJ-80mps-Lr75 and this is consistent with the profiles shown in Fig. 4 where the mean scalar dissipation profiles overlap around stoichiometric.

Richer mixture fraction ranges ($0.075<\xi<0.085$ and $0.125<\xi< 0.135$), indicate marked differences between the homogeneous and inhomogeneous cases with the latter showing much flatter profiles that extend to much

lower values of $\chi_r$. This is consistent with the fact that in the inhomogeneous flames (FJ-80mps-Lr75), broader and flatter mixture fraction profiles lead to zones to lower stretch rate where premixed and stratified fluid samples burn readily and lead to improved flame stabilization. This is contrasted with the narrower profiles shown for case FJ-59mps-Lr300 which is indicative of non-premixed combustion. This is also consistent with the mean profiles of scalar dissipation shown in Fig. 4 where the homogeneous cases show much higher values of $<\chi_r>$ on the rich side of stoichiometric. Larger values for homogeneous flames in these two mixture fraction regions suggest increased species transport as would be expected in diffusion dominated flames.

The richest zone shown in Fig. 5 ($0.195<\xi<0.205$) indicates yet another transition where here, the inhomogeneous case shows higher values of $\chi_r$ spilling over to the $\chi_r$ >100/s. This is due to steeper gradients and much richer mixtures that exist in the inhomogeneous cases. It is worth noting that mixtures in this range are rather too rich to be reactive.

## 4. Conclusion

The initial look at a new data set with a finer resolution shows promising results. The comparison with the previously reported data shows similar results in key physical phenomena. The similarity in results validates use of the higher resolution data as a continuation of the previous work on these flames. Improvements in symmetry and processing methods in this current campaign should improve use in numerical model validation.

Further potential investigations into characterising turbulent partially premixed combustion are hinted at by the initial analysis into scalar dissipation. A combination of improved resolution and increased shot density allows the opportunity to better describe the characteristics of these flames. The additional axial locations also give the potential for a closer examination into inhomogeneous mixtures as they transition from premixed to diffusion dominated combustion.

## 5. Acknowledgement

Work at the University of Sydney was supported by the Australian Research Council. Work at Sandia was supported by the Division of Chemical Sciences, Geosciences and Biosciences, Office of Basic Energy Sciences, US Department of Energy. Sandia National Laboratories is a multiprogram laboratory operated by Sandia Corporation, a Lockheed Martin Company, for the United States Department of Energy under contract DE-AC04-94-AL85000. Contributions by Bob Harmon in support of these experiments are gratefully acknowledged.

## 6. References

[1] P. Kutne, B.K. Kapadia, W. Meier, M. Aigner, Proc. Combust. Inst., 33, (2) (2011) 3383–3390.

[2] P. Weigand, W. Meier, X.R. Duan, *Combust. Flame*, **144**, (1-2) (2006) 225–236.

[3] B. Böhm, J.H. Frank, a. Dreizler, *Proc. Combust. Inst.*, **33**, (1) (2011) 1583–1590.

[4] F. Seffrin, F. Fuest, D. Geyer, a. Dreizler, *Combust. Flame*, **157**, (2) (2010) 384–396.

[5] M.S. Sweeney, S. Hochgreb, M.J. Dunn, R.S. Barlow, *Combust. Flame*, **159**, (9) (2012) 2896–2911.

[6] M.S. Sweeney, S. Hochgreb, M.J. Dunn, R.S. Barlow, *Combust. Flame*, **160**, (2) (2013) 322–334.

[7] R.S. Barlow, S. Meares, G. Magnotti, H. Cutcher, A.R. Masri, *Combust. Flame*, **162**, (10) (2015) 3516–3540.

[8] S. Meares, A.R. Masri, *Combust. Flame*, **161**, (2) (2014) 484–495.

[9] S. Meares, V.N. Prasad, G. Magnotti, R.S. Barlow, a. R. Masri, *Proc. Combust. Inst.*, **35**, (2) (2014) 1477–1484.

[10] M.S. Sweeney, S. Hochgreb, M.J. Dunn, R.S. Barlow, *Combust. Flame*, **159**, (9) (2012) 2896–2911.

[11] R.S.S. Barlow, G.-H.G.-H. Wang, P. Anselmo-Filho, M.S.S. Sweeney, S. Hochgreb, *Proc. Combust. Inst.*, **32**, (1) (2009) 945–953.

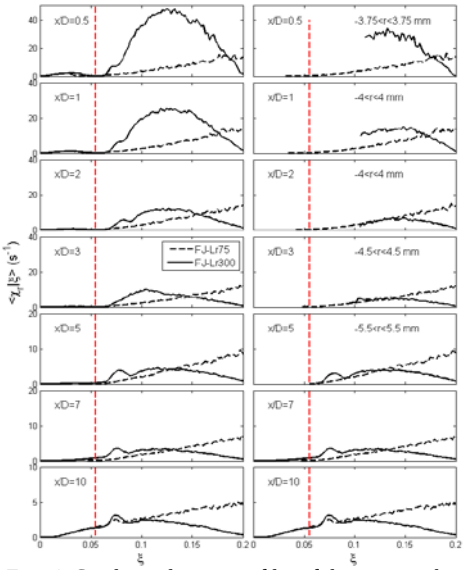


Fig. 4: Conditional mean profiles of density-weighted scalar dissipation (radial contribution only). Solid lines are for FJ-59mps-Lr300 and dashed lines for FJ-80mps-Lr75. The right hand column has restricted spatial range to reduce the effect of pilot samples.

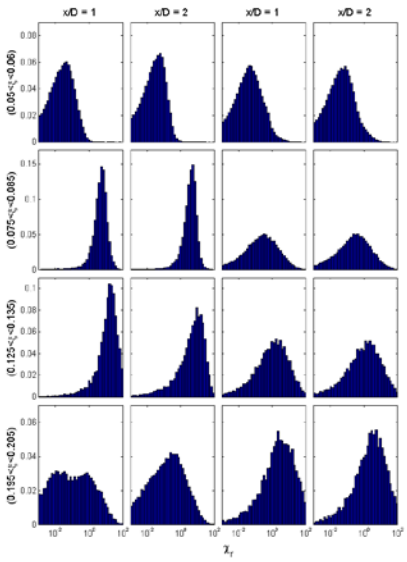


Fig. 5: Probability density functions of scalar dissipation (radial contribution only) for the selected mixture fraction intervals shown.

**Proceedings of the Australian Combustion Symposium**
**December 7-9, 2015, The University of Melbourne**

# Performing High Spatial and Temporal Resolution Measurements on Forced Premixed Laminar Flames

Samuel M. Wiseman[1, *], Michael J. Brear, Robert L. Gordon, Ivan Marusic
[1]Melbourne School of Engineering
University of Melbourne VIC 3010 Australia

**Abstract**
Forced, laminar, premixed flames have been used extensively to study different flame phenomena. In these experiments, a velocity modulation is usually imparted on the unburned gases by a speaker. Since these flames are ideally periodic, they can permit collection of high resolution data by using low speed, phase locked measurements, thereby avoiding the cost and complexity of high speed data acquisition. However, measurement resolution is then limited by the cycle-to-cycle non-repeatability of the flame.

This paper therefore first presents some key problems encountered when attempting to establish a high degree of cycle-to-cycle repeatability during experiments on forced, laminar, premixed flames. Solutions to these problems are then discussed and demonstrated. It is shown that a high degree of cycle-to-cycle repeatability can be achieved during experiments lasting of order several hours.

*Keywords: Acoustically Excited Flames, Forced Flames, Laminar Premixed Flames, Flame Imaging*

## 1. Introduction

Forced, premixed, laminar flames have been extensively used in premixed combustion studies. In one of the most widely used configurations, velocity modulations are imposed on the unburned gases upstream of a laminar flame by use of a speaker driver. The flame response can produce flame surface geometries useful in studying the effect of curvature and stretch rate on burning speeds [1,2]. Flame annihilation events can also be produced and have recently been of interest due to their potential role in noise production and thermoacoustic instability [3,4,5,6].

In some experimental configurations the flame response is sufficiently repeatable that the temporal evolution of the flame can be captured using phase shifted measurements taken in different flame cycles [1,6,7,8]. These stroboscopic methods have three main advantages: more commonly available, less expensive, and more sensitive low repetition rate diagnostics may be used; multiple diagnostics may be applied sequentially; and signal to noise ratios can be improved by averaging several measurements at the same phase of the flame cycle.

However, achieving sufficient repeatability can be challenging. For example, to reduce the impact of buoyancy induced flame flickering Baillot and Bourehla [1] conducted their experiments at 0.25 atm, and the minimization of disturbances was a significant factor in the choice of experimental conditions. Candel et al. [6] conducted experiments at atmospheric conditions and took 100 images at each phase of the cycle to smooth out cycle-to-cycle fluctuations. Indeed, under some conditions sufficient repeatability simply cannot be achieved and high speed diagnostics must be used [2,9].

This paper therefore presents some key problems encountered when attempting to establish a high degree of cycle-to-cycle repeatability during experiments on forced, laminar, premixed flames. Solutions to these problems are then discussed and demonstrated.

## 2. Experiment Setup

A flame holder with a square port was used to produce a laminar, premixed flame. The sides of the port are 22 mm long with rounded corners, as shown in Figure 1. Air and propane are mixed approximately three metres upstream of the burner to ensure a thorough mixing at the burner port [3]. The flow rates of both gases were controlled with mass flow controllers. An equivalence ratio of 0.75 was used in all experiments. The unburned gases pass through a 60 mm honeycomb flow straightener in the burner plenum before entering a contraction upstream of the flame holder. Layers of fine steel mesh before and after the contraction are used to dissipate unsteadiness. A 230 mm long removable quartz tube protects the flame from ambient disturbances while still allowing optical access.

Velocity modulations in the unburned gases are produced using an L8S800 8” speaker driver that is fixed to the bottom of the burner plenum. It is driven by a B&K Type 2706 amplifier. The amplitude of the velocity modulation was not measured, but was adjusted so that the forced flame cycle contained two flame annihilation events: flame neck collapse and flame island burnout. A low temperature coefficient 20 ohm resistor was placed in series with the speaker driver. Voltages across both the speaker driver and the series resistor were acquired at 100 kHz using a LabVIEW 6040E data acquisition card.

* Corresponding author:
Phone: (+61) 3 8344 8876
Email: wisemans@student.unimelb.edu.au

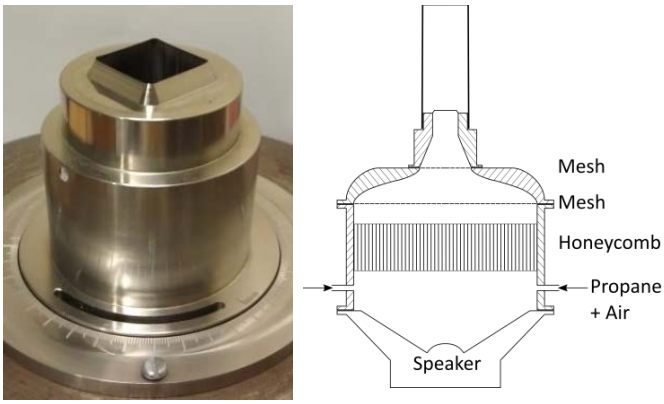


Figure 1. Left: Photograph of square port flame holder. Right: Schematic of burner plenum and flow conditioning.

A LaVision Flowmaster 3S camera system was used to image the visible light emission of the flame. The camera is equipped with a 150 mm Sigma lens at f/2.8, and a LaVision high-speed IRO image intensifier. A gate width of 100 μs was used. The 12 bit camera has a resolution of 1280×1024 and a maximum frame rate of 8 frames per second. In all experiments, the forced flame was allowed to stabilize for at least 3 hours before imaging was commenced.

An Arduino Due microcontroller was used to generate a 50 Hz sinusoidal input voltage signal to the speaker amplifier. A phase locked square wave was also generated. A second microcontroller, an Arduino MEGA 2560, was used to trigger the camera exposure. The Arduino MEGA counts the falling edges of the square wave and after a specified number of counts, an additional programmed time delay generates a camera trigger pulse. The flame cycle was imaged at different phases of the sinusoidal forcing signal by varying the time delay. This separation of tasks between the two microcontrollers allowed for more flexible control of the phase of the camera trigger without compromising the accuracy of the timing. Using an oscilloscope, the trigger delay was found to be accurate throughout the cycle to better than 5 μs.

## 3. Results and Discussion

Departures from the repeatability of the flame response can be classified by their time-scale. Non-repeatability on the order of, or less than, the period of the flame cycle produces noticeable variations in consecutive flame cycles and appear to be random. However, non-repeatability is also observed over a large number of flame cycles and appears to be systematic. Both forms of non-repeatability are now discussed.

### 3.1 Cycle-To-Cycle Periodicity

There are numerous potential causes of short term, cycle-to-cycle variations in the flame response. Unsteadiness in the incoming flow can be significant, and these are usually suppressed using flow straightening and meshes [10,11], as done in this study. Flame flickering can be a buoyancy induced disturbance in which the tip of the flame oscillates at frequencies typically between 10 and 20 Hz, and is due to the formation of toroidal vortices downstream of the flame. Flame flickering in open flames is reduced in low pressure environments [12], low gravity environments [13] and with co-flow [14]. Confining flames can also greatly reduce flame flickering, and is the approach used in our own experiments.

However, flame confinement can also introduce thermo-acoustic instability, where flame disturbances are amplified due to a coupling between the acoustic modes of the combustion chamber and the heat release rate of the flame. For our experiments, the length of the confining quartz tube was chosen so that the longitudinal fundamental frequency of the system was significantly greater than the frequencies at which the flame responds [3].

The repeatability of the flame over 60 consecutive cycles is demonstrated in Figure 2. At the sampling resolution of 50 μs and within this total time interval of 1.2 seconds, differences between images at the same phase are essentially random and appear to be primarily due to the camera's noise. If the sampling resolution is increased below 10 μs, random, cycle-to-cycle differences in flame neck collapse and island formation begin to appear, likely due to one of more of the disturbances discussed above. Thus, a conservative lower limit of short term, cycle-to-cycle periodicity is 50 μs, which is less than 1 deg phase at the flame's

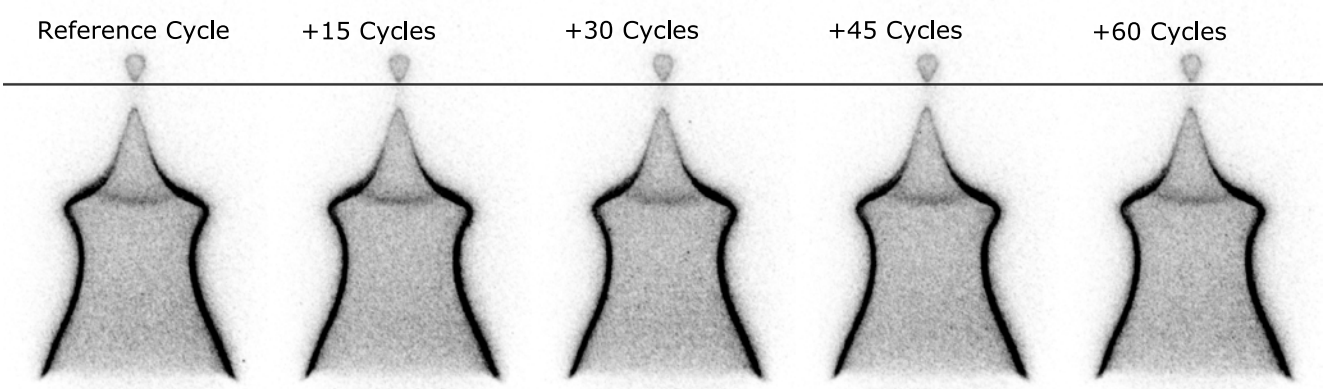


Figure 2. Images at the same phase of the forcing signal over 60 consecutive cycles. The horizontal line has been included to illustrate the precision of the phase timing.

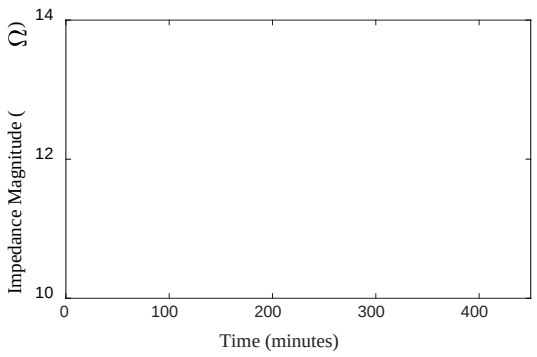


Figure 3. Measured speaker impedance over time during 50 Hz forcing of $\phi$=0.75 propane-air flame.

forcing frequency of 50Hz.

## 3.2 Longer Term Repeatability

The system relating the flame response to the amplifier forcing is comprised of four coupled subsystems [15]. The electrical subsystem of the speaker relates the amplifier forcing to the force on the voice coil. The mechanical subsystem relates the force on the voice coil to the velocity of the speaker cone. The acoustic system of the burner relates the speaker cone velocity to the velocity modulation at the flame. Lastly, the flame response to velocity modulation is a complicated system that has itself been studied extensively [3].

Figure 3 shows both the magnitude and phase of the speaker impedance over time. This impedance was determined from the measured speaker voltage and current, and is shown from when a given flame forcing experiment commences until after the flame is extinguished at about 420 minutes. The images in the first row of Figure 4 were taken at 180 minutes and those in the last row just prior to extinguishing the flame. The impedance magnitude was observed to increase by about 3% over the imaging period. Additional experiments found that the timing of the flame neck collapse relative to a reference phase of the forcing signal is only weakly dependent on the forcing amplitude. Therefore, a change in the magnitude of the velocity modulation is not thought to be the main cause of the phase shift seen in Figure 4. Further, the change in the impedance's phase over this same imaging period is only about 1 degree. Thus, the phase shift in the electrical subsystem alone does not appear to account for the phase shift seen in Figure 4.

However, the impedance of the speaker is the sum of the voice coil impedance and the motional impedance. The latter is a result of the so-called 'back emf' generated by the voice coil moving through the speaker's magnetic field. This motional impedance depends on both the mechanical stiffness and damping of the speaker and also the acoustic impedance of the burner plenum acting via the static pressure acting on the speaker cone. In this study, the effect of the motional impedance is easily demonstrated by simply turning off the fuel flow and extinguishing the flame at about 420 minutes in Figure 3. A step change is

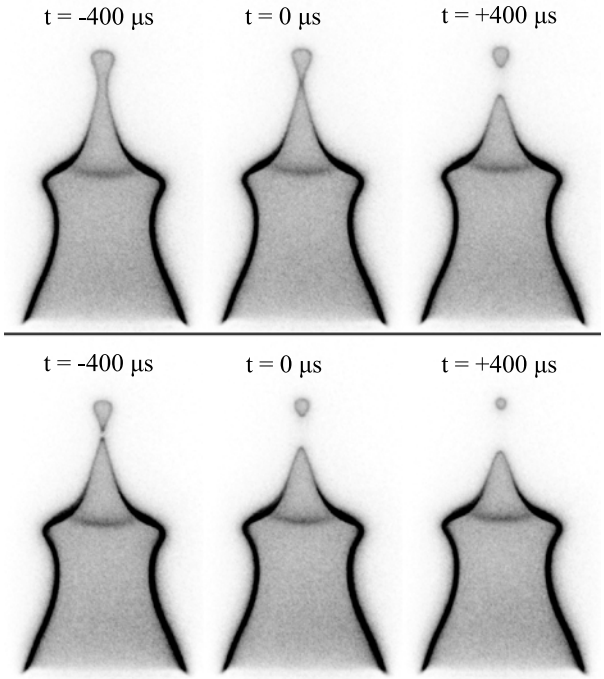


Figure 4. Images of the forced flame at three phases of the forcing signal. The indicated time refers to the time the image exposure was started relative to a reference phase of the forcing signal. The bottom row of images were taken 4 hours after the top row. Images within each row were taken within 20 seconds of one another.

immediately apparent, followed by a more gradual change in impedance as the rig cools.

Figure 3 also suggests that the rig approaches thermal equilibrium over a period of several hours. Conduction through the burner plenum is thought to be the main heat transfer path. However, it was also found that when forcing the flow without a flame present, the speaker impedance can drift randomly in magnitude and phase by 5-10% and 1-2 degrees respectively, presumably in response to fluctuations in the ambient conditions.

It was also observed that the flame height varied over periods on the order of minutes, as shown for an unforced flame in Figure 5. These changes are likely due to changes in the temperature of the flame holder, and therefore the preheating of the gases near the flame holder walls. This likely affects flame anchoring and hence the entire flame geometry.

Thus, whilst we cannot be categorical as to all the causes of these observed forms of drift in the rig, these variations are slow at a given operating condition and can therefore be compensated for manually. This is done in two ways once thermal equilibrium is approximated. The unforced flame height is first measured. This height then becomes a reference, with the premixture flow rate adjusted regularly by order of 1% at constant equivalence ratio to maintain this height throughout a given set of measurements. Second, the timing of the flame neck collapse is used for on-line re-referencing of the phase response, as these events have a duration of less than 1 deg phase at 50Hz forcing frequency.

Figure 6 shows that use of these two methods results in almost identical flames at a given phase, even though

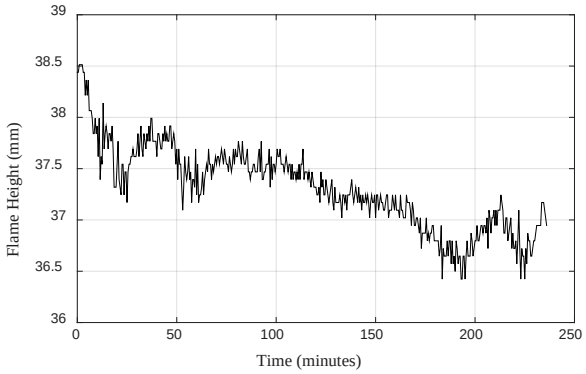


Figure 5. Variation in unforced flame height over time. Determined from flame images.

these images are taken hours apart. As discussed in Section 3.1, the flame neck collapse can be located well within a 50 μs time interval, and this is within 1 deg phase at this operating condition. The spatial resolution is also dependent on the periodicity of the flame, but is additionally a function of the accuracy of the measurement timing and the flame velocity. Again comparing the images in Figure 6, we also estimate a spatial resolution of better than 3 pixels or 200 μm.

## 4. Conclusions

The cycle-to-cycle and longer term repeatability of a forced, laminar, premixed flame has been investigated experimentally. It was found that for periods greater than a few minutes, drift in the flame's response to its forcing was significant, with thermal variations in the burner rig and resulting changes in the electro-mechanical response of the speaker both appearing responsible. Compensation via variations in the mixture flow rate of order 1% at fixed equivalence ratio coupled with on-line re-referencing of the phase response relative to a particular, short lived feature in each cycle was then demonstrated. This showed that cycle-to-cycle periodicity better than 1deg in phase for forcing cycles of order 50Hz frequency, and a spatial resolution of better than 200 μm, can both be established during experiments lasting of order several hours.

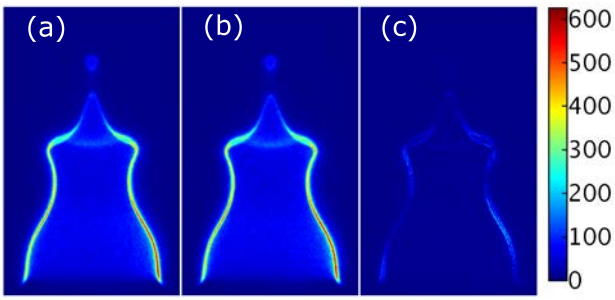


Figure 6. (a) and (b) are flame images taken 3 hours apart, at the same time delay after the flame neck collapse. (c) shows the absolute difference between the images on the same scale.

## 5. Acknowledgements

This research was supported by the Advanced Centre for Automotive Research and Testing (ACART, www.acart.com.au) and the Australian Research Council.

## 6. References

[1] F. Baillot and A. Bourehla, Combust. Sci. Technol. **126** (1997), pp 201-224.

[2] D. Durox, S. Ducruix, and S. Candel, Comb. Flame **125** (2001) pp. 982-1000.

[3] N. Karimi, M. J. Brear, S. Jin, and J. P. Monty, Comb. Flame **156** (2009) pp. 2201-2212.

[4] M. Talei, M. J. Brear, and E.R. Hawkes, J. Fluid Mech. **679** (2011) pp. 194-218.

[5] M. Talei, M. J. Brear, and E.R. Hawkes, Comb. Flame **159** (2012) pp. 757-769

[6] S. Candel, D. Durox, A. L. Birbaud, N. Noiray, and T. Schuller, Int. J. Aeroacoustics **8** (2009), pp. 1-56.

[7] T. Schuller, D. Durox, and S. Candel, Combust. Flame **128** (2002), pp. 88-110.

[8] S. Candel, D. Durox, and T. Schuller, 10th AIAA/CEAS Aeroacoustics Conference AIAA2004-2928 (2004), pp. 1444-1454.

[9] F. Baillot, D. Durox, and D. Demare, Proc. Combust. Inst. **29** (2002) pp. 1453-1460.

[10] J. Groth and A. V. Johansson, J. Fluid Mech. **197** (1988) pp. 139-155.

[11] V. Kulkarni, N. Sahoo, and S. D. Chavan, J. Wind Eng. Ind. Aerodyn. **99** (2011) pp. 37-45.

[12] D. Durox, F. Baillot, P. Scouflaire, and R. Prud'homme, Combust. Flame **82** (1990) pp.66-74.

[13] L. W. Kostiuk and R. K. Cheng, Combust. Flame **103** (1995) pp. 27-40.

[14] H. Gohari Darabkhani, Q. Wang, L. Chen, and Y. Zhang, Energ. Convers. Manage. **52** (2011) pp. 2996-3003.

[15] J. Whitaker and B. Benson, Standard Handbook of Audio Engineering Second Edition, McGraw-Hill, 2002, Chapter 15.

# An Experimental and Numerical Study into Laminar Flame Speeds of $H_2$/CO/Air Mixtures with $CO_2$ and $N_2$ Dilution

Rongxue Shang, Yang Zhang*, Mingming Zhu, Zhezi Zhang, Dongke Zhang
Centre for Energy (M473)
The University of Western Australia WA 6009 Australia

## Abstract

The effect of $N_2$ and $CO_2$ dilution on the laminar flame speed of $H_2$/CO/air mixtures was experimentally and numerically studied. Experiments were conducted at atmospheric pressure and 298K using a modified Bunsen flame approach, taking the flame stretch effect into account and using the Schlieren imaging technique. The $H_2$/CO mixtures with $H_2$ mole fraction of 25%, 50% and 75%, and the equivalence ratio for each fuel/air mixture ranging from 0.7 to 4.0, respectively, were tested. The numerical simulation was performed using Chemkin-Pro, employing three detailed kinetic mechanisms, namely Li-Mech, Frassoldati-Mech and Davis-Mech. The results showed that the modified Bunsen flame approach could accurately measure the laminar flame speeds. The laminar flame speeds of $H_2$/CO/air mixtures decreased with increasing $CO_2$ or $N_2$ dilution. $CO_2$ had a more profound effect than $N_2$ in reducing the laminar flame speed. It was also found that Davis-Mech and Li-Mech mechanism were capable of predicting the laminar flame speeds of $H_2$/CO/air at equivalence ratios tested, while Frassoldati-Mech under-predicted the laminar flame speed for $H_2$-rich fuels. With $N_2$ dilution, both Davis-Mech and Li-Mech adequately estimated the laminar flame speeds of all mixtures except for the case with 60 vol% $N_2$ dilution when the equivalence ratio was larger than 2. For $CO_2$ dilution, Li-Mech showed better predictions than the other two mechanisms, which successfully predicting the flame speeds at most conditions. Considering all of the tested conditions, Li-Mech presented the better prediction than Davis-Mech and Frassoldati-Mech but still need to be improved at large equivalence ratios under highly-$N_2$ diluted conditions.

*Keywords: Bunsen flame, Laminar flame speed, Mechanisms validation, $N_2$ and $CO_2$ dilution, Syngas.*

## 1. Introduction

Synthetic gas (syngas), produced by pyrolysis or gasification of coal or biomass, mainly contains $H_2$ and CO, $CO_2$ and $N_2$ with small amounts of other hydrocarbons such as $CH_4$. Such syngas can be an attractive alternative fuel for the internal combustion engines for small scale combined heat and power (CHP) applications [1]. It is necessary to understand the combustion characteristics of synthetic gas in order to optimise the engine performance.

Laminar flame speed ($S_u^0$, method-independent), an important combustion property, has been extensively investigated in previous studies. A detailed review of the laminar flame speed studies on syngas/air flames can be found in [2]. However, as stated in [2], the experimental data obtained using different methods presented poor agreement between each other, especially under highly diluted conditions with $CO_2$ or $N_2$.

Meanwhile, some comprehensive $H_2$/CO/$O_2$ combustion kinetic models have been also developed based on those experimental data [3-6]. However, the accuracy of the existing kinetic models has not been adequately validated for diluted $H_2$/CO/$O_2$ flames.

In the present study, $S_u^0$ of $H_2$/CO/air mixtures over a wide range of $H_2$ content in the fuel (from 25 vol% to 75 vol%) were measured over a range of equivalence ratios ($\phi$) varying from 0.7 to 4.0 under atmospheric conditions via a modified Bunsen flame method. The laminar flame speeds of the $H_2$/CO/air mixtures were also simulated using three mechanisms, namely Li-Mech [4], Frassoldati-Mech [5] and Davis-Mech [6] and the results were validated against the experimental data of $S_u^0$'s. In addition, the effect of $N_2$ (0% - 60 vol%) and $CO_2$ (0% - 40 vol%) dilution on the laminar flame speed of $H_2$/CO/air mixtures was also studied.

## 2. Experimental

Several methods were employed to measure $S_u^0$, including spherically propagating flame method [7], counter-flow flame method [2], heat flux method [8], among others. On account of simplicity, $S_u^0$ in the present study was measured using a Bunsen flame method. The experimental determination of $S_u$ (method-dependent flame propagation speed) was based on the flame area method by applying the mass conservation balance [9]:

$$\dot{m} = \rho_u S_u A = \rho_u \dot{Q} \rightarrow S_u = \frac{\dot{Q}}{A} \quad (1)$$

where $\rho_u$ denotes the unburned gas density and $\dot{Q}$ is the total volumetric flow rate of the unburned mixture. By definition, $A$ is the flame front area viewed from the unburned mixture side.

The flow rates of the fuel and air streams were respectively controlled by adjusting the upstream pressures of the sonic nozzles. The Reynolds number of the gas flow at the burner exit remained within the range 400 - 1400. The fuels were mixtures of pure $H_2$ (>99.99%) and CO (>99.9%). Diluents were pure $N_2$ (>99.9%) and $CO_2$ (>99.99%). The oxidiser was compressed air, pre-dried by desiccators. Two straight cylindrical stainless steel tubes with inner diameters of 4.44 mm and 7.56 mm, respectively, were employed as the Bunsen burners. The length of each tube was at least

* Corresponding author: Dr Yang Zhang
Phone: (+61) 8 6488 5528
Email: yang.zhang@uwa.edu.au

50 times of its diameter, ensuring that the flow was laminar and fully developed at the burner exit [10]. A *Z*-type two-mirror Schlieren system was deployed to obtain the Schlieren images, which were captured using a digital CMOS camera. A MATLAB program was developed to process the edge of the flame on the unburned mixture side.

The uncertainty of the $S_u^0$ measurement was estimated following Moffat's [11] method. The uncertainty of $\phi$ caused by the uncertainties in the $H_2$, CO and air flow rates, were estimated from the calibration data of the gas flowmeters.

## 3. Numerical modelling

$S_u^0$ were also calculated using the Chemkin-Pro package. The thermal diffusion (Soret) effect and multi-component transport were included in the calculations due to the strong mass diffusivity of hydrogen.

For comparison, three kinetic mechanisms denoted as Li-Mech [4], Frassoldati-Mech [5], and Davis-Mech [6], respectively, were employed in the current modelling. The initial temperature was set to 298 K and initial pressure at 1 atm. The grid control parameters, GRAD and CURV, were set at 0.05-0.1, and the grid number was 800 – 3000.

## 4. Results and discussion

### 4.1 Validation of the modified Bunsen flame methodology

Previous studies [9, 12] revealed that the accurate measurements of flame front and flame area were key to the determination of $S_u^0$ using the Bunsen flame approach. Thus, the present study compared two flame areas, namely, one visible to bear eyes (natural light image) and the other, the Schlieren areas, respectively (shown in Fig.1). The flame visible edge, reflecting the chemiluminescence area, was obtained within the narrow reaction region (Edge A), while the Schlieren visualization based on the deflection of light by a refractive index gradient, was directly related to flow density gradient, i.e., temperature gradient [13]. Therefore, the outer edge of the Bunsen flame on the Schlieren image was located at the maximum of the brightness gradient, representing the largest temperature gradient (Edge B shown in Fig.1c). The brightest edge

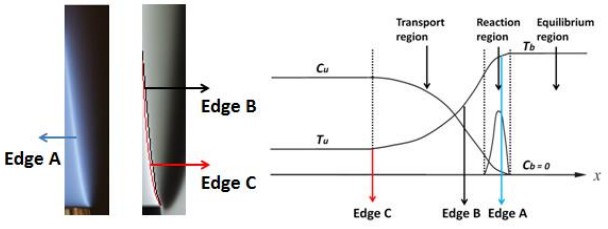


(a) (b) (c)

Fig.1 Bunsen flame image processing: (a) natural light images ($H_2$:CO = 25:75, $\phi$ = 0.8), (b) Schlieren images ($H_2$:CO = 25:75, $\phi$ = 0.8), (c) detailed structure of a corresponding premixed flame(Edge A: visible edge, Edge B: maximum of brightness gradient of Schlieren edge, Edge C: brightest Schlieren edge)

of the flame on the Schlieren image, denoted the region where the temperature begins to increase (Edge C). Edge C was much closer to the flame front viewed from the unburned mixture side, matching the definition of $S_u^0$. Therefore, Edge C was adopted in $A$ calculation in the present study.

The effect of curvature at the flame top tip and the heat dissipation at the flame bottom also affected the accuracy of the $S_u^0$ measurements. These effects could be suppressed by allowing the highest possible flow velocity of mixtures [10]. However, increasing the flow velocity would also bring in other problems. Since the flame stretch increases with the flow velocity, the flame stretch effect grows to an extent that would considerably affect the measured $S_u^0$ values by as much as 15% under the current conditions, as indicated in Fig. 2. This means that simply assuming $S_u^0 = S_u$, as many previous studies did, is simply inadequate. Therefore, the effect of flow rate on $S_u^0$, which was seldom inspected in previous studies, cannot be simply neglected. By definition, $S_u^0$ is the velocity of unburned mixture propagating towards the 1-D flat, stretch-free, stable and adiabatic flame. In the Bunsen flame structure, this ideal flame can only be theoretically achieved when the flow velocity $\omega$ exactly equals to $S_u^0$. Therefore, a similar approach to the ones in a spherically propagating flame or counter-flow flame was used. Basically, the experimentally measured $S_u$ at various flow velocities were linearly extrapolated. The flame speed at which $S_u = \omega$ was regarded as the theoretical stretch-free laminar flame speed $S_u^0$, as presented in Fig. 2.

The modified Bunsen flame approach was put to test to investigate $S_u^0$ of various $H_2$/CO/air mixtures as a function of $\phi$ ranging from 0.7 – 4.0. Both the experimental data and predicted data are shown in Fig. 3 and both sets of data are compared with the literature experimental data. As shown in Fig.3a, the present results agreed excellently well with the data measured using the combustion bomb [14-17] and counter-flow methods [18]. The calculated results using Davis-Mech and Li-Mech matched very well with the experimental data while Frassoldati-Mech under-predicted $S_u^0$ when $H_2$ content was more than 50%, and when the mixtures were close to the stoichiometry. Compared to the

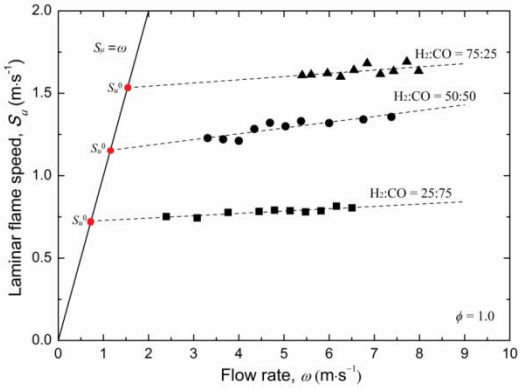


Fig.2 Variations of flame propagation speed with respect to flow rate ($\phi$ = 1.0, symbols: experimental data; solid line: $S_u = \omega$; dash lines: linear extrapolation)

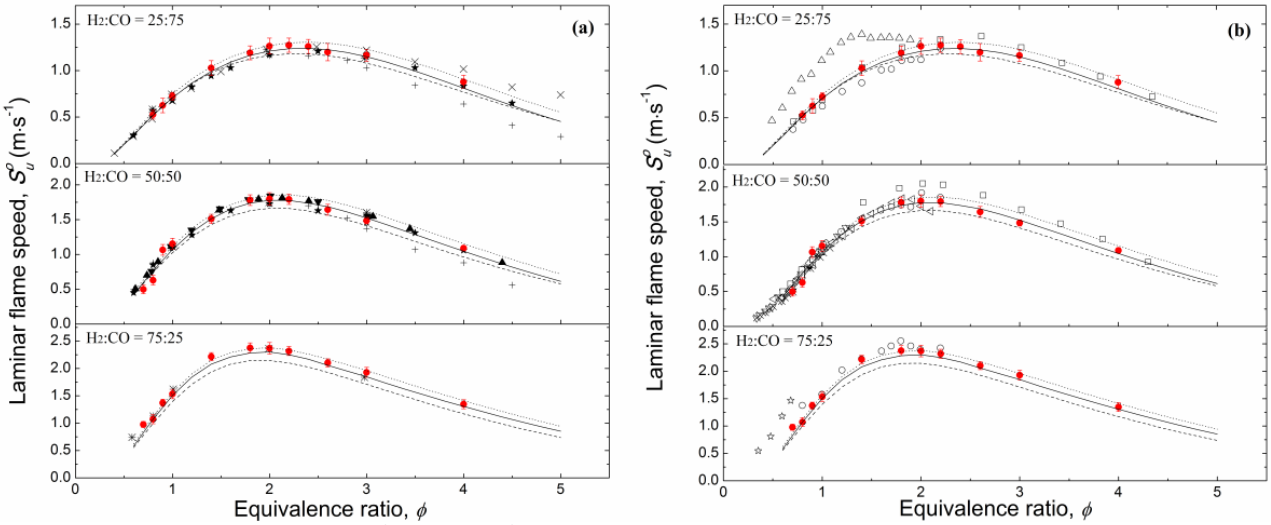


Fig. 3 Experimental and computed laminar flame speeds of $H_2$/CO/air mixtures: (a) comparison with previous results using combustion bomb and counter-flow method; (b) comparison with previous results using Bunsen flame method. (●: Present work; △: B. Dam et al.[19]; □: H. J. Burbano et al. [12]; ○: D. Lapalme et al. [20]; ▽: N. Bouvet et al.[9]; ◇: J. Natarajan et al. [10]; ◁: C.Dong et al. [21]; ☆: Z.H. Wang et al.[8]; ×: N. Bouvet et al.[22]; ★: H.Y. Sun et al. [15]; +: M.I.Hassan et al. [16]; ✳: Deepti Singh et al.[17]; ▲: Ian C. Mclean et al.[14]; ▼: J.S. Kim et al.[18]; and solid line: Davis-Mech; dash line: Li-Mech; dot line: Frassoldati-Mech)

literature data obtained using the Bunsen flame method as shown in Fig 3b, the present data largely diminished the experimental uncertainty. These results suggest that this modified Bunsen flame approach is adequately reliable in the determination of the laminar flame speeds of premixed flames.

## 4.2 $N_2$ and $CO_2$ dilution effect

Experimental and numerical results of $S_u^0$'s of $H_2$/CO/air mixtures diluted with 20%, 40% and 60% of $N_2$ and 20% and 40% of $CO_2$ by volume are presented in Fig. 4. Some literature experimental data was also included for comparison [8-10, 12, 14-22]. As seen from Fig. 4a, $N_2$ dilution considerably decreased $S_u^0$ of the syngas mixtures. In addition, increasing $N_2$ dilution shifted the peaks of the $S_u^0$ - $\phi$ curves to the leaner side of the mixture. For $H_2$/CO/air mixtures diluted with 20 vol% and 40 vol% $N_2$, the present experimental results agreed well with the calculated results using Davis-Mech and Li-Mech while the Frassoldati-Mech under-estimated $S_u^0$ at 75% $H_2$. For the $H_2$/CO/air mixtures with 60 vol% $N_2$ dilution, all mechanisms under-predicted $S_u^0$ when $\phi$ was larger than 2.

$CO_2$ addition was also shown to reduce the laminar flame speed. At the same dilution ratio, $CO_2$ showed a stronger dilution effect than $N_2$ in reducing $S_u^0$ (shown in Fig. 4b), consistent with the literature data [23]. The $CO_2$ dilution effect was correctly predicted by Li-Mech under most conditions. For the fuels with 25% $H_2$ content, Davis-Mech predictions showed better agreement with the results of 20 vol% $CO_2$ dilution when $\phi$ at 2.6 and 3.0. Again, Frassoldati-Mech under-estimated $S_u^0$ for $H_2$-rich fuels, especially for mixtures with 20 vol% $CO_2$ dilution.

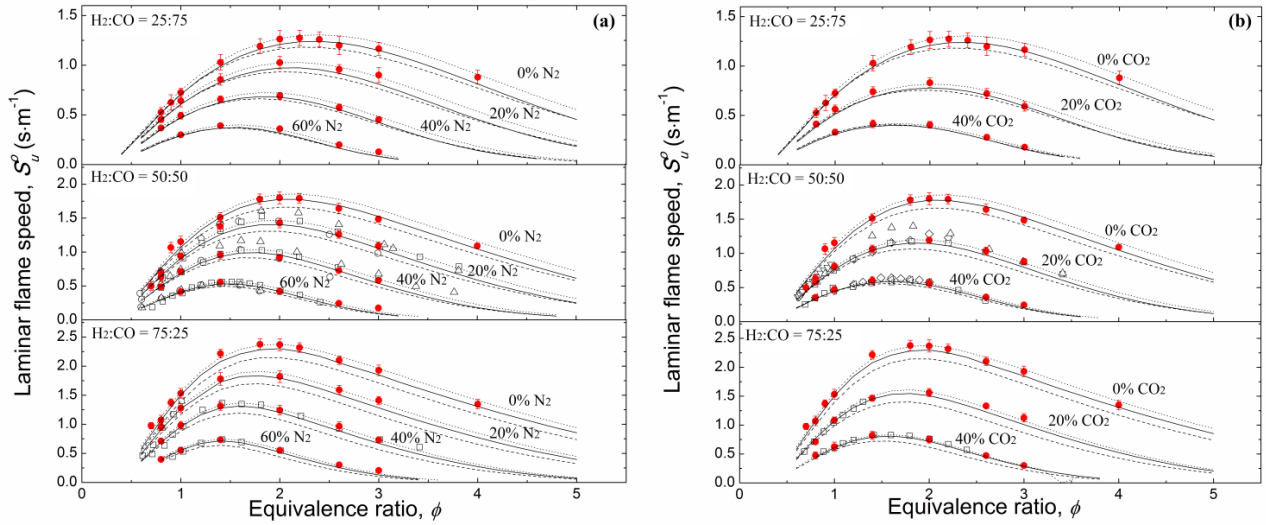


Fig. 4 Experimental and computed laminar flame speeds of $H_2$/CO/air mixtures: (a) with $N_2$ dilution; (b) with $CO_2$ dilution. (●: Present work; △: B. Dam et al.[19]; □: H. J. Burbano et al. [12]; ○: D. Lapalme et al. [20]; ▽: N. Bouvet et al.[9]; ◇: J. Natarajan et al. [10]; ◁: C.Dong et al. [21]; ☆: Z.H. Wang et al.[8]; ×: N. Bouvet et al.[22]; ★: H.Y. Sun et al. [15]; +: M.I.Hassan et al. [16]; ✳: Deepti Singh et al.[17]; ▲: Ian C. Mclean et al.[14]; ▼: J.S. Kim et al.[18]; and solid line: Davis-Mech; dash line: Li-Mech; dot line: Frassoldati-Mech)

Considering all of the tested conditions including those without dilution, with $N_2$ and $CO_2$ dilution, Li-Mech presented better prediction than Davis-Mech and Frassoldati-Mech. However, Li-Mech still noticeably under-predicted at large equivalence ratios under highly-$N_2$ diluted conditions.

## 5. Conclusions

Laminar flame speeds of $H_2$/CO/air mixtures with $N_2$ (0 – 60 vol%) and $CO_2$ (0 – 40 vol%) dilution were measured using a modified Bunsen flame approach under atmospheric conditions. $H_2$ content in the $H_2$/CO fuels varied from 25% to 75% and $\phi$ varied from 0.7 to 4.0 for each mixture. Numerical simulations were also performed using three kinetic mechanisms.

Due to the more accurate measurement of the flame area and appropriate reduction of stretch effect on the Bunsen flame, the measured data showed good agreement with the literature data using the combustion bomb and counter-flow methods, which are more complex than the Bunsen flame approach. The results proved that the modified Bunsen flame approach is simple yet accurate in measuring the laminar flame speeds. Both Davis-Mech and Li-Mech adequately predicted the flame laminar speeds of the mixtures, while Frassoldati-Mech under-predicted the $S_u^0$ for $H_2$-rich fuels and when flames were close to the stoichiometric conditions.

Increasing $N_2$ and $CO_2$ dilution resulted in a significant decrease in the $S_u^0$ of the syngas mixtures, and shifted the highest $S_u^0$ to the lean side. The effect of $CO_2$ dilution was more profound than that of $N_2$ in reducing $S_u^0$. For $N_2$ dilution, both Davis-Mech and Li-Mech are capable of predicting the flame speeds except for cases with 60 vol% $N_2$ dilution when $\phi$ was greater than 2. For $CO_2$ dilution, Li-Mech showed better predictions than the other two mechanisms, which successfully predicted the flame speeds under most conditions. Moreover, for both $CO_2$ and $N_2$ dilution, Frassoldati-Mech again under-estimated $S_u^0$ for $H_2$-rich fuels.

Considering all of the tested conditions, Li-Mech presented better prediction than Davis-Mech and Frassoldati-Mech but still need to be improved at large equivalence ratios under highly-$N_2$ diluted conditions.

## 6. Acknowledgments

This study received partial financial supports from the ARC under Linkage Project Scheme (LP100200135) and Discovery Project Scheme (DP110103699), and the Australia-India Strategic Research Fund Project (GCF020010).

## 7. References

[1] J. Zhu, D.K. Zhang, K.D. King, CHEMECA **96**(3**)** (1996), pp. 131-136.

[2] Y. Zhang, W. Shen, M. Fan, H. Zhang, S. Li, Combust. Flame, **161**(10)(2014), pp. 2492-2495.

[3] A. Kéromnès, W.K. Metcalfe, K.A. Heufer, N. Donohoe, A.K. Das, C.-J. Sung, J. Herzler, C. Naumann, P. Griebel, O. Mathieu, M.C. Krejci, E.L. Petersen, W.J. Pitz, H.J. Curran, Combust. Flame,, **160**(6) (2013), pp. 995-1011.

[4] J. Li, Z. Zhao, A. Kazakov, M. Chaos, F.L. Dryer, J.J. Scire, Int. J. Chem. Kinet., **39**(3) (2007), pp. 109-136.

[5] A. Frassoldati, T. Faravelli, E. Ranzi, Int. J. Hydrogen Energy, **32**(15) (2007), pp. 3471-3485.

[6] S.G. Davis, A.V. Joshi, H. Wang, F. Egolfopoulos, Proc. Combust. Inst., **30**(1) (2005), pp. 1283-1292.

[7] C. Prathap, A. Ray, M.R. Ravi, Combust. Flame, **159**(2) (2012), pp. 482-492.

[8] Z.H. Wang, W.B. Weng, Y. He, Z.S. Li, K.F. Cen, Fuel, **141** (2015), pp. 285-292.

[9] N. Bouvet, C. Chauveau, I. Gökalp, S.-Y. Lee, R. Santoro, Int. J. Hydrogen Energy, **36**(1) (2011), pp. 992-1005.

[10] J. Natarajan, T. Lieuwen, J. Seitzman, Combust. Flame, **151**(1-2) (2007), pp. 104-119.

[11] R.J. Moffat, Exp. Therm Fluid Sci., **1**(1) (1988), pp. 3-17.

[12] H.J. Burbano, J. Pareja, A.A. Amell, Int. J. Hydrogen Energy, **36**(4) (2011), pp. 3232-3242.

[13] G. Settles, Schlieren and shadowgraph techniques: visualizing phenomena in transparent media, Springer Science & Business Media, 2001.

[14] I.C. McLean, D.B. Smith, S.C. Taylor, Symp. (Int.) Combust, **25**(1994), pp. 749-757.

[15] H. Sun, S. Yang, G. Jomaas, C. Law, Proc. Combust. Inst., **31**(1) (2007), pp. 439-446.

[16] M. Hassan, K. Aung, G. Faeth, J. Propul. Power, **13**(2) (1997), pp. 239-245.

[17] D. Singh, T. Nishiie, S. Tanvir, L. Qiao, Fuel, **94** (2012), pp. 448-456.

[18] J.S. Kim, J. Park, D.S. Bae, T.M. Vu, J.S. Ha, T.K. Kim, Int. J. Hydrogen Energy, **35**(3) (2010), pp. 1390-1400.

[19] B. Dam, V. Ardha, A. Choudhuri, J. of Energy Resour. Technol., **132**(4) (2010), pp. 044501.

[20] D. Lapalme, P. Seers, Int. J. Hydrogen Energy, **39**(7) (2014), pp. 3477-3486.

[21] C. Dong, Q. Zhou, Q. Zhao, Y. Zhang, T. Xu, S. Hui, Fuel, **88**(10) (2009), pp. 1858-1863.

[22] N. Bouvet, C. Chauveau, I. Gökalp, F. Halter, Proc. Combust. Inst., **33**(1) (2011), pp. 913-920.

[23] Y. Zhang, W. Shen, H. Zhang, Y. Wu, J. Lu, Fuel, **157** (2015), pp. 115-121.

# Lewis number effects on edge-flame propagation in lifted turbulent flames

Shahram Karami[1,*], Mohsen Talei[2], Evatt R. Hawkes[1,3], Hongfeng Yu[4]
[1] School of Photovoltaic and Renewable Energy
The University of New South Wales, NSW 2052, Australia
[2] Department of Mechanical Engineering
University of Melbourne, Melbourne, VIC 3010, Australia
[3] School of Mechanical Engineering
The University of New South Wales, NSW 2052, Australia
[4]Computer Science and Engineering
University of Nebraska-Lincoln, Lincoln, NE 68588, United States of America

## Abstract

Three turbulent lifted slot-jet flames of different fuel Lewis numbers are studied using direct numerical simulation (DNS). To reduce the computational cost, a one-step chemistry model is employed with a mixture-fraction dependent activation energy reproducing the dependence of the laminar flame speed on the equivalence ratio which is representative of hydrocarbon fuels. In addition to turbulent flames, axisymmetric laminar jet flames with a same chemistry model to that of turbulent flames are simulated. It is found that the maximum reaction rate decreases as the Lewis number increases in the laminar cases. Analysis of the turbulent cases reveals that the extinction limit is affected by the Lewis number of the fuel. The scalar dissipation rate of the extinction limit increases as the Lewis number decreases. For a given positive curvature, the conditional edge-flame propagation velocity on the curvature increases as the Lewis number decreases. This is similar to the observation in premixed flames and can be explained based on thermo-diffusive effects.

*Keywords: Turbulent lifted flames, Lewis Number, Edge-flames, Triple flames.*

## 1. Introduction

Recently, we are witnessing a global movement towards using alternative and cleaner fuels to produce energy. One of the challenges with these fuels such as syngas and hydrogen is the possible impacts of thermo-diffusive instabilities on the combustion efficiency and pollutant emissions. The non-dimensional number describing this effect is known as Lewis number which is defined as the ratio of thermal diffusivity to molecular diffusivity. It is well-known that the propagation velocity of a laminar premixed flame depends on the Lewis number of reactants and the flame front curvature [1]. For triple flames, the curvature of the flame front is dominantly positive which means the flame structure is convex towards reactant, therefore it is expected to observe a higher propagation velocity for triple flames with increasing the fuel Lewis number [2-4]. This can be explained based on heat and species diffusion. When the flame front is convex towards the reactant and the Lewis number is smaller than unity, the reactants will diffuse into the reaction zone more rapidly than the heat diffused away from this region. Consequently, the temperature will increase, resulting in a rapid increase of the reaction rate [4]. Chen et al. [5] studied the effect of Lewis number in a counter flow and a laminar lifted flame configuration. The methane- and propane-air flames with different dilution levels in the fuel stream, facilitating a wide range of fuel Lewis number, were studied. They reported that the reactant effective Lewis number at the flame base is an important parameter in the counter-flow configuration whereas the fuel Lewis number is important in lifted triple flames.

The importance of the Lewis number has been also investigated in turbulent premixed [6-9] and non-premixed flames [10]. The experimental studies of lifted turbulent non-premixed flames [11] have also investigated the effects of the fuel Lewis number on the stabilisation process. Cessou et. al. [11] found that the lifted height and the blow-out limit of hydrocarbon fuels depend on the Lewis number.

It is very challenging to measure the edge-flame propagation velocity, curvature of the flame front and scalar dissipation rate simultaneously in experimental setups. However, this simultaneous measurement is required to understand the edge-flame dynamics in lifted flames in addition to the stabilization mechanism. Therefore, this paper seeks to address this gap by analysing the response of the flame propagation and flame front curvature to the scalar dissipation rate as a key parameter in this problem when the fuel Lewis number of fuel varies.

## 2. Numerical method and simulation parameters

The non-dimensionalised conservation equations of mass, momentum, sensible energy and species are solved. These equations are non-dimensionalised with respect to the inlet jet width, H, the speed of sound, temperature and thermodynamic properties on the jet centreline at the inlet. A single-step irreversible reaction

* Corresponding author:
Phone: (+61) 2 9385 4602
Email: s.karami@unsw.edu.au

of F+rO→(1+r)P where r is the stoichiometric ratio, i.e. the mass of oxidant disappearing with unit mass of fuel was used. The DNS code S3D_SC [12] is employed here. The solver uses high-order accurate, low dissipative numerical schemes and a 3D structured, Cartesian mesh. The spatial derivatives were discretised using an 8$^{th}$ order central differencing scheme and the time integration was performed with a 6-stage, 4$^{th}$ order, explicit Runge-Kutta method. To suppress the numerical fluctuations at high wave numbers, a 10th order filter was applied every 10 time steps. Non-reflecting outflow boundary conditions were used in the streamwise and transverse directions, and periodic boundary conditions were applied in the spanwise direction. The simulation parameters along with their values are presented in table 1. The configuration is a slot jet flame. The mean inlet axial velocity, $U_{in}$, and fuel mass fraction, $Y_F$, were specified using a tanh-based profile with an inlet momentum (and mixing layer) thickness, $\delta$, is equal to 0.05H. To describe the velocity fluctuations at the inlet, a homogeneous isotropic turbulence field based on a prescribed turbulent energy spectrum with a turbulence intensity of 5% is first produced. These velocity fluctuations are then added to the mean inlet velocity using the Taylor's frozen turbulence hypothesis [12, 13].

A uniform grid spacing of 0.02H was chosen for the streamwise and spanwise directions. An algebraically stretched mesh was applied [14] in the transverse direction which maintained uniform spacing of 0.02H in $|y|<7.5H$ and less than 3% of grid stretching in the region of $|y| > 7.5H$. The simulation was run for 18.0 jet flow through times, $t_j = L_x/U_j$ (where $L_x$ is the length of the computational domain in the streamwise direction), and the data of the last $12.0t_j$ were used for analysis. The simulations were performed for three different Lewis numbers of the fuel as 0.7, 1.0 and 1.3.
The turbulence and chemistry resolutions are discussed in more details in Ref. [12].

Table 1 Numerical and physical parameters of the simulation.

| **Description** | **Value** |
|---|---|
| Domain size ($L_x \times L_y \times L_z$) | 16H×24H×6H |
| Number of grid points ($N_x \times N_y \times N_z$ ) | 800×800×300 |
| Mean inlet jet Mach number ($U_j/a_{ref}$) | 0.48 |
| Laminar co-flow Mach number ($U_{co}/a_{ref}$) | 0.001 |
| Jet non-dimensional temperature ($T_{jet}$) | 2.5 |
| Co-flow non-dimensional temperature ($T_{co\text{-}flow}$) | 2.5 |
| Jet Reynolds number (Re) | 5280 |
| Inlet velocity fluctuation intensity | 5% |
| Fuel mass fraction in the fuel stream ($Y_{F,o}$) | 1.0 |
| Oxidiser mass fraction in the oxidiser stream ($Y_{O,o}$) | 0.233 |
| Stoichiometric oxidiser to fuel mass ratio (r) | 4.0 |
| Heat-release parameter ($\alpha$) | 0.86 |
| Zel'dovich number ($\beta$) | 5.0 |
| Non-dimensionalisation Damköhler number (Da) | 800 |
| Lewis number (Le) | 0.7 – 1.0 – 1.3 |
| Prandtl number (Pr) | 0.7 |

## 3. Mathematical background

Three components of the flow velocity in a time-resolved manner have been measured simultaneously by the most advanced experiments [15]. These have provided very useful information; however, flame propagation velocities relative to the flow have never been measured. In our previous study of stabilization mechanism of a turbulent lifted flame with unity Lewis number of the fuel, it was shown that flame propagation plays a key role, in the stabilization process. However, to the best of our knowledge, there is no study on the effects of the fuel Lewis number on the edge-propagation velocity in lifted flames. Therefore, this study will focus on Lewis number effects in turbulent lifted flames. For this purpose, the flame edge is defined as the intersection of a mixture-fraction iso-surface with a product mass-fraction iso-surface. The mixture-fraction iso-values were 0.077, 0.07 and 0.066 which correspond to the mixture-fractions having the highest laminar flame speeds in one-dimensional flat premixed laminar flames with the Lewis numbers of 0.7, 1.0 and 1.3, respectively. The product iso-values were selected at the point of the maximum reaction rate for each laminar flame corresponding to a given Lewis number.

The edge-flame displacement speed, $S_e$, in the plane of the mixture-fraction iso-surface in the direction $T_2$, which is the tangent vector to the mixture-fraction iso-surface that is normal to the intersection line which defines the edge, pointing towards the unburned reactants is given in terms of the product mass-fraction self-displacement speed $S_d$, the mixture-fraction self-displacement speed $S_z$, and the inner product of the normal vectors to product and mixture-fraction iso-surfaces k as [16]:

$$S_e^* = \frac{S_d^* - kS_Z^*}{\sqrt{1-k^2}} \tag{1}$$

The iso-surface self-displacement speeds are given by [17]:

$$\rho_u S_Z^* = \rho S_Z = \frac{1}{|\nabla Z|}\left(-\frac{\partial}{\partial x_j}\left(\frac{\mu}{ScRe}\frac{\partial Z}{\partial x_j}\right)\right), \text{ and}$$
$$\rho_u S_d^* = \rho S_d = \frac{1}{|\nabla Z|}\left(-\dot{\omega}_P - \frac{\partial}{\partial x_j}\left(\frac{\mu}{ScRe}\frac{\partial Y_P}{\partial x_j}\right)\right), \tag{2}$$

The curvature of product mass fraction iso-surfaces is defined as $|\nabla \cdot \mathbf{N}_{Yp}|$. Figure 1 presents schematic of the edge-flame propagation velocity.

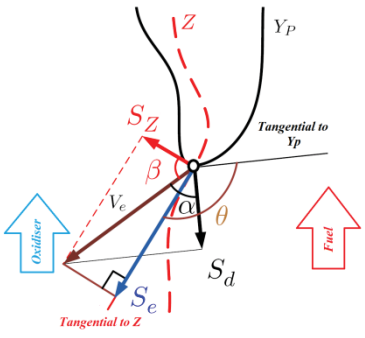


Figure 1. Schematic of the edge-propagation velocity.

## 4. Results

For an orientation first, symmetric laminar lifted flames with the same chemistry parameters to those of turbulent flames were simulated. Figure 2 shows the reaction rates of laminar triple flames for different fuel

Lewis numbers. It is observed that the maximum reaction rates decreases as the Lewis number increases which is expected as the curvature is positive [18]. Also it is noted that the lifted height increases and the diffusion tail disappears as the Lewis number increases.

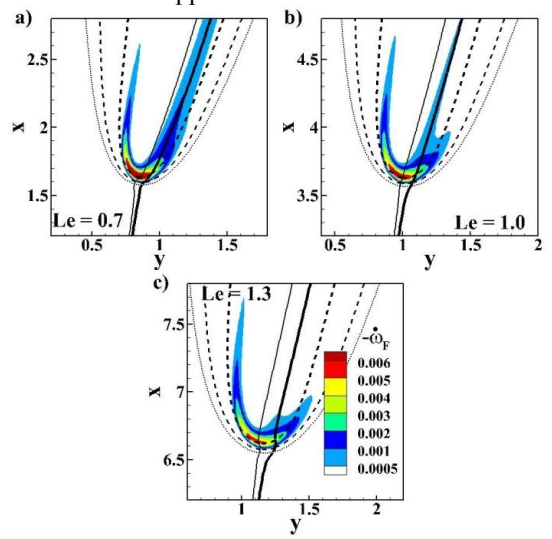


Figure 2. The contour plots of reaction rates of laminar triple flames with fuel Lewis number of a) 0.7, b) 1.0 and c)1.3 ( The solid lines are mixture fraction iso-lines and the dashed lines are different levels of product mass fraction).

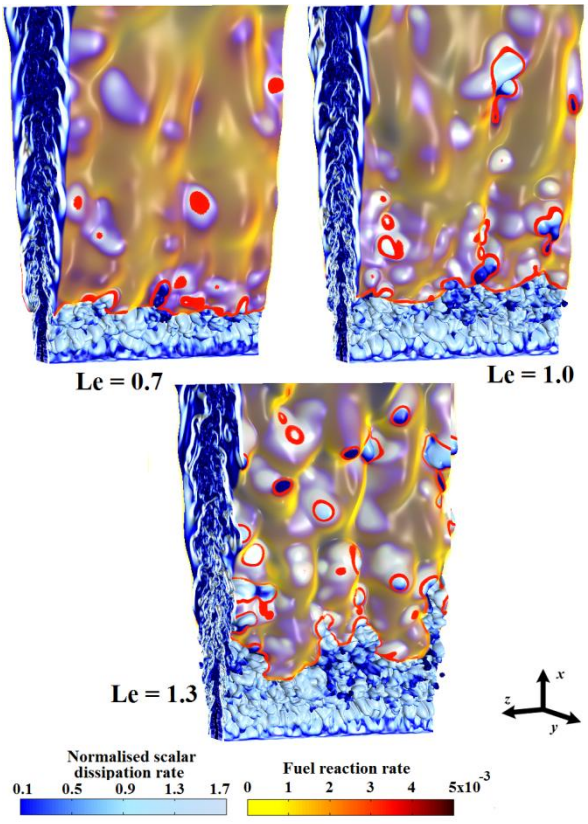


Figure 3. Three-dimensional volume rendering of logarithm of the scalar dissipation rate (blue/white) and reaction rate (red/orange) for different Lewis number of fuels.

Moving to the turbulent cases, Fig. 3 presents the volume rendering of logarithm of the scalar dissipation rate (blue/white) and reaction rate (red/orange) for different Lewis numbers of the fuel stream. From left to right are cases with the Lewis numbers of 0.7, 1.0 and 1.3. The reaction sheet is strongly positive for Le = 0.7 but becomes weaker as the Lewis number increases. The flame base also experiences a higher level of distortion. As the Lewis number increases, the shield generated by the flame becomes weaker and therefore the probability of being broken by large-eddy structures is higher. As a result, more holes are observed for Le = 1.3. Also, it is noted that the holes are highly convoluted for this case.

The roles of the scalar dissipation rate and curvature are now discussed. Figure 4 shows the conditional mean of the edge-propagation velocity on the scalar dissipation rates for different Lewis numbers. The results are consistent with those observed with regards to the triple flame response to the scalar dissipation rate [2, 4, 19-21]. The edge-flame propagation velocity decreases as the scalar dissipation rate increases and the flame is extinguished at a critical value. However, the extinction limits are different for different cases. The Le = 0.7 case has a higher extinction limit and a higher propagation velocity for all values of scalar dissipation rates. On the other hand, the extinction limit for Le = 1.3 is the smallest. This implies that the flame with a higher Lewis number will be extinguished more easily. This is in agreement with the observation in the literature that the critical scalar dissipation rate marking the triple flame extinction increases as the Lewis number decreases [4, 22, 23]. Furthermore, this explains formation of a larger number of local extinctions on the flame sheet and a higher convolution at the flame base for Le > 1 observed in Fig. 3.

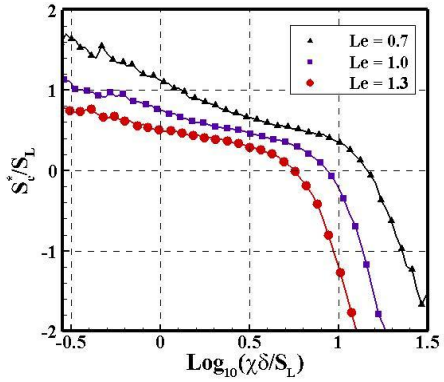


Figure 4. Conditionally averaged edge-propagation velocity on normalised scalar dissipation rate at the flame base for three cases of Lewis number 0.7, 1.0 and 1.3.

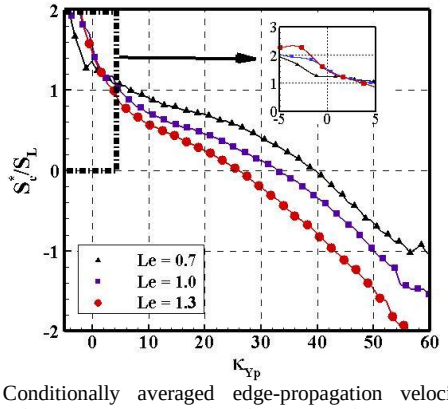


Figure 5. Conditionally averaged edge-propagation velocity on product-mass fraction curvature at the flame base for three cases of Lewis number 0.7, 1.0 and 1.3.

Another important parameter is the flame front curvature which has been shown to play an important role in flame propagation [7, 8]. Figure 5 presents the

conditional mean of the edge-flame propagation velocity on the curvature of the product mass-fraction iso-surface. In contrast to laminar triple flames, there is a small region of negative curvatures which is due to the effects of turbulence. The edge-flame propagation velocity non-linearly decreases as the curvature increases. It is well-known that a higher scalar dissipation rate causes a larger curvature and consequently two premixed flames merge on the diffusion tails [24]. This is consistent with what is observed in Fig. 5 as high scalar dissipation rates are coincident with large curvatures. Figure 5 also shows that for a given positive curvature, the edge propagation velocity increases as Lewis number of the fuel decreases. This observation can be explained using the thermo-diffusive properties of the fuel. When the curvature is positive and Le < 1, the fuel diffuses faster into the flame front than the heat diffusing out. This will increase the reaction rate and therefore the edge-propagation velocity. The opposite behaviour is however expected for Le > 1.

## 5. Conclusion

Direct numerical simulation (DNS) was used to study the effects of fuel Lewis number on the edge-flame propagation in laminar and turbulent lifted flames. It was found that the maximum reaction rate decreases as the Lewis number increases in the laminar cases. For the turbulent cases, an increased number of extinction holes and more distortion of the flame base were observed as the Lewis number was increased. In contrast to laminar triple flames in which the curvatures of the flame fronts are positive, negative curvatures were also observed at the flame base of the turbulent cases. It was observed that the edge-flame propagation velocity of the fuel with Le < 1 is higher than other cases for all values of the scalar dissipation rate when the curvature of the product mass-fraction is positives. This is similar to effects of Lewis number observed in premixed flames.

## 4. Acknowledgments

This work was supported by the Australian Research Council (ARC). The research was also supported by access to computational resources on the Australian NCI National Facility through the National Computational Merit Allocation Scheme and Intersect Australia partner share.

## 5. References

[1] P. A. Libby, A. Liñán, F. A. Williams, Combust. Sci. Technol. **34** (1-6) (1983), pp. 257-293.
[2] J. Daou, F. Al-Malki, Combust. Theor. Model. **14** (2) (2010), pp. 177-202.
[3] R. Daou, J. Daou, J. Dold, Combust. Theor. Model. **8** (4) (2004), pp. 683-699.
[4] J. Daou, A. Liñán, Combust. Theor. Model. **2** (4) (1998), pp. 449-477.
[5] R. H. Chen, M. Chaos, A. Kothawala, Proc. Combust. Inst. **31** (1) (2007), pp. 1231-1237.
[6] A. J. Aspden, M. S. Day, J. B. Bell, J. Fluid Mech. **680** (2011), pp. 287-320.
[7] A. J. Aspden, M. S. Day, J. B. Bell, Proc. Combust. Inst. **33** (1) (2011), pp. 1463-1471.
[8] A. J. Aspden, M. S. Day, J. B. Bell, Proc. Combust. Inst. **33** (1) (2011), pp. 1473-1480.
[9] J. B. Bell, R. K. Cheng, M. S. Day, I. G. Shepherd, Proc. Combust. Inst. **31** (1) (2007), pp. 1309-1317.
[10] H. Hesse, N. Chakraborty, E. Mastorakos, Proc. Combust. Inst. **32** (1) (2009), pp. 1399-1407.
[11] A. Cessou, C. Maurey, D. Stepowski, Combust. Flame **137** (4) (2004), pp. 458-477.
[12] S. Karami, E. R. Hawkes, M. Talei, J. H. Chen, J. Fluid Mech. **777** (2015), pp. 633-689.
[13] C. S. Yoo, R. Sankaran, J. H. Chen, J. Fluid Mech. **640** (2009), pp. 453-481.
[14] E. R. Hawkes, O. Chatakonda, H. Kolla, A. R. Kerstein, J. H. Chen, Combust. Flame **159** (8) (2012), pp. 2690-2703.
[15] I. Boxx, C. Heeger, R. Gordon, B. Böhm, A. Dreizler, W. Meier, Combust. Flame **156** (1) (2009), pp. 269-271.
[16] E. Hawkes, R. Sankaran, J. Chen, 16th Australasian Fluid Mechanics Conference (AFMC) (2007), pp. 1271-1274.
[17] S. B. Pope, Int. J. Eng. Sci. **26** (5) (1988), pp. 445-469.
[18] J. Buckmaster, M. Matalon, Symp. (Int.) Combust. **22** (1) (1989), pp. 1527-1535.
[19] J. Boulanger, L. Vervisch, J. Reveillon, S. Ghosal, Combust. Flame **134** (4) (2003), pp. 355-368.
[20] V. Favier, L. Vervisch, Combust. Flame **125** (1–2) (2001), pp. 788-803.
[21] S. Ghosal, L. Vervisch, J. Fluid Mech. **415** (2000), pp. 227-260.
[22] M. Matalon, Proc. Combust. Inst. **32** (1) (2009), pp. 57-82.
[23] M. Matalon, Combust. Sci. Technol. **31** (3-4) (1983), pp. 169-181.
[24] I. A. Mulla, S. R. Chakravarthy, Combust. Flame (2014), pp.

# Large Eddy Simulation of Evaporating Acetone in a Turbulent Multiphase Flow

M. N. Khan* and M. J. Cleary
School of Aerospace, Mechanical and Mechatronic Engineering
The University of Sydney, NSW 2006 Australia

**Abstract**

A combination of Eulerian large eddy simulation (LES) and two parallel Lagrangian particle schemes is used to model a non-reacting evaporating acetone spray. In addition to momentum coupling between the LES and Lagrangian fuel particles, a novel conserved scalar approach is used to account for interphase heat and mass transfer. The model has been implemented in an OpenFOAM compatible CFD code called *mmcFoam*. The dispersion of the acetone droplets of various size classes is found to be in good agreement with experimental data for a dilute, evaporating turbulent acetone spray. The effects of mass transfer coupling with LES are explored.

*Keywords: Multiphase, Mixture Fraction, Evaporation.*

## 1. Introduction

The mixture fraction concept has been a powerful one in advancing our understanding of mixing and combustion in turbulent flows that are non-premixed [1]. Models for turbulent combustion of gaseous fuels are widely reviewed [2]. However, most practical combustion processes involve the use of either solid or liquid fuels as a spray. Research on sprays has mostly focused on atomization, dispersion and evaporation. Less emphasis has been placed on the modelling of pollutant species such as soot, oxides of nitrogen and carbon monoxide. Many turbulent combustion models, such as CMC [3] and MMC [4], use conserved scalars to accurately and affordably predict harmful pollutants. Coupling such methods with turbulent heat and mass transfer to and from liquid droplets is our focus. Spalding [5] derived greatly simplified transfer relations using a conserved scalar approach for a single component evaporating liquid droplet. He showed the consistency of using the transfer relations for conditions with and without gas-phase reactions. Some publications [6] use transfer relations for combustion of spray modelling, which are strictly speaking valid in the absence of gas-phase combustion. A consistent approach is needed, which can use the transfer relations in such a way that the closure of turbulent gas-phase reaction, heat and mass transfer coupling between continuous and dispersed phases are done elegantly.

Here we use mixture fraction based heat and mass transfer equations. Separate stochastic particle methods are used for the gas phase composition [4] and liquid phase dispersion. The numerical simulation of this study is done on an LES based OpenFOAM code. As a first step we previously published simulations of a non-reacting and non-evaporating kerosene sprays [7]. In the present case we extend the model to account for evaporation. An evaporating (but still non-reacting ) acetone spray is considered [8].

* Corresponding author:
Phone: (+61) 2 93515360
Email: mkha1785@uni.sydndey.edu.au

## 2. Models

### 2.1 Heat and Mass Transfer for an Isolated Fuel Particle

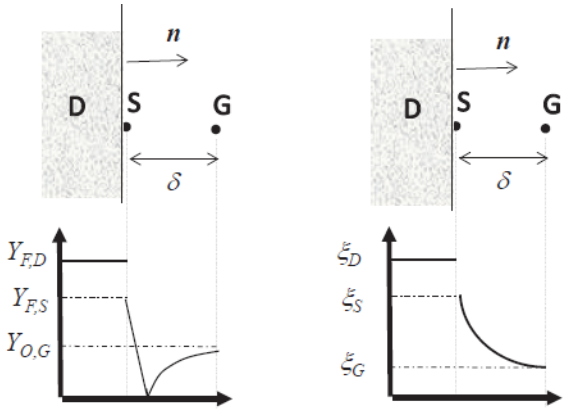


Figure 1: Schematic of mass fraction profile (left) of evaporative fuel $Y_F$ and Oxidizer $Y_O$ and mixture fraction profile (right).

Our validation case is a dilute spray. The model building block for the simulations is simultaneous heat and mass transfer between a single isolated liquid fuel particle and an infinite, quiescent gaseous environment as shown in Figure 1. We denote the dispersed phase (fuel particle) as 'D', gas phase as 'G' and surface state as 'S'. In the mass fraction profile, there is a discontinuity, where the mass fraction is totally consumed at the radial location corresponding to a stoichiometric mixture. Turns [9] derives expressions for additional boundary conditions for the reaction zone which is assumed to be infinitely thin. In practice, reaction proceeds in a wider reaction zone due to

intense turbulent mixing or quenching. The mixture fraction profile as shown on the right side of Figure 1 is continuous as it is conserved through the reaction zone and can therefore be used in both reacting and non-reacting cases.

The mixture fraction is defined as

$$\xi = \frac{\beta - \beta_0}{\beta_1 - \beta_0} \tag{1}$$

where $\beta$ is any conserved scalar and subscripts *0* and *1* represent the values in pure oxidiser and pure fuel, respectively. The standardised enthalpy is defined as

$$h_D = C_{P,D}\left(T_D - T_r\right) \tag{2}$$

$$h_G = \sum_{\alpha=1}^{N_S}\left[h_f^r + \int_{T_r}^{T_G} C_{p,G}\,dT\right]_\alpha \tag{3}$$

where $C_{P,D}$ is the specific heat, $T_r$ is a reference temperature and $h_f$ is enthalpy of formation. $\xi$ and $h$ have the same definition in both phases.

The heat and mass transfer relations in the diffusive layer about a fuel particle are derived elsewhere [7] . We summarise here the final equations for heat and mass fluxes

$$\dot{Q}'' = \dot{m}''\left(h_S - h_D + q_D - q_R\right) \tag{4}$$

$$\dot{m}'' = Nu\frac{\rho\alpha}{L}ln\left(1+B_H\right) = Sh\frac{\rho D}{L}ln\left(1+B_M\right) \tag{5}$$

where, Spalding transfer numbers ($B_H$ and $B_M$) and internal heating ($q_D$ ) is given by

$$B_H = \frac{h_G - h_S}{h_S - h_D + q_D - q_R} \tag{6}$$

$$B_M = \frac{\xi_G - \xi_S}{\xi_S - 1} \tag{7}$$

$$q_D = \frac{h_G - h_S}{\left(1+B_M\right)^Z - 1} - \left(h_S - h_D\right) + q_R \tag{8}$$

$L$ is the characteristic length scale of the phase interface. *Nu* and *Sh*, are the Nusselt and Sherwood numbers respectively, to cover both quiescent and convective transfer environments. $q_R$ is heat transfer due to radiation which can be used a solid body radiation model. *Le* is Lewis number ($Le=\alpha/D$) and $Z=Le^{-1}Sh/Nu$.

Finally we require values for $h$ and $\xi$ at the 'S' and 'G' states. For the 'G' state $h$ and $\xi$, we will use gas phase simulation (e.g. MMC-LES [10] or CMC-LES [3] which provides reactive species at the 'G' state. $\xi_G$ is sampled randomly with an assumed Clipped Gaussian model (see section 2.3). It is assumed that a species, *i*, is a unique function of the mixture fraction, $Y_i = F(\xi)$, where $F$ is given by gas phase combustion model. The inverse function then gives $\xi_S = F^{-1}(Y_{i,S})$. $Y_{i,S}$ is calculated from the phase equilibrium model as described below for acetone case. It is reasonable to set $T_S = T_D$, where $T_D$ is obtained from a simple lumped capacitance approach [6].

We adopt the Clausius Clapeyron phase equilibrium model for the surface condition. The species mass fraction of a fuel component is given by

$$Y_{i,S} = \left[1 + \frac{MW_{air}}{MW_\alpha}\left(\frac{P}{P_\alpha} - 1\right)\right]^{-1} \tag{9}$$

where $MW_{air}$ and $MW_\alpha$ are the molecular weight of air and species respectively, $P$ is the thermodynamic pressure (assumed to be atmospheric in low Mach number flows) and $P_\alpha$ is the saturation pressure of evaporative species.

## 2.2 Particle Dispersion Model

The dispersion of fuel particles are tracked in Lagrangian fashion in parcels which represent some identical particles. We adopt a method for modelling of polydispersed, spherical fuel particles that is based on the approach of Dukowicz [11]. The governing equations of location and velocity of the fuel parcels are

$$\frac{dx_i^{fp}}{dt} = u_{D,i}^{fp} \tag{10}$$

$$du_{D,i}^{fp} = \left(a_{D,i}^{fp} + g_i\right)dt + b_{D,i}^{fp}dw_i \tag{11}$$

where $a_{D,i}^{fp}$ is the acceleration of fuel parcels due to drag force imparted by the gas phase, $g_i$ is the acceleration due to gravity and $b_{D,i}^{fp}dw_i$ is a stochastic term which simulates the subfilter differential velocity. $b_{D,i}^{fp}dw_i$ has a very small effect in LES and may be neglected as a first approximation [3]. $a_{D,i}^{fp}$ is modelled by as relaxation to the filtered gas phase velocity for spherical particles [12]. In return, the particles impart a momentum change on the gas-phase, appearing as a source term in the Navier-Stokes equation.

## 2.3 Clipped Gaussian model

Mixture fraction in the gas phase is calculated by the LES filtered mean and subgrid variance passed through a clipped Gaussian sampling model. It is a Gaussian distribution for turbulent region between $0 < \eta < 1$ and Delta functions for intermittent appearance of unmixed fluid at $\eta = 0$ and $\eta = 1$. In Favre form, it is given by

$$\tilde{P}(\eta) = \alpha_1\delta(\eta) + \left(1 - \alpha_1 - \alpha_2\right)\frac{G(\eta)}{I_G} + \alpha_2\delta(1-\eta) \tag{12}$$

where,

$$I_G = \int_0^1 G(\eta)d\eta \tag{13}$$

and $\delta(\eta)$ is the Dirac Delta function whose integral is unity if $\eta = 0$ and is zero otherwise. The $\alpha_1$ and $\alpha_2$ are

the strength of intermittency spikes. A flow dependent empirical formula is used here to avoid costly iterative method. $G(\eta)$ is clipped at two standard deviations so that

$$G(\eta) = \frac{1}{\sqrt{2\pi g}} exp\left(-\frac{(\eta - f)^2}{\sqrt{g}}\right) \text{ for } \frac{|\eta - f|}{\sqrt{g}} \le 2 \text{ and}$$

$$= 0 \text{ for } \frac{|\eta - f|}{\sqrt{g}} > 2 \quad (14)$$

where, $f$ and $g$ are the mean and variance of $G(\eta)$. The strength of intermittency spikes are determined from first and second moment of $\tilde{P}(\eta)$.

## 3. Numerical Methods

The model has been implemented in a new OpenFOAM C++ compatible LES code, called *mmcFoam*, which was recently developed at the University of Sydney. The object oriented code is structured with nested templates (i.e. generic code which is instantiated at runtime). Each level of the nested templates represents specific physics. Our implementation retains all the generality of OpenFOAM allowing for structured and unstructured grids, numerous discretisation and integration schemes, and the full range of thermodynamic and kinetic flexibility.

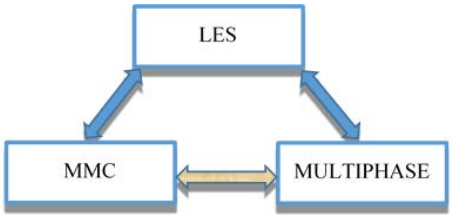


Figure 2: The coupling between different code packages.

The two-way communication among the different packages of code library is shown in Figure 2. Multiphase uses the gas phase's properties, for example gas mixture fraction, species mass fraction etc to calculate multiphase properties as described in the section 2. In return, the gas phase species mass, mixture fraction and enthalpy must be updated as multiphase simulation is in progress.

## 4. Results

The non-reacting evaporating acetone SP6 from the University of Sydney spray burner by Gounder *et al.* [8] is simulated. The 3D flow domain extends 104mm transversely by 320mm axially with a total of 466,560 LES cell. Zero gradient pressure boundary conditions are applied for the jet and coflow while fixed (total) pressure boundary conditions are applied at the domain sides and outlet. Realistic jet turbulent velocity boundary conditions are applied; this is based on the exit plane experimental data of acetone SP6 case [8].

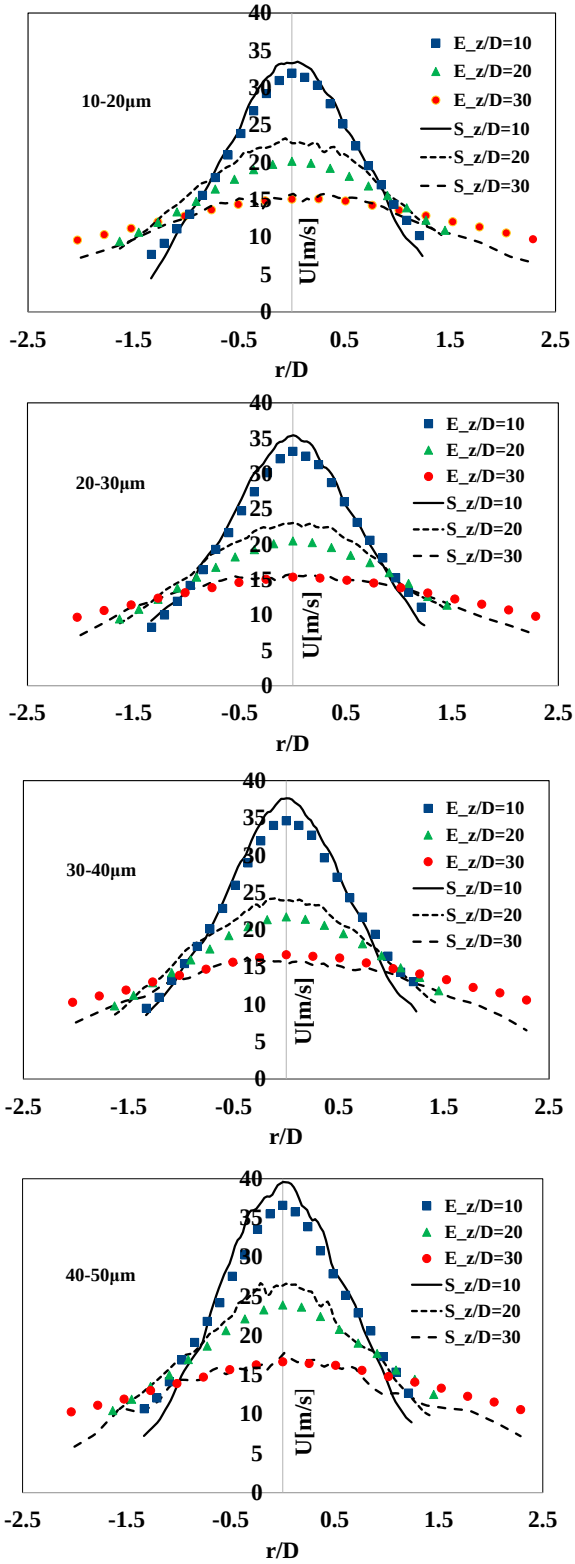


Figure 3: Radial profiles at three axial stations of size conditioned droplet mean droplet velocity for acetone SP6 case; E stands for experimental data [8] and S stands for simulation results.

Figure 3 shows radial profiles of axial velocity for a set of size classes of fuel droplets starting from the 10-20µm to 40-50 µm range in three positions; z/D = 10,

20 and 30, where D is the diameter of jet (10.5 mm) and z is the axial distance from the jet exit plane. The simulation results are in excellent agreement with experimental data with slight deviation in the z/D = 20 location. It is also found that the larger droplets (40-50μm) have experienced higher velocity as 39.58 m/s against than the smaller droplets' (10-20μm) velocity as 33.38 m/s, which is expected because the Stoke's number of large particles is greater than unity and slip velocities are high.

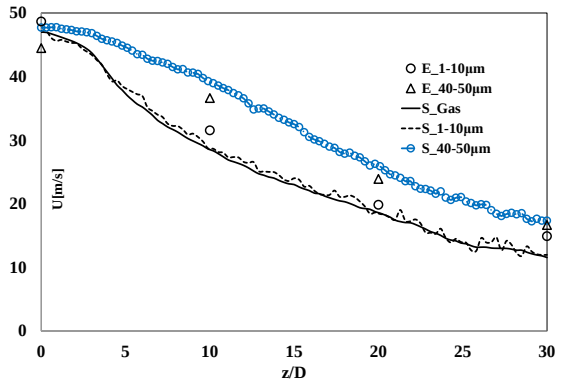


Figure 4: Axial profiles of mean velocity for smaller droplets (E_1-10μm), bigger droplets (E_40-50μm) Gas velocity (Gas) [8], E stands for Experimental data.

Figure 4 shows axial profiles of droplet mean velocity along centreline for the smallest droplets (1-10μm), large droplets (40-50μm), gas velocity (Gas) and experimental data (E). The axial profiles are very close to each other which justifies the accuracy of our simulation results. For the bigger droplets (40-50μm size) shows a clear difference from the others. In the simulation, the jet break up at point z/D = 5 and subsequent decay is nicely captured as expected.

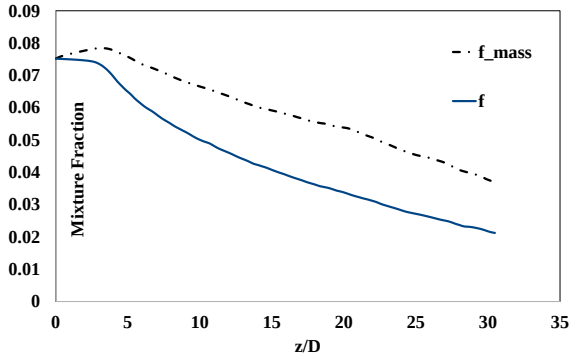


Figure 5: Mixture fraction in axial centreline, with mass coupling (f_mass) and without mass coupling (f).

As the droplets evaporate, there is gas production from them, which we couple with LES code as a source term in the mixture fraction equation. For testing the effects of mass coupling with LES, we conduct a simulation with mass coupling and without mass coupling. Figure 5 shows the clear indication that the mixture fraction increases with mass coupling (f_mass) comparing to without mass transfer coupling (f). It demonstrates that our mass transfer is physically correct but more testing is required to confirm that all coupling are accurate.

## 5. Conclusion

The non-reacting evaporating acetone case SP6 is simulated based on the mixture fraction approach. In LES, the simulation is extended to multiphase flow by coupling both gas and liquid phases for heat and mass transfer. The model is validated against experimental data of acetone cases of Sydney University sprays and shows excellent agreement. The future works will focus on validation of reacting cases, followed by multicomponent bio-fuels.

## 6. Acknowledgments

We acknowledge support from the ARC under grant number DP130100763.

## 7. References

[1] R. W. Bilger, Combustion and Flame 158 (2) (2011), pp. 191-202.

[2] R. Bilger, S. Pope, K. Bray and J. Driscoll, Proceedings of the Combustion Institute 30 (1) (2005), pp. 21-42.

[3] S. Ukai, A. Kronenburg and O. T. Stein, Flow, Turbulence and Combustion 93 (3) (2014), pp. 405-423.

[4] M. J. Cleary and A. Y. Klimenko, in: T. Echekki and E. Mastorakos (Eds.), Turbulent Combustion Modeling, Springer Netherlands, (2011), pp. 143-173.

[5] S. D. B., Some Fundamentals of Combustion, Buttersworth Scientific Publications, London, (1955), pp.

[6] W. P. Jones, S. Lyra and S. Navarro-Martinez, Combustion and Flame 159 (4) (2012), pp. 1539-1561.

[7] M. N. Khan, L. F. Zhao, M. J. Cleary, R. W. Bilger, O. T. Stein and A. Kronenburg, A Mixture Fraction-Based Model for Evaporation, Pyrolysis and Char Conversion of Dilute Fuel Dispersions, RMIT University, Melbourne, 2014, pp. 1-4.

[8] J. D. Gounder, A. Kourmatzis and A. R. Masri, Combustion and Flame 159 (11) (2012), pp. 3372-3397.

[9] S. R. Turns, in: (Eds.), McGraw-Hill, (2012), pp.

[10] Y. Ge, M. J. Cleary and A. Y. Klimenko, Proceedings of the Combustion Institute 34 (1) (2013), pp. 1325-1332.

[11] J. K. Dukowicz, Journal of Computational Physics 35 (2) (1980), pp. 229-253.

[12] M. C. Yuen and L. W. Chen, Combustion Science and Technology 14 (4-6) (1976), pp. 147-154.

**Proceedings of the Australian Combustion Symposium**
**December 7-9, 2015, The University of Melbourne**

# DNS of hydrogen auto-ignition under HCCI-like conditions with wall heat transfer; parametric study

J. Behzadi[1, *], M. Bolla[1], M. Talei[2], E.R. Hawkes[1,3], S. Kook[1]
[1]School of Mechanical and Manufacturing Engineering, University of New South Wales, NSW 2052 Australia
[2] Department of Mechanical Engineering, University of Melbourne, VIC 3010, Australia
[3] School of Photovoltaic and Renewable Energy Engineering, University of New South Wales, Sydney, NSW 2052, Australia

## Abstract

Two-dimensional direct numerical simulations (DNSs) are performed to study the effect of wall heat transfer on the auto-ignition of lean hydrogen-air mixtures in the presence of temperature stratifications at conditions relevant to homogeneous charge compression ignition (HCCI) engines. The DNS are used to further advance combustion modelling for HCCI combustion previously developed using periodic boundary conditions. The simulations are initialised using the statistics available from a previous DNS study of compression heating under HCCI conditions which considered an idealised engine geometry [1]. Three different wall temperatures, leading to three different levels of temperature stratification, are chosen. The results for these wall-HCCI cases are compared to their counterparts with periodic boundary conditions. The heat release rate (HRR) for the wall-HCCI cases exhibit lower peaks and longer combustion duration compared to the cases with periodic boundaries. Using the DNS data for the wall-HCCI cases, an attempt is made to study the effect of the wall on the HCCI combustion from a modelling point of view, with particular attention to conditional moment closure (CMC). A first-order closure hypothesis with enthalpy (chemical + sensible) as conditioning variable and ignoring the spatial variations of conditional statistics is first tested and found to break down at high levels of stratification. Accounting for the dependence of conditional statistics on the distance from the wall cannot provide a closure either. Second order evaluation of the reaction rates, however, yields satisfactory closure, even without accounting for the spatial dependence of conditional statistics. The three-way interaction between chemistry, turbulence and wall is illustrated using temperature, enthalpy, mass fraction of $H_2O$ and the distance from the wall. Some remarks on the challenge of addressing the conditional fluctuations in the vicinity of the wall are made and the scope of future modelling work is outlined.

*Keywords: HCCI, DNS, CMC, wall-HCCI, SCCI, stratification*

## 1. Introduction

Despite their low emissions and high fuel economy, homogeneous charge compression ignition (HCCI) engines suffer from a number of technical challenges which need to be overcome before they could be adopted in widespread usage. At high load conditions they suffer from rapid pressure rise rates [2], which in turn are the result of high heat release rates (HRR). It is known from previous experimental [2] and numerical research [3-7] that thermal stratification in the fuel-air charge results in significant reductions of HRR compared with fully homogeneous operating conditions. Investigation of wall heat transfer is therefore important, considering it is the main mechanism for introducing this thermal stratification into the cylinder. Wall heat transfer effects are also potentially important for understanding emissions of unburned hydrocarbons, which can be significant at low-load conditions [2], and are thought to result mainly from cooler regions of the cylinder near the wall.

Direct numerical simulation (DNS) of HCCI-like conditions has been widely attempted in the past 10 years to better understand this combustion mode. In this approach, instead of solving transport equations for a realistically sized HCCI engine, an affordable computational domain, usually in two dimensions, is initialised such that the integral time scales in this domain matches that of the top dead centre (TDC) conditions in a real HCCI engine, e.g. [3, 4]. In all these DNS-based works on HCCI, periodic boundary conditions were utilised to simulate the auto-ignition in the *bulk* and the cooling effect of the wall with proper initialisation for the wall boundary layer, to the best of knowledge of the authors, has not been studied using DNS so far [8].

In the present work a first-of-a-kind attempt is made to study the effect of wall temperature on auto-ignition characteristics of hydrogen-air mixtures using two-dimensional (2D) DNS. The 2D approximation is necessary here because of computational cost considerations, following most other DNS studies of HCCI, e.g. [3, 4]. While it is acknowledged that full features of the wall-flame interaction through turbulent transport may not be captured in the present 2D framework, the present work, as a first step toward more realistic HCCI simulations, provides a platform to generate DNS statistics for developing and testing HCCI combustion models. The DNS data are used to assess, in *a priori*, the potential of conditional moment closure (CMC) to model HCCI in the presence of walls. The study is an extension to previous attempts using CMC and flamelet modelling approaches that did not explicitly address the wall, e.g. [7, 9].

## 2. Numerical method and initial conditions

### 2.1 DNS solver

S3D, an explicit DNS solver developed in Fortran at the Combustion Research Facility at Sandia National Laboratories is used [10]. S3D is a high-order yet low-dissipation numerical solver which utilises a Cartesian grid to solve the Navier-Stokes, species mass-fraction transport and total energy equations. The governing equations are discretised using a central, 8$^{th}$ order finite differencing scheme for spatial derivatives and a 6 stage,

* Corresponding author: Jalal Behzadi
Phone: (+61) 2 9385 4602
Email: J.Behzadi@unsw.edu.au

4th order explicit Runge-Kutta scheme for time integration. Viscosity is found using Sutherland's formula. Prandtl number and Lewis number[1] are assumed 0.705 and 1, respectively.

**Table 1** Simulation parameters

| Case | $W \times H$ (mm$^2$) | $N_x \times N_y$ | $T'_{bulk}$ (K) | $T_{wall}$ (K) |
|---|---|---|---|---|
| W0 | 30 × 7.5 | 5120 × 1280 | 30 | 500 |
| W1 | 7.5 × 7.5 | 1280 × 1280 | 30 | 500 |
| W2 | 7.5 × 7.5 | 1280 × 1280 | 15 | 800 |
| W3 | 7.5 × 7.5 | 1280 × 1280 | 7.5 | 950 |
| P1 | 7.5 × 7.5 | 1280 × 1280 | 30 | - |
| P2 | 7.5 × 7.5 | 1280 × 1280 | 15 | - |
| P3 | 7.5 × 7.5 | 1280 × 1280 | 7.5 | - |

## 2.2 Test cases and initial conditions

Table 1 outlines the details of all seven cases studied. The initial conditions of temperature are illustrated in Fig. (1.a). While cases denoted with the letter P have periodic boundary conditions (BCs) in all directions, the cases denoted with the letter W have wall BCs on two sides and periodic BCs are applied elsewhere. The cases are intended to simulate auto-ignition in lean $H_2$/air mixtures with inhomogeneities in temperature. The pressure-dependent hydrogen–air chemistry is based on a detailed chemical mechanism with 9 reactive species and 19 reversible reactions [11]. All cases initially have a uniform mixture composition with a mean equivalence ratio of 0.1, mean temperature of 1090 K, and pressure of 23 atm. Three wall temperatures are chosen leading to three stratification levels in the bulk temperature. Temperature distribution in the bulk of the wall cases is identical to the bulk of the periodic cases. This is to highlight the effect of the walls when compared to periodic cases. The case W0 is initialised similar to the case W1. It provides more statistics to confirm the domain size chosen for the other cases is appropriate.

For the periodic cases, the initial velocity field is generated using a 2D Passot-Pouquet spectrum for the turbulent kinetic energy, similar to Ref. [3]. This initial field has an integral length scale of 2 mm and velocity root mean square (RMS) of 1 m/s. The temperature fluctuations are generated using the analogous Passot-Pouquet spectrum with a dominant length scale of 2 mm.

In order to specify a realistic initial condition for the cases with walls, statistics obtained from a previous three-dimensional DNS of (non-reacting) compression heating in an idealised HCCI engine geometry including a moving piston with a single valve are used [1]. A centrally located slice of the temperature field taken at top dead centre (TDC) of this DNS is illustrated in Fig. (1.b). The domain size of this previous DNS at TDC is 75x7.5 mm$^2$. In the previous DNS, the statistics are relatively homogeneous in the radial direction over the considered slice, such that variation in the statistics in the normal direction to the piston and head wall only needs to be considered. The mean and RMS of temperature taken from this slice, as shown in dark blue in Fig. (1.c) and (1.d), are used as reference profiles to construct the mean and RMS profiles for temperature in the present wall cases, shown in red. The mean and RMS profiles for all W-cases are constructed based on the fixed length scales, $y_1$=140µm and $y_2$=1.25mm, from the TDC case. The target RMS profile chosen is capable of scaling the temperature fluctuations in the thermal boundary layer of the wall cases when compared to the periodic cases. The $T'_{wall}$ changes for each wall case subject to the temperature difference between the bulk's mean and the wall. A similar methodology is used to superimpose the wall boundary layer for velocity. The resulting turbulent Reynolds number based on integral length scale of 2 mm and the RMS velocity fluctuations of 1 m/s is 87.

[1] Here a unity Lewis number has been assumed - although not valid for hydrogen - as the main scope of this work is to explore the performance of the CMC model where Le=1 is usually employed in practical *a posteriori* implementations and in perspective of future calculations with more relevant hydrocarbon fuels.

## 3. Results and discussion

Figure (2) illustrates results for spatially-averaged HRR, $<\omega_T>$. The HRR is calculated based on chemical enthalpy definition. Figure (2.a) demonstrates the HRR results for the case W0 whereas Fig. (2.b,c,d) present the results for all other cases. In Fig. (2.b,c,d), the HRR for periodic cases are labeled as $<\omega_T>_{\text{periodic}}$. Apart from these curves, all other curves in Fig. (2) correspond to the wall cases. The label $<\omega_T>_{1st}$ corresponds to the mean HRR obtained from reaction rates that are calculated by first order closure with respect to enthalpy (chemical + sensible) as conditioning variable. Furthermore, $<\omega_T>_{2nd}$ represents the mean HRR based on the reaction rates obtained using second order closure approach. The label $<\omega_T>_{\text{dbl}}$ presents the mean HRR that uses the reaction rates that are calculated using first order closure with enthalpy as conditioning variable; however, unlike $<\omega_T>_{1st}$ and $<\omega_T>_{2nd}$, the conditional means are calculated by reference to $y$ as well as enthalpy. This is to see whether considering the distance from the wall can improve the conditioning operation.

The cases in Fig. (2.a) and (2.b) have similar $T'_{bulk}$ but their domain sizes differ. By comparing Fig. (2.a) to (2.b) the only difference observed is that the former shows a smoother mean profile for HRR compared to the latter. This confirms that the size of 7.5x7.5 mm$^2$ is large enough to capture the major trends in the mean values. Furthermore, comparing $<\omega_T>_{\text{periodic}}$ to $<\omega_T>$ in Fig. (2.b,c,d) shows that the wall heat transfer spreads out the HRR curve and lowers its peak compared to the periodic cases. A longer combustion duration is due to the presence of cool boundaries at the walls, which delays the auto-ignition of fuel in these regions. Therefore, a longer mixing time is needed for these cold pockets to migrate to warmer regions toward the bulk and become more reactive.

From Fig. (2.a,b) it is clear that $<\omega_T>_{1st}$ for $T'$=30K exhibits deviations compared to $<\omega_T>$. For the cases with $T'$=15K and $T'$=7.5K the differences are negligible. In an attempt to fix the deviations, $<\omega_T>_{\text{dbl}}$ are calculated. The $<\omega_T>_{\text{dbl}}$ curves in Fig. (2) are closely following the $<\omega_T>_{1st}$ lines. This shows that calculating the conditional moments by taking into account their distance from the wall does not provide a better first-order closure. This confirms that even though the largest tempera-

ture fluctuations initially lie in the near-wall regions, they are not solely responsible for breakdown of the first-order closure hypothesis, and contributions from the bulk region are as important. Second-order evaluation of the reaction rates without considering spatial dependence of the conditional statistics, $<\omega_T>_{2nd}$, provides a satisfactory closure when the result are compared to $<\omega_T>$. This is an important indication for future modelling directions. The level of modelling complexity, however, needs to be further investigated *a priori*.

In Fig. (3), the temporal evolution of temperature (top row) and mass fraction of $H_2O$ (bottom row) for the case W0 are illustrated. By reference to Fig. (3.a,b,c) a basic understanding of the chemistry-turbulence-wall interaction can be established. By $t$=1.0ms some of the hottest spots, mostly in the bulk, have already started to autoignite resulting in some hot islands of product species surrounded by a cold unburned bulk. The islands grow in size and approach the near-wall zone, chosen here to have a thickness of 1.0 mm. The 1 mm thickness is comparable to $y_2$=1.25 mm in Fig.(1). Turbulent transport along with flame propagation pushes the high concentrations of $Y_{H2O}$ from the bulk into the near-wall region. Upon contact with a wall, the hot products start to cool down, leading to a reduced reactivity in the near-wall region with an increase in concentration of the cold product species.

The presence of walls can also delay the flame enclosure in the bulk. This is very well depicted in Fig. (3.c) showing that cold unburned gases migrate from the wall into the bulk region. While the core of these structures contain unburned reactants, they do not tend to autoignite as their temperature is low. As a result, the front propagation in these cold extensions from the wall is hindered, and it takes more time for the hot bulk to close in and consume all the fuel.

In Fig. (3.d) to (3.h) the temporal evolution of $Y_{H2O}$ in enthalpy space is depicted to provide some further insight in terms of the CMC modelling. In Fig. (3.d,e) the conditional mean of $Y_{H2O}$, black dashed line, is zero on the cold side (low enthalpies). This is because no reaction has yet taken place in the near-wall regions. It should be emphasised here that the black line is calculated using the statistics from the *entire* domain and not only the near-wall region, whereas the scatter plot is only representative of the 1 mm boundary layer. At later times shown in Fig. (3.f,g,h), the cold side experiences a sharp increase in $Y_{H2O}$. Based on the "$\log_{10}$y" colours on the scatter plot in the background, the far left tail of the black line corresponds to the wall and *very near* to the wall regions. This observation is consistent with those in Fig. (3.b,c), explained previously, where turbulent transport injects the $Y_{H2O}$, located on the flame front of the hot islands, into the cold near-wall region. The changes in conditional mean of $Y_{H2O}$ in the near-wall region is not thought to be due to the chemistry effects, rather it is proposed to be driven by turbulent transport of burnt products to the wall region. Therefore, the success of any modelling attempt at predicting the rise of the left tail of the $Y_{H2O}$ black line in Fig. (3.f,g,h) heavily relies on correctly capturing the turbulent mixing effects. This point needs further investigation, which is within the scope of our future work.

Figures (3.g,h) also provide a reason for why including the distance from the wall as the second conditioning variable does not lead to any improvement for prediction of the HRR. As can be seen, significant conditional fluctuations in a large range of enthalpies are observed near the wall (shown by the blue colour) and therefore, the distance from the wall cannot solely capture these fluctuations.

## 4. Conclusion

Two-dimensional DNS is used to perform a parametric study on the effect of wall temperature on the auto-ignition of a lean hydrogen-air mixture under HCCI-relevant conditions. This is an attempt to set up a first-of-a-kind DNS platform for parametric study of HCCI combustion in presence of wall heat transfer, with a particular attention to implications for the CMC modelling. The initialisation is based on the TDC statistics taken from a previous three-dimensional DNS study of non-reacting compression heating in an HCCI engine [1]. Three different wall temperatures, leading to three different levels of temperature stratification in the bulk, are studied. The DNS cases provide a platform to gain insight about future directions for the CMC modelling of HCCI with wall heat transfer. This is one further step forward to model HCCI combustion compared to previous works based on periodic boundary conditions, e.g. [7, 9]. The following observations were made in this study.

- Comparing the HRR for the wall-HCCI cases to their periodic counterparts show that the wall heat transfer leads to a more distributed heat release event with a lower peak of HRR. This is attributed to the extra temperature stratification that wall introduces combined with the turbulent transport from/to the wall.
- The first-order closure hypothesis with enthalpy as conditioning variable breaks down at higher levels of stratification. Inclusion of the spatial dependence of the conditional moments with respect to the walls does not provide a better closure either. This is an important non-trivial finding. Second-order evaluation of the reaction rates, however, satisfactorily provides a closure. The level of model complexity to determine which conditional co-variances contribute more dominantly, especially for larger chemical mechanisms, is left for future modelling work.
- The near-wall regions are found to exhibit high levels of conditional fluctuations in species mass fractions. Unlike the bulk where the fluctuations are mainly generated and controlled via the chemistry source term, due to the cold nature of the wall region the source of the fluctuations is not immediately clear. Further qualitative and quantitative investigation regarding turbulent transport to/from the bulk is needed to understand the source of the fluctuations in this region that defines the scope of the future work.

## 5. Acknowledgement

This work was supported by the Australian Research Council. The research benefited from computational resources provided through the Na-

tional Computational Merit Allocation Scheme, supported by the Australian Government. The computational facilities supporting this project included the Australian NCI National Facility, the partner share of the NCI facility provided by Intersect Australia Pty Ltd., the Peak Computing Facility of the Victorian Life Sciences Computation Initiative (VLSCI), iVEC (Western Australia), and the UNSW Faculty of Engineering.

## 6. References

[1] M. Schmitt; C. E. Frouzakis; A. G. Tomboulides; Y. M. Wright; K. Boulouchos, Proc. Combust. Inst. 35 (3) (2015) 3069-3077.
[2] J. E. Dec, Proc. Combust. Inst. 32 (2) (2009) 2727-2742.
[3] J. H. Chen; E. R. Hawkes; R. Sankaran; S. D. Mason; H. G. Im, Combust. Flame 145 (1-2) (2006) 128-144.
[4] C. S. Yoo; T. Lu; J. H. Chen; C. K. Law, Combust. Flame 158 (9) (2011) 1727-1741.
[5] F. Bisetti; J. Y. Chen; E. R. Hawkes; J. H. Chen, Combust. Flame 155 (4) (2008) 571-584.
[6] R. Yu; T. Joelsson; X. S. Bai; B. Johansson, SAE paper 2008-01-1669 (2008).
[7] V. Mittal; D. J. Cook; H. Pitsch, Combust. Flame 159 (8) (2012) 2767-2776.
[8] M. Katayama; N. Fukushima; M. Shimura; M. Tanahashi; T. Miyauchi, in: *8th ASME/JSME Therm. Eng. Joint Conf.*, Honolulu, Hawaii, USA, 2011.
[9] F. Salehi; M. Talei; E. R. Hawkes; C. S. Yoo; T. Lucchini; G. D'Errico; S. Kook, Proc. Combust. Inst. 35 (3) (2015) 3087-3095.
[10] J. H. Chen; A. Choudhary; B. de Supinski; M. DeVries; E. R. Hawkes; S. Klasky; W. K. Liao; K. L. Ma; J. Mellor-Crummey; N. Podhorszki; R. Sankaran; S. Shende; C. S. Yoo, Comput. Sci. Discovery 2 (1) (2009) 015001.
[11] A. Gruber; R. Sankaran; E. R. Hawkes; J. H. Chen, J. Fluid Mech. 658 (2010) 5-32.

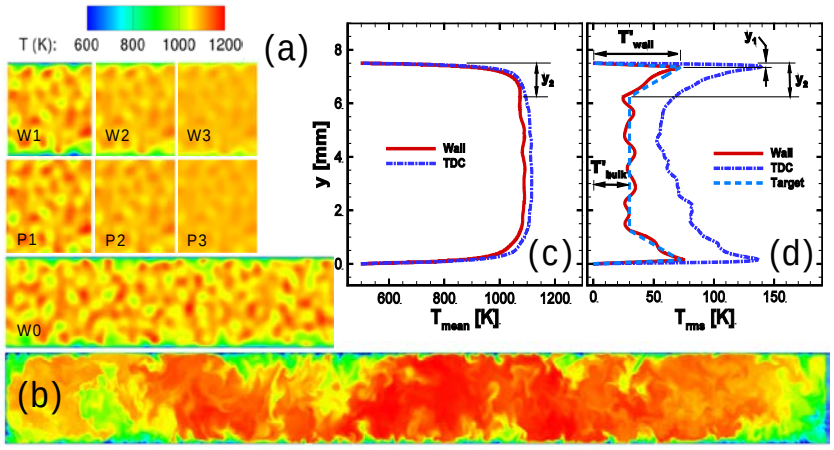


**Figure 1.** **(a)** The initial fields of temperature for all seven cases present in table 1; **(b)** A two-dimensional slice of the temperature field taken from top dead centre (TDC) of the reference case [1]; **(c)** Initial mean temperature profiles; the blue line represents the reference case (TDC); the red line represents the case W0; **(d)** Root mean square (RMS) of initial temperature; the blue line represents the reference case (TDC); the red line represents the case W0; the light blue line represents the target profile for the case W0.

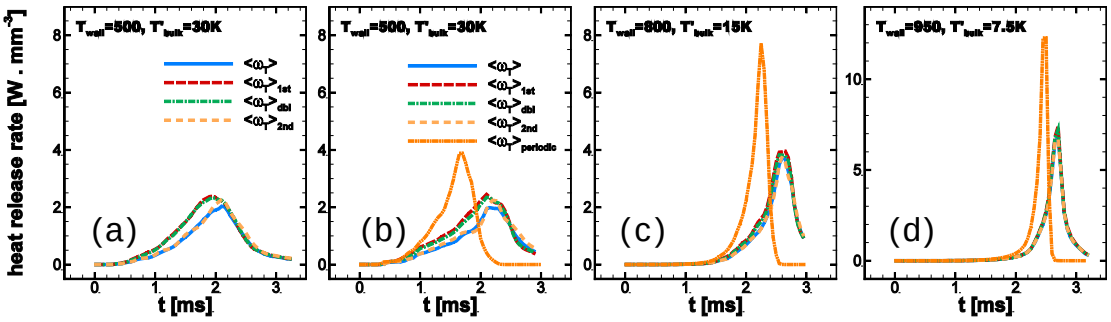


**Figure 2.** The heat release rate (HRR) for all seven cases; the $<\omega_T>$ line represents the exact mean HRR for the wall cases; the $<\omega_T>_{1st}$ line represents the mean HRR of the wall cases calculated using first-order closure for reaction rate by single-conditioning on enthalpy; the $<\omega_T>_{dbl}$ line illustrates the mean HRR of the wall cases calculated using first-order closure doubly conditioned on enthalpy and *y*-distance; the $<\omega_T>_{2nd}$ line shows the mean HRR of the wall cases calculated by second-order closure for the reaction rates; the $<\omega_T>_{periodic}$ line depicts the mean HRR for the periodic cases. **(a)** Case W0; **(b)** Case W1 and P1; **(c)** Case W2 and P2; **(d)** Case W3 and P3.

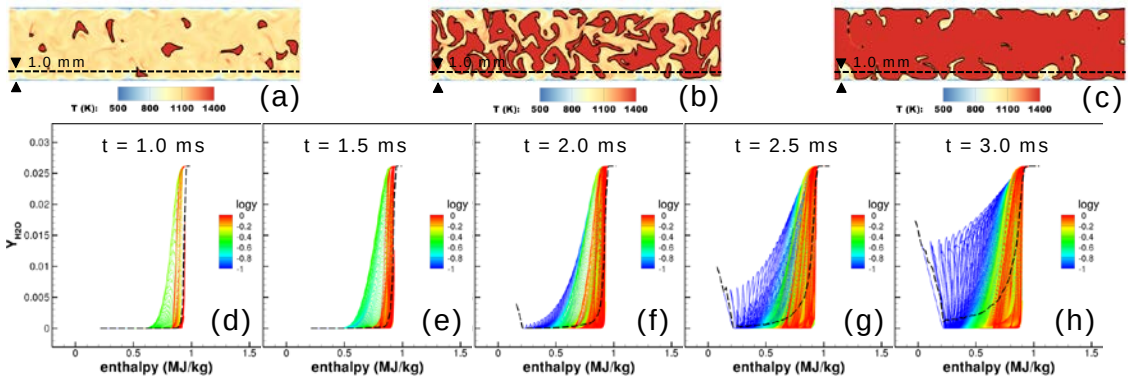


**Figure 3.** **Top row:** Temporal evolution of the temperature field at $t$=1.0, 2.0 and 3.0 ms for the case W0. The thin reaction zone is located on the flame front marked with black lines for a representative product species at a mass fraction $Y_{H2O}$=0.02, which corresponds to almost 75% of maximum $Y_{H2O}$. **Bottom row:** Temporal evolution of the mass fraction of a product species, $Y_{H2O}$, as a function of enthalpy, the conditioning variable. The scatter plots are coloured using the $\log_{10}$ of distance from the bottom wall in mm. Only the data points in 1mm proximity of the bottom wall are illustrated, the rest of the data are blanked out. The conditional mean of $Y_{H2O}$, which is calculated using statistics from entire domain, is shown using a black dashed line for reference. The data is extracted from the case W0.

# Towards the LES-MMC Calculation of Turbulent Piloted Flames with Inhomogeneous Inlets

S. Galindo*, M.J. Cleary and A.R. Masri
School of Aerospace, Mechanical and Mechatronic Engineering
The University of Sydney, NSW 2006, Australia

**Abstract**

This paper presents large eddy simulations (LES) of piloted turbulent flames where fuel and oxidant are compositionally inhomogeneous. This is a first step towards the computation of the structure of flames with inhomogeneous inlets that exhibit enhanced stability compared with the homogeneous counterparts. The studied burner is a modification from the standard piloted Sydney burner configuration with the addition of a central tube carrying methane fuel that can slide within the outer tube carrying air to induce the compositional in-homogeneity at the burner exit plane. A mixture fraction approach is used to compute the flame structure along with a simplified chemistry treatment. Comparisons between the predictions and the experimental measurements are made. The flame structure is adequately predicted and it serves as a good starting point to use multiple mapping conditioning (MMC) to compute the structure of flames with inhomogeneous inlets.

Keywords: Turbulent combustion, partially premixed, Inhomogeneous inlets, LES, MMC

## 1. Introduction

In recent years, there have been significant advances in the capabilities to compute the structure of turbulent non-premixed as well as premixed flames [1]. These codes have mostly transitioned form RANS-based approaches to large eddy due to the advent of faster computers [2]. Employed combustion models range from variants of the laminar flamelet concept, to conditional moment closure (CMC) and pdf-based methods where either Eulerian stochastic fields or Lagrangian Monte-Carlo methods are used [3]–[6]. Sparse Lagrangian multiple mapping conditioning (SL-MMC) has proven to be an important variant where the number of particles used is reduced significantly and hence the computational time [7].

While successful for specific modes of combustion, such as premixed or non-premixed, none of these modeling approaches have yet demonstrated universal capability to compute multi-modes where flames transition across a broad range of mixture fractions. Such variability is common in practical combustors [8], yet to date, there has not been a simple laboratory-based burner that can stabilize such versatile flames. The Sydney piloted burner with compositionally inhomogeneous inlets has recently provided such a platform with capabilities to stabilize multi-mode flames with premixed, stratified and non-premixed fluid samples co-existing within the same jet [9], [10]. This is a simple variant of the standard piloted burner [11] which has already formed a very effective computational platform to advance the modeling of turbulence-chemistry interaction in turbulent non-premixed flames [12].

The objective of this project is to apply the MMC approach to the piloted flames with inhomogeneous inlets to test and develop its capability to compute multiple modes of combustion. This paper is only concerned with the preliminary set and formulation as well as with demonstrating the initial, but necessary step, of computing the structure of turbulent, homogeneous, but partially premixed flames.

## 2. Experiments and numerical approach

### 2.1 Experiments

A thorough description of the burner, its stability characteristics and study case is reported in [9], [13] and only a brief account is given here. The complete data set for a range of flames with varying inlet conditions is also posted on the web and may be made available on request [14]. Figure 1a shows a schematic of the burner that consists of two concentric tubes surrounded by an annular pilot. The inner tube can slide within the annulus so that, at the right recess distance, the fuel/air issuing from the exit plane may be compositionally inhomogeneous. Homogeneously partially premixed conditions may be obtained at sufficiently large recession distances, while the non-premixed condition prevails when both tubes are flush at the burner exit plane. The burner assembly is centered in a wind tunnel providing a uniform air co-flow, which is fixed here at $U_c$=15 m/s.

The blow-off limits for this burner are shown in Fig. 1b for the case where the volumetric air to fuel ratio in the inner tube and the annulus is $V_A/V_F$=2. The fuel used here is methane. It is notable that maximum stability, reflected by higher jet velocities at blow-off, $U_J$ are obtained at an intermediate recess distance of around Lr=75mm. Note that when the inner tube carries fuel while the outer carries air, the conditions are referred to as FJ, while the reverse case is labelled FA. The FJ200-5GP is evidently showing the better stability

* Corresponding author:
Phone: (+61) 2 93515092
Email: sgal8842@uni.sydney.edu.au

while the FA200-5GP transition gradually to the homogeneous limit at Lr=300mm. Note that 5GP refers to a five-gas pilot which is a stoichiometric mixture of acetylene, hydrogen, oxygen, nitrogen and carbon dioxide. This is designed to have the same C/H ratio as methane while at the same time matching its adiabatic flame temperature.

Two cases are selected for further study and these are indicated by the stars on Fig.1b. These are referred to as FJ200-5GP-Lr300-59 and FJ200-5GP-Lr75-80. Both cases correspond to the FJ configuration where fuel is injected in the central pipe and have similar departure from blow-off such that $U_J/U_{BO}$=0.7. However, these cases have different recess distance and hence one is homogeneous with Lr=300mm and the other is inhomogeneous with Lr=75mm.

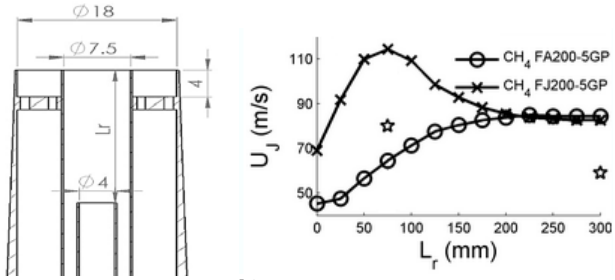


a) b)

Figure 1: a) Inhomogeneous inlets burner cutout b) Bulk jet velocity at blow-off limits plot as a function of recess distance (Lr)

## 2.2 Numerical approach

All computations presented here use the LES platform and are performed using mmcFoam, a solver developed using OpenFOAM library [15]. The code solves equations for the filtered conservation of mass, momentum, and reference mixture fraction. Closure of the sub-filter stress adopts an eddy viscosity approach. The eddy viscosity is computed with a standard Smagorinsky model. Similarly, the sub-filter turbulent fluxes are computed according to an eddy diffusivity model where the eddy diffusivity is determined with a constant turbulent Schmidt number of 0.4 in accordance previous results for jet flames [16]. Transport equations for major species are solved and the chemical source term is treated as a relaxation term towards a single precomputed low strain flamelet solution, where rich side of the curve has been modified to match mixing conditions at the value issuing from the partially premixed jet ($\tilde{\xi}$=0.22) and relaxation time ($\tau_{rel}$) determined by numerical factors. In this work, is set to approximately ten times the characteristic numerical time step.

Calculations presented here are restricted to the homogeneous case (FJ200-5GP-Lr300-59) and commence at the jet exit plane. The boundary conditions are therefore made to match the experimental profiles reported for this case at the jet exit plane. The computational domain consists of a box that extends 50 jet diameters axially and 10 jet diameters in the radial direction. 768 cells are used in axial direction and 56 cells in the radial direction with clustering in the jet and pilot region, giving a total of about 1.4 million cells. The velocity inlet condition in the turbulent jet is generated using the method described in [17]. Further description of the model and how this incorporated in a MMC approach can be found in [18]–[21].

# 3. Results

## 3.1 The homogeneous case

Numerical results are presented here for the homogeneous case (FJ200-5GP-Lr300-59) in the form of radial profiles, conditional means as well as scatter plots and these are compared with the relevant measurements. The flame computed here present low levels of local extinction, which is ideal to test the simple relaxation treatment of the chemical source term and the ideas behind conditioning techniques.

Figure 2a shows computed and measured mean radial profiles of mixture fraction. The agreement in the mean mixture fraction profiles is generally good along the entire length indicating good reproduction of the mixing rate and jet spread except for a slight over prediction at x/D=30 where experiments shows a more homogeneously mixed jet with a larger spread.

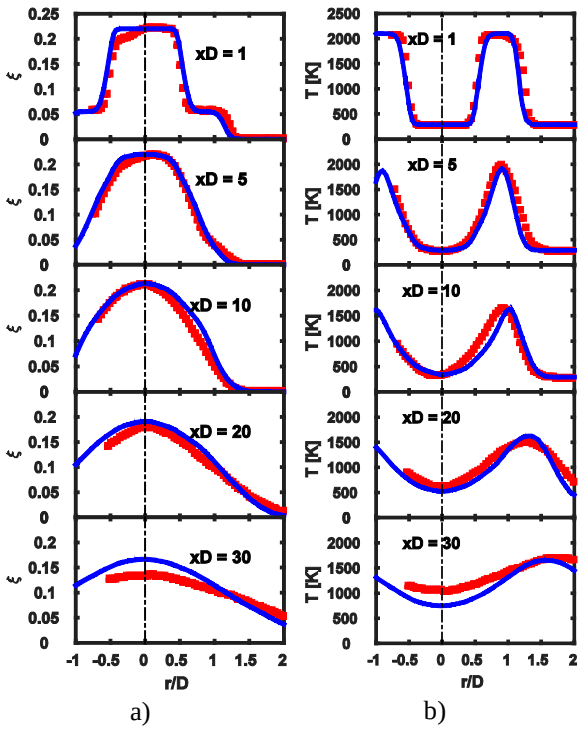


a) b)

Figure 2: Mean mixture fraction and mean temperature radial profiles for flame FJ200-5GP-Lr300-59 at x/D locations of 1, 5, 10, 15, 20 and 30. Symbols, experiment; lines: LES calculations

The good agreement of the mixing field translates in a good agreement in the reactive scalar fields (Fig. 2)

and this is expected for this case which is close to a diffusion flame with some departure from blowoff so that local extinction levels are generally low. This aspect is discussed next.

Figure 3 shows scatter plots for temperature versus mixture fraction, ξ, at x/D = 1, 5, 15 and 30. Computed values are on the left column and measurements on the right. It should be noted the dual branch observed in the experimental values at x/D=1 is due to difficulties to center inner pipe in the burner thus the existence of a slight asymmetry in the jet. As pointed out earlier it can be observed that the flame burns in a diffusion-like manner. Some degree of local extinction is detected downstream of the exit plane between x/D=10 and x/D=15 and the model is able to reproduce this features to some extent. The differences in the range of the mixture fraction values near the exit plane can be attributed mostly to the boundary condition used in the simulation, where a fully homogeneous mixture is issuing from the jet (ξ=0.22) whereas in the experiments is not the case (0.18≤ξ≤0.25).

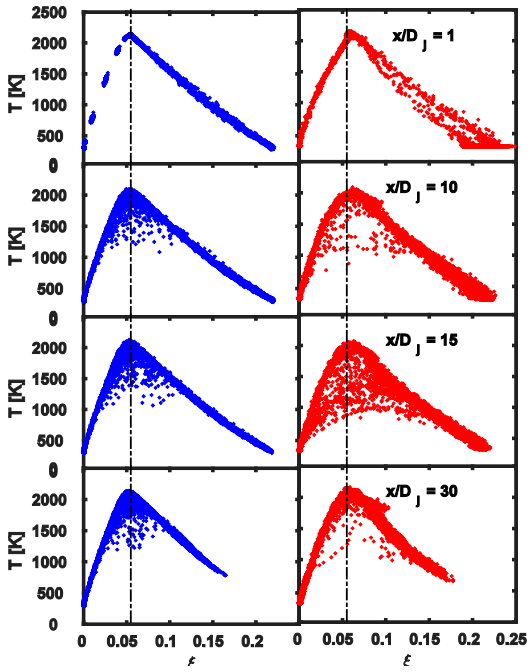


Figure 3: Predicted (left) and experimental (right) temperature scatter plots for flame FJ200-5GP-Lr300-59 at x/D locations of 1, 10, 15 and 30.

To clarify the information in the scatter plots conditional means plots for temperature and the mass fraction of CO are presented versus mixture fraction in Fig 4. Both measurements and calculations are shown for various axial location in the flame. While there is good agreement for temperature, there is clearly a significant difference in the mass fraction of CO which is under-predicted for all axial location shown here. While not shown here due to space limitations, a similar discrepancy is obtained for hydrogen while the agreement for major species such as carbon dioxide and water is adequate and similar to that of temperature. This is somewhat expected considering that the simple flamelet approach is employed so that chemistry of minor species such as CO are not well reproduced. The use of detailed chemistry should significantly improve such calculations and such calculations are currently being performed. Overall, this is a good starting point showing that mixture fraction is suitable to represent the main features of the flame establishing the validity of the approach as a promising tool for initiating calculation of flame with compositionally inhomogeneous inlets.

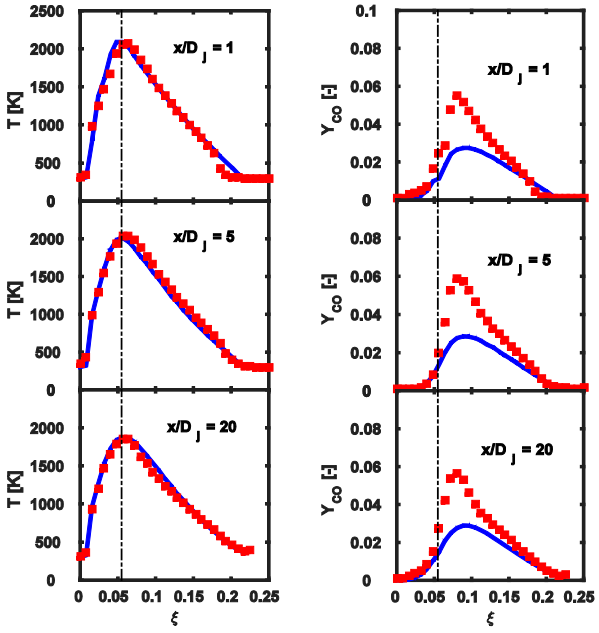


Figure 4: conditional mean of a) temperature and b) carbon monoxide at x/D =1, 5, and 20 predictions (solid lines) and experiments (symbols). Vertical dashed line indicates stoichiometric mixture fraction

## 3.2 The inhomogeneous case

Now that the calculations for the homogeneous case are established, attention shifts to the more challenging inhomogeneous case (FJ200-5GP-Lr75-80). Here calculations cannot be initiated at the jet exit plane due to the steep concentration gradients so that flow inside the pipe needs to be computed. Essentially, flow and mixing between the fuel and air stream is computed within the recess distance using inlet conditions that are specified within the inner fuel stream and the outer air annulus. Results presented here are preliminary pipe simulations with length 100mm and a bulk jet velocity $U_j$=82m/s, which correspond to the case FJ200-Lr100-82. The mesh was generated considering y+ requirements, however under the flow conditions the resolution requirements are very limiting and for this reason Spalding's wall functions have been used in OpenFOAM.

Figure 5 shows computed mean radial profiles for axial velocity and mixture fraction at the exit plane and compared with experimental results taken at x/D = 0.5 from the exit plane. Since the computational domain just considers the region where fuel and air mix, appropriate inlet conditions are not available thus two simulations were performed. One simulation has been performed imposing a mean velocity profile without any fluctuations (Case1) and a second one adding

fluctuations to this mean profile with an approximate turbulence intensity of 10% (Case2). As it can be seen from mixing profiles the lack of turbulent fluctuations gives under predicts mixing while 10% intensity over predicts mixing. Further work is in process to evaluate the appropriate inlet conditions and modeling issues.

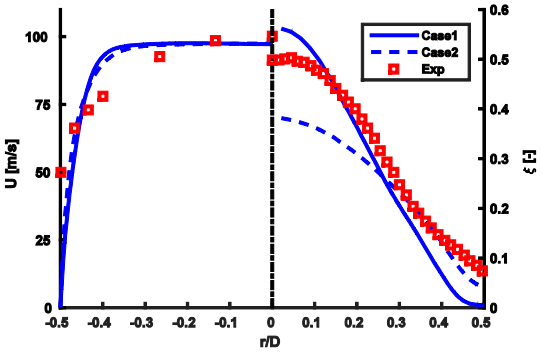


Figure 5: mean radial profiles of axial velocity (left) and mixture fraction (right). Case1 inlet mean velocity profile without fluctuations. Case2 inlet mean velocity profile with fluctuations (I ≈10%).

## 4. Conclusions

The LES approach combined with a simplified chemistry treatment is used to compute the structure of a turbulent partially premixed piloted flame as a starting point to compute flames with compositionally inhomogeneous inlets. The results are satisfactory with scalar fields well reproduced albeit there are some discrepancies. The usefulness of mixture fraction for conditioning purposes is demonstrated and supports future work towards the computation of the structure of turbulent flames using MMC. The compositionally inhomogeneity at the exit plane allows for the existence of mixed mode combustion accompanied by finite rate chemistry effects that will have to be accounted for in future work.

## Acknowledgements

This work is supported by the Australian Research Council.

## References

[1] H. Pitsch, 'Large-Eddy Simulation of Turbulent Combustion', *Annu. Rev. Fluid Mech.*, vol. 38, no. 1, pp. 453–482, 2006.

[2] T. Poinsot and D. Veynante, *Theoretical and Numerical Combustion*. R.T. Edwards, Inc., 2005.

[3] N. Peters, 'Laminar diffusion flamelet models in non-premixed turbulent combustion', *Prog. Energy Combust. Sci.*, vol. 10, no. 3, pp. 319–339, 1984.

[4] A. Y. Klimenko and R. W. Bilger, 'Conditional moment closure for turbulent combustion', *Prog. Energy Combust. Sci.*, vol. 25, no. 6, pp. 595–687, Dec. 1999.

[5] S. B. Pope, 'PDF methods for turbulent reactive flows', *Prog. Energy Combust. Sci.*, vol. 11, no. 2, pp. 119–192, 1985.

[6] S. B. Pope, 'Lagrangian PDF Methods for Turbulent Flows', *Annu. Rev. Fluid Mech.*, vol. 26, no. 1, pp. 23–63, 1994.

[7] M. J. Cleary, A. Y. Klimenko, J. Janicka, and M. Pfitzner, 'A sparse-Lagrangian multiple mapping conditioning model for turbulent diffusion flames', *Proc. Combust. Inst.*, vol. 32, no. 1, pp. 1499–1507, 2009.

[8] A. R. Masri, 'Partial premixing and stratification in turbulent flames', *Proc. Combust. Inst.*, vol. 35, no. 2, pp. 1115–1136, 2015.

[9] S. Meares and A. R. Masri, 'A modified piloted burner for stabilizing turbulent flames of inhomogeneous mixtures', *Combust. Flame*, vol. 161, no. 2, pp. 484–495, Feb. 2014.

[10] S. Meares, V. N. Prasad, M. Juddoo, K. H. Luo, and A. R. Masri, 'Simultaneous planar and volume cross-LIF imaging to identify out-of-plane motion', *Proc. Combust. Inst.*, vol. 35, no. 3, pp. 3813–3820, 2015.

[11] A. R. Masri, R. W. Dibble, and R. S. Barlow, 'The structure of turbulent nonpremixed flames revealed by Raman-Rayleigh-LIF measurements', *Prog. Energy Combust. Sci.*, vol. 22, no. 4, pp. 307–362, 1996.

[12] 'TNF Workshop'. [Online]. Available: http://www.sandia.gov/TNF/abstract.

[13] S. Meares, V. N. Prasad, G. Magnotti, R. S. Barlow, and A. R. Masri, 'Stabilization of piloted turbulent flames with inhomogeneous inlets', *Proc. Combust. Inst.*, vol. 35, no. 2, pp. 1477–1484, 2015.

[14] A. R. Masri, [Online]. Available: http://web.aeromech.usyd.edu.au/thermofluids/database.php.

[15] Y. Ge, B. Sundaram, M. Cleary, and A. Klimenko, 'A bluff body jet mixer simulation with a new developed OpenFOAM based sparse-Lagrangian Multiple Mapping Conditioning model', presented at the 18th Australasian Fluid Mechanics Conference, Launceston, Australia, 2012.

[16] H. Pitsch and Steiner, 'Large-eddy simulation of a turbulent piloted methane/air diffusion flame (Sandia flame D)', *Phys. Fluids 1994-Present*, vol. 12, no. 10, p. 2541, 2000.

[17] A. Kempf, M. Klein, and J. Janicka, 'Efficient Generation of Initial- and Inflow-Conditions for Transient Turbulent Flows in Arbitrary Geometries', *Flow Turbul. Combust.*, vol. 74, no. 1, pp. 67–84, Jan. 2005.

[18] M. J. Cleary and A. Y. Klimenko, 'A Generalised Multiple Mapping Conditioning Approach for Turbulent Combustion', *Flow Turbul. Combust.*, vol. 82, no. 4, pp. 477–491, Jun. 2008.

[19] M. J. Cleary and A. Y. Klimenko, 'A detailed quantitative analysis of sparse-Lagrangian filtered density function simulations in constant and variable density reacting jet flows', *Phys. Fluids 1994-Present*, vol. 23, no. 11, p. 115102, Nov. 2011.

[20] Y. Ge, M. J. Cleary, and A. Y. Klimenko, 'A comparative study of Sandia flame series (D–F) using sparse-Lagrangian MMC modelling', *Proc. Combust. Inst.*, vol. 34, no. 1, pp. 1325–1332, 2013.

[21] Y. Ge, M. J. Cleary, and A. Y. Klimenko, 'Sparse-Lagrangian FDF simulations of Sandia Flame E with density coupling', *Proc. Combust. Inst.*, vol. 33, no. 1, pp. 1401–1409, 2011.

# Simulations of an *n*-dodecane flame with LES/sparse-Lagrangian MMC method

Fatemeh Salehi[1, *], Matthew J. Cleary[1], Assaad R. Masri[1]
[1]School of Aerospace, Mechanical and Mechatronic Engineering
University of Sydney NSW 2006 Australia

## Abstract

This paper presents simulations for *n*-dodecane spray A of the engine combustion network (ECN) using a sparse-Lagrangian multiple mapping conditioning (MMC) model coupled with a large eddy simulation (LES) approach. A 106-species chemistry mechanism is employed. A gas-jet model is used for the fuel injection to focus on the turbulence-chemistry interactions in the gas phase. The LES/sparse-Lagrangian MMC method is first evaluated for a baseline non-reacting case with ambient temperature and oxygen of 900 K and 15%, respectively. The LES/sparse-Lagrangian MMC shows a good agreement with experiment for vapor penetration lengths and the radial profiles of mixture fraction at different axial locations. The model is then applied to reacting cases, featuring transient ignition and combustion with a lifted flame base. Simulations are performed at various ambient temperatures (800 K-1100 K) that correspond to conditions in both conventional and advanced (e.g., low-temperature) diesel engines. The trend towards decreasing ignition delay time and lift-off length with increasing ambient temperature is predicted very well. The agreement between the computed ignition delay times and the experiment is satisfactory although the simulations reveal a longer lift-off length at all ambient temperatures. This may be partly due to the gas-jet assumption which assumes that the main flame does not overlap with the liquid phase. For the high ambient temperature cases this assumption may not hold.

*Keywords: LES/ Sparse-Lagrangian MMC, diesel spray, n-dodecane, Gas-jet model.*

## 1. Introduction

Formation of pollutants, particularly particles, remains a key challenge with diesel engines despite of their continued use as main source of power in transportation. In order to reduce the formation of the pollutants and optimise efficiency, further developments of the combustion process in diesel engines are required. Reliable numerical tools capable of predicting combustor performance can be highly valuable to achieve these aims. Recently, the Engine Combustion Network (ECN) [1] has been established to provide an effective and a collaborative platform for experimental and numerical researchers in engine combustion. A single hole *n*-dodecane spray which is known as spray A is one of the main ECN targets focusing on high pressure diesel spray flames at engine-like conditions. Various modelling approaches, with varying degrees of success, have been employed to treat turbulence-chemistry interactions (TCI) in spray A simulations. They mainly include the well-mixed model [2], multiple-flamelet representative interactive flamelets (mRIF) [3,4], unsteady flamelet progress variable (UFPV) [5] and the probability density function (PDF) approach [6,7].

In this study, the sparse-Lagrangian multiple mapping conditioning (MMC) is applied in the LES framework to treat TCI in modelling combustion in spray A. The sparse-Lagrangian MMC approach model combines the advantages of PDF and conditional moment closure (CMC) [8] methods. Since the filtered chemical source term in the LES framework cannot be closed by the resolved scalars, the concept of a PDF for sub-filter fluctuations, known as the filter density function (FDF), was introduced. However, with the FDF approach, an enormous number of particles are required to enforce localness in physical space. For instance, 60 to 200 particles per Eulerian grid cell were employed to model the gas phase in the ECN spray A [6,7] which is computationally costly particularly in the LES framework. The sparse-Lagrangian method offers a more effective alternative where a precise mixing process can be achieved using the enforcement of localness in composition space. Hence, the reacting composition can be simulated using a fewer number of particles with a very low computational cost while retaining comparable accuracy. This approach has been successfully applied to simulate various statistically stationary reacting flows [9-11]. The current work represents the first application of the sparse models for transient reacting flows under more realistic, engine-like conditions.

## 2. Experimental setup and test case studied

The experimental platform employed here is spray A which is provided by Sandia National Laboratories [12] through the ECN. The experimental configuration is a constant-volume cubic vessel of size 108 mm. High pressure *n*-dodecane fuel is injected into a high temperature ($T_{amb}$) and high pressure environment ($P_{amb}$). The parameters that can be varied are the ambient temperature ($T_{amb}$) and density ($\rho_{amb}$) as well as level of oxygen ($O_2$%) and injector pressure ($P_{inj}$). For the cases studied in this work, the injection pressure, the fuel temperature and the ambient density are held constant at 150 MPa, 363 K and 22.8 kg/m$^3$, respectively, whereas the ambient temperature are varied. Relevant parameters are summarised in Table 1. Ambient composition for

* Corresponding author:
Phone: (+61) 2 9351 2835
Email: fatemeh.salehi@sydney.edu.au

both non-reacting and reacting cases is also shown in Table 2.

Table 1 Simulated conditions for Spray A.

| Case | $T_{amb}$ (K) | $O_2$% | $N_2$% | $CO_2$ % | $H_2O$ % |
|---|---|---|---|---|---|
| 1 | 900 | 0 | 89.71 | 6.52 | 3.77 |
| 2 | 900 | 15 | 75.15 | 6.22 | 3.62 |
| 3 | 800 | 15 | 75.15 | 6.22 | 3.62 |
| 4 | 1000 | 15 | 75.15 | 6.22 | 3.62 |
| 5 | 1100 | 15 | 75.15 | 6.22 | 3.62 |

## 3. Methodology

### 3.1 Fuel injection model

In the present study, a gas-jet model is employed to represent liquid fuel injection in the chamber. In order to match the mass and momentum flow rates of as the experimental liquid jet, the orifice diameter is accordingly modified to account for density differences. This assumption is reasonable for the ECN spray A at conditions where there is not an overlap between the flame and the liquid phase. For instance, the liquid length in the baseline case with ambient temperature of 900 K (Case 2 in Table 2) is 10.6 mm from the nozzle exit while the lift-off length is 16.5 mm so that the flame is stabilised downstream of the liquid region. For this condition, after about 0.2 ms, a quasi-steady liquid length is established whereas the ignition delay time is 0.44 ms. Therefore, the main ignition occurs after the transient liquid phase development. The gas-jet model has been successfully employed in earlier simulations for ECN sprays [4, 13].

### 3.2 Turbulence and combustion models

The LES/sparse-Lagrangian MMC (LES-MMC) approach is a hybrid Eulerian/Lagrangian method. The Eulerian LES formulation simulates velocity, pressure, reference mixture fraction fields whereas a Lagrangian formulation is used for the simulation of the reactive composition field in the gas phase. Differential stochastic equations are solved on Pope particles (i.e. notional particles). The MMC mixing model used here is similar to Curl's model [14] in which the particles interact directly with each other. However, the mixing particle pairs are selected specifically rather than randomly. The enforcement of localness in composition space has been introduced to provide an accurate mixing model [15]. Mixture fraction, a conserved variable, was suggested as a reference variable to enforce localness in composition space. Two global parameters including a characteristic physical scale, $r_m$, and a characteristic reference mixture fraction scale, $f_m$, control the mixing localisation structure. Equations and more details can be found in Ref. [9].

### 3.3 Numerical setup

The model is implemented into an open source object oriented C++ CFD code known as OpenFOAM. The LES-MMC solver, known as mmcFOAM, was recently developed at the University of Sydney, and employs both structured and unstructured meshes with parallel processing capability. The sparse-Lagrangian MMC model is fully coupled with a transient LES solver. The LES code implicitly solves the mass, momentum, and reference mixture fraction equations. A pressure-implicit algorithm with splitting of operators (PISO) is adopted to treat the pressure-velocity coupling. Then, using the solution on an Eulerian LES mesh, velocity, turbulent diffusivity and reference mixture fraction are interpolated for particles and then passed to the sparse-Lagrangian MMC solver. In the next fractional step, the solution for stochastic equations for particles is advanced in time. Density coupling is achieved through adopted the equivalent enthalpy method [16]. In mmcFOAM, this is done by solving equivalent composition equations related to the enthalpy. The standard Smagorinsky turbulent viscosity model [17] is used for the subgrid scale stresses.

The ambient conditions in the simulations are the same as for the experiments however the fuel properties and orifice diameter are modified to match the experimental mass flow rate. The spray parameters calculated for the baseline case (Case 1) are presented in Table 2. A three-dimensional rectangular computational domain of 108 mm in x-direction (axial) and 30 mm in both y- and z-directions was considered. The computational domain has the same length as the experimental chamber in the axial direction but it is shorter in other directions. Free stream boundary conditions were applied in these directions while wall boundary conditions were applied at either ends of the axial domains. A level of 15% for turbulent intensity and a ratio of 0.125 for the integral length to the orifice diameter were imposed for the turbulent velocity boundary condition. A hexahedral mesh with about 600 thousands cells was employed in the present study. The mesh size near the nozzle is 0.02 mm whereas it is about 3 mm close to the free stream boundaries. One particle per 8 Eulerian LES cells and a value of $f_m$ = 0.01 were used in the simulations. Various chemistry mechanism have been used in earlier simulations for spray A [2-7] and a skeletal-chemistry mechanism including 106 species and 420 reactions [18] is employed here as recommended by the ECN.

Table 2 Experimental and numerical parameters for Spray A.

| | Experiment | Model |
|---|---|---|
| Injected fuel | Liquid | Gas |
| Fuel density (kg/m$^3$) | 713 | 341 |
| Injection velocity (m/s) | 577.3 | 577.3 |
| Fuel Temperature (K) | 363 | 363 |
| Nozzle diameter (mm) | 0.085 | 0.13 |

## 4. Results

Figure 1 presents vapor penetration versus time computed by the LES-MMC model in comparison with experimental data for Case 1 with $T_{amb}$ = 900 K. The computed vapor penetration length is defined as the axial distance from the nozzle exit where the mixture fraction drops to 0.001 as recommended by the ECN. The agreement between the LES-MMC and experiment is satisfactory and errors in prediction of vapor penetration using the LES-MMC are less than 10% in all times. Various parameters such as gird resolutions, integral

length and turbulence intensity have been examined to investigate the reason for observed over-prediction. It was found the inlet jet turbulent intensity significantly influenced the prediction of the jet penetration. The best agreement was obtained using the turbulence intensity of 15%. A dynamic Smagorinsky turbulence model was also applied however it did not significantly affect the results.

The simulated and measured radial profiles of azimuthally averaged mixture fraction at axial locations of 35 and 45 mm and quasi-steady state are shown in Fig 2. As can be seen, the LES-MMC results are in excellent agreement with the experiment at both axial locations. The axial profile of mixture fraction extracted on the jet centerline is also shown in Fig. 2 and this is predicted fairly well.

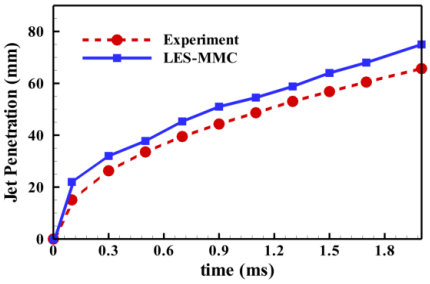


Fig. 1: Vapor penetration for case 1 with $T_{amb}$ = 900 K.

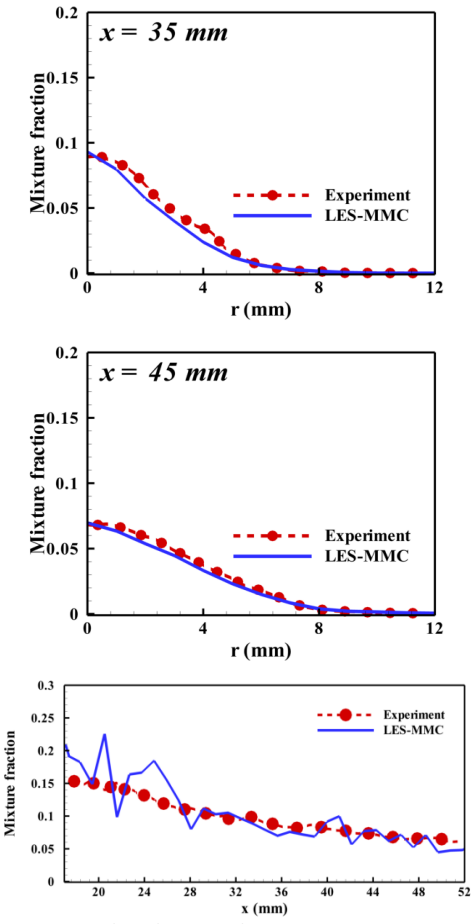


Fig. 2: Radial profile of mixture fraction at various axial locations (top and middle) and centreline mixture fraction (bottom) for Case 1 with $T_{amb}$ = 900 K.

To evaluate the LES-MMC performance in reacting cases, global quantities including the ignition delay time and the lift-off length are compared with the experimental data. As recommended by ECN [1], the ignition delay time is defined as the duration from the start of injection until the occurrence of the maximum rate of rise of peak temperature occurs. The definition of the lift-off length is the axial distance from the nozzle exit at which the OH mass fraction reaches 2% of its maximum value at each operating condition.

Figure 3 shows the computed ignition delay time and lift-off length versus ambient temperature. As can be seen, the trend towards decreasing ignition delay time with increasing ambient temperature is predicted well although the predicted ignition delay times are slightly longer than the experimental values at all ambient temperatures. The longer ignition delay times have been observed in earlier simulations [2-7]. Pei et al. [6] and D'Errico et al. [3] showed that the reasons for the discrepancy are largely linked to the chemistry mechanism using the analysis of ignition delay time provided for shock tubes.

As shown in Fig. 3.b), the LES-MMC model predicts a longer lift-off length at all ambient temperatures but the trend is qualitatively well predicted. It can be seen that the LES-MMC predictions at lower ambient temperatures are in better agreement than those at higher ambient temperatures. This may be due to the gas-jet model which provides a reasonable approximation at lower ambient temperatures where there is no overlap between the main flame and the liquid phase. However, at higher ambient temperatures, the flame is stabilised close to the nozzle exit and there is a high chance of overlapping with the liquid phase.

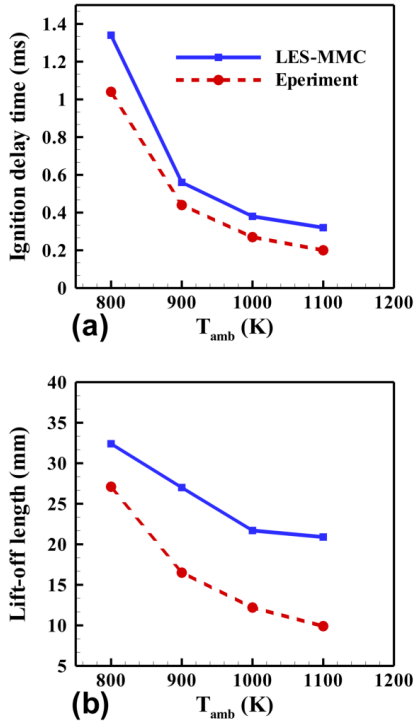


Fig. 3: Ignition delay time and lift-off length versus ambient temperature.

Figure 4 illustrates the temporal evolution of the quasi-steady state lift-off length for different ambient temperatures obtained using the LES-MMC. As can be seen, the lift-off length reaches a quasi-steady state value after 1.8 ms and 0.8 ms for the cases with $T_{amb}$ = 800 and 900 K, respectively which is long enough after the quasi-steady liquid phase is stablished. However, the quasi-steady state lift-off length for the cases with $T_{amb}$ = 1000 and 1100 K is shorter and occurs at about t = 0.4 ms where the flame may overlap with development of liquid phase. Then, it can be concluded that the use of gas-jet model especially at higher ambient temperatures may be the main reason for predicting longer lift-off length in comparison with experimental data. The longer lift-off lengths can be also linked to the over-predicted ignition delay times which is due the chemistry model. As discussed in the ECN [1], the prediction of lift-off length, compared to the ignition delay time, is less sensitive to the chemistry mechanism but it can be improved using more appropriate chemistry mechanism.

Another reason for the observed discrepancy can be associated to the mixing model. Since the ignition delay times at higher ambient temperatures is relatively shorter than those with lower ambient temperatures, the effect of turbulence-chemistry interactions are more significant in the former. The use of a global mixing parameter, $f_m$, in these cases may not be sufficient for predicting the intense turbulence-chemistry interactions and the strong variations. Local values of $f_m$ may improve results but it is beyond the scope of this study.

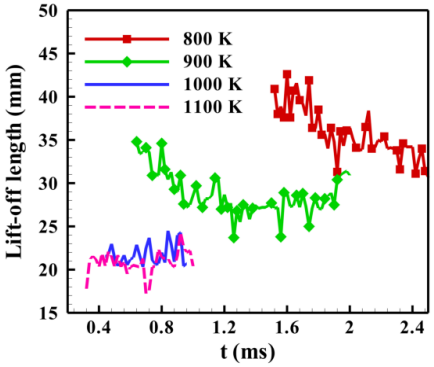


Fig. 4: Temporal evolution of the lift-off length for various ambient temperature cases.

## 5. Conclusion

Simulations for the ECN *n*-dodecane spray known as spray A at various ambient temperatures were presented using the LES-MMC approach. A gas-jet approach was employed for the fuel injection model. The LES-MMC results for the non-reacting case were initially investigated. The LES-MMC prediction for vapor penetration and the radial profiles of the mixture fraction at various axial locations were satisfactory.

The model was then applied to the reacting spray at various ambient temperatures using a 106-species chemistry model for *n*-dodecane. A slightly longer ignition delay time was predicted at all ambient temperature which can be due to the chemistry model. The LES-MMC model predicted the trend of decreasing lift-off of length with increasing ambient temperature very well. However, the computed lift-off length was longer than the experiment. At lower ambient temperatures, the lift-off length was found to be in a better agreement with the experiment compared to one at higher ambient temperatures. One of the reasons for the over-predicted lift-off length may be associated with the use the gas-jet assumption. It becomes problematic at higher ambient temperatures due to the potential overlap between the liquid phase and the flame.

## 6. Acknowledgments

This work was supported by the Australian Research Council (ARC). The research was also supported by access to the University of Sydney high performance computing facility, Artemis.

## 7. References

[1] http://www.sandia.gov/ecn/index.php, 2014.

[2] Z. Luo, S. Som, S.M. Sarathy, M. Plomer, W.J. Pitz, D.E. Longman, T. Lu, Combust. Theor. Model. **18** (2014) 187–203.

[3] G. D'Errico, T. Lucchini, F. Contino, M. Jangi, X.S. Bai, Combust. Theor. Model. **18** (2014).

[4] P. Kundu, Y. Pei, M. Wang, R. Mandhapati, S. Som, Atomization Sprays **24** (2014).

[5] C. Bajaj, M. Ameen, J. Abraham, Combust. Sci. Tech. **185** (2013) 454–472.

[6] Y. Pei, E.R. Hawkes, S. Kook, G.M. Goldin, T. Lu, Combust. Flame **162** (2015) 2006–2019.

[7] S. Bhattacharjee, D.C. Haworth, Combust. Flame **160** (2013) 2083–2102.

[8] A.Y. Klimenko, R.W. Bilger, Prog. Energ. Combust. Sci. **25** (1999) 595–687.

[9] M.J. Cleary, A. Klimenko, Phys. Fluids **23** (2011) 115102.

[10] Y. Ge, M.J. Cleary, A. Klimenko, Proc. Combus. Inst. **33** (2011) 1401–1409.

[11] Y. Ge, M. Cleary, A. Klimenko, Proc. Combust. Inst. **34** (2013) 1325–1332.

[12] L.M. Pickett, J. Manin, C.L. Genzale, D.L. Siebers, M.P. Musculus, C.A. Idicheria, SAE Int. J. Eng. **4** (2011) 764–799, 2011-01-0686.

[13] Y. Pei, E.R. Hawkes, S. Kook, Proc. Combus. Inst. **34** (2013) 3039–3047.

[14] R. Curl, A.I.Ch.E. J. **9** (1963) 175–181.

[15] S. Subramaniam, S. Pope, Combust. Flame **115** (1998) 487–514.

[16] M. Muradoglu, S.B. Pope, D.A. Caughey, J. Comput. Phys. **172** (2001) 841–878.

[17] J. Smagorinsky, Mon. Weather Rev. **91** (1963) 99–164.

[18] S. Som, D.E. Longman, Z. Luo, M. Plomer, T. Lu, Three dimensional simulations of diesel sprays using n-dodecane as a surrogate, Fall Technical Meeting of the Eastern States Section of the Combustion Institute, Storrs, CT, 9–11 October 2011.

# The effect of equivalence ratio on sound generation by turbulent premixed flames

A. Haghiri[1,*], M. Talei[1], M. J. Brear[1], E. R. Hawkes[2,3]
[1]Department of Mechanical Engineering, University of Melbourne, Parkville 3010, Australia
[2]School of Mechanical and Manufacturing Engineering, University of New South Wales, Sydney 2052, Australia
[3]School of Photovoltaic and Renewable Energy Engineering, University of New South Wales, Sydney 2052, Australia

**Abstract**
Direct numerical simulation (DNS) is used to study sound generation by open, turbulent premixed flames. Two cases of methane/air combustion with different equivalence ratios ($\phi = 0.7$ and $1$) are considered. The computational grid is set up such that both the near and far fields are fully resolved. A simple-chemistry model is used to reduce the computational cost. The results show that flame annihilation events are significant monopolar sources of noise. Spectral analysis of the radiated sound shows a broadband spectrum where the observed frequency of the peak amplitude matches that observed experimentally. Furthermore, it is observed that the stoichiometric flame ($\phi = 1$) is a much stronger source of noise than the lean flame ($\phi = 0.7$).

*Keywords: Direct numerical simulation, Combustion noise, Annihilation event, Turbulent premixed flames.*

## 1. Introduction

In addition to being a significant form of noise pollution, combustion noise has an intimate relationship with combustion instability [1], which is a major challenge in developing low emission gas turbine combustors. Combustion instability is usually initiated by combustion-generated sound and other disturbances generated by the turbulent flame inside the combustor. The interaction of the reflected acoustic waves from the combustor's walls with the flame can introduce instability leading to failure in extreme cases. Hence, the mechanism of sound generation by turbulent flames needs to be first understood.

There are a considerable number of studies indicating that sound generation due to unsteady combustion in lean-premixed flames can lead to combustion instability, e.g. [2–8]. To develop clean and more efficient combustors, it is therefore important to address the issues associated to lean premixed flames. As a result, understanding the mechanism(s) of sound generation by premixed flames is a natural first step.

Sound generation by premixed flames has been topic of interest in the last 60 or so years. In one early study, Smith et al. [9] experimentally investigated sound generation by open turbulent premixed flames. They showed that the emitted sound originates from a distribution of monopolar sources throughout the reaction zone. This work appears to be the first to report experimentally that sound generation by a turbulent premixed flame can be essentially monopolar. They also showed that combustion noise is a broad, continuous spectrum of frequencies where its peak amplitude and associated frequency can be related to the burner diameter, the flow velocity, and the flame speed. In the same year, Bragg [10] established a simple theory to clarify the relationship between the sound production and turbulent combustion. He assumed that the generated noise is the result of changes in the flame volume or the heat release rate. It is now well established that fluctuations of the heat release rate play a significant role in generation of combustion noise, e.g. [2,3,7,8,11].

One mechanism that may result in significant fluctuations of the heat release rate is flame annihilation. Flame annihilation can occur when two flame surfaces collide with each other resulting in a rapid, unsteady consumption of the unburned gas trapped between these surfaces. There are a few experimental studies that have investigated this mechanism of combustion noise [12-14]. In a number of one- (1D) and two-dimensional (2D) numerical studies [7,8,15,16], flame annihilation has also been shown to have a significant contribution to the rate of change of heat release rate, and therefore the generated sound in laminar premixed flames. However, it is unclear whether these events are also significant sources of noise in turbulent premixed flames.

This paper therefore presents a 3D, fully-resolved DNS study of sound generation by open turbulent premixed flames. It appears that a DNS study of sound generation by an open turbulent premixed flame has not yet been reported. A simple-chemistry model is used and a comparison is made between simulations of two cases of methane-air flames with different equivalence ratios ($\phi = 0.7$ and $1$), in which the premixture is preheated at $T_u$=800 K for both cases. The spectral content of the radiated sound is also examined with regards to experimental studies performed by others.

* Corresponding author:
Phone: (+61) 3 83446743
Email: a.haghiri@student.unimelb.edu.au

## 2. Computational Model

### 2.1 Governing Equations

Using a single-step chemistry model, the governing equations for the conservation of momentum, mass, total energy, and deficient species mass are, respectively, as follows:

$$\frac{\partial \rho u_j}{\partial t} + \frac{\partial \rho u_i u_j}{\partial x_i} = -\frac{\partial p}{\partial x_j} + \frac{\partial \tau_{ij}}{\partial x_i}, \quad (1)$$

$$\frac{\partial \rho}{\partial t} + \frac{\partial \rho u_i}{\partial x_i} = 0, \quad (2)$$

$$\frac{\partial \rho E_t}{\partial t} + \frac{\partial u_j(\rho E_t + p)}{\partial x_j} = \frac{\partial u_i \tau_{ij}}{\partial x_j} - \frac{\partial q_j}{\partial x_j}, \quad (3)$$

and

$$\frac{\partial \rho Y_F}{\partial t} + \frac{\partial \rho u_j Y_F}{\partial x_j} = \frac{\partial}{\partial x_j}\left(\rho D \frac{\partial Y_F}{\partial x_j}\right) - \dot{\omega}_F, \quad (4)$$

where $x$ and $t$ are the spatial coordinate and time, respectively. In addition, $\rho$ is the density, $u_j$ is the j-component of flow velocity, $Y_F$ is the fuel mass fraction, $p$ is the pressure, $E_t$ is the total energy per unit mass (internal energy plus kinetic energy), $q_j$ is the heat flux vector considering constant heat capacity, and $\tau_{ij}$ is the $ij$-component of the viscous stress tensor. The quantities $E_t$ , $q_j$ and $\tau_{ij}$ are given by,

$$E_t = \frac{p}{\rho(\gamma - 1)} + Y_F Q + \frac{1}{2} u_i u_i, \quad (5)$$

$$q_j = -\lambda \frac{\partial T}{\partial x_j} - \sum_{k=1}^{N_s=2} \left( \Delta h_k^0 \rho D \frac{\partial Y_k}{\partial x_j} \right), \quad (6)$$

$$\tau_{ij} = \mu \left[ \frac{\partial u_i}{\partial x_j} + \frac{\partial u_j}{\partial x_i} - \frac{2}{3} \frac{\partial u_k}{\partial x_k} \delta_{ij} \right], \quad (7)$$

where γ is the heat capacity ratio, $Q$ is the heat of reaction per unit mass of reactant, $\Delta h_k^0$ is the chemical enthalpy of formation evaluated at reference temperature $T_0$, μ is the dynamic viscosity, $D$ is the binary mass diffusion coefficient, λ is the mixture thermal conductivity, and $\delta_{ij}$ is the Kronecker delta. The fuel reaction rate $\dot{\omega}_F$ may be obtained using the Arrhenius law as follows:

$$\dot{\omega}_F = \Lambda \rho Y_F \exp\left[ -\frac{\beta(1-\theta)}{1-\alpha(1-\theta)} \right], \quad (8)$$

where

$$\Lambda = B \exp(-\beta/\alpha), \ \theta = \frac{T - T_0}{T_f - T_0}, \quad (9)$$

$$\alpha = \frac{T_f - T_0}{T_f}, \ and \ \beta = \frac{E_a (T_f - T_0)}{R T_f^2}. \quad (10)$$

Note that $B$ is the pre-exponential factor, $\beta$ is the Zel'dovich number, $T_f$ is the adiabatic flame temperature, $T_0$ is the fresh mixture temperature at jet inlet, $E_a$ is the activation energy, $R$ is the universal gas constant, and $\alpha$ is the heat release parameter.

### 2.2 Numerical Method

Direct numerical simulation (DNS) of the governing equations (1-4) was carried out using a modified version of the code S3D [17] (referred to as S3D-SC [18]) which features an 8th order central differencing scheme for spatial derivatives, combined with a 4th order explicit Runge–Kutta time integrator. S3D is an MPI-compatible solver and can be run on parallel processors with a high performance.

Figure 1 shows a schematic of the computational domain. The computational domain was resolved using a 3D structured Cartesian mesh. The boundary conditions were based on 3D Navier-Stokes Characteristic Boundary Condition (3DNSCBC) [19]. All boundaries were carefully treated to avoid spurious noise reflections.

A subsonic round jet of unburned premixed mixture (reactant) is injected into an open environment of adiabatic combustion products. The environment's temperature is equal to the product temperature. Two cases of methane/air combustion were considered with different equivalence ratios ( $\phi = 0.7$ and $1$ ), in which the reactants are preheated at $T_u$=800 K in both cases. A coflow with a low velocity magnitude (1% of the jet mean velocity) surrounds the jet flame at the product temperature to mimic natural convection around jet flames in real conditions. The simulation parameters for both cases are presented in Table 1.

The mean inlet streamwise velocity was adapted from the DNS study of Wu and Moin [20] where a fully developed turbulent pipe flow at the Reynolds number $Re_D$=5300 was simulated. To impose the velocity fluctuations at the inlet boundary, homogeneous isotropic turbulence, obtained based on the Passot-Pouquet energy spectrum [21] with a centreline turbulence intensity of 3.7 %, was first generated. The velocity fluctuations at the inlet were then obtained by rescaling the streamwise velocities of the turbulence field with the turbulence intensity profile of the pipe flow simulation in the streamwise direction [20]. The resulting frozen velocity field was then added to the mean inlet velocity using the Taylor hypothesis.

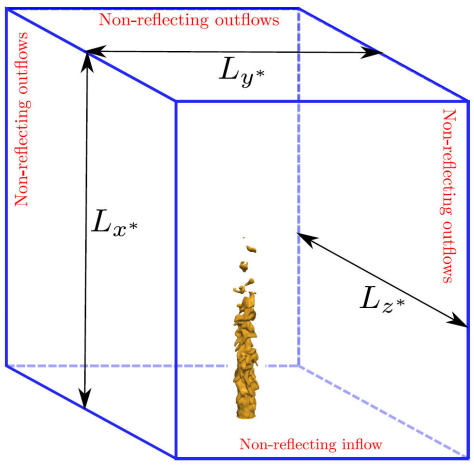


Figure 1: The computational domain (not to scale).

Table 1: The simulation parameters used in the present study.

| | $\phi = 1$ | $\phi = 0.7$ |
|---|---|---|
| Jet diameter | D | |
| Domain size | 20D × 16D × 16D | |
| Grid resolution | 2412 × 1040 × 1040 | |
| Mean inlet jet Mach number | 0.35 | 0.26 |
| co-flow Mach number | 0.0035 | 0.0026 |
| Heat release parameter (α) | 0.675 | 0.637 |
| Jet Reynolds number (Re) | 5300 | 5300 |
| $\delta_{th} / D$ | 0.07 | 0.07 |
| $S_L / a_{ref}$ | 0.00422 | 0.00325 |
| $\beta$ | 7.9 | 5.5 |
| Pr | 0.72 | 0.72 |
| Le | 1.0 | 1.0 |

The simulations for both cases were performed using a constant time step for six complete jet flow-through times to achieve a statistically stationary solution. The data of the last four flow-through times were used for post-processing.

## 3. Results and Discussion

### 3.1 Flame-Generated Sound and Related Acoustic Field

Instantaneous snapshots of the temperature and dilation fields ($(D/a_{ref})\nabla.\vec{u}$ ) extracted at the central X-Y plane through the jet are shown in Fig. 2 for each case. (It can be readily shown that the dilatation and the pressure are related in the far field [22]). Flame annihilation evidently occurs, in particular near the flame tip. Looking at the dilatation fields, it can be seen that the acoustic fields for both the stoichiometric and lean flames feature discrete monopolar sound sources. The sound produced from these sources, originating some distance downstream of the nozzle, clearly dominate the incoming noise at the inflow.

It should be also noted that weaker monopolar sources of sound appear in the lean flame. Since both simulated cases have the same Reynolds numbers and turbulence intensities, this observation is most likely related to a difference in chemical parameters, such as flame speeds, between two cases. However, a more detailed analysis is required to quantify the contribution of annihilation events and the role of the flame key parameters to the overall radiated sound.

### 3.2 Spectral Analysis

The spectrum of the produced sound is calculated on a plane perpendicular to the jet axis at $x/D$=10. Eight uniformly-distributed virtual microphones at $r/D$=6 are placed on the plane to measure the sound intensity. The mean frequency spectrum is then obtained by averaging the spectrum of all individual microphones. To reduce the so-called 'spectral leakage' and to obtain the smallest spectral variance per data point, a modified Hanning window [23] with 50% overlap [24] was used to perform the fast Fourier transform (FFT) at each probe.

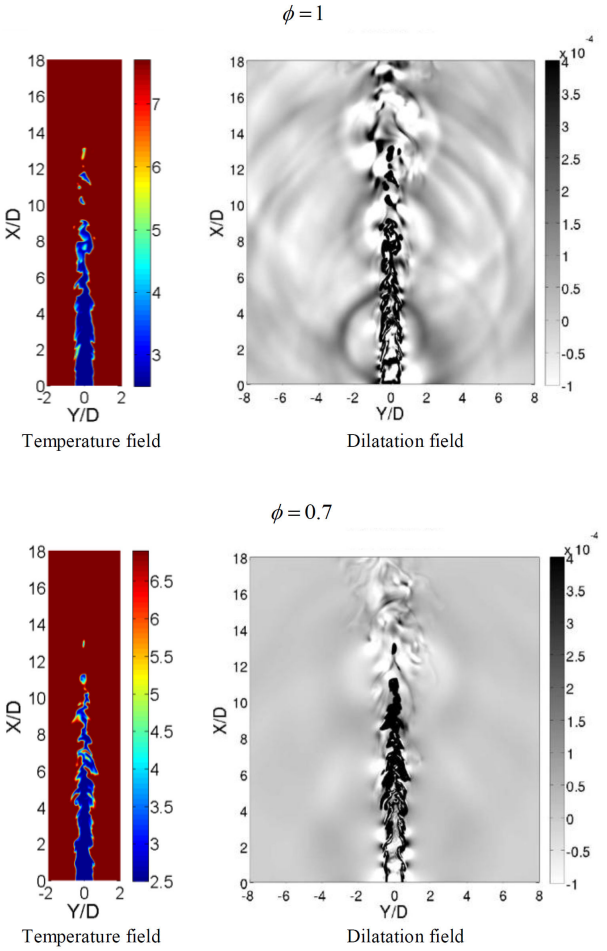


Figure 2: The instantaneous dimensionless temperature and dilatation fields for each case.

The averaged calculated spectrum for each case is shown in Fig. 4. Similar to earlier experimental studies (e.g [25]), the produced sound is broadband in nature in our study. Furthermore, the magnitude of the noise radiated by the stoichiometric flame is significantly greater than that of the lean flame.

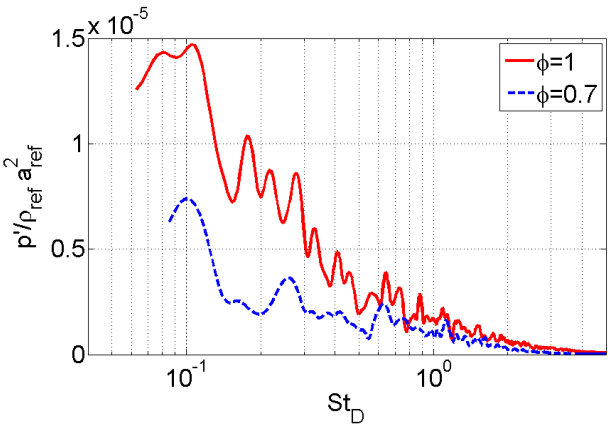


Figure 3: The calculated noise spectrum for each case at $x/D$=10, $r/D$=6. The horizontal axis shows Strouhal number ($St_D=fD/U_{av}$) and the vertical axis shows the non-dimensional acoustic pressure.

Rajaram and Lieuwen [25] investigated noise generation by a number of turbulent premixed flames and found that the frequency of peak emissions $f_{peak}$ across all burners, flow velocities, fuel/air ratios, and fuel types, is mainly a function of the flame length and the mean inlet velocity. They calculated the flame length based on the variance of every pixel in the intensity of chemiluminescence emitted by the flame. This intensity was regarded as a measure of the heat release at that location. The flame length $L_{flame}$ was then defined as the distance between the heights where the horizontally integrated intensity of the variance image crosses a quarter of the maximum value. They showed that the peak Strouhal number ($St_{peak} = f_{peak} L_{flame}/U_{av}$) is close to unity for the experimental conditions that they tested.

In the present study the flame length was calculated using the variance of the reaction rate field by following the method proposed by Rajaram and Lieuwen [25]. The flame lengths were approximately equal to 12.8*D* and 11.8*D* for the stoichiometric and lean cases, respectively. Using these values for the flame lengths, the peak Strouhal numbers for the stoichiometric and lean flames are equal to 1.3 and 1.2, respectively. These values therefore agree well with the peak Strouhal numbers found experimentally [25].

## 4. Conclusion

This paper presented a direct numerical simulation (DNS) study of sound generation by turbulent premixed flames. Two cases of methane/air flames with different equivalence ratios ($\phi = 0.7$ and $1$) were considered. A single-step chemistry model was used to reduce the computational cost. Care was taken to fully resolve both the near and far fields and avoid spurious reflections at the outflow boundaries using the three dimensional Navier-Stokes Characteristic Boundary Condition (3D-NSCBC).

It was observed that the interaction of flame surfaces led to flame annihilation events, specifically in the downstream region near the flame tip. The acoustic fields for both the stoichiometric and lean flames also featured discrete monopolar sound sources originating from these annihilation events, with the strength of these sources clearly dependent on equivalence ratio. The spectra of the radiated noise were then examined. These were found to be broadband in nature, with a frequency of the peak amplitude that follows the scaling proposed by Rajaram and Lieuwen [25].

A more detailed analysis is required to quantify the contribution of annihilation events and the flame key parameters to the overall radiated sound. This is a topic of our future research.

## 5. Acknowledgments

This study was supported by the Advanced Centre for Automotive Research and Testing (ACART, www.acart.com.au), the Australian Research Council (ARC) and the National Computational Merit Allocation Scheme, supported by the Australian Government. The computational facilities supporting this project included the Australian National Facility (NCI), the partner share of the NCI facility provided by Intersect Australia Pty Ltd., the Peak Computing Facility of the Victorian Life Sciences Computation Initiative (VLSCI) and iVEC (Western Australia).

## 6. References

[1] N. Swaminathan, K. N. C. Bray, (Eds.) Turbulent premixed flames. Cambridge University Press, 2011.

[2] I.R. Hurle, R.B. Price, T.M. Sugden, A. Thomas, Proc. R. Soc. Lond. A **303** (1968), pp. 409–427.

[3] W.C. Strahle, Prog. Energy Combust. Sci. **4** (1978), pp. 157–176.

[4] D.G. Crighton, A.P. Dowling, J.E. Ffowcs Williams, M. Heckl, F.G. Leppington, Modern Methods in Analytical Acoustics: Lecture Notes, Springer-Verlag, London, 1992.

[5] N. Swaminathan, R. Balachandran, G. Xu, A.P. Dowling, Proc. Combust. Inst. **33** (2011), pp. 1533–1541.

[6] N. Swaminathan, G. Xu, A.P. Dowling, R. Balachandran, J. Fluid Mech. **681** (2011), pp. 80–115.

[7] M. Talei, M.J. Brear, E.R. Hawkes, J. Fluid Mech. **679** (2011), pp. 194–218.

[8] M. Talei, M.J. Brear, E.R. Hawkes, Combust. Flame **159** (2) (2012), pp 757–769.

[9] T.J.B Smith, T. J. B., J.K Kilham, J. Acoust. Soc. Am. **35** (1963), pp. 715-724.

[10] S.L Bragg, J. Inst. Fuel **36** (1) (1963), pp. 12-16.

[11] C.K. Tam, Int. J. Aeroacoust., **14**(3-4) (2015), pp. 431-456.

[12] N. Kidin, V. Librovicht, J. Roberts, M. Vuillermoz, Dyn. Flames React. Syst. (1984), pp. 343–355.

[13] T. Schuller, D. Durox, S. Candel, Combust. Flame **135** (2003), pp. 525–537.

[14] S. Candel, D. Durox, T. Schuller, in: 10th AIAA/ CEAS Aeroacoustics Conference, Paper No. 2004- 2928, pp. 1444–1454.

[15] M. Talei, M.J. Brear, E.R. Hawkes, Proc. Combust. Inst. **34** (1) (2012), pp. 1093–1100.

[16] C. Jiménez, A. Haghiri, M.J. Brear, M. Talei, E.R. Hawkes, Proc. Combust. Inst. **35**(3) (2015), pp. 3317-3325.

[17] J.H. Chen, A. Choudhary, B. De Supinski, M. Devries, E.R. Hawkes, S. Klasky, W.K. Liao, K.L. Ma, J. Mellor-Crummey, N. Podhorszki, R. Sankaran, S. Shende, C.S. Yoo, Comput. Sci. Discovery **2** (2009), 015001.

[18] S. Karami, E.R. Hawkes, M. Talei, J.H. Chen, J. Fluid Mech. **777** (2015), pp. 633- 689.

[19] C.S. Yoo, H.G. Im, Combust. Theor. Model., **11**(2) (2007), pp. 259-286.

[20] X. Wu, P. Moin, J. Fluid Mech. **608** (2008), pp. 81-112.

[21] T. Passot, and A. Pouquet, J. Fluid Mech., **181** (1987), pp. 441–466.

[22] T. Colonius, S.K. Lele, P. Moin, J. Fluid Mech., **330** (1997), pp. 375–409.

[23] D.P. Lockard, J. Sound Vib. **229**(4) (2000), pp. 897–911.

[24] T.P. Bui, W. Schröder, M Meinke,. Comput. Fluids **37**(9) (2008), pp. 1157-1169.

[25] R. Rajaram, T. Lieuwen, J. Fluid Mech. **637** (2009), pp. 357–385.

# Flame interaction identification in turbulent premixed flames

D. Brouzet[1, *], A. Haghiri[1], T. Kulkarni[2], M. Talei[1], M. J. Brear[1], E. R. Hawkes[3,4]
[1]Department of Mechanical Engineering, University of Melbourne, Parkville 3010, Australia
[2]Department of Mechanical Engineering, Indian Institute of Technology Madras, Chennai, India
[3]School of Mechanical and Manufacturing Engineering, University of New South Wales, Sydney 2052, Australia
[4]School of Photovoltaic and Renewable Engineering, University of New South Wales, Sydney 2052, Australia

**Abstract**

An efficient formulation of the method of Griffiths et al. [1] is used to identify premixed flame interactions. This method identifies flame interactions by finding critical points in the progress variable field, and is applied to a DNS dataset featuring sound generation by a premixed jet flame. The results show that different types of flame interaction events occur, including tunnel formation, tunnel closure and pocket burn-out. A large number of these events occur close to the flame tip. The developed method, optimised for parallel processing, will be used to gain a detailed understanding of sound generation in turbulent premixed flames in future studies.

*Keywords: Flame interaction events, Turbulent premixed flame, Combustion noise, Optimization method.*

## Nomenclature

$\delta_{th}$: Flame thickness
$S_L$: Flame laminar speed
$u$: Velocity field

## 1. Introduction

Lean premixed combustion is a promising method of decreasing greenhouse emissions in modern gas turbines. However, the combustors operating under lean conditions are susceptible to so called 'thermo-acoustic instability' [2]. This phenomenon involves a strong coupling between the flame dynamics and acoustic waves and results in large pressure fluctuations leading to the combustor failure in extreme cases [3-8]. As a result, achieving an improved understanding of how flames produce sound is of great importance for environmental and safety reasons.

One of the first theoretical studies of combustion noise was performed by Strahle [9]. He used Lighthill's acoustic analogy [10] to describe sound generation in turbulent combusting flows as a function of flame key parameters. The time derivative of the heat release rate ($\partial\dot{Q}/\partial t$) was found to be the main source term of Lighthill's equation. Much of the subsequent work used this theoretical framework and showed reasonable agreement with experimental results (See Ref. [11] for a review of these studies). One phenomenon that can result in large fluctuations of heat release rate, and therefore large $\partial\dot{Q}/\partial t$, is flame annihilation [6,7,12-14]. When two flame surfaces approach each other, the unburned gas trapped between them is rapidly consumed, resulting in large fluctuations of the heat release rate.

Several investigations by the group have highlighted the importance of flame annihilation in the sound generation process using one-dimensional (1D) and two-dimensional (2D) numerical simulations of laminar premixed flames [6,7,15,16]. However, the contribution of flame annihilation events to the noise generation by turbulent premixed flames has not been examined closely. In a recent study, Haghiri et al. [17] performed a three-dimensional (3D) DNS of sound generation by a turbulent premixed flame. They showed that annihilation events were strong monopolar sources of sound. However, the annihilation events have not been examined in detail in this work.

Studies are also now emerging that identify flame interaction events. For instance, Dunstan et al. [18] investigated flame interactions in turbulent, premixed, twin V-flames. They used an automatic feature extraction (AFE) technique to identify flame interactions through topological changes of a progress variable iso-surface. The effects of the different types of interactions on the turbulent flame brush, and especially on the flame stretch rate, were discussed in this work. Griffiths et al. [1] used a different approach to identify flame interactions in a temporally evolving premixed flame. They identified flame interactions by finding the critical points in the progress variable field. They classified different types of flame interactions into four groups: product pocket, tunnel formation, tunnel closure and pocket burn-out events. They then performed some statistical analysis of those interactions in two flames with different Damkhöler numbers.

The present paper applies the method proposed by Griffiths et al. [1] to DNS data of a turbulent jet, premixed flame [17]. The ultimate goal is a detailed examination of the annihilation events and their contribution to the overall radiated sound from turbulent premixed flames.

The structure of this paper is as follows. First the DNS dataset is briefly presented. Then, the numerical method developed to identify the flame interactions is outlined. Next, the importance of flame interactions in the sound generation process is discussed, and finally the identified critical points with different types of annihilation events are visualised.

* Corresponding author:
Phone: (+61) 423 598 451
Email: brouzetd@student.unimelb.edu.au

## 2. DNS Dataset and Numerical Method

A direct numerical simulation (DNS) database of sound generation by a turbulent premixed flame was used in this study [17]. The DNS were performed using a modified version of S3D [19], referred to as S3D-SC [20-22]. S3D-SC uses an 8$^{th}$ order central differencing scheme for spatial derivatives, combined with a 6-stage, 4$^{th}$ order explicit Runge-Kutta time integrator. The simulation was performed on a 3D structured Cartesian mesh. The boundary conditions were based on 3D Navier-Stokes Characteristic Boundary Conditions (3DNSCBC) [23]. All non-reflecting outflow boundaries were carefully treated to avoid spurious noise reflections.

The DNS data features a round jet of unburned premixed mixture (reactant) issuing into an open environment of combustion products at the adiabatic flame temperature. The jet Reynolds number was equal to 4000 and a homogeneous turbulence field with a turbulence intensity of 10% was fed into the mean velocity field using the Taylor hypothesis. A single step chemistry model was used to reduce the computational cost. The fuel mass fraction $Y_f$ was used as the progress variable.

Table 1 summarises the DNS parameters. A representation of the flame, with 2 iso-surface values of the progress variable, can be seen in Fig. 1.

Table 1: DNS parameters

| | |
|---|---|
| Jet diameter | D |
| Domain size | 15D × 16D × 16D |
| Grid resolution | 1800 × 800 × 800 |
| Mean inlet Mach number | 0.4 |
| Co-flow Mach number | 0.004 |
| Non-dim. Fresh mixture temperature | 2.5 |
| Heat release parameter (α) | 3 |
| Jet Reynolds number (Re) | 4000 |
| Inlet turbulence intensity ($u'/\bar{U}_j$) | 0.1 |
| $\delta_{th}/D$ | 0.07 |
| $S_L/a_{ref}$ | 0.007 |
| Zeldovich number (β) | 8.0 |
| Damkhöler number (Da) | 19.44 |
| Prantl number (Pr) | 0.75 |
| Lewis number (Le) | 1.0 |

The flame annihilation events were identified by finding the critical points in the progress variable field, i.e. points where the progress variable gradients in all directions is zero [1]. An optimised form of Newton's algorithm was used to find these critical points. At first, a linear interpolation of the three components of the gradient vector was computed for the entire domain. Then, the cells which were likely to include a critical point were found using a linear interpolation of the gradient vector. If a cell passed this test, the cell's centre was given as a first estimate for Newton's method. Before commencing the iterative process to find the critical point, a tri-cubic convolution algorithm was used to calculate the progress variable field inside a given cell. This method reduces the computational cost as the spatial derivatives can be calculated analytically anywhere inside the cell. The next step is then to obtain the next guess for the critical point position $\boldsymbol{v}_{i+1}$ as follows:

$$\boldsymbol{v}_{i+1} = \boldsymbol{v}_i - [Hf(\boldsymbol{v}_i)]^{-1} * \nabla f(\boldsymbol{v}_i)\,, \qquad (1)$$

where $\nabla f(\boldsymbol{v}_i)$ and $[Hf(\boldsymbol{v}_i)]^{-1}$ are respectively the gradient vector and the inverse of the Hessian matrix of the progress variable at the current estimate point. This iterative process is continued until convergence is reached based on a given position tolerance.

The critical points of interest were those located in the region with a non-zero reaction rate. From a calculation of a 1D laminar flame with the same chemical model as the 3D simulation, the progress variable $Y_f$ between 0.02 and 0.5 was found to satisfy the non-zero reaction rate condition, as per the two iso-surfaces shown in Fig. 1.

This routine was implemented in S3D-SC, to post-process the data on parallel processors. A large number of tests on 2D and 3D data were performed to ensure that the proposed algorithm works effectively.

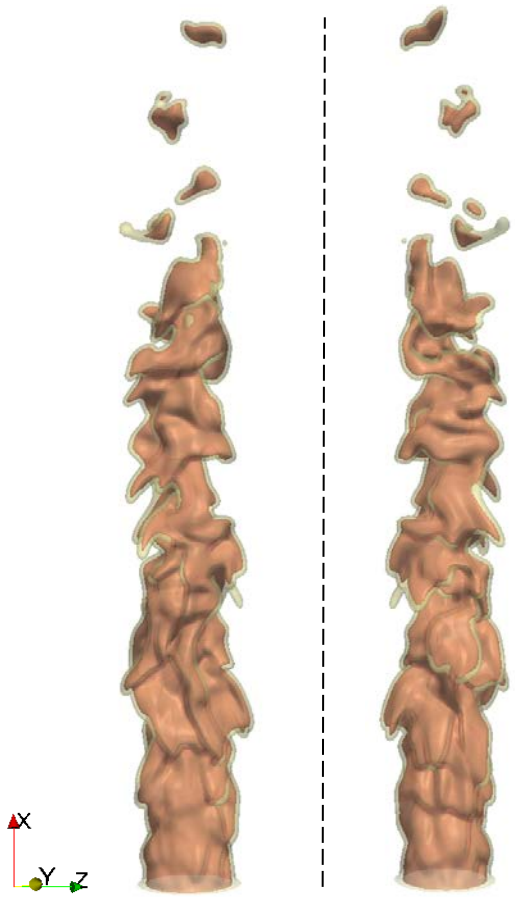


Figure 1: Back and front views of the computed turbulent premixed flame [17] represented by 2 progress variable iso-surfaces (yellow: $Y_f$=0.02 and orange: $Y_f$=0.5)

## 3. Results and Discussions

Figure 2 shows the dilatation field at two different time steps in an X-Y plane cutting through a flame interaction event. (It can be readily shown that the dilatation $\nabla.\vec{u}$

and pressure are related in the far field [25].) It can be seen that annihilation events produce strong sound waves, motivating our study of flame interactions.

There are four different types of flame interactions, defined by Griffiths et al [1]. First, a 'product pocket' is a pocket of burnt gases, propagating outwards. This type of event did not appear in the premixed flame studied here. In flames with a moderate level of turbulence product pocket will only appear during an auto-ignition event, which does not occur in a stable premixed flame. This explains why no 'product pockets' were found in the flame. Second, a 'tunnel formation' (Fig. 3.a) occurs when a hole appears in the $Y_f$ iso-surface. Third, a 'tunnel closure' (Fig 3.b) appears when a pocket of unburnt gases pinches off from part the flame surface. Finally, a 'pocket burn-out' is a pocket of unburnt gases propagating inwards until all the fuel is burnt (Fig 3.c). Mathematically, it is the signs of the eigenvalues of the progress variable Hessian matrix by which the event type is specified (Table 2). For a product pocket, all eigenvalues are positive whereas for a pocket burn-out,

Table 2: Relation between the types of interactions and the eigenvalues signs

| Flame interaction type | Eigenvalues' signs |
|---|---|
| Product pocket | + + + |
| Tunnel formation | + + - |
| Tunnel closure | + - - |
| Pocket burn-out | - - - |

the eigenvalues are all negative. A tunnel formation is found when there is only one negative eigenvalue whereas the tunnel closure corresponds to only one positive eigenvalue.

Figure 4 shows the location and types of these events at a given time step in one simulation studied. Similar to other studies in the literature [1,18], the majority of flame interactions were found close to the flame tip. Several pocket burn-outs (shown with red points) events are observed in Fig. 4. A tunnel formation (shown with blue point) can also be seen.

To examine the significance of annihilation events in the sound generation process in a later study, this method will be applied to the large dataset introduced in this paper. Identifying different types of flame interactions and their relation to important acoustic properties at the critical points will shed light on the contribution of those events to the overall noise generated by the turbulent premixed flame.

## 4. Conclusion

An efficient formulation of the method of Griffiths et al. [1] was used to identify premixed flame interactions. This method identified flame interactions by finding critical points in the progress variable field, and was applied to a DNS dataset featuring sound generation by a premixed jet flame. The dilatation field of the DNS

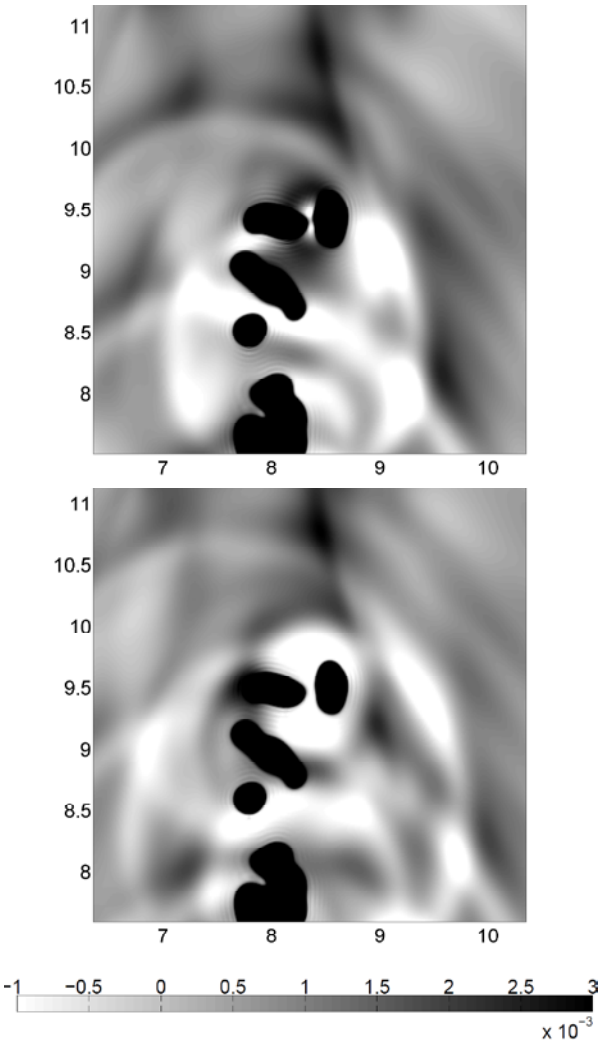


Figure 2: Dilatation field close to a flame interaction event

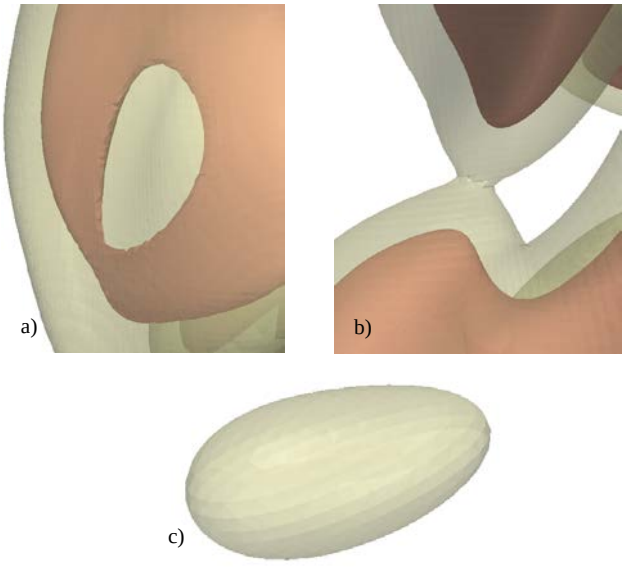


Figure 3: Three different types of flame interactions: a) Tunnel formation, b) Tunnel closure, c) Pocket burn-out

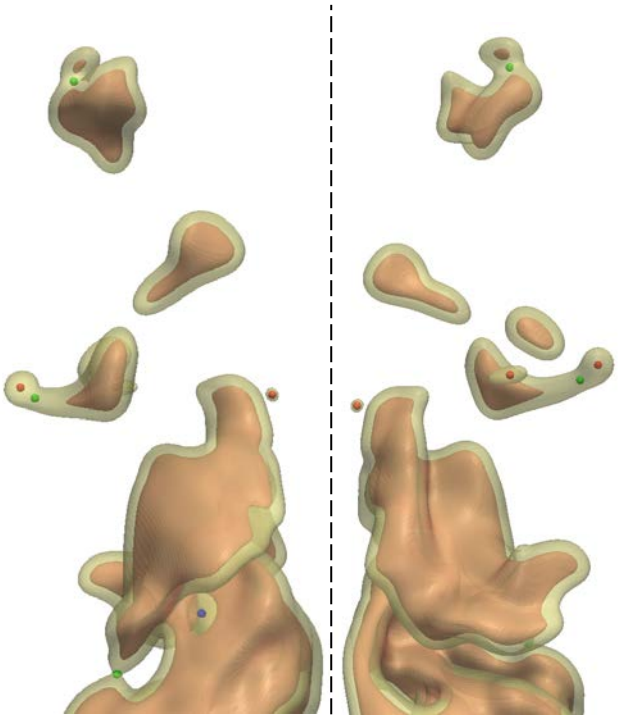

Figure 4: Back and front view of flame interactions at the flame tip (blue: tunnel formation, green: tunnel closure, red: pocket burn-out)

dataset was also used to examine the sound generation process.

The results showed that different types of flame interaction events occurred, including tunnel formation, tunnel closure and pocket burn-out. A large number of these events occurred close to the flame tip. Visual inspection suggested reasonable identification of the critical points within the progress variable field. Preliminary analysis also suggested that these identified events played a significant role in sound generation, although this requires further research to be definitive.

## 5. Acknowledgments

This study was supported by the Advanced Centre for Automotive Research and Testing (ACART, www.acart.com.au), the Australian Research Council (ARC) and the National Computational Merit Allocation Scheme, supported by the Australian Government. The computational facilities supporting this project included the Australian National Facility (NCI), the partner share of the NCI facility provided by Intersect Australia Pty Ltd., the Peak Computing Facility of the Victorian Life Sciences Computation Initiative (VLSCI) and iVEC (Western Australia).

## 6. References

[1] Griffiths, R. A. C., Chen, J. H., Kolla, H., Cant, R. S. & Kollmann, W., Proc. Combust. Inst. 35(2) (2015), pp.1341-1348.

[2] T. Poinsot, D. Veynante, Theoretical and Numerical Combustion, R.T. Edwards, 2001.

[3] L. Rayleigh, Nature 18 (1878), pp. 319-321.

[4] F. Nicoud, T. Poinsot, Combust. and Flame 142 (2005), pp.153-159.

[5] N. Swaminathan, G. Xu, A.P. Dowling and R. Balachandran, J. Fluid Mech. 681 (2011), pp. 80-115.

[6] M. Talei, M.J. Brear, E.R. Hawkes, J. Fluid Mech. 679 (2011), pp. 194-218.

[7] M. Talei, M.J. Brear, E.R. Hawkes, Combust. Flame 159 (2) (2012), pp. 757-769.

[8] Strahle W.C., Prog. Energy Combust. Sci. 4 (1978), pp. 157-176.

[9] Strahle, W.C., J. Fluid Mech. 49 (2) (1971), pp. 399-414.

[10] Lighthill, M. J., Proc. R. Soc. Lond. 211 (1951), pp. 564-587.

[11] Candel, S., Durox, D., Ducruix, S., Birbaud, A. L., Noiray, N. & Schuller, T., Intl J. Aeroacoust. 8 (1 & 2) (2009), pp. 1–56.

[12] T. Schuller, D. Durox, S. Candel, Combust. Flame 135 (2003), pp. 525-537.

[13] Kidin, N., Librovich, V., Roberts, J. & Vuillermoz, M., Dyn. Flames Reactive Syst (1984), pp. 343–355.

[14] Candel, S., Durox, D. & Schuller, T., In 10th AIAA/CEAS Aeroacoustics Conference, Paper 2004-2928, pp. 1444–1454.

[15] Jiménez, C., Haghiri, A., Brear, M. J., Talei, M., and Hawkes, E. R., Proc. Combust. Inst. 35(3) (2015), pp. 3317-3325.

[16] M. Talei, M.J. Brear, E.R. Hawkes, Proc. Combust. Inst. 34 (1) (2012), pp. 1093-1100.

[17] Haghiri, A., Talei, M., Brear, M. J., & Hawkes, E. R., TSFP-9 (2015) 1C-2.

[18] T.D. Dunstan, N. Swaminathan, K.N.C. Bray, N.G. Kingsbury, Combust. Sci. and Tech. 185(1) (2013), pp. 134-159.

[19] J.H. Chen, A. Choudhary, B. De Supinski, M. Devries, E.R. Hawkes, S. Klasky, W.K. Liao, K.L. Ma, J. Mellor-Crummery, N. Podhorszki, R. Sankaran, S. Shende, C.S. Yoo, Comput. Sci. Discovery 2 (2009), 015001.

[20] Karami, S., Hawkes, E.R., Talei, M., Chen, J.H., J. Fluid Mech. 777 (2015), pp. 633-689.

[21] Karami, S., Talei, M., Hawkes, E.R. and Chatakonda, 9th Asia-Pacific Conf. on Combust., Korea (2013), pp. 19-22.

[22] Karami, S., Hawkes, E.R. and Talei, M., 18th Aus. Fluid Mech. Conf., Launceston (2012), pp. 3-7.

[23] Yoo, C.S & Im, H.G., Combust. Theory and Modelling, 11(2) (2007), pp. 259-286.

[24] Keys, R. G., Acoustics, Speech and Signal Proc., IEEE Transactions on, *29*(6) (1981), pp. 1153-1160.

[25] T. Colonius, S.K. Lele, P. Moin, J. Fluid Mech., 330 (1997), pp. 375–409.

# A study of pressure enhancement influence on the radiative reabsorption in CO2-diluted methane laminar premixed flames

S. Karimkashi[1, *], M. Bolla[1], H. Wang[1], E.R. Hawkes[1,2], H.G. Im[3], P.G. Arias[3]
[1]School of Mechanical and Manufacturing Engineering
University of New South Wales NSW 2052 Australia
[2]School of Photovoltaic and Renewable Energy Engineering
University of New South Wales NSW 2052 Australia
[3]Clean Combustion Research Center,
King Abdullah University of Science and Technology, Thuwal 23955, Saudi Arabia

## Abstract

In this paper, the effect of radiative heat transfer reabsorption in a laminar fuel-lean $CO_2$-diluted methane-air premixed flame is studied numerically for high-pressure premixed-mode burners. Of particular interest is the radiative transport at the flame front region. The radiative transport equation is solved using discrete ordinate method (DOM) and with grey radiation characteristics assumption. For the range of pressure variations from atmospheric to 80atm, flame properties and radiative heat transport characteristics are investigated. Radiation penetration depth, normalized with the flame thickness, is defined and reported at different pressures to illustrate the reabsorption importance across the flame region. The results indicate that for combustion at intermediate to high pressure (20-80atm) not only is the radiative heat transfer considerable, but reabsorption of gaseous species play an important role as it can change the flame characteristics because the penetration depth can be of the same order as the flame thickness. It is concluded that at intermediate to high pressures, the effect of radiative reabsorption is important, even for the short residence time of the reactants mixture.

*Keywords: radiation, reabsorption, high pressure, penetration depth, laminar, premixed flame, non-luminous.*

## 1. Introduction

Many developed premixed combustion devices employ exhaust-gas or flue-gas recirculation where significant amounts of highly radiation absorbent $CO_2$ and $H_2O$ are present in the unburned mixture, which can increase the importance of radiative heat transfer. To better estimate the thermal environment in the simulation of real combustors, it is required to consider radiation reabsorption. However, it is still difficult to address reabsorption in the simulation of real combustors, such as performing a large-eddy simulation (LES) of a gas turbine combustor, due to numerical constraints on grid resolution [1]. Therefore, modeling of laminar premixed-gas flames with reabsorption in conditions relevant to combustion at high pressures could be useful to assess the importance of considering reabsorption in these devices.

In the previous studies of laminar premixed flames, with a high percentage of $H_2O$ or $CO_2$ in the mixture, some of the experiments have observed a minor effect of reabsorption on the reactants [2-5]. Some simulation works have also confirmed the same findings as in those experiments [2, 4-8]. This is because the apparatus dimension was generally smaller than the radiation length scale (inverse of the absorption coefficient) and consequently optically thin conditions applied.

However, few numerical studies have shown that radiation reabsorption could play an important role if the domain size is considerably larger than the radiation length scale; i.e. an optically thick condition [9-11]. In these works it is shown that a preheat layer forms in the reactant side. This occurs due to the absorption of the emitted radiation from high temperature products, called reabsorption, which does considerably affect flame properties such as the flame speed and the flammability limit. This effect has been observed to become more prominent for elevated pressures. Namely, the importance of radiation reabsorption is increased at higher pressure. The radiation length scale (inverse of the absorption coefficient) does linearly decrease with pressure, whereas the flame length scale (flame thickness) is also reduced but by a smaller extent. Therefore, radiation is reabsorbed with a smaller amount of length scales, comparable with the flame thicknesses.

However, most of the previous experimental [2, 4] and numerical studies [4, 6, 8, 10] of laminar flames have reported the effect of radiative transport only up to a pressure of 5atm, which is one order of magnitude lower than the pressure typically encountered in industrial gas-turbines. To the best of our knowledge, to date, there is only one numerical study [7] reporting results up to 50 atm.

Therefore, the aim of this paper is to study the effect of radiative heat transfer in a laminar fuel-lean CO2-diluted methane-air premixed flame at different ambient pressures (from 1 up to 80atm) relevant for high-pressure premixed-mode burners. In particular, the typical length and times scales of the flame and of radiation are evaluated to estimate the importance of radiation interactions across the flame front region and the role of radiation reabsorption at high pressures.

* Corresponding author:
Phone: (+61) 431694697
Email: s.karimkashiarani@unsw.edu.au

## 2. Governing equations

The code used here is called S3D. S3D is a fully compressible Navier–Stokes solver coupled with an integrator for combustion chemistry, and is based on 8th-order finite differencing [12], 4th-order explicit Runge–Kutta time integration [13], a Navier-Stokes characteristic boundary condition treatment [14], a CHEMKIN-compatible description of chemical kinetics [15], and a conventional rectangular Cartesian mesh capability. Chemical reactions are described by a skeletal chemical kinetics mechanism for methane combustion in air, involving 29 species and 268 elementary reaction steps.

Assuming grey radiation characteristics, the radiation source term, $\dot{Q}_{rad}$, which is added to the right hand side of the energy (enthalpy) equation, can be expressed as the divergence of the radiative heat flux, $q_{rad}$:

$$\dot{Q}_{rad} = \nabla . q_{rad} = \dot{Q}_{rad,em} - \dot{Q}_{rad,abs} = k_p \left( 4\pi I_b - \int_{4\pi} I d\Omega \right) \quad (1)$$

where $k_p$ is the Planck-mean absorption coefficient and $\sigma$ is the Stefan–Boltzmann constant. $\dot{Q}_{rad,em}$, corresponds to emission and $\dot{Q}_{rad,abs}$ to absorption. Here $\Omega$ is the solid angle, $I_b$ is the Planck function (a known function of local temperature: $(I_b = I_b(T))$, and $I$ is the radiative intensity. For a grey non-scattering medium, the intensity, $I$, is determined from the radiative transfer equation (RTE) as [16]:

$$\frac{dI}{ds} = \hat{s} . \nabla I = k_p (I_b - I) \quad (2)$$

where $\hat{s}$ denotes direction.

The RTE results into an integro-differential equation with five independent variables (three spatial coordinates and two direction coordinates). Radiation properties correspond to a fictitious gray gas with Planck mean absorption coefficient [16],

$$kp_i = P_i \times [C_0 + C_1(T) + C_2(T)^2 + C_3(T)^3 + C_4(T)^4 + C_5(T)^5] \quad (3)$$

where $C_j$, the polynomial coefficients are found in [16]. The species responsible for radiation are: $CO_2$, $H_2O$, CO and $CH_4$ and $P_i$ denotes their partial pressure in the mixture. The relevance of this model at higher pressures could be evaluated and justified with the available spectral radiation properties databases for $CO_2$, $H_2O$ and CO, calculated using HITEMP2010, in [17] and for $CH_4$, calculated using HITRAN2008, in [18] for pressures from 0.1atm to 80atm, temperatures from 300 to 3000K and for various mole fractions. The total absorption coefficient, $k_p$, is the sum of all Planck mean absorption coefficients. The penetration depth is defined as the inverse of the total absorption coefficient; $X = kp^{-1}$. The normalized penetration depth is defined as $L = {}^{X}/_{\delta f}$ where $\delta f$ is the flame thickness. This definition is useful to compare the radiation length scale with the flame length scale, in order to study the importance of radiation reabsorption in the flame front region.

The discrete ordinate method (DOM) is applied to solve the RTE. In DOM [19], the calculation of the radiative source term at a given location is based on the discretization of the RTE according to a chosen number of discrete directions, *Sn* ($\mu_i$, $\eta_i$, $\xi_i$), associated to the corresponding weights $\omega_i$, contained in the solid angle $4\pi$, where ($\mu_i$, $\eta_i$, $\xi_i$) are directional cosines and always satisfy the identity $\xi^2_n+\eta^2_n+\mu^2_n=1$. Different angular discretization may be used. Equation of transfer is solved for a set of "*n*" different directions in the total of $4\pi$ solid angle and the integrals over directions are replaced by numerical quadrature. Assuming a single grey assumption and no scattering, the one-dimensional RTE may be written for each quadrature point *n* in Cartesian coordinates as:

$$\xi_n \frac{\partial I^n}{\partial x} = -k_p I^n + k_p \frac{\sigma T^4}{\pi} \quad (4)$$

In this paper, the S2 approximation has been used for solving the transfer equation. More details about the DOM model implemented in S3D can be found in [20].

## 3. Numerical test cases

To elucidate the importance of radiative transport at elevated pressures, a CO2-diluted methane-air premixed flame is considered. N2 is partially replaced with CO2 so that the composition is $CH4 + \{0.21O2 + (0.79 - 0.3)N2 + 0.3CO2\}$ in molar fraction. The reactant temperature is 600K. This high temperature is intended to be similar to the reactant temperature in gas turbines arising from the compression stages. The reactant composition is homogenous with an equivalence ratio of 0.7. This is a typical value for lean low-NOx gas turbines strategies. At the given conditions, the adiabatic flame temperature is 1880K.

Pressure is gradually increased from atmospheric pressure and a set of simulations are performed at pressures of 1, 5, 10, 20, 40 and 80atm. At each pressure, two simulations have been carried out for the sake of comparison; an adiabatic (non-radiative) and a radiative simulation. The laminar flame thicknesses, based on the temperature gradient, and the laminar flame speed, based on the reaction rates for various runs, are reported. Also for the radiative cases, the time needed for the radiative heat transfer equilibrium -reabsorption response time-, normalized penetration depth and the length of the reactants preheat region are reported.

The 1D simulation is initialized as a freely propagating laminar premixed flame, for both of the non-radiative and radiative cases. Subsequently, the flame fronts propagate until they reach a steady state as a classical premixed flame.

## 4. Results and discussion

In this section, first the effects of pressure increment on the adiabatic (non-radiative) flame properties and the expected normalized penetration depths are reported. Then, the quasi-steady adiabatic and radiative

atmospheric pressure cases are compared and discussed to provide an insight of how the laminar flame structure is influenced by the radiative transport. Finally, the importance of radiation reabsorption is evaluated for the 80atm device-relevant pressure.

Fig 1 shows the pressure dependence of: (a) the flame thickness, (b) the flame speed and (c) the radiation reabsorption length in the reactant side normalized by the flame thickness (normalized penetration depth for the cold side). All the quantities are evaluated for the adiabatic cases. When increasing the pressure, the laminar flame thickness and speed are gradually decreased, Fig. 1(a and b). For the pressure range considered here (1-80atm), the flame thickness is found to scale with pressure as $\sim P^{-0.64}$ and the flame speed as $\sim P^{-0.38}$. The normalized penetration depth could be estimated without simulating radiation as shown in Fig.1(c). In this figure, the normalized penetration depth is reported at the reactants side which is more likely to absorb energy as it is at a lower temperature than the products side. It is observed that penetration depth decreases with pressure and therefore the radiative penetration depth will become closer to the flame thickness at higher pressure. To investigate this effect in the flame front region, cases that exhibit radiation are required.

Figure 2 displays the temperature and the normalized penetration depth profiles for the adiabatic and radiative cases at quasi-steady conditions at atmospheric pressure. The domain size is normalized with the flame thickness because here we aim to investigate the effect of radiation on the flame region properties. The radiative case is initialized with a freely propagating and adiabatic laminar flame profile and it takes approximately 90ms to reach radiative heat transfer equilibrium in the system. After this time the length of the preheat region and the flame temperature do not change as the time evolves. As observed in this figure, the temperature profile of the radiative case exhibits a stronger exchange of energy between the products and the reactants, leading to a considerable increase in the preheat zone temperature of approximately 300-350K. As a consequence of this heating, the peak temperature of the flame front is increased by roughly 200K compared to the case without radiation. The peak on the hot side of the reaction zone is a consequence of the absorption coefficient profile. Ju et. al. [9] had used the same composition at atmospheric pressure but with ambient temperature and an increase of the maximum flame temperature of around 100K compared to their adiabatic case was reported. The normalized penetration depth is also shown in Fig. 2. In the flame region the normalized penetration depth is rapidly decreased so that its minimum value suggests a radiative reabsorption length of 25 times larger than the flame thickness.

Another interesting parameter, which is not shown here for the sake of brevity, is the reabsorption response time. This is the time required to obtain the quasi-steady solution for radiative cases when initializing with the adiabatic solution. This time decreases with pressure so that it varies from 90ms at atmospheric pressure to 32ms

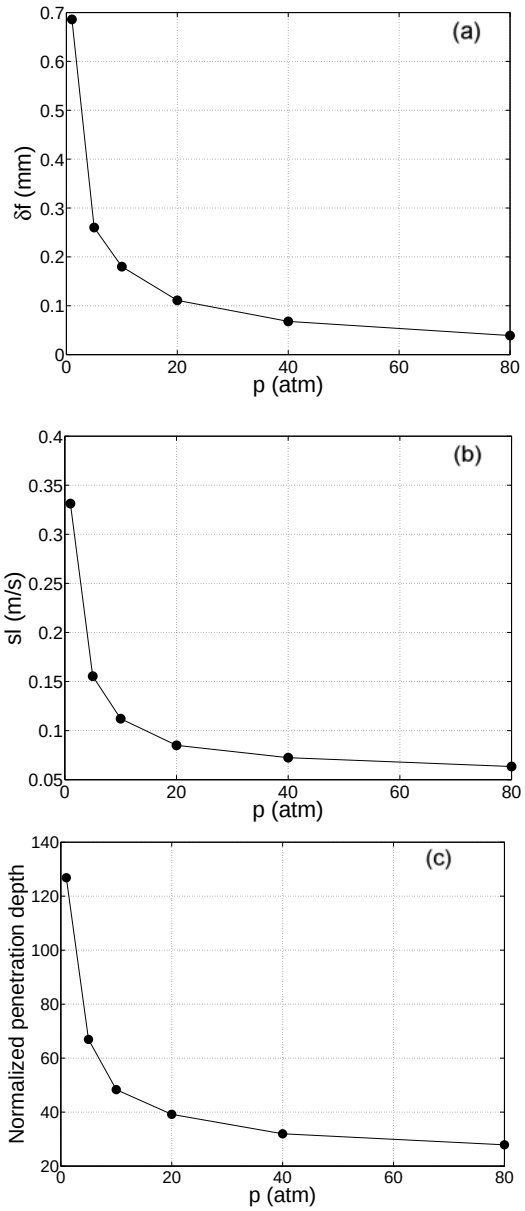


Figure 1. Pressure effects on: (a) flame thickness, (b) flame speed, (c) normalized penetration depth for the cold side of adiabatic cases.

at 40atm and 25ms at 80atm. Also, it is found that in the quasi-steady conditions the preheat zone length for all pressure cases are around 150-300 times larger than their corresponding flame thickness; the lower limits relate to

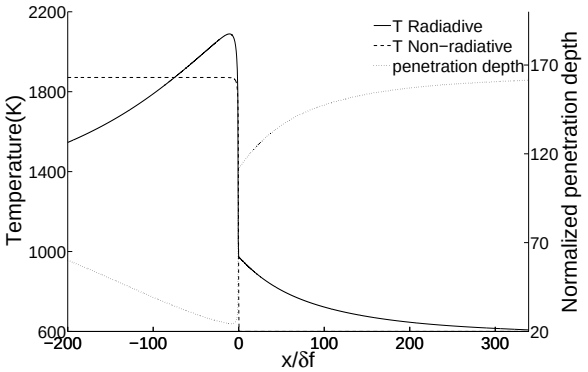


Figure 2. Temperature profiles of the adiabatic and radiative cases and the normalized penetration depth profile at atmospheric pressure after 90ms in the quasi-steady condition.

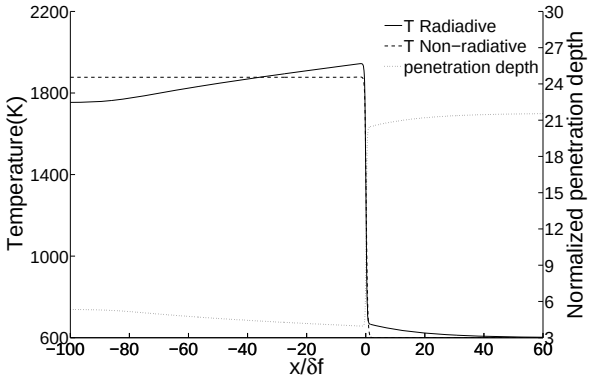


Figure 3. Temperature profiles of the adiabatic and radiative cases and the normalized penetration depth profile at 80atm after 10ms (required time for radiative transport equilibrium at this pressure is 25ms).

higher pressures and vice versa.

The typical fluid residence time in gas-turbines combustors is around 5-10ms or even more. Therefore, the radiative heat transfer effects after 10ms could be of relevance for intermediate to high pressure cases. Figure 3 shows the temperature and normalized penetration depth profiles at 80atm after 10ms. Note, however, that for this pressure it takes 25ms for the equilibrium solution to be obtained. From Fig. 3 it is observed that the reactants are preheated by around 100K due to the reabsorption with a preheated length of around 40-60 times larger than the flame thickness. The maximum flame temperature is also increased by around 90K compared to the adiabatic case. The characteristic radiation reabsorption length across the flame varies from only 4 to 21 times greater than the flame thickness. This result reveals that for the simulation of the non-luminous premixed flames, reabsorption could play an important role, especially at intermediate to high pressure cases. In other words, flame properties could be subjected to changes because there are cases where the penetration depth is of the same order as the flame thickness in the relevant residence time of reactants in a real high-pressure combustor.

## 5. Conclusion

The parametric study of pressure on the premixed laminar methane-air mixture with CO2 diluents shows that radiation reabsorption is more prominent at the intermediate to high pressures (20-80atm). When at elevated pressure, radiation becomes very important due to the faster response time to radiation and the decreased penetration depth which is of the same order as the flame thickness. This suggests that in many industrial applications where the pressure is more than 20atm and the fuel is diluted with CO2, radiative heat transfer will preheat the fuel mixture and it affects the flame characteristics.

## 6. Acknowledgments

The work was supported by funding from the Australian Renewable Energy Agency (ARENA). This research used resources of the National Computational Infrastructure (NCI), Pawsey, and Intersect.

## 7. References

[1] L. Y. M. Gicquel, G. Staffelbach and T. Poinsot, Prog. Energy Combust. Sci. **38** (6) (2012), pp. 782-817.
[2] D. L. Zhu, F. N. Egolfopoulos and C. K. Law, Symp. (Int.) Combust. **22** (1) (1989), pp. 1537-1545.
[3] A. Abbud-Madrid and P. D. Ronney, Symp. (Int.) Combust. **23** (1) (1991), pp. 423-431.
[4] Z. Chen, X. Qin, B. Xu, Y. Ju and F. Liu, Proc. Combust. Inst. **31** (2) (2007), pp. 2693-2700.
[5] Y. Xie, J. Wang, M. Zhang, J. Gong, W. Jin and Z. Huang, Energy & Fuels **27** (10) (2013), pp. 6231-6237.
[6] H. Yu, W. Han, J. Santner, X. Gou, C. H. Sohn, Y. Ju and Z. Chen, Combust. Flame **161** (11) (2014), pp. 2815-2824.
[7] C. H. Sohn, Z. Chen and Y. Ju, Int. J. Heat Mass Transfer **86** (2015), pp. 820-825.
[8] J. Jayachandran, R. Zhao and F. N. Egolfopoulos, Combust. Flame **161** (9) (2014), pp. 2305-2316.
[9] Y. Ju, G. Masuya and P. D. Ronney, Symp. (Int.) Combust. **27** (2) (1998), pp. 2619-2626.
[10] J. Ruan, H. Kobayashi, T. Niioka and Y. Ju, Combust. Flame **124** (1–2) (2001), pp. 225-230.
[11] H. Guo, Y. Jub, K. Maruta, T. Niioka and F. Liu, Combust. Sci. Technol. **135** (1-6) (1998), pp. 49-64.
[12] S. K. Lele, J. Comput. Phys. **103** (1) (1992), pp. 16-42.
[13] C. A. Kennedy, M. H. Carpenter and R. M. Lewis, Appl. Numer. Math. **35** (3) (2000), pp. 177-219.
[14] C. S. Yoo and H. G. Im, Combust. Theor. Model. **11** (2) (2007), pp. 259-286.
[15] R. J. Kee, F. M. Rupley, E. Meeks and J. A. Miller, CHEMKIN-III: A FORTRAN chemical kinetics package for the analysis of gas-phase chemical and plasma kinetics, Sandia National Laboratories Livermore, CA, 1996.
[16] Y. Ju, H. Guo, K. Maruta and F. Liu, J. Fluid Mech. **342** (1997), pp. 315-334.
[17] L. S. Rothman, I. E. Gordon, R. J. Barber, H. Dothe, R. R. Gamache, A. Goldman, V. I. Perevalov, S. A. Tashkun and J. Tennyson, J. Quant. Spectrosc. Radiat. Transfer **111** (15) (2010), pp. 2139-2150.
[18] L. S. Rothman, I. E. Gordon, A. Barbe, D. C. Benner, P. F. Bernath, M. Birk, V. Boudon, L. R. Brown, A. Campargue, J. P. Champion, K. Chance, L. H. Coudert, V. Dana, V. M. Devi, S. Fally, J. M. Flaud, R. R. Gamache, A. Goldman, D. Jacquemart, I. Kleiner, N. Lacome, W. J. Lafferty, J. Y. Mandin, S. T. Massie, S. N. Mikhailenko, C. E. Miller, N. Moazzen-Ahmadi, O. V. Naumenko, A. V. Nikitin, J. Orphal, V. I. Perevalov, A. Perrin, A. Predoi-Cross, C. P. Rinsland, M. Rotger, M. Šimečková, M. A. H. Smith, K. Sung, S. A. Tashkun, J. Tennyson, R. A. Toth, A. C. Vandaele and J. Vander Auwera, J. Quant. Spectrosc. Radiat. Transfer **110** (9–10) (2009), pp. 533-572.
[19] M. F. Modest, Radiative Heat Transfer, Academic Press, Boston, 2013.
[20] C. S. Yoo and H. G. Im, Proc. Combust. Inst. **31** (1) (2007), pp. 701-708.

# Preliminary Experimental and Computational Study of Time-varying Laminar Non-Premixed Ethylene/Nitrogen Flames

K.K.Foo[1*], A. Jocher[2,3], C.X. Thong[1], B.B. Dally[1], G.J. Nathan[1], P.R. Medwell[1], Z.T. Alwahabi[4], H. Pitsch[3]
[1] School of Mechanical Engineering, The University of Adelaide, Adelaide, SA 5005 Australia
[2] Inst Jean le Rond dAlembert, Univ Paris 06, Univ Paris 04, UMR 7190, Paris, France
[3]RWTH Aachen University, Institute for Combustion Technology, Aachen, Germany
[4] School of Chemical Engineering, The University of Adelaide, Adelaide, SA 5005 Australia

## Abstract

Time-varying laminar non-premixed $C_2H_4/N_2$ flames were investigated experimentally and numerically in this work. These laminar non-premixed flames were acoustically driven by imposing a sinusoidal perturbation on the fuel flow. In order to assess the level of synchronisation between the oscillation of flames and the forcing frequencies, the phase-locked centreline velocities at the near-field region were measured using Particle Imaging Velocimetry (PIV). The flames sooting tendencies were also examined using luminosity images of each flame under different acoustic frequencies and amplitudes. The preliminary results offer some initial validation of numerical models. The simulations show a good agreement with the experimental results, in terms of the overall flame structure and the location of peak soot volume fraction.

*Keywords: time-varying, laminar, non-premixed flame, PIV, soot volume fraction, acoustic*

## Nomenclature

| | |
|---|---|
| $d$ | Diameter of the fuel tube |
| $f$ | Frequency |
| $St$ | Strouhal number |
| $Stk$ | Stokes number |
| $u$ | Jet exit velocity |
| $V_{pp}$ | Peak-to-peak voltage |

## 1. Introduction

Since understanding of combustion processes in laminar non-premixed flames has matured, increased attention has been shifted toward turbulent flames which are more practical. However, due to the three-dimensional unsteady nature of turbulent flames, it requires multiple parameters to be measured simultaneously to fully understand the interactions between these parameters. The experimental difficulties of simultaneous spatial and temporal measurements increase as the number of parameters increases. Furthermore, the complex coupling between fluid transport and chemistry in turbulent flames raises the cost and time required for detailed modelling.

The gap between laminar and turbulent flames can be bridged by time-varying laminar flames. Time-varying laminar flames exhibit a broader range of temperature, pressure, residence time, and strain than are observed under steady conditions. Owing to their axisymmetric feature, two-dimensional measurements performed in time-varying laminar flames are relatively simple compared to in turbulent diffusion flames. Furthermore, due to the periodic oscillating behaviours, it is possible to apply phase-locked measurement techniques to acquire phase-resolved data of unsteady laminar flames.

Time-varying flames have been studied experimentally [1-5], computationally [6, 7], and combination of both [8, 9]. In most of these experiments, unsteady laminar flames were acoustically forced using a membrane loudspeaker. Generally, the studies were focused on the global response of the flames and soot field due to the frequency and amplitude of the imposed fluctuation.

Experiments reported in the literature can be categorised into two different frequency regimes: (i) frequencies near natural flickering ($St = fd/u < 5$) [1, 2, 5, 6, 8-10], (ii) high frequencies ($St > 10$) [3, 4, 7]. Here, $f$ is the oscillation frequency, $d$ is the characteristic diameter of the jet, and $u$ is the jet exit velocity. Low frequency oscillations ($St < 5$) tend to enhance the global soot concentration within unsteady flames over their steady counterparts. Shaddix and Smyth [2] reported the total soot volume fraction in flickering flames ($St = 1.4$) are enhanced by a factor of four relative to the equivalent steady flame. Kaplan *et al.* [6] have simulated the flickering flames reported in [2] and successfully predicted the enhancement of soot volume fraction. They concluded that the enhancement was attributed to the increased residence time due to the oscillation. In contrast, Sapmaz and Ghenai [5] reported that low frequency oscillations ($St = 2.8$) suppressed the total soot volume fraction measured in a flicking flame.

The amplitude of the forced oscillations directly affects the fluctuation of the fuel flow rate and with it, the local unsteady strain rate at the jet exit. The maximum strain rate increases along with the amplitude of the imposed fluctuation, which leads to suppression

* Corresponding author:
Phone: (+61) 4 25058494
Email: kae.foo@adelaide.edu.au

in total soot produced [11]. If the flow velocity amplitude exceeds the average jet exit velocity, the flow will reverse back into the burner and cause premixing of the oxidiser and the fuel [12]. Ezekoye *et al.* [12] reported this phenomenon as acoustically induced partial premixing.

A combination of computational and experimental study has been planned to deepen the current understanding on the flame structure and soot characteristics in a time-varying field. Computationally, a statistical model has been employed to predict the formation of soot precursors, Polycyclic Aromatic Hydrocarbon (PAH) and the growth of soot particles. Experimentally, Particle Imaging Velocitmetry (PIV) was used to determine the fuel jet exit velocity and the phase of the time-varying flames. Luminescence images were used to examine the overall flame shape during the forcing cycle and the variations in soot concentration due to the acoustic pulsing.

The flame properties and soot behaviour response to the presence of acoustic field in a coupled and complex way. So far, there is no general agreed trend in the variation of the soot produced in acoustic driven flames. Further investigation on these interdependent parameters and coupled mechanisms will provide deeper insight in the evolution of soot particles in unsteady flow field. This paper aims to perform a preliminary assessment on the global flame response and sooting tendency of ethylene flame under time-dependent acoustic field. This assessment will offer a guideline for detailed measurements in the future.

## 2. Experimental and numerical procedures

### 2.1 Burner configuration

An axisymmetric, steady, non-premixed laminar flame with an approximate 26 mm flame height was established over a non- premixed flame burner. The burner was adopted from Connelly [13] to duplicate the steady and unsteady flames reported in her work. The burner system as shown in Fig. 1, consists of a fuel tube with an inner diameter ID=4.0 mm (wall thickness 0.38 mm) in a concentric co-flow housing with an inner diameter ID=74 mm. A speaker is attached to the bottom of fuel plenum where the fuel flows in, and allows a sinusoidal wave to be imposed on the fuel flow rate. An axisymmetric, co-flowing, non-premixed laminar flame is generated on the burner under atmospheric pressure.

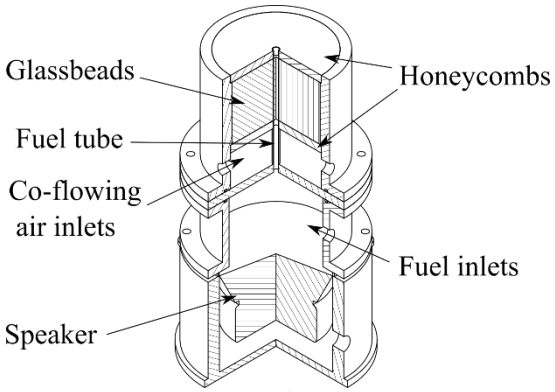


**Figure 1: The CAD drawing of the burner used in the experiment. It consists of co-flow housing, fuel plenum and a speaker in the bottom part.**

### 2.2 Flow conditions

The central jet fuel contains a mixture of 32% $C_2H_4$ and 68% $N_2$, by volume. Air is used for the co-flowing. The fuel composition is consistent with [13] for validation purposes. This mixture prevents scattering from soot particles interfering with the optical diagnostics. Both the fuel and co-flow are kept at a bulk exit velocity of 0.35 m/s using Alicat mass flow controllers. The co-flow housing contains two HAST-X honeycomb sections (0.8 mm cell size) at the top and bottom of the co-flow housing. The space in between is filled with 2.0 mm glass beads to provide a uniform exit flow profile.

### 2.3 Optical diagnostic measurements

Two-dimensional in-plane velocity profiles of the flames were captured at different phases of the time-varying flames using PIV. The fuel flow was seeded with $TiO_2$ particles less than 5-μm diameter with a calculated Stokes number, $Stk$ = 0.34. The light was sourced from a Quantel Brilliant Twin B Nd: YAG laser frequency-doubled to 532 nm and double-pulsed at 10Hz. The laser light sheet was approximately 1 mm thick, formed using a combination of spherical and cylindrical optics. The laser sheet was oriented vertically and aligned with the centreline of the burner such that the centreline velocity was included in the region of interest.

The PIV images were collected in non-reacting flow and phase-locked to the oscillation frequency. 214 pairs of PIV images were collected using a Princeton Instruments' CCD Megaplus II ES4020 camera with a 530 nm bandpass filter (FWHM = 10 nm). The CCD camera has a pixel resolution of 2048×2048 and the physical imaging window is approximately 84×84 mm, which leads to a spatial resolution of 24.38 px/ mm.

The luminescence images were phase-locked to the flames oscillation frequency (20 Hz) and taken using the same CCD. The images were recorded over 200 oscillation cycles with 1 ms exposure time.

### 2.4 Control signals

The speaker was driven by a signal generator that generated a sinusoidal wave with adjustable frequency

and amplitude. The speaker was operated at 20 Hz so that the flames oscillated at $St = 0.22$. In order to examine the global flame response to the amplitude of pulsing, the amplitudes of the signals were selected to be peak-to-peak voltages of $10.0V_{pp}$ which generate an acoustic pressure of 81 µPa. A digital delay generator was utilised to synchronise the Nd:YAG laser with the flame oscillations. The delay generator triggered both the CCD camera and the laser. In order to acquire phase-resolved images, the laser pulse was placed temporally relative to the speaker oscillation by controlling the delay in the delay generator. The paired images were separated by 100 µs. The optical setup layout for PIV measurement is illustrated in Fig. 2.

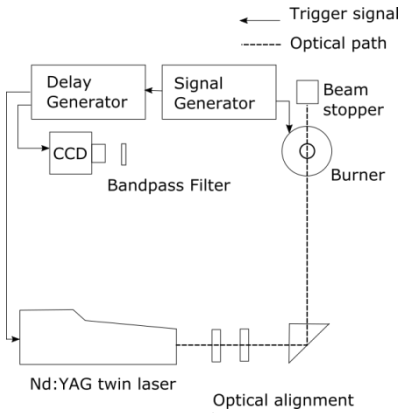


**Figure 2: Schematic diagram of the optical setup layout**

## 2.5 Numerical simulations

Computationally, the CIAO in-house code and multi-grid HYPRE solver were employed to solve the Navier-Stokes equations and the Poisson equation for pressure. The simulations adopted the numerical scheme detailed in [14]. In order to computationally reproduce the flames measured in the experiment, two-dimensional axisymmetric numerical simulations were carried out using the CIAO in-house code. The prediction of soot precursors, Polycyclic Aromatic Hydrocarbon (PAH) were simulated based on a chemical kinetic mechanism that contains 47 species and 290 reactions [15]. The radiation model used in the modelling included four gas-phase species: $CO_2$, $H_2O$, $CH_4$, and CO. The soot model adopted a statistical model that integrate the advantages of the Method of Moments with Interpolative Closure (MOMIC) and the Direct Quadrature Method of Moment (DQMOM), known as the Hybrid Method of Moments (HMOM) [16].

# 3. Results and discussion

## 3.1 Centreline velocity profiles

For each phase, the velocity profiles of the fuel flow were obtained by averaging 214 pairs of PIV images at the same phase. Figure 3 plots the centreline axial velocities at the exit plane, about 2mm height above the burner (HAB) throughout the oscillation. It resembles a 20 Hz sine with maximum velocity of 0.75 m/s and minimum velocity near zero. This result confirms that the flame oscillation was well synchronised with the acoustic forcing.

## 3.2 Luminosity images

Figure 3 shows a complete cycle of the luminescence of the pulsed flame (f = 20 Hz) from phase angle, $\phi = 0^\circ$ to $320^\circ$ with a separation of $40^\circ$. The flame luminescence serves as a preliminary indicator for the location of soot and its relative concentration level. It also shows the global response of the unsteady flame dependent on the phase angle over one cycle.

It is clearly shown that the increase in strain rate is stretching the flame front, which leads to elongation in flame length. Further increase in strain rate causes local flame extinction at the near exit region. Figure 3 shows the soot region pinches off from the flame region at phase angle between $320^\circ$ and $360^\circ$. The pinched-off region contains unburned gas and high concentration of soot. Once it pinches off, the unburned gas burns inward to the core and consumes all of the unburned gas and soot particles.

## 3.3 Numerical simulations validation

The computed time-varying laminar flame at $\phi = 36^\circ$ intervals of the 20 Hz cycle are depicted in Fig. 5. Although different phase angle intervals are adopted in experimental and numerical results, several characteristic resemblances are observed in both results. At $\phi = 0^\circ$, the pinched-off soot region appear to have similar height (~40 mm) in both computational and experimental results. Although the luminescence of flame cannot be directly compared to the soot volume fraction, in this paper it is used to perform qualitative comparison of sooting tendency between computational and experimental results. The numerical simulations successfully predicted the soot volume fraction peaks at the core of the pinched-off region. However, from $\phi = 216^\circ$ to $324^\circ$, the computed soot contour shows the peak soot volume fraction shifted from the centreline towards the wings of the flame, which is not observable in the luminosity images, as shown in Fig. 4. This may be one of the drawbacks to compare luminescence to soot volume fraction.

Figure 6 plots the comparison between the height of the peak soot volume fraction computed from numerical simulations, and the height of the maximum luminescence intensity measured from experimental results. Both of the results have a similar increasing trend, and the matching sudden drop at phase angle $\phi = 72^\circ$ (computational) and $\phi = 80^\circ$ (experimental).

Despite all the resemblances, the width of the reaction zone measured in experiment is narrower relative to the computed results. The experimental result shows that the flame experience necking earlier than the computed result. This indicates that the numerical simulation maybe underpredicted the strain rate experienced by the flame.

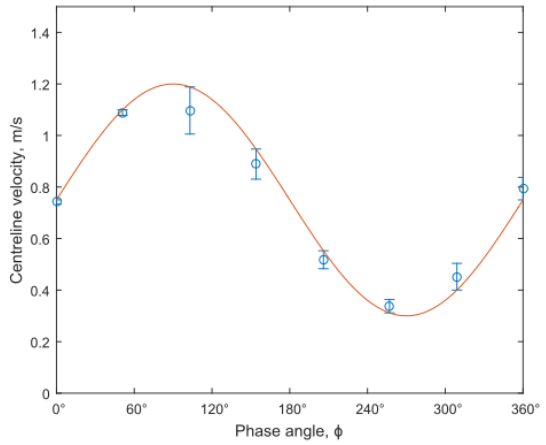


**Figure 3: Centreline axial velocity of the non-reacting fuel flow at exit plane (~2 mm HAB). The bulk exit velocity is 0.35 m/s.**

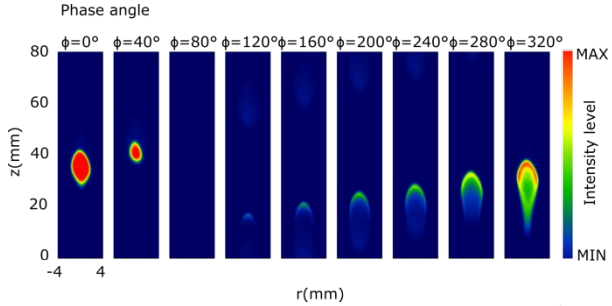


**Figure 4: Cycle-resolved soot luminosity image sequence of an ethylene flame oscillates at 20 Hz. Each image is temporally spaced with an interval of ϕ= 40˚.**

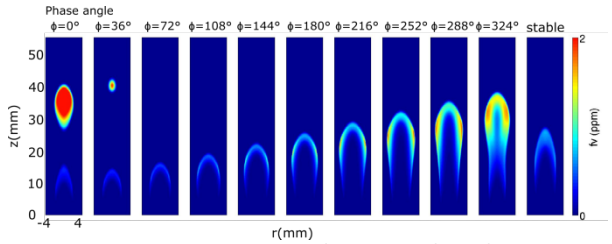


**Figure 5: Computed soot volume fraction profiles of an ethylene flame oscillate at 20 Hz. Each image is temporally spaced with an interval of ϕ= 36˚.**

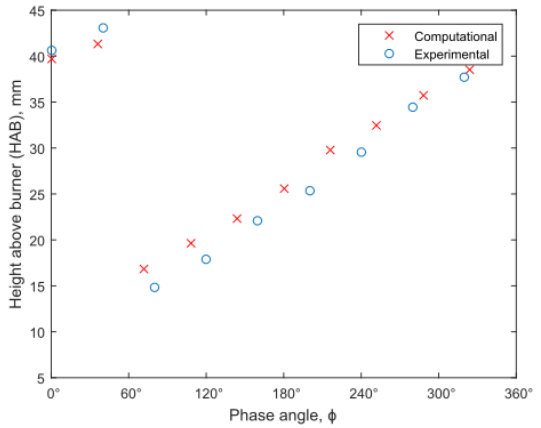


**Figure 6: The comparison between the experimental and computational results in term of the height of the peak luminescence intensity and the peak soot volume fraction as a function of phase angle.**

## 4. Conclusion

A preliminary comparison between computational and experimental results in terms of the flame profiles and the sooting tendencies have been presented. Particle imaging velocimetry was performed to measure the centreline velocity at the exit of the fuel jet to verify that the frequency of the fuel flow oscillation is synchronised to the pulsing frequency. The experimental observation has been computationally reproduced using the CIAO in-house code. The overall appearance of the flame and the soot volume fraction profiles predicted by the numerical simulations are in good qualitative agreement with the experimental results. Further examination is required into the global response of the flame structure due to the frequency and magnitude of the fuel flow perturbation, and the effect of local unsteady strain on the soot volume fraction within flame.

## 5. Acknowledgments

The authors thank the Australian Research Council for supporting the experimental work. The numerical work was performed using HPC resources from GENCI-CINES (Grant 2015-C20132B7144) and financially supported by Université franco-allemande/Deutsch-Französische Hochschule.

## 6. References

[1] C.R. Shaddix, and K.C. Smyth, Combust. Flame 107(4)(1996) , pp. 418-452.

[2] C.R. Shaddix, J.E. Harrington, and K.C Smyth, Combust. Flame, 99(3) (1994) , pp. 723-732.

[3] F.L.d. Oliveira, L.G. Barreta, and P.T. Lacava, Journal of the Brazilian Society of Mechanical Sciences and Engineering, 31(2) (2009) , pp. 137-141.

[4] M. Saito, M. Sato, and A. Nishimura, Fuel, 77(9) (1998) , pp. 973-978.

[5] H. Sapmaz, C.-X. Lin, and C. Ghenai, Experiments in Fluids, 44(1) (2008) , pp. 137-144.

[6] C.R. Kaplan, S.W. Baek, E.S. Oran, and J.L. Ellzey, Combust. Flame, 96 (1-2) (1994) , pp. 1-21.

[7] M. Sánchez-Sanz, B.A.V. Bennett, M.D. Smooke, and A. Liñán, Combustion Theory and Modelling, 14 (3) (2010) , pp. 453-478.

[8] S.B. Dworkin, B.C. Connelly, A.M. Schaffer, B.A.V. Bennett, M.B. Long, M.D. Smooke, M.P. Puccio, B. McAndrews, and J.H. Miller, Proc. Combust. Inst. 31(1) (2007) , pp. 971-978.

[9] R.K. Mohammed, M.A. Tanoff, M.D. Smooke, A.M. Schaffer, and M.B. Long Proc. Combust. Inst. (1998) , pp. 693-702.

[10] T.C. Williams, C.R. Shaddix, R.W. Schefer, P. Desgroux,Combust. Flame. 151(4) (2007) , pp. 676 - 684.

[11] W.L. Roberts, Soot, Temperature, and OH Measurements in a Unsteady Counterflow Diffusion Flame, Report No. ADA366140, North Carolina State Univ at Raleigh, 1998.

[12] O.A. Ezekoye, K.M. Martin, and F. Bisetti, Proc. Combust. Inst. 30(1) (2005) , pp. 1485 - 1492.

[13] B.C. Connelly, Quantitative Characterization of Steady and Time-Varying, Sooting, Laminar Diffusion Flames using Optical Techniques, PhD Thesis, Department of Mechanical Engineering, Yale University, 2009.

[14] O. Desjardins, G. Blanquart, G. Balarac, and H. Pitsch, J. Comput. Phys. 227(15) (2008) , pp. 7125-7159.

[15] F. Bisetti, G. Blanquart, M.E. Mueller, and H. Pitsch, Combust. Flame, 159(1) (2012) , pp. 317-335.

[16] M.E. Mueller,G. Blanquart, and H. Pitsch, Combust. Flame, 156(6) (2009) , pp. 1143-1155.

**Proceedings of the Australian Combustion Symposium**
**December 7-9, 2015, The University of Melbourne**

# Soot measurements in a $N_2$-diluted ethylene/air counterflow diffusion flame at elevated pressures

Hafiz M.F. Amin* and William L. Roberts
Clean Combustion Research Center
King Abdullah University of Science and Technology, Saudi Arabia

**Abstract**

Measurements of soot volume fraction ($f_v$) and primary particle diameter ($d_p$) were made in a $N_2$-diluted, ethylene/air, counterflow diffusion flame at elevated pressures, using light scattering/extinction technique. To provide a well-controlled pressurized environment for the flame with the required optical access, a pressure vessel was built. Soot volume fraction was measured by light extinction technique from 2 to 5 atm while maintaining the same global strain rate at all pressures. Scattered light from soot particles was measured at 135° and primary particle diameter was calculated using scattering/extinction ratio. Both soot volume fraction and primary particle diameter showed a progressive increase with pressure.

*Keywords: Counterflow diffusion flames, Soot, Scattering, High pressure.*

## 1. Introduction

Soot emissions are of primary concern due to their detrimental effects on human health and environment. Soot is the result of inefficient combustion. Many practical combustion devices operate at high pressure in order to optimize their efficiency and size. Pressure is one of the parameters which significantly affect soot emissions. Mechanisms of soot formation at high pressure are different than the ones at atmospheric pressure. Soot formation increases strongly with pressure [1].

While a significant number of studies have been carried out about soot morphology at atmospheric pressure [2-4], our understanding on the effects of pressure on combustion process and on soot formation is limited. Soot studies done in high pressure flames have shown increase in soot volume fractions [5, 6]. Other morphological parameters of soot investigated up to 2.5 atm in flames are average diameter and number density of soot particles which also showed increase with pressure [7].

Effective primary particle diameter measured in a co-flow flame, using LII, showed an increase in particle size between 5 atm to 40 atm [8]. Increase in effective particle diameter does not confirm increase in primary particle diameter which can be investigated by light scattering technique.

Most of the high pressure flames focused on soot structure are coflow flames in which valuable conclusion obtained is the relation between pressure and soot volume fraction. Although high pressure can be achieved, coflow flames exhibit some problems, such as buoyancy instabilities and heat loss to the burner [9].

In this study, a counterflow diffusion flame has been established at elevated pressures to understand the effects of pressure on soot formation. Counterflow flame configuration allows to control the residence time and is relatively immune from buoyancy instabilities. This work focuses on the volume fraction and particle size measurements of the soot in a $N_2$-diluted ethylene/air counterflow flame, using light scattering and extinction technique.

## 2. Experimental Setup

The experimental set up as shown in Fig. 1, consists of a pressure vessel which has four quartz windows of curved shape providing 10 to 170 degree optical access in the angular direction. Sealing between the metal parts of pressure vessel and optical windows is achieved using RTV silicone. Fuel, air and inert supply inside the pressure vessel is provided from the bottom flange of the vessel which is holding the burner while the exhaust line from the top of the vessel is connected to an electronically controlled pressure regulator which is operated by LabVIEW program.

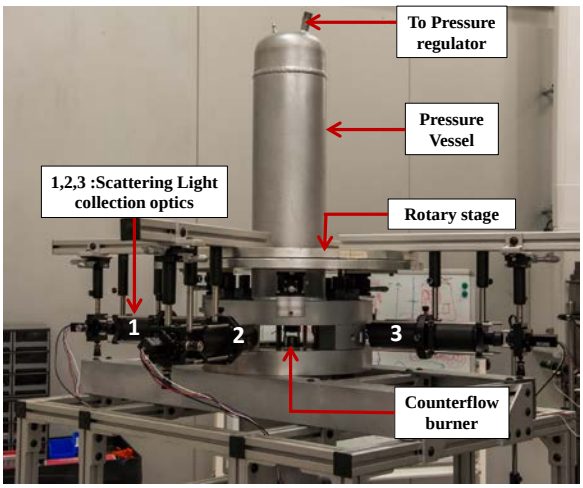


Figure 1. Pressure vessel holding counterflow burner inside and scattered light collection optics attached on the rotary stage.

A counterflow burner has been designed and built which is mounted on translation stages. The translation stages and the burner are mounted on the bottom flange

* Corresponding author:
Email: hafiz.amin@kaust.edu.sa

as shown in Fig. 2. These translation stages facilitate the burner to move in xyz-direction inside the pressure vessel. Bottom flange can be raised or lowered for moving the counterflow burner inside and outside the pressure vessel through a motorized mechanism.

The counterflow burner inside the pressure vessel produced a steady 1-D diffusion flame. At high soot loadings, it was found that the soot accumulates around optical windows which reduced optical transmissivity over time. Also the flow rate through the burner at operating conditions was not enough to force the soot out of the vessel. Uniformly distributed flow around the inside diameter of pressure vessel was introduced through the bottom flange, which prevented the soot accumulation around the optical windows without disturbing the flame.

Counterflow burner consists of two concentric straight tubes of internal diameter 8.1 mm which are separated by 8.2 mm. Nitrogen/Ethylene stream was supplied from the bottom side while the air stream through the top side of counterflow burner and both the streams had equal momentum. Global strain rate (GSR) of $30s^{-1}$ was maintained at all pressures. In order to minimize the entrainment, shroud flow with the same velocities as that of the main streams was provided through the outer tubes having internal diameter of 28 mm. Ethylene, nitrogen mole fraction was $X_F = 0.3$, $X_{N2} = 0.7$ vs air and stoichiometric mixture fraction was $Z_{st} = 0.184$. The flame studied was soot formation (SF) flame located on the oxidizer side of the stagnation plane.

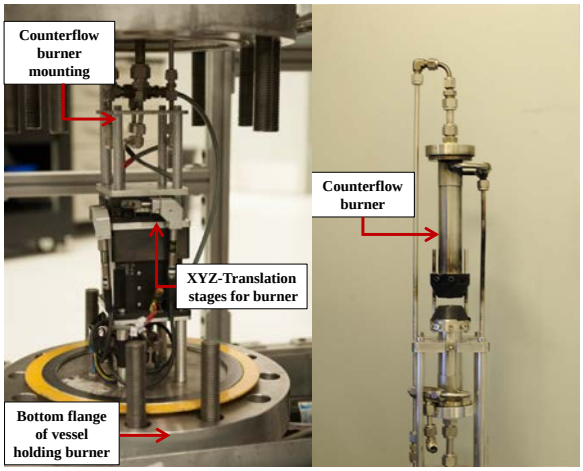


Figure 2. xyz-translation stages (on left) and the counterflow burner (on right)

A vertically polarized laser beam emitted from Ar/Kr ion laser at a wavelength of 514.5 nm was chopped and focused at the center of the flame using combination of optics. The focused laser beam, with a beam waist diameter of 150 μm, passed through the flame and the light scattered by soot particles was collected by optics which were mounted on a rotary stage. A schematic of laser diagnostics is shown in Fig. 3.

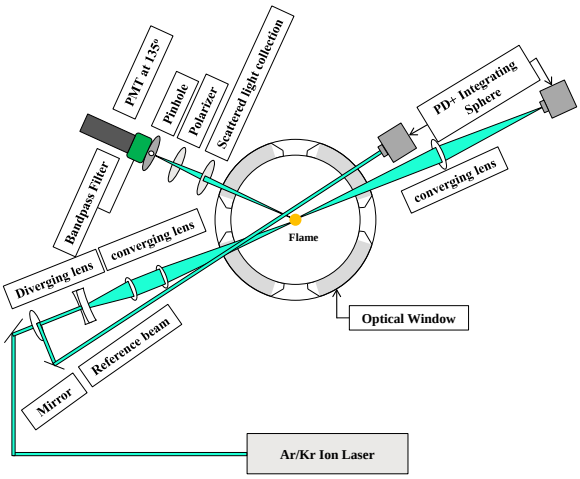


Figure 3. Schematic of Laser Diagnostics.

Scattered light was collected by a lens which focused it on a pinhole of diameter 150 μm. Before the pinhole, a polarizer was mounted, which allowed only the vertically polarized light to pass. Optical windows had anti-reflection coatings. Unwanted light from the surrounding, reflections from the burner and flame radiations were minimized by placing a band pass filter in front of the PMT and using a lock in amplifier.

For light extinction measurements, attenuated laser beam signal was collected by the lens and then focused on integrating sphere on which band pass filter and photodetector were attached. Integrating sphere was used to avoid the effects of beam steering on the detector. To compensate the effect of soot accumulation on optical windows and change in laser power, a reference beam was passed through the pressure vessel and the reference signal was also measured using integrating sphere. Incident $(I_o)$ and transmitted $(I)$ light intensities were measured without and with the flame, respectively. The flame was scanned along the centerline by moving the burner inside the pressure vessel in axial direction and the measured signals from PMT and photodetectors were transferred to the computer using a data-acquisition system and stored for further analysis.

## 3. Theoretical methods

The analysis detailed in [2] was followed and the essential properties of soot were found by measuring its scattering coefficient, $K_{vv}(\theta)$, and extinction coefficient, $K_{ext}$, which is given by Beer's law

$$K_{ext} = \frac{1}{L} ln\left(\frac{I_o}{I}\right) \quad (1)$$

Where, $I_o$ and $I$ are the incident and transmitted signals measured without and with the flame. $L$ is the absorption length which is calculated by imaging the flame. Soot volume fraction is calculated from $K_{ext}$ as

$$f_v = \frac{\lambda}{6\pi E(m)} \frac{K_{ext}}{1+\rho_{sa}} \quad (2)$$

and

$$E(m) = im\left(\frac{m^2-1}{m^2+2}\right) \quad (3)$$

Here, $m$ is the refractive index of soot, $\rho_{sa}$ is scattering to absorption ratio and $\lambda$ is the wavelength of

laser beam incident on the flame. To estimate the value of $\rho_{sa}$, knowledge about several parameters of soot morphology is required. As these parameters are under investigation at the moment, $\rho_{sa}$ is assumed zero for the present study. The absorption coefficient, $K_{abs}$, is equal to extinction coefficient, $K_{ext}$, scaled by $(1+\rho_{sa})^{-1}$. So, for $\rho_{sa}=0$, $K_{ext}$, becomes equal to, $K_{abs}$. $K_{vv}(\theta)$ of soot is calculated using

$$K_{vv}(\theta) = K_{vv}^{gas} \frac{I_{vv}}{I_{vv}^{gas}} \quad (4)$$

Where, $I_{vv}^{gas}$ and $I_{vv}$ are the scattered intensities of calibration gas and soot, respectively. $K_{vv}^{gas}$ is the known scattering coefficient of the calibration gas. Propane was used as a calibration gas and to account for the stray light from internal reflections, scattering from nitrogen was also measured. Noise was calculated from the known ratio of the scattering cross sections of propane and nitrogen. Neutral density filters were used, while measuring the scattered signal from soot particles, due to several order of magnitude differences between scattering intensities of soot particles and calibration gas. Mean primary particle diameter was calculated from the ratio of $K_{vv}(\theta)$ and $K_{ext}$

$$d_p = \frac{\lambda}{\pi}\left[4\pi \frac{E(m)}{F(m)} \frac{K_{vv}(\theta_L)}{K_{abs}} \frac{(2sin\theta_L/2)^{D_f}}{k_f}\right]^{1/(3-D_f)} \quad (5)$$

where,

$$F(m) = \left|\frac{m^2-1}{m^2+2}\right|^2 \quad (6)$$

$K_f$ and $D_f$ are the fractal prefactor and fractal dimension of aggregates, respectively. $D_f$ = 1.8 and $k_f$ = 2 were used in this study as they are found to be representing for wide range of combustion conditions [10]. The value of complex refractive index of soot particles was taken to be $m$ = 1.62+0.66i because the wavelength used to conclude this value was the same as used in this study [11]. The scattered light was measured at an angle $\theta$ = 135° corresponding to power law regimes.

## 4. Results and discussions

Soot volume fraction profiles obtained from the extinction measurements in a counterflow flame are shown in Fig. 4 at pressures of 2, 3, 4 and 5 atm. At atmospheric pressure, it was not possible to measure the soot volume fraction profile due to low soot loading. Error bars show combined uncertainty due to $E$ $(m)$, detector's response, the path length and scattering to absorption ratio $(\rho_{sa})$. The value of $1+\rho_{sa}$ was considered to vary from 1 to 1.1 for the uncertainty analysis as the values of $\rho_{sa}$ changes from 0.036 to 0.11 in a non-premixed ethylene/air flame at atmospheric pressure for the current wavelength [12]. For a non-zero value of $\rho_{sa}$, $K_{abs}$ will decrease and hence the value of $f_v$ will decrease. The soot volume fraction profiles show that the value of $f_v$ increases with the pressure and the particle stagnation plane shifts towards the flame when the pressure is raised while keeping the global strain rate constant. The soot volume fraction profiles are skewed towards the particle stagnation plane and the gradient is increased as the pressure is increased. The flame studied here is SF flame in which the soot particles appear on the fuel side of the flame and they keep growing as they are convected away towards the particle stagnation plane where they leak out, eventually. If the peak soot volume fraction $(f_v^{peak})$ values are fitted to the power law relationship then peak value scales with $P^{3.32}$. Due to the buoyancy effects, soot produced in the flame leaks upward, absorbs part of the laser light, because of which the soot volume fraction values on the oxidizer side of the flame remains non-zero.

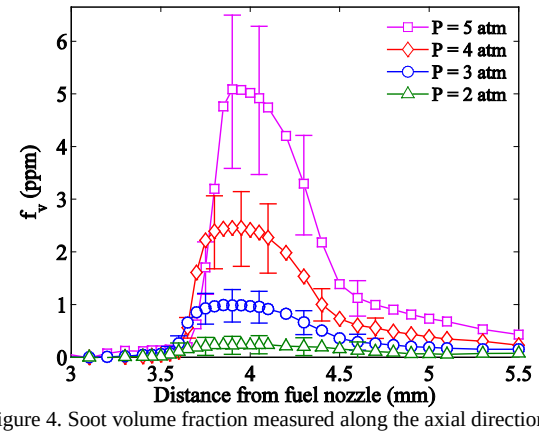


Figure 4. Soot volume fraction measured along the axial direction in a counterflow diffusion flame at elevated pressures (GSR = 30s$^{-1}$)

Scattering cross sections of soot from 2 to 5 atm are presented in Fig. 5. Significant change in the scattering cross section is observed with pressure because $K_{vv}(\theta)$ is proportional to $d_p^6$ and is more sensitive to large particles. Error bars are not shown here, as the error due to the detector was small.

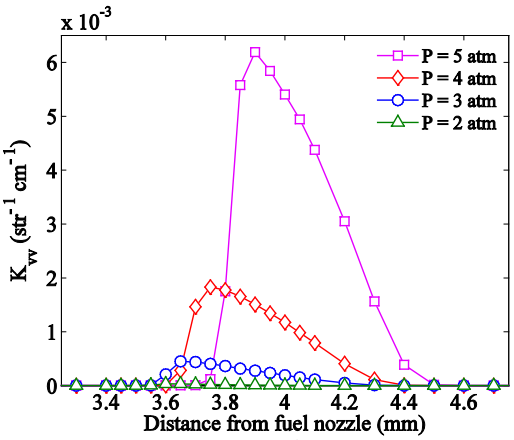


Figure 5. Scattering cross section of soot measured along the axial direction in a counterflow diffusion flame at elevated pressures.

Figure 6 shows the profiles of the primary particle diameter, calculated using scattering/extinction ratio. To our knowledge, there are not any reported measurements of primary particle diameter in a counterflow flame at these pressures. Error bars are shown only at few points in order to keep the visibility clear. Error bars represent the combined uncertainty due to refractive index, $\rho_{sa}$ and measurement of $K_{vv}(\theta)$ and $K_{abs}$. A non-zero value of $\rho_{sa}$, will increase the diameter of primary particle due to decrease in $K_{abs}$. Soot particles appear on the fuel side of the flame and they grow as they move towards the

stagnation plane because no oxidation is present in SF flame. The location of the peak diameter of primary particles is shifted towards the flame with pressure. This shift indicates that soot zone thickness is decreased with increasing the pressure. This trend is similar to the one in $f_v$ but here it is much more prominent. The peak diameter of 16 nm at 2 atm has increased to 48 nm at 5 atm, approximately. Increase in diameter can be due to coagulation or surface growth or both with increasing the pressure.

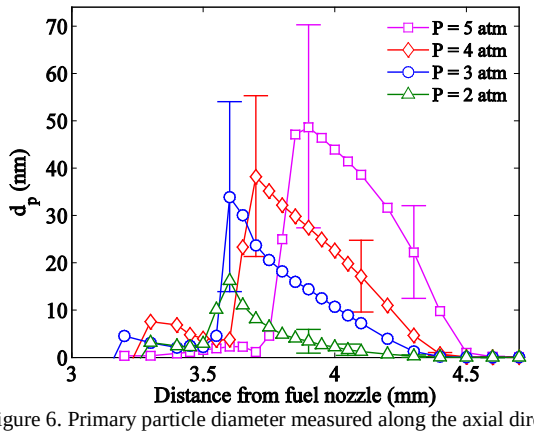


Figure 6. Primary particle diameter measured along the axial direction in a counterflow diffusion flame at elevated pressures (GSR = $30s^{-1}$)

Increased soot loading at high pressure caused extinction of the laser beam which required the correction of the raw scattering data and it was done by taking into account the attenuation of the light before the scattering volume and the attenuation from the scattering volume to the detector.

## 5. Conclusion

An experimental setup, which was recently built at KAUST to study the soot morphology at elevated pressures using multi-angle light scattering, is presented. A sooting counterflow diffusion flame is stabilized inside the pressure vessel up to 5 atm. Soot volume fraction and primary particle diameter profiles are measured in a $N_2$-diluted ethylene/air counterflow diffusion flame, from 2 to 5 atm. Peak integrated soot volume fraction and integrated soot volume fraction increased with pressure. The peak diameter is shifted towards the flame and soot zone thickness is reduced with increasing pressure. Size of the primary particle diameter is increased with pressure which can be due to surface growth and coagulation at elevated pressures. In future, multi-angle light scattering at elevated pressures will be conducted to investigate the influence of pressure on other morphological parameters like fractal dimension and aggregate size distribution.

## 6. Acknowledgement

The work is supported by King Abdullah University of Science and Technology (KAUST) Office of Sponsored Research (OSR) under award no. 1402. The authors also thank Mr. Scott A. Steinmetz for his assistance.

## 7. References

1. W.L. Flower, C.T.Bowman, Soot production in axisymmetric laminar diffusion flames at pressures from one to ten atmospheres. The Combustion Institute, 1986: p. 1 I 15-1124.
2. U.O. Koylu, Quantitative analysis of in situ optical diagnostics for inferring particle/aggregate parameters in flames: Implications for soot surface growth and total emissivity. Combustion and Flame, 1997. 109(3): p. 488-500.
3. U. O. Koylu, G.M. Faeth, Optical properties of overfire soot in bouyant turbulent diffusion flames at long residence times. Journal of Heat Transfer, 1994. 116: p. 152 - 159.
4. B. Yang, and U.O. Koylu, Soot processes in a strongly radiating turbulent flame from laser scattering/extinction experiments. Journal of Quantitative Spectroscopy and Radiative Transfer, 2005. 93(1-3): p. 289-299.
5. L.L. McCrain and W.L. Roberts, Measurements of the soot volume field in laminar diffusion flames at elevated pressures. Combustion and Flame, 2005. 140(1-2): p. 60-69.
6. K.A. Thomson, et al., Soot concentration and temperature measurements in co-annular, nonpremixed CH/air laminar flames at pressures up to 4 MPa. Combustion and Flame, 2005. 140(3): p. 222-232.
7. W.L. Flower and C. T. Bowman., Measurements of the structure of sooting laminar diffusion flames at elevated pressures. Symposium (International) on Combustion 1985. 20: p. 1035-1044.
8. K.A. Thomson, et al., Laser induced incandescence measurements of soot volume fraction and effective particle size in a laminar co-annular non-premixed methane/air flame at pressures between 0.5–4.0 MPa. Applied Physics B, 2006. 83(3): p. 469-475.
9. H.I. Joo, and Ö.L. Gülder, Soot formation and temperature structure in small methane–oxygen diffusion flames at subcritical and supercritical pressures. Combustion and Flame, 2010. 157(6): p. 1194-1201.
10. B. Hu, B. Yang, and U.O. Koylu, Soot measurements at the axis of an ethylene/air non-premixed turbulent jet flame. Combustion and flame, 2003. 134(1): p. 93-106.
11. S. Krishnan, K.-C. Lin, and G.M. Faeth, Optical properties in the visible of overfire soot in large buoyant turbulent diffusion flames. Journal of Heat Transfer, 2000. 122(3): p. 517-524.
12. F. Migliorini, K.A. Thomson, and G. Smallwood, Investigation of optical properties of aging soot. Applied Physics B, 2011. 104(2): p. 273-283.

**Proceedings of the Australian Combustion Symposium**
**December 7-9, 2015, The University of Melbourne**

# High pressure considerations for Yield Sooting Index

S.A. Steinmetz*, W.L. Roberts
Clean Combustion Research Center
King Abdullah University of Science and Technology, Saudi Arabia

## Abstract

Yield Sooting Index (YSI) is a useful tool for characterizing the sooting tendencies of liquid fuels. YSI can be used to predict fuel sooting tendencies, aid in surrogate development, and evaluate fuel structure effects. However, the applicability of YSI, measured at atmospheric pressure, to high pressure flames is unknown. In this work, YSI is evaluated for several n- and cyclo-alkanes and benzene at pressures from 1-5 bar, using n-hexane and n-dodecane as reference fuels. The effect of fuel structure on its soot pressure sensitivity is investigated. The flexibility of applying the YSI methodology to a new geometry is also investigated. At pressures up to 5 bar, when referencing YSI to two n-alkane fuels, there is no appreciable change in the YSI of n-alkanes, despite the change in geometry and large variation in soot loads. For the same reference fuels, there is a small change in the YSI of cyclopentane, and a large change in the YSI of benzene. Peak soot concentrations in flames of n-alkanes were found to scale faster with pressure than cyclo-alkanes, which scale faster than benzene, for the same number of fuel carbon atoms.

*Keywords: YSI, pressure, soot, liquid fuel*

## 1. Introduction

Soot is known to impact human health and the environment [1], and increased understanding of its formation is key to its reduction. Numerous sooting indices have been developed to characterize soot formation, including threshold soot index [2], soot temperature index, soot sensitivity index [3], and yield sooting index (YSI) [4-6]. These indices give insight into the structural effect of a fuel on soot formation and aid in surrogate development. However, there is uncertainty in the relevance of these indices when applying them to high pressure combustion.

McEnally and Pfefferle developed the YSI [4-6] to characterize sooting tendency of a fuel based on the peak soot volume fraction ($f_v$) in a methane coflow flame doped with the fuel of interest. Sooting tendency can be more reliably measured with this method than smoke point. The use of small doping concentrations (400 ppm of gas volume) allows for testing with fairly constant temperature and species fields at constant residence times. YSI is defined as $YSI = f_{v,max} \times C + D$, where $C$ and $D$ are apparatus-specific parameters chosen to satisfy the YSI requirement of two reference fuels. Most recently, they were chosen to satisfy $YSI_{n\text{-}hexane} = 0$, and $YSI_{benzene} = 100$ [6]. Another advantage of this method is that exact knowledge of soot optical properties is not needed, as these properties can be absorbed into the apparatus-specific constants. However, this assumes that optical properties are consistent for each fuel, which may not be the case.

The flexibility of the YSI methodology has recently been investigated [7]. Kashif et al. demonstrated consistent YSI measurements even with much larger dopant concentrations (up to 6.14%). Additionally, they showed that evaluating YSI with peak integrated $f_v$, peak centerline $f_v$, or global peak $f_v$ produced comparable results [7]. There have been few studies on the effect of pressure on the sooting tendencies of liquid fuels [8-10], and fewer still investigating the effect of fuel structure [11]. Zhou et al. investigated linear and cyclic $C_6$ alkanes and alcohols doped into n-heptane flames at different liquid volume fractions.

The objectives of this study are to 1) evaluate the robustness of YSI in high pressure conditions, 2) evaluate what effect the structure of a fuel may have on its soot pressure sensitivity.

## 2. Methodology

Nitrogen-diluted methane flames were doped with 10,000 ppm (gas volume) of liquid fuel. Flames were diluted to limit soot formation at high pressures, while still keeping soot concentrations at detectable levels at atmospheric pressure, and to produce an appropriately sized flame for measurement (20-25 mm). Doping was at higher levels in this work compared to [6] to produce a greater change in soot yield at elevated pressures between different fuels. However, [7] showed the robustness of the YSI method at even higher dopant concentrations. Methane and nitrogen flow rates were 1.0 mg/s (90 sccm) and 0.39 mg/s (20 sccm), respectively. Air flow rates were 0.6 g/s (30 slpm), 1 g/s (50 slpm), and 1.4 g/s (70 slpm) at 1-2, 3, and 4-5 bar, respectively. Increasing coflow rate may suppress soot formation [12], though it was necessary to maintain flame stability.

Flames were established on a coflow burner, similar to previous studies [6-7]. The burner consists of a fuel nozzle with a 4 mm inside diameter which extends 8 mm beyond the exit plane of a 50 mm diameter air coflow section. The knife-edged fuel nozzle tip tapers out to a 6.5 mm outside diameter where it meets the coflow exit plane. The coflow section is filled with 2 mm copper beads to facilitate uniform heating. Both the nozzle and

* Corresponding author:
Phone: (+966) 5 44701913
Email: scott.steinmetz@kaust.edu.sa

the coflow contain nickel-chrome foam at the exit plane of the coflow. It should be noted that this burner is smaller than the Santoro burner used in previous studies [6-7]. This is necessary, as smaller flames are required to maintain stability at elevated pressures.

Combustion gases were heated to 150 C with a process heater and rope heaters. Liquid fuel, metered by a syringe pump, was injected into the heated methane/nitrogen steam to vaporize. The burner was externally heated to maintain 150 C to prevent condensation of the liquid fuel. In previous studies, only the fuel stream was heated to prevent condensation [6-7]. Gas temperatures were monitored at the base of the fuel nozzle in the burner, and at the burner coflow exit. Complete fuel vaporization was verified by ensuring a change in fuel vaporization temperature had no effect on the soot field.

Soot volume fraction was measured using the diffuse-light two-dimensional line of sight attenuation technique [13]. As the location of peak soot volume fraction is on the centerline of these flames at 1 and 2 bar, but in the annulus above 2 bar, full 2D soot field measurement is necessary. A similar technique was used in [7]. A 6500 K LED was used as the light source, and images were captured with a PIXIS 400F CCD camera. A 445-455 nm bandpass filter was used to limit flame luminosity, allowing full use of the CCD dynamic range for measurement of the light source. The exposure time was chosen to keep measured intensities just below saturation, and was 850 ms. 50 sets of images (with and without flame, with and without light source) were collected for each measurement. Measurements were done at 1, 2, 3, 4, and 5 bar, and 5 measurements were done for each fuel at each pressure. Integrated extinction coefficients were tomographically inverted using Tikhonov regularized onion peeling [14].

YSI was measured for 5 n-alkanes, 3 cyclo-alkanes, and benzene. YSI was evaluated using the peak $f_v$ in the flame. The fuels chosen are shown in table 1. Fuels were chosen to span a wide range of YSI, and to have both n- and cyclo-alkanes with the same carbon number. They were also chosen to include the two reference fuels from [6], n-hexane and benzene.

Table 1. Selected liquid fuels

| Fuel | Formula | $YSI_{McEnally}$ [6] |
|---|---|---|
| n-hexane | $C_6H_{14}$ | 0 (reference) |
| n-heptane | $C_7H_{16}$ | 8.7 |
| cyclopentane | $C_5H_{10}$ | 14.0 |
| n-octane | $C_8H_{18}$ | 18.9 |
| cyclohexane | $C_6H_{12}$ | 19.1 |
| n-decane | $C_{10}H_{22}$ | 41.7 |
| cyclooctane | $C_8H_{16}$ | 42.4 |
| n-dodecane | $C_{12}H_{26}$ | 64.2 |
| benzene | $C_6H_6$ | 100 (reference) |

## 3. Results

Application of the YSI method to the current flame geometry is first assessed. In order to isolate potential fuel structure effects, two n-alkanes are chosen as reference fuels, n-hexane and n-dodecane, Rather than n-hexane and benzene. They are assigned the corresponding YSI values from [6] of 0.0 and 64.2, respectively. Figure 1 shows the measured YSI at 1 bar, compared to the original measurements by McEnally [6]. Error bars represent precision of repeated measurements (95% confidence). Other measurement uncertainties (soot refractive index, PAH absorption, tomographic inversion) would either cancel during YSI conversion or be consistent between fuels. Dotted lines indicate the uncertainty reported in [6]. Due to rescaling, uncertainties in $f_v$ result in larger uncertainties in YSI.

The current measurements of alkanes agree well with previous measurements, within uncertainties. Average cyclo-alkane YSIs measure consistently high, but the difference is small compared to the uncertainty. However, peak soot measured in benzene doped flames is consistently greater than expected. A similar observation was made in [7]. Kashif et al. were able to reconcile this by adjusting their dimensionless extinction coefficient to account for the different soot produced by a fuel with a different H/C ratio, like benzene. However, a similar adjustment for the wavelength in this work does not result in agreement. The discrepancy could be due to refractive index, or an indication that YSI is not apparatus independent.

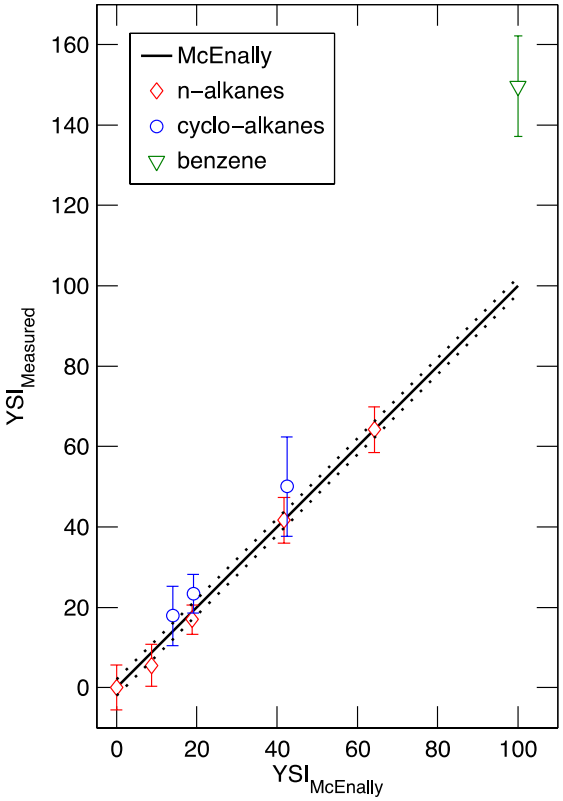


Figure 1. Comparison of measured and literature values of YSI at 1 bar. Error bars indicate uncertainty due to measurement precision (95% confidence).

Figure 2 shows measured YSI as a function of carbon number at 1, 3, and 5 bar. Measurements at 2 and 4 bar are not shown, for clarity. Error bars indicate uncertainty due to measurement precision. Uncertainties tend to be highest at 1 and 2 bar. This is due to the lower overall soot concentrations, and propagation of error

through tomographic inversion to centerline, where soot concentrations are peak. In general, the YSI of n-alkanes is not affected by pressure up to 5 bar. This could be expected, as the YSI is referenced to two n-alkane fuels. Considering uncertainties, a small change in the YSI of cyclopentane is observed. There is a noticeable change in relative sooting tendancy of benzene, though this change brings the measured YSI back into range of the original YSI value.

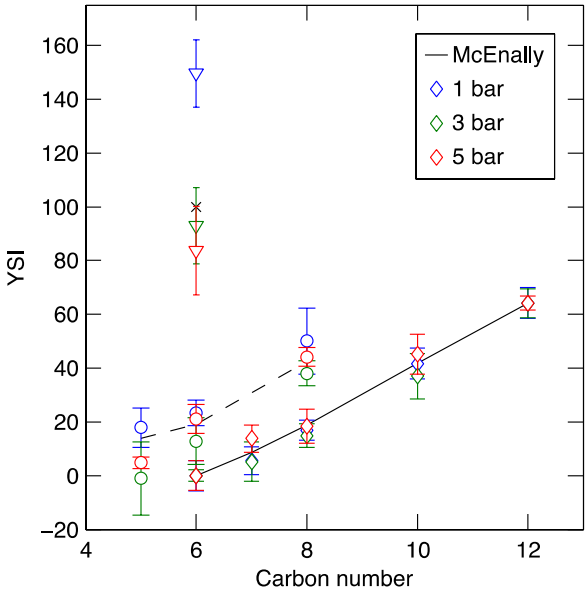


Figure 2. YSI of liquid fuels at 1, 3, and 5 bar. Diamond symbols indicate n-alkanes, circles indicate cyclo-alkanes, triangles indicate benzene. Black lines indicate YSI measured by McEnally (solid – n-alkanes, dashed – cyclo-alkanes, x – benzene).

At atmospheric pressure, soot concentrations (0.25-0.9 ppm peak) are strongly influence by dopants, which increased peak $f_v$ by factors of 2-8 compared to the base diluted methane flame (0.1 ppm peak). At 5 bar, dopants increased peak $f_v$ (15-20 ppm) only by factors of 1.5-2 compared to the base flame (10 ppm). These results show the wide range of soot loads over which YSI can be applied.

YSI was also evaluated using the peak soot volume fraction on centerline at each pressure, producing comparable results. While there is a larger increase in soot concentrations in the flame annulus, compared to centerline, with pressure, this difference is consistent for each fuel. Similar observations were made in [7] for different evaluation methods of YSI at atmospheric pressure.

While a change in YSI may be observed, this may not be the result in a change in sooting tendency. The ability to accurately measure $f_v$ requires knowledge of soot optical properties. Accurate measurement of YSI requires knowledge of the relative difference in soot optical properties. The effect of pressure on soot optical properties is unknown, though it would be unlikely to cause large variations for soot from similar alkane fuels.

Another way of visualizing the effect of pressure ($P$) on sooting tendency is to fit peak soot volume fraction to a power law, where soot scales as $P^n$. This has frequently been done in flames of gaseous fuels [15]. Due to the change in coflow rate suppressing soot formation at elevated pressures, the scaling here is not solely due to pressure, but is consistent for each fuel. Peak soot in the nitrogen-diluted methane base flame scales with pressure as $P^{2.8}$. The exponents of the pressure power law scaling of liquid fuels are shown in Fig. 3.

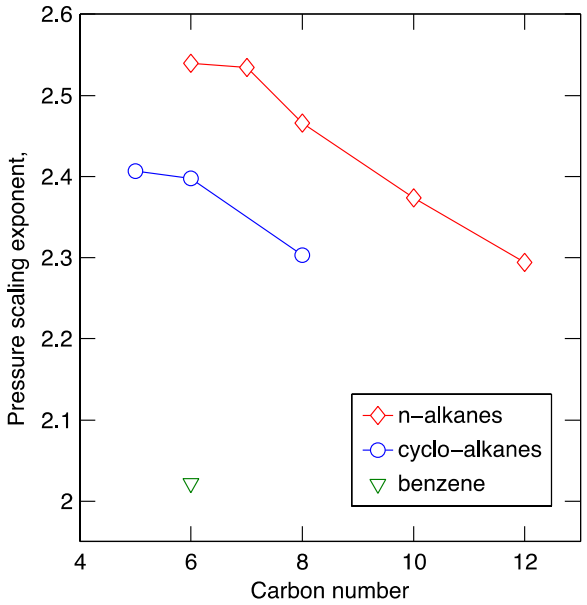


Figure 3. Power law scaling of peak soot volume fraction in nitrogen-diluted methane flames doped with different liquid fuels from 1-5 bar.

A general decrease in scaling is seen with carbon number. However, this is largely due to the higher soot concentrations in flames doped by these high carbon number fuels at 1 bar. As the relative difference in soot yield between fuels is smaller at elevated pressures, the scaling appears smaller. A reduced scaling with carbon number for one fuel class does not necessarily compromise the validity of YSI, as long as the reduction is linearly proportional to the YSI at atmospheric pressure. However, if different fuel classes have very different scaling rates, a breakdown in YSI would be expected at elevated pressures. The slight reduction in relative soot yield in cyclo-alkane doped flames, and the large reduction in relative soot yield in benzene doped flames could be explained by this scaling. Extending measurements to higher pressures may make scaling effects clearer. Additionally, investigation of other alkanes, alkenes, and alcohols may reveal further effects.

## 4. Conclusions

YSI has been measured for 5 n-alkanes, 3 cyclo-alkanes, and benzene, from 1-5 bar. Soot formation for many of these fuels was investigated elevated pressures for the first time. The following conclusions can be made over the pressure range of 1-5 bar:

YSI calculated with either peak centerline $f_v$ or peak global $f_v$ are comparable, and YSI is not affected by the change in geometry or large variation in soot load.

When YSI values are calculated in reference to two n-alkanes, there is little affect of pressure on the YSI of other n-alkanes.

With n-alkane reference fuels, there may be a small change in YSI for cyclo-alkanes from.

With n-alkane reference fuels, there is a large change in the YSI of benzene from 1-5 bar. The discrepancy in YSI of benzene at 1 bar could be due to measurement error, a result of different soot optical properties.

Peak soot concentrations in n-alkane doped flames scale faster with pressure than cyclo-alkane doped flames, which scale faster than benzene doped flames, for the same number of fuel carbon atoms. Extending measurements to higher pressures could make scaling differences more apparent.

## 5. Acknowledgements

This work was funded by the Clean Combustion Research Center at King Abdullah University of Science and Technology.

## 6. References

[1] U. P¨oschl, Atmospheric aerosols: composition, transformation, climate and health effects, Angew. Chem. Int. Ed. Engl. 44 (46) (2005) 7520–40.

[2] M. P. Hanson, D. H. Rouvray, Novel Applications of Topological Indices. 2. Prediction of the Threshold Soot Index for Hydrocarbon Fuels, J. Phys. Chem. 91 (19) (1987) 2981–2985.

[3] Y. Wang, S. H. Chung, Effect of strain rate on sooting limits in counterflow diffusion flames of gaseous hydrocarbon fuels: Sooting temperature index and sooting sensitivity index, Combust. Flame 161 (5) (2014) 1224–1234.

[4] C. S. McEnally, L. D. Pfefferle, Improved sooting tendency measurements for aromatic hydrocarbons and their implications for naphthalene formation pathways, Combust. Flame 148 (4) (2007) 210–222.

[5] C. S. McEnally, L. D. Pfefferle, Sooting tendencies of nonvolatile aromatic hydrocarbons, Proc. Combust. Inst. 32 (1) (2009) 673–679.

[6] C. S. McEnally, L. D. Pfefferle, Sooting tendencies of oxygenated hydrocarbons in laboratory-scale flames., Environ. Sci. Technol. 45 (6) (2011) 2498–503.

[7] M. Kashif, P. Guibert, J. Bonnety, G. Legros, Sooting tendencies of primary reference fuels in atmospheric laminar diffusion flames burning into vitiated air, Combust. Flame 161 (6) (2014) 1575–1586.

[8] A. G. Mouis, A. Menon, V. Katta, T. A. Litzinger, M. Linevsky, R. J. Santoro, S. P. Zeppieri, M. B. Colket, W. M. Roquemore, Effects of m-xylene on aromatics and soot in laminar, N2-diluted ethylene co-flow diffusion flames from 1 to 5 atm, Combust. Flame 159 (10) (2012) 3168–3178.

[9] A. E. Karata, G. Intasopa, O. L. Gulder, Sooting behaviour of n-heptane laminar diffusion flames at high pressures, Combust. Flame 160 (9) (2013) 1650–1656.

[10] L. Zhou, N. J. Dam, M. D. Boot, L. P. H. de Goey, Measurements of sooting tendency in laminar diffusion flames of n-heptane at elevated pressure, Combust. Flame 160 (11) (2013) 2507–2516.

[11] L. Zhou, N. J. Dam, M. D. Boot, L. P. H. de Goey, Investigation of the effect of molecular structure on sooting tendency in laminar diffusion flames at elevated pressure, Combust. Flame 161 (10) (2014) 2669–2677.

[12] Z. Dai, G. M. Faeth, Hydrodynamic suppression of soot formation in laminar coflowing jet diffusion flames, Proc. Combust. Inst. 28 (1) (2000) 2085–2092.

[13] K. A. Thomson, M. R. Johnson, D. R. Snelling, G. J. Smallwood, Diffuse-light two-dimensional line-of-sight attenuation for soot concentration measurements, Appl. Opt. 47 (5).

[14] E. O. Akesson, K. J. Daun, Parameter selection methods for axisymmetric flame tomography through Tikhonov regularization., Appl. Opt. 47 (3) (2008) 407–16.

[15] A. E. Karata, O. L. Gulder, Soot formation in high pressure laminar diffusion flames, Prog. Energy Combust. Sci. 38 (6) (2012) 818–845.

**Proceedings of the Australian Combustion Symposium**
**December 7-9, 2015, The University of Melbourne**

# Variations of In-Flame Soot Particles in the Presence of a Neighbouring Flame in a Diesel Engine

R. Zhang[1, *], Y. Zhang[1] and S. Kook[1]
[1]School of Mechanical and Manufacturing Engineering
The University of New South Wales, NSW 2052 Australia

## Abstract

A thermophoresis-based sampling of in-flame soot particles has been performed in a working diesel engine. The sampled soot particles were analysed using a transmission electron microscope and in-house-developed image post-processing code to obtain size distributions of both soot aggregates and primary particles. Of particular interests is the influence of jet-jet interactions on the soot particle size given that the high soot formation occurs in a fuel-rich region. Three different injector nozzle configurations were used to address this question including two single-jets (Jet A and Jet B) and a double-jet (Jet A&B). The result shows an interesting trend of the increased particle number when a neighbouring flame impacts the in-flame soot particles. This supports higher soot production due to locally rich mixtures in the jet-jet interaction regions. However, both the aggregate and primary particle sizes of the double jet appear to be lower than those of the single-jets, suggesting that soot particles in the fuel-rich jet-jet interaction region are in an earlier stage of soot formation.

*Keywords: Diesel Engine, Soot Particles, Radius of Gyration, Primary Particle Diameter, Jet-Jet Interaction*

## 1. Introduction

Diesel soot particles with complex fractal structures are a product of multi-stage formation processes including the nucleation, surface growth and agglomeration occurring within the diesel flame [1]. The soot particles are well known to have negative impacts on environment and health [2], which calls for an improved understanding of the size and structures of soot particles at key formation and oxidation stages.

Direct sampling of in-flame soot particles from a single reacting jet and subsequent transmission electron microscope (TEM) image analysis has been used widely for the investigation of soot particle size and structure [3-6]. However, the previous studies focused on a single diesel flame with no neighbouring diesel flames, which cannot address the significant impact of flame-to-flame interactions on mixture conditions and soot particles. In realistic engine conditions, multiple fuel jets impinge on the bowl-wall and then travel along the wall before they merge with neighbouring jets. This jet-jet interaction creates locally fuel-rich zones [7, 8] and decreases the lift-off length [9, 10], leading to the increased soot production [11].

In our recent study [12], how nano-scale structures of soot primary particles are impacted by jet-jet interactions was investigated, which reported that soot primaries under the influence of jet-jet interactions show more reactive and pre-mature structures than those without jet-jet interactions. The present study provides additional information about the particle number count and size distributions of soot aggregates and primaries to better understand the influence of jet-jet interactions on soot particle morphology.

## 2. Experiments

### 2.1 Diesel Engine and Operating Conditions

A single-cylinder, automotive-size optical diesel engine was used for in-flame soot particles sampling. Engine specifications and operating conditions are listed in Table 1. Figure 1 depicts the combustion chamber through the side-view (top) and top-view (bottom) orientations. A modified piston was used to omit the risk of potential collisions between a sampling probe and fast moving engine parts (e.g., valves and piston). This includes a 30-mm-wide bowl-rim cut-out

Table 1. Engine specifications and operating conditions

| | |
|---|---|
| Displacement volume | 498 $cm^3$ (single cylinder) |
| Bore / Stroke | 83 mm / 92 mm |
| Compression ratio | 15.2 |
| Swirl ratio | 1.4 |
| Coolant temperature | 90 °C |
| Intake air temperature | 30 °C |
| Engine speed | 1200 rpm |
| Injection system | Bosch second-generation common-rail injector |
| Fuel | Ultra-low-sulfur diesel |
| Cetane number | 51 |
| Nozzle hole diameter | 134 μm (nominal) |
| Number of holes | single-hole (Jet A) |
| | single-hole (Jet B) |
| | double-hole (Jet A&B) |
| Injection pressure | 70 MPa |
| Injection duration | 2.34 ms |
| Injection timing | -6 °CA aTDC (Jet A) |
| | -8 °CA aTDC (Jet B) |
| | -7 °CA aTDC (Jet A&B) |

* Corresponding author:
Phone: (+61) 4 2509 1230
Email: renlin.zhang@unsw.edu.au

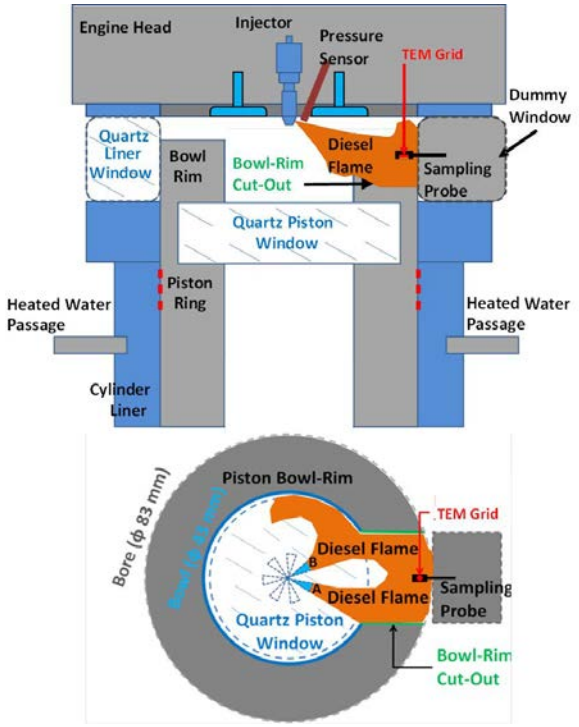


Fig. 1. Schematics of the combustion chamber of the diesel engine. The engine modifications for soot sampling and the sooting diesel flame development relative to the sampling probe are illustrated in the side-view (top) and top-view (bottom) orientations.

and a dummy side window replacing the optical window to hold a soot sampling probe. Heated water at 90°C was circulated through the cylinder liner, engine block and engine head to simulate a thermally stable, warmed-up engine condition. The temperature of naturally aspirated intake air was measured at 30°C throughout the experiments. The engine speed was fixed at 1200 revolutions per minute (rpm) using a 37-kW AC motor. The fuel injection system is comprised of a common-rail system (Bosch CP3) and solenoid injector which are controlled by a universal injection and timing controller (Zenobalti 5100). A conventional ultra-low-sulphur diesel fuel with cetane number of 51 was used in the present study.

The original injector had a 7-hole nozzle with a nominal nozzle-hole diameter of 134 µm. In this study, the sampling experiments were performed for three different jet configurations of Jet A, Jet B and Jet A&B as shown in Fig. 1 (bottom). A laser welding technique was used to produce these jet configurations. For instance, Jet A nozzle was crafted by leaving the 4 o'clock hole open while blocking all other holes. For all three jet configurations, the injection pressure and injection duration were held constant at 70 MPa and 2.34 ms, respectively, which delivered 9 mg per injection per hole [5, 6, 13]. The injection timing for Jet A was set at -6 crank angle degrees after top dead centre (°CA aTDC), which was slightly adjusted for other jet configurations to match the combustion phasing. This was to isolate the effect of ambient gas conditions at the start of combustion on soot processes. More details about the engine specification and operating conditions are found in our previous work conducted in the same engine [12].

## 2.2 Soot Sampling

As depicted in Fig. 1 (bottom), the jets would penetrate into the bowl-rim cut-out region. As a result, a 3-mm diameter carbon coated TEM grid at the tip of the sampling probe was exposed to the sooting diesel flame. The high temperature gradient between hot soot laden gas and the cold TEM grid surface would induce thermophoretic deposition of soot particles onto the carbon film while causing sudden reaction quenching, and thereby preserving their in-flame morphology [14]. Soot loading on the TEM grid was controlled by the number of injections per sampling run. In the present study, a total of 10 injections were executed to collect sufficient soot particles for statistical analysis while avoiding soot overloading. More details about this sampling technique are found in our previous work focused on the diagnostics and error analysis [6].

## 2.3 TEM Imaging and Image Processing

A transmission electron microscope (JEOL 1400 TEM) with a point resolution of 0.38 nm and a 100 kV acceleration voltage was used to observe sampled soot particles. The magnified soot images were then digitised using a CCD camera with an 11-mega pixel resolution. For each soot sample, multiple TEM images were obtained at various on-grid locations considering the spatial variations of soot particles. The magnification was set at x100,000 for high image quality. The obtained TEM images were then post-processed using a Matlab-based image processing code similar to our previous work [5, 6]. The post-processing yielded the number of particles per image, radius of gyration of soot aggregates ($R_g$) and diameter of primary particles ($d_p$).

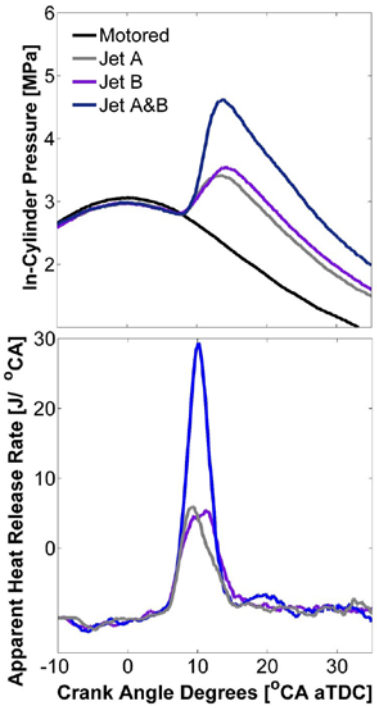


Fig. 2. Average in-cylinder pressure and correspond apparent heat release rate (aHRR) traces versus crank angle degree after the top dead centre (°CA aTDC) for various jet configurations.

## 3. Results and Discussions

### 3.1 In-cylinder Combustion Conditions

Figure 2 shows the ensemble averaged in-cylinder pressure and corresponding apparent heat release rates (aHRR) for all tested jet configurations in the present study. It is noticeable that the differences between Jet A and Jet B are minor and well within the cycle-to-cycle variations [6]. The start of combustion is also similar in all three jet configurations as the injection timing was adjusted accordingly. Therefore, the diesel combustion and soot processes started to occur at the same ambient conditions regardless of the jet configurations. However, Jet A&B shows almost twice higher peak pressure and aHRR than the single-jet cases. It is simply due to the twice higher fuel mass for Jet A&B configuration because the injection duration was fixed at 2.34 ms. This was necessary to keep the dynamics of double-jet as its single-jet counterparts and to maintain the long jet-jet interactions. Since the bulk-gas pressure and temperature is higher for Jet A&B in the present study, one might expect that in-flame soot particles would be in a more mature stage of soot formation.

### 3.2 TEM Images of In-Flame Soot Particles

Figure 3 shows example TEM images for all three tested jet configurations in the present study. It is observed that the majority of soot particles are aggregates comprised of near spherical primary particles. The soot particles exhibit various sizes and structures, ranging from small aggregates with only a few primary particles to large aggregates with fractal-like structures. It is noticeable that Jet B sample shows the increased number of small soot particles than Jet A. Furthermore, the particle number of Jet A&B is higher than both of the single-jets. It is also found that Jet A&B soot particles show a noticeable decrease in the overall particle size compared to that of Jet A and Jet B.

### 3.3 The Particle Number Count

The particle number counts per TEM image are plotted in Fig. 4. It is clear that Jet B has higher particle number than Jet A. This is attributed to the differences in the spatial development of a wall-interacting jet and associated changes in the soot particle development. As shown in Fig. 1, Jet A penetrated fully into the bowl-rim cut-out region while Jet B was targeted at the edge of the cut-out, leaving only half of the jet penetrating into the cut-out region. As a result, the TEM grid was closer to the wall-impingement point of Jet A. On the other hand, the grid was exposed to the wall-jet head region of Jet B after the flame-wall impingement. Our previous study performed in the same engine reported the fragmentation of soot aggregates due to the jet-wall interaction, leading to the increased number of soot particles [5]. Between the double-jet and single-jets, the number of soot particles are much higher for Jet A&B. This is consistent with the well-known increase in soot formation due to jet-jet interactions. That is, the increased locally rich mixtures in the jet-jet interaction regions [7, 8] and the penetration of the jet back towards the nozzle to decrease the lift-off length (i.e. re-entrainment) [9, 10] would increase the soot production [11].

### 3.4 Size Distribution of Soot Particles

The size of soot particles was quantified by measuring $R_g$ and $d_p$. In the present study, more than 600 soot aggregates and 7000 primary particles were processed for each jet configuration. The results are presented using a probability density function (pdf) in Fig. 5.

Figure 5 shows that the mean $R_g$ for Jet B is about 26 nm, which is smaller than that of Jet A. The pdf also shows that the likelihood of observing soot aggregate with an $R_g$ smaller than 50 nm is considerably higher for Jet B. This can be explained by the soot fragmentation during the flame-wall impingement [5], as mentioned previously. The large soot aggregates would breakdown into small fragments due to the enhanced mixing in the wall-jet head-vortex region, resulting in the increased number of soot particles and decreased $R_g$. However, this process would not affect the primary particles significantly. This is confirmed by the almost identical mean $d_p$ ($\approx$ 17.5 nm) and distribution profiles of $d_p$ for Jet A and Jet B samples (Fig. 5 bottom).

The mean $R_g$ and $d_p$ of Jet A&B are about 21 and 13 nm, respectively while the pdfs display further shift towards smaller size ranges compared to the single-jet cases. This suggests that Jet A&B soot particles are smaller than those of Jet A or Jet B. The result is consistent with the visual inspection of TEM images (Fig. 3). Our recent study focused on the jet-jet interaction effect on soot nanostructures reported that a double-jet produces more pre-mature carbon fringe

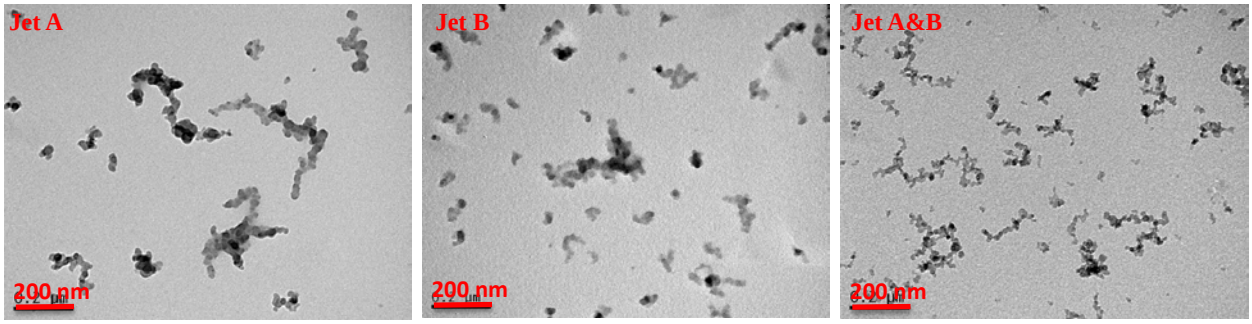

Fig. 3. Example TEM images of in-flame soot particles for various jet configurations. The red scale bars of 200 nm are shown in the bottom-left corner of each image.

structures than those of a single jet [12]. This suggests that the smaller particle size seen in Fig. 5 is associated with the pre-mature internal structure of Jet A&B soot particles. In other words, soot particles formed in fuel-rich jet-jet interaction regions are in an earlier stage of soot formation than that of a single jet with no jet-jet interactions. This is consistent with previous studies reporting that soot particle collected from the early formation zone show smaller sizes [3, 4]. It was noted that the pre-mature soot particle structures are directly opposite to our earlier prediction based on the higher bulk-gas temperature, suggesting that the influence of locally rich mixtures in the jet-jet interaction region outperformed the higher bulk-gas temperature effect to cause more mature soot structures.

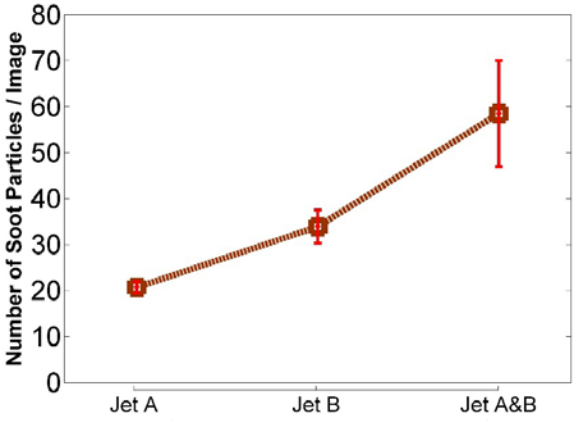


Fig. 4. Number of soot particles per each TEM image for various jet configurations. Error ranges were estimated at 95% confidence.

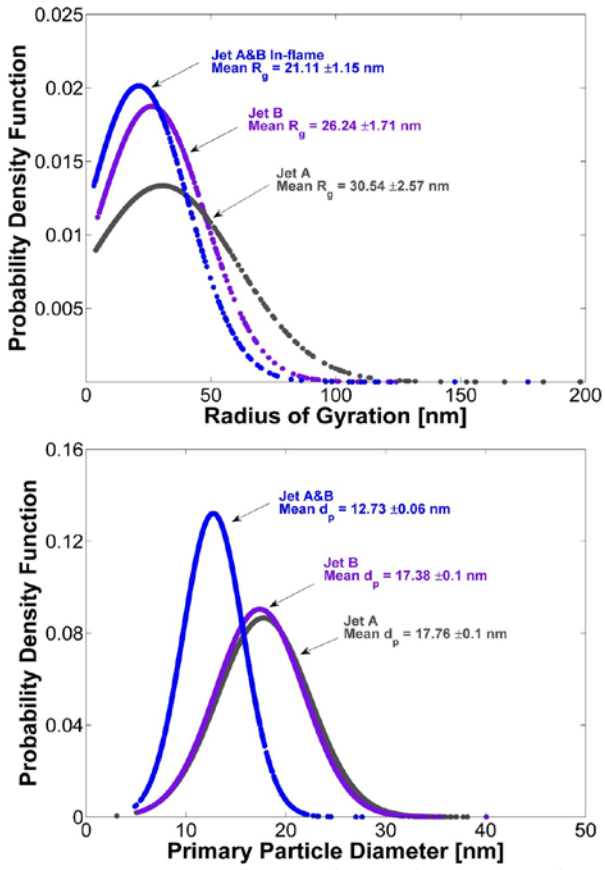


Fig. 5. Probability density functions of radius of gyration ($R_g$) of soot aggregates (top) and diameter ($d_p$) of primary particles (bottom) for various jet configurations. The mean values and error ranges (95% confidence) are noted for each jet configuration.

## 3. Conclusions

A thermophoretic soot particles sampling was performed directly from flames in a diesel engine. Soot samples collected from three nozzle configurations including two single-jets (Jet A and Jet B) and a double-jet (Jet A&B) were imaged by a TEM. The subsequent image processing yielded the number of particles and the size distributions of both soot aggregates and primary particles. The major findings of this study can be summarised as follows:

1) Regardless of the jet configurations, soot particles sampled directly from diesel flames show overall similar agglomerated structures.
2) Soot particles sampled from two single-jets show measurable differences in the number count and aggregate size due to different flame development with respect to the bowl-wall and sampling probe. However, the primary particles show near identical size distributions.
3) Soot particles sampled from fuel-rich jet-jet interaction regions show higher particle number due to the increased soot production.
4) Soot particles formed in fuel-rich jet-jet interaction regions are in an earlier stage of soot formation than that of single jets.

## 4. Acknowledgments

Experiments were conducted at the UNSW Engine Research Laboratory. Support for this research was provided by the Australian Research Council.

## 5. References

[1] D.R. Tree and Svensson K.I, Prog. Energy Combust. Sci. **33** (3) (2007), pp. 272-309.

[2] D.M. Broday and R. Rosenzweig, J. Aerosol Sci. **42** (6) (2011), pp. 372-386.

[3] S. Kook and L.M. Pickett, SAE Int. J. Fuels Lubr. **5** (2) (2012), pp. 647-664.

[4] K. Kondo, T. Yamaguchi, H. Nishigai, S. Takano and T. Aizawa, SAE Technical Paper No. 2011-24-0068, 2011.

[5] R. Zhang and S. Kook, Combust. Flame **162** (6) (2015), pp. 2720-2728.

[6] S. Kook, R. Zhang, K. Szeto, L. M. Pickett and T. Aizawa, SAE Int. J. Fuels Lubr. **6** (1) (2013), pp. 80-97.

[7] C. Chartier, J. Sjoholm, E. Kristensson, O. Andersson, M. Richter, B. Johansson and M. Alden, SAE Int. J. Fuels Lubr. **5**(4) (2012), pp. 1684-1692.

[8] J. Abraham, A. Khan and V. Magi, SAE Technical Paper No. 1999-01-0513, 1999.

[9] A.M. Rusly, M. Le, S. Kook and E. Hawkes, Fuel **125** (0) (2014), pp. 1-14.

[10] C. Chartier, U. Aronsson, O. Andersson, R. Egnell and B. Johansson, Fuel, **112** (2013), pp. 311-318.

[11] L.M. Pickett, D.L. Siebers, Combust. Flame **138** (1-2) (2004), pp. 114-135.

[12] Y. Zhang, R. Zhang and S. Kook, SAE Int. J. Engines **8** (5) (2015).

[13] R. Zhang, S. Kook, Environ. Sci. Technol. **48** (14) (2014), pp. 8243-8250.

[14] R.A. Dobbins and C.M. Megaridis, Langmuir **3** (2) (1987), pp. 254-259.

# The influence of high flux broadband radiation on soot concentration and temperature in a sooty flame

Xue Dong[1, 2, *], Zhiwei Sun[1, 3], Dahe Gu[1, 3], Graham J. Nathan[1, 3*], Peter J. Ashman[1, 2], Zeyad T. Alwahabi[1, 2], Bassam B. Dally[1,3]
[1]Centre for Energy Technology, [2]School of Chemical Engineering and [3]School of Mechanical Engineering, The University of Adelaide, SA 5005, Australia

## Abstract

This paper reports the first set of measurements of the influence of concentrated solar radiation (CSR) on a laminar sooty flame. Broad-band radiation at fluxes of up to 0.45 MW/m$^2$ and wavelengths that simulate those in concentrated solar receivers was produced by a metal-halide lamp configured in series with three optical concentrators to irradiate an entire Santoro-type laminar flame of 64 mm length. The soot volume fraction and temperature of the flame was measured using laser induced incandescence and two-line atomic fluorescence, respectively. The results show that the soot volume fraction was increased due to CSR by 40-50% at downstream locations (height above burner>26 mm). The spatially-average flame temperature along the radial direction was increased due to CSR by about 8% at most of the downstream locations.

*Keywords: combustion-radiation interactions, concentrated solar radiation, soot volume fraction, temperature*

## 1. Introduction

Hybrids of concentrated solar thermal energy and fossil-fuelled technologies are receiving growing attention because the combination of the two energy sources can provide lower emissions of carbon and other pollutants than pure fossil fuels, lower cost than pure solar thermal energy, and continuous supply. While most of the previously reported hybrid concepts employ stand-alone solar receivers and combustors [1, 2], Nathan *et al.* have been developing an alternative approach with which to fully combine a combustor and a solar cavity receiver into a single device [3, 4]. This offers the potential for significant savings from reduced infrastructure investment and reduced start-up and shut-down losses [3]. Besides, this hybrid also results in the direct interaction between concentrated solar radiation and a flame, which is already known to be coupled [5]. However, the influence of concentrated solar radiation (CSR) on a flame has not been experimentally investigated.

Soot is one of the key components in many combustion systems. This is because, within a flame, an increased presence of soot acts to increase the flame emissivity and hence the radiation— the dominant heat transfer mode in kilns and furnaces [6, 7]. Therefore, in these applications, an increase of soot concentration within the flame is highly desirable. It has been demonstrated by Medwell *et al.* [8] that laser radiation at 10.6 μm with a fluence of 4 MW/m$^2$ can approximately double the peak concentration of soot in an ethylene flame, and translate the soot layer towards the oxidising side of the flame [8]. However, the previous investigation was undertaken with a single excitation wavelength on a small area of the flame (5 mm in diameter) [8], while the CSR is broadband and would irradiate an entire flame in a hybrid reactor. Therefore, the influence of broadband radiation of relevance to CSR on the soot volume fraction of the whole flame is yet to be studied.

In addition to soot concentration, flame temperature is another key parameter of interest. Molecular absorption of CSR is expected to increase the temperature of these molecules. Furthermore, the absorption of CSR by soot is also expected to increase the radiant heat transfer, and hence increase the temperature of the gas phase species. In this case, the diffusion rate and reaction rate of species within the flame are likely to be enhanced because they are highly dependent on the flame temperature. It is therefore important to measure temperature distribution in this challenging high flux environment.

Therefore, this paper aims to quantify the influence of CSR on the soot volume fraction and temperature of a sooty laminar flame.

## 2. Methodology

### 2.1 High flux solar simulator

The configuration of the solar simulator is shown in Figure 1. The solar simulator consists of a 6 kW

* Corresponding author:
Email: xue.dong@adelaide.edu.au
graham.nathan@adelaide.edu.au

Metal Halide Lamp, close-coupled with an elliptical reflector and co-aligned with a conical secondary concentrator to further concentrate the radiation, and then a tertiary concentrator to enable the concentrated radiation to double pass the focal area. The optical design of the solar simulator using the experimentally validated Monte-Carlo ray-tracing code is reported elsewhere [9]. This study employs a metal halide lamp as the light source of the solar simulator, the spectrum of which is reported by Dong *et al.* [10]. The elliptical reflector is made of aluminium alloy 1050, with a physical vapour deposition (PVD) coating comprising alumina and silica, similar to that used by Petrasch *et al.* [11]. The secondary concentrator is cone shaped with an inlet diameter $D$ = 500 mm, an outlet diameter d = 55 mm and length $L$ = 1100 mm. The tertiary concentrator is also conical with $D$ = 200 mm, $d$ = 0 and $L$ = 60 mm. Both the secondary and tertiary concentrators were made of polished stainless steel with a reflectivity of 65% and are water cooled to under 50 °C during operation, to minimize the thermal impact of the facility on the flame. The flame was placed 50 mm downstream of the secondary concentrator and 50 mm upstream of the tertiary concentrator. This configuration provides a peak radiant flux of 0.45 MW/m$^2$ and on average of 0.27 MW/m$^2$ in the flame area.

### 2.2 Burner setup

A laminar non-premixed ethylene flame was employed due to its high soot loading [7, 12], hence potentially high absorption of CSR. The burner consists of a central fuel jet with an inner diameter of 11 mm and an annular co-flow cylinder with an inner diameter of 98 mm, both made of brass. The conditioning of the co-flow gas stream was achieved with the use of stainless steel mesh, steel honey comb and glass beads. Steel honey comb was also employed in the fuel jet to ensure uniform velocity distribution at the jet exit. Industrial grade ethylene (>99.5% C2H4) at a flow rate of 0.184 standard litres per minute (SLM) and air at a flow rate of 127.7 SLM were used as the fuel and co-flow, respectively. This flame is desirable for resolving the spatial variations that arise from the irradiation [13].

### 1.1 Planar LII measurement

The experimental arrangement used for the present Laser Induced Incandescence, LII, measurements follows that described previously [7]. A schematic diagram of the experimental layout is shown in Figure 1. An Nd:YAG laser operating at 1064 nm was used for the LII excitation. The laser beam was circularly polarised and formed into a sheet of ~0.3 mm thick and was aligned with the nozzle axis. The LII laser sheet was clipped with a rectangular aperture to 25 mm in height. The LII signals were detected with an ICCD camera through a 410-nm optical filter (10-nm bandwidth) [7]. The gate width of the camera was set to 30 ns. The LII signals were calibrated using laser extinction measurements following Qamar et al. [14]. The soot extinction coefficient ($K_e$) was taken to be 4.03, computed from the formula obtained from Mie theory [15], with the complex refractive index $m$=*2.75-2.25i* [16].

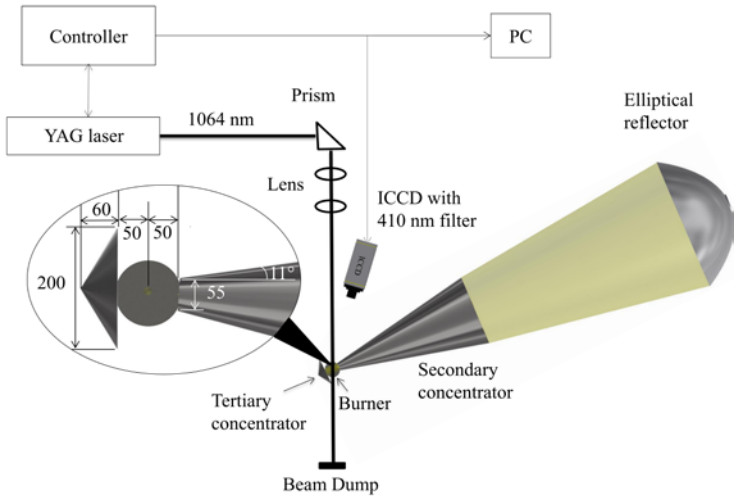


Figure 1. Schematic diagram of the LII setup in the solar-flame interacting system, dimensions in the zoomed-in part are in mm.

The LII measurements of the Santoro flame were conducted with and without the irradiation from the solar simulator. Images of the flame with the lamp-on and the laser-off were also taken to be used for the background correction. This was later substraced from the LII signal with the lamp-on to correct for the interferences of scattering from soot. The 25 mm high laser beam was traversed axially, to allow imaging of the entire flame. The measurement of $f_v$ was repeatable to within 5% as determined from 6 separate measurements. The images presented for this laminar flame were median-averaged 200 frames to improve the SNR.

### 1.2 TLAF measurement

The temperature was measured using two-line atomic fluorescence (TLAF). However, the application of this technique in this high flux environment is very challenging due to its strong background scattering. The TLAF technique were further developed specifically for this environment to enable the measurements to be undertaken reliably, and strong light scattering background from the irradiation was accounted for by recording the pure light scattering background and subtracted from the raw LIF images. as reported elsewhere by Gu *et al.* [17].

## 2. Results and Discussion

Figure 2 presents images of the soot volume fraction for the cases with and without the irradiation from the solar simulator. It can be seen from Fig. 2 that the $f_v$ is

higher in the flame with CSR, especially on the fuel rich side, although there is no visible change to the length and width of the flame. The reason why the distribution of soot with radiation on is not symmetric along the flame axis is that, in the plane where the laser beam intersects with the flame, the profile of simulated solar radiation is not symmetric along the flame axis.

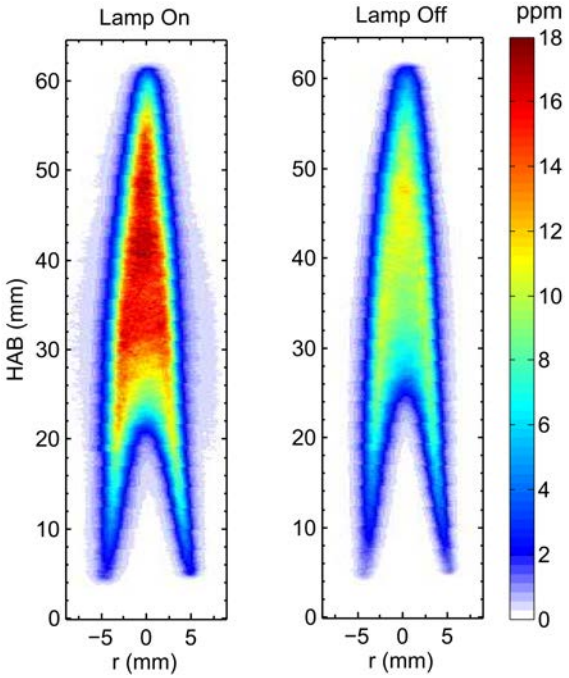


Figure 2. Measured soot volume fraction of flame with simulated solar radiation on (left) and off (right).

Figure 3 presents the profiles of $f_v$ along the centre line of the flame as a function of the normalized height above burner (HAB), i.e. HAB/$L_f$, here $L_f$ is the flame length. It can be seen that $f_v$ along the flame centre line was increased by CSR, starting from HAB/$L_f$=0.16, and peaked at HAB/$L_f$=0.5-0.8 with an increase of ~50%. Importantly, the magnitude and distribution of $f_v$ is different for the current reference case from that for preheating of the fuel as reported by Konsur *et al.* [18]. This is because they employed a jet burner of 1.6 mm inner diameter without co-flow, and a fuel mixture of 50% (volume) $C_2H_2$–50% $N_2$[18]. Results reported by Konsur *et al.* [18] shows that the $f_v$ can be increased by fuel preheating. This is because preheating the fuel can potentially promote pyrolysis rates which, in turn, create more soot in this region and shortened soot growth [18]. However, the extent of this influence is less than that which occurs from solar irradiation. Significantly, the amount of preheating of the fuel in the current study was limited to below 13 °C. In contrast, the exposure to high flux radiation increased the temperature of the fuel jet by ~100 °C. In addition, the difference in $f_v$ caused by lamp radiation is more significant than the fuel preheating, because as can be seen in Figure 5a that the fuel preheating only translates the position of soot formation upstream, while the lamp radiation not only brings the soot inception upstream, but also significantly increases the peak $f_v$. Furthermore, the TLAF measurement shows that the centre line flame temperature was increased due to CSR by 50-100 K at HAB/$L_f$ =0.35-0.6. These results indicate that the solar flux interacts with the full flames, which has more profound influence on $f_v$ than preheating the fuel. Noteworthy is that the measurement of $f_v$ is repeatable to within 5% as determined from 6 separate measurements. A measurement precision of 80 K is achieved in the sooting flame without solar irradiation [17].

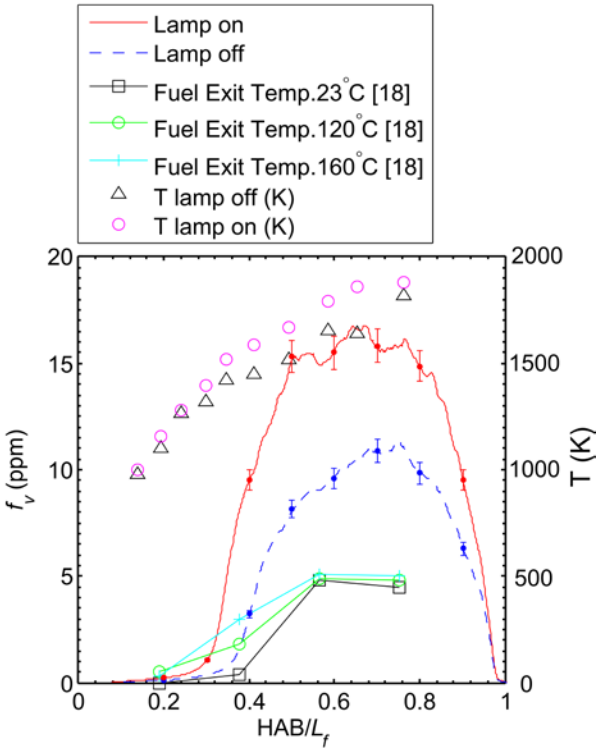


Figure 3. Profiles of $f_v$ and temperature along the centre line of the flame, i.e. at $r$ =0, for the current measurements and those of preheating a fuel mixture of $C_2H_2/N_2$ (50%/50%) reported by Konsur *et al.*[18];

Figure 4 presents the radial profiles of $f_v$ and T at different flame heights, from HAB=12 mm to 49 mm. It can be seen from Figure 6 that, the soot volume fraction along the radial direction was increased due to CSR by 40% - 50 % at downstream locations (HAB >26 mm). While the spatially averaged flame temperature along the radial direction was also increased due to CSR by a fraction of about 8% for 26 mm < HAB < 49 mm. The fact that the increase of temperature is less significant than that of $f_v$ indicates that, although more soot is generated by CSR, which leads to increased soot absorption of CSR, hence of flame temperature, the radiation from soot to the surroundings is also increased, which can be expected to decrease the flame temperature. That is, the balance between these two mechanisms results in only a slight increase in gas temperature in this case.

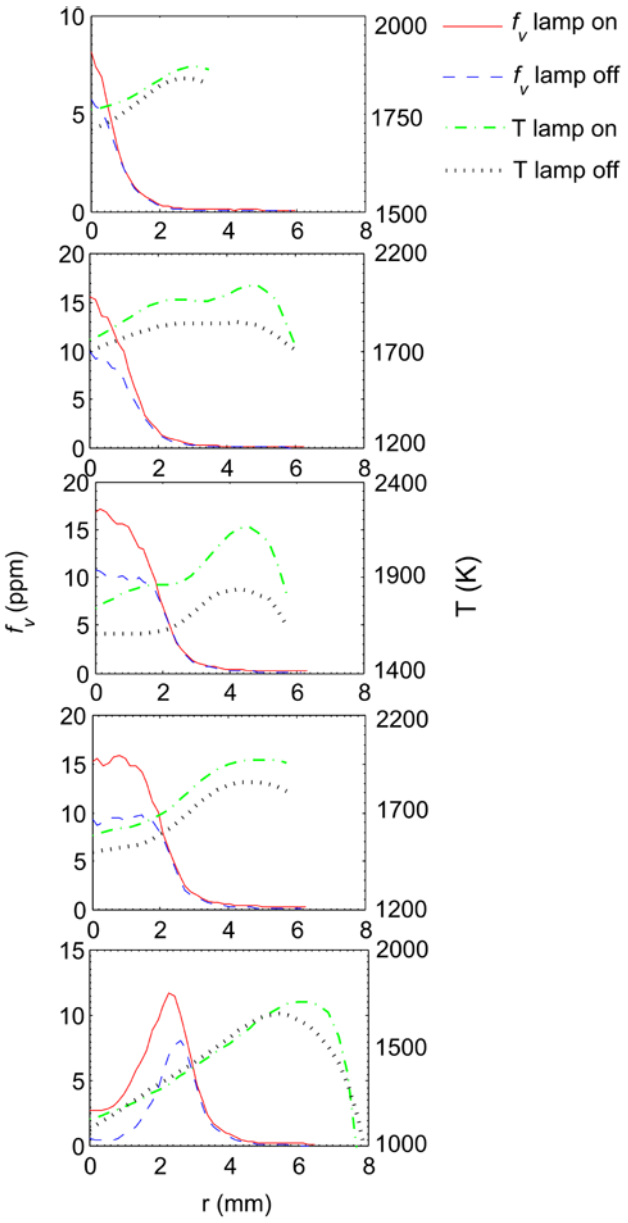


Figure 4. Radial distribution of $f_v$ and T at HAB=12, 26, 32, 42 and 49 mm (from bottom to top).

## 3. Conclusions

The influence of simulated concentrated solar radiation on laminar non-premixed ethylene flame was found to be significant. Specifically:

- The $f_v$ is higher in the flame with CSR by 40% - 50 % at downstream location (HAB > 26 mm), especially in the fuel rich side, although there is no visible change to the length and width of the flame.
- The spatially-averaged flame temperature along the radial direction was increased due to CSR by a fraction of about 8% at 26 mm< HAB <49 mm.

## 4. Acknowledgments

This work was funded by Australian Research Council Linkage under Project ID: LP110200060. Partial support for the work was also provided by the Australian Government through the Australian Renewable Energy Agency, ARENA grant 1-US034. The authors would also like to acknowledge the financial support from the China Scholarship Council (Grant no: 2011673002) to the first author.

## Reference:

1. F. A. Grange B, Bellard D, Vrinat M, Couturier R, Fan Y. , Journal of Solar Energy Engineering 133: (31004) (2011) 1-11
2. C. R. Gou C, Hong H. , Energy 32 (2007) 1707–1714.
3. G. J. Nathan; D. L. Battye; P. J. Ashman, Applied Energy 113 (2014) 1235-1243
4. G. J. Nathan; B. B. Dally; P. J. Ashman; A. Steinfeld A hybrid receiver combustor. Provisional Patent Application No. 2012/901258. Adelaide Research and Innovation Pty. Ltd. 2012.
5. P. Coelho, Progress in Energy and Combustion Science 33 (4) (2007) 311-383
6. M. A. Delichatsios; J. De Ris; L. Orloff, Symposium (International) on Combustion 24 (1) (1992) 1075-1082
7. Q. N. Chan; P. R. Medwell; P. A. Kalt; Z. T. Alwahabi; B. B. Dally; G. J. Nathan, Proceedings of the Combustion Institute 33 (1) (2011) 791-798
8. P. R. Medwell; G. J. Nathan; Q. N. Chan; Z. T. Alwahabi; B. B. Dally, Combustion and Flame 158 (9) (2011) 1814-1821
9. X. Dong; G. J. Nathan; Z. W. Sun; D. H. Gu; P. J. Ashman, Solar Energy 122 (2015) 293-306
10. X. Dong; Z. W. Sun; G. J. Nathan; P. J. Ashman; D. H. Gu, Solar Energy 115 (2015) 613-620
11. J. Petrasch; P. Coray; A. Meier; M. Brack; P. Häberling; D. Wuillemin; A. Steinfeld, Journal of Solar Energy Engineering 129 (4) (2007) 405-411
12. A. Gomez; M. Littman; I. Glassman, Combustion and Flame 70 (2) (1987) 225-241
13. Q. N. Chan; P. R. Medwell; Z. T. Alwahabi; B. B. Dally; G. J. Nathan, Applied Physics B 104 (1) (2011) 189-198
14. N. Qamar; G. Nathan; Z. Alwahabi; K. King, Proceedings of the Combustion Institute 30 (1) (2005) 1493-1500
15. W. H. Dalzell; A. F. Sarofim, Journal of Heat Transfer 91 (1) (1968) 100-104
16. H. Chang; T. Charalampopoulos, Proc. R. Soc. London,Ser. A 430 (1990) 577–591
17. D. Gu; Z. Sun; G. J. Nathan; X. Dong; Z. Alwahabi; B. B. Dally, in: *The 10th Asia-Pacific Conference on Combustion*, Beijing, China, 2015.
18. B. Konsur; C. M. Megaridis; D. W. Griffin, Combustion and Flame 116 (3) (1999) 334-347

**Proceedings of the Australian Combustion Symposium**
**December 7-9, 2015, The University of Melbourne**

# A technique for the measurement and classification of soot precursors and soot particles in turbulent flames

Daniel Bartos[1,*], Matthew Dunn[1], Mariano Sirignano[2], Andrea D'Anna[2], Assaad R. Masri[1]
[1] School of Aerospace, Mechanical and Mechatronic Engineering, the University of Sydney, Sydney Australia
[2] Dipartimento di Ingegneria Chimica, dei Materiali e della Produzione Industriale, Universita`degli Studi di Napoli 'Federico II, Napoli, Italy

**Abstract**

This paper explores an experimental technique for the point-wise measurement and classification of soot precursors as well as soot particles in turbulent flames. Soot precursor characterization is based on monitoring the spatial and temporal evolution of fluorescence emissions by mean of UV excitation in selected regions of the visible and the UV spectra. Simultaneous characterization of soot particles is achieved by measurements of elastic scattering and laser induced incandescence. The trends for soot precursors and soot particles obtained in a laminar ethylene flame agree well with previous measurements obtained in the same flame with a similar technique. It is found that pyrogenically formed soot precursors display bi-exponential fluorescence decay in the visible and UV spectral regions. Measurements in a piloted turbulent ethylene flame are successfully acquired. The use of 266nm picosecond excitation pulses and fast collection optics are crucial in observing these phenomena. The further development and application of this technique to well-posed sooting and near-sooting turbulent flames will enable the study of soot formation and destruction pathways in these complex flows.

*Keywords: laser-induced emission, time resolved, polycyclic aromatic hydrocarbon, turbulent combustion.*

## 1. Introduction

Improving the current understanding of soot formation and oxidation mechanisms in turbulent flames is increasingly important considering that regulations on the emission of particles are becoming more stringent [1]. Satisfying such regulations necessitates an improved understanding of particle evolution processes in flames. While extensive research has already been undertaken on sooting laminar premixed and diffusion flames [2–4], the same degree of progress has not been made for turbulent flames due to the difficulty of applying the same diagnostic methods whilst simultaneously resolving the relevant time and spatial scales. Extensive efforts are currently under way, through venues such as the International Sooting Flame Workshop [5] to enhance experimental and numerical capabilities for resolving the evolution of soot nanoparticles in laminar flames and to extend such capabilities to turbulent flows at normal and high pressures relevant to engine applications.

Measurements of soot evolution in laminar flames [6–16] reveal the existence of a bimodal number density distribution with small nanoparticles in the size range less than 10nm (referred to herein as Mode I structures ) and larger particles and aggregates potentially up to hundreds of nanometres which are generally identified as soot (referred to as Mode II particles). Mode I structures are formed and directly linked with the nucleation of small polycyclic aromatic hydrocarbons (PAHs). Mode I structures may exhibit unusual optical properties that bridge those of PAH molecules and condensed phase material: they are visible transparent but absorb light in the UV spectral region. Also a small excess of scattering signal with respect to gas phase compounds can be attributed to these structures due to their condensed phase feature, and, if excited with UV light source, they exhibit a laser induced fluorescence signal which remains below 500nm suggesting a basic aromatic structure not larger than gas phase PAHs [2]. The exact processes involved remain the subject of intense research. Mode II particles appear to have predominantly chain-like structure in which primary particles can be distinguished within aggregates [2]. They exhibit usual optical properties of large excess of scattering respect to gas phase as well as a visible absorption, and are responsible for natural incandescence of flame as well as for laser induced incandescence signal. The transition from Mode I structures to Mode II particles is also important and current understanding of the mechanisms controlling such transition are not well understood [2,3].

In this study, a UV wavelength and short pulse-width laser excitation (266nm with a pulse duration of 30ps), is applied to induce emissions. The temporal evolution of these signals are monitored at a range of wavelengths including elastic scattering, two fluorescence bands centred at about 350 and 440nm as well as the LII band at wavelength larger than 550nm. It is noted that using the same laser source for LII was problematic and has resulted in excessive laser fluence which rendered the LII quantitatively unreliable.

## 2. Experimental Methods

This section provides descriptions on the configuration of the burners and the optical set-up. The collection of the temporal evolution of the LIF signals is crucial in understanding the structure of emitting particles. These behaviours have been already explored and found in laminar flames with techniques similar to those presented in this paper [15,17].

* Corresponding author:
Phone: (+61) 4 05650510
Email: dbar4475@uni.sydney.edu.au

## 2.1 Burners and Flames

Initial studies are performed on a laminar flame to check reproducibility of the technique and to ensure consistency with previous measurements [15]. A Santoro style burner [18] with an 12.5mm inner diameter nozzle and 70mm co-flow diameter is used to stabilize a non-premixed flame at atmospheric conditions. The fuel is ethylene (0.23SLPM, 25°C, 101.3kPa) injected in a co-flow of air (10SLPM). The visible laminar flame length was 70mm but the very tip was flickering slightly causing measurements at the downstream locations to contain some intermittency.

A piloted burner is used to stabilize a turbulent jet flame burning a mixture of ethylene and nitrogen (1/1 by volume) with Reynolds number, Re=4800. Although this is modest, the flame is sufficiently turbulent to form an adequate test to check the in-principle applicability of the approach. The fuel jet with a diameter of 4mm is surrounded by a pilot annulus of diameter 18mm which is recessed by 15 mm upstream of the jet exit plane. The pilot is a mixture of hydrogen, acetylene and air (Ø=0.71) with the same C/H ratio as the main fuel. The unburned bulk velocity in the pilot stream is 4.5m/s and this provides sufficient heat release to stabilize the main flame to the exit plane of the burner. The visible flame length is 450mm and sufficient soot is produced to enable the detection of LIF signals.

## 2.2 Optical Setup

The technique employed here is similar to that used by Sirignano et al. [15] but with refined capabilities to enable time-resolved measurements to be made in turbulent flames. The key premise of the technique involves exciting the flame with UV light to induce fluorescence in the UV as well as visible bands around 350 nm and 440 nm, respectively. Soot precursors that contain PAHs with low ring numbers tend to fluoresce in the UV whereas those with higher ring numbers or highly packed structures are inclined fluoresce in the visible spectrum [6,15,19]. Scattering, as well as LII from soot particles are also collected so that, in total, four wavelength bands are measured providing useful information about Mode I structures and Mode II particles.

A schematic of the experimental setup is shown in Fig. 1. The flame is probed by the 4th harmonic (266nm) of a mode locked ND: YAG 10Hz pulsed laser (Ekspla PL2251 Series Laser). A wavelength of 266nm is chosen to avoid excitation of other products present in the flame, including CO2 and H2O, which are known to fluoresce at wavelengths below 230 nm [6,20]. Although not typically used for LII, the 266nm laser pulse will still induce LII in larger soot particles [6,15,19]. Additionally, this wavelength will reduce fragmentation compared to 213 nm and C2 emissions that would interfere with the LIF [15]. The probe volume of the focused laser is measured at a diameter of 30 microns FWHM using knife edge scanning technique. This results in a fluence of 60 J/cm2.

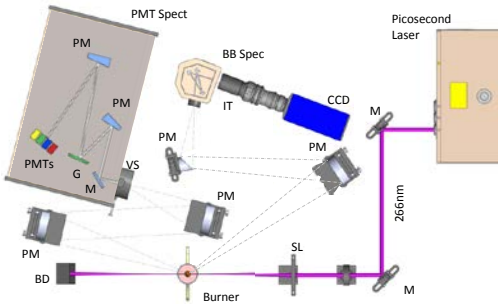


Fig 1. (Colour). Experiment Setup. (M) Mirror, (SL) UV fused silica plano-convex lens 455mm focal length, (BD) Beam dump, (PM) Aluminium off-axis parabolic mirror, (G) Ruled diffraction grating , (PMTs) x4 fast response photomultiplier tube, (IT) Intensifier 18mm diameter, (CCD) CCD Camera: La Vision Flowmaster 3. (VS) Variable slit, (BB Spec) Oriel 0.125m Spectrometer, (PMT Spec) Custom PMT Spectrometer.

The very short laser pulse is essential for capturing the short LIF lifetimes expected from PAHs at high temperatures [17]. A 30ps pulse is employed here and there is provision for 80ps pulse to be used as well. The use of longer pulses, such 8ns pulses originating from typical ND-YAG lasers is adequate for measurements in laminar flames where averaging can be applied but no suitable for turbulent flames where the signal to noise ratio is a crucial factor. The use of sub-nanosecond laser pulses with sufficiently high energies brings with it possible problems of multi-photon processes which were indeed observed in the upstream region of the jets. A peak in the emission signals, without accompanying scattering intensity was detected at the exit plane of the turbulent jet, indicative of fragmentation of the ethylene fuel. This signal decreases significantly by 100mm above the exit plane. Measurements presented here are substantially downstream and are expected not to be affected by this phenomenon.

A novel set-up that consists of a purpose-built spectrometer is designed to collect temporally resolved signals. Four fast-response PMTs (Hamamatsu H10721-210 and H10721-20) are mounted at the focal plane of the spectrometer and are positioned, respectively, to intercept signals in the following spectral bands: (i) 244 to 275 nm, (ii) 339 to 370 nm, (iii) 434 to 465 nm, and (iv) 562 to 592 nm. These spectral bins were chosen to best match the two distinct fluorescence bands reported by Sirignano et al. [15] and to avoid interference from 532nm. This interference is possible from the residual second harmonic of the laser or second order reflection of the grating. The PMTs are connected to a fast high-resolution oscilloscope (Tektronix DSA70404C) capable of a sampling rate of 25 Giga-samples/s.

The choice of parabolic mirrors was driven by the need to avoid spherical and chromatic aberration. This is particularly important to avoid considering the broad collection span.

Another collection system (Oriel Spectrometer and coupled intensifier/camera) that provided details on the spectrum but not on time evolution was employed to monitor signal contributions. These details are not provided here.

## 3. Data Processing

To obtain the true lifetime of the collected LIF signals, a deconvolution process is required to extract the exponential decay function ($I_E$). The signal is convoluted by both the length of the laser pulse and the system response whose combined effect is approximately captured in the near Gaussian scattering signal illustrated in Fig. 2a. The combined system response ($I_S$) function measured a rise time of 0.85ns. Figure 2 also shows time-traces of the signals collected in the four PMTs (Elastic scattering, UV-LIF, visible LIF and LII) at various heights above the burner. While it is acknowledged that the LII signal is affected by the excessive laser fluence, it is worth noting the longer temporal decay which is typical of incandescence signal.

The collected signal ($I_C$) undergoes a deconvolution to extract the exponential emission signal ($I_E$), as per $I_C = I_S$ x $I_E$. Previous work by Sirignano et al. [15] concluded that a single term exponential was sufficient to fit the emission signal. It was found here with the short 30ps laser pulse and the quick system response that the LIF decay was better fit with a bi-exponential ($I_E(t) = A1e^{(-t/\tau 1)} + A_2e^{(-t/\tau 2)}$). This is consistent with PAH-LIF decay responses at elevated temperatures that were explored extensively by Ossler et al. [17]. Figure 3 highlights the superiority of the bi-exponential fit (Fig. 3b) over the single exponential (Fig. 3a). The effective decay time ($\tau_{eff}$) is found by curve fitting the convoluted function of bi-exponential $I_E$ and $I_S$ to $I_C$ using the exponential coefficients as weighting the effective decay is computed by: $\tau_{eff} = (A_1\tau_1 + A_2\tau_2)/(A_1 + A_2)$. The curve is fitted using a least squares technique.

## 4. Results and Discussion

The results are presented here in two sections. The first section shows measurements in laminar flames and compares with existing data while the second section demonstrates the validity of the approach in turbulent flames.

### 4.1 Laminar flame

At each centreline location in the flame 150 data points are collected and typical traces are shown in Fig. 2. These are then averaged for further analysis. The temporally resolved elastic scattering signal observed in Fig. 2a is very short with a FWHM of about 2ns. However, this is longer than what is expected from a 30ps laser pulse, showing that this signal is distorted by the response of the optical collection system. The signals collected from PMT-2 and PMT-3 shown in Figs. 2b and 2c display decay signatures not typical of gas phase PAH fluorescence. Decay times of LIF from 1 to 10ns are what are expected for these flame temperatures for Mode I particles. In the laminar flame, high levels of signal were achieved on every shot allowing for easy interpretation.

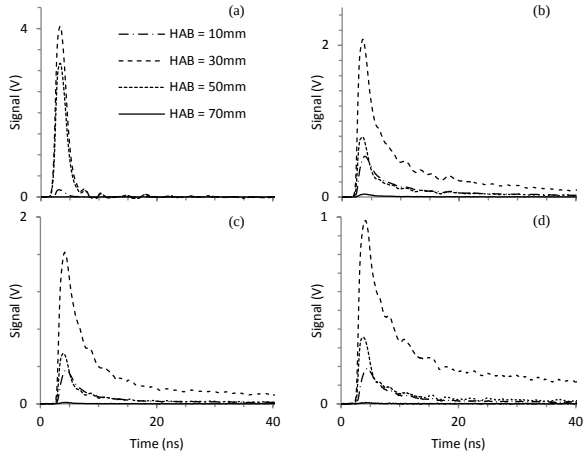


Fig 2. Temporal response of laser induced emission signals captured by PMTS in a laminar Santoro style flame. (a) Elastic scattering, (b) UV-LIF, (c) Visible LIF, (d) LII. The signals captured at a number of heights above the burner (HAB) are displayed. (In Volts).

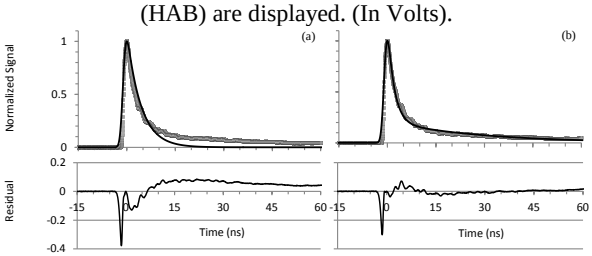


Fig 3. Exponential decay of LIF signals. A typical LIF signal fitted with Gaussian approximation for the system response function showing: (a) single exponential decay, (b) bi-exponential decay fit.

Figure 4 shows peak signal profiles along the centreline of the co-flowing laminar diffusion flame. Scattering signal shows a maximum at 40mm HAB, indicating a strong presence of Mode II soot particles in this region. An appreciable LII signal is also measured here. This corresponds well to the visibly sooting region of the flame. At a HAB of 30mm, both UV-LIF and visible-LIF peak just prior to the scattering peak by Mode II particles. This behaviour is consistent with previous works in laminar flames and also fits in with the current understanding of the soot evolution mechanisms [15]. The drop off of signal at 60mm and above is expected due to soot oxidation. However, flame tip flickering can also play a minor role. The measured slow decaying LIF indicates the presence of Mode I particles.

The decay times observed in this laminar flame are presented in Fig. 5. The longer component ($\tau 2$) for both UV-LIF and visible-LIF exist between 10 and 40ns, whereas the shorter component ($\tau 1$) is consistently below 2.5ns. This shorter component would be difficult, if not impossible, to capture with a longer system response. For HAB ranging from 30 to 50mm HAB, where the presence of fluorescing species is significant, and visible-LIF maintains a longer decay time than UV-LIF. Due to the more rigid structure of stacked PAH clusters, the fluorescence from these particles should display a longer decay time. Moving downstream the flame (higher HAB) there is an obvious trend of decreasing decay times for both UV- and visible-LIF. This

correlates well with the increase in temperature [17] typical of these diffusion flames.

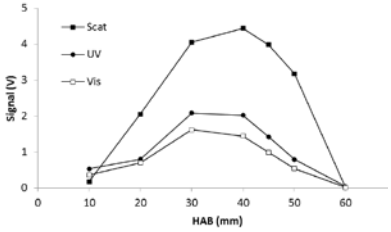


Fig 4. Laser induced emission trace along flame length. Measurements taken along the centreline of laminar Santoro [18] style flame. Signal in volts (V).

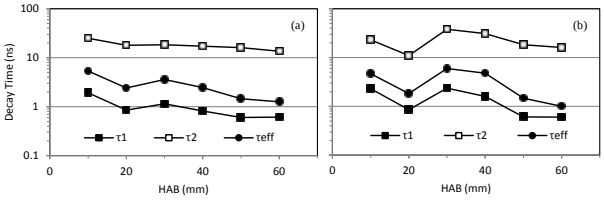


Fig 5. Bi-exponential decay time constants plotted against HAB for laminar flame. Both short (τ1) and long (τ2) time constant along with the effective (τeff) time constant. (a) UF LIF (b) Visible LIF.

## 4.2 Turbulent flame

Figure 6 shows representative samples of instantaneous traces collected from PMT-2 and PMT-3 in the turbulent flame at 300mm above the jet exit plane. Notwithstanding some expected fluctuations in the signals, such traces show very realistic patterns similar to those observed in laminar flames. The overall signal level is significantly lower in these turbulent flames compared to the laminar counterpart. This is expected since the turbulent flame studied here uses ethylene diluted with nitrogen and hence is less sooting that the pure ethylene laminar flame. Discussions on Turbulent flame results are not presented here due paper limitations but some results are presented to highlight successful measurement in turbulent flames with the ability to temporally resolve instantaneous signals.

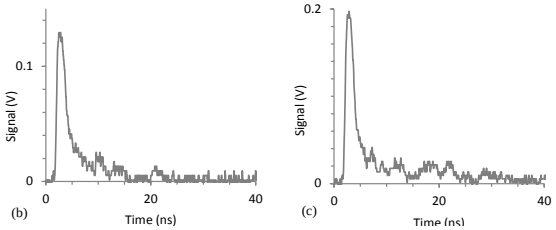


Fig 6. Instantaneous temporal response of Laser induced emission signals captured by PMTS in semi-turbulent jet flame. Taken at HAB = 300mm and radial position r = 6mm. (b) UV LIF, (c) Visible LIF (in Volts).

## 5. Conclusions

Measurements of soot evolution in an intermittent turbulent jet flame were successfully taken using a novel technique based on laser induced emission. An excitation wavelength of 266nm and picoseconds laser pulse has proven to be very suitable for the excitation of Mode I structures resulting in a laser induced fluorescence in both the UV and visible spectral region within turbulent flames while inducing additional incandescence in Mode II particles. Four collection wavelengths were monitored: elastic scattering at 266nm, UV-LIF and visible-LIF from PAH centred at 350nm and 440nm, respectively; and laser induced incandescence at 570nm. The 30ps laser pulse and fast system response was necessary to capture the temporal response of the LIF signal. It is also found that the decay times of the fluorescence signals are best represented using a bi-exponential. Reported results are consistent with those found in literature and the application in the turbulent case demonstrates that this technique can indeed be extended to track soot evolution processes in turbulent flames, however some improvements are needed.

## 6. Acknowledgments

Research at the University of Sydney was supported by the Australian Research Council. In Italy, thanks for the financial support of the Accordo di Programma MSE/CNR ‘‘Miglioramento dell'efficienza energetica dei sistemi di conversione locale di energia’’ 2013–2014.

## 5. References

[1] European Commission, http://ec.europa.eu/growth/sectors/automotive/environment-protection/emissions/index_en.htm,.
[2] A. D’Anna, Proc. Combust. Inst. **32**, 593 (2009).
[3] P. Desgroux, X. Mercier, and K. a. Thomson, Proc. Combust. Inst. **34**, 1713 (2013).
[4] H. Wang, Proc. Combust. Inst. **33**, 41 (2011).
[5] T. U. of Adelaide, http://www.adelaide.edu.au/cet/isfworkshop/,.
[6] S. Bejaoui, X. Mercier, P. Desgroux, and E. Therssen, Combust. Flame **161**, 2479 (2014).
[7] H. Bladh, N.-E. Olofsson, T. Mouton, J. Simonsson, X. Mercier, A. Faccinetto, P.-E. Bengtsson, and P. Desgroux, Proc. Combust. Inst. **35**, 1 (2014).
[8] Q. N. Chan, P. R. Medwell, P. a M. Kalt, Z. T. Alwahabi, B. B. Dally, and G. J. Nathan, Proc. Combust. Inst. **33**, 791 (2011).
[9] M. Commodo, G. Tessitore, G. De Falco, A. Bruno, P. Minutolo, and A. D’Anna, Proc. Combust. Inst. **35**, 1795 (2014).
[10] A. D’Anna, M. Commodo, M. Sirignano, P. Minutolo, and R. Pagliara, Proc. Combust. Inst. **32 I**, 793 (2009).
[11] G. De Falco, M. Commodo, C. Bonavolontà, G. P. Pepe, P. Minutolo, and A. D’Anna, Combust. Flame **161**, 3201 (2014).
[12] A. Faccinetto, P. Desgroux, M. Ziskind, E. Therssen, and C. Focsa, Combust. Flame **158**, 227 (2011).
[13] L. A. Sgro, A. D’Anna, and P. Minutolo, Combust. Flame **158**, 1418 (2011).
[14] M. Sirignano, M. Alf, A. Tregrossi, A. Ciajolo, and A. D’Anna, Proc. Combust. Inst. **33**, 633 (2011).
[15] M. Sirignano, A. Collina, M. Commodo, P. Minutolo, and A. D’Anna, Combust. Flame **159**, 1663 (2012).
[16] M. Sirignano and A. D’Anna, Proc. Combust. Inst. **34**, 1877 (2013).
[17] F. Ossler, T. Metz, and M. Ald, Appl. Phys. B **478**, 465 (2001).
[18] R. J. Santoro, H. G. Semerjian, and R. a. Dobbins, Combust. Flame **51**, 203 (1983).
[19] I. B. Berlman, *Handbook of Fluorescence Spectra of Aromatic Molecules* (1971).
[20] T. Joutsenoja, A. D’Anna, A. D’Alessio, and M. . Nazzaro, Appl. Spectrosc. **55**, 130 (2001).

# The Effect of Exit Strain Rate on Soot Volume Fraction in Turbulent Non-Premixed Jet Flames

S. M. Mahmoud [a], Z. W. Sun [a], B. B. Dally [a], Z. T. Alwahabi [b], P. R. Medwell [a] and G. J. Nathan[a]
Schools of [a] Mechanical and [b] Chemical Engineering
Centre for Energy Technology, University of Adelaide, S.A. 5005, AUSTRALIA
saleh.mahmoud@adelaide.edu.au

## Abstract

Laser-Induced Incandescence (LII) measurements from soot were conducted in three attached turbulent non-premixed jet flames spanning various locations in each flame. The effect of the variation of the strain rate on soot behaviour is assessed through the comparison of the mean and integrated data for the three flames. The change is strain rate was achieved through the simultaneous variation of the jet burner diameter and the fuel exit velocity at the nozzle, thus allowing a systematic study of the influence of the exit strain rate in turbulent combustion while keeping the exit Reynold's number constant. These measurements, which are part of an ongoing comprehensive study of the effect of strain rate on mean, instantaneous, integrated soot volume fraction as well as intermittency data, reveal an inverse relationship between the exit strain rate with the mean and instantaneous soot volume fraction (SVF), and agree with radiation tests performed previously for the same flames.

## Introduction

Soot is one of the key features of many combustion systems since it plays a significant and a highly effective role in radiative heat transfer [1,2]. The complex processes of soot formation and oxidation in flames are governed by interdependent parameters such as fuel type, strain rate, pressure, temperature, and mixing rate [3]. Importantly, many of these dependencies are coupled in the presence of turbulence. The effect of the local flame strain rate on soot formation has been investigated in various studies, but mostly in laminar flames because such flames allow stable and well-defined conditions that are not achievable in turbulent conditions. These studies found out that both soot concentration and soot zone thickness decrease with increasing flame strain rate [4-6]. However, in turbulent sooty flames the measurements of strain rate are predominantly limited to characteristic, or global, rather than local values due to the difficulties of performing such measurements in unsteady flames containing soot.

Qamar *et al.* [7] measured the soot volume fraction in three different turbulent diffusion flames using laser-induced incandescence (LII). Their work provided insight into the effect of global mixing rate on the instantaneous local and the average soot volume fraction. The global mixing rate calculated by Qamar *et al*. is defined as the inverse global residence time, and is calculated as the volume flow rate of fuel divided by the flame volume [7, 8]. Their measurements reveal an inverse relationship between global mixing rate and both the total amount of soot in the flame and local instantaneous soot volume fractions, broadly consistent with trends in laminar flames. Qamar *et al*. work, despite its significance, was performed on three different burners albeit with similar operating conditions. Their measurements do not provide information on the dependency of the exit strain rate or the Reynolds number, which together characterize the mixing processes, as well as the soot formation and evolution processes. Kent and Bastin [9] investigated the effect of mixing in acetylene turbulent jet flames from simple pipe nozzles and showed that the average soot volume fraction decreases with increasing characteristic strain rate. Additionally, the rate of this decrease is higher at high mixing rates than at low mixing rates. Noteworthy is that, soot extinction which is a line-of-sight technique was used for their measurement, thus limiting the data presented to averaged values with no information about the local soot in the flames. Besides, stabilizers were added some distance from the nozzle to the flames with high Reynolds number, which would interfere with the flame chemical and physical scales.

The three-dimensional and unsteady nature of turbulent flames makes it highly desirable to provide measurements in multiple dimensions, allowing the acquisition of spatially correlated scalars and their gradients which influence soot evolution [10]. In order to allow the joint application of experiments and computational fluid dynamics, from which the major advances in combustion research have been derived, it is necessary for the experiments to be performed under very well characterized conditions. In a similar vein, owing to the complexity of soot evolution in turbulent flames, it is desirable that measurements be performed in attached turbulent

flames, since lifted flames are not only more difficult to predict but also strongly inhibit soot formation through partial premixing. Hence for this purpose, LII imaging of soot in a series of five attached turbulent non-premixed jet flames was performed and some preliminary results are present in this paper. The effect of two parameters, the exit strain rate and the exit Reynolds number, was assessed in this study. The exit strain rate was defined as the ratio of the exit fuel velocity to the exit jet diameter, and is assessed separately through a simultaneous variation of the jet burner diameter and the fuel exit velocity at the nozzle. This variation allows a systemic study of the influence of the aforesaid parameter in turbulent combustion through isolating its effects. While the results presented here are preliminary and restricted to strain rate effect, detailed results of the study will be reported in the near future. This study aims at contributing towards achieving a better understanding of soot evolution in turbulent flames by the joint application of high fidelity databases and model development.

## Experimental Setup

### *Flames*

Three attached turbulent non-premixed jet flames were used in this study. The jet flames burn an identical mixture of ethylene-hydrogen-nitrogen at 40-41-19 percent composition by volume, respectively, with co-flowing air at ambient temperature and atmospheric pressure. Full details of the flame conditions are provided in Table 1. Time-averaged photographs with long-time exposures of flames 1 to 3 are presented in Figure 1. Ethylene ($C_2H_4$) was selected as the fuel to examine soot formation and destruction due to its relatively well-defined chemistry and high soot yields. Hydrogen ($H_2$) was premixed with ethylene in order to keep the flames attached at high Reynolds numbers. Nitrogen ($N_2$) was also added as a diluent to achieve a high Reynolds number and higher stoichiometric mixture fraction through increasing

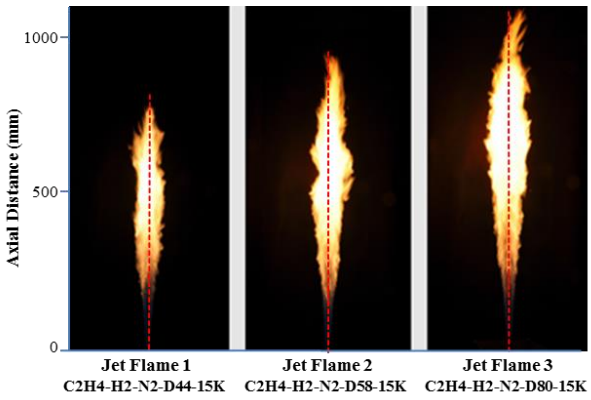


**Fig 1**. Photographs of the attached jet flames 1 to 3, from left to right, respectively. Dashed red line corresponds to the centreline location. Each photograph is 500 mm width by 1100 mm height.

Reynolds number, as well as to influence soot formation through thermal means. Flames from this set have been employed in previous studies, such in simultaneous planar measurements of temperature and soot concentration by the authors [11] and a study of the global characteristics of hydrogen–hydrocarbon blended fuels by Dong *et al*. [12].

### *Burners*

The burners used to stabilise the flames comprise a set of round aluminium tube of 4.4 mm, 5.8 mm, and 8 mm ID, with a tapered end and a wall thickness of 1 mm each. The pipes were mounted in the centre of a contraction delivering co-flowing air at ambient temperature and at a mean velocity of 1.1 m/s. The contraction has a square cross-section of dimensions 150 mm by 150 mm, and the pipe jet burner outlet rises above the contraction edge by a distance of 18 mm. A traverse was used to move the burner and contraction vertically through the optical diagnostic beams to enable measurements throughout various heights of the entire flame.

The extraction hood was traversed with the flame to avoid any influence of the exhaust extraction on the flames. Measurements were performed at thirteen axial locations spanning most regions of the flame. Data from five axial locations, $x/Lf$= 0.24, 0.42, 0.61, 0.73 and 0.90, where $x$ is the axial distance from the nozzle exit, as well as integrated data over full flame length are presented in this paper.

### *Laser Induced Incandescence (LII)*

Soot concentration was measured quantitatively using the LII technique. Soot Incandescence was recorded on an ICCD camera and then converted to meaningful *SVF* data. Calibration for the LII technique was performed via soot extinction from an ethylene flat flame generated by a McKenna burner, using a CW DPSS laser at 1064 nm. LII was performed with a pulsed Nd:YAG laser at 1064 nm, while the incandescence was collected with an ICCD camera through a 430-nm (10 nm bandwidth) interference filter. This arrangement was selected to suppress the $C_2$ laser-induced emission and to minimize interference from flame radiation [13]. The gate-width of the LII camera was set to 50 ns, while the timing was set to coincide with the LII excitation, as this has been proven to decrease the sensitivity of the signal to the soot particle size [14]. The LII laser sheet was approximately 24 mm high and 500 µm thick and captures the full flame width. The laser fluence was kept above 0.5 J/cm$^2$, in the plateau region of the LII response curve, to minimize any influence on the LII signal due to fluence variation from attenuation or from beam "steering". The influence of beam steering and signal trapping on the accuracy of soot volume

**Table 1.** Flow conditions of the attached jet flames

| Flame name | | Central Jet Diameter (D) | Average Exit Velocity (U) | Exit Strain Rate (U/D) | Exit Reynolds Number | Visible Flame Length |
|---|---|---|---|---|---|---|
| | | (mm) | (m/sec) | ($s^{-1}$) | (-) | (mm) |
| C2H4-H2-N2-D44-15K | **Flame 1** | 4.4 | 56.8 | 12,900 | 15,000 | 750 |
| C2H4-H2-N2-D58-15K | **Flame 2** | 5.8 | 42.4 | 7,300 | 15,000 | 975 |
| C2H4-H2-N2-D80-15K | **Flame 3** | 8 | 31.5 | 4,000 | 15,000 | 1190 |

fraction has been fully investigated in turbulent non-premixed sooting flames by Sun *et al.* [15]. The maximum "steering" of the laser beams in the flames was measured to be 2 milli-rad, corresponding to a 50% increase in the laser sheet thickness from one side of the flame to the other. This in turn leads to the spatial resolution in the out-of-plane direction varying from 300 to 450 µm throughout the flame. The data was binned over 3 pixels in height and width, resulting in a final volume imaged by each binned pixel being 0.72 x 0.72 x 0.75 mm for all measurements.

## Results

A comparison of the axial-radial distribution of the mean and the room mean square (RMS) of the SVF in parts per billion (ppb), collected from 500 instantaneous images, is presented in Figure 2.

The minimum detection limit is 20 ppb, while the uncertainty in the measurements is calculated to be 20%. At any given height, from $x/L_f$ = 0.1 throughout to the flame tip region, a consistent trend of soot radial distribution within the three flames is found, where more soot is found in flames with lower exit strain rate, a trend noticeable for both mean and RMS data. It is observed that the maximum mean soot volume fraction, for the three flames, occurs on the nozzle axis, while its axial location is consistent for the three flames ($x/L_f$ ~ 0.60). This is consistent with the trends in radiant heat profiles for the same profiles reported by Xue *et al.*, where the peak heat flux from the flames was found in the downstream region of $0.6 < x/L_f < 0.7$ [12], confirming the significant role of soot in flame radiation and temperature. It is also close to the SVF peak at $x/L_f$ =0.6 reported for the simple jet flame measured by Qamar *et al.* [7].

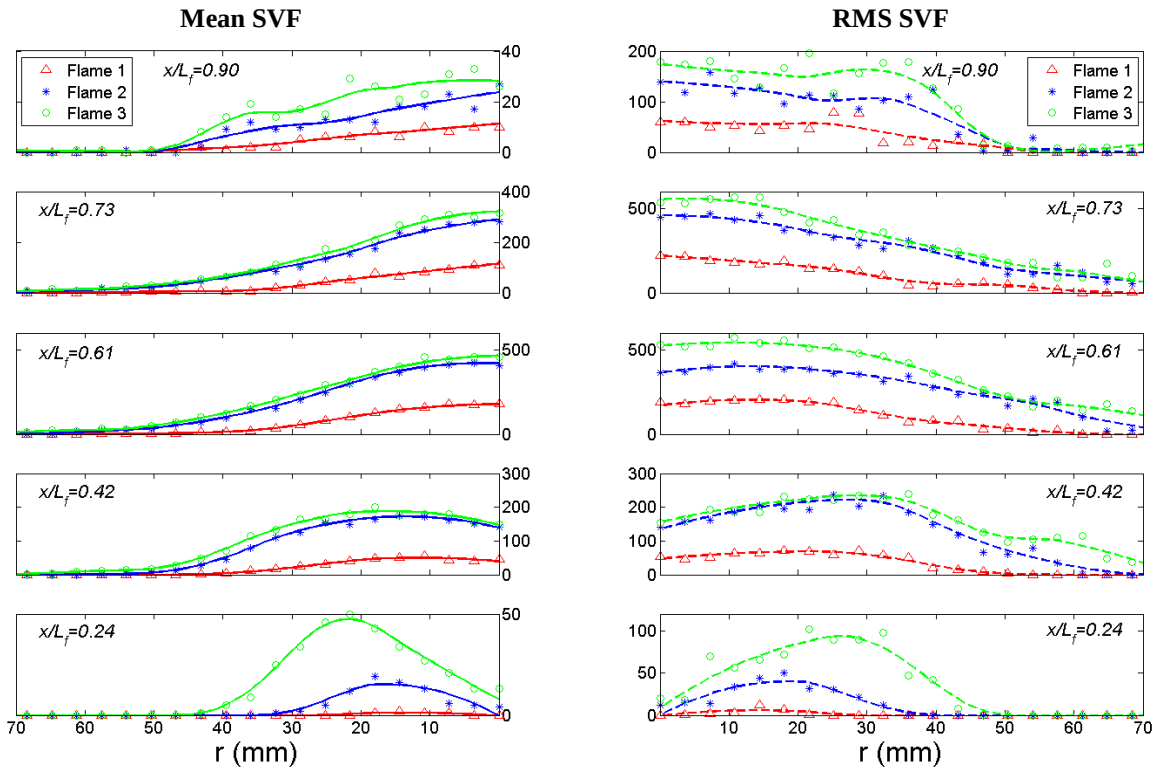


**Fig 2.** Mean and RMS radial profiles of soot volume fraction, at various downstream locations. Mean profiles of flames 1-3 is on the left side, RMS profiles on the right side. Flames 1, 2 and 3 have the same Reynolds number (15,000) and different exit strain rates of 12,900, 7,300 and 4,000 $sec^{-1}$ respectively. Measurements were conducted across the full flame width. Profiles for one side of the flames are presented since symmetry tests for all flames showed good results.

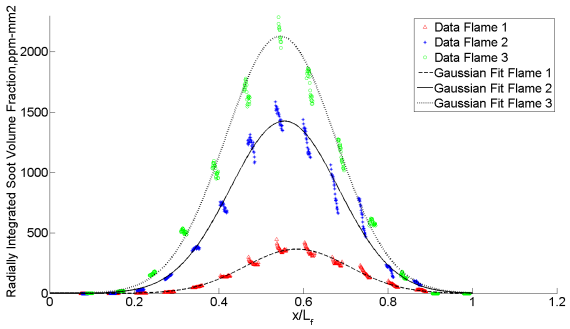


**Fig 3.** Axial profiles of radially integrated SVF, in ppm, over full flame length. Markers represent experimental data, while the profiles are Gaussian fits for the experimental data.

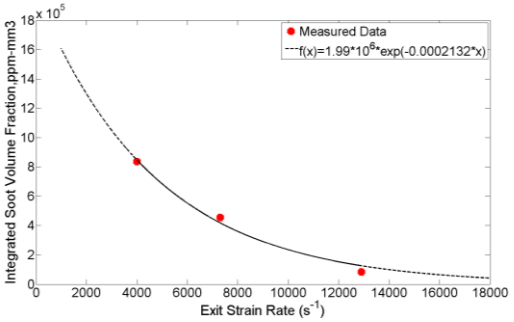


**Fig 4.** Integrated SVF over full flame volume. Markers represent values of integrated data. Curve plot is an exponential function of the integrated data.

High RMS values for SVF are reported throughout the flame, owing to large fluctuations of soot concentration. Higher ratio of RMS to mean SVF values is observed at far downstream and upstream location measurements, indicating high intermittency at these locations.

Total soot per axial length is measured by integrating mean SVF over the cross-section of the flame at each axial height. The integrated values, which have the units of soot volume per unit length, are presented in Figure 3. These results show a similar trend of the inverse relationship between exit strain rate and integrated SVF in the mean and RMS data. The data was fitted with a Gaussian distribution function with $R^2$ value of 0.98. Consistent with Figure 2, the location of peak SVF for all flames is in the range of $0.56 < x/Lf < 0.58$.

Figure 4 presents total soot per unit volume of each flame, calculated by estimating the area under the Gaussian curve plots from radially integrated SVF over non-normalized flame length (plots are not presented here). It is deduced from figure 4 that flame 3 has about 1.8 more soot than flame 2, which in turn has 5 times more soot than flame 1. The data points were then fitted with an exponential curve function, with an $R^2$ value of 0.90. This function is chosen since the volume integrated SVF is predicted to peak at very low strain rates and is predicted to decay with increasing exit strain rate. The reciprocal fit, while plausible, can be used to predict the total amount of soot concentration for various strain rates, for turbulent non-premixed flames of similar composition and exit flow conditions. A detailed analysis of the effect of the strain rate on the mean, integrated, and instantaneous SVF, as well as intermittency studies is currently underway, and will be presented in future publications.

## Conclusions

Preliminary results of the effect of varying the exit strain rate on soot behaviour in turbulent diffusion flames are presented. These results reveal an inverse relationship between SVF and exit strain rate and shows consistency of the mean and integrated SVF profiles which peak at the same location for all flames investigated in this study, and with radiation heat profiles from literature. Further analysis will follow in upcoming publications.

## References

1. C. R. Shaddix and T. C. Williams, *Am. Sci*. **95**, 232–239 (2007).
2. D.W. Dockery and P. H. Stone, *N. Engl. J. Med*. **356**, 511–513 (2007).
3. J.H. Kent, D. Honnery, *Combust. Sci. Technol*. **54**, 383–397 (1987).
4. M.E. Decroix, W.L. Roberts, *Combust. Sci. Technol*. **160**, 165–189 (2000).
5. A. Beltrame, P. Porshnev, W. Merchan-Merchan, A. Saveliev, A. Fridman, L.A. Kennedy, O. Petrova,S. Zhdanouk, F. Amouri, O. Charon, *Combust. Flame* **124**, 295–310 (2001).
6. H. Wang, D.X. Du, C.J. Sung, C.K. Law, *Proc.Combust. Inst.* **26** (1996) 2359–2368.
7. N.H. Qamar, G.J. Nathan, Z.T. Alwahabi, D.K. King, *Proc. Combust.* Inst. **30** (2005) 1493–1500.
8. S.R. Turns, F.H. Myhr, Combust. Flame 87 (1991) 319–335.
9. J.H. Kent, S.J. Bastin, *Combust. Flame* **56,** 29–42 (1984).
10. R.S. Barlow, *Proc. Combust. Inst.* **31**, 49–75 (2007).
11. S.M. Mahmoud, G.J. Nathan, P.R. Medwell et al, *Proc.Combust. Inst.*, **35**, 1931-1938 (2015).
12. X. Dong, G.J. Nathan, S. Mahmoud, P.J. Ashman, D. Gu, B.B. Dally, *Combust. Flame* **162**, 1326–1335 (2015).
13. C. Schulz, B.F. Kock, M. Hofmann, et al. *Appl.Phys*. B **83**, 333–354 (2006).
14. R.L. Vander Wal, *Appl. Opt.* **35,** 6548–6559 (1996).
15. Z. W. Sun, Z. T. Alwahabi, D. H. Gu, S. M. Mahmoud, G. J. Nathan, B. B. Dally, *Appl. Phys. B*, DOI 10.1007/s00340-015-6080-6.

**Proceedings of the Australian Combustion Symposium**
**December 7-9, 2015, The University of Melbourne**

# Development of an in-flame thermophoretic soot sampling device

C. Wang[1], Q.N. Chan[1,*], S. Kook[1], E.R. Hawkes[1,2], P.R. Medwell[3], J. Lee[4]
[1]School of Mechanical and Manufacturing Engineering
[2]School of Photovoltaic and Renewable Energy Engineering
UNSW Australia NSW 2052 Australia
[3]School of Mechanical Engineering
The University of Adelaide, Adelaide SA 5005 Australia
[4]School of Mechanical Engineering, Korea University of Technology and Education,
1600 Choongjeol ro, Byeongcheonmyeon, Cheonan, South Korea

## Abstract
A pneumatically-driven thermophoretic sampling system that can sample soot particles directly from flame is presented. The instantaneous probe motion of the sampling system at different piston actuating pressure settings for the sampling piston and the effect of its intrusion on the flame are directly analyzed using high-speed imaging. The assessments reveal that spatial uncertainties of the soot sampling system are ~2.2 and 2.6 mm in vertical and the lateral directions, when operated at an optimum piston actuating pressure of 4 bar. The results also demonstrate that whilst the flame is perturbed when the sampling probe is inserted into the flame, there are no indications of significant instabilities or turbulence in the upstream or downstream regions from the probe.

*Keywords: Soot, Transmission electron microscope, Laminar flame, Thermophoretic soot sampling.*

## 1. Introduction

Soot particles are often formed in combustion processes of hydrocarbon fuels, and mainly consist of carbon and appear as aggregated structures of near-spherical primary particles. Many previous studies have reported strong correlations between the soot morphological information and their impact on soot growth and destruction process within flame, which in turn have a strong influence on the flame radiative heat transfer and pollutant emission processes [1, 2]. Knowledge of the soot morphology information has also been reported to provide critical insights to its environmental and health impact [3, 4]. The investigation and quantification of soot morphology is therefore important and have motivated considerable interest (*e.g.* [1, 3]).

There are many techniques for soot diagnostics [5-7], both intrusive and non-intrusive, which are employed by the research community however thermophoretic sampling technique remains the only method that permits a direct observation of soot morphological information. Thermophoretic sampling, as its name implies, relies on thermophoresis effect to drive the deposition of soot particles from hot medium, such as flame, towards the cold surface of the sampling grid. The sampled soot particles are later examined using electron microscope (most often transmission electron microscope, TEM) to provide well-resolved soot TEM images. Such images can be analyzed to provide important soot morphological information, such as primary particle diameters, radius of gyration and fractal dimensions [1]. A thermophoretic sampling system typically comprises of a sampling probe on which a sampling grid is mounted. The sampling probe is usually attached to the end of the arm of a pneumatic system, and is moved quickly through the flame for soot sampling. One challenge is assembling a probe insertion system that can enable a rapid insertion and extraction of the grid holder, given that a typical exposure or sampling time used for the method ranges from 10 to 200 ms. Such short sampling time is necessary to minimize probe heating, in addition to ensuring a low grid coverage (less than 10%), so that the soot particles sampled are sufficiently isolated [8]. It is also essential that the probe transit time (insertion and extraction) is kept shorter than the sampling time (less than 20%) so that an insignificant number of samples are collected anywhere in the flame, other than the intended location [2]. Another challenge is to minimize flame perturbations when the intrusive sampling method is used. A thin sampling probe is therefore normally designed and used, to minimize the blocking of flow stream. Nonetheless, using a thin probe can be problematic as it has low bending stiffness [9]. The thin probe can therefore bend excessively during the rapid insertion/extraction process, which will then impact on the accuracy of the soot sampling process, if used without due caution. In view of the challenges described above, the design of the sampling probe and probe insertion system is therefore of great importance.

It should be noted that despite the substantial research work that were performed with thermophoretic sampling, very little known/reported about the spatial uncertainties and the degree of flame perturbation that are associated with the sampling devices used. The current work aims to assess the instantaneous probe motion and the spatial uncertainties of a pneumatically-driven thermophoretic soot sampling device that is designed and built in-house. The current work also assesses the effect of the intrusive sampling method on

* Corresponding author:
Phone: (+61) 2 93854116
Email: qing.chan@unsw.edu.au

the flame, when the probe is inserted in the flame. The knowledge of the uncertainties/effect is important to enable the sampling device to be used with higher confidence. Accordingly, the present paper details the steps that are needed for the assessments.

## 2. Experimental

The thermophoretic soot sampling system was tested in a laminar ethylene-air diffusion flame produced using a Wolfhard-Parker style burner [10, 11], which is shown in Fig. 1. The burner consists of three parallel rectangular slots that are 41 mm in length. The outer slots, which carried the oxidizer, are 16 mm wide each, whilst the inner fuel slot has a width of 8 mm. For the current work, the air co-flow and ethylene gas were supplied to the outer and central slots, at flow rates of 2.4 and 9 SLM, respectively. A nitrogen co-flow was introduced at a flow rate of 3 SLM to the short ends of the inner fuel slot to prevent the formation of end-flames and draft [10]. A two-dimensional contraction made of two curved wire mesh screens was used to stabilize the flames and to prevent flickering [10]. A stainless steel sampling probe with a 4 mm width and 2 mm thickness was machined and used. The probe was designed to have an aspect ratio (thickness/width) of 0.5, as a minimum aspect ratio value of 0.2 was recommended for reasonable bending stiffness [9]. When sampling was performed, a 3 mm diameter carbon-supported TEM grid (Agar Scientic, Agar-S160-H) was attached to a 3.1 mm diameter circular recess at the tip of the sampling probe. The probe was mounted onto the end of a pneumatically-driven double-acting cylinder system (Bimba Manufacturing, P/N: NR-096-DXPB). A double-acting pneumatic cylinder with damper was selected as the damper can help to dampen the sudden impact between the piston and the end cap of the cylinder, when the piston reaches the end of its stroke. Such motion can cause the probe to deflect and sample from locations other than its intended sampling position. The cylinder was controlled by a four-way solenoid valve (Mac Valves, P/N: 411A-DOA-DM-DDA-J2JD) with compressed nitrogen as the actuating gas. The inlet pressure of the compressed gas was regulated using a pressure regulator (CKD, P/N: W3000-10-W) with an operating pressure ranging from 0 to 7 bar. The sampling system is mounted on a translational stage (Thorlabs, P/N: L490/M) to permit vertical translation and therefore, soot sampling at different heights above burner (HABs). An Arduino microcontroller was used to trigger and control the sampling system.

## 3. Results and Discussion

In order to assess the positional uncertainty associated with the dampened motion and its impact on the spatial accuracy of the sampling technique, a series of instantaneous images of the probe during operation were captured using a high-speed camera (Phantom v7.3) against a bright background. Figures 2(a) and 2(b) present the typical instantaneous images of the same sampling probe, when inserted with horizontal and

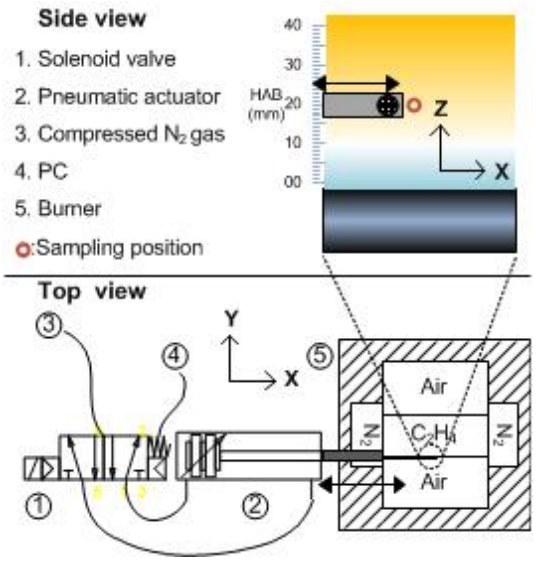

Fig. 1: Experimental setup.

vertical orientation, at the moment of maximum deflection from the centerline. The horizontal and vertical displacements of the probe, from the instance when it reached its final position, are subsequently plotted as a function of time at three selected piston actuating pressure settings, as shown in Fig. 3. The imaging of the probe motion was performed three times and the uncertainties associated with each data point, which are not presented in the figures for clarity, are found to be generally small (less than 0.26 mm). From the figure, it can be seen that the maximum horizontal and vertical displacement from the centerline caused by the impact vary from 2.2 to 2.8 mm, depending on the piston actuating pressure and the orientation of the sampling probe. The deviation is found to increase with the piston actuating pressure used, and is generally observed to be greater in the horizontal or lateral direction. The effect of the piston actuating pressure of the sampling piston on the probe motion is also further assessed by plotting the insertion velocity of the sampling probe, as a function of time after the start of triggering, as shown in Fig 4, for the three selected piston actuating pressures. From the plot, it can be seen the lowest maximum velocity value (3.4 m/s) and therefore the longest the transition period is attained when an piston actuating pressure of 2 bar was applied, which is to be expected. From the figure, it can also be seen that whilst the maximum velocity value of the probe increases when higher piston actuating pressures of 4 and 6 bar were applied, the average speed attained during the transition period is similar for both. These results imply that for the present system, even though a shorter probe transition period can be attained with higher piston actuating pressure, the reduction is not significant once the pressure exceeds 4 bar. In view of the need to minimize the probe transition period whilst maintaining a reasonably low spatial uncertainty for accurate soot particle sampling, an piston actuating pressure of 4 bar was therefore specified for all experiments. The spatial uncertainties associated with the sampling system were therefore ~2.2 and 2.6 mm in

the vertical and lateral directions, respectively, when operated with a piston actuating pressure of 4 bar.

Following the approach of Leschowski *et al.* [12], a series of raw soot luminosity images were captured using the high-speed camera (Phantom v7.3), as shown in Fig. 5, and was used to help examine the effect of the probe penetrating the flame. It is noted that no spectral filter was used as signal separation is not important for the purpose of the present assessment [12]. Figures 5(a) and 5(b) present the typical raw soot luminosity images of the flame that were observed, when the sampling probe was 5 ms from reaching its intended sampling position, and when the probe was at its final location. It is noted that the sampling probe was positioned at 20 mm HAB for these set of images. The measured signal profiles acquired at the two different timings are then examined more quantitatively by averaging the signal intensities horizontally in the white-dashed regions indicated in the soot luminosity images in Fig. 5, to generate the vertical profiles in Fig. 6. The white-dashed region was selected so that its horizontal position coincided with the position where the TEM grid was located on the probe, when the sampling probe was at its final position. From Fig. 6, it can be seen that there are some discrepancies in the vertical profile shapes. As is noted in the earlier section, the sampling probe used was 4 mm wide, and was therefore positioned from 18 to 22 mm HAB when fully inserted into the flame at a HAB of 20 mm. The drop in the signal intensity observed between 18 and 22 mm HAB in the vertical profile for the second image is therefore attributed the blocking of the soot luminosity signal by the sampling probe. Nonetheless, the measured signal intensity in the regions from 2 mm below to 3 mm above specified region is also found to be different from the vertical profile of the first image. The discrepancies in the profiles observed demonstrate that the flame is inevitably perturbed by the presence of the sampling probe. It is, however, important to note that the measured intensity profiles are still similar in the upstream region (HAB<16 mm), and are observed to overlap again at the downstream region (HAB>25 mm) after the probe. The finding indicates that the intrusion of the sampling probe does not significantly affect the upstream region of the diffusion flame, and that the combustion gases can flow smoothly across the probe without experiencing significant instabilities or turbulences [12].

Using the current device, soot was sampled from the burner, firing laminar ethylene-air flame. It is noted that the characteristic insertion and retraction times were adjusted to 12 ms each, and the sampling time of the sampling probe in the flame was set to ~100 ms. The probe was aligned so that it was inserted in line with the peak soot layer [11], to maximize the amount of soot particles being sampled. The sample acquired was imaged using a TEM (JEOL 1400) at UNSW Australia, operated at an electron acceleration voltage of 120 keV. It is beyond the scope of this paper to analyze the structure of the soot samples in detail, although an example for sample acquired at 20 mm HAB is shown in Fig. 7. From the figure, it can be seen that the soot

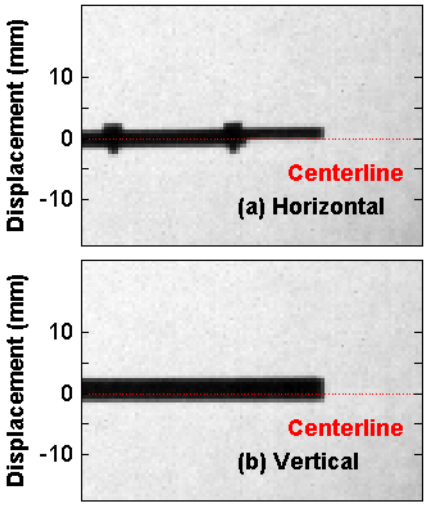


Fig. 2: Typical images of the (a) horizontally and (b) vertically inserted sampling probe at the moment of maximum deviation from the centreline (red dashed line).

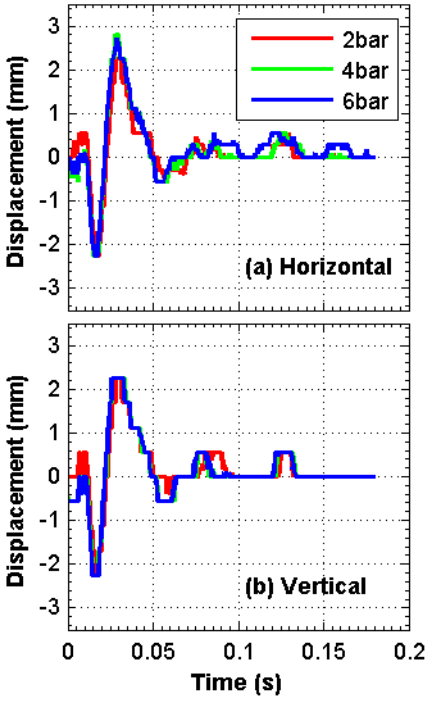


Fig. 3: (a) Horizontal and (b) vertical vibration motions of the sampling probe at its final position, as a function of time.

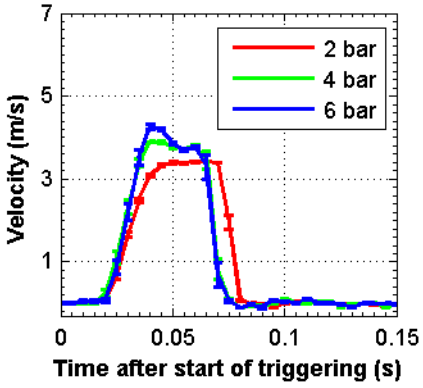


Fig. 4: Velocity of the sampling probe as a function of time after start of triggering, at three selected piston actuating pressure settings.

particles collected possess liquid-like appearances that are poly-dispersed in size with diffused boundaries. In the image, it can also be seen that some of the larger droplets have black nucleus or nuclei immersed inside them. The presence of the liquid structures, with and without the black nucleus or nuclei, indicates that soot inception was still taking place at the sampling position. It is noted that the liquid-like structures, which are also termed as soot precursors in the literature, are commonly observed for soot samples previously acquired from low flame regions in other burners, where intense particle inception and coagulation are expected to occur [9]. The absence of the aggregated/more mature particles implies the contamination of the sampling grid by soot material originating from locations other than its intended sampling position is not significant. The device can therefore be used to sample soot reliably [9].

## 4. Conclusions

A pneumatically-driven device for thermophoretic sampling of soot particles in a flame was built and tested. The operation of the device was analyzed by high-speed measurements of the position of sampling probe and its effect on the flame. The sampling system was observed to have spatial uncertainties of ~2.2 and 2.6 mm in vertical and the lateral directions, when used with an optimum piston actuating pressure of 4 bar. The sampling process was observed to have an influence on the soot luminosity in the region up to 2 mm below and 3 mm above the probe. No indications of significant instabilities or turbulence were found.

## 5. Acknowledgments

The authors wish to acknowledge the financial support of Australia Research Council (ARC) and UNSW Australia.

## 6. References

1 S. Kook, R. Zhang, Q. N. Chan, T. Aizawa, K. Kondo, L. M. Pickett, E. Cenker, G. Bruneaux, O. Andersson, J.H. Pagels and E.Z. Nordin, SAE Paper No. 2015-01-1991, 2015.

2 Ü.Ö. Köylü, G.M. Faeth, T.L. Farias and M.G. Carvalho, Combustion and Flame 100 (1995), pp. 621-633.

3 Grishin, K. Thomson, F. Migliorini and J.J. Sloan, Applied Optics 51 (2012), pp. 610-620.

4 B. Frank, R. Schlögl and D.S. Su, Environ. Sci. Technol. 47 (2013), pp. 3026-3027.

5 Q.N. Chan, P.R. Medwell, Z.T. Alwahabi, B.B. Dally and G.J. Nathan, Applied Physics B 104 (2011), pp. 189-198

6 P.R. Medwell, Q.N. Chan, B.B. Dally, S. Mahmoud, Z.T. Alwahabi, GJ Nathan, Proceedings of the Combustion Institute 34 (2013), pp. 3619-3627

7 A.E. Karataş, Ö.L. Gülder, Progress in Energy and Combustion Science 38 (2012), pp. 818-845

8 J. Lee and S.Y. Yang, International Journal of Mechanical Sciences 76 (2013), pp. 152-157.

9 J. Lee, I. Altman and M. Choi, Journal of Aerosol Science 39 (2008), pp. 418-431

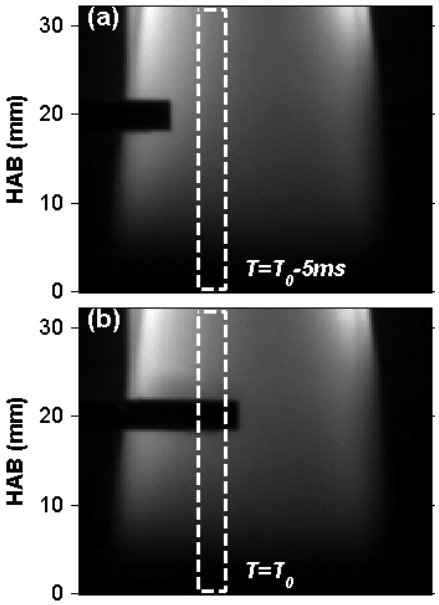


Fig. 5: Raw soot luminosity images of the ethylene/air flame captured with the sampling probe penetrating through the sooting area of the flame. The images were captured when the holder was (a) 5 ms before reaching its intended sampling location, and (b) when it was at its final position. The white dashed region is the image area that was horizontally integrated to assess the impact of the probe intrusion on the flame region.

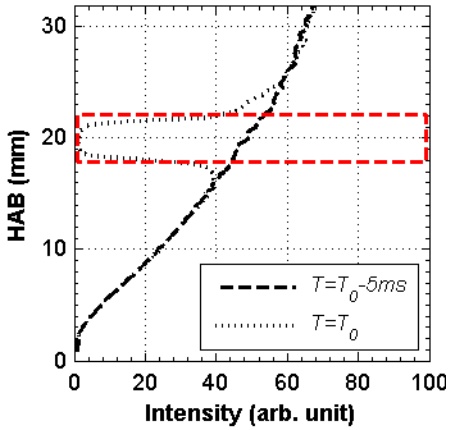


Fig. 6: Vertical profiles for the flame soot luminosity images in Fig. 5, which were captured with the sampling probe inserted at two different timings/positions. The red-dashed region indicates the position of the in relation to the height above flame region.

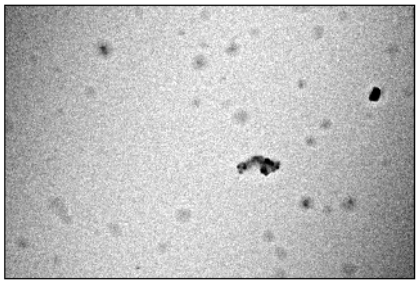

Fig. 7: A typical TEM image of soot, sampled at 20 mm HAB.

10 C. Wey, E.A. Powell and J.I. Jagoda, Combustion Science and Technology 41 (1984), pp. 173-190.

11 T.C. Williams, C.R. Shaddix, K.A. Jensen and J.M. Suo-Anttila, International Journal of Heat and Mass Transfer 50 (2007), pp. 1616-1630

12 M. Leschowski, T. Dreier, C. Schulz, Review of Scientific Instruments 85 (2014), 045103.

**Proceedings of the Australian Combustion Symposium**
**December 7-9, 2015, The University of Melbourne**

# External Irradiation Effect on the Evolution of In-flame Soot Species

C. Wang[1], Q.N. Chan[1, *], S. Kook[1], E.R. Hawkes[1, 2], P.R. Medwell[3], J.Lee[4]
[1]School of Mechanical and Manufacturing Engineering
[2]School of Photovoltaic and Renewable Energy Engineering
UNSW Australia NSW 2052 Australia
[3]School of Mechanical Engineering
The University of Adelaide, Adelaide SA 5005 Australia
[4]School of Mechanical Engineering, Korea University of Technology and Education,
1600 Choongjeol ro, Byeongcheonmyeon, Cheonan, South Korea

## Abstract

Soot samples that are thermophoretically sampled from a laminar non-premixed ethylene-air flame from a Wolfhard-Parker style burner are presented. The soot samples are collected at 20 and 40 mm above the burner, with and without the introduction of external broadband irradiation, to assess the effect of external irradiation on the evolution of in-flame soot species. The soot samples acquired are imaged using both normal-resolution and high-resolution transmission electron microscopes (TEMs) and the images are compared and analysed in detail. The assessments reveal that the soot samples acquired, from both within and at the downstream region after the vicinity of the external irradiation, are of more mature appearances when external irradiation is introduced. The results imply that the application of external irradiation source can accelerate the in-flame soot generation process, and that the effect can persist downstream from the irradiation location.

*Keywords: Soot morphology, Thermophoretic sampling, Laminar Flame, External irradiation*

## 1. Introduction

The interaction of radiation and soot species is a subject that is of great interest to the research and industrial communities due to the complexity of the interaction and also its impact on the ensuing combustion processes. Soot, at flame temperatures, behaves like a black-body to emit visible and infrared radiation in accordance to Planck's law [1]. In a highly sooty flame, the radiative heat transfer from the flame due to soot emission can result in a drop in the peak flame temperature of more than ~150 K [2]. Such change can impact on other quantities that are temperature sensitive, such as the formation of NOx, unburned hydrocarbons and also soot generation itself. Radiation, on the other hand, can be coupled with the combustion process through soot species and gas molecular absorption. For example, it has been reported fuel molecules can be simulated to undergo oxidative or pyrolysis reactions to promote or suppress soot formation, when sufficient radiation heating is present [3]. Whilst the importance of soot-radiation interaction is well-recognized with considerable efforts undertaken towards understanding it [1], many of the research works are focusing on the coupling of soot with natural radiation from a flame. Less research efforts are extended towards the understanding the interaction between externally introduced irradiation with flame [3], which is the focus of the present work.

Whilst many of the physical and chemical mechanisms involved in the coupling of soot and radiation remain inadequately-understood, the introduction of externally irradiated light source to interact with in-flame soot species, nevertheless, has seen increasing applications in both research and industrial sectors for different purposes. Some examples include the laser-heating of soot particles for soot diagnostics, *i.e.* laser-induced incandescence (LII) [5] and nanomaterial synthesis purposes [6, 7], by the combustion and material research communities. The recent advent of the hybrid solar receiver-combustor (HRC) concept [3, 8] has also drawn further interest to the flame-radiation interaction process. In a HRC, both the solar receiver and combustor are combined into a single device to achieve significant savings from reduced infrastructure investment and potential thermodynamic synergies [8]. The approach, however, would also result in the direct interaction of concentrated solar radiation with flame species under certain operating cycles, which can then impact on the combustion and emission performances of the hybrid system. An improved fundamental understanding of the external irradiation and soot species can therefore help to optimize the aforementioned applications.

The aim of the present work is therefore to assess the effect of an external broadband irradiation on the in-flame evolution of soot species - a topic that is not addressed in the literature to the best of the authors' knowledge. A Wolfhard-Parker style burner is used to generate a planar laminar ethylene-air flame and a lab-scale solid-state plasma light is used to provide a highly-controllable external broadband light source. An in-house assembled thermophoretic soot sampling system, as described in a companion paper [9], is used to sample the soot species at targeted heights above burner, with and without the introduction of external irradiation. The soot samples obtained are then imaged using a transmission electron microscope (TEM), and the

* Corresponding author:
Phone: (+61) 2 93854116
Email: qing.chan@unsw.edu.au

acquired images are analyzed and compared to assess the external irradiation effect.

## 2. Experimental Details

A Wolfhard-Parker style burner, as shown in Fig. 1, which consists of three parallel 41 mm long rectangular slots, was used. The outer slots, which carried the oxidizer, are each 16 mm wide, whilst the inner fuel slot is 8 mm wide. For the present work, air co-flow and ethylene gas were supplied to the outer and central slots at 2.4 and 9 SLM, respectively. Nitrogen co-flow was also introduced at 3 SLM to the short ends of the inner fuel slot to prevent the formation of end-flames and draft [9]. The planar flame sheets were therefore confined to the thin regions between the inner and outer slots. A two-dimensional contraction made of two curved wire mesh screens was used to stabilize the flames and to prevent flickering [9]. It should be noted that the heating rates are lower in a two-dimensional flame due to its planar geometry, which only permits thermal conduction of heat from the flame front (as opposed to the cylindrical configuration that is present in a co-annular flame) [9]. The soot precursors therefore persist to higher flame heights in the planar flame, as their conversion to soot is slower than an axisymmetric because of the lower heating rates. The current burner therefore facilitate a better targeting of soot species *i.e.* soot precursors. The light source used is a solid-state plasma light source (Thorlabs, P/N: 43 HPLS-30-04) with a spectrum that approximates a black body at 6500 K with 2800 lumens and 13.9 W of total power, as shown in Fig 2. The lamp emits converging light rays from its 17 mm circular aperture, which converges down to a 9 mm spot from the aperture. In addition, two plano-convex lenses of 37 mm and 80 mm focal lengths were placed in front of the light source, to collimate and to focus the light rays down to a 12 mm diameter spot within the flame. The radiation was focused at height of 15 mm above the burner exit plane (15mm HAB), where soot precursors are expected to be present in abundance, with very little or no mature soot. The average irradiation achieved, after focusing, was measured to be ~120 kW/m$^2$ (or 120 suns), with a flux variation of ~0.5% (1 standard deviation). It is noted that the irradiation was focused on the flame sheet that was located closer the light source (see Fig. 2). The soot samples were also sampled from the same flame sheet.

The soot samples were extracted at 20 and 40 mm HABs using either a carbon-supported TEM grid (Agar Scientific, Agar-S160-H) or a lacey carbon TEM film (Emgrid, LC300-CU-150) for low resolution and high resolution TEM imaging studies, respectively. The grids were attached to a 3.1 mm diameter circular recess at the tip of a 4 mm wide and 2 mm thick stainless steel probe that functioned as the grid holder (see Fig. 1). The grid holder was aligned parallel to the flow-field during experiments to minimize flow disturbances, and was mounted onto the end of a pneumatically-driven double-acting cylinder system with adjustable sampling timing. The cylinder was controlled by a four-way solenoid valve, with compressed nitrogen as the actuating gas.

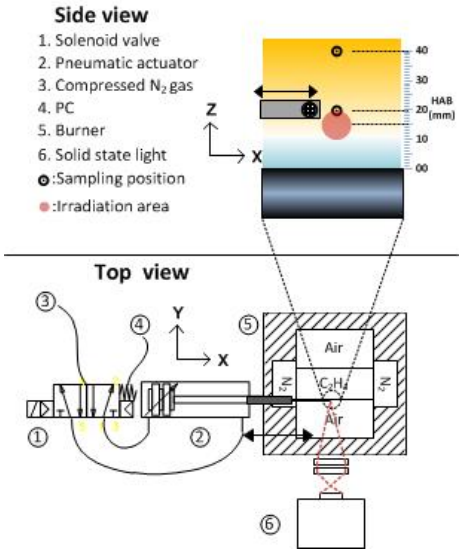


Figure 1: Layout for experimental setup.

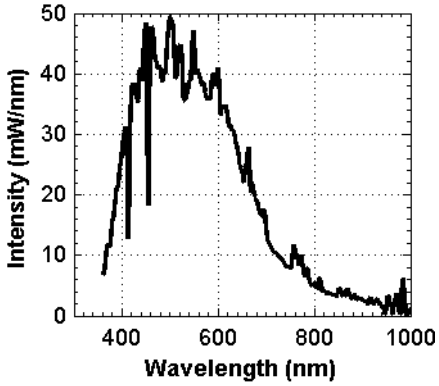


Figure 2: Spectra power distribution for the solid-state plasma light source.

The incoming pressure was regulated using a pressure regulator. The sampling pneumatic system was operated at a piston actuating pressure of 4 bar for all experiments, which was previously assessed to give spatial uncertainties ~2.2 and 2.6 mm in vertical and the lateral directions [9]. The sampling system is mounted on a translational stage to permit vertical translation and therefore, soot sampling at 20 and 40 mm HABs, directly above the focal point of the external irradiation source. An Arduino microcontroller was used to trigger and control the sampling system. For the experiments, the characteristic insertion and retraction times of the sampling system were adjusted to 12 ms each, and the sampling/exposure time in the flame was set to 100 ms. The exposure time was selected to ensure that the TEM grid surface coverage by the sampled soot particles is sufficiently small. This is to prevent excessive overlapping of the soot samples acquired, which can lead to changes in the particle sizes or degree of agglomeration information [9].

The carbon-supported TEM grids collected at the different sampling locations were imaged using a nromal-resolution TEM (JEOL 1400) at UNSW Australia, operated at an electron acceleration voltage of 120 keV. The TEM images were digitized using a CCD camera with a resolution of 11 mega-pixels. It is noted

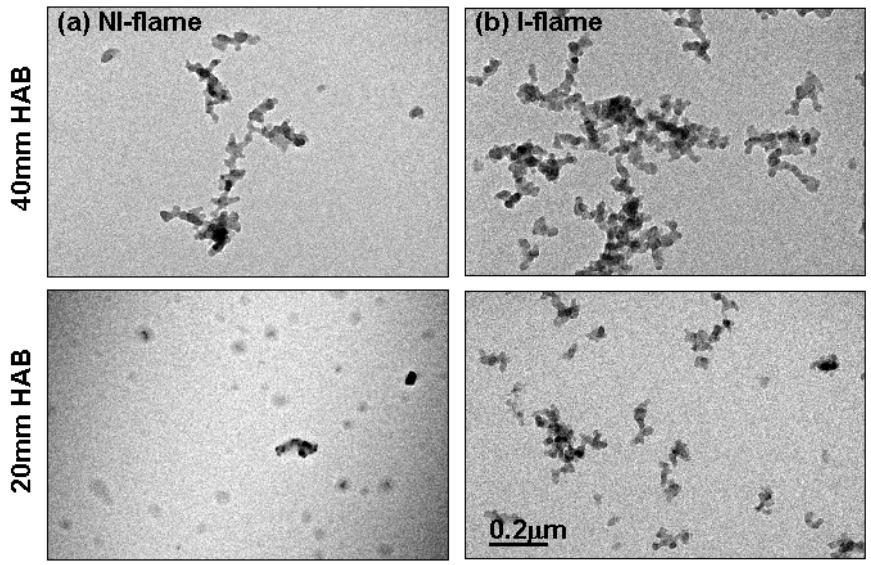


Figure 3: Typical normal-resolution TEM images of the soot samples acquired from the (a) non-irradiated (NI-flame) and (b) irradiated (I-flame) flames, at 20 and 40 mm heights above burner (HABs). The scale is the same for all images.

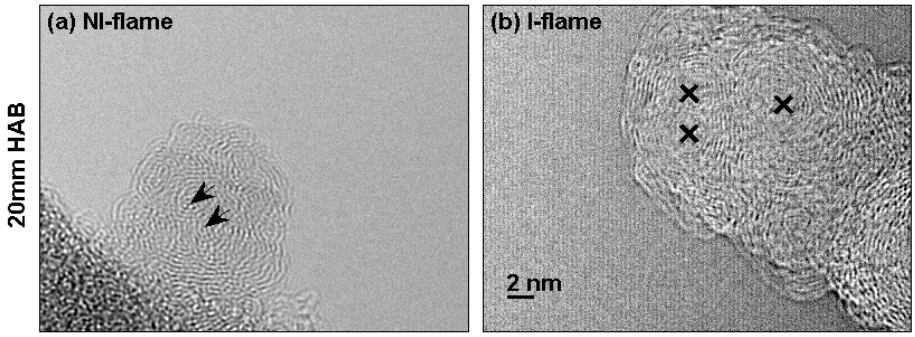


Figure 4: Typical high-resolution TEM images of the soot samples acquired from the (a) non-irradiated (NI-flame) and (b) irradiated (I-flame) flames, at 20 mm height above burner (HAB). The arrows are used to indicate regions within the primary particles where the underlying structures are discernible. The crosses are used to indicate the inner cores detected within the soot sample. The scale is the same for all images.

that an image magnification of 100k was used to achieve a better resolution for primary particles identification. The lacey carbon TEM films, on the other hand, were imaged using a high-resolution TEM (Phillips CM200) at UNSW Australia, operated at an electron acceleration voltage of 200kV and an image magnification of 470k. A CCD camera with a resolution of 7.2 mega-pixels was used to digitize the images. No thermal or chemical pretreatment was performed on the sampled soot to ensure that the original properties of the soot particles are maintained as much as possible.

## 3. Results and Discussion

Figures 3(a) and 3(b) present the low resolution TEM images of the soot particulates that were sampled from 20 and 40 mm HABs of the laminar diffusion ethylene-air flame, with and without the introduction of external irradiation. The non-externally irradiated and the externally irradiated flames are herein referred to as NI-flame and I-flame respectively. Throughout the current work, a comparison of the two flames is made in terms of their thermophoretic observations. For the NI-flame, the soot particulates collected at 20 mm HAB, as seen in Fig. 3(a) possess liquid-like appearances that are poly-dispersed in size and are partially transparent to the electron beam. The boundaries of the translucent liquid-like structures are hard to define due to their diffuseness. In the image, it can be seen that some of the larger structures have black nucleus or nuclei immersed inside them. The presence of the liquid-like structures, with and without the black nucleus or nuclei, is a strong indication that soot inception and coagulation take place at the sampling location (20 mm HAB). It is noted that the liquid-like structures, which are typically termed as soot precursors in the literature, were also sampled from low flame regions in other burner configurations, where intense particle inception and coagulation were expected to occur [11]. The soot particulates sampled at 40 mm HAB of the NI-flame, however, are comprised of highly opaque carbonaceous aggregates with distinct boundaries. The aggregates are observed to contain primary particles that are joined together, whereby the profiles of the particles can be identified from their spherical-like outlines. From the image, it can be observed that the number and the size of aggregates detected generally increase with height. Nonetheless, small aggregates and even single solid primary particles can still be detected. From Fig. 3(b), it can also be seen that the translucent substances detected at 20 mm HAB are not observed at 40 mm HAB. Together, the observations imply that precursors detected at the lower flame height, *i.e.* 20 mm HAB, experience a greater level of carbonization with increased flame residence time and

that the soot inception process is less prevalent at the higher flame region, *i.e.* 40 mm HAB. The current findings are consistent with the trends observed in previous studies [11]. Figure 3(b), on the other hand, presents the TEM photographs of the soot samples that were extracted from the I-flame. From the images, the soot samples from the I-flame have a more mature appearance, when compared with the soot particulates sampled at comparative heights from the NI-flame. The soot samples from the I-flame are observed to consist of solid soot particles that are fused together to form aggregates with clear boundaries, even at 20 mm HAB. The number and the size of the soot aggregates are found to increase with flame height in the flame, as is observed in the NI-flame. It is noted that the translucent structures that were observed at 20 mm HABs in the NI-flame, are not detected in the TEM images obtained for the I-flame at both 20 mm and 40 mm HAB. From the images, it can be seen that the size of the primary particles, the morphologies and the degree of agglomeration of the aggregates are strongly influenced by their positions within the flame, and also by the presence or absence of the external irradiation. The changes in the soot morphological information observed when comparing the soot TEM images obtained from the flames imply that the introduction of external irradiation may accelerate the soot processes such that the soot generation evolves more quickly. The effect of the enhanced soot formation process is also observed to persist downstream, after the irradiation point, as the size and number of the soot aggregates collected at 40 mm HAB are found to be generally larger for the I-flame.

To further examine the internal nanostructure of the soot samples, high-resolution soot TEM images at 20 mm HAB for the NI-flame and I-flame were sampled and analyzed. Figures 4(a) and 4(b) present the high-resolution TEM photographs of soot samples that were acquired from the flames. In Fig. 4(a), it can be seen that the soot primary particles from the NI-flame comprise of randomly-orientated, discernible striations, with lengths that are generally not continuous for more than a few nanometers. There are also regions of carbon layers with less defined structures observed along the outer edges of the primary particles. Together, the observations indicate that the soot sample acquired do not have a significant long range order. In addition, in the central regions of the primary particle, as annotated by arrows, the structures of the underlying particles can be vaguely discerned. The detection of the underlying structures, despite the presence of the overlaying particles, implies that the observed particles are not highly graphitized. This is because carbonaceous material, when present, would interfere with the electron beam path from the microscope and therefore, obscure the underlying particles from view. The absence of long range order, in addition to the translucent nature of the soot samples in Fig. 4(a), suggest that the soot sample acquired from the NI-flame are relatively young [4].

Figure 4(b), on the other hand, presents the high-resolution TEM image of soot particulates sampled from the I-flame. In the figure, highly concentrically orientated graphitic layers (GLs) are observed within and along the outer periphery of the soot primary particles. Typically, 6 to 10 layers of GLs are found to stack orderly on the periphery of inner cores, as indicated using crosses in Fig. 4(b), to form shell-like nanostructures. Although still not continuous, the length of the GLs observed are generally longer than that of the striations detected in Fig. 4(a). Further inspection of the image reveals that the primary particles are still embedded in amorphous coalesced material, although such layers are thinner. Together, the presence of longer range order, in addition to the more carbonaceous nature of the sample imply that soot presented in Fig. 4(b) are more mature than the soot sample in Fig. 4(a). The more mature internal nanostructure observed in the high-resolution TEM images of the soot primary particles obtained from the I-flame, when compared with the sample collected form the NI-flame, again supports the earlier assertion that the introduction of external irradiation can accelerate the soot formation processes.

## 4. Conclusions

Soot samples were thermophoretically sampled from a laminar non-premixed ethylene-air flame. The soot samples obtained were imaged using both normal-resolution and high-resolution transmission electron microscopes (TEMs) and the images were compared and analyzed in detail, to assess the effect of external irradiation on the evolution of in-flame soot species. The comparisons revealed that the soot samples acquired from both within and after the vicinity of the external irradiation were found to have more mature appearances. The results suggested that the application of external irradiation source to flame can accelerate the in-flame soot generation process, and the effect can persist downstream from the irradiation location.

## 6. References


1. I.K. Puri (eds.), Environmental Implications of Combustion Processes, CRC Press, U.S., 1993, pp. 71-95.
2. R. S. Mehta, Detailed Modelling of Soot Formation and Turbulence-Radiation Interactions in Turbulent Jet Flames, The Pennsylvania State University, U.S., 2008.
3. P.R. Medwell, G.J. Nathan, Q.N. Chan, Z.T. Alwahabi and B.B. Dally, Combust Flame **158** (2011), pp. 1814-1821.
4. R.L. Vander Wal and M.Y. Choi, Carbon **37** (1999), pp. 231-239.
5. N.H. Qamar, G.J. Nathan, Z.T. Alwahabi and Q.N. Chan, Combust Flame **158** (2011), pp. 2458-2464.
6. M. Choi, I.S. Altman, Y.-J. Kim, P.V. Pikhitsa, S. Lee, G.-S. Park, T. Jeong and J.-B. Yoo, Adv Mate **16** (2004), pp. 1721-1725.
7. L. Hu, S. Wang, B. Zhang and Y. Zeng, Carbon **44** (2006), pp. 1725-1729.
8. G.J. Nathan, D.L. Battye and P.J. Ashman, Appl Energ **113** (2014), pp. 1235-1243.
9. C. Wang, Q.N. Chan, S. Kook, E.R. Hawkes, J. Lee and P.R. Medwell, Development of an in-flame thermophoretic soot sampling device, in the Proceedings Australian Combustion Symposium, University of Melbourne, 2015.
10. T.C. Williams, C.R. Shaddix, K.A. Jensen and J.M. Suo-Anttila, Int J Heat Mass Tran **50** (2007), pp. 1616-1630.
11. J. Lee, I. Altman and M. Choi, J Aerosol Sci **39** (2008), pp. 418-431.

# On the Structure of Turbulent Flames of DME/$N_2$ with Inhomogeneous inlets

T.F. Guiberti[1,2*], M. Juddoo[1], M.D. Dunn[1], W.L. Roberts[2], A.R. Masri[1]
[1]School of Aerospace, Mechanical and Mechatronic Engineering, The University of Sydney, NSW 2006, Australia
[2]Clean Combustion Research Center, KAUST, Thuwal 23955, Saudi Arabia

## Abstract

This paper reports an experimental and numerical analysis of the stabilization of turbulent DME/$N_2$ piloted jet flames with inhomogeneous inlets. The burner employs two concentric tubes with the pilot stream, so that the inner fuel, when recessed, leads to a varying degree of inhomogeneity in mixing with the outer air stream. While the trends are similar to those obtained earlier with methane fuel, the increase in stability for DME/$N_2$ with recess distance is very marginal. Using PLIF-$CH_2O$, it is shown that modifying the degree of inhomogeneity influences the $CH_2O$ layer thickness as measured downstream of the burner exit plane. A set of 1-D laminar counterflow simulations demonstrate that the $CH_2O$ layer thickness of a flame burning in contact with the pilot hot burnt gases increases with the equivalence ratio. It is shown that tailoring the degree of inhomogeneity at the burner exit plane allows modifying the local equivalence ratio of the DME/$N_2$/air mixture in contact with the pilot burnt gases, which then burns with an equivalence ratio closer to unity in comparison to the fully homogeneous case.

*Keywords: Turbulent jet flames, piloted flames, inhomogeneous inlets, PLIF-$CH_2O$, DME.*

## 1. Introduction

Compositional inhomogeneity is quite common in practical combustion devices even if these are designed to operate with homogeneous mixtures [1,2]. Such inhomogeneity may have beneficial effects in enhancing stability and this has been demonstrated recently [3-5] where varying concentration gradients are imposed on the jet exit conditions of laboratory-based piloted burners. These gradients are introduced by recessing a fuel tube within an air annulus both of which are located within the piloted stream. Only methane fuel was studied earlier and the objective of this paper is to extend this study to dimethyl ether (DME).

DME is one of the simplest oxygenated fuels and is a reasonable first step in the study of the combustion of complex oxygenated fuels, which are a promising option for clean compression ignition (CI) engines [6]. DME fuels have a low sooting propensity and lend themselves for advanced laser diagnostics, such as laser induced fluorescence of formaldehyde, LIF-$CH_2O$, which is part of the DME consumption pathway [7]. While subsequent analysis is performed for LIF-$CH_2O$ only due to space limitation, the measurements include joint LIF-$CH_2O$-OH hence providing a useful tool to describe the structure of the turbulent reaction zones [8].

This paper reports the stability limits for DME/$N_2$ (1/1 by vol.) flames as well as a joint experimental and numerical study of selected flames of DME/$N_2$/air with varying inhomogeneity at the inlets. High-speed PLIF-$CH_2O$, with a repetition rate of 10 kHz, is used to describe the influence of inlet inhomogeneities on the $CH_2O$ layer thickness. A set of 1-D laminar counterflow simulations is also conducted to better understand the physics of the stabilization of theses piloted flames.

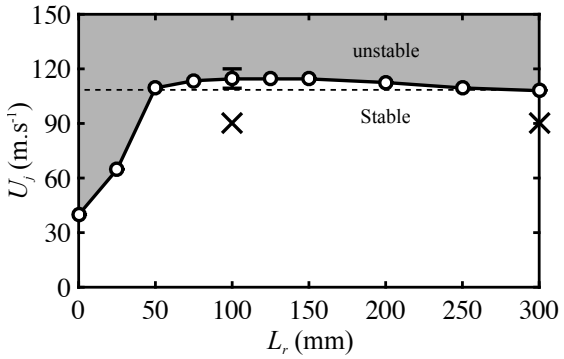


**Figure 1: Bulk jet velocity $U_j$ at blow-off (circle symbols) as a function of the recession distance $L_r$. Cross symbols show the bulk jet velocities and recess distances chosen for PLIF experiments.**

## 2. Experimental set-up

The burner is similar to that used in [3-5] for the investigation of piloted turbulent $CH_4$/Air flames with inhomogeneous inlets. It includes two tubes surrounded by an annular pilot and an air co-flow. The inner tube (inner diameter $D_i = 4$ mm), supplying a mixture of DME and $N_2$, can recess within the main tube (inner diameter $D = 7.5$ mm), supplying air, which varies the degree of mixing between fuel and air at the burner exit plane. A recession distance $L_r = 0$ mm corresponds to a fully inhomogeneous case, where fuel and air only mix after the exit plane of the burner. The global volumetric $N_2$ to DME and air to DME ratios are fixed to $V_{N2}/V_{DME} = 1$ and $V_{AIR}/V_{DME} = 5$ respectively. The $N_2$ dilution is adopted here for practical consideration since with pure DME, not enough fuel can be metered to drive the flame to blow-off. This is achieved with nitrogen dilution since this tends to reduce the blow-off limits.

* Corresponding author:
Phone: (+61) 4 06964242
Email: Thibault.guiberti@kaust.edu.sa

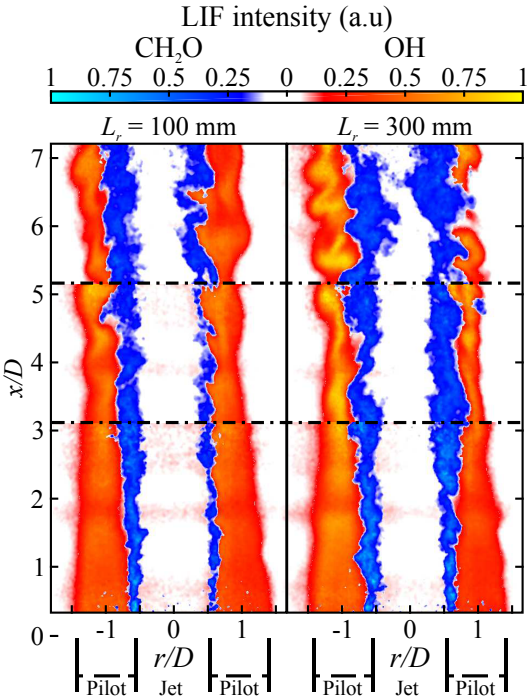


**Figure 2: $CH_2O$ (blue colorbar) and OH (red colorbar) PLIF intensities for two recess distances $L_r$ = 100 mm (left) and $L_r$ = 300 mm (right). The three windows separated by the horizontal dash-dotted lines do not correspond to the same time.**

A stoichiometric $C_2H_2/H_2$/Air mixture with the same C/H ratio as DME powers the pilot flame stabilized in a perforated plate with $D_p$ = 18 mm tube. The unburnt bulk velocity of the pilot stream is 1.54 m.s$^{-1}$, corresponding to an overall heat release of 1.14 kW. The burner assembly is located in a 15×15 cm square wind tunnel providing a uniform air co-flow at 15 m.s$^{-1}$. The mass flow rates of DME, $N_2$, $C_2H_2$, $H_2$, and air are regulated with thermal mass flow controllers (Alicat MC series) with a relative accuracy better than 2%. Some excess heat issues from the pilot due to the higher adiabatic flame temperature of $T$ = 2492 K.

The distribution of hot burnt gases downstream of the burner exit plane is deduced from planar laser induced fluorescence of OH (PLIF-OH) at 10 kHz. The PLIF-OH set-up is described in details in [4] and these are complemented by simultaneous imaging of $CH_2O$-PLIF. Formaldehyde is excited by the third harmonic at 355 nm of a Nd:YAG (Edgewave HD30II-E) also fired at a repetition rate of 10 kKz with a power output of approximately 36 W and a pulse length of around 7 ns. The signal is detected with a 768×768 pixel high-speed CMOS camera (LaVision HSS6) coupled to a two-stage intensifier (LaVision High-Speed IRO) and equipped with a 409 nm longpass filter (Semrock FF02-409/LP-25) and a 500 nm shortpass filter (CVI SPF-500-50.0M). The image resolution is 57 µm/pixel. The $CH_2O$ laser sheet has a 15 mm height and a thickness of approximately 200 µm. Snapshot images of PLIF-OH and $CH_2O$ are corrected to laser shot-to-shot energy variations and laser sheet inhomogeneities.

## 3. Results and discussions

### 3.1 Stability limits

Figure 1 shows the bulk jet velocity $U_j$ leading to flame blow-off as a function of the recession distance $L_r$. A higher bulk jet velocity at blow-off indicates better flame stability. For $L_r$ = 0 mm, corresponding to a fully non-premixed case, the flame blows off at $U_j$ = 40 m.s$^{-1}$. With homogeneously partially premixed inlets, obtained for $L_r$ = 300 mm, the flame is more stable and blows off at $U_j$ = 108 m.s$^{-1}$. Meares *et al*. [3-4] reported a similar behavior with $CH_4$/air mixtures. In Fig 1, the bulk jet velocity at blow-off increases rapidly between $L_r$ = 0 mm and $L_r$ = 100 mm, where it reaches a global maximum of $U_j$ = 115 m.s$^{-1}$. Between $L_r$ = 110 mm and $L_r$ = 300 mm, $U_j$ slowly decreases. As in [3-5], there exists an optimal recess distance that allows maximizing the flame stability. For a DME/$N_2$/Air mixture with $V_{Air}/V_{DME}$ = 5 and $V_{DME}/V_{N2}$ = 1, the optimal recess distance is $L_r \approx$ 100 mm, which yields a 6.5 % increase of flame stability in reference to the case with homogeneous inlets. While useful, this is much lower than the 50% gain reported earlier for flames of methane [3-5]. This is partly attributed to the lower pilot heat release of 1.14 kW used here compared to the pilot heat release of 2.22 kW used for $CH_4$/Air mixtures. Other more subtle reasons may also contribute to this difference such as different mixing patterns between the fuel and air as recess distance is increased. These issues are currently the subjects of further investigations.

### 3.2 PLIF experiments

To better understand the influence of the recession distance on the flame stability, the fluorescence from OH and $CH_2O$ was measured for two nearly identical operating conditions, where only the recess distance differs. These two operating conditions, shown by the crosses on Fig. 1, feature the same bulk jet velocity $U_j$ = 90 m.s$^{-1}$ but with recess distances of either $L_r$ = 100 mm or $L_r$ = 300 mm. Figure 2 shows examples of the distribution of LIF-OH (red colorbar) and LIF-$CH_2O$ (blue colorbar) measured downstream the burner's exit plane for $L_r$ = 100 mm (left) and $L_r$ = 300 mm (right). The OH-PLIF distribution is first described. While both flames show the same qualitative features, some subtle differences exist as demonstrated in the remainder of this paper. The region $0 < x/D \leq 2$ and $0.6 \leq |r/D| \leq 1.5$ is filled with hot burnt gases from the pilot flame and shows a high OH-PLIF intensity. This region is barely affected by turbulence and the OH-PLIF does not fluctuate significantly with time. On the contrary, burnt gases from the turbulent jet flame ($x/D > 3$) start to exhibit fluctuations due to turbulence.

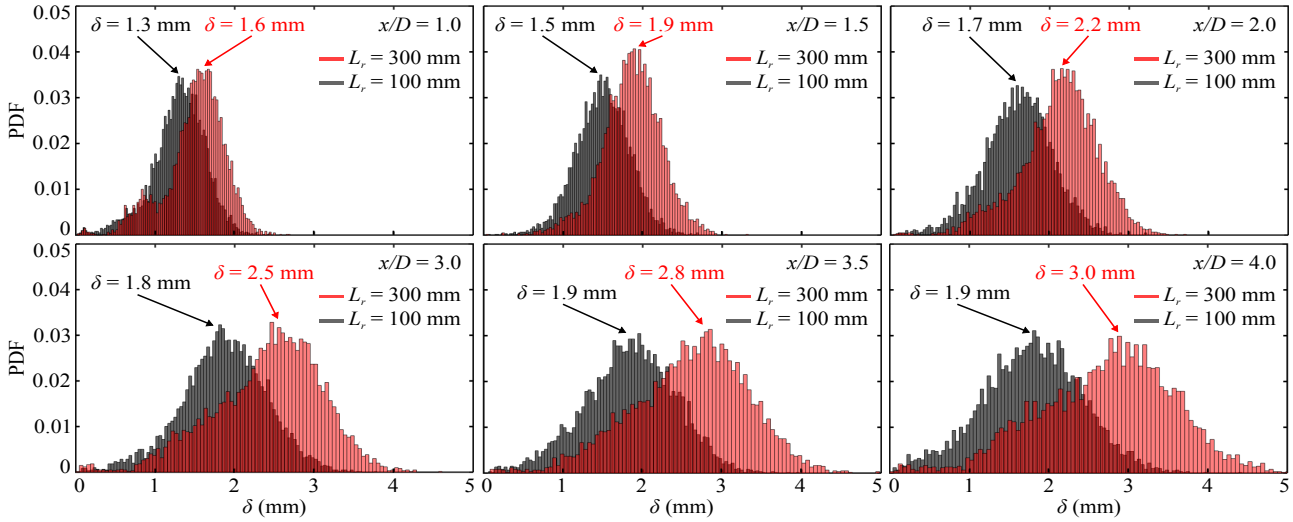


**Figure 3: Probability density function (PDF) of the thickness $\delta$ of the $CH_2O$ layer for six heights above the burner exit plane and two recess distances $L_r$ = 100 mm (black) and $L_r$ = 300 mm (red).**

The regions of the flow featuring large quantities of $CH_2O$ appear in blue in Fig. 2. For $x/D \leq 1$, a thin zone of $CH_2O$ can be observed in the shear layer between the central jet and the burnt gases from the pilot flame. Independently of the recession distance, the thickness of the $CH_2O$ layer increases with distance from the burner exit. For the same height above the burner, it appears that the $CH_2O$ layer is consistently thicker for the homogeneous case at $L_r = 300$ mm. This suggests that fluid mixtures at $L_r = 100$ mm are less homogeneous than those at $L_r = 300$ mm. This is now confirmed using a more thorough statistical analysis of the thicknesses of measured $CH_2O$ layers.

Figure 3 shows the probability density function (PDF) of the thickness $\delta$ of the $CH_2O$ layer measured by PLIF for six heights above the burner exit plane $x/D = 1.0, 1.5, 2.0, 3.0, 3.5$, and 4 and for two recess distances $L_r$ = 100 mm (black) and $L_r$ = 300 mm (red). For a given height above the burner exit plane, the thickness $\delta$ is defined here as the distance between the two radial positions $r$ where the $CH_2O$ PLIF signal reaches 10 % of the maximum PLIF image intensity. A total of 2000 PLIF snapshots were taken at each position to ensure statistical convergence of the data. Overall, the distribution of the thickness $\delta$ takes a Gaussian shape. It is possible to define the most probable $CH_2O$ layer thickness for each position and for both recess distances. Independently of $L_r$, Fig. 3 confirms that the $CH_2O$ layer thickness increases with height above the burner exit plane. The most probable thickness increases from $\delta \approx 1.6$ mm at $x/D = 1$ to $\delta \approx 3.0$ mm at $x/D = 4$ if $L_r = 300$ mm.

More importantly, Fig. 3 demonstrates that the $CH_2O$ layer thickness is globally larger for the homogeneous case at $L_r = 300$ mm than for $L_r = 100$ mm. At $x/D = 1$, $\delta$ is 19 % smaller for $L_r = 100$ mm than for $L_r = 300$ mm. At $x/D = 4$, the discrepancy is even larger and $\delta$ is 37 % smaller for $L_r = 100$ mm than for $L_r = 300$ mm. This confirms that the burning conditions are different for these two recess distances implying that the case with $L_r = 100$ mm is most probably not homogeneous. The PLIF experiments are however not sufficient to precisely describe the conditions under which the non-homogeneous jet burns in contact with the hot pilot burnt gases for $L_r = 100$ mm. Additional information is obtained by comparing PLIF results to 1-D laminar counterflow simulations.

## 3.3 1-D laminar flame simulations

We conducted a set of 1-D laminar counterflow direct simulations with the software CHEMKIN [9] and the detailed chemistry mechanism from Zhao *et al.* [10]. A DME/$N_2$/Air homogeneous mixture at $T = 298$ K is injected at a velocity $u$ on one side of the computational domain while on the other side, which is located $L = 20$ mm away, a homogeneous and hot mixture of $N_2/CO_2/H_2O/O_2$ at $T = 2492$ K is injected with a velocity $-u$. This counter-flowing mixture roughly corresponds to the composition and temperature of the burnt gases from the pilot flame, computed with CHEMKIN beforehand. We conducted simulations for a range of air to DME ratios $V_{Air}/V_{DME}$ = [5:1:13, 14.29] and strain rates $a$ = [100, 500, 2000] $s^{-1}$. The nitrogen dilution ratio is fixed to $V_{N2}/V_{DME} = 1$. The case $V_{Air}/V_{DME} = 5$ corresponds to an equivalence ratio of $\phi = 2.86$. For $V_{Air}/V_{DME} = 14.29$, the equivalence ratio is $\phi = 1$. The strain rate is here defined as $a = 2u/L$.

Figure 4 (top) shows the evolution of species molar fraction, X(i) and temperature for the case $V_{Air}/V_{DME} = 5$ and $a = 500$ $s^{-1}$. The red solid line shows the molar fraction of $CH_2O$. It is seen that $CH_2O$ is located in the pre-heat region of the premixed flame with a maximum concentration at $x = 14.6$ mm. It is now possible to calculate the thickness $\delta$ of the $CH_2O$ layer which, by analogy with the PLIF experiments, is defined as the separation distance between the positions $x$ where the $CH_2O$ molar fraction reaches 10 % of the peak. Figure 4 (bottom) plots the evolution of the calculated $CH_2O$ layer thickness $\delta$ (black) as a function of $V_{Air}/V_{DME}$. Results for the three strain rates $a$ = [100, 500, 2000] $s^{-1}$ are overlapped. To facilitate further comparisons with the PLIF experiments, Fig. 4 (bottom) also plots the thickness of a simulated $CH_2O$ LIF layer (red). In reality the $CH_2O$ LIF signal intensity is a

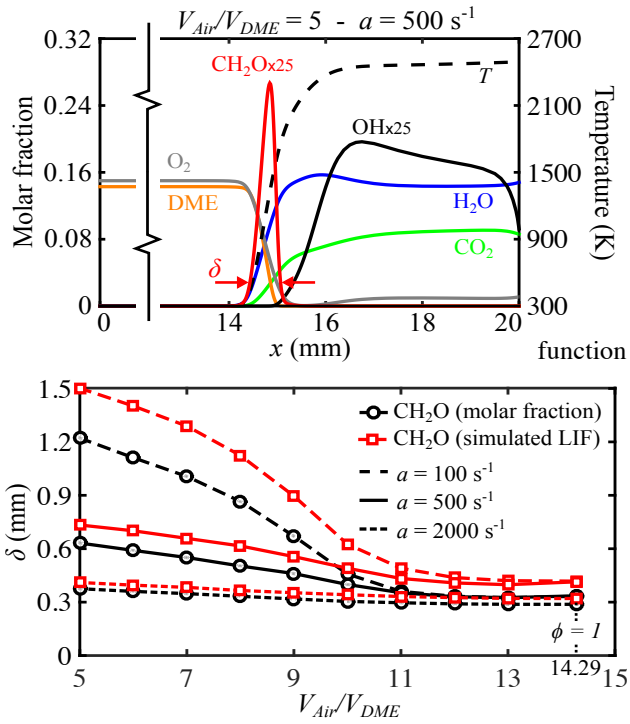


**Figure 4: Top: Simulated species molar fraction and temperature in a 1-D laminar counterflow flame (strain rate $a = 500\ s^{-1}$) opposing a DME/$N_2$/air mixture ($V_{Air}/V_{DME} = 5$ and $V_{DME}/V_{N2} = 1$) at $T = 298$ K to the burnt gases of the pilot. Bottom: Simulated thickness $\delta$ of the $CH_2O$ layer, based on the molar fraction (black) and simulated LIF signal (red), as a function of $V_{Air}/V_{DME}$ for three different strain rates.**

of the $X_{CH2O}$ and temperature [11]. It is then necessary to correct the $CH_2O$ molar fraction $X_{CH2O}$ profile in 1-D simulations with the local temperature to compute a somewhat comparable $CH_2O$ fluorescence signal profile $I_{CH2O}$. This is here modeled as follows: $I_{CH2O} = X_{CH2O} \times T^{-2.6}$ [11]. The simulated LIF profile is shifted towards the lower temperatures and the corresponding thickness is larger than the thickness based on the $CH_2O$ molar fraction profile.

Figure 4 (bottom) shows that the $CH_2O$ layer thickness decreases when $V_{Air}/V_{DME}$ increases, *i.e.* when the equivalence ratio decreases. However, the rate of decay of $\delta$ is a strong function of the strain rate $a$. For $a = 100\ s^{-1}$, the thickness based on the simulated LIF decreases from $\delta = 1.5$ mm for $V_{Air}/V_{DME} = 5$ ($\phi = 2.86$) to $\delta = 0.41$ mm for $V_{Air}/V_{DME} = 14.29$ ($\phi = 1$). For $a = 2000\ s^{-1}$, the thickness only decreases from $\delta = 0.41$ mm for $V_{Air}/V_{DME} = 5$ ($\phi = 2.86$) to $\delta = 0.32$ mm for $V_{Air}/V_{DME} = 14.29$ ($\phi = 1$). These values are lower that the thicknesses measured with PLIF and this is attributed to turbulence, which broadens the $CH_2O$ layer. While the equivalent strain rate experienced by the turbulent flames is not known, both experiments for $L_r = 100$ mm and $L_r = 300$ mm are realized at the same bulk jet velocity $U_j = 90$ m.s$^{-1}$. It is, therefore, reasonable to assume that both flames experience a similar strain rate. Consequently, the very different $CH_2O$ layer thicknesses measured by PLIF and described in Fig. 3 demonstrate that the flames with $L_r = 100$ mm and $L_r = 300$ mm are not burning with the same local equivalence ratio.

For $L_r = 300$ mm, the DME/$N_2$/Air jet mixture is homogeneous and has a rich equivalence ratio $\phi = 2.86$ ($V_{Air}/V_{DME} = 5$). The measured $CH_2O$ thickness is lower for $L_r = 100$ mm than for $L_r = 300$ mm, independently of the distance above the burner's exit plane (see Fig. 3). From Fig. 4 (bottom), this indicates that the flame at $L_r = 100$ mm burns locally with an equivalence ratio lower than $\phi = 2.86$, *i.e.* closer the stoichiometric and hence more robust than the flame for $L_r = 300$ mm. This explains why the bulk jet velocity at blow-off is higher for the recess distance $L_r = 100$ mm than for $L_r = 300$ mm. This result corroborates the findings of [3-5] for the same burner but different mixtures of $CH_4$/Air.

## 3. Conclusions

The influence of compositional inhomogeneities on the stability of DME/$N_2$/Air turbulent jet piloted flames is analyzed and the $CH_2O$ layer thickness was measured with PLIF-$CH_2O$. It was shown that $CH_2O$ depends on the local equivalence ratio of the turbulent jet burning in contact with burnt gases from the pilot flame. The homogeneous case with $L_r = 300$ mm corresponds to an equivalence ratio $\phi = 2.86$ and yields a thicker $CH_2O$ layer than the flame with $L_r = 100$ mm which is inhomogeneous. Comparisons with 1-D direct laminar counterflow simulations confirms these findings and demonstrates that thicker $CH_2O$ layers are obtained with partially premixed flames.

## 4. Acknowledgments

This work is supported by the Australian Research Council and CCRC-KAUST. We thank S. Gali and A. MacFarlane for their help with the experiment and H. Cutcher for his assistance with CHEMKIN.

## 5. References

[1] M. Yao, Z. Zheng and H. Liu, Prog. Energy Combust. Sci. **35** (2009), pp. 398-437.

[2] F. Jaegle, J.M. Senoner, M. Garcia, F. Bismes, R. Lecourt, B. Cuenot and T. Poinsot, Proc. Combust. Inst. **33** (2011), pp. 2099-2107.

[3] S. Meares and A.R. Masri, Combust. Flame **161** (2014), pp. 484-495.

[4] S. Meares, V.N. Prasad, G. Magnotti, R.S. Barlow and A.R. Masri, Proc. Combust. Inst. **35** (2015), pp. 1477-1484.

[5] R.S. Barlow, S. Meares, G. Magnotti, H. Cutcher and A.R. Masri, Combust. Flame (2015), **In press**.

[6] C. Arcoumanis, C. Bae, R. Crookes and E. Kinoshita, Fuel **87** (2008), pp. 1014-1030

[7] K.N. Gabet, H. Shen, R.A. Patton, F. Fuest and J.A. Sutton, Proc. Combust. Inst. **34** (2013), pp. 1447-1454.

[8] B. Coriton, M. Zendehdel, S. Ukai, A. Kronenburg, O.T. Stein, S.K. Im, M. Gamba and J.H. Frank, Proc. Combust. Inst. **35** (2015), pp. 1251-1258.

[9] CHEMKIN 10113, Reaction Design: San Diego, 2012.

[10] Z. Zhao, M. Chaos, A. Kazakov and F.L. Dryer, Int. J. Chem. Kinet., **40 (1)** (2008), pp. 1-18.

[11] P.H. Paul and H.M. Najm, Proc. Combust. Inst. **27** (1998) pp. 43-50.

# Stabilization of Turbulent Auto-Igniting DME Jets Issuing in Hot Vitiated Coflows

A.R.W. Macfarlane, M.J. Dunn, M. Juddoo, A.R. Masri
School of Aerospace, Mechanical and Mechatronic Engineering,
The University of Sydney, NSW 2006, Australia

**Abstract**

This paper presents a study of a dimethyl ether (DME) fuelled jet issuing into a large coaxial vitiated hot coflow of lean premixed $H_2$/air combustion products. The DME in the fuel jet has been partially premixed with varying volumetric ratios of air and the flame lift-off heights measured for a range of coflow temperatures. To gain further insight into the auto-ignition processes that occur in these flames, high-speed chemiluminescence imaging of CH* has been applied with a repetition rate of 10 kHz to track the formation rate, growth and consumption of auto-igniting flame kernels and their interaction with the primary flame front. The results presented in this paper indicate that the dynamics and interaction of the flame kernels with the main flame base may provide a useful indicator as to the nature of the primary flame stabilisation mechanism.

*Keywords: Vitiated hot coflow, auto-ignition, turbulent flames, kernel, lift-off height*

## 1 Introduction

Dimethyl ether is receiving considerable attention as a possible alternative fuel in applications such as CI engines [1]. This is not only due to its high cetane number and low auto-ignition temperature, but also because of its high oxygen content which is around 35% by mass. This increased content has the potential of reducing the sooting propensity [2] which is a key advantage, particularly in diesel engines. It is important therefore, to develop an improved understanding of the combustion and auto-ignition characteristics of this fuel in turbulent flows not unlike those encountered in real devices.

The stabilization mechanism of lifted flames remains subject to controversy particularly at moderate temperatures where auto-ignition may be occurring. Transition from stabilization by propagation of premixed flames or flames edges to stabilization by auto-ignition kernels occurs at relevant temperatures and the demarcation between these regimes remains vague. Lyons [3] provides a comprehensive review of classical lifted flames and the relevant stabilization mechanisms. Auto-igniting flames for hydrogen and methane have been studied extensively using the hot co-flow burner configuration adopted here [4,5]. In these flames, it is now established that kernel generation is the key mechanism for stabilization. This is confirmed by DNS studies of similar flows showing that particular species, such as formaldehyde in the case of methane fuel, populate these auto-igniting kernels at lean mixtures (which are referred to as most reactive mixture fractions) and low dissipation rates [6,7].

The hot vitiated coflow burner employed here was introduced by Cabra [4] and was subsequently used by many groups to study turbulent auto-ignition as well as premixed flames. In this paper, the same burner is used to study DME which may be partially premixed with air to varying proportions. Measurements of lift-off heights are presented along with high-speed chemiluminescence images which provide insights about the mode of flame stabilization.

## 2 The setup

The burner employed is very similar to that used by Cabra and Dibble [4]. The wide coflow diameter of 197 mm has ~1800x1.6 mm diameter holes which stabilize lean $H_2$/air flames. The coflow products shroud the fuel jet at a constant burnt velocity of 4 m/s for all cases. The temperature of the co-flow is varied by varying the equivalence ratio and the range covered in the present study is 1200 to 1500 K. The "valid cone' is defined as the region downstream of the exit plane within which the central flames remain fully engulfed by the co-flow gases and not affected by the laboratory air. This region is measured to be around 270 mm or $60D_j$ downstream of the central nozzle ($D_j$ =4.45 mm). The entire burner assembly is placed in a wind tunnel providing a co-flowing stream of air at a fixed velocity of 0.8 m/s. The air diluent ratios were

varied within the central fuel jet while maintaining a constant 50 m/s bulk velocity. The operating conditions are summarised in Table 1 for selected cases that are further analysed within this paper. An example coflow temperature at 1400 K (where the equivalence ratio is 0.39) is shown with the stoichiometric mixture fractions, $\xi_{st}$, for pure DME as well as air/DME dilution ratios of 3/1 and 1/1, respectively.

**Table 1 Selected burner conditions**

| | Fuel Jet | | |
|---|---|---|---|
| | air/DME =3/1 | air/DME =1/1 | Pure DME |
| V(m/s) | 50 | 50 | 50 |
| Re | 16650 | 22990 | 38610 |
| T (K) | 298 | 298 | 298 |
| QDME (SLM) | 11.7 | 23.4 | 46.8 |
| Qair (SLM) | 35.0 | 23.4 | - |
| $\xi_{st}$ | 0.197 | 0.107 | 0.064 |

## 2.1 Experimental method

Flame Lift off heights (LH) were determined using a digital camera by extracting the individual movie frames. This method is preferred over still images as observed features are more distinct, owing to faster shutter speed, reducing potential error in the flame base location. Each frame is taken at a rate of 24 Hz with a 1 ms exposure and the LH is based on the lowest intensity that exceeds the background. Aproximately 430 frames were used to determine the average, standard deviation and extremes of the LH's. Furthermore, sound level measurements were taken using a Bruel and Kjaer type 2250 to determine any correlation of igntion events to acoustical emissions.

Due to the tubulence of the flames and short time scales, 24 Hz was insufficient to capture any temporal resolution. Therefore a high speed CMOS camera operating at 10 kHz was used to capture the chemiluminescence from CH* camera at 10 kHz. The camera was operrated using LaVision software with a 25 µs intensifier gate and a 50 mm $f_{\#}2$ visible lens. Figure 1 shows selected images (low/high LH and kernel formation) for coflow temperatures of 1275 K and 1400K using air/DME=3/1. The images show the relative fluctuations of the flame base and the difference in flame structure where at 1275 K the flucuations in the flame are more significant. This is discussed further in the next section with resepct to the chemilumenescence images.

## 2.2 Results

Figure 2 shows the lift-off heights plotted versus temperature of the co-flow for pure DME as well as for air/DME=1/1 and 3/1 by volume. The horizontal dashed line on each plot marks the end of the "valid cone". The trends observed from Figure 1 are similar to those reported earlier for methane, in that the lift-off heights are highly influenced by the co-flow temperature and decrease as the latter decreases. Pure DME fuel has the lowest LH which increases with increasing partial premixing with air. For temperatures lower than 1300K the slope of LH increases significantly with the decreasing temperature of the coflow.

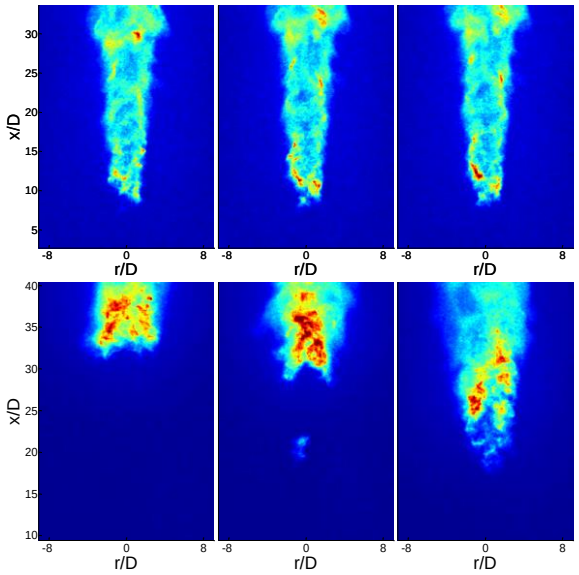


**Figure 1 CH* 10 KHz images showing the fluctuation of the Flame base: 1400 K (Top) 1275 K (Bottom)**

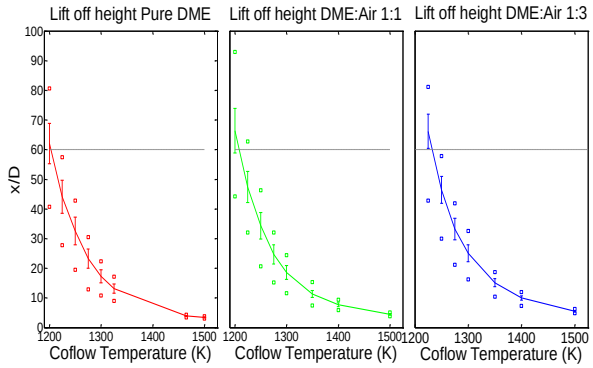


**Figure 2 LH curves for selected cases: For each condition a range of 1σ from the mean is indicated with a vertical line. The absolute minimum and maximum LH is illustrated with square symbols.**

Figure 2 shows that for lower coflow temperatures the fluctuation in the LH's increases. It is noted that for subsequent analysis, flame conditions that are likely to fall downstream of the 'valid cone' are excluded, as it is possible they might be invalid due to entrainment of laboratory air.

Sound level data taken simultaneously with the chemiluminescence movies is presented in Figure 3

for the three flames studied in this paper. The higher diluent ratios indicate an increase in noise levels with decreased temperature (increased LH). The 1/1 and pure case extended outside the 'valid cone' before a peak sound level was reached. However for higher diluent ratios 1/5, 1/7 (not displayed here) follow the same trend, that is increased diluent has reduced peak noise.

For each of the fuel mixtures studied here, three cases were selected for further study: One at high coflow temperature corresponding to a premixed propagating flame, another at lower temperature corresponding to autoignition stabilisation and finally a potential intermediate flame condition. These cases were selected such that the flame sits within the valid cone. For the partially premixed air/DME=3/1 the selected cases were; 1400 K, 1325 K and 1275 K. For the 1/1 diluent and pure case, coflow temperatures of 1250 K and 1225 K respectively were chosen.

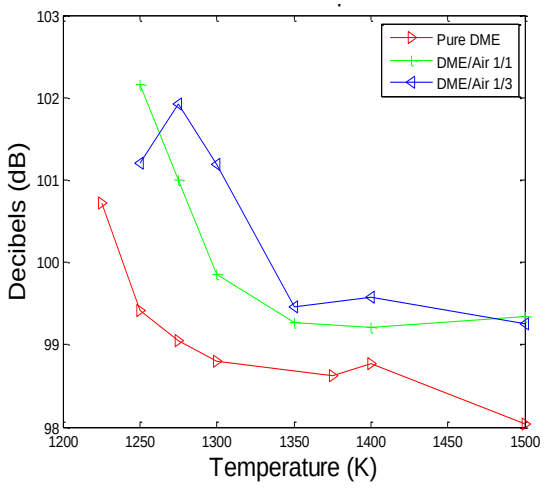


**Figure 3 Sound levels that were exceeded 5% of the time ($Le_{05}$) for various coflow and diluent ratios for LH's inside the 'valid cone'**

## 2.3 HS Kernel Tracking

Figure 4 below shows a sample sequence of chemiluminescence images collected for two temperatures in the air/DME=3/1 flames. The range covered here extends from $x/D$~10 to 40 and includes the flame base. The horizontal dashed line marks the leading edge of the main flame base at the start of the sequence shown here. For the higher coflow temperature of 1400 K, the flame kernel formed upstream of the flame base are very small and the leading edge of the flame remains almost fixed right through the entire sequence. Conversely, at 1275K, the flame kernels grow significantly while the flame base is advected downstream. This continues until such a time when the kernel is attached to the main flame base as shown from the last image in the sequence. This process is typical of the images with lower coflow temperatures and large fluctuating LH's given in Figure 2.

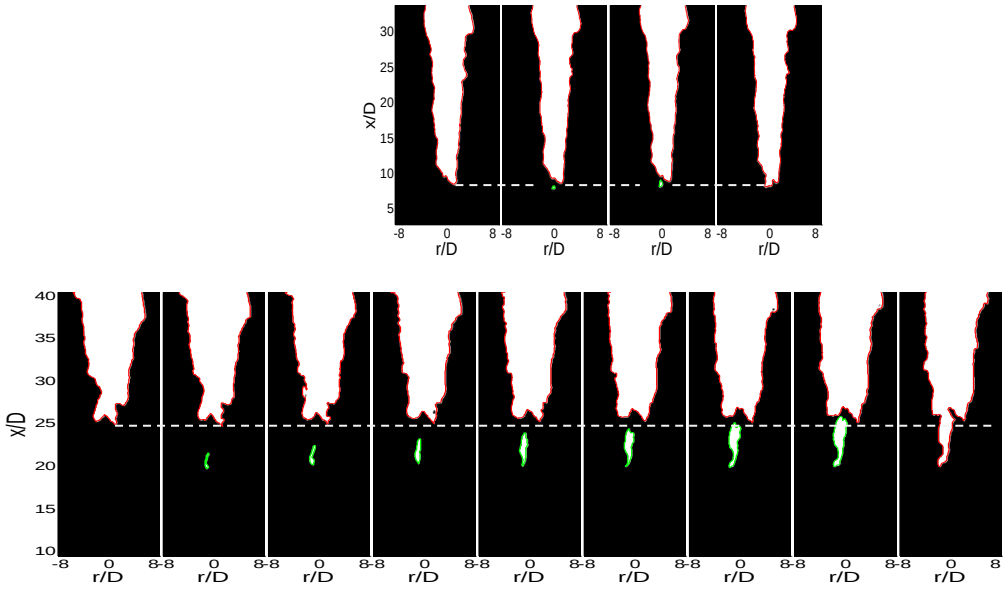


**Figure 4 Consecutive 10 kHz Chemiluminescence CH* images for air/DME=3/1: 1400 K (Top) 1275 K (Bottom). The horizontal dashed line indicates the flame base for the first image. Green highlights the kernels and red for the flame base**

After de-noising the images, the path and size of a kernel is mapped on the preceding image. If the new centroid of the kernel doesn't exist within the boundaries of the projected centroid it is determined to be kernel initiation otherwise it was deemed to be kernel growth. The axial location of

each of these new kernels (sorted based on 15mm axial bin sizes) was obtained for the various fuel mixtures and coflow temperatures seen in Figure 5.

Figure 5 shows the location of kernel formation and consumption given by the first and last data points respectively. The termination is found to line up closely with the average lift off height found in Figure 2. It can be seen that the higher temperature case (1400 K) has a very small axial distance with which kernel initiation and consumption occurs (only two axial positions), and this increases for lower temperatures. There is a definite peak where kernels form for each case and this reduces in relative magnitude for lower temperatures. This peak position marks the most desirable location for auto ignition. Additionally, with decreasing temperatures the range of kernel formation spreads out over a broader range of axial locations as is evident from the flatter profiles.

Increasing partial premixing while keeping a similar temperature range in the coflow (1225 K to 1275 K) leads to narrower profiles with sharper peaks in the frequency of kernel formation. This is consistent since increasing partial premixing facilitates the formation of ignitable mixtures and hence enhances the likelihood of auto ignition.

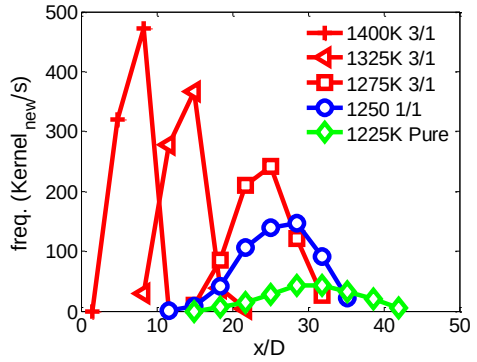


**Figure 5 Frequency of kernel initiation for a given axial location**

Figure 6 shows the average flame base advection velocity for air/DME=3/1 at three coflow temperatures. It displays the average of the flame base velocity fluctuations, having removed any discontinuity of kernel consumption as this would incur an unrealistic upstream flame base propagation.

This figure indicates as per the images in Figure 4 that for lower temperatures the downstream advection of the flame base is greater. That is, for the flame base to be stabilised and not get blow off (oscillate about the mean LH), kernel stabilisation is more important at lower coflow temperatures.

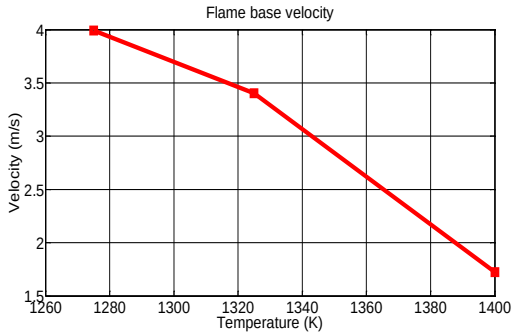


**Figure 6 Downstream flame base advection for air/DME= 3/1 at various coflow temperatures**

## 3 Conclusion

A study on the lift off heights of auto igniting flames with DME diluted with air was performed using a vitiated hot coflow burner. LH's are found to increase for a given coflow temperature for an increase in dilution ratio. Also LH's are seen to increase for a given diluent with reduced coflow temperature.

Finally, through the tracking of auto ignition kernels a method was developed to determine the location of kernel initiation and consumption. By measuring the velocity fluctuation of the flame base excluding any kernel consumption it was possible to define the importance of kernels for flame stabilisation.

## 4 References


[1] C. Arcoumanis, C. Bae, R. Crookes, and E. Kinoshita, *Fuel*, vol. 87, no. 7, pp. 1014–1030, Jun. 2008.

[2] H. J. Curran, E. . Fisher, P. . Glaude, N. . Marinov, W. . Pitz, C. . Westbrook, P. . Flynn, R. . Durett, A. O. zur Loye, O. C. Akinyemi, and F. L. Dryer, *Symp. Combust.*, 2000.

[3] K. M. Lyons, *Prog. Energy Combust. Sci.*, vol. 33, no. 2, pp. 211–231, Apr. 2007.

[4] R. Cabra, J. Chen, R. Dibble, A. Karpetis, and R. Barlow, *Combust. Flame*, vol. 143, no. 4, pp. 491–506, Dec. 2005.

[5] R. Cabra, T. Myhrvold, J. Y. Chen, R. W. Dibble, A. N. Karpetis, and R. S. Barlow, *Proc. Combust. Inst.*, vol. 29, pp. 1881–1888, 2002.

[6] R. Hilbert and D. Thévenin, *Combust. Flame*, vol. 128, no. 1, pp. 22–37, 2002.

[7] R. L. Gordon, A. R. Masri, and E. Mastorakos, *Combust. Flame*, vol. 155, no. 1–2, pp. 181–195, Oct. 2008.

# An Experimental Study of the Effect of Soap on Ignition and Combustion Characteristics of Single Droplets of Glycerol

Hendrix Y. Setyawan, Mingming Zhu*, Zhezi Zhang and Dongke Zhang
Centre for Energy (M473)
The University of Western Australia, 35 Stirling Highway, WA 6009 Australia

## Abstract

The effect of soap, as an impurity in the glycerol of biodiesel manufacturing, on the ignition and combustion characteristics of single droplets of glycerol was studied experimentally. Soap was added into a pure glycerol at concentrations of 1 to 5 wt%. Single droplets of pure glycerol with and without soap addition were suspended on the tip of a silicon carbide fibre and exposed to an air temperature of 1023 K in an electrically heated tube furnace. The ignition and combustion behaviour of the droplets was recorded using a CCD camera and the ignition delay time, burnout time and burning rate were then estimated. It was found that the ignition and combustion process of droplets of glycerol with soap additions consisted of two stages: (1) ignition and combustion of the glycerol; and (2) ignition and combustion the solid residue formed from the first stage. The ignition delay time of glycerol was slightly reduced with increasing concentration of soap added, while the burning rate was enhanced. The burnout time of the glycerol slightly decreased with increasing soap concentration due to the increased burning rate.

*Keywords: Droplet, Glycerol, Ignition, Soap.*

## 1. Introduction

Crude glycerol is an inevitable by-product of biodiesel production. In 2014, production of crude glycerol was approximately 2.8 million metric tonnes (MMT), higher than the global market could absorb at approximately 2 MMT [1]. A number of glycerol utilisation technologies have been proposed and reviewed in [2]. However, either the costs of these technologies are expensive or the values of the products generated are too low.

Combustion of crude glycerol for combined heat and power generation has been identified as the simplest glycerol utilisation method, but a number of challenges remain and the major one is the impurities contained in the crude glycerol [3-5]. These impurities include methanol, water, soap, fatty acid methyl ester (FAME), glycerides, free fatty acid (FFA), as well as ash. The amount of each impurity in crude glycerol depends on the process and operating condition of biodiesel production.

In order to utilise crude glycerol as a fuel, it is essential to understand the effect of each of these impurities. Our previous work studied the effects of water [6] and methanol [7] on the ignition and combustion of pure glycerol droplets. The present experimental work, as an extension of our previous studies, discussed the effect of soap on the ignition and combustion characteristics of glycerol.

The soap in crude glycerol is derived from sodium hydroxide (NaOH), a base catalyst for biodiesel production. The sodium hydroxide reacts with methanol producing sodium methoxide [8], which then reacts with glycerol to produce soap and methanol at certain conditions. The sodium hydroxide also reacts with free fatty acid in the presence of water producing soap during transesterification process. The amount of soap in crude glycerol can reach up to 26.5wt% [3-7]. The reaction routes for the soap formation are illustrated in the following:

$$C_3H_5(OCOR)_3+CH_3OH \overset{NaOH}{\rightleftharpoons} 3COOR+C_3H_5(OH)_3 \quad (1)$$

$$CH_3OH + NaOH \rightarrow CH_3ONa + H_2O \quad (2)$$

$$C_3H_5(OH)_3+3CH_3ONa \rightarrow C_3H_5(ONa)_3+3CH_3OH \quad (3)$$

$$NaOH + H_2O \rightarrow Na^+ + OH^- + HOOCR_1 \rightarrow NaOOCR_1 + H_2O \quad (4)$$

The knowledge on the effect of soap on the ignition and combustion of glycerol is essential in utilising crude glycerol as a fuel but such information is not available in the literature. Sodium, the main component of soap could affect the ignition and combustion characteristics of hydrocarbon fuels [9]. Thus, it is expected that soap have a significant impact on the ignition and combustion of crude glycerol. This paper investigated the effect of soap on the combustion behaviour including ignition delay time, burnout time, and burning rate of glycerol droplets using the single droplet combustion method that widely used to study the ignition and combustion fundamentals of liquid fuels [10].

## 2. Experimental

Employed for the current study, a pure glycerol and olive oil based soap were purchased from Sigma Aldrich and a local store, respectively. The soap was added into the pure glycerol at 1%, 3% and 5% by weight. To shorten, the pure glycerol and the glycerol with soap additions were denoted as PG and

* Corresponding author:
Phone: (+61) 8 6488 5528
Email: mingming.zhu@uwa.edu.au

PGSx, respectively, with x indicating the weight percentage of soap in the glycerol (ie: PGS1 means pure glycerol with 1 wt % of soap addition).

The ignition and combustion behaviour was studied using the single droplet combustion technique described in [10]. As illustrated in Fig. 1, the experimental setup consisted of a droplet suspension system, a horizontal tube electric furnace with temperature control for providing a hot air environment, a step motor (equipped with backlight) for delivering the droplet into the furnace, and a CCD camera (Basler PIA-210gc) controlled by a computer for capturing the images [10].

In brief, a droplet was produced using a 10 µL micro pipette and deposited on the tip of silicon carbide fibre of 0.142 mm in diameter. The initial droplet diameter ($d_o$) in the current study was around 1 mm. Aided by a step motor, the droplet was delivered at a linear velocity of 1 $ms^{-1}$ to the centre of the furnace. The droplet then stopped when it reached the centre of furnace. The temperature of the furnace was set at 1023 K. In order to record the combustion processes, the CCD camera was used to capture images of the combustion history. A halogen lamp was provided as a back light to capture the change of droplet size during combustion.

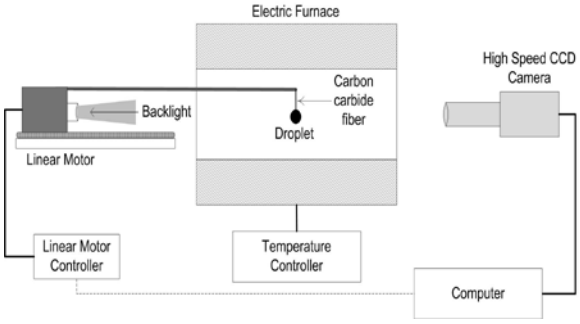


Figure 1 A schematic diagram of experimentation apparatus of single droplet combustion

The images of backlit burning droplets, captured by the camera at 200 fps, were processed using self-developing Matlab program to calculate the evolution of droplet size during combustion. The equivalent droplet diameter was determined from measuring the width ($d_{min}$) and height ($d_{max}$) of the droplet according to the following equation [11].

$$d = \sqrt[3]{(d_{\min}^2)(d_{\max})} \quad (5)$$

The un-backlit images taken from the camera at 50fps were used to approximate ignition delay time and burnout time. The ignition delay time ($t_i$) was defined as the period between the moments when the droplet reached the centre of the furnace to the moment when the first visible flame was observed. The burnout time ($t_b$) was defined as the period from the moment when the first visible flame was observed until the combustion of glycerol completed. The total combustion time, the sum of the ignition delay time and burnout time, was also calculated. The burning rate ($k$) then was determined using $d^2$-Law of droplet combustion by measuring the rate of droplet size reduction, which taken as the ratio of the droplet size at the moment when ignition occurred divided by the burnout time [12].

## 3. Results and Discussion

### 3.1 Ignition and Combustion Phenomena of Single Glycerol Droplets

In combustion of a typical single droplet of a fuel [13], when the droplet is subjected to heat from ambience at a certain temperature, the surface temperature of the droplet increases and the droplet starts to vaporise when the temperature reaches over the boiling point of the droplet. The fuel vapour diffuses into the ambience and mixes with oxygen to form a combustible mixture. Once the ignition criterion is met, the ignition is occurred and a flame is formed surrounding the droplet. The combustion is completed when the mass of the droplet has been completely evaporated.

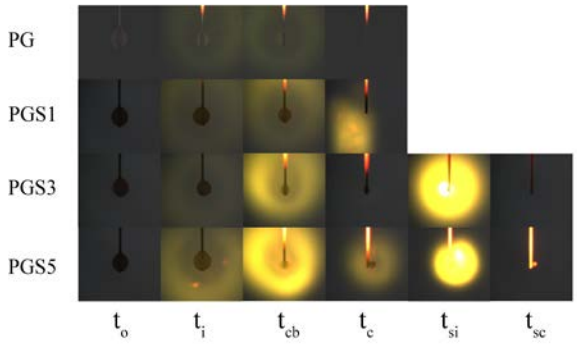


Figure 2 The typical images of burning glycerol droplets with and without soap addition at 1023K; $t_o$ is the moment when the droplets arrived at the centre of the furnace; $t_i$ the time when the droplets ignited, $t_{cb}$ the time when combustion was steady, $t_c$ the time when the combustion of liquid glycerol completed, $t_{si}$ the time when the ignition of the solid residue occurred, $t_{sc}$ the time when the combustion of solid residue completed

Figure 2 shows the time sequenced un-backlit images of typical glycerol droplets with and without soap addition at 1023K. From left to right hand side are the images of the droplets from the moment the droplets arrived at the centre of the furnace until the completion of the combustion. Seen from Figure 2, upon arrival at the centre of the furnace, the glycerol droplets with and without soap addition were the same in size. Upon ignition, flames were formed surrounding the droplets. The flame of the pure glycerol droplet was blue/greenish and dim, suggesting a clean combustion with very little amount of soot particles formed. At the end of combustion, the combustion of the pure glycerol droplet showed a clean fibre without any solid residues formed. However, for the droplets with soap additions, the flames turned to be yellow and became brighter with increasing the soap concentration. When the combustion approached to the end, some solid residues were produced and attached on the tip

of the fibre. The solid residues from the combustion of glycerol droplets with addition of 3 wt% and 5 wt% of soap were then ignited and burned, producing bright yellow flames again. The combustion of the solid residue lasted a few milliseconds when there was still a small proportion left on the tip of the fibre, which was believed to be the ash. An initial speculation as to reason is that the solid residue was the unevaporated sodium from the soap. It has been found that sodium was the main component of the fly ash in the combustion of demethylated glycerol using swirl burners [5]. However, an investigation into chemical compositions of the solid residues is required and warrants further research.

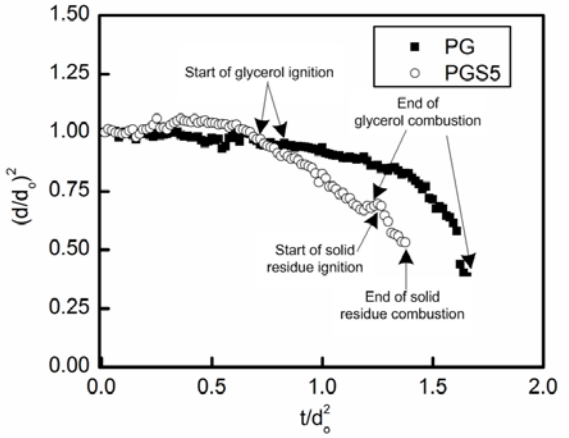


Figure 3 The normalised temporal evolution of the squared diameter $(d/d_o)^2$ for a pure glycerol droplet and a droplet with 5 wt % soap addition at 1023K

Figure 3 illustrates the temporal variation of the square of the normalised droplet diameter $(d/d_0)^2$ for droplets of pure glycerol and pure glycerol with the 5wt% soap addition at 1023K. The droplet size was measured from the moment of the droplet at the centre of the furnace until the completion of combustion. It is evident that the droplet size remained almost constant during the ignition delay period and then showed an approximately linear reduction after ignition, implying that the droplet combustion conformed to the $d^2$-law [12]. However, for the glycerol droplet with the soap addition, the droplet size decreased linearly with time upon ignition and then levelled off for a few milliseconds before the droplet size decreasing linearly again with time. This is in accordance with the phenomena observed in Figure 2 and the explanations above. The combustion process of the glycerol droplets with soap additions was composed of two stages: (1) the ignition and combustion of liquid glycerol followed by (2) the ignition and combustion of solid residue generated from the first stage of combustion. Note that in the following discussion, we mainly focused on the effect of soap addition on the ignition delay time, burnout time, total combustion time and burning rate of the liquid glycerol occurred in the first stage of the combustion. Discussion on the ignition and combustion characteristics of the solid residues was not included.

## 3.2 Effect of Soap on Ignition Delay Time and Burnout Time of Glycerol Droplets

Figure 4 illustrates the effect of soap addition on the ignition delay time, burnout time and total combustion time of glycerol droplets. It is evident that the ignition delay time of glycerol droplets was slightly reduced with increasing concentration of the soap. This suggested that the soap addition may change the evaporation rates of the glycerol droplets, particularly at the surface of the droplets. On the other hand, it was speculated that the sodium evaporated into the gas phase promoted the chemical reaction rate between the glycerol vapour and air during the ignition delay period, shorting the ignition delay time [14].

It is also evident that the burnout time and total combustion time decreased with increasing soap concentration in the glycerol, which may be attributed to the enhanced burning rate as discussed in the following section.

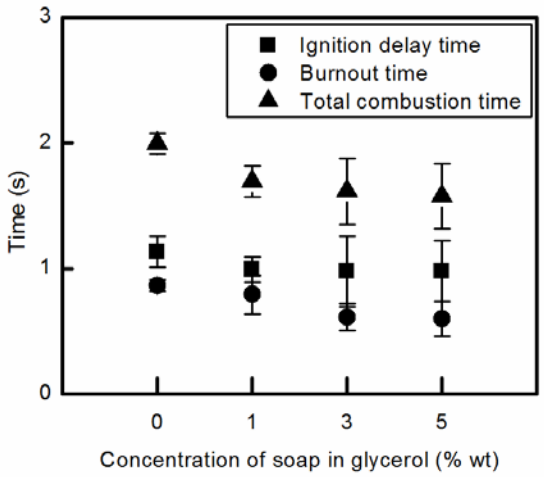


Figure 4 The ignition delay time burnout time and total combustion time of glycerol droplets with soap addition at different concentrations at 1023K

## 3.3 Effect of Soap on Burning Rate of Glycerol Droplets

Figure 5 displays the effect of soap addition on the burning rates of glycerol droplets at 1023K. As stated in the above, for the droplets with soap addition, which consist of two combustion stages, the burning rate in Figure 5 was the burning rate of the liquid droplet in the first stage, excluding the combustion of the solid residues in the second stage.

It can be seen from Figure 5 that the addition of soap increased the burning rates of glycerol droplets. As shown in Figure 2, the combustion of glycerol droplets with the soap addition showed brighter flames than that of the pure glycerol, suggesting that the flame temperatures of the soap added glycerol droplets were higher. According to the classic droplet combustion theory, for a droplet with higher flame temperature, its combustion rate would subsequently augment [12].

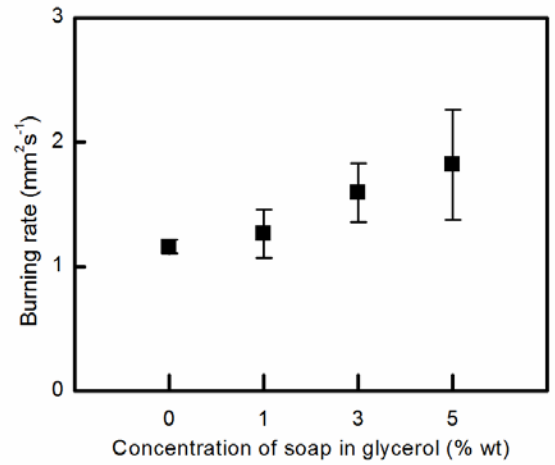


Figure 5 The burning rates of glycerol droplets with soap addition at different concentrations

## 4. Conclusions

The ignition delay time, burnout time, and burning rate of single droplets of glycerol with and without addition of soap were experimentally studied at air temperature 1023K. The ignition and combustion process of single droplets of glycerol with soap addition consisted of (1) ignition and combustion of glycerol stage and (2) subsequent ignition and combustion of solid residue stage. With increasing soap to the glycerol ratio, the ignition delay time of the glycerol was slightly shortened, while the burning rate was enhanced. The burnout time of the glycerol slightly decreased with increasing soap addition due to the increased burning rate.

## 5. Acknowledgments

Financial supports have been received from the Australian Research Council under the ARC Discovery Project scheme (DP110103699) and ARC Linkage Project scheme (LP100200135). Financial and other supports have also been received from BHP Billiton Iron Ore Pty Ltd and Ansac Pty Ltd. Hendrix Setyawan also acknowledges the Australian Commonwealth Government for providing the Australia Awards Scholarship (AAS).

## 6. References

[1] R. Ciriminna, C. Della-Pina, M. Rossi and M. Pagliaro. European Journal of Lipid Science. **116** (8) (2014).

[2] H.W. Tan, A.R. Abdul Aziz and M.K. Aroua. Renewable and Sustainable Energy Reviews. **27** (2013), pp.118-127.

[3] C.A.G. Quispe, C.J.R. Coronado and J.A. Carvalho Jr. Renewable and Sustainable Energy Reviews. **27** (2013), pp. 475-493.

[4] J. Mcneil, P. Day and F. Sirovski. Process Safety and Environmental Protection. **90 (**2012), pp. 180-188;

[5] M.D. Bohon, B.A. Metzger, W.P. Linak, C.J. King and W.L. Roberts. Proceedings of The Combustion Institute. **33 (**2011), pp. 2717-2724.

[6] H. Y. Setyawan, M. Zhu, Z. Zhang and D. Zhang. Proceeding of International Conference of Applied Energy. Abu Dhabi (2015).

[7] H. Y. Setyawan, M. Zhu, W. Zhou and D. Zhang. Proceedings of The Australian Combustion Symposium Nov 6th to 8th. The University of Western Australia. (2013), pp. 332-335.

[8] A. Singh, B. He, J. Thompson and J. V. Gerpen. Applied Engineering in Agriculture. **22** (2006) (4).

[9] V. V. Lissianski, V. M. Zamansky and P. M. Maly. Combustion and Flame, 125 (2001), pp.1118-1127.

[10] M. Zhu, Y. Ma and D. Zhang. Proceedings of the Combustion Institute. **34** (2013), pp.1537-1544.

[11] M. Zhu, Y. Ma and D. Zhang. Chemeca. Engineers Australia, Wellington, New Zealand. (2012), pp. 543-553.

[12] C.K. Law. Combustion Physics. Cambridge University Press, New York. United States of America. (2006)

[13] S. K. Aggarwal. Progress in Energy and Combustion Science. **45** (2014), pp. 79-107.

[14] A. Makino and H. Fukada, Proceedings of the Combustion Institute. **30** (2005), 2047-2054.

# Soot Reduction in Cookstoves due to Turbulent Mixing

K.M. Lask[1,3*], P.R. Medwell[2], C.H. Birzer[2], A.J. Gadgil[1,3]
[1]Applied Science & Technology, University of California Berkeley, Berkeley, CA 94720, USA
[2]School of Mechanical Engineering, The University of Adelaide, Adelaide, SA 5005, Australia
[3]Energy Technologies Area, Lawrence Berkeley National Laboratory, Berkeley, CA 94720, USA

## Abstract

Emissions from solid-fuel cookstoves, used by almost three billion people worldwide, create major issues for both human health and the environment. These emissions cause an estimated 4.3 million premature deaths annually and significantly contribute to environmental issues such as global climate change. One of the harmful emissions is soot and a promising option for reducing soot emissions from cookstoves is injecting air into the combustion chamber to increase turbulent mixing. Typically aerosol measurement systems are used to explore the effects of such modifications. However, these systems collect data relatively far away from the source, which makes it difficult to explore how the design modifications affect the actual flames. In this study, soot produced by a proxy-cookstove burner was measured in-situ using luminescence to explore the effects of different air injection modifications. The soot reduction trends were compared between different air injection angles and different air injection flow rates. Black carbon aerosol measurements were collected to compare with the values for in-situ soot and also to gain a quantitative value of black carbon produced in each case. It was found that overall trends appear to be consistent between the two measurement systems with all air injection modifications reducing black carbon over the baseline flame case and higher airflows proving to be more beneficial for soot reduction. Despite major differences in the amount of black carbon emitted from the flames recorded by the aerosol system, the luminosity intensity is similar for all cases, suggesting a significant increase in the soot oxidation with forced air flow. This indicates that the halo air injection systems are performing as desired, inducing turbulent mixing to reduce soot emissions.

*Keywords: Cookstove, Luminescence, Soot, Black Carbon, Aethalometer*

## 1. Introduction

Worldwide, nearly three billion people cook using solid fuels such as biomass and emissions from these fires lead to enormous health and environmental issues [1]. Smoke from biomass stoves has been found to be the largest environmental threat to health in the world, prematurely killing an estimated 4.3 million people every year [1, 2]. The burning of residential solid fuels also significantly contributes to outdoor air pollution and climate change, providing an estimated 25% of global black carbon emissions [3]. Due to these undesirable side effects, there is considerable interest in reducing soot emissions from biomass stoves [4].

One promising technique for soot reduction is injecting air into the combustion chamber of the stove to promote turbulent mixing. Mixing is a crucial component in soot reduction for non-premixed flames because a large fuel-rich zone exists where particulates are less likely to be exposed to oxidizers. Increased mixing breaks up this large fuel-rich zone into smaller pockets, raising the likelihood that soot particles will be exposed to air and thus oxidized prior to emission.

When evaluating cookstove performance, it is common practice to use an aerosol-based emissions measurement system, sampling far downstream from the stove in a duct which captures the emissions [5-7]. Aerosol emission measurements are useful when evaluating stove performance, but are not as informative about what is occurring in the flame zone itself because impacts to the flame must be hypothesized from measurements taken far downstream. Nonintrusive, in-situ measurements, like luminescence, provide a better view of how design modifications, such as air injection, are affecting the combustion in a stove.

The aim of this paper is to evaluate the impacts of air injection modifications on soot within a cookstove. The performance is assessed using a combination of both in-situ luminescence and ex-situ aerosol measurements. This systematic study of applying different injection angles and airflow rates to deduce promising modifications will guide future exploration and provide a comparison between concentrations of in-situ soot and ex-situ soot emissions.

## 2. Experimental methodology

Glowing soot particles formed in the fuel-rich regions of the flame produce a yellow luminescence [8]. This luminescence can be observed and recorded using a light collection device, such as a camera or photodiode, thus providing an estimation of soot in the flame based on the amount of light output, or luminosity.

Luminescence was chosen for these experiments as it is an uncomplicated, adaptable, and nonintrusive method of measuring soot concentration in a flame. A limitation of luminescence is that it does not provide a quantitative concentration, only qualitative results. However, these qualitative results allow for straightforward comparisons between different air injection modifications and provide insight on the locations of soot reduction in the flames. Aerosol measurements, on the other hand, provide a

* Corresponding author:
Phone: (+1) 510 486 7435
Email: klask@berkeley.edu

quantitative measurement of emitted black carbon, but do not offer information on locations of soot reduction.

Comparing results from the two techniques emphasizes the difference between in-situ soot (soot within the flame) and soot emitted from the flame. While it is desirable to reduce the soot emitted from a fire, the presence of soot within the flame is not entirely unwelcome as it increases radiative heat transfer to a cooking pot. Luminescence only measures in-situ soot, so soot may still be oxidized prior to leaving the stove but this would not be captured in the luminosity. As aerosol techniques measure the soot emitted, comparing luminescence and aerosol measurements can provide an idea of the amount of soot being oxidized outside of the flame front by each modification.

## 2.1 Burner and Air Injection System

A gaseous burner was developed that mimicked the thermal power and particulate emissions of an improved wood-burning cookstove, the Berkeley-Darfur Stove [5, 6], for proof of concept. The approach of having a well-controlled gas burner as a proxy for a wood-burning cookstove was chosen as wood fires are too variable for future laser-based experiments. The burner, shown in Fig. 1, is a trident-like system consisting of three parallel stainless steel pipes (each 254 mm long with a 21 mm outer diameter) spaced 19 mm apart. Nine 3.76 mm holes were drilled in each pipe situated such that the multiple small flames could interact, similar to a wood fire. Liquefied petroleum gas (LPG) was combusted in non-premixed flames with the flow of fuel held constant by an Alicat mass flow controller.

A toroidal manifold mounted above the burner, referred to in this paper as a halo, was used as the air injection modification. Three different halos were explored in this study; each halo injected air downwards onto the flames but were differentiated by the angle of air injected relative to the burner.

- The "Straight" halo had holes that aimed air directly downward onto the flames.
- The "Angled" halo aimed air inwardly at a 30 degree angle.
- The "Swirled" halo had the inward 30 degree angle of the Angled halo, but also included a 30 degree tangential component to add a swirling effect.

Each halo had ten 2.4 mm holes equidistantly spaced around the halo. The halo was mounted 154 mm above the burner, centered over the holes in the burner tubes. Three volumetric airflow rates were used for the experiments (28.3, 35.4, and 42.5 standard L/min), along with a baseline case where no air was added.

# 3. Luminescence Experiments

Images of the flames under the different halo and airflow cases were taken using a digital SLR camera. Several exposure times, ISO settings, and aperture settings were assessed to achieve the highest signal

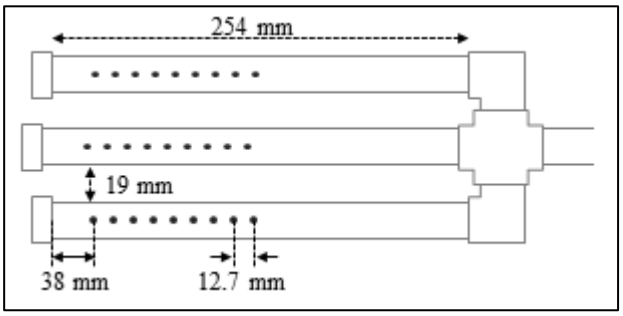


**Figure 1:** LPG burner designed as a proxy for an improved wood-burning cookstove. The parallel burner pipes are 21 mm diameter stainless steel with 3.76 mm diameter holes. The fuel enters the burner from the right of the image.

output with limited saturation for all halo and flow rate combinations. The signal-to-noise ratio of the images was found to be less than 2%. Total light emitted from the flames was also recorded with a photodiode. No filter was used, so the photodiode detected broadband flame emission. Background noise was removed from the total intensity before processing. The camera and photodiode were both mounted inline with the centre pipe of the burner.

## 3.1 Total Intensity

The average total luminosity intensity, shown in Fig. 2, was measured with the photodiode. All halo cases decreased intensity compared to the baseline, with the Straight halo leading to the largest reduction on average. As the measured intensity is taken as a proxy for the luminescing soot concentration in the flame, air injection through any halo appears to reduce soot production within the flame. Furthermore, in general an increase in air flow through the halo appears to suppress soot formation, consistent with the expected trend due to higher strain rate.

## 3.2 Intensity Radial Profiles

To visualise the effect of the different halos on the flames, mean profiles of the recorded intensity were developed from the luminescence images. Radial profiles of intensity (integrated over the total flame height) from the centreline of the burner outward are shown in Fig. 3.

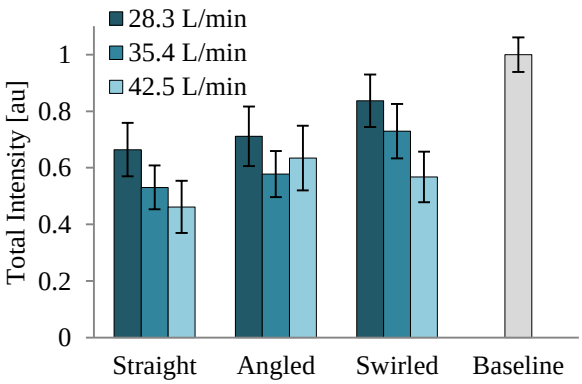


**Figure 2:** Total signal intensity of flames under different cases. All halos reduced soot compared to the baseline with the Straight halo providing the largest reductions on average. Error bars represent standard deviation (n > 1000).

Luminescence images for each halo are shown in Fig. 4. Each image is the average of approximately 1000 still images and represents a viewing area of 238 mm by 162 mm. These sample images are for the lowest halo airflow rate, 28.3 L/min.

The baseline case profile shown in Fig. 3 has two strong intensity peaks in the radial direction, one at the centreline and the other at approximately 40 mm. This corresponds to the flames from the centre pipe and one of the outer pipes of the burner. In the images, it is the same with three strong flames shown in Fig. 4A.

The Straight halo pushes these flames downward, theoretically increasing mixing so the soot is exposed to oxidizers. At low flow rates, like shown in Fig. 4B, flames still rise through the centre of the Straight halo, but as the flow increases, all flames are more equally mixed. This explains the strong soot reduction shown in Fig. 2 and why the soot decreased as airflow increased.

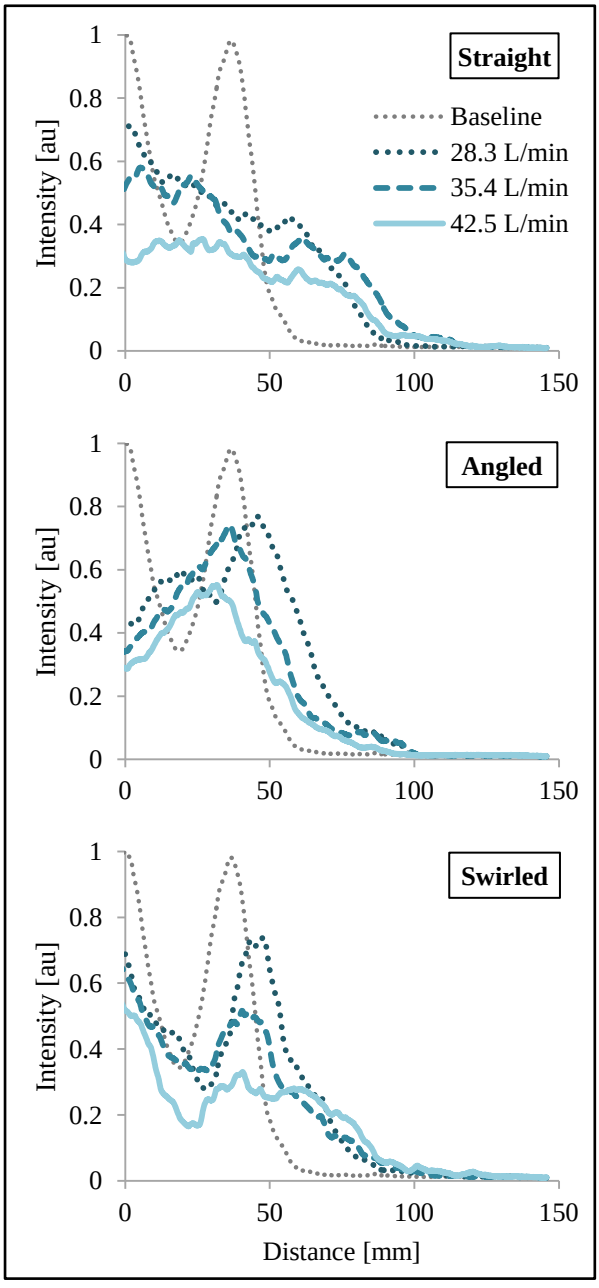


**Figure 3:** Mean radial profiles of signal intensity for each Halo: Straight (Top), Angled (Middle), Swirled (Bottom). The baseline case is shown on all three graphs for comparison.

The Angled halo primarily breaks up the fuel-rich zone in the centre flame where the air converges, leading to the reduced intensity seen in Fig. 4C and explaining the improved soot reductions over the baseline in Fig. 2. However, it allows the flame from the outer pipe to rise up the outer edge of the injected air (around 40-50 mm in the radial direction of the profile), which is likely why the Straight halo had larger reductions.

The Swirled halo profile has two interesting trends apparent. An almost constant peak is maintained along the centreline even with increased air flow. As this peak is not observed in the Angled halo case, it is most likely due to a swirl effect caused by the tangential component of the Swirled halo because the two halos are otherwise identical. Indeed, a swirling central vortex was visually observed during experiments. Similar to the Angled halo, the outer flame is present at low flow rates as the air injection does not greatly impact the flames near the burner, shown in Fig. 4D. However, as seen in the profile, if the flow rate increases, this outer flame is reduced almost to the level of the Straight halo as that soot is likely oxidized by air entrained by the central vortex.

## 4. Ex-situ Measurements

Black carbon aerosol measurements were taken using a rack-mounted aethalometer, Model AE22, manufactured by Magee Scientific. An aethalometer is an instrument that determines the mass concentration of black carbon by passing an aerosol sample through a filter and measuring the light absorption as carbon particles collect on the filter. The aerosol experiments were conducted with the burner and halo in an exhaust hood system which controlled and monitored airflow rates through the duct. Real time (1 Hz) measurements were taken by the aethalometer from the exhaust ducting, sampled approximately 2.5 m downstream of the burner.

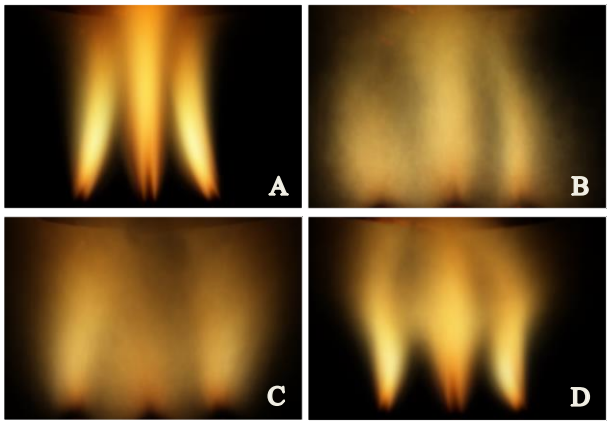


**Figure 4:** Averaged images of flames in each halo case: (A) Baseline, (B) Straight, (C) Angled, and (D) Swirled. Images represent a 238 mm by 162 mm viewing window and the lowest airflow rate is used in all halo images.

The ex-situ results shown in Fig. 5 follow similar trends to the in-situ results shown in Fig. 2: (1) all halo and air combinations reduce soot in comparison to the baseline; (2) the Straight halo performs best followed by the Angled and then the Swirled; and (3) as the flow rate of air increases, the soot decreases.

An important distinction is noted in the level of soot reduction measured between the baseline and halo cases; the difference between baseline and halos is far larger and more significant in the ex-situ results. This is likely due to the air injection modifications performing as desired – soot still forms within the flame, resulting in high luminosity, but the increased turbulent mixing from the air injection oxidizes soot prior to its emission.

## 5. Discussion

An important consideration is the effect of the air on the flame strain rate. If air strains the flame too much this could lead to local extinction. It could be expected as the airflow rates increase, the probability of quenching occurring also increases, and this could lead to an increase in soot released from the flame. A further sign of flame quenching is an increase in carbon monoxide (CO) emissions [9]. To help identify quenching, a California Analytical Instruments NDIR gas analyzer measured CO emissions in the same aerosol system as the aethalometer. The baseline case emits three times the amount of CO as any of the halo cases so any quenching effects appear to be small in this system. However when optimizing an airflow rate for these modifications, closer consideration will need to be taken to evaluate and mitigate quenching effects.

It is also important to note that the burner used in this work is a proof of concept; the real cookstove is a very complex system with many important aspects besides soot emissions, such as gaseous emissions, fuel consumption, thermal efficiency, cultural relevance, and ease of implementation. In a real cookstove, for example, there is a cylindrical combustion chamber which will provide containment for the flames and injected air and promote mixing, especially for the Swirled halo Future work is therefore necessary to evaluate effects of the halos in the real stove.

## 6. Conclusions

The soot emitted from the global use of cookstoves has large adverse impacts on health and the environment; forced air modifications are proposed as a possible technique for decreasing the amount of soot emitted from cookstoves. In this paper, the potential for soot reduction using air injection was explored using both luminescence and aerosol systems. The comparison of in-situ and ex-situ measurements of soot reductions due to air injection modifications has shown similar trends: all air injection cases evaluated reduced soot compared to the baseline and generally as the air flow increased, the soot concentration decreased. However, the difference in magnitude between the in-situ and ex-situ

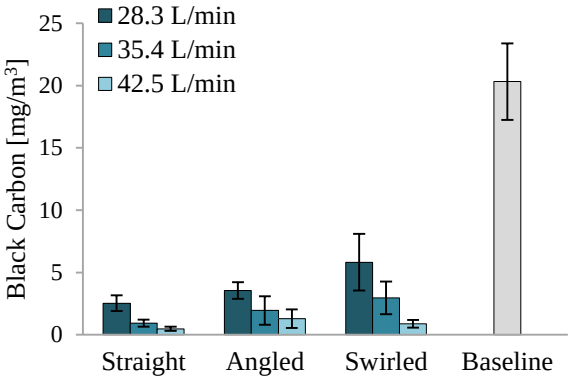


**Figure 5:** Ex-situ average black carbon emissions. Similar to the in-situ results, all halos reduced soot compared to the baseline with the Straight halo providing the largest reductions on average. Error bars represent standard deviation (n > 1000).

reductions indicates that the halos do not affect soot formation in the flame, so high luminosity is measured, but the forced air is successful at promoting oxidation of the soot prior to its emissions and measurement ex-situ.

## 7. Acknowledgments

Funding for this research was generously provided by a grant through the GROW program sponsored by the U.S. National Science Foundation and the University of Adelaide. The authors would like to thank Jingjing Ye, Chia Thong, and Sharon Chen for their assistance with the experiments and Vi Rapp, Daniel Wilson, Julien Caubel and the UC Berkeley engineering machine shop for their help with burner and halo development. The authors are grateful for the support from the Centre for Energy Technology (CET) and acknowledge the Australian Research Council for equipment funding.

## 8. References

[1] World Health Organization (WHO), Indoor air quality guidelines: household fuel combustion, WHO Document Production Services, Geneva, 2014, p. 1.

[2] S.S. Lim, T. Vos, A.D. Flaxman, G. Danaei, K. Shibuya, H. Adair-Rohani, et al., Lancet, **380** (9859) (2012), p. 2224 – 2260.

[3] T.C. Bond, S.J. Doherty, D.W. Fahey, P.M. Forster, T. Berntsen, B.J. DeAngelo, et al., J Geophys Res-Atmos, **118** (11) (2013), p. 5380 – 5552.

[4] Department of Energy, "Biomass cookstoves technical meeting: summary report," DOE, Alexandria, VA, 2011.

[5] J. Jetter, Y. Zhao, K.R. Smith, B. Khan, T. Yelverton, P. DeCarlo, and M. Hays, Environ Sci Technol, **46** (19) (2012), p. 10827 – 10834.

[6] C.V. Preble, O.L. Hadley, A.J. Gadgil, and T.W. Kirchstetter, Environ Sci Technol, **48** (11) (2014), p. 6484 – 6491.

[7] N. MacCarty, D. Still, and D. Ogle, Energ Sustain Dev, **14** (3) (2010), p. 161 – 171.

[8] J. Warnatz, U. Maas, and R. Dibble, Combustion: Physical and Chemical Fundamentals, Modeling and Simulation, Experiments, Pollutant Formation, Springer-Verlag, Berlin, 2006, p. 8.

[9] A.R. Morr, J.B. Heywood, and A.H. Fitch, Combust Sci Technol, **11** (3-4) (1975), p. 97 – 109.

**Proceedings of the Australian Combustion Symposium**
**December 7-9, 2015, The University of Melbourne**

# Assessment of natural draft combustion properties of a top-lit up-draft research furnace

T. Kirch*, P.R. Medwell, C.H. Birzer
School of Mechanical Engineering
The University of Adelaide, SA 5005, Australia

**Abstract**

Worldwide, over four million people die each year due to emissions from cookstoves. To address this problem advanced cookstoves are being developed with one system, called a top-lit up-draft (TLUD) gasifier stove, showing particular potential in reducing the production of harmful emissions. A novel research furnace analogy of a TLUD gasifier stove has been designed to study the TLUD combustion process. A commissioning procedure was performed under natural draft conditions. This included an assessment to establish the design operates as a TLUD gasifier and described the visual attributes of the TLUD's performance for in-field evaluation. Emissions profiles were recorded to identify combustion phases. The efficiency was evaluated through the nominal combustion efficiency (NCE = $CO_2/(CO_2 + CO)$) which is very high in the migrating pyrolysis phase, averaging 0.997. A value of this magnitude has previously not been reported for a cookstove. In the lighting phase and char gasification phase the NCE falls to 0.841 and 0.657 respectively. High $H_2$ emissions are also found in the lighting and char gasification phases, the latter indicating incomplete pyrolysis. The low NCE in the lighting and char gasification phase, compared to the NCE of an open fire, clearly demonstrate the need for combustion optimisation and emissions mitigation of these phases. The precise description of all the combustion phases, in combination with the emissions profiles and efficiency evaluation provide the means for in-field stove evaluation, aid in determining stove deficiencies and set baseline measurements against which TLUD stove designs can be compared.

*Keywords: Top-lit up-draft, Natural draft, Gasification, Pyrolysis, Cookstove.*

## 1. Introduction

Energy consumption in private households in developing countries is still primarily based on biomass fuels. Over the last three decades, and into the foreseeable future, 2.7 billion people [1] consistently rely on traditional, open fires and simple cookstoves to satisfy their cooking needs. These methods have very low efficiency and produce harmful emissions through incomplete combustion. In addition to the potential environmental consequences of deforestation and the contribution to climate change, there are major health problems related to traditional household cooking methods.

Worldwide, approximately 4.3 million premature deaths occur each year from cooking-related illnesses: more than 50% of premature deaths of children under the age of five years are the result of household air pollution [2]. The implementation of more efficient cookstoves that could decrease the consumption of biomass fuels would reduce the environmental consequences as well as people's exposure to pollutants, offering both health and environmental benefits [3].

In order to achieve substantial health benefits, cleaner burning cookstoves than are currently in use are needed [4,5]. One type of cookstove that has been recognised as potentially able to achieve this goal are gasifier stoves [6]. These use the thermochemical process of gasification to transform the fuel into combustible gases and burn them separately in time and location [7].

Gasifier stoves can be used under natural draft conditions, as in the present study, or with the assistance of a fan that creates a forced airflow. Compared with other cookstoves, gasifier stoves have been shown to produce low carbon monoxide (CO) and particulate matter (PM) emissions under laboratory conditions [8,9]. Specific studies on the TLUD combustion behaviour are limited but it has been shown that variation in stove geometry and the utilized fuel have an important impact on the stove performance [10,11]. It has been observed that the burn rate of wood increases with the initial wood density [12] and that the heat transfer to a vessel on the stove is a strong function of the vessel diameter while swirl of secondary air has a negligible impact [13]. Arora *et al.* [14] compared the influence of different standardised tests, kindling material and fuel feeding intervals on the cookstove performance. With different test protocols as well as fuel feeding intervals the emissions factors, primarily of CO and PM, showed variation and increased with lower calorific value of the kindling material. All of these studies have evaluated specific designs and analysed the performance while performing cooking tasks. An analysis of the unobstructed combustion process could lead to a deeper understanding and present further optimization possibilities to reduce harmful emissions consistently.

In the current study, a research furnace was specifically designed to study the operational properties of TLUD stoves in order to optimise for combustion and fuel efficiency. The designed furnace allows for various combustion-relevant parameters to be individually altered and is larger than normal household stoves, to be able to address scaling issues for stoves for communal use versus stoves for private households. Furthermore the increase in size enables a greater variability of adjustable parameters, such as amounts and locations of

* Corresponding author:
Phone: (+61) 8313 5460
Email: thomas.kirch@adelaide.edu.au

the fuel within the combustion chamber, to be studied. Through the commissioning test procedure, under natural draft conditions, the combustion phases will be determined, both visually and through emissions testing over the whole burning cycle. Furthermore, the phases will be clearly separated and analysed individually. This will allow future studies on TLUD cookstoves to be compared with these basic natural draft conditions to determine how design alternations affect the combustion process. An investigation of what is visually perceptible, in addition to the emissions profiles of all combustion phases, is especially relevant for in-field stove assessment. This article, therefore, provides the means to relate visual findings to emissions profiles and sets a baseline against which to compare TLUD stove designs.

## 2. Experimental details

The research furnace was designed as a TLUD stove with the general characteristics of a primary air inlet at the bottom of the furnace, and a lateral secondary air inlet in the upper region, as shown in Fig. 1.

The central component of the research furnace is the stove body, consisting of a cylindrical steel cylinder (600 mm tall, 206 mm inner diameter, 8 mm wall thickness) and a fuel grate. The perforated fuel grate (26% open-area ratio) is located inside the cylinder to hold the fuel stack in place. The depth of the fuel grate is adjustable. The stove body is placed on top of a steel frame, which serves as the primary air inlet chamber. The steel frame of the primary air inlet allows all sides to be closed off, so air can be applied through only one inlet. If the sides are not closed off, air enters freely. In the present study air can enter freely via natural draft over the whole stove diameter. The secondary air inlet is provided by a detachable stove extension to the top of the stove body. There are two possible stove extensions. The first extension is equipped with a diffuser ring around the air inlet that it can be attached to compressed air to control the in-flow. The second extension, which was used for testing in this study, allows air to enter by natural draft.

Emissions data was collected in one central location while the temperature data was constantly measured in two locations. For emissions testing a measuring probe of a Testo 350XL was placed in the centre of a fume hood inlet at a distance of 0.83 m above the exit plane of the extension. The Testo 350XL was used to record the CO, $CO_2$, $H_2$ concentrations, on a dry basis. Temperature data were collected via two K-type thermocouples (locations A and B in Fig. 1) and via an infra-red thermometer (location C).

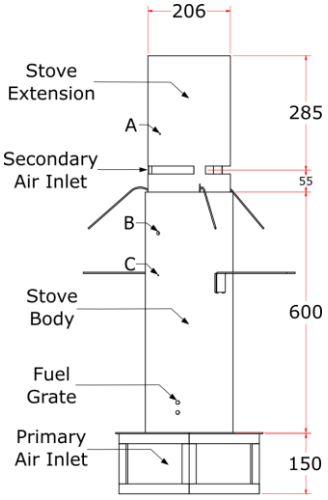


**Figure 1: Schematic TLUD research furnace configuration for natural draft conditions**

A normalisation process was performed for all gathered emissions concentrations. The emissions data are related to the sum of all carbon emissions, here CO and $CO_2$. The emissions are each normalised with respect to the sum of the carbon emissions because these can be attributed to the combustion process and provide the relationship between the intensity of the combustion process and the release of certain products.

The fuel for each test consisted of 700 g of dried locally sourced pine bark chips. Bark chips were chosen as fuel because wood is the most commonly combusted biomass [15]. In every test the furnace was pre-heated, supplied with one batch of fuel and lit at the top, using 5 mL of methylated spirits to aid ignition.

## 3. Results

Preliminary results were gathered through visual assessment. In further tests, emissions and temperature profiles were also recorded. Through the emissions measurements, the performance of the stove in terms of the nominal combustion efficiency (NCE) (defined as $CO_2/(CO + CO_2)$ [9]) was evaluated and a mathematical separation of the combustion phases was conducted. By relating all the findings (visual, emissions and temperature measurements) to one another, a full picture of the process could be drawn.

After lighting, combustion takes place directly at the fuel stack. This can be seen by flames spreading from the kindling material over the surface of the biomass. Once the upper layer of the fuel stack is ignited, the temperature increases and small amounts of smoke start to be released. This suggests that the remaining water evaporates and volatile compounds are released from the fuel. A change can be observed once thick white smoke is released from the fuel stack which is subsequently ignited and clean burning. This indicates that a second phase, termed *migrating pyrolysis*, has begun.

In the transition period from the lighting phase to the migrating pyrolysis volatile compounds are released from the fuel, observable as thick white smoke. The thick smoke indicates that there are high amounts of vaporised pyrolysis products, such as tars, heavier hydrocarbons and water, in the gas stream. This suggests that the process of cracking pyrolytic products into lighter hydrocarbons, which occurs at high temperatures and for which hot char particles act as a catalyst [16], is restricted. Varunkumar *et al.* [13] hypothesised that cracking in gasifier based stoves might be restrained due to the limited char bed thickness.

The thick smoke released from the fuel rises to the secondary air inlet where it should be ignited, after mixing with oxygen from the entering air. In the pre-

heated tests the flames that established on the fuel stack in the lighting phase ignite the thick smoke at the secondary air inlet. In some cold start tests, it was observed that the flames on top of the fuel stack would not ignite a flame at the secondary air inlet. This implies that the flames that establish in the lighting phase need to bridge the distance between the fuel stack and the location where a combustible mixture of secondary air with gasification products from the fuel is present. This has previously not been observed when testing smaller TLUD stoves and needs to be considered when designing bigger TLUD stoves, where the distance between fuel and secondary air inlet increases. Once the thick smoke is ignited a bright yellow flame establishes that burns very cleanly. This separation between the migrating pyrolysis taking place in the fuel stack and the pyrolytic products being burned separately in time and location, at the secondary air inlet, is a distinctive characteristic of TLUD stoves [17].

The end of the migrating pyrolysis phase is indicated by the extinction of the flame at the secondary air inlet. The char gasification phase begins because insufficient combustible volatiles are released from the fuel stack to sustain the flame at the secondary air inlet. It can be seen that hot glowing char remains, with small irregular flames above the char bed until only ash is left on the fuel grate.

Tests were carried out with the natural draft stove and emissions concentrations were recorded, as presented in Fig. 2. Three phases can be identified in each of the profiles presented in Fig. 2. The three phases are the lighting phase, the migrating pyrolysis phase and the char gasification phase. Numerically, a change in phase is identified here when the temporal derivative of the normalised CO profile exceeds $\pm 0.002\ s^{-1}$. This value was determined following a rigorous verification based on inspection of the profiles and found to be reliable at identifying each phase. Table 1 presents the results of the combustion phase specific calculations of time weighted average (TWA) values for all emissions and peak values for the nominal combustion efficiency (NCE) and $H_2$ emissions.

It is apparent from Fig. 2 that in the lighting phase, the NCE can be extremely low, with one peak reaching below 0.6 compared to an average of 0.9965 in the migrating pyrolysis phase (see Table 1). These profiles can be related to incomplete combustion of the kindling material and the top layer of the biomass. In the lighting phase the combustion of kindling material and the top layer of biomass takes place inside the stove body where the surrounding oxygen is quickly consumed and insufficient primary air enters through the fuel stack for complete combustion. It should be noted, though, that only three of the eight tests show very low $CO_2$ peak values, which suggests that a consistently higher NCE in this phase could be achieved. To find ways to ensure lower emissions in this phase requires further investigation.

Once a flame front establishes at the secondary air inlet, the NCE rises to an average of 0.9965, which is much higher than in the other phases, while the $H_2$

**Table 1: Averaged normalised data for the three phases, with the standard deviation of eight tests in parentheses underneath**

| | Lighting | Migrating pyrolysis | Char gasification |
|---|---|---|---|
| Time in Phase [s] | 95.1 | 285.4 | 221.5 |
| | (9.9) | (27.7) | (17.1) |
| Min NCE | 0.8404 | – | 0.6572 |
| | (0.1658) | – | (0.0569) |
| Time to Peak [s] | 54.4 | – | 523.4 |
| | (10.5) | – | (40.9) |
| Peak $H_2/(CO_2 + CO)$ | 0.0418 | – | 0.0556 |
| | (0.0538) | – | (0.0240) |
| Time to Peak [s] | 71.9 | – | 539.1 |
| | (11.4) | – | (41.9) |
| TWA - NCE | – | 0.9965 | 0.8518 |
| | – | (0.0006) | (0.0427) |
| TWA - $CO/(CO_2 + CO)$ | – | 0.0035 | 0.1482 |
| | – | (0.0006) | (0.0427) |
| TWA - $NO_x/(CO_2 + CO)$ | – | 0.00059 | 0.00036 |
| | – | (0.00005) | (0.00007) |
| TWA - $H_2/(CO_2 + CO)$ | – | 0.00013 | 0.01368 |
| | – | (0.00015) | (0.00727) |

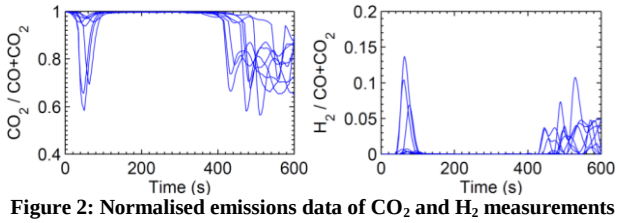


**Figure 2: Normalised emissions data of $CO_2$ and $H_2$ measurements for eight tests**

emissions remain consistently low (Fig. 2). In this phase the migrating pyrolytic front steadily moves down the fuel stack, which provides the necessary gaseous products for the flame at the secondary air inlet to be sustained. This phase is highly efficient and exhibits extremely low emissions. Comparing these with the results of Jetter *et al.* [9] and Johnson *et al.* [18] it can be seen that only very few stoves can achieve a NCE of this magnitude. It should be borne in mind, though, that this comparison is limited because the test conditions in the compared studies are different. The comparison still clearly verifies the high efficiency of the research furnace and the potential of this type of stove.

In the char gasification phase, average CO and $H_2$ emissions are higher than in the other phases, resulting in a low NCE. The high CO emissions were to be expected and were also detected by Mukunda *et al.* [19]. These emissions can be explained by an increase in the surface oxidation due to a higher relative surface area [20]. The high $H_2$ emissions should be noted carefully in this phase because they cannot necessarily be explained by char gasification. These emissions might indicate that the release of hydrocarbon compounds in the migrating pyrolysis phase is incomplete. Therefore it might be possible, through further study, to optimise the migrating pyrolysis phase to achieve a higher overall efficiency.

The temperature profiles presented in Fig. 3 reflect the results from both the visual assessment and the emissions data. The three phases can be identified, based on the slope of the temperature profile. In the lighting phase, the gas temperature inside the stove body heats up much more quickly than in the stove extension because combustion takes place on the fuel stack.

Once the migrating pyrolysis phase starts and a flame front establishes at the secondary air inlet, the gas temperature inside the stove extension rises above the

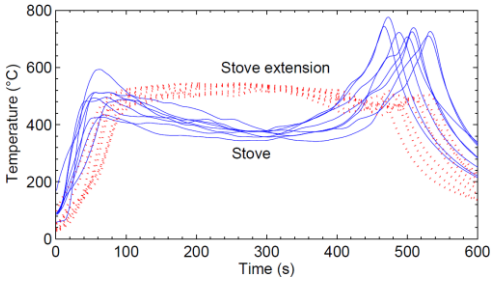


**Figure 3: Mean temperatures in the stove (location B in Fig. 1) and in the stove extension (location A)**

temperature in the stove body. In the stove body, the endothermic (energy absorbing) pyrolysis is mainly sustained by the released energy from the partial oxidation of the pyrolysis products, which causes the temperature to drop. The gas temperature inside the stove body reduces to below 400 °C, which means that the temperature of the pyrolysis products, once they reach the secondary air inlet, can be below this value. This drop of pyrolysis product temperature from ≈ 600 °C, when leaving the fuel bed [19], to below 400 °C when reaching the secondary air inlet suggests a cooling effect. This cooling effect can be assumed to be due to the heat loss through the furnace walls and would increase with the size of the stove. Especially when increasing the size, beyond the size of the presented research furnace, the condensation of liquid pyrolysis products could occur. This cooling effect needs to be considered when designing large stoves. Towards the end of the migrating pyrolysis phase, the gas temperature inside the stove body starts increasing until it peaks in the char gasification phase. This can be explained by the decline of endothermic, pyrolytic reactions with a simultaneous increase of exothermic, char gasification reactions inside the fuel bed. Highest temperatures can be achieved in the char gasification phase within the stove body, as has previously been observed [11, 12].

## 4. Conclusions

In order to better understand the combustion process in TLUD stoves, and to enable future optimisation of TLUD designs for various conditions, a research furnace has been designed, built and commissioned. A visual assessment presented the attributes of TLUD stoves that can be observed; primarily the separation of the solid fuel and the combustion of the gasification products. Furthermore, the emissions profiles were normalised and presented to show the combustion behaviour of TLUD stoves under natural draft conditions. Three distinct phases: the lighting phase, the migrating pyrolysis phase and the char gasification phase, were identified. The lighting and char gasification phases are characterised by low nominal combustion efficiency (NCE) and high emissions of incomplete combustion. It has been seen that a consistently shorter and more efficient lighting phase should be possible to achieve. Also scaling issues are shown to occur when increasing the distance between the fuel bed and the secondary air inlet. These issues include ignition problems at the secondary air inlet and heat loss between the fuel bed and the secondary air inlet. The migrating pyrolysis phase, conversely to the other two phases, displayed an extremely high NCE. High traces of $H_2$ emissions in the char gasification phase suggest that the pyrolysis process is incomplete in the migrating pyrolysis phase. The high emissions in the lighting phase and char gasification phase are in contrast to the low emissions in the migrating pyrolysis phase. This leads to the conclusion that further research to prolong the migrating pyrolysis phase, while mitigating the release of emissions of incomplete combustion in the lighting and char gasification phases, could be of benefit to future stove designs.

These results identify research topics that need to be addressed to optimise stove performance and shed light on relevant parameters that need to be considered when designing larger TLUD stoves for communal use. Additionally they enable the in-field visual assessment of TLUD stoves and set a baseline against which such stoves can be compared.

## 5. Acknowledgements

The authors wish to acknowledge the support of The University of Adelaide, Marc Simpson, Aleksis Xenophon, James Metcalfe and Oliver Robson.

## 6. References

[1] S. Bonjour, H. Adair-Rohani, J. Wolf, N. G. Bruce, S. Mehta, A. Prüss-Ustün, M. Lahiff, E. a. Rehfuess, V. Mishra, and K. R. Smith, Environ. Health Perspect., **121** (7) ( 2013), pp. 784–790.
[2] WHO, (2014). [Online]. Available: http://www.who.int/iris/handle/10665/141496. [Accessed: 04-Aug-2015].
[3] C. A. Ochieng, C. Tonne, and S. Vardoulakis, Biomass and Bioenergy, **58** (2013), pp. 258–266.
[4] K. R. Smith, J. P. McCracken, M. W. Weber, A. Hubbard, A. Jenny, L. M. Thompson, J. Balmes, A. Diaz, B. Arana, and N. Bruce, Lancet, **378** (2011), pp. 1717–1726.
[5] J. Baumgartner, K. R. Smith, and A. Chockalingam, Glob. Heart, **7** (3) (2012), pp. 243–247.
[6] G. L. Simon, R. Bailis, J. Baumgartner, J. Hyman, and A. Laurent, Energy Sustain. Dev., **20** (2014), pp. 49–57.
[7] P. S. Anderson and T. B. Reed, LAMNET Project International Workshop (2004).
[8] J. J. Jetter and P. Kariher, Biomass and Bioenergy, **33** (2) (2009), pp. 294–305.
[9] J. Jetter, Y. Zhao, K. R. Smith, B. Khan, T. Yelverton, P. Decarlo, and M. D. Hays, Environ. Sci. Technol., **46 (**19) (2012), pp. 10827–10834.
[10] C. Birzer, P. Medwell, J. Wilkey, T. West, M. Higgins, G. Macfarlane, and M. Read, J. Humanitarian Eng., **2 (**1) (2013), pp. 1–8.
[11] J. Tryner, B. D. Willson, and A. J. Marchese, Energy Sustain. Dev., **23** (2014), pp. 99–109.
[12] S. Varunkumar, N. K. S. Rajan, and H. S. Mukunda, Combust. Sci. Technol., **183 (**11) (2011), pp. 1147–1163.
[13] S. Varunkumar, N. K. S. Rajan, and H. S. Mukunda, Energy Convers. Manag., **53** (1) (2012), pp. 135–141.
[14] P. Arora, P. Das, S. Jain, and V. V. N. Kishore, Energy Sustain. Dev., **21**, (1) (2014), pp. 81–88.
[15] R. Yevich, Global Biogeochem. Cycles, **17 (**4) (2003).
[16] P. Basu, Elsevier Inc., 2013, p. 118.
[17] P. S. Anderson, T. B. Reed, and P. W. Wever, Boil. Point, **53** (53) (2007), pp. 35–37.
[18] M. Johnson, R. Edwards, V. Berrueta, and O. Masera, Environ. Sci. Technol., **44** (1) (2010), pp. 368–374.
[19] H. S. Mukunda, S. Dasappa, P. J. Paul, N. K. S. Rajan, M. Yagnaraman, D. Ravi Kumar, and M. Deogaonkar, Curr. Sci., **98** (5) (2010), pp. 627–638.
[20] P. S. Arora and S. Jain, Environ. Sci. Technol., **49** (2015), pp. 3958 – 3965.

**Proceedings of the Australian Combustion Symposium**
**December 7-9, 2015, The University of Melbourne**

# Numerical simulation of premixed methane/air flame dynamics in narrow channels

X. Kang, R. J. Gollan, P. A. Jacobs and A. Veeraragavan*
School of Mechanical & Mining Engineering, The University of Queensland, QLD 4072, Australia

**Abstract**

Numerical simulations of premixed methane/air combustion in a submillimetre narrow channel between two parallel heated plates are performed. The problem is modelled by solving the two-dimensional, transient, full Navier-Stokes equations with the detailed reaction mechanism (DRM-19) in our in-house code (Eilmer). The effects of the inflow velocity on the flame propagation characteristics are investigated. For a range of inlet velocities tested, flame dynamics such as flames with repetitive extinction and ignition (FREI), chaotically oscillating flames, symmetric stable flames, slightly and periodically wobbling flames, and asymmetric stable flames are observed.

*Keywords: Premixed combustion; Microchannel; Flame dynamics; Flames with repetitive extinction and ignition (FREI)*

## 1 Introduction

Microcombustion can be defined as combustion in narrow channels with the characteristic dimension (the diameter of a circular tube or the distance between parallel plates) less than 1 mm which is typically lower than the flame quenching distance while mesoscale combustion is viewed as that whose characteristic dimension is larger than 1 mm but still on the order of the flame thickness [1]. As hydrocarbons have considerably higher specific energy per unit mass compared to the traditional electrochemical batteries (45 vs. 0.6 MJ/kg), micro/mesoscale combustion finds potential application in portable power systems and propulsion systems for small scale rockets [1]. Past work on experimental micro/mesoscale combustion [2–5] established operational regimes and stability limits [2], investigated ability to make fundamental temperature and species concentration measurements in simulated mesocale combustors [3] as well as demonstrated a range of flame features such as flames with repetitive extinction and ignition (FREI) [4] and various flame patterns [5].

In order to make quantitatively accurate predictions of experimental observations and to develop reliable design tools for microcombustors, it is necessary to develop numerical models that include accurate physical features. Simulations of hydrogen combustion in narrow channels have been intensively performed and various types of flame dynamics were reported [6–8]. Methane, as the largest constituent of natural gas, is a safer and more reliable fuel for small scale power generation but its micro/mesoscale combustion features need to be better characterised. For numerical simulations of methane/air combustion within narrow channels, there are a limited number of works investigating the transient flame behaviours using fully elliptic models with detailed reaction mechanisms. Miyata et al. [9] recently performed direct numerical simulations (DNS) of premixed methane/air microcombustion. Three types of flame modes i.e. steady flame, oscillating flame and FREI were observed under different wall temperature gradients. Our previous work [10] simulating methane/air microcombustion investigated the effects of the wall temperature magnitude on the flame propagation. The decrease of the wall temperature was found to induce a transition from spatially stable flames to FREI.

Our previous simulation adopted a reservoir inflow boundary condition in which the total pressure and temperature were set and a plenum upstream of the combustor was used to minimize the effect of the inlet boundary [10]. In this paper, a more standard and well-known inflow mass flux boundary condition is used in the time-accurate simulations of premixed methane/air flames in a narrow, heated parallel channel using the detailed chemical kinetics model. The effects of the inflow velocity on the flame behaviours are investigated.

## 2 Numerical Approach

The premixed methane/air flame propagation in a two-dimensional, planar micro-channel is numerically studied by using the Eilmer code [11], which is a Navier-Stokes solver for transient, compressible flow in 2D or 3D developed at the University of Queensland. The cell-centred, finite volume method is employed for the discretization of the governing equations. Time-accurate and numerically stable solutions are obtained by using the explicit three-stage Runge-Kutta time-stepping scheme and setting the Courant-Friedrichs-Lewy (CFL) number to 0.3 to choose the simulation time step.

Figure 1 shows the computational domain and boundary conditions used for the numerical model. The combustor length ($L$) is 5 mm and channel height ($H$) is 600 $\mu$m. In order to capture the asymmetric features of

*Corresponding author: Phone: (+61) 7 33654069; Email: anandv@uq.edu.au

the flame, simulations were performed for a full channel without any symmetry boundary condition imposed at the midplane of the combustor. At the inlet of the combustor, a mass flux boundary condition was set, in which the gas total temperature ($T_0$ = 300 K), mass fractions of incoming species of the stoichiometric mixture and a uniform mass flux ($\dot{M}$) across the boundary were specified. At the outlet, the pressure was set at atmospheric pressure while zero Neumann boundary conditions were imposed for the rest of the variables. At the wall of the combustor, a no-slip boundary condition with a prescribed hyperbolic tangent temperature profile to mimic the heat recirculation by the exhaust gases (as done in [4, 6, 7]) was employed. The wall temperature ramped from the mixture inlet temperature of 300 K to a high temperature at 1400 K over the initial 1 mm of the channel length and maintained at this value for the remaining length of the combustor.

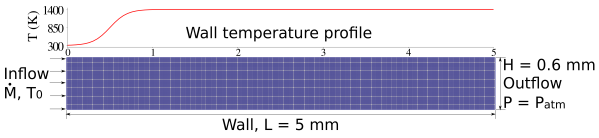


Figure 1: Computational domain/mesh of the micro-channel.

The simulations used the 19-species and 84-reaction methane/air chemical kinetics (DRM-19) [12]. As the subset of a full GRI-Mech3.0 chemistry, this truncated mechanism DRM-19 is able to save computational costs but has also been proved to provide accurate modelling of ignition delay and heat release [13] and therefore is considered to be applicable for closely reproducing the main physical features of transient flames. The evaluation of thermodynamic (specific heat, enthalpy and entropy) and transport (viscosity and thermal conductivity) properties for the component species used curve fits collated by McBride and Gordon [14] for their CEA2 program. The state for the gas mixture was then calculated based on a mass fraction weighted sum of individual species for thermodynamic properties and using Wilke's mixing rule [15] for transport properties. Unity Lewis number assumption [16] was used to evaluate the species mass diffusion for premixed methane/air combustion in present study. A more detailed diffusion model using Fick's law with the mixture-averaged diffusion coefficients will be implemented in future studies.

A uniform mesh consisting of 390×46 cells with the cell size of 12.8 $\mu$m was employed to keep an equal spatial accuracy over the whole domain for the transient micro-flame problem. A grid refinement study was performed by comparing the temperature and species concentration profiles along the channel centreline for several mesh levels (not shown here). The grid resolution used here was found to be adequate for spatial accuracy as the simulation results were not significantly affected when finer resolution was adopted.

The simulations were performed in parallel using MPI with each simulation using 64 cores on the Australian national computing cluster Raijin [17]. The computational time depended on the flame dynamics mode: it ranged from ∼90 hours of wall clock time for an asymmetric stable flame with the simulation time up to 3 ms, to more than 500 hours for the dynamics of FREI with the simulation time above 20 ms.

## 3 Results and Discussion

In order to quantitatively characterise the process of the flame ignition and propagation, methyl radicals ($CH_3$) which represent the flame front are chosen to monitor the flame temporal variations. Moreover, the total heat release rate (THRR) [7] over the whole computational domain is calculated according to the definition:

$$THRR = \int_V \sum_{species} \dot{\omega}_s h_s \, dV \qquad (1)$$

where $\dot{\omega}_s$ is the summation of production/loss rates of species $s$ over all reactions and $h_s$ is the standard enthalpy of formation of species $s$.

An ignition strategy of "Ignition-zone" to trigger the combustion is adopted: an artificial rate-controlling temperature (set at 2000 K) is used within a small zone (located between $0.75L$-$0.8L$) to inflate the Arrhenius chemical reaction rate but the thermodynamic temperature remains unaffected. This zone is in effect for the first 1 ms of the simulation time to establish the flame and then "switched-off" subsequently. This paper mainly focuses on the dynamic behaviours of the flame after it is established. The artificial ignition process is not discussed in detail here. A range of inflow velocities $U_{in}$ of 15, 30, 45, 60 and 65 cm/s were investigated. The results for these cases are as follows.

### 3.1 Flames with repetitive extinction and ignition ($U_{in}$ = 15 cm/s)

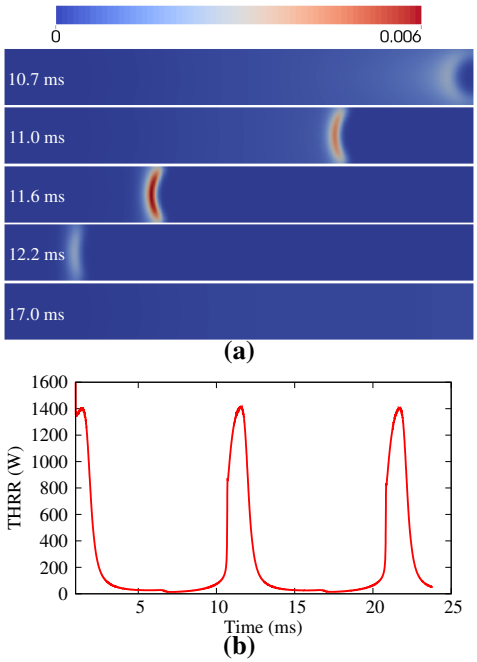


Figure 2: (a) Temporal evolution of $CH_3$ mole fractions and (b) Total heat release rate versus the simulation time for FREI mode at $U_{in}$ = 15 cm/s.

For $U_{in}$ at a relatively low value of 15 cm/s, the flame mode of FREI is observed. One cycle of this mode is shown in Figure 2 (a), where the flame reignites near the exit of the channel at t = 10.7 ms due to the preheating by the "hot" walls, after the extinction from the previous cycle. After that, the flame travels upstream at a quite high propagation speed (up to several metres per second), consuming the fuel rapidly. As the flame reaches the cold inflow at t = ∼12.2 ms, it gets weakened significantly. Eventually the flame cannot be sustained and is considered to be extinguished (t = ∼17.0 ms). Then the tiny amount of remaining $CH_3$ radicals are pushed away far downstream by the fresh incoming mixture, which marks the prelude to the next cycle. The temporal evolution of THRR (Figure 2 (b)) successfully captures this interesting flame behaviour and the period of this mode is determined to be ∼10 ms.

### 3.2 Chaotic oscillation ($U_{in}$ = 30 cm/s)

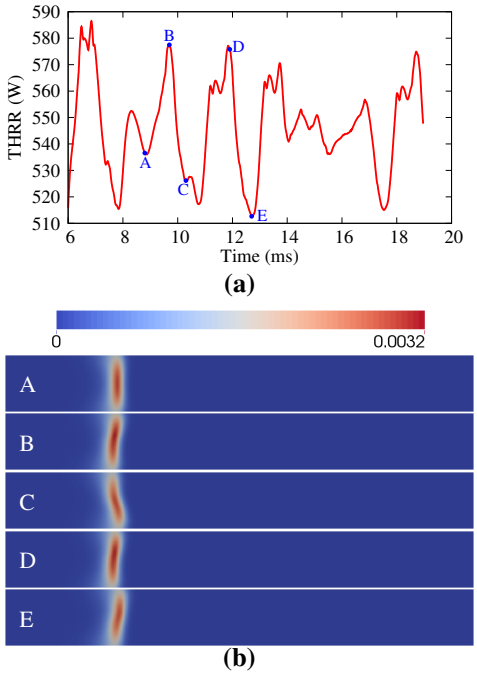


Figure 3: (a) Temporal variation of total heat release rate for chaotically oscillating flames at $U_{in}$ = 30 cm/s. (b) Distribution of $CH_3$ mole fractions at five time instants A to E marked.

When $U_{in}$ increases from 15 to 30 cm/s, as more input energy is supplied, the flame can be sustained within the channel without extinction rather than undergoing FREI. However, this new flame mode is still unsteady and even chaotic. This is captured in Figure 3 (a), where the THRR fluctuates non-periodically while the amplitude of the THRR for this mode is much smaller compared to that for FREI. Behaviours of the flame front at the five time instants marked on the THRR curve are shown in Figure 3 (b). The flame exhibits a variety of temporal behaviours ranging from symmetric to asymmetric shapes (with either an obtuse or an acute angle with respect to the streamwise direction) at various time instants. However, the flame shows only a small spatial variaton in the flame position. This chaotic oscillation mode has also been observed for premixed hydrogen/air combustion in a mesoscale channel [7].

### 3.3 Symmetric stable flames ($U_{in}$ = 45 cm/s)

When $U_{in}$ is increased to 45 cm/s, the flame becomes quite stable, showing a symmetric shape with respect to the channel midplane (Figure 4 (a)). The mole fraction profiles of combustion reactants/products and radicals/intermediates along the channel centreline for the stable flame are plotted in Figure 4 (b). The ratio between carbon monoxide (CO) and carbon dioxide ($CO_2$) mole fractions at the channel exit plane is only 0.04, which represents a relatively high degree of combustion completeness.

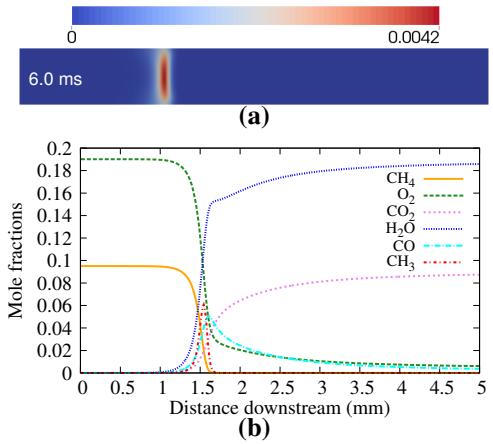


Figure 4: (a) 2-D distribution of $CH_3$ mole fractions and (b) Species mole fraction profiles ($X_{CH_4}$, $X_{O_2}$, $X_{CO_2}$, $X_{H_2O}$, $X_{CO}$ and $15\times X_{CH_3}$) along the channel centreline for the symmetric stable flame at $U_{in}$ = 45 cm/s and t = 6.0 ms.

### 3.4 Slightly and periodically wobbling flames ($U_{in}$ = 60 cm/s)

When $U_{in}$ is further increased to 60 cm/s, the symmetric stable flame mode loses stability and exhibits another type of instability: the flame starts to wobble, with a slight and periodic change between a symmetric and an asymmetric shape. The THRR in this mode (shown in Figure 5 (a)) varies between 1012 and 1021 W with a period of ∼0.47 ms. Figure 5 (b) shows the distributions of $CH_3$ mole fractions with isolines at two time instants on the THRR curve near the peak and the crest. The flame front is found to be quite symmetric at the THRR crest (t = $t_1$) while it exhibits a slightly asymmetric shape near the THRR peak (t = $t_2$). The change from a symmetric to an asymmetric shape results in a slightly more pronounced flame curvature near the channel lower wall, and then leading to a small increase in the THRR owing to the minor increase in the surface area of the flame front. This unsteady flame behaviour is considered as a transition from a symmetric stable flame to an asymmetric stable flame which is discussed in the next section.

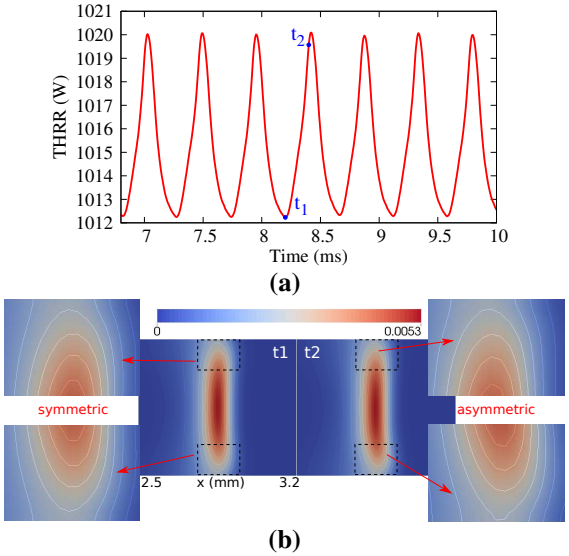


Figure 5: (a) Total heat release rate versus the simulation time for slightly and periodically wobbling flames at $U_{in}$ = 60 cm/s. (b) Distribution of $CH_3$ mole fractions with isolines represented at two time instants $t_1$ and $t_2$ marked.

### 3.5 Asymmetric stable flames ($U_{in}$ = 65 cm/s)

Finally, as $U_{in}$ is increased to 65 cm/s, the flame ceases wobbling and becomes steady again, with an asymmetric shape (Figure 6 (a)). Pizza et al. [6] explained this steady asymmetric solution as a result of a symmetry-breaking pitchfork bifurcation from the dynamical system point of view. The species mole fractions along the channel centreline for this flame mode are shown in Figure 6 (b). The ratio between CO and $CO_2$ mole fractions at the channel exit plane increases to 0.26. This can be attributed to the further downstream location of flame stabilisation at higher $U_{in}$, which results in a lower degree of combustion completeness. Further increase of $U_{in}$ to the value above 75 cm/s will lead to the flame being blown out of the channel.

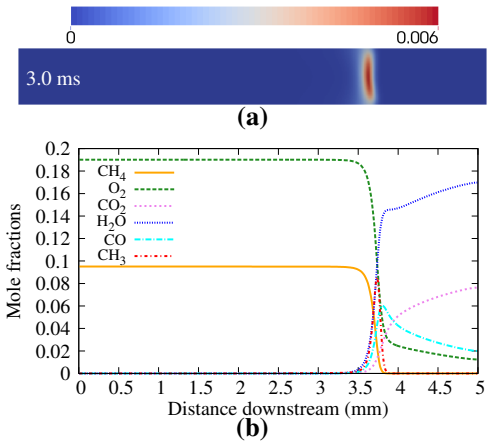


Figure 6: (a) 2-D distribution of $CH_3$ mole fractions and (b) Species mole fraction profiles ($X_{CH_4}$, $X_{O_2}$, $X_{CO_2}$, $X_{H_2O}$, $X_{CO}$ and $15\times X_{CH_3}$) along the channel centreline for the asymmetric stable flame at $U_{in}$ = 65 cm/s and t = 3.0 ms.

## 4 Conclusion

Simulations of premixed methane/air combustion in a narrow, heated channel were performed with detailed chemistry DRM-19. The effects of the inflow velocity on the flame behaviour were investigated. For a range of inflow velocities from 15 to 65 cm/s, various flame dynamics such as flames with repetitive extinction and ignition (FREI), chaotically oscillating flames, symmetric stable flames, slightly and periodically wobbling flames, and asymmetric stable flames were observed. The effects of other parameters such as mixture equivalence ratio, channel dimensions on the flame propagation will be examined in future works.

## 5 Acknowledgements

This research was undertaken with the assistance of resources from the National Computational Infrastructure (NCI) which is supported by the Australian Government and was supported under Australian Research Council's LIEF funding scheme (project number LE120100181).

## References

[1] N. S. Kaisare, D. G. Vlachos, Prog. Energy Combust. Sci. 38 (3) (2012) 321 – 359.

[2] C. J. Evans, D. C. Kyritsis, Proceedings of the Combustion Institute 32 (2) (2009) 3107 – 3114.

[3] S. Heatwole, A. Veeraragavan, C. Cadou, S. Buckley, Nanosc. Microsc. Therm. 13 (1) (2009) 54–76.

[4] K. Maruta, T. Kataoka, N. I. Kim, S. Minaev, R. Fursenko, Proc. Combust. Inst. 30 (2) (2005) 2429 – 2436.

[5] A. Fan, S. Minaev, S. Kumar, W. Liu, K. Maruta, J. Micromech. Microeng. 17 (12) (2007) 2398.

[6] G. Pizza, C. E. Frouzakis, J. Mantzaras, A. G. Tomboulides, K. Boulouchos, Combust. Flame 152 (3) (2008) 433 – 450.

[7] G. Pizza, C. E. Frouzakis, J. Mantzaras, A. G. Tomboulides, K. Boulouchos, Combust. Flame 155 (12) (2008) 2 – 20.

[8] A. Alipoor, K. Mazaheri, Energy 73 (2014) 367–379.

[9] E. Miyata, N. Fukushima, Y. Naka, M. Shimura, M. Tanahashi, T. Miyauchi, Proc. Combust. Inst. 35 (3) (2015) 3421 – 3427.

[10] X. Kang, R. Gollan, P. Jacobs, A. Veeraragavan, Numerical simulations of premixed combustion in narrow channels, in: 19th Australasian Fluid Mechanics Conference, Melbourne, Australia, 2014.

[11] R. Gollan, P. Jacobs, Int. J. Numer. Meth. Fl. 73 (1) (2013) 19–57.

[12] A. Kazakov, M. Frenklach, Reaction Set DRM19. URL `http://www.me.berkeley.edu/drm/`

[13] B. O'Flaherty, Reducing the global warming potential of coal mine ventilation air by combustion in a free-piston engine, Ph.D. thesis, The University of Queensland (2012).

[14] B. J. McBride, S. Gordon, Computer program for calculation of complex chemical equilibrium compositions and applications. part 2: Users manual and program description, Reference Publication 1311, NASA (1996).

[15] C. R. Wilke, J. Chem. Phys. 18 (1950) 517–519.

[16] R. B. Pember, L. H. Howell, J. B. Bell, P. Colella, W. Y. Crutchfield, W. A. Fiveland, J. P. Jessee, Combust. Sci. Technol. 140 (1-6) (1998) 123–168.

[17] National computing cluster raijin. URL `http://nci.org.au/nci-systems/`

**Proceedings of the Australian Combustion Symposium**
**December 7-9, 2015, The University of Melbourne**

# Surface Temperature Distribution along the Brick-Clay or Porcelain Tube Due to the Flame Spreading

C Luo, J. Zanganeh, E. Doroodchi and B. Moghtaderi*
Centre for Frontier Energy Technologies
The University of Newcastle, Australia, NSW 2308
Australia

## Abstract

The heat loss of the $CH_4$-air flame in a closed tube due to the convective heat transfer which is needed for predicting the flame speed is proportional to the difference between the inner surface temperature of the tube and the gas mixture temperature. For the tube wall, the solid thermal conduction equation is discretised using the finite volume method and the relationship between the surface temperature and the gas mixture temperature is derived. Two non-dimensional parameters are identified as the key to control the surface temperature distribution and the heat loss. Finally the flame heat loss due to convective heat transfer is analysed for varying thermal properties and tube sizes.

*Keywords: convective heat transfer, finite volume method, flame speed.*

## 1. Introduction

Ventilation Air Methane (VAM) from underground coal mines is comprised of 0.1-1.2% methane ($CH_4$), and 98.8-99.9% air. The VAM RAB is analogous to an oven operating at around 800 °C to 1,100 °C converting the $CH_4$ into carbon dioxide ($CO_2$) and water vapour with the $CO_2$ either released to atmosphere or using Carbon Capture and Storage (CCS) technology to treat the product $CO_2$.

The gas flow path of Corky's VAM-RAB is illustrated in Figure 1. In the Corky's VAM-RAB design, Honeycomb brick or Clay-brick, with their sizes summarized at Table 1, would be used for storing the heat to minimize the temperature fluctuation due to unstable $CH_4$ concentration from the VAM.

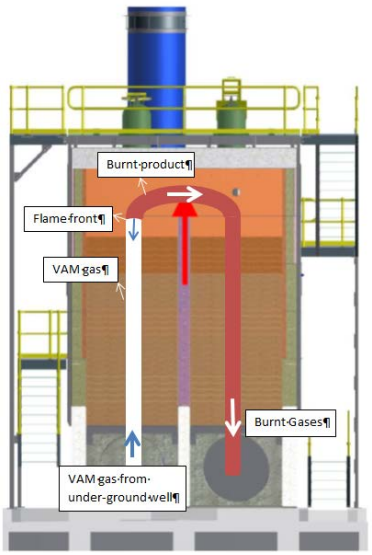


**Figure 1 Gas flow pathway in the Corky's VAM-RAB demonstration plant.**

One of the concerns for safe operation of the VAM-RAB is to understand whether or not the flame in the VAM-RAB would propagate back to the underground mine well. To address this safety problem, flame speeds of the VAM in the tube along the holes of the Honeycomb brick, as shown in Fig. 2, or the slits of the Clay-bricks, as shown in Fig. 3, will be calculated by considering the heat loss due to the convective heat transfer between the tube wall and the flame.

The surface temperature of the tube and heat transfer can be obtained by solving the Fourier thermal diffusion equation. Luo et al. [1] derived two equations relating the surface temperatures and surface heat fluxes at both inner and outer surfaces of a solid wall using finite volume method, without involving inner nodes of the solid wall. Given two boundary conditions at both inner and outer surfaces of the solid wall, surface temperatures and surface heat fluxes will be calculated using the discretized finite volume equations derived from the solid thermal conduct equations of the tube wall. And the heat loss, due to the convective heat transfer, will be analyzed in terms of two non-dimensional parameters.

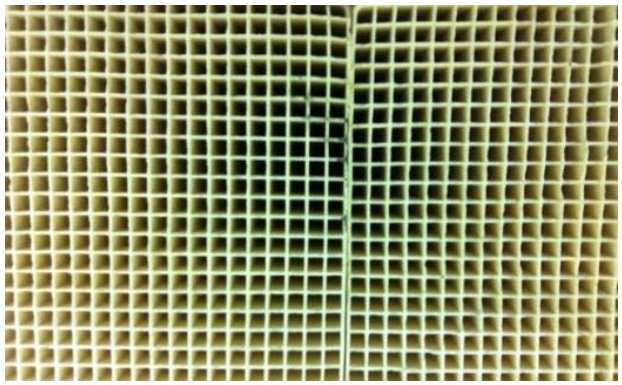

**Figure 2 Honeycomb brick (porcelain) used in the VAM-RAB**

Corresponding author: B Moghtaderi
Phone: (+61) 2 40339062
Email: Behdad.Moghtaderi@newcastle.edu.au

**Figure 3 Clay-brick used in the VAM-RAB**

## 2. Mathematics Description

To model the gas flow pathway as shown in Fig. 1, a simplified 1D model is presented in Fig. 4.

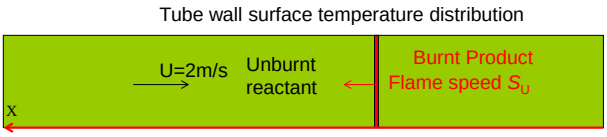


**Figure 4 Coordinate system for calculating the tube surface temperature distribution due to the flame spreading.**

The velocity of unburnt reactant could be any value and is used to assess whether or not the flame front could propagate back to the under-mining wells. The surface temperature distribution of the tube is heated by the burnt product and is calculated by solving the solid thermal conducting equation.

According to [1-4], the surface temperature at the time instant $t^n$ can be calculated by the following formula (for details, refer to the Appendix A),

$$T_{s0}^{\ n} = \frac{N_t T_{s0}^{\ n-1} + \frac{5L_t}{27k} N_t h T_{air}^{\ n} + \frac{L_t}{k} h T_{air}^{\ n} + \frac{5L_t}{27k} N_t h (T_{s0} - T_{air})^{n-1} - \frac{L_t}{k} h (T_{s0} - T_{air})^{n-1}}{\left( N_t + \frac{5L_t}{27k} N_t h + \frac{L_t}{k} h \right)} \quad (1)$$

in which $\frac{L_t^{\ 2}}{\alpha \Delta t} = N_t$, $L_t$ is the thickness of the tube wall, $k$ is the thermal conductivity of the tube wall, $h$ is the Convective Heat Transfer Coefficient (CHTC) between the wall surface and gas mixture (fuel + oxidant), $T_{air}$ is the mixture temperature, $T_{s0}$ is the surface temperature, $n$ and $n$-1 are the time instants $t_n$ and $t_{n-1}$, $\Delta t$ is the time step, $\alpha$ is the thermal diffusivity defined as $k/\rho C_p$. The gas mixture temperature is defined as:

$$\begin{aligned} T_{air} &= T_{flame} \qquad x \le x_{flame} \\ T_{air} &= 298.15\ \text{K} \qquad x > x_{flame} \end{aligned} \quad (2)$$

$$x_{flame} = u_{flame} \times t \quad (3)$$

$$k = 1.5207 \times 10^{-11} \times T^3 - 4.8574 \times 10^{-8} \times T^2 + 1.0184 \times 10^{-4} \times T - 0.00039333 \quad (4)$$

$$\mu = 1.827 \times 10^{-5} \times (0.555 \times 291.15 + 120) / (0.555 \times T + 120) \times (T/291.15)^{3/2} \quad (5)$$

## 3. Results and Discussions

Four calculation cases are studied with details of thermal properties summarized in Table 1. Please note that the CHTC $h$ is dependent on the flow speed and whether the flow is laminar or turbulent flow. In the present trial calculation, as shown in Fig 5, $T_{flame}$ = 1800 K, $u_{flame}$ = 0.41 m/s, $\Delta t$ = 0.001 s; At the instant of 10 s the flame front will move 4.1 m from the inlet and the total length of the tube is 5 m. As shown in Fig 5, the surface temperature at the left inlet increases with the time. And the temperature distribution along the distance is linear or nonlinear depending on the thermal properties of the wall material. It can be expected that the surface temperature of the tube will be heated to the flame temperature with enough time. However, for lower $\rho C_p$ a longer time is needed to heat the surface to the flame temperature, as shown in Fig 5.

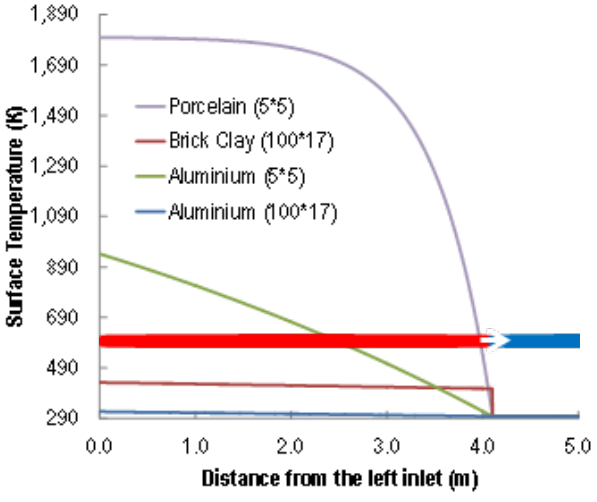


**Figure 5 Surface temperature distributions along the tube for porcelain, clay-brick and aluminium honeycomb with 1 and 14 mm in thickness at the instant of 10 s.**

From Equation 1, calculating the VAM tube surface temperature depends on the following two non-dimensional parameters: $\frac{L_t^{\ 2}}{\alpha \Delta t} = N_t$ and $\frac{h}{k} L_t$. Table 1

summarizes the total heat loss due to convective heat transfer between the VAM inner surface and the flame. The size column in Table 1 represents the hole size, and the thickness stands for the wall surface thickness (or $L_t$ in Equation 1). The heat loss is calculated by Equation (6) as following:

$$Q_{loss} = P_{eri} h_{conv} (T - T_{surf}) \qquad (6)$$

In which $h_{conv}$ the convective heat transfer coefficient, $P_{eri}$ the perimeter of the tube cross section, $T_{surf}$ the tube surface temperature

**Table 1 Total heat loss due to convective heat transfer between the VAM tube and the flame.**

| Material | Size (mm) | Thickness (mm) | $\rho C_p$ (J/m$^3$K) | $K$ (W/mK) | $h$ (W/m$^2$K) | Total heat loss (W/m$^2$)* |
|---|---|---|---|---|---|---|
| Brick clay | 100 × 17 | 14 | $1.58 \times 10^6$ | 0.7 | 21.3 | 120485.0 |
| Porcelain | 5 × 5 | 1 | $1.95 \times 10^5$ | 2.2 | 68.7 | 59980.0 |
| Aluminium alloy | 100 × 17 | 14 | $2.46 \times 10^6$ | 221 | 21.3 | 130282.9 |
| Aluminium alloy | 5 × 5 | 1 | $2.46 \times 10^6$ | 221 | 68.7 | 323945.0 |

Note: * Calculation for 1 metre unit length

It can be observed from Table 1 that total heat loss of the clay-brick is higher than that of the porcelain even though Convective Heat Transfer Coefficient (CHTC) of the clay-brick is three times less than that of porcelain honeycomb. This can be explained by Figs 7 and 8 which show the tube surface temperature distribution at instants ranging from 1 s to 10 s for clay-brick and aluminum alloy honeycomb respectively. The surface temperature for clay-brick is as low as 400 K, due to its 14 mm thickness, while the surface temperature for the porcelain honeycomb is as high as 1700 K as shown in Fig. 6, due to 1 mm thickness. The total heat loss due to convective heat transfer as calculated by Equation (6) depends both on CHTC and the temperature difference $T_{flame}$ - $T_{s0}$, hinting that the temperature difference for porcelain honeycomb is high enough to overcome the relatively low value of its CHTC. However, the difference in Figs 6 and 7 could be caused by the different material. To overcome the difference caused by the different tube wall materials, the same aluminum alloy tube wall being used as shown in Figs 8 and 9, higher heat loss is obtained for smaller hole geometry 5 mm × 5 mm than the bigger hole geometry 100 mm × 17 mm as illustrated in Table 1.

In conclusion, high thermal mass (thick tube wall, and high $\rho C_p$) will incur lower surface temperature, and smaller hole geometry will result in higher flow velocity and higher CHTC accordingly. Clay-brick presents more heat loss than the porcelain honeycomb due to its huge thermal mass effect.

## 4. Conclusions

The solid thermal conduction equation was discretised using the finite volume method and the relationship between the surface temperature and the gas mixture temperature was derived. Two non-dimensional parameters were identified as the key to control the surface temperature distribution and heat loss. Conclusions are summarized as followings:

- A higher thermal mass ($\rho C_p$), for the same CHTC, has lower surface temperature after the flame passing and a longer time is needed to heat the surface to the flame temperature;
- For the same temperature of the unburnt reactant, porcelain honeycomb has lower flame speed than the clay-brick;
- Accordingly, porcelain honeycomb is safer to prevent the flame front propagating back to the underground mines;
- At higher flow speeds and higher convective heat transfer coefficients, more combustion energy is transmitted to the tube surface and a lower the flame speed results;
- Accordingly, it is significant to predict the temperature of the "cold" reactant. And the "cold" reactant can be preheated by the channels, showing that the thermal mass of the channels is important for the temperature distribution along the channels;

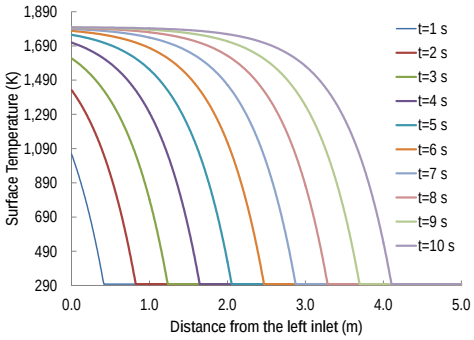


**Figure 6 Surface temperature distribution along the tube for porcelain honeycomb with $\rho$ = 260 kg/m$^3$, $C_p$ = 750 J/kg K, $k$ = 2.2 W/mK, and $h$ = 68.7 W/m$^2$K with 1 mm in thickness.**

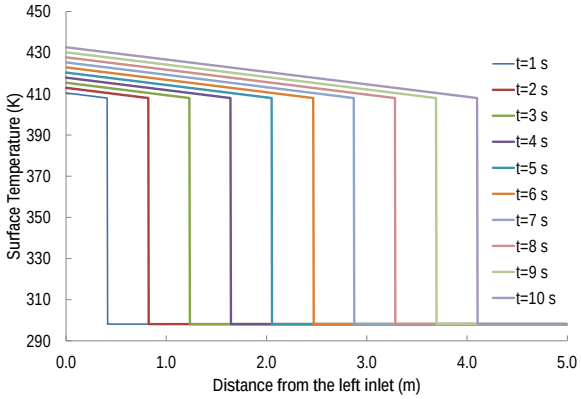


**Figure 7 Surface temperature distribution along the tube for clay-brick with $\rho$ = 800 kg/m$^3$, $C_p$ = 1970 J/kg K, $k$ = 0.7 W/mK, and $h$ = 21.3 W/m$^2$K with 14 mm in thickness.**

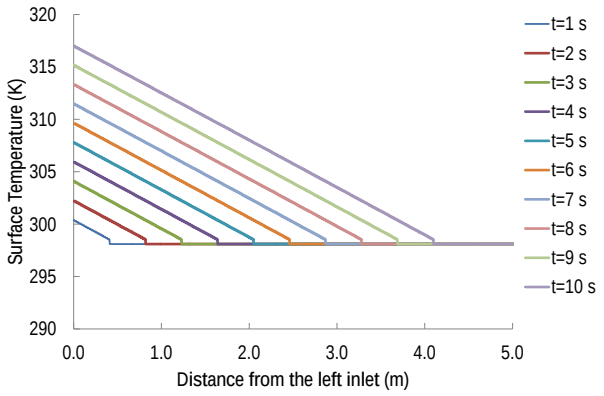


**Figure 8 Surface temperature distribution along the tube for aluminium alloy honeycomb (100mm × 17mm) with $\rho$ = 896 kg/m$^3$, $C_p$ = 2740 J/kg K, $k$ = 221.0 W/mK, and $h$ = 21.3 W/m$^2$K with 14 mm in thickness.**

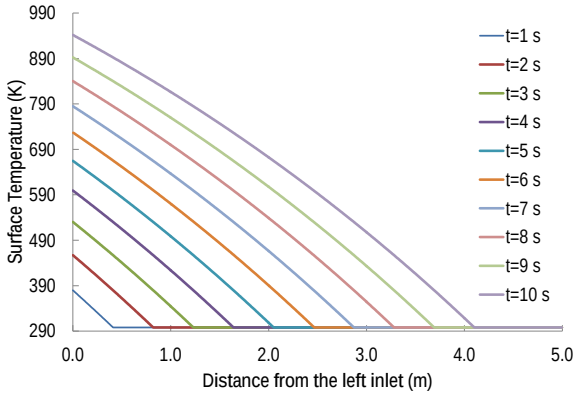


**Figure 9 Surface temperature distribution along the tube for aluminium alloy honeycomb (5mm × 5mm) with $\rho$ = 896 kg/m$^3$, $C_p$ = 2740 J/kg K, $k$ = 221.0 W/mK, and $h$ = 68.7 W/m$^2$K with 1 mm in thickness.**

## 5. References


[1] C. Luo, B. Moghtaderi, H. Sugo and A. Page, "A new stable finite volume method for predicting thermal performance of a whole building", *Building and Environment* 2008, 43, 37-43..

[2] C. Luo, B. Moghtaderi, A. Page (2010), "Modelling of wall heat transfer using modified conduction transfer function, finite volume and complex Fourier analysis methods", *Energy and Buildings*, Vol.42, Issue 5, 605-617.

[3] C. Luo, B. Moghtaderi, A. Page (2010), "The implication of ground model and initial conditions for zone models", *Applied Thermal Engineering*, Vol.30, issue 16, 2602-2609.

[4] C. Luo, B. Moghtaderi, A. Page (2011), "Determining the thermal capacitance, conductivity and the convective heat transfer coefficient of a brick wall by annually monitored temperatures and total heat fluxes", *Energy and Buildings*, Vol.43, 379-385.


## Appendix A: Derivation for the un-steady tube surface temperature based on the air temperature

The Fourier thermal diffusion equation for a solid wall is

$$\rho C_p \frac{\partial T}{\partial t} = k \frac{\partial^2 T}{\partial x^2} \tag{A1}$$

in which $\rho$ denotes density, $C_p$ is the specific capacity, $k$ is the thermal conductivity of the layer, $T$ is the temperature across the layer, $t$ is the time and $x$ is the distance across the layer. A new finite volume scheme and a hybrid finite volume- finite difference are introduced below for discretizing the partial differential equation (A1). Without considering the thermal conduction along the tube, the governing equation for the surface temperature and surface heat flux can be derived from [1],

$$\frac{1}{162k} L^2{}_t \rho_b Cp_b \left[ \left( 81T_{s0} - \frac{15L_t}{k} q''_{s0} \right)^n - \left( 81T_{s0} - \frac{15L_t}{k} q''_{s0} \right)^{n-1} \right] = \frac{\Delta t}{2} \left[ \left( \frac{L_t}{k} q''_{s0} \right)^n + \left( \frac{L_t}{k} q''_{s0} \right)^{n-1} \right] \tag{A2}$$

$$\frac{1}{81k\Delta t} L^2{}_t \rho_b Cp_b \left[ \left( 81T_{s0} - \frac{15L_t}{k} q''_{s0} \right)^n - \left( 81T_{s0} - \frac{15L_t}{k} q''_{s0} \right)^{n-1} \right] = \left[ \left( \frac{L_t}{k} q''_{s0} \right)^n + \left( \frac{L_t}{k} q''_{s0} \right)^{n-1} \right] \tag{A3}$$

$$\frac{L^2 t}{\alpha \Delta t} = N_t \tag{A4}$$

$$N_t \left( {T_{s0}}^n - {T_{s0}}^{n-1} \right) = \frac{5L_t}{27k} N_t \left( {q''_{s0}}^n - {q''_{s0}}^{n-1} \right) + \frac{L_t}{k} \left( {q''_{s0}}^n + {q''_{s0}}^{n-1} \right) \tag{A5}$$

$$q''_{s0} = -h(T_{s0} - T_{air}) \text{ and assuming } h \text{ is constant} \tag{A6}$$

$${T_{s0}}^n = \frac{N_t {T_{s0}}^{n-1} + \frac{5L_t}{27k} N_t h {T_{air}}^n + \frac{L_t}{k} h {T_{air}}^n + \frac{5L_t}{27k} N_t h (T_{s0} - T_{air})^{n-1} - \frac{L_t}{k} h (T_{s0} - T_{air})^{n-1}}{\left( N_t + \frac{5L_t}{27k} N_t h + \frac{L_t}{k} h \right)} \tag{A7}$$

**Proceedings of the Australian Combustion Symposium**
**December 7-9, 2015, The University of Melbourne**

# Turbojet Exhaust Plume Heat Transfer

Y.D. Kuo[1,*], N.S.A. Smith[2], D.R. Honnery[1]
[1]Department of Mechanical and Aerospace Engineering Monash University VIC 3800 Australia
[2]Defence Science & Technology Group (DST Group) Department of Defence VIC 3207 Australia

## Abstract

Exhaust jet plume heats up airframe surfaces during operations which may cause structural integrity and survivability issues. This paper presents the predictions of a real exhaust jet plume and its heat transfer onto the surface of a flat plate simulated by Computational Fluid Dynamics (CFD) using Reynolds-averaged Navier Stokes (RANS) equations in SST k-omega turbulence model. By using the exit conditions of a jet engine throttle setting (maximum velocity magnitude 155 m/s and maximum temperature 672 ºC), the expansion of the exhaust plume downstream from the nozzle exit was simulated in the CFD model. Velocity and temperature line profiles of the modelled exhaust plume were then compared to that of the experimental plume characterisation data to justify the plume prediction. The top surface temperature distribution of the CFD simulated flat plate was examined and was found to exhibit similar features to the flat plate in experiment. The CFD results were found to be able to predict the overall heat transfer coefficient of the convection of the exhaust plume onto a flat plate to within 7% error.

*Keywords: exhaust plume, CFD modelling, surface heat transfer*

## 1. Introduction

In most aerospace application cases, the exhaust plume from gas turbine engines impinges parallel to the airframe surfaces. The heating of aircraft surfaces may cause structural integrity problems and also vulnerability to threats. To increase the survivability of aircraft, it is crucial to understand and predict the convective heat transfer phenomenon that occurs in between the exhaust plume and aircraft surfaces.

Examining the heat interaction between real jet exhaust plume and aircraft surfaces has had the problem of there being a limited range of easily adaptable, realistic laboratory scale systems that enable investigation of a large parameter space at low cost. The development of the micro gas turbine for model aircraft and the advance of Computational Fluid Dynamics (CFD) have made this possible.

This paper presents the CFD predictions of a micro jet gas turbine exhaust plume and its heat transfer onto a sample plate. To test the capability of the CFD model, three parameters are investigated: (a) exhaust plume expansion, (b) sample plate surface temperature distribution, and (c) overall heat transfer coefficient of convection by the plume. The prediction results are then compared with the experimental results, followed by some discussions.

## 2. Methods

### 2.1 Experimental Setup

For the experiment, a thin 7075-T6 aluminium alloy at plate with the dimension 8D (360mm) x 2D (90mm) x 0.03D (1.27mm) was chosen to be placed in a developed plume region downstream of the 45mm diameter (D) nozzle of a micro jet engine which was set to a particular throttle setting. The plate was placed at X = 7D and Z = -1D, referenced to the leading edge of the plate as shown in Figure 1.

The plate was painted with a black paint with a measured average emissivity of 0.94. A 384 x 288 pixel thermal imaging camera with spectral range 7.5µm to 14µm and temperature measurement range -40ºC to 1200ºC, mounted on a rail over the top of the engine, was used to capture the thermal images of the top surface of the sample plate during surface heating experiments.

In order to characterise the flow, a few measurement approaches were taken place. Velocity and temperature were measured at the exit of the nozzle by using a 1.2mm stagnation hole pitot static tube and a bare wire type-K thermocouple sheathed in a ceramic tube [6].

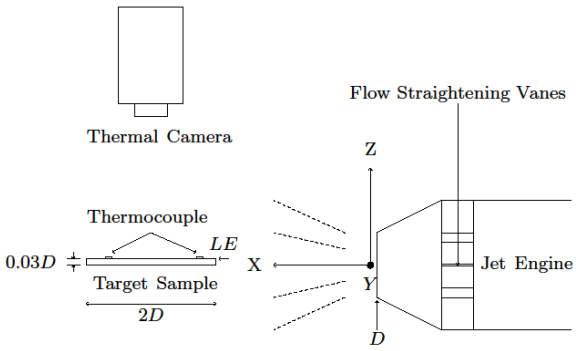


Figure 1: Experiment layout.

* Corresponding author:
Phone: (+61) 3 9905 1008
Email: yee.dah.kuo@monash.edu

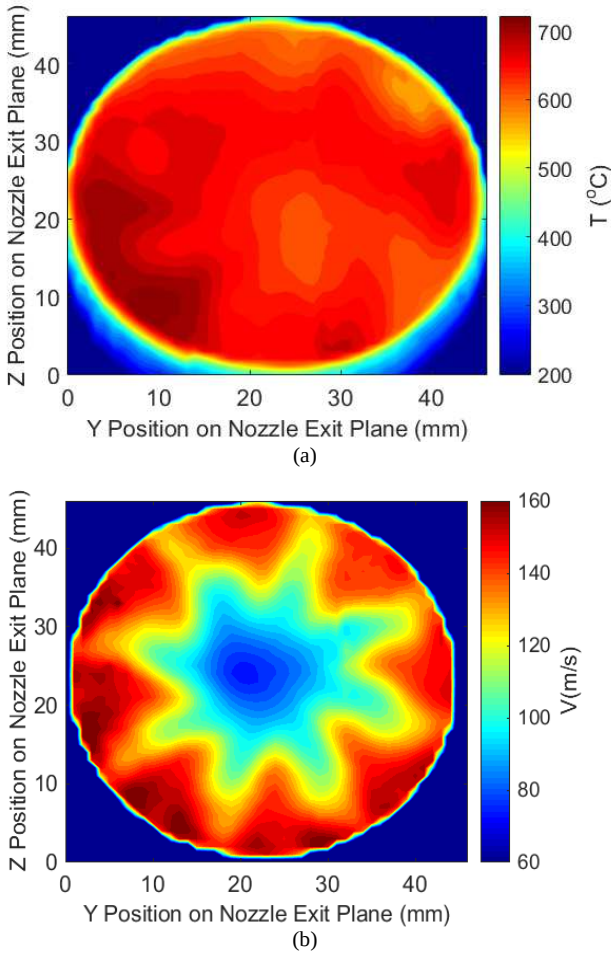


Figure 2: (a) Temperature and (b) velocity contours of the nozzle exit measured experimentally at the designated throttle setting.

The velocity components of the flow were measured by a five-hole conventional probe at different locations downstream of the nozzle exit. The degree of swirl is represented by swirl number, *S* which is calculated based on the equation by Chigier and Chervinsky (1967) [2]. It is defined as the ratio of axial flux of azimuthal momentum to axial momentum multiplied by an equivalent nozzle radius. The gas composition of the exhaust plume were measured and averaged at the nozzle exit using a gas analyser. While the nozzle exit temperature is generally uniform, it has some degree of asymmetry as shown in Figure 2(a). The exhaust plume at the nozzle exit exhibits a velocity profile of an annular jet as shown in Figure 2(b).

It was believed that there is considerable amount of swirl at the nozzle exit. Due to the five-hole probe material's limitation, the swirl component of the flow at the nozzle exit could not be measured. The swirl number at X = 7D is 0.07 which is considered low as discussed in Toh et al. (2010) [4]. The exhaust gas composition, with an average molecular weight of 28.7 kg/mol, consists of approximately 75% $N_2$, 16% $O_2$, 3% $CO_2$ and 3% $H_2O$. Detailed description of the conditions and parameters used in CFD model is discussed in the next section.

## 2.1 Computational Setup

Commercial package, ANSYS FLUENT was utilised as the platform for the exhaust plume surface heating CFD simulation. To model the flow of the plume, the Reynolds-averaged Navier Stokes equations were employed using the SST k-omega turbulence model. An inflow turbulence intensity of 5% and turbulence viscosity ratio of 10 was chosen. A 13D diameter and 10D long half-cylindrical domain was created and meshed with 10 million cut cells assuming the exhaust plume is symmetrical on the other plane.

The nozzle exit was modelled as a velocity inlet of the domain where the surface-averaged inlet temperature and velocity magnitude boundary conditions were taken from the experiment data. The other remaining cylindrical surfaces of the setup domain were set as atmospheric pressure-outlets. The real exhaust jet plume has complicated annular flow structures at the nozzle exit. The velocity components at the nozzle exit were guessed based on the measurements further downstream. The exhaust plume was treated as an incompressible ideal gas and its specific heat and viscosity were modelled by polynomials as functions of temperature.

The infrared radiation from the exhaust gas, computed by using a numerical narrow-band gas infrared radiation model was found insignificant compared to other form of heat transfer mechanisms in the absence of solid particles such as soot [3] [4]. In the CFD simulation, radiation was neglected.

The computational plume prediction results were then compared to the measured data at the location used for the surface heating experiments. An aluminium plate was placed in the CFD model to simulate the surface heating experiments. The prediction results of a steady-state case are shown in the next section.

# 3. Results and Discussions

## 3.1 CFD Plume Prediction

As mentioned in the previous section, the velocity components at the nozzle exit were unknown. Therefore, trial and error approach was attempted. Iterations were performed until the results are comparable to the velocity and temperature measurement at X = 7D downstream of the nozzle exit and the centreline velocity magnitude from X = 0D to X = 7D. The cross-section velocity and temperature contours of the exhaust plume, predicted by the CFD model, are shown in Figure 3.

High radial and tangential velocities, up to 40m/s, were estimated for the flow conditions at the nozzle exit. The plume prediction result suggested that the plume near the nozzle exit has complicated flow structures. The velocity magnitude at the nozzle exit ranges from 80 m/s to 155 m/s while the temperature ranges from 550 $^oC$ to 672 $^oC$.

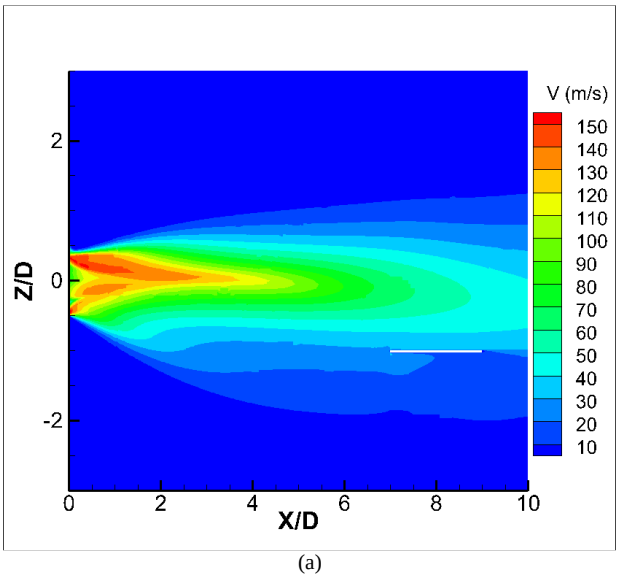


(a)

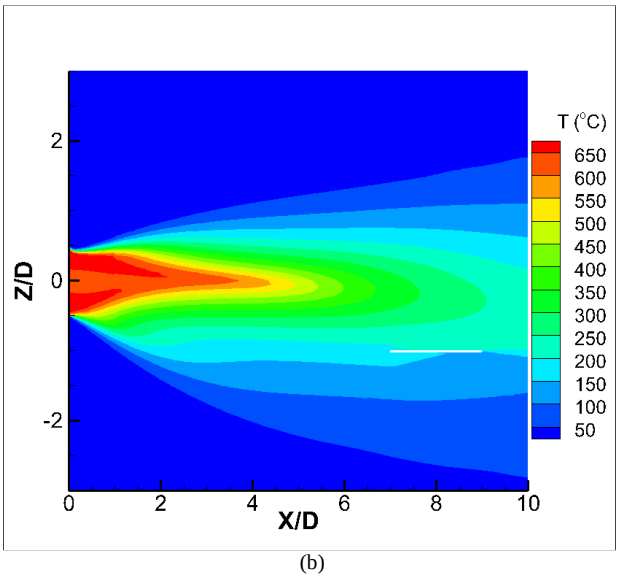


(b)

Figure 3: (a) Velocity and (b) temperature middle cross-sections of the exhaust plume predicted by CFD. The flat plate is represented by a rectangular in the plume.

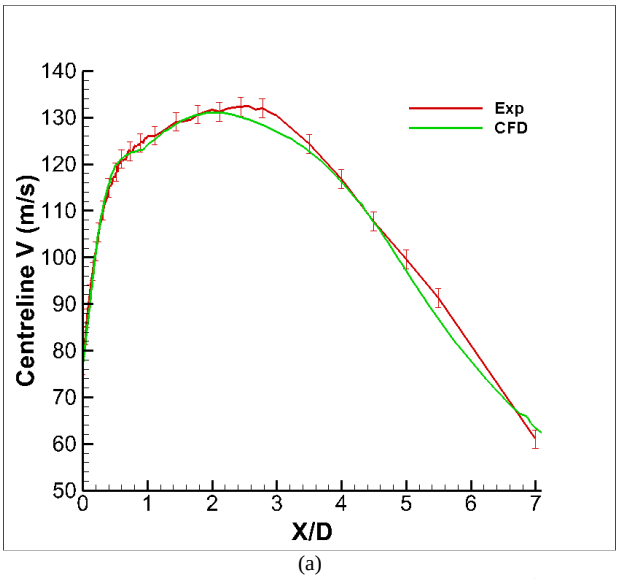


(a)

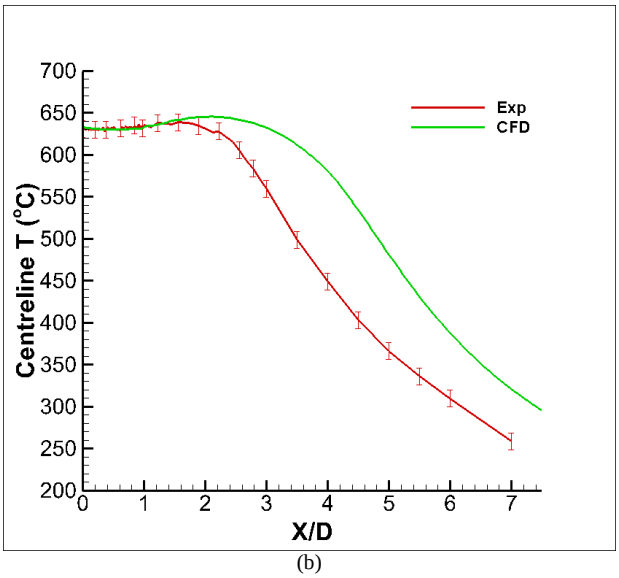


(b)

Figure 4: (a) Velocity magnitude and (b) temperature line profiles along the centreline, downstream of the nozzle exit.

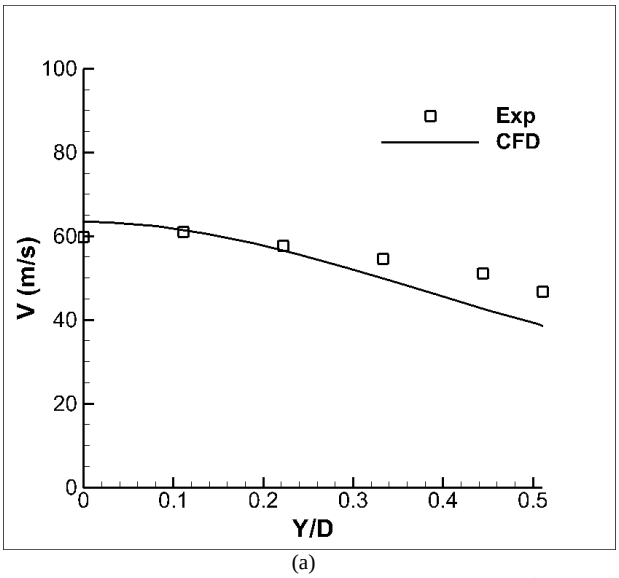


(a)

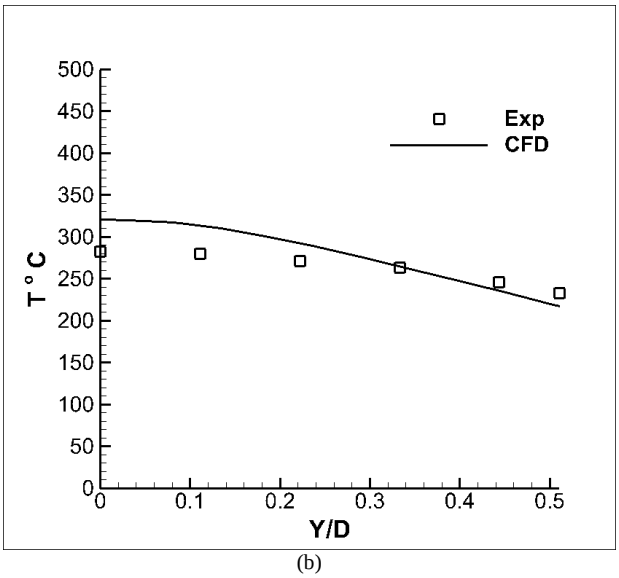


(b)

Figure 5: (a) Velocity magnitude and (b) temperature line profile at X = 7D and Z = 0.

The CFD simulation agreed well with the centreline velocity magnitude measurement. The higher the radial velocity at the nozzle exit, the steeper the slope at the beginning of the curve shown in Figure 4(a). Tangential velocity component behaves so that the plume expands faster and more, hence decreasing the centreline velocity magnitude. The CFD model, however, underestimated the cooling of the plume as shown in Figure 4(b). The decrease in plume temperature after X = 2D is due to free atmospheric expansion and is also caused by the heat transfer between the hot exhaust plume with the surrounding air. It is possible that the actual air entrainment rate was higher than what the CFD model anticipated. Generally, the predicted velocity magnitude of the plume at further downstream from the nozzle exit is found close to the expected results as shown in Figure 5 (a). The predicted temperature at X = 7D and Z = 0 is higher at the centre, Y = 0 but it gradually converges towards the experimental data as it moves away from the core of the plume.

## 3.2 Heat Transfer by the Plume

The exhaust plume heats up the sample plate due to convection and the heat spreads over the plate by conduction. Assuming steady-state case, the local convective heat transfer coefficient, $h_{i,j}$ on the surface of the sample plate in a control volume can be calculated by finite element method as discussed in Kuo et al. (2015) [4] and Bergman et al. [1] such that

$$h_{i,j} = \frac{k_s d[4T_{i,j} - (T_{i-1,j} + T_{i,j+1} + T_{i+1,j} + T_{i,j-1})]}{\Delta x^2 f(T_\infty - T_{i,j})} \quad (1)$$

where $k_s$ is the thermal conductivity of the plate, d is the thickness of the plate, $T_{i,j}$ is the local surface temperature of the node $i,j$, $f$ is a heating factor, $\Delta x$ is the distance between nodes and $T_\infty$ is temperature of the plume at infinity referenced to the averaged nozzle exit temperature.

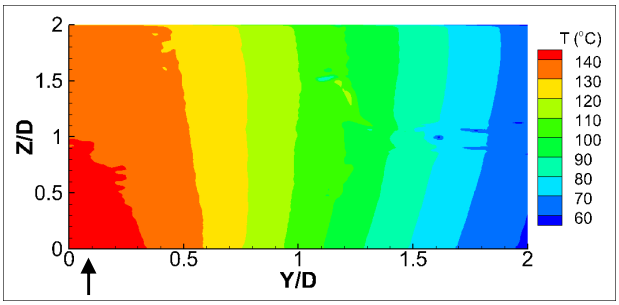

(a)

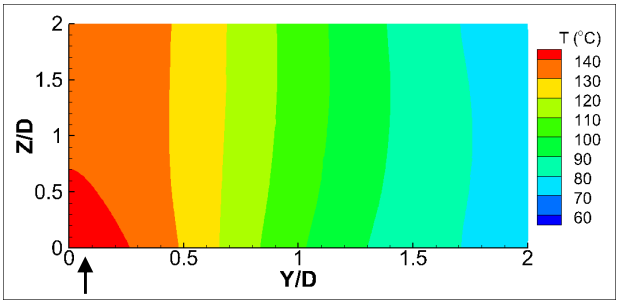

(b)

Figure 6: Surface temperature contours of half flat plate (a) experiment (b) CFD. The arrow shows plume direction.

Figure 6 shows that the CFD surface heating prediction result possessed similar surface temperature distribution and magnitude to the actual experiment result. The overall heat transfer coefficient, $\bar{h}$ of the CFD flat plate was found to be 1.96 W/m$^2$ compared to 1.84 W/m$^2$ calculated from the experimental result.

## 4. Conclusion

In conclusion, the Computational Fluid Dynamics (CFD) model can approximate the expansion of the high speed exhaust plume and its convective heat transfer event onto surfaces. The model was able to predict the overall heat transfer coefficient of the exhaust plume to within 7% error. However, the model could not predict the cooling of the plume at downstream of the nozzle exit. It is suspected that the air entrainment from the surrounding might not be taken account effectively by the model.

## 5. Acknowledgments

The first author acknowledges the financial, facilities and equipment support given by Laboratory for Turbulence Research in Aerospace and Combustion (LTRAC), Faculty of Engineering, Monash University and Defence Science & Technology Group (DST Group), Department of Defence.

## 6. References

[1] Bergman, T. L., Lavine, A. S., Incropera, F. P., and Dewitt, D. P. *Fundamentals of Heat and Mass Transfer*, 7 ed. John Wiley and Sons.

[2] Chigier, N. A., and Chervinsky, A. *Experimental Investigation of Swirling Vortex Motion in Jets.* Journal of Applied Mechanics 34 (1967), 443-451.

[3] Grosshandler, W. L. *RADCAL: A Narrow-Band Model for Radiation Calculations in a Combustion Environment.* techreport 1402, National Institute of Standards and Technology (NIST), 1993.

[4] Kuo, Y. D., Smith, N. S. A., and Honnery, D. R. *Experimental Study of Surface Heating by a High Speed Exhaust Plume*, Experimental Thermal and Fluid Science (Accepted 2015).

[5] Kuo, Y. D., Smith, N. S. A., and Honnery, D. R. *Airframe Surface Heating by a High Speed Micro Gas Turbine Exhaust Plume - Preliminary Results.* In 16th Australian International Aerospace Congress (23-24 February 2015).

[6] Toh, I. K., Honnery, D., and Soria, J. *Axial Plus Tangential Entry Swirling Jet.* Experiments in Fluids 48 (2010), 3.

# AUTHOR INDEX